MASARYK UNIVERSITY

FACULTY OF SCIENCE

DEPARTMENT OF BIOCHEMISTRY

Advanced Immunochemical Biosensors and Assays: From Label-Free to Single-Molecule Detection

Habilitation Thesis

Zdeněk Farka

Brno 2022

Abstract

The ability of rapid detection of low analyte concentrations, in particular of biomarkers, microorganisms and their products, or pharmaceuticals, is of fundamental importance in many fields, including clinical diagnostics, food control, and environmental screening. Immunochemical biosensors and assays combine the excellent selectivity provided by antibodies with highly sensitive detection based on various readout techniques. This habitation thesis presents a commented summary of 22 scientific papers focused on advanced immunoanalytical techniques, to which I have contributed as a corresponding author, first author, or co-author. After introducing the field of immunosensing, the thesis starts with label-free biosensors and continues through catalytic and luminescent labels to the detection by laser-induced breakdown spectroscopy. Numerous assays were developed for a wide range of analytes, starting from small molecules (pharmaceuticals, mycotoxins), through proteins (disease biomarkers), to bacteria (*Salmonella*, honeybee pathogens). The research was focused not only on testing new methodologies but also on the practical applicability of the sensors, as represented by a large focus on the analysis of representative real samples.

Acknowledgments

Table of Contents

1 Commentary to Habilitation Thesis

This habitation thesis presents a commented summary of 22 scientific papers published between 2014 and 2021, to which I have contributed as a corresponding author, first author, or co-author. All these publications are focused on immunochemical biosensors and assays; however, they are based on different sensing schemes and the detection of various analytes. After introducing the field of immunosensing, the thesis starts with label-free biosensors and continues through catalytic and luminescent labels to the detection by laser-induced breakdown spectroscopy. The research was focused not only on testing new methodologies but also on the practical applicability of the sensors, as represented by a large focus on the analysis of representative real samples.

The label-free sensors especially provide rapid and straightforward analysis, making them suitable for in-field detection, especially of larger analytes. The thesis discusses the development and performance of biosensor based on electrochemical impedance spectroscopy for *Salmonella* and quartz crystal microbalance biosensor for aerosolized biological warfare agents. We have also focused on biosensor surface modifications by plasma-polymerized films and their application in surface plasmon resonance biosensing.

The catalytic labels are beneficial due to their ability of signal enhancement. Apart from the conventional use of horseradish peroxidase in a sandwich immunoassay for European foulbrood diagnosis, the thesis demonstrates advanced approaches based on enzymatically-catalyzed precipitation for signal enhancement in surface plasmon resonance and the catalytic Prussian blue nanoparticles as a promising alternative to enzymes.

The luminescence detection was done with photon-upconversion nanoparticles, which overcome the optical background interference by the ability to be excited in the near IR region, followed by the emission in the visible range. The methods of their surface modification and conjugation with biomolecules were thoroughly studied. The conjugates were used for immunochemical detection of a wide range of analytes from small molecules, through proteins, to bacteria, demonstrating even the capabilities of single-molecule detection.

Finally, laser-induced breakdown spectroscopy was introduced as a novel way of signal readout, which is not dependent on the catalytic or luminescent properties of the labels. This approach was used in the microtiter plate-based immunoassay but also as the readout method in immunocytochemical imaging.

Roman numerals will be used to address the individual publications in the following text. Full articles have been reproduced in the appendix with permissions from the respective copyright holders. Asterisk denotes corresponding author.

I. Farka, Z.; Juřík, T.; Kovář, D.; Trnková, L.; Skládal, P., Nanoparticle-Based Immunochemical Biosensors and Assays: Recent Advances and Challenges. *Chem. Rev.* **2017**, *117* (15), 9973–10042.
Contribution: Literature research, manuscript writing
(Supervision 10%, Manuscript 30%, Research direction 30%)

II. <u>Farka, Z.</u>; Mickert, M. J.; Pastucha, M.; Mikušová, Z.; Skládal, P.; Gorris, H. H., Advances in Optical Single-Molecule Detection: En Route to Super-Sensitive Bioaffinity Assays. *Angew. Chem. Int. Ed*. **2020**, *59* (27), 10746–10773. (Z.F. and M.J.M. contributed equally)
Contribution: Outline of review, literature research, manuscript writing
(Supervision 50%, Manuscript 30%, Research direction 40%)

III. <u>Farka, Z.</u>; Juřík, T.; Pastucha, M.; Kovář, D.; Lacina, K.; Skládal, P., Rapid immunosensing of *Salmonella* Typhimurium using electrochemical impedance spectroscopy: the effect of sample treatment. *Electroanalysis* **2016**, *28* (8), 1803–1809. (Z.F. and T.J. contributed equally)
Contribution: Design of experiments, development and optimization of EIS immunosensor, characterization of sensing surface by AFM, data evaluation, manuscript writing
(Experimental work 30%, Supervision 30%, Manuscript 50%, Research direction 40%)

IV. Kovář, D.; <u>Farka, Z.</u>; Skládal, P., Detection of aerosolized biological agents using the piezoelectric immunosensor. *Anal. Chem.* **2014**, *86* (17), 8680–8686. (D.K. and Z.F. contributed equally)
Contribution: Development and optimization of QCM immunosensor, data evaluation, manuscript writing
(Experimental work 50%, Supervision 10%, Manuscript 50%, Research direction 30%)

V. Makhneva, E.; <u>Farka, Z.</u>; Skládal, P.; Zajíčková, L., Cyclopropylamine plasma polymer surfaces for label-free SPR and QCM immunosensing of *Salmonella*. *Sens. Actuators B Chem.* **2018**, *276*, 447–455.
Contribution: Development and optimization of SPR and QCM immunosensors, characterization of sensing surface by AFM, data evaluation, participation in manuscript writing
(Experimental work 30%, Supervision 10%, Manuscript 30%, Research direction 20%)

VI. Makhneva, E.; <u>Farka, Z.*</u>; Pastucha, M.; Obrusník, A.; Horáčková, V.; Skládal, P.; Zajíčková, L., Maleic anhydride and acetylene plasma copolymer surfaces for SPR immunosensing. *Anal. Bioanal. Chem.* **2019**, *411* (29), 7689–7697.
Contribution: Design of experiments, development and optimization of SPR immunosensor, characterization of sensing surface by AFM, data evaluation, manuscript writing
(Experimental work 20%, Supervision 50%, Manuscript 50%, Research direction 40%)

VII. Makhneva, E.; Barillas, L.; <u>Farka, Z.</u>; Pastucha, M.; Skládal, P.; Weltmann, K. D.; Fricke, K., Functional Plasma Polymerized Surfaces for Biosensing. *ACS Appl. Mater. Interfaces* **2020**, *20* (14), 17100–17112.
Contribution: Development and optimization of SPR immunosensor, data evaluation, participation in manuscript writing
(Experimental work 20%, Supervision 10%, Manuscript 20%, Research direction 20%)

VIII. Mikušová, Z.; <u>Farka, Z.*</u>; Pastucha, M.; Poláchová, V.; Obořilová, R.; Skládal, P., Amperometric Immunosensor for Rapid Detection of Honeybee Pathogen *Melissococcus plutonius*. *Electroanalysis* **2019**, *31* (10), 1969–1976.

Contribution: Design of experiments, preparation of immunization antigen and antibody, optimization of electrochemical immunosensor, data evaluation, manuscript writing
(Experimental work 30%, Supervision 80%, Manuscript 50%, Research direction 80%)

IX. Farka, Z.; Juřík, T.; Pastucha, M.; Skládal, P. Enzymatic Precipitation Enhanced Surface Plasmon Resonance Immunosensor for the Detection of *Salmonella* in Powdered Milk. *Anal. Chem.* **2016**, *88* (23), 11830–11836.
Contribution: Design of experiments, development and optimization of precipitation-enhanced SPR assay, characterization of precipitation reaction by AFM, data evaluation, manuscript writing
(Experimental work 40%, Supervision 50%, Manuscript 50%, Research direction 50%)

X. Farka, Z.*; Čunderlová, V.; Horáčková, V.; Pastucha, M.; Mikušová, Z.; Hlaváček, A.; Skládal, P., Prussian Blue Nanoparticles as a Catalytic Label in a Sandwich Nanozyme-Linked Immunosorbent Assay. *Anal. Chem.* **2018**, *90* (3), 2348–2354. (Z.F. and V.Č. contributed equally)
Contribution: Design of experiments, bioconjugation and characterization of PBNPs, development and optimization of sandwich assay, data evaluation, manuscript writing
(Experimental work 40%, Supervision 60%, Manuscript 60%, Research direction 60%)

XI. Hlaváček, A.; Farka, Z.; Hübner, M.; Horňáková, V.; Němeček, D.; Skládal, P.; Knopp, D.; Gorris, H. H., Competitive Upconversion-Linked Immunosorbent Assay for the Sensitive Detection of Diclofenac. *Anal. Chem.* **2016**, *88* (11), 6011–6017.
Contribution: Design of experiments, bioconjugation and characterization of UCNPs, development and optimization of competitive immunoassay, data evaluation, participation in manuscript writing
(Experimental work 30%, Supervision 10%, Manuscript 30%, Research direction 20%)

XII. Hlaváček, A.; Peterek, M.; Farka, Z.; Mickert, M. J.; Prechtl, L.; Knopp D.; Gorris, H. H., Rapid single-step upconversion-linked immunosorbent assay for diclofenac. *Microchim. Acta* **2017**, *184* (10), 4159–4165.
Contribution: Development and optimization of competitive immunoassay, data evaluation, participation in manuscript writing
(Experimental work 20%, Supervision 10%, Manuscript 20%, Research direction 10%)

XIII. Peltomaa, R.; Farka, Z.; Mickert, M. J.; Brandmeier, J. C.; Pastucha, M.; Hlaváček, A.; Martínez-Orts, M.; Canales, Á.; Skládal, P.; Benito-Peña, E.; Moreno-Bondi, M. C.; Gorris, H. H., Competitive upconversion-linked immunoassay using peptide mimetics for the detection of the mycotoxin zearalenone. *Biosens. Bioelectron.* **2020**, *170*, 112683.
Contribution: Design of experiments, bioconjugation and characterization of UCNPs, development and optimization of competitive immunoassay, data evaluation, participation in manuscript writing
(Experimental work 30%, Supervision 30%, Manuscript 30%, Research direction 30%)

XIV. Poláchová, V.; Pastucha, M.; Mikušová, Z.; Mickert, M. J.; Hlaváček, A.; Gorris, H. H.; Skládal, P.; Farka, Z.*, Click-conjugated photon-upconversion nanoparticles in an immunoassay for honeybee pathogen *Melissococcus plutonius*. *Nanoscale* **2019**, *11* (17), 8343–8351.

Contribution: Design of experiments, preparation of immunization antigen and antibody, bioconjugation and characterization of UCNPs, development and optimization of sandwich immunoassay, data evaluation, manuscript writing

(Experimental work 20%, Supervision 80%, Manuscript 50%, Research direction 80%)

XV. Kostiv, U.; <u>Farka, Z.</u>; Mickert, M. J.; Gorris, H. H.; Velychkivska, N.; Pop-Georgievski, O.; Pastucha, M.; Odstrčilíková, E.; Skládal, P.; Horák, D., Versatile bioconjugation strategies of PEG-modified upconversion nanoparticles for bioanalytical applications. *Biomacromolecules* **2020**, *21* (11), 4502–4513. (U.K. and Z.F. contributed equally)

Contribution: Design of experiments, bioconjugation of UCNPs, development and optimization of sandwich immunoassay, data evaluation, participation in manuscript writing

(Experimental work 30%, Supervision 40%, Manuscript 40%, Research direction 40%)

XVI. Pastucha, M.; Odstrčilíková, E.; Hlaváček, A.; Brandmeier, J. C.; Vykoukal, V.; Weisová, J.; Gorris, H. H.; Skládal, P.; <u>Farka Z.*</u>, Upconversion-linked Immunoassay for the Diagnosis of Honeybee Disease American Foulbrood. *IEEE J. Sel. Top. Quantum Electron.* **2021**, *27* (5), 6900311.

Contribution: Design of experiments, preparation of immunization antigen and antibody, bioconjugation and characterization of UCNPs, development and optimization of sandwich immunoassay, data evaluation, manuscript writing

(Experimental work 20%, Supervision 80%, Manuscript 50%, Research direction 80%)

XVII. <u>Farka, Z.</u>; Mickert, M. J.; Hlaváček, A.; Skládal P.; Gorris, H. H., Single Molecule Upconversion-Linked Immunosorbent Assay with Extended Dynamic Range for the Sensitive Detection of Diagnostic Biomarkers. *Anal. Chem.* **2017**, *89* (21), 11825–11830. (Z.F. and M.J.M. contributed equally)

Contribution: Design of experiments, optimization of single-particle microscope setup, bioconjugation and characterization of UCNPs, development and optimization of sandwich immunoassay, data evaluation, manuscript writing

(Experimental work 40%, Supervision 20%, Manuscript 40%, Research direction 20%)

XVIII. Mickert, M. J.; <u>Farka, Z.</u>; Kostiv, U.; Hlaváček, A.; Horák, D.; Skládal, P.; Gorris, H. H., Measurement of Sub-femtomolar Concentrations of Prostate-Specific Antigen through Single-Molecule Counting with an Upconversion-Linked Immunosorbent Assay. *Anal. Chem.* **2019**, *91* (15), 9435–9441. (M.J.M and Z.F. contributed equally)

Contribution: Design of experiments, bioconjugation and characterization of UCNPs, development and optimization of sandwich immunoassay, data evaluation, manuscript writing

(Experimental work 30%, Supervision 20%, Manuscript 30%, Research direction 30%)

XIX. Brandmeier, J. C.; Raiko, K.; <u>Farka, Z.*</u>; Peltomaa, R.; Mickert, M. J.; Hlaváček, A.; Skládal, P.; Soukka, T.; Gorris, H. H., Effect of Particle Size and Surface Chemistry of Photon-Upconversion Nanoparticles on Analog and Digital Immunoassays for Cardiac Troponin. *Adv. Healthc. Mater.* **2021**, *10* (18), 2100506.

Contribution: Design of experiments, bioconjugation and characterization of UCNPs, development and optimization of sandwich immunoassay, data evaluation, manuscript writing

(Experimental work 20%, Supervision 30%, Manuscript 30%, Research direction 30%)

XX. <u>Farka, Z.*</u>; Mickert, M. J.; Mikušová, Z.; Hlaváček, A.; Bouchalová, P.; Xu, W.; Bouchal, P.; Skládal, P.; Gorris, H. H., Surface design of photon-upconversion nanoparticles for high-contrast immunocytochemistry. *Nanoscale* **2020**, *12* (15), 8303–8313. (Z.F. and M.J.M. contributed equally)
Contribution: Design of experiments, optimization of microscope setup, bioconjugation and characterization of UCNPs, development and optimization of ICC assay, data evaluation, manuscript writing
(Experimental work 40%, Supervision 40%, Manuscript 50%, Research direction 40%)

XXI. Modlitbová, P.; <u>Farka, Z.</u>; Pastucha, M.; Pořízka, P.; Novotný, K.; Skládal, P.; Kaiser, J., Laser-induced breakdown spectroscopy as a novel readout method for nanoparticle-based immunoassays. *Microchim. Acta* **2019**, *186*, 629.
Contribution: Design of experiments, development and optimization of sandwich immunoassay, data evaluation, participation in manuscript writing
(Experimental work 40%, Supervision 30%, Manuscript 30%, Research direction 30%)

XXII. Pořízka, P.; Vytisková, K.; Obořilová, R.; Pastucha, M.; Gábriš, I.; Brandmeier, J. C.; Modlitbová, P.; Gorris, H. H.; Novotný, K.; Skládal, P.; Kaiser, J.; <u>Farka, Z.</u>, Laser-Induced Breakdown Spectroscopy as a Readout Method for Immunocytochemistry with Upconversion Nanoparticles. *Microchim. Acta* **2021**, *188*, 147.
Contribution: Design of experiments, bioconjugation and characterization of UCNPs, development and optimization of ICC assay, data evaluation, manuscript writing
(Experimental work 20%, Supervision 40%, Manuscript 50%, Research direction 50%)

2 Introduction (Papers I and II)

The capability to rapidly detect small analyte concentrations, particularly of low-abundance biomarkers, is critical for diagnosing diseases in their early stages. The majority of bioaffinity methods are employing antibodies;[1, 2] however, also aptamers[3] and molecularly imprinted polymers (MIPs)[4] can be used for specific capture of the target analyte. Antibodies with high affinity can be prepared against generally any analyte molecule. The limit of affinity, represented by a binding constant, is approximately 10^{10} M^{-1},[5] which is worse than 10^{14} M^{-1} in the case of (strept)avidin-biotin interaction.[6] Due to the relatively large size of antibodies, single binding site antibodies (camelids) are also attracting attention recently.[7] Aptamers are beneficial due to their easier large-scale production, and MIPs excel in chemical stability. MIPs are particularly suitable for detecting small molecules with a rigid structure. However, they are less suitable for the detection of bigger, more flexible analytes, as proteins.

Two approaches can be used for the detection of binding events: (i) Label-free assays exploit the possibility to generate a signal directly upon analyte binding to the detection element. (ii) The so-called sandwich format is based on binding a second affinity reagent bearing a label that provides signal generation. Both approaches can be carried out in a competitive (or inhibition) mode, based on competition of immunoreagents for a limited amount of binding sites, resulting in lower signals for higher analyte concentrations. The first immunoassays were based on radioactive labels;[8] however, these were soon replaced by enzymes, which allow higher safety. Furthermore, a single enzyme molecule can generate a high number of measurable product molecules (signal amplification step). The enzyme-linked immunosorbent assay (ELISA) is nowadays considered as a method of choice for quantitative analysis of various analytes, from clinical diagnosis, through food control, up to environmental protection.

Throughout the past 60 years, the progress in immunoassays was primarily focused on enhancing sensitivity, specificity, and reproducibility. Even though ELISA can detect picomolar analyte concentrations, even higher sensitivities are necessary. Only a few toxin molecules can be harmful,[3] individual infectious viruses or bacteria can initiate a disease,[9] and trace cancer biomarker quantities indicate the onset of a malignant transformation.[10] Furthermore, developing immunoassays with higher sensitivity is critical to allow discovering new biomarkers, which cannot be analyzed using the current methodology.[11, 12]

The conventional ELISA is carried out the laboratory conditions and is based on relatively long incubation times and several washing steps. Therefore, the recent development in the field aims also at faster analysis, with higher throughput and smaller sample consumption. Such assays allow on-line analysis, e.g., at the bedside for clinical tests,[13] or in the field for environmental or military applications. Such methods are often referred to as point-of-care (PoC) tests.[14] It is preferred to use samples that require minimal invasiveness during their collection, such as urine or saliva. Furthermore, assays without washing steps are desired. The most famous PoC test based on antibodies is the home pregnancy test, the representative of lateral flow immunoassays (LFIAs), which were developed in the 1980s.[15] The user-friendly operation, along with the possibility to provide reliable results, is necessary to allow the PoC

test to be used in predictive, preventive, personalized, and participatory medicine, commonly termed P4 medicine.[16]

The group of label-based bioaffinity assays can be further divided according to the used detection label (**Figure 1**). (i) Enzymes represent the most widespread approach, whereas (ii) fluorescent molecular labels are generally easier, without the requirement of the product generation step. However, the fluorescence immunoassays (FIAs) are typically limited by the fluorescence of the background. Furthermore, fluorescence readout was adapted in homogeneous assays based on fluorescence polarization and methods based on signal amplification (e.g., based on Immuno PCR). Significant progress regarding the limitation of background fluorescence was achieved by the development of time-resolved (TR) approaches that exploit lanthanide-based labels with long lifetimes (μs) compared to small fluorophores (ns).[17] The time-gated approach is based on the luminescence excitation, which is not directly followed by the signal acquisition, but the measurement is delayed by a few μs, so the autofluorescence signal decays, and only specific lanthanide signals are measured. The dissociation-enhanced lanthanide fluorescent immunoassay (DELFIA) is currently the most widespread commercially available TR approach.[18]
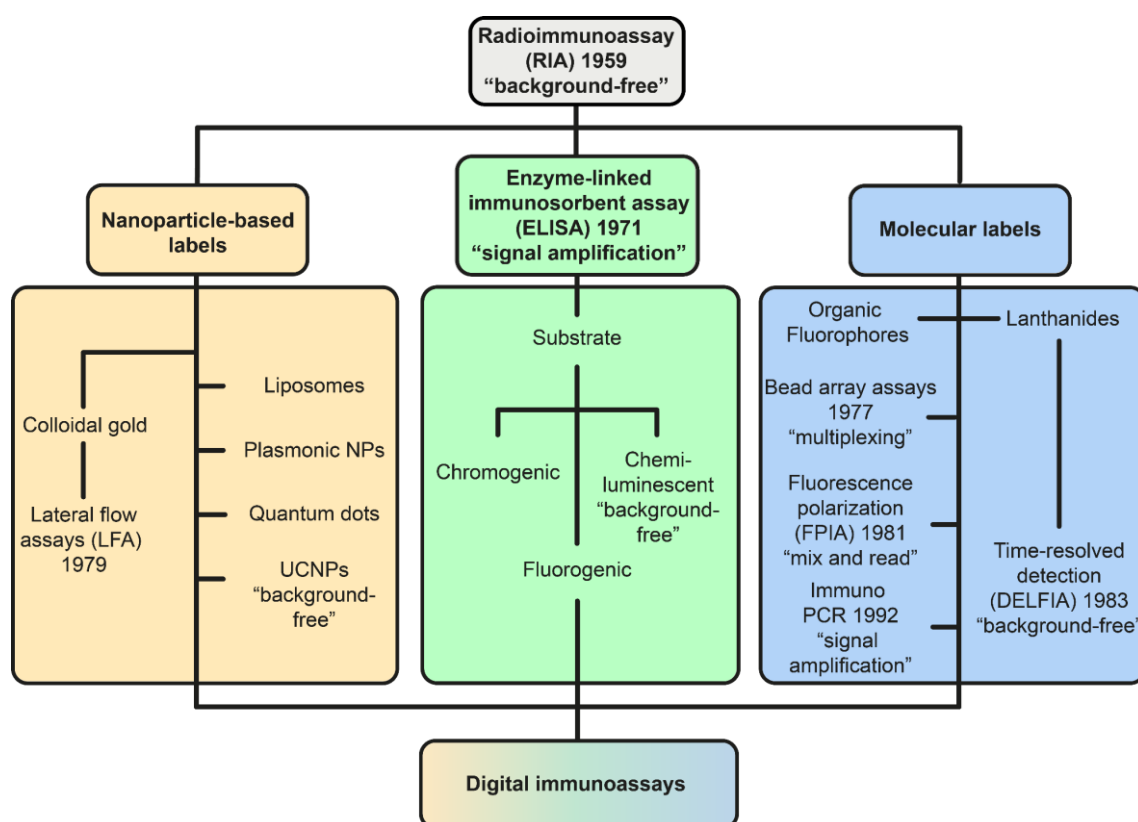
Figure 1: History of the development of label-based immunoassays with optical readout. Radioisotopes were replaced by enzymes, fluorescent molecules, and nanoparticles. By choosing a suitable readout method, all these labels can be used for the measurement at the single-molecule level. Reprinted from Paper II under the permission of Creative Commons Attribution-NonCommercial 4.0 International License.

As an alternative label type (iii), various kinds of nanoparticles (NPs) are gaining increasing popularity (**Figure 1**).[2, 19] Gold nanoparticles (Au NPs) are widely used for the readout of LFIAs. Because of their plasmonic properties, Au NPs exhibit strong absorption and scattering of light, which makes them easily visible by the eye, and the color-based readout is possible without the need for sophisticated instrumentation. Apart from the plasmonic NPs, many other types of NPs and nanocomposites are being used for optical detection. Quantum dots (QDs) represent an alternative to organic fluorophores due to their better photostability and higher brightness, which is an essential aspect in immunoassay readout. Photon-upconversion nanoparticles (UCNPs) are another kind of luminescent labels, which allow excitation by near-infrared light, followed by the emission of light with a shorter wavelength. This anti-Stokes emission avoids autofluorescence and light scattering, leading to detection without optical background interference.[20] Nanocontainers (e.g., liposomes) can be packed by many fluorescent molecules to generate strong signals. Compared to the enzyme-based labels, which produce the fluorophores *in situ* from the non-fluorescent substrate, the fluorophores encapsulated in nanocontainers can be released on demand, limiting the self-quenching inside the confined environment.[21] Furthermore, various mixed detection schemes, e.g., electrochemiluminescence, can be employed to generate strong signals without background.

Overall, the various detection schemes present different advantages and disadvantages in terms of sensitivity, analysis time, miniaturization potential, etc. Therefore, a suitable method has to be chosen not only concerning the target analyte but also for the intended application and user base.

3 Label-Free Biosensing

3.1 Electrochemical Impedance Spectroscopy Biosensing of *Salmonella* (Paper III)

Electrochemical immunosensors are receiving increasing focus because they can combine highly sensitive measurements with portability and low cost. Electrochemical impedance spectroscopy (EIS) is a technique, which allows the measurement of small changes in the interface between the electrode and solution. EIS provides a fast response in combination with high sensitivity and potential for real-time measurement and miniaturization.[22] When used in biosensors, EIS provides insight into the individual immobilized layers and coating on the electrode in general. The EIS measurement is based on applying a low-amplitude sinusoidal potential (or current) through the electrochemical cell with the electrolyte solution, typically ferro/ferricyanide. The output current (or potential) is then measured over a range of frequencies by a potentiostat, allowing the calculation of the impedance parameters. Compared to the other electrochemical techniques, including cyclic voltammetry, the applied potential is smaller, preventing the undesired influence on biomolecular layers and binding processes.[23]

The biosensors based on EIS typically employ antibodies immobilized in the electrode, directly capturing the target analyte. The accumulated mass hinders the electron transfer; this is evaluated as the increase of impedance. This allows operation in label-free mode, providing robust and straightforward analysis. The label-free EIS can be used for rapid analysis of pathogens within small sample amounts.

Our research focused on *Salmonella enterica* serovar Typhimurium, a non-typhoidal strain, which is one of the leading causes of gastrointestinal diseases. *Salmonella* is a gram-negative bacterium, which can cause diarrhea, fever, and abdominal spasm within 12 to 72 h after infection. In the worst scenario, *Salmonella* can enter blood, bones, brain, or nervous system, which can cause even lethal infections.[24] The infection is typically caused by consuming contaminated food.[25] *Salmonella* can be present in raw animal food products, including meat, eggs, and unpasteurized dairy products. There are globally 94 million cases of gastroenteritis and 155,000 deaths attributed to *Salmonella* each year.[26] According to the Centers for Disease Control and Prevention (CDC), there are 1.2 million illnesses and 450 deaths per year in the United States caused by non-typhoidal *Salmonella* strains.[26] This highlights the danger of *Salmonella* to human health and the importance of developing devices that can allow rapid and sensitive *Salmonella* detection.

The standard approaches allowing the detection of *Salmonella* include traditional cultivation-based methods, ELISA, and polymerase chain reaction (PCR). The cultivation-based approaches are considered a gold standard for *Salmonella* detection because of the high sensitivity and selectivity. However, the long analysis times (5–7 days) with labor-intensive procedures do not allow using cultivation for rapid screening purposes.[27] The ELISA can provide sensitive results generally within 24 h.[28] Usually, a time-consuming pre-enrichment step is necessary to increase the bacteria count in the samples.[29] PCR overcomes the sensitivity and analysis times on conventional methods; however, it requires expensive instrumentation

and trained personnel to carry out the analysis.[30] Furthermore, the above-mentioned methods are typically limited only to laboratory conditions and do not allow PoC operation.

We have developed an EIS approach for the detection of *Salmonella* Typhimurium, based on a simple, easy to fabricate, and low-cost immunosensor. The screen-printed electrodes (SPEs) were modified by a self-assembled monolayer of cysteamine, followed by binding of glutaraldehyde and specific antibody (**Figure 2**). The increase of impedance after incubation with the sample revealed the presence of bacteria. Different sample treatment methods (viable bacteria and combinations of

Figure 2: Scheme of antibody immobilization (blocking by BSA not shown) and the design of the SPE electrode. Reprinted from Paper III with permission. Copyright 2016 Wiley-VCH.

heat-treatment and sonication) were tested to find the optimal way of sample preparation regarding the specificity of the chosen antibody. The achieved results have shown that the antibody did not exhibit the necessary affinity towards native *Salmonella*. After the heat-treatment (80 ℃, 40 min), the affinity of the antibody to the microbe increased significantly. This allowed reaching a limit of detection (LOD) of 7×10^4 CFU/mL with a wide linear range up to 10^8 CFU/mL. The treatment by heat does not present significant technical difficulty for the real sample analyses. Furthermore, it can even be beneficial to work with the killed or weakened bacteria due to the reduced level of pathogenicity.

To improve the sensitivity further, the *Salmonella* cells were disrupted by sonication. The sonicated heat-treated sample has shown a higher level of specific binding than whole cells, resulting in an LOD of 1×10^3 CFU/mL; the linear range was up to 10^8 CFU/mL. The total analysis time (including the incubation of the sensor with the sample) was 20 min. The treatment by sonication is also not a technical problem for practical analysis. Even though additional instrumentation is required, sonication is beneficial because it is less time-consuming than heat-treatment. The presence of bacteria on the sensor surface was confirmed by atomic force microscopy (AFM; **Figure 3**). It was shown that the sensor captured a large number of cell fragments, with the size and structure corresponding to heat-treated and sonicated bacteria adsorbed on the glass.

In the case of the cross-reactivity with *E. coli* K-12, only negligible increases of impedance were observed, confirming the excellent selectivity of the method. Because both *Salmonella* and *E. coli* are relatively similar gram-negative bacteria, a low level of cross-reactivity can also be expected in the case of more phylogenetically distant bacteria.[31]
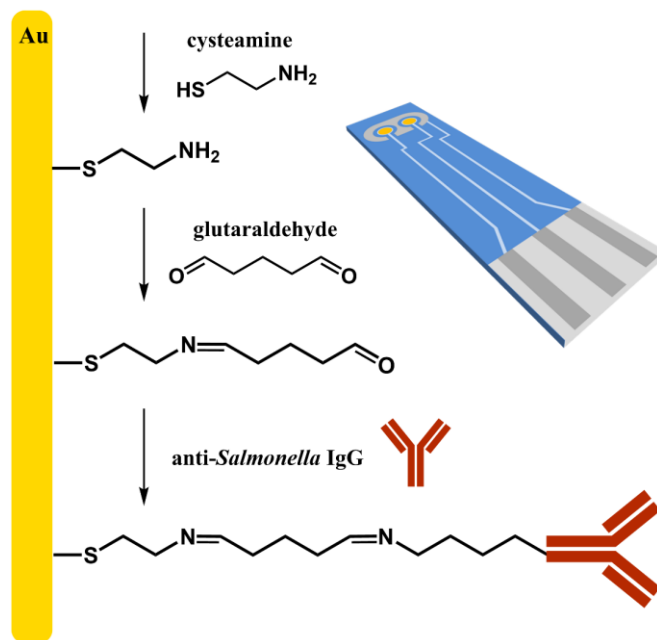
The practical applicability of the sensor was demonstrated by the analysis of real samples of milk spiked with *Salmonella*. The electrode had to be washed thoroughly after the incubation with complex samples; insufficient washing was connected with the increase of non-specific signals. The detection capabilities in the case of complex samples decreased slightly compared to the detection in the buffer, resulting in the LOD of 9×10^3 CFU/mL and linear range up to 10^7 CFU/mL. These results are comparable to the infection dose of *Salmonella*[32] and highlight the potential of the developed method.
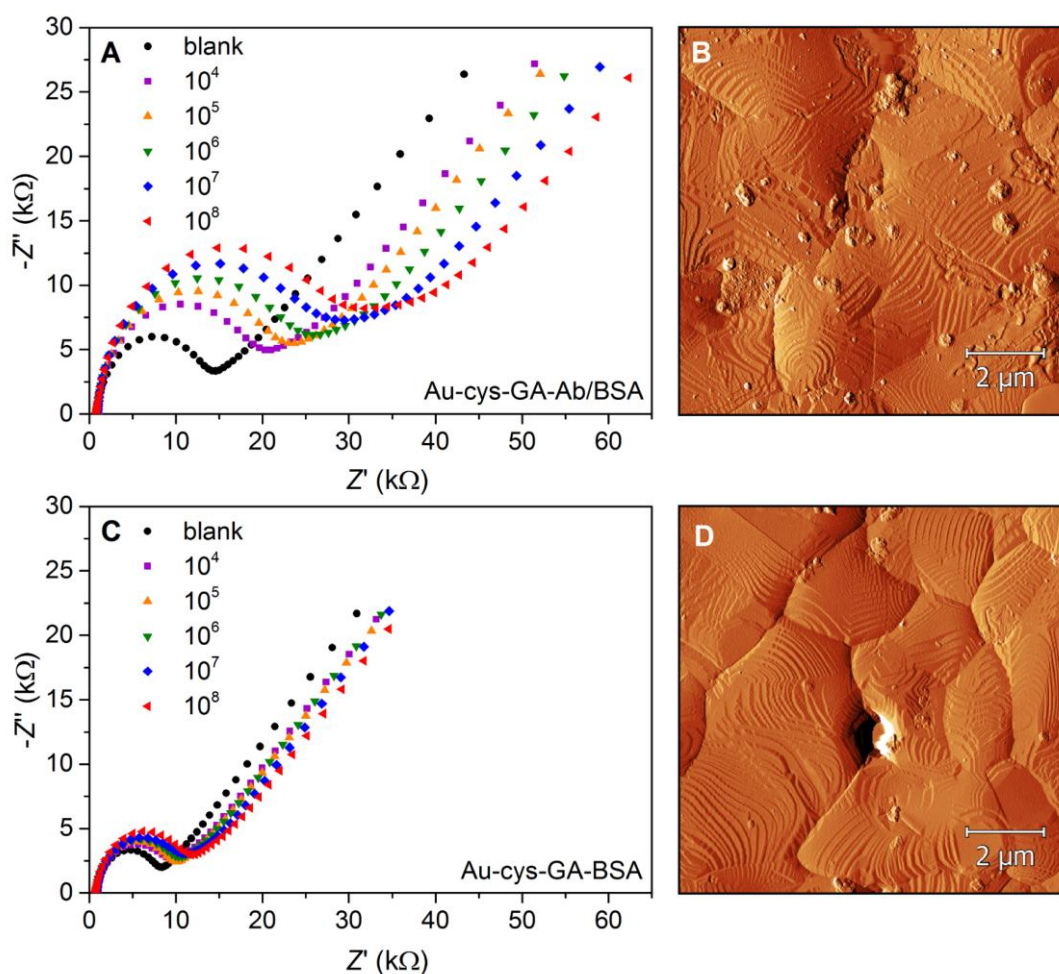
Figure 3: **(A)** EIS response of the SPE immunosensor to different concentrations of heat-treated and sonicated *Salmonella*; **(B)** AFM scan of the electrode after binding (error signal); **(C)** negative control (no antibody on the surface); **(D)** AFM scan of the blank electrode. Reprinted from Paper III with permission. Copyright 2016 Wiley-VCH.

3.2 Quartz Crystal Microbalance Biosensor for Aerosolized Bacteria (Paper IV)

In 1959, Sauerbrey described the dependence between the resonant frequency of quartz sensor and the mass accumulated on the sensor surface, which led to the development of the microgravimetric biosensing approach – quartz crystal microbalance (QCM). QCM allows detecting binding events based on the measurement of changes of frequency of the quartz

resonator.[33] The great advantage of QCM is the ability to provide the results in real-time, finding applications in monitoring of surface modifications, adsorption/desorption effects, and binding interactions. When the analyte is captured on the surface, it increases the loaded mass, which can be directly estimated from the decrease of the resonance frequency.

We employed the QCM biosensor for the detection of bioaerosols. Airborne microorganisms (bacteria, viruses, fungi, etc.) are an integral part of the environment. Bacteria can be spread to the air by natural as well as anthropogenic sources; the misuse of pathogens can result in targeted biological attacks.[34, 35] Modern history has shown that the potential of abuse of biological warfare agents is very high.[36]

The contamination of outdoor and indoor air by bacteria can infect a large number of people within a short timeframe.[37] The detection of bioaerosols is difficult due to the low levels of target bacteria, combined with a potentially complex sample matrix containing pollen grains, mold, fungi, dust, and ubiquitous microbial organisms.[38] Further interferences might be caused by industrial products, which are emitted into the atmosphere in large quantities. The low visibility and lack of odor present additional challenges for sampling and analysis. In contrast to chemical agents, also the delayed effect of biological agents has to be considered, leading to a potentially large number of casualties before protective steps are taken.[36] The bioaerosols can contribute to the spread of epidemics and pandemics in places with high population densities. In such cases, rapid detection and identification of the pathogen are critical to allow early treatment. Therefore, the specific detection of bacteria in the air is of particular importance also during peacetime.

The bioaerosol analysis consists of two critical parts: collection of the bioaerosol and detection of the bacteria. The systems for the collection of bioaerosols (samplers) have been extensively developed in recent years;[39] their function can be based on various physical principles.[40]

The two main approaches for the detection are based on the analysis of general biological compounds in the air or specific detection of target bacteria. The non-specific detection is typically based on optical methods, exploiting the fluorescence of the molecules present in biological systems (ATP, NADH, tryptophan, etc.).[41, 42] These systems, however, cannot differentiate between pathogenic and non-pathogenic bacteria, and the presence of atmospheric pollutants with fluorescence properties can interfere with the analysis.[43] Furthermore, this principle is only useful for living bacteria, and it does to allow detection of spores, as they exhibit only low ATP levels.[44] The specific detection of bacteria typically exploits culture-based techniques, PCR,[45, 46] Raman spectroscopy, or mass spectrometry.[47] The culture-based methods are time-consuming and usually require collection of samples for subsequent laboratory analysis. The PCR is highly sensitive; however, various interfering substances can be present in the complex samples, which hinders the analysis.[48] Therefore, PCR is often combined with other methods to prevent false-positive results.[49] In the case of MS, the widespread use for in-field detection is limited mainly by the requirement of vacuum and extensive instrumentation in general.

We have employed the immunosensor technology to overcome these disadvantages, aiming at quick-response, real-time, and on-site detection. First, a bioaerosol chamber was

constructed for safe and controlled dissemination of biological agents and applied for experiments with model bacterial aerosols of *E. coli* (**Figure 4A**). The samples were disseminated using a piezoelectric humidifier, distribution of bioaerosol inside the chamber was achieved using three 12-cm fans. The disseminated bacteria were collected and preconcentrated using the wetted-wall cyclone SASS 2300; the analysis was done using the on-line linked QCM immunosensor. The measurement was fully automated; the flow system was used for the on-line delivery of the samples from the cyclone to the QCM, allowing to perform one detection cycle within 16 min. The achieved LOD of *E. coli* in the bioaerosol was 10^4 CFU/L of air, based on the amounts of the disseminated microbe (**Figure 4B**). The whole experiment, including sample collection, detection, sensor surface regeneration, and bioaerosol chamber ventilation, took 40 min. The reference experiments based on cultivation showed that the disseminated amount of *E. coli* was reduced, probably because of the surface adsorption, desiccation, and mechanical stress caused by the cyclone. The great benefit of the developed detection system is the possibility of entirely remote operation; the users do not come into contact with potentially dangerous microorganisms during the experiments. Furthermore, the system is fully portable (desk-top size) and requires only power and ethernet connections.

The achieved results proved the suitability of the developed QCM immunosensor combined with cyclone sampling to detect aerosolized bacteria. In the future, multiplexed detection based on monoclonal antibodies specific to different pathogens can allow comprehensive screening of the air quality in a reasonably short time. The system based on single-step analysis provides the necessary simplicity, robustness, and reliability, making it a suitable option for in-field applications.
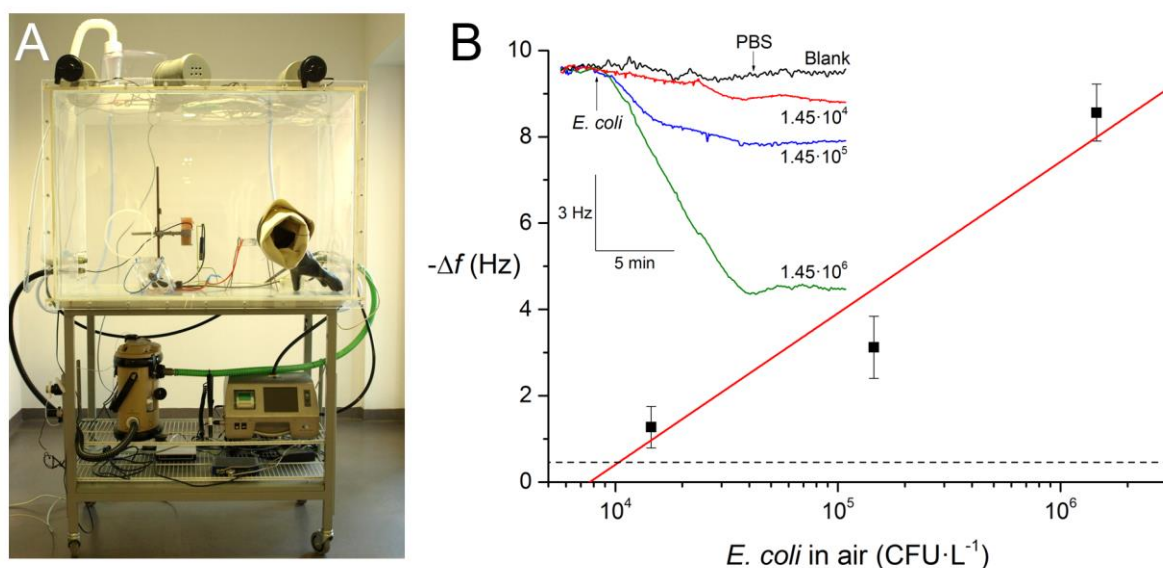
Figure 4: (A) The constructed bioaerosol chamber. **(B)** Calibration curve for the QCM detection of *E. coli* in bioaerosol. The inset shows the binding curves of samples captured by the cyclone. Adapted from Paper IV with permission. Copyright 2014 American Chemical Society.

3.3 Plasma-Polymerized Surfaces for SPR Biosensing (Papers V–VII)

Surface plasmon resonance (SPR) biosensors are based on the oscillations of electrons in conduction bands of metal films (typically gold) upon the excitation by light. This effect strongly depends on the dielectric constant of the environment[50] and can be exploited in immunosensing because the biological interactions lead to the changes in oscillation frequency. The measurement can be based on changes of intensity, angle, refractive index, or phase of the reflected light.[51]

The SPR biosensors can be divided into two main groups: (i) propagating SPRs (PSPRs; also simply referred to as SPRs) and localized SPRs (LSPRs).[52] The excitation of PSPR is typically done on continuous metal thin films using a prism or grating. The resonance then spreads along the metal/dielectric surface to a distance up to hundreds of micrometers.[53] In the case of the LSPR, the plasmon resonance is not propagating and is excited on nanostructured metal surfaces. The properties can be adjusted by the size, shape, or composition of the nanostructures or nanoparticles.[54]

The SPR experiments are typically done in a direct,[55] sandwich,[56] or inhibition format.[57] The direct assays are useful for bigger analytes that provide a sufficient response upon binding (**Figure 5**). The sandwich assay is based on a two-step procedure. The antibody first binds the analyte as in the direct format, followed by the capture of secondary antibodies (potentially labeled with enzymes or nanoparticles) to enhance the signal.[58] The inhibition assay is based on mixing the analyte with respective antibodies, followed by the injection to the flow cell containing a chip with a known amount of immobilized analyte. The binding of free antibodies from the solution is evaluated to determine the analyte concentration.

To efficiently immobilize the capture molecules to the sensor surface, coatings bearing chemical groups that allow the formation of covalent bonds are typically used.[59, 60] Apart from the amount of the functional groups, sufficient layer stability under various conditions is necessary. Typically, the biomolecules are immobilized *via* primary amines or carboxyl groups; therefore, there should be either carboxyls or primary amines available on the surface to provide immobilization *via* the common carbodiimide / *N*-hydroxysuccinimide zero-length coupling reactions providing amide-based bonds. Numerous methodologies were investigated for surface modification with the desired chemical groups. Typically, wet-chemical procedures are being used, including binding of thiols on the surfaces of noble metals.[61] However, these methods are time-consuming and often require the use of aggressive chemicals.

Alternatively, plasma polymerization can be used to prepare thin

Figure 5: Scheme of SPR immunoassay in direct format. Adapted from Paper VII with permission. Copyright 2020 American Chemical Society.

polymer films on various surfaces in a fast and eco-friendly procedure without the requirement of washing steps or reagent additions. Physical plasma is (partially) ionized gas consisting of photons, electrons, positive and negative ions, atoms, free radicals, and exci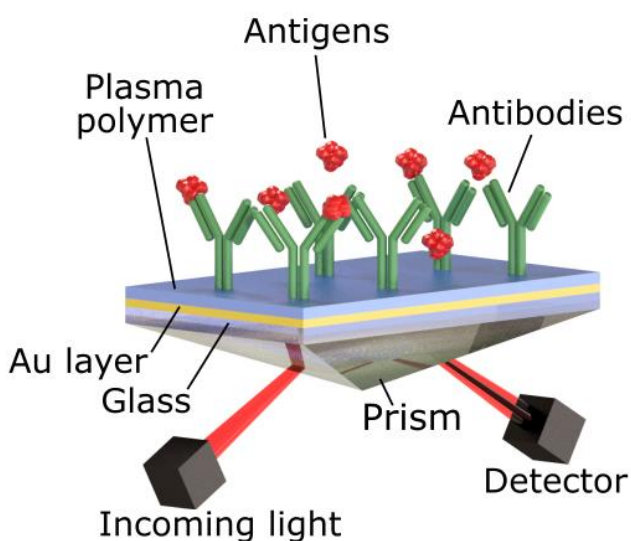ted or non-excited molecules. Generation of plasma can be done by applying energy at low-, atmospheric-, or high-pressure conditions. Non-thermal plasmas are gaining increasing attention in many applications due to the possibility to provide enhanced gas-phase chemistry with high concentrations of chemically active species without the need for increased gas temperatures. The prepared plasma-polymerized (PP) coatings typically exhibit high branching and cross-linking, excellent adhesion to practically any surfaces, and high stability.

The amine-rich PP coatings are the most commonly used and studied to allow biomolecule immobilization and cell binding.[62, 63] The use of amine-rich PP films was demonstrated in biosensing, cell proliferation, and other biological applications.[64, 65] Compared with the conventional layers, e.g., carboxymethylated dextran (CMD), faster and more cost-effective layer preparation can be achieved by employing plasma processes. PP films with carboxyl groups are usually prepared by plasma polymerization of various acrylates.[66] Alternative approaches can be based on gas mixtures of CO_2 and ethylene[67] or deposition from maleic anhydride (MA). The MA-based coating provided a highly reactive surface; however, the polymerization required fine-tuning as the layer was initially not sufficiently stable.[68]

We have explored different ways of surface modification by PP films for biosensing applications. First, we explored amine-based PP films composed of cyclopropylamine (CPA). The pulsed plasma polymerization of CPA can be used to prepare reactive nitrogen-containing films in a fast and eco-friendly way. As the layer stability is one of the critical aspects, we have first investigated the behavior of CPA PP films in aqueous media. The immersion in the buffer for 18 h before the glutaraldehyde activation turned out to be a critical step in maintaining long-term layer stability. The FT-IR and ellipsometry showed that the number of amine groups decreased, which was connected by the decreases of thickness by up to 17% after the immersion in the buffer. The results were explained by the hydrolysis of enamines or imines in the CPA PP; the chemical changes without thickness losses were caused by the hydrolysis of nitriles. The activation by glutaraldehyde led to the growth of a 5–7 nm thick film of glutaraldehyde and its oligomers. This surface was used to immobilize antibodies against human serum albumin (HSA) or *Salmonella* for the biosensing experiments. Furthermore, regeneration with 10 mM NaOH allowed multiple measurements with a single sensor.

Since the commercial SPR sensors are most commonly based on carboxyl-containing layers,[69] we have also examined the field of carboxyl-rich PP films. In our preliminary study, we have demonstrated the potential of PP films in SPR biosensing.[70] We compared two kinds of PP films prepared under different plasma conditions; the first was based on polymerization from gas mixtures of maleic anhydride, acetylene, and argon (MA/C_2H_2/Ar; **Figure 6A**), the other on the mixture of CO_2, ethylene, and argon (CO_2/C_2H_4/Ar). The capacity of both surfaces to bind anti-HSA antibody was demonstrated, and the specific binding of HSA showed the biosensing potential. The layer based on CO_2/C_2H_4 exhibited lower stability and smaller binding capacity, which resulted in the drift of the baseline and small response upon HSA injection. In contrast, the film based on MA/C_2H_2 allowed efficient immobilization of the

20

antibody and provided a stable baseline signal, which resulted in a higher response to HSA compared to the immunosensor based on CO_2/C_2H_4.

Based on these results and with the aim to develop a robust biosensing layer, we continued studying the preparation and properties of films based on MA/C_2H_2. We carried out a systematic comparison of MA/C_2H_2 PP films with sensors based on a mixed self-assembled monolayer of mercaptoundecanoic acid with mercaptohexanol (MUA/MCH) and with carboxymethylated dextrans (2D and 3D CMD) in term of the performance in the detection of HSA (**Figure 6B**). Compared with MUA/MCH and 2D CMD layers, the MA/C_2H_2 PP films showed better performance, demonstrated by about two times higher signals. On the other hand, the sensor based on 3D CMD still exhibited higher performance, especially providing a wider working range. This, however, can be explained by the significantly smaller surface area of the planar PP film compared to the 3D CMD.
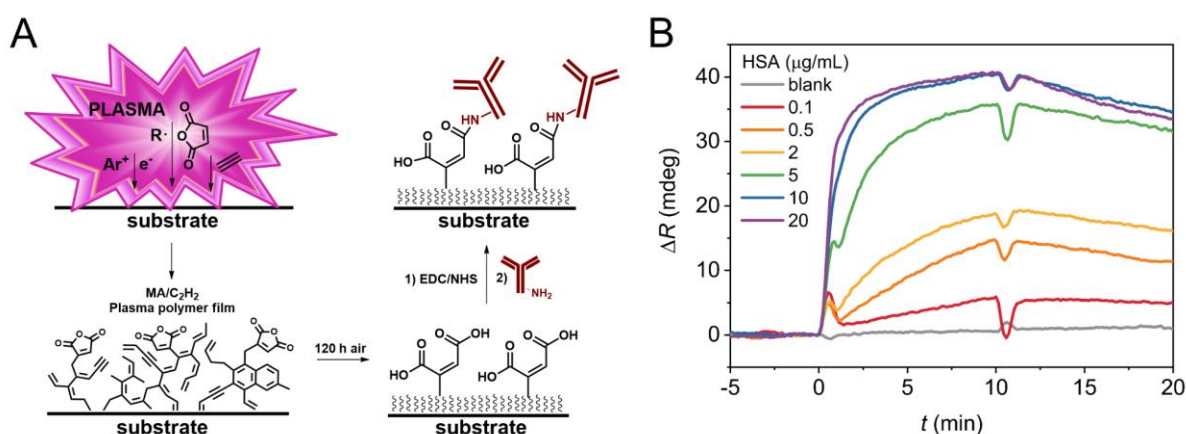
Figure 6: (A) Scheme of sensor surface modification by MA/C_2H_2 PP film with subsequent immobilization of the antibody *via* EDC/NHS chemistry. **(B)** SPR binding curves of HSA on antibody-modified MA/C_2H_2 PP film. Adapted from Paper VI with permission. Copyright 2019 Springer.

In our next contribution, we used a high frequency-driven atmospheric-pressure plasma jet (APPJ; **Figure 7**) to prepare PP coatings based on 1,2,4-trivinylcyclohexane (TVC), tetrahydrofurfuryl methacrylate (THFMA), and a mixture of thereof. THFMA was selected because of the presence of the vinylidene group that can form polymers chains and tetrahydrofuran (THF) group, which served as a protective group against the breakdown of the THFMA. TVC contains three vinyl groups, which makes it effective as a monomer, but TVC also served as the source of carbon functionalities to adjust the carbon content and stability of the resulting PP films. Under plasma-induced polymerization conditions, the THF or cyclohexane ring-opening can happen, which results in further polymer chain cross-linking. Both the TVC and the THFMA are non-toxic, which fits the eco-friendly procedure of plasma polymerization.

The behavior of the films in an aqueous environment was studied. The highest stability was observed in the case of ppTVC, which contained the lowest amount of oxygen. In the case of ppTHFMA and ppTHFMA-co-TVC, more significant thickness losses occurred during the initial storage in water, however, with no impact on the chemical composition. After the stabilization for 24 h in liquid, all films have shown a high level of stability. The initial losses of film thickness can be explained by the removal of loosely bound oligomers from the film surface. AFM has demonstrated that the thickness losses were connected with the formation of characteristic morphological

Figure 7: Scheme of the atmospheric-pressure plasma jet (APPJ; left) and photograph of the operating APPJ (right). Reprinted from Paper VII with Permission. Copyright 2020 American Chemical Society.

features. These led to an increase in the surface area and can be beneficial for the immobilization of a higher amount of antibody, resulting in higher sensor sensitivity.

After the immobilization of the specific antibody, the PP-modified chips were used for the SPR detection of HSA. We have demonstrated that not only the number of functional groups affect the sensitivity of the measurement, but also the layer morphology is an essential factor. The ppTHFMA-co-TVC layer with the highest surface roughness provided the largest binding capacity. The sensors exhibited an excellent level of stability; the regeneration allowed to perform up to 9 measurements with a single sensor. The achieved LOD of 50 ng/mL is comparable with the performance of the 3D CMD chip, which confirms that the PP films are a promising alternative to the conventional surface modification techniques.

4   Catalytic Labels

4.1   Amperometric Detection of *M. plutonius* (Paper VIII)

Amperometric biosensors are devices based on the measurement of the current, corresponding to the analyte concentration, as a function of electrode potential or time. The amperometric methods can be used to determine the redox potential of the analyte, its electrochemical activity (adsorption, interaction with modified layers, electrocatalysis), but they are also sensitive to the changes of the electrode surface. In the case of amperometric catalytic biosensors, a suitab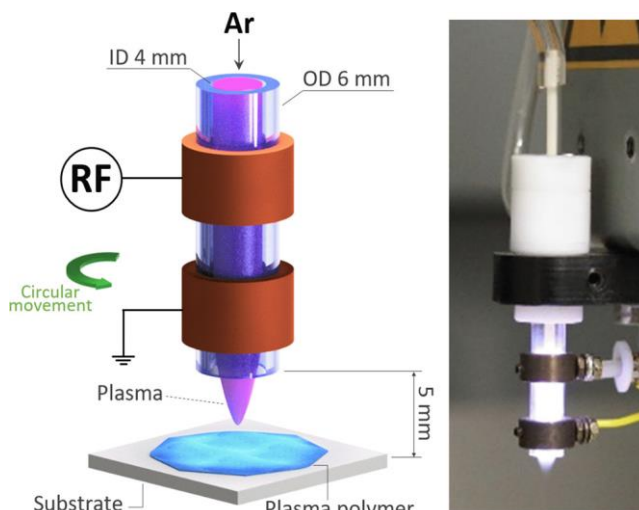le enzyme (or multi-enzyme system) is typically immobilized on the electrode, which catalyzes the transformation of the analyte; the concentration is determined from the measured current. In the case of amperometric immunosensors, the most common approach is based on labeling the analyte with a tracer (antibody conjugated with suitable enzyme); the analyte concentration is determined from the current measured upon the addition of the substrate solution.

The most common potential-controlled (potentiostatic) measurement techniques include (i) chronoamperometry based on the measurement of a current at a fixed potential in time; (ii) single-potential amperometry based on the measurement of direct current as a function of the potential difference between two electrodes, and (iii) multiple-potential amperometry based on sweeping the potential in time and recording the corresponding current in the whole potential window.[2]

We have developed a chronoamperometric biosensor for the detection of *Melissococcus plutonius*, the causative agent of honeybee disease European foulbrood (EFB). EFB can typically be found in honeybee larvae up to five days of age, which get infected by the ingestion of food contaminated with *M. plutonius*. Upon the infection, the larvae color changes from white to yellow or brown, and larvae usually die displaced in the brood cells instead of normal coiled position.[71] Because the infection can affect a large percentage of the brood, it can severely weaken the colony or even cause its collapse.

It is crucial to prevent the uncontrolled spreading of the EFB to limit the economic and environmental consequences of the honeybee colony losses. Therefore, there is a high demand for methods that can detect *M. plutonius* in the stages of EFB infections, ideally in the PoC format. The typical detection approach is based on the microscopic evaluation of smears stained by carbol fuchsin. However, the sensitivity of this approach is not high enough to reveal the EFB in its early stages. Cultivation-based methods traditionally exhibit very high sensitivity at the cost of high time demands. However, in the case of EFB, the analysis is complicated by the low cultivation recoveries of *M. plutonius* and overgrowing by secondary invaders.[71] The sensitivity, time-requirements, and throughput of the conventional methods can be overcome by using molecular detection methods based on either DNA or antibodies. Nowadays, real-time PCR is considered the gold standard for laboratory confirmation of *M. plutonius*.[71] Even though antibody-based methods are widely used to detect various pathogens,[72] they are not yet commonly used in the EFB diagnosis. There are no antibodies against *M. plutonius* commercially available; the need to prepare the antibodies in-house is clearly one of the factors limiting the faster growth of antibody-based methods for EFB. There is only a single report on the ELISA for the laboratory detection of *M. plutonius*.[73] Furthermore, an LFIA assay for EFB

was recently reported.[74] However, it allows only qualitative disease confirmation, suggesting room for more sensitive approaches.

To start working in the field of EFB diagnosis, we have first prepared a rabbit polyclonal anti-*M. plutonius* antibody, and tested it in an ELISA assay.[75] To develop an amperometric immunosensor based on a sandwich assay (**Figure 8A**), the antibody was immobilized to the gold working electrode via a self-assembled monolayer of cysteamine and glutaraldehyde. As the tracer, antibody conjugated with horseradish peroxidase (HRP) was used to provide electrochemical readout based on reducing the enzymatically oxidized 3,3′,5,5′-tetramethylbenzidine (TMB). Due to the use of the sandwich format, the effect of the complex sample matrix was suppressed compared to the label-free procedure based on EIS. Therefore, the amperometric approach is preferred for the analysis of complex samples of bees and larvae. The specific capture of *M. plutonius* on the sensor was verified by AFM. Even though the electrode exhibited substantial roughness, the bacteria were clearly visible.

The achieved LOD was 6.6×10^4 CFU/mL for the pure bacterial sample in the buffer, and the sensor provided a working range up to 10^9 CFU/mL (**Figure 8B**). In the case of the real sample analysis, LODs of 2.4×10^5 and 7.0×10^5 CFU/mL were achieved for homogenized bees and larvae, respectively. The experiments with *P. alvei* as a negative control confirmed the high selectivity of the assay. The achieved sensitivity, together with a short analysis time of 2 h, confirm the suitability of the developed sensor in PoC diagnosis of EFB.
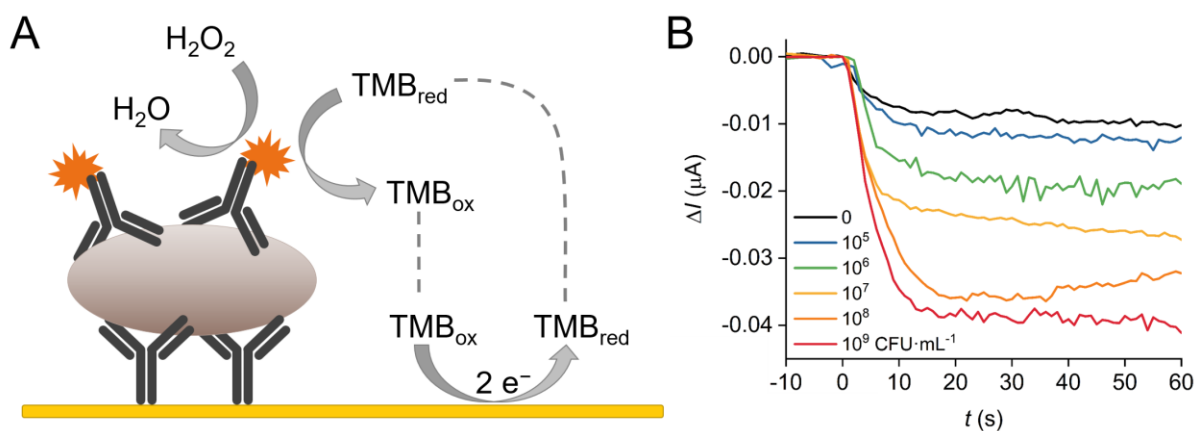
Figure 8: (A) Scheme of an amperometric immunoassay for the detection of *M. plutonius*. **(B)** Amperometric response traces after the addition of TMB in the *M. plutonius* detection. Adapted from Paper VIII with permission. Copyright 2019 Wiley-VCH.

4.2 Enzymatic Precipitation-Enhanced SPR Detection of *Salmonella* (Paper IX)

In recent years, various kinds of nanoparticles are being employed to enhance the performance of SPR immunosensors. For example, the application of gold nanoparticles in a sandwich format allowed to significantly increase the refractive index in the *Salmonella* detection.[76] Magnetic nanoparticles can provide signal amplification due to the increased refractive index and the immunomagnetic preconcentration.[77] However, the nanoparticle-based labels often suffer from a higher level of non-specific interactions compared to smaller molecules. To

overcome this limitation, a method of amplification based on enzyme-catalyzed precipitation of solid product on the sensor surface was developed.[78, 79] The approach found application mainly in electrochemical sensing, with reports on the detection of prostate-specific antigen (PSA),[80, 81] carcinoembryonic antigen (CEA),[82] as well as *E. coli*.[83]

We introduced a method for the detection of *Salmonella* using SPR immunosensor enhanced by biocatalyzed precipitation. Our strategy aimed to develop a highly sensitive, robust, and straightforward assay while maintaining a reasonably short analysis time. The assay was based on the formation of sandwich immunocomplex of capture antibody, *Salmonella*, and HRP-conjugated detection antibody (Ab$_2$-HRP). The HRP then catalyzed the conversion of 4-chloro-1-naphthol (4-CN) to insoluble benzo-4-chlorocyclohexadienone, which served as the signal enhancement step (**Figure 9A**).
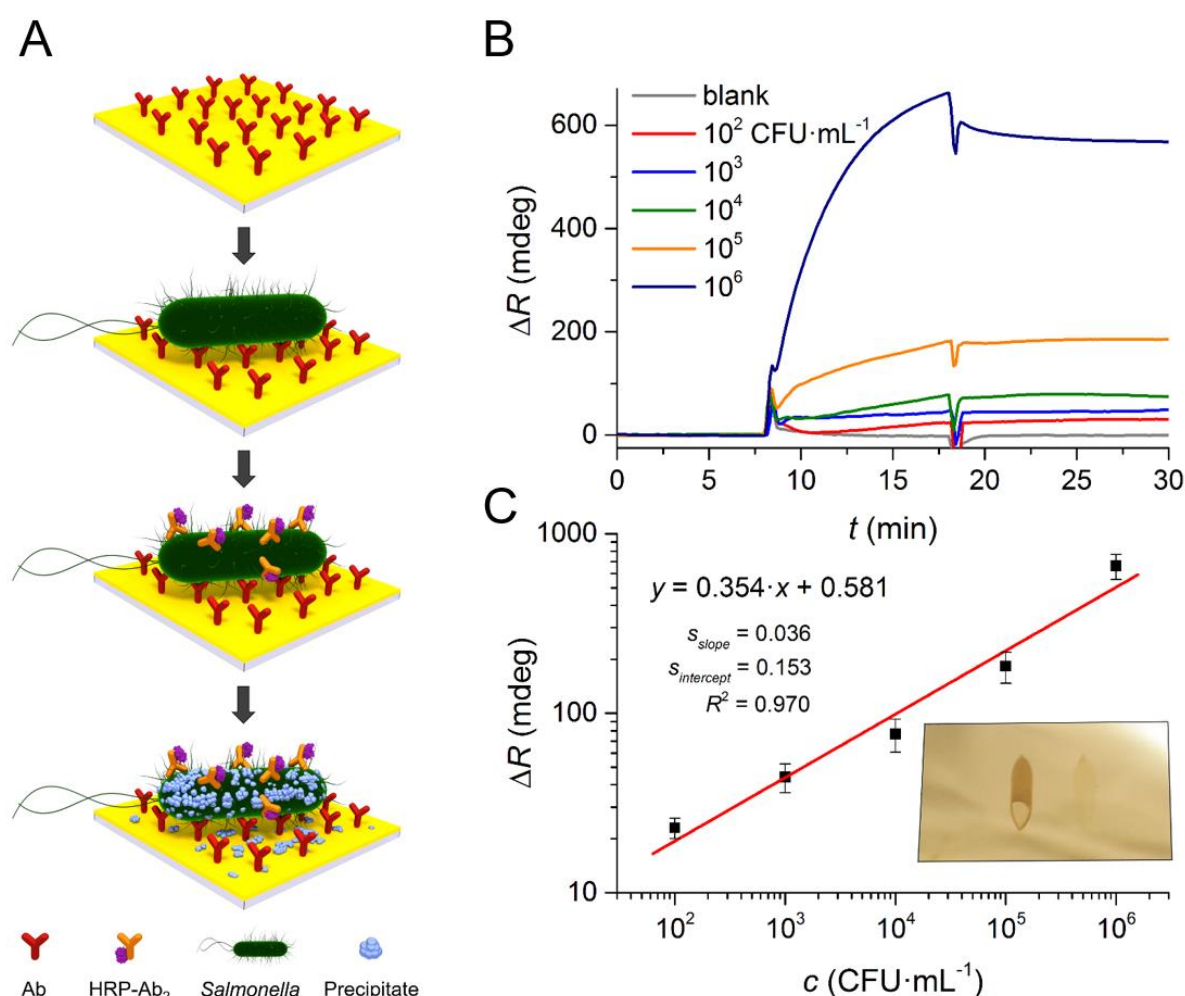
Figure 9: (A) Scheme of biocatalyzed precipitation-enhanced SPR detection of *Salmonella*. **(B)** SPR sensorgrams of the final step of biocatalyzed precipitation enhancement for different *Salmonella* concentrations. **(C)** Calibration curve. The inset shows the measuring chip after the precipitation reaction (antibody-modified channel – left, reference – right). Adapted from Paper IX with permission. Copyright 2016 American Chemical Society.

At the concentration of 10^7 CFU/mL, the signal change after precipitation enhancement was 40× higher than the signal with the bare bacterium. A closer look at the SPR signal changes in binding and reference channels revealed that even though some response was observed for the non-specific binding of *Salmonella*, there was practically no signal change upon injection of Ab$_2$-HRP conjugate. This led to the increase of the ratio between the binding and reference channel from 3.5 (after *Salmonella* binding) to 8.6 (after biocatalyzed precipitation). Even though the injection of *Salmonella* in a very low concentration of 100 CFU/mL led to signal change comparable to the level of noise, the following precipitation reaction allowed to increase the signal to clearly distinguishable levels, allowing to reliably determine even very low *Salmonella* concentrations (**Figure 9B**).

With the increasing concentration of bacteria, the measured signal increased exponentially. This suggests that several Ab$_2$-HRP conjugates can be bound on a single *Salmonella* cells, leading to the precipitation of a large number of 4-CN molecules. This is a significant advantage to nanoparticle-based signal amplification, which leads only to linear enhancement of the signal.[84] The obtained dependence of $\log(\Delta R)$ on $\log(c)$ was linear from 10^2 to 10^6 CFU/mL, and the LOD was evaluated to be 100 CFU/mL (**Figure 9C**).

The total assay time was 60 min, which is substantially shorter than the conventional methods for the detection of bacteria, including cultivation (~ days),[85] ELISA (~ 10 h),[86] and PCR (~ hours).[87, 88] The analysis time is also shorter than in other reports on the amplification of SPR response with nanoparticles while achieving similar or better LOD.[76, 84] Furthermore, the real-time operation of SPR can reveal higher bacteria concentrations in a short time upon sample injection (~ 10 min), allowing a rapid reaction even before the signal amplification is finished.

After the measurement, the SPR chip was removed from the system and analyzed by the AFM. It was visible already by the naked eye that there was more precipitate formed in the measuring channel compared to the reference. AFM revealed the presence of bacteria and a large number of precipitate particles (~ 22,000 particles on the area of $20{\times}20\ \mu m^2$). Even though the reference channel also contained some precipitate particles, the number was significantly lower (~ 3,000 particles on $20{\times}20\ \mu m^2$). The 6.9-fold difference in the number of precipitate particles found by AFM corresponds to the 8.6-fold difference in SPR response for the same concentration. A closer look at the individual *Salmonella* before and after the precipitation revealed the presence of precipitate particles, leading to a three times increase of the height upon the precipitation (**Figure 10**).

To demonstrate the applicability of the developed method for analyzing real samples, *Salmonella* was detected in powdered milk. Although immunosensors used specific antibodies to ensure selective detection, components of complex samples can still exhibit non-specific binding towards the sensor surface. However, as the Ab$_2$-HRP conjugate used in our method is specific towards *Salmonella*, the potential non-specific binding is not transferred to the signal amplification step, contributing to the high selectivity of the method. In powdered milk, the achieved LOD was 10^3 CFU/mL, which is deterioration by one order of magnitude compared to the analysis in the buffer. This was probably caused by the non-specific adsorption of milk components, which can block some of the antibodies in the sensor surface or conceal some

epitopes on *Salmonella*. The ID_{50} (the number of bacteria that have to be ingested to result in 50% infection probability) of *Salmonella* is considered to be $> 10^4$ CFU.[89] Furthermore, it was shown that ingestion of low *Salmonella* levels below 10^2 CFU/g does not pose a risk to human health.[90] Therefore, the performance of the developed SPR immunosensor is suitable for the practical analysis of *Salmonella* in contaminated food samples.
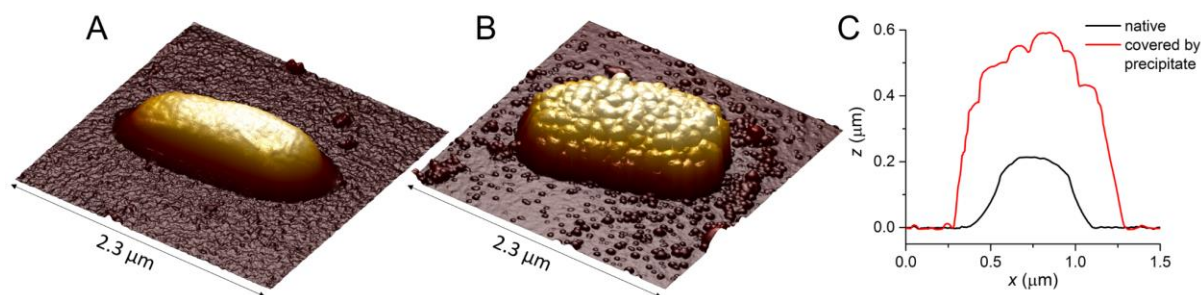
Figure 10: 3D representation of the AFM scan of **(A)** native and **(B)** precipitate-covered individual *Salmonella* cells. **(C)** Cross-sections of the bacteria evaluated as perpendicular lines in the center. Reprinted from Paper IX with permission. Copyright 2016 American Chemical Society.

4.3 Nanozyme-Linked Immunosorbent Assay (Paper X)

The typical catalytical labels used in immunoassays are represented by enzymes, especially HRP. However, the enzymes suffer from several disadvantages, including the high cost of their production, limited stability, and activity reduction upon conjugation with immunoreagents. The properties of conventional enzymes can be overcome by using catalytic nanomaterials – nanozymes.[91, 92] Compared to the biomolecules, the inorganic nanomaterials provide very high thermal and chemical stability.[93] In particular, nanozymes with high peroxidase-like activity are preferred for immunoassays due to the compatible assay procedure with conventional ELISA.

Nanozyme production can be done using aqueous solutions and benign precursors, making the procedure eco-friendly.[94] The peroxidase-like activity was first discovered for magnetite nanoparticles (Fe_3O_4), followed by many other nanomaterials, including CeO_2, CuO, Co_3O_4, and MnO_2 nanoparticles, graphene oxide nanoplates, or Prussian blue nanoparticles (PBNPs).[95, 96]

We have introduced a method for the conjugation of PBNPs with antibodies and applied the conjugates in a nanozyme-linked immunosorbent assay (NLISA). The conjugation was based on the modification of the PBNP surface by reductively denatured bovine serum albumin (BSA), followed by the oxidation of antibodies by sodium periodate and binding them to the amino group of BSA (**Figure 11**). We have developed two sandwich NLISA assays, first for the detection of HSA in urine and the other for the detection of *Salmonella* in powdered milk. Because the oxidation of TMB to the blue product was utilized in the assay, the readout could be done using a standard colorimetric reader without special requirements on instrumentation.

For the analysis of HSA in urine, the possible trace amounts of HSA present in the urine of healthy donors were first removed using centrifugal ultrafiltration on a 10-kDa membrane, followed by spiking known HSA concentrations. Even though the urine contains various ions,

which can cause undesired oxidation of TMB, the heterogeneous format with several washing steps allowed to overcome this limitation. As a result, only small differences were observed between HSA analysis in the buffer and urine. Microalbuminuria, which happens due to diabetic nephropathy, is connected with HSA concentrations from 20 to 200 µg/mL in the 24 h specimens.[97] The optimized NLISA provided an LOD of 1.2 ng/mL of HSA in urine and a working range up to 1 µg/mL (**Figure 12**). This confirms that the NLISA is suitable for the practical diagnosis of microalbuminuria.

Figure 11: Scheme of PBNP-Ab conjugate synthesis. The PBNPs are modified by denatured BSA to introduce amino groups on their surface, and the oxidized antibody is conjugated *via* the aldehyde groups. Reprinted from Paper X with permission. Copyright 2018 American Chemical Society.

Comparing the performance of NLISA with ELISA based on the same immunoreagents has shown only a small difference in LODs (1.2 ng/mL for NLISA and 3.7 ng/mL for ELISA). The comparable results suggest that the primary limiting step of the assay is not the detection step but rather the antibody affinity. Nevertheless, PBNPs offer several practical advantages, including higher stability, simple and cheap synthesis, and the possibility of catalyzing higher concentrations of TMB. As the shelf-life of PBNPs is practically unlimited (several years at 4 °C), antibodies are becoming the main limiting element. Therefore, the overall stability of the detection label could be, in the future, improved by replacing antibodies with MIPs or aptamers.

Figure 12: Scheme of sandwich NLISA and calibration curve for HSA detection in spiked urine. Reprinted from Paper X with permission. Copyright 2018 American Chemical Society.

The universal applicability of PBNPs as immunoassay labels was also demonstrated by detecting *Salmonella* in powdered milk. The incubation with milk served as an additional blocking step and had a minimum effect on the LOD. The optimized assay provided LOD of 6×10^3 CFU/mL with a working range up to 10^6 CFU/mL. This performance is better than the published ELISA assays that provide LODs between 10^4 and 10^6 CFU/mL.[28, 98] The comparison with ELISA based on the same immunoreagents (LOD 3×10^3 CFU/mL) confirmed that the choice of antibodies affects the assay performance more significantly than the label. Overall, PBNPs proved to be a suitable alternative to conventionally used HRP; the detection of peroxidase-like activity is compatible with standard instrumentation and methodologies. Furthermore, the nanoparticle-based labels provide higher stability than biomolecules with the possibilities for cheap and large-scale production.

5 Photon-Upconversion Nanoparticles

Photon-upconversion nanoparticles (UCNPs) are lanthanide-doped nanocrystals, which exhibit anti-Stokes emission. The energy transfer upconversion belongs to the non-linear optical processes and is based on the absorption of two or more photons, resulting in the emission of a single photon with higher energy (shorter wavelength).[99] Compared with other anti-Stokes processes, including two-photon excitation and second harmonic generation, the excitation of upconversion can be done at lower energy densities. Even though the upconversion process was discovered already in the 1960s,[100] it was only used in the form of bulk crystalline or glass materials.[101] The composition of inorganic upconversion phosphor is based on a crystalline host matrix (typically $NaYF_4$) with a dopant included at a low concentration (typically Yb^{3+} and Er^{3+} or Tm^{3+}). The dopant ensures luminescence, while the crystal structure of the host lattice provides a matrix to bring the dopant ions into the optimal position.[102]

Due to the remarkable progress in nanotechnology, methods for the synthesis of upconversion nanomaterials were discovered, leading to UCNPs with high luminescence efficiency. Compared to conventional luminescence labels, such as organic fluorophores or QDs, UCNPs can be detected without autofluorescence background, they provide large anti-Stokes shifts allowing easy separation of the excitation and detection channels, exhibit excellent photostability, and the emission wavelength is tunable to enable multiplexed detection.[102]

The synthesis of UCNPs is typically done in hydrophobic solvents, such as oleic acid and octadecene. Therefore, their surface has to be modified for biological applications.[103] One of the most widespread surface modification techniques is silanization. It is based on the hydrolysis and condensation of siloxane precursors, typically tetraethyl orthosilicate[104] with other derivatives of silane, to provide functional groups for further bioconjugations.[105] Other modification techniques are based on exchanging the hydrophobic surface ligands by ligands with hydrophilic properties. Ligands bearing phosphonate or carboxylate groups can coordinate to the lanthanide ions on the UCNP surface; the functional groups on the other end of the ligand are then used for the bioconjugation.[106]

Throughout our extensive work in the UCNP field, we have explored different ways of UCNPs surface modifications and employed the conjugates to develop immunoassays for a wide range of analytes, from small molecules to bacteria.

5.1 Competitive Upconversion-Linked Immunosorbent Assays

5.1.1 Competitive ULISA for Diclofenac (Papers XI and XII)

Diclofenac (DCF) is a widely used non-steroidal anti-inflammatory drug. The widespread use of DCF for cattle treatment in the Indian subcontinent has led to significant vulture population losses in the 1990s because DCF caused renal failure in vultures feeding on contaminated carcasses.[107] DCF is one of the most frequently analyzed pharmaceuticals in the water-cycle in Europe because it cannot be easily degraded in water treatment plants. It was detected in the amounts of low µg/L wastewater effluents and amounts of ng/L in surface waters,[108] groundwater, and drinking water.[109] The sensitive detection of DCF is typically done by LC-TOF-MS or high-resolution mass spectrometers.[110] However, these methods require expensive

instrumentation with trained personnel, and the analysis is lengthy. On the other hand, ELISA assays are highly suitable for analyzing a large number of samples, even in smaller, less-equipped laboratories.[111]

In our pioneering work on the immunoassay based on UCNPs – the upconversion linked immunosorbent assay (ULISA) – we have synthesized conjugates of UCNPs with detection anti-mouse antibody and applied them in an indirect competitive assay for DCF (**Figure 13A**). We have synthesized oleic acid-capped UCNPs and coated them with a silica shell bearing carboxyl groups on the surface. This modification was used to improve the water dispersibility and conjugate antibodies using EDC/sulfo-NHS chemistry.[112]

The coating antigen in a competitive immunoassay has to be, on hand, in low-enough concentration to allow efficient competition for the binding sites of the detection antibodies, but, on the other hand, its concentration still has to provide strong-enough signals. To achieve the optimal assay performance, we have prepared and characterized two different coating conjugates by modifying bovine serum albumin (BSA) with DCF. The MALDI-TOF mass spectrometry analysis revealed that the conjugates carried either 5.7 or 10 DCF molecules per BSA. Even though the conjugate with the higher degree of derivatization provided about twice as high signals, larger signal fluctuations and hook effect were observed. On the other hand, the conjugate with 5.7 DCF molecules per BSA provided better signal stability, slightly lower IC_{50} value (1.2 ng/mL compared to 1.5 ng/mL), and lower LOD. The optimized ULISA assay provided an LOD of 0.05 ng/mL, which was five times higher than the LOD of a conventional ELISA (0.01 ng/mL; **Figure 13B**). However, the ULISA allowed for a faster and easier signal generation. However, it was most notably a first step in the further development of ULISA assays that were eventually going to reach a single-molecule sensitivity.
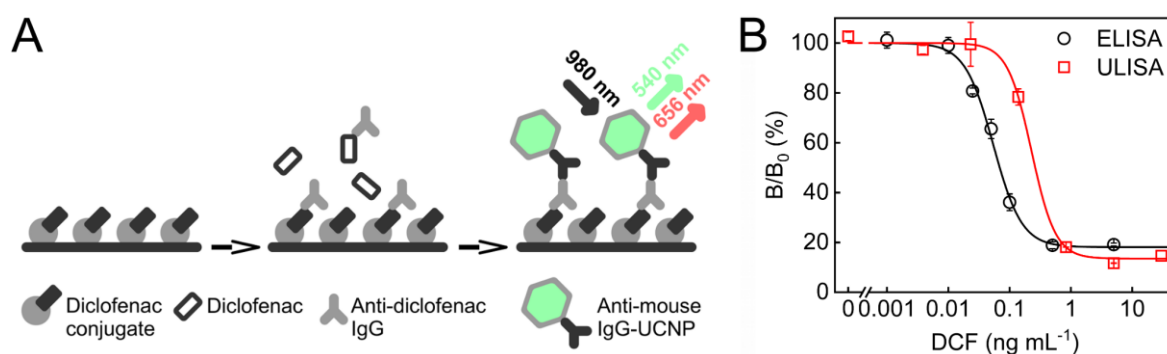
Figure 13: (A) Scheme of indirect competitive ULISA for the detection of DCF. A microtiter plate is coated with a BSA-DCF conjugate, dilution series of DCF are prepared in the microtiter plate followed by the addition of anti-DCF mouse antibody, and the attachment of anti-DCF antibody is detected by a conjugate of secondary antibody with UCNP. **(B)** Normalized calibration curves of ULISA and ELISA. Adapted from Paper XI with permission. Copyright 2016 American Chemical Society.

In the follow-up work, we focused on improving the LOD and reducing the analysis time by designing a single-step ULISA assay (**Figure 14A**). For the synthesis of the DCF tracer, we have prepared a conjugate to DCF with bovine γ-globulin (BGG) and conjugated it on the surface of UCNPs with a carboxylated silica shell. The DCF-BGG conjugate was used

because it provided structural flexibility between the DCF and the UCNPs, and it prevented non-specific binding of the tracer to the microtiter plate. Because the UCNP-DCF tracer was used to directly compete with the analyte DCF for the binding on the immobilized anti-DCF antibody, the assay was done in a single step. Furthermore, we have optimized a method for the lyophilization of the tracer, which did not negatively affect its performance even after prolonged storage at room temperature. The single-step analysis and the possibility of storing the tracer in a dry state without the necessity of cooling makes the ULISA an excellent option for environmental analysis in low-resource settings.[113]

The optimized assay provided an LOD of 0.02 ng/mL with a signal-to-background (*S*/*B*) ratio of 82 (**Figure 14B**). The high value of *S*/*B* was enabled by (i) the high brightness of the used UCNPs with a diameter of 90 nm, (ii) the low level of non-specific interaction due to the coating with BGG, and (iii) the presence of multiple DCF molecules per single UCNP ensures efficient competition even when the molar concentration of tracer is significantly lower than the concentration of DCF. Finally, we have demonstrated the practical potential of the method on the successful analysis of real samples of drinking and river water.
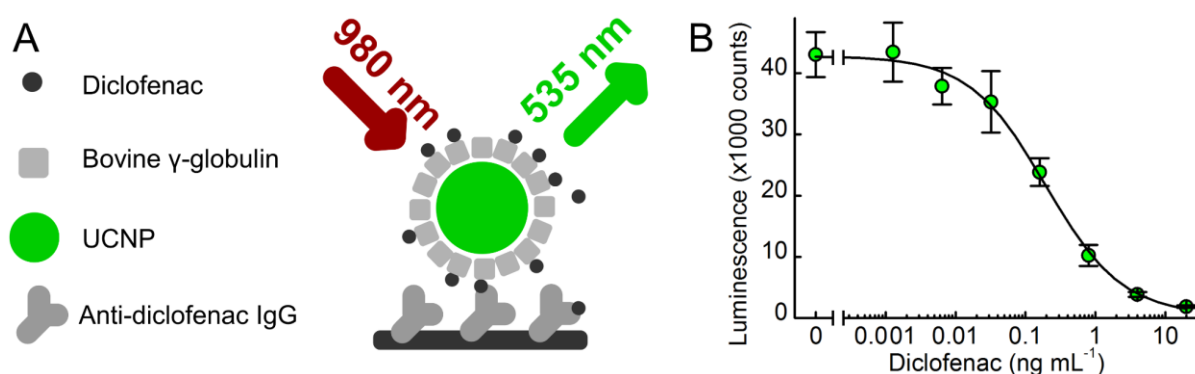
Figure 14: (A) Scheme of single-step competitive ULISA for the detection of DCF and **(B)** calibration curve. Adapted from Paper XII with permission. Copyright 2017 Springer.

5.1.2   Competitive ULISA for Zearalenone (Paper XIII)

We have also developed an assay for the analysis of mycotoxin zearalenone, based on the competition with epitope mimicking peptide. Microbial toxins are produced by many pathogenic microorganisms (bacteria and fungi) and act as their virulence agents. They are represented by a heterogeneous group of compounds that interfere with biochemical processes, including the function of membranes, transport of ions, release of transmitters, and synthesis of macromolecules. Exposure to the toxins either in food or in the environment can cause significant health problems; the individual symptoms vary significantly between the different toxins.[114] Unlike in the case of viable bacteria, toxins are typically not affected by the heat processing of the product.

Zearalenone (ZEA) is a non-steroidal estrogenic mycotoxin produced by several fungi species of the *Fusarium* genus.[115] Even though the acute toxicity of ZEA is relatively low, it is chronically toxic and has been connected with reproduction disorders of farm animals, mainly pigs.[116] ZEA exhibits estrogenic, genotoxic, haematotoxic, and anabolic effects.[117] Along with

other mycotoxins, ZEA is often found in agricultural products, including maize, wheat, barley, rice, and oats.[118]

Epitope mimicking peptides, also referred to as mimotopes, are used as an alternative to conventional analyte-conjugates in competitive immunosensing. Such peptides mimic the epitope of the analyte and allow competition with the native analyte for binding to the antibody. Even though antibodies with high affinity are required in all immunoassay, competing peptides with lower affinity can be beneficial for competitive assays. They shift the equilibrium towards analyte binding, making a smaller amount of analyte produce the same response level.[119]

Based on the previously identified amino acid sequence,[120] we have synthesized the peptide mimetic of ZEA, introduced biotin on its C-terminus, and used it in an ULISA assay for ZEA detection (**Figure 15**). The specific anti-ZEA antibody was bound on the surface of the microtiter plate, allowing competition between analyte ZEA and biotinylated peptide mimetic. The detection was carried out using the conjugate of UCNPs with streptavidin. The optimized assay provided an LOD of 20 pg/mL with a working range up to 0.5 ng/mL, representing a 200-fold improvement of LOD and 3-fold improvement of working range compared to the previously reported bioluminescence immunoassay with the same peptide mimetic.[120]
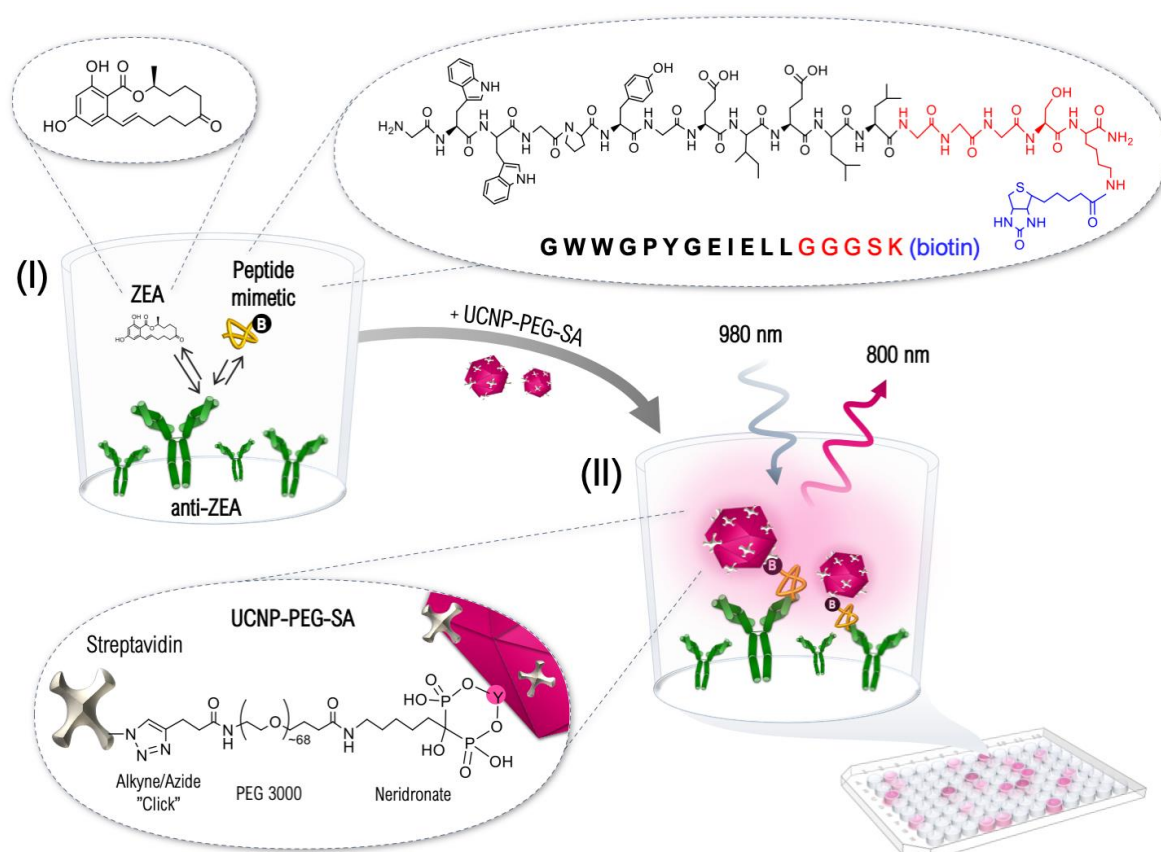
Figure 15: Scheme of competitive ULISA for ZEA. In the first step, a microtiter plate is coated with an anti-ZEA antibody, and ZEA in the sample competes with the biotinylated peptide mimetic for a limited amount of antibody binding sites. In the second step, the conjugates of UCNPs with streptavidin bind to the biotinylated peptide. Reprinted from Paper XIII with permission. Copyright 2020 Elsevier.

To confirm the potential of ULISA for the analysis of complex samples, analysis of ZEA-free maize samples (as confirmed by UPLC-MS/MS) spiked with ZEA was done. The recoveries between 77% and 105% demonstrate the suitable accuracy for quantitative real sample analysis. Furthermore, in comparison with UPLC-MS/MS, ULISA is based only on a simple extraction in methanol and does not require extensive sample pre-treatment. The achieved performance fulfills the requirements given by the European legislation, which confirms the suitability of ULISA as a tool for simple analysis of food samples contaminated by mycotoxins.

5.2   Sandwich Upconversion-Linked Immunosorbent Assays

5.2.1   Detection of *M. plutonius* with BSA-Modified UCNPs (Paper XIV)

UCNPs are also highly useful as labels in sandwich immunoassays. We have introduced a method to conjugate UCNPs with streptavidin based on a copper-free click reaction and used this conjugate to detect *M. plutonius*, the causative agent of European foulbrood (**Figure 16**). The conjugation was based on strain-promoted cycloaddition between bicyclo[6.1.0]nonyne (BCN) groups bound on the UCNP surface via BSA and azide-modified streptavidin.[121] Apart from serving as an intermediate to bind the BCN, BSA also contributes to the reduction of non-specific binding of the UCNP conjugates.
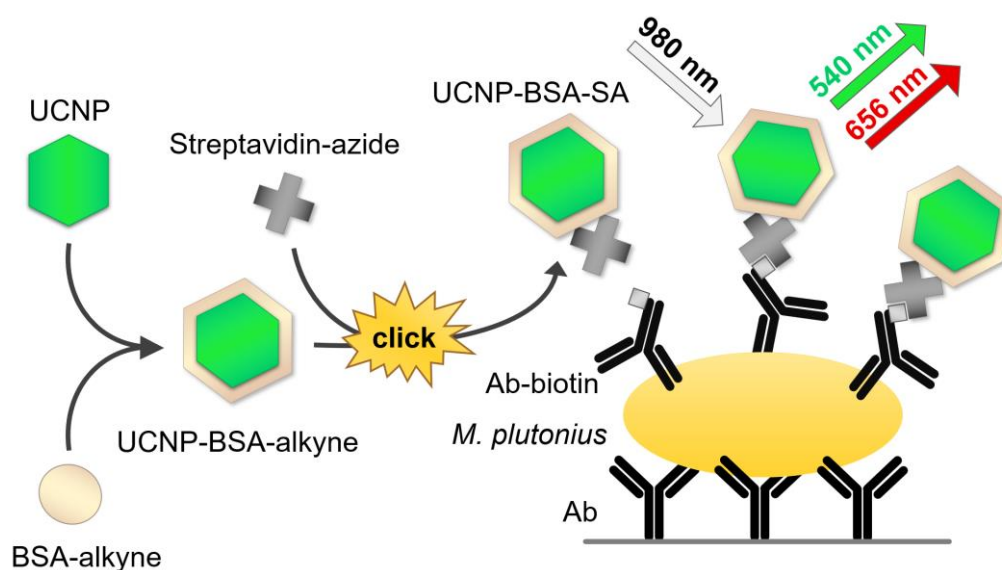
Figure 16: Scheme of the conjugation of UCNP with streptavidin based on functionalization of UCNP surface with alkyne-modified BSA and click reaction with azide-modified streptavidin. The conjugates are then employed as a label in a sandwich ULISA for the detection of *M. plutonius*. Reprinted from paper XIV with permission. Copyright 2019 Royal Society of Chemistry.

The bioconjugation reaction was followed using agarose gel electrophoresis based on fluorescence labeling of BSA-BCN and streptavidin-azide. The overlap of the fluorescence signals, together with the mobility shift, confirmed the successful progress of the conjugation reaction. Furthermore, the presence of BSA and streptavidin on the UCNP surface was confirmed by mass spectrometry. After the digestion of proteins on the UCNP conjugates by trypsin, the UCNP cores were removed by centrifugation, and the samples were analyzed by

LC-MS/MS. Both BSA and streptavidin were successfully identified; according to the integrated signal intensities, BSA was detected as the most abundant protein in the sample. The amount of streptavidin was approximately one order of magnitude lower than the amount of BSA.

First, we have optimized ULISA on the detection of *M. plutonius* in the buffer. The assay provided an LOD of 340 CFU/mL and a wide working range up to 10^9 CFU/mL. This LOD is 400 times better in comparison with ELISA (**Figure 17**). Since the same antibodies were used in both assays, the most significant impact on

Figure 17: Comparison of sandwich ULISA and ELISA assays for the detection of *M. plutonius*. The normalized signals were calculated by dividing the data by y_{MAX} value from the logistic fit. Reprinted from Paper XIV with permission. Copyright 2019 Royal Society of Chemistry.

enhancement can be accounted to the high label performance, providing a highly sensitive readout of anti-Stokes emission and the low non-specific binding. To demonstrate the practical applicability of the assay, real samples of bees, larvae, and bottom hive debris were analyzed, representing the typical matrices where *M. plutonius* has to be detected during the infection by EFB. The achieved LODs were 540 CFU/mL for bee extract, 8.5×10^3 CFU/mL for larvae extract, and 570 CFU/mL for bottom hive debris. The level of *M. plutonius* in infected apiaries with clinical symptoms is typically around 10^5 CFU/mL,[122] demonstrating the suitability of the developed ULISA for the practical EFB diagnosis in the early stages of the infection.

5.2.2 Preparation of PEG-Modified UCNPs and Analysis of HSA (Paper XV)

In our next work, we have introduced a different strategy for UCNP surface modification based on coating the particles with a PEG linker and applying the conjugates in a sandwich immunoassay for the detection of albuminuria marker HSA. For the surface modifications, we have chosen heterobifunctional PEG with neridronate, and alkyne or maleimide functional end-groups based on these considerations; (i) PEG can sterically stabilize the particles and resist the non-specific interactions with surfaces and biomolecules;[123] (ii) neridronate shows strong coordination towards lanthanide ions of UCNPs;[124] and (iii) the alkyne or maleimide groups can be used for the subsequent conjugation of biomolecules.[125] The first conjugation approach was based on attaching azide-modified antibody or streptavidin to the alkyne groups *via* click reaction (**Figure 18**). Alternatively, the disulfide bonds in the antibody were reduced by TCEP, and the generated thiol moieties were bound to the maleimide groups.
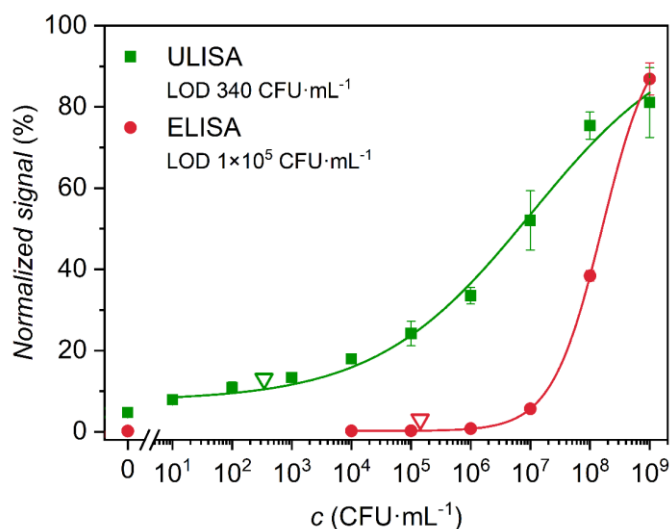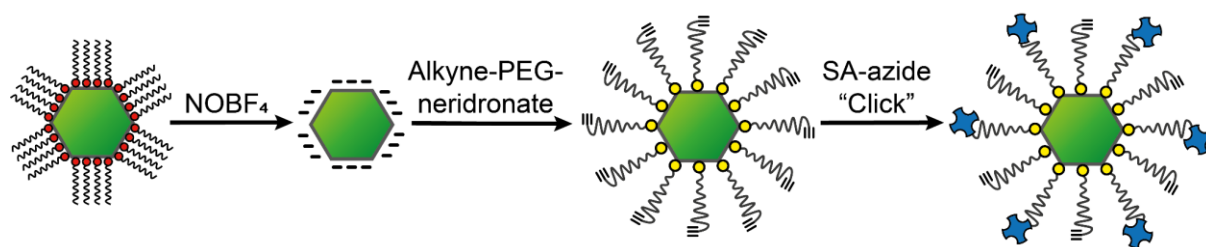
Figure 18: Scheme of the preparation of PEG-based conjugates of UCNPs with streptavidin. The oleic acid on the surface of as-synthesized UCNPs was removed by a ligand exchange reaction with nitrosonium tetrafluoroborate to prepare water-dispersible nanoparticles. The particles were then coated with an alkyne-PEG-neridronate linker, and streptavidin-azide was coupled *via* copper-catalyzed click reaction.

The prepared bioconjugates were used in the sandwich ULISA assay for HSA detection. To allow efficient use in immunoassay, the nanoparticle-based labels must provide not only a high level of modification with biorecognition molecule to allow specific binding, but the conjugates must also show high uniformity with a small number of aggregates to reduce the signal fluctuations.

First, we have tested the UCNPs modified by antibody *via* alkyne-azide click reaction. Two different ratios between the antibody and NHS-PEG-N$_3$ were tested. Even though higher signals were observed in the case of conjugate based on antibody with a higher number of azide molecules, there was no positive effect on the LOD. This can be explained by the higher number of aggregated conjugates, resulting in higher signal fluctuation. The optimized ULISA based on these particles provided an LOD of 3.5 ng/mL and a working range up to 1 μg/mL. In contrast, the antibody conjugates based on maleimide coupling provided higher signals and slightly lower background, resulting in the improvement of the LOD to 0.24 ng/mL and an unchanged working range up to 1 μg/mL. The conjugates with streptavidin reached an even lower LOD of 0.17 ng/mL (**Figure 19**). This can be explained by the more efficient binding of the streptavidin-coated UCNPs to the biotinylated antibody, caused mainly by the flexibility of the additional antibody present in the immunocomplex compared to the binding directly to the antigen. The comparison with ELISA (LOD 0.56 ng/mL) and fluorescence immunoassay (LOD of 0.59 ng/mL) based on the same immunoreagents demonstrated that the use of UCNPs is advantageous in term of assay performance compared to the conventional labels.
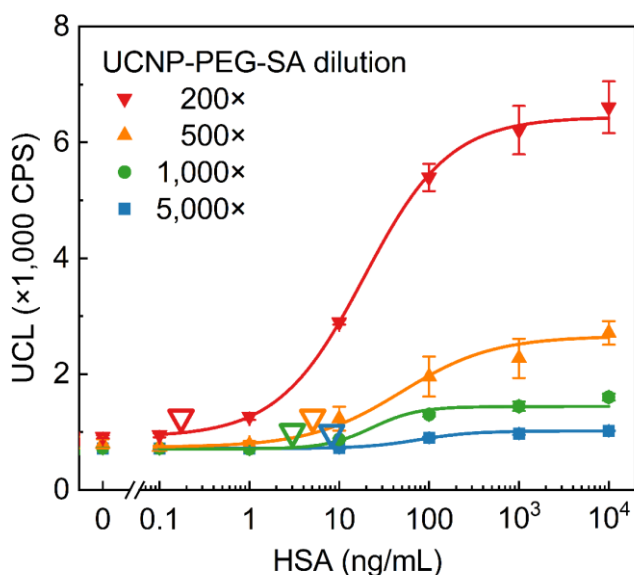
Figure 19: ULISA for the detection of HSA with UCNP-PEG-SA label. Adapted from Paper XV with permission. Copyright 2020 American Chemical Society.

The optimized assay based on streptavidin-conjugated UCNPs was then used for the analysis of HSA in spiked urine. A slightly higher baseline was observed for the urine compared to the buffer, which was probably caused by the presence of some HSA levels, even in the samples from healthy donors. However, this did not affect the ability to specifically detect the HSA, demonstrating the potential of the method for practical applications.

5.2.3 Detection of *P. larvae* with PEG-Modified UCNPs (Paper XVI)

Afterward, we have employed the PEG-based UCNP conjugates to detect spore-forming bacterium *Paenibacillus larvae*, the causative agent of American foulbrood (AFB). AFB represents the most dangerous honeybee brood disease and causes significant economic losses throughout the world.[126] The honeybee larvae are infected by ingesting the fee contaminated by spores. The spores then germinate and colonize the midgut of the larvae, which is followed by spreading the bacteria over the midgut epithelium and the body cavity of the larva.[127] The dead larvae are found as a glue-like mass sticking to the side of the honeycomb cell, which is used as the typical sign for the AFB diagnosis. Afterward, the bacteria sporulate, and the spores are spread around the hive by the adult honeybees, which results in the infection of more larvae by the ingestion of contaminated food reserves. The spores can be found not only in the diseased larvae and the resulting dry scales but also in adult worker bees, honey, bottom hive debris, beehive surfaces, and beekeeping equipment.[128]

Because the spores are highly resilient, the discovery of infection is usually connected with burning down the honeybee colonies, as well as the contaminated equipment.[129] Therefore, sensitive diagnostic approaches are required to allow early diagnosis, preventing the infection from spreading further.[130] The traditional diagnosis of AFB is based on observing the clinical signs within the hive. Microscopic evaluation of stained smears from diseased larvae can be used for fast detection; however, the sensitivity of this approach is not high enough to diagnose the infection in its early stages.[131] On the other hand, culture-based methods provide excellent sensitivity, but the cultivation takes several days, making this approach not suitable for screening purposes.[132] Currently, PCR is considered the gold standard for AFB diagnosis, as it combines high sensitivity with fast analysis.[132, 133] However, PCR-inhibitors and other contaminants in the honeybee material can complicate the analysis of real samples.[134] The development of immunochemical methods for AFB diagnosis is generally hampered by the lack of commercially available antibodies against *P. larvae*. Even though there was a single report on the ELISA for the AFB diagnosis,[135] its sensitivity did not allow detecting sub-clinical *P. larvae* levels.

We have prepared a rabbit polyclonal anti-*P. larvae* antibody and used it in ULISA assay to allow early diagnosis of AFB. Cell wall fraction of *P. larvae* was used for the immunization of two rabbits. However, only one serum was used for further experiments because the other showed high cross-reactivity with *M. plutonius*. Even though affinity purification is generally used to suppress the cross-reactivity of generated antibodies, it was not possible here because of the complex nature of the used antigen.[136] Therefore, all IgGs present in the antiserum were isolated by the purification on protein G affinity column.

First, an ELISA assay was used for testing the antibody specificity. To allow performing a sandwich assay, the antibody was conjugated with biotin, and the conjugate of streptavidin

with HRP (SA-HRP) was used as a tracer. The assay provided an LOD of 6.5×10^4 CFU/mL and a *S/B* ratio of 34. This performance is comparable with the LOD of 1×10^5 CFU/mL published by Olsen et al.;[135] however, it is not sufficient to analyze sub-clinical levels of the bacterium.

Therefore, the SA-HRP conjugate was replaced by the streptavidin-coated UCNPs (**Figure 20A**) in the ULISA assay (**Figure 20B**). The *S/B* value of 128 was achieved in the optimized assay, representing a 4-fold improvement compared to the ELISA. In the case of negative controls of *P. alvei*, *M. plutonius*, and *B. laterosporus*, only small signal changes were observed compared to the target bacterium *P. larvae*. The assay provided an LOD of 2.9×10^3 CFU/mL (**Figure 20C**), which is 22 times better than the ELISA with the same antibody, clearly demonstrating the advantage of the labels based on UCNPs. Finally, the successful analysis of real samples of bees, larvae, and bottom hive debris showed the potential of ULISA in the practical diagnosis of AFB.
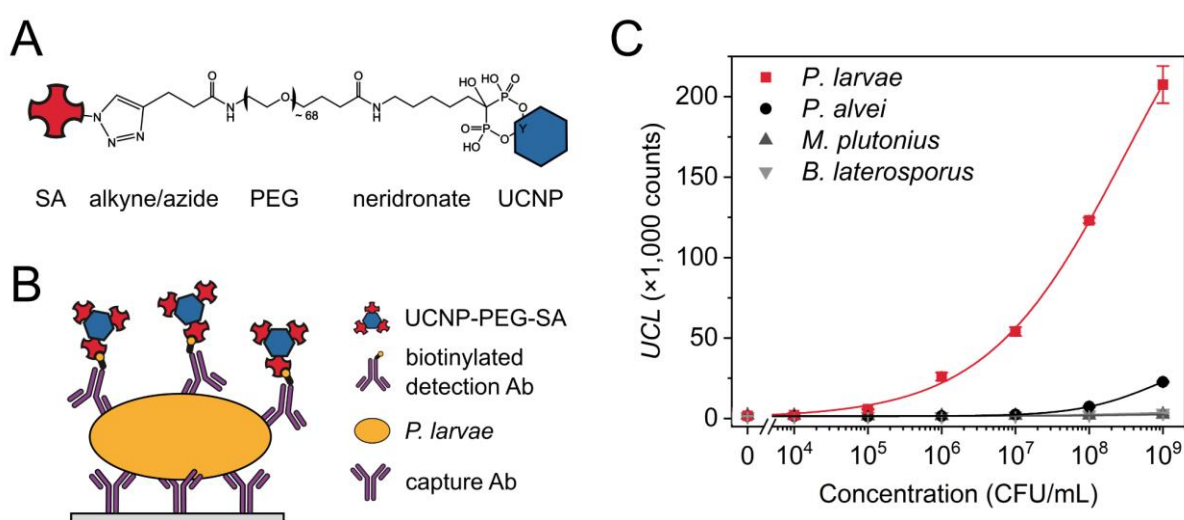
Figure 20: (A) Structure of UCNP-PEG-SA conjugate. **(B)** Scheme of sandwich ULISA for the detection of *P. larvae*. **(C)** Cross-reactivity testing of ULISA with P. *larvae* as a specific target and *P. alvei*, *M. plutonius*, and *B. laterosporus* as negative controls. Adapted from Paper XVI with permission. Copyright 2021 IEEE.

5.3 Single-Molecule Upconversion-Linked Immunosorbent Assays

5.3.1 Digital ULISA for PSA (Papers XVII and XVIII)

Due to the very low optical background, it is even possible to detect individual UCNPs. We have developed an approach allowing visualization of single UCNPs under a conventional epiluminescence microscope and used it in a single-molecule assay of cancer biomarker prostate-specific antigen (PSA). Prostate cancer is globally the fifth leading cause of death from cancer and the most often diagnosed cancer type among men.[137] PSA is secreted by the epithelial cells of the prostate in a typical concentration in healthy men below 4 ng/mL; the increase above this level can be used in the prostate cancer diagnosis.[138] When the carcinoma is removed by the radical prostatectomy, the PSA levels decrease significantly.[139] However,

repeated monitoring of PSA is still necessary because the increase from levels below 0.1 ng/mL to consistently above 0.2 ng/mL is connected with the biochemical recurrence,[140] which occurs in up to 40% of cases after the surgery.[141] This highlights the need for sensitive assays to detect the recurrence of cancer as early as possible.

In the first step, we have modified an epifluorescence microscope Nikon Eclipse Ti-E for the imaging of UCNPs (**Figure 21**). The microscope was equipped with a 980-nm excitation laser, 100× heat resistant objective, and suitable filter sets to detect upconversion luminescence of Er- and Tm-doped UCNPs. For optimizing the setup, carboxylated UCNPs with sizes from 37 to 90 nm were immobilized on a glass slide modified by cationized BSA. The excitation by 980-laser resulted in a very low background that – when there were no UCNPs present on the surface – depended

Figure 21: Scheme of upconversion microscope. The inset shows individual UCNPs as diffraction-limited spots. Adapted from Paper XVII with permission. Copyright 2017 American Chemical Society.

only on the signal noise of the camera. All tested UCNP types were visible as individual diffraction-limited spots with a diameter of ~ 400 nm; the number of detected UCNPs was directly proportional to their concentration.

Microtiter plates with a thin foil (190 µm) at the bottom of each well were used in an immunoassay because of the short working distance of the objective with the high numerical aperture. The assay was based on the sandwich immunocomplex of the capture antibody, PSA, and the conjugate of silica-coated UCNPs with detection antibody. First, the upconversion luminescence was read out by a conventional microtiter plate reader (analog ULISA), followed by counting the individual immunocomplexes under the microscope (digital ULISA). There was a small number of upconversion spots visible, in the case of the blank with no PSA in the samples, which corresponds to the non-specific binding of UCNPs to the surface of the microtiter plate and defines the LOD similarly as in the conventional immunoassays. However, compared to the analog readout, digital detection offers several advantages: Because the signal of an individual label can be reliably distinguished from the background noise, the background fluctuations do not influence the measurement. Therefore, the LOD is limited only by the affinity and non-specific binding of the immunoreagents used in the assay. Furthermore, in contrast to the intensity-based readout, where a few big aggregates can strongly affect the overall intensity, the digital approach counts the aggregates as single binding events, reducing their effect on the measured signal.[142] This enhances the robustness of the measurement and indirectly allows for achieving lower LODs.
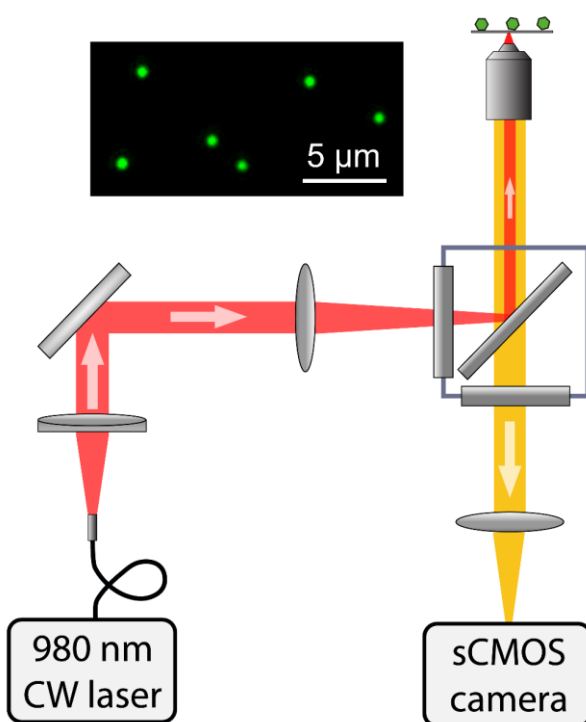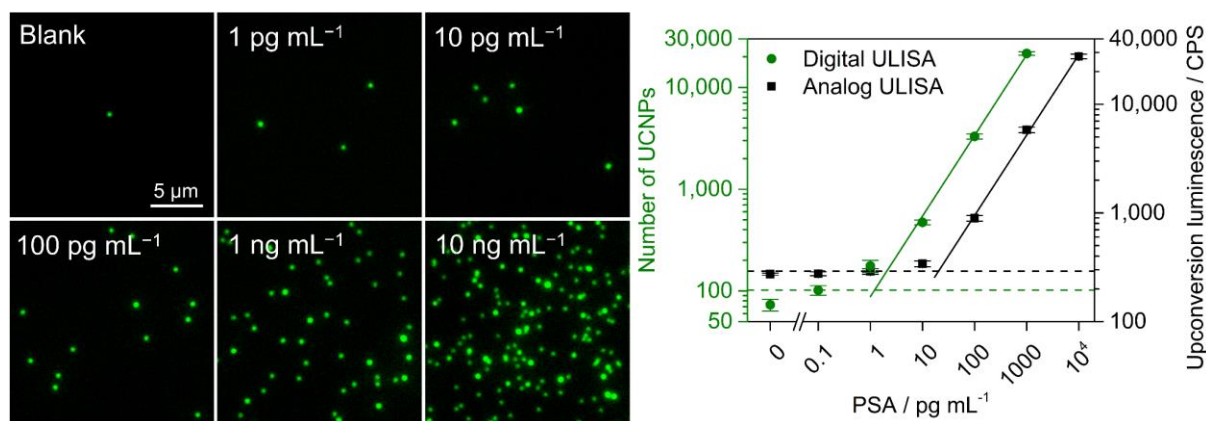
Figure 22: Upconversion microscopy images of microtiter plate after binding of serial dilutions of PSA in 25% serum. The calibration curves yield LOD of 1.2 pg/mL in the digital and 20.3 pg/mL in the analog mode. Adapted from Paper XVII with permission. Copyright 2017 American Chemical Society.

The analog readout of the immunoassay for PSA in 25% serum provided an LOD of 20.3 pg/mL with a working range from 100 pg/mL to 10 ng/mL. This is comparable with the commercial ELISA assays for the PSA.[143] The digital readout of the same microtiter plate (**Figure 22**) allowed to lower the LOD by more than one order of magnitude down to 1.2 pg/mL, with a working range from 10 pg/mL to 1 ng/mL. It was not possible to analyze higher PSA concentrations because the point-spread functions of the UCNPs started to overlap and did not allow reliable counting. It is also possible to combine both readout options, extending the overall working range to three orders of magnitude from 10 pg/mL to 10 ng/mL. The PSA detection in the buffer provided practically identical results, confirming that the 25% serum has a negligible matrix effect.

In our follow-up work, we have further improved the single-molecule assay scheme by replacing the conjugates of silica-coated UCNPs with antibody by PEG-coated UCNPs conjugated with streptavidin (**Figure 23**). Such conjugate was expected to provide better performance because (i) the PEG provides resistance of UCNPs against aggregation and ensures high dispersibility in water; (ii) the steric hindrance of the PEG reduces the level of non-specific interactions;[144, 145] and (iii) the subsequent addition of biotinylated detection antibody and streptavidin-coated UCNPs allows using a relatively high detection antibody concentration to efficiently label all PSA molecules while being able to reduce the UCNP concentration due to the high affinity between streptavidin and biotin,[146] which leads to a lower amount of non-specifically adsorbed UCNPs.
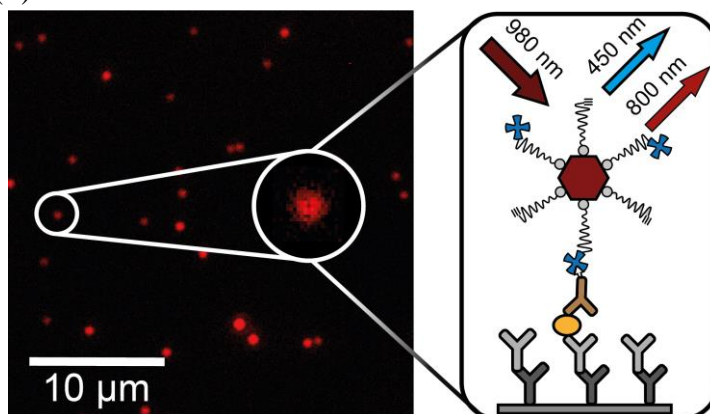
Figure 23: Upconversion microscopy image of a microtiter plate after the specific capture of PSA and a scheme of individual sandwich immunocomplex. Reprinted from Paper XVIII with permission. Copyright 2019 American Chemical Society.

Compared to our previous study,[147] the new assay design lowered the LOD by 50 times. The comparison of an assay based on Er-doped (LOD 23 fg/mL, 800 aM) and Tm-doped UCNPs LOD 24 fg/mL, 840 aM; **Figure 24A**) demonstrated that the advantages of the digital readout are not dependent on the label type. The three times lower value of IC_{50} further confirms that the two-step label design provides improved binding kinetics. For the real sample analysis, random samples of human serum were collected in the hospital and analyzed by electrochemiluminescence immunoassay as a reference method. The dilution linearity experiments have shown that human serum has a low matrix effect on the assay, as represented by the recovery rate fluctuations below 20%. The results from electrochemiluminescence assay and ULISAs (both analog and digital) were in great agreement, confirming the potential of UCNPs to be used as a label in assays for the diagnosis of prostate cancer (**Figure 24B**).
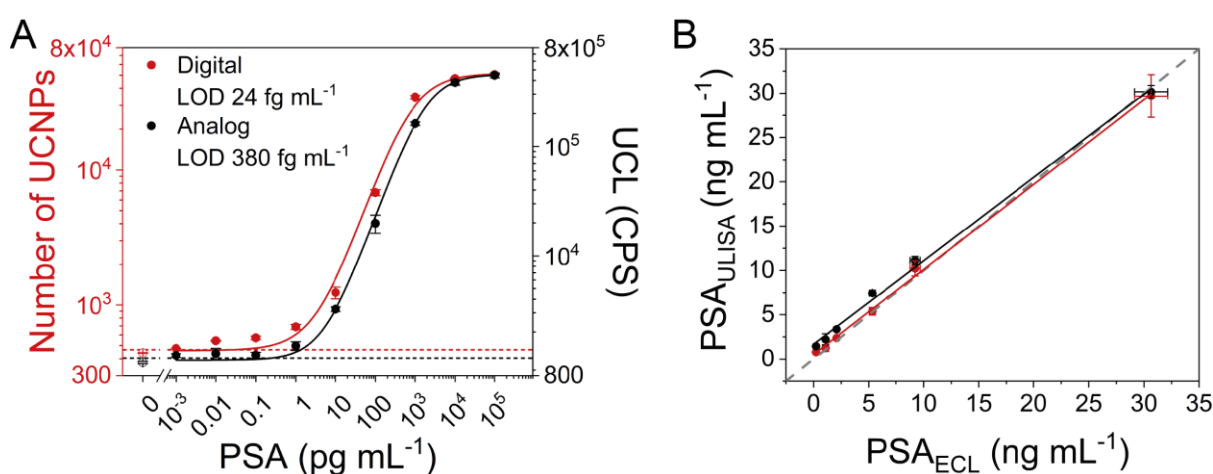
Figure 24: (A) Calibration curves of the ULISA in the digital (red) and analog (black) mode. The logarithmic scale of the *y*-axis highlights the signals in the low PSA concentration range. **(B)** Correlation between the PSA concentrations in human serum samples determined by the digital (red) or analog (black) ULISA and an electroluminescence immunoassay. Reprinted from Paper XVIII with permission. Copyright 2019 American Chemical Society.

5.3.2 Digital ULISA for Cardiac Troponin (Paper XIX)

The digital ULISA can be adapted for the detection of other biomarkers by simply exchanging the immunoreagents. Thus, to demonstrate the universal nature of the approach, we focused on detecting cardiac troponin, a biomarker of acute myocardial infarction (AMI). Heart diseases represent the leading cause of death worldwide. There is typically only a short time available since the symptoms start before the treatment is necessary, creating demand for rapid and reliable diagnostic assays.[148] Cardiac troponin is one of the recommended biomarkers for the diagnosis of AMI. Because it is located only in myocardial tissue in healthy individuals, its elevated concentration in blood can indicate the onset of AMI.[149] Cardiac troponin is a heterotrimeric complex, which consists of three distinct subunits – cTnI, cTnT, and TnC.[150] The subunits cTnI and cTnT are present only in the myocardium (heart muscle), and during the AMI, they are released into the bloodstream.[151, 152] The diagnosis of AMI can be made based on measuring the changes in the cTnI levels.[153]

However, cTnI is a challenging analyte for the detection by immunochemical methods as its recognition by antibodies can be affected by several factors.[154, 155] The N- and C-terminal parts of cTnI are susceptible to proteolytic degradation,[156] favoring the use of antibodies that target epitopes in the central region.[157] In addition, cTnI is typically present in blood in the form of a binary cTnI-TnC complex,[158] thus, the antibodies should recognize free as well as complex form cTnI. Furthermore, the epitopes can be phosphorylated or blocked by autoantibodies or heterophile antibodies, hindering immunochemical recognition.[159] For this reason, assays for cTnI are often based on the combination of two capture or two detection antibodies.[154]

In our work, we studied the impact of size and surface modification of UCNP labels on analog and digital ULISA for the detection of cTnI. The size of UCNP-based detection labels is one of the critical factors affecting assay performance. On the one hand, the particles should be as small as possible to (i) provide stable dispersions, (ii) minimize the level of non-specific binding, and (iii) limit the influence of the UCNPs and the immunochemical interaction. On the other hand, larger size leads to higher brightness of the UCNPs, making them more easily detectable. Furthermore, we tested two ways of surface modification, based on (i) alkyne-PEG-neridronate linker and streptavidin and (ii) poly(acrylic acid) (PAA) and antibody; the corresponding assay schemes are shown in **Figure 25**.
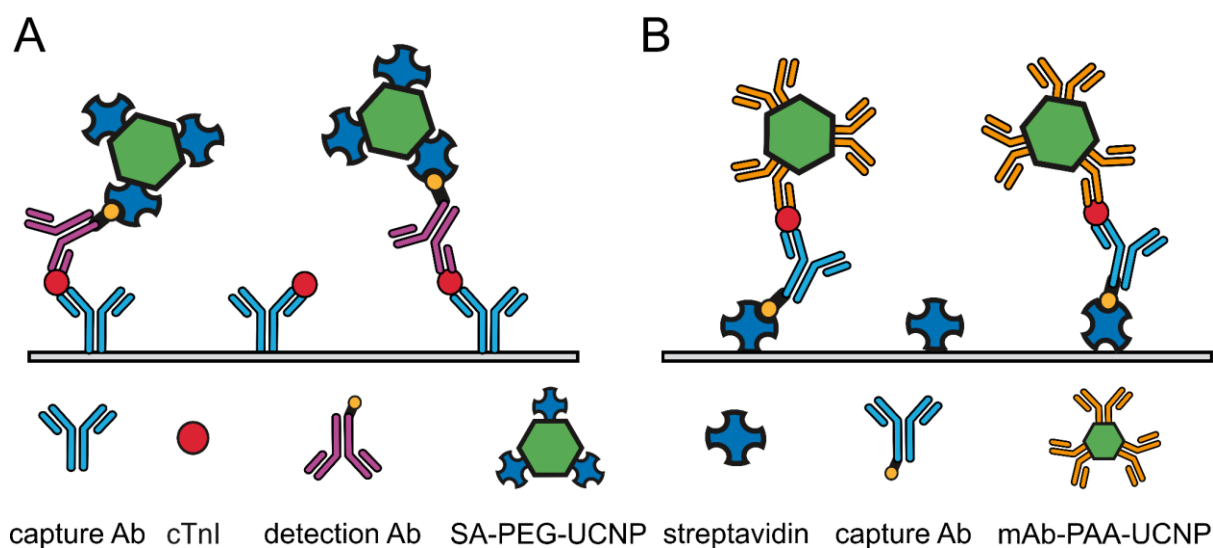
Figure 25: ULISA configurations for the detection of cTnI with labels based on **(A)** UCNP-PEG-SA and **(B)** UCNP-PAA-Ab. Adapted from Paper XIX under the permission of Creative Commons Attribution-NonCommercial 4.0 International License.

We found out that the size and surface modification of UCNPs affect the assay performance more than the difference between analog and digital readout modes. Varying the UCNPs size affected especially the assays in human plasma; the increasing size resulted in a higher level of non-specific binding; however, the smaller UCNPs exhibited a slightly higher degree of aggregation. The highest sensitivity was achieved when using PAA-based UCNPs with a diameter of 48 nm. Surprisingly, the LODs in human plasma provided by analog (8.6 pg/mL) and digital (9.8 pg/mL) readout were very similar. This contradicts with the results

achieved when detecting PSA where digital readout showed significantly higher sensitivity than the analog one. This discrepancy might be caused by the different affinity of the antibody-antigen pairs for PSA and cTnI. The analog readout provided a 10-fold lower LOD for PSA compared to cTnI, and the difference increased to 200-fold in the digital mode. These results thus suggest that a large enough antibody affinity is required to allow the digital readout to further increase the sensitivity of the ULISA.

5.4 UCNP-Based Immunocytochemistry (Paper XX)

We have also demonstrated that UCNPs can be advantageously used to label breast cancer biomarkers in immunocytochemistry (ICC) and immunohistochemistry (IHC). With around 2.1 million new cases reported every year, breast cancer is the second most common type of cancer worldwide.[160] Even though mammographic screening and advances in adjuvant systemic therapy help fighting the disease, its incidence continues growing.[161] Human epidermal growth factor receptors (HER or ErbB) belong to membrane receptors, which play essential roles in biological processes, including apoptosis and migration, differentiation, and proliferation of cells. The overexpression of the HER2 receptor on cancer cells happens in 10–30% of all patients with breast cancer. Due to the association with an increased rate of cell proliferation, which results in rapid cancer growth and poor prognosis, HER2 is often used as a biomarker in cancer diagnostics.[162]

IHC allows detecting and localizing antigens within histological tissues, which can be used to identify cancerous cells.[163] The optimization of protocols and testing of new staining and labeling methods can be done in ICC, which targets cultivated cells prepared similarly as the tissue samples. The most common counterstaining approach is based on the combination of hematoxylin and eosin (H&E).[164] However, to allow specific detection of cancer biomarkers, conjugates of antibodies with enzymes,[165] fluorophores,[166] or nanoparticles[167] have to be used. Typically, HRP is employed to oxidize 3,3'-diaminobenzidine to a brown precipitation product, which is evaluated by light microscopy.[168] The evaluation of the tissue sections is typically done by a time-consuming visual inspection by the trained pathologists. To increase the throughput, the current research focuses on the automation of imaging and evaluation aided by artificial intelligence in so-called digital pathology.[169] However, the automation requires labels providing high specific signals and low non-specific binding.[170]

Due to their high brightness and low non-specific adsorption, we have explored the capabilities of BSA-based[75] and PEG-based[143] conjugates of UCNPs with streptavidin for labeling of HER2 biomarker on cancer cells (**Figure 26**). The conjugates based on PEG provided a higher *S*/*B* ratio,
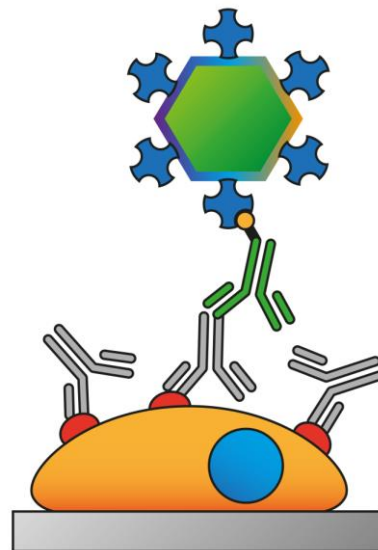
Figure 26: Scheme of the ICC assay. The primary antibody binds to the HER2 receptor on the cell surface, followed by a biotinylated secondary antibody, and detection UCNP-streptavidin conjugate. Adapted from Paper XX with permission. Copyright 2020 Royal Society of Chemistry.

probably due to the non-specific adsorption of BSA to the cell surface. The efficiency of labeling was strongly dependent on the blocking conditions. The *S*/*B* ratios were calculated as the ratio of signals between HER2-positive BT-474 cells incubated with and without primary antibody, as evaluated by upconversion scanning. Even though the assay buffer based on BSA and BGG allowed to reach an acceptable *S*/*B* ratio of 23, the use of commercial SuperBlock solution reduced the non-specific binding more efficiently while even slightly increasing the specific signals (**Figure 27**). This resulted in the improvement of the *S*/*B* ratio by more than one order of magnitude to 319. This finding agrees with the previous results, suggesting that the presence of serum proteins is not optimal for achieving low backgrounds in ICC. The comparison of HER2-positive BT-474 cells with HER2-negative MDA-MB-231 cells under the same experimental conditions also confirmed a high level of specific binding, producing 40 times higher signals in the case of BT-474. We have also shown that upconversion-based labeling is compatible with the H&E counterstaining, suggesting good applicability in IHC, where the H&E is the typical counterstaining method.

The performance of UCNP-based labels was compared with conventional fluorescence labeling using a conjugate of streptavidin with carboxyfluorescein (SA-FAM). The fluorescence labeling resulted in *S*/*B* value of only 6.1, which is connected with relatively high background signals due to the cellular autofluorescence and cross-talk between the detection channels (fluorescein and DAPI). Due to the 50-fold wider dynamic range, the upconversion labeling allows a much finer distinction of HER2 expression within different cell lines. Furthermore, the high *S*/*B* ratio can enable the application of UCNP labeling for IHC with automated data evaluation in digital pathology.
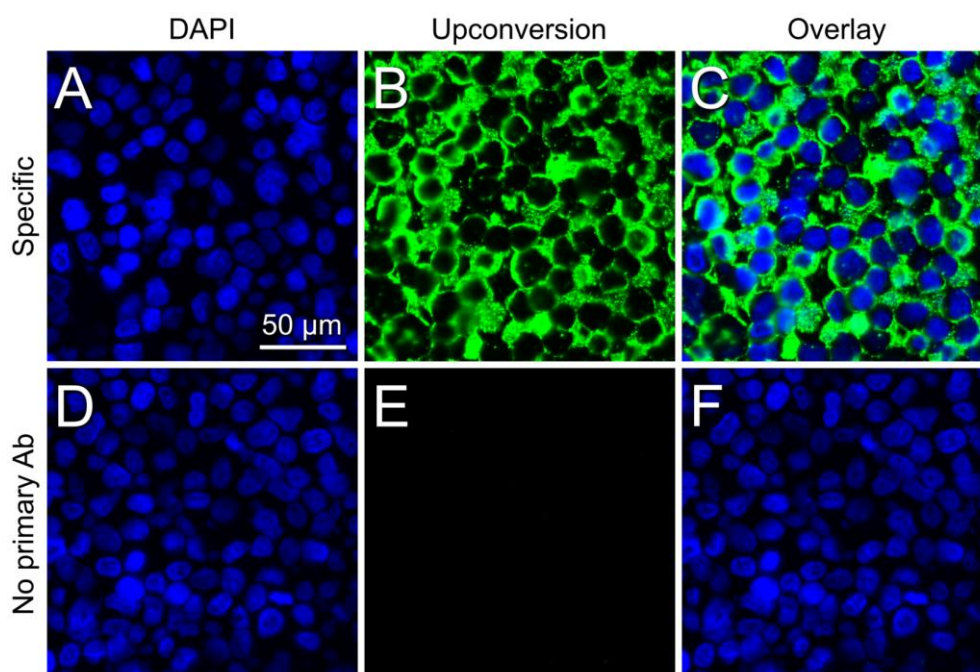
Figure 27: Labeling of HER2-positive FFPE BT-474 cells using UCNP-PEG-SA conjugates: **(A)** DAPI, **(B)** upconversion, **(C)** overlay. Negative control (without primary antibody): **(D)** DAPI, **(E)** upconversion, **(F)** overlay. Adapted from Paper XX with permission. Copyright 2020 Royal Society of Chemistry.

6 Laser-Induced Breakdown Spectroscopy (Papers XXI and XXII)

The direct nanoparticle-based immunoassay readout (i.e., not employing catalytic transformation of the substrate) is typically based on luminescence detection, which combines high sensitivity and simple instrumentation. However, the requirement of luminescence properties limits the range of potential labels. Therefore, there is a demand for alternative readout techniques that would allow universal detection independent of the luminescent or catalytic properties of the label.

Laser-induced breakdown spectroscopy (LIBS) is an optical emission technique complementary to the conventional methods in bioimaging.[171] LIBS combines high sensitivity, rapid analysis, and the possibility to detect halogens and light elements. However, its main advantage is the possibility of multi-elemental imaging on a large scale (few cm) and with a high resolution (units of μm).[172] LIBS can be used to detect different kinds of nanoparticles on various matrices, from the analysis of QDs on a filter paper[173] to UCNPs in model organisms.[174] Furthermore, LIBS can be used for surface mapping, providing information about the 2D or even 3D element distribution within the sample.[175]

We have developed a method for the detection of Ag NPs and Au NPs by LIBS from the bottom of the conventional 96-well microtiter plate (**Figure 28**). The optimized setup was then applied for the readout of a sandwich immunoassay to detect HSA based on streptavidin-conjugated Ag NPs. The performance of the LIBS-based assay was compared with a conventional fluorescence readout based on the conjugate of detection antibody with fluorescein isothiocyanate (FITC). Even though slightly higher sensitivity was observed in the case of fluorescence, the great advantage of LIBS was the wider dynamic range. Furthermore, LIBS allows detecting labels without luminescence properties and presents the possibility of multi-elemental analysis without the necessity to consider spectral overlaps of the conventional luminescence labels.

In the following work, we pioneered the application of LIBS for the readout of nanoparticle-labeled ICC sections. The cell pellets were labeled with UCNPs according to our previous report,[176] and the characteristic signal of the Y II 437.49 nm emission line was used to construct the 2D map of the sample surface with a resolution of 100 μm. The results demonstrated the ability of LIBS to map the yttrium distribution and showed a clear difference between HER2-positive and HER2-negative cells. The results from LIBS were then compared with upconversion optical microscopy and upconversion luminescence
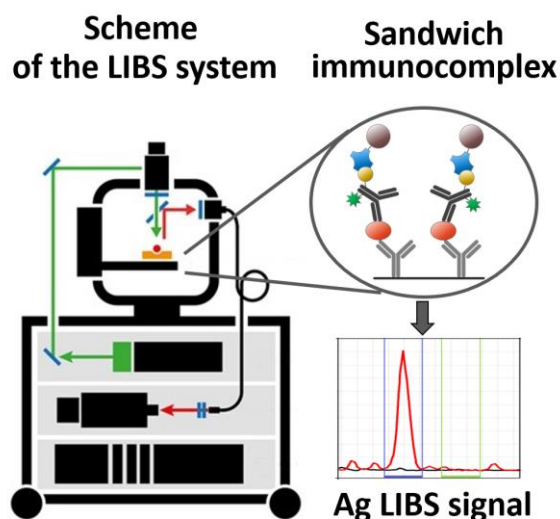
Figure 28: Scheme of LIBS immunoassay with label based on conjugate of Ag NPs with streptavidin. Reprinted from Paper XXI with permission. Copyright 2019 Springer.

scanning. The main advantage of microscopy compared to scanning-based approaches is the high resolution, which allows studying the target distribution within cellular structures. However, it is not possible to use conventional optical microscopy to quantitatively determine the amount of label (and therefore indirectly also of the target antigen) within the whole cell pellet. The S/B ratio of LIBS was 5, whereas the upconversion scanning of the identical pellets provided S/B of 159 (**Figure 29**). Because there was the same amount of UCNPs, the worse S/B of LIBS was probably given by the lower measurement sensitivity. Despite the successful results of the preliminary work, further improvements of LIBS are necessary to meet the practical requirement of IHC, especially in terms of sensitivity and lateral resolution. In the future, LIBS can significantly improve the multiplexing capabilities in IHC due to the possibility of using multiple nanoparticle labels without having to deal with spectral overlaps, as in the case of optical readout.
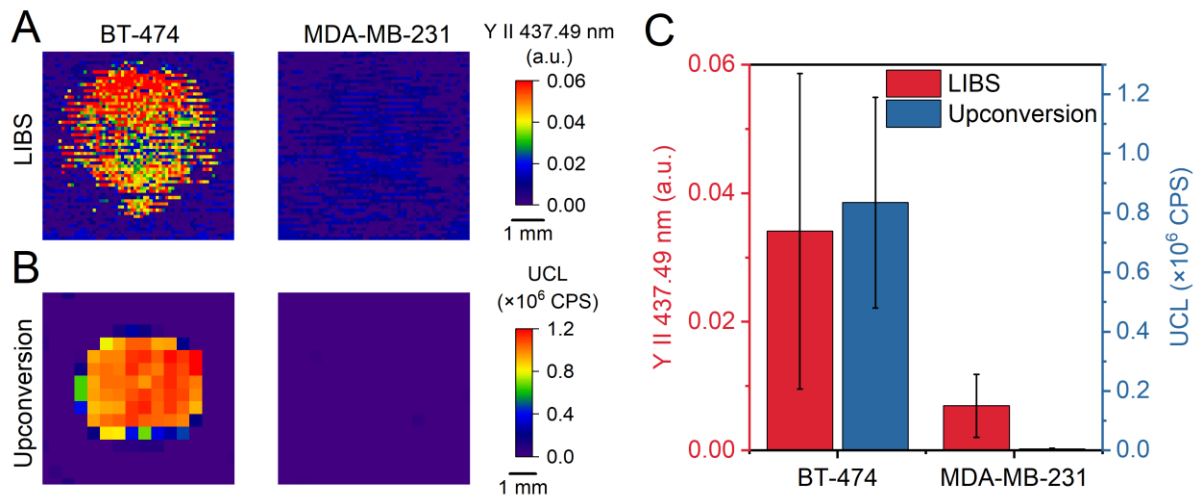
Figure 29: Comparison of **(A)** LIBS and **(B)** upconversion scanning of BT-474 and MDA-MB-231 cells with HER2 biomarker labeled with UCNP-PEG-SA conjugate. **(C)** The average intensities evaluated by the two methods. Error bars correspond to standard deviations of intensities within the cell pellet. Reprinted from Paper XXII. Copyright 2021 Springer.

7 Conclusions and Outlook

This thesis has summarized the recent progress in the rapidly developing field of immunochemical biosensors and assays. This research topic represents an interdisciplinary effort to combine various kinds of physicochemical transducers with appropriate assay strategies to achieve highly sensitive and specific detection. Furthermore, the use of nanoparticles, in particular with catalytic or luminescent properties, can further enhance the performance of such assays.

The label-free biosensing was represented by EIS biosensor for *Salmonella* in milk, QCM biosensor for aerosolized biological warfare agents, and application of plasma-polymerized layers in SPR biosensing of HSA and *Salmonella*. Overall, the main advantage of these approaches is the rapid analysis and simple procedure. However, the sensitivity can be limited by the lack of the signal-amplification step.

On the other hand, the use of catalytic labels is typically connected with higher sensitivity and reduced effect of the complex sample matrix, but the analysis requires the substrate conversion step and, therefore, longer time. Enzyme-based labels were employed in an amperometric biosensor for the diagnosis of EFB and in precipitation-based SPR assay for *Salmonella*. As an alternative to enzymes, we have also used catalytic PBNPs in an NLISA for HSA and *Salmonella*. Even though the sensitivity was similar to the conventional ELISA, PBNPs provide several practical advantages, particularly higher stability and the possibility of easy synthesis from cheap precursors.

UCNPs allow highly sensitive detection due to the anti-Stokes luminescence and lack of optical background. We have thoroughly studied the different ways of UCNP surface modification and conjugation with biorecognition molecules. The conjugates were then employed in ULISA assays for a wide range of analytes, from small molecules (DCF, ZEA), through proteins (HSA, PSA, troponin), to bacteria (*M. plutonius* and *P. larvae*). UCNPs also proved useful for labeling HER2 biomarker on the surface of breast cancer cells in ICC imaging.

Finally, we have explored the possibilities of LIBS as an alternative way of signal readout not dependent on the catalytic or luminescent properties of the labels. We have employed it in microtiter plate-based immunoassay for HSA and in ICC detection of HER2 biomarker.

Even though reaching ever lower LODs is one of the main challenges from the scientific point of view, it is equally important to address the simplicity and robustness of the assay procedure. An ideal assay should provide results within a few minutes and be based either on a fully automated system or a cheap disposable sensor that requires minimum manipulation. The ongoing advances in transducer technology and labels, especially based on nanoparticles, promise that the performance of immunochemical biosensors and assays will keep improving in the future. This will be beneficial for the biochemical and biological research field, and for the large community of immunoassay users in clinical diagnosis, detection of biological agents, food safety, and environmental protection.

References

1. Tighe, P. J.; Ryder, R. R.; Todd, I.; Fairclough, L. C., ELISA in the multiplex era: Potentials and pitfalls. *Proteomics Clin. Appl.* **2015,** *9* (3–4), 406–422.
2. Farka, Z.; Juřík, T.; Kovář, D.; Trnková, L.; Skládal, P., Nanoparticle-Based Immunochemical Biosensors and Assays: Recent Advances and Challenges. *Chem. Rev.* **2017,** *117* (15), 9973–10042.
3. Peltomaa, R.; Benito-Pena, E.; Moreno-Bondi, M. C., Bioinspired recognition elements for mycotoxin sensors. *Anal. Bioanal. Chem.* **2018,** *410* (3), 747–771.
4. Surugiu, I.; Danielsson, B.; Ye, L.; Mosbach, K.; Haupt, K., Chemiluminescence imaging ELISA using an imprinted polymer as the recognition element instead of an antibody. *Anal. Chem.* **2001,** *73* (3), 487–491.
5. Foote, J.; Eisen, H. N., Kinetic and affinity limits on antibodies produced during immune responses. *Proc. Natl. Acad. Sci. U.S.A.* **1995,** *92* (5), 1254–1256.
6. Green, N. M., Avidin and streptavidin. In *Methods Enzymol.*, Wilchek, M.; Bayer, E. A., Eds. Academic Press: 1990; Vol. 184, pp 51–67.
7. Harmsen, M. M.; De Haard, H. J., Properties, production, and applications of camelid single-domain antibody fragments. *Appl. Microbiol. Biotechnol.* **2007,** *77* (1), 13–22.
8. Yalow, R. S.; Berson, S. A., Assay of Plasma Insulin in Human Subjects by Immunological Methods. *Nature* **1959,** *184* (4699), 1648–1649.
9. Kunze, A.; Pei, L.; Elsasser, D.; Niessner, R.; Seidel, M., High performance concentration method for viruses in drinking water. *J. Virol. Methods* **2015,** *222*, 132–137.
10. Anderson, N. L.; Anderson, N. G., The human plasma proteome – History, character, and diagnostic prospects. *Mol. Cell. Proteomics* **2002,** *1* (11), 845–867.
11. Hanash, S. M.; Pitteri, S. J.; Faca, V. M., Mining the plasma proteome for cancer biomarkers. *Nature* **2008,** *452* (7187), 571–579.
12. Walt, D. R., Clinical testing should be individualized, not based on populations. *J. Clin. Invest.* **2019,** *129* (9), 3472–3473.
13. Rusling, J. F.; Kumar, C. V.; Gutkind, J. S.; Patel, V., Measurement of biomarker proteins for point-of-care early detection and monitoring of cancer. *Analyst* **2010,** *135* (10), 2496–2511.
14. St John, A.; Price, C. P., Existing and Emerging Technologies for Point-of-Care Testing. *Clin. Biochem. Rev.* **2014,** *35* (3), 155–167.
15. Litman, D. J.; Hanlon, T. M.; Ullman, E. F., Enzyme Channeling Immunoassay – A New Homogeneous Enzyme-Immunoassay Technique. *Anal. Biochem.* **1980,** *106* (1), 223–229.
16. Hood, L., A Personal Journey of Discovery: Developing Technology and Changing Biology. *Annu. Rev. Anal. Chem.* **2008,** *1*, 1–43.
17. Siitari, H.; Hemmila, I.; Soini, E.; Lovgren, T.; Koistinen, V., Detection of hepatitis B surface antigen using time-resolved fluoroimmunoassay. *Nature* **1983,** *301* (5897), 258–260.
18. Rui, M.; Hampe, C. S.; Wang, C.; Ling, Z. D.; Gorus, F. K.; Lernmark, A.; Pipeleers, D. G.; De Pauw, P. E. M., Species and epitope specificity of two 65 kDa glutamate decarboxylase time-resolved fluorometric immunoassays. *J. Immunol. Methods* **2007,** *319* (1–2), 133–143.

19. Pastucha, M.; Farka, Z.; Lacina, K.; Mikušová, Z.; Skládal, P., Magnetic nanoparticles for smart electrochemical immunoassays: a review on recent developments. *Microchim. Acta* **2019,** *186* (5), 26.

20. Gorris, H. H.; Wolfbeis, O. S., Photon-Upconverting Nanoparticles for Optical Encoding and Multiplexing of Cells, Biomolecules, and Microspheres. *Angew. Chem. Int. Ed.* **2013,** *52* (13), 3584–3600.

21. Hofmann, C.; Duerkop, A.; Baeumner, A. J., Nanocontainers for Analytical Applications. *Angew. Chem. Int. Ed.* **2019,** *58* (37), 12840–12860.

22. Mejri, M. B.; Baccar, H.; Baldrich, E.; Del Campo, F. J.; Helali, S.; Ktari, T.; Simonian, A.; Aouni, M.; Abdelghani, A., Impedance biosensing using phages for bacteria detection: Generation of dual signals as the clue for in-chip assay confirmation. *Biosens. Bioelectron.* **2010,** *26* (4), 1261–1267.

23. Daniels, J. S.; Pourmand, N., Label-free impedance biosensors: Opportunities and challenges. *Electroanalysis* **2007,** *19* (12), 1239–1257.

24. Scharff, R. L., Economic Burden from Health Losses Due to Foodborne Illness in the United States. *J. Food Prot.* **2012,** *75* (1), 123–131.

25. Desin, T. S.; Koster, W.; Potter, A. A., *Salmonella* vaccines in poultry: past, present and future. *Expert Rev. Vaccines* **2013,** *12* (1), 87–96.

26. Majowicz, S. E.; Musto, J.; Scallan, E.; Angulo, F. J.; Kirk, M.; O'Brien, S. J.; Jones, T. F.; Fazil, A.; Hoekstra, R. M., The Global Burden of Nontyphoidal *Salmonella* Gastroenteritis. *Clin. Infect. Dis.* **2010,** *50* (6), 882–889.

27. Alocilja, E. C.; Radke, S. M., Market analysis of biosensors for food safety. *Biosens. Bioelectron.* **2003,** *18* (5–6), 841–846.

28. Roda, A.; Mirasoli, M.; Roda, B.; Bonvicini, F.; Colliva, C.; Reschiglian, P., Recent developments in rapid multiplexed bioanalytical methods for foodborne pathogenic bacteria detection. *Microchim. Acta* **2012,** *178* (1–2), 7–28.

29. de Boer, E.; Beumer, R. R., Methodology for detection and typing of foodborne microorganisms. *Int. J. Food Microbiol.* **1999,** *50* (1–2), 119–130.

30. Velusamy, V.; Arshak, K.; Korostynska, O.; Oliwa, K.; Adley, C., An overview of foodborne pathogen detection: In the perspective of biosensors. *Biotechnol. Adv.* **2010,** *28* (2), 232–254.

31. Aydintug, M. K.; Inzana, T. J.; Letonja, T.; Davis, W. C.; Corbeil, L. B., Cross-Reactivity of Monoclonal Antibodies to *Escherichia coli* J5 with Heterologous Gram-Negative Bacteria and Extracted Lipopolysaccharides. *J. Infect. Dis.* **1989,** *160* (5), 846–857.

32. Kothary, M. H.; Babu, U. S., Infective dose of foodborne pathogens in volunteers: A review. *J. Food Saf.* **2001,** *21* (1), 49–73.

33. Sauerbrey, G., Verwendung von Schwingquarzen zur Wägung dünner Schichten und zur Mikrowägung. *Z. Phys.* **1959,** *155* (2), 206–222.

34. Sternbach, G., The history of anthrax. *J. Emerg. Med.* **2003,** *24* (4), 463–467.

35. Török, T. J.; Tauxe, R. V.; Wise, R. P.; Livengood, J. R.; Sokolow, R.; Mauvais, S.; Birkness, K. A.; Skeels, M. R.; Horan, J. M.; Foster, L. R., A Large Community Outbreak of Salmonellosis Caused by Intentional Contamination of Restaurant Salad Bars. *JAMA* **1997,** *278* (5), 389–395.

36. Danzig, R.; Berkowsky, P. B., Why should we be concerned about biological warfare? *JAMA* **1997,** *278* (5), 431–432.

37. Khardori, N.; Kanchanapoom, T., Overview of biological terrorism: Potential agents and preparedness. *Clin. Microbiol. Newsl.* **2005,** *27* (1), 1–8.

38. Polymenakou, P. N., Atmosphere: A Source of Pathogenic or Beneficial Microbes? *Atmosphere* **2012,** *3* (1), 87–102.

39. Mandal, S.; Koirala, D.; Selvam, S.; Ghimire, C.; Mao, H. B., A Molecular Tuning Fork in Single-Molecule Mechanochemical Sensing. *Angew. Chem. Int. Ed.* **2015,** *54* (26), 7607–7611.

40. Su, W. C.; Tolchinsky, A. D.; Chen, B. T.; Sigaev, V. I.; Cheng, Y. S., Evaluation of physical sampling efficiency for cyclone-based personal bioaerosol samplers in moving air environments. *J. Environ. Monit.* **2012,** *14* (9), 2430–2437.

41. Joshi, D.; Kumar, D.; Maini, A. K.; Sharma, R. C., Detection of biological warfare agents using ultra violet-laser induced fluorescence LIDAR. *Spectrochim. Acta Pt. A Mol. Biomol. Spectrosc.* **2013,** *112*, 446–456.

42. Park, C. W.; Park, J. W.; Lee, S. H.; Hwang, J., Real-time monitoring of bioaerosols via cell-lysis by air ion and ATP bioluminescence detection. *Biosens. Bioelectron.* **2014,** *52*, 379–383.

43. Pohlker, C.; Huffman, J. A.; Poschl, U., Autofluorescence of atmospheric bioaerosols – fluorescent biomolecules and potential interferences. *Atmos. Meas. Tech.* **2012,** *5* (1), 37–71.

44. Venkateswaran, K.; Hattori, N.; La Duc, M. T.; Kern, R., ATP as a biomarker of viable microorganisms in clean-room facilities. *J. Microbiol. Methods* **2003,** *52* (3), 367–377.

45. Hospodsky, D.; Yamamoto, N.; Peccia, J., Accuracy, Precision, and Method Detection Limits of Quantitative PCR for Airborne Bacteria and Fungi. *Appl. Environ. Microbiol.* **2010,** *76* (21), 7004–7012.

46. Usachev, E. V.; Agranovski, I. E., Internally controlled PCR system for detection of airborne microorganisms. *J. Environ. Monit.* **2012,** *14* (6), 1631–1637.

47. Alam, S. I.; Kumar, B.; Kamboj, D. V., Multiplex Detection of Protein Toxins Using MALDI-TOF-TOF Tandem Mass Spectrometry: Application in Unambiguous Toxin Detection from Bioaerosol. *Anal. Chem.* **2012,** *84* (23), 10500–10507.

48. Green, H. C.; Field, K. G., Sensitive detection of sample interference in environmental qPCR. *Water Res.* **2012,** *46* (10), 3251–3260.

49. Maher, N.; Dillon, H. K.; Vermund, S. H.; Unnasch, T. R., Magnetic bead capture eliminates PCR inhibitors in samples collected from the airborne environment, permitting detection of *Pneumacystis carinii* DNA. *Appl. Environ. Microbiol.* **2001,** *67* (1), 449–452.

50. Wijaya, E.; Lenaerts, C.; Maricot, S.; Hastanin, J.; Habraken, S.; Vilcot, J. P.; Boukherroub, R.; Szunerits, S., Surface plasmon resonance-based biosensors: From the development of different SPR structures to novel surface functionalization strategies. *Curr. Opin. Solid State Mat. Sci.* **2011,** *15* (5), 208–224.

51. Guo, X. W., Surface plasmon resonance based biosensor technique: A review. *J. Biophotonics* **2012,** *5* (7), 483–501.

52. Stewart, M. E.; Anderton, C. R.; Thompson, L. B.; Maria, J.; Gray, S. K.; Rogers, J. A.; Nuzzo, R. G., Nanostructured plasmonic sensors. *Chem. Rev.* **2008,** *108* (2), 494–521.

53. Zeng, S. W.; Yu, X.; Law, W. C.; Zhang, Y. T.; Hu, R.; Dinh, X. Q.; Ho, H. P.; Yong, K. T., Size dependence of Au NP-enhanced surface plasmon resonance based on differential phase measurement. *Sens. Actuators B Chem.* **2013,** *176*, 1128–1133.

54. Zeng, S. W.; Yong, K. T.; Roy, I.; Dinh, X. Q.; Yu, X.; Luan, F., A Review on Functionalized Gold Nanoparticles for Biosensing Applications. *Plasmonics* **2011,** *6* (3), 491–506.

55. Nakamura, C.; Hasegawa, M.; Nakamura, N.; Miyake, J., Rapid and specific detection of herbicides using a self-assembled photosynthetic reaction center from purple bacterium on an SPR chip. *Biosens. Bioelectron.* **2003,** *18* (5–6), 599–603.

56. Wei, J. Y.; Mu, Y.; Song, D. Q.; Fang, X. X.; Liu, X.; Bu, L. S.; Zhang, H. Q.; Zhang, G. Z.; Ding, J. H.; Wang, W. Z.; Jin, Q. H.; Luo, G. M., A novel sandwich immunosensing method for measuring cardiac troponin I in sera. *Anal. Biochem.* **2003,** *321* (2), 209–216.

57. Gobi, K. V.; Tanaka, H.; Shoyama, Y.; Miura, N., Continuous flow immunosensor for highly selective and real-time detection of sub-ppb levels of 2-hydroxybiphenyl by using surface plasmon resonance imaging. *Biosens. Bioelectron.* **2004,** *20* (2), 350–357.

58. Farka, Z.; Juřík, T.; Pastucha, M.; Skládal, P., Enzymatic Precipitation Enhanced Surface Plasmon Resonance Immunosensor for the Detection of *Salmonella* in Powdered Milk. *Anal. Chem.* **2016,** *88* (23), 11830–11836.

59. Howell, S.; Kenmore, M.; Kirkland, M.; Badley, R. A., High-density immobilization of an antibody fragment to a carboxymethylated dextran-linked biosensor surface. *J. Mol. Recognit.* **1998,** *11* (1–6), 200–203.

60. Wadu-Mesthrige, K.; Amro, N. A.; Liu, G. Y., Immobilization of proteins on self-assembled monolayers. *Scanning* **2000,** *22* (6), 380–388.

61. Vericat, C.; Vela, M. E.; Benitez, G.; Carro, P.; Salvarezza, R. C., Self-assembled monolayers of thiols and dithiols on gold: new challenges for a well-known system. *Chem. Soc. Rev.* **2010,** *39* (5), 1805–1834.

62. Chen, Q.; Forch, R.; Knoll, W., Characterization of pulsed plasma polymerization allylamine as an adhesion layer for DNA adsorption/hybridization. *Chem. Mater.* **2004,** *16* (4), 614–620.

63. Jung, D.; Yeo, S.; Kim, J.; Kim, B.; Jin, B.; Ryu, D. Y., Formation of amine groups by plasma enhanced chemical vapor deposition and its application to DNA array technology. *Surf. Coat. Technol.* **2006,** *200* (9), 2886–2891.

64. Yang, Z. L.; Wang, J.; Luo, R. F.; Maitz, M. F.; Jing, F. J.; Sun, H.; Huang, N., The covalent immobilization of heparin to pulsed-plasma polymeric allylamine films on 316L stainless steel and the resulting effects on hemocompatibility. *Biomaterials* **2010,** *31* (8), 2072–2083.

65. Ren, T. B.; Weigel, T.; Groth, T.; Lendlein, A., Microwave plasma surface modification of silicone elastomer with allylamine for improvement of biocompatibility. *J. Biomed. Mater. Res. Part A* **2008,** *86A* (1), 209–219.

66. Nisol, B.; Watson, S.; Lerouge, S.; Wertheimer, M. R., Energetics of Reactions in a Dielectric Barrier Discharge with Argon Carrier Gas: III Esters. *Plasma Process. Polym.* **2016,** *13* (9), 900–907.

67. Rupper, P.; Vandenbossche, M.; Bernard, L.; Hegemann, D.; Heuberger, M., Composition and Stability of Plasma Polymer Films Exhibiting Vertical Chemical Gradients. *Langmuir* **2017,** *33* (9), 2340–2352.

68. Mishra, G.; McArthur, S. L., Plasma Polymerization of Maleic Anhydride: Just What Are the Right Deposition Conditions? *Langmuir* **2010,** *26* (12), 9645–9658.

69. Rich, R. L.; Myszka, D. G., Advances in surface plasmon resonance biosensor analysis. *Curr. Opin. Biotechnol.* **2000,** *11* (1), 54–61.

70. Makhneva, E.; Obrusník, A.; Farka, Z.; Skládal, P.; Vandenbossche, M.; Hegemann, D.; Zajíčková, L., Carboxyl-rich plasma polymer surfaces in surface plasmon resonance immunosensing. *Jpn. J. Appl. Phys.* **2018,** *57* (1), 5.

71. Forsgren, E.; Budge, G. E.; Charriere, J. D.; Hornitzky, M. A. Z., Standard methods for European foulbrood research. *J. Apic. Res.* **2013,** *52* (1), 14.

72. Ahmed, A.; Rushworth, J. V.; Hirst, N. A.; Millner, P. A., Biosensors for Whole-Cell Bacterial Detection. *Clin. Microbiol. Rev.* **2014,** *27* (3), 631–646.

73. Pinnock, D. E.; Featherstone, N. E., Detection and quantification of *Melissococcus pluton* infection in honeybee colonies by means of enzyme-linked immunosorbent assay. *J. Apic. Res.* **1984,** *23* (3), 168–170.

74. Tomkies, V.; Flint, J.; Johnson, G.; Waite, R.; Wilkins, S.; Danks, C.; Watkins, M.; Cuthbertson, A. G. S.; Carpana, E.; Marris, G.; Budge, G.; Brown, M. A., Development and validation of a novel field test kit for European foulbrood. *Apidologie* **2009,** *40* (1), 63–72.

75. Poláchová, V.; Pastucha, M.; Mikušová, Z.; Mickert, M. J.; Hlaváček, A.; Gorris, H. H.; Skládal, P.; Farka, Z., Click-conjugated photon-upconversion nanoparticles in an immunoassay for honeybee pathogen *Melissococcus plutonius*. *Nanoscale* **2019,** *11* (17), 8343–8351.

76. Vaisocherová-Lísalová, H.; Víšová, I.; Ermini, M. L.; Špringer, T.; Song, X. C.; Mrázek, J.; Lamačová, J.; Scott Lynn Jr, N.; Šedivák, P.; Homola, J., Low-fouling surface plasmon resonance biosensor for multi-step detection of foodborne bacterial pathogens in complex food samples. *Biosens. Bioelectron.* **2016,** *80*, 84–90.

77. Liu, X.; Hu, Y.; Zheng, S.; Liu, Y.; He, Z.; Luo, F., Surface plasmon resonance immunosensor for fast, highly sensitive, and in situ detection of the magnetic nanoparticles-enriched *Salmonella enteritidis*. *Sens. Actuators B Chem.* **2016,** *230*, 191–198.

78. Juřík, T.; Skládal, P., Detection of hydrogen peroxide and glucose by enzyme product precipitation on sensor surface. *Chem. Pap.* **2015,** *69* (1), 167–175.

79. Li, J.; Wang, J. J.; Guo, X.; Zheng, Q.; Peng, J.; Tang, H.; Yao, S. Z., Carbon Nanotubes Labeled with Aptamer and Horseradish Peroxidase as a Probe for Highly Sensitive Protein Biosensing by Postelectropolymerization of Insoluble Precipitates on Electrodes. *Anal. Chem.* **2015,** *87* (15), 7610–7617.

80. Akter, R.; Rahman, M. A.; Rhee, C. K., Amplified Electrochemical Detection of a Cancer Biomarker by Enhanced Precipitation Using Horseradish Peroxidase Attached on Carbon Nanotubes. *Anal. Chem.* **2012,** *84* (15), 6407–6415.

81. Hou, L.; Tang, Y.; Xu, M. D.; Gao, Z. Q.; Tang, D. P., Tyramine-Based Enzymatic Conjugate Repeats for Ultrasensitive Immunoassay Accompanying Tyramine Signal Amplification with Enzymatic Biocatalytic Precipitation. *Anal. Chem.* **2014,** *86* (16), 8352–8358.

82. Hou, L.; Cui, Y. L.; Xu, M. D.; Gao, Z. Q.; Huang, J. X.; Tang, D. P., Graphene oxide-labeled sandwich-type impedimetric immunoassay with sensitive enhancement based on enzymatic 4-chloro-1-naphthol oxidation. *Biosens. Bioelectron.* **2013,** *47*, 149–156.

83. Ruan, C. M.; Yang, L. J.; Li, Y. B., Immunobiosensor chips for detection of *Escherichia coli* O157:H7 using electrochemical impedance spectroscopy. *Anal. Chem.* **2002,** *74* (18), 4814–4820.

84. Torun, O.; Boyaci, I. H.; Temur, E.; Tamer, U., Comparison of sensing strategies in SPR biosensor for rapid and sensitive enumeration of bacteria. *Biosens. Bioelectron.* **2012,** *37* (1), 53–60.

85. Fratamico, P. M., Comparison of culture, polymerase chain reaction (PCR), TaqMan *Salmonella*, and Transia Card *Salmonella* assays for detection of *Salmonella* spp. in naturally-contaminated ground chicken, ground turkey, and ground beef. *Mol. Cell. Probes* **2003,** *17* (5), 215–221.

86. Cudjoe, K. S.; Hagtvedt, T.; Dainty, R., Immunomagnetic separation of *Salmonella* from foods and their detection using immunomagnetic particle (IMP)-ELISA. *Int. J. Food Microbiol.* **1995,** *27* (1), 11–25.

87. Li, Y.; Mustapha, A., Simultaneous detection of *Escherichia coli* O157:H7, *Salmonella*, and *Shigella* in apple cider and produce by a multiplex PCR. *J. Food Prot.* **2004,** *67* (1), 27–33.

88. Rodriguez-Lazaro, D.; D'Agostino, M.; Herrewegh, A.; Pla, M.; Cook, N.; Ikonomopoulos, J., Real-time PCR-based methods for detection of *Mycobacterium avium* subsp. *paratuberculosis* in water and milk. *Int. J. Food Microbiol.* **2005,** *101* (1), 93–104.

89. Teunis, P. F. M.; Kasuga, F.; Fazil, A.; Ogden, L. D.; Rotariu, O.; Strachan, N. J. C., Dose-response modeling of *Salmonella* using outbreak data. *Int. J. Food Microbiol.* **2010,** *144* (2), 243–249.

90. Scott, V. N.; Powell, M.; Cabrera, J.; Carullo, M. E.; Martinez, I.; Lohachoompol, V., Development of microbiological criteria to assess the acceptability of a food lot – An example for milk powder. *Food Control* **2015,** *58*, 12–16.

91. Kuah, E.; Toh, S.; Yee, J.; Ma, Q.; Gao, Z. Q., Enzyme Mimics: Advances and Applications. *Chem. Eur. J.* **2016,** *22* (25), 8404–8430.

92. Ragg, R.; Tahir, M. N.; Tremel, W., Solids Go Bio: Inorganic Nanoparticles as Enzyme Mimics. *Eur. J. Inorg. Chem.* **2016,** *2016* (13–14), 1906–1915.

93. Gao, L. Z.; Zhuang, J.; Nie, L.; Zhang, J. B.; Zhang, Y.; Gu, N.; Wang, T. H.; Feng, J.; Yang, D. L.; Perrett, S.; Yan, X., Intrinsic peroxidase-like activity of ferromagnetic nanoparticles. *Nat. Nanotechnol.* **2007,** *2* (9), 577–583.

94. Shokouhimehr, M.; Soehnlen, E. S.; Khitrin, A.; Basu, S.; Huang, S. P. D., Biocompatible Prussian blue nanoparticles: Preparation, stability, cytotoxicity, and potential use as an MRI contrast agent. *Inorg. Chem. Commun.* **2010,** *13* (1), 58–61.

95. Wei, H.; Wang, E. K., Nanomaterials with enzyme-like characteristics (nanozymes): next-generation artificial enzymes. *Chem. Soc. Rev.* **2013,** *42* (14), 6060–6093.

96. Wu, J. J. X.; Wang, X. Y.; Wang, Q.; Lou, Z. P.; Li, S. R.; Zhu, Y. Y.; Qin, L.; Wei, H., Nanomaterials with enzyme-like characteristics (nanozymes): next-generation artificial enzymes (II). *Chem. Soc. Rev.* **2019,** *48* (4), 1004–1076.

97. Doumas, B. T.; Peters, T., Serum and urine albumin: A progress report on their measurement and clinical significance. *Clin. Chim. Acta* **1997,** *258* (1), 3–20.

98. Wang, W. B.; Liu, L. Q.; Song, S. S.; Tang, L. J.; Kuang, H.; Xu, C. L., A Highly Sensitive ELISA and Immunochromatographic Strip for the Detection of *Salmonella typhimurium* in Milk Samples. *Sensors* **2015,** *15* (3), 5281–5292.

99. Haase, M.; Schafer, H., Upconverting Nanoparticles. *Angew. Chem. Int. Ed.* **2011,** *50* (26), 5808–5829.

100. Auzel, F., Upconversion and Anti-Stokes Processes with f and d Ions in Solids. *Chem. Rev.* **2004,** *104* (1), 139–173.

101. Chamarro, M. A.; Cases, R., Energy upconversion in (Yb, Ho) and (Yb, Tm) doped fluorohafnate glasses. *J. Lumin.* **1988,** *42* (5), 267–274.

102. Li, X. M.; Zhang, F.; Zhao, D. Y., Lab on upconversion nanoparticles: optical properties and applications engineering via designed nanostructure. *Chem. Soc. Rev.* **2015,** *44* (6), 1346–1378.

103. Wang, M.; Abbineni, G.; Clevenger, A.; Mao, C. B.; Xu, S. K., Upconversion nanoparticles: synthesis, surface modification and biological applications. *Nanomed. Nanotechnol. Biol. Med.* **2011,** *7* (6), 710–729.

104. Li, Z. Q.; Zhang, Y., Monodisperse silica-coated polyvinylpyrrolidone/NaYF$_4$ nanocrystals with multicolor upconversion fluorescence emission. *Angew. Chem. Int. Ed.* **2006,** *45* (46), 7732–7735.

105. Liu, Z. E.; Wang, J.; Li, Y.; Hu, X. X.; Yin, J. W.; Peng, Y. Q.; Li, Z. H.; Li, Y. W.; Li, B. M.; Yuan, Q., Near-Infrared Light Manipulated Chemoselective Reductions Enabled by an Upconversional Supersandwich Nanostructure. *ACS Appl. Mater. Interfaces* **2015,** *7* (34), 19416–19423.

106. Sedlmeier, A.; Gorris, H. H., Surface modification and characterization of photon-upconverting nanoparticles for bioanalytical applications. *Chem. Soc. Rev.* **2015,** *44* (6), 1526–1560.

107. Oaks, J. L.; Gilbert, M.; Virani, M. Z.; Watson, R. T.; Meteyer, C. U.; Rideout, B. A.; Shivaprasad, H. L.; Ahmed, S.; Chaudhry, M. J. I.; Arshad, M.; Mahmood, S.; Ali, A.; Khan, A. A., Diclofenac residues as the cause of vulture population decline in Pakistan. *Nature* **2004,** *427* (6975), 630–633.

108. Koutsouba, V.; Heberer, T.; Fuhrmann, B.; Schmidt-Baumler, K.; Tsipi, D.; Hiskia, A., Determination of polar pharmaceuticals in sewage water of Greece by gas chromatography-mass spectrometry. *Chemosphere* **2003,** *51* (2), 69–75.

109. Heberer, T., Occurrence, fate, and removal of pharmaceutical residues in the aquatic environment: a review of recent research data. *Toxicol. Lett.* **2002,** *131* (1–2), 5–17.

110. Petrovic, M.; Hernando, M. D.; Diaz-Cruz, M. S.; Barcelo, D., Liquid chromatography-tandem mass spectrometry for the analysis of pharmaceutical residues in environmental samples: a review. *J. Chromatogr. A* **2005,** *1067* (1–2), 1–14.

111. Deng, A. P.; Himmelsbach, M.; Zhu, Q. Z.; Frey, S.; Sengl, M.; Buchberger, W.; Niessner, R.; Knopp, D., Residue analysis of the pharmaceutical diclofenac in different water types using ELISA and GC-MS. *Environ. Sci. Technol.* **2003,** *37* (15), 3422–3429.

112. Algar, W. R.; Prasuhn, D. E.; Stewart, M. H.; Jennings, T. L.; Blanco-Canosa, J. B.; Dawson, P. E.; Medintz, I. L., The Controlled Display of Biomolecules on Nanoparticles: A Challenge Suited to Bioorthogonal Chemistry. *Bioconjugate Chem.* **2011,** *22* (5), 825–858.

113. Petrie, B.; Barden, R.; Kasprzyk-Hordern, B., A review on emerging contaminants in wastewaters and the environment: Current knowledge, understudied areas and recommendations for future monitoring. *Water Res.* **2015,** *72*, 3–27.

114. Scognarniglio, V.; Arduini, F.; Palleschi, G.; Rea, G., Biosensing technology for sustainable food safety. *Trends Anal. Chem.* **2014,** *62*, 1–10.

115. Bennett, J. W.; Klich, M., Mycotoxins. *Clin. Microbiol. Rev.* **2003,** *16* (3), 497–516.

116. Zinedine, A.; Soriano, J. M.; Molto, J. C.; Manes, J., Review on the toxicity, occurrence, metabolism, detoxification, regulations and intake of zearalenone: An oestrogenic mycotoxin. *Food Chem. Toxicol.* **2007,** *45* (1), 1–18.

117. Maaroufi, K.; Chekir, L.; Creppy, E. E.; Ellouz, F.; Bacha, H., Zearalenone induces modifications of haematological and biochemical parameters in rats. *Toxicon* **1996,** *34* (5), 535–540.

118. Schothorst, R. C.; van Egmond, H. P., Report from SCOOP task 3.2.10 "Collection of occurrence data of *Fusarium* toxins in food and assessment of dietary intake by the population of EU member states" – Subtask: Trichothecenes. *Toxicol. Lett.* **2004,** *153* (1), 133–143.

119. Xiong, Y.; Leng, Y. K.; Li, X. M.; Huang, X. L.; Xiong, Y. H., Emerging strategies to enhance the sensitivity of competitive ELISA for detection of chemical contaminants in food samples. *Trends Anal. Chem.* **2020,** *126*, 19.

120. Peltomaa, R.; Fikacek, S.; Benito-Pena, E.; Barderas, R.; Head, T.; Deo, S.; Daunert, S.; Moreno-Bondi, M. C., Bioluminescent detection of zearalenone using recombinant peptidomimetic *Gaussia* luciferase fusion protein. *Microchim. Acta* **2020,** *187* (10), 11.

121. Becer, C. R.; Hoogenboom, R.; Schubert, U. S., Click Chemistry beyond Metal-Catalyzed Cycloaddition. *Angew. Chem. Int. Ed.* **2009,** *48* (27), 4900–4908.

122. Roetschi, A.; Berthoud, H.; Kuhn, R.; Imdorf, A., Infection rate based on quantitative real-time PCR of *Melissococcus plutonius*, the causal agent of European foulbrood, in honeybee colonies before and after apiary sanitation. *Apidologie* **2008,** *39* (3), 362–371.

123. Schottler, S.; Becker, G.; Winzen, S.; Steinbach, T.; Mohr, K.; Landfester, K.; Mailander, V.; Wurm, F. R., Protein adsorption is required for stealth effect of poly(ethylene glycol)- and poly(phosphoester)-coated nanocarriers. *Nat. Nanotechnol.* **2016,** *11* (4), 372–377.

124. Nsubuga, A.; Sgarzi, M.; Zarschler, K.; Kubeil, M.; Hubner, R.; Steudtner, R.; Graham, B.; Joshi, T.; Stephan, H., Facile preparation of multifunctionalisable 'stealth' upconverting nanoparticles for biomedical applications. *Dalton Trans.* **2018,** *47* (26), 8595–8604.

125. Gorris, H. H.; Resch-Genger, U., Perspectives and challenges of photon-upconversion nanoparticles – Part II: bioanalytical applications. *Anal. Bioanal. Chem.* **2017,** *409* (25), 5875–5890.

126. Genersch, E., American Foulbrood in honeybees and its causative agent, *Paenibacillus larvae*. *J. Invertebr. Pathol.* **2010,** *103*, S10–S19.

127. Ebeling, J.; Knispel, H.; Hertlein, G.; Funfhaus, A.; Genersch, E., Biology of *Paenibacillus larvae*, a deadly pathogen of honey bee larvae. *Appl. Microbiol. Biotechnol.* **2016,** *100* (17), 7387–7395.

128. Dobbelaere, W.; De Graaf, D. C.; Reybroeck, W.; Desmedt, E.; Peeters, J. E.; Jacobs, F. J., Disinfection of wooden structures contaminated with *Paenibacillus larvae* subsp. *larvae* spores. *J. Appl. Microbiol.* **2001,** *91* (2), 212–216.

129. Stephan, J. G.; de Miranda, J. R.; Forsgren, E., American foulbrood in a honeybee colony: spore-symptom relationship and feedbacks. *BMC Ecology* **2020,** *20* (1), 14.

130. Locke, B.; Low, M.; Forsgren, E., An integrated management strategy to prevent outbreaks and eliminate infection pressure of American foulbrood disease in a commercial beekeeping operation. *Prev. Vet. Med.* **2019,** *167*, 48–52.

131. Hornitzky, M. A. Z.; Wilson, S. C., A system for the diagnosis of the major bacterial brood diseases of honeybees. *J. Apic. Res.* **1989,** *28* (4), 191–195.

132. De Graaf, D. C.; Alippi, A. M.; Brown, M.; Evans, J. D.; Feldlaufer, M.; Gregorc, A.; Hornitzky, M.; Pernal, S. F.; Schuch, D. M. T.; Titera, D.; Tomkies, V.; Ritter, W., Diagnosis of American foulbrood in honey bees: a synthesis and proposed analytical protocols. *Lett. Appl. Microbiol.* **2006,** *43* (6), 583–590.

133. Sopko, B.; Zitek, J.; Nesvorna, M.; Markovic, M.; Kamler, M.; Titera, D.; Erban, T.; Hubert, J., Detection and quantification of *Melissococcus plutonius* in honey bee workers exposed to European foulbrood in Czechia through conventional PCR, qPCR, and barcode sequencing. *J. Apic. Res.* **2020,** *59* (4), 503–514.

134. Forsgren, E.; Laugen, A. T., Prognostic value of using bee and hive debris samples for the detection of American foulbrood disease in honey bee colonies. *Apidologie* **2014,** *45* (1), 10–20.

135. Olsen, P. E.; Grant, G. A.; Nelson, D. L.; Rice, W. A., Detection of American foulbrood disease of the honeybee, using a monoclonal antibody specific to *Bacillus larvae* in an enzyme-linked immunosorbent assay. *Can. J. Microbiol.* **1990,** *36* (10), 732–735.

136. Huse, K.; Böhme, H.-J.; Scholz, G. H., Purification of antibodies by affinity chromatography. *J. Biochem. Biophys. Methods* **2002,** *51* (3), 217–231.

137. Torre, L. A.; Bray, F.; Siegel, R. L.; Ferlay, J.; Lortet-Tiulent, J.; Jemal, A., Global Cancer Statistics, 2012. *CA Cancer J. Clin.* **2015,** *65* (2), 87–108.

138. Center, M. M.; Jemal, A.; Lortet-Tiulent, J.; Ward, E.; Ferlay, J.; Brawley, O.; Bray, F., International Variation in Prostate Cancer Incidence and Mortality Rates. *Eur. Urol.* **2012,** *61* (6), 1079–1092.

139. Giljohann, D. A.; Mirkin, C. A., Drivers of biodiagnostic development. *Nature* **2009,** *462* (7272), 461–464.

140. Rissin, D. M.; Kan, C. W.; Campbell, T. G.; Howes, S. C.; Fournier, D. R.; Song, L.; Piech, T.; Patel, P. P.; Chang, L.; Rivnak, A. J.; Ferrell, E. P.; Randall, J. D.; Provuncher, G. K.; Walt, D. R.; Duffy, D. C., Single-molecule enzyme-linked immunosorbent assay detects serum proteins at subfemtomolar concentrations. *Nat. Biotechnol.* **2010,** *28* (6), 595–599.

141. Thaxton, C. S.; Elghanian, R.; Thomas, A. D.; Stoeva, S. I.; Lee, J. S.; Smith, N. D.; Schaeffer, A. J.; Klocker, H.; Horninger, W.; Bartsch, G.; Mirkin, C. A., Nanoparticle-based bio-barcode assay redefines "undetectable" PSA and biochemical recurrence after radical prostatectomy. *Proc. Natl. Acad. Sci. U. S. A.* **2009,** *106* (44), 18437–18442.

142. Liebherr, R. B.; Hutterer, A.; Mickert, M. J.; Vogl, F. C.; Beutner, A.; Lechner, A.; Hummel, H.; Gorris, H. H., Three-in-one enzyme assay based on single molecule detection in femtoliter arrays. *Anal. Bioanal. Chem.* **2015,** *407* (24), 7443–7452.

143. Mickert, M. J.; Farka, Z.; Kostiv, U.; Hlaváček, A.; Horák, D.; Skládal, P.; Gorris, H. H., Measurement of Sub-femtomolar Concentrations of Prostate-Specific Antigen through Single-Molecule Counting with an Upconversion-Linked Immunosorbent Assay. *Anal. Chem.* **2019,** *91* (15), 9435–9441.

144. Salvati, A.; Pitek, A. S.; Monopoli, M. P.; Prapainop, K.; Bombelli, F. B.; Hristov, D. R.; Kelly, P. M.; Aberg, C.; Mahon, E.; Dawson, K. A., Transferrin-functionalized nanoparticles lose their targeting capabilities when a biomolecule corona adsorbs on the surface. *Nat. Nanotechnol.* **2013,** *8* (2), 137–143.

145. Shi, Y.; Shi, B. Y.; Dass, A. V. E.; Lu, Y. Q.; Sayyadi, N.; Kautto, L.; Willows, R. D.; Chung, R.; Piper, J.; Nevalainen, H.; Walsh, B.; Jin, D. Y.; Packer, N. H., Stable Upconversion Nanohybrid Particles for Specific Prostate Cancer Cell Immunodetection. *Sci. Rep.* **2016,** *6*, 11.

146. Weber, P. C.; Ohlendorf, D. H.; Wendoloski, J. J.; Salemme, F. R., Structural origins of high-affinity biotin binding to streptavidin. *Science* **1989,** *243* (4887), 85–88.

147. Farka, Z.; Mickert, M. J.; Hlaváček, A.; Skládal, P.; Gorris, H. H., Single Molecule Upconversion-Linked Immunosorbent Assay with Extended Dynamic Range for the Sensitive Detection of Diagnostic Biomarkers. *Anal. Chem.* **2017,** *89* (21), 11825–11830.

148. Anderson, J. L.; Morrow, D. A., Acute Myocardial Infarction. *New Engl. J. Med.* **2017,** *376* (21), 2053–2064.

149. Thygesen, K.; Alpert, J. S.; Jaffe, A. S.; Simoons, M. L.; Chaitman, B. R.; White, H. D., Third Universal Definition of Myocardial Infarction. *Circulation* **2012,** *126* (16), 2020–2035.

150. Takeda, S.; Yamashita, A.; Maeda, K.; Maeda, Y., Structure of the core domain of human cardiac troponin in the Ca^{2+}-saturated form. *Nature* **2003,** *424* (6944), 35–41.

151. Jaffe, A. S.; Ravkilde, J.; Roberts, R.; Naslund, U.; Apple, F. S.; Galvani, M.; Katus, H., It's time for a change to a troponin standard. *Circulation* **2000,** *102* (11), 1216–1220.

152. Thygesen, K.; Mair, J.; Katus, H.; Plebani, M.; Venge, P.; Collinson, P.; Lindahl, B.; Giannitsis, E.; Hasin, Y.; Galvani, M.; Tubaro, M.; Alpert, J. S.; Biasucci, L. M.; Koenig, W.; Mueller, C.; Huber, K.; Hamm, C.; Jaffe, A. S., Recommendations for the use of cardiac troponin measurement in acute cardiac care. *Eur. Heart J.* **2010,** *31* (18), 2197–2204.

153. Westermann, D.; Neumann, J. T.; Sorensen, N. A.; Blankenberg, S., High-sensitivity assays for troponin in patients with cardiac disease. *Nat. Rev. Cardiol.* **2017,** *14* (8), 472–483.

154. Apple, F. S.; Collinson, P. O., Analytical Characteristics of High-Sensitivity Cardiac Troponin Assays. *Clin. Chem.* **2012,** *58* (1), 54–61.

155. Savukoski, T.; Twarda, A.; Hellberg, S.; Ristiniemi, N.; Wittfooth, S.; Sinisalo, J.; Pettersson, K., Epitope Specificity and IgG Subclass Distribution of Autoantibodies to Cardiac Troponin. *Clin. Chem.* **2013,** *59* (3), 512–518.

156. Katrukha, A. G.; Bereznikova, A. V.; Filatov, V. L.; Esakova, T. V.; Kolosova, O. V.; Pettersson, K.; Lovgren, T.; Bulargina, T. V.; Trifonov, I. R.; Gratsiansky, N. A.; Pulkki, K.; Voipio-Pulkki, L. M.; Gusev, N. B., Degradation of cardiac troponin I: implication for reliable immunodetection. *Clin. Chem.* **1998,** *44* (12), 2433–2440.

157. Panteghini, M., Assay-related issues in the measurement of cardiac troponins. *Clin. Chim. Acta* **2009,** *402* (1–2), 88–93.

158. Apple, F. S.; Sandoval, Y.; Jaffe, A. S.; Ordonez-Llanos, J., Cardiac Troponin Assays: Guide to Understanding Analytical Characteristics and Their Impact on Clinical Care. *Clin. Chem.* **2017,** *63* (1), 73–81.

159. Herman, D. S.; Kavsak, P. A.; Greene, D. N., Variability and Error in Cardiac Troponin Testing An ACLPS Critical Review. *Am. J. Clin. Pathol.* **2017,** *148* (4), 281–295.

160. Bray, F.; Ferlay, J.; Soerjomataram, I.; Siegel, R. L.; Torre, L. A.; Jemal, A., Global cancer statistics 2018: GLOBOCAN estimates of incidence and mortality worldwide for 36 cancers in 185 countries. *CA Cancer J. Clin.* **2018,** *68* (6), 394–424.

161. Gluz, O.; Liedtke, C.; Gottschalk, N.; Pusztai, L.; Nitz, U.; Harbeck, N., Triple-negative breast cancer-current status and future directions. *Ann. Oncol.* **2009,** *20* (12), 1913–1927.

162. Swain, S. M.; Kim, S. B.; Cortes, J.; Ro, J.; Semiglazov, V.; Campone, M.; Ciruelos, E.; Ferrero, J. M.; Schneeweiss, A.; Knott, A.; Clark, E.; Ross, G.; Benyunes, M. C.; Baselga, J., Pertuzumab, trastuzumab, and docetaxel for HER2-positive metastatic breast cancer (CLEOPATRA study): overall survival results from a randomised, double-blind, placebo-controlled, phase 3 study. *Lancet Oncol.* **2013,** *14* (6), 461–471.

163. Ross, J. S.; Slodkowska, E. A.; Symmans, W. F.; Pusztai, L.; Ravdin, P. M.; Hortobagyi, G. N., The HER-2 Receptor and Breast Cancer: Ten Years of Targeted Anti-HER-2 Therapy and Personalized Medicine. *Oncologist* **2009,** *14* (4), 320–368.

164. Titford, M., Progress in the development of microscopical techniques for diagnostic pathology. *J. Histotechnol.* **2009,** *32* (1), 9–19.

165. Nakane, P. K.; Pierce, G. B., Enzyme-Labeled Antibodies: Preparation and Application for the Localization of Antigens. *J. Histochem. Cytochem.* **1966,** *14* (12), 929–931.

166. Susaki, E. A.; Ueda, H. R., Whole-body and Whole-Organ Clearing and Imaging Techniques with Single-Cell Resolution: Toward Organism-Level Systems Biology in Mammals. *Cell Chem. Biol.* **2016,** *23* (1), 137–157.

167. Nayak, T. R.; Andreou, C.; Oseledchyk, A.; Marcus, W. D.; Wong, H. C.; Massague, J.; Kircher, M. F., Tissue factor-specific ultra-bright SERRS nanostars for Raman detection of pulmonary micrometastases. *Nanoscale* **2017,** *9* (3), 1110–1119.

168. Fan, L.; Tian, Y. Y.; Yin, R.; Lou, D. D.; Zhang, X. Z.; Wang, M.; Ma, M.; Luo, S. H.; Li, S. Y.; Gu, N.; Zhang, Y., Enzyme catalysis enhanced dark-field imaging as a novel immunohistochemical method. *Nanoscale* **2016,** *8* (16), 8553–8558.

169. Bera, K.; Schalper, K. A.; Rimm, D. L.; Velcheti, V.; Madabhushi, A., Artificial intelligence in digital pathology – new tools for diagnosis and precision oncology. *Nat. Rev. Clin. Oncol.* **2019,** *16* (11), 703–715.

170. Griffin, J.; Treanor, D., Digital pathology in clinical use: where are we now and what is holding us back? *Histopathology* **2017,** *70* (1), 134–145.

171. Modlitbova, P.; Porizka, P.; Kaiser, J., Laser-induced breakdown spectroscopy as a promising tool in the elemental bioimaging of plant tissues. *Trends Anal. Chem.* **2020,** *122*, 10.

172. El Haddad, J.; Canioni, L.; Bousquet, B., Good practices in LIBS analysis: Review and advices. *Spectrochim. Acta Part B Atom. Spectr.* **2014,** *101*, 171–182.

173. Škarková, P.; Novotný, K.; Lubal, P.; Jebavá, A.; Pořízka, P.; Klus, J.; Farka, Z.; Hrdlička, A.; Kaiser, J., 2D distribution mapping of quantum dots injected onto filtration paper by laser-induced breakdown spectroscopy. *Spectrochim. Acta Part B Atom. Spectr.* **2017,** *131*, 107–114.

174. Modlitbová, P.; Hlaváček, A.; Švestková, T.; Pořízka, P.; Šimoníková, L.; Novotný, K.; Kaiser, J., The effects of photon-upconversion nanoparticles on the growth of radish and duckweed: Bioaccumulation, imaging, and spectroscopic studies. *Chemosphere* **2019,** *225*, 723–734.

175. Gimenez, Y.; Busser, B.; Trichard, F.; Kulesza, A.; Laurent, J. M.; Zaun, V.; Lux, F.; Benoit, J. M.; Panczer, G.; Dugourd, P.; Tillement, O.; Pelascini, F.; Sancey, L.; Motto-Ros, V., 3D Imaging of Nanoparticle Distribution in Biological Tissue by Laser-Induced Breakdown Spectroscopy. *Sci. Rep.* **2016,** *6*, 29936.

176. Farka, Z.; Mickert, M. J.; Mikusova, Z.; Hlavacek, A.; Bouchalova, P.; Xu, W. S.; Bouchal, P.; Skladal, P.; Gorris, H. H., Surface design of photon-upconversion nanoparticles for high-contrast immunocytochemistry. *Nanoscale* **2020,** *12* (15), 8303–8313.

List of Abbreviations

4-CN	4-chloro-1-naphthol
Ab	antibody
AFB	American foulbrood
AFM	atomic force microscopy
AMI	acute myocardial infarction
BSA	bovine serum albumin
CFU	colony-forming unit
CMD	carboxymethylated dextran
CPA	cyclopropylamine
DCF	diclofenac
EDC	1-ethyl-3-(3-dimethylaminopropyl)carbodiimide
EFB	European foulbrood
EIS	electrochemical impedance spectroscopy
ELISA	enzyme-linked immunosorbent assay
HRP	horseradish peroxidase
HSA	human serum albumin
ICC	immunocytochemistry
IHC	immunohistochemistry
LFIA	lateral flow immunoassay
LIBS	laser-induced breakdown spectroscopy
LOD	limit of detection
MIP	molecularly imprinted polymer
NHS	N-hydroxysuccinimide
NLISA	nanozyme-linked immunosorbent assay
PAA	poly(acrylic acid)
PBNP	Prussian blue nanoparticle
PCR	polymerase chain reaction
PoC	point-of-care
PP	plasma polymerization

PSA   prostate-specific antigen

QCM   quartz crystal microbalance

QD   quantum dot

SPE   screen-printed electrode

SPR   surface plasmon resonance

THFMA   tetrahydrofurfuryl methacrylate

TVC   1,2,4-trivinylcyclohexane

UCNP   photon-upconversion nanoparticle

ULISA   upconversion-linked immunosorbent assay

ZEA   zearalenone

Appendix

List of Publications

1. Hlaváček, A.; <u>Farka, Z.*</u>; Mickert, M. J.; Kostiv, U.; Brandmeier, J. C.; Horák, D.; Skládal, P.; Foret, F.; Gorris, H. H., Bioconjugates of photon-upconversion nanoparticles for cancer biomarker detection and imaging. *Nat. Protoc*. Accepted.

2. Obořilová, R.; Šimečková, H.; Pastucha, M.; Klimovič, Š.; Víšová, I.; Přibyl, J.; Vaisocherová-Lísalová, H.; Pantůček, R.; Skládal, P.; Mašlaňová, I.; <u>Farka Z.*</u>, Atomic force microscopy and surface plasmon resonance for real-time single-cell monitoring of bacteriophage-mediated lysis of bacteria. *Nanoscale* **2021**, *13* (31), 13538–13549.

3. Brandmeier, J. C.; Raiko, K.; <u>Farka, Z.*</u>; Peltomaa, R.; Mickert, M. J.; Hlaváček, A.; Skládal, P.; Soukka, T.; Gorris, H. H., Effect of Particle Size and Surface Chemistry of Photon-Upconversion Nanoparticles on Analog and Digital Immunoassays for Cardiac Troponin. *Adv. Healthc. Mater*. **2021**, *10* (18), 2100506.

4. Pastucha, M.; Odstrčilíková, E.; Hlaváček, A.; Brandmeier, J. C.; Vykoukal, V.; Weisová, J.; Gorris, H. H.; Skládal, P.; <u>Farka Z.*</u>, Upconversion-linked Immunoassay for the Diagnosis of Honeybee Disease American Foulbrood. *IEEE J. Sel. Top. Quantum Electron*. **2021**, *27* (5), 6900311.

5. Pořízka, P.; Vytisková, K.; Obořilová, R.; Pastucha, M.; Gábriš, I.; Brandmeier, J. C.; Modlitbová, P.; Gorris, H. H.; Novotný, K.; Skládal, P.; Kaiser, J.; <u>Farka, Z.</u>, Laser-Induced Breakdown Spectroscopy as a Readout Method for Immunocytochemistry with Upconversion Nanoparticles. *Microchim. Acta* **2021**, *188*, 147.

6. Petruš, O.; Macko, J.; Oriňaková, R.; Oriňak, A.; Múdra, E.; Kupková, M.; Pastucha, M.; <u>Farka, Z.</u>; Socha, V., Detection of organic dyes by surface-enhanced Raman spectroscopy using plasmonic NiAg nanocavity films. *Spectrochim. Acta A* **2020**, 249, 119322.

7. Trnková, L.; Třísková, I.; Čechal, J.; <u>Farka, Z.</u>, Polymer pencil leads as a porous nanocomposite graphite material for electrochemical applications: The impact of chemical and thermal treatments. *Electrochem. Commun*. **2021**, *126*, 107018.

8. <u>Farka Z.*</u>, Nanoparticle-Based Biosensing: En Route to Ultimate Sensitivity (Meet the Board). *Anal. Sens*. **2021**, *1* (4), 136–137.

9. <u>Farka, Z.</u>; Mickert, M. J.; Pastucha, M.; Mikušová, Z.; Skládal, P.; Gorris, H. H., Advances in Optical Single-Molecule Detection: En Route to Super-Sensitive Bioaffinity Assays. *Angew. Chem. Int. Ed.* **2020**, *59* (27), 10746–10773. (Z.F. and M.J.M. contributed equally)

10. <u>Farka, Z.*</u>; Mickert, M. J.; Mikušová, Z.; Hlaváček, A.; Bouchalová, P.; Xu, W.; Bouchal, P.; Skládal, P.; Gorris, H. H., Surface design of photon-upconversion nanoparticles for high-contrast immunocytochemistry. *Nanoscale* **2020**, *12* (15), 8303–8313. (Z.F. and M.J.M. contributed equally)

11. Peltomaa, R.; <u>Farka, Z.</u>; Mickert, M. J.; Brandmeier, J. C.; Pastucha, M.; Hlaváček, A.; Martínez-Orts, M.; Canales, Á.; Skládal, P.; Benito-Peña, E.; Moreno-Bondi, M. C.; Gorris, H. H., Competitive upconversion-linked immunoassay using peptide mimetics for the detection of the mycotoxin zearalenone. *Biosens. Bioelectron.* **2020**, *170*, 112683.

12. Makhneva, E.; Barillas, L.; <u>Farka, Z.</u>; Pastucha, M.; Skládal, P.; Weltmann, K. D.; Fricke, K., Functional Plasma Polymerized Surfaces for Biosensing. *ACS Appl. Mater. Interfaces* **2020**, *20* (14), 17100–17112.

13. Kostiv, U.; <u>Farka, Z.</u>; Mickert, M. J.; Gorris, H. H.; Velychkivska, N.; Pop-Georgievski, O.; Pastucha, M.; Odstrčilíková, E.; Skládal, P.; Horák, D., Versatile bioconjugation strategies of PEG-modified upconversion nanoparticles for bioanalytical applications. *Biomacromolecules* **2020**, *21* (11), 4502–4513. (U.K. and Z.F. contributed equally)

14. Víšová, I.; Smolková, B.; Uzhytchak, M.; Vrabcová, M.; Chafai, D. E.; Houska, M.; Pastucha, M.; Skládal, P.; <u>Farka, Z.*</u>; Dejneka, A.; Vaisocherová-Lísalová, H., Functionalizable Antifouling Coatings as Tunable Platforms for the Stress-Driven Manipulation of Living Cell Machinery. *Biomolecules* **2020**, *10* (8), 1146.

15. Šišoláková, I.; Hovancová, J.; Oriňaková, R.; Oriňak, A.; Trnková, L.; Trísková, I.; <u>Farka, Z.</u>; Pastucha, M.; Radoňák, J., Electrochemical determination of insulin on CuNPs/chitosan-MWCNTs and CoNPs/chitosan-MWCNTs modified screen printed carbon electrodes. *J. Electroanal. Chem.* **2020**, *860*, 113881.

16. Poláchová, V.; Pastucha, M.; Mikušová, Z.; Mickert, M. J.; Hlaváček, A.; Gorris, H. H.; Skládal, P.; <u>Farka, Z.*</u>, Click-conjugated photon-upconversion nanoparticles in an immunoassay for honeybee pathogen *Melissococcus plutonius*. *Nanoscale* **2019**, *11* (17), 8343–8351.

17. Mickert, M. J.; <u>Farka, Z.</u>; Kostiv, U.; Hlaváček, A.; Horák, D.; Skládal, P.; Gorris, H. H., Measurement of Sub-femtomolar Concentrations of Prostate-Specific Antigen through Single-Molecule Counting with an Upconversion-Linked Immunosorbent Assay. *Anal. Chem.* **2019**, *91* (15), 9435–9441. (M.J.M and Z.F. contributed equally)

18. Pastucha, M.; <u>Farka, Z.</u>; Lacina, K.; Mikušová, Z.; Skládal, P., Magnetic nanoparticles for smart electrochemical immunoassays: a review on recent developments. *Microchim. Acta* **2019**, *186*, 312.

19. Modlitbová, P.; <u>Farka, Z.</u>; Pastucha, M.; Pořízka, P.; Novotný, K.; Skládal, P.; Kaiser, J., Laser-induced breakdown spectroscopy as a novel readout method for nanoparticle-based immunoassays. *Microchim. Acta* **2019**, *186*, 629.

20. Mikušová, Z.; <u>Farka, Z.*</u>; Pastucha, M.; Poláchová, V.; Obořilová, R.; Skládal, P., Amperometric Immunosensor for Rapid Detection of Honeybee Pathogen *Melissococcus plutonius*. *Electroanalysis* **2019**, *31* (10), 1969–1976.

21. Makhneva, E.; <u>Farka, Z.*</u>; Pastucha, M.; Obrusník, A.; Horáčková, V.; Skládal, P.; Zajíčková, L., Maleic anhydride and acetylene plasma copolymer surfaces for SPR immunosensing. *Anal. Bioanal. Chem.* **2019**, *411* (29), 7689–7697.

22. <u>Farka, Z.*</u>; Čunderlová, V.; Horáčková, V.; Pastucha, M.; Mikušová, Z.; Hlaváček, A.; Skládal, P., Prussian Blue Nanoparticles as a Catalytic Label in a Sandwich Nanozyme-Linked Immunosorbent Assay. *Anal. Chem.* **2018**, *90* (3), 2348–2354. (Z.F. and V.Č. contributed equally)

23. Makhneva, E.; <u>Farka, Z.</u>; Skládal, P.; Zajíčková, L., Cyclopropylamine plasma polymer surfaces for label-free SPR and QCM immunosensing of *Salmonella*. *Sens. Actuators B Chem.* **2018**, *276*, 447–455.

24. Hegemann, D.; Indutnyi, I.; Zajíčková, L.; Makhneva, E.; <u>Farka, Z.</u>; Ushenin, Y.; Vandenbossche, M., Stable, nanometer-thick oxygen-containing plasma polymer films suited for enhanced biosensing. *Plasma Process. Polym.* **2018**, *15* (11), 1800090.

25. Modlitbová, P.; Pořízka, P.; Novotný, K.; Drbohlavová, J.; Chamradová, I.; <u>Farka, Z.</u>; Zlámalová-Gargošová, H.; Romih, T.; Kaiser, J., Short-term assessment of cadmium toxicity and uptake from different types of Cd-based Quantum Dots in the model plant *Allium cepa* L. *Ecotoxicol. Environ. Saf.* **2018**, *153*, 23–31.

26. Makhneva, E.; Obrusník, A.; Farka, Z.; Skládal, P.; Vandenbossche, M.; Hegemann, D.; Zajíčková, L., Carboxyl-rich plasma polymer surfaces in surface plasmon resonance immunosensing. *Jpn. J. Appl. Phys.* **2018**, *57* (01AG06), 1–5.

27. Modlitbová, P.; Klepárník, K.; Farka, Z.; Pořízka, P.; Skládal, P.; Novotný, K.; Kaiser, J., Time-Dependent Growth of Silica Shells on CdTe Quantum Dots. *Nanomaterials* **2018**, *8* (6), 439.

28. Farka, Z.; Juřík, T.; Kovář, D.; Trnková, L.; Skládal, P., Nanoparticle-Based Immunochemical Biosensors and Assays: Recent Advances and Challenges. *Chem. Rev.* **2017**, *117* (15), 9973–10042.

29. Farka, Z.; Mickert, M. J.; Hlaváček, A.; Skládal P.; Gorris, H. H., Single Molecule Upconversion-Linked Immunosorbent Assay with Extended Dynamic Range for the Sensitive Detection of Diagnostic Biomarkers. *Anal. Chem.* **2017**, *89* (21), 11825–11830. (Z.F. and M.J.M. contributed equally)

30. Hlaváček, A.; Peterek, M.; Farka, Z.; Mickert, M. J.; Prechtl, L.; Knopp D.; Gorris, H. H., Rapid single-step upconversion-linked immunosorbent assay for diclofenac. *Microchim. Acta* **2017**, *184* (10), 4159–4165.

31. Škarková, P.; Novotný, K.; Lubal, P.; Jebavá, A.; Pořízka, P.; Klus, J.; Farka, Z.; Hrdlička, A.; Kaiser, J., 2D distribution mapping of quantum dots injected onto filtration paper by laser-induced breakdown spectroscopy. *Spectrochim. Acta B. At. Spectrosc.* **2017**, *131*, 107–114.

32. Kubesa, O.; Horáčková, V.; Moravec, Z.; Farka, Z.; Skládal, P., Graphene and graphene oxide for biosensing. *Monatsh. Chem.* **2017**, *148* (11), 1937–1944.

33. Kovář, D.; Malá, A.; Mlčochová, J.; Kalina, M.; Fohlerová, Z.; Hlaváček, A.; Farka, Z.; Skládal, P.; Starčuk, Z.; Jiřík, R.; Slabý, O.; Hubálek, J., Preparation and Characterisation of Highly Stable Iron Oxide Nanoparticles for Magnetic Resonance Imaging. *J. Nanomater.* **2017**, *2017* (7859289), 1–8.

34. Trnková, L.; Farka, Z., Advanced nano- and biomaterials in biophysical chemistry (Editorial). *Monatsh. Chem.* **2017**, *148* (11), 1899–1900.

35. Farka, Z.; Juřík, T.; Pastucha, M.; Skládal, P. Enzymatic Precipitation Enhanced Surface Plasmon Resonance Immunosensor for the Detection of *Salmonella* in Powdered Milk. *Anal. Chem.* **2016**, *88* (23), 11830–11836.

36. Farka, Z.; Juřík, T.; Pastucha, M.; Kovář, D.; Lacina, K.; Skládal, P., Rapid immunosensing of *Salmonella* Typhimurium using electrochemical impedance spectroscopy: the effect of sample treatment. *Electroanalysis* **2016**, *28* (8), 1803–1809. (Z.F. and T.J. contributed equally)

37. Hlaváček, A.; Farka, Z.; Hübner, M.; Horňáková, V.; Němeček, D.; Skládal, P.; Knopp, D.; Gorris, H. H., Competitive Upconversion-Linked Immunosorbent Assay for the Sensitive Detection of Diclofenac. *Anal. Chem.* **2016**, *88* (11), 6011–6017.

38. Juřík, T.; Podešva, P.; Farka, Z.; Kovář, D.; Skládal, P.; Foret, F., Nanostructured gold deposited in gelatin template applied for electrochemical assay of glucose in serum. *Electrochim. Acta* **2016**, *188*, 277–285.

39. Trnková, L.; Farka, Z., Physical and electrochemical aspects of bio- and nanomaterials (Editorial). *Monatsh. Chem*. **2016**, *147* (5), 845.

40. Farka, Z.; Kovář, D.; Skládal, P., Rapid detection of microorganisms based on active and passive modes of QCM. *Sensors* **2015**, *15* (1), 79–92. (Z.F. and D.K. contributed equally)

41. Kovář, D.; <u>Farka, Z.</u>; Skládal, P., Detection of aerosolized biological agents using the piezoelectric immunosensor. *Anal. Chem.* **2014**, *86* (17), 8680–8686. (D.K. and Z.F. contributed equally)

42. <u>Farka, Z.</u>; Kovář, D.; Přibyl, J.; Skládal, P., Piezoelectric and surface plasmon resonance biosensors for *Bacillus atrophaeus* spores. *Int. J. Electrochem. Sci.* **2013**, *8* (1), 100–112.

43. <u>Farka, Z.</u>; Kovář, D.; Skládal, P., Piezoelectric biosensor coupled to cyclone air sampler for detection of microorganisms. *Chem. Listy* **2013**, *107* (S3), s302–s304.

* corresponding author

Paper I

Nanoparticle-Based Immunochemical Biosensors and Assays: Recent Advances and Challenges

Farka, Z.; Juřík, T.; Kovář, D.; Trnková, L.; Skládal, P.

Contribution:

Literature research, manuscript writing

Nanoparticle-Based Immunochemical Biosensors and Assays: Recent Advances and Challenges

Zdeněk Farka,[†] Tomáš Juřík,[†,‡] David Kovář,[†] Libuše Trnková,[§] and Petr Skládal*[†,‡]

[†]Central European Institute of Technology (CEITEC), [‡]Department of Biochemistry, Faculty of Science, and [§]Department of Chemistry, Faculty of Science, Masaryk University, Kamenice 5, 625 00 Brno, Czech Republic

ABSTRACT: We review the progress achieved during the recent five years in immunochemical biosensors (immunosensors) combined with nanoparticles for enhanced sensitivity. The initial part introduces antibodies as classic recognition elements. The optical sensing part describes fluorescent, luminescent, and surface plasmon resonance systems. Amperometry, voltammetry, and impedance spectroscopy represent electrochemical transducer methods; electrochemiluminescence with photo-electric conversion constitutes a widely utilized combined method. The transducing options function together with suitable nanoparticles: metallic and metal oxides, including magnetic ones, carbon-based nanotubes, graphene variants, luminescent carbon dots, nanocrystals as quantum dots, and photon up-converting particles. These sources merged together provide extreme variability of existing nanoimmunosensing options. Finally, applications in clinical analysis (markers, tumor cells, and pharmaceuticals) and in the detection of pathogenic microorganisms, toxic agents, and pesticides in the environmental field and food products are summarized.

CONTENTS

1. INTRODUCTION

This review focuses on advances in immunochemical biosensors (immunosensors) combined with nanoparticles for the enhanced sensitivity of the resulting assays. When reading the papers published in *Chemical Reviews* during the recent five years, we noticed a strong interest in various types of nanoparticles and other nanomaterials applied for the improvement of biosensors as well as other bioanalytical assays. The relevant publications typically concentrated on the type of nano-object being chosen. On the basis of our long experience in the construction and application of immunosensors, or biosensors based on antibodies, we find it challenging to set the primary focus on antibodies and to propose a review of the most promising trends regarding the combination with nanoparticles for immunosensing. Despite the numerous attempts to replace them with alternative recognition molecules (aptamers, biomimetic polymers, artificial receptors), classic antibodies still remain the most common recognition elements in research and commercial affinity assays. Thus, we consider it beneficial to aim the attention of the review on this point, summarizing the novel nanotrends to improve the classic immunoanalytical and, in particular, immunosensing concepts. We believe that such an approach will be interesting for not only chemists working in the analytical field but also the large community of immunoassay users within medical (clinical assays) and biological research.

The targeted scientific resources cover the recent five years, namely, the period from 2012 to 2016 (September). The initial, and rather wide, literature search yielded approximately 4500 hits. After manual preselection, 3300 papers were evaluated as relevant to our field.

The critically selected results cover all possible types of immunosensors and immunoassays applied usually in heterogeneous formats; i.e., several separation and washing steps are involved. Homogeneous formats, providing simplified working procedures, were rather rare. The initial part introduces antibodies as classic recognition elements, which, however, continue to develop and improve the usage of tools from molecular biology and protein engineering. The sensing techniques covered mostly optical and electrochemical transducers. The former area included classic label-based fluorescence and luminescence but only a few chemiluminescence examples; advanced label-less surface plasmon resonance was rather common together with its localized variants. One of the chapters also discusses the promising surface-enhanced Raman scattering. Electrochemistry was mainly represented by the simplest amperometric measurements, followed by voltammetric approaches and impedance spectroscopy; potentiometric techniques were rare and consisted of miniaturized field-effect transducers. Furthermore, combined electro-optical techniques, namely, electrochemiluminescence and photoelectric conversion, proved very fruitful. Special examples of magnetic transduction are focused both on assays and on imaging

techniques using magnetic nanoparticles modified with target-specific antibodies.

The transducing options are combined with all suitable nanoparticles: metallic and metal oxides, with special attention to magnetic ones, carbon-based nanotubes, graphene variants, and luminescent carbon dots. Luminescent nanocrystals are represented by quantum dots and photon up-converting particles. Individual sensors also often contain other components, including enzymes (peroxidase, glucose oxidase, alkaline phosphatase) generating redox-active donors/acceptors, molecular fluorophores, and electroactive molecules (e.g., ferrocene).

The above-mentioned groups of transducers and nanoparticles ensure an extremely wide range of potential combinations, and this precondition is really reflected in the exceptional variability of the existing nanoimmunosensing options. Finally, we have tried to provide an overview of applications aimed especially at clinical analysis, followed by the detection of pathogenic organisms and toxic agents; the environmental field and food assay then complement the list.

2. ANTIBODIES

Currently, the detection and quantification of different analytes exhibits an increasing tendency toward broader application. In multiple immunoassays, antibodies (Ab's) are employed as a biorecognition element, and the utilization in biosensors brings new tools for analysis in the biochemical, clinical, and environmental fields. It is commonly known that the high sensitivity and selectivity of immunosensors to recognize a biomolecular component are ensured by specific interactions and the extremely high equilibrium association constants (10^{10} M^{-1} and greater) attainable between an antibody and its corresponding antigen.

Antibodies are a unique natural family of (immune system) related glycoproteins known as immunoglobulins (Ig's), produced by differentiated B cells in response to the attendant of an immunogen during an immune response. The role of Ab is essential to life and plays an unsubstitutable role in the immune systems of higher animals. A typical mammalian antibody unit is a heterodimer consisting of two identical long heavy chains (approximately 450−600 amino acid residues) and two identical short light chains (approximately 220 residues).[1] The heavy chains are a large polypeptide subunit and vary between different animals. These four chains are joined to form a "Y"-shaped molecule (Figure 1).

Both Ig chains consist of conserved protein structures called domains corresponding to approximately 110 amino acids. The light chains have two domains—variable (V_L) and constant (C_L). The heavy chains also have one variable domain (V_H) and, depending on the Ig types, another three (in the case of IgG, IgA, and IgD) or four (in the case of IgM and IgE) constant domains (C_H1, C_H2, C_H3, C_H4). The domains are identical between the two light and two heavy chains. The heavy chains are connected with each other by covalent disulfide bridges and noncovalent bonds. Similarly, the light chains are connected to the heavy chains. The arms of the "Y" consist of the N-termini of each heavy chain associated with one of the light chains to create two antigen-binding domains. This region is termed the "antigen-binding fragment" (Fab fragment or domain). The tail of the "Y" is formed by a combination of the C-termini of the two heavy chains and is termed the "crystallizable fragment" (Fc fragment or domain). Physiologically, the Fc fragment is responsible for the effector role of the Ig (i.e., the cell receptor interaction, complement activation, etc.).[2]
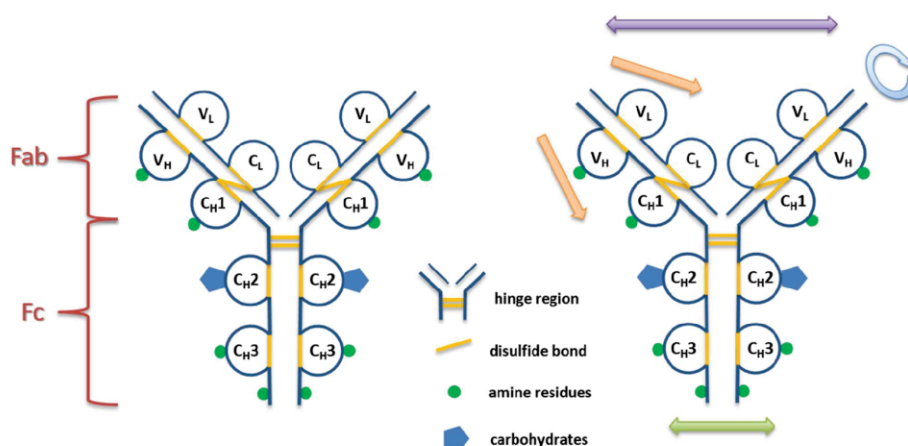
Figure 1. Unique structure of antibodies comprised of four polypeptide units joined together to form a "Y"-shaped molecule—two identical heavy chains and two identical light chains. The disulfide bonds depicted between C_L and C_H1 are relevant for most IgG subclasses. The two Fab's are antigen-binding fragments, and Fc is a crystallizable fragment. In the right-hand structure, flexibility is outlined: Fab arm waving (violet), Fab rotation (blue), Fab elbow bend (orange), and Fc wagging (green).

The chains have another region, known as the hinge region, located between the C_H1 and C_H2 domains The hinge region gives flexibility—namely, arm rotation and waving—to the Fab fragment. The other possible type of flexibility rests in the Fab elbow bend and Fc wagging.[3] The hinge region contains a high amount of proline accountable for the flexibility and sensitivity to proteolytic enzymes. A controlled scission using proteolytic enzymes (pepsin or papain) leads to the fragmentation of a molecule; as well as reaction with disulfide reducing agents. The sensitivity of IgG subclasses to proteolytic cleavage depends on the sequence and length of their hinge regions; also, the strength of the reducing agents plays a role regarding the position of reduced − S−S− bridges.[4]

A minimal antigen-binding fragment consisting of V_H and V_L chains and referred to as the Fv fragment is obtainable by the pepsin digestion of F(ab′). A recombinant single-chain Fv (scFv) fragment contains a small flexible linker between the V_H and V_L chains and is more stable than the native Fv fragment. The progress in the molecular recombinant DNA technology allows scFv fragments retaining the antigen-binding capacity of the parent immunoglobulin or totally newly designed scFv fragments to be obtained in a routine manner (Figure 2).[5,6]

Due to the variability of the V_L and V_H domains, the Fab fragment determines the specificity and ability to interact and bind the immunogen. This variability is located in three segments within the domains called hypervariable regions or complementarity-determining regions (CDRs).[7] These regions exhibit about 10 amino acids and are usually denoted as CDR1, CDR2, and CDR3. Each antibody molecule has two antigen-binding sites formed by the regions, localized at the tip of each arm of the "Y"-shaped molecule.

The classification of antibodies is based on the sequence of the heavy chains and the content of carbohydrates. The heavy chains are highly conserved and can be separated into isotypes or classes of Ig (μ, IgM; γ, IgG; ε, IgE; α, IgA; δ, IgD). Similarly, the light chains are described as κ and λ, but contrariwise, they are the same for all Ig classes. Isotypes α and γ have approximately 450 amino acids, whereas μ and ε exhibit 550 amino acids. Over this diversity, the individual classes of antibodies differ in the

quaternary molecular structure: IgM has a pentameric structure, IgA has a dimeric one, and the others are monomers.

As mentioned above, the discussed antibodies are glycoproteins. The carbohydrates are localized in the constant domains of the heavy chains, mainly around the C_H2 and hinge regions.[8] The share of carbohydrates is 15% of the heavy chains. The exact role of the carbohydrate residues is not fully understood; we can speculate on their relation to catabolism or to some of the Ig unknown functions. Experimentally, it was shown that the oxidation or deglycosylation of the Ig does not affect the change of the molecular structure; only the effector functionality is affected.[9,10]

The eminent dogma of the structure of antibodies was reinterpreted by discovering a new antibody type in the Camelidae species in the 1990s.[11] Camelids (i.e., *Camelus dromedarius*, *Lama glama*) produce heavy-chain antibodies (hcAb's) missing the light chains; these antibodies are more stable than classic antibodies and are capable of strongly binding antigens. The recombinant variable domain (V_HH) of hcAb is commercially produced and called a "nanobody".[12] The items may possess inherent thermal and protease stability and are able to bind epitopes that cannot interact with whole antibodies.[13] Other heavy-chain antibodies have been isolated from cartilaginous fish and termed "IgNAR" or "vNAR" (the variable domain of a new antigen receptor in sharks).[14,15] Genetic engineering allows making, e.g., recombinant fusion products of nanobodies with the superfolder green fluorescent protein[16] or intraspike cross-linked antibodies for HIV therapy.[17]

Antibodies harvested from blood plasma are mixture products of many different plasma cell clones, and they react with many epitopes. The number of producing clones varies on the inducing epitopes. In practice, it is not possible to isolate specific antibodies of one clone from these mixtures known as polyclonal antibodies (pAb's). The immunoglobulins produced by the single plasma cell originating clone are specific against one epitope of the immunogen. These specific antibodies are called monoclonal and are mainly produced via the hybridoma technique using the fusion of B-cells with the immortal myeloma cell line.[18] Another in vitro technique, known as the phage display method, is based on selecting recombinant structures
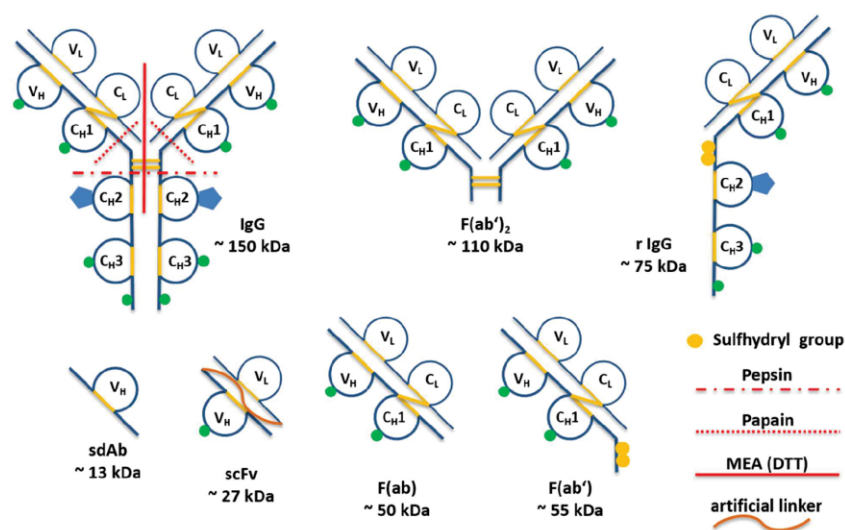
69

Figure 2. Fragments of an IgG molecule prepared via the application of protease enzymes and disulfide reducing agents. The image includes recombinant fragments of classic antibodies, i.e., single-chain Fv (scFv) and camelized single-domain Ab (sdAb), also known as V_HH or nanobodies, which can be prepared in the same form by recombinant engineering.

presented on the bacteriophage surface and tested for the interaction with the target antigen.[19]

The specificity and sensitivity of antibodies are crucial parameters for the construction of immunosensors.[20] Suo et al. reported a comparative study of the efficacy of seven antibodies for the binding of the living cells of *Salmonella enterica*. The results suggest that an antibody should target a surface antigen extending out from the bacterial surface and closely attaching to the bacterial cell wall. In the studied case, the best results were achieved using antifimbria antibodies.[21]

As regards the immunosensing formats, the most common competitive and sandwich options are shown in Figure 3.

3. NANOPARTICLES FOR IMMUNOSENSING

3.1. Metallic Nanoparticles

3.1.1. Gold Nanoparticles. Because of their unique optical, chemical, electrical, and catalytic properties, Au NPs are the most common signal amplification labels for various kinds of immunosensors and immunoassays, including lateral flow assays, electrochemistry, colorimetric assays, and plasmonic sensing (SPR, LSPR, SERS).[22] The particular properties and applications of Au NPs are strongly influenced by their sizes and shapes. The color of a colloidal Au NP solution is either intense red (particles smaller than 100 nm) or dirty yellow (larger particles).[23] These optical properties are caused by localized surface plasmon resonance. The free electrons of Au NPs undergo oscillation in the presence of an oscillating electromagnetic field, and resonance occurs at a specific frequency of the light.[24]

The currently most common technique for the synthesis of Au NPs was developed by Turkevich et al. in 1951[25] and further improved by Frens in 1973.[26] This method is based on the chemical reduction of gold salts (e.g., hydrogen tetrachloroaurate, $HAuCl_4$) by citrate; the products of the reaction are monodisperse spherical Au NPs. The particle size and shape can be controlled by the concentration of the reagents or the selected reducing agent or by using a surfactant (i.e., cetyltrimethylammonium bromide, CTAB).[27] Further optimizations of the

experimental conditions allowed the preparation of Au NPs with various shapes, such as nanorods,[28] nanostars,[29] nanoclusters,[30] core−shell structures,[31] and irregularly shaped NPs.[32]

Au NPs have drawn the particular focus of scientists in the bioanalytical field due to their distinct physical and chemical properties, including easy preparation and modification, superior biocompatibility, intensive color, and catalytic activity.[33,34] Au NPs enable the conjugation of biological ligands, exploiting the strong affinity of the mercapto[35] and amino[36] functional groups to gold. Au NPs also provide a microenvironment compatible with biomolecules; thus, their activity remains even after immobilization. For this reason, Au NPs are often modified using different biomolecules, such as antibodies, enzymes, or DNA, to create specific nanoprobes applicable for detecting various analytes.[37]

The applications of Au NPs in immunosensing cover the majority of possible transducers. For example, due to the high molar extinction coefficient and significant color changes during aggregation, a number of colorimetric immunoassays have been developed.[38] Fluorescence immunoassays can be constructed on the basis of the energy transfer between fluorophores and Au NPs, which causes the quenching of the fluorescence signal.[39] The plasmonic properties of Au NPs can be used to amplify SPR immunosensing,[40] the catalytic properties of Au NPs are utilizable for the amplification of optical or electrochemical signals,[41] and the electrochemical properties can be exploited in EIS biosensors.[42] Many in vitro studies have demonstrated that Au NPs are generally nontoxic for cells, this being in contrast with other NPs (e.g., carbon nanotubes and metal oxides).[43] The precondition then enables the application of Au NPs within in vivo diagnostics and imaging.[44]

More details about the amplification of the sensor response by Au NPs are provided in sections devoted to individual transducers. Au NPs appear to be quite universal and fully established; the excellent stability compared to that of other metals in combination with routine procedures for bioconjugation, pronounced colors, and sensitive plasmon changes makes

70

them typically the first nanomaterial to be considered for improving the performance of classic immunoassays.

3.1.2. Silver Nanoparticles. Ag NPs embody the most common commercially produced type of NPs. They are used as antimicrobials within multiple consumer products, including cosmetics, clothing, shoes, and detergents, and as surface coatings in respirators and water filters.[45,46] Ag NPs are characterized by an extinction coefficient higher than that of Au NPs exhibiting the same size and also provide stronger Raman and fluorescence enhancement,[47] which enables their use in optical applications.[48] Moreover, Ag NPs can be oxidized more easily and offer improved electrochemical activity compared to Au NPs, making them excellent candidates for detection tags in electrochemical sensing. However, the practical applications of Ag NPs in immunosensing are restricted by their significantly lower stability, more prominent difficulty to functionalize, and limited biocompatibility compared to those of Au NPs.[49] In recent years, the application of Ag NPs in immunosensing has been increasing with the improvement in the relevant methods of synthesis, stabilization, and functionalization.

Spherical Ag NPs can be synthesized using the Turkevich method described for spherical Au NPs. Experimentally, due to its good solubility in polar solvents, $AgNO_3$ is the most commonly used precursor in the preparation of Ag NPs via the reduction route. The reduction using citrate typically leads to the production of particles with larger diameters (50−100 nm) and broad surface plasmon absorption. Smaller spherical nanoparticles (5−20 nm) can be synthesized using $NaBH_4$ as the reducing agent.[50,51] The Ag NP dispersions are usually stabilized by poly(vinyl alcohol), poly(vinylpyrrolidone), BSA, citrate, or cellulose.[34]

Besides the amplification of traditional immunosensors, Ag NPs are also used in specialized applications. A metalloimmunoassay based on the dissolution of Ag NPs was developed by Szymanski et al.[52] After the sandwich reaction with the Ag NP label, the Ag NPs aggregated due to the addition of thiocyanate, and the negatively charged aggregates were attracted to the positively charged carbon electrode during pretreatment. Once in direct contact with the electrode surface, the Ag NPs were oxidized at +0.6 V to form soluble silver ions, which were immediately complexed by the thiocyanate and detected via anodic stripping voltammetry.[52]

Furthermore, the silver-based enhancement approach is suitable for the amplification of biosensors based on Au NP labels. Au NPs can act as a catalyst, reducing silver ions into metallic silver in the presence of a reducing agent. The reaction leads to the deposition of silver on the gold surface as the nucleation site and to the growth of NPs, resulting in signal enhancement (Figure 4). This approach was originally used to improve the properties of microscopic imaging; the applications in DNA sensing[53] and immunosensing[54,55] followed.

Even though Ag NPs do not typically show fluorescencent properties, very small Ag NPs or nanoclusters[56,57] can be used in fluorescence applications. The fluorescence of these particles is assumed to originate from either the quantum states within the metal core or mixed ligand states at the inorganic−organic interface.[58] There are also reports about the preparation of larger luminescent Ag NPs. Zheng et al. synthesized fluorescent polycrystalline Ag NPs with a diameter of 18 nm.[59] The luminescence was claimed to arise from small domains, with sizes similar to the Fermi electron wavelength (∼0.5 nm), that provide discrete energy states and permit optical transitions. However,
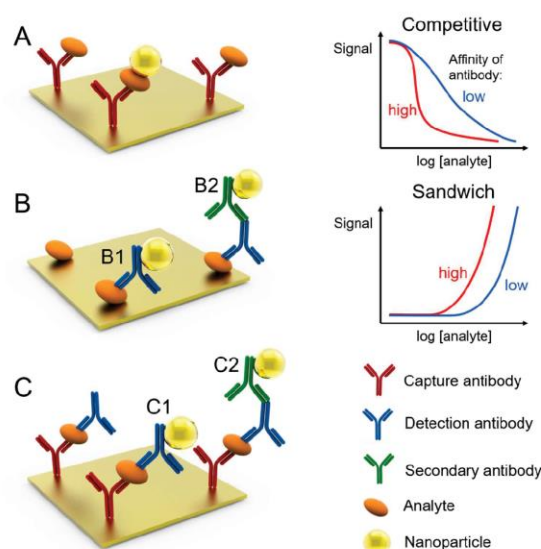
Figure 3. Formats suitable for electrochemical immunosensing include competitive (A, B) and sandwich (C) immunoassays. For competition, the immobilized recognition molecule can be either an antibody (A) or an antigen (B, antigen, hapten, or their derivatives); the signal-generating labeled molecule, or the tracer, includes analyte−NP (A) or antibody−NP (B1) conjugates. The latter variant can also employ an unlabeled primary antibody and a secondary labeled antibody (B2). For sandwich assays, the capture (primary) antibody is immobilized (C), and a signal is generated using the labeled secondary antibody (C1) or even the third labeled antibody (C2). The general calibration graphs for both competitive and sandwich assays are shown in the right-hand section of the image.
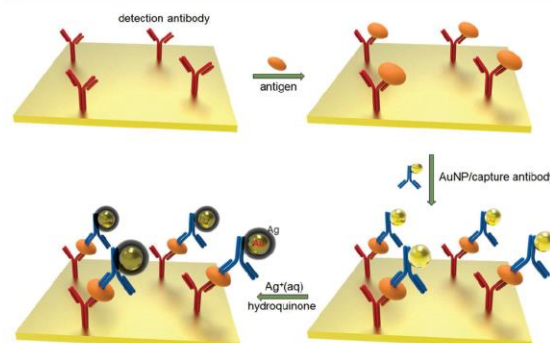
Figure 4. Principle of the enhanced response for sandwich immunoassays with Au NP-labeled secondary antibodies. Au NPs act as a catalyst and help to reduce Ag^+ ions into metallic silver with hydroquinone as a reducing agent. Based on ref 54.

no immunoassays based on the direct exploitation of the fluorescent properties of Ag NPs have been reported thus far.

At present, the secondary signal enhancement step seems to be the most important role of Ag NPs in the immunoanalytical field, followed by the important role in the SERS techniques.

3.2. Magnetic Nanoparticles

Magnetic NPs constitute a type of nanomaterial with unique physicochemical properties and an extremely wide variety of applications. Due to the good biocompatibility, MPs have been

71
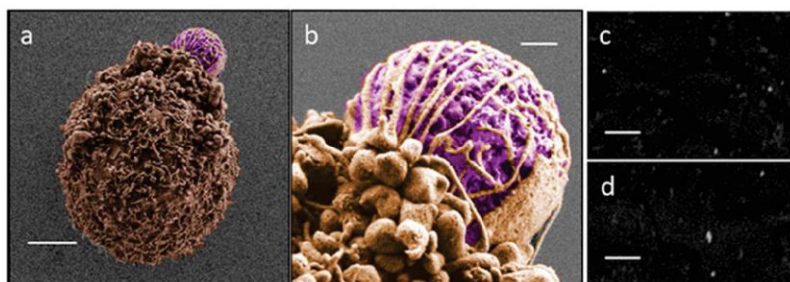
Figure 5. Scanning electron microscopy images of Caco2 cells captured with MB/anti-EpCAM and simultaneously labeled with AuNPs/anti-EpCAM in the presence of THP-1 cells: (a, b) SEM images (falsely colored with Corel Paint Shop Pro) of a Caco2 cell captured by MBs/anti-EpCAM. (c, d) Higher magnification backscattered images of the Caco2 cell surface showing AuNPs distributed along the cell plasma membrane. Scale bars: 3 μm (a), 400 nm (b), and 200 nm (c, d). Reprinted from ref 82. Copyright 2012 American Chemical Society.

widely used in biomedical domains such as drug delivery,[60,61] hyperthermia,[62,63] and magnetic resonance imaging.[64,65] Environmental and catalytic applications are no less important.[66,67]

Analytical applications based on magnetic NPs are represented mainly by three strategies. The basic strategy is the magnetic preconcentration of an analyte due to its interaction with biofunctionalized nanoparticles. In this manner, one can preconcentrate the analyte, minimize the effect of a sample matrix with interferents, or attract the immunocomplex onto the surface of the sensor via an external magnetic field. This is perhaps the most important and unique advantage. Another procedure rests in applications where functionalized MPs are used as tags for the visualization and sensitive detection of immunocomplexes with a specific analyte. The third common approach is the integration of magnetic NPs into the transducer material or the modification of the sensor surface to improve the analytical signal. In many cases, the aforementioned approaches are combined and improve the final effects, e.g., the sensitivity, selectivity, signal-to-noise ratio, and limit of detection.

3.2.1. Magnetic Preconcentration. A very attractive, simple, and promising field is magnetic preconcentration, where one can easily separate the analyte from the matrix of the sample using an external magnetic field and, in the second step, detect the analyte in the form of an immunosandwich. For example, magnetic NPs were used for the preconcentration of myeloperoxidase from human plasma and magnetically entrapped on the electrode surface.[68] The activity of the myeloperoxidase was determined via the chronoamperometric detection of converted TMB. The main advantage consisted of direct detection without the necessity of any tags. Commercial Dynabeads were used for the competitive magneto-immunoassay.[69] Ochratoxin A from diluted instant coffee samples competed with the enzymatic tracer on the immunobeads, and after washing, the immunocomplex was measured amperometrically. The LOD in the spiked coffee samples corresponded to 0.26 μg/mL, a value which was, interestingly, comparable to that of the samples diluted in PBS (an LOD of 0.32 μg/mL). Magnetic nanoparticles with immobilized primary antibodies against p24 HIV antigen were also used as the capture probe.[70] The immunocomplex was attracted to the SPE electrode surface, and the HRP tag consisting of HRP immobilized via the dextrin amine skeleton on the Au NPs amplified the signal via the oxidation of catechol by H_2O_2. The electrochemical response for the p24 HIV antigen was linear in a wide range, and an LOD of 0.5 pg/mL was achieved. An immunosensor for detecting phosphorylated butyrylcholinesterase was described by Zhang et

al.[71] The prepared Fe_3O_4/TiO_2 NPs selectively interacted with the phosphorylated moiety, and the complexes were magnetically separated from the human serum samples. The secondary anti-BChE Ab's with quantum dot tags made an immunosandwich that was analyzed using SPR. In addition, Cd^{2+} ions were measured using square wave voltammetry. The LOD for the phosphorylated BChE was at a concentration of 10 pM.

Magnetic NPs with a gold shell and antibodies immobilized in an oriented manner were used for the preconcentration of the bovine leukemia virus antigen gp51.[72] The screening method for the clenbuterol in bovine hair was described by Regiart et al.,[73] who took advantage of a combination between a microfluidic chip and nanogold-modified screen-printed electrodes. The competitive indirect immunoassay used magnetic microparticles with primary Ab's for the preconcentration of the antigen. The microparticles were magnetically entrapped on the Au NP-modified SPE, and a mixture of the analyte and phosphatase-modified clenbuterol was injected. This combination minimized the consumption of the reagents and samples to a few microliters and facilitated an improvement in the detection limit of up to 8 pg/mL. Magnetic preconcentration was also applied on brevetoxin B in a competitive assay with guanine-assembled graphene nanoribbons conjugated with brevetoxin B.[74] Ru-$(bpy)_3Cl_2$ was electrochemically detected on a magnetic carbon paste electrode, and the signal was proportional to the concentration of the brevetoxin. Magnetic NPs with specific antibodies were used for the preconcentration of hepatitis B surface antibodies.[75] Secondary Ab with HRP formed an immunosandwich, and the produced 2-hydroxy-3-aminophenoxazine was detected using the DPV technique with a very low detection limit of 8 ng/L. The strategy of magnetic preconcentration in combination with an electrochemical transducer was also used for, e.g., the impedance detection of *Listeria monocytogenes*,[76] amperometric detection of iterleukin-6,[77] chronoamperometric detection of Alzheimer's disease biomarkers in cerebrospinal fluid, human serum, and plasma,[78] and chronoamperometric detection of the human colon adenocarcinoma cell line as a model of cancer circulating cells (Figure 5).[79] Similarly, the combined detection of cancer cells and tumor biomarkers was described by Yang et al.[80] Doubly functionalized magnetic nanobeads with anti-avian influenza A (H7N9) and alkaline phosphatase were used for the preconcentration of the target virus.[81] These immunocomplexed nanobeads were interacted with an mAb-modified GCE to make a stable immunosandwich. A double electrode signal was measured during the enzyme-induced metallization reaction. Anodic

72

stripping voltammetry helped to analyze the H7N9 virus with an LOD of 6.8 pg/mL.

A comparative study of the immunomagnetic separation and electrochemical detection of *Salmonella* was proposed by Brandão et al.[83] The authors realized the separation of *Salmonella enterica* in different media, such as BHI broth or diluted and whole milk. A slight matrix effect when using mag NPs at a higher bacteria concentration was shown. Miniaturization and its combination with nanobiotechnology can provide powerful and sensitive analytical instruments. Microfluidics combined with nanostructured microelectrodes has been reported.[84] Otieno et al. described sensitive preconcentration using mag NPs and the ultralow accurate detection of cancer biomarkers, which can be helpful for the early detection of cancer. Interleukin-6 and interleukin-8 were detected with ultralow limits of detection equal to 5 and 7 fg/mL, respectively.

β-Amyloid as an Alzheimer's disease biomarker was magnetically separated from the whole blood sample and detected using a portable SERS probe with an LOD of 100 fg/mL.[85] One multifunctional nanoplatform was made of a magnetic core–plasmonic Au shell nanoparticle attached to hybrid graphene oxide.

3.2.2. Renewable Sensor Surfaces and Modification Methods.
The reusable sensor layer based on immunomagnetic particles has several advantages, including magnetic preconcentration, ecological aspects, and automation possibilities. This kind of assay has been described several times for, e.g., the detection of aminoterminal probrain natriuretic peptides,[86] *α*-fetoprotein,[87] and phosphorylated p53 protein.[88] Electrochemically active magnetite NPs were described by Cheng et al.[89] The magnetic core was interlayered with Prussian blue and AEAPS. This cluster was coated with gold nanoparticles supporting the immobilization of anti-*Escherichia coli* antibodies. The sophisticated system produced a renewable amperometric immunosensor. These four-layer functionalized magnetic NPs were entrapped on the electrode using an internal electromagnet. The final size of these combined particles was approximately 100 nm. The observed detection limit corresponded to 4.3×10^2 cfu/mL *E. coli* O157:H7. An amperometric magneto-immunoassay was also developed using core–shell magnetic particles attached to a carbon paste electrode.[90] The tracer was used for the specific label of the captured *Legionella pneumophila*, and the electric current was recorded after the addition of H_2O_2 in the presence of hydroquinone.

The sensing signal can be enhanced by enlargement of the sensor area and thus via increasing its binding capacity. Electrochemical impedance spectroscopy with a modified magnetic glassy carbon electrode (MGCE) was used for the detection of CD146, a biomarker of human malignant melanoma.[91] Au@Fe_3O_4@graphene clusters were used to modify the MGCE electrode and thus to produce a conductive and extra-area platform for the immobilization of specific antibodies. The sensor was tested with several interferent molecules and then applied for detection in real human serum samples. A wide linear range from 5 pg/mL to 500 ng/mL and a detection limit of 2.5 pg/mL showed good specificity of this label-free immunosensor. A new sensing platform for the ultralow detection (LOD = 0.33 pg/mL) of the CEA was provided by the modification of the GCE with Fe_3O_4/porous graphitic carbon nanocomposites and self-polymerized dopamine.[92] Mag NPs coated on an ITO electrode were used as the active layer for the immobilization of mAb anti-*Vibrio cholerae*.

The impedimetric behavior of this system was studied using a ferro/ferricyanide redox probe.[93]

A combination of several different nanomaterials is also common, bringing new options and improved sensor properties. For example, the GCE was modified using graphene sheets with thionine, and the magnetic NPs covered by a silver shell were immobilized through glutaraldehyde chemistry.[94] The anti-kanamycin antibodies were thus immobilized on the surface in a significantly higher amount. The improved electrical behavior of the sensor was characterized using cyclic voltammetry and square wave voltammetry. The ability of the sensor was also evaluated using real pork samples. Kanamycin was detected in less than 5 min with an LOD of 15 pg/mL. An electrochemical sensor for the CEA tumor marker was prepared with an enhanced electrode layer.[95] The GCE electrode was modified with Au NP-functionalized magnetic carbon nanotubes together with lead ions (Pb^{2+}/Au/MWCNTs–Fe_3O_4). This setup enhanced the electrochemical signal, and the CEA was detected with an LOD of 1.7 fg/mL.

QCM sensors are mostly used for the direct monitoring of emerging immunocomplexes at their surfaces, and magnetic NPs can be used beneficially for the amplification of QCM-based bacteria detection. Zhou et al. described a different approach, one based on monitoring the insoluble product given by the reaction of 3-amino-9-ethylcarbazole with H_2O_2 catalyzed by the HRP tag.[96] First, a change in the monitored frequency was given by the magnetic attraction of the immunocomplex (CRP and anti-CRP@MPs) to the QCM sensor. An additional frequency change arose due to the catalytic reaction and formation of the insoluble product. Using this amplification, C-reactive protein was determined in the serum with an LOD of 0.3 pg/mL.

3.2.3. Magnetic Particles as Tags.
An analytical signal can be enhanced using a suitably selected tag. Mag NPs are usable individually or in combination with other NPs or signal mediators; for example, the simultaneous detection of tumor markers was based on the electrochemical determination of two mag-particle-based probes on the electrode surface.[97] The primary Ab was immobilized on the poly[1-methyl-3-(1-methyl-4-piperidinylmethylene)thiophene-2,5-diyl chloride]-modified GCE electrode. Two electrochemical probes were made via the modification of Fe_3O_4 nanoparticles with thionine and ferrocenecarboxylic acid possessing two separate analytical peaks after the sandwich-type interaction of a labeled secondary Ab with tumor markers. The LODs for the squamous cell carcinoma-associated antigen (SCCA) and carcinoembryonic antigen corresponded to 4 and 5 pg/mL, respectively.

Mag NPs coated with streptavidin were used as a tag for the detection of the PSA using spectral correlation interferometry, where the change of the thickness of the bioactive layer consisting of the primary Ab, PSA, biotinylated second Ab, and mag NPs was monitored.[98] Compared to other NPs used in the study, interestingly, the MPs were more effective, and an LOD of 92 pg/mL was achieved. Immunomagnetic NPs were also used as an enhancing tag for the direct competitive immunoassay for okadaic acid monitored using SPR.[99] The magnetic preconcentration with SPR was used for the enhanced detection of AFP[100] and human interleukin 17A.[101]

Similarly, the core–shell magnetite@Au NPs were used for the preconcentration of the human epididymis protein 4 (an ovarian tumor marker) and further SERS detection of this immunocomplex with an LOD of 100 fg/mL.[102] The same concept was also employed to detect *E. coli*;[103] likewise, the anti-CEA/

73

aminothiophenol/Fe_3O_4−Au tag was used for the improved detection of the CEA expressed by A459 lung cancer cells.[104]

The analytical response can also be enhanced via special tags affecting the signal or increasing the amount of mediators. A controlled release system was developed for the detection of the SCCA.[105] Mesoporous magnetite NPs with encapsulated toluidine blue (TB) were used as a tag and source of mediator molecules. The interaction of conjugated Ab's led to the release of TB, and the released probe was electrochemically detected by CV. The strategy of "huge" molecular tags carrying several electrochemically active molecules is represented by cadmium ion-doped magnetic poly(styrene−acrylic acid) nanospheres and carbon nanospheres with protein cage NPs.[106]

Enzyme mimic tags are very attractive due to their high stability and resistance against harsh conditions. There are many applications of magnetic particles serving as enzyme mimic tags. A nonenzymatic label based on magnetic beads with immobilized TMB and CEA was used for competitive binding between this complex and free analyzed CEA.[107] CV and DPV were used to monitor the oxidation of ascorbic acid catalyzed by mag beads@ TMB. A low detection limit, 1 pg/mL, was achieved. The corralite-like nanocomposite $Fe_3O_4/MnO_2/Pt$ mimics peroxidase activity and was tested as a tag conjugated on the secondary Ab.[108] The amperometric signal was proportional to the concentration of the CEA with an LOD of 0.16 pg/mL. A hematin-decorated magnetic $NiCo_2O_4$ superstructure was used for the construction of an enzyme-free ultrasensitive photoelectrochemical and electrochemical assay to facilitate the detection of the CEA.[109]

A magnetic immunoassay on porous 3D filters (Figure 6) made of twisted fibers of polyethylene coated with polypropylene
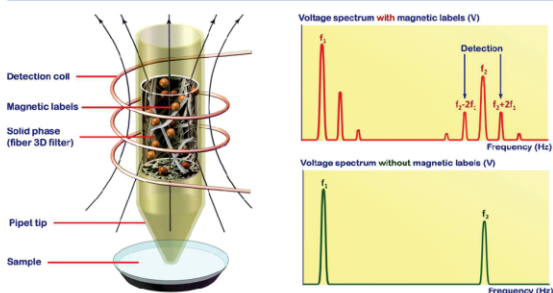
Figure 6. Detection of superparamagnetic nanolabels by their nonlinear response at combinatorial frequencies from the whole volume of the 3D solid phase located inside a pipet tip. Reprinted from ref 110. Copyright 2013 American Chemical Society.

(Figure 7) seems to be a promising tool for automatic detection in various applications. A model experiment was presented on the detection of the staphylococcal enterotoxin A and toxic shock syndrome toxin from milk. The antigens were captured using antibodies covalently attached in the filter, and the immunosandwich arose by interaction with the magnetic NPs labeled with secondary Ab's. The mag NPs served as an active signal tag, and their nonlinear magnetization indicated the presence of an antigen in the sample.

Magnetic NPs became indispensable for specific preconcentration of analytes present at very low concentrations; the simultaneous sample cleanup represents an additional benefit. Unique magnetic properties allowed the proposal of interesting sensing mechanisms, though the development and transfer to commercial devices seems to be slow. The applications in targeted drug delivery will grow. The highest potential exists in the magnetic resonance imaging for specific contrast enhancement.

3.3. Carbon-Based Nanomaterials

3.3.1. Carbon Nanotubes. Carbon nanotubes (CNTs), discovered by Iijima in 1991,[111] can be considered graphite sheets rolled up into nanoscale tubes. CNTs can be divided into two main categories: single-walled carbon nanotubes (SWCNTs) and multiwalled carbon nanotubes (MWCNTs). SWCNTs consist of a single sheet of graphene wrapped into a cylindrical tube. SWCNTs are typically about 0.4−2 nm in diameter and 1−100 μm in length, depending on the method used for their synthesis. MWCNTs are composed of concentric cylinders of rolled up graphene sheets; the diameter of MWCNTs usually ranges between 1 and 10 nm, depending on the number of sheets. CNTs exhibit metallic or semiconducting character, according to their chirality and the diameter of the tubes.[112] The chirality can be designated as armchair, zigzag, or chiral, depending on the axis upon which the CNT was rolled.[113]

The three main types of CNT synthesis are arc discharge,[111] chemical vapor deposition (CVD),[114] and laser ablation.[115] CNTs were first synthesized using carbon-arc discharge. Depending upon the catalyst used, this approach provides MWCNTs or SWCNTs with a high yield (∼90%) and ensures good control over the dimensions of the synthesized tubes. Due to the high yield and reproducibility, this technique allows large-scale commercial production. Chemical vapor deposition is also catalyst dependent and results in small-diameter CNTs. The yield of the CNTs is lower, but the created CNTs are significantly cleaner, and the purification procedures can be simplified. Laser ablation offers the cleanest CNTs, though at a higher price and lower yield. All these synthesis techniques provide a mixture of metallic and semiconducting CNTs.[113]
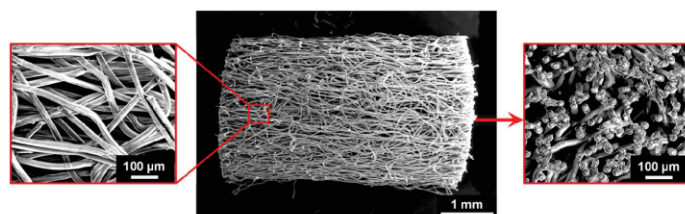
Figure 7. SEM surface morphology of cylindrical 3D fiber filters obtained with an FEI Quanta 200 scanning electron microscope: left, magnified lateral surface fragment (500× magnification); center, overview of the lateral surface of the filter (60× magnification); right, top surface fragment (500× magnification). Reprinted from ref 110. Copyright 2013 American Chemical Society.

74
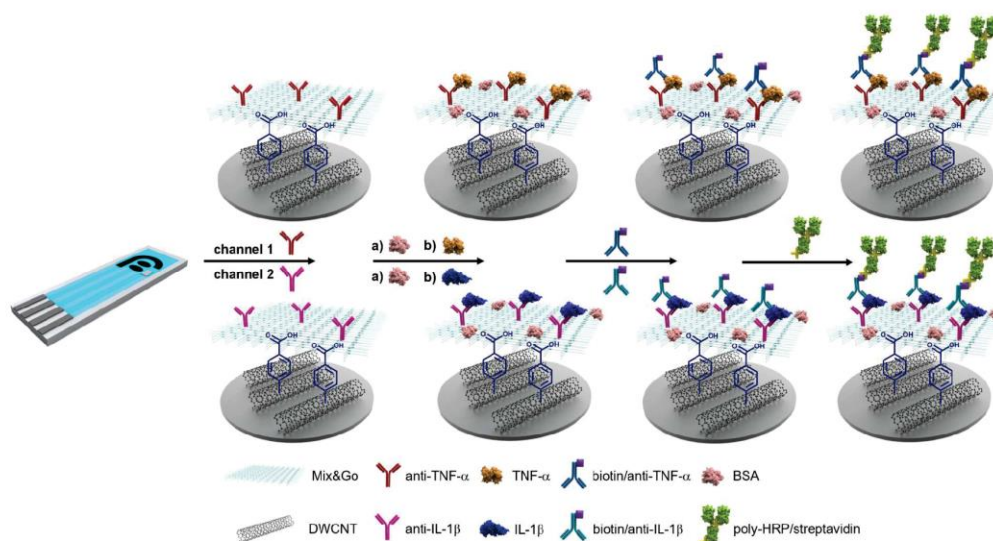
Figure 8. Schematic display of the different steps involved in the preparation of the dual electrochemical immunosensor for multiplexed determination of IL-1β and TNF-α cytokines. Based on ref 126.

CNTs are often used in immunosensing[116] due to their unique physical and chemical properties, e.g., the high surface-to-volume ratio, high electrical conductivity, and rapid electrode kinetics.[117,118] The functionalization of CNTs can be performed via covalent or noncovalent binding with different chemical groups, which allows high compatibility of CNTs for the conjugation with biomolecules.[119] The large surface area of CNTs facilitates a massive loading capacity for the conjugation of biomolecules or incorporation of other nanoparticles; this property can improve the sensitivity via amplification of the electrical[120] or optical[121] signals. The high conductivity of CNTs was also demonstrated to mediate electron transfer, which further enhances the measured current.[122] The chemical functionalization of CNTs also allows us to enhance their solubility and biocompatibility.[123]

In electrochemical immunosensing, CNTs can be used either to directly modify the electrode surface or as labels in sandwich assays. CNTs as an electrode nanomaterial offer improved sensitivities, wide detection ranges, and lower limits of detection compared to traditional carbon electrodes.[124] The CNTs in sandwich-based immunoassays can be used as signal labels and to provide surface enlargement for the immobilization of the secondary antibodies.[125]

Double-walled carbon nanotubes (DWCNTs) were used to modify two-channel SPEs for the simultaneous determination of two cytokines (interleukin-1β (IL-1β) and tumor necrosis factor α (TNF-α); relevant details are shown in Figure 8).[126] DWCNTs offer improved lifetimes and a higher stability compared to MWCNTs,[127] and they also exhibit better electrochemical behavior than SWCNTs; such features then enhance the electron transfer and allow considerable over-potential reduction for various species. After chemical mod-ification of DWCNTs, the outer cylinder works as a protective sheath to guard the electric properties of the inner tube. Covalent sidewall chemistry can be performed on DWCNTs without any loss of the intrinsic properties.[128] Sandwich-type immunoassays with amperometric signal amplification using poly-HRP–streptavidin conjugates, H_2O_2 as the HRP substrate, and

hydroquinone as the redox mediator were conducted for each cytokine. LODs of 0.38 pg/mL (IL-1β) and 0.85 pg/mL (TNF-α) were achieved, and the application of a sensor was demonstrated in real samples of human serum and saliva.

A label-free electrochemical immunosensor based on GCE modified by MWCNTs and Au–Pt NPs was developed by Liu et al.[129] The modifications of the electrode increased the surface area for the immobilization of a large amount of antibodies and enhanced the electrochemical performance. The mAb captured the analyte (mycotoxin zearalenone), which was subsequently directly oxidized by DPV. However, this assay scheme can only be applied in detecting electrochemically active analytes; in other cases, a sandwich or a competitive assay has to be performed.

3.3.2. Graphene. Graphene is a two-dimensional single-atom-thick planar sheet of sp^2-bonded carbon atoms organized in a hexagonal lattice. The first mechanical exfoliation of graphene was demonstrated by Novoselov et al. in 2004;[130] since then, the number of studies on graphene has constantly increased. Graphene offers outstanding electrochemical, mechanical, and thermal properties, optical transparency (~97.7%), and flexibility. Due to these features, graphene embodies an attractive candidate for the preparation of biosensors.[113] As graphene is conductive, transparent, and inexpensive, it constitutes an ideal material for the development of biosensors based on diverse transducers, from electrochemical to optical ones.[131]

Various types of graphene have been synthesized and applied in biosensing.[132] Pristine graphene, obtained via the mechanical cleavage of graphite, is strongly hydrophobic, which heavily reduces its applications in immunosensing. Graphene oxide (GO) significantly improves the hydrophilicity of graphene layers, but GO is an electrical insulator, causing the reduction of conductivity by several orders of magnitude. When the oxygen-containing groups of GO are eliminated, the reduced graphene oxide (rGO) achieves a unique combination of high conductivity, large surface area, high electrochemical activity, and simple functionalization.[133]

GO is produced using the Hummers method, which is based on a treatment by potassium permanganate and concentrated

75

sulfuric acid for the simultaneous oxidation and exfoliation of graphite.[134] The acid treatment introduces polar functional groups, such as epoxy, carbonyl, and hydroxyl, inducing the hydrophilicity of GO. The colloidal solution of GO can be reduced by means of various treatments, such as chemical reduction by directly adding reducing agents (e.g., hydrazine)[135] or thermal reduction using high temperatures (200−900 °C).[136] Electrochemical reduction based on immobilizing GO on an electrode surface and performing reducing scans by sweeping the potential from 0 to 1.5 V is a simple and convenient procedure to produce rGO-modified electrodes.[137]

Chemical vapor deposition (CVD) on transition-metal substrates (typically Cu[138]) is a promising, cost-effective, and high-throughput approach for the synthesis of large-area graphene films. The CVD synthesis of graphene is practically the subsequent diffusion and surface segregation of the carbon atoms obtained by the thermal decomposition of hydrocarbons, upon the cooling of the carbon−metal solid solution. This technique enables the control of the grain size, crystallinity, and number of graphene layers via adjustment of the gas flow rate, growth time, and cooling rate. CVD allows the integration of graphene in conventional Si-based electronics and serves as a platform for the production of miniaturized FET biosensors.[113]

Similarly to the application of CNTs, the applications of graphene in electrochemical immunosensing can also be divided into direct modifications of the sensor surface and usage as a label in sandwich assays. The modifications of electrode surfaces can be performed with graphene directly or by using nanocomposites of graphene with metallic NPs to enhance the sensitivity even further. A simple one-step method for the preparation of a graphene−thionine−Au nanocomposite was demonstrated by Han et al.[139] HAuCl$_4$ was reduced in the presence of GO and thionine; the formed nanocomposite was then adsorbed to a GCE, and the anti-CEA antibody was immobilized to Au via physical adsorption. The binding of the CEA hindered the electron transfer to the thionine, which was monitored by SWV. A low detection limit of 0.05 fg/mL was achieved, even though the amount of Au NPs on the surface was not very high; this could restrict the antibody immobilization and, therefore, also the binding of the CEA.[140]

A sandwich assay based on HRP-modified GO and biocatalyzed precipitation was developed by Hou et al.[141] The antigen (CEA) was captured by an antibody immobilized on a Au NP-modified GCE followed by the binding of a conjugate of GO with multiple molecules of HRP and a detection antibody. The HRP catalyzed the precipitation of 4-chloro-1-naphthol, resulting in increased impedance. The conjugate with GO allowed improvement of the LOD by 3 orders of magnitude (to 0.64 pg/mL) compared to that of a simple conjugate of the antibody with the HRP. The details of the procedure are shown in Figure 9.

Furthermore, graphene is also suitable for fluorescent and chemiluminescent immunoassays, where it acts as the energy acceptor to quench the luminescence signal.[142] A complex immunosensing strategy based on ssDNA labeled by 6-carboxyfluorescein (FAM-DNA) and exonuclease for signal amplification was developed by Liu et al.[143] After the formation of a sandwich with a biotinylated detection antibody and the subsequent binding of streptavidin, biotin-labeled ssDNA, and FAM-DNA, the FAM-DNA was hydrolyzed by exonuclease. Thus, a small amount of the target protein could produce a large amount of fluorescent fragments that cannot be adsorbed on the
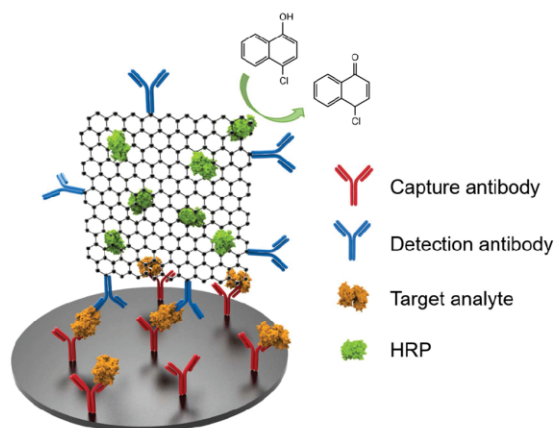
Figure 9. Schematic illustration of the graphene oxide-labeled sandwich-type impedimetric immunoassay with signal enhancement based on in situ 4-chloro-1-naphthol precipitation. Based on ref 141.

surface of GO. The remaining FAM-DNA was adsorbed on the surface of GO, and the fluorescence quenching was evaluated.

3.3.3. Other Carbon-Based Nanomaterials.
Apart from CNTs and graphene, other types of carbon-based nanostructures (such as fullerene, carbon nanohorns, and carbon dots) have also been recently used for immunosensing applications.[144]

Fullerene C60, the smallest stable and most abundant member of the fullerene group, is an electroactive nanomaterial characterized by unique properties that make it well suited for the development of electrochemical sensors.[145] Fullerene C60 has multiple redox states in a wide range of potentials undergoing six different one-electron reversible reductions to form stable intermediates. The capability of signal mediation and the simple functionalization allow applications in the field of immunosensors.[146,147] Electrodes modified by fullerene C60 have an increased electroactive surface area and high electric conductivity. The disadvantage of fullerene is the hydrophobicity and insolubility in water, which complicates the conjugation of biologically active molecules.[144]

Single-walled carbon nanohorns (CNHs) are a novel type of carbon allotrope. CNHs can be produced by vaporizing pure graphite rods via CO$_2$ laser ablation. Advantageously, no metal catalyst is necessary; the prepared CNHs can thus be essentially metal-free[148] and are usable directly, without post-treatment. CNHs are convenient as a scaffold for the immobilization of antibodies or antigens and also for the amplification of the electrochemical signal.[149]

Carbon dots (further divided into carbon quantum dots and graphene quantum dots) are a type of 0D carbon nanomaterial with a size of approximately 10 nm.[150] Since the discovery of carbon dots by Xu et al. in 2004,[151] substantial research effort has been devoted to this material. As carbon dots are characterized by quantum confinement and edge effects, they can exhibit optical and electro-optical properties similar to those of conventional QDs and offer potential for application within.[152,153] Recently, also the electrochemical properties of carbon dots were exploited to develop electrochemical biosensors.[154]

Carbon quantum dots and Ag@SiO$_2$ NPs were combined into a nanoplatform for sandwich fluorescence and SERS immunoassays.[155] The Raman reporter 4,4′-dimercaptoazobenzene was generated from the apparent reporter p-aminothiophenol bound

76
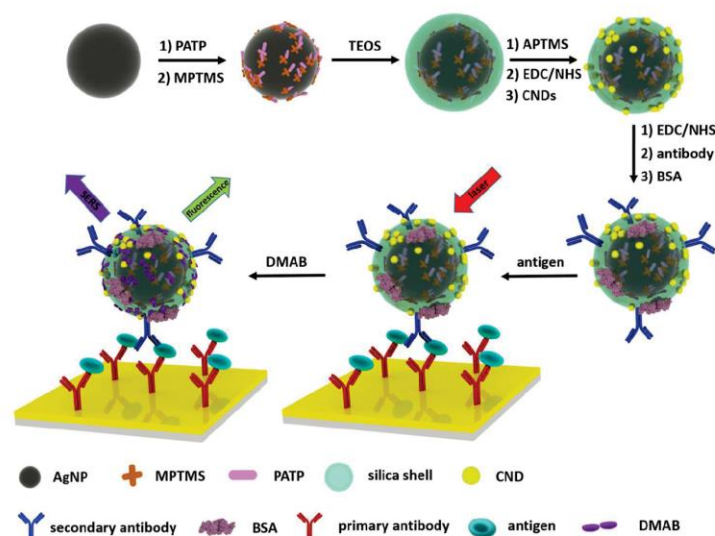
Figure 10. Illustration of the construction of bifunctional CND-decorated Ag/PATP/SiO₂ nanoparticles for fluorescence and SERS immunoassays. PATP = *p*-aminothiophenol, MPTMS = (3-mercaptopropyl)trimethoxysilane, TEOS = tetraethyl orthosilicate, and APTMS = (3-aminopropyl)-trimethoxysilane. Based on ref 155.

on the surfaces of Ag NPs upon the illumination of a laser. The large Raman scattering cross sections compensated for the reduction of SERS signals resulting from the silica coating (Figure 10). IgG molecules were detected in a proof-of-concept experiment with an LOD of 2.5 ng/mL.

Graphene quantum dots prepared via the autoclaving of graphene oxide were employed for the electrochemilumines-cence detection of cancer cells.[156] Cubic Cu₂O was used as a template for the formation of a surface villous Au nanocage, which was then bound to graphene quantum dots. The performance of a sandwich ECL sensor was demonstrated on the detection of MCF-7 breast cancer cells. Similar labels were used for core−shell NPs combining fluorescence and the SERS response.

The main role of graphene variants and carbon nanotubes is enhancement of the electron transfer rate in electrochemical immunosensors. The higher current density is favorable for an improved signal-to-noise ratio. At the lowest level, these carbon-based nanomaterials function as molecular wires interconnecting redox centers of proteins, conductive metal NPs, and the electrode surface.

3.4. Luminescent Nanocrystals

3.4.1. Quantum Dots. Quantum dots (QDs) are fluorescent semiconductor nanocrystals characterized by dimensions typically in the range of 1−10 nm.[157] They enable various applications, for example, light-emitting devices, photodetectors, solar cells, field-effect transistors, memory elements, luminescent biolabels, biosensors, and bioimaging probes.[158] QDs show size-tunable photoluminescence properties, wide excitation spectra, and a narrower emission bandwidth compared to classic organic fluorophores.[159,160] The fluorescence color can be controlled by the QD size, i.e., by modifying the temperature during the synthesis or the duration of the nanocrystal growth. QDs with emission wavelengths ranging from 380 to 2000 nm can be prepared using an appropriate semiconductor material and nanocrystal size.[161] Furthermore, multiplexed color encoding

can be carried out by embedding QDs with different sizes into polymeric microbeads at precisely controlled ratios.[162]

Most of the QDs for analytical applications are prepared as core−shell structures, with the core nanocrystal coated with another semiconductor material for the protection and improve-ment of the optical properties (Figure 11). QDs with large quantum yields and a narrow size distribution are commonly synthesized at a high temperature in organic solvents.[163] To transfer these hydrophobic QDs to an aqueous solution, the hydrophobic ligand layer has to be changed. The two principal hydrophilization methods are ligand exchange and encapsulation
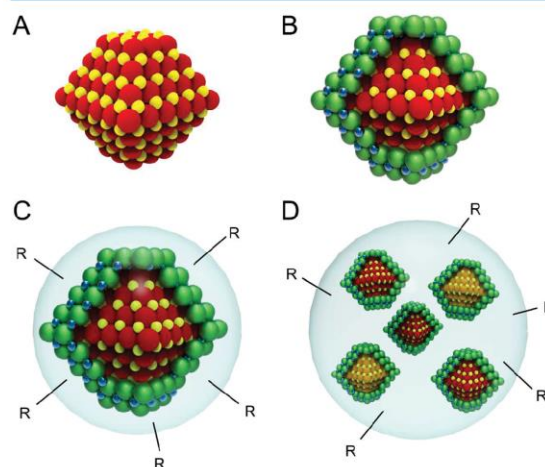
Figure 11. Schematic view of quantum dots as labels in immunoassays: (A) QDs formed by a single semiconductor material; (B) core−shell QDs; (C) core−shell QDs with a hydrophilic coating and reactive groups R for bioconjugation; (D) a polymeric particle containing several QDs for signal multiplexing.

77

with an amphiphilic polymer.[164,165] Most of the hydrophilic ligands employed for ligand exchange include mercapto groups since they offer a high binding affinity to the QD surface.[166]

The conjugates of QDs with antibodies are stable and provide an easily detectable analytical signal, which makes them useful as sensitive fluorescent labels in immunoassays[167−169] and bioimaging.[170,171] The application of QDs in quantitative LFIA for CRP detection was demonstrated by Hu et al.[172] Fluorescent nanospheres were produced by embedding hydrophobic CdSe/ZnS QDs into a poly(styrene−acrylamide) copolymer, which strongly increased the fluorescence intensities compared to single QDs. The QD-based assay was more sensitive (an LOD of 34.8 pM in serum) than the conventional LFIA based on Au NPs.

QDs have also become very popular in ECL immunosensing.[173,174] Zhang et al.[175] synthesized CdSe nanocrystals for the single-molecule analysis of the CEA (Figure 12). Mercaptopro-
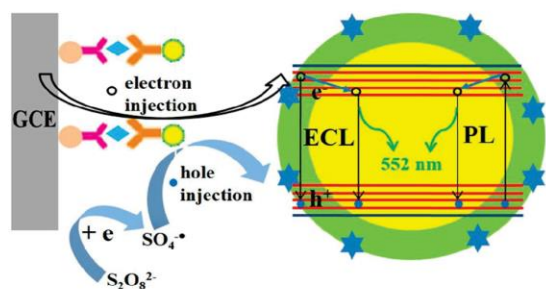

Figure 12. Scheme of a sandwich ECL immunosensor for the determination of the CEA. Reprinted from ref 175. Copyright 2016 American Chemical Society.

pionic acid and sodium hexametaphosphate were used as the capping agents to facilitate the electrochemically involved hole (or electron) injecting process and improve the nanocrystal stability. A very low LOD of ∼6−8 CEA antigen molecules in 20 μL of serum samples was achieved, which could be ascribed to the effective ECL generation of the well-passivated and stable NPs.

Tasso et al.[176] capped QDs with a multidentate dithiol/zwitterion copolymer ligand. This approach exploited the thiol groups for both anchoring and the bioconjugation of up to 10 protein A molecules per QD while preserving long-term colloidal stability of QDs. Protein A provides a simple and universal platform for the immobilization of various antibodies. The authors demonstrated the low toxicity of the conjugates and the usage of the QDs for visualizing E-cadherin in fixed MCF-7 cells and tracking the cannabinoid CB1 receptor in live HEK cells.

3.4.2. Photon-Upconverting Nanoparticles. Photon-upconverting nanoparticles (UCNPs) are lanthanide-doped nanocrystals that show anti-Stokes emission. The energy transfer up-conversion is a nonlinear optical process characterized by the absorption of two or more photons and leading to the emission of a single photon at the shorter wavelength.[177] Unlike other anti-Stokes processes, such as the two-photon excitation and second harmonic generation, up-conversion can be efficiently excited at lower excitation densities. Upconversion has been known since the 1960s;[178] however, the applications of the upconversion effect were limited to bulk glass or crystalline materials.[179] An inorganic upconversion phosphor contains a crystalline host and a dopant (typically lanthanide ions) added at a low concentration. The dopant provides luminescent centers, and

the host lattice with its crystal structure ensures a matrix to bring these centers into optimal positions.[180]

The progress in nanocrystal research has evoked an increasing interest in the development of synthesis procedures, facilitating the preparation of highly efficient, small UCNPs with a narrow size distribution that can form transparent solutions in various solvents. Unlike commonly used luminescent biological labels (for example, organic dyes and QDs), UCNPs are advantageous in many aspects; they are characterized by a practically zero autofluorescence background, large anti-Stokes shifts allowing easy separation of the excitation and detection channels, multiple and narrow emission bands tunable individually for the multiplexed detection of analytes, and excellent photostability.[180] Small and homogeneous lanthanide-doped UCNPs showing high upconversion efficiency are typically synthesized in organic solvents. UCNP functionalization methods to ensure a hydrophilic surface and allow bioconjugation reactions were reviewed by Sedlmeier and Gorris.[181]

The unique photophysical properties of UCNPs make them suitable as reporters in optical biosensors and biomolecular binding assays. The potential of UCNPs in diagnostics was first demonstrated by Tanke et al. in 1999.[182,183] Since then, UCNPs have been used in the design of heterogeneous[184−186] and homogeneous[187,188] microtiter plate immunoassays and in lateral flow immunoassays[189] for the detection of various analytes.

Competitive upconversion-linked immunosorbent assay (ULISA; Figure 13) for the detection of the pharmaceutical
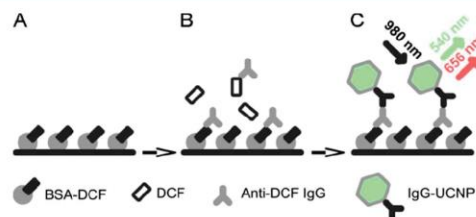
Figure 13. Scheme of the indirect competitive ULISA for the detection of diclofenac (DCF). (A) A microtiter plate is coated with a BSA−DCF conjugate. (B) Dilution series of DCF are prepared in the microtiter plate followed by the addition of an anti-DCF mouse antibody. (C) The attachment of the anti-DCF antibody is then detected by the antimouse IgG−UCNP secondary antibody conjugate. Reprinted from ref 190. Copyright 2016 American Chemical Society.

diclofenac was developed by Hlaváček et al.[190] The competitive reaction based on the immobilized BSA−diclofenac conjugate and free diclofenac and a primary antibody was followed by the detection step involving the binding of the UCNP−secondary antibody conjugate. The optimized ULISA achieved an LOD of 0.05 ng/mL, which came close to that of the conventional ELISA without the necessity of the enzyme-mediated signal amplification step.

Li et al. developed an immunoassay based on FRET between UCNPs and Au NPs[191] (Figure 14). The glass slide was covalently modified by UCNPs and the capture antibody. A competition between the free antigen and the antigen conjugated with BSA and Au NPs was performed. When the conjugate was bound, FRET occurred, and this was measured as a decrease of luminescence compared to that of free UCNPs. The single-step method offers several advantages against the commonly used multistep reactions due to less washing steps and the overall shorter analysis time.

78
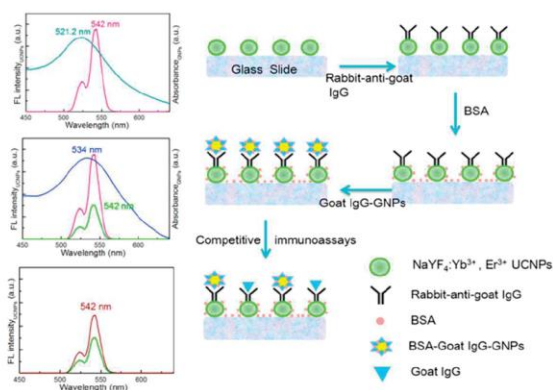
Figure 14. Schematic illustration of the one-step in situ immunoassay based on FRET between the UCNPs covalently immobilized on the substrate surface and Au NPs. Reprinted with permission from ref 191. Copyright 2016 Elsevier.

The excitation by near-infrared light that is within the optical transparency window and, therefore, can penetrate tissues makes UCNPs helpful also for the visualization of specific markers in optical microscopy.[192] Thus far, most UCNP applications in bioimaging were based on UCNPs not labeled by an antibody.[193] Wang et al.[194] applied conjugates of UCNPs with an anti-CEA8 antibody as fluorescent biolabels for the specific detection of the carcinoembryonic antigen (CEA) expressed on the surface of HeLa cells. A strong luminescence signal from the UCNPs was obtained, and no autofluorescence from the cells was observed under 980 nm excitation.

The properties of luminescent NPs can be easily fine-tuned through simple modifications of the synthetic procedures; the time-dependent size allows the emission bands of QDs to be shifted, and the amount of dopants influences the UCNPs. The main optical advantage is high brightness and stability of the derived labels. Additional benefits include a single excitation wavelength for several types of NPs; this is significant for multilabel procedures. Quite unique for the future seems to be the anti-Stokes infrared excitation of UCNPs completely removing the background fluorescence of biological samples.

4. TRANSDUCTION MECHANISMS

Nanoparticles appeared compatible with almost all transducing systems suitable for the affinity types of biosensors. The technological aspects of the most common types are provided in the subsections below, with a focus on the employed nanoparticles.

4.1. Optical Transducers

4.1.1. Fluorescence. The sensitivity of a fluorescence-based (immuno)assay relies primarily on three factors: the brightness of the fluorescent labels, the packing density of the fluorophores, and the parameters of the detection optics. The two initial aspects can be conveniently addressed using novel fluorescent nanomaterials.

The embedding of hydrophobic CdSe/ZnS QDs into poly(styrene–acrylamide) copolymer nanospheres provided labels containing around 330 QDs per NP sized 270 nm. The surface carboxyls served in antibody coupling using the EDC/NHS chemistry. The thus obtained fluorescent nanoconjugate was used in the lateral flow strip format for the rapid detection of

CRP.[195] The assay was 260× more sensitive compared to alternative labeling with Au NPs.

The Ag_2S QDs (80 nm in diameter) were protected with a silica shell (45 nm in thickness) providing for label emitting in the IR region (896 nm).[196] This allowed a sensitive sandwich assay of *Cryptosporidium parvum* in the microplate format, ensuring an LOD of 10 oocysts/mL. Fluorescein-loaded porous silica NPs served as a label in a sandwich assay for the pathogenic strain of *E. coli*.[197] General aspects of embedding labels inside silicate and similar nanoparticles were reviewed by Wei.[198]

An interesting amplification strategy involving the covalent coupling step was based on CuO NPs labeling a secondary Ab. The label was dissolved in HCl and reduced to Cu^+ ions catalyzing the click-chemistry-based alkyne–azide cycloaddition of weak fluorescent 3-azido-7-hydroxycoumarin and propargyl alcohol to form a strong fluorescent compound.[199]

4.1.2. FRET Assays. A FRET-based immunosensor for the detection of troponin using graphene QDs and graphene as the quencher has already been described.[200] The capture anti-cardiac troponin I Ab was covalently conjugated with amine-functionalized graphene quantum dots. This fluorescent nanoprobe (excitation at 360 nm, emission at 437 nm) was further investigated in the presence of graphene, which resulted in the quenching of the fluorescence intensity due to dipole–dipole interaction. The addition of the target troponin expelled the stacked graphene apart from the immunocomplex and recovered the fluorescence.

The fluorescence of CdTe modified with the capture Ab was quenched by the present H_2O_2. The competitive assay format for ochratoxin used the tracer based on an ochratoxin–catalase conjugate. Thus, in the absence of ochratoxin, the bound catalase decomposed the H_2O_2, and the fluorescence was recovered. The achieved LOD of 0.05 pg/mL was 300× lower compared to that of the conventional ELISA technique with HRP as the label.[201]

The optical advantages of QDs were combined with the long-lasting luminescence of lanthanides.[202] The amphiphilic polymer backbone was covalently decorated with biotin (future conjugation reactions) and chelate complexes with embedded atoms of Eu. This was used to coat the surface of CdSe QDs using trioctylphosphine oxide as a contacting interlayer. The close proximity of QD and Eu resulted in an efficient FRET transfer, and the overall system exhibited long-lasting luminescence suitable for measurement using the time-resolved approach, which provides an excellent signal-to-noise ratio. Several other similar approaches based on luminescent terbium complexes were also reviewed and considered for a multiplexed assay when combined with QDs of different sizes (colors).[203] The immunosensor based on luminescence resonance energy transfer used near-infrared (980 nm) excitation of UCNPs $NaYF_4$:Yb^{3+}, Er^{3+} as the donor modified with the capture Ab. The analyte (glycated hemoglobin HbA1c) was bound and functioned as the acceptor. HbA1c absorbs at 541 nm, which overlaps with the UCNP emission, and the signal is quenched.[204]

4.1.3. Chemiluminescent Nanolabels. The common option is to prepare nanomaterials loaded with suitable chemiluminescent dyes. Mesoporous silicate NPs were loaded with rhodamine 6G and fluorescein and coupled to the detection antibody.[205] The classic microplate heterogeneous format was used for the sandwich immunoassay of staphyloccocal enterotoxin C1; the final luminescence was triggered by the addition of bis(2,4,6-trichlorophenyl) oxalate, H_2O_2, and imidazole. Resonant energy transfer occurs onto the internal dyes with an enhanced signal.
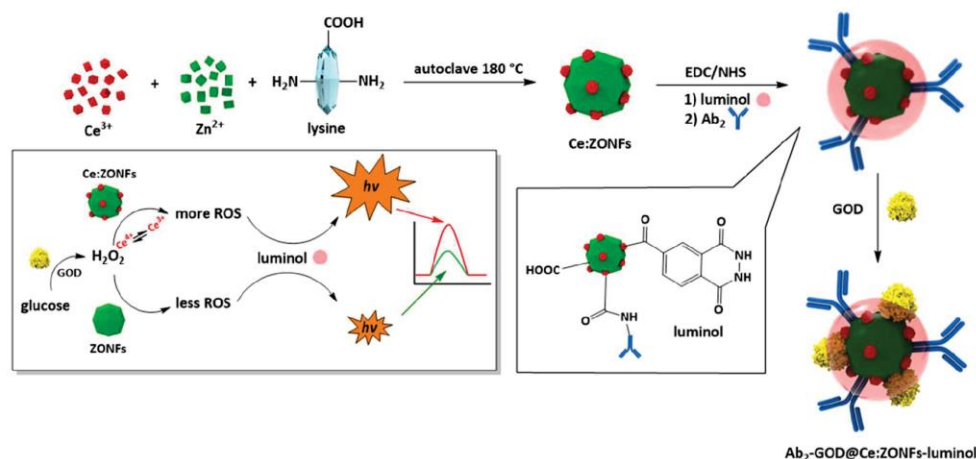
Figure 15. Preparation of the hybrid Ab−NP/luminol/GOD label and the subsequent ECL of luminol using in situ generated ROS radicals. Ce:ZONFs = ceria-doped zinc oxide nanoflowers. Based on ref 222.

4.1.4. Electrochemiluminescence. The conversion of electrochemical energy to light at the surface of an electrode is known as electrochemiluminescence (ECL). The relaxation of the excited states of the molecules formed within the electrochemical reaction is accompanied by luminescence. The process is initiated by applying a suitable potential on the electrode, and the intensity of the released light is measured by a photodetector, typically a photomultiplier.[206] The simple instrumentation and low background signal compared to those of other luminescent methods resulted in numerous analytical applications of ECL.[207] A high response is often obtained due to the repeated conversion of such labels, e.g., ruthenium complexes represented by Ru(bpy)$_3^{2+}$.

The ECL of various NPs is a relatively new technique; suitable variants include the common binary, core−shell, and doped QDs, single-element NPs (Si, Ge, Ag, Au), metal oxide semiconductors, up-converting NPs, molecular nanoaggregates, and more complex hierarchical assemblies providing several ECL mechanisms and reaction courses.[208]

The composite QDs Cd/ZnSe served as a label for the sandwich assay of AFP. The ECL was carried out on glassy carbon via a cathodic pathway with $(NH_4)_2S_2O_8$ as the coreactant. The procedure employed spectral evaluation instead of the common simple light intensity measurement;[195] the authors proposed this approach for multicolor ECL immuno-assays. The resulting emission spectra were similar for ECL and photoexcitation, thus confirming the similar mechanism. The authors used a comparable approach with CdSe for the assay of the CEA; the remarkably low LOD was 0.1 fg/mL, which corresponds to few (7) molecules of the CEA in 20 μL of sample, thus approaching the single-molecule detection capabilities.[209] For CdTe-based QDs, significantly enhanced ECL was obtained after deposition of these QDs onto graphene sheets.[210] The multicolor sensing could also be achieved with common band-pass filters and PMT detectors.[211] The graphene-modified glassy carbon was linked to two different capture antibodies (anti-AFP and anti-CEA) in the sandwich format; the biotinylated secondary Ab's were labeled with different streptavidin−QD conjugates. The achieved LOD was 0.4 fg/mL for both markers.

The QDs as labels in ECL sandwich assays are usually excited on differently modified electrodes. Thus, glassy carbon coated with PANI nanofibers/graphene sheets and subsequently deposited Au NPs on magnetic beads were used for the sensitive assay of interferon γ (LOD = 30 fg/mL).[212]

Labels based on poly(amidoamine)-dendrimer-functionalized carbon nanodots were combined with an electrode modified using the composite consisting of fullerene, graphene oxide (in situ electroreduced to graphene), and chitosan; the sandwich assay of AFP provided an LOD of 0.33 fg/mL.[213]

For large analytes, such as microbes, ECL blocking assays are suitable: the signal decreases with the rising amount of the surface-bound analyte. The magnetic Fe_3O_4/graphene oxide nanocomposite was activated with EDC/NHS and isoluminol (ABEI), and the capture Ab's were covalently attached. The product was simply drop-coated on a magnetic electrode; the ECL signal decreased with increasing amounts of the target pathogen *Vibrio parahemolyticus* (an LOD of 5 cfu/g in seafood samples).[214] The concept also functioned for N-terminal pro-brain natriuretic peptide with an ITO electrode modified with ABEI−Au nanodots/chitosan/MWCNT as the ECL interface. After activation with glutaraldehyde and the covalent binding of the capture Ab, the presence of the analyte resulted in decreased ECL (LOD = 3.9 fg/mL).[215]

A similar performance was also obtained for a direct assay of deoxynivalenol.[216] Network-like Co NPs were produced by the alkaline dissolution of Al from the CoAl alloy; Co_3O_4 was further grown on the surface followed by Au NP functionalization, deposition of the capture Ab, and further modification with Ru(bpy)$_3^{2+}$-loaded silicate NPs. This assembly was drop-coated on glassy carbon and allowed to dry. The ECL signal was measured in the presence of $K_2S_2O_8$; it continuously decreased with higher amounts of deoxynivalenol in the solution. However, the authors did not explain why the ECL decreases, as the analyte is a rather small molecule for reasonable blocking of the surface.

The novel ECL system was designed by a rather extensive Mn^{2+} doping level of the NaYF$_4$:Yb/Er UCNPs.[217] The UCNPs were coated with an aminosilicate shell, dropped on glassy carbon, and Au NPs were bound through interaction with amino groups. Eventually, the capture Ab was linked through adsorption on the Au surface. The ECL was measured with $K_2S_2O_8$, and it continuously decreased with higher concentrations of the CEA (LOD = 5.2 pg/mL).

80

Small analytes, such as mercury ions, are typically measured using competitive assays. The electrode surface was modified with a poly(diallyldimethylammonium chloride)—graphene—CdSe composite secured with chitosan, and the assembly provided a strong ECL signal with cathodically produced H_2O_2. The methylmercury—6-mercaptonicotinic acid linked to albumin was further immobilized as a coating antigen. This competed with the free mercury ions for the tracer, or a specific Ab—Au NP—HRP tracer. After the binding of the tracer, HRP decomposes the H_2O_2 by the oxidation of o-phenylenediamine, and the ECL intensity drops.[218] Alternatively, ALP as a label enzymatically produced p-nitrophenol, which was oxidized to p-benzoquinone acting as the quencher of the surface-deposited QDs.[219]

The quenching of ECL also occurs due to the resonance energy transfer within the sandwich complex.[220] The carbonization of diethylenetriaminepentaacetic acid provided N-doped C-QDs, which, deposited on an electrode, function as a luminophore. However, the binding of the analyte (AFP) and its labeling with the secondary Ab linked to aminated graphene resulted in the resonant loss of excitation and decreased the ECL signal. A similar principle was employed using ferrocene—chitosan NPs as labels in a sandwich assay.[221]

Hybrid luminol/nanoparticles constitute a combination of organic and inorganic labels. An enhanced response can be achieved by various combinations of organic and nanocrystal-based luminophores. The cerium-doped ZnO nanoflowers were prepared by autoclaving Ce^{3+} and Zn^{2+} salts with lysine, which afterward served in the EDC/NHS coupling of the sequentially added luminol, secondary Ab, and GOD enzyme (in excess to block the surface, Figure 15). The capture Ab was deposited through Ag NWs on glassy carbon. After completion of the sandwich immunoassay, the added glucose with GOD generated in situ H_2O_2, which was, in the presence of Ce^{4+}, electrochemically oxidized to ROS radicals reacting with the embedded luminol. The application for an assay of the amyloid-β protein resulted in an LOD of 52 fg/mL within about 90 min.[222]

Luminol was also bound to Au NPs, and the product was coated on magnetic Fe_3O_4 NPs together with a secondary Ab. The ECL was measured on a Au electrode modified with Au/ZnO NPs containing the capture Ab. An LOD of 4.5 fg/mL was achieved for mucin.[223] For the analysis of CEA-125, the luminol was covalently coupled to the poly-(diethylenetriaminepentaacetic acid—ethylene glycol) ester dendrimers.[224]

The SiO_2 NPs were doped with $Ru(bpy)_3^{2+}$ and further combined with Au/graphene and a secondary Ab to form a composite bioconjugate. This approach significantly enhances the amount of Ru complexes per molecule of tracer in sandwich assays. The other components increase the rate of the electron transfer and provide multiple antibody binding sites. For the HIV-1 p24 antigen in a human serum, the achieved LOD was 1 pg/mL.[225]

Tris(4,4′-dicarboxy-2,2′-bipyridyl)ruthenium(II) was linked with cysteine using EDC/NHS coupling chemistry to obtain a self-enhanced ECL label for reagentless use.[226] This makes the procedure independent of common coreactants such as peroxydisulfate, oxalate, or tripropylamine and, consequently, more robust. After being linked to Au nanorods and the attachment of a secondary Ab, it served in a sandwich assay for cardiac troponin I with an LOD of 83 fg/mL. Compared to the use of free cysteine as the coreactant, the use of Cys@Ru(II) provided a much higher ECL signal since the intramolecular ECL reaction exhibits a shorter electron transfer path and lower energy loss.

4.1.5. Photoelectrochemical Conversion.
A suitable photoactive nanomaterial absorbs the photon, and charge separation occurs as the electron—hole pair formed by the excitation of the electron from the valence to the conductive band. An anodic photocurrent occurs when the electrons are transferred to the electrode and the electron donor (D) in the solution replaces the hole (Figure 16). Alternatively, if the
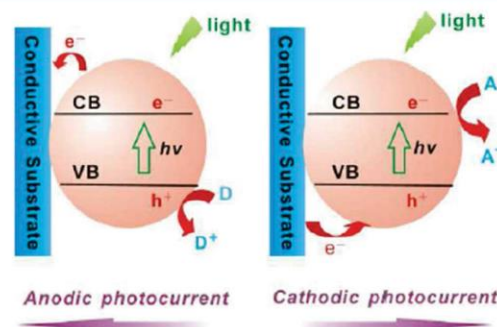
Figure 16. Principle of the origin of photocurrents. The nanoparticles contain valence and conductive bands (VB and CB, respectively). The electrons are provided (accepted) by the donors (acceptors) present in the surrounding solution. Reprinted with permission from ref 227. Copyright 2015 Elsevier.

electrons are transferred to the acceptor (A), complementary electrons from the electrode neutralize the holes, yielding a cathodic photocurrent.[227] General applications of QDs for PEC systems were recently reviewed by Lisdat.[228]

CuS (p-type semiconductor) constitutes a suitable PEC material; it was on-site coated to a Au paper electrode (cellulose coated with Au NPs) modified with ZnO nanoflakes, and the capture Ab was linked through a chitosan layer.[229] The sandwich with the CEA analyte was labeled with the Au NP/secondary Ab/GOD enzyme assembly. The H_2O_2 resulting from the enzymatic oxidation of glucose served as the electron donor for the PEC process. The wide band gap of ZnO allows its excitation with UV light, and this problem is overcome by the introduction of CuS serving as the primary light capture system. Tetracarboxyl naphthalocyanine zinc can serve as an alternative sensitizer; it was covalently linked to ZnO using aminothiophenol as a bridge and the EDC/NHS coupling.[230] This brings the option for near-infrared photoexcitation; ascorbic acid served as the electron donor. The CEA was the analyzed marker, blocking the surface and thus lowering the photocurrent with its increasing concentrations.

A similar approach was used with CdS QDs deposited on TiO_2 and galactosidase as a label, producing p-aminophenol by enzymatic hydrolysis of p-aminophenyl galactopyranoside. Aminophenol as a donor is photooxidized to quinonimine.[231] A more complex interface consisted of TiO_2 nanotubes coated sequentially with Mn-doped CdS and CdTe QDs (Figure 17) suitable for visible light excitation due to the gradual transfer of electron/hole entities.[232] The sandwich immunosensing for matrix metalloproteinase brings a secondary Ab linked to silicate NPs functioning as a shield for the ascorbic acid donor and decreasing the photocurrent. This strategy also worked with ZnO as the primary electrode coating.[233]

81
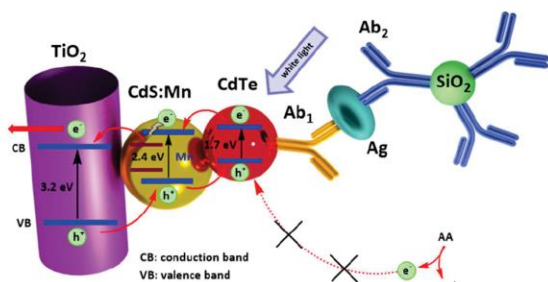
Figure 17. System for the sequential transfer of electrons/holes through overlapping energy levels. Based on ref 232.

Alternatively, Fe (0.1%) doping of TiO_2 enhanced its photoactivity 10-fold and shifted the excitation toward the visible light range. A further 3-fold enhancement was achieved by CdS QDs; when the coupled capture Ab binds the corresponding squamous cell carcinoma antigen, the photocurrent decreases.[234]

Bi_2S_3 nanorods on an ITO electrode served as the photo-interface for a sandwich-based assay of avian leukosis virus. A secondary Ab linked to ALP provided for the enzymatic production of ascorbate from ascorbate phosphate.[235] This donor system was applied also to the CdS QD/TiO_2 assembly.[236]

The SnO_2 QD/graphene composite functioned as a label for the sandwich sensing of the CEA; a capture Ab was deposited on an ITO through Au NPs. This required near-UV (365 nm) irradiation.[237] A similar format for the CEA used a label based on carboxylated MWCNT—Congo red—C60 fullerene nanohybrids prepared by mechanical grinding. This photolabel was suitable for green laser excitation.[238]

An interesting and smartly conceived approach employed a charge-collecting component in the electronic amplification interface. The chemiluminescent illumination system was combined with PEC transduction.[239] The CL excitation part as the tracer employed Au NP labels containing attached CEA, bound isoluminol (ABEI), and GOD for the enzymatic generation of H_2O_2. The PEC surface consisted of TiO_2 nanospheres and CdS QDs and was modified with a capture Ab (Figure 18). To further enhance the signal, the photocurrent electrons were collected in a supercapacitor formed by paper
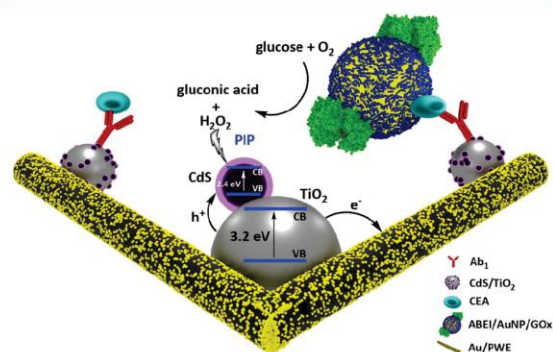
**Figure 18.** Principle of CL illumination with a PEC transducer. The response is enhanced by the flow of electrons to the supercapacitor charge collection system. PIP = p-iodophenol, and PWE = paper working electrode. Based on ref 239.

coated with a carbon layer as the counter electrode from the other side. The 60 s accumulated charge was evaluated as the corresponding potential change after the measuring circuit was switched on with a simple multimeter.

An alternative system employed the CL generated by the classic HRP-catalyzed luminol reaction.[240] The PEC layer was also obtained using an SWCNT coated with the photovoltaic polymer poly(m-phenylenevinylene-co-2,5-dioctoxy-p-phenyle-nevinylene), which forms excitons under the incident light. As its valence band is aligned with the CNT, the holes in the excitons are injected into the carbon nanotube, leaving the electrons in the vicinity of the CNT on a Si wafer and finally resulting in the measured current.[241] Illumination resulted from the HRP/luminol reaction within the sandwich complex with troponin labeled by the secondary Ab—HRP conjugate.

A PEC blocking assay was based on an ITO electrode coated using the layer-by-layer technique by CdSe QDs and poly-(diallyldimethylammonium chloride) layers. A capture Ab was linked using EDC/NHS chemistry, and a sandwich was formed with the target analyte—model immunoglobulin—labeled by the secondary Ab—HRP conjugate. After the addition of 4-chloro-1-naphthol and H_2O_2, enzyme conversion produced a precipitating product which blocked the generation of a photocurrent.[242] The precipitation of the product helps to keep the signaling molecules close to the point of formation and minimizes their loss by diffusion to the surrounding bulk medium. Thus, this simple approach can be considered an amplification strategy.

4.1.6. Visual Evaluation and Colorimetric Systems. The wide use of colored nanoparticles seems to shift colorimetric immunoassays closer to real clinical applications.[243] The intuitive approach utilizes colored NPs directly as a label for evaluation. The use of Au NPs as labels remains the most common option for lateral flow immunoassays,[244,245] being a convenient format for the visual evaluation of immunoassays performed out of laboratory. A significant sensitivity improvement was obtained when Au NPs were combined with silica nanorods.[246]

Conversely, NPs without any pronounced color can help to catalyze the conversion of chromogenic substrates. Pt NPs were used in the lateral flow format as a catalytic system mimicking the enzyme action of peroxidase; the evaluation might be realized using a colorimetric system or simply visually using TMB and H_2O_2 as substrates, though chemiluminescence with luminol is suitable too.[247] Pt NPs were also combined with magnetic NPs for convenient manipulation, and the catalytic properties were enhanced using graphene oxide; in this way, breast cancer cells can be identified, with short time periods around 5 min.[248]

The straightforward blue/red color change discrimination helped to identify food allergies.[249] The principle was based on HRP as the label on a secondary Ab specific against the target IgE present in the blood of patients suffering from allergies. Bound HRP decomposes H_2O_2, and in this way, small blue Au NPs appear. In the absence of HRP, H_2O_2 reduces Au^{3+} to Au, which increases the size of the NPs, resulting in the red color. The IgE can be quantified according to the absorbance at 550 nm. A similar color change allowed the detection of several pathogens (Salmonella, Listeria, and E. coli O157) in the sample; the triggered chemical cascade led to a large red to dark blue shift visible to the naked eye. The breakdown of cysteine-loaded nanoliposomes initiated the aggregation of plasmonic gold nanoparticles.[250]

Ag nanocubes, Au/Ag alloy nanoparticles, and Au/Ag nanocages were evaluated for a multiplexed dot immunoassay

82

Figure 19. Principle of the single-particle photon burst counting applied for homogeneous immunosensing. Based on ref 252.

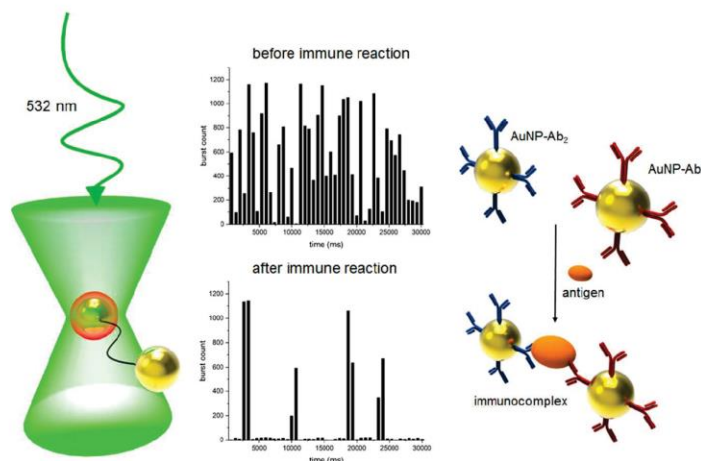carried out on a nitrocellulose membrane strip; multicolor NPs were conjugated with specific antibodies. The NPs were prepared via galvanic replacement between the Ag atoms of silver nanocubes and $AuCl_3$. Depending on the Ag/Au conversion ratio, the particle plasmon resonance was tuned from 450 to 700 nm, and the suspension color changed from yellow to blue, suitable for visual evaluation on the sensing strip.[251]

4.1.7. Single-Molecule Detection Techniques. Enhanced immunoassays have recently been evaluated digitally by single-molecule analysis based on counting individual molecular or nanoparticle labels instead of measuring the overall (analog) signal. The setup typically comprises a microscope, a sensitive camera, and suitable software to count the individual spots. The high brightness of luminescent NPs is a significant advantage. The noise-free digital readout allows the elimination of the instrumental background, which has a crucial impact on lowering the LOD.

The single-particle method (Figure 19) combines photon burst counting with Au NPs as labeling probes.[252] The photon bursting of a single NP is generated in a highly focused laser beam (<1 fL) due to the plasmon resonance scattering and Brownian motion. A linear relationship was found between the burst counts and the number of particles in a solution. Upon the immunoaggregation of NPs through the present molecules of the antigen (PSA), the number of counts decreases. The linear range of the PSA was 1−1000 pmol/L, and the LOD corresponded to 0.8 pmol/L.

4.2. Surface Plasmon Resonance

Surface plasmon resonance (SPR) biosensors are based on the light-stimulated oscillation of electrons in the conduction band of metal films (usually gold), called resonant surface plasmons. This effect is strongly dependent on the dielectric constant of its environment[253] and is highly advantageous for biosensing applications because the biological receptor−analyte interaction causes a change of the oscillation frequency. The signal can be measured as a change of the angle, intensity, refractive index, or phase of the reflected light.[254]

SPR sensors can be classified into two main categories: propagating SPRs (PSPRs, also simply referred to as SPRs) and localized SPRs (LSPRs).[255] PSPR is typically excited on continuous metal thin films through prism couplers or a grating,

and the resonance is spread along the metal/dielectric surface up to hundreds of micrometers.[256] LSPR embodies nonpropagating surface plasmon resonance excited on nanostructured metal surfaces; it can be tuned by the size, shape, or composition of nanostructures or nanoparticles.[257]

SPR measurements mostly consist of direct detection[258] and sandwich[259] or competitive inhibition[260] assays. Direct detection is appropriate for applications where the direct binding of the analyte yields a sufficient response. The detection limits can be enhanced using a sandwich or an inhibition assay. In a sandwich assay, the measurement is carried out in two steps: First, the analyte is bound to the antibodies on the sensor surface, and in the second step, the sensor surface is incubated with a solution containing secondary antibodies (which can be labeled by nanoparticles or enzymes[261] to further improve the signal), which bind to the previously captured analyte and increase the sensor response. In an inhibition assay, the examined sample is first mixed with respective antibodies (which, again, can be labeled to enhance the signals), and then the mixture is brought into contact with the sensor surface exhibiting immobilized analyte molecules. The free antibodies remaining in the solution can subsequently bind to the surface.

4.2.1. Amplification by Nanoparticles. Various formats for the detection of chemical and biological analytes have been used in SPR immunosensing. The detection scheme is chosen with respect to the analyte size, binding characteristics of the biomolecular recognition element, range of the concentrations to be measured, and sample matrix.[262] Direct SPR biosensors are applicable in the case of medium and large molecular weight analytes, which induce measurable refractive index changes upon their binding on the surface. The typical detection limits are above nanograms per milliliter.[263]

The enhancement of the sensor sensitivity via labeling the secondary Ab's in a sandwich assay by latex particles[264] and Au NPs[265] was presented in the 1990s. Throughout the years, Au NPs have become a standard for SPR signal amplification tags and enhanced sensing surfaces. Nevertheless, substantial effort was also put into the development of other nanomaterials for SPR amplification, such as nanoparticles based on Ag,[266] CdS,[267] NiO,[268] Pd,[269] and NPs,[270] also including various kinds of magnetic NPs.[271,272]

83

The principles of signal enhancement using nanomaterials can be divided into three categories: (1) plasmonic NP-based SPR sensing, where LSPR is coupled with the surface plasmon wave excited on the sensing film (Au and Ag NPs), (2) large surface mass loading to improve the sensitivity (latex and magnetic NPs), and (3) charge transfer from the nanomaterial to the metallic sensing film that induces a larger evanescent field enhancement, thereby magnifying the SPR signals (graphene).[273]

Au NPs constitute the most common signal-amplification labels in SPR immunosensing. It has been shown that electronic coupling between the localized surface plasmons of Au NPs and the surface plasmon waves associated with the Au SPR chip can significantly increase the SPR response (Figure 20).[274−276] The
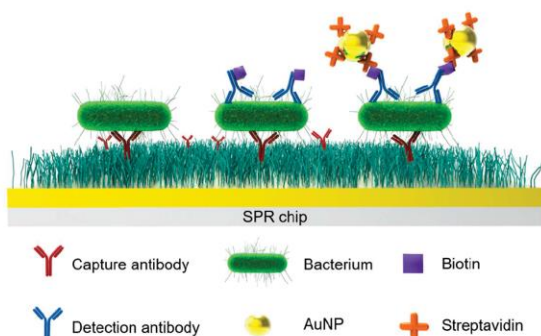
Figure 20. Scheme of the sandwich SPR assay amplified by Au NPs for the detection of bacteria. Based on ref 276.

LSPR peaks of Au NPs are determined by their size and shape and the dielectric constant of the surrounding medium. The large local electromagnetic field enhancement is closely related to metal nanostructures with sharp corners or large curvatures since electric charges can preferentially accumulate in these regions.[277] The LSPR of Au NRs can be systematically adjusted from the visible to the near-infrared wavelengths by manipulating their aspect ratios.[273]

Besides the use of Au NPs in a solution, the incorporation of additional plasmonic nanostructures directly in the SPR sensor chip is one of the perspective ways to enhance SPR signals.[273,278] The excitation of LSPRs by light is related to the strong absorption and scattering of light and also high enhancement of the electromagnetic field close to the nanostructure.[279] Metal NPs with controlled sizes and lateral distances[280] and different types of plasmonic nanostructures,[281] including nanogratings,[282] nanoholes,[283,284] and nanodots,[285] were used in SPR sensors. In addition, even a single nanohole in a metal layer has been proved to support LSPRs.[286]

Ag NP-coated SPR sensors were found to exhibit stronger enhancement of the SPR response compared to those coated with Au NPs[287] due to the larger negative real part and smaller imaginary part in their complex dielectric constants.[288,289] The major disadvantage of Ag NPs is their limited stability and pronounced susceptibility to oxidation. To overcome this challenge, Au−Ag alloy nanocomposites were applied in SPR immunoassays.[290] The nanocomposites present high resistance to oxidization and enable high sensitivity enhancement. Using the Au−Ag alloy, the human IgG was detected with an LOD of 150 ng/mL, while the Au NPs provided an LOD of 300 ng/mL.

Magnetic NPs have been employed in SPR immunosensing to increase binding-induced refractive index changes[291] and for the preconcentration and purification of the analyte in complex samples.[292,293] The nanohybrids of Au NPs and magnetic NPs
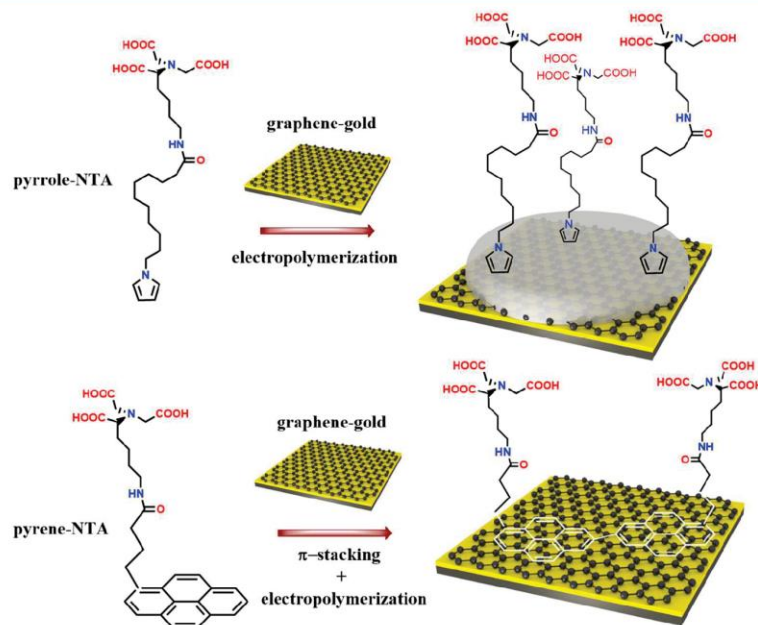
Figure 21. Functionalization of the graphene layer on a Au SPR chip via (top) the electropolymerization of polypyrrole−NTA and (bottom) the π−π stacking of pyrene−NTA followed by electropolymerization for the reinforcement of the layer. Based on ref 303.

84

offer the advantages of both of the above-mentioned amplification approaches.[294] Zhang et al.[295] synthesized particles consisting of a Au nanorod core and a magnetic shell. The NPs were assembled on the sensor surface via a magnetic pillar without any chemical covalent link; this procedure simplified the immunoassay and facilitated easy regeneration. The authors demonstrated the detection of IgG with an LOD of 150 ng/mL.

Carbon-based nanomaterials, such as graphene[296] and carbon nanotubes,[297] have also been used for the enhancement of SPR immunosensing. Theoretical models predicted that the incorporation of a single layer of graphene can strongly amplify the optical sensitivity of SPR sensors.[298,299] GO and rGO were introduced on a gold film using the layer-by-layer assembly, and their effect on the refractive index increase was systematically investigated by Chung et al.[300] The practical applications of graphene in SPR immunosensing were demonstrated by several research groups.[301,302] Singh et al.[303] bound graphene non-covalently to a gold surface to enhance the SPR detection of anticholera toxin antibodies (Figure 21). NTA functional groups were attached to the graphene via the electropolymerization of polypyrrole or $\pi-\pi$ stacking of pyrene. A biotinylated cholera toxin was bound to these layers, and anti-cholera toxin antibodies were detected. The presence of a single graphene sheet increased the SPR sensor performances by 80% (an LOD of 4 pg/mL) compared to a graphene-devoid setup.

The sandwich approach based on the above-mentioned NP labels is generally applicable to enhance the detection of any analyte large enough to allow the binding of two antibodies (the capture and detection Ab's). The sandwich NP-enhanced SPR has been used for the detection of various proteins (e.g., cardiac troponin T,[304] ErbB2 receptor tyrosine kinase 2,[305] or CEA[306]) and bacterial pathogens (e.g., *Salmonella*[272,276]).

Small chemical compounds with a mass inadequate to cause significant changes in the refractive index that do not possess at least two epitopes are hardly detectable by the direct or sandwich approaches. To enhance the SPR response in these situations, a competition for binding to the surface between an antigen conjugated with a high molecular weight label and the unlabeled antigen in the sample can be performed. Another method is based on immobilizing the antigen to the sensor surface followed by the injection of the primary antibody and a sample containing a free antigen. In this case, the signal can be further amplified by the use of the secondary Ab's labeled by NPs (e.g., Au[307−309] or magnetic[292] ones).

4.3. Localized Surface Plasmon Resonance

LSPR is an optical phenomenon caused by the collective oscillations of the electron gas in metal nanostructures (with dimensions smaller than the wavelength of light) surrounded by a dielectric. Typical materials for plasmonic applications are the nanoparticles or nanostructures of noble metals such as Au or Ag, which exhibit LSPR in the visible range of the spectrum.[310] When the nanostructures interact with light, a portion of the incident photons are absorbed, while another portion are scattered in different directions.[311] Both the absorption and the scattering are significantly enhanced when the LSPR is excited. The LSPR resonant frequency depends on the composition, size, and shape of the NPs as well as on the refractive index of the surrounding dielectric medium.[312,313]

4.3.1. Solution-Based LSPR. The very strong and highly confined electromagnetic fields induced by LSPR yield a very sensitive probe for the monitoring of small changes in the dielectric environment around the nanostructures.[314] Local

refractive index changes, including those induced by the biomolecular interactions at the surface of the nanostructures, can be observed using the LSPR peak shift.

Plasmon-enabled assays are usually performed with stable colloid plasmonic NPs. The NPs are characterized by a large surface area for sensing because of their small size; the high diffusion rates of the NPs enable fast analysis. Assays based on the direct capture of the analyte on the NP surface usually provide relatively small shifts in the LSPR peak, and therefore, an absorbance spectroscopy setup is required to allow sensitive detection.[315]

Various materials (typically Au[316] but also Ag or Cu[317]) and shapes (typically spherical NPs[318] or nanorods[319,320]) of plasmonic NPs have been recently employed for solution-based LSPR immunosensing. The NP shape has a significant impact on the detection sensitivity; Au nanorods were significantly more influenced by bulk refractive index changes than spherical Au NPs.[321]

LSPR spectroscopy is usually carried out with large ensembles of NPs. However, each nanoparticle in the ensemble can be potentially used as an independent sensor. The use of single-nanoparticle sensors can ensure improved absolute detection limits (the evaluation of the total number of molecules in a sample) and also increase the spatial resolution in multiplexed assays.[322] Moreover, single nanoparticles with especially narrow bandwidths can be selected from the field of view to enhance the signal-to-noise ratio (S/N) resolution.[323] Typically, the LSPR mode of single NPs, inducing absorption and scattering, can be monitored by dark-field microscopy.[324]

4.3.2. Surface-Based LSPR. Changes in the ionic strength, pH, or temperature can cause the aggregation of NPs. To prevent such a complication, LSPR immunosensing can be performed with nanostructures on solid surfaces. Various approaches to preparing surfaces for LSPR have been developed.

The family of bottom-up techniques is based on capturing NPs on the substrate. The assembly can be performed via chemical binding, exploiting the high affinity of Au and Ag to the mercapto[325] and amino[326] functional groups. Other methods include electrostatic interactions between oppositely charged surfaces and metal NPs,[327] thermal annealing,[328] and the thermal growing of NPs.[329]

Top-down techniques can also be used for the preparation of metal nanostructures on solid supports. Photolithography enables the formation of plasmonic nanostructures with various shapes.[330] Advanced lithographic techniques, such as electron beam lithography (EBL)[331] or focused ion beam (FIB),[332] allow the production of metal nanostructures with accurate control of the size, shape, and spatial distribution. As an alternative way of LSPR surface preparation, inexpensive and large-scale lithographic methods were established, including nanosphere lithography (NSL),[333] colloidal lithography,[334] soft lithography,[335] nanoimprint lithography (NIL),[336] and templating by self-organized nanoporous anodized aluminum oxide (AAO).[337]

A significant benefit of surface-based assays is that the washing steps can be performed with sequential washes over static sensor components, while solution-based nanobiosensors require nanoparticle capture (e.g., using a magnet) or precipitation followed by washing, which is a time-consuming task. Nevertheless, moving from solution-based to surface-based sensing negates the enlarged sensing surface of small particles dispersed in a solution.[315]

The label-free detection based on the immobilization of the antibody to the sensing surface and direct capture of the antigen
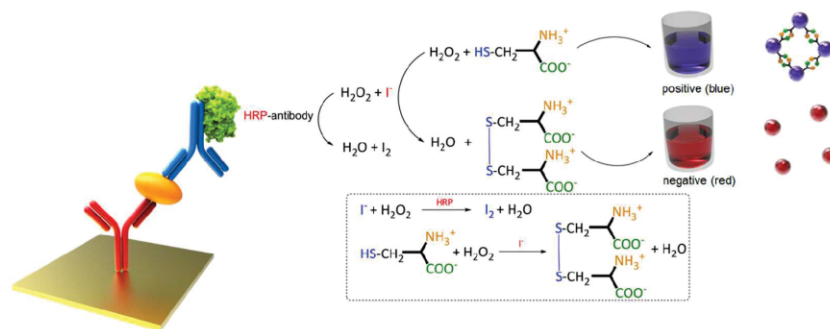
85

Figure 22. Plasmonic immunoassay based on the HRP-mediated aggregation of Au NPs that enables naked-eye readout. Based on ref 342.

is performed as a typical procedure. However, enhancing the LSPR immunoassay with 400% amplification of the shift upon antibody binding to the analyte was demonstrated using antibodies labeled by Au NPs.[338]

4.3.3. Plasmonic Nanoparticle Assemblies. The optical properties of plasmonic NPs depend on the organization and distances between them. When the NPs are in close proximity, the interparticle plasmon coupling causes a red shift in the absorbance peak.[339] The ability to functionalize the NPs and link their aggregation to the presence of the analyte enables the development of various assays based on color change.[340] These methods demonstrate the potentially simple assay scheme with easy colorimetric readout. Aggregation-based methods typically provide a larger LSPR shift compared to the direct analyte capture. Because in some of the techniques the color changes can also be seen with the naked eye, this approach is applicable to point-of-care diagnosis.[341] Aggregation-based colorimetric sensing also has some disadvantages, including mainly the narrow dynamic range and complicated quantification. An additional limitation lies in that the LSPR shifts commonly occur in a region of high absorbance by native proteins, and thus, the sensitivity of measurement in real samples can be restricted.[315]

A sandwich assay based on an HRP-labeled detection antibody and an enzymatic cascade leading to the aggregation of Au NPs (Figure 22) was developed by Xianyu et al.[342] The HRP-catalyzed oxidation of iodide and iodide-catalyzed oxidation of cysteine were used to modulate the plasmonic signals of Au NPs. The method enabled sensitive naked-eye readout and has a potential for point-of-care applications in resource-constrained settings.

4.3.4. Controlled Nanoparticle Growth. Large LSPR shifts are detectable when physical changes, such as the nucleation and growth of new particles or controlled growth of shell structures on pre-existing core NPs, occur in the nanomaterial structure. Ultrasensitive immunoassays can be developed by linking the changes of the nanomaterial structure to the presence or absence of an analyte.[343,344] This approach can bring advantages to aggregation assays based on preformed NPs since the complex matrixes of real samples might induce the aggregation of NPs independently from the analyte presence.

The plasmonic ELISA-based enzymatically controlled NP growth was pioneered by the group of Stevens.[345,346] The detection procedure exploited a classic ELISA sandwich with a biotinylated secondary Ab and streptavidin-labeled catalase, which catalyzes the decomposition of H_2O_2 to H_2O and O_2. The Au NP precursor material ($HAuCl_4$) was added into the ELISA wells, where it reacted to form NPs. The biocatalytic cycle was linked to the growth of Au NPs to obtain blue (or red) solutions in the presence (or absence) of the analyte. In the absence of the analyte, the reduction of Au^{3+} by H_2O_2 occurred at a fast rate, and nonaggregated Au NPs (red color) were formed. In the presence of the analyte, the catalase consumed the H_2O_2, slowing the crystal growth kinetics and causing the growth of nanocrystals with ill-defined morphology and aggregated NPs (blue). The naked-eye detection of low levels of the PSA and HIV-1 capsid antigen p24 was demonstrated, both with an LOD of 10^{-18} g/mL.

4.4. Surface-Enhanced Raman Scattering

Raman spectroscopy is a spectroscopic technique that monitors the vibrational, rotational, and other low-frequency states in a molecule or system. The vibrational mode provides a major contribution to the chemical constitution of a specific analyte. The Raman spectrum ensures a chemical fingerprint for the identification of the analyte. However, Raman signals are generally weak because of the very small number of scattered photons (1 in 10^6 to 10^{10}), which causes serious limitations to identifying analytes at low concentrations.[347]

A substantial signal enhancement (surface-enhanced Raman scattering) was first observed by Fleischmann et al. in 1974,[348] when pyridine was adsorbed to a electrochemically roughened Ag surface. Even though the electromagnetic (EM) basis of SERS is currently well established, surface enhancement has also been connected with the charge transfer (CT) effects in the metal−adsorbate system (chemical enhancement).[349]

An EM enhancement appears if an EM field is induced by the LSPR of a noble-metal surface (e.g., Au and Ag) via the excitation of the electrons on the metal surface by the photons from a laser source.[350] When the analyte molecules are directly on or close to the surface of the metallic nanostructures, the number of induced dipoles increases and subsequently participates in the formation of the SERS effect, resulting in the detectable enhancement of otherwise low Raman signals.[351] The signals increase in conjunction with enhanced EM fields, usually ranging between 10^4 and 10^8.[352]

The CT mechanism can be defined as the grouping of the resonant and nonresonant electronic processes that occur between the metal surface and molecule and are dependent upon the adsorption of the molecule. Because the incident laser causes excited resonance states with the metal surface or molecule, the promoted charge transfer between the two changes the resonance of the system. This participates in the polarizability of the molecule and enhances the Raman signal.[353,354] The effect

86
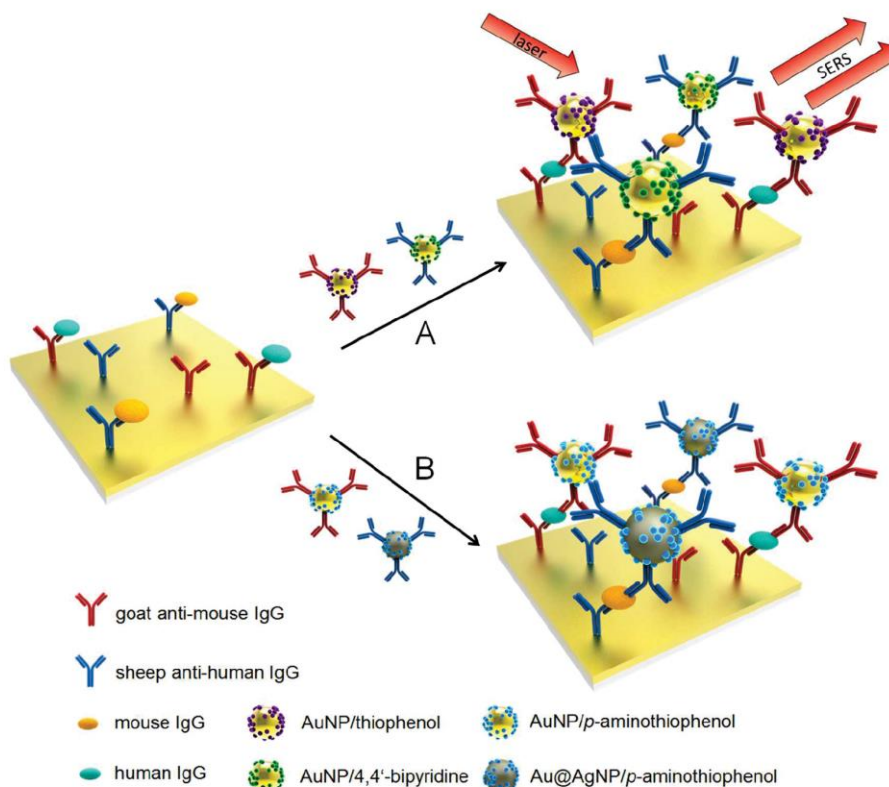
Figure 23. Two strategies for a multianalyte SERS immunoassay based on the sandwich approach. Based on ref 363.

of CT interactions is significantly lower (on the order of 10^1 to 10^2) compared to the discussed EM enhancement.[355]

For most of the reported immunosensing applications, SERS-active substrates have been prepared using Au or Ag.[356] Similarly to SPR and LSPR, the factors influencing the preference of Au or Ag are connected with the differences in the surface chemistries that allow the desired modifications, for example, surface passivation or the conjugation of biomolecules. The higher levels of enhancement provided by Ag NPs go together with the deterioration of the optical properties, caused by rapid oxidation in air and aqueous solutions.[357] To address the particular limitations, the synthesis of composites comprising Ag coated with Au was demonstrated; the process connects high chemical stability and significant enhancement of SERS signals.[358,359]

SERS-based immunosensing can be divided into two main schemes: label-free intrinsic SERS, where the Raman spectra of the target molecule are directly measured, and extrinsic SERS, where the metal surface is functionalized with Raman reporter molecules and target-specific ligands and an amplified signal from the Raman reporter is measured after binding to the target analyte. Extrinsic SERS is typically used for the detection of macromolecules. The complex biochemical composition of biological samples complicates the interpretation of intrinsic SERS spectra, making the identification of a particular biomolecule a difficult task. Macromolecules also exhibit a lower SERS effect compared to smaller molecules.[360] Therefore, different SERS labels or nanotags are used extensively in bioanalytical applications, where the known signature of the tag allows the identification of the target analyte. A typical SERS

nanotag comprises three parts: Raman reporter molecules providing characteristic Raman signatures, a plasmonic metal NP (typically Au or Ag) to enhance the Raman signal, and a recognition element to bind the target molecule.[315] The Raman reporters that can be used also as a conjugation linker (e.g., p-mercaptobenzoic acid) have gained significant attention in recent years due to the simplified nanotag preparation.

A typical SERS immunoassay is based on a sandwich scheme: the capture antibody is immobilized on the surface, it binds the antigen from the sample, and SERS nanotags are applied to allow the detection. The application of extrinsic SERS in cellular and in vivo sensing is extensive because the nanotags associated with the target biomolecules can stand out in the background signals from a complex biological matrix.

The sandwich approach can also be applied in simultaneous detection of multiple analytes through the use of different Ab's and different Raman reporters to prepare specific nanotags. Contrary to the wide emission profiles of fluorescent compounds, the individual Raman spectral peaks show a higher resolution and are, on the average, 10–100 times narrower in width.[361] Furthermore, all Raman labels can be excited by a single laser source, which is not possible in fluorescence-based multiplex analysis. Another advantage of SERS is the high optical stability of the Raman labels. Contrary to fluorescence, photobleaching does not occur in Raman spectroscopy. The signal intensities can be improved by increasing the power of the excitation laser.[362] However, due to the strong local heating induced by the plasmonic nanostructures, the laser power

Figure 24. Number of studies that have used electrochemical methods combined with immunochemical recognition principles in the past five years. Combinations containing, in addition, some types of nanoparticles are shown too.

densities at the sample must still be carefully controlled to prevent damaging the sample.
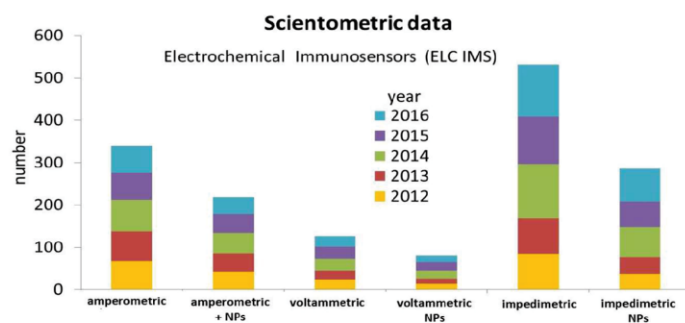
Another multiplexing scheme is based on the combination of identical reporters with different kinds of NPs, arising from the fact that the SERS spectrum of one reporter molecule is influenced by the plasmonic NP enhancement (Figure 23). The ability to encode the reporter NPs was presented by the application of Au NPs and bimetallic Ag–Au NPs to distinguish human and mouse antibodies.[363]

A label-free SERS immunoassay based on the frequency shift due to the binding of the analyte was developed by Tang et al.[364] A Ag NP film for SERS substrates was grown on mercaptosilanized slides using a high-temperature modification of Tollen's method. Poly(dimethylsiloxane) (PDMS) stamps were used to chemisorb two Raman reporters in small square domains on the substrate via microcontact printing followed by repeating with two antibodies. For the multiplex sensing of AFP and glypican-3 (GPC3), the patterned antibody-conjugated substrates were immersed in the sample, and SERS spectra were recorded.

The recent progress in SERS-based immunosensing was devoted to the development of NPs with different shapes and compositions to achieve higher SERS enhancement factors. Compared to conventional nanospheres, nanorods have a stronger SERS effect due to the more intensive scattering derived from the electromagnetic radiation.[365] Other shapes of noble-metal nanoparticles include hollow nanospheres,[366] nanocubes,[367] nanostars,[368,369] nanoprisms,[370] nanoflowers,[371] and tetrapods.[372]

The combination of magnetic beads with SERS nanotags enables some of the limitations of immunoassays on solid substrates (e.g., the long incubation times and the requirement of repeated washing) to be overcome.[373,374] A sensor based on a competitive SERS immunoassay and magnetic separation was presented by Yang et al.[375] Au NPs were labeled by the chloramphenicol–BSA conjugate and a Raman reporter to prepare the nanotag. With the addition of free chloramphenicol, a competitive immune reaction was initiated between free chloramphenicol and the nanotag for binding to the antichloramphenicol antibody-modified magnetic NPs. Instead of the solid substrate, the antibody-conjugated magnetic beads were applied as supporting materials and separation tools. Using a magnet, the mixture was removed from the supernatant for concentration effects. The SERS signals were recorded directly from the supernatant; an LOD of 1 pg/mL was achieved.

SERS techniques have also progressed toward the use in microscopy and small-animal in vivo imaging.[376] The potential of the noninvasive application of SERS is highly valuable for live imaging. SERS also provides a very high resolution for the monitoring of the intracellular environment and the tracking of the cellular distribution of extrinsic molecules. While SERS can be used for the direct imaging of Raman fingerprints in single cells, SERS microscopy mostly depends on extrinsic detection based on nanotags. Various substrates have been adapted for the conjugation of antibodies for targeted cancer imaging in live cells.[377] For example, Au–Ag core–shell NPs were bound to mAb's via a poly(ethylene glycol) (PEG) linker and applied for the imaging of the expression of phospholipase Cγ1 on the surface of HEK293 cells.[378] A multiplexed mixture of receptor-targeted SERS nanotags enabled the rapid quantitative molecular phenotyping of the surface of freshly excised breast cancer tissues to detect the presence of residual tumors. To reduce the ambiguity caused by nonspecific sources of contrast such as off-target binding or uneven delivery, a ratiometric method was used for the quantification of the specific vs nonspecific binding. This technique provides results in less than 15 min and allows the potential intraoperative use in guiding breast-conserving surgeries.[379]

4.5. Electrochemical Transducers

Electrochemical immunosensors and immunoassays are gaining growing attention due to their high sensitivity, selectivity, low cost, good portability, reproducibility, and compatibility with micromachining technology. With the development of nanotechnology and nanoscience, electrochemical immunosensing not only opened the door to substantial improvement of the sensitivity of immunoassays but also led toward implementing further inherent merits, such as miniaturization, portability, and the immense scope of modifications. Together with antibodies (the biorecognition element) and electroactive mediators (either as carriers or as electroactive labels), these approaches secure low detection limits with relatively fast responses. While direct immunosensors are able to follow fast electric signals during the immunocomplex formation, indirect sensors use signal-generating labels incorporated into the immunocomplex during its formation. The latter allow more sensitive and versatile detection. Recently, electrochemical immunosensing has experienced major development, and the application of nanoparticles in electrochemical techniques contributes to this. The scientometric data for the past five years (Figure 24) show that the most increasing trend is associated with impedimetric immunosensors. The second position is then occupied by amperometric immunosensors.

88

4.5.1. Amperometric and Voltammetric Measurements. The amperometric immunosensor is based on measuring the current changes of a conductive material due to the interaction of an analyte with the surface functionalized with antibodies (immuno); in other words, the amperometric immunosensor is a device that transforms chemical information, such as the concentration of a specific sample component, into an analytically useful signal. Usually, the current is measured as a function of the electrode potential (E) or time (t). Both modes are used in immunosensing. With respect to the variation of parameters, amperometric detection in potential-controlled methods (potentiostatic methods) can be realized by different techniques (Figure 25, right). These are as follows: (a)
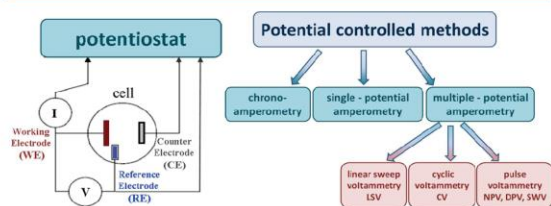

Figure 25. Scheme of the three-electrode setup used in potentiostatic electrochemical methods (left). Potential-controlled methods suitable for electrochemical immunosensing (right).

chronoamperometry, in which the current is measured at a fixed potential in time (usually a short time), (b) single-potential amperometry, where the direct current (dc) is recorded as a function of the potential difference between two electrodes (usually in stirred solutions for a longer time), and (c) multiple-potential amperometry, in which the potential is swept in time by the scan rate (dE/dt) and the corresponding current is recorded in the whole potential window as a voltammetric curve, i.e., $I = f(E)$. Then, linear sweep (LSV), cyclic (CV), normal pulse (NPV), differential pulse (DPV), and square wave (SWV) voltammetric responses characterize electrochemical systems at different potentials and time together.[380]

To control the potential value and to avoid the current load of the reference electrode, an electrochemical cell containing three electrodes, namely, working (WE), counter or auxiliary (CE or AE), and reference (RE) electrodes, is used. The current flows between the WE and CE electrodes, and the desired potential is controlled between the WE and RE electrodes (Figure 25, left).

The above-mentioned methods can reveal not only the reduction and/or oxidation potential of an analyte but also its electrochemical activity (adsorption, interaction with modified layers, electrocatalysis, and preceding chemical reactions). The techniques are sensitive to electrode surface changes, and as such, they find application in the electrochemical immunoassay. Moreover, they can be regarded as nondestructive since only a very small amount of the analyte is consumed at the surface of the working electrode. The explosive development of nanoscience and nanotechnology, giving new improved electroanalytical tools, is also reflected in the area of immunosensors.[381]

As well as nanomaterial-based biosensors, the enhancement of the analytical performance of electrochemical immunosensors by NPs consists of lowering overpotentials (at higher surface area, the current density tends to be smaller and electrocatalysis efficiency to be higher) and increasing current yields (redox conversion stemming from the large surface area of NPs). NPs also improve the reproducibility of nanoimmunosensors because

a high and targeted surface area allows faster and more complete and controlled charge transfer at lower overpotentials, which lessens the complications associated with electrode fouling. NPs can guarantee enhancement of biomolecule compatibility and functionalization. On the basis of the knowledge of electrostatic interactions or the formation of bonds, the NP functionalization is able to attach specifically certain biomolecules, allowing their efficient immobilization and increased electroanalytical responses.[382]

An electrochemical (amperometric) immunosensor, being a chemical biosensor, contains two basic functional units: a bioreceptor and a transducer. Some immunosensors may include a separator consisting of, for example, a membrane. From the bioreceptor part, the important information is transformed into a form of energy measurable as electrical work by the transducer. Thus, in amperometric immunosensors, the response is derived from the interaction between chemistry and electric current (Figure 26).
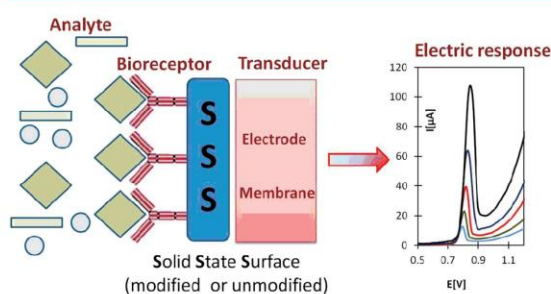
Figure 26. Scheme of the electrochemical (amperometric) immunosensor design, depicting the integration of immunological recognition at the solid-state surface.

Undoubtedly, nanotechnology has had a major impact on biosensor research. In the field of electrochemical biosensors (immunosensors), nanotechnology brings new and varied opportunities connected with the modification of a transducer and/or biomolecules via nanomaterials. This is often related to the miniaturization of the transducer. Apart from the very specific biorecognition reaction, antibodies (Ab's) and antigens (Ag's) can be produced to obtain a specific binding partner for the target of interest.[383]

Finally, it should be noted that electrochemical sensors based on enzyme labels produce or consume an electroactive substrate or cofactor which can be monitored at an electrode interface. The most common enzyme labels—horseradish peroxidase (HRP), glucose oxidase (GOD), and alkaline phosphatase (ALP), together with nanomaterials (nanoparticles, nanocomposites)—open up an exceptional potential for powerful electrochemical immunosensors. For example, ALP cleaves the nonelectroactive p-aminophenyl phosphate into p-aminophenol, which undergoes reversible oxidation. Moreover, p-aminophenol can be recycled thanks to the reduction by p-benzoquinonimine at the second electrode.

Multiple strategies to enhance the amperometric responses of immunosensors have been reported; however, no clear formulation or optimum procedure has been proposed to date, and thus, we acquire an attractive topic in the electrochemical investigation of immunosensors. The research problems may rest in or be related to (a) the optimization of a suitable interaction or binding mechanism between the analyte and the electrode

89

surface, (b) the modification of the electrode surface (nano-composites, polymers, nanoparticles, self-assembled monolayers (SAMs)), (c) the immobilization of the antibody, (d) the effect of the pH, ionic strength, and temperature on the individual steps within electrochemical immunodetection, and (e) the effect of the Ab (length), polymers, and nanoparticles on electron transfer processes. In this field, recent research activities have been focused on the modification of electrode surfaces by using metal (prominently gold and silver) or metal oxide nanoparticles, nanocomposites, and allotropic modifications of carbon (e.g., CNTs and graphene). Some papers discuss electrode surface modification performed by means of SAMs, diazonium, or sol–gel chemistry. Within the development of electrochemical immunosensors, conducting polymers have attracted considerable attention stemming from a set of crucial reasons. Polymers embody a suitable (very often also biocompatible) matrix for the entrapment of enzymes, and they can be prepared in situ on electrode surfaces via electropolymerization, enabling control over their film thickness. Moreover, electropolymerization can establish a direct connection of the polymer layer with the electrode surface, which is important for increasing the robustness of the electrochemical immunosensor.

Metallic nanoparticles have become a much-favored tool in electroanalysis because of their superior physical and chemical properties, including the high surface-to-volume ratio, good electrical qualities, strong adsorption ability, and positive surface characteristics. The implementation of metallic or metal oxide nanoparticles is used also in electrochemical immunosensors.

4.5.2. Electrochemical Immunosensors with Metals or Metal Oxides. Electrochemical applications of nanomaterials are predominated by carbon and metallic nanoparticles, which are used in modifying active surfaces of conventional macro- and microelectrodes. A large variety of designs employing metallic NPs for immunosensors were reported. For example, one design was developed for ultrasensitive electrochemical immunoassay of small molecules based on a host–guest interaction of adamantine with a β-cyclodextrin-functionalized Au/Pd bimetallic nanoprobe. In that design, the electrocatalysis of Au/Pd NPs toward the oxidation of $NaBH_4$ was employed to produce a voltammetric analytical signal. The highly efficient electrocatalysis by AuPd nanoparticles for $NaBH_4$ oxidation produced an ultrasensitive response (LOD = 4.6 ng/L) to chloramphenicol as a model of a small-molecule antigen.[384]

A highly sensitive electrochemical CEA immunosensor was fabricated by covalently immobilizing a monoclonal CEA antibody (anti-CEA, Ab1) and a mediator (thionine, Th) on the Au NP-encapsulated dendrimer. The highly sensitive detection was achieved by the increased HRP-electrocatalyzed reduction of hydrogen peroxide locally generated by GOD. The immunosensor surface was characterized using EIS, AFM, and QCM; dendrimer-modified NPs and the Ab2/MWCNT/GOx/HRP bioconjugates were characterized using high-resolution TEM, SEM, and X-ray photoelectron spectroscopy. Cyclic and square wave voltammetry techniques were used to monitor the increased electrocatalyzed reduction of hydrogen peroxide by HRP.[385]

In the other voltammetric immunoassay of CEA, a polystyrene microbead was covered with chemically deposited Au NPs, which were also employed as a tracing tag to label the signal antibody. A triple signal amplification was achieved using graphene to modify the immunosensor surface for accelerating electron transfer, poly(styrene-*co*-acrylic acid) microbeads carried Au NPs as a tracing tag on the Ab2, and Au NPs induced

silver deposition for anodic stripping analysis. The immunosensor was constructed by covalently immobilizing capture Ab on the Chit/rGO film-modified GCE. The in situ synthesis of Au NPs led to the enhanced loading of the label on the bead surface.[386]

Mao et al.[387] used the Nafion membrane modified by titanium dioxide (TiO_2) nanoparticles for human chorionic gonadotropin and a Nafion–TiO_2–Gr homogeneous composite with a GCE for the detection of CEA.[388] To detect sulfamethoxazole, a new electrochemical immunosensor was based on a CeO_2–chitosan nanocomposite modifying a GCE.[389] A detection limit of 0.11 pg/mL CEA was achieved in a sandwich-type immunoassay (anti-horseradish peroxidase bonded to anti-carcinoembryonic antigen, HRP–anti-CEA) by using biometallic AuPt nanochains.[390] The biometallic nanochains were considered as promising candidates for the next-generation sandwich-type electrochemical immunoassays. To determine the prostate-specific antigen (PSA) with a low limit of detection (1.16 fg/mL in serum), TiO_2 NPs and a monoclonal antibody in combination with ICP–MS were used.[391] The amperometric/coulombimetric signal produced of the CdS NP was employed for the detection of sulfonamide antibiotic residues in food samples.[392] Au NPs were invented to recognize the trombin captured on the screen-printed carbon electrode.[393] For the electrochemical detection of staphylococcal enterotoxin B, GCEs were modified with platinum nanoparticles,[394] and to facilitate the rapid detection of *Salmonella pullorum*, a system containing ionic liquids (Au NP/HRP/ILs) was used.[395]

Carbon nanotubes (SWCNTs or MWCNTs) and graphene, graphene oxide (GO), and reduced graphene oxide (rGO) nanosheets all belong to the allotropes of carbon with a two-dimensional nanostructure, offering unique chemical, geometrical, and mechanical properties such as high strength flexibility and thermal stability. From the perspective of their application in electrochemical sensing, we should highlight electrical properties such as the high conductivity and electron transfer capability.

4.5.3. Allotropic Modification. Papers on novel electrochemical immunodetection platforms based on carbon nanotubes have been published; selected examples describe modifications with a thionine–chitosan nanocomposite film,[396] MWCNTs with graphene sheets and poly(ethylenimine)–Au,[397] GCE/Bi NPs/Nafion–MWCNTs/GCE,[398] and electrospun carbon nanotube nanofibers.[399]

Advanced electrochemical immunodetection platforms based on graphene have been presented in many papers. The electrochemical reduction of GO was chosen for preparing rGO-modified ITO surfaces.[400] Graphene oxide sheets were initially deposited on amine-terminated benzenediazonium-modified indium tin oxide (ITO) surfaces through both electrostatic and π–π interactions between the modified surfaces and GO. Using the ultrasensitive detection of an antigen by the sandwich ELISA method, a very low limit of detection (ca. 100 fg/mL, which corresponds to ca. 700 aM) was achieved. Graphene-based immunosensors were fabricated for the detection of aflatoxin B1, an extremely toxic substance among mycotoxins in contaminated food products.

A dual enhancing strategy[401] has been employed to develop an electrochemical immunosensor for the ultrasensitive detection of AFP, which is enhanced by a polydopamine-functionalized N-doped multiwalled carbon nanotube (PDA-N-MWCNT) and the nanocomposite of graphene-loaded Au/Pt mesoporous nanodendrites.
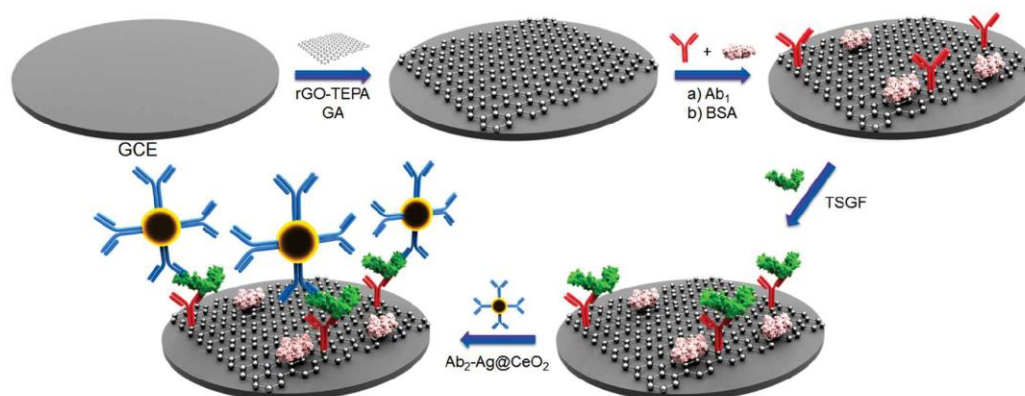
Figure 27. Schematic representation of the preparation of an immunosensor. The reticular structures represent rGO−TEPA. Ab1 represents the anti-TSGF antibody. rGO−TEPA, GA, Ab1, BSA, TSGF, and Ab2−Ag@CeO$_2$ are modified onto the GCE in sequence. Based on ref 402.
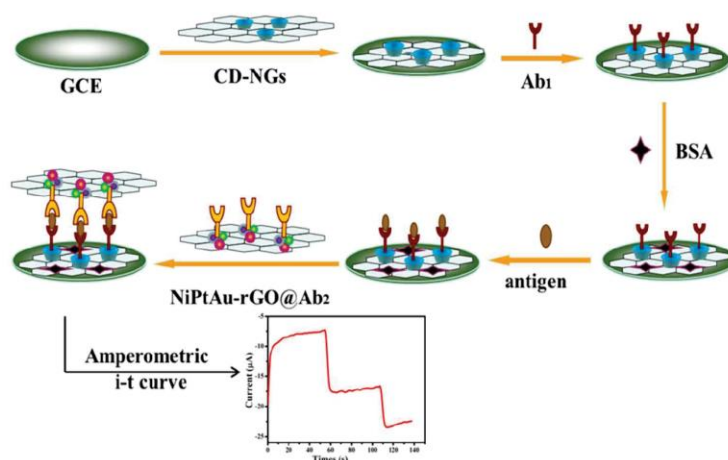
Figure 28. Schematic illustration of the fabrication process related to the sandwich-type electrochemical immunosensor for detecting the carcinoembryonic antigen. CD−NGs = cyclodextrin−nanosheets of graphene. Reprinted from ref 403 with the permission of the Creative Commons Attribution 4.0 International License (http://creativecommons.org/licenses/by/4.0/). Copyright 2016 Nature Publishing Group.

The application of nanomaterials in electrochemical immunosensors of the sandwich ELISA type is presented in many variations. For example, one of the referenced papers describes an ultrasensitive amperometric immunosensor developed to detect a tumor-specific grow factor—the endometrial cancer marker.[402] Reduced graphene oxide−tetraethylenepentamine (rGO−TEPA) was used to modify the surface of a glassy carbon electrode (GCE), and a Ag (silver)@CeO$_2$ nanocomposite was applied as the secondary antibody (Ab2) label (Figure 27). The amperometric response of the immunosensor for the reduction of H$_2$O$_2$ was recorded. Thus, the anti-TSGF primary antibody (Ab1) was immobilized onto the rGO−TEPA-modified GCE via cross-linking with glutaraldehyde (GA), and then the tumor-specific growth factor antigen and Ab2−Ag@CeO$_2$ were modified onto the electrode surface in sequence. Under optimal experimental conditions, this immunosensor exhibited a low detection limit of 0.2 pg/mL. A possible explanation can be outlined as follows: First, the large specific surface area of rGO−TEPA can increase the loading capacity of the Ab1 and then raise the amount of combined antigen and Ab2, leading to a higher

response. In addition, the good electroconductivity and electron transfer capability of rGO−TEPA can be beneficial for the detection of H$_2$O$_2$. Second, Ag@CeO$_2$ exhibits fine catalytic activity toward H$_2$O$_2$, which can improve the immunosensor performance significantly. The authors have discussed the effect of the irreversible agglomeration of rGO on the stability of these nanostructured electrochemical sensors and their potential application in the detection of other cancer biomarkers.

Tumor markers are highly popular analytes for modified electrochemical immunosensors. The explanation is simple: Clinical practice requires an uncomplicated, reliable, low-cost, and sensitive detection method for tumor markers to reveal cancer at an early stage. In other words, tumor markers can reflect the existence and growth of a tumor. CEA, a widely used tumor marker produced abundantly in essentially all human colon carcinomas and in a high proportion of carcinomas at many other sites, is applied for clinical research and early diagnosis in the serum. The authors of a referenced source developed a novel and ultrasensitive sandwich-type electrochemical immunosensor for the quantitative detection of the CEA (Figure 28).[403] This

91

immunosensor was developed by using trimetallic NiAuPt nanoparticles on graphene nanosheets as excellent labels and β-cyclodextrin-functionalized reduced graphene oxide nanosheets as the platform. Such an assembly with a high specific surface area, good biocompatibility, and ideal dispersibility was used to capture the primary Ab_1 efficiently. The trimetallic NiAuPt–NG nanocomposites were used as the labels for the signal amplification, showing improved electrocatalytic activity toward the reduction of hydrogen peroxide (H_2O_2), which is substantially better than that of monometallic Pt–NGs, bimetallic NiPt–NGs, and AuPt–NGs due to the synergetic effect presented in the NiAuPt–NGs. The NiAuPt–NG nanocomposites consist of tightly coupled nanostructures of Au, Ni, and Pt, which have neither an alloy nor a core–shell structure. Under optimal conditions, a linear range of 0.001−100 ng/mL and a low detection limit of 0.27 pg/mL were obtained for the CEA. The proposed electrochemical sandwich-type immunosensor may have promising application in bioassays and enriches electrochemical immunoassays.

In general, electroactive nanomaterials were used as labels for constructing a sandwich-type immunoassay to enhance the sensitivity. According to the discussions concerning this application, there are some drawbacks related to (a) the activity of the biomolecules in the systems after the application of nanoparticles or nanocomposites, (b) the aggregation of nanoparticles and the effect of their shells on both the aggregation process and the electrochemical activity of nanoparticles, and (c) the electron transfer and its rate influenced by a linker (length, cleavage) between the electrode surface and the electron transfer mediator. In amperometric immunosensors, the main disadvantage of having an indirect sensing system is, however, compensated for by excellent sensitivity compared to that of classic ELISA. This is due to the linear analyte concentration range compared to the logarithmic relationship in potentiometric systems. Special attention must be directed to the system-inherent transport rate limitations for redox partners on the electrode surface.

4.5.4. Electrochemical Impedance Spectroscopy.

Electrochemical impedance spectroscopy (EIS) has received substantial attention in the field of immunosensors during the recent years, especially due to the possibility of ultrasensitive, nondestructive, and rapid electrochemical sensing and characterization of various biological analytes and interfaces. EIS embodies a powerful technique to explore the physicochemical properties of the biorecognition events connected to a respective transducer or, generally, an electrode. In the case of biosensors, EIS may provide valuable information about the individual immobilized layers, polymers, and diverse coatings on the electrode; furthermore, the charge transfer resistances, capacitances, and diffusion coefficients can be readily evaluated. The method also enables us to examine the electrochemical behavior of a composite electrode, surface roughness, porosity, and eventual adsorption mechanism. As the technical background of EIS has been comprehensively described elsewhere,[404,405] this section will focus especially on the recently utilized approaches associated with nanoparticle-enhanced immunosensing. The principle of impedimetric measurement rests in the application of a sinusoidal potential (or current) with a low amplitude through the two- or three-electrode cells containing an electrolyte solution, mainly ferro/ferricyanide. The resulting current (or potential) is recorded by a potentiostat over a range of frequencies, and the overall impedance is calculated by appropriate software according to

$$Z = \frac{V(t)}{I(t)} = \frac{V_0 \sin(2\pi f t)}{I_0 \sin(2\pi f t + \theta)}$$

where V_0 and I_0 are the maximum potential and current signals, f denotes the frequency, t represents the time, and θ is the phase shift between the voltage−time and current−time functions. Generally, the applied potential is rather small, which provides a practical advantage compared to other electrochemical methods (CV, DPV, SWV). Higher potential values can cause an unfavorable disruption of the biomolecular layer, influence the binding, or oxidize/reduce the attached components.[406] In certain immunosensing assays, EIS is used to monitor particular immobilization steps and support the data obtained from the above-mentioned common electrochemical approaches.[407] The central role of EIS is, however, associated with label-free detection. Since the impedance-based technique exhibits extreme dependency on the interfacial binding events occurring at the electrode surface, the labeling is not required in certain cases.[408] Principally, the analyte of interest is bound to a specific Ab immobilized on the electrode, and the impedance increment is registered in the solution of the redox probe as a result of the accumulated mass hindering the electron transfer.

Various nanomaterials have been used to enlarge the surface area, to improve the stability of the immobilized biomolecules, and to enhance the sensitivity of the developed sensor.[409−411] The most frequent items, or Au NPs/nanostructures/nanocomposites[412,413] and graphene sheets,[414,415] assembled on the electrode represent highly effective and biocompatible layers providing an extended surface/volume ratio and thus also more space for antibody immobilization. Moreover, the nanostructure-designed surface is considered to be an excellent promoter of the electron transfer between the electrode and the redox probe.[416,417] Multiple nanocomposites have been fabricated to enhance the signal intensity. For instance, Raymundo-Pereira et al. revealed the synergistic effect of Au and Pt nanostructure-based electrodes accelerating the electron transfer more efficiently than just bare Au or Pt electrodes.[418] The NP-modified label-free impedimetric sensor demonstrates an ideal arrangement for point-of-care applications.[419] For practical purposes and ease of operation, the single-frequency mode of impedance suggests a desirable alternative, facilitating the data analysis and excluding the need for equivalent circuit modeling and fitting of electrochemical parameters.[420] In some cases, the label-free approach does not provide satisfactory LODs and is substituted with the sandwich format. Here, the response and selectivity are further improved by the attachment of a detection Ab, ordinarily conjugated to a label. Several NPs[402,421] and nanomaterials (carbon nanotubes, graphene)[422−424] have been used to assemble an increased load of antibodies/labels, e.g, enzymes, catalyzing the conversion of the substrate to insoluble products on the electrode, thus amplifying the signal by the extension of the charge transfer resistance.[425] Another variant of immunosensors, the signal-off group, is based on "electron wiring" between the electrode and the highly conductive NPs conjugated either to the detection Ab or whole cells (Figure 29).[426] It has been reported that the electron transfer (ET) at the interface of the AuNPs/insulating barrier/electrode is similar to or even more efficient than the ET between the bare electrode and the redox probe.[427] In this case, a decrease of the charge transfer resistance is observed with an increased concentration of the nanoparticle-modified analyte. The above principles can be ranged within faradic impedance spectroscopy: the charge is transferred in the presence of a redox probe across the interface.
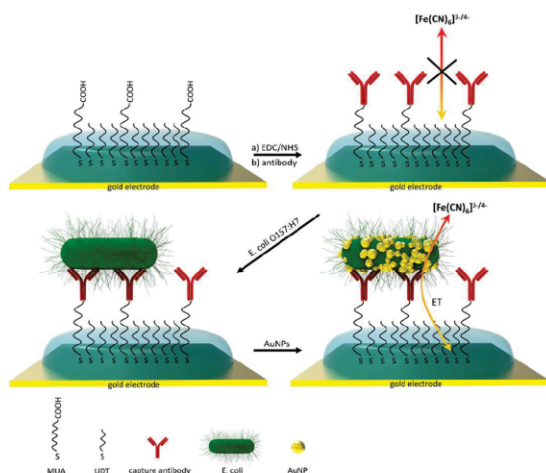
Figure 29. Scheme of the signal-off impedimetric immunosensor. Based on ref 42.

Contrariwise, nonfaradic EIS is usually performed in a dielectric solution, which becomes more conductive when a charged material, e.g., a negatively charged cell membrane of bacteria, is attached to the electrode.[428] Then the solution resistance and double-layer capacitance are monitored as the most variable parameters. Nguyen et al. successfully applied such an approach in the detection of *Salmonella* adhered to magnetic silica nanotubes and achieved a remarkable limit of detection.[429]

Although the nanosurfaces provide a large number of advantages within impedimetric immunosensing, the orientation of the immobilized antibodies remains questionable. Some Ab's may be deeply buried in the branched nanostructures inaccessible for larger analytes. These phenomena could result in uneasily reproducible impedance spectra among the individual sensors. However, multiple reports dealing with EIS illustrate that this technique finds its potential in many bioanalytical applications.

4.5.5. Field-Effect Transistors. Within the effort to achieve a deeper understanding of both these and the biomolecule–surface interactions at the atomic level, potentiometric immunosensors based on the field-effect transistor (FET) have attracted wide interest.[430] Field-effect transistors (FETs) are active electronic components enabling us to control the current flowing between the drain (D) and source (S) terminals via the voltage (charge) on the gate (G) terminal. The principle of the FET was patented by J. E. Lilienfeld in 1925. Depending on the architecture, FET devices can be classified into two main branches: insulated gate FETs (or MOSFETs, metal oxide semiconductor field-effect transistors) and junction FETs (JFETs).

Most FET devices applicable in the field of sensing are MOSFETs. When using MOSFETs as (bio)chemical sensors, the gate terminal is in direct contact with the measured environment (samples). Interestingly, the name is now a misnomer because the previous metal gate material is often replaced with a layer of polycrystalline Si (Figure 30) due to the capacity of the latter to form self-aligned gates. Typical gate materials are SiO_2, Si_3N_4, Al_2O_3, and Ta_2O_5; the surfaces of these oxidic materials contain amphoteric hydroxyl groups capable of both donating and binding protons. The pH changes induce variations in the surface charge which controls the conductance of the drain–source channel of the resulting ISFET (ion-selective FET) devices. ISFETs are easily adaptable for the measurement of ions other than H^+ (e.g., K^+ and Ca^{2+}) by coating the gate with an additional ion-selective membrane. By coating the ISFET gate with an enzyme layer, a range of enzyme FET (ENFET) devices can be constructed provided that the corresponding enzymatic reactions involve a pH change. This technique can also be applied to immunosensors, and ISFETs are good candidates for ultrasensitive immunosensor applications.

Typical graphene-based field-effect transistors (GFETs) on Si/SiO_2 or poly(ethylene terephthalate) (PET) substrates are presented in Figure 31. While the output characteristics of FET devices correspond to the drain current I_D (μA) as a function of the drain voltage V_D or V_{ds} (V), the transfer characteristics are measured as the drain current I_D (μA) dependent on the gate voltage V_G or V_g (V).[431] Then the drain current versus the time for an FET during the injection of various concentrations of the
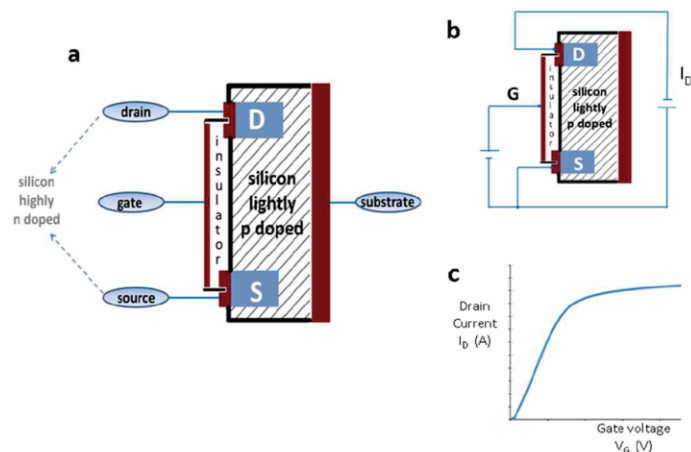

Figure 30. Conceptual enhancement mode, n-channel MOSFET: (a) basic MOSFET structure; (b) schematic diagram with the applied voltage; (c) transfer characteristics of the FET (the drain current I_D as a function of the gate voltage V_G).
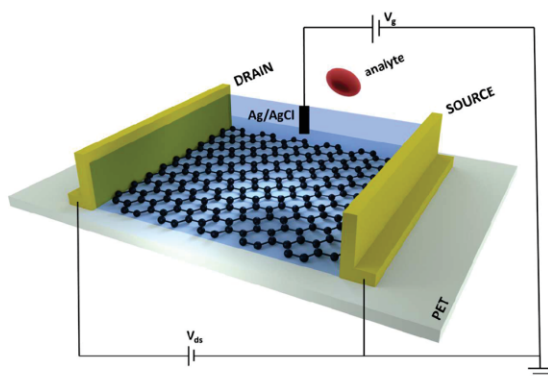
93

Figure 31. Typical back-gate graphene-based field-effect transistors (GFETs) on a flexible poly(ethylene terephthalate) (PET) substrate (as the chemical and biological sensor in an aqueous solution). Based on ref 431.

studied analyte is registered (e.g., serum ferritin in the concentration range between 50 pg/mL and 500 pg/mL).[432]

An advantage of FETs as potentiometric sensors is the simplicity of operation, which can be suitably used for automation; this is complemented with the small size of the solid-state FET sensors, which require very little current (usually less than 1 mA). Possible drawbacks may consist of the nonspecific effects of binding or the signaling influences from other ions present within the sample. The referenced paper[433] pointed to detecting biomolecules in complex biosamples with high ionic strength (>100 mM), where screening effects can be expected. Most sensors operate under low ionic strength conditions, requiring ex situ biosample manipulation steps (desalting processes). The authors demonstrated an effective approach for the direct detection of the biomolecules in an untreated serum, based on the fragmentation of the antibody-capturing units. Moreover, the size-reduced antibody fragments permit the biorecognition event to occur in closer proximity to the nanowire surface, falling within the charge-sensitive Debye screening length (the dimensions of macromolecules).

In FET immunosensors (also EISFET, or the electrolyte−insulator−semiconductor field-effect transistor), the gate is decorated by covalently immobilizing antibodies as binding entities that specifically capture the desired analyte. Two proposed basic mechanisms (the intrinsic charge of the detectable macromolecule and/or the charge redistribution that follows the intermolecular interaction) were discussed.[433] Numerous research efforts have been devoted to realizing the idea of these approaches; however, most of the reported results turned out to be disappointing.

The immunosensor is based on an FET where a network of SWCNTs acts as the conductor channel, constituting carbon nanotube field-effect transistors (CNTFETs). Anti-atrazine antibodies were adsorbed onto the SWCNTs, and subsequently, the SWCNTs were protected with Tween 20 to prevent the nonspecific binding of bacteria or proteins.[434] The principle of the immunoreaction consists of the direct adsorption of atrazine-specific antibodies (anti-atrazine) onto SWCNT networks. After being exposed to increasing concentrations of atrazine, CNTFETs could be used as convenient label-free platforms to detect atrazine. Under optimal conditions, a detection limit as low as 0.001 ng/mL was obtained, which is lower than that found

in other methods for atrazine detection, and falls within the working range between 0.001 and 10 ng/mL. Single-walled carbon nanotubes (SWCNTs), but horizontally aligned, were applied in a liquid-gated field-effect transistor (FET) of interleukin-6 (IL-6; from the family of secreted proteins).[435] The proposed immunosensor exhibits not only good sensitivity (the LOD is 1.37 pg/mL) but also improved stability attributed to the strong adhesion of CNTs to the quartz substrate because of the good horizontal alignment of these tubes. This facile approach could be customized to also detect food toxins (e.g., *Clostridium perfringens*) and biomarkers upon appropriate functionalization of the aligned CNTs.[436]

The superior physical and electrical properties, including the high carrier mobility, ambipolar electric field effect, high surface area, flexibility, and compatibility with microfabrication techniques, make carbon allotropic nanomaterials such as graphene (G) and carbon nanotubes (CNTs) easy to integrate into FET immunosensors. Ramnani et al.[437] presented an approach toward integration into these devices using various fabrication methods, evaluated different sensing platforms that incorporate biomolecules such as enzymes, antibodies, and aptamers as the recognition elements, and pointed to problems connected with the same properties of GFETs or CNTFETs. The discussed issues included, for example, impurities, the number of layers, edge structure, substrate, length and diameter of the tubes, or level of agglomeration. In view of our experience, this evaluation can be supplemented with two aspects: the amount and distribution of hydroxyl, carbonyl, carboxyl, or other functionalized groups and their distribution on the surface area with respect to edge effects.

Park et al. used a modified FET immunosensor for very sensitive determination of the CEA.[438] For this purpose, they fabricated aptamer-functionalized multidimensional conducting polymer (poly(pyrrole-3-carboxylate)) nanotubes (Apt-C-PPy MNTs). To produce an FET-type biosensor transducer, functionalized NTs were integrated with the CEA-binding aptamer immobilized on an interdigitated array electrode substrate by covalent bonding with amide groups. The resulting liquid-gated C-PPy MNT-based FET sensors exhibit both a rapid response in real time (<1 s) and ultrasensitivity toward the CEA with a detection limit of 1 fg/mL.

Within the domain of FET immunosensing, another paper[439] from the same laboratory examines the highly sensitive and label-free detection of cardiac troponin I (cTnI), a biomarker for the diagnosis of acute myocardial infarction. Monoclonal antibodies for cTnI were covalently immobilized on a silicon nanowire surface with a honeycomb-like structure, and the attachment of the antibodies is clearly visualized by an atomic force microscope. The detection limit of the silicon nanowire FETs is about 5 pg/mL.

An alternative solution for recognizing tumor-related proteins by using an FET, usually based on antibodies, is presented in a corresponding paper.[440] Here, the platelet-derived growth factor (PDGF) was detected via an aptamer (fragment single-stranded DNA), and the LOD equals 8.8 pM.

Some possible applications of immuno-FETs as quantitative point-of-care devices are presented in the form of next-generation tools for serological disease diagnosis to compete with pathogen serology using enzyme-linked immunosorbent assay (ELISA). Exploiting the model pathogen bovine herpes virus-1 (BHV-1; a major viral pathogen of bovine respiratory disease), this study employs an extended-gate FET for direct potentiometric serological diagnosis.[441] To demonstrate the

94

capabilities of the FET sensor as a diagnostic instrument, the BHV-1 viral protein gE was expressed and immobilized on the sensor surface to serve as a capture antigen for the BHV-1-specific antibody (anti-gE). This FET sensor is significantly faster than ELISA (<10 min). By using another type of FET immunosensor, one based on a hornlike polycrystalline silicon nanowire (poly-Si NW FET), the intracellular protein ferritin was detected in a microfluidic channel with an LOD of 50 pg/mL.[442]

FET immunosensors also occupy a significant position within the diagnosis of various diseases. For example, nanowire immuno-FETs and ion-sensitive field-effect transistors (ISFETs) were used for the real-time and label-free detection of antibodies from avian influenza (anti-AI)[443] and hepatitis B surface antigens,[444] respectively. Newly developed ISFET-based portable sensors hold a large potential for point-of-care (POC) tools in a variety of diseases, without being limited by the need for expensive equipment such as spectrophotometers.[445] Similarly, the label-free, low-cost, and miniaturized silicon nanowire field-effect transistor (Si NW FET) chip, detecting the human thyroid-stimulating hormone[446] or human immunodeficiency virus (HIV),[447] has a potential in the point-of-care diagnosis of thyroid or AIDS diseases. The type of transistor channels may vary according to the organic molecules used as semiconductors (e.g., n channel for pentacene and p channel for naphthalenetracarboxylic diimide); these organic molecules are in conjunction with a new dielectric layer (fluorinated polymer and vapor-deposited hydrocarbon).[448] Organic thin film transistors (OTFTs) are able to detect a wide range of analytes, including gases, chemicals associated with explosives, and biomolecules (nucleic acids, proteins). Compared to inorganic semiconductors, organic ones are flexible materials promising (a) integration into wearable or implantable medical care devices, (b) the fabrication of thin layers by spin-coating and/or printing procedures, and (c) the modification of the transistor surface via simple chemical tailoring.

4.6. Magnetic Sensors

4.6.1. Diagnostic Magnetic Resonance.
Magnetic NPs offer unique possibilities for biosensing methods. Biological samples exhibit no magnetic background, and thus, such procedures are highly sensitive and can be performed in complex matrixes without further preprocessing. Several methods have been developed for the analysis of biomolecules and other particles using a magnetic field and MP-based labels.[449] Some authors referred to functionalized magnetic NPs as magnetic nanosensors.[450] Biomolecules and cells labeled with magnetic nanoparticles can be detected using a technique based on nuclear magnetic resonance effects. This method is termed diagnostic magnetic resonance (DMR) and has been advanced by designing a miniaturized chip-based μNMR system.[451,452] In a magnetic field, MPs induce a change in the proton relaxation rate and the transverse relaxation time T_2 of the measured samples. Two forms of DMR assays can be used considering the size of the target. First, the magnetic relaxation switching (MRS) effect can be exploited to detect small molecules making aggregates with MPs and thus changing the magnetic relaxivity. For example, kanamycin was detected using a competitive MRS immunoassay with an LOD of 0.1 ng/mL and an analysis time of less than 1 h.[453] Furthermore, not only small molecules but also larger targets such as bacteria or cells are labeled with MPs; the unbound MPs are removed, and the relaxation time is measured. Liao et al. used dynamic magnetic resonance to detect C-reactive

protein (CRP), a key indicator of infectious/noninfectious diseases or an acute tissue.[454] Dextran-coated magnetite nanoparticles were conjugated with specific anti-CRP antibodies. The interaction of magnetic nanoparticles with CRP was monitored as a decreasing change of the T_2 relaxation time, which corresponds to the concentration of the analyte in the sample. A compact-size DMR system suitable for POC detection was constructed and tested using *Staphylococcus aureus*.[455]

4.6.2. Magnetoresistance.
Magnetic particles serving as labels interact with an external magnetic field, which induces a change in the electrical resistance. Specifically bound antigens can be detected by magnetoresistive (MR) sensors. Various MR-based sensors have been derived, including the giant (GMR), tunneling (TMR), colossal (CMR), and anisotropic (AMR) types.[456] Since their discovery by Grünberg and simultaneously by Fert in 1988,[457] GMR sensors have become popular.[458,459] GMR is a quantum mechanical effect based on spin-polarized electron transport in magnetic/nonmagnetic multilayers.[460] A detected nonmagnetic layer is sandwiched between two ferromagnetic layers. The upper layer consisting of MPs is referred to as the free layer, and its magnetization can be changed by an external magnetic field. However, the penetration depth of the magnetic field is only approximately 150 nm. The magnetization of the bottom fixed layer remains unchangeable. The imbalance of the spin populations results in a magnetic moment in the film and affects the electric resistivity, and small changes in the magnetization of the free layer are detected.

A GMR sensor arranged in a microfluidic cell was used for detecting a D-dimer—a biomarker of thrombosis.[461] Magnetic NPs with an average size of 100 nm were used as the signal probe. The detection limit corresponded to 5 ng/mL, and the results were in good correlation with the applied Sysmex CA1500 commercial analyzer. The use of a GMR sensor for detecting *E. coli* and *E. coli* O157:H7 was presented by Kokkinis et al.[462] and Sun et al.,[463] respectively. This technique also introduces new possibilities into the study of protein interactions. The monitoring of the binding affinities of programmed cell death proteins 1 and 2 (PD-1 and PD-2) was described.[464] Another interesting application consists of the multiplexed monitoring of food allergens.[465] The clinically important peanut allergens Ara h 1 and Ara h 2 and wheat allergen gliadin were simultaneously analyzed, with LODs of 7.0, 0.2, and 1.5 ng/mL, respectively. Yet another application of GMR sensors was focused on the detection of representative biomarkers for radiation exposure and cancer, including the phosphorylated structural maintenance of chromosome 1 (phosphor-SMC1), granulocyte colony stimulation factor (GCSF), and interleukin-6.[466]

TMR sensors take advantage from replacing the spacer layer with a thin insulator; NPs are entrapped magnetically.[467] The TMR sensor with an electromagnetic trap of *E. coli* bound to IMPs was constructed as a miniature device (Figure 32).[468] Even though the LOD was not sufficiently low (6.6×10^6 cfu/mL), the concept seems to be promising.

4.6.3. Superconducting Quantum Interference Device.
A superconducting quantum interference device (SQUID) is the most sensitive tool for monitoring a magnetic field at low frequencies. In its simplest form, it consists of a superconducting loop broken by one or two weak links called Josephson junctions. Two main types of SQUID sensors are utilized: the direct current (DC-SQUID) variant, which uses two Josephson junctions, and the radio frequency (RF-SQUID) embodiment, where only one junction is employed. RF-SQUIDs are cheaper but also less sensitive.[469] If the current is below the critical value, these
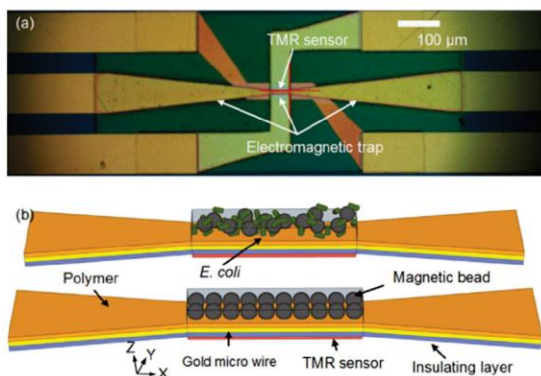
95

Figure 32. (a) Optical image of a microfabricated tunnel magneto-resistive sensor supplemented by an electromagnetic trap. (b) Schematic representation of the detection method. Reprinted with permission from ref 468. Copyright 2014 Elsevier.

junctions allow it to pass with zero voltage; otherwise, the voltage appears across the junction. In the case of RF-SQUIDs, other components such as a radio frequency coil and a large antenna loop are incorporated. The working principle is based on the interaction of a magnetic field (affected by the analyte labeled with MPs) and an electric current. A SQUID sensor utilizing magnetic NPs as a label was constructed and tested on the streptavidin/biotin system.[470] The sensor was capable of distinguishing between captured and free magnetic markers. A highly interesting aspect rests in the low detection limit for biotin, achieving a concentration of 9.5×10^{-16} mol/L. An original comparison of three different magnetic methods was presented by a team of Japanese researchers;[471] the paper focused on SQUID, an MR sensor, and a fluxgate sensor. In addition to this problem, the authors discussed using magnetic markers with a large magnetic moment to attain a higher signal.

4.6.4. Other Magnetic Sensors. The immunointeractions of MP-labeled molecules can be monitored via magnetic particle quantification (MPQ). The method uses the nonlinear magnetization of particles in a magnetic field at two ac frequencies; the particle responses are recorded. Orlov et al. detected the PSA in a human serum, with a detection limit as low as 25 pg/mL.[472] Grapevine fanleaf virus was captured on an immunofiltration column via specific monoclonal Ab's. The viruses were labeled with a second Ab conjugated to magnetic NPs, and the frequency generated by MPs in a magnetic field was recorded.[473] A planar microcoil array was exploited as a sensor of magnetic beads through the bottom of classic ELISA plates.[474] The immuno-sandwich of mouse IgG with magnetically labeled secondary Ab's was detected with a sensitivity comparable to that of optical detection with an LOD of 100 pg/mL.

An integrated platform to perform the manipulation with and detection of cells and biomolecules was described.[475] Electro-magnetic microcoils and capacitive biosensors on a CMOS chip were constructed, and the functionality was characterized on the model interaction between anti-streptavidin antibodies and streptavidin-coated magnetic microbeads. A microfluxgate sensor was developed and tested on AFP and the CEA model antigen.[476] An MEMS[477] microfluxgate sensor was described by Sun et al.[478] Primary anti-PSA antibodies were immobilized on a small glass plate with a gold film via an SAM and EDC/NHS chemistry. Dynabeads with the anti-PSA were mixed with

samples containing various amounts of the PSA, and the mixture was incubated. In the following step, the immunocomplex on the Dynabeads was magnetically separated, and a small volume was dropped onto the immunochip. After incubation, the chip was washed with PBS, and changes in the magnetic field were measured (Figure 33). The magnetic change correlated with the concentration of the PSA in the sample, and the LOD corresponded to 0.1 ng/mL.
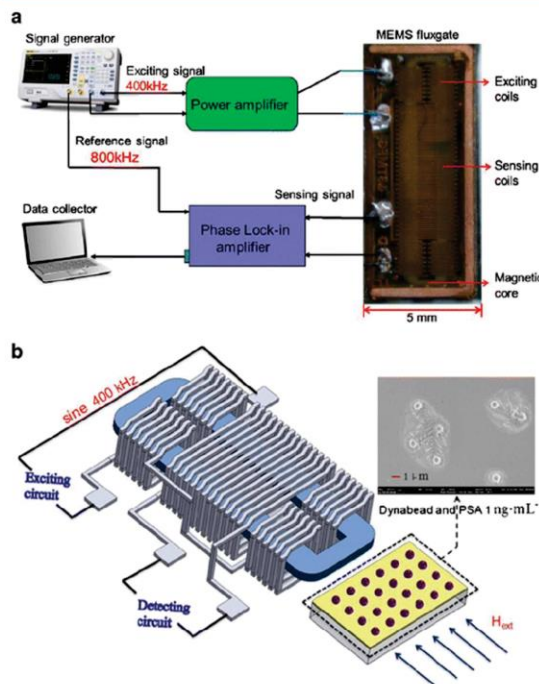
Figure 33. (a) Block diagram of the microfluxgate-based biosensing system. (b) Detection discipline of the microfluxgate-based biosensing system. Reprinted with permission from ref 478. Copyright 2016 Springer.

The Dynabeads magnetic particles were used to label the antigen, and the changes in the magnetic fields generated by two excitation coils and affected by the presence of an amount of Dynabeads were detected by the sensing coil at a minimum detectable concentration of 1 pg/mL. Planar-frequency mixing magnetic detection (p-FMMD) as a technique based on nonlinear magnetization was presented by Kim et al.[479] The immunocomplexes with superparamagnetic iron oxide (SPIO) nanoparticles were measured conveniently in planar microfluidic channels. The Alzheimer's disease biomarker amyloid β 42 was detected at a minimal concentration of 23.8 pg/mL.

4.7. Piezoelectric Systems

In 1959, the relationship between quartz resonant frequency and the mass accumulated on the sensor surface was established by Sauerbrey, leading to the development of a commonly used microgravimetric biosensing technique—quartz crystal micro-balance (QCM). Shortly explained, QCM is a mass-sensitive instrument detecting binding events by measuring the frequency change of the quartz resonator. The corresponding mass can be easily deduced from the Sauerbrey equation:[480]

96

$$\Delta f = \frac{-2\Delta m f_0^2}{A\sqrt{\mu_q \rho_q}} = -C_f \Delta m$$

where Δf is a change in the resonant frequency of the crystal (Hz), Δm denotes a mass change, f_0 represents the intrinsic crystal frequency (MHz), A is the piezoelectrically active area (cm^2), ρ_q is the density of a quartz (g/cm^3), μ_q denotes the shear modulus of a quartz (Pa), and C_f is the constant of a crystal. The significance of QCM rests in the possibility of rapid and real-time monitoring of surface modifications, adsorption/desorption effects, and biomolecule interactions, e.g., antigen−antibody recognition and DNA hybridization. The QCM apparatus often suffers from the influence of the surrounding noise and may lack sensitivity, especially in the case of low molecular weight analytes. Thus, recent approaches propose the application of novel NPs, nanomaterials, and nanocomposites.[481,482] For instance, highly biocompatible Au NPs providing a high surface-to-volume ratio were used by Chu et al. to improve the sensor performance.[483] The surface coverage by Au NPs increased the number of the binding sites for Ab's and, subsequently, the mass of the target analyte. Another way to enhance the signal intensity consists of the secondary Ab-functionalized Au NPs bound to the antigen in a sandwich format.[484] This additional binding step further extends the mass on the surface, resulting in a broader shift of the frequency.[485,486]

One might assume that the larger the secondary ligand assembled, the higher the signal observed. This, however, is not always correct, as the Sauerbrey frequency decrease takes into account only thin films rigidly attached to the surface.[487] An interesting option to overcome this limitation was proposed by Liu et al.;[488] a complex of 150 nm magnetic particles, detection antibody, and enzyme catalase was used to amplify the signal. Once this complex was attached to the antigen on the QCM surface, hydrogen peroxide was introduced into the system, initiating the biocatalyzed conversion to water and oxygen. The generated oxygen influenced the shear modulus of the immunocomplex layer, with the viscosity and density of the adjacent liquid layer resulting in a significant frequency increase.

The frequently applied mechanism of the biocatalyzed precipitation of an insoluble product on the surface appeared to be beneficial for increased signal generation also in the case of QCM.[489] Akter et al. exploited the dual merit of magnetic NPs, i.e., the surface enlargement for antibody/enzyme capturing and the possibility of easy sample purification, and developed a sensitive QCM sensor based on the bienzymatic (GOD/HRP) conversion of the initial substrate—glucose—to a solid product, resulting in extended rigidity of the layer and a concomitant frequency change.[490] This approach, however, significantly lowers the detection limit, and regeneration is practically impossible, making the sensor disposable. A solution to this problem arises from a paper by Zhou et al.,[491] who omitted the covalent immobilization of the primary antibody and attracted the MNP−Ab$_1$/antigen/Ab$_2$−HRP immunocomplex to the QCM surface by an external magnet. The surface covered by the precipitate can be regenerated chemically or electrochemically.[492] The data obtained from the microgravimetric measurements can be promptly verified by employing electrochemical quartz crystal microbalance (EQCM). The assay is ordinarily performed in an electrochemical cell composed of a gold-coated quartz crystal as a working electrode, a reference electrode, an auxiliary electrode, and a certain electrolyte solution.[493] For instance, the accumulation of the secondary ligand, e.g., Au NPs,

results in a frequency decrease; however, a current increase will be observed during the voltammetric scan because of the wiring effect of the conducting nanoparticles.

In the domain of immunosensors, QCM apparently constitutes an obsolete technique, but the incorporation of various nanoparticles and nanomaterials nevertheless makes it a promising instrument for future applications dealing with the fast, sensitive, and real-time detection of many toxins,[494] proteins,[495−497] and bacteria.[498,499]

Typically, different types of nanoparticles are best compatible with selected types of transducers. In the field of biosensors, electrochemical transduction is most popular, as the good performance can be achieved with rather simple and miniature devices. Measuring techniques are the simplest amperometry and differential pulsed voltammetry when the highest sensitivity is required. Potentiometric measurements are rare because of complications with a reliable reference, and the complex sample matrixes also limit a wider use of field-effect transistors. The carbon- and metal-based NPs help to improve the transport of electrons from traditional enzyme-based labels, though combinations of two (or even more) nanomaterials are common. The wide variety of "nano"-modified screen-printed electrodes are already easily obtained from several suppliers. Many authors favor the impedimetric techniques, which provide the direct measurement without the need for any labeling. The EIS measurements might appear quite simple and straightforward, but in real samples, complications with nonspecifically adsorbed biomolecules create significant complications and irreproducible results.

Optical techniques have gained interest because of the excellent photochemical stability and brightness of the luminescent nanocrystal and even the use of some hybrid NPs as labels. On the other hand, the high expectations related to quantum dots are fulfilled only gradually; reliable bioconjugation procedures for often hydrophobic QDs were not readily available, and the simplified adsorption of biomolecules was not robust enough. Currently, the interest in up-converting NPs as labels is growing. It was rather surprising that optoelectrochemical combined techniques such as electrochemiluminescence and photoelectrochemical conversion are represented by a high number of contributions; evidently, this is the field where optically active NPs have brought significant benefits. For direct assays with real-time data collection, surface plasmon resonance traditionally serves in immunosensing; noble-metal NPs help to moderately increase the measured signals. Due to the very high costs of instruments and limited portability, classic SPR functions in biochemical research laboratories and allows more precise screening of drug candidates in pharma industries. Much more interest is focused on localized SPR variants, which allow simple evaluation based on a change of color.

Rapid development of Raman spectroscopy and especially the surface-enhanced variants with nanomaterials and nanoparticles was also successfully combined with the specific antibodies, and applications are rapidly growing. Here, the imaging variants are suitable for living cells and are tested also for specific visualization of malignant tissues during surgery.

Magnetic transducers are highly variable and often complex; the bioanalytical applications exist rather rarely. The main field here will be the magnetic resonance imaging with the help of specifically binding magnetic NPs. Finally, piezoelectric transduction, despite the very long tradition, will most probably remain a rather exotic laboratory approach; nanoparticles might shift the sensitivity, but the improvement will be only limited.

Table 1. Selected Examples of Immunoassays for Clinical Markers Based on Nanoparticles

marker sample matrix	LOD	range	time (min)	surface	label(s)	procedure	year and ref
α-Fetal Protein (AFP)							
serum	0.8 pg/mL	0.001–200 ng/mL	250	mpt–Ab$_1$	PbS NP/Ab$_2$; Ag NP/DNA	RCA, DPV FIG–RCA	2013[527]
PBS (model)	0.01 pg/mL	0.1–50 pg/mL	150	GCE/Ab$_1$	CdZnSe QD/Ab$_2$	sw, ECL	2016[528]
serum	0.33 fg/mL	1 fg/mL to 80 ng/mL	180	GCE/grox/chit–fuller-ene/Ab$_1$	C–QD/PAAD/Ab$_2$	sw, ECL	2016[213]
Amyloid A							
serum	43 ng/mL	9.4–600 ng/mL	45	GCE/PPy-COOH/chit/MWCNT/Ab$_1$	– (direct)	blocked DPV	2015[529]
Amyloid-β							
serum	1 pg/mL	1–10000 pg/mL	120	Au/Al$_2$O$_3$ array/Au NP/Ab$_1$	– (direct)	EIS	2014[530]
serum	50 fg/mL	0.08 to 10^5 pg/mL	90	GCE/Ag NW/Cys/Ab$_1$	ZnO/CeO$_2$ NP/luminol/GOD/Ab$_2$	sw, ECL	2016[222]
Apolipoprotein-A1							
serum	0.02 pg/mL	0.0001–50 ng/mL	130	SPE–C/Au NP/Ab$_1$	Ag NP/hydroxyapatite/Ab$_2$	sw, stripping SWV	2015[531]
Apolipoprotein-A2							
urine	6.7 pg/mL	20 pg/mL to 2 mg/mL	12	polycrystalline Si NW/graphene/Ab$_1$	– (direct)	FET	2015[532]
Apoptosis Regulators Bcl-2 and BAX							
cell lysate	1 ng/mL	1–300 ng/mL	340	GCE/rGO/Ab$_{1a}$,Ab$_{1b}$	SiO$_2$/CdSeTe NP/PDDA/Ab$_2$a; SiO$_2$/Ag NC/PEI/Ab$_2$b	dual sw, stripping SWV	2016[533]
Butyrylcholinesterase, Phosphorylated							
plasma	0.01 nM	0.02–10 nM	80	SPE–C; Fe$_3$O$_4$/TiO$_2$ NP/Ab$_1$	CdS QD/Ab$_2$	sw, mag sep, DPV	2013[534]
Calmodulin							
tumor cells	18 pg/mL	0.05–200 ng/mL	240	GCE/chit–thionine/graphene/Au Ag NP/Ab$_1$	Au NR/HRP/Ab$_2$	sw, DPV	2014[535]
Cancer Antigen CA-125							
serum	1.6 mU/mL	2–100 mU/mL	65	Au/Au NP/SiO$_2$CdS QD/Ab$_1$	– (direct)	blocked EIS	2015[536]
Carbohydrate Antigen 19-9							
PBS (model)	0.04 U/mL	0.01–200 U/mL	130	ITO/TiO$_2$ NWs/Au NP/CdSe–ZnS/Ab$_1$	(bipyridinium^{2+})–Ab$_2$	sw, blocked PEC	2016[537]
serum, urine	0.5 mU/mL	0.001–5 U/mL	60	GCE/grox/Au NP/ABEI/Ab$_1$	– (direct)	blocked ECL	2015[538]
Carbohydrate Antigen 15-3							
serum	14 mU/mL	0.05–120 U/mL	105	GCE/PEI–MWCNT/Au NP/Ab$_1$	Mn–ZnO NR/Lys/Ru(bpy-di-COOH)$_3^{2+}$/Pt NP/Ab$_2$	sw, ECL	2015[539]
Carcinoembryonic Antigen (CEA)							
serum	0.1 pg/mL	1 pg/mL to 50 ng/mL	35	Fe$_3$O$_4$/Au NP/Ab$_1$	PANI NF/HRP/Ab$_2$	sw, mag sep, DPV in flow	2012[540]
serum	0.36 fg/mL	0.005–10 ng/mL	65	ITO/Au NP/Ab$_1$	graphene–SnO$_2$ NP/PDDA/Ab$_2$	sw, PEC	2013[237]
serum	0.1 pg/mL	0.0001–10 ng/mL	150	microplate–mAb$_1$	NaEuF$_4$ NP/av/Ab$_2$	Eu^{3+} dissolution, time-resolved PL	2014[541]
serum	0.86 fg/mL	1 fg/mL to 10 ng/mL	80	Au NR/SiO$_2$/ rhodamine-6G/Ab$_2$	– (direct)	SERS	2014[542]
serum	1 pg/mL	0.05–80 ng/mL	?	ITO–Au/Au NP/Ab$_1$		blocked EIS and UV spectra	2015[543]
serum	0.1 pg/mL	1.0 pg/mL to 500 ng/mL	45	Au/PANI–ferricyanide/Au NP/Ab$_1$	– (direct)	blocked DPV	2015[544]
serum	3.2 fg/mL	0.01 to 10$_5$ pg/mL	150	GCE/ZnO NP/Ab$_1$	Au,Pd NP/Ab$_2$	sw, catalytic, amp	2015[545]
serum	0.16 fg/mL	1 fg/mL to 200 ng/mL	45	GCE/PPy–phytic acid/Au NP/Ab$_1$	– (direct)	blocked DPV	2015[546]
serum	0.1 fg/mL	1.0–1000 fg/mL	150	GCE/PABA/Ab$_1$	CdSe QD/Ab$_2$	sw, ECL	2016[209]
serum	0.65 pg/mL	0.001–80 ng/mL	75	GCE/Au NP/Ab$_1$	GO/HRP/Ab$_2$	sw, precipitation, EIS	2016[547]
serum	0.16 pg/mL	0.0005–100 ng/mL	140	microplate/Ab$_1$	Cu NP/Ab$_2$	sw, Cu-click conjugation, F	2016[199]
serum	0.2 pg/mL	0.001–80 ng/mL	>45	GCE/GO/Au NP/Ab$_1$	Fe$_3$O$_4$ NP/silicate/ferrocene/HRP/Ab$_2$	sw, DPV	2016[548]

Table 1. continued

marker sample matrix	LOD	range	time (min)	surface	label(s)	procedure	year and ref
Cortisol							
saliva	1 pM	1 pM to 100 nM	35	Si/Au/ZnO NR/Ab$_1$	– (direct)	CV	2015[549]
C-Reaction Protein (CRP)							
plasma	3.9 ng/mL	0.025–1.6 ng/mL	20	nitrocellulose/mAb$_1$	CdZnSe QD/mAb$_2$	sw, LFIA, F	2016[195]
C-Terminal Telopeptide							
serum	50 pg/mL	50–600 pg/mL	90	CNT (aligned)–epoxy/Au NP/Ab$_1$	– (direct)	EIS	2016[550]
Cystatin C							
serum	0.14 pM	0.72 pM to 3.6 nM	45	Ti/TiO$_2$ NT/rAb	– (direct)	blocked PEC	2016[551]
Cytokeratins Antigen 21-1							
serum	2.3 pg/mL	0.01–200 ng/mL	45	GCE/rGO/polyhydroquinone/Au NP/Ab$_1$	– (direct)	blocked DPV	2016[552]
Epidermal Growth Factor Receptor							
serum	2 fg/mL	1–14 fg/mL	?	SPE–C/SWCNT/Ab$_1$	– (direct)	EIS	2014[553]
Enolase, Neuron-Specific							
serum	5 pg/mL	0.01–120 ng/mL	45	GCE/graphene–C nanospheres/poly(thionine)/Ab$_1$	Pt NP/HRP/Ab$_2$	sw, DPV	2013[554]
serum	0.2 pg/mL	0.001–100 ng/mL	35	ITO/ZnCdHgSe QD/pAb$_1$	– (direct)	blocked PEC	2015[555]
Epidermal Growth Factor Receptor 2							
serum	10 fg/mL	0.01–100 pg/mL	40	Au/Ab$_1$	Au,Ag NP/SiO$_2$/malachite green/Ab$_2$	sw, SERS	2015[556]
cell homogenate	0.05 pg/mL	0.1–1000 pg/mL		SPE–Pt/poly(thiophene)/Ab$_1$	Fe$_3$O$_4$/chit/Au NP/Ab$_2$	sw, mag sep, DPV	2015[557]
Epithelial Cell Adhesion Molecule							
blood cells extract	1.2 pg/mL	2.5–2000 pg/mL	40	glass/ZnO NP/PVA/Ab$_1$	Ab$_2$–HRP	sw, fluidics, F	2016[558]
Erythropoietin							
serum	0.0027 mIU/mL	0.01–80 mIU/mL	135	GCE/AuNP/Ab$_1$	fullerene–PAMAM NP/Au NP/Ab$_2$	sw, DPV	2015[559]
Ethinylestradiol							
urine	65 pg/mL	0.1–50 ng/mL	65	GCE/GO/Ag NP/SiO$_2$/Ab$_1$	HRP– ethinylestradiol	comp, amp	2016[560]
Ferritin							
serum	50 pg/mL	0.05–500 ng/mL	5	polycrystalline Si NW/Ab$_1$	– (direct)	FET	2016[561]
Hemoglobin, Glycated (HbA1c)							
blood	2.5%	5.6–11.5%	12	– (in solution)	(NaYF$_4$:Yb^{3+}, Er^{3+}) NP/silicate/Ab$_1$	UCNP PL quenched by hemoglobin	2016[204]
Human Chorionic Gonadotrophin							
serum	0.0026 mIU/mL	0.005–500 mIU/mL	150	graphene/CNT/Au NP/Ab$_1$	silica NP/Au NPs/thionine/HRP/Ab$_2$	sw, DPV	2012[562]
serum	8.6 pg/mL	0.01–16 ng/mL	65	GCE/sulfographene/thionin/Pd–SiO$_2$ NP/Ab$_1$	– (direct)	DPV	2013[563]
urine	0.016 ng/mL	0.1–25 ng/mL	20	SPE–C/graphene/chi/Au NP/Ab$_1$	– (direct)	blocked EIS	2014[564]
Insulin							
serum	0.086 nM	1–10000 ng/mL	30	ITO/rGO/Ab$_1$	– (direct)	capacitance	2015[565]
serum	15 pM	1–100 pM	25	PGE/MWCNT–pyrenebutyric acid	Fe3O4 NP/insulin	comp, DPV	2015[566]
Interferon γ							
blood cells supernatant	30 fg/mL	0.1–500 pg/mL	170	grox/PANI NF/mAb$_1$	CdS QD/pAb$_2$	sw, ECL	2016[212]
blood, serum, saliva	400 fg/mL	1 pg/mL to 10 μg/mL	60	PS/PLL/Au NP/Ab$_1$	– (direct)	LSPR	2016[567]
Interleukin-6							
serum	0.01 fg/mL	0.01–100 fg/mL	45	Si/SiO$_2$/SWCNT/Au NP/mAb$_1$	– (direct)	EIS	2013[568]
serum	0.3 pg/mL	1–40 pg/mL	150	ITO/graphene–Au NP–silicate/Ab$_1$	Au NP/MWCNT/PDOPA/HRP/Ab$_2$	sw, amp	2014[569]

99

Table 1. continued

marker sample matrix	LOD	range	time (min)	surface	label(s)	procedure	year and ref
Interleukin-17							
serum	50 fg/mL	0.1−1000 pg/mL	125	GCE/graphene/Ab$_1$	PS−Cd/Au NP/Ab$_2$	sw, DPV of re-leased Cd^{2+}	2013[570]
Matrix Metalloproteinase-2							
serum	3.6 fg/mL	0.01−500 pg/mL	140	TiO$_2$ NT/CdS,Mn,CdTe QD/Ab$_1$	SiO$_2$ NP/Ab$_2$	sw, blocked PEC	2014[232]
Monocyte Chemotactic Protein-1							
serum	0.03 pg/mL	0.09−360 pg/mL	65	Au NP/Au,Pt NW/	− (direct)	blocked DPV	2015[571]
Mucin							
cell culture	0.5 nM	1−500 nM	125	GCE/graphene/Ab$_1$	Ag NP/aptamer; Ag deposition	sw, SWV	2015[572]
Natriuretic Peptide							
PBS (model)	0.33 fg/mL	0.001−2 pg/mL	55	GCE/PAMAM/Ab$_1$	chit−ferrocene NP/Ab$_2$	sw, blocked ECL	2014[221]
serum	0.75 fg/mL	1 fg/mL to 1 ng/mL	110	CoFe$_2$O$_4$/Au NP/Ab$_1$	metal−organic frame/Au tetrapods/toluidine blue/Ab$_2$	sw, SERS	2016[573]
Netrin-1							
serum	30 fg/mL	0.09−1800 pg/mL	50	GCE/MWCNT/chit/thi-onin/Au NP/pAb$_1$	− (direct)	blocked DPV	2015[574]
Osteopontin							
serum	0.3 pg/mL	1 pg/mL to 1 μg/mL	65	Au/ITO gap with SWCNT-COOH/Ab$_1$	− (direct)	blocked EIS	2015[575]
Procalcitonin							
serum	0.4 pg/mL	0.02−500 ng/mL	120	GCE/Au NP/Ab$_1$	PAMAM−Au NP/β-cyclodextrin−ferrocene/Ab$_2$	catalytic, DPV	2015[576]
serum	1.2 pg/mL	0.01−100 ng/mL	∼60	GCE/Au NP/Ab$_1$	MWCNT/CoPC NP/choline oxi-dase/Ab$_2$	sw, DPV	2016[577]
Prostate-Specific Antigen (PSA)							
serum	0.4 pg/mL	1−10000 pg/mL	125	Au/MWCNT/Au NP/Ab$_1$	MWCNT/HRP/Ab$_2$	sw, precipitation, SWV	2012[578]
serum	10^{-18} g/mL	− (qualitative)	300	mtp/Ab$_1$	catalase−Ab$_2$	generation of Au NP, color, visual	2012[579]
serum	0.3 ng/mL	0.3−100 ng/mL	12	Au/Ab$_1$	Au NP/Ab$_2$	sw, SPR	2012[580]
serum	0.3 fg/mL	10 fg/mL to 10 ng/mL	12	Au NW/polypyrrole/Ab$_1$	− (direct)	blocked DPV	2014[581]
serum, saliva	0.04 fg/mL	0.04−10 fg/mL	85	Au/Au NP/Ab$_1$	SiO$_2$−Au nanosphere/ABEI/Ab$_2$	sw, ECL	2014[582]
serum	0.32 pg/mL	0.001−3 ng/mL	140	microplate/Ab$_1$; Ti/TiO$_2$ NT/CdS QD	Au NP/ssDNA primer/Ab2; av-ALP	ligase RCA, PEC	2015[583]
serum	0.05 pg/mL	0.1−1000 pg/mL	50	PGE/SWCNT/Ab1	SiO$_2$ NP/Ru(bpy)$_3^{2+}$/Ab$_2$	sw, ECL (CCD multiplex)	2015[584]
Protein p53							
PBS (model)	1 pg/mL	1−1000 pg/mL	105	GCE/MWCNT−polya-mide/polythionine/Ab$_1$	HRP−Ab$_2$	sw, DPV	2015[585]
PBS (model)	50 pg/mL	0.05−100 ng/mL	?	Ti/TiO$_2$ NT/Au NP/ALP/Ab$_1$	− (blocked ALP)	LSPR-enhanced PEC	2016[586]
Selectin-P							
	0.85 pg/mL	1 pg/mL to 10 μg/mL	90	SPE−C/MWCNT/Au NP/Ab$_1$	lipo(ferricyanide)/Ab$_2$	sw, DPV	2012[587]
Thrombin							
serum	1 aM	1 aM to 200 nM	60	Au/Ab$_1$	Au NP (diff. shapes)/aptamers	sw, SPR	2016[588]
Thyroid-Stimulating Hormone							
serum	0.005 μIU/mL	0.01−20 μIU/mL		Au/Au NP/Ab$_1$	Au−PANI NP/HRP/Ab$_2$	sw, DPV	2012[589]
serum	100 zM	100 zM to 100 fM	>180	Au dots/Ab$_1$	Ag NP/Ab$_2$	sw, dark field light scattering	2016[590]
Thyroxin (T4)							
PBS (model)	15 fg/mL	0.05−5000 pg/mL	230	GCE/MWCNT/Nafion/Ab$_1$	Fe$_3$O$_4$/graphene/Au NP/PDDA/ssDNAAb$_2$; ssDNA/cytochrome c/GOD	sw, mag. sep, hy-bridization, DPV	2013[591]
Tissue Polypeptide Antigen							
serum	5 pg/mL	0.01−30 ng/mL	36	GCE/Ab$_1$	Au−PB NP/HRP/Ab$_2$	sw, catalytic, DPV	2014[592]
serum	0.3 pg/mL	0.001−100 ng/mL	90	GCE/Ab$_1$	Au−PB NP/polytyramine/HRP/Ab$_2$	sw, catalytic, DPV	2015[593]
3,3′,5-Triiodothyronine (T3)							
PBS (model)	30 fg/mL	0.1−10000 pg/mL	85	GCE/PLL/Au NP/Ab$_1$	Fe$_3$O$_4$/GO/Ru(bpy)$_3^{2+}$/Ab$_2$	sw, enhanced ECL	2013[594]
Troponin I, Cardiac (cTnI)							
serum	0.08 pg/mL	0.25−100 pg/mL	60	GCE/Au NP/Ab$_1$	Au NR/Ru(dcbpy)$_3^{2+}$/Cys/Ab$_2$	sw, enhanced ECL	2014[226]
plasma	3.1 pg/mL	0.01−50 pg/mL	45	microplate/mAb$_1$	NaYF$_4$:Yb^{3+}, Er^{3+} NP/PAA/mAb$_2$	sw, UCNP PL	2016[595]
serum	0.19 pg/mL	0.001−1000 ng/mL	∼15	graphene QD/Ab1	graphene (as FRET quencher)	homogen., re-stored PL	2016[200]

100

Table 1. continued

marker sample matrix	LOD	range	time (min)	surface	label(s)	procedure	year and ref
Trypsin							
serum	1.2 pg/mL	20−20000 pg/mL	?	GCE/polythionine/AuNP/Ab$_1$	− (direct)	blocked DPV	2015[596]
Tumor Necrosis Factor α							
serum	2 pg/mL	5−5000 pg/mL	125	GCE/MWCNT/Au NP/Ab$_1$	chit−PB−CeO$_2$ NP/Ab$_2$	sw, catalytic, amp	2012[597]
serum	2 pg/mL	5 pg/mL to 10 ng/mL	125	GCE/peptide, ferrocene NW/Au NP/Ab$_1$	Au NR/GOD/Ab$_2$	sw, DPV	2013[598]
Vascular Endothelial Growth Factor							
plasma	7 fg/mL	0.1 pg/mL to 10 ng/mL	30	Au triangular nanospots/Ab$_1$	Au NP/Ab$_2$	sw, SERS	2016[599]

5. APPLICATIONS

This part of the review starts with clinical assays, namely, procedures for the determination of markers such as proteins, small molecules, tumor cells, and drugs.

5.1. Clinical Assays

5.1.1. Proteins and Small Molecules as Markers. In medicine, biomarkers indicate the severity or presence of some disease or particular physiological state of the organism (https://fnih.org/what-we-do/biomarkers-consortium). Substances chosen as clinical markers are currently analyzed in specialized central laboratories using large and fully automated analyzers, or "black boxes", where users introduce the samples and supply immunoreagents in the form of disposable kits. Inside, immunoassays and immunosensors function as independent modules. The system is well-established, fully sufficient for the clinically relevant levels of analytes, and rather conservative with respect to novel technologies. For less common biomarkers, the classic ELISA kits are supplied.

Thus, the community of researchers in the field should be initially addressed because the scope of the assays is larger than the options existing in analyzers or as ELISA kits, and new markers are being introduced within the current preventive medicine trends. The convenient overview of blood tests is available online (https://en.wikipedia.org/wiki/Reference_ranges_for_blood_tests); a much more comprehensive database is maintained by the American Association for Clinical Chemistry (https://labtestsonline.org).

Immunosensors with NPs should be considered for special situations, especially when new markers not yet used within analyzer procedures need to be measured. The most promising application situations will occur when either a rapid analysis at critical moments or a measurement cycle to be performed directly in an ambulance (or generally out of laboratory) becomes a priority. For this purpose, the point-of-care immunosensor format is the most appropriate. The performance is simple, and POC devices are typically portable and suitable for nontrained users. The results are obtained in sufficiently short time to make decisions immediately improving the patient's state. The POC immunosensors will play a key role also in personalized medicine.

Selected applications of immunosensors with nanoparticles are summarized in Table 1. The examples provided include protein markers indicating the health condition; insulin and also glycated hemoglobin as indicators of long-term treatment in diabetic patients are prominently mentioned in the given context.

Endocrinological markers include thyroid hormones such as the thyroid-stimulating hormone, trijodothyronine, and thyroxin, which require highly sensitive assays ensured via

immunosensors. The Clearblue pregnancy test based on human chorionic gonadotropin constitutes one of the first commercially available personal electrochemical immunosensor tests. Other sex hormones are represented by cortisol and ethinylestradiol.

Urgent cardiac states are evaluated using troponin I. CRP is the most important acute phase protein. Neuronal disorders, including Alzheimer's disease, are studied by means of amyloid fragments. Numerous systems are centered on cancer markers such as fetoprotein, cancer and carbohydrate antigens, protein p53, and the prostate-specific and (perhaps the most frequently assayed) carcinoembryonic antigens. From the technological point of view, the CEA molecule might serve well for the critical comparison of tens of different sensing approaches. Recent concern has focused on regulatory factors such as interferon, interleukins, growth factor receptors, and apoptosis.

5.1.2. Cancer Cells. Cancer constitutes a most serious cause of death. Despite the fact that cancer cells emerge from the body's own cells, it is very difficult to analyze cancerous growth at an early stage. Fortunately, there are many genes overexpressed in a cancerous tissue that offer a potential for analytical and therapeutic exploitation.[500] Tumor markers are widely used in oncology and play an indispensable role in cancer detection and clinical screening.[501,502] Any effort to detect cancer as early as possible places increasing demands on the detection methods and analytical protocols; this is then reflected also in the field of biosensors.[503] Another situation arises when the cancer is fully manifested and metastases may occur. Metastatic tumors are formed through the spread of cancer cells from the original tumor. From this perspective, circulating tumor cells (CTCs) have assumed a key role in the process, and their early diagnosis brings an opportunity to conduct effective treatment.

CTCs are dissipated populations of tumor cells in the bloodstream, characterized by their very rare occurrence, plasticity, and heterogeneity. The detection of CTCs is a fundamental prerequisite for the detailed understanding of particulars such as the characteristics of CTCs and their prognosis, predictive significance, and, above all, use in both clinical practice and the development of new drugs. The separation and detection of CTC cells is based on detecting epithelial characters. Unfortunately, there are several limitations to current diagnostic methods; relevant deficiencies include, for example, the inability to detect cells with mesenchymal characteristics or the lack of morphological verification of CTCs, making their isolation and characterization a major technological challenge.

On the basis of the aforementioned properties of tumor cells, numerous platforms for CTC detection have been developed. Generally, one can refer to two major categories:[504] (1)

101

Table 2. Assays for Cells Related to Malignant Transformations

marker sample matrix	LOD	range	time (min)	surface	label(s)	procedure	year and ref
Basal Cell Carcinoma							
skin tissue sections	—	—	5	skin tissue	Au NPs/4-ATP/Ber–EP4	SERS detection of cells via interaction of label with EpCAM	2016[600]
Chondroitin Sulfate Proteoglycan 4 (CSPG4), Alias High Molecular Weight Melanoma-Associated Antigen (HMW-MAA)							
cell lysate of M14 human melanoma line (model)	—	yes/no detection system	~120	PANI@GO film on ITO	label-free	EIS	2016[601]
HepG$_2$ Cells							
HepG$_2$ cells (model)	5 cells/mL	10 to 10^5 cells/mL	60	ITO/CNT/anti/EpCAM	label-free	EIS	2014[602]
Human Breast Cancer (MCF-7) Cells and Adriamycin-Resistant MCF-7 (MCF-7/ADR) Cells							
MCF-7 and MCF-7/ADR (model)	170 cells/mL	5×10^2 to 1.6×10^6 cells/mL	>180	(Bcl-2)—BSA/PLL/GCE	Au NP/Ab	EIS detection of cells with expressed Bcl-2 protein	2015[603]
Human Cervical Carcinoma (HeLa) Cells							
HeLa cell line (model)	10 cells/mL	10 to 10^6 cells/mL	>30	Au/MPA/PEI–Fc/SWCNT/FA	label-free	DPV detection of cells with expressed folate receptor	2013[604]
	6 cells/mL	6 to 10^3 and 10^3 to 10^5 cells/mL	NA	Au/1,6-dimercaptohexane/Au NPs/MUA/FA	label-free	EIS detection of cells with expressed folate receptor	2012[605]
Human Epithelial Carcinoma (A431) Cells							
detection of EGFR in cell lysate (model)	~100 pg in a sample volume of ~10 nL	NA	150	optical fiber/PLL	Au NPs/MGITC/anti-EGFR	combination of SERS with hollow core photonic crystal fiber (HCPCF)	2012[606]
Human Ovarian Cancer (SKOV-3) Cells							
SKOV-3 cell line (model)	5.2 cells/mL	6.5–65000 cells/mL	NA	GCE/GO/anti-HER2	ssDNA-labeled anti-HER2 antibody and hybridization with cDNA	DPV detection of daunorubicin after intercalation	2012[607]

102

Table 3. Assays for Drugs and Other Pharmaceuticals

pharmaceutical sample matrix	LOD	range	time (min)	surface	label(s)	procedure	year and ref
Chloramphenicol							
w (environmental; river)	1 pg/mL	1 pg/mL to 10 ng/mL	120	MNP/Ab$_1$	Au NP/SERS reporter/Ab$_2$	mag sep, sw SERS	2016[608]
eye drops	4.6 pg/mL	50 pg/mL to 50 μg/mL	45	GCE/MWCNTs/chloramphenicol—BSA	Ab—adamantine, AuPd NP/cyclodextrin	comp LSV	2013[609]
Clenbuterol							
w (model)	6.57 pg/mL	0.01—10 ng/mL	NA	Au/graphene/Ab	— (direct)	SPR (and EIS)	2015[610]
urine	6.8 pg/mL	0.01—10 ng/mL	150	GCE/MWCNT/Ab$_1$	Ag—graphene oxide—clenbuterol	comp DPV	2012[611]
pork meat, liver	20 pg/mL	50 pg/mL to 1 μg/mL	240	GCE/QDs/clenbuterol—OVA	Ab$_1$, Ab$_2$—HRP	comp ECL	2013[612]
urine	0.35 ng/mL	1.22—6 ng/mL	24	glass/clenbuterol—BSA	Au NP/Ab	comp capillary immunochromatograpy	2016[613]
swine urine	5 pg/mL	0.01—1 ng/mL	90	GCE/Au NP/clenbuterol—BSA	Ab—Ru(bpy)	comp ECL	2012[614]
pork	1.38 pg/mL	0.01—100 ng/mL	60	SPCE/rGO/clenbuterol	AgPd NP/Ab	comp LSV	2013[615]
swine feed	0.25 ng/mL	0.5—1000 ng/mL	60	GCE/MWNCTs/Ab	graphene oxide/Au NP/GOD/clenbuterol	comp enzyme amplified DPV	2013[616]
pig urine	5.5 pg/mL	0.01—10 ng/mL	NA	Au/QD/PANI nanowire/Ab	— (direct)	EIS	2016[617]
Diclofenac							
w (environmental; river, lake, tap water)	50 pg/mL	50 pg/mL to 0.5 ng/mL	180	microplate/diclofenac—BSA	Ab$_1$,Ab$_2$—UCNP	comp luminescence	2016[618]
Doxorubicin							
human serum	1.7 pg/mL	2.5—100 pg/mL	60	stainless steel/Au NP/Ab	— (direct)	EIS	2013[619]
human serum, urine	90 fg/mL	2.5—50 pg/mL	60	Au/Au NP/Ab	— (direct)	EIS	2014[620]
Infliximab							
human serum	0.3 ng/mL	0.3—100 ng/mL	150	Au/Ab$_1$	Au NP/Ab$_2$	sw SPR	2016[621]
Kanamycin							
milk	2 pg/mL	2 pg/mL to 80 ng/mL	10	MNP/Ab$_1$	Au@Ag NP/SERS reporter/Ab$_2$	sw SERS	2014[622]
chicken liver	5.8 pg/mL	0.01—12 ng/mL	NA	GCE/graphene/nafion/thionine/Pt NP/Ab	— (direct)	CV	2012[623]
pork meat	15 pg/mL	0.05—16 ng/mL	NA	GCE/graphene—thionin/Ag@Fe$_3$O$_4$/Ab	— (direct)	LSV	2013[624]
Morphine							
urine	0.82 ng/mL	2—200 ng/mL	NA	ITO/Au NP/Ab	— (direct)	ECL	2015[625]
Ofloxacin							
w (model)	30 pg/mL	0.08—410 ng/mL	180	GCE/Au nanocluster/ofloxacin—OVA	Au NR/HRP/Ab$_2$	comp, enzymatic amplification, CV	2013[626]
w (model)	0.15 ng/mL	0.26—25.6 ng/mL	120	GCE/MWCNTs/ofloxacin	Ab$_1$, Ab$_2$—Au nanoflower	comp CV	2015[627]
Pefloxacin							
seafood	1 ng/mL	1—20 ng/mL	120	Au NR/Ab	magnetosome/pefloxacin—ova	comp LSPR	2013[628]
Ractopamine (Growth Promoter, Feed Additive)							
fodder	10 pg/mL	0.01—25 ng/mL	40	Au/MNP/cyclodextrin	Ab$_2$—poly-HRP	sw QCM, precipitation enhancement	2015[629]
pork	1.52 pg/mL	0.01—100 ng/mL	60	SPCE/rGO/ractopamine	AgPd NP/Ab	comp LSV	2013[517]
pig urine	7.5 pg/mL	0.1—10 ng/mL	NA	Au/Cu/Cu$_2$O nanocrystal/rGO/Ab	— (direct)	EIS	2015[630]
serum	2.5 pg/mL	0.01—10 ng/mL	20	GCE/magnetic chitosan/Au@Ag$_2$S NP/Ab	— (direct)	SWV	2015[631]
Salbutamol							
pig feed, pork liver	10 ng/mL	20 ng/mL to 0.8 μg/mL	30	ITO/Ag nanoprism/Ab	— (direct)	LSPR	2013[632]
animal feed, pork liver	50 ng/mL	50 ng/mL to 0.8 μg/mL	30	ITO/hollow Au NP/Ab	— (direct)	LSPR	2013[633]
porcine serum	4 fg/mL	0.1 pg/mL to 1 μg/mL	60	SPCE/Au NP/Au NS/Ab	— (direct)	EIS	2016[634]

103

Table 3. continued

pharmaceutical sample matrix	LOD	range	time (min)	surface	label(s)	procedure	year and ref
Salbutamol							
pork	1.44 pg/mL	0.01−100 ng/mL	60	SPCE/rGO/salbutamol	AgPd NP/Ab	comp LSV	2013[517]
serum	7 pg/mL	0.02−15 ng/mL	NA	GCE/graphene/Ab₁	mesoporous silica/Pd NP/Ab₂	sw amperometry	2012[635]

morphological methods based on the gradient density, size, and deformability of CTCs and (2) immunological methods based on the interaction between specific Ab's and expressed epithelial cell surface markers such as EpCAM (the epithelial cell adhesion molecule). Moreover, CellSearch (Janssen Diagnostics) as the only FDA-approved platform for CTC detection in clinical practice utilizes the magnetic preconcentration of CTCs using anti-EpCAM antibodies immobilized on magnetic particles. The fluorescent detection is provided for by the second anti-cytokeratin and anti-CD45 antibodies labeled with fluorescent dyes.[505]

A basic prerequisite for the application of CTCs in clinical practice is the unification of the preanalytical and analytical phases of detection and the ability to implement the current knowledge of liquid biopsy and immunochemical assays. The noninvasive detection of CTCs may ideally replace metastatic tissue biopsies. An open challenge currently lies within the newly emerging area of detecting CTCs for the industry of biosensors. Regrettably, biosensor-based detections of cancer cells are very rare, and they are usually described on the model cell lines. Table 2 provides a summary of representative studies where the nanoparticles are simultaneously utilized.

5.1.3. Pharmaceutical Detection. The development and extensive availability of sensitive analytical techniques enabled a rising amount of pharmaceuticals to be detected after medical or veterinary application. During medical procedures, the drug levels in biological fluids (i.e., urine and blood) often have to be monitored to ensure efficient and safe treatment. The pharmaceutical residues in the environment also have to be controlled due to possible side effects and within the monitoring of the increasing bacterial antibiotic resistance. In livestock production, veterinary drugs and anabolic steroids (endogenous or synthetic hormones) are employed to a considerable extent. Any inappropriate or unauthorized use of such compounds may leave residues in edible tissues, which might then be harmful for consumers. Overall, there are a wide array of matrixes in which the pharmaceuticals have to be analyzed, ranging from biological fluids through environmental samples to food products.

Chloramphenicol is a broad-spectrum antibiotic offering outstanding antibacterial and pharmacokinetic effects. However, its application is limited since it may cause aplastic anemia and other adverse reactions.[506] The use of chloramphenicol in food-producing animals is prohibited in the European Union (EU), and any residues found in a sample are considered a violation under EU legislation. Nevertheless, chloramphenicol residues have been detected in a wide variety of foodstuffs, such as prawn, honey, and milk-based products imported from non-EU countries.[507]

Diclofenac is an extensively used nonsteroidal anti-inflammatory drug. In the Indian subcontinent, the widespread use of diclofenac for the veterinary treatment of cattle since the 1990s has led to an abrupt decline in the vulture population because the substance can cause renal failure in vultures that feed on contaminated carcasses.[508] In Europe, diclofenac belongs to pharmaceuticals most frequently analyzed in relation to the water

cycle, mainly due to their poor degradability in wastewater treatment plants. Diclofenac has been detected in low microgram per liter amounts in wastewaters and also in nanogram per liter amounts in surface waters, groundwater, and drinking water.[190]

Doxorubicin constitutes an anthracycline antibiotic that has been extensively used for the chemotherapeutic treatment of a variety of cancers, such as lymphoblastic leukemia and sarcomas.[509] The detection of doxorubicin in biological and clinical samples is important, mainly because of its high cardiotoxicity effects.[510]

Kanamycin embodies an aminoglycoside antibiotic produced by the bacterium *Streptomyces kanamyceticus*; it finds application in the treatment of various bacterial infections by inducing mistranslation and indirectly inhibiting translocation in the course of protein synthesis. Analogously to other aminoglycosides, kanamycin is characterized by a narrow safety margin and can generate several side effects, e.g., the loss of hearing, damage to the kidneys, and allergic reactions to drugs.[511] In addition, residual amounts of kanamycin in the given foodstuff can cause antibiotic resistance of the pathogenic bacterial strains.[512]

Pefloxacin is an antibiotic drug within the group of fluoroquinolones. Due to its broad spectrum of activity against Gram-positive and Gram-negative bacteria, pefloxacin is used in the aquaculture industry to treat and prevent various infectious diseases. However, overusing the drug generates the risk of residues in seafood and contributes to bacterial resistance.[513]

Ofloxacin represents a new generation of fluorinated quinolones structurally related to nalidixic acid. It has been commonly used against most Gram-negative bacteria, many Gram-positive bacteria, and some anaerobes through the inhibition of their DNA gyrase. The drug exhibits rapid absorption and potent inhibition ability at a reasonable price.[514] Unlike most other wide-spectrum antibacterial pharmaceuticals, ofloxacin can be orally administered as well as intravenously transported into body tissues.[515] Additionally, ofloxacin is applied not only in human medicine but also in the treatment and prevention of veterinary diseases in food-producing animals, and even as a growth-promoting substance. The residues of ofloxacin in food products of animal origin are potentially dangerous via, e.g., toxic influence, an allergic hypersensitivity reaction, and the promotion of bacterial antibiotic resistance.[516]

Ractopamine, clenbuterol, and salbutamol are a group of β-adrenergic agonists with comparable chemical structures and effects. Although they were first developed to treat diseases, the side effects of reducing fat levels and increasing muscle protein anabolism were discovered in the drug when administered to animals. Hoewever, the residues accumulating in animal tissues can induce symptoms of serious poisoning in humans; therefore, β-adrenergic agonists have been forbidden as an animal feed additive in numerous countries worldwide.[517]

To date, tools such as liquid chromatography (HPLC,[518,519] LC−MS,[520] GC−MS[521]) capillary electrophoresis,[522,523] and spectroscopic techniques (colorimetry,[524] fluorometry,[525] chemiluminescence[526]) have been used for the detection of

104

pharmaceuticals. The chromatographic and electrophoretic procedures are nevertheless time-consuming and labor-intensive, which renders them usable mainly for confirmatory analysis. Since the pharmaceuticals are a rather heterogeneous group of compounds, the immunosensor-based detection methods vary appropriately. Most of the drugs are compounds of relatively low molecular weights, and therefore, sandwich assay is not as common as competitive or direct detection.

The relevant applications of NP-based immunoanalytical techniques and sensors for the detection of pharmaceuticals are provided in Table 3.

5.2. Toxic Substances and Pathogens

The assays within this category very often need to be realized out of regular laboratories to quickly screen and identify potentially dangerous substances. The rapid immunoassays suitable for field use are represented by the lateral flow immunoassay format (Figure 34); a drop of the sample spontaneously moves through
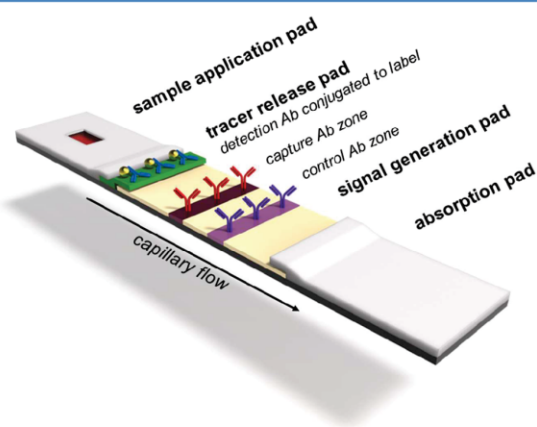
Figure 34. Schematic view of the lateral flow immunoassay format widely used for rapid assays out of the laboratory.

the porous strip material with the help of capillary forces, dissolving the immunoreagents deposited at the beginning of the flow path in the tracer release pad. Finally, the concentration level is evaluated in the measuring part embodied in the capture zone, and the performance of the assay is confirmed in the control zone. Sophisticated immunosensors should compete with the fast performance of this format.

5.2.1. Detection of Toxins. Microbial toxins are the main virulent subunits of many pathogenic microorganisms (bacteria and fungi); they represent a heterogeneous set of compounds which can interfere with biochemical processes, including the membrane function, ion transport, transmitter release, and macromolecule synthesis. Human exposure to toxins in either food or the environment may cause serious health problems, with the individual symptoms varying substantially between the toxins.[636] Thermal processing methods such as pasteurization or heating typically kill only the bacteria and do not affect the toxins. Thus, the detection of food toxins should be carried out by immunological rather than microbiological procedures because the latter detect only the bacteria.

Botulinum neurotoxins represent the most potent natural toxins. The group comprises seven different immunogenic serotypes (A–G) produced by various strains of the spore-forming bacterium *Clostridium botulinum*. The toxicity is caused

by the cleavage of the proteins associated with the release of acetylcholine after targeted binding with nerve cells or cholinergic nerve endings; the process induces muscular paralysis, respiratory collapse, or death.[637] The fatal dose of botulinum neurotoxins ranges between 0.1 and 1 ng/kg in humans, and we thus have to consider the risk that the aerosolized toxin might be also used as a biological weapon.[638]

Brevetoxin B is an efficient neurotoxin produced by the red tide organism *Gymnodinium breve* Davis.[639] Many filter-feeding shellfish are known to accumulate brevetoxins with no obvious adverse effects; however, eating brevetoxin-contaminated shellfish poses a major health hazard. Brevetoxin can bind to voltage-gated sodium channels in nerve cells, which leads to gastrointestinal and neurological symptoms. The lethal dose of brevetoxins in mice is around 200 μg/kg of body weight for intraperitoneal injection and varies between 520 and 6600 μg/kg for oral administration.[640] Brevetoxin can also influence respiratory irritation via aerosol exposure at seashores.[641]

Cholera toxin constitutes an enterotoxin protein secreted by the bacterium *Vibrio cholerae*, a causative agent for diarrhea and acidosis in humans with high lethality.[642] Cholera toxin is composed of two subunits: cholera toxin subunit A and cholera toxin subunit B. The latter is responsible for binding to the ganglioside GM1 receptor on intestinal cell walls, whereas the former is the active function protein that activates the production of cyclic AMP, causing a dramatic efflux of ions and water from the infected enterocytes; the process leads to watery diarrhea.[643]

Microcystins are the most widespread lethal cyanotoxins. They are produced by the blooming cyanobacteria *Microcystis aeruginosa* in fresh and brackish waters.[644] Within over 80 mycrocystin types, microcystin-LR (containing leucin (L) and arginine (R) as the two variable amino acids) is the most prevalent and abundant toxin, accounting for 46.0–99.8% of the overall concentration of microcystins in the toxic cyanobacterial blooms.[645] It is a hepatotoxin capable of inducing functional and structural disturbances of the liver; the substance can accumulate in aquatic organisms and transfer to higher trophic levels.[646] The LD_{50} of microcystin-LR in mice and rats is 36–122 μg/kg through various routes, including aerosol inhalation.[647]

Mycotoxins embody secondary metabolites produced by microfungi having the ability to cause disease and death in humans and animals. The most important mycotoxins are the aflatoxins and ochratoxin A produced by the fungi *Aspergillus* and *Penicillium*. In general terms, aflatoxins are difuranocoumarin derivatives produced via a polyketide pathway by many strains of *Aspergillus flavus* and *Aspergillus parasiticus*. More than 20 aflatoxins have been identified, those of major concern being B1, B2, G1, and G2; the classification defines the fluorescence under UV light (blue or green) and relative chromatographic mobility during thin-layer chromatography.[648] AFB1 is normally predominant in amount and also exhibits the highest toxicity.[649] When aflatoxin B1 is consumed by cows, it metamorphosizes into its hydroxylated product, aflatoxin M1, which is secreted through the milk.[650] Because of the differences in aflatoxin susceptibility in test animals, it is difficult to extrapolate the possible effects of aflatoxin on humans. The acute lethal dose for adults was calculated to lie between approximately 10 and 20 mg of aflatoxins.[651] Ochratoxin A is produced by many filamentous species belonging to the genera *Aspergillus* and *Penicillium*.[652] The substance constitutes a potent nephrotoxic mycotoxin linked to kidney problems in both livestock and human populations, and it also exhibits carcinogenic, genotoxic, and immunotoxic properties.[653] The LD_{50} of ochratoxin A in mice

Table 4. Overview of Immunosensors for Toxic Molecules

toxin sample matrix	LOD	range	time (min)	surface	label(s)	procedure	year and ref
Aflatoxin A1							
peanuts	8 pg/mL	8 pg/mL to 1 ng/mL	90	Au/aflatoxin−BSA	Au NP/Ab$_2$	comp SPRi	2014[698]
Aflatoxin B1							
peanuts	0.16 ng/mL	0.5−50 ng/mL	45	−	Au NR/AFB1−BSA	comp, optical (reader)	2013[699]
peanuts	0.6 pg/mL	0.6 pg/mL to 10 ng/mL	180	microplate/Ab$_1$	biotin/Ab$_2$; sa; nanoliposome/biotin	sw, commercial glucometer readout	2016[700]
w (environmental; tap water)	0.1 ng/mL	0.1 ng/mL to 100 μg/mL	30	MNP/Ab$_1$	hollow Au NP/Ab$_2$	sw SERS	2014[701]
w (model)	80 pg/mL	0.25−1.4 ng/mL	NA	ITO/MWCNTs/Ab	− (direct)	CV	2013[702]
w (model)	30 pg/mL	NA	12	LFIA strip/AFB−BSA	Au NP/Ab	comp LFIA	2014[703]
olive oil	0.03 ng/mL	0.1−10 ng/mL	40	GCE/MWCNT/ionic liquid/Ab	− (direct)	EIS	2015[704]
milk, peanut oil	0.2 pg/mL	1 pg/mL to 100 ng/mL	90	SPCE/Au NP/Ab$_1$	Cu−apatite/AFB−BSA	comp ASV	2016[705]
w (model)	1 pg/mL	1 pg/mL to 10 μg/mL	NA	Si/PMMA/Pt NP/Ab	− (direct)	EIS	2016[706]
corn powder	3.5 pg/mL	0.01−100 ng/mL	210	chitosan/SWCNTs/AFB$_1$−BSA	Ab$_1$, Ab$_2$−ALP	comp DPV	2016[707]
peanuts	5 pg/mL	5 pg/mL to 5 ng/mL	30	GCE/AFB$_1$−BSA	graphene oxide/CoTPP/Pt NP/Ab	comp peroxidase-like DPV	2016[708]
corn	0.2 ng/mL	0.05−200 ng/mL	90	magnetic electrode/CNHs/MNPs/Ab	− (direct)	ECL	2016[709]
peanuts	2.7 pg/mL	3 pg/mL to 20 ng/mL	80	GCE/graphene/conA/SiO2 NP/Ab	Au NP/invertase/AFB$_1$−BSA	comp, displacement DPV	2015[710]
w (model)	0.12 ng/mL	0.125−1.5 ng/mL	NA	ITO/rGO/Ab	− (direct)	CV	2013[711]
w (model)	0.16 ng/mL	1−8 ng/mL	NA	ITO/rGO−Ni NP/Ab	− (direct)	DPV	2016[712]
corn	10 fg/mL	10 fg/mL to 10 pg/mL	50	GCE/PPy/PPa/rGO/Ab	− (direct)	EIS	2015[713]
Aflatoxin M1							
milk	18 pg/mL	18 pg/mL to 1 μg/mL	55	Au/pHEMA/BSA−AFM$_1$	Au NPs/Ab$_2$	indirect comp, SPR	2016[714]
Botulinum Neurotoxin							
orange juice, milk	5 pg/mL	10 pg/mL to 10 ng/mL	65	GCE/graphene/Ab$_1$	Au NP/Ag NP/Ab$_2$/ALP	sw LSV of product of enzymatic reaction	2015[715]
orange juice	150 fg/mL	150 fg/mL to 2.5 ng/mL	240	nanoporous silica/Ab$_1$	dye-doped NP/Ab$_2$	sw F	2012[716]
Brevetoxin							
seafood	0.6 pg/mL	1 pg/mL to 10 ng/mL	75	Au/graphene/ConA/sa/Ab$_1$	Au NP/glucoamalyse	comp, hydrolytic reaction, displacement QCM	2013[717]
seafood	6 pg/mL	0.01−3.5 ng/mL	80	mesoporous silica nanocontainer/Ab	methylene blue, aminated polystyrene microspheres	controlled release, SWV	2013[718]
seafood	5 pg/mL	0.01−10 ng/mL	50	GCE/brevetoxin−BSA	mesoporous enriched PdNS/Ab	comp, DPV	2015[719]
Cholera Toxin							
w (model)	1.1 μg/mL	1.1−6 μg/mL	25	buoyant silica microspheres/Ab$_1$	Au NP/Ab$_2$	sw, SERS	2012[720]
w (model)	0.6 ng/mL	37−350 ng/mL	30	ITO/NiO NWs/(SpA)/Ab	− (direct)	EIS	2013[721]
Microcystin-LR							
w (drinking water)	0.04 ng/mL	0.05−20 ng/mL	45	Si/MWCNTs/Ab	− (direct)	EIS	2012[722]
w (environmental; lake, tap water)	4 pg/mL	5−50 pg/mL	150	Au/CNT@Co silicate/Ag NP/microcystin	Ab$_1$ and MNP/dopamine/Au NP/Ab$_2$	comp CV	2016[723]
w (environmental; lake)	4 pg/mL	0.01−100 ng/mL	90	GCE/Au NP/microcystin−BSA	Ab−HRP	comp EIS	2016[724]
w (environmental; lake)	1.7 ng/mL	2.5 ng/mL to 5 μg/mL	150	GCE/CNT/Ab$_1$	Au NP/Ab$_2$	comp ASV	2016[725]
w (environmental; lake, river, tap)	0.6 pg/mL	1−1000 pg/mL	60	Au/MWCNT/microcystin	− (direct)	resistivity	2015[726]
w (environmental; lake)	0.5 ng/mL	0.5 ng/mL to 10 μg/mL	180	glass/graphene oxide/Ab$_1$	Au NP/aptamer	sw F quenching	2012[727]
w (environmental)	21 pg/mL	0.1−25 ng/mL	60	fluorine doped tin oxide/QD−graphene/Ab	− (direct)	photocurrent decrease	2012[728]
w (drinking water)	1.7 ng/mL	5 ng/mL to 1 μg/mL	15	GCE/ionic liquid/MWCNTs/Ab	− (direct)	EIS	2012[729]

106

Table 4. continued

toxin sample matrix	LOD	range	time (min)	surface	label(s)	procedure	year and ref
Ochratoxin							
peanuts	30 pg/mL	30 pg/mL to 1 ng/mL	90	Au/ochratoxin—BSA	Au NP/Ab$_2$	comp SPRi	2014[308]
corn, wheat, rice, coffee	10 zg/mL	10 zg/mL to 1 ag/mL	180	microplate/Ab$_1$	SiO$_2$ NP/catalase/ ochratoxin	comp plasmonic ELISA, naked eye or reader	2015[730]
ground corn	0.2 ng/mL	1 ng/mL to 1 μg/mL	120	GCE/Au NPs/ ochratoxin—OVA	Ab	comp CV	2013[731]
corn, wheat, rice	0.05 pg/mL	0.05—10 pg/mL	195	microplate/Ab$_1$	OTA—CAT and QDs	comp F quenching	2016[732]
milk	2 pg/mL	10 pg/mL to 50 ng/mL	NA	ITO/TiO2/QD/Ab	— (direct)	PEC	2015[733]
instant coffee	0.26 ng/mL	1—104 ng/mL	15	MNP/Ab	ochratoxin—HRP	comp amperometry	2015[734]
Staphylococcal Enterotoxin A							
milk	10 pg/mL	0.01—10 ng/mL	120	3D fiber/Ab$_1$	MNP/Ab$_2$	sw, mag. Separation, mag. detection	2013[735]
Staphylococcal Enterotoxin B							
w (model)	1 pg/mL	1 pg/mL to 1 ng/mL	10	LFA strip/Ab$_1$	hollow Au NP/Ab$_2$	sw, LFIA, naked eye	2016[736]
w (model)	8.15 ng/mL	10 ng/mL to 1 μg/mL	NA	sepharose/Ab$_1$	QD/Ab$_2$	comp F	2012[737]
milk	17 pg/mL	50 pg/mL to 5 ng/mL	45	magnetosome/PANI— Au NPs/Ab$_1$	— (direct)	EIS	2013[738]
milk	2.5 ng/mL	5—100 ng/mL	15	LFIA strip/Ab$_1$	Au NP/Ab$_2$	LFIA naked eye readout	2016[739]
w (model)	1 ng/mL	NA	20	PMMA/SWCNTs/Ab	— (direct)	electrical percolation	2013[740]
Staphylococcal Enterotoxin C1							
milk	19 pg/mL	0.025—2 ng/mL	160	microplate/Ab$_1$	SiO$_2$ NP/Ab$_2$	sw CL	2016[741]
Zearalenon							
peanuts	15 pg/mL	15 pg/mL to 1 ng/mL	90	Au/zearalenon—BSA	Au NP/Ab$_2$	comp SPRi	2014[742]
feed sample	1 pg/mL	5 pg/mL to 5 ng/mL	180	glass/zearalenone—BSA	Au NP/Ab	comp SERS	2014[743]
pig feed	2.1 pg/mL	5 pg/mL to 25 ng/mL	NA	GCE/nitrogen-doped graphene/Ab$_1$	PtCo NP/Ab$_2$	sw, chronoamperometry	2013[744]

oscillates within the range of 38—56 mg/kg, depending on the mouse strain.[654] Staphylococcal enterotoxins form a category of toxic proteins produced by *Staphylococcus aureus*. Enterotoxins are often found in protein-rich food, such as meat and milk,[655] and they exhibit heat stability, resistance to gut proteases, and activity over a wide range of pH values.[656] Thus far, 20 serologically distinct staphylococcal enterotoxins have been discovered; staphylococcal enterotoxin B (SEB) is most often connected with food poisoning. The SEB infection is very rapid and causes symptoms such as nausea, violent vomiting, and abdominal cramping that may result in diarrhea even at a dose of less than 1 μg or 100—200 ng in highly sensitive people.[657,658]

Zearalenone is a mycotoxin produced mainly by fungi belonging to the genus *Fusarium*. Contaminations by zearalenone are frequent in agricultural commodities and cereal products such as flour, malt, soybeans, and beer.[659] Consuming contaminated products might cause various toxic effects in humans and animals, including teratogenesis, carcinogenicity, neurotoxicity, abortion, and the estrogenic effect.[660] The LD_{50} of zearalenone in mice equals 500 mg/kg of body weight.[661]

The selected applications of NP-based immunoanalytical techniques and sensors for the detection of toxins are provided in Table 4.

5.2.2. Pesticides as Environmental Pollutants. Pesticides constitute significant pollutants as they are constantly spread in large amounts into the environment. The negative influence of these compounds on the environment was emphasized by pesticides being listed as priority hazard agents within European water policy. The substances exhibit adverse health effects, and therefore, most countries have defined maximum residue levels (MRLs) of pesticides in food and animal feed. The common feature of most pesticides is bioaccumulation risk and the relatively high toxicity to humans.[662] In the EU, pesticides in drinking water are currently regulated by the Drinking Water Directive, which stipulates the maximum allowable concentration of 0.1 μg/L per pesticide or 0.5 μg/L for the total pesticide concentration.[663]

2,4-Dichlorophenoxyacetic acid (2,4-D) embodies one of the most frequently applied herbicides in agriculture. It is a synthetic plant growth regulator, structurally and functionally akin to auxin.[664] At low concentrations, 2,4-D is a component of the plant tissue culture medium; at high ones, however, it functions as a herbicide for broadleaf weeds. The compound is potentially toxic to humans, can be accumulated in the human body, and has a certain potential of carcinogenicity and mutagenicity.[665,666] The oral LD_{50} of 2,4-D in rats is 375 mg/kg of body weight.[667] The U.S. Environmental Protection Agency (EPA) has set the enforceable regulation for 2,4-D, or the maximum contaminant level (MCL), at 70 μg/L.[668]

Atrazine is a widely used herbicide that enables the control of annual grasses and broadleaf weeds in agriculture worldwide. It is persistent in the environment and can thus remain in the ecological system, including soil, natural water, and food (e.g., maize). When accumulated in vivo, atrazine can antagonize, impair, enhance, or inhibit the actions of endogenous hormones, leading to abnormalities in growth, reproduction, development, behavior, immune functions, or malignant tumors.[669] The atrazine toxicity (LD_{50}) by oral ingestion in humans is 1000 mg/kg.[670]

Carbofuran constitutes a broad-spectrum insecticide commonly applied in agriculture to control insects and nematodes for the purposes of production enhancement.[671] It is highly toxic to

107

mammals and reportedly embryotoxic and teratogenic. Due to its extensive use in agriculture and relatively good solubility in water, carbofuran can contaminate surface and ground waters and, therefore, poses a risk to consumers and the environment. The U.S. EPA prescribes the maximum contaminant level (MCL) for carbofuran in drinking water at 40 μg/L.[672]

Chlorpyrifos is an organophosphorus acetylcholinesterase inhibitor. Exposures to chlorpyrifos can result in a series of neurotoxic injuries to the central nervous system as well as the cardiovascular and respiratory functions.[673] The acute and chronic reference doses of chlorpyrifos are 5 and 0.3 μg/kg/day, respectively, with the oral LD$_{50}$ amounting to 50−250 mg/kg/day.[674]

Diuron is a substituted phenylurea herbicide employed for wide-spectrum pre-emergence weed control. The compound is a potent photosynthesis inhibitor, interrupting the photosynthetic electron transport chain; the process then leads to reduced formation of high-energy substances such as ATP.[675] This herbicide can be classified as an endocrine disruptor.[676] It is rather persistent in soil, having a half-life in the range between 90 and 180 days, depending on the type of environment.[677] Diuron exhibits only slight acute toxicity to mammals; the oral LD$_{50}$ in rats is 3.4 g/kg.[678]

Endosulfan constitutes a broad-spectrum organochlorine pesticide widely used in agriculture to control insects and mites. The substance has been regarded as a relatively environmentally safe pesticide with a short half-life and little evidence of bioaccumulation. However, due to its high application rate (750 g/ha) and relatively high acute toxicity to fish (LC$_{50}$ = 0.1−20 g/L), endosulfan poses a potential environmental threat.[679]

Imidacloprid is an insecticide that kills insects by binding to the nicotinic acetylcholine receptors (nAChR's) in their central nervous system. The compound is highly specific for nAChR's and is less harmful to mammals. However, it is soluble in water and has a lifetime greater than 1000 days, which enables it to accumulate in soils and water sources.[680] The short-term oral LD$_{50}$ is 450 mg/kg for rats and 150 mg/kg for mice.[681]

Metolcarb is an N-methylcarbamate pesticide widely used in agricultural production to control rice leafhoppers, planthoppers, and fruit flies. The compound is based on inhibiting acetylcholinesterase transmission at nerve endings.[682] It is potentially dangerous to mammals; the LD$_{50}$ equals 268 mg/kg.[683]

Paraquat is a widely used and fast-acting organic heterocyclic herbicide. The use of paraquat has been banned in the EU since 2007; however, this rule does not apply to non-European countries exporting to the EU. The maximum residue limit (MRL) of 20 μg/kg has been established for many food products such as barley, wheat, or potato.[684] The LD$_{50}$ of paraquat in rats is 79 mg/kg.[685]

Parathion and methyl parathion are organophosphorus pesticides. The symptoms of poisoning include nausea, vomiting, diarrhea, muscle cramping/twitching, and shortness of breath.[686] The LD$_{50}$ values of parathion and methyl parathion in mice were found to be 13.5 and 11 mg/kg, respectively.[687]

Among the many pesticides used in agriculture, insecticides from organophosphorus and carbamic groups are often applied because they exhibit high insecticidal activity and rather small persistence in the environment. The substances are commonly detected by inhibition-based enzymatic sensors, which are not discussed in this review and were summarized elsewhere.[688,689]

The relevant applications of immunosensing techniques and sensors used for pesticides are summarized in Table 5.

5.2.3. Microbial Detection. The rapid detection and reliable identification of hazardous microbial agents constitutes a challenging task. The prevention or early treatment of infectious diseases is a concern of modern society. Even human deaths due to possible bioterrorist attacks are threats to modern society, and it is thus understandable that the growing demands for the detection of bioagents originated from the military, civil rescue, and security services, protection of public buildings, and homeland security, all of which constitute major domains of current public interest. The Centers for Disease Control and Prevention sorted the critical biological agents for public health into the three categories.[690] The properties of biological agents such as lethal dose and infectiveness make these agents suitable candidates for use as biological warfare agents (BWAs). The most dangerous bacteria are, for example, *Francisella tularensis* (tularemia), *Yersinia pestis* (plague), *Clostridium botulinum* (botulism), and *Bacillus anthracis* (anthrax). The last one is feared because it has already been used. As regards the practical use, the Department of Homeland Security in the United States requires the sensitivity of field devices in the range from 10^2 to 10^5 organisms/L.[691] The most dangerous bioagents cannot be easily used in common laboratory conditions; therefore, the safe strains of *E. coli* (DH5α) and *Bacillus atrophaeus* are used for the development of detection technologies.

Microbial detection is nevertheless indispensable also for the everyday inspection of potentially contaminated food, including meat, poultry, and milk products, vegetables, and fruits; possible contaminants then comprise the strains of *Escherichia*, *Salmonella*, and *Listeria*. *Salmonella* was evaluated as a leading cause of foodborne infections in the United States, with approximately 1.2 million illnesses and 450 deaths per year.[692] *Legionella* should be seriously considered too as it occasionally contaminates water supplies.

Viruses and viral antigens are typically assayed in clinical diagnostics; classic examples are hepatitis surface antigens and human immunodeficiency virus. Each year, outbreaks of viral infections (the most common being influenza with potentially highly dangerous mutated variants) cause illness, disability, death, and economic loss. As learned from past incidents, the detrimental impact grows exponentially without effective quarantine. Therefore, rapid on-site detection and analysis are highly desired.[693] Recently, the lack of laboratory facilities resulted in diagnostic complications during the West African Ebola virus outbreak in 2013−2015, thus compromising outbreak control. Nearly 28000 confirmed, probable, and suspected cases were reported; owing to limited laboratory capacity and local transport infrastructure, the delays from sample collection to test results were often 2 days or more.[694]

Even though suitable analytical procedures (cultivation tests, polymerase chain reaction,[695] enzyme-linked immunosorbent assays) and devices (mass spectrometry[696]) are readily available, drawbacks such as slow operation, complicated portability, and high running costs often limit their applicability. Conventional microbiological methods are time-consuming and usually require the collection of samples for subsequent laboratory analysis. The complexities of analyzed samples containing interfering (bio)-substances disadvantage PCR methods, and additional methods are needed to avoid false conclusions. In the case of MS, extensive instrumentation limits widespread use for the field detection. The actual assays of bioagents are further complicated by minor differences between hazardous and commonly used microbial

108

Table 5. Assays for Pesticides and Other Environmental Pollutants

pesticide sample matrix	LOD	range	time (min)	surface	label(s)	procedure	year and ref
2,4-Dichlorophenoxyacetic Acid							
w (model)	13 ng/mL	13.3–666.7 ng/mL	70	Au/2,4-D–BSA	Ab₁, Ab₂–Au NP	comp QCM	2014[745]
Atrazine							
w (model)	50 pg/mL	50 pg/mL to 5 ng/mL	180	glass/Au NPs/Ab	– (direct)	LSPR	2012[746]
maize	1 ng/mL	1–15.6 ng/mL	10	Au/Au NP/Ab	– (direct)	SPR	2015[747]
crop	16 pg/mL	0.05–0.5 ng/mL	45	Au/Au NP/Ab	– (direct)	DPV	2014[748]
w (model)	0.01 ng/mL	0.01–50 ng/mL	20	SPE/styrene sulfonic acid doped nanostructured PANI/Ab	– (direct)	EIS	2014[749]
orange juice	3.5 pM	0.9–4.5 nM	20	boron doped diamond/Pt NP/magnetic bead/Ab	atrazine–HRP	mag sep, comp, chronoamperometry	2016[750]
w (environmental), feed, corn flakes	1.2 ng/mL	0.01–1000 ng/mL	120	GCE/Au NP/atrazine–BSA	Ab₁, Ab₂–HRP	comp CV	2014[751]
w (environmental)	1 pg/mL	1 pg/mL to 10 ng/mL	15	FET/SWCNTs/Ab	– (direct)	FET	2016[752]
w (environmental)	0.2 pg/mL	0.2–20 pg/mL	90	SPCE/magnetic bead/Ab	phage particles/HRP	mag sep, noncompetitive, chronoamperometry	2014[753]
Carbofuran							
lettuces, cabbages, green peppers, tomatoes, Chinese chives, strawberries	60 pg/mL	0.1 to 10⁶ ng/mL	45	Au/deposited Au nanocrystals/Ab	– (direct)	DPV	2012[754]
cabbage, lettuce	0.021 ng/mL	0.1–1 μg/mL	15	Au/Au NP/Prussian blue–MWCNT–chitosan/SpA/Ab	– (direct)	CV	2012[755]
cabbages, green peppers, tomatoes, Chinese chives, peaches	0.03 ng/mL	0.5–500 ng/mL	25	GCE/MWCNTs/graphene–PEI–Au/Au NP/Ab	– (direct)	CV	2013[756]
cabbage	0.11 ng/mL	1 ng/mL to 200 μg/mL	30	GCE/Au NP/thiourea/Au NP/Ab	– (direct)	amperometry	2012[757]
Chlorsulfuron							
w (model)	NA	0.1 pg/mL to 10 ng/mL	170	microplate/chlorsulfuron–BSA	Au NP/Ab	comp ASV (SWV)	2012[758]
Chlorpyrifos							
cabbage, pakchoi, lettuce, leek	52 pg/mL	5 ng/mL to 2 mg/mL	30	GCE/NiAl/graphene/hollow Au NP/Ab	– (direct)	CV	2015[759]
w (environmental)	6.3 pg/mL	0.01–1000 ng/mL	120	GCE/polydopamine nanospheres/chlorpyrifos–OVA	Ab₁, Ab₂/CNT/Fe₃O₄/HRP	comp CV enzymatic amplification	2015[760]
Diuron							
w (model)	0.01 ng/mL	1 pg/mL to 10 μg/mL	150	microplate/diuron–BSA/Ag NP (blocking)	Ab–FITC	comp plasmon enhanced FL	2013[761]
w (environmental)	0.1 pg/mL	0.01 pg/mL to 10 mg/mL	185	SPE/MWCNTs/diuron hapten	Ab₂–ALP	comp DPV	2012[762]
w (environmental)	5.46 ng/mL	1–1000 ng/mL	NA	SPCE/Au NP/Ab	– (direct)	EIS	2012[763]
w (model)	0.01 pg/mL	0.01 pg/mL to 10 μg/mL	120	SPCE/functionalized graphene–GO/diuron–BSA	Ab₁, Ab₂–ALP	comp LSV	2013[764]

109

Table 5. continued

pesticide sample matrix	LOD	range	time (min)	surface	label(s)	procedure	year and ref
Endosulfan							
w (environmental)	0.01 ppb	0.01–20 ppb	180	GCE/SWCNTs/endosulfan hapten	Ab	comp SWV	2012[765]
Imidacloprid							
w (model)	1 ppb	1–10 ppb	20	Al$_2$O$_3$/Ag nanostructures/imidacloprid–BSA	Ab	comp SPR	2016[766]
Metolcarb							
orange juice	19 ng/mL	0.1–50 µg/mL	120	Au/MWCNT–PAMAM/Ab	– (direct)	QCM	2013[767]
Paraquat							
potato	1.4 µg/kg	3.1–67.8 µg/kg	30	magnetic microparticle/paraquat–BSA	QD/Ab	mag sep, comp, ASV	2014[768]
Parathion							
comato, carrot	52 fg/mL	0.1–1000 pg/mL	10	SPCE/graphene/Ab	– (direct)	EIS	2016[769]

species. Evidently, a reliable device suitable for rapid on-site POC detection was missing.

Nanoparticles bring important advantages to immunoassays. Magnetic NPs appeared to be a useful tool providing a favorable dual benefit for the signal amplification: immunomagnetic separation, and preconcentration of the sample. Microbial species captured in the sensing area provide a sufficiently large surface ideally suited for further binding of "decorating" nanoparticle-based labels (Figure 35). The relevant example applications of NP-based immunoanalytical techniques and sensors are provided for bacteria (Table 6) and viruses (including viral antigens, Table 7).
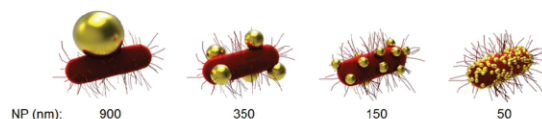
Figure 35. Enhanced response of an immunosensor for the detection of microbes. A comparison of the different sizes of the NP labels binding to *E. coli*. Based on ref 697.

6. CONCLUSION AND OUTLOOK

This review has summarized recent advances, challenges, and trends in the rapidly developing domain of immunochemical biosensing supported and enhanced by nanoparticles. The research topic represents the interdisciplinary effort to combine the unique electronic, magnetic, optical, catalytic, and mechanical properties of nanoparticles with the optimized recognition function of biomaterials such as antibodies. In the review, nano-objects were introduced in broad contexts, and the role of nanoparticles in immunosensing was discussed. Attention was paid to not only several applications of nanoparticles in individual immunomethods but also the architecture and transduction strategies that have proposed perspectives for further development.

The review has demonstrated that NP-based immunosensors provide very good results with a promising sensitivity and reproducibility and, in combination with novel devices (such as microfluidic sample delivery, microelectromechanical systems, or sensors with embedded electronic signal treatment, namely, concepts well-known from the lab-on-the-chip field), offer an attractive analytical approach for the fast, low-cost, and accessible detection of trace prognostic biomarkers, drugs, toxins, microbial pathogens, and environmental pollutants. The key advantages of immunochemical biosensors—small size and portability, reasonable assay costs, simplified use, and straightforward interpretation of results—are being further enhanced through incorporation of nanoparticles improving particular steps completing both the immunorecognition and sensing function.

The relative complexity of the sensing structures and procedures should not constitute an obstacle, as the production technologies for the robust deposition of thin layers and immobilization of biocomponents are already available. The actual reliability in real situations, however, might pose certain difficulties, especially if we consider the fact that the results obtained from the testing of newly developed bioanalytical technologies almost invariably appear to be flawless. Thus, extensive, critical test cycles supervised by independent specialists should be realized prior to considering any production and commercialization-related steps. Importantly, what looks ideal in

110

Table 6. Immunosensing for Pathogenic Bacteria

bacteria sample matrix	LOD (cfu/mL)	range (cfu/mL)	time (min)	surface	label(s)	procedure	year and ref
Alexandrium minutum (Microalgae, Shellfish Toxins)							
w (sea)	100	100 to 10^8	30	nitrocellulose/mAb_1	mag NP/mAb_2	sw, mag sep and reader, LFIA	2016[770]
Bacillus anthracis							
(spores) milk powder	400	4×10^3 to 10^6	30	nitrocellulose/mAb_1	mag NP/mAb_2	sw, mag sep and reader, LFIA	2013[771]
Bacillus cereus							
cell culture	10	50 to 10^4	30	glassy C/chit–Au NP/Ab_1	– (direct)	blocked chronoamp	2012[772]
Cryptosporidium parvum (Protozoan Parasite, Oocysts)							
w (model)	5	5–100	65	glass/mAb_1	Ag_2S/SiO_2/mAb_2	sw, F (NIR)	2014[196]
Enterobacter sakazakii							
w (model)	1000	10^4 to 10^{10}	45	SPE C/MWCNT–alginate–chit/HRP/thionin–Ab_1	– (direct)	blocked CV	2013[773]
Escherichia coli							
w (model)	10	10 to 10^9	30	Au/cystine flowers/Ab_1	– (direct)	blocked EIS	2014[774]
w (model) (DH5α)	210	100 to 10^7	1	aligned C nanofibers	Fe_2O_3/Au nano-ovals/Ab	dielectrophoretic capture; SERS	2015[775]
urine	30	100 to 10^8	120	Fe_3O_4/Au NP/Ab_1	CdTe QD/chit/Ab_2	sw, F	2016[776]
dairy	50	100 to 10^6	150	glassy C/PAMAM dendrimer/AuNP/mAb_1	MWCNT/HRP/pAb_2	enzyme PANI deposition, DPV	2016[777]
Escherichia coli O157:H7							
w (model)	250	400 to 4×10^5	45	Au/Au NP/chit–MWCNT–SiO_2/thionine/mAb_1	– (direct)	blocked CV	2012[778]
stool (model)	15	30 to 3×10^6	90	C/fullerene, ferrocene/Au, SiO_2 NP/Ab1	Pt NP/GOD/Ab_2	sw, CV of GOD–ferrocene transfer	2013[779]
brassica	430	4×10^3 to 4×10^8	35	Fe_3O_4/PB/Au NP/Ab_1	– (direct)	mag sep, catalytic NP, CV	2014[780]
w (model)	100	100 to 10^7	10	nitrocellulose/pAb_1	Au NP/mAb_2	LFIA, color visual/reader	2015[244]
w (model)	10	10 to 10^6	60	mag NP/PANI/mAb_1	Au NP/Pb NP/mAb_2	mag sep, sw, SWV of dissolved Pb^{2+}	2015[781]
milk	10	10	30	Fe_3O_4/Pt/Ab_1	–	mag sep, catalytic, color visual	2015[782]
milk, orange juice, w	3	4 to 4×10^6	75	Fe_3O_4/SiO_2/PAA/Ab_1	SiO_2/FITC/Ab_2	sw, mag sep, F	2016[197]
w (model)	100	100 to 10^6	15	nitrocellulose/pAb_1	AuPt NP/Ab_2	LFIA, catalytic NP, color visual/reader	2016[783]
w (model)	100	300 to 10^5	150	Au/pAb_1	Au NP/pAb_2	sw, EIS	2016[42]
food (hamburger)	57	10 to 10^4	80	Au/PCBAA brush/Ab_1	Ab2–bt; Au NP/sav	sw, SPR	2016[276]
food	1–10	10^4 to 10^6	24 h	Au/Ab_1	Au NP/Ab_2	sw, QCM, on-chip cultivation	2016[784]
Legionella pneumophila							
w (preconcentrated 2000×)	10	10 to 10^5	180	SPE–C; Fe_3O_4 NP/PDOPA/pAb_1	pAb_2–HRP	sw, mag sep, amp	2015[785]
Listeria innocua							
w (model)	10^4	10^4 to 10^8	20	mag NP/Ab_1	Au NP/Ab_2	sw, SERS	2016[786]
Listeria monocytogenes							
lettuce	300	300 to 10^4	150	IDE; Fe_3O_4 NP/mAb_1	Au NP/pAb_2/urease	sw, urease/urea impedance	2015[787]
milk	100	100 to 10^7	<10	SPE–Au/grox–chit/Ag NP/Ru $(bpy)_3^{2+}$/mAb_1	– (direct)	blocked amp	2015[788]
Pseudomonas aeruginosa							
w	900	10 to 10^7	90	glassy C/Ca–pectin/Au NP/Ab_1	Ab_2–HRP	sw, DPV	2016[789]
Salmonella galinarum							
chicken	32	100 to 10^6	120	SPE; Fe_3O_4/SiO_2/Ab_1	Ab_2–HRP	sw, mag sep, CV	2015[790]
Salmonella pullorum							
chicken liver	90	100 to 10^6	150	SPE; Fe_3O_4/SiO_2/Ab_1	grox-r/AuNP/Ab_2	sw, mag sep, DPV	2016[791]
Salmonella typhimurium							
milk, egs, sprouts	13	10 to 10^6	150	SPE–avidin; Fe_3O_4–latex NP/ssDNA code/$mAb1$	pAb_2–biotin	sw, Ag-enhanced stripping DPV	2013[792]
w (model)	100	100 to 10^5	25	glass/ZnO NR/pAb	– (direct)	blocked PL (UV)	2014[793]
milk	5	10 to 10^5	150	glassy C/chit/Au NP/Ab1	Ab_2–HRP	sw, DPV	2015[413]
apple juice	<10	10 to 1000	180	polystyrene/mAb_1	bt–Ab2, sa, Cys/bt–lipo, Au NP	sw, NP aggreg., SPR color visual	2015[250]
chicken extract	1000	10^3 to 10^6	70	mag NP/Ab_1	CdSe/ZnS QDs/Ab_2	sw, mag sep, fluidics, F	2015[794]
w (model)	100	100 to 10^5	40	–	Au NP/Ab	SERS; ICP-MS	2015[795]

111

Table 6. continued

bacteria sample matrix	LOD (cfu/mL)	range (cfu/mL)	time (min)	surface	label(s)	procedure	year and ref
Vibrio cholerae							
w (model)	100	100 to 10^4	90	Pt/CeO_2 NW/Ab_1	− (direct)	blocking EIS	2016[796]
Vibrio parahemolyticus							
sea w, seafood	5	10 to 10^8	65	$GCE/grox/ABEI/Ab_1$	− (direct)	blocked ECL	2016[214]

Table 7. Immunosensors for Viruses and Viral Antigens

virus (antigen) sample matrix	LOD	range	time (min)	surface	label(s)	procedure	year and ref
Avian Leucosis ALVs-J (TCID Is the 50% Tissue Culture Infective Dose)							
serum (avian)	$10^{2.08}$ TCID/mL	$10^{2.1}$ to $10^{3.7}$ $TCID_{50}/mL$	~100	ITO/Bi_2S_3 $NR/chit/Ab_1$	Au NP/ALP/Ab_2	sw, generated ascorbate, PEC	2014[235]
Bacteriophage MS2							
w (river)	9 pfu/mL	10 to 10^{11} pfu/mL	210	SPE–Au/Fe_2O_3/ SWCNT/Ab_1	Ab_2–ALP	sw, DPV	2015[797]
Cytomegalovirus pp65 Antigen							
saliva	30 pg/mL	0.1–80 ng/mL	60	Pt, Pd NP/SWCNT/HRP/ thionine/Ab_1	− (direct)	blocking DPV	2016[798]
Dengue							
cell culture	1 pfu/mL	1–900 pfu/mL	45	Al_2O_3 nanochannels/Ab_1	− (direct)	blocked EIS	2012[799]
cell culture	0.04 pfu/mL	3–45 pfu/mL	5	Al_2O_3 Pt nanochannels/PB nanotubes/Ab_1	− (direct)	blocked PB catalysis, fuel cell	2012[800]
Hepatitis B Aurface Antigen							
w (model)	5 mIU/mL	5–1000 mIU/mL	90	Au NP 50 nm/Ab_1	Au NP 10 nm/Ab_2	sw, enhanced DLS	2012[801]
serum	0.1 ng/mL	0.5–800 ng/mL	30	CPE/graphene/Au NP/ Nafion–Cys/Ab_1	− (direct)	blocked DPV	2012[802]
serum (human)	0.11 pg/mL	1–100 pg/mL	70	Fe_3O_4 NP/rAb_1	PAA–$Ru(bpy)_3^{2+}$/SiO_2/ Nafion/pAb_2	mag sep, sw, ECL	2015[803]
serum (human)	0.3 pg/mL	0.001–20 ng/mL	?	glassy C/Au NP/Ab_1	halloysite NT/MnO_2–Pd NP/Ab_2	sw, LSV	2016[804]
Hepatitis C Core Antigen							
serum (human)	10 fg/mL	0.25–300 pg/mL	90	Au/graphitized C–MB/Au NP/Ab_1	MWCNT/dsDNA–multi-HRP/Ab_2	sw, SWV	2013[805]
Human Immunodeficiency							
blood	98 pfu/mL	100 to 10^6 pfu/mL	70	polystyrene/PLL/Au NP/ Ab_1	− (direct)	LSPR	2012[806]
Influenza (Avian) Antigen(s)							
serum (human)	0.4 pg/mL	1–100 pg/mL	60	glassy C, Au,Pd NP/Ab_1	grox/Pt, CeO_2 NP/ALP/ Ab_2	sw, DPV	2015[807]
Influenza H1N1 and H5N1 Antigens (Avian)							
w (model)	8.3 pM	25–500 pM	45	SPE–C/grox/MB/chit– protein A–Ab_1	− (direct)	blocked DPV	2016[808]
Influenza H7 Antigen							
w (model)	1.6 pg/mL	1.6 to 1.6×10^4 pg/mL	80	Au/graphene–chit/Au NP–mAb_1	graphene/Ag NP/pAb_2	sw, LSV	2016[809]
Influenza H7N9 Antigen							
w (model)	0.8 pg/mL	8–60 pg/mL	80	glassy C/Au NP/SiO_2– ADH/protein A/mAb_1	MWCNT/oligo-DNazyme/hemin/MB/ pAb_2	sw, electrocatalytic, amp	2015[810]
Orchid (*Cymbidium* Mosaic or *Odontoglossum* Ringspot)							
plant extract	42 pg/mL	0.04–100 ng/mL	10	fiber/silicate/Au NR/Ab_1	− (direct)	LSPR	2014[811]
Rift Valley Fever, West Nile Antigen							
serum (fetal bovine)	5 fg/mL	0.005–50 pg/mL	60	Fe_3O_4/SiO_2/Ab_1	Au NP/IR dye/Ab_2	mag separ, SERS	2013[812]
Vaccinia							
fruit juice	4000 pfu/mL	10^4 to 10^7 pfu/mL	65	ITO/grox/mAb_1	Ab_2–ALP	sw, amp	2015[813]

a scientific paper or on the Web can be markedly less optimal in reality; moreover, the typical end user does not examine the principles of the sensing devices but rather focuses on the reliable performance, fast results, and economical use as his or her central criteria for success.

Researchers involved in the field currently seem to concentrate upon achieving the best possible performance limits, namely, the lowest detection threshold, ideally at the level of a few molecules. However, it is also vital to stress the aspects that are seldom brought to the limelight, and these prominently include the rather long duration of the whole analytical process, starting from the application of a sample and ending with the reading of the result. The high sensitivity and very low measured concentrations are indeed nice indicators, but they should always be

112

compared with the practical needs and existing levels of analytes in real samples.

We have summarized various strategies and approaches which can be used for the further development of nanoparticle-based immunosensors. It is clear that there are still many challenges, but one may consider some current issues making the repeatable production of these devices harder: (i) heterogeneity existing at the nanoscale level, (ii) stable shape, size, and surface modification of nanomaterials, (iii) high variability of such produced immunosensors depending on rarely optimized preparation methods and not completely defined properties of the components, and (iv) general problems with immobilization of antibodies on solid-state surfaces.

In our view, three main requirements have to be taken into account with probe immobilization and modification by NPs because none of the immobilization techniques and NPs used are nowadays optimal for this purpose. First, the immobilization and modification processes need to be stable and involve well-defined probes (Ab's), second, the probes (Ab's) have to remain functional, and third, they have to be in appropriate orientation and configuration. From the physicochemical point of view, the perspective future can also be supported by the improved knowledge of involved transport properties, kinetics of interactions, reaction mechanism of the used systems, and last but not least interactions between molecules of antibodies and nanoparticles.

AUTHOR INFORMATION

Corresponding Author

*E-mail: skladal@chemi.muni.cz.

ORCID

David Kovář: 0000-0002-5550-6143
Petr Skládal: 0000-0002-3868-5725

Notes

The authors declare no competing financial interest.

Biographies

Zdeněk Farka received his M.Sc. with honors in analytical biochemistry at Masaryk University in 2014; his thesis was focused on the immunosensing of bacteria in bioaerosols. He is currently pursuing his Ph.D. at CEITEC, Masaryk University, Czech Republic, under the supervision of Dr. Petr Skládal. His research interests include the detection of bacteria and proteins via immunoanalytical techniques. He is developing label-free point-of-care sensors and examines the amplification of the immunosensor response by means of nanoparticles and enzymes. In 2016, he spent an internship at the University of Regensburg (Germany), working on applications of photon-upconverting nanoparticles under the supervision of Dr. Gorris.

Tomáš Juřík received his B.Sc. and M.Sc. in biochemistry from Masaryk University while working in the biosensors laboratory of Dr. Petr Skládal. He is currently a Ph.D. student/researcher at CEITEC, Masaryk University, Czech Republic. In 2014, he spent an internship at the Autonomous University of Barcelona, investigating magnetic separation-based immunosensors under the supervision of Dr. Pividori. His present research concentrates on nanostructured materials and surfaces for the detection of clinical markers and microbes via electrochemical techniques.

David Kovář received his Ph.D. in biomolecular chemistry in 2015 under the supervision of Dr. Petr Skládal at Masaryk University, Czech Republic. His Ph.D. studies were focused on immunospecific sensors exploiting nanoparticles and nanostructures with the main applications

of magnetic nanoparticles. He then joined the group of Prof. Maria Hepel at the State Univeristy of New York (SUNY; Potsdam, NY) as a postdoctoral researcher in physical electrochemistry. His current research activities at Masaryk University relate to microfluidic platforms for screening and selection methods in directed enzyme evolution.

Libuše Trnková is an Associated Professor in the Faculty of Science, Masaryk University (Brno, Czech Republic). She graduated in physical chemistry from the university, receiving her Ph.D. in 1983. She currently heads the Laboratories of Biophysical Chemistry and Electrochemistry (LABIFEL). Her research interests are focused on the electrochemical properties of biopolymers and their components in solutions, electrode/electrolyte interfaces, electrochemical processes, and the development of biosensors. She is the founder of elimination voltammetry, a novel electrochemical method.

Petr Skládal is an Associated Professor in the Department of Biochemistry, Faculty of Science, Masaryk University. He received his Ph.D. in the field of amperometric biosensors in 1992. After completing research stays (1991, 1993) at the University of Florence, Italy, with Marco Mascini, he continued to investigate biosensors at Masaryk University. He currently heads the Nanobiotechnology Laboratory at the Central European Institute of Technology in Brno. His research is focused on enzyme and immunochemical biosensors using electrochemical and piezoelectric transducers, affinity kinetics with surface plasmon resonance systems, and applications of atomic force microscopy in life sciences.

ABBREVIATIONS

Ab	antibody (mAb, monoclonal; pAb, polyclonal; rAb, recombinant; Ab_1, primary/capture; Ab_2, secondary/detection)
ABEI	N-(4-aminobutyl)-N-ethylisoluminol
ADH	alcohol dehydrogenase
AEAPS	[3-[(2-aminoethyl)amino]propyl]trimethoxysilane
AFP	α-fetal protein
ALP	alkaline phosphatase
amp	amperometric
av	avidin
bpy	2,2′-bipyridine
BSA	bovine serum albumin
bt	biotin
CEA	carcinoembryonic antigen
chit	chitosan
CL	chemiluminescence
CNDs	carbon nanodots
comp	competitive immunoassay
CTCs	circulating tumor cells
CV	cyclic voltammetry
DLS	dynamic light scattering
DPV	differential pulse voltammetry
ECL	electrochemiluminescence
EDC	1-[3-(dimethylamino)propyl]-3-ethylcarbodiimide hydrochloride
EIS	electrochemical impedance spectroscopy
F	fluorescence
FET	field-effect transistor
FITC	fluoresceine isothiocyanate
FRET	fluorescence resonance energy transfer
GCE	glassy carbon electrode
GOD	glucose oxidase
GO	graphene oxide
rGO	reduced graphene oxide
HRP	horseradish peroxidase

113

ICP-MS	inductively coupled plasma mass spectrometry
Ig	immunoglobulin
ITO	indium tin oxide
LFIA	lateral flow immunoassay
lipo	liposome
LSPR	localized surface plasmon resonance
mag	magnetic
MB	methylene blue
MEMS	microelectromechanical system
mtp	microtitration plate
MWCNTs	multiwalled carbon nanotubes
NC	nanocrystal
NF	nanofiber
NHS	N-hydroxysuccinimide
NIR	near-infrared
NP	nanoparticle
NT	nanotube
NTA	nitrilotriacetic acid
NW	nanowire
PAA	poly(acrylic acid)
PABA	poly(aminobenzoic acid)
PAMAM	poly(amidoamine)
PB	Prussian blue
PBS	phosphate-buffered saline
PC	phthalocyanine
PCBAA	poly(carboxybetaine acrylamide)
PDDA	poly(diallyldimethylammonium chloride)
PANI	poly(aniline)
PDOPA	poly(dopamine)
PEC	photoelectrochemical conversion
PEI	poly(ethylenimine)
PGE	pyrolytic graphite electrode
PL	photoluminescence
PLL	poly(lysine)
PMT	photomultiplier tube
POC	point-of-care detection
PS	poly(styrene)
PVA	poly(vinyl alcohol)
QD	quantum dot
RCA	rolling cycle amplification
ROS	reactive oxygen species
sav	streptavidin
SCCA	squamous cell carcinoma-associated antigen
scFv	single-chain variable fragment
sep	separation
SERS	surface-enhanced Raman spectroscopy
SPE	screen-printed electrode
SPR	surface plasmon resonance
sw	sandwich immunoassay
SWCNTs	single-walled carbon nanotubes
SWV	square wave voltammetry
TMB	3,3′,5,5′-tetramethylbenzidine
UCNP	up-converting nanoparticle
UV	ultraviolet
vis	visible
w	water

REFERENCES

(1) Bengtén, E.; Wilson, M.; Miller, N.; Clem, L. W.; Pilström, L.; Warr, G. W. Immunoglobulin Isotypes: Structure, Function, and Genetics. In *Origin and Evolution of the Vertebrate Immune System*; Du Pasquier, L., Littman, G. W., Eds.; Current Topics in Microbiology and Immunology, Vol. *248*; Springer: Berlin, 2000; p 189.

(2) Vidarsson, G.; Dekkers, G.; Rispens, T. IgG subclasses and allotypes: from structure to effector functions. *Front. Immunol.* **2014**, *5*, 520.

(3) Kontermann, R.; Dübel, S. *Antibody Engineering*; Springer: Berlin, 2001.

(4) Hermanson, G. T. *Bioconjugate Techniques*, 3rd ed.; Elsevier: Amsterdam, 2013.

(5) Ahmad, Z. A.; Yeap, S. K.; Ali, A. M.; Ho, W. Y.; Alitheen, N. B. M.; Hamid, M. scFv Antibody: Principles and Clinical Application. *Clin. Dev. Immunol.* **2012**, *2012*, 980250.

(6) Jeong, H. J.; Kawamura, T.; Dong, J.; Ueda, H. Q-Bodies from Recombinant Single-Chain Fv Fragment with Better Yield and Expanded Palette of Fluorophores. *ACS Sensors* **2016**, *1*, 88−94.

(7) Choi, Y.; Deane, C. M. Predicting Antibody Complementarity Determining Region Structures without Classification. *Mol. BioSyst.* **2011**, *7*, 3327.

(8) Gala, F. A.; Morrison, S. L. The Role of Constant Region Carbohydrate in the Assembly and Secretion of Human IgD and IgA1. *J. Biol. Chem.* **2002**, *277*, 29005−29011.

(9) Zheng, K.; Bantog, C.; Bayer, R. The Impact of Glycosylation on Monoclonal Antibody Conformation and Stability. *mAbs* **2011**, *3*, 568−576.

(10) Higel, F.; Seidl, A.; Sörgel, F.; Friess, W. N-Glycosylation Heterogeneity and the Influence on Structure, Function and Pharmacokinetics of Monoclonal Antibodies and Fc Fusion Proteins. *Eur. J. Pharm. Biopharm.* **2016**, *100*, 94−100.

(11) Hamers-Casterman, C.; Atarhouch, T.; Muyldermans, S.; Robinson, G.; Hammers, C.; Songa, E. B.; Bendahman, N.; Hammers, R. Naturally Occurring Antibodies Devoid of Light Chains. *Nature* **1993**, *363*, 446−448.

(12) Gibbs, W. W. Nanobodies. *Sci. Am.* **2005**, *293*, 78−83.

(13) Hassanzadeh-Ghassabeh, G.; Devoogdt, N.; De Pauw, P.; Vincke, C.; Muyldermans, S. Nanobodies and Their Potential Applications. *Nanomedicine* **2013**, *8*, 1013−1026.

(14) Juarez, K.; Dubberke, G.; Lugo, P.; Koch-Nolte, F.; Buck, F.; Haag, F.; Licea, A. Monoclonal Antibodies for the Identification and Purification of vNAR Domains and IgNAR Immunoglobulins from the Horn Shark. *Hybridoma* **2011**, *30*, 323−329.

(15) Feige, M. J.; Grawert, M. A.; Marcinowski, M.; Hennig, J.; Behnke, J.; Auslander, D.; Herold, E. M.; Peschek, J.; Castro, C. D.; Flajnik, M.; et al. The Structural Analysis of Shark IgNAR Antibodies Reveals Evolutionary Principles of Immunoglobulins. *Proc. Natl. Acad. Sci. U. S. A.* **2014**, *111*, 8155−8160.

(16) Abbady, A. Q.; Al-Shemali, R.; Mir Assaad, J.; Murad, H. Generation and Characterization of Nanobodies against rhGH Expressed as sfGFP Fusion Protein. *Gen. Comp. Endocrinol.* **2014**, *204*, 33−42.

(17) Galimidi, R. P.; Klein, J. S.; Politzer, M. S.; Bai, S.; Seaman, M. S.; Nussenzweig, M. C.; West, A. P., Jr.; Bjorkman, P. J. Intra-Spike Crosslinking Overcomes Antibody Evasion by HIV-1. *Cell* **2015**, *160*, 433−446.

(18) Tomita, M.; Tsumoto, K. Hybridoma Technologies for Antibody Production. *Immunotherapy* **2011**, *3*, 371−380.

(19) Hammers, C. M.; Stanley, J. R. Antibody Phage Display: Technique and Applications. *J. Invest. Dermatol.* **2014**, *134*, 1−5.

(20) Sharma, S.; Byrne, H.; O'Kennedy, R. J. Antibodies and Antibody-Derived Analytical Biosensors. *Essays Biochem.* **2016**, *60*, 9−18.

(21) Suo, Z.; Yang, X.; Avci, R.; Deliorman, M.; Rugheimer, P.; Pascual, D. W.; Idzerda, Y. Antibody Selection for Immobilizing Living Bacteria. *Anal. Chem.* **2009**, *81*, 7571−7578.

(22) Fenzl, C.; Hirsch, T.; Baeumner, A. J. Nanomaterials as Versatile Tools for Signal Amplification in (Bio)analytical Applications. *TrAC, Trends Anal. Chem.* **2016**, *79*, 306−316.

(23) Murphy, C. J.; Gole, A. M.; Stone, J. W.; Sisco, P. N.; Alkilany, A. M.; Goldsmith, E. C.; Baxter, S. C. Gold Nanoparticles in Biology: Beyond Toxicity to Cellular Imaging. *Acc. Chem. Res.* **2008**, *41*, 1721−1730.

114

(24) Haes, A. J.; Van Duyne, R. P. A Unified View of Propagating and Localized Surface Plasmon Resonance Biosensors. *Anal. Bioanal. Chem.* **2004**, *379*, 920−930.

(25) Turkevich, J.; Stevenson, P. C.; Hillier, J. A Study of the Nucleation and Growth Processes in the Synthesis of Colloidal Gold. *Discuss. Faraday Soc.* **1951**, *11*, 55.

(26) Frens, G. Controlled Nucleation for the Regulation of the Particle Size in Monodisperse Gold Suspensions. *Nature, Phys. Sci.* **1973**, *241*, 20−22.

(27) Xia, Y.; Xiong, Y.; Lim, B.; Skrabalak, S. E. Shape-Controlled Synthesis of Metal Nanocrystals: Simple Chemistry Meets Complex Physics? *Angew. Chem., Int. Ed.* **2009**, *48*, 60−103.

(28) Baek, S. H.; Wark, A. W.; Lee, H. J. Dual Nanoparticle Amplified Surface Plasmon Resonance Detection of Thrombin at Subattomolar Concentrations. *Anal. Chem.* **2014**, *86*, 9824−9829.

(29) Nguyen, A. H.; Lee, J.; Il Choi, H.; Seok Kwak, H.; Jun Sim, S. Fabrication of Plasmon Length-Based Surface Enhanced Raman Scattering for Multiplex Detection on Microfluidic Device. *Biosens. Bioelectron.* **2015**, *70*, 358−365.

(30) Rasheed, P. A.; Sandhyarani, N. A Highly Sensitive DNA Sensor for Attomolar Detection of the BRCA1 Gene: Signal Amplification with Gold Nanoparticle Clusters. *Analyst* **2015**, *140*, 2713−2718.

(31) Chen, H.; Qi, F.; Zhou, H.; Jia, S.; Gao, Y.; Koh, K.; Yin, Y. Fe3O4@Au Nanoparticles as a Means of Signal Enhancement in Surface Plasmon Resonance Spectroscopy for Thrombin Detection. *Sens. Actuators, B* **2015**, *212*, 505−511.

(32) Dreaden, E. C.; Alkilany, A. M.; Huang, X.; Murphy, C. J.; El-Sayed, M. A. The Golden Age: Gold Nanoparticles for Biomedicine. *Chem. Soc. Rev.* **2012**, *41*, 2740−2779.

(33) Jans, H.; Huo, Q. Gold Nanoparticle-Enabled Biological and Chemical Detection and Analysis. *Chem. Soc. Rev.* **2012**, *41*, 2849−2866.

(34) Mody, V.; Siwale, R.; Singh, A.; Mody, H. Introduction to Metallic Nanoparticles. *J. Pharm. BioAllied Sci.* **2010**, *2*, 282.

(35) Lin, H.-Y.; Huang, C.-H.; Lu, S.-H.; Kuo, I.-T.; Chau, L.-K. Direct Detection of Orchid Viruses Using Nanorod-Based Fiber Optic Particle Plasmon Resonance Immunosensor. *Biosens. Bioelectron.* **2014**, *51*, 371−378.

(36) Inci, F.; Filippini, C.; Baday, M.; Ozen, M. O.; Calamak, S.; Durmus, N. G.; Wang, S.; Hanhauser, E.; Hobbs, K. S.; Juillard, F.; et al. Multitarget, Quantitative Nanoplasmonic Electrical Field-Enhanced Resonating Device (NE2RD) for Diagnostics. *Proc. Natl. Acad. Sci. U. S. A.* **2015**, *112*, E4354−E4363.

(37) Wang, X.; Niessner, R.; Tang, D.; Knopp, D. Nanoparticle-Based Immunosensors and Immunoassays for Aflatoxins. *Anal. Chim. Acta* **2016**, *912*, 10−23.

(38) Vilela, D.; González, M. C.; Escarpa, A. Sensing Colorimetric Approaches Based on Gold and Silver Nanoparticles Aggregation: Chemical Creativity behind the Assay. A Review. *Anal. Chim. Acta* **2012**, *751*, 24−43.

(39) Mayilo, S.; Kloster, M. A.; Wunderlich, M.; Lutich, A.; Klar, T. A.; Nichtl, A.; Kürzinger, K.; Stefani, F. D.; Feldmann, J. Long-Range Fluorescence Quenching by Gold Nanoparticles in a Sandwich Immunoassay for Cardiac Troponin T. *Nano Lett.* **2009**, *9*, 4558−4563.

(40) Vaisocherová-Lísalová, H.; Víšová, I.; Ermini, M. L.; Špringer, T.; Song, X. C.; Mrázek, J.; Lamačová, J.; Scott Lynn, N., Jr.; Šedivák, P.; Homola, J. Low-Fouling Surface Plasmon Resonance Biosensor for Multi-Step Detection of Foodborne Bacterial Pathogens in Complex Food Samples. *Biosens. Bioelectron.* **2016**, *80*, 84−90.

(41) Liu, R.; Zhang, Y.; Zhang, S.; Qiu, W.; Gao, Y. Silver Enhancement of Gold Nanoparticles for Biosensing: From Qualitative to Quantitative. *Appl. Spectrosc. Rev.* **2014**, *49*, 121−138.

(42) Wan, J.; Ai, J.; Zhang, Y.; Geng, X.; Gao, Q.; Cheng, Z. Signal-off Impedimetric Immunosensor for the Detection of Escherichia Coli O157:H7. *Sci. Rep.* **2016**, *6*, 19806.

(43) Li, N.; Zhao, P.; Astruc, D. Anisotropic Gold Nanoparticles: Synthesis, Properties, Applications, and Toxicity. *Angew. Chem., Int. Ed.* **2014**, *53*, 1756−1789.

(44) Dinish, U. S.; Balasundaram, G.; Chang, Y.-T.; Olivo, M. Actively Targeted in Vivo Multiplex Detection of Intrinsic Cancer Biomarkers Using Biocompatible SERS Nanotags. *Sci. Rep.* **2015**, *4*, 4075.

(45) Bondarenko, O.; Juganson, K.; Ivask, A.; Kasemets, K.; Mortimer, M.; Kahru, A. Toxicity of Ag, CuO and ZnO Nanoparticles to Selected Environmentally Relevant Test Organisms and Mammalian Cells in Vitro: A Critical Review. *Arch. Toxicol.* **2013**, *87*, 1181−1200.

(46) Turner, A. P. F. Biosensors: Sense and Sensibility. *Chem. Soc. Rev.* **2013**, *42*, 3184.

(47) Nooney, R.; Clifford, A.; LeGuevel, X.; Stranik, O.; McDonagh, C.; MacCraith, B. D. Enhancing the Analytical Performance of Immunoassays That Employ Metal-Enhanced Fluorescence. *Anal. Bioanal. Chem.* **2010**, *396*, 1127−1134.

(48) Liang, A.; Liu, Q.; Wen, G.; Jiang, Z. The Surface-Plasmon-Resonance Effect of Nanogold/Silver and Its Analytical Applications. *TrAC, Trends Anal. Chem.* **2012**, *37*, 32−47.

(49) Li, H.; Xu, D. Silver Nanoparticles as Labels for Applications in Bioassays. *TrAC, Trends Anal. Chem.* **2014**, *61*, 67−73.

(50) Fang, Y. Optical Absorption of Nanoscale Colloidal Silver: Aggregate Band and Adsorbate-Silver Surface Band. *J. Chem. Phys.* **1998**, *108*, 4315−4318.

(51) Austin, L. A.; Mackey, M. A.; Dreaden, E. C.; El-Sayed, M. A. The Optical, Photothermal, and Facile Surface Chemical Properties of Gold and Silver Nanoparticles in Biodiagnostics, Therapy, and Drug Delivery. *Arch. Toxicol.* **2014**, *88*, 1391−1417.

(52) Szymanski, M.; Turner, A. P.F.; Porter, R. Electrochemical Dissolution of Silver Nanoparticles and Its Application in Metal-loimmunoassay. *Electroanalysis* **2010**, *22*, 191−198.

(53) Taton, T. A. Scanometric DNA Array Detection with Nano-particle Probes. *Science* **2000**, *289*, 1757−1760.

(54) Yeh, C.-H.; Hung, C.-Y.; Chang, T. C.; Lin, H.-P.; Lin, Y.-C. An Immunoassay Using Antibody-Gold Nanoparticle Conjugate, Silver Enhancement and Flatbed Scanner. *Microfluid. Nanofluid.* **2009**, *6*, 85−91.

(55) Omidfar, K.; Khorsand, F.; Darziani Azizi, M. New Analytical Applications of Gold Nanoparticles as Label in Antibody Based Sensors. *Biosens. Bioelectron.* **2013**, *43*, 336−347.

(56) Díez, I.; Ras, R. H. A. Fluorescent Silver Nanoclusters. *Nanoscale* **2011**, *3*, 1963.

(57) Singh, A. K.; Kanchanapally, R.; Fan, Z.; Senapati, D.; Ray, P. C. Synthesis of Highly Fluorescent Water-Soluble Silver Nanoparticles for Selective Detection of Pb(ii) at the Parts per Quadrillion (PPQ) Level. *Chem. Commun.* **2012**, *48*, 9047.

(58) Ashenfelter, B. A.; Desireddy, A.; Yau, S. H.; Goodson, T., III; Bigioni, T. P. Fluorescence from Molecular Silver Nanoparticles. *J. Phys. Chem. C* **2015**, *119*, 20728−20734.

(59) Zheng, J.; Ding, Y.; Tian, B.; Wang, Z. L.; Zhuang, X. Luminescent and Raman Active Silver Nanoparticles with Polycrystalline Structure. *J. Am. Chem. Soc.* **2008**, *130*, 10472−10473.

(60) Ulbrich, K.; Holá, K.; Šubr, V.; Bakandritsos, A.; Tuček, J.; Zbořil, R. Targeted Drug Delivery with Polymers and Magnetic Nanoparticles: Covalent and Noncovalent Approaches, Release Control, and Clinical Studies. *Chem. Rev.* **2016**, *116*, 5338−5431.

(61) Huang, J.; Li, Y.; Orza, A.; Lu, Q.; Guo, P.; Wang, L.; Yang, L.; Mao, H. Magnetic Nanoparticle Facilitated Drug Delivery for Cancer Therapy with Targeted and Image-Guided Approaches. *Adv. Funct. Mater.* **2016**, *26*, 3818−3836.

(62) Obaidat, I.; Issa, B.; Haik, Y. Magnetic Properties of Magnetic Nanoparticles for Efficient Hyperthermia. *Nanomaterials* **2015**, *5*, 63−89.

(63) Salunkhe, A. B.; Khot, V. M.; Pawar, S. H. Magnetic Hyperthermia with Magnetic Nanoparticles: A Status Review. *Curr. Top. Med. Chem.* **2014**, *14*, 572−594.

(64) Shin, T.-H.; Choi, Y.; Kim, S.; Cheon, J. Recent Advances in Magnetic Nanoparticle-Based Multi-Modal Imaging. *Chem. Soc. Rev.* **2015**, *44*, 4501−4516.

(65) Busquets, M. A.; Estelrich, J.; Sánchez-Martín, M. J. Nanoparticles in Magnetic Resonance Imaging: From Simple to Dual Contrast Agents. *Int. J. Nanomed.* **2015**, 1727.

115

(66) Govan, J.; Gun'ko, Y. Recent Advances in the Application of Magnetic Nanoparticles as a Support for Homogeneous Catalysts. *Nanomaterials* **2014**, *4*, 222−241.

(67) Pratt, A. Environmental Applications of Magnetic Nanoparticles. *Nanomagnetism: Fundamentals and Applications*; Elsevier: Amsterdam, 2014; p 259.

(68) Barallat, J.; Olivé-Monllau, R.; Gonzalo-Ruiz, J.; Ramírez-Satorras, R.; Muñoz-Pascual, F. X.; Ortega, A. G.; Baldrich, E. Chronoamperometric Magneto Immunosensor for Myeloperoxidase Detection in Human Plasma Based on a Magnetic Switch Produced by 3D Laser Sintering. *Anal. Chem.* **2013**, *85*, 9049−9056.

(69) Jodra, A.; Hervás, M.; López, M. Á.; Escarpa, A. Disposable Electrochemical Magneto Immunosensor for Simultaneous Simplified Calibration and Determination of Ochratoxin A in Coffee Samples. *Sens. Actuators, B* **2015**, *221*, 777−783.

(70) Gan, N.; Du, X.; Cao, Y.; Hu, F.; Li, T.; Jiang, Q. An Ultrasensitive Electrochemical Immunosensor for HIV p24 Based on Fe3O4@SiO2 Nanomagnetic Probes and Nanogold Colloid-Labeled Enzyme−Antibody Copolymer as Signal Tag. *Materials* **2013**, *6*, 1255−1269.

(71) Zhang, X.; Wang, H.; Yang, C.; Du, D.; Lin, Y. Preparation, Characterization of Fe3O4 at TiO2Magnetic Nanoparticles and Their Application for Immunoassay of Biomarker of Exposure to Organophosphorus Pesticides. *Biosens. Bioelectron.* **2013**, *41*, 669−674.

(72) Baniukevic, J.; Hakki Boyaci, I.; Goktug Bozkurt, A.; Tamer, U.; Ramanavicius, A.; Ramanaviciene, A. Magnetic Gold Nanoparticles in SERS-Based Sandwich Immunoassay for Antigen Detection by Well Oriented Antibodies. *Biosens. Bioelectron.* **2013**, *43*, 281−288.

(73) Regiart, M.; Fernández-Baldo, M. A.; Spotorno, V. G.; Bertolino, F. A.; Raba, J. Ultra Sensitive Microfluidic Immunosensor for Determination of Clenbuterol in Bovine Hair Samples Using Electrodeposited Gold Nanoparticles and Magnetic Micro Particles as Bio-Affinity Platform. *Biosens. Bioelectron.* **2013**, *41*, 211−217.

(74) Tang, J.; Hou, L.; Tang, D.; Zhou, J.; Wang, Z.; Li, J.; Chen, G. Magneto-Controlled Electrochemical Immunoassay of Brevetoxin B in Seafood Based on Guanine-Functionalized Graphene Nanoribbons. *Biosens. Bioelectron.* **2012**, *38*, 86−93.

(75) Ding, F. L.; Cheng, Q.; Li, J. F.; Jiang, F. E. Magnetic Nanospheres-Based Electrochemical Immunoassay Amplified by Hyperbranched Polymer Conjugate. *Chin. J. Anal. Chem.* **2012**, *40*, 1514−1518.

(76) Chen, Q.; Lin, J.; Gan, C.; Wang, Y.; Wang, D.; Xiong, Y.; Lai, W.; Li, Y.; Wang, M. A Sensitive Impedance Biosensor Based on Immunomagnetic Separation and Urease Catalysis for Rapid Detection of Listeria mnocytogenes Using an Immobilization-Free Interdigitated Array Microelectrode. *Biosens. Bioelectron.* **2015**, *74*, 504−511.

(77) Ojeda, I.; Moreno-Guzmán, M.; González-Cortés, A.; Yáñez-Sedeño, P.; Pingarrón, J. M. Electrochemical Magnetoimmunosensor for the Ultrasensitive Determination of Interleukin-6 in Saliva and Urine Using Poly-HRP Streptavidin Conjugates as Labels for Signal Amplification. *Anal. Bioanal. Chem.* **2014**, *406*, 6363−6371.

(78) de la Escosura-Muñiz, A.; Plichta, Z.; Horák, D.; Merkoçi, A. Alzheimer's Disease Biomarkers Detection in Human Samples by Efficient Capturing through Porous Magnetic Microspheres and Labelling with Electrocatalytic Gold Nanoparticles. *Biosens. Bioelectron.* **2015**, *67*, 162−169.

(79) Maltez-da Costa, M.; de la Escosura-Muñiz, A.; Nogués, C.; Barrios, L.; Ibáñez, E.; Merkoçi, A. Simple Monitoring of Cancer Cells Using Nanoparticles. *Nano Lett.* **2012**, *12*, 4164−4171.

(80) Yang, H.-W.; Lin, C.-W.; Hua, M.-Y.; Liao, S.-S.; Chen, Y.-T.; Chen, H.-C.; Weng, W.-H.; Chuang, C.-K.; Pang, S.-T.; Ma, C.-C. M. Combined Detection of Cancer Cells and a Tumor Biomarker Using an Immunomagnetic Sensor for the Improvement of Prostate-Cancer Diagnosis. *Adv. Mater.* **2014**, *26*, 3662−3666.

(81) Wu, Z.; Zhou, C.-H.; Chen, J.-J.; Xiong, C.; Chen, Z.; Pang, D.-W.; Zhang, Z.-L. Bifunctional Magnetic Nanobeads for Sensitive Detection of Avian Influenza A (H7N9) Virus Based on Immunomagnetic Separation and Enzyme-Induced Metallization. *Biosens. Bioelectron.* **2015**, *68*, 586−592.

(82) Maltez-da Costa, M.; de la Escosura-Muñiz, A.; Nogués, C.; Barrios, L.; Ibáñez, E.; Merkoçi, A. Simple Monitoring of Cancer Cells Using Nanoparticles. *Nano Lett.* **2012**, *12*, 4164−4171.

(83) Brandão, D.; Liébana, S.; Campoy, S.; Alegret, S.; Isabel Pividori, M. Immunomagnetic Separation of Salmonella with Tailored Magnetic Micro and Nanocarriers. A Comparative Study. *Talanta* **2015**, *143*, 198−204.

(84) Otieno, B. A.; Krause, C. E.; Latus, A.; Chikkaveeraiah, B. V.; Faria, R. C.; Rusling, J. F. On-Line Protein Capture on Magnetic Beads for Ultrasensitive Microfluidic Immunoassays of Cancer Biomarkers. *Biosens. Bioelectron.* **2014**, *53*, 268−274.

(85) Demeritte, T.; Viraka Nellore, B. P.; Kanchanapally, R.; Sinha, S. S.; Pramanik, A.; Chavva, S. R.; Ray, P. C. Hybrid Graphene Oxide Based Plasmonic-Magnetic Multifunctional Nanoplatform for Selective Separation and Label-Free Identification of Alzheimer's Disease Biomarkers. *ACS Appl. Mater. Interfaces* **2015**, *7*, 13693−13700.

(86) Liang, W.; Li, Y.; Zhang, B.; Zhang, Z.; Chen, A.; Qi, D.; Yi, W.; Hu, C. A Novel Microfluidic Immunoassay System Based on Electrochemical Immunosensors: An Application for the Detection of NT-proBNP in Whole Blood. *Biosens. Bioelectron.* **2012**, *31*, 480−485.

(87) Tsai, H. Y.; Gao, B. Z.; Yang, S. F.; Li, C. S.; Fuh, C. B. Detection of Alpha-Fetoprotein in Magnetic Immunoassay of Thin Channels Using Biofunctional Nanoparticles. *J. Nanopart. Res.* **2014**, *16*, 2182.

(88) Luo, Y.; Asiri, A. M.; Zhang, X.; Yang, G.; Du, D.; Lin, Y. A Magnetic Electrochemical Immunosensor for the Detection of Phosphorylated p53 Based on Enzyme Functionalized Carbon Nanospheres with Signal Amplification. *RSC Adv.* **2014**, *4*, 54066−54071.

(89) Cheng, P.; Huang, Z.-G.; Zhuang, Y.; Fang, L.-C.; Huang, H.; Deng, J.; Jiang, L.-L.; Yu, K.-K.; Li, Y.; Zheng, J.-S. A Novel Regeneration-Free E. Coli O157:H7 Amperometric Immunosensor Based on Functionalised Four-Layer Magnetic Nanoparticles. *Sens. Actuators, B* **2014**, *204*, 561−567.

(90) Martín, M.; Salazar, P.; Jiménez, C.; Lecuona, M.; Ramos, M. J.; Ode, J.; Alcoba, J.; Roche, R.; Villalonga, R.; Campuzano, S.; et al. Rapid *Legionella pneumophila* Determination Based on a Disposable Core−shell Fe$_3$O$_4$@poly(dopamine) Magnetic Nanoparticles Immunoplatform. *Anal. Chim. Acta* **2015**, *887*, 51−58.

(91) Wang, Y.; Guo, Z.; Ma, H.; Li, Y.; Cao, W.; Du, B.; Wei, Q. Magnetic Electrode-Based Label-Free Electrochemical Impedance Spectroscopy Immunosensor for Sensitive Detection of Human Malignant Melanoma Markers Using Gold Nanoparticles Functionalized Magnetic Graphene Sheets as Signal Amplifier. *RSC Adv.* **2014**, *4*, 59106−59113.

(92) Ji, L.; Yan, T.; Li, Y.; Gao, J.; Wang, Q.; Hu, L.; Wu, D.; Wei, Q.; Du, B. Preparation of Au-Polydopamine Functionalized Carbon Encapsulated Fe$_3$O$_4$ Magnetic Nanocomposites and Their Application for Ultrasensitive Detection of Carcino-Embryonic Antigen. *Sci. Rep.* **2016**, *6*, 21017.

(93) Sharma, A.; Baral, D.; Rawat, K.; Solanki, P. R.; Bohidar, H. B. Biocompatible Capped Iron Oxide Nanoparticles for *Vibrio cholerae* Detection. *Nanotechnology* **2015**, *26*, 175302.

(94) Yu, S.; Wei, Q.; Du, B.; Wu, D.; Li, H.; Yan, L.; Ma, H.; Zhang, Y. Label-Free Immunosensor for the Detection of Kanamycin Using Ag@Fe$_3$O$_4$ Nanoparticles and Thionine Mixed Graphene Sheet. *Biosens. Bioelectron.* **2013**, *48*, 224−229.

(95) Li, F.; Jiang, L.; Han, J.; Liu, Q.; Dong, Y.; Li, Y.; Wei, Q. A Label-Free Amperometric Immunosensor for the Detection of Carcinoembryonic Antigen Based on Novel Magnetic Carbon and Gold Nanocomposites. *RSC Adv.* **2015**, *5*, 19961−19969.

(96) Zhou, J.; Gan, N.; Li, T.; Zhou, H.; Li, X.; Cao, Y.; Wang, L.; Sang, W.; Hu, F. Ultratrace Detection of C-Reactive Protein by a Piezoelectric Immunosensor Based on Fe$_3$O$_4$@SiO$_2$ Magnetic Capture Nanoprobes and HRP-Antibody Co-Immobilized Nano Gold as Signal Tags. *Sens. Actuators, B* **2013**, *178*, 494−500.

(97) Zhang, X.; Ren, X.; Cao, W.; Li, Y.; Du, B.; Wei, Q. Simultaneous Electrochemical Immunosensor Based on Water-Soluble Polythiophene Derivative and Functionalized Magnetic Material. *Anal. Chim. Acta* **2014**, *845*, 85−91.

116

(98) Orlov, A. V.; Nikitin, M. P.; Bragina, V. A.; Znoyko, S. L.; Zaikina, M. N.; Ksenevich, T. I.; Gorshkov, B. G.; Nikitin, P. I. A New Real-Time Method for Investigation of Affinity Properties and Binding Kinetics of Magnetic Nanoparticles. *J. Magn. Magn. Mater.* **2015**, *380*, 231−235.

(99) Garibo, D.; Campbell, K.; Casanova, A.; de la Iglesia, P.; Fernández-Tejedor, M.; Diogène, J.; Elliott, C. T.; Campàs, M. SPR Immunosensor for the Detection of Okadaic Acid in Mussels Using Magnetic Particles as Antibody Carriers. *Sens. Actuators, B* **2014**, *190*, 822−828.

(100) Liang, R.-P.; Yao, G.-H.; Fan, L.-X.; Qiu, J.-D. Magnetic Fe3O4@Au Composite-Enhanced Surface Plasmon Resonance for Ultrasensitive Detection of Magnetic Nanoparticle-Enriched α-Fetoprotein. *Anal. Chim. Acta* **2012**, *737*, 22−28.

(101) Guo, X. Fe_3O_4@Au Nanoparticles Enhanced Surface Plasmon Resonance for Ultrasensitive Immunoassay. *Sens. Actuators, B* **2014**, *205*, 276−280.

(102) Ge, M.; Wei, C.; Xu, M.; Fang, C.; Yuan, Y.; Gu, R.; Yao, J. Ultra-Sensitive Magnetic Immunoassay of HE4 Based on Surface Enhanced Raman Spectroscopy. *Anal. Methods* **2015**, *7*, 6489−6495.

(103) Ondera, T. J.; Hamme, A. T., II Magnetic-Optical Nanohybrids for Targeted Detection, Separation, and Photothermal Ablation of Drug-Resistant Pathogens. *Analyst* **2015**, *140*, 7902−7911.

(104) Qiu, Y.; Deng, D.; Deng, Q.; Wu, P.; Zhang, H.; Cai, C. Synthesis of Magnetic Fe_3O_4−Au Hybrids for Sensitive SERS Detection of Cancer Cells at Low Abundance. *J. Mater. Chem. B* **2015**, *3*, 4487−4495.

(105) Gao, J.; Guo, Z.; Yu, S.; Su, F.; Ma, H.; Du, B.; Wei, Q.; Pang, X. A Novel Controlled Release System-Based Homogeneous Immuno-assay Protocol for SCCA Using Magnetic Mesoporous Fe_3O_4 as a Nanocontainer and Aminated Polystyrene Microspheres as a Molecular Gate. *Biosens. Bioelectron.* **2015**, *66*, 141−145.

(106) Zhang, B.; Cui, Y.; Liu, B.; Chen, H.; Chen, G.; Tang, D. Cadmium Ion-Doped Magnetic Poly(styrene-Acrylic Acid) Nano-spheres for Sensitive Electrochemical Immunoassay. *Biosens. Bioelectron.* **2012**, *35*, 461−465.

(107) Akter, R.; Kyun Rhee, C.; Aminur Rahman, M. Sensitivity Enhancement of an Electrochemical Immunosensor through the Electrocatalysis of Magnetic Bead-Supported Non-Enzymatic Labels. *Biosens. Bioelectron.* **2014**, *54*, 351−357.

(108) Wu, D.; Ma, H.; Zhang, Y.; Jia, H.; Yan, T.; Wei, Q. Corallite-like Magnetic Fe_3O_4@MnO_2@Pt Nanocomposites as Multiple Signal Amplifiers for the Detection of Carcinoembryonic Antigen. *ACS Appl. Mater. Interfaces* **2015**, *7*, 18786−18793.

(109) Dai, H.; Gong, L.; Zhang, S.; Xu, G.; Li, Y.; Hong, Z.; Lin, Y. All-in-One Bioprobe Devised with Hierarchical-Ordered Magnetic $NiCo_2O_4$ Superstructure for Ultrasensitive Dual-Readout Immunosen-sor for Logic Diagnosis of Tumor Marker. *Biosens. Bioelectron.* **2016**, *77*, 928−935.

(110) Orlov, A. V.; Khodakova, J. A.; Nikitin, M. P.; Shepelyakovskaya, A. O.; Brovko, F. A.; Laman, A. G.; Grishin, E. V.; Nikitin, P. I. Magnetic Immunoassay for Detection of Staphylococcal Toxins in Complex Media. *Anal. Chem.* **2013**, *85*, 1154−1163.

(111) Iijima, S. Helical Microtubules of Graphitic Carbon. *Nature* **1991**, *354*, 56−58.

(112) Wilder, J. W. G.; Venema, L. C.; Rinzler, A. G.; Smalley, R. E.; Dekker, C. Electronic Structure of Atomically Resolved Carbon Nanotubes. *Nature* **1998**, *391*, 59−62.

(113) Ramnani, P.; Saucedo, N. M.; Mulchandani, A. Carbon Nanomaterial-Based Electrochemical Biosensors for Label-Free Sensing of Environmental Pollutants. *Chemosphere* **2016**, *143*, 85−98.

(114) Kong, J.; Soh, H. T.; Cassell, A. M.; Quate, C. F.; Dai, H. Synthesis of Individual Single-Walled Carbon Nanotubes on Patterned Silicon Wafers. *Nature* **1998**, *395*, 878−881.

(115) Guo, T.; Nikolaev, P.; Thess, A.; Colbert, D. T.; Smalley, R. E. Catalytic Growth of Single-Walled Manotubes by Laser Vaporization. *Chem. Phys. Lett.* **1995**, *243*, 49−54.

(116) Oliveira, O. N.; Iost, R. M.; Siqueira, J. R.; Crespilho, F. N.; Caseli, L. Nanomaterials for Diagnosis: Challenges and Applications in Smart Devices Based on Molecular Recognition. *ACS Appl. Mater. Interfaces* **2014**, *6*, 14745−14766.

(117) Baughman, R. H. Carbon Nanotubes–the Route Toward Applications. *Science* **2002**, *297*, 787−792.

(118) Jiang, L.; Han, J.; Li, F.; Gao, J.; Li, Y.; Dong, Y.; Wei, Q. A Sandwich-Type Electrochemical Immunosensor Based on Multiple Signal Amplification for α-Fetoprotein Labeled by Platinum Hybrid Multiwalled Carbon Nanotubes Adhered Copper Oxide. *Electrochim. Acta* **2015**, *160*, 7−14.

(119) Kumar, S.; Ahlawat, W.; Kumar, R.; Dilbaghi, N. Graphene, Carbon Nanotubes, Zinc Oxide and Gold as Elite Nanomaterials for Fabrication of Biosensors for Healthcare. *Biosens. Bioelectron.* **2015**, *70*, 498−503.

(120) Chang, Y.-T.; Huang, J.-H.; Tu, M.-C.; Chang, P.; Yew, T.-R. Flexible Direct-Growth CNT Biosensors. *Biosens. Bioelectron.* **2013**, *41*, 898−902.

(121) Huang, J.-H.; Hong, Y.-J.; Chang, Y.-T.; Chang, P.; Yew, T.-R. Carbon Nanotubes for Highly Sensitive Colorimetric Immunoassay Biosensor. *J. Mater. Chem. B* **2013**, *1*, 5389.

(122) Tu, M.-C.; Chen, H.-Y.; Wang, Y.; Moochhala, S. M.; Alagappan, P.; Liedberg, B. Immunosensor Based on Carbon Nanotube/manganese Dioxide Electrochemical Tags. *Anal. Chim. Acta* **2015**, *853*, 228−233.

(123) Balasubramanian, K.; Burghard, M. Electrochemically Function-alized Carbon Nanotubes for Device Applications. *J. Mater. Chem.* **2008**, *18*, 3071.

(124) Feng, T.; Wang, Y.; Qiao, X. Recent Advances of Carbon Nanotubes-Based Electrochemical Immunosensors for the Detection of Protein Cancer Biomarkers. *Electroanalysis* **2017**, *29*, 662−675.

(125) Lim, W. Q.; Gao, Z. Metal Oxide Nanoparticles in Electro-analysis. *Electroanalysis* **2015**, *27*, 2074−2090.

(126) Sánchez-Tirado, E.; Salvo, C.; González-Cortés, A.; Yáñez-Sedeño, P.; Langa, F.; Pingarrón, J. M. Electrochemical Immunosensor for Simultaneous Determination of Interleukin-1 Beta and Tumor Necrosis Factor Alpha in Serum and Saliva Using Dual Screen Printed Electrodes Modified with Functionalized Double−walled Carbon Nanotubes. *Anal. Chim. Acta* **2017**, *959*, 66−73.

(127) Green, A. A.; Hersam, M. C. Properties and Application of Double-Walled Carbon Nanotubes Sorted by Outer-Wall Electronic Type. *ACS Nano* **2011**, *5*, 1459−1467.

(128) Moore, K. E.; Flavel, B. S.; Ellis, A. V.; Shapter, J. G. Comparison of Double-Walled with Single-Walled Carbon Nanotube Electrodes by Electrochemistry. *Carbon* **2011**, *49*, 2639−2647.

(129) Liu, N.; Nie, D.; Tan, Y.; Zhao, Z.; Liao, Y.; Wang, H.; Sun, C.; Wu, A. An Ultrasensitive Amperometric Immunosensor for Zearale-nones Based on Oriented Antibody Immobilization on a Glassy Carbon Electrode Modified with MWCNTs and AuPt Nanoparticles. *Micro-chim. Acta* **2017**, *184*, 147−153.

(130) Novoselov, K. S. Electric Field Effect in Atomically Thin Carbon Films. *Science* **2004**, *306*, 666−669.

(131) Pumera, M. Graphene in Biosensing. *Mater. Today* **2011**, *14*, 308−315.

(132) Wang, Z.; Dai, Z. Carbon Nanomaterial-Based Electrochemical Biosensors: An Overview. *Nanoscale* **2015**, *7*, 6420−6431.

(133) Loh, K. P.; Bao, Q.; Eda, G.; Chhowalla, M. Graphene Oxide as a Chemically Tunable Platform for Optical Applications. *Nat. Chem.* **2010**, *2*, 1015−1024.

(134) Hummers, W. S.; Offeman, R. E. Preparation of Graphitic Oxide. *J. Am. Chem. Soc.* **1958**, *80*, 1339−1339.

(135) Stankovich, S.; Dikin, D. A.; Piner, R. D.; Kohlhaas, K. A.; Kleinhammes, A.; Jia, Y.; Wu, Y.; Nguyen, S. T.; Ruoff, R. S. Synthesis of Graphene-Based Nanosheets via Chemical Reduction of Exfoliated Graphite Oxide. *Carbon* **2007**, *45*, 1558−1565.

(136) McAllister, M. J.; Li, J.-L.; Adamson, D. H.; Schniepp, H. C.; Abdala, A. A.; Liu, J.; Herrera-Alonso, M.; Milius, D. L.; Car, R.; Prud'homme, R. K.; Aksay, I. A. Single Sheet Functionalized Graphene by Oxidation and Thermal Expansion of Graphite. *Chem. Mater.* **2007**, *19*, 4396−4404.

(137) Zhou, M.; Zhai, Y.; Dong, S. Electrochemical Sensing and Biosensing Platform Based on Chemically Reduced Graphene Oxide. *Anal. Chem.* **2009**, *81*, 5603−5613.

117

(138) Mattevi, C.; Kim, H.; Chhowalla, M. A Review of Chemical Vapour Deposition of Graphene on Copper. *J. Mater. Chem.* **2011**, *21*, 3324−3334.

(139) Han, J.; Ma, J.; Ma, Z. One-Step Synthesis of Graphene oxide−thionine−Au Nanocomposites and Its Application for Electrochemical Immunosensing. *Biosens. Bioelectron.* **2013**, *47*, 243−247.

(140) Han, J.; Ma, J.; Ma, Z. One-Step Synthesis of Graphene oxide−thionine−Au Nanocomposites and Its Application for Electrochemical Immunosensing. *Biosens. Bioelectron.* **2013**, *47*, 243−247.

(141) Hou, L.; Cui, Y.; Xu, M.; Gao, Z.; Huang, J.; Tang, D. Graphene Oxide-Labeled Sandwich-Type Impedimetric Immunoassay with Sensitive Enhancement Based on Enzymatic 4-Chloro-1-Naphthol Oxidation. *Biosens. Bioelectron.* **2013**, *47*, 149−156.

(142) Lee, J. S.; Joung, H.-A.; Kim, M.-G.; Park, C. B. Graphene-Based Chemiluminescence Resonance Energy Transfer for Homogeneous Immunoassay. *ACS Nano* **2012**, *6*, 2978−2983.

(143) Liu, Y.; Luo, M.; Xiang, X.; Chen, C.; Ji, X.; Chen, L.; He, Z. A Graphene Oxide and Exonuclease-Aided Amplification Immuno-Sensor for Antigen Detection. *Chem. Commun.* **2014**, *50*, 2679.

(144) Yáñez-Sedeño, P.; González-Cortés, A.; Agüí, L.; Pingarrón, J. M. Uncommon Carbon Nanostructures for the Preparation of Electrochemical Immunosensors. *Electroanalysis* **2016**, *28*, 1679−1691.

(145) Pilehvar, S.; De Wael, K. Recent Advances in Electrochemical Biosensors Based on Fullerene-C60 Nano-Structured Platforms. *Biosensors* **2015**, *5*, 712−735.

(146) Afreen, S.; Muthoosamy, K.; Manickam, S.; Hashim, U. Functionalized Fullerene (C60) as a Potential Nanomediator in the Fabrication of Highly Sensitive Biosensors. *Biosens. Bioelectron.* **2015**, *63*, 354−364.

(147) Han, J.; Zhuo, Y.; Chai, Y.-Q.; Xiang, Y.; Yuan, R. New Type of Redox Nanoprobe: C60-Based Nanomaterial and Its Application in Electrochemical Immunoassay for Doping Detection. *Anal. Chem.* **2015**, *87*, 1669−1675.

(148) Shi, L.; Liu, X.; Niu, W.; Li, H.; Han, S.; Chen, J.; Xu, G. Hydrogen Peroxide Biosensor Based on Direct Electrochemistry of Soybean Peroxidase Immobilized on Single-Walled Carbon Nanohorn Modified Electrode. *Biosens. Bioelectron.* **2009**, *24*, 1159−1163.

(149) Liu, F.; Xiang, G.; Yuan, R.; Chen, X.; Luo, F.; Jiang, D.; Huang, S.; Li, Y.; Pu, X. Procalcitonin Sensitive Detection Based on Graphene−gold Nanocomposite Film Sensor Platform and Single-Walled Carbon Nanohorns/hollow Pt Chains Complex as Signal Tags. *Biosens. Bioelectron.* **2014**, *60*, 210−217.

(150) Wang, Y.; Hu, A. Carbon Quantum Dots: Synthesis, Properties and Applications. *J. Mater. Chem. C* **2014**, *2*, 6921.

(151) Xu, X.; Ray, R.; Gu, Y.; Ploehn, H. J.; Gearheart, L.; Raker, K.; Scrivens, W. A. Electrophoretic Analysis and Purification of Fluorescent Single-Walled Carbon Nanotube Fragments. *J. Am. Chem. Soc.* **2004**, *126*, 12736−12737.

(152) Lim, S. Y.; Shen, W.; Gao, Z. Carbon Quantum Dots and Their Applications. *Chem. Soc. Rev.* **2015**, *44*, 362−381.

(153) Zou, F.; Zhou, H.; Tan, T. V.; Kim, J.; Koh, K.; Lee, J. Dual-Mode SERS-Fluorescence Immunoassay Using Graphene Quantum Dot Labeling on One-Dimensional Aligned Magnetoplasmonic Nanoparticles. *ACS Appl. Mater. Interfaces* **2015**, *7*, 12168−12175.

(154) Wang, Z.; Dai, Z. Carbon Nanomaterial-Based Electrochemical Biosensors: An Overview. *Nanoscale* **2015**, *7*, 6420−6431.

(155) Zhang, X.; Du, X. Carbon Nanodot-Decorated Ag@SiO2Nanoparticles for Fluorescence and Surface-Enhanced Raman Scattering Immunoassays. *ACS Appl. Mater. Interfaces* **2016**, *8*, 1033−1040.

(156) Liu, F.; Ge, S.; Su, M.; Song, X.; Yan, M.; Yu, J. Electrochemiluminescence Device for in-Situ and Accurate Determination of CA153 at the MCF-7 Cell Surface Based on Graphene Quantum Dots Loaded Surface Villous Au Nanocage. *Biosens. Bioelectron.* **2015**, *71*, 286−293.

(157) Alivisatos, P. The Use of Nanocrystals in Biological Detection. *Nat. Biotechnol.* **2004**, *22*, 47−52.

(158) Wu, P.; Yan, X.-P. Doped Quantum Dots for Chemo/biosensing and Bioimaging. *Chem. Soc. Rev.* **2013**, *42*, 5489.

(159) Burda, C.; Chen, X.; Narayanan, R.; El-Sayed, M. A. Chemistry and Properties of Nanocrystals of Different Shapes. *Chem. Rev.* **2005**, *105*, 1025−1102.

(160) Resch-Genger, U.; Grabolle, M.; Cavaliere-Jaricot, S.; Nitschke, R.; Nann, T. Quantum Dots Versus Organic Dyes as Fluorescent Labels. *Nat. Methods* **2008**, *5*, 763−775.

(161) Petryayeva, E.; Algar, W. R.; Medintz, I. L. Quantum Dots in Bioanalysis: A Review of Applications Across Various Platforms for Fluorescence Spectroscopy and Imaging. *Appl. Spectrosc.* **2013**, *67*, 215−252.

(162) Han, M.; Gao, X.; Su, J. Z.; Nie, S. *Nat. Biotechnol.* **2001**, *19*, 631−635.

(163) Peng, Z. A.; Peng, X. Formation of High-Quality CdTe, CdSe, and CdS Nanocrystals Using CdO as Precursor. *J. Am. Chem. Soc.* **2001**, *123*, 183−184.

(164) Medintz, I. L.; Uyeda, H. T.; Goldman, E. R.; Mattoussi, H. Quantum Dot Bioconjugates for Imaging, Labelling and Sensing. *Nat. Mater.* **2005**, *4*, 435−446.

(165) Yu, W. W.; Chang, E.; Drezek, R.; Colvin, V. L. Water-Soluble Quantum Dots for Biomedical Applications. *Biochem. Biophys. Res. Commun.* **2006**, *348*, 781−786.

(166) Lees, E. E.; Nguyen, T.-L.; Clayton, A. H. A.; Mulvaney, P. The Preparation of Colloidally Stable, Water-Soluble, Biocompatible, Semiconductor Nanocrystals with a Small Hydrodynamic Diameter. *ACS Nano* **2009**, *3*, 1121−1128.

(167) Speranskaya, E. S.; Beloglazova, N. V.; Lenain, P.; De Saeger, S.; Wang, Z.; Zhang, S.; Hens, Z.; Knopp, D.; Niessner, R.; Potapkin, D. V.; et al. Polymer-Coated Fluorescent CdSe-Based Quantum Dots for Application in Immunoassay. *Biosens. Bioelectron.* **2014**, *53*, 225−231.

(168) Sun, B.; Chen, L.; Xu, Y.; Liu, M.; Yin, H.; Ai, S. Ultrasensitive Photoelectrochemical Immunoassay of Indole-3-Acetic Acid Based on the MPA Modified CdS/RGO Nanocomposites Decorated ITO Electrode. *Biosens. Bioelectron.* **2014**, *51*, 164−169.

(169) Fan, D.; Wu, D.; Cui, J.; Chen, Y.; Ma, H.; Liu, Y.; Wei, Q.; Du, B. An Ultrasensitive Label-Free Immunosensor Based on CdS Sensitized Fe−TiO2 with High Visible-Light Photoelectrochemical Activity. *Biosens. Bioelectron.* **2015**, *74*, 843−848.

(170) Gao, X.; Cui, Y.; Levenson, R. M.; Chung, L. W. K.; Nie, S. In Vivo Cancer Targeting and Imaging with Semiconductor Quantum Dots. *Nat. Biotechnol.* **2004**, *22*, 969−976.

(171) Rakovich, T. Y.; Mahfoud, O. K.; Mohamed, B. M.; Prina-Mello, A.; Crosbie-Staunton, K.; Van Den Broeck, T.; De Kimpe, L.; Sukhanova, A.; Baty, D.; Rakovich, A.; et al. Highly Sensitive Single Domain Antibody−Quantum Dot Conjugates for Detection of HER2 Biomarker in Lung and Breast Cancer Cells. *ACS Nano* **2014**, *8*, 5682−5695.

(172) Hu, J.; Zhang, Z.-L.; Wen, C.-Y.; Tang, M.; Wu, L.-L.; Liu, C.; Zhu, L.; Pang, D.-W. Sensitive and Quantitative Detection of C-Reaction Protein Based on Immunofluorescent Nanospheres Coupled with Lateral Flow Test Strip. *Anal. Chem.* **2016**, *88*, 6577−6584.

(173) Zhang, X.; Tan, X.; Zhang, B.; Miao, W.; Zou, G. Spectrum-Based Electrochemiluminescent Immunoassay with Ternary CdZnSe Nanocrystals as Labels. *Anal. Chem.* **2016**, *88*, 6947−6953.

(174) Qiu, Y.; Wen, Q.; Zhang, L.; Yang, P. Label-Free and Dynamic Evaluation of Cell-Surface Epidermal Growth Factor Receptor Expression via an Electrochemiluminescence Cytosensor. *Talanta* **2016**, *150*, 286−295.

(175) Zhang, X.; Zhang, B.; Miao, W.; Zou, G. Molecular-Counting-Free and Electrochemiluminescent Single-Molecule Immunoassay with Dual-Stabilizers-Capped CdSe Nanocrystals as Labels. *Anal. Chem.* **2016**, *88*, 5482−5488.

(176) Tasso, M.; Singh, M. K.; Giovanelli, E.; Fragola, A.; Loriette, V.; Regairaz, M.; Dautry, F.; Treussart, F.; Lenkei, Z.; Lequeux, N.; et al. Oriented Bioconjugation of Unmodified Antibodies to Quantum Dots Capped with Copolymeric Ligands as Versatile Cellular Imaging Tools. *ACS Appl. Mater. Interfaces* **2015**, *7*, 26904−26913.

(177) Haase, M.; Schäfer, H. Upconverting Nanoparticles. *Angew. Chem., Int. Ed.* **2011**, *50*, 5808−5829.

118

(178) Auzel, F. Upconversion and Anti-Stokes Processes with f and d Ions in Solids. *Chem. Rev.* **2004**, *104*, 139−174.

(179) Chamarro, M. A.; Cases, R. Energy up-Conversion in (Yb, Ho) and (Yb, Tm) Doped Fluorohafnate Glasses. *J. Lumin.* **1988**, *42*, 267−274.

(180) Li, X.; Zhang, F.; Zhao, D. Lab on Upconversion Nanoparticles: Optical Properties and Applications Engineering via Designed Nanostructure. *Chem. Soc. Rev.* **2015**, *44*, 1346−1378.

(181) Sedlmeier, A.; Gorris, H. H. Surface Modification and Characterization of Photon-Upconverting Nanoparticles for Bioanalytical Applications. *Chem. Soc. Rev.* **2015**, *44*, 1526−1560.

(182) Zijlmans, H. J. M. A. A.; Bonnet, J.; Burton, J.; Kardos, K.; Vail, T.; Niedbala, R. S.; Tanke, H. J. Detection of Cell and Tissue Surface Antigens Using Up-Converting Phosphors: A New Reporter Technology. *Anal. Biochem.* **1999**, *267*, 30−36.

(183) Van de Rijke, F.; Zijlmans, H.; Li, S.; Vail, T.; Raap, A. K.; Niedbala, R. S.; Tanke, H. J. Up-Converting Phosphor Reporters for Nucleic Acid Microarrays. *Nat. Biotechnol.* **2001**, *19*, 273−276.

(184) Päkkilä, H.; Ylihärsilä, M.; Lahtinen, S.; Hattara, L.; Salminen, N.; Arppe, R.; Lastusaari, M.; Saviranta, P.; Soukka, T. Quantitative Multianalyte Microarray Immunoassay Utilizing Upconverting Phosphor Technology. *Anal. Chem.* **2012**, *84*, 8628−8634.

(185) Huang, P.; Zheng, W.; Zhou, S.; Tu, D.; Chen, Z.; Zhu, H.; Li, R.; Ma, E.; Huang, M.; Chen, X. Lanthanide-Doped LiLuF₄ Upconversion Nanoprobes for the Detection of Disease Biomarkers. *Angew. Chem., Int. Ed.* **2014**, *53*, 1252−1257.

(186) Sirkka, N.; Lyytikäinen, A.; Savukoski, T.; Soukka, T. Upconverting Nanophosphors as Reporters in a Highly Sensitive Heterogeneous Immunoassay for Cardiac Troponin I. *Anal. Chim. Acta* **2016**, *925*, 82−87.

(187) Wu, S.; Duan, N.; Zhu, C.; Ma, X.; Wang, M.; Wang, Z. Magnetic Nanobead-Based Immunoassay for the Simultaneous Detection of Aflatoxin B1 and Ochratoxin A Using Upconversion Nanoparticles as Multicolor Labels. *Biosens. Bioelectron.* **2011**, *30*, 35−42.

(188) Arppe, R.; Mattsson, L.; Korpi, K.; Blom, S.; Wang, Q.; Riuttamäki, T.; Soukka, T. Homogeneous Assay for Whole Blood Folate Using Photon Upconversion. *Anal. Chem.* **2015**, *87*, 1782−1788.

(189) Corstjens, P. L. A. M.; van Lieshout, L.; Zuiderwijk, M.; Kornelis, D.; Tanke, H. J.; Deelder, A. M.; van Dam, G. J. Up-Converting Phosphor Technology-Based Lateral Flow Assay for Detection of Schistosoma Circulating Anodic Antigen in Serum. *J. Clin. Microbiol.* **2008**, *46*, 171−176.

(190) Hlaváček, A.; Farka, Z.; Hübner, M.; Horňáková, V.; Němeček, D.; Niessner, R.; Skládal, P.; Knopp, D.; Gorris, H. H. Competitive Upconversion-Linked Immunosorbent Assay for the Sensitive Detection of Diclofenac. *Anal. Chem.* **2016**, *88*, 6011−6017.

(191) Li, C.; Zuo, J.; Li, Q.; Chang, Y.; Zhang, Y.; Tu, L.; Liu, X.; Xue, B.; Zhao, H.; Zhang, H.; Kong, X. One-Step in Situ Solid-Substrate-Based Whole Blood Immunoassay Based on FRET Between Upconversion and Gold Nanoparticles. *Biosens. Bioelectron.* **2017**, *92*, 335−341.

(192) Zhou, J.; Sun, Y.; Du, X.; Xiong, L.; Hu, H.; Li, F. Dual-Modality in Vivo Imaging Using Rare-Earth Nanocrystals with Near-Infrared to Near-Infrared (NIR-to-NIR) Upconversion Luminescence and Magnetic Resonance Properties. *Biomaterials* **2010**, *31*, 3287−3295.

(193) Liu, Q.; Yang, T.; Feng, W.; Li, F. Blue-Emissive Upconversion Nanoparticles for Low-Power-Excited Bioimaging in Vivo. *J. Am. Chem. Soc.* **2012**, *134*, 5390−5397.

(194) Wang, M.; Mi, C.-C.; Wang, W.-X.; Liu, C.-H.; Wu, Y.-F.; Xu, Z.-R.; Mao, C.-B.; Xu, S.-K. Immunolabeling and NIR-Excited Fluorescent Imaging of HeLa Cells by Using NaYF₄:Yb,Er Upconversion Nanoparticles. *ACS Nano* **2009**, *3*, 1580−1586.

(195) Hu, J.; Zhang, Z.-L.; Wen, C.-Y.; Tang, M.; Wu, L.-L.; Liu, C.; Zhu, L.; Pang, D.-W. Sensitive and Quantitative Detection of C-Reaction Protein Based on Immunofluorescent Nanospheres Coupled with Lateral Flow Test Strip. *Anal. Chem.* **2016**, *88*, 6577−6584.

(196) Srinivasan, K.; Thiruppathiraja, C.; Subramanian, K.; Dinakaran, K. Sensitive Detection of C. Parvum Using near Infrared Emitting

(197) Hu, R.-R.; Yin, Z.-Z.; Zeng, Y.-B.; Zhang, J.; Liu, H.-Q.; Shao, Y.; Ren, S.-B.; Li, L. A Novel Biosensor for Escherichia Coli O157:H7 Based on Fluorescein-Releasable Biolabels. *Biosens. Bioelectron.* **2016**, *78*, 31−36.

(198) Wei, W.; Wei, M.; Liu, S. Silica Nanoparticles as a Carrier for Signal Amplification. *Reviews in Analytical Chemistry*; De Gruyter: Berlin, 2012; Vol. *31*.

(199) Xie, Q.; Weng, X.; Lu, L.; Lin, Z.; Xu, X.; Fu, C. A Sensitive Fluorescent Sensor for Quantification of Alpha-Fetoprotein Based on Immunosorbent Assay and Click Chemistry. *Biosens. Bioelectron.* **2016**, *77*, 46−50.

(200) Bhatnagar, D.; Kumar, V.; Kumar, A.; Kaur, I. Graphene Quantum Dots FRET Based Sensor for Early Detection of Heart Attack in Human. *Biosens. Bioelectron.* **2016**, *79*, 495−499.

(201) Huang, X.; Zhan, S.; Xu, H.; Meng, X.; Xiong, Y.; Chen, X. Ultrasensitive Fluorescence Immunoassay for Detection of Ochratoxin A Using Catalase-Mediated Fluorescence Quenching of CdTe QDs. *Nanoscale* **2016**, *8*, 9390−9397.

(202) Cywinski, P. J.; Hammann, T.; Hühn, D.; Parak, W. J.; Hildebrandt, N.; Löhmannsröben, H.-G. Europium-Quantum Dot Nanobioconjugates as Luminescent Probes for Time-Gated Biosensing. *J. Biomed. Opt.* **2014**, *19*, 101506.

(203) Hildebrandt, N.; Wegner, K. D.; Algar, W. R. Luminescent Terbium Complexes: Superior Förster Resonance Energy Transfer Donors for Flexible and Sensitive Multiplexed Biosensing. *Coord. Chem. Rev.* **2014**, *273−274*, 125−138.

(204) Jo, E.-J.; Mun, H.; Kim, M.-G. Homogeneous Immunosensor Based on Luminescence Resonance Energy Transfer for Glycated Hemoglobin Detection Using Upconversion Nanoparticles. *Anal. Chem.* **2016**, *88*, 2742−2746.

(205) Tao, L.; Zhang, C.; Zhang, J.; Sun, Y.; Li, X.; Yan, K.; Jin, B.; Zhang, Z.; Yang, K. Sensitive Chemiluminescence Immunoassay for Staphylococcal Enterotoxin C1 Based on the Use of Dye-Encapsulated Mesoporous Silica Nanoparticles. *Microchim. Acta* **2016**, *183*, 2163−2168.

(206) Richter, M. M. Electrochemiluminescence (ECL). *Chem. Rev.* **2004**, *104*, 3003−3036.

(207) Li, L.; Chen, Y.; Zhu, J.-J. Recent Advances in Electrochemiluminescence Analysis. *Anal. Chem.* **2017**, *89*, 358−371.

(208) Deng, S.; Ju, H. Electrogenerated Chemiluminescence of Nanomaterials for Bioanalysis. *Analyst* **2013**, *138*, 43−61.

(209) Zhang, X.; Zhang, B.; Miao, W.; Zou, G. Molecular-Counting-Free and Electrochemiluminescent Single-Molecule Immunoassay with Dual-Stabilizers-Capped CdSe Nanocrystals as Labels. *Anal. Chem.* **2016**, *88*, 5482−5488.

(210) Gan, N.; Zhou, J.; Xiong, P.; Li, T.; Jiang, S.; Cao, Y.; Jiang, Q. An Ultrasensitive Electrochemiluminescence Immunoassay for Carbohydrate Antigen 19−9 in Serum Based on Antibody Labeled Fe₃O₄ Nanoparticles as Capture Probes and Graphene/CdTe Quantum Dot Bionanoconjugates as Signal Amplifiers. *Int. J. Mol. Sci.* **2013**, *14*, 10397−10411.

(211) Guo, Z.; Hao, T.; Du, S.; Chen, B.; Wang, Z.; Li, X.; Wang, S. Multiplex Electrochemiluminescence Immunoassay of Two Tumor Markers Using Multicolor Quantum Dots as Labels and Graphene As Conductingbridge. *Biosens. Bioelectron.* **2013**, *44*, 101−107.

(212) Zhu, M.; Tang, Y.; Wen, Q.; Li, J.; Yang, P. Dynamic Evaluation of Cell-Secreted Interferon Gamma in Response to Drug Stimulation via a Sensitive Electro-Chemiluminescence Immunosensor Based on a Glassy Carbon Electrode Modified with Graphene Oxide, Polyaniline Nanofibers, Magnetic Beads, and Gold Nanoparticles. *Microchim. Acta* **2016**, *183*, 1739−1748.

(213) Zhang, S.; Zang, L.; Zhang, X.; Dai, H.; Xu, G.; Zhang, Q.; Yang, C.; Lin, Y. Signal-on Electrochemiluminescent Immunosensor Based on Poly(amidoamine) Dendrimer Functionalized Carbon Nanodots Amplification for Ultrasensitive Detection of α-Fetoprotein. *Electrochim. Acta* **2016**, *196*, 67−74.

Ag₂S@silica Core−Shell Nanospheres. *RSC Adv.* **2014**, *4*, 62399−62403.

119

(214) Sha, Y.; Zhang, X.; Li, W.; Wu, W.; Wang, S.; Guo, Z.; Zhou, J.; Su, X. A Label-Free Multi-Functionalized Graphene Oxide Based Electrochemiluminscence Immunosensor for Ultrasensitive and Rapid Detection of Vibrio Parahaemolyticus in Seawater and Seafood. *Talanta* **2016**, *147*, 220−225.

(215) Zhang, H.; Han, Z.; Wang, X.; Li, F.; Cui, H.; Yang, D.; Bian, Z. Sensitive Immunosensor for N-Terminal Pro-Brain Natriuretic Peptide Based on N-(Aminobutyl)-N-(Ethylisoluminol)-Functionalized Gold Nanodots/Multiwalled Carbon Nanotube Electrochemiluminescence Nanointerface. *ACS Appl. Mater. Interfaces* **2015**, *7*, 7599−7604.

(216) Lv, X.; Li, Y.; Yan, T.; Pang, X.; Cao, W.; Du, B.; Wu, D.; Wei, Q. Electrochemiluminescence Modified Electrodes Based on RuSi@ Ru(bpy)$_3^{2+}$ Loaded with Gold Functioned Nanoporous CO/Co$_3$O$_4$ for Detection of Mycotoxin Deoxynivalenol. *Biosens. Bioelectron.* **2015**, *70*, 28−33.

(217) Liu, M.; Ye, Y.; Yao, C.; Zhao, W.; Huang, X. Mn2+-Doped NaYF4:Yb/Er Upconversion Nanoparticles with Amplified Electrogenerated Chemiluminescence for Tumor Biomarker Detection. *J. Mater. Chem. B* **2014**, *2*, 6626−6633.

(218) Cai, F.; Zhu, Q.; Zhao, K.; Deng, A.; Li, J. Multiple Signal Amplified Electrochemiluminescent Immunoassay for Hg2+Using Graphene-Coupled Quantum Dots and Gold Nanoparticles-Labeled Horseradish Peroxidase. *Environ. Sci. Technol.* **2015**, *49*, 5013−5020.

(219) Yang, M.; Chen, Y.; Xiang, Y.; Yuan, R.; Chai, Y. In Situ Energy Transfer Quenching of Quantum Dot Electrochemiluminescence for Sensitive Detection of Cancer Biomarkers. *Biosens. Bioelectron.* **2013**, *50*, 393−398.

(220) Zhou, J.; Han, T.; Ma, H.; Yan, T.; Pang, X.; Li, Y.; Wei, Q. A Novel Electrochemiluminescent Immunosensor Based on the Quenching Effect of Aminated Graphene on Nitrogen-Doped Carbon Quantum Dots. *Anal. Chim. Acta* **2015**, *889*, 82−89.

(221) Zhuo, Y.; Han, J.; Tang, L.; Liao, N.; Gui, G.-F.; Chai, Y.-Q.; Yuan, R. Quenching of the Emission of Peroxydisulfate System by Ferrocene Functionalized Chitosan Nanoparticles: A Sensitive "signal Off" Electrochemiluminescence Immunosensor. *Sens. Actuators, B* **2014**, *192*, 791−795.

(222) Wang, J.-X.; Zhuo, Y.; Zhou, Y.; Wang, H.-J.; Yuan, R.; Chai, Y.-Q. Ceria Doped Zinc Oxide Nanoflowers Enhanced Luminol-Based Electrochemiluminescence Immunosensor for Amyloid-β Detection. *ACS Appl. Mater. Interfaces* **2016**, *8*, 12968−12975.

(223) Wang, J.-X.; Zhuo, Y.; Zhou, Y.; Yuan, R.; Chai, Y.-Q. Electrochemiluminescence Immunosensor Based on Multifunctional Luminol-Capped AuNPs@Fe$_3$O$_4$ Nanocomposite for the Detection of Mucin-1. *Biosens. Bioelectron.* **2015**, *71*, 407−413.

(224) Li, J.; Xu, Q.; Fu, C.; Zhang, Y. A Dramatically Enhanced Electrochemiluminescence Assay for CA125 Based on Dendrimer Multiply Labeled Luminol on Fe$_3$O$_4$ Nanoparticles. *Sens. Actuators, B* **2013**, *185*, 146−153.

(225) Zhou, L.; Huang, J.; Yu, B.; Liu, Y.; You, T. A Novel Electrochemiluminescence Immunosensor for the Analysis of HIV-1 p24 Antigen Based on P-RGO@Au@Ru-SiO$_2$Composite. *ACS Appl. Mater. Interfaces* **2015**, *7*, 24438−24445.

(226) Zhou, Y.; Zhuo, Y.; Liao, N.; Chai, Y.; Yuan, R. Ultrasensitive Electrochemiluminescent Detection of Cardiac Troponin I Based on a Self-Enhanced Ru(II) Complex. *Talanta* **2014**, *129*, 219−226.

(227) Zhou, H.; Liu, J.; Zhang, S. Quantum Dot-Based Photoelectric Conversion for Biosensing Applications. *TrAC, Trends Anal. Chem.* **2015**, *67*, 56−73.

(228) Lisdat, F.; Schäfer, D.; Kapp, A. Quantum Dots on Electrodes—new Tools for Bioelectroanalysis. *Anal. Bioanal. Chem.* **2013**, *405*, 3739−3752.

(229) Sun, G.; Yang, H.; Ma, C.; Zhang, Y.; Yu, J.; He, W.; Song, X. Application of CuS-Functionalized ZnO Nanoflakes for a Paper-Based Photoelectrochemical Immunoassay Using an in Situ Electron Donor Producing Strategy. *New J. Chem.* **2015**, *39*, 7012−7018.

(230) Sun, G.; Wang, P.; Zhu, P.; Ge, L.; Ge, S.; Yan, M.; Song, X.; Yu, J. A near-Infrared Light Photoelectrochemical Immunosensor Based on a Au-Paper Electrode and Naphthalocyanine Sensitized ZnO Nanorods. *J. Mater. Chem. B* **2014**, *2*, 4811.

(231) Zhao, W.-W.; Chen, R.; Dai, P.-P.; Li, X.-L.; Xu, J.-J.; Chen, H.-Y. A General Strategy for Photoelectrochemical Immunoassay Using an Enzyme Label Combined with a CdS Quantum Dot/TiO$_2$ Nanoparticle Composite Electrode. *Anal. Chem.* **2014**, *86*, 11513−11516.

(232) Fan, G.-C.; Han, L.; Zhu, H.; Zhang, J.-R.; Zhu, J.-J. Ultrasensitive Photoelectrochemical Immunoassay for Matrix Metalloproteinase-2 Detection Based on CdS:Mn/CdTe Cosensitized TiO$_2$ Nanotubes and Signal Amplification of SiO$_2$@Ab2Conjugates. *Anal. Chem.* **2014**, *86*, 12398−12405.

(233) Li, W.; Sheng, P.; Cai, J.; Feng, H.; Cai, Q. Highly Sensitive and Selective Photoelectrochemical Biosensor Platform for Polybrominated Diphenyl Ether Detection Using the Quantum Dots Sensitized Three-Dimensional, Macroporous ZnO Nanosheet Photoelectrode. *Biosens. Bioelectron.* **2014**, *61*, 209−214.

(234) Fan, D.; Wu, D.; Cui, J.; Chen, Y.; Ma, H.; Liu, Y.; Wei, Q.; Du, B. An Ultrasensitive Label-Free Immunosensor Based on CdS Sensitized Fe−TiO$_2$ with High Visible-Light Photoelectrochemical Activity. *Biosens. Bioelectron.* **2015**, *74*, 843−848.

(235) Sun, B.; Qiao, F.; Chen, L.; Zhao, Z.; Yin, H.; Ai, S. Effective Signal-on Photoelectrochemical Immunoassay of Subgroup J Avian Leukosis Virus Based on Bi$_2$S$_3$ Nanorods as Photosensitizer and in Situ Generated Ascorbic Acid for Electron Donating. *Biosens. Bioelectron.* **2014**, *54*, 237−243.

(236) Zhao, W.-W.; Ma, Z.-Y.; Yan, D.-Y.; Xu, J.-J.; Chen, H.-Y. In Situ Enzymatic Ascorbic Acid Production as Electron Donor for CdS Quantum Dots Equipped TiO$_2$ Nanotubes: A General and Efficient Approach for New Photoelectrochemical Immunoassay. *Anal. Chem.* **2012**, *84*, 10518−10521.

(237) Wang, Y.; Li, M.; Zhu, Y.; Ge, S.; Yu, J.; Yan, M.; Song, X. A Visible Light Photoelectrochemical Sensor for Tumor Marker Detection Using Tin Dioxide Quantum Dot−graphene as Labels. *Analyst* **2013**, *138*, 7112−7118.

(238) Hu, C.; Zheng, J.; Su, X.; Wang, J.; Wu, W.; Hu, S. Ultrasensitive All-Carbon Photoelectrochemical Bioprobes for Zeptomole Immunosensing of Tumor Markers by an Inexpensive Visible Laser Light. *Anal. Chem.* **2013**, *85*, 10612−10619.

(239) Wang, Y.; Liu, H.; Wang, P.; Yu, J.; Ge, S.; Yan, M. Chemiluminescence Excited Photoelectrochemical Competitive Immunosensing Lab-on-Paper Device Using an Integrated Paper Supercapacitor for Signal Amplication. *Sens. Actuators, B* **2015**, *208*, 546−553.

(240) Sun, G.; Zhang, Y.; Kong, Q.; Ma, C.; Yu, J.; Ge, S.; Yan, M.; Song, X. Chemiluminescence Excited Paper-Based Photoelectrochemical Competitive Immunosensing Based on Porous ZnO Spheres and CdS Nanorods. *J. Mater. Chem. B* **2014**, *2*, 7679−7684.

(241) Shim, J. S.; Ahn, C. H. Optical Immunosensor Using Carbon Nanotubes Coated with a Photovoltaic Polymer. *Biosens. Bioelectron.* **2012**, *34*, 208−214.

(242) Zhao, W.-W.; Ma, Z.-Y.; Yu, P.-P.; Dong, X.-Y.; Xu, J.-J.; Chen, H.-Y. Highly Sensitive Photoelectrochemical Immunoassay with Enhanced Amplification Using Horseradish Peroxidase Induced Biocatalytic Precipitation on a CdS Quantum Dots Multilayer Electrode. *Anal. Chem.* **2012**, *84*, 917−923.

(243) Zheng, W.; Jiang, X. Integration of Nanomaterials for Colorimetric Immunoassays with Improved Performance: A Functional Perspective. *Analyst* **2016**, *141*, 1196−1208.

(244) Cui, X.; Huang, Y.; Wang, J.; Zhang, L.; Rong, Y.; Lai, W.; Chen, T. A Remarkable Sensitivity Enhancement in a Gold Nanoparticle-Based Lateral Flow Immunoassay for the Detection of *Escherichia coli* O157:H7. *RSC Adv.* **2015**, *5*, 45092−45097.

(245) Ge, X.; Asiri, A. M.; Du, D.; Wen, W.; Wang, S.; Lin, Y. Nanomaterial-Enhanced Paper-Based Biosensors. *TrAC, Trends Anal. Chem.* **2014**, *58*, 31−39.

(246) Xu, H.; Chen, J.; Birrenkott, J.; Zhao, J. X.; Takalkar, S.; Baryeh, K.; Liu, G. Gold-Nanoparticle-Decorated Silica Nanorods for Sensitive Visual Detection of Proteins. *Anal. Chem.* **2014**, *86*, 7351−7359.

(247) Park, J.-M.; Jung, H.-W.; Chang, Y. W.; Kim, H.-S.; Kang, M.-J.; Pyun, J.-C. Chemiluminescence Lateral Flow Immunoassay Based on Pt Nanoparticle with Peroxidase Activity. *Anal. Chim. Acta* **2015**, *853*, 360−367.

120

(248) Kim, M. I.; Kim, M. S.; Woo, M.-A.; Ye, Y.; Kang, K. S.; Lee, J.; Park, H. G. Highly Efficient Colorimetric Detection of Target Cancer Cells Utilizing Superior Catalytic Activity of Graphene Oxide–magnetic-Platinum Nanohybrids. *Nanoscale* **2014**, *6*, 1529–1536.

(249) Bose, P. P.; Mandal, G.; Chatterjee, U.; Singh, M.; Chatterjee, B. P. Gold Nanoparticle-Based Novel Visual Diagnostic Method for the Detection of Specific IgE to Test for Food Allergies. *Anal. Methods* **2016**, *8*, 3878–3884.

(250) Bui, M.-P. N.; Ahmed, S.; Abbas, A. Single-Digit Pathogen and Attomolar Detection with the Naked Eye Using Liposome-Amplified Plasmonic Immunoassay. *Nano Lett.* **2015**, *15*, 6239–6246.

(251) Panfilova, E.; Shirokov, A.; Khlebtsov, B.; Matora, L.; Khlebtsov, N. Multiplexed Dot Immunoassay Using Ag Nanocubes, Au/Ag Alloy Nanoparticles, and Au/Ag Nanocages. *Nano Res.* **2012**, *5*, 124–134.

(252) Lan, T.; Wang, J.; Dong, C.; Huang, X.; Ren, J. Homogeneous Immunoassays by Using Photon Burst Counting Technique of Single Gold Nanoparticles. *Talanta* **2015**, *132*, 698–704.

(253) Wijaya, E.; Lenaerts, C.; Maricot, S.; Hastanin, J.; Habraken, S.; Vilcot, J.-P.; Boukherroub, R.; Szunerits, S. Surface Plasmon Resonance-Based Biosensors: From the Development of Different SPR Structures to Novel Surface Functionalization Strategies. *Curr. Opin. Solid State Mater. Sci.* **2011**, *15*, 208–224.

(254) Guo, X. Surface Plasmon Resonance Based Biosensor Technique: A Review. *J. Biophotonics* **2012**, *5*, 483–501.

(255) Stewart, M. E.; Anderton, C. R.; Thompson, L. B.; Maria, J.; Gray, S. K.; Rogers, J. A.; Nuzzo, R. G. Nanostructured Plasmonic Sensors. *Chem. Rev.* **2008**, *108*, 494–521.

(256) Zeng, S.; Yu, X.; Law, W.-C.; Zhang, Y.; Hu, R.; Dinh, X.-Q.; Ho, H.-P.; Yong, K.-T. Size Dependence of Au NP-Enhanced Surface Plasmon Resonance Based on Differential Phase Measurement. *Sens. Actuators, B* **2013**, *176*, 1128–1133.

(257) Zeng, S.; Yong, K.-T.; Roy, I.; Dinh, X.-Q.; Yu, X.; Luan, F. A Review on Functionalized Gold Nanoparticles for Biosensing Applications. *Plasmonics* **2011**, *6*, 491–506.

(258) Nakamura, C.; Hasegawa, M.; Nakamura, N.; Miyake, J. Rapid and Specific Detection of Herbicides Using a Self-Assembled Photosynthetic Reaction Center from Purple Bacterium on an SPR Chip. *Biosens. Bioelectron.* **2003**, *18*, 599–603.

(259) Wei, J.; Mu, Y.; Song, D.; Fang, X.; Liu, X.; Bu, L.; Zhang, H.; Zhang, G.; Ding, J.; Wang, W.; Jin, Q.; Luo, G. A Novel Sandwich Immunosensing Method for Measuring Cardiac Troponin I in Sera. *Anal. Biochem.* **2003**, *321*, 209–216.

(260) Gobi, K. V.; Tanaka, H.; Shoyama, Y.; Miura, N. Continuous Flow Immunosensor for Highly Selective and Real-Time Detection of Sub-Ppb Levels of 2-Hydroxybiphenyl by Using Surface Plasmon Resonance Imaging. *Biosens. Bioelectron.* **2004**, *20*, 350–357.

(261) Farka, Z.; Juřík, T.; Pastucha, M.; Skládal, P. Enzymatic Precipitation Enhanced Surface Plasmon Resonance Immunosensor for the Detection of Salmonella in Powdered Milk. *Anal. Chem.* **2016**, *88*, 11830–11836.

(262) Shankaran, D.; Gobi, K.; Miura, N. Recent Advancements in Surface Plasmon Resonance Immunosensors for Detection of Small Molecules of Biomedical, Food and Environmental Interest. Sens. *Sens. Actuators, B* **2007**, *121*, 158–177.

(263) Habauzit, D.; Armengaud, J.; Roig, B.; Chopineau, J. Determination of Estrogen Presence in Water by SPR Using Estrogen Receptor Dimerization. *Anal. Bioanal. Chem.* **2008**, *390*, 873–883.

(264) Kubitschko, S.; Spinke, J.; Brückner, T.; Pohl, S.; Oranth, N. Sensitivity Enhancement of Optical Immunosensors with Nanoparticles. *Anal. Biochem.* **1997**, *253*, 112–122.

(265) Lyon, L. A.; Musick, M. D.; Smith, P. C.; Reiss, B. D.; Peña, D. J.; Natan, M. J. Surface Plasmon Resonance of Colloidal Au-Modified Gold Films. *Sens. Actuators, B* **1999**, *54*, 118–124.

(266) Wu, Q.; Song, D.; Zhang, D.; Sun, Y. An Enhanced SPR Immunosensing Platform for Human IgG Based on the Use of Silver Nanocubes and Carboxy-Functionalized Graphene Oxide. *Microchim. Acta* **2016**, *183*, 2177–2184.

(267) Golub, E.; Pelossof, G.; Freeman, R.; Zhang, H.; Willner, I. Electrochemical, Photoelectrochemical, and Surface Plasmon Reso-nance Detection of Cocaine Using Supramolecular Aptamer Complexes and Metallic or Semiconductor Nanoparticles. *Anal. Chem.* **2009**, *81*, 9291–9298.

(268) Chen, H.; Liu, F.; Koh, K.; Lee, J.; Ye, Z.; Yin, T.; Sun, L. Sensitive Detection of Tuberculosis Using Nanoparticle-Enhanced Surface Plasmon Resonance. *Microchim. Acta* **2013**, *180*, 431–436.

(269) Lin, K.; Lu, Y.; Chen, J.; Zheng, R.; Wang, P.; Ming, H. Surface Plasmon Resonance Hydrogen Sensor Based on Metallic Grating with High Sensitivity. *Opt. Express* **2008**, *16*, 18599.

(270) Golub, E.; Pelossof, G.; Freeman, R.; Zhang, H.; Willner, I. Electrochemical, Photoelectrochemical, and Surface Plasmon Reso-nance Detection of Cocaine Using Supramolecular Aptamer Complexes and Metallic or Semiconductor Nanoparticles. *Anal. Chem.* **2009**, *81*, 9291–9298.

(271) Pollet, J.; Delport, F.; Janssen, K. P. F.; Tran, D. T.; Wouters, J.; Verbiest, T.; Lammertyn, J. Fast and Accurate Peanut Allergen Detection with Nanobead Enhanced Optical Fiber SPR Biosensor. *Talanta* **2011**, *83*, 1436–1441.

(272) Liu, X.; Hu, Y.; Zheng, S.; Liu, Y.; He, Z.; Luo, F. Surface Plasmon Resonance Immunosensor for Fast, Highly Sensitive, and in Situ Detection of the Magnetic Nanoparticles-Enriched *Salmonella enteritidis*. *Sens. Actuators, B* **2016**, *230*, 191–198.

(273) Zeng, S.; Baillargeat, D.; Ho, H.-P.; Yong, K.-T. Nanomaterials Enhanced Surface Plasmon Resonance for Biological and Chemical Sensing Applications. *Chem. Soc. Rev.* **2014**, *43*, 3426.

(274) Maurer, T.; Adam, P.-M.; Lévêque, G. Coupling between Plasmonic Films and Nanostructures: From Basics to Applications. *Nanophotonics* **2015**, *4*, 361–382.

(275) Li, R.; Feng, F.; Chen, Z.-Z.; Bai, Y.-F.; Guo, F.-F.; Wu, F.-Y.; Zhou, G. Sensitive Detection of Carcinoembryonic Antigen Using Surface Plasmon Resonance Biosensor with Gold Nanoparticles Signal Amplification. *Talanta* **2015**, *140*, 143–149.

(276) Vaisocherová-Lísalová, H.; Víšová, I.; Ermini, M. L.; Špringer, T.; Song, X. C.; Mrázek, J.; Lamačová, J.; Scott Lynn, N.; Šedivák, P.; Homola, J. Low-Fouling Surface Plasmon Resonance Biosensor for Multi-Step Detection of Foodborne Bacterial Pathogens in Complex Food Samples. *Biosens. Bioelectron.* **2016**, *80*, 84–90.

(277) Pettinger, B.; Ren, B.; Picardi, G.; Schuster, R.; Ertl, G. Nanoscale Probing of Adsorbed Species by Tip-Enhanced Raman Spectroscopy. *Phys. Rev. Lett.* **2004**, *92*, 096101.

(278) Spackova, B.; Wrobel, P.; Bockova, M.; Homola, J. Optical Biosensors Based on Plasmonic Nanostructures: A Review. *Proc. IEEE* **2016**, *104*, 2380–2408.

(279) Maier, S. A. *Plasmonics: Fundamentals and Applications*; Springer: New York, 2007.

(280) Jang, Y. H.; Chung, K.; Quan, L. N.; Špačková, B.; Šípová, H.; Moon, S.; Cho, W. J.; Shin, H.-Y.; Jang, Y. J.; Lee, J.-E.; Kochuveedu, S. T.; Yoon, M. J.; Kim, J.; Yoon, S.; Kim, J. K.; Kim, D.; Homola, J.; Kim, D. H. Configuration-Controlled Au Nanocluster Arrays on Inverse Micelle Nano-Patterns: Versatile Platforms for SERS and SPR Sensors. *Nanoscale* **2013**, *5*, 12261.

(281) Joshi, S.; Segarra-Fas, A.; Peters, J.; Zuilhof, H.; van Beek, T. A.; Nielen, M. W. F. Multiplex Surface Plasmon Resonance Biosensing and Its Transferability Towards Imaging Nanoplasmonics for Detection of Mycotoxins in Barley. *Analyst* **2016**, *141*, 1307–1318.

(282) Moon, S.; Kim, Y.; Oh, Y.; Lee, H.; Kim, H. C.; Lee, K.; Kim, D. Grating-Based Surface Plasmon Resonance Detection of Core-Shell Nanoparticle Mediated DNA Hybridization. *Biosens. Bioelectron.* **2012**, *32*, 141–147.

(283) Im, H.; Sutherland, J. N.; Maynard, J. A.; Oh, S.-H. Nanohole-Based Surface Plasmon Resonance Instruments with Improved Spectral Resolution Quantify a Broad Range of Antibody-Ligand Binding Kinetics. *Anal. Chem.* **2012**, *84*, 1941–1947.

(284) Im, H.; Shao, H.; Park, Y. I.; Peterson, V. M.; Castro, C. M.; Weissleder, R.; Lee, H. Label-Free Detection and Molecular Profiling of Exosomes with a Nano-Plasmonic Sensor. *Nat. Biotechnol.* **2014**, *32*, 490–495.

(285) Kravets, V. G.; Schedin, F.; Jalil, R.; Britnell, L.; Gorbachev, R. V.; Ansell, D.; Thackray, B.; Novoselov, K. S.; Geim, A. K.; Kabashin, A. V.;

121

Grigorenko, A. N. Singular Phase Nano-Optics in Plasmonic Metamaterials for Label-Free Single-Molecule Detection. *Nat. Mater.* **2013**, *12*, 304–309.

(286) Degiron, A.; Lezec, H. J.; Yamamoto, N.; Ebbesen, T. W. Optical Transmission Properties of a Single Subwavelength Aperture in a Real Metal. *Opt. Commun.* **2004**, *239*, 61–66.

(287) Lee, Y. H.; Chen, H.; Xu, Q.-H.; Wang, J. Refractive Index Sensitivities of Noble Metal Nanocrystals: The Effects of Multipolar Plasmon Resonances and the Metal Type. *J. Phys. Chem. C* **2011**, *115*, 7997–8004.

(288) Hutter, E.; Fendler, J. H.; Roy, D. Surface Plasmon Resonance Studies of Gold and Silver Nanoparticles Linked to Gold and Silver Substrates by 2-Aminoethanethiol and 1,6-Hexanedithiol. *J. Phys. Chem. B* **2001**, *105*, 11159–11168.

(289) Lu, H.; Zhang, H.; Yu, X.; Zeng, S.; Yong, K.-T.; Ho, H.-P. Seed-Mediated Plasmon-Driven Regrowth of Silver Nanodecahedrons (NDs). *Plasmonics* **2012**, *7*, 167–173.

(290) Wang, J.; Song, D.; Wang, L.; Zhang, H.; Zhang, H.; Sun, Y. Design and Performances of Immunoassay Based on SPR Biosensor with Au/Ag Alloy Nanocomposites. *Sens. Actuators, B* **2011**, *157*, 547–553.

(291) Wang, J.; Munir, A.; Zhu, Z.; Zhou, H. S. Magnetic Nanoparticle Enhanced Surface Plasmon Resonance Sensing and Its Application for the Ultrasensitive Detection of Magnetic Nanoparticle-Enriched Small Molecules. *Anal. Chem.* **2010**, *82*, 6782–6789.

(292) Wang, Y.; Dostalek, J.; Knoll, W. Magnetic Nanoparticle-Enhanced Biosensor Based on Grating-Coupled Surface Plasmon Resonance. *Anal. Chem.* **2011**, *83*, 6202–6207.

(293) Liu, X.; Hu, Y.; Zheng, S.; Liu, Y.; He, Z.; Luo, F. Surface Plasmon Resonance Immunosensor for Fast, Highly Sensitive, and in Situ Detection of the Magnetic Nanoparticles-Enriched Salmonella Enteritidis. *Sens. Actuators, B* **2016**, *230*, 191–198.

(294) Torun, Ö.; Hakkı Boyacı, İ.; Temür, E.; Tamer, U. Comparison of Sensing Strategies in SPR Biosensor for Rapid and Sensitive Enumeration of Bacteria. *Biosens. Bioelectron.* **2012**, *37*, 53–60.

(295) Zhang, H.; Sun, Y.; Gao, S.; Zhang, H.; Zhang, J.; Bai, Y.; Song, D. Studies of Gold Nanorod-Iron Oxide Nanohybrids for Immunoassay Based on SPR Biosensor. *Talanta* **2014**, *125*, 29–35.

(296) Sreekanth, K. V.; Zeng, S.; Yong, K.-T.; Yu, T. Sensitivity Enhanced Biosensor Using Graphene-Based One-Dimensional Photonic Crystal. *Sens. Actuators, B* **2013**, *182*, 424–428.

(297) Cui, S.; Pu, H.; Lu, G.; Wen, Z.; Mattson, E. C.; Hirschmugl, C.; Gajdardziska-Josifovska, M.; Weinert, M.; Chen, J. Fast and Selective Room-Temperature Ammonia Sensors Using Silver Nanocrystal-Functionalized Carbon Nanotubes. *ACS Appl. Mater. Interfaces* **2012**, *4*, 4898–4904.

(298) Wu, L.; Chu, H. S.; Koh, W. S.; Li, E. P. Highly Sensitive Graphene Biosensors Based on Surface Plasmon Resonance. *Opt. Express* **2010**, *18*, 14395.

(299) Gosciniak, J.; Tan, D. T. H. Graphene-Based Waveguide Integrated Dielectric-Loaded Plasmonic Electro-Absorption Modulators. *Nanotechnology* **2013**, *24*, 185202.

(300) Chung, K.; Rani, A.; Lee, J.-E.; Kim, J. E.; Kim, Y.; Yang, H.; Kim, S. O.; Kim, D.; Kim, D. H. Systematic Study on the Sensitivity Enhancement in Graphene Plasmonic Sensors Based on Layer-by-Layer Self-Assembled Graphene Oxide Multilayers and Their Reduced Analogues. *ACS Appl. Mater. Interfaces* **2015**, *7*, 144–151.

(301) Hu, W.; He, G.; Zhang, H.; Wu, X.; Li, J.; Zhao, Z.; Qiao, Y.; Lu, Z.; Liu, Y.; Li, C. M. Polydopamine-Functionalization of Graphene Oxide to Enable Dual Signal Amplification for Sensitive Surface Plasmon Resonance Imaging Detection of Biomarker. *Anal. Chem.* **2014**, *86*, 4488–4493.

(302) Zhang, J.; Sun, Y.; Xu, B.; Zhang, H.; Gao, Y.; Zhang, H.; Song, D. A Novel Surface Plasmon Resonance Biosensor Based on Graphene Oxide Decorated with Gold Nanorod–Antibody Conjugates for Determination of Transferrin. *Biosens. Bioelectron.* **2013**, *45*, 230–236.

(303) Singh, M.; Holzinger, M.; Tabrizian, M.; Winters, S.; Berner, N. C.; Cosnier, S.; Duesberg, G. S. Noncovalently Functionalized Monolayer Graphene for Sensitivity Enhancement of Surface Plasmon Resonance Immunosensors. *J. Am. Chem. Soc.* **2015**, *137*, 2800–2803.

(304) Pawula, M.; Altintas, Z.; Tothill, I. E. SPR Detection of Cardiac Troponin T for Acute Myocardial Infarction. *Talanta* **2016**, *146*, 823–830.

(305) Eletxigerra, U.; Martinez-Perdiguero, J.; Barderas, R.; Pingarrón, J. M.; Campuzano, S.; Merino, S. Surface Plasmon Resonance Immunosensor for ErbB2 Breast Cancer Biomarker Determination in Human Serum and Raw Cancer Cell Lysates. *Anal. Chim. Acta* **2016**, *905*, 156–162.

(306) Li, R.; Feng, F.; Chen, Z.-Z.; Bai, Y.-F.; Guo, F.-F.; Wu, F.-Y.; Zhou, G. Sensitive Detection of Carcinoembryonic Antigen Using Surface Plasmon Resonance Biosensor with Gold Nanoparticles Signal Amplification. *Talanta* **2015**, *140*, 143–149.

(307) Jiang, Z.; Qin, Y.; Peng, Z.; Chen, S.; Chen, S.; Deng, C.; Xiang, J. The Simultaneous Detection of Free and Total Prostate Antigen in Serum Samples with High Sensitivity and Specificity by Using the Dual-Channel Surface Plasmon Resonance. *Biosens. Bioelectron.* **2014**, *62*, 268–273.

(308) Hu, W.; Chen, H.; Zhang, H.; He, G.; Li, X.; Zhang, X.; Liu, Y.; Li, C. M. Sensitive Detection of Multiple Mycotoxins by SPRi with Gold Nanoparticles as Signal Amplification Tags. *J. Colloid Interface Sci.* **2014**, *431*, 71–76.

(309) Karczmarczyk, A.; Dubiak-Szepietowska, M.; Vorobii, M.; Rodriguez-Emmenegger, C.; Dostálek, J.; Feller, K.-H. Sensitive and Rapid Detection of Aflatoxin M1 in Milk Utilizing Enhanced SPR and p(HEMA) Brushes. *Biosens. Bioelectron.* **2016**, *81*, 159–165.

(310) Caucheteur, C.; Guo, T.; Albert, J. Review of Plasmonic Fiber Optic Biochemical Sensors: Improving the Limit of Detection. *Anal. Bioanal. Chem.* **2015**, *407*, 3883–3897.

(311) Haes, A. J.; Van Duyne, R. P. A Unified View of Propagating and Localized Surface Plasmon Resonance Biosensors. *Anal. Bioanal. Chem.* **2004**, *379*, 920–930.

(312) Liz-Marzán, L. M. Tailoring Surface Plasmons through the Morphology and Assembly of Metal Nanoparticles. *Langmuir* **2006**, *22*, 32–41.

(313) Haes, A. J.; Stuart, D. A.; Nie, S.; Van Duyne, R. P. Using Solution-Phase Nanoparticles, Surface-Confined Nanoparticle Arrays and Single Nanoparticles as Biological Sensing Platforms. *J. Fluoresc.* **2004**, *14*, 355–367.

(314) Sepúlveda, B.; Angelomé, P. C.; Lechuga, L. M.; Liz-Marzán, L. M. LSPR-Based Nanobiosensors. *Nano Today* **2009**, *4*, 244–251.

(315) Howes, P. D.; Rana, S.; Stevens, M. M. Plasmonic Nanomaterials for Biodiagnostics. *Chem. Soc. Rev.* **2014**, *43*, 3835–3853.

(316) Byun, J.-Y.; Shin, Y.-B.; Li, T.; Park, J.-H.; Kim, D.-M.; Choi, D.-H.; Kim, M.-G. The Use of an Engineered Single Chain Variable Fragment in a Localized Surface Plasmon Resonance Method for Analysis of the C-Reactive Protein. *Chem. Commun.* **2013**, *49*, 9497.

(317) Valdez, J.; Bawage, S.; Gomez, I.; Singh, S. R. Facile and Rapid Detection of Respiratory Syncytial Virus Using Metallic Nanoparticles. *J. Nanobiotechnol.* **2016**, *14*, 13.

(318) Lee, J. U.; Nguyen, A. H.; Sim, S. J. A Nanoplasmonic Biosensor for Label-Free Multiplex Detection of Cancer Biomarkers. *Biosens. Bioelectron.* **2015**, *74*, 341–346.

(319) Chen, S.; Zhao, Q.; Zhang, L.; Wang, L.; Zeng, Y.; Huang, H. Combined Detection of Breast Cancer Biomarkers Based on Plasmonic Sensor of Gold Nanorods. *Sens. Actuators, B* **2015**, *221*, 1391–1397.

(320) Sun, X.; Wu, L.; Ji, J.; Jiang, D.; Zhang, Y.; Li, Z.; Zhang, G.; Zhang, H. Longitudinal Surface Plasmon Resonance Assay Enhanced by Magnetosomes for Simultaneous Detection of Pefloxacin and Microcystin-LR in Seafoods. *Biosens. Bioelectron.* **2013**, *47*, 318–323.

(321) Chen, C.-D.; Cheng, S.-F.; Chau, L.-K.; Wang, C. R. C. Sensing Capability of the Localized Surface Plasmon Resonance of Gold Nanorods. *Biosens. Bioelectron.* **2007**, *22*, 926–932.

(322) McFarland, A. D.; Van Duyne, R. P. Single Silver Nanoparticles as Real-Time Optical Sensors with Zeptomole Sensitivity. *Nano Lett.* **2003**, *3*, 1057–1062.

122

(323) Anker, J. N.; Hall, W. P.; Lyandres, O.; Shah, N. C.; Zhao, J.; Van Duyne, R. P. Biosensing with Plasmonic Nanosensors. *Nat. Mater.* **2008**, *7*, 442−453.

(324) Choi, I.; Choi, Y. Plasmonic Nanosensors: Review and Prospect. *IEEE J. Sel. Top. Quantum Electron.* **2012**, *18*, 1110−1121.

(325) Lin, H.-Y.; Huang, C.-H.; Lu, S.-H.; Kuo, I.-T.; Chau, L.-K. Direct Detection of Orchid Viruses Using Nanorod-Based Fiber Optic Particle Plasmon Resonance Immunosensor. *Biosens. Bioelectron.* **2014**, *51*, 371−378.

(326) Inci, F.; Filippini, C.; Baday, M.; Ozen, M. O.; Calamak, S.; Durmus, N. G.; Wang, S.; Hanhauser, E.; Hobbs, K. S.; Juillard, F.; Kuang, P. P.; Vetter, M. L.; Carocci, M.; Yamamoto, H. S.; Takagi, Y.; Yildiz, U. H.; Akin, D.; Wesemann, D. R.; Singhal, A.; Yang, P. L.; Nibert, M. L.; Fichorova, R. N.; Lau, D. T.-Y.; Henrich, T. J.; Kaye, K. M.; Schachter, S. C.; Kuritzkes, D. R.; Steinmetz, L. M.; Gambhir, S. S.; Davis, R. W.; Demirci, U. Multitarget, Quantitative Nanoplasmonic Electrical Field-Enhanced Resonating Device (NE2RD) for Diagnostics. *Proc. Natl. Acad. Sci. U. S. A.* **2015**, *112*, E4354−E4363.

(327) Mock, J. J.; Smith, D. R.; Schultz, S. Local Refractive Index Dependence of Plasmon Resonance Spectra from Individual Nano-particles. *Nano Lett.* **2003**, *3*, 485−491.

(328) Qiu, G.; Ng, S. P.; Wu, L. C.-M. Dielectric Functionalization for Differential Phase Detecting Localized Surface Plasmon Resonance Biosensor. *Sens. Actuators, B* **2016**, *234*, 247−254.

(329) Liu, C.; Meng, F.; Zheng, W.; Xue, T.; Jin, Z.; Wang, Z.; Cui, X. Plasmonic ZnO nanorods/Au Substrates for Protein Microarrays with High Sensitivity and Broad Dynamic Range. *Sens. Actuators, B* **2016**, *228*, 231−236.

(330) He, J.; Boegli, M.; Bruzas, I.; Lum, W.; Sagle, L. Patterned Plasmonic Nanoparticle Arrays for Microfluidic and Multiplexed Biological Assays. *Anal. Chem.* **2015**, *87*, 11407−11414.

(331) Gunnarsson, L.; Rindzevicius, T.; Prikulis, J.; Kasemo, B.; Käll, M.; Zou, S.; Schatz, G. C. Confined Plasmons in Nanofabricated Single Silver Particle Pairs: Experimental Observations of Strong Interparticle Interactions. *J. Phys. Chem. B* **2005**, *109*, 1079−1087.

(332) Brolo, A. G.; Gordon, R.; Leathem, B.; Kavanagh, K. L. Surface Plasmon Sensor Based on the Enhanced Light Transmission through Arrays of Nanoholes in Gold Films. *Langmuir* **2004**, *20*, 4813−4815.

(333) Haes, A. J.; Van Duyne, R. P. A Nanoscale Optical Biosensor: Sensitivity and Selectivity of an Approach Based on the Localized Surface Plasmon Resonance Spectroscopy of Triangular Silver Nano-particles. *J. Am. Chem. Soc.* **2002**, *124*, 10596−10604.

(334) Larsson, E. M.; Alegret, J.; Käll, M.; Sutherland, D. S. Sensing Characteristics of NIR Localized Surface Plasmon Resonances in Gold Nanorings for Application as Ultrasensitive Biosensors. *Nano Lett.* **2007**, *7*, 1256−1263.

(335) Stewart, M. E.; Mack, N. H.; Malyarchuk, V.; Soares, J. A. N. T.; Lee, T.-W.; Gray, S. K.; Nuzzo, R. G.; Rogers, J. A. Quantitative Multispectral Biosensing and 1D Imaging Using Quasi-3D Plasmonic Crystals. *Proc. Natl. Acad. Sci. U. S. A.* **2006**, *103*, 17143−17148.

(336) Jo, N. r.; Lee, K. j.; Shin, Y.-B. Enzyme-Coupled Nanoplasmonic Biosensing of Cancer Markers in Human Serum. *Biosens. Bioelectron.* **2016**, *81*, 324−333.

(337) Yeom, S.-H.; Han, M.-E.; Kang, B.-H.; Kim, K.-J.; Yuan, H.; Eum, N.-S.; Kang, S.-W. Enhancement of the Sensitivity of LSPR-Based CRP Immunosensors by Au Nanoparticle Antibody Conjugation. *Sens. Actuators, B* **2013**, *177*, 376−383.

(338) Hall, W. P.; Ngatia, S. N.; Van Duyne, R. P. LSPR Biosensor Signal Enhancement Using Nanoparticle−Antibody Conjugates. *J. Phys. Chem. C* **2011**, *115*, 1410−1414.

(339) Gunnarsson, L.; Rindzevicius, T.; Prikulis, J.; Kasemo, B.; Käll, M.; Zou, S.; Schatz, G. C. Confined Plasmons in Nanofabricated Single Silver Particle Pairs: Experimental Observations of Strong Interparticle Interactions. *J. Phys. Chem. B* **2005**, *109*, 1079−1087.

(340) Gupta, S.; Andresen, H.; Ghadiali, J. E.; Stevens, M. M. Kinase-Actuated Immunoaggregation of Peptide-Conjugated Gold Nano-particles. *Small* **2010**, *6*, 1509−1513.

(341) Nie, X.-M.; Huang, R.; Dong, C.-X.; Tang, L.-J.; Gui, R.; Jiang, J.-H. Plasmonic ELISA for the Ultrasensitive Detection of Treponema Pallidum. *Biosens. Bioelectron.* **2014**, *58*, 314−319.

(342) Xianyu, Y.; Chen, Y.; Jiang, X. Horseradish Peroxidase-Mediated, Iodide-Catalyzed Cascade Reaction for Plasmonic Immuno-assays. *Anal. Chem.* **2015**, *87*, 10688−10692.

(343) Soh, J. H.; Lin, Y.; Rana, S.; Ying, J. Y.; Stevens, M. M. Colorimetric Detection of Small Molecules in Complex Matrixes via Target-Mediated Growth of Aptamer-Functionalized Gold Nano-particles. *Anal. Chem.* **2015**, *87*, 7644−7652.

(344) Peng, C.; Duan, X.; Khamba, G. W.; Xie, Z. Highly Sensitive "signal on" Plasmonic ELISA for Small Molecules by the Naked Eye. *Anal. Methods* **2014**, *6*, 9616−9621.

(345) De la Rica, R.; Stevens, M. M. Plasmonic ELISA for the Ultrasensitive Detection of Disease Biomarkers with the Naked Eye. *Nat. Nanotechnol.* **2012**, *7*, 821−824.

(346) De la Rica, R.; Stevens, M. M. Plasmonic ELISA for the Detection of Analytes at Ultralow Concentrations with the Naked Eye. *Nat. Protoc.* **2013**, *8*, 1759−1764.

(347) Raman, C. V.; Krishnan, K. S. A New Type of Secondary Radiation. *Nature* **1928**, *121*, 501−502.

(348) Fleischmann, M.; Hendra, P. J.; McQuillan, A. J. Raman Spectra of Pyridine Adsorbed at a Silver Electrode. *Chem. Phys. Lett.* **1974**, *26*, 163−166.

(349) Chrimes, A. F.; Khoshmanesh, K.; Stoddart, P. R.; Mitchell, A.; Kalantar-zadeh, K. Microfluidics and Raman Microscopy: Current Applications and Future Challenges. *Chem. Soc. Rev.* **2013**, *42*, 5880.

(350) Banholzer, M. J.; Millstone, J. E.; Qin, L.; Mirkin, C. A. Rationally Designed Nanostructures for Surface-Enhanced Raman Spectroscopy. *Chem. Soc. Rev.* **2008**, *37*, 885−897.

(351) Qian, X.-M.; Nie, S. M. Single-Molecule and Single-Nanoparticle SERS: From Fundamental Mechanisms to Biomedical Applications. *Chem. Soc. Rev.* **2008**, *37*, 912−920.

(352) Jensen, L.; Aikens, C. M.; Schatz, G. C. Electronic Structure Methods for Studying Surface-Enhanced Raman Scattering. *Chem. Soc. Rev.* **2008**, *37*, 1061−1073.

(353) Morton, S. M.; Jensen, L. Understanding the Molecule−Surface Chemical Coupling in SERS. *J. Am. Chem. Soc.* **2009**, *131*, 4090−4098.

(354) Muehlethaler, C.; Leona, M.; Lombardi, J. R. Review of Surface Enhanced Raman Scattering Applications in Forensic Science. *Anal. Chem.* **2016**, *88*, 152−169.

(355) Moskovits, M. Surface-Enhanced Raman Spectroscopy: a Brief Retrospective. *J. Raman Spectrosc.* **2005**, *36*, 485−496.

(356) Willets, K. A.; Van Duyne, R. P. Localized Surface Plasmon Resonance Spectroscopy and Sensing. *Annu. Rev. Phys. Chem.* **2007**, *58*, 267−297.

(357) Driscoll, A. J.; Harpster, M. H.; Johnson, P. A. The Development of Surface-Enhanced Raman Scattering as a Detection Modality for Portable in Vitro Diagnostics: Progress and Challenges. *Phys. Chem. Chem. Phys.* **2013**, *15*, 20415.

(358) Gutés, A.; Maboudian, R.; Carraro, C. Gold-Coated Silver Dendrites as SERS Substrates with an Improved Lifetime. *Langmuir* **2012**, *28*, 17846−17850.

(359) Wang, Y.; Vaidyanathan, R.; Shiddiky, M. J. A.; Trau, M. Enabling Rapid and Specific Surface-Enhanced Raman Scattering Immunoassay Using Nanoscaled Surface Shear Forces. *ACS Nano* **2015**, *9*, 6354−6362.

(360) Liao, W.; Lu, X. Determination of Chemical Hazards in Foods Using Surface-Enhanced Raman Spectroscopy Coupled with Advanced Separation Techniques. *Trends Food Sci. Technol.* **2016**, *54*, 103−113.

(361) Wang, G.; Park, H.-Y.; Lipert, R. J.; Porter, M. D. Mixed Monolayers on Gold Nanoparticle Labels for Multiplexed Surface-Enhanced Raman Scattering Based Immunoassays. *Anal. Chem.* **2009**, *81*, 9643−9650.

(362) Haisch, C. Raman-Based Microarray Readout: a Review. *Anal. Bioanal. Chem.* **2016**, *408*, 4535−4545.

(363) Cui, Y.; Ren, B.; Yao, J.-L.; Gu, R.-A.; Tian, Z.-Q. Multianalyte Immunoassay Based on Surface-Enhanced Raman Spectroscopy. *J. Raman Spectrosc.* **2007**, *38*, 896−902.

123

(364) Tang, B.; Wang, J.; Hutchison, J. A.; Ma, L.; Zhang, N.; Guo, H.; Hu, Z.; Li, M.; Zhao, Y. Ultrasensitive, Multiplex Raman Frequency Shift Immunoassay of Liver Cancer Biomarkers in Physiological Media. *ACS Nano* **2016**, *10*, 871−879.

(365) Wu, L.; Wang, Z.; Zong, S.; Huang, Z.; Zhang, P.; Cui, Y. A SERS-Based Immunoassay with Highly Increased Sensitivity Using Gold/silver Core-Shell Nanorods. *Biosens. Bioelectron.* **2012**, *38*, 94−99.

(366) Hwang, J.; Lee, S.; Choo, J. Application of a SERS-Based Lateral Flow Immunoassay Strip for the Rapid and Sensitive Detection of Staphylococcal Enterotoxin B. *Nanoscale* **2016**, *8*, 11418−11425.

(367) Jiang, T.; Zhang, L.; Zhou, J. Silver Nanocube-Mediated Sensitive Immunoassay Based on Surface-Enhanced Raman Scattering Assisted by Etched Silicon Nanowire Arrays. *Analyst* **2014**, *139*, 5893−5900.

(368) Nguyen, A. H.; Lee, J.; Il Choi, H.; Seok Kwak, H.; Jun Sim, S. Fabrication of Plasmon Length-Based Surface Enhanced Raman Scattering for Multiplex Detection on Microfluidic Device. *Biosens. Bioelectron.* **2015**, *70*, 358−365.

(369) Li, M.; Kang, J. W.; Sukumar, S.; Dasari, R. R.; Barman, I. Multiplexed Detection of Serological Cancer Markers with Plasmon-Enhanced Raman Spectro-Immunoassay. *Chem. Sci.* **2015**, *6*, 3906−3914.

(370) Ciou, S.-H.; Cao, Y.-W.; Huang, H.-C.; Su, D.-Y.; Huang, C.-L. SERS Enhancement Factors Studies of Silver Nanoprism and Spherical Nanoparticle Colloids in The Presence of Bromide Ions. *J. Phys. Chem. C* **2009**, *113*, 9520−9525.

(371) Kamińska, A.; Witkowska, E.; Winkler, K.; Dzięcielewski, I.; Weyher, J. L.; Waluk, J. Detection of Hepatitis B Virus Antigen from Human Blood: SERS Immunoassay in a Microfluidic System. *Biosens. Bioelectron.* **2015**, *66*, 461−467.

(372) He, Y.; Wang, Y.; Yang, X.; Xie, S.; Yuan, R.; Chai, Y. Metal Organic Frameworks Combining CoFe2O4 Magnetic Nanoparticles as Highly Efficient SERS Sensing Platform for Ultrasensitive Detection of N-Terminal Pro-Brain Natriuretic Peptide. *ACS Appl. Mater. Interfaces* **2016**, *8*, 7683−7690.

(373) Li, J.; Skeete, Z.; Shan, S.; Yan, S.; Kurzatkowska, K.; Zhao, W.; Ngo, Q. M.; Holubovska, P.; Luo, J.; Hepel, M.; Zhong, C.-J. Surface Enhanced Raman Scattering Detection of Cancer Biomarkers with Bifunctional Nanocomposite Probes. *Anal. Chem.* **2015**, *87*, 10698−10702.

(374) Zengin, A.; Tamer, U.; Caykara, T. Extremely Sensitive Sandwich Assay of Kanamycin Using Surface-Enhanced Raman Scattering of 2-Mercaptobenzothiazole Labeled Gold@silver Nanoparticles. *Anal. Chim. Acta* **2014**, *817*, 33−41.

(375) Yang, K.; Hu, Y.; Dong, N. A Novel Biosensor Based on Competitive SERS Immunoassay and Magnetic Separation for Accurate and Sensitive Detection of Chloramphenicol. *Biosens. Bioelectron.* **2016**, *80*, 373−377.

(376) Dinish, U. S.; Balasundaram, G.; Chang, Y.-T.; Olivo, M. Actively Targeted In Vivo Multiplex Detection of Intrinsic Cancer Biomarkers Using Biocompatible SERS Nanotags. *Sci. Rep.* **2015**, *4*, 4075.

(377) Vendrell, M.; Maiti, K. K.; Dhaliwal, K.; Chang, Y.-T. Surface-Enhanced Raman Scattering in Cancer Detection and Imaging. *Trends Biotechnol.* **2013**, *31*, 249−257.

(378) Lee, S.; Kim, S.; Choo, J.; Shin, S. Y.; Lee, Y. H.; Choi, H. Y.; Ha, S.; Kang, K.; Oh, C. H. Biological Imaging of HEK293 Cells Expressing PLCγ1 Using Surface-Enhanced Raman Microscopy. *Anal. Chem.* **2007**, *79*, 916−922.

(379) Wang, Y.; Kang, S.; Khan, A.; Ruttner, G.; Leigh, S. Y.; Murray, M.; Abeytunge, S.; Peterson, G.; Rajadhyaksha, M.; Dintzis, S.; Javid, S.; Liu, J. T. C. Quantitative Molecular Phenotyping with Topically Applied SERS Nanoparticles for Intraoperative Guidance of Breast Cancer Lumpectomy. *Sci. Rep.* **2016**, *6*, 21242.

(380) Bard, A. J.; Faulkner, L. R. *Electrochemical Methods: Fundamentals and Applications*, 2nd ed.; Wiley: Hoboken, NJ, 2001.

(381) Merkoci, A.; Ambrosi, A.; de la Escosura-Muniz, A.; Perez-Lopez, B.; Guix, M.; Maltez, M.; Marin, S. Nanomaterials for Electroanalysis. In *Encyclopedia of Analytical Chemistry*; Meyer, R. A., Ed.; John Wiley & Sons Ltd.: Hoboken, NJ, 2010.

(382) Lim, S. A.; Ahmed, M. U. Electrochemical Immunosensors and Their Recent Nanomaterial-Based Signal Amplification Strategies: A Review. *RSC Adv.* **2016**, *6*, 24995−25014.

(383) Borgmann, S.; Schulte, A.; Neugebauer, S.; Schuhmann, W. Amperometric Biosensors. In *Advances in Electrochemical Science and Engineering*; Alkire, R. C., Kolb, D. M., Lipkowski, J., Eds.; Wiley-VCH: Weinheim, Germany, 2011.

(384) Wang, L.; Lei, J.; Ma, R.; Ju, H. Host−Guest Interaction of Adamantine with a β-Cyclodextrin-Functionalized AuPd Bimetallic Nanoprobe for Ultrasensitive Electrochemical Immunoassay of Small Molecules. *Anal. Chem.* **2013**, *85*, 6505−6510.

(385) Jeong, B.; Akter, R.; Han, O. H.; Rhee, C. K.; Rahman, M. A. Increased Electrocatalyzed Performance through Dendrimer-Encapsulated Gold Nanoparticles and Carbon Nanotube-Assisted Multiple Bienzymatic Labels: Highly Sensitive Electrochemical Immunosensor for Protein Detection. *Anal. Chem.* **2013**, *85*, 1784−1791.

(386) Lin, D.; Wu, J.; Wang, M.; Yan, F.; Ju, H. Triple Signal Amplification of Graphene Film, Polybead Carried Gold Nanoparticles as Tracing Tag and Silver Deposition for Ultrasensitive Electrochemical Immunosensing. *Anal. Chem.* **2012**, *84*, 3662−3668.

(387) Li, J.; Li, S.; Yang, C. F. Electrochemical Biosensors for Cancer Biomarker Detection. *Electroanalysis* **2012**, *24*, 2213−2229.

(388) Huang, K.-J.; Wu, Z.-W.; Wu, Y.-Y.; Liu, Y.-M. Electrochemical Immunoassay of Carcinoembryonic Antigen Based on TiO$_2$ − Graphene/Thionine/Gold Nanoparticles Composite. *Can. J. Chem.* **2012**, *90*, 608−615.

(389) Cai, M.; Zhu, L.; Ding, Y.; Wang, J.; Li, J.; Du, X. Determination of Sulfamethoxazole in Foods Based on CeO2/Chitosan Nanocomposite-Modified Electrodes. *Mater. Sci. Eng., C* **2012**, *32*, 2623−2627.

(390) Cao, X.; Wang, N.; Jia, S.; Guo, L.; Li, K. Bimetallic AuPt Nanochains: Synthesis and Their Application in Electrochemical Immunosensor for the Detection of Carcinoembryonic Antigen. *Biosens. Bioelectron.* **2013**, *39*, 226−230.

(391) Cho, H. K.; Lim, H. B. Determination of Prostate-Specific Antigen (PSA) Tagged with TiO2 Nanoparticles Using ICP-MS. *J. Anal. At. Spectrom.* **2013**, *28*, 468.

(392) Valera, E.; Muriano, A.; Pividori, I.; Sánchez-Baeza, F.; Marco, M.-P. Development of a Coulombimetric Immunosensor Based on Specific Antibodies Labeled with CdS Nanoparticles for Sulfonamide Antibiotic Residues Analysis and Its Application to Honey Samples. *Biosens. Bioelectron.* **2013**, *43*, 211−217.

(393) Yeh, F.-Y.; Liu, T.-Y.; Tseng, I.-H.; Yang, C.-W.; Lu, L.-C.; Lin, C.-S. Gold Nanoparticles Conjugates-Amplified Aptamer Immunosensing Screen-Printed Carbon Electrode Strips for Thrombin Detection. *Biosens. Bioelectron.* **2014**, *61*, 336−343.

(394) Sharma, A.; Kameswara Rao, V.; Vrat Kamboj, D.; Jain, R. Electrochemical Immunosensor for Staphylococcal Enterotoxin B (SEB) Based on Platinum Nanoparticles-Modified Electrode Using Hydrogen Evolution Inhibition Approach. *Electroanalysis* **2014**, *26*, 2320−2327.

(395) Wang, D.; Dou, W.; Zhao, G.; Chen, Y. Immunosensor Based on Electrodeposition of Gold-Nanoparticles and Ionic Liquid Composite for Detection of Salmonella Pullorum. *J. Microbiol. Methods* **2014**, *106*, 110−118.

(396) Sun, X.; Cao, Y.; Gong, Z.; Wang, X.; Zhang, Y.; Gao, J. An Amperometric Immunosensor Based on Multi-Walled Carbon Nanotubes-Thionine-Chitosan Nanocomposite Film for Chlorpyrifos Detection. *Sensors* **2012**, *12*, 17247−17261.

(397) Zhu, Y.; Cao, Y.; Sun, X.; Wang, X. Amperometric Immunosensor for Carbofuran Detection Based on MWCNTs/GS-PEI-Au and AuNPs-Antibody Conjugate. *Sensors* **2013**, *13*, 5286−5301.

(398) Sharma, M. K.; Narayanan, J.; Upadhyay, S.; Goel, A. K. Electrochemical Immunosensor Based on Bismuth Nanocomposite Film and Cadmium Ions Functionalized Titanium Phosphates for the Detection of Anthrax Protective Antigen Toxin. *Biosens. Bioelectron.* **2015**, *74*, 299−304.

(399) Dai, H.; Xu, G.; Zhang, S.; Gong, L.; Li, X.; Yang, C.; Lin, Y.; Chen, J.; Chen, G. Carbon Nanotubes Functionalized Electrospun

124

Nanofibers Formed 3D Electrode Enables Highly Strong ECL of Peroxydisulfate and Its Application in Immunoassay. *Biosens. Bioelectron.* **2014**, *61*, 575−578.

(400) Haque, A.-M. J.; Park, H.; Sung, D.; Jon, S.; Choi, S.-Y.; Kim, K. An Electrochemically Reduced Graphene Oxide-Based Electrochemical Immunosensing Platform for Ultrasensitive Antigen Detection. *Anal. Chem.* **2012**, *84*, 1871−1878.

(401) Jiao, L.; Mu, Z.; Zhu, C.; Wei, Q.; Li, H.; Du, D.; Lin, Y. Graphene Loaded Bimetallic Au@Pt Nanodendrites Enhancing Ultrasensitive Electrochemical Immunoassay of AFP. *Sens. Actuators, B* **2016**, *231*, 513−519.

(402) Yu, S.; Zou, G.; Wei, Q. Ultrasensitive Electrochemical Immunosensor for Quantitative Detection of Tumor Specific Growth Factor by Using Ag@CeO$_2$ Nanocomposite as Labels. *Talanta* **2016**, *156−157*, 11−17.

(403) Tian, L.; Liu, L.; Li, Y.; Wei, Q.; Cao, W. Ultrasensitive Sandwich-Type Electrochemical Immunosensor Based on Trimetallic Nanocomposite Signal Amplification Strategy for the Ultrasensitive Detection of CEA. *Sci. Rep.* **2016**, *6*, 30849.

(404) Randviir, E. P.; Banks, C. E. Electrochemical Impedance Spectroscopy: An Overview of Bioanalytical Applications. *Anal. Methods* **2013**, *5*, 1098.

(405) Lisdat, F.; Schäfer, D. The Use of Electrochemical Impedance Spectroscopy for Biosensing. *Anal. Bioanal. Chem.* **2008**, *391*, 1555−1567.

(406) Daniels, J. S.; Pourmand, N. Label-Free Impedance Biosensors: Opportunities and Challenges. *Electroanalysis* **2007**, *19*, 1239−1257.

(407) Ma, H.; Li, Y.; Wang, Y.; Hu, L.; Zhang, Y.; Fan, D.; Yan, T.; Wei, Q. Cubic Cu$_2$O Nanoframes with a Unique Edge-Truncated Structure and a Good Electrocatalytic Activity for Immunosensor Application. *Biosens. Bioelectron.* **2016**, *78*, 167−173.

(408) Katz, E.; Willner, I. Probing Biomolecular Interactions at Conductive and Semiconductive Surfaces by Impedance Spectroscopy: Routes to Impedimetric Immunosensors, DNA-Sensors, and Enzyme Biosensors. *Electroanalysis* **2003**, *15*, 913−947.

(409) Yagati, A. K.; Choi, Y.; Park, J.; Choi, J.-W.; Jun, H.-S.; Cho, S. Silver Nanoflower−reduced Graphene Oxide Composite Based Micro-Disk Electrode for Insulin Detection in Serum. *Biosens. Bioelectron.* **2016**, *80*, 307−314.

(410) Wang, X.; Deng, W.; Shen, L.; Yan, M.; Yu, J. A 3D Electrochemical Immunodevice Based on an Au Paper Electrode and Using Au Nanoflowers for Amplification. *New J. Chem.* **2016**, *40*, 2835−2842.

(411) Wang, Y.; Li, Y.; Hu, L.; Ren, X.; Du, B.; Ma, H.; Wei, Q. Application of Three-Dimensional Flower-like Nanomaterials in the Fabrication of Sandwich-Type Electrochemical Immunosensors. *RSC Adv.* **2015**, *5*, 88160−88165.

(412) Raghav, R.; Srivastava, S. Core−shell Gold−silver Nanoparticles Based Impedimetric Immunosensor for Cancer Antigen CA125. *Sens. Actuators, B* **2015**, *220*, 557−564.

(413) Xiang, C.; Li, R.; Adhikari, B.; She, Z.; Li, Y.; Kraatz, H.-B. Sensitive Electrochemical Detection of Salmonella with Chitosan−gold Nanoparticles Composite Film. *Talanta* **2015**, *140*, 122−127.

(414) Yu, S.; Zou, G.; Wei, Q. Ultrasensitive Electrochemical Immunosensor for Quantitative Detection of Tumor Specific Growth Factor by Using Ag@CeO2 Nanocomposite as Labels. *Talanta* **2016**, *156−157*, 11−17.

(415) Tuteja, S. K.; Chen, R.; Kukkar, M.; Song, C. K.; Mutreja, R.; Singh, S.; Paul, A. K.; Lee, H.; Kim, K.-H.; Deep, A.; et al. A Label-Free Electrochemical Immunosensor for the Detection of Cardiac Marker Using Graphene Quantum Dots (GQDs). *Biosens. Bioelectron.* **2016**, *86*, 548−556.

(416) Jia, X.; Chen, X.; Han, J.; Ma, J.; Ma, Z. Triple Signal Amplification Using Gold Nanoparticles, Bienzyme and Platinum Nanoparticles Functionalized Graphene as Enhancers for Simultaneous Multiple Electrochemical Immunoassay. *Biosens. Bioelectron.* **2014**, *53*, 65−70.

(417) Ma, H.; Sun, J.; Zhang, Y.; Bian, C.; Xia, S.; Zhen, T. Label-Free Immunosensor Based on One-Step Electrodeposition of Chitosan-Gold Nanoparticles Biocompatible Film on Au Microelectrode for Determination of Aflatoxin B1 in Maize. *Biosens. Bioelectron.* **2016**, *80*, 222−229.

(418) Raymundo-Pereira, P. A.; Shimizu, F. M.; Coelho, D.; Piazzeta, M. H. O.; Gobbi, A. L.; Machado, S. A. S.; Oliveira, O. N., Jr. A Nanostructured Bifunctional Platform for Sensing of Glucose Biomarker in Artificial Saliva: Synergy in Hybrid Pt/Au Surfaces. *Biosens. Bioelectron.* **2016**, *86*, 369−376.

(419) Kavosi, B.; Hallaj, R.; Teymourian, H.; Salimi, A. Au Nanoparticles/PAMAM Dendrimer Functionalized Wired Ethyleneamine−viologen as Highly Efficient Interface for Ultra-Sensitive α-Fetoprotein Electrochemical Immunosensor. *Biosens. Bioelectron.* **2014**, *59*, 389−396.

(420) Ramanathan, M.; Patil, M.; Epur, R.; Yun, Y.; Shanov, V.; Schulz, M.; Heineman, W. R.; Datta, M. K.; Kumta, P. N. Gold-Coated Carbon Nanotube Electrode Arrays: Immunosensors for Impedimetric Detection of Bone Biomarkers. *Biosens. Bioelectron.* **2016**, *77*, 580−588.

(421) Li, L.; Feng, D.; Zhang, Y. Simultaneous Detection of Two Tumor Markers Using Silver and Gold Nanoparticles Decorated Carbon Nanospheres as Labels. *Anal. Biochem.* **2016**, *505*, 59−65.

(422) Akter, R.; Jeong, B.; Choi, J.-S.; Rahman, M. A. Ultrasensitive Nanoimmunosensor by Coupling Non-Covalent Functionalized Graphene Oxide Platform and Numerous Ferritin Labels on Carbon Nanotubes. *Biosens. Bioelectron.* **2016**, *80*, 123−130.

(423) Wang, G.; He, X.; Chen, L.; Zhu, Y.; Zhang, X. Ultrasensitive IL-6 Electrochemical Immunosensor Based on Au Nanoparticles-Graphene-Silica Biointerface. *Colloids Surf., B* **2014**, *116*, 714−719.

(424) Sun, B.; Gou, Y.; Ma, Y.; Zheng, X.; Bai, R.; Ahmed Abdelmoaty, A. A.; Hu, F. Investigate Electrochemical Immunosensor of Cortisol Based on Gold Nanoparticles/Magnetic Functionalized Reduced Graphene Oxide. *Biosens. Bioelectron.* **2017**, *88*, 55−62.

(425) Hou, L.; Tang, Y.; Xu, M.; Gao, Z.; Tang, D. Tyramine-Based Enzymatic Conjugate Repeats for Ultrasensitive Immunoassay Accompanying Tyramine Signal Amplification with Enzymatic Biocatalytic Precipitation. *Anal. Chem.* **2014**, *86*, 8352−8358.

(426) Wan, J.; Ai, J.; Zhang, Y.; Geng, X.; Gao, Q.; Cheng, Z. Signal-off Impedimetric Immunosensor for the Detection of Escherichia Coli O157:H7. *Sci. Rep.* **2016**, *6*, 19806.

(427) Shein, J. B.; Lai, L. M. H.; Eggers, P. K.; Paddon-Row, M. N.; Gooding, J. J. Formation of Efficient Electron Transfer Pathways by Adsorbing Gold Nanoparticles to Self-Assembled Monolayer Modified Electrodes. *Langmuir* **2009**, *25*, 11121−11128.

(428) Mihailescu, C.-M.; Stan, D.; Iosub, R.; Moldovan, C.; Savin, M. A Sensitive Capacitive Immunosensor for Direct Detection of Human Heart Fatty Acid-Binding Protein (h-FABP). *Talanta* **2015**, *132*, 37−43.

(429) Nguyen, P.-D.; Tran, T. B.; Nguyen, D. T. X.; Min, J. Magnetic Silica Nanotube-Assisted Impedimetric Immunosensor for the Separation and Label-Free Detection of Salmonella Typhimurium. *Sens. Actuators, B* **2014**, *197*, 314−320.

(430) Shalev, G.; Rosenwaks, Y.; Levy, I. The Interplay between pH Sensitivity and Label-Free Protein Detection in Immunologically Modified Nano-Scaled Field-Effect Transistor. *Biosens. Bioelectron.* **2012**, *31*, 510−515.

(431) He, Q.; Wu, S.; Yin, Z.; Zhang, H. Graphene-Based Electronic Sensors. *Chem. Sci.* **2012**, *3*, 1764.

(432) Yen, L.-C.; Pan, T.-M.; Lee, C.-H.; Chao, T.-S. Label-Free and Real-Time Detection of Ferritin Using a Horn-like Polycrystalline-Silicon Nanowire Field-Effect Transistor Biosensor. *Sens. Actuators, B* **2016**, *230*, 398−404.

(433) Elnathan, R.; Kwiat, M.; Pevzner, A.; Engel, Y.; Burstein, L.; Khatchtourints, A.; Lichtenstein, A.; Kantaev, R.; Patolsky, F. Biorecognition Layer Engineering: Overcoming Screening Limitations of Nanowire-Based FET Devices. *Nano Lett.* **2012**, *12*, 5245−5254.

(434) Belkhamssa, N.; Justino, C. I. L.; Santos, P. S. M.; Cardoso, S.; Lopes, I.; Duarte, A. C.; Rocha-Santos, T.; Ksibi, M. Label-Free Disposable Immunosensor for Detection of Atrazine. *Talanta* **2016**, *146*, 430−434.

(435) Chen, H.; Choo, T. K.; Huang, J.; Wang, Y.; Liu, Y.; Platt, M.; Palaniappan, A.; Liedberg, B.; Tok, A. I. Y. Label-Free Electronic

125

Detection of Interleukin-6 Using Horizontally Aligned Carbon Nanotubes. *Mater. Des.* **2016**, *90*, 852−857.

(436) Palaniappan, Al.; Goh, W. H.; Fam, D. W. H.; Rajaseger, G.; Chan, C. E. Z.; Hanson, B. J.; Moochhala, S. M.; Mhaisalkar, S. G.; Liedberg, B. Label-free electronic detection of bio-toxins using aligned carbon nanotubes. *Biosens. Bioelectron.* **2013**, *43*, 143−147.

(437) Ramnani, P.; Saucedo, N. M.; Mulchandani, A. Carbon Nanomaterial-Based Electrochemical Biosensors for Label-Free Sensing of Environmental Pollutants. *Chemosphere* **2016**, *143*, 85−98.

(438) Park, J. W.; Na, W.; Jang, J. One-Pot Synthesis of Multidimensional Conducting Polymer Nanotubes for Superior Performance Field-Effect Transistor-Type Carcinoembryonic Antigen Biosensors. *RSC Adv.* **2016**, *6*, 14335−14343.

(439) Kim, K.; Park, C.; Kwon, D.; Kim, D.; Meyyappan, M.; Jeon, S.; Lee, J.-S. Silicon Nanowire Biosensors for Detection of Cardiac Troponin I (cTnI) with High Sensitivity. *Biosens. Bioelectron.* **2016**, *77*, 695−701.

(440) Lin, M.-Y.; Hsu, W.-Y.; Yang, Y.-S.; Huang, J.-W.; Chung, Y.-L.; Chen, H. Immobilized Rolling Circle Amplification on Extended-Gate Field-Effect Transistors with Integrated Readout Circuits for Early Detection of Platelet-Derived Growth Factor. *Anal. Bioanal. Chem.* **2016**, *408*, 4785−4797.

(441) Tarasov, A.; Gray, D. W.; Tsai, M.-Y.; Shields, N.; Montrose, A.; Creedon, N.; Lovera, P.; O'Riordan, A.; Mooney, M. H.; Vogel, E. M. A Potentiometric Biosensor for Rapid on-Site Disease Diagnostics. *Biosens. Bioelectron.* **2016**, *79*, 669−678.

(442) Brince Paul, K.; Kumar, S.; Tripathy, S.; Vanjari, S. R. K.; Singh, V.; Singh, S. G. A Highly Sensitive Self Assembled Monolayer Modified Copper Doped Zinc Oxide Nanofiber Interface for Detection of Plasmodium Falciparum Histidine-Rich Protein-2: Targeted towards Rapid, Early Diagnosis of Malaria. *Biosens. Bioelectron.* **2016**, *80*, 39−46.

(443) Ahn, J.-H.; Im, M.; Park, T. J.; Lee, S. Y.; Choi, Y.-K. Label-Free and Real-Time Detection of Avian Influenza Using Nanowire Field Effect Transistors. *J. Biomed. Nanotechnol.* **2015**, *11*, 1640−1643.

(444) Lee, I.-K.; Jeun, M.; Jang, H.-J.; Cho, W.-J.; Lee, K. H. A Self-Amplified Transistor Immunosensor under Dual Gate Operation: Highly Sensitive Detection of Hepatitis B Surface Antigen. *Nanoscale* **2015**, *7*, 16789−16797.

(445) Jang, H.-J.; Ahn, J.; Kim, M.-G.; Shin, Y.-B.; Jeun, M.; Cho, W.-J.; Lee, K. H. Electrical Signaling of Enzyme-Linked Immunosorbent Assays with an Ion-Sensitive Field-Effect Transistor. *Biosens. Bioelectron.* **2015**, *64*, 318−323.

(446) Lu, N.; Dai, P.; Gao, A.; Valiaho, J.; Kallio, P.; Wang, Y.; Li, T. Label-Free and Rapid Electrical Detection of hTSH with CMOS-Compatible Silicon Nanowire Transistor Arrays. *ACS Appl. Mater. Interfaces* **2014**, *6*, 20378−20384.

(447) Kim, J.-Y.; Ahn, J.-H.; Moon, D.-I.; Park, T. J.; Lee, S. Y.; Choi, Y.-K. Multiplex Electrical Detection of Avian Influenza and Human Immunodeficiency Virus with an Underlap-Embedded Silicon Nanowire Field-Effect Transistor. *Biosens. Bioelectron.* **2014**, *55*, 162−167.

(448) Huang, W.; Besar, K.; LeCover, R.; Dulloor, P.; Sinha, J.; Martínez Hardigree, J. F.; Pick, C.; Swavola, J.; Everett, A. D.; Frechette, J.; et al. Label-Free Brain Injury Biomarker Detection Based on Highly Sensitive Large Area Organic Thin Film Transistor with Hybrid Coupling Layer. *Chem. Sci.* **2014**, *5*, 416−426.

(449) Issadore, D.; Park, Y. I.; Shao, H.; Min, C.; Lee, K.; Liong, M.; Weissleder, R.; Lee, H. Magnetic Sensing Technology for Molecular Analyses. *Lab Chip* **2014**, *14*, 2385−2397.

(450) Syed, M. A. Advances in Nanodiagnostic Techniques for Microbial Agents. *Biosens. Bioelectron.* **2014**, *51*, 391−400.

(451) Shao, H.; Min, C.; Issadore, D.; Liong, M.; Yoon, T.-J.; Weissleder, R.; Lee, H. Magnetic Nanoparticles and microNMR for Diagnostic Applications. *Theranostics* **2012**, *2*, 55−65.

(452) Haun, J. B.; Yoon, T.-J.; Lee, H.; Weissleder, R. Magnetic Nanoparticle Biosensors. *Wiley Interdisciplinary Reviews: Nanomedicine and Nanobiotechnology* **2010**, *2*, 291−304.

(453) Chen, Y. P.; Zou, M. q.; Qi, C.; Xie, M.-X.; Wang, D.-N.; Wang, Y.-F.; Xue, Q.; Li, J.-F.; Chen, Y. Immunosensor Based on Magnetic

(454) Liao, S.-H.; Chen, K.-L.; Wang, C.-M.; Chieh, J.-J.; Horng, H.-E.; Wang, L.-M.; Wu, C.; Yang, H.-C. Using Bio-Functionalized Magnetic Nanoparticles and Dynamic Nuclear Magnetic Resonance to Characterize the Time-Dependent Spin-Spin Relaxation Time for Sensitive Bio-Detection. *Sensors* **2014**, *14*, 21409−21417.

(455) Issadore, D.; Min, C.; Liong, M.; Chung, J.; Weissleder, R.; Lee, H. Miniature Magnetic Resonance System for Point-of-Care Diagnostics. *Lab Chip* **2011**, *11*, 2282−2287.

(456) Jogschies, L.; Klaas, D.; Kruppe, R.; Rittinger, J.; Taptimthong, P.; Wienecke, A.; Rissing, L.; Wurz, M. Recent Developments of Magnetoresistive Sensors for Industrial Applications. *Sensors* **2015**, *15*, 28665−28689.

(457) Ennen, I.; Albon, C.; Weddemann, A.; Auge, A.; Hedwig, P.; Wittbracht, F.; Regtmeier, A.; Akemeier, D.; Dreyer, A.; Peter, M.; et al. From Magnetic Nanoparticles to Magnetoresistive Biosensors. *Acta Phys. Pol., A* **2012**, *121*, 420−425.

(458) Manteca, A.; Mujika, M.; Arana, S. GMR Sensors: Magnetoresistive Behaviour Optimization for Biological Detection by Means of Superparamagnetic Nanoparticles. *Biosens. Bioelectron.* **2011**, *26*, 3705−3709.

(459) Wang, W.; Wang, Y.; Tu, L.; Feng, Y.; Klein, T.; Wang, J.-P. Magnetoresistive Performance and Comparison of Supermagnetic Nanoparticles on Giant Magnetoresistive Sensor-Based Detection System. *Sci. Rep.* **2015**, *4*, 5716.

(460) Chu, Y. W.; Engebretson, D. A.; Carey, J. R. Bioconjugated Magnetic Nanoparticles for the Detection of Bacteria. *J. Biomed. Nanotechnol.* **2013**, *9*, 1951−1961.

(461) Gao, Y. Z.; Zhang, L.; Huo, W. S.; Shi, S.; Lian, J.; Gao, Y. H. An Integrated Giant Magnetoresistance Microfluidic Immuno-Sensor for Rapid Detection and Quantification of D-Dimer. *Chin. J. Anal. Chem.* **2015**, *43*, 802−807.

(462) Kokkinis, G.; Jamalieh, M.; Cardoso, F.; Cardoso, S.; Keplinger, F.; Giouroudi, I. Magnetic-Based Biomolecule Detection Using Giant Magnetoresistance Sensors. *J. Appl. Phys.* **2015**, *117*, 17B731.

(463) Sun, X.; Lei, C.; Guo, L.; Zhou, Y. Separable Detecting of Escherichia Coli O157H:H7 by a Giant Magneto-Resistance-Based Bio-Sensing System. *Sens. Actuators, B* **2016**, *234*, 485−492.

(464) Lee, J.-R.; Bechstein, D. J. B.; Ooi, C. C.; Patel, A.; Gaster, R. S.; Ng, E.; Gonzalez, L. C.; Wang, S. X. Magneto-Nanosensor Platform for Probing Low-Affinity Protein−protein Interactions and Identification of a Low-Affinity PD-L1/PD-L2 Interaction. *Nat. Commun.* **2016**, *7*, 12220.

(465) Ng, E.; Nadeau, K. C.; Wang, S. X. Giant Magnetoresistive Sensor Array for Sensitive and Specific Multiplexed Food Allergen Detection. *Biosens. Bioelectron.* **2016**, *80*, 359−365.

(466) Kim, D.; Lee, J.-R.; Shen, E.; Wang, S. X. Modeling and Experiments of Magneto-Nanosensors for Diagnostics of Radiation Exposure and Cancer. *Biomed. Microdevices* **2013**, *15*, 665−671.

(467) Li, F.; Kosel, J. A Magnetic Biosensor System for Detection of E. coli. *IEEE Trans. Magn.* **2013**, *49*, 3492−3495.

(468) Li, F.; Kosel, J. An Efficient Biosensor Made of an Electromagnetic Trap and a Magneto-Resistive Sensor. *Biosens. Bioelectron.* **2014**, *59*, 145−150.

(469) Pizzella, V.; Penna, S. D.; Gratta, C. D.; Romani, G. L. SQUID Systems for Biomagnetic Imaging. *Supercond. Sci. Technol.* **2001**, *14*, R79−R114.

(470) Uchida, S.; Higuchi, Y.; Ueoka, Y.; Yoshida, T.; Enpuku, K.; Adachi, S.; Tanabe, K.; Tsukamoto, A.; Kandori, A. Highly Sensitive Liquid-Phase Detection of Biological Targets With Magnetic Markers and High SQUID. *IEEE Trans. Appl. Supercond.* **2014**, *24*, 1−5.

(471) Bhuiya, A. K.; Asai, M.; Watanabe, H.; Hirata, T.; Higuchi, Y.; Yoshida, T.; Enpuku, K. Characterization of Magnetic Markers and Sensors for Liquid-Phase Immunoassays Using Brownian Relaxation. *IEEE Trans. Magn.* **2012**, *48*, 2838−2841.

(472) Orlov, A. V.; Bragina, V. A.; Nikitin, M. P.; Nikitin, P. I. Rapid Dry-Reagent Immunomagnetic Biosensing Platform Based on Volu-

126

metric Detection of Nanoparticles on 3D Structures. *Biosens. Bioelectron.* **2016**, *79*, 423−429.

(473) Rettcher, S.; Jungk, F.; Kühn, C.; Krause, H.-J.; Nölke, G.; Commandeur, U.; Fischer, R.; Schillberg, S.; Schröper, F. Simple and Portable Magnetic Immunoassay for Rapid Detection and Sensitive Quantification of Plant Viruses. *Appl. Environ. Microbiol.* **2015**, *81*, 3039−3048.

(474) Zheng, Y.; Shang, N.; Haddad, P. S.; Sawan, M. A Microsystem for Magnetic Immunoassay Based on Planar Microcoil Array. *IEEE Trans. Biomed. Circ. Syst* **2016**, *10*, 477−486.

(475) Chang, A.-Y.; Lu, M. S.-C. A CMOS Magnetic Microbead-Based Capacitive Biosensor Array with on-Chip Electromagnetic Manipulation. *Biosens. Bioelectron.* **2013**, *45*, 6−12.

(476) Yang, Z.; Lei, J.; Sun, X.; Lei, C.; Zhou, Y.; Liu, Y. A Dynabeads-Labeled Immunoassay Based on a Fluxgate Biosensor for the Detection of Biomarkers. *Anal. Methods* **2015**, *7*, 2391−2398.

(477) Bogue, R. Recent developments in MEMS sensors: a review of applications, markets and technologies. *Sens. Rev.* **2013**, *33*, 300−304.

(478) Sun, X.; Lei, C.; Guo, L.; Zhou, Y. Sandwich Immunoassay for the Prostate Specific Antigen Using a Micro-Fluxgate and Magnetic Bead Labels. *Microchim. Acta* **2016**, *183*, 2385−2393.

(479) Kim, C.-B.; Lim, E.-G.; Shin, S. W.; Krause, H. J.; Hong, H. Magnetic Immunoassay Platform Based on the Planar Frequency Mixing Magnetic Technique. *Biosens. Bioelectron.* **2016**, *83*, 293−299.

(480) Sauerbrey, G. Verwendung von Schwingquarzen Zur Wägung Dünner Schichten Und Zur Mikrowägung. *Eur. Phys. J. A* **1959**, *155*, 206−222.

(481) Ramos-Jesus, J.; Pontes-de-Carvalho, L. C.; Melo, S. M. B.; Alcântara-Neves, N. M.; Dutra, R. F. A Gold Nanoparticle Piezoelectric Immunosensor Using a Recombinant Antigen for Detecting Leishmania Infantum Antibodies in Canine Serum. *Biochem. Eng. J.* **2016**, *110*, 43−50.

(482) Ding, J.; Lu, Z.; Wang, R.; Shen, G.; Xiao, L. Piezoelectric Immunosensor with Gold Nanoparticles Enhanced Competitive Immunoreaction Technique for 2,4-Dichlorophenoxyacetic Acid Quantification. *Sens. Actuators, B* **2014**, *193*, 568−573.

(483) Chu, P.-T.; Lin, C.-S.; Chen, W.-J.; Chen, C.-F.; Wen, H.-W. Detection of Gliadin in Foods Using a Quartz Crystal Microbalance Biosensor That Incorporates Gold Nanoparticles. *J. Agric. Food Chem.* **2012**, *60*, 6483−6492.

(484) Kleo, K.; Schäfer, D.; Klar, S.; Jacob, D.; Grunow, R.; Lisdat, F. Immunodetection of Inactivated Francisella Tularensis Bacteria by Using a Quartz Crystal Microbalance with Dissipation Monitoring. *Anal. Bioanal. Chem.* **2012**, *404*, 843−851.

(485) Yan, Z.; Yang, M.; Wang, Z.; Zhang, F.; Xia, J.; Shi, G.; Xia, L.; Li, Y.; Xia, Y.; Xia, L. A Label-Free Immunosensor for Detecting Common Acute Lymphoblastic Leukemia Antigen (CD10) Based on Gold Nanoparticles by Quartz Crystal Microbalance. *Sens. Actuators, B* **2015**, *210*, 248−253.

(486) Luo, Y.; Liu, T.; Zhu, J.; Kong, L.; Wang, W.; Tan, L. Label-Free and Sensitive Detection of Thrombomodulin, a Marker of Endothelial Cell Injury, Using Quartz Crystal Microbalance. *Anal. Chem.* **2015**, *87*, 11277−11284.

(487) Voinova, M. V.; Jonson, M.; Kasemo, B. Missing Mass" Effect in Biosensor's QCM Applications. *Biosens. Bioelectron.* **2002**, *17*, 835−841.

(488) Liu, W.; Huang, R.; Qi, W.; Wang, M.; Su, R.; He, Z. A Gas-Phase Amplified Quartz Crystal Microbalance Immunosensor Based on Catalase Modified Immunoparticles. *Analyst* **2015**, *140*, 1174−1181.

(489) Chen, S.; Pan, D.; Gan, N.; Wang, D.; Zhu, Y.; Li, T.; Cao, Y.; Hu, F.; Jiang, S. A QCM Immunosensor to Rapidly Detect Ractopamine Using Bio-Polymer Conjugate and Magnetic β-Cyclodextrins. *Sens. Actuators, B* **2015**, *211*, 523−530.

(490) Akter, R.; Rhee, C. K.; Rahman, M. A. A Highly Sensitive Quartz Crystal Microbalance Immunosensor Based on Magnetic Bead-Supported Bienzymes Catalyzed Mass Enhancement Strategy. *Biosens. Bioelectron.* **2015**, *66*, 539−546.

(491) Zhou, J.; Gan, N.; Li, T.; Zhou, H.; Li, X.; Cao, Y.; Wang, L.; Sang, W.; Hu, F. Ultratrace Detection of C-Reactive Protein by a Piezoelectric Immunosensor Based on Fe$_3$O$_4$@SiO$_2$ Magnetic Capture

Nanoprobes and HRP-Antibody Co-Immobilized Nano Gold as Signal Tags. *Sens. Actuators, B* **2013**, *178*, 494−500.

(492) Juřík, T.; Skládal, P. Detection of Hydrogen Peroxide and Glucose by Enzyme Product Precipitation on Sensor Surface. *Chem. Papers* **2015**, *69*, 167−175.

(493) Chauhan, R.; Singh, J.; Solanki, P. R.; Basu, T.; O'Kennedy, R.; Malhotra, B. D. Electrochemical Piezoelectric Reusable Immunosensor for Aflatoxin B1 Detection. *Biochem. Eng. J.* **2015**, *103*, 103−113.

(494) Chauhan, R.; Singh, J.; Solanki, P. R.; Manaka, T.; Iwamoto, M.; Basu, T.; Malhotra, B. D. Label-Free Piezoelectric Immunosensor Decorated with Gold Nanoparticles: Kinetic Analysis and Biosensing Application. *Sens. Actuators, B* **2016**, *222*, 804−814.

(495) Ly, T. N.; Park, S.; Park, S. J. Detection of HIV-1 Antigen by Quartz Crystal Microbalance Using Gold Nanoparticles. *Sens. Actuators, B* **2016**, *237*, 452−458.

(496) Ding, P.; Liu, R.; Liu, S.; Mao, X.; Hu, R.; Li, G. Reusable Gold Nanoparticle Enhanced QCM Immunosensor for Detecting C-Reactive Protein. *Sens. Actuators, B* **2013**, *188*, 1277−1283.

(497) Reddy, S. B.; Mainwaring, D. E.; Al Kobaisi, M.; Zeephongsekul, P.; Fecondo, J. V. Acoustic Wave Immunosensing of a Meningococcal Antigen Using Gold Nanoparticle-Enhanced Mass Sensitivity. *Biosens. Bioelectron.* **2012**, *31*, 382−387.

(498) Salam, F.; Uludag, Y.; Tothill, I. E. Real-Time and Sensitive Detection of *Salmonella* Typhimurium Using an Automated Quartz Crystal Microbalance (QCM) Instrument with Nanoparticles Amplification. *Talanta* **2013**, *115*, 761−767.

(499) Masdor, N. A.; Altintas, Z.; Tothill, I. E. Sensitive Detection of Campylobacter Jejuni Using Nanoparticles Enhanced QCM Sensor. *Biosens. Bioelectron.* **2016**, *78*, 328−336.

(500) Kohn, K. W.; Zeeberg, B. M.; Reinhold, W. C.; Pommier, Y. Gene Expression Correlations in Human Cancer Cell Lines Define Molecular Interaction Networks for Epithelial Phenotype. *PLoS One* **2014**, *9* (6), e99269.

(501) Duffy, M. J. Tumor Markers in Clinical Practice: A Review Focusing on Common Solid Cancers. *Med. Princ. Pract.* **2013**, *22*, 4−11.

(502) Wu, L.; Qu, X. Cancer biomarker detection: recent achievements and challenges. *Chem. Soc. Rev.* **2015**, *44* (10), 2963−2997.

(503) Topkaya, S. N.; Azimzadeh, M.; Ozsoz, M. Electrochemical Biosensors for Cancer Biomarkers Detection: Recent Advances and Challenges. *Electroanalysis* **2016**, *28*, 1402−1419.

(504) Yu, M.; Stott, S.; Toner, M.; Maheswaran, S.; Haber, D. A. Circulating Tumor Cells: Approaches to Isolation and Characterization. *J. Cell Biol.* **2011**, *192*, 373−382.

(505) Riethdorf, S.; Fritsche, H.; Muller, V.; Rau, T.; Schindlbeck, C.; Rack, B.; Janni, W.; Coith, C.; Beck, K.; Janicke, F.; Jackson, S.; Gornet, T.; Cristofanilli, M.; Pantel, K. Detection of Circulating Tumor Cells in Peripheral Blood of Patients with Metastatic Breast Cancer: A Validation Study of the CellSearch System. *Clin. Cancer Res.* **2007**, *13*, 920−928.

(506) Yang, K.; Hu, Y.; Dong, N. A Novel Biosensor Based on Competitive SERS Immunoassay and Magnetic Separation (for Accurate and Sensitive Detection of Chloramphenicol. *Biosens. Bioelectron.* **2016**, *80*, 373−377.

(507) Ashwin, H. M.; Stead, S. L.; Taylor, J. C.; Startin, J. R.; Richmond, S. F.; Homer, V.; Bigwood, T.; Sharman, M. Development and Validation of Screening and Confirmatory Methods for the Detection of Chloramphenicol and Chloramphenicol Glucuronide Using SPR Biosensor and Liquid Chromatography−tandem Mass Spectrometry. *Anal. Chim. Acta* **2005**, *529*, 103−108.

(508) Oaks, J. L.; Gilbert, M.; Virani, M. Z.; Watson, R. T.; Meteyer, C. U.; Rideout, B. A.; Shivaprasad, H. L.; Ahmed, S.; Iqbal Chaudhry, M. J.; Arshad, M.; Mahmood, S.; Ali, A.; Ahmed Khan, A. Diclofenac Residues as the Cause of Vulture Population Decline in Pakistan. *Nature* **2004**, *427*, 630−633.

(509) Rezaei, B.; Askarpour, N.; Ensafi, A. A. A Novel Sensitive Doxorubicin Impedimetric Immunosensor Based on a Specific Monoclonal Antibody−Gold Nanoaprticle−Sol−Gel Modified Electrode. *Talanta* **2014**, *119*, 164−169.

(510) Zhang, Y.-W.; Shi, J.; Li, Y.-J.; Wei, L. Cardiomyocyte Death in Doxorubicin-Induced Cardiotoxicity. *Arch. Immunol. Ther. Exp.* **2009**, *57*, 435−445.

(511) Finegold, S. M. Toxicity of Kanamycin in Adults. *Ann. N. Y. Acad. Sci.* **1966**, *132*, 942−956.

(512) Zengin, A.; Tamer, U.; Caykara, T. Extremely Sensitive Sandwich Assay of Kanamycin Using Surface-Enhanced Raman Scattering of 2-Mercaptobenzothiazole Labeled Gold@silver Nanoparticles. *Anal. Chim. Acta* **2014**, *817*, 33−41.

(513) Sun, X.; Wu, L.; Ji, J.; Jiang, D.; Zhang, Y.; Li, Z.; Zhang, G.; Zhang, H. Longitudinal Surface Plasmon Resonance Assay Enhanced by Magnetosomes for Simultaneous Detection of Pefloxacin and Microcystin-LR in Seafoods. *Biosens. Bioelectron.* **2013**, *47*, 318−323.

(514) Monk, J. P.; Campoli-Richards, D. M. Ofloxacin. *Drugs* **1987**, *33*, 346−391.

(515) Todd, P. A.; Faulds, D. Ofloxacin. *Drugs* **1991**, *42*, 825−876.

(516) Zang, S.; Liu, Y.; Lin, M.; Kang, J.; Sun, Y.; Lei, H. A Dual Amplified Electrochemical Immunosensor for Ofloxacin: Polypyrrole Film-Au Nanocluster as the Matrix and Multi-Enzyme-Antibody Functionalized Gold Nanorod as the Label. *Electrochim. Acta* **2013**, *90*, 246−253.

(517) Wang, H.; Zhang, Y.; Li, H.; Du, B.; Ma, H.; Wu, D.; Wei, Q. A Silver−Palladium Alloy Nanoparticle-Based Electrochemical Biosensor for Simultaneous Detection of Ractopamine, Clenbuterol and Salbutamol. *Biosens. Bioelectron.* **2013**, *49*, 14−19.

(518) Alhareth, K.; Vauthier, C.; Gueutin, C.; Ponchel, G.; Moussa, F. HPLC Quantification of Doxorubicin in Plasma and Tissues of Rats Treated with Doxorubicin Loaded Poly(alkylcyanoacrylate) Nanoparticles. *J. Chromatogr. B: Anal. Technol. Biomed. Life Sci.* **2012**, *887−888*, 128−132.

(519) Morales-Trejo, F.; León, S. V.; Escobar-Medina, A.; Gutiérrez-Tolentino, R. Application of High-Performance Liquid chromatography−UV Detection to Quantification of Clenbuterol in Bovine Liver Samples. *J. Food Drug Anal.* **2013**, *21*, 414−420.

(520) Impens, S.; Reybroeck, W.; Vercammen, J.; Courtheyn, D.; Ooghe, S.; De Wasch, K.; Smedts, W.; De Brabander, H. Screening and Confirmation of Chloramphenicol in Shrimp Tissue Using ELISA in Combination with GC−MS2 and LC−MS2. *Anal. Chim. Acta* **2003**, *483*, 153−163.

(521) He, L.; Su, Y.; Zeng, Z.; Liu, Y.; Huang, X. Determination of Ractopamine and Clenbuterol in Feeds by Gas Chromatography−mass Spectrometry. *Anim. Feed Sci. Technol.* **2007**, *132*, 316−323.

(522) Lu, H.; Yuan, G.; He, Q.; Chen, H. Rapid Analysis of Anthracycline Antibiotics Doxorubicin and Daunorubicin by Microchip Capillary Electrophoresis. *Microchem. J.* **2009**, *92*, 170−173.

(523) Horstkötter, C.; Blaschke, G. Stereoselective Determination of Ofloxacin and Its Metabolites in Human Urine by Capillary Electrophoresis Using Laser-Induced Fluorescence Detection. *J. Chromatogr., Biomed. Appl.* **2001**, *754*, 169−178.

(524) He, P.; Shen, L.; Liu, R.; Luo, Z.; Li, Z. Direct Detection of β-Agonists by Use of Gold Nanoparticle-Based Colorimetric Assays. *Anal. Chem.* **2011**, *83*, 6988−6995.

(525) Martínez Ferreras, F.; Wolfbeis, O. S.; Gorris, H. H. Dual Lifetime Referenced Fluorometry for the Determination of Doxorubicin in Urine. *Anal. Chim. Acta* **2012**, *729*, 62−66.

(526) Francis, P. S.; Adcock, J. L. Chemiluminescence Methods for the Determination of Ofloxacin. *Anal. Chim. Acta* **2005**, *541*, 3−12.

(527) Zhang, B.; Liu, B.; Zhou, J.; Tang, J.; Tang, D. Additional Molecular Biological Amplification Strategy for Enhanced Sensitivity of Monitoring Low-Abundance Protein with Dual Nanotags. *ACS Appl. Mater. Interfaces* **2013**, *5*, 4479−4485.

(528) Zhang, X.; Tan, X.; Zhang, B.; Miao, W.; Zou, G. Spectrum-Based Electrochemiluminescent Immunoassay with Ternary CdZnSe Nanocrystals as Labels. *Anal. Chem.* **2016**, *88*, 6947−6953.

(529) Xia, C.; Li, Y.; Yuan, G.; Guo, Y.; Yu, C. Immunoassay for serum amyloid A using a glassy carbon electrode modified with carboxy-polypyrrole, multiwalled carbon nanotubes, ionic liquid and chitosan. *Microchim. Acta* **2015**, *182*, 1395−1402.

(530) Wu, C. C.; Ku, B. C.; Ko, C. H.; Chiu, C. C.; Wang, G. J.; Yang, Y. H.; Wu, S. J. Electrochemical impedance spectroscopy analysis of A-beta (1−42) peptide using a nanostructured biochip. *Electrochim. Acta* **2014**, *134*, 249−257.

(531) Wang, H.; Li, G.; Zhang, Y.; Zhu, M.; Ma, H.; Du, B.; Wei, Q.; Wan, Y. Nanobody-Based Electrochemical Immunoassay for Ultrasensitive Determination of Apolipoprotein-A1 Using Silver Nanoparticles Loaded Nanohydroxyapatite as Label. *Anal. Chem.* **2015**, *87*, 11209−11214.

(532) Chen, H. C.; Chen, Y. T.; Tsai, R. Y.; Chen, M. C.; Chen, S. L.; Xiao, M. C.; Chen, C. L.; Hua, M. Y. A Sensitive and Selective Magnetic Graphene Composite-Modified Polycrystalline-Silicon Nanowire Field-Effect Transistor for Bladder Cancer Diagnosis. *Biosens. Bioelectron.* **2015**, *66*, 198−207.

(533) Zhou, S. W.; Wang, Y. Y.; Zhu, J. J. Simultaneous Detection of Tumor Cell Apoptosis Regulators Bcl-2 and Bax through a Dual-Signal-Marked Electrochemical Immunosensor. *ACS Appl. Mater. Interfaces* **2016**, *8*, 7674−7682.

(534) Zhang, X.; Wang, H.; Yang, C.; Du, D.; Lin, Y. Preparation, Characterization of Fe_3O_4 at TiO_2 magnetic nanoparticles and their application for immunoassay of biomarker of exposure to organophosphorus pesticides. *Biosens. Bioelectron.* **2013**, *41*, 669−674.

(535) Geng, P.; Fu, Y.; Yang, M.; Sun, Q.; Liu, K.; Zhang, X.; Xu, Z.; Zhang, W. Amplified Electrochemical Immunosensor for Calmodulin Detection Based on Gold-Silver-Graphene Hybrid Nanomaterials and Enhanced Gold Nanorods Labels. *Electroanalysis* **2014**, *26*, 2002−2009.

(536) Johari-Ahar, M.; Rashidi, M. R.; Barar, J.; Aghaie, M.; Mohammadnejad, D.; Ramazani, A.; Karami, P.; Coukos, G.; Omidi, Y. An Ultra-Sensitive Impedimetric Immunosensor for Detection of the Serum Oncomarker CA-125 in Ovarian Cancer Patients. *Nanoscale* **2015**, *7*, 3768−3779.

(537) Zhu, H.; Fan, G. C.; Abdel-Halim, E. S.; Zhang, J. R.; Zhu, J. J. Ultrasensitive Photoelectrochemical Immunoassay for CA19−9 Detection Based on CdSe@ZnS Quantum Dots Sensitized TiO_2 NWs/Au Hybrid Structure Amplified by Quenching Effect of Ab(2)@V^{2+} Conjugates. *Biosens. Bioelectron.* **2016**, *77*, 339−346.

(538) Sha, Y.; Guo, Z.; Chen, B.; Wang, S.; Ge, G.; Qiu, B.; Jiang, X. A One-Step Electrochemiluminescence Immunosensor Preparation for Ultrasensitive Detection of Carbohydrate Antigen 19−9 Based on Multifunctionalized Graphene Oxide. *Biosens. Bioelectron.* **2015**, *66*, 468−473.

(539) Zhang, L.; He, Y.; Wang, H.; Yuan, Y.; Yuan, R.; Chai, Y. A Self-Enhanced Electrochemiluminescence Immunosensor Based on L-Lys-Ru(dcbpy)(3)(2+) Functionalized Porous Six Arrises Column Nanorods for Detection of CA15−3. *Biosens. Bioelectron.* **2015**, *74*, 924−930.

(540) Cui, Y.; Tang, D.; Liu, B.; Chen, H.; Zhang, B.; Chen, G. Biofunctionalized Dendritic Polyaniline Nanofibers for Sensitive Electrochemical Immunoassay of Biomarkers. *Analyst* **2012**, *137*, 1656−1662.

(541) Zhou, S.; Zheng, W.; Chen, Z.; Tu, D.; Liu, Y.; Ma, E.; Li, R.; Zhu, H.; Huang, M.; Chen, X. Dissolution-Enhanced Luminescent Bioassay Based on Inorganic Lanthanide Nanoparticles. *Angew. Chem., Int. Ed.* **2014**, *53*, 12498−12502.

(542) Quyen, T. T. B.; Chang, C.-C.; Su, W.-N.; Uen, Y.-H.; Pan, C.-J.; Liu, J.-Y.; Rick, J.; Lin, K.-Y.; Hwang, B.-J. Self-Focusing Au@SiO$_2$ Nanorods with Rhodamine 6G as Highly Sensitive SERS Substrate for Carcinoembryonic Antigen Detection. *J. Mater. Chem. B* **2014**, *2*, 629−636.

(543) Zeng, H.; Agyapong, D. A. Y.; Li, C.; Zhao, R.; Yang, H.; Wu, C.; Jiang, Y.; Liu, Y. A Carcinoembryonic Antigen Optoelectronic Immunosensor Based on Thiol-Derivative-Nanogold Labeled Anti-CEA Antibody Nanomaterial and Gold Modified ITO. *Sens. Actuators, B* **2015**, *221*, 22−27.

(544) He, S.; Wang, Q.; Yu, Y.; Shi, Q.; Zhang, L.; Chen, Z. One-Step Synthesis of Potassium Ferricyanide-Doped Polyaniline Nanoparticles for Label-Free Immunosensor. *Biosens. Bioelectron.* **2015**, *68*, 462−467.

(545) Wang, Y.; Li, Y.; Hu, L.; Ren, X.; Du, B.; Ma, H.; Wei, Q. Application of Three-Dimensional Flower-Like Nanomaterials in the

128

Fabrication of Sandwich-Type Electrochemical Immunosensors. *RSC Adv.* **2015**, *5*, 88160−88165.

(546) Rong, Q.; Han, H.; Feng, F.; Ma, Z. Network Nanostructured Polypyrrole Hydrogel/Au Composites as Enhanced Electrochemical Biosensing Platform. *Sci. Rep.* **2015**, *5*, 11440.

(547) Hou, L.; Cui, Y.; Xu, M.; Gao, Z.; Huang, J.; Tang, D. Graphene Oxide-Labeled Sandwich-Type Impedimetric immunoassay with sensitive Enhancement Based on Enzymatic 4-Chloro-1-naphthol oxidation. *Biosens. Bioelectron.* **2013**, *47*, 149−156.

(548) Feng, T.; Qiao, X.; Wang, H.; Sun, Z.; Hong, C. A Sandwich-Type Electrochemical Immunosensor for Carcinoembryonic Antigen Based on Signal Amplification Strategy of Optimized Ferrocene Functionalized Fe₃O₄@SiO₂ as Labels. *Biosens. Bioelectron.* **2016**, *79*, 48−54.

(549) Vabbina, P. K.; Kaushik, A.; Pokhrel, N.; Bhansali, S.; Pala, N. Electrochemical Cortisol Immunosensors Based on Sonochemically Synthesized Zinc Oxide 1D Nanorods and 2D Nanoflakes. *Biosens. Bioelectron.* **2015**, *63*, 124−130.

(550) Ramanathan, M.; Patil, M.; Epur, R.; Yun, Y.; Shanov, V.; Schulz, M.; Heineman, W. R.; Datta, M. K.; Kumta, P. N. Gold-Coated Carbon Nanotube Electrode Arrays: Immunosensors for Impedimetric Detection of Bone Biomarkers. *Biosens. Bioelectron.* **2016**, *77*, 580−588.

(551) Mi, L.; Wang, P. Y.; Yan, J. R.; Qian, J.; Lu, J. S.; Yu, J. C.; Wang, Y. Z.; Liu, H.; Zhu, M.; Wan, Y. K.; Liu, S. Q. A Novel Photoelectrochemical Immunosensor by Integration of Nanobody and TiO₂ Nanotubes for Sensitive Detection of Serum Cystatin C. *Anal. Chim. Acta* **2016**, *902*, 107−114.

(552) Wang, H. Q.; Rong, Q. F.; Ma, Z. F. Polyhydroquinone-Graphene Composite as New Redox Species for Sensitive Electro-chemical Detection of Cytokeratins Sntigen 21-1. *Sci. Rep.* **2016**, *6*, 30623.

(553) Asav, E.; Sezginturk, M. K. A Novel Impedimetric Disposable Immunosensor for Rapid Detection of a Potential Cancer Biomarker. *Int. J. Biol. Macromol.* **2014**, *66*, 273−280.

(554) Zhang, Y.; Ren, W. Carbon Nanosphere-Functionalized Graphene Nanosheets for Sensing Biomolecules Based on Platinum Nanoflower Labeling. *Anal. Methods* **2013**, *5*, 3379−3385.

(555) Yu, X.; Wang, J.; Chen, X.; Wu, K.; Chen, D.; Ma, M.; Huang, Z.; Wu, W.; Li, C. White-Light-Exciting, Layer-by-Layer-Assembled ZnCdHgSe Quantum Dots/Polymerized Ionic Liquid Hybrid Film for Highly Sensitive Photoelectrochemical lmmunosensing of Neuron Specific Enolase. *Anal. Chem.* **2015**, *87*, 4237−4244.

(556) Wang, Y.; Vaidyanathan, R.; Shiddiky, M. J. A.; Trau, M. Enabling Rapid and Specific Surface-Enhanced Raman Scattering Immunoassay Using Nanoscaled Surface Shear Forces. *ACS Nano* **2015**, *9*, 6354−6362.

(557) Omidfar, K.; Darzianiazizi, M.; Ahmadi, A.; Daneshpour, M.; Shirazi, H. A High Sensitive Electrochemical Nanoimmunosensor Based on Fe₃O₄/TMC/Au Nanocompo Dite and Pt-Modified Electrode for the Detection of Cancer Biomarker Epidermal Growth Factor Receptor. *Sens. Actuators, B* **2015**, *220*, 1311−1319.

(558) Fernandez-Baldo, M. A.; Ortega, F. G.; Pereira, S. V.; Bertolino, F. A.; Serrano, M. J.; Lorente, J. A.; Raba, J.; Messina, G. A. Nanostructured Platform Integrated into a Microfluidic Immunosensor Coupled to Laser-Induced Fluorescence for the Epithelial Cancer Biomarker Determination. *Microchem. J.* **2016**, *128*, 18−25.

(559) Han, J.; Zhuo, Y.; Chai, Y. Q.; Xiang, Y.; Yuan, R. New Type of Redox Nanoprobe: C-60-Based Nanomaterial and Its Application in Electrochemical Immunoassay for Doping Detection. *Anal. Chem.* **2015**, *87*, 1669−1675.

(560) Cincotto, F. H.; Martinez-Garcia, G.; Yanez-Sedeno, P.; Canevari, T. C.; Machado, S. A. S.; Pingarron, J. M. Electrochemical Immunosensor for Ethinylestradiol using Diazonium Salt Grafting onto Silver Nanoparticles-Silica-Graphene Oxide Hybrids. *Talanta* **2016**, *147*, 328−334.

(561) Yen, L. C.; Pan, T. M.; Lee, C. H.; Chao, T. S. Label-Free and Real-Time Detection of Ferritin using a Horn-Like Polycrystalline-Silicon Nanowire Field-Effect Transistor Biosensor. *Sens. Actuators, B* **2016**, *230*, 398−404.

(562) Lu, J.; Liu, S.; Ge, S.; Yan, M.; Yu, J.; Hu, X. Ultrasensitive Electrochemical Immunosensor Based on Au Nanoparticles Dotted Carbon Nanotube-Graphene Composite and Functionalized Meso-porous Materials. *Biosens. Bioelectron.* **2012**, *33*, 29−35.

(563) Wu, D.; Zhang, Y.; Shi, L.; Cai, Y.; Ma, H.; Du, B.; Wei, Q. Electrochemical Immunosensor for Ultrasensitive Detection of Human Chorionic Gonadotropin Based on Pd@SBA-15. *Electroanalysis* **2013**, *25*, 427−432.

(564) Teixeira, S.; Ferreira, N. S.; Conlan, R. S.; Guy, O. J.; Sales, M. G. F. Chitosan/AuNPs Modified Graphene Electrochemical Sensor for Label-Free Human Chorionic Gonadotropin Detection. *Electroanalysis* **2014**, *26*, 2591−2598.

(565) Yagati, A. K.; Park, J.; Cho, S. Reduced Graphene Oxide Modified the Interdigitated Chain Electrode for an Insulin Sensor. *Sensors* **2016**, *16*, 109.

(566) Singh, V.; Krishnan, S. Voltammetric Immunosensor Assembled on Carbon-Pyrenyl Nanostructures for Clinical Diagnosis of Type of Diabetes. *Anal. Chem.* **2015**, *87*, 2648−2654.

(567) Inci, F.; Filippini, C.; Baday, M.; Ozen, M. O.; Calamak, S.; Durmus, N. G.; Wang, S. Q.; Hanhauser, E.; Hobbs, K. S.; Juillard, F.; et al. Multitarget, Quantitative Nanoplasmonic Electrical Field-Enhanced Resonating Device ((NERD)-R-2) for Diagnostics. *Proc. Natl. Acad. Sci. U. S. A.* **2015**, *112*, E4354−E4363.

(568) Yang, T.; Wang, S.; Jin, H.; Bao, W.; Huang, S.; Wang, J. An Electrochemical Impedance Sensor for the Label-Free Ultrasensitive Detection of Interleukin-6 Antigen. *Sens. Actuators, B* **2013**, *178*, 310−315.

(569) Wang, G.; He, X.; Chen, L.; Zhu, Y.; Zhang, X. Ultrasensitive IL-6 Electrochemical Immunosensor Based on Au Nanoparticles-Graphene-Silica Biointerface. *Colloids Surf., B* **2014**, *116*, 714−719.

(570) Jiang, W.; Li, T.; Qu, F.; Ding, L.; Shen, Z.; Yang, M. Electrochemical Immunosensor for the Detection of Interleukin-17 Based on Cd²⁺ Incorporated Polystyrene Spheres. *Sens. Actuators, B* **2013**, *185*, 658−662.

(571) Li, Y.; He, J.; Xia, C.; Gao, L.; Yu, C. Ultrasensitive Electrochemical Immunosensor Based on Orderly Oriented Conductive Wires for the Detection of Human Monocyte Chemotactic Protein-1 in Serum. *Biosens. Bioelectron.* **2015**, *70*, 392−397.

(572) Guo, Q.; Li, X.; Shen, C.; Zhang, S.; Qi, H.; Li, T.; Yang, M. Electrochemical Immunoassay for the Protein Biomarker Mucin 1 and for MCF-7 Cancer Cells Based on Signal Enhancement by Silver Nanoclusters. *Microchim. Acta* **2015**, *182*, 1483−1489.

(573) He, Y.; Wang, Y.; Yang, X.; Xie, S. B.; Yuan, R.; Chai, Y. Q. Metal Organic Frameworks Combining CoFe₂O₄ Magnetic Nanoparticles as Highly Efficient SERS Sensing Platform for Ultrasensitive Detection of N-Terminal Pro-Brain Natriuretic Peptide. *ACS Appl. Mater. Interfaces* **2016**, *8*, 7683−7690.

(574) Xu, W.; He, J.; Gao, L.; Zhang, J.; Yu, C. Immunoassay for Netrin 1 via a Glassy Carbon Electrode Modified with Multi-Walled Carbon Nanotubes, Thionine and Gold Nanoparticles. *Microchim. Acta* **2015**, *182*, 2115−2122.

(575) Sharma, A.; Hong, S.; Singh, R.; Jang, J. Single-Walled Carbon Nanotube Based Transparent Immunosensor for Detection of a Prostate Cancer Biomarker Osteopontin. *Anal. Chim. Acta* **2015**, *869*, 68−73.

(576) Shen, W. J.; Zhuo, Y.; Chai, Y. Q.; Yang, Z. H.; Han, J.; Yuan, R. Enzyme-Free Electrochemical Immunosensor Based on Host-Guest Nanonets Catalyzing Amplification for Procalcitonin Detection. *ACS Appl. Mater. Interfaces* **2015**, *7*, 4127−4134.

(577) Yang, Z. H.; Zhuo, Y.; Yuan, R.; Chai, Y. Q. Electrochemical Activity and Electrocatalytic Property of Cobalt Phthalocyanine Nanoparticles-Based Immunosensor for Sensitive Detection of Procalcitonin. *Sens. Actuators, B* **2016**, *227*, 212−219.

(578) Akter, R.; Rahman, Md. A.; Rhee, C. K. Amplified Electro-chemical Detection of a Cancer Biomarker by Enhanced Precipitation Using Horseradish Peroxidase Attached on Carbon Nanotubes. *Anal. Chem.* **2012**, *84*, 6407−6415.

129

(579) de la Rica, R.; Stevens, M. M. Plasmonic ELISA for the Ultrasensitive Detection of Disease Biomarkers with the Naked Eye. *Nat. Nanotechnol.* **2012**, *7*, 821−824.

(580) Uludag, Y.; Tothill, I. E. Cancer Biomarker Detection in Serum Samples Using Surface Plasmon Resonance and Quartz Crystal Microbalance Sensors with Nanoparticle Signal Amplification. *Anal. Chem.* **2012**, *84*, 5898−5904.

(581) Moon, J.-M.; Kim, Y. H.; Cho, Y. A nanowire-Based Label-Free Immunosensor: Direct Incorporation of a PSA Antibody in Electropolymerized Polypyrrole. *Biosens. Bioelectron.* **2014**, *57*, 157−161.

(582) Du, S.; Guo, Z.; Chen, B.; Sha, Y.; Jiang, X.; Li, X.; Gan, N.; Wang, S. Electrochemiluminescence Immunosensor for Tumor Markers Based on Biological Barcode Mode with Conductive Nanospheres. *Biosens. Bioelectron.* **2014**, *53*, 135−141.

(583) Zhuang, J.; Tang, D.; Lai, W.; Xu, M.; Tang, D. Target-Induced Nano-Enzyme Reactor Mediated Hole-Trapping for High-Throughput Immunoassay Based on a Split-Type Photoelectrochemical Detection Strategy. *Anal. Chem.* **2015**, *87*, 9473−9480.

(584) Kadimisetty, K.; Malla, S.; Sardesai, N. P.; Joshi, A. A.; Faria, R. C.; Lee, N. H.; Rusling, J. F. Automated Multiplexed ECL Immunoarrays for Cancer Biomarker Proteins. *Anal. Chem.* **2015**, *87*, 4472−4478.

(585) Wang, X.; Gao, C.; Shu, G.; Wang, Y.; Liu, X. The Enzyme Electrocatalytic Immunosensor Based on Functional Composite Nanofibers for Sensitive Detection of Tumor Suppressor Protein p53. *J. Electroanal. Chem.* **2015**, *756*, 101−107.

(586) Zhu, Y. C.; Zhang, N.; Ruan, Y. F.; Zhao, W. W.; Xu, J. J.; Chen, H. Y. Alkaline Phosphatase Tagged Antibodies on Gold Nanoparticles/ TiO2 Nanotubes Electrode: A Plasmonic Strategy for Label-Free and Amplified Photoelectrochemical Immunoassay. *Anal. Chem.* **2016**, *88*, 5626−5630.

(587) Ho, J. A.; Jou, A. F.; Wu, L.; Hsu, S. L. Development of an Immunopredictor for the Evaluation of the Risk of Cardiovascular Diseases Based on the Level of Soluble P-selectin. *Methods* **2012**, *56*, 223−229.

(588) Kwon, M. J.; Lee, J.; Wark, A. W.; Lee, H. J. Nanoparticle-Enhanced Surface Plasmon Resonance Detection of Proteins at Attomolar Concentrations: Comparing Different Nanoparticle Shapes and Sizes. *Anal. Chem.* **2012**, *84*, 1702−1707.

(589) Cui, Y.; Chen, H.; Hou, L.; Zhang, B.; Liu, B.; Chen, G.; Tang, D. Nanogold-Polyaniline-Nanogold Microspheres-Functionalized Molecular Tags for Sensitive Electrochemical Immunoassay of Thyroid-Stimulating Hormone. *Anal. Chim. Acta* **2012**, *738*, 76−84.

(590) Lee, S.; Nan, H.; Yu, H.; Kang, S. H. Quantitative Nanoimmunosensor Based on Dark-Field Illumination with Enhanced Sensitivity and On-Off Switching using Scattering Signals. *Biosens. Bioelectron.* **2016**, *79*, 709−714.

(591) Han, J.; Zhuo, Y.; Chai, Y.; Yu, Y.; Liao, N.; Yuan, R. Electrochemical Immunoassay for Thyroxine Detection using Cascade Catalysis as Signal Amplified Enhancer and Multi-Functionalized Magnetic Graphene Sphere as Signal Tag. *Anal. Chim. Acta* **2013**, *790*, 24−30.

(592) Li, Q.; Lou, F.; Tang, D. Biofunctional Nanogold Microsphere Doped with Prussian Blue Nanoparticles for Sensitive Electrochemical Immunoassay of Cancer Marker. *Anal. Methods* **2014**, *6*, 3442−3448.

(593) Xu, T.; Zhang, H.; Li, X.; Xie, Z.; Li, X. Enzyme-Triggered Tyramine-Enzyme Repeats on Prussian Blue-Gold Hybrid Nanostructures for Highly Sensitive Electrochemical Immunoassay of Tissue Polypeptide Antigen. *Biosens. Bioelectron.* **2015**, *73*, 167−173.

(594) Liao, N.; Zhuo, Y.; Chai, Y. Q.; Xiang, Y.; Han, J.; Yuan, R. Reagentless Electrochemiluminescent Detection of Protein Biomarker using Graphene-Based Magnetic Nanoprobes and Poly-L-lysine as Co-Reactant. *Biosens. Bioelectron.* **2013**, *45*, 189−194.

(595) Sirkka, N.; Lyytikainen, A.; Savukoski, T.; Soukka, T. Upconverting Nanophosphors as Reporters in a Highly Sensitive Heterogeneous Immunoassay for Cardiac Troponin I. *Anal. Chim. Acta* **2016**, *925*, 82−87.

(596) Weng, S.; Liu, Q.; Zhao, C.; Hong, G.; Jiang, Z.; Lin, L.; Chen, Y.; Lin, X. Sensitive Electrochemical Immunoassay Based on Polythionine-

Au Nanocomposites as Enhanced Sensing Signal for Selective Detection of Biomarker with High Isoelectric Point. *Sens. Actuators, B* **2015**, *216*, 307−315.

(597) Li, T.; Si, Z.; Hu, L.; Qi, H.; Yang, M. Prussian Blue-Functionalized Ceria Nanoparticles as Label for Ultrasensitive Detection of Tumor Necrosis Factor-alpha. *Sens. Actuators, B* **2012**, *171-172*, 1060−1065.

(598) Sun, Z.; Deng, L.; Gan, H.; Shen, R.; Yang, M.; Zhang, Y. Sensitive Immunosensor for Tumor Necrosis Factor alpha Based on Dual Signal Amplification of Ferrocene Modified Self-Assembled Peptide Nanowire and Glucose oxidase Functionalized Gold Nanorod. *Biosens. Bioelectron.* **2013**, *39*, 215−219.

(599) Li, M.; Cushing, S. K.; Zhang, J.; Suri, S.; Evans, R.; Petros, W. P.; Gibson, L. F.; Ma, D.; Liu, Y.; Wu, N. Three-Dimensional Hierarchical Plasmonic Nano-Architecture Enhanced Surface-Enhanced Raman Scattering Immunosensor for Cancer Biomarker Detection in Blood Plasma. *ACS Nano* **2013**, *7*, 4967−4976.

(600) Quynh, L. M.; Nam, N. H.; Kong, K.; Nhung, N. T.; Notingher, I.; Henini, M.; Luong, N. H. Surface-Enhanced Raman Spectroscopy Study of 4-ATP on Gold Nanoparticles for Basal Cell Carcinoma Fingerprint Detection. *J. Electron. Mater.* **2016**, *45*, 2563−2568.

(601) Fu, J.; Shi, Z.; Li, M.; Wang, Y.; Yu, L. Label-Free Detection of Chondroitin Sulphate Proteoglycan 4 by a Polyaniline/Graphene Nanocomposite Functionalized Impedimetric Immunosensor. *J. Nanomater.* **2016**, *2016*, 7834657.

(602) Liu, Y.; Zhu, F.; Dan, W.; Fu, Y.; Liu, S. Construction of Carbon Nanotube Based Nanoarchitectures for Selective Impedimetric Detection of Cancer Cells in Whole Blood. *Analyst* **2014**, *139*, 5086−5092.

(603) Chen, L.; Luo, Y.; Liu, T.; Yuan, Y.; Gu, H.; Yang, Y.; Li, L.; Tan, L. Label-Free Electrochemical Immunoassay of Bcl-2 Protein Expression on Tumor Cells. *Talanta* **2015**, *132*, 479−485.

(604) Liu, J.; Qin, Y.; Li, D.; Wang, T.; Liu, Y.; Wang, J.; Wang, E. Highly Sensitive and Selective Detection of Cancer Cell with a Label-Free Electrochemical Cytosensor. *Biosens. Bioelectron.* **2013**, *41*, 436−441.

(605) Wang, R.; Di, J.; Ma, J.; Ma, Z. Highly Sensitive Detection of Cancer Cells by Electrochemical Impedance Spectroscopy. *Electrochim. Acta* **2012**, *61*, 179−184.

(606) Dinish, U. S.; Fu, C. Y.; Soh, K. S.; Ramaswamy, B.; Kumar, A.; Olivo, M. Highly Sensitive SERS Detection of Cancer Proteins in Low Sample Volume Using Hollow Core Photonic Crystal Fiber. *Biosens. Bioelectron.* **2012**, *33*, 293−298.

(607) Xia, Y.; Gao, P.; Bo, Y.; Wang, W.; Huang, S. Immunoassay for SKOV-3 Human Ovarian Carcinoma Cells using a Graphene Oxide-Modified Electrode. *Microchim. Acta* **2012**, *179*, 201−207.

(608) Yang, K.; Hu, Y.; Dong, N. A Novel Biosensor Based on Competitive SERS Immunoassay and Magnetic Separation for Accurate and Sensitive Detection of Chloramphenicol. *Biosens. Bioelectron.* **2016**, *80*, 373−377.

(609) Wang, L.; Lei, J.; Ma, R.; Ju, H. Host−Guest Interaction of Adamantine with a *β*-Cyclodextrin-Functionalized AuPd Bimetallic Nanoprobe for Ultrasensitive Electrochemical Immunoassay of Small Molecules. *Anal. Chem.* **2013**, *85*, 6505−6510.

(610) Yan, F.; Zhang, Y.; Zhang, S.; Zhao, J.; Liu, S.; He, L.; Feng, X.; Zhang, H.; Zhang, Z. Carboxyl-Modified Graphene for Use in an Immunoassay for the Illegal Feed Additive Clenbuterol Using Surface Plasmon Resonance and Electrochemical Impedance Spectroscopy. *Microchim. Acta* **2015**, *182*, 855−862.

(611) Bai, J.; Lai, Y.; Jiang, D.; Zeng, Y.; Xian, Y.; Xiao, F.; Zhang, N.; Hou, J.; Jin, L. Ultrasensitive Electrochemical Immunoassay Based on Graphene oxide−Ag Composites for Rapid Determination of Clenbuterol. *Analyst* **2012**, *137*, 4349.

(612) Yao, X.; Yan, P.; Tang, Q.; Deng, A.; Li, J. Quantum Dots Based Electrochemiluminescent Immunosensor by Coupling Enzymatic Amplification for Ultrasensitive Detection of Clenbuterol. *Anal. Chim. Acta* **2013**, *798*, 82−88.

(613) Qu, X.; Lin, H.; Du, S.; Sui, J.; Zhang, X.; Cao, L. Development of a Nano-Gold Capillary Immunochromatographic Assay for Rapid and

130

Semi-Quantitative Detection of Clenbuterol Residues. *Food Anal. Methods* **2016**, *9*, 2531−2540.

(614) Li, Z.; Wang, Y.; Kong, W.; Wang, Z.; Wang, L.; Fu, Z. Ultrasensitive Detection of Trace Amount of Clenbuterol Residue in Swine Urine Utilizing an Electrochemiluminescent Immunosensor. *Sens. Actuators, B* **2012**, *174*, 355−358.

(615) Wang, H.; Zhang, Y.; Li, H.; Du, B.; Ma, H.; Wu, D.; Wei, Q. A Silver−palladium Alloy Nanoparticle-Based Electrochemical Biosensor for Simultaneous Detection of Ractopamine, Clenbuterol and Salbutamol. *Biosens. Bioelectron.* **2013**, *49*, 14−19.

(616) Lai, Y.; Bai, J.; Shi, X.; Zeng, Y.; Xian, Y.; Hou, J.; Jin, L. Graphene Oxide as Nanocarrier for Sensitive Electrochemical Immunoassay of Clenbuterol Based on Labeling Amplification Strategy. *Talanta* **2013**, *107*, 176−182.

(617) Zhang, Z.; Duan, F.; He, L.; Peng, D.; Yan, F.; Wang, M.; Zong, W.; Jia, C. Electrochemical Clenbuterol Immunosensor Based on a Gold Electrode Modified with Zinc Sulfide Quantum Dots and Polyaniline. *Microchim. Acta* **2016**, *183*, 1089−1097.

(618) Hlaváček, A.; Farka, Z.; Hübner, M.; Horňáková, V.; Němeček, D.; Niessner, R.; Skládal, P.; Knopp, D.; Gorris, H. H. Competitive Upconversion-Linked Immunosorbent Assay for the Sensitive Detection of Diclofenac. *Anal. Chem.* **2016**, *88*, 6011−6017.

(619) Rezaei, B.; Havakeshian, E.; Ensafi, A. A. Stainless Steel Modified with an Aminosilane Layer and Gold Nanoparticles as a Novel Disposable Substrate for Impedimetric Immunosensors. *Biosens. Bioelectron.* **2013**, *48*, 61−66.

(620) Rezaei, B.; Askarpour, N.; Ensafi, A. A. A Novel Sensitive Doxorubicin Impedimetric Immunosensor Based on a Specific Monoclonal Antibody−gold Nanoaprticle−sol−gel Modified Electrode. *Talanta* **2014**, *119*, 164−169.

(621) Lu, J.; Van Stappen, T.; Spasic, D.; Delport, F.; Vermeire, S.; Gils, A.; Lammertyn, J. Fiber Optic-SPR Platform for Fast and Sensitive Infliximab Detection in Serum of Inflammatory Bowel Disease Patients. *Biosens. Bioelectron.* **2016**, *79*, 173−179.

(622) Zengin, A.; Tamer, U.; Caykara, T. Extremely Sensitive Sandwich Assay of Kanamycin Using Surface-Enhanced Raman Scattering of 2-Mercaptobenzothiazole Labeled Gold@silver Nanoparticles. *Anal. Chim. Acta* **2014**, *817*, 33−41.

(623) Wei, Q.; Zhao, Y.; Du, B.; Wu, D.; Li, H.; Yang, M. Ultrasensitive Detection of Kanamycin in Animal Derived Foods by Label-Free Electrochemical Immunosensor. *Food Chem.* **2012**, *134*, 1601−1606.

(624) Yu, S.; Wei, Q.; Du, B.; Wu, D.; Li, H.; Yan, L.; Ma, H.; Zhang, Y. Label-Free Immunosensor for the Detection of Kanamycin Using Ag@Fe3O4 Nanoparticles and Thionine Mixed Graphene Sheet. *Biosens. Bioelectron.* **2013**, *48*, 224−229.

(625) Ya, Y.; Xiaoshu, W.; Qing, D.; Lin, J.; Yifeng, T. Label-Free Immunosensor for Morphine Based on the Electrochemiluminescence of Luminol on Indium−tin Oxide Coated Glass Functionalized with Gold Nanoparticles. *Anal. Methods* **2015**, *7*, 4502−4507.

(626) Zang, S.; Liu, Y.; Lin, M.; Kang, J.; Sun, Y.; Lei, H. A Dual Amplified Electrochemical Immunosensor for Ofloxacin: Polypyrrole Film-Au Nanocluster as the Matrix and Multi-Enzyme-Antibody Functionalized Gold Nanorod as the Label. *Electrochim. Acta* **2013**, *90*, 246−253.

(627) He, Z.; Zang, S.; Liu, Y.; He, Y.; Lei, H. A Multi-Walled Carbon Nanotubes-Poly(l-Lysine) Modified Enantioselective Immunosensor for Ofloxacin by Using Multi-Enzyme-Labeled Gold Nanoflower as Signal Enhancer. *Biosens. Bioelectron.* **2015**, *73*, 85−92.

(628) Sun, X.; Wu, L.; Ji, J.; Jiang, D.; Zhang, Y.; Li, Z.; Zhang, G.; Zhang, H. Longitudinal Surface Plasmon Resonance Assay Enhanced by Magnetosomes for Simultaneous Detection of Pefloxacin and Microcystin-LR in Seafoods. *Biosens. Bioelectron.* **2013**, *47*, 318−323.

(629) Chen, S.; Pan, D.; Gan, N.; Wang, D.; Zhu, Y.; Li, T.; Cao, Y.; Hu, F.; Jiang, S. A QCM Immunosensor to Rapidly Detect Ractopamine Using Bio-Polymer Conjugate and Magnetic β-Cyclodextrins. *Sens. Actuators, B* **2015**, *211*, 523−530.

(630) Wang, M.; Kang, M.; Guo, C.; Fang, S.; He, L.; Jia, C.; Zhang, G.; Bai, B.; Zong, W.; Zhang, Z. Electrochemical Biosensor Based on Cu/Cu2O Nanocrystals and Reduced Graphene Oxide Nanocomposite for

Sensitively Detecting Ractopamine. *Electrochim. Acta* **2015**, *182*, 668−675.

(631) Zhang, Y.; Ma, H.; Wu, D.; Li, Y.; Du, B.; Wei, Q. Label-Free Immunosensor Based on Au@Ag2S Nanoparticles/magnetic Chitosan Matrix for Sensitive Determination of Ractopamine. *J. Electroanal. Chem.* **2015**, *741*, 14−19.

(632) Wu, Y.; Dong, P.; Deng, A.; Di, J. Development of a Label-Free and Reagentless Plasmonic Immunosensor for the Detection of Salbutamol. *Anal. Methods* **2013**, *5*, 5222.

(633) Yan, Z.; Hu, T.; Guo, W.; Deng, A.; Di, J. A Label-Free Immunosensor for Determination of Salbutamol Based on Localized Surface Plasmon Resonance Biosensing. *Bioprocess Biosyst. Eng.* **2014**, *37*, 651−657.

(634) Lin, C.-H.; Wu, C.-C.; Kuo, Y.-F. A High Sensitive Impedimetric Salbutamol Immunosensor Based on the Gold Nanostructure-Deposited Screen-Printed Carbon Electrode. *J. Electroanal. Chem.* **2016**, *768*, 27−33.

(635) Cui, Z.; Cai, Y.; Wu, D.; Yu, H.; Li, Y.; Mao, K.; Wang, H.; Fan, H.; Wei, Q.; Du, B. An Ultrasensitive Electrochemical Immunosensor for the Detection of Salbutamol Based on Pd@SBA-15 and Ionic Liquid. *Electrochim. Acta* **2012**, *69*, 79−85.

(636) Scognamiglio, V.; Arduini, F.; Palleschi, G.; Rea, G. Biosensing Technology for Sustainable Food Safety. *TrAC, Trends Anal. Chem.* **2014**, *62*, 1−10.

(637) Narayanan, J.; Sharma, M. K.; Ponmariappan, S.; Sarita; Shaik, M.; Upadhyay, S. Electrochemical Immunosensor for Botulinum Neurotoxin Type-E Using Covalently Ordered Graphene Nanosheets Modified Electrodes and Gold Nanoparticles-Enzyme Conjugate. *Biosens. Bioelectron.* **2015**, *69*, 249−256.

(638) Arnon, S. S.; Schechter, R.; Inglesby, T. V.; Henderson, D. A.; Bartlett, J. G.; Ascher, M. S.; Eitzen, E.; Fine, A. D.; Hauer, J.; Layton, M.; Lillibridge, S.; Osterholm, M. T.; O'Toole, T.; Parker, G.; Perl, T. M.; Russell, P. K.; Swerdlow, D. L.; Tonat, K.; for the Working Group on Civilian Biodefense.. Botulinum Toxin as a Biological Weapon: Medical and Public Health Management. *JAMA* **2001**, *285*, 1059−1070.

(639) Kadota, I.; Takamura, H.; Nishii, H.; Yamamoto, Y. Total Synthesis of Brevetoxin B. *J. Am. Chem. Soc.* **2005**, *127*, 9246−9250.

(640) Plakas, S. M.; Dickey, R. W. Advances in Monitoring and Toxicity Assessment of Brevetoxins in Molluscan Shellfish. *Toxicon* **2010**, *56*, 137−149.

(641) Lin, Y.; Zhou, Q.; Lin, Y.; Lu, M.; Tang, D. Mesoporous Carbon-Enriched Palladium Nanostructures with Redox Activity for Enzyme-Free Electrochemical Immunoassay of Brevetoxin B. *Anal. Chim. Acta* **2015**, *887*, 67−74.

(642) Solanki, P. R.; Ali, M. A.; Agrawal, V. V.; Srivastava, A. K.; Kotnala, R. K.; Malhotra, B. D. Highly Sensitive Biofunctionalized Nickel Oxide Nanowires for Nanobiosensing Applications. *RSC Adv.* **2013**, *3*, 16060.

(643) Bunyakul, N.; Promptmas, C.; Baeumner, A. J. Microfluidic Biosensor for Cholera Toxin Detection in Fecal Samples. *Anal. Bioanal. Chem.* **2015**, *407*, 727−736.

(644) Han, C.; Doepke, A.; Cho, W.; Likodimos, V.; de la Cruz, A. A.; Back, T.; Heineman, W. R.; Halsall, H. B.; Shanov, V. N.; Schulz, M. J.; Falaras, P.; Dionysiou, D. D. A Multiwalled-Carbon-Nanotube-Based Biosensor for Monitoring Microcystin-LR in Sources of Drinking Water Supplies. *Adv. Funct. Mater.* **2013**, *23*, 1807−1816.

(645) Hou, L.; Ding, Y.; Zhang, L.; Guo, Y.; Li, M.; Chen, Z.; Wu, X. An Ultrasensitive Competitive Immunosensor for Impedimetric Detection of Microcystin-LR via Antibody-Conjugated Enzymatic Biocatalytic Precipitation. *Sens. Actuators, B* **2016**, *233*, 63−70.

(646) Gan, C.; Ling, L.; He, Z.; Lei, H.; Liu, Y. In-Situ Assembly of Biocompatible Core−shell Hierarchical Nanostructures Sensitized Immunosensor for Microcystin-LR Detection. *Biosens. Bioelectron.* **2016**, *78*, 381−389.

(647) Dawson, R. M. The Toxicology of Microcystins. *Toxicon* **1998**, *36*, 953−962.

(648) Bennett, J. W.; Klich, M. Mycotoxins. *Clin. Microbiol. Rev.* **2003**, *16*, 497−516.

131

(649) Xu, X.; Liu, X.; Li, Y.; Ying, Y. A Simple and Rapid Optical Biosensor for Detection of Aflatoxin B1 Based on Competitive Dispersion of Gold Nanorods. *Biosens. Bioelectron.* **2013**, *47*, 361−367.

(650) Stroka, J.; Anklam, E. New Strategies for the Screening and Determination of Aflatoxins and the Detection of Aflatoxin-Producing Moulds in Food and Feed. *TrAC, Trends Anal. Chem.* **2002**, *21*, 90−95.

(651) Pitt, J. I. Toxigenic Fungi: Which Are Important? *Med. Mycol.* **2000**, *38* (Suppl. 1), 17−22.

(652) El Khoury, A.; Atoui, A. Ochratoxin A: General Overview and Actual Molecular Status. *Toxins* **2010**, *2*, 461−493.

(653) Cabañes, F. J.; Bragulat, M. R.; Castellá, G. Ochratoxin A Producing Species in the Genus Penicillium. *Toxins* **2010**, *2*, 1111−1120.

(654) Creppy, E. E.; Chiarappa, P.; Baudrimont, I.; Borracci, P.; Moukha, S.; Carratù, M. R. Synergistic Effects of Fumonisin B1 and Ochratoxin A: Are in Vitro Cytotoxicity Data Predictive of in Vivo Acute Toxicity? *Toxicology* **2004**, *201*, 115−123.

(655) Blaiotta, G.; Ercolini, D.; Pennacchia, C.; Fusco, V.; Casaburi, A.; Pepe, O.; Villani, F. PCR Detection of Staphylococcal Enterotoxin Genes in *Staphylococcus* Spp. Strains Isolated from Meat and Dairy Products. Evidence for New Variants of seG and seI in S. Aureus AB-8802. *J. Appl. Microbiol.* **2004**, *97*, 719−730.

(656) Wang, W.; Liu, L.; Xu, L.; Kuang, H.; Zhu, J.; Xu, C. Gold-Nanoparticle-Based Multiplexed Immunochromatographic Strip for Simultaneous Detection of Staphylococcal Enterotoxin A, B, C, D, and E. Part. *Part. Sys. Charact.* **2016**, *33*, 388−395.

(657) Vinayaka, A. C.; Thakur, M. S. An Immunoreactor-Based Competitive Fluoroimmunoassay for Monitoring Staphylococcal Enterotoxin B Using Bioconjugated Quantum Dots. *Analyst* **2012**, *137*, 4343.

(658) Ricci, F.; Volpe, G.; Micheli, L.; Palleschi, G. A Review on Novel Developments and Applications of Immunosensors in Food Analysis. *Anal. Chim. Acta* **2007**, *605*, 111−129.

(659) Schatzmayr, G.; Streit, E. Global Occurrence of Mycotoxins in the Food and Feed Chain: Facts and Figures. *World Mycotoxin J.* **2013**, *6*, 213−222.

(660) Liu, J.; Hu, Y.; Zhu, G.; Zhou, X.; Jia, L.; Zhang, T. Highly Sensitive Detection of Zearalenone in Feed Samples Using Competitive Surface-Enhanced Raman Scattering Immunoassay. *J. Agric. Food Chem.* **2014**, *62*, 8325−8332.

(661) Abbès, S.; Ouanes, Z.; ben Salah-Abbès, J.; Houas, Z.; Oueslati, R.; Bacha, H.; Othman, O. The Protective Effect of Hydrated Sodium Calcium Aluminosilicate Against Haematological, Biochemical and Pathological Changes Induced by Zearalenone in Mice. *Toxicon* **2006**, *47*, 567−574.

(662) Arduini, F.; Cinti, S.; Scognamiglio, V.; Moscone, D. Nanomaterials in Electrochemical Biosensors for Pesticide Detection: Advances and Challenges in Food Analysis. *Microchim. Acta* **2016**, *183*, 2063−2083.

(663) Dolan, T.; Howsam, P.; Parsons, D. J.; Whelan, M. J. Is the EU Drinking Water Directive Standard for Pesticides in Drinking Water Consistent with the Precautionary Principle? *Environ. Sci. Technol.* **2013**, *47*, 4999−5006.

(664) Grossmann, K. Auxin Herbicides: Current Status of Mechanism and Mode of Action. *Pest Manage. Sci.* **2010**, *66*, 113−120.

(665) Park, K.; Park, J.; Kim, J.; Kwak, I.-S. Biological and Molecular Responses of Chironomus Riparius (Diptera, Chironomidae) to Herbicide 2,4-D (2,4-Dichlorophenoxyacetic Acid). *Comp. Biochem. Physiol., Part C: Toxicol. Pharmacol.* **2010**, *151*, 439−446.

(666) Ding, J.; Lu, Z.; Wang, R.; Shen, G.; Xiao, L. Piezoelectric Immunosensor with Gold Nanoparticles Enhanced Competitive Immunoreaction Technique for 2,4-Dichlorophenoxyacetic Acid Quantification. *Sens. Actuators, B* **2014**, *193*, 568−573.

(667) Seiler, J. P. The Genetic Toxicology of Phenoxy Acids Other Than 2,4,5-T. *Mutat. Res., Rev. Genet. Toxicol.* **1978**, *55*, 197−226.

(668) Fusco, G.; Gallo, F.; Tortolini, C.; Bollella, P.; Ietto, F.; De Mico, A.; D'Annibale, A.; Antiochia, R.; Favero, G.; Mazzei, F. AuNPs-Functionalized PANABA-MWCNTs Nanocomposite-Based Impedimetric Immunosensor for 2,4-Dichlorophenoxy Acetic Acid Detection. *Biosens. Bioelectron.* **2017**, *93*, 52−56.

(669) Liu, X.; Yang, Y.; Mao, L.; Li, Z.; Zhou, C.; Liu, X.; Zheng, S.; Hu, Y. SPR Quantitative Analysis of Direct Detection of Atrazine Traces on Au-Nanoparticles: Nanoparticles Size Effect. *Sens. Actuators, B* **2015**, *218*, 1−7.

(670) Ghosh, P. K.; Philip, L. Environmental Significance of Atrazine in Aqueous Systems and Its Removal by Biological Processes: An Overview. *Global NEST J.* **2006**, *8*, 159−178.

(671) Sun, X.; Zhu, Y.; Wang, X. Amperometric Immunosensor Based on Deposited Gold Nanocrystals/4,4′-Thiobisbenzenethiol for Determination of Carbofuran. *Food Control* **2012**, *28*, 184−191.

(672) Brkić, D. V.; Vitorović, S. L.; Gašić, S. M.; Nešković, N. K. Carbofuran in Water: Subchronic Toxicity to Rats. *Environ. Toxicol. Pharmacol.* **2008**, *25*, 334−341.

(673) Sun, Z.; Wang, W.; Wen, H.; Gan, C.; Lei, H.; Liu, Y. Sensitive Electrochemical Immunoassay for Chlorpyrifos by Using Flake-Like Fe_3O_4 Modified Carbon Nanotubes as the Enhanced Multienzyme Label. *Anal. Chim. Acta* **2015**, *899*, 91−99.

(674) Schwartz, R.; Lahav, O.; Ostfeld, A. Integrated Hydraulic and Organophosphate Pesticide Injection Simulations for Enhancing Event Detection in Water Distribution Systems. *Water Res.* **2014**, *63*, 271−284.

(675) Bazot, S.; Bois, P.; Joyeux, C.; Lebeau, T. Mineralization of Diuron [3-(3,4-Dichlorophenyl)-1, 1-Dimethylurea] by Co-Immobilized Arthrobacter Sp. and Delftia Acidovorans. *Biotechnol. Lett.* **2007**, *29*, 749−754.

(676) Tixier, C.; Sancelme, M.; Sancelme, M.; Bonnemoy, F.; Cuer, A.; Veschambre, H. Degradation Products of a Phenylurea Herbicide, Diuron: Synthesis, Ecotoxicity, and Biotransformation. *Environ. Toxicol. Chem.* **2001**, *20*, 1381−1389.

(677) Sharma, P.; Bhalla, V.; Tuteja, S.; Kukkar, M.; Suri, C. R. Rapid Extraction and Quantitative Detection of the Herbicide Diuron in Surface Water by a Hapten-Functionalized Carbon Nanotubes Based Electrochemical Analyzer. *Analyst* **2012**, *137*, 2495.

(678) Giacomazzi, S.; Cochet, N. Environmental Impact of Diuron Transformation: A Review. *Chemosphere* **2004**, *56*, 1021−1032.

(679) Lee, N.; Beasley, H. L.; Kimber, S. W. L.; Silburn, M.; Woods, N.; Skerritt, J. H.; Kennedy, I. R. Application of Immunoassays to Studies of the Environmental Fate of Endosulfan. *J. Agric. Food Chem.* **1997**, *45*, 4147−4155.

(680) Lee, K.-L.; You, M.-L.; Tsai, C.-H.; Lin, E.-H.; Hsieh, S.-Y.; Ho, M.-H.; Hsu, J.-C.; Wei, P.-K. Nanoplasmonic Biochips for Rapid Label-Free Detection of Imidacloprid Pesticides with a Smartphone. *Biosens. Bioelectron.* **2016**, *75*, 88−95.

(681) Proença, P.; Teixeira, H.; Castanheira, F.; Pinheiro, J.; Monsanto, P. V.; Marques, E. P.; Vieira, D. N. Two Fatal Intoxication Cases with Imidacloprid: LC/MS Analysis. *Forensic Sci. Int.* **2005**, *153*, 75−80.

(682) Pan, M.; Kong, L.; Liu, B.; Qian, K.; Fang, G.; Wang, S. Production of Multi-Walled Carbon Nanotube/poly(aminoamide) Dendrimer Hybrid and Its Application to Piezoelectric Immunosensing for Metolcarb. *Sens. Actuators, B* **2013**, *188*, 949−956.

(683) Sun, J.; Dong, T.; Zhang, Y.; Wang, S. Development of Enzyme Linked Immunoassay for the Simultaneous Detection of Carbaryl and Metolcarb in Different Agricultural Products. *Anal. Chim. Acta* **2010**, *666*, 76−82.

(684) Valera, E.; García-Febrero, R.; Pividori, I.; Sánchez-Baeza, F.; Marco, M.-P. Coulombimetric Immunosensor for Paraquat Based on Electrochemical Nanoprobes. *Sens. Actuators, B* **2014**, *194*, 353−360.

(685) Melchiorri, D.; Reiter, R. J.; Sewerynek, E.; Hara, M.; Chen, L.; Nisticò, G. Paraquat Toxicity and Oxidative Damage. *Biochem. Pharmacol.* **1996**, *51*, 1095−1099.

(686) Mehta, J.; Vinayak, P.; Tuteja, S. K.; Chhabra, V. A.; Bhardwaj, N.; Paul, A. K.; Kim, K.-H.; Deep, A. Graphene Modified Screen Printed Immunosensor for Highly Sensitive Detection of Parathion. *Biosens. Bioelectron.* **2016**, *83*, 339−346.

(687) Benke, G. M.; Cheever, K. L.; Mirer, F. E.; Murphy, S. D. Comparative Toxicity, Anticholinesterase Action and Metabolism of Methyl Parathion and Parathion in Sunfish and Mice. *Toxicol. Appl. Pharmacol.* **1974**, *28*, 97−109.

132

(688) Scognamiglio, V.; Arduini, F.; Palleschi, G.; Rea, G. Biosensing Technology for Sustainable Food Safety. *TrAC, Trends Anal. Chem.* **2014**, *62*, 1−10.

(689) Arduini, F.; Cinti, S.; Scognamiglio, V.; Moscone, D. Nanomaterials in Electrochemical Biosensors for Pesticide Detection: Advances and Challenges in Food Analysis. *Microchim. Acta* **2016**, *183*, 2063−2083.

(690) Rotz, L. D.; Khan, A. S.; Lillibridge, S. R.; Ostroff, S. M.; Hughes, J. M. Public Health Assessment of Potential Biological Terrorism Agents. *Emerging Infect. Dis.* **2002**, *8*, 225−230.

(691) Sabelnikov, A.; Zhukov, V.; Kempf, R. Probability of Real-Time Detection versus Probability of Infection for Aerosolized Biowarfare Agents: A Model Study. *Biosens. Bioelectron.* **2006**, *21*, 2070−2077.

(692) Scallan, E.; Hoekstra, R. M.; Angulo, F. J.; Tauxe, R. V.; Widdowson, M. A.; Roy, S. L.; Jones, J. L.; Griffin, P. M. Foodborne Illness Acquired in the United States - Major Pathogens. *Emerging Infect. Dis.* **2011**, *17*, 7−15.

(693) Weidemaier, K.; Carrino, J.; Curry, A.; Connor, J. H.; Liebmann-Vinson, A. Advancing Rapid Point-of-Care Viral Diagnostics to a Clinical Setting. *Future Virol.* **2015**, *10*, 313−28.

(694) Nouvellet, P.; Garske, T.; Mills, H. L.; Nedjati-Gilani, G.; Hinsley, W.; Blake, I. M.; Van Kerkhove, M. D.; Cori, A.; Dorigatti, I.; Jombart, T.; Riley, S.; Fraser, C.; Donnelly, C. A.; Ferguson, N. M. The Role of Rapid Diagnostics in Managing Ebola Epidemics. *Nature* **2015**, *528*, S109−16.

(695) Hospodsky, D.; Yamamoto, N.; Peccia, J. Accuracy, Precision, and Method Detection Limits of Quantitative PCR for Airborne Bacteria and Fungi. *Appl. Environ. Microbiol.* **2010**, *76*, 7004−7012.

(696) van Wuijckhuijse, A. L.; Stowers, M. A.; Kleefsman, W. A.; van Baar, B. L. M.; Kientz, C. E.; Marijnissen, J. C. M. Matrix-Assisted Laser Desorption/Ionisation Aerosol Time-of-Flight Mass Spectrometry for the Analysis of Bioaerosols: Development of a Fast Detector for Airborne Biological Pathogens. *J. Aerosol Sci.* **2005**, *36*, 677−687.

(697) Jiang, X.; Wang, R.; Wang, Y.; Su, X.; Ying, Y.; Wang, J.; Li, Y. Evaluation of Different Micro/Nanobeads used as Amplifiers in QCM Immunosensor for More Sensitive Detection of *E. coli* O157:H7. *Biosens. Bioelectron.* **2011**, *29*, 23−28.

(698) Hu, W.; Chen, H.; Zhang, H.; He, G.; Li, X.; Zhang, X.; Liu, Y.; Li, C. M. Sensitive Detection of Multiple Mycotoxins by SPRi with Gold Nanoparticles as Signal Amplification Tags. *J. Colloid Interface Sci.* **2014**, *431*, 71−76.

(699) Xu, X.; Liu, X.; Li, Y.; Ying, Y. A Simple and Rapid Optical Biosensor for Detection of Aflatoxin B1 Based on Competitive Dispersion of Gold Nanorods. *Biosens. Bioelectron.* **2013**, *47*, 361−367.

(700) Tang, J.; Huang, Y.; Liu, H.; Zhang, C.; Tang, D. Novel Glucometer-Based Immunosensing Strategy Suitable for Complex Systems with Signal Amplification Using Surfactant-Responsive Cargo Release from Glucose-Encapsulated Liposome Nanocarriers. *Biosens. Bioelectron.* **2016**, *79*, 508−514.

(701) Ko, J.; Lee, C.; Choo, J. Highly Sensitive SERS-Based Immunoassay of Aflatoxin B1 Using Silica-Encapsulated Hollow Gold Nanoparticles. *J. Hazard. Mater.* **2015**, *285*, 11−17.

(702) Singh, C.; Srivastava, S.; Ali, M. A.; Gupta, T. K.; Sumana, G.; Srivastava, A.; Mathur, R. B.; Malhotra, B. D. Carboxylated Multiwalled Carbon Nanotubes Based Biosensor for Aflatoxin Detection. *Sens. Actuators, B* **2013**, *185*, 258−264.

(703) Urusov, A. E.; Zherdev, A. V.; Dzantiev, B. B. Use of Gold Nanoparticle-Labeled Secondary Antibodies to Improve the Sensitivity of an Immunochromatographic Assay for Aflatoxin B1. *Microchim. Acta* **2014**, *181*, 1939−1946.

(704) Yu, L.; Zhang, Y.; Hu, C.; Wu, H.; Yang, Y.; Huang, C.; Jia, N. Highly Sensitive Electrochemical Impedance Spectroscopy Immunosensor for the Detection of AFB1 in Olive Oil. *Food Chem.* **2015**, *176*, 22−26.

(705) Wang, H.; Zhang, Y.; Chu, Y.; Ma, H.; Li, Y.; Wu, D.; Du, B.; Wei, Q. Disposable Competitive-Type Immunoassay for Determination of Aflatoxin B1 via Detection of Copper Ions Released from Cu-Apatite. *Talanta* **2016**, *147*, 556−560.

(706) Mondal, K.; Ali, M. A.; Srivastava, S.; Malhotra, B. D.; Sharma, A. Electrospun Functional Micro/nanochannels Embedded in Porous Carbon Electrodes for Microfluidic Biosensing. *Sens. Actuators, B* **2016**, *229*, 82−91.

(707) Zhang, X.; Li, C.-R.; Wang, W.-C.; Xue, J.; Huang, Y.-L.; Yang, X.-X.; Tan, B.; Zhou, X.-P.; Shao, C.; Ding, S.-J.; Qiu, J.-F. A Novel Electrochemical Immunosensor for Highly Sensitive Detection of Aflatoxin B1 in Corn Using Single-Walled Carbon Nanotubes/chitosan. *Food Chem.* **2016**, *192*, 197−202.

(708) Shu, J.; Qiu, Z.; Wei, Q.; Zhuang, J.; Tang, D. Cobalt-Porphyrin-Platinum-Functionalized Reduced Graphene Oxide Hybrid Nanostructures: A Novel Peroxidase Mimetic System For Improved Electrochemical Immunoassay. *Sci. Rep.* **2015**, *5*, 15113.

(709) Xu, G.; Zhang, S.; Zhang, Q.; Gong, L.; Dai, H.; Lin, Y. Magnetic Functionalized Electrospun Nanofibers for Magnetically Controlled Ultrasensitive Label-Free Electrochemiluminescent Immune Detection of Aflatoxin B1. *Sens. Actuators, B* **2016**, *222*, 707−713.

(710) Lin, Y.; Zhou, Q.; Lin, Y.; Tang, D.; Niessner, R.; Knopp, D. Enzymatic Hydrolysate-Induced Displacement Reaction with Multifunctional Silica Beads Doped with Horseradish Peroxidase−Thionine Conjugate for Ultrasensitive Electrochemical Immunoassay. *Anal. Chem.* **2015**, *87*, 8531−8540.

(711) Srivastava, S.; Kumar, V.; Ali, M. A.; Solanki, P. R.; Srivastava, A.; Sumana, G.; Saxena, P. S.; Joshi, A. G.; Malhotra, B. D. Electrophoretically Deposited Reduced Graphene Oxide Platform for Food Toxin Detection. *Nanoscale* **2013**, *5*, 3043.

(712) Srivastava, S.; Kumar, V.; Arora, K.; Singh, C.; Ali, M. A.; Puri, N. K.; Malhotra, B. D. Antibody Conjugated Metal Nanoparticle Decorated Graphene Sheets for a Mycotoxin Sensor. *RSC Adv.* **2016**, *6*, 56518−56526.

(713) Wang, D.; Hu, W.; Xiong, Y.; Xu, Y.; Li, C. M. Multifunctionalized Reduced Graphene Oxide-Doped Polypyrrole/pyrrolepropylic Acid Nanocomposite Impedimetric Immunosensor to Ultra-Sensitively Detect Small Molecular Aflatoxin B1. *Biosens. Bioelectron.* **2015**, *63*, 185−189.

(714) Karczmarczyk, A.; Dubiak-Szepietowska, M.; Vorobii, M.; Rodriguez-Emmenegger, C.; Dostálek, J.; Feller, K.-H. Sensitive and Rapid Detection of Aflatoxin M1 in Milk Utilizing Enhanced SPR and p(HEMA) Brushes. *Biosens. Bioelectron.* **2016**, *81*, 159−165.

(715) Narayanan, J.; Sharma, M. K.; Ponmariappan, S.; Sarita; Shaik, M.; Upadhyay, S. Electrochemical Immunosensor for Botulinum Neurotoxin Type-E Using Covalently Ordered Graphene Nanosheets Modified Electrodes and Gold Nanoparticles-Enzyme Conjugate. *Biosens. Bioelectron.* **2015**, *69*, 249−256.

(716) Bok, S.; Korampally, V.; Darr, C. M.; Folk, W. R.; Polo-Parada, L.; Gangopadhyay, K.; Gangopadhyay, S. Femtogram-Level Detection of Clostridium Botulinum Neurotoxin Type A by Sandwich Immunoassay Using Nanoporous Substrate and Ultra-Bright Fluorescent Suprananoparticles. *Biosens. Bioelectron.* **2013**, *41*, 409−416.

(717) Tang, D.; Zhang, B.; Tang, J.; Hou, L.; Chen, G. Displacement-Type Quartz Crystal Microbalance Immunosensing Platform for Ultrasensitive Monitoring of Small Molecular Toxins. *Anal. Chem.* **2013**, *85*, 6958−6966.

(718) Zhang, B.; Liu, B.; Liao, J.; Chen, G.; Tang, D. Novel Electrochemical Immunoassay for Quantitative Monitoring of Biotoxin Using Target-Responsive Cargo Release from Mesoporous Silica Nanocontainers. *Anal. Chem.* **2013**, *85*, 9245−9252.

(719) Lin, Y.; Zhou, Q.; Lin, Y.; Lu, M.; Tang, D. Mesoporous Carbon-Enriched Palladium Nanostructures with Redox Activity for Enzyme-Free Electrochemical Immunoassay of Brevetoxin B. *Anal. Chim. Acta* **2015**, *887*, 67−74.

(720) Schmit, V. L.; Martoglio, R.; Carron, K. T. Lab-on-a-Bubble Surface Enhanced Raman Indirect Immunoassay for Cholera. *Anal. Chem.* **2012**, *84*, 4233−4236.

(721) Solanki, P. R.; Ali, M. A.; Agrawal, V. V.; Srivastava, A. K.; Kotnala, R. K.; Malhotra, B. D. Highly Sensitive Biofunctionalized Nickel Oxide Nanowires for Nanobiosensing Applications. *RSC Adv.* **2013**, *3*, 16060.

133

(722) Han, C.; Doepke, A.; Cho, W.; Likodimos, V.; de la Cruz, A. A.; Back, T.; Heineman, W. R.; Halsall, H. B.; Shanov, V. N.; Schulz, M. J.; Falaras, P.; Dionysiou, D. D. A Multiwalled-Carbon-Nanotube-Based Biosensor for Monitoring Microcystin-LR in Sources of Drinking Water Supplies. *Adv. Funct. Mater.* **2013**, *23*, 1807−1816.

(723) Gan, C.; Ling, L.; He, Z.; Lei, H.; Liu, Y. In-Situ Assembly of Biocompatible Core−shell Hierarchical Nanostructures Sensitized Immunosensor for Microcystin-LR Detection. *Biosens. Bioelectron.* **2016**, *78*, 381−389.

(724) Hou, L.; Ding, Y.; Zhang, L.; Guo, Y.; Li, M.; Chen, Z.; Wu, X. An Ultrasensitive Competitive Immunosensor for Impedimetric Detection of Microcystin-LR via Antibody-Conjugated Enzymatic Biocatalytic Precipitation. *Sens. Actuators, B* **2016**, *233*, 63−70.

(725) Zhang, J.; Sun, Y.; Dong, H.; Zhang, X.; Wang, W.; Chen, Z. An Electrochemical Non-Enzymatic Immunosensor for Ultrasensitive Detection of Microcystin-LR Using Carbon Nanofibers as the Matrix. *Sens. Actuators, B* **2016**, *233*, 624−632.

(726) Tan, F.; Saucedo, N. M.; Ramnani, P.; Mulchandani, A. Label-Free Electrical Immunosensor for Highly Sensitive and Specific Detection of Microcystin-LR in Water Samples. *Environ. Sci. Technol.* **2015**, *49*, 9256−9263.

(727) Shi, Y.; Wu, J.; Sun, Y.; Zhang, Y.; Wen, Z.; Dai, H.; Wang, H.; Li, Z. A Graphene Oxide Based Biosensor for Microcystins Detection by Fluorescence Resonance Energy Transfer. *Biosens. Bioelectron.* **2012**, *38*, 31−36.

(728) Tian, J.; Zhao, H.; Zhao, H.; Quan, X. Photoelectrochemical Immunoassay for Microcystin-LR Based on a Fluorine-Doped Tin Oxide Glass Electrode Modified with a CdS-Graphene Composite. *Microchim. Acta* **2012**, *179*, 163−170.

(729) Sun, X.; Guan, L.; Shi, H.; Ji, J.; Zhang, Y.; Li, Z. Determination of Microcystin-LR with a Glassy Carbon Impedimetric Immunoelectrode Modified with an Ionic Liquid and Multiwalled Carbon Nanotubes. *Microchim. Acta* **2013**, *180*, 75−83.

(730) Huang, X.; Chen, R.; Xu, H.; Lai, W.; Xiong, Y. Nanospherical Brush as Catalase Container for Enhancing the Detection Sensitivity of Competitive Plasmonic ELISA. *Anal. Chem.* **2016**, *88*, 1951−1958.

(731) Liu, X.; Yang, Z.; Zhang, Y.; Yu, R. A Novel Electrochemical Immunosensor for Ochratoxin A with Hapten Immobilization on Thionine/gold Nanoparticle Modified Glassy Carbon Electrode. *Anal. Methods* **2013**, *5*, 1481.

(732) Huang, X.; Zhan, S.; Xu, H.; Meng, X.; Xiong, Y.; Chen, X. Ultrasensitive Fluorescence Immunoassay for Detection of Ochratoxin A Using Catalase-Mediated Fluorescence Quenching of CdTe QDs. *Nanoscale* **2016**, *8*, 9390−9397.

(733) Yang, J.; Gao, P.; Liu, Y.; Li, R.; Ma, H.; Du, B.; Wei, Q. Label-Free Photoelectrochemical Immunosensor for Sensitive Detection of Ochratoxin A. *Biosens. Bioelectron.* **2015**, *64*, 13−18.

(734) Jodra, A.; Hervás, M.; López, M. Á.; Escarpa, A. Disposable Electrochemical Magneto Immunosensor for Simultaneous Simplified Calibration and Determination of Ochratoxin A in Coffee Samples. *Sens. Actuators, B* **2015**, *221*, 777−783.

(735) Orlov, A. V.; Khodakova, J. A.; Nikitin, M. P.; Shepelyakovskaya, A. O.; Brovko, F. A.; Laman, A. G.; Grishin, E. V.; Nikitin, P. I. Magnetic Immunoassay for Detection of Staphylococcal Toxins in Complex Media. *Anal. Chem.* **2013**, *85*, 1154−1163.

(736) Hwang, J.; Lee, S.; Choo, J. Application of a SERS-Based Lateral Flow Immunoassay Strip for the Rapid and Sensitive Detection of Staphylococcal Enterotoxin B. *Nanoscale* **2016**, *8*, 11418−11425.

(737) Vinayaka, A. C.; Thakur, M. S. An Immunoreactor-Based Competitive Fluoroimmunoassay for Monitoring Staphylococcal Enterotoxin B Using Bioconjugated Quantum Dots. *Analyst* **2012**, *137*, 4343.

(738) Wu, L.; Gao, B.; Zhang, F.; Sun, X.; Zhang, Y.; Li, Z. A Novel Electrochemical Immunosensor Based on Magnetosomes for Detection of Staphylococcal Enterotoxin B in Milk. *Talanta* **2013**, *106*, 360−366.

(739) Wang, W.; Liu, L.; Xu, L.; Kuang, H.; Zhu, J.; Xu, C. Gold-Nanoparticle-Based Multiplexed Immunochromatographic Strip for Simultaneous Detection of Staphylococcal Enterotoxin A, B, C, D, and E. *Part. Part. Sys. Charact.* **2016**, *33*, 388−395.

(740) Bruck, H. A.; Yang, M.; Kostov, Y.; Rasooly, A. Electrical Percolation Based Biosensors. *Methods* **2013**, *63*, 282−289.

(741) Tao, L.; Zhang, C.; Zhang, J.; Sun, Y.; Li, X.; Yan, K.; Jin, B.; Zhang, Z.; Yang, K. Sensitive Chemiluminescence Immunoassay for Staphylococcal Enterotoxin C1 Based on the Use of Dye-Encapsulated Mesoporous Silica Nanoparticles. *Microchim. Acta* **2016**, *183*, 2163−2168.

(742) Hu, W.; Chen, H.; Zhang, H.; He, G.; Li, X.; Zhang, X.; Liu, Y.; Li, C. M. Sensitive Detection of Multiple Mycotoxins by SPRi with Gold Nanoparticles as Signal Amplification Tags. *J. Colloid Interface Sci.* **2014**, *431*, 71−76.

(743) Liu, J.; Hu, Y.; Zhu, G.; Zhou, X.; Jia, L.; Zhang, T. Highly Sensitive Detection of Zearalenone in Feed Samples Using Competitive Surface-Enhanced Raman Scattering Immunoassay. *J. Agric. Food Chem.* **2014**, *62*, 8325−8332.

(744) Feng, R.; Zhang, Y.; Ma, H.; Wu, D.; Fan, H.; Wang, H.; Li, H.; Du, B.; Wei, Q. Ultrasensitive Non-Enzymatic and Non-Mediator Electrochemical Biosensor Using Nitrogen-Doped Graphene Sheets for Signal Amplification and Nanoporous Alloy as Carrier. *Electrochim. Acta* **2013**, *97*, 105−111.

(745) Ding, J.; Lu, Z.; Wang, R.; Shen, G.; Xiao, L. Piezoelectric Immunosensor with Gold Nanoparticles Enhanced Competitive Immunoreaction Technique for 2,4-Dichlorophenoxyacetic Acid Quantification. *Sens. Actuators, B* **2014**, *193*, 568−573.

(746) Jia, K.; Bijeon, J. L.; Adam, P. M.; Ionescu, R. E. Sensitive Localized Surface Plasmon Resonance Multiplexing Protocols. *Anal. Chem.* **2012**, *84*, 8020−8027.

(747) Liu, X.; Yang, Y.; Mao, L.; Li, Z.; Zhou, C.; Liu, X.; Zheng, S.; Hu, Y. SPR Quantitative Analysis of Direct Detection of Atrazine Traces on Au-Nanoparticles: Nanoparticles Size Effect. *Sens. Actuators, B* **2015**, *218*, 1−7.

(748) Liu, X.; Li, W.-J.; Li, L.; Yang, Y.; Mao, L.-G.; Peng, Z. A Label-Free Electrochemical Immunosensor Based on Gold Nanoparticles for Direct Detection of Atrazine. *Sens. Actuators, B* **2014**, *191*, 408−414.

(749) Deep, A.; Saraf, M.; Neha; Bharadwaj, S. K.; Sharma, A. L. Styrene Sulphonic Acid Doped Polyaniline Based Immunosensor for Highly Sensitive Impedimetric Sensing of Atrazine. *Electrochim. Acta* **2014**, *146*, 301−306.

(750) Medina-Sánchez, M.; Mayorga-Martinez, C. C.; Watanabe, T.; Ivandini, T. A.; Honda, Y.; Pino, F.; Nakata, K.; Fujishima, A.; Einaga, Y.; Merkoçi, A. Microfluidic Platform for Environmental Contaminants Sensing and Degradation Based on Boron-Doped Diamond Electrodes. *Biosens. Bioelectron.* **2016**, *75*, 365−374.

(751) Giannetto, M.; Umiltà, E.; Careri, M. New Competitive Dendrimer-Based and Highly Selective Immunosensor for Determination of Atrazine in Environmental, Feed and Food Samples: The Importance of Antibody Selectivity for Discrimination Among Related Triazinic Metabolites. *Anal. Chim. Acta* **2014**, *806*, 197−203.

(752) Belkhamssa, N.; Justino, C. I. L.; Santos, P. S. M.; Cardoso, S.; Lopes, I.; Duarte, A. C.; Rocha-Santos, T.; Ksibi, M. Label-Free Disposable Immunosensor for Detection of Atrazine. *Talanta* **2016**, *146*, 430−434.

(753) González-Techera, A.; Zon, M. A.; Molina, P. G.; Fernández, H.; González-Sapienza, G.; Arévalo, F. J. Development of a Highly Sensitive Noncompetitive Electrochemical Immunosensor for the Detection of Atrazine by Phage Anti-Immunocomplex Assay. *Biosens. Bioelectron.* **2015**, *64*, 650−656.

(754) Sun, X.; Zhu, Y.; Wang, X. Amperometric Immunosensor Based on Deposited Gold Nanocrystals/4,4′-Thiobisbenzenethiol for Determination of Carbofuran. *Food Control* **2012**, *28*, 184−191.

(755) Sun, X.; Du, S.; Wang, X. Amperometric Immunosensor for Carbofuran Detection Based on Gold Nanoparticles and PB-MWCNTs-CTS Composite Film. *Eur. Food Res. Technol.* **2012**, *235*, 469−477.

(756) Zhu, Y.; Cao, Y.; Sun, X.; Wang, X. Amperometric Immunosensor for Carbofuran Detection Based on MWCNTs/GS-PEI-Au and AuNPs-Antibody Conjugate. *Sensors* **2013**, *13*, 5286−5301.

134

(757) Sun, X.; Li, Q.; Wang, X. Amperometric Immunosensor Based on Gold Nanoparticles and Saturated Thiourea for Carbofuran Detection. *IEEE Sens. J.* **2012**, *12*, 2071−2076.

(758) Nangia, Y.; Bhalla, V.; Kumar, B.; Suri, C. R. Electrochemical Stripping Voltammetry of Gold Ions for Development of Ultra-Sensitive Immunoassay for Chlorsulfuron. *Electrochem. Commun.* **2012**, *14*, 51−54.

(759) Qiao, L.; Guo, Y.; Sun, X.; Jiao, Y.; Wang, X. Electrochemical Immunosensor with NiAl-Layered Double Hydroxide/graphene Nanocomposites and Hollow Gold Nanospheres Double-Assisted Signal Amplification. *Bioprocess Biosyst. Eng.* **2015**, *38*, 1455−1468.

(760) Sun, Z.; Wang, W.; Wen, H.; Gan, C.; Lei, H.; Liu, Y. Sensitive Electrochemical Immunoassay for Chlorpyrifos by Using Flake-Like Fe₃O₄ Modified Carbon Nanotubes as the Enhanced Multienzyme Label. *Anal. Chim. Acta* **2015**, *899*, 91−99.

(761) Sharma, P.; Kukkar, M.; Ganguli, A. K.; Bhasin, A.; Suri, C. R. Plasmon Enhanced Fluoro-Immunoassay Using Egg Yolk Antibodies for Ultra-Sensitive Detection of Herbicide Diuron. *Analyst* **2013**, *138*, 4312.

(762) Sharma, P.; Bhalla, V.; Tuteja, S.; Kukkar, M.; Suri, C. R. Rapid Extraction and Quantitative Detection of the Herbicide Diuron in Surface Water by a Hapten-Functionalized Carbon Nanotubes Based Electrochemical Analyzer. *Analyst* **2012**, *137*, 2495.

(763) Bhalla, V.; Sharma, P.; Pandey, S. K.; Suri, C. R. Impedimetric Label-Free Immunodetection of Phenylurea Class of Herbicides. *Sens. Actuators, B* **2012**, *171−172*, 1231−1237.

(764) Sharma, P.; Tuteja, S. K.; Bhalla, V.; Shekhawat, G.; Dravid, V. P.; Suri, C. R. Bio-Functionalized Graphene−graphene Oxide Nanocomposite Based Electrochemical Immunosensing. *Biosens. Bioelectron.* **2013**, *39*, 99−105.

(765) Liu, G.; Wang, S.; Liu, J.; Song, D. An Electrochemical Immunosensor Based on Chemical Assembly of Vertically Aligned Carbon Nanotubes on Carbon Substrates for Direct Detection of the Pesticide Endosulfan in Environmental Water. *Anal. Chem.* **2012**, *84*, 3921−3928.

(766) Lee, K.-L.; You, M.-L.; Tsai, C.-H.; Lin, E.-H.; Hsieh, S.-Y.; Ho, M.-H.; Hsu, J.-C.; Wei, P.-K. Nanoplasmonic Biochips for Rapid Label-Free Detection of Imidacloprid Pesticides with a Smartphone. *Biosens. Bioelectron.* **2016**, *75*, 88−95.

(767) Pan, M.; Kong, L.; Liu, B.; Qian, K.; Fang, G.; Wang, S. Production of Multi-Walled Carbon Nanotube/poly(aminoamide) Dendrimer Hybrid and Its Application to Piezoelectric Immunosensing for Metolcarb. *Sens. Actuators, B* **2013**, *188*, 949−956.

(768) Valera, E.; García-Febrero, R.; Pividori, I.; Sánchez-Baeza, F.; Marco, M.-P. Coulombimetric Immunosensor for Paraquat Based on Electrochemical Nanoprobes. *Sens. Actuators, B* **2014**, *194*, 353−360.

(769) Mehta, J.; Vinayak, P.; Tuteja, S. K.; Chhabra, V. A.; Bhardwaj, N.; Paul, A. K.; Kim, K.-H.; Deep, A. Graphene Modified Screen Printed Immunosensor for Highly Sensitive Detection of Parathion. *Biosens. Bioelectron.* **2016**, *83*, 339−346.

(770) Gas, F.; Baus, B.; Queré, J.; Chapelle, A.; Dreanno, C. Rapid Detection and Quantification of the Marine Toxic Algae, Alexandrium Minutum, Using a Super-Paramagnetic Immunochromatographic Strip Test. *Talanta* **2016**, *147*, 581−589.

(771) Wang, D.-B.; Tian, B.; Zhang, Z.-P.; Deng, J.-Y.; Cui, Z.-Q.; Yang, R.-F.; Wang, X.-Y.; Wei, H.-P.; Zhang, X.-E. Rapid Detection of Bacillus Anthracis Spores Using a Super-Paramagnetic Lateral-Flow Immunological Detectionsystem. *Biosens. Bioelectron.* **2013**, *42*, 661−667.

(772) Kang, X.; Pang, G.; Chen, Q.; Liang, X. Fabrication of Bacillus Cereus Electrochemical Immunosensor Based on Double-Layer Gold Nanoparticles and Chitosan. *Sens. Actuators, B* **2013**, *177*, 1010−1016.

(773) Dou, W.; Tang, W.; Zhao, G. A Disposable Electrochemical Immunosensor Arrays Using 4-Channel Screen-Printed Carbon Electrode for Simultaneous Detection of *Escherichia coli* O157:H7 and *Enterobacter sakazakii*. *Electrochim. Acta* **2013**, *97*, 79−85.

(774) Mouli Pandey, C.; Sumana, G.; Tiwari, I. Nanostructuring of Hierarchical 3D Cystine Flowers for High-Performance Electrochemical Immunosensor. *Biosens. Bioelectron.* **2014**, *61*, 328−335.

(775) Madiyar, F. R.; Bhana, S.; Swisher, L. Z.; Culbertson, C. T.; Huang, X.; Li, J. Integration of a Nanostructured Dielectrophoretic Device and a Surface-Enhanced Raman Probe for Highly Sensitive Rapid Bacteria Detection. *Nanoscale* **2015**, *7*, 3726−3736.

(776) Dogan, Ü.; Kasap, E.; Cetin, D.; Suludere, Z.; Boyaci, I. H.; Türkyılmaz, C.; Ertas, N.; Tamer, U. Rapid Detection of Bacteria Based on Homogenous Immunoassay Using Chitosan Modified Quantum Dots. *Sens. Actuators, B* **2016**, *233*, 369−378.

(777) Zhang, X.; Shen, J.; Ma, H.; Jiang, Y.; Huang, C.; Han, E.; Yao, B.; He, Y. Optimized Dendrimer-Encapsulated Gold Nanoparticles and Enhanced Carbon Nanotube Nanoprobes for Amplified Electrochemical Immunoassay of E. Coli in Dairy Product Based on Enzymatically Induced Deposition of Polyaniline. *Biosens. Bioelectron.* **2016**, *80*, 666−673.

(778) Li, Y.; Cheng, P.; Gong, J.; Fang, L.; Deng, J.; Liang, W.; Zheng, J. Amperometric Immunosensor for the Detection of Escherichia Coli O157:H7 in Food Specimens. *Anal. Biochem.* **2012**, *421*, 227−233.

(779) Li, Y.; Fang, L.; Cheng, P.; Deng, J.; Jiang, L.; Huang, H.; Zheng, J. An Electrochemical Immunosensor for Sensitive Detection of Escherichia Coli O157:H7 Using C60 Based Biocompatible Platform and Enzyme Functionalized Pt Nanochains Tracing Tag. *Biosens. Bioelectron.* **2013**, *49*, 485−491.

(780) Cheng, P.; Huang, Z.-G.; Zhuang, Y.; Fang, L.-C.; Huang, H.; Deng, J.; Jiang, L.-L.; Yu, K.-K.; Li, Y.; Zheng, J.-S. A Novel Regeneration-Free E. Coli O157:H7 Amperometric Immunosensor Based on Functionalised Four-Layer Magnetic Nanoparticles. *Sens. Actuators, B* **2014**, *204*, 561−567.

(781) Wang, Y.; Fewins, P. A.; Alocilja, E. C. Electrochemical Immunosensor Using Nanoparticle-Based Signal Enhancement for Escherichia Coli O157:H7 Detection. *IEEE Sens. J.* **2015**, *15*, 4692−4699.

(782) Kwon, D.; Lee, S.; Ahn, M. M.; Kang, I. S.; Park, K.-H.; Jeon, S. Colorimetric Detection of Pathogenic Bacteria Using Platinum-Coated Magnetic Nanoparticle Clusters and Magnetophoretic Chromatography. *Anal. Chim. Acta* **2015**, *883*, 61−66.

(783) Jiang, T.; Song, Y.; Wei, T.; Li, H.; Du, D.; Zhu, M.-J.; Lin, Y. Sensitive Detection of *Escherichia coli* O157:H7 Using Pt−Au Bimetal Nanoparticles with Peroxidase-like Amplification. *Biosens. Bioelectron.* **2016**, *77*, 687−694.

(784) Guo, X.; Lin, C.-S.; Chen, S.-H.; Ye, R.; Wu, V. C. H. A Piezoelectric Immunosensor for Specific Capture and Enrichment of Viable Pathogens by Quartz Crystal Microbalance Sensor, Followed by Detection with Antibody-Functionalized Gold Nanoparticles. *Biosens. Bioelectron.* **2012**, *38*, 177−183.

(785) Martín, M.; Salazar, P.; Jiménez, C.; Lecuona, M.; Ramos, M. J.; Ode, J.; Alcoba, J.; Roche, R.; Villalonga, R.; Campuzano, S.; et al. Rapid Legionella Pneumophila Determination Based on a Disposable Core−shell Fe₃O₄@poly(dopamine) Magnetic Nanoparticles Immunoplatform. *Anal. Chim. Acta* **2015**, *887*, 51−58.

(786) Uusitalo, S.; Kögler, M.; Välimaa, A.-L.; Popov, A.; Ryabchikov, Y.; Kontturi, V.; Siitonen, S.; Petäjä, J.; Virtanen, T.; Laitinen, R.; et al. Detection of Listeria Innocua on Roll-to-Roll Produced SERS Substrates with Gold Nanoparticles. *RSC Adv.* **2016**, *6*, 62981−62989.

(787) Chen, Q.; Lin, J.; Gan, C.; Wang, Y.; Wang, D.; Xiong, Y.; Lai, W.; Li, Y.; Wang, M. A Sensitive Impedance Biosensor Based on Immunomagnetic Separation and Urease Catalysis for Rapid Detection of Listeria Monocytogenes Using an Immobilization-Free Interdigitated Array Microelectrode. *Biosens. Bioelectron.* **2015**, *74*, 504−511.

(788) Veerapandian, M.; Neethirajan, S. Graphene Oxide Chemically Decorated with Ag−Ru/Chitosan Nanoparticles: Fabrication, Electrode Processing and Immunosensing Properties. *RSC Adv.* **2015**, *5*, 75015−75024.

(789) Krithiga, N.; Viswanath, K. B.; Vasantha, V. S.; Jayachitra, A. Specific and Selective Electrochemical Immunoassay for *Pseudomonas aeruginosa* Based on Pectin−gold Nano Composite. *Biosens. Bioelectron.* **2016**, *79*, 121−129.

(790) Fei, J.; Dou, W.; Zhao, G. A Sandwich Electrochemical Immunoassay for *Salmonella pullorum* and Salmonella Gallinarum Based on a AuNPs/SiO₂/Fe₃O₄ adsorbing Antibody and 4 Channel

135

Screen Printed Carbon Electrode Electrodeposited Gold Nanoparticles. *RSC Adv.* **2015**, *5*, 74548−74556.

(791) Fei, J.; Dou, W.; Zhao, G. Amperometric Immunoassay for the Detection of *Salmonella pullorum* Using a Screen - Printed Carbon Electrode Modified with Gold Nanoparticle-Coated Reduced Graphene Oxide and Immunomagnetic Beads. *Microchim. Acta* **2016**, *183*, 757−764.

(792) Pratiwi, F. W.; Rijiravanich, P.; Somasundrum, M.; Surareungchai, W. Electrochemical Immunoassay for *Salmonella* Typhimurium Based on Magnetically Collected Ag-Enhanced DNA Biobarcode Labels. *Analyst* **2013**, *138*, 5011.

(793) Viter, R.; Khranovskyy, V.; Starodub, N.; Ogorodniichuk, Y.; Gevelyuk, S.; Gertnere, Z.; Poletaev, N.; Yakimova, R.; Erts, D.; Smyntyna, V.; et al. Application of Room Temperature Photoluminescence From ZnO Nanorods for *Salmonella* Detection. *IEEE Sens. J.* **2014**, *14*, 2028−2034.

(794) Kim, G.; Moon, J.-H.; Moh, C.-Y.; Lim, J. A Microfluidic Nano-Biosensor for the Detection of Pathogenic *Salmonella*. *Biosens. Bioelectron.* **2015**, *67*, 243−247.

(795) Lin, Y.; Hamme, A. T., II Gold Nanoparticle Labeling Based ICP-MS Detection/Measurement of Bacteria, and Their Quantitative Photothermal Destruction. *J. Mater. Chem. B* **2015**, *3*, 3573−3582.

(796) Tam, P. D.; Thang, C. X. Label-Free Electrochemical Immunosensor Based on Cerium Oxide Nanowires for *Vibrio cholerae* O1 Detection. *Mater. Sci. Eng., C* **2016**, *58*, 953−959.

(797) Prieto-Simón, B.; Bandaru, N. M.; Saint, C.; Voelcker, N. H. Tailored Carbon Nanotube Immunosensors for the Detection of Microbial Contamination. *Biosens. Bioelectron.* **2015**, *67*, 642−648.

(798) Huang, W.; Xiang, G.; Jiang, D.; Liu, L.; Liu, C.; Liu, F.; Pu, X. Electrochemical Immunoassay for CytomegalovirusAntigen Detection with Multiple Signal Amplification Using HRP and Pt-Pd Nanoparticles Functionalized Single-Walled Carbon Nanohorns. *Electroanalysis* **2016**, *28*, 1126−1133.

(799) Nguyen, B. T. T.; Peh, A. E. K.; Chee, C. Y. L.; Fink, K.; Chow, V. T. K.; Ng, M. M. L.; Toh, C.-S. Electrochemical Impedance Spectroscopy Characterization of Nanoporous Alumina Dengue Virus Biosensor. *Bioelectrochemistry* **2012**, *88*, 15−21.

(800) Wei, Y.; Wong, L. P.; Toh, C.-S. Fuel Cell Virus Sensor Using Virus Capture within Antibody-Coated Nanochannels. *Anal. Chem.* **2013**, *85*, 1350−1357.

(801) Wang, X.; Li, Y.; Quan, D.; Wang, J.; Zhang, Y.; Du, J.; Peng, J.; Fu, Q.; Zhou, Y.; Jia, S.; et al. Detection of Hepatitis B Surface Antigen by Target-Induced Aggregation Monitored by Dynamic Light Scattering. *Anal. Biochem.* **2012**, *428*, 119−125.

(802) Huang, K.-J.; Li, J.; Liu, Y.-M.; Cao, X.; Yu, S.; Yu, M. Disposable Immunoassay for Hepatitis B Surface Antigen Based on a Graphene Paste Electrode Functionalized with Gold Nanoparticles and a Nafion-Cysteine Conjugate. *Microchim. Acta* **2012**, *177*, 419−426.

(803) Ge, Z.-L.; Song, T.-M.; Chen, Z.; Guo, W.-R.; Xie, H.-P.; Xie, L. Polyelectrolyte-Based Electrochemiluminescence Enhancement for $Ru(bpy)_3^{2+}$ Loaded by SiO_2 Nanoparticle Carrier and Its High Sensitive Immunoassay. *Anal. Chim. Acta* **2015**, *862*, 24−32.

(804) Li, Y.; Tian, L.; Liu, L.; Liu, L.; Li, J.; Wei, Q.; Cao, W. An Ultrasensitive Sandwich-Type Electrochemical Immunosensor Based on δ-MnO2and Palladium Nanoparticles Covered Natural Halloysite Nanotubes for the Detection of Hepatitis B Surface Antigen. *New J. Chem.* **2016**, *40*, 558−563.

(805) Ma, C.; Liang, M.; Wang, L.; Xiang, H.; Jiang, Y.; Li, Y.; Xie, G. Multi sHRP-DNA-Coated CMWNTs as Signal Labels for an Ultrasensitive Hepatitis C Virus Core Antigen Electrochemical Immunosensor. *Biosens. Bioelectron.* **2013**, *47*, 467−474.

(806) Inci, F.; Tokel, O.; Wang, S.; Gurkan, U. A.; Tasoglu, S.; Kuritzkes, D. R.; Demirci, U. Nanoplasmonic Quantitative Detection of Intact Viruses from Unprocessed Whole Blood. *ACS Nano* **2013**, *7*, 4733−4745.

(807) Yang, Z.-H.; Zhuo, Y.; Yuan, R.; Chai, Y.-Q. An Amplified Electrochemical Immunosensor Based on in Situ-Produced 1-Naphthol as Electroactive Substance and Graphene Oxide and Pt Nanoparticles

Functionalized CeO_2 Nanocomposites as Signal Enhancer. *Biosens. Bioelectron.* **2015**, *69*, 321−327.

(808) Veerapandian, M.; Hunter, R.; Neethirajan, S. Dual Immunosensor Based on Methylene Blue-Electroadsorbed Graphene Oxide for Rapid Detection of the Influenza A Virus Antigen. *Talanta* **2016**, *155*, 250−257.

(809) Huang, J.; Xie, Z.; Xie, Z.; Luo, S.; Xie, L.; Huang, L.; Fan, Q.; Zhang, Y.; Wang, S.; Zeng, T. Silver Nanoparticles Coated Graphene Electrochemical Sensor for the Ultrasensitive Analysis of Avian Influenza Virus H7. *Anal. Chim. Acta* **2016**, *913*, 121−127.

(810) Yang, J.; Xiang, Y.; Song, C.; Liu, L.; Jing, X.; Xie, G.; Xiang, H. Quadruple Signal Amplification Strategy Based on Hybridization Chain Reaction and an Immunoelectrode Modified with Graphene Sheets, a Hemin/G-Quadruplex DNAzyme Concatamer, and Alcohol Dehydrogenase: Ultrasensitive Determination of Influenza Virus Subtype H7N9. *Microchim. Acta* **2015**, *182*, 2377−2385.

(811) Lin, H.-Y.; Huang, C.-H.; Lu, S.-H.; Kuo, I.-T.; Chau, L.-K. Direct Detection of Orchid Viruses Using Nanorod-Based Fiber Optic Particle Plasmon Resonance Immunosensor. *Biosens. Bioelectron.* **2014**, *51*, 371−378.

(812) Neng, J.; Harpster, M. H.; Wilson, W. C.; Johnson, P. A. Surface-Enhanced Raman Scattering (SERS) Detection of Multiple Viral Antigens Using Magnetic Capture of SERS-Active Nanoparticles. *Biosens. Bioelectron.* **2013**, *41*, 316−321.

(813) Park, S.; Kim, J.; Ock, H.; Dutta, G.; Seo, J.; Shin, E.-C.; Yang, H. Sensitive Electrochemical Detection of Vaccinia Virus in a Solution Containing a High Concentration Of l-Ascorbic Acid. *Analyst* **2015**, *140*, 5481−5487.

136

Paper II

Advances in Optical Single-Molecule Detection: En Route to Super-Sensitive Bioaffinity Assays

Farka, Z.; Mickert, M. J.; Pastucha, M.; Mikušová, Z.; Skládal, P.; Gorris, H. H.

(Z.F. and M.J.M. contributed equally)

Contribution:

Outline of review, literature research, manuscript writing

Single-Molecule Detection

Advances in Optical Single-Molecule Detection: En Route to Supersensitive Bioaffinity Assays

Zdeněk Farka[+], Matthias J. Mickert[+], Matěj Pastucha, Zuzana Mikušová, Petr Skládal, and Hans H. Gorris*
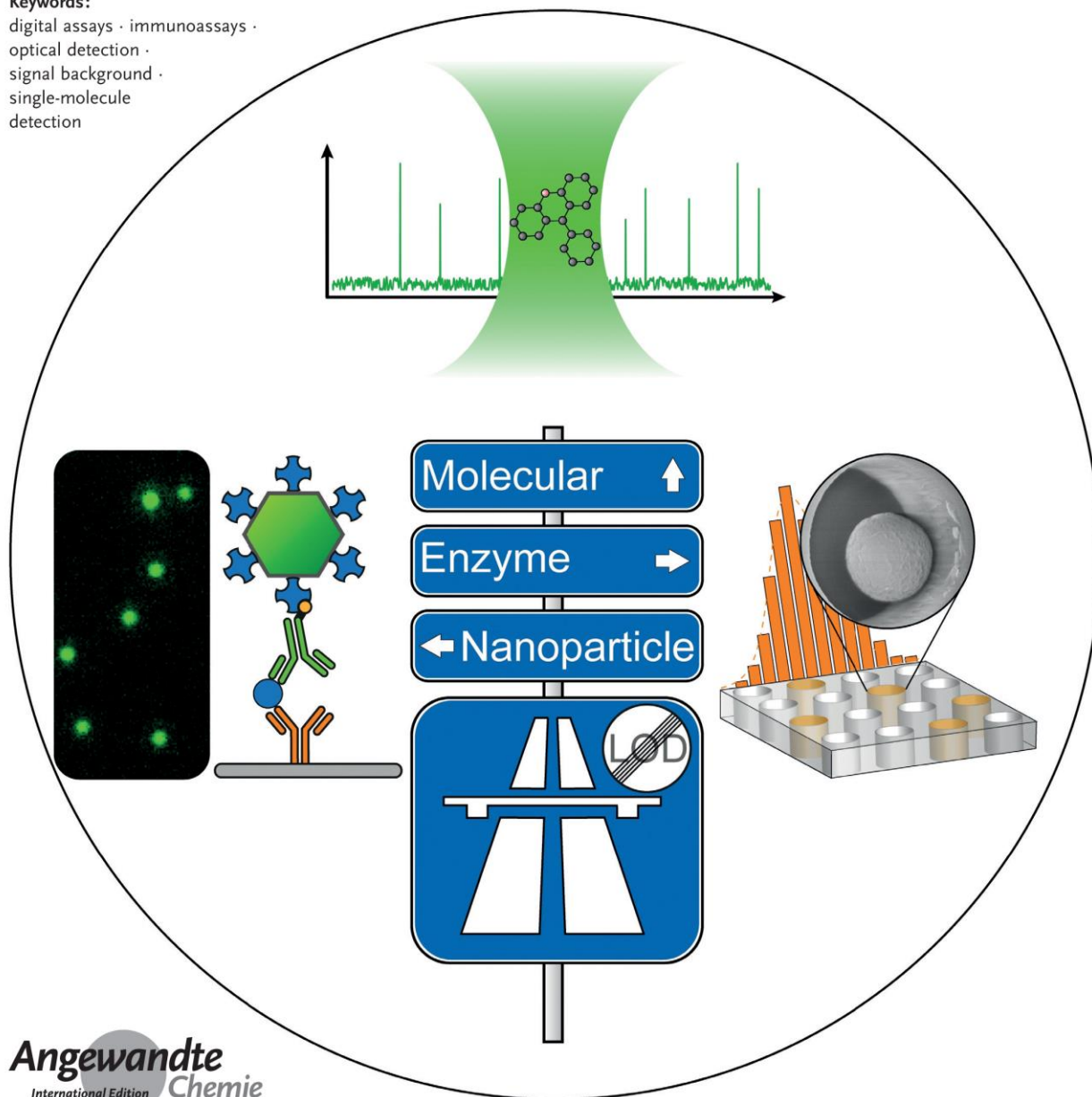
*T*he ability to detect low concentrations of analytes and in particular low-abundance biomarkers is of fundamental importance, e.g., for early-stage disease diagnosis. The prospect of reaching the ultimate limit of detection has driven the development of single-molecule bio-affinity assays. While many review articles have highlighted the potentials of single-molecule technologies for analytical and diagnostic applications, these technologies are not as widespread in real-world applications as one should expect. This Review provides a theoretical background on single-molecule—or better digital—assays to critically assess their potential compared to traditional analog assays. Selected examples from the literature include bioaffinity assays for the detection of biomolecules such as proteins, nucleic acids, and viruses. The structure of the Review highlights the versatility of optical single-molecule labeling techniques, including enzymatic amplification, molecular labels, and innovative nanomaterials.*

From the Contents

1. Introduction

The ability to detect individual molecules—at first sight—holds the promise to reach the ultimate sensitivity. Thus, it is not surprising to see a surge in the number and variety of single-molecule approaches. While there have been many review articles on the advantages of single-molecule fluorescence spectroscopy in the field of biophysics,[1] more recent reviews have discussed the potential and limitations of single-molecule applications for analytical chemistry.[2] Our Review is focused on single-molecule bioaffinity assays and does not cover similar techniques for fundamental biophysical or biomolecular research. Furthermore, it was necessary to limit the Review to optical single-molecule techniques. Other emerging single-molecule applications of electrochemical[3] and force-based techniques[4] can be found elsewhere. As the labeling technique is the key element for the ability to detect a single analyte target molecule, the structure of the Review follows different types of optical detection labels. We have also included illustrative examples of label-free optical techniques reported for single-molecule assays.[5]

Most bioaffinity techniques rely on antibodies, though aptamers or molecularly imprinted polymers (MIPs)[6] have also been used to specifically bind and capture an analyte of interest. Antibodies can be generated with high specificity against almost any analyte. Only the affinity ceiling limits their binding constant to approximately $10^{10} M^{-1}$,[7] which is much lower than that of (strept)avidin–biotin binding ($10^{14} M^{-1}$).[8] Since antibodies are rather large, cameloid antibodies that consist only of a single binding site have attracted some attention. The advantage of aptamers is the easy large-scale production, whereas MIPs stand out for their high chemical stability. MIPs are especially useful for the detection of small molecules with a rigid structure. MIPs, however, seem less suitable for the detection of structurally flexible analytes such as proteins.

For detecting the binding event, two approaches can be distinguished: 1) In label-free assays, the binding of the analyte to the detection element results in a signal change that can be directly measured. 2) In the so-called sandwich format, a second affinity reagent, which carries a signal-generating label, binds to the analyte. As a detection label can strongly amplify the signal, this approach is more amenable for implementing single-molecule assays. The first immunoassays used radioactive labels,[9] but enzyme labels have gradually replaced radionuclides for safety reasons and because each enzyme label generates thousands of measurable product molecules (intrinsic signal-amplification step). The enzyme-linked immunosorbent assay (ELISA) is still considered to be the gold standard for the quantitative measurement of various analytes ranging from clinical diagnosis to environmental applications not the least because it is relatively easy to perform.

[*] Dr. Z. Farka,[+] M. Pastucha, Z. Mikušová, Prof. Dr. P. Skládal
    CEITEC – Central European Institute of Technology
    Masaryk University
    625 00 Brno (Czech Republic)

    M. J. Mickert,[+] Priv.-Doz. Dr. H. H. Gorris
    Institute of Analytical Chemistry, Chemo- and Biosensors
    University of Regensburg
    Universitätsstraße 31, 93040 Regensburg (Germany)
    E-mail: hans-heiner.gorris@ur.de

    M. Pastucha, Z. Mikušová, Prof. Dr. P. Skládal
    Department of Biochemistry, Faculty of Science
    Masaryk University
    625 00 Brno (Czech Republic)

[+] These authors contributed equally to this work.

The ORCID identification number(s) for the author(s) of this article can be found under:
https://doi.org/10.1002/anie.201913924

139

Over the last 60 years, the development of immunoassays has been mainly driven by making measurements more sensitive, specific, and reproducible. While conventional ELISAs can measure picomolar concentrations of analytes, higher sensitivities are required because even few molecules of toxins can be harmful,[10] individual pathogens can initiate an infectious disease,[11] and trace amounts of a cancer marker indicate the beginning of a malignant transformation.[12] Additionally, the development of more sensitive immuno-assays is essential for the discovery of new potential biomarkers that are not accessible using current diagnostic tests.[13]

A conventional ELISA is performed in a laboratory and requires several washing steps and relatively long incubation times. Thus, the second line of immunoassay development has aimed at a faster throughput using lower sample volumes, and assays that can be performed directly at the site of sample collection (on-site testing), for example, at the bedside for diagnostic tests,[14] or in the field for environmental and food products applications. In diagnostics, such assays are commonly known as point-of-care (POC) tests.[15] Minimally invasive sample collection methods, for example, from urine or saliva, and no washing steps are preferred to maintain the user-friendly operation of POC tests. The most famous antibody-based POC test is the home pregnancy test, a very successful example of a lateral flow assay (LFA) first described in the 1980s.[16] The wide acceptance and user-friendliness is a precondition for POC methods to become a cornerstone in the predictive, preventive, personalized, and participatory medicine, commonly termed P4 medicine.[17]

The family of bioaffinity assays, in particular immuno-assays, can be subdivided depending on the detection label as shown in Figure 1. 1) Enzyme labels represent the central branch and continue to be the most common detection route.

2) Fluorescent molecular labels are in principle easier to implement because the detection antibody is directly labeled with a fluorophore and no enzymatic amplification step is necessary. The simplest form, the fluorescence immunoassay (FIA), however, is limited by background fluorescence without the advantage of enzymatic amplification. In addition to the direct intensity-based fluorescence detection, this scheme was adapted for signal amplification (e.g. by Immuno PCR) or for the development of homogeneous assays using fluorescence polarization. Nevertheless, the non-zero background of fluorescence remains. A decisive breakthrough was the development of time-resolved (TR) detection by employing lanthanide-based labels that display a long lifetime (microseconds) compared to organic fluorophores (nanoseconds).[18] In a time-gated approach, after luminescence excitation, the signal acquisition is delayed by a few microseconds to let the autofluorescence signal decay, and only the specific signal of the lanthanide is recorded. The TR-FIA is a background-free optical detection method that, however, requires a more sophisticated instrumental setup. The dissociation-enhanced lanthanide fluorescent immunoassay (DELFIA) is the most prominent TR-FIA system on the market.[19]

Nanoparticles (NP) currently constitute the most rapidly branching labeling strategy for immunoassays.[20] Colloidal gold has been used for the readout of LFAs. Due to their plasmonic properties, gold nanoparticles (Au NPs) strongly absorb and scatter light such that a direct color read-out by eye is possible, and the user is able to make a yes/no decision. In the meantime, the use of NPs in immuno- and other bioaffinity assays has experienced a fast growth as a result of concurrent progress in nanomaterials research. Plasmonic NPs are now in widespread use, but also other NPs and nanocomposites have been designed that enable a convenient optical readout. For example, quantum dots (QDs) are

Zdeněk Farka received his PhD in structural biology in 2017 under the supervision of Petr Skládal at the Central European Institute of Technology (CEITEC), Masaryk University (Brno, Czech Republic). He completed research internships at the University of Regensburg (Germany) with Hans-Heiner Gorris and at the University of Rouen (France) with Niko Hildebrandt. He is currently working as a Senior Researcher at CEITEC. His research interests include the detection of proteins and bacteria via various immunoanalytical techniques.

Matěj Pastucha is a PhD student of biochemistry at Masaryk University. He received a Master's degree in analytical biochemistry in 2015 and is currently pursuing his PhD under the supervision of Petr Skládal. His research focuses on the development of immunochemical assays and sensors for the detection of proteins and bacteria. This includes antibody immobilization to diverse substrates, their conjugation with nanoparticles or other labels, and detection utilizing optical or electrochemical readout.

Matthias J. Mickert is a PhD student at the Institute of Analytical Chemistry, Chemo- and Biosensors of the University of Regensburg in the group of Hans-Heiner Gorris. His research interests include single-molecule enzyme kinetics in femtoliter arrays and the development of digital immunoassays using photon-upconversion nanoparticles as background-free luminescent labels. He is specialized in the surface modification, characterization, and imaging of upconversion nanoparticles.

Zuzana Mikušová graduated with a degree in biotechnology at the Slovak University of Technology in Bratislava in 2014. She is now a PhD student under the supervision of Petr Skládal at Masaryk University. She is currently focusing on immunosensing in the electrochemistry field as well as the immunocytochemistry of cells, both using nanoparticles as labels.

140

a better alternative to organic fluorophores because they are more photostable and brighter, which is an important feature for single-molecule applications. Photon-upconversion nanoparticles (UCNPs) are another emerging class of labels that can be excited by near-infrared light and emit shorter-wavelength light. The anti-Stokes emission prevents autofluorescence and light scattering and thus allows for an optical readout without background interference.[21] The background-free detection renders UCNPs an excellent candidate for single-molecule applications.[22] Furthermore, nanocontainers such as liposomes can be filled with large numbers of fluorophores to generate a strong signal. In contrast to enzyme labels that generate the fluorophores in situ, the encapsulated fluorophores are released on demand from the nanocontainer to avoid self-quenching inside the confined environment.[23] There are also mixed detection schemes, e.g., in the form of electrochemiluminescence that generates a strong signal without background.

All three branches shown in Figure 1 have now blossomed into single-molecule assays as a consequence of innovative assay designs as well as advances in instrumental techniques, detector sensitivities and data processing capabilities. In simple terms, single-molecule assays can be considered as the result of driving conventional assays to the highest sensitivity—either by increasing the specific signal to very high levels or by background reduction. Therefore, any standard analytical method can, in principle, reach "single-molecule sensitivity" but background interference such as matrix effects, readout noise or non-specific binding typically prevents it.

It is furthermore essential to understand that the ability to detect a single molecule is not synonymous with the most

Petr Skládal is an Associate Professor and Head of the Department of Biochemistry, Faculty of Science, Masaryk University. He received his PhD in the field of amperometric biosensors in 1992. After research stays (1991, 1993) at the University of Florence (Italy) with Marco Mascini, he continued to investigate biosensors at Masaryk University. He currently also heads the Nanobiotechnology Research Group at CEITEC. His research interests include enzymatic and immunochemical biosensors using electrochemical and piezoelectric transducers.

Hans-Heiner Gorris studied biology at the University of Münster (Germany) and obtained his PhD degree from the University of Lübeck (Germany). After working on single-molecule enzyme assays with David Walt at Tufts University (USA), he joined the Institute of Analytical Chemistry, Chemo- and Biosensors at the University of Regensburg (Germany) in 2009. He has been a Heisenberg-Fellow of the DFG since 2016. His research interests include background-free luminescent bioaffinity assays based on UCNPs with single-molecule sensitivity as well as new methods for investigating enzyme kinetics at the single-molecule level.

sensitive analytical assay. For example, some immunoassays from the pre-single-molecule era actually had higher sensitivities than current single-molecule assays.[24] If we shift our attention from the detection of a single molecule as the "ultimate" sensitivity to the distinct readout mode, however, it becomes clear that single-molecule detection is a unique and powerful tool for background reduction. Since the signal of a single detection label can be reliably distinguished from the background noise of the instrument and reagents, the measurement is completely independent of background fluctuations. Thus, the term "digital assay" (as opposed to a conventional "analog assay") is a much better description of the advantages conferred by single-molecule detection in analytical chemistry. The digital readout, in turn, makes the measurement more robust and thus indirectly leads to lower detection limits.

The signal-to-noise (S/N) ratio determines whether a single molecule can be detected or not. The strength of the specific optical signal depends on the type of label and can be strongly amplified, as discussed in the next section. In a digital assay, however, each detectable response is derived from a single analyte molecule, and thus the specific signal strength is ultimately fixed. The only option to assure single-molecule detection is the reduction of the background signal, which decreases with the detection volume. This problem has been extensively discussed for fluorescence spectroscopy, one of the earliest and most important methods for single-molecule detection, but similar considerations also hold for nonfluorescent single-molecule detection methods. Fluorescent molecules are capable of generating a strong signal because each fluorophore can emit up to a million photons before it finally photobleaches. Fluorescence excitation, however, also leads to an optical background signal due to autofluorescence and light scattering.[25] In order to observe a single fluorescent molecule, it is essential to reduce the detection volume to a femtoliter (fL) volume—commonly by using confocal microscopy, fluorescence correlation spectroscopy (FCS), or total internal reflection microscopy (TIRF).

The requirement for a very small detection volume is associated with two closely related problems that must be addressed in order to achieve higher sensitivity with digital assays. The first problem is analyte sampling. At very low analyte concentrations, there are not enough molecules present in an analyte sample to reach the detection volume by diffusion on a reasonable timescale. For example, it was estimated that it takes on average more than ten minutes for a molecule present in a concentration of 1 fM to reach a detection volume of 10 fL by diffusion.[26] Stochastic fluctuations are the second problem.[27] At low analyte concentrations, a small observation volume is randomly at one time occupied by a single analyte molecule and, at another time, empty. The so-called Poisson noise $((\sqrt{n})/n)$ depends on the number of counted events (n) and is negligible in conventional analog assays where n is very large. For digital assays, however, it presents a problem because a single detection event of an analyte molecule does not contain enough analytical information. Therefore, it is necessary to make either many parallel measurements on a larger area or many sequential measurements in the same detection volume.

Figure 1. Progress in the development of immunoassays using optical detection schemes towards single-molecule detection. Radioisotopes were replaced by labels based on enzymes, fluorescent molecules, and nanoparticles. Through the choice of an appropriate readout method, all these labels can be exploited for measurement at the single-molecule level.

2. Enzyme Labels

ELISA has been successfully transformed into single-molecule immunoassays. The generation of thousands of fluorescent molecules per enzyme label molecule multiplied by up to a million photons per fluorophore generates a very strong signal that can be detected by simple wide-field fluorescence microscopy. In particular, β-galactosidase from *Escherichia coli* is an excellent enzyme label for single-molecule applications because it is robust and can turn over up to 1000 substrate molecules per second. Based on this strategy, Rotman[28] reported the very first single-molecule experiment already in 1961. The enzymatic substrate turnover, however, is a kinetic process and requires time, which leads to product diffusion. Consequently, the signal is not detectable at the same location as the analyte. There are two options to spatially allocate the signal to the analyte.

2.1. Assays Based on Localized Product Deposition

In the easiest case, the enzymatic reaction generates a product that precipitates around the analyte. The group of Suzuki[29] designed a digital sandwich immunoassay on beads

by using a conjugate of detection antibody and horseradish peroxidase. The enzyme label converted a fluorescence-labeled tyramide substrate to a short-lived radical which immediately coupled the fluorescent labels only to the analyte-bearing beads. This led to a high local fluorescence signal at the site of analyte binding. It was noted, however, that the detection of the tyramide signal on the beads by flow cytometry was less efficient than that of digital ELISAs in confined environments.

2.2. Assays in Confined Environments

Alternatively, the enzyme label converts a substrate to a soluble fluorescent product. In this case, the reaction must be confined in a very small compartment in order to prevent product diffusion.[30] The concentration of the reaction product exceeds the detection threshold in small confined volumes. For example, a single molecule of β-galactosidase enclosed in a volume of 50 fL (50 μm³) can produce a fluorophore concentration of 2 μM in 1 min, which can be easily detected via conventional epifluorescence microscopy.[31] Enzymatic reactions were confined in water-in-oil emulsion[28] or microfluidic droplets, fused silica capillaries,[32] virus

142

capsids,[33] lipid vesicles,[34] or so-called femtoliter arrays. In particular, femtoliter arrays and water-in-oil microfluidic droplets have found analytical applications.

2.2.1. Femtoliter Arrays

Femtoliter arrays consist of a large number of homogeneous wells fabricated in the surface of optical fiber bundles,[35] fused silica slides,[36] or polydimethylsiloxane (PDMS).[37] The Walt group[38] pioneered single-molecule immunoassays based on a fluorogenic enzymatic reaction in femtoliter arrays, which was commercialized by Quanterix. In the so-called Simoa platform (single-molecule arrays, Figure 2), magnetic beads with a capture antibody were dispersed in a sample. The bead concentration was typically much higher than the analyte concentration. The beads were magnetically separated and incubated with a biotinylated antibody, followed by the addition of a streptavidin–β-galactosidase conjugate. A high bead-to-analyte ratio resulted in a small fraction of beads labeled with a single enzyme molecule and a large excess of unlabeled beads. The beads were loaded with a fluorogenic substrate onto a femtoliter array and sealed with a gasket or oil film. A highly fluorescent product accumulated only in wells that contained a bead with a bound analyte molecule. The analyte concentration was determined digitally by counting the number of fluorescent wells. Prostate-specific antigen (PSA) and tumor necrosis factor-α (TNF-α) were detected with a limit of detection (LOD) of 1.5 fg mL^{-1} (≈ 50 aM) and 2.5 fg mL^{-1} (≈ 150 aM), respectively. Other clinically relevant analytes included cancer biomarkers,[39] urinary biomarkers,[40] p24 protein of HIV,[41] and the neurofilament light chain protein (NFL),

a neuronal injury marker of various neurodegenerative conditions and brain injuries. Traditionally, cerebrospinal fluid must be obtained for analysis by lumbar puncture because the concentration of NFL in the blood is too low for a conventional ELISA. Shahim et al.[42] developed an ultrasensitive immunoassay with an LOD of 0.29 pg mL^{-1}, which enabled NFL measurements in the serum of healthy subjects. Olivera et al.[43] determined tau protein in blood plasma (LOD of 0.012 pg mL^{-1}) to examine the relationship between increased tau protein levels and chronical neurological and psychological symptoms in military personnel after a traumatic brain injury. The ultrasensitive detection of biothreats such as ricin has also been demonstrated.[44]

The Noji group[45] developed larger arrays of one million femtoliter wells. Counting a very high number of individual immunocomplexes in the arrays reduced the Poisson noise. The assay was employed for the detection of PSA with an LOD of 60 ag mL^{-1} (≈ 2 aM). The authors also showed that the digital assay in femtoliter arrays is amenable to multiplexing by using two different enzyme/substrate labels.[46] Recently, a competitive femtoliter array format was demonstrated for the detection of small molecules such as cortisol in saliva.[47] The assay achieved an IC$_{50}$ down to 0.42 ng mL^{-1}, which was 44 times lower than for a conventional ELISA.

2.2.2. Microdroplets

Different methods for the generation of water-in-oil microdroplets have been reviewed earlier.[30] Water-in-oil droplets enclose the reactants and the product into pico- to femtoliter volumes. While microdroplets generated by emulsification methods tend to be rather heterogeneous, more homogeneous microdroplets can be generated and handled by microfluidic devices. Microfluidic droplets separate the reactants from the liquid substances, reduce the assay volume, and enable rapid handling, which increases the assay throughput.[48] Microfluidic droplets have also been used to study single enzyme molecule reactions[49] and single cells.[50]

Water-in-oil femtoliter droplets generated by a microfluidic device were used to establish a bead-based ELISA (Figure 3).[51] A capture antibody on the surface of polystyrene beads immobilized PSA. The presence of PSA was then detected by a biotinylated detection antibody and a streptavidin–β-galactosidase conjugate using fluorescein-di-β-D-galactopyranoside (FDG) as the substrate. The enzyme product fluorescein was recorded by fluorescence microscopy while the beads were identified and counted based on their red autofluor-
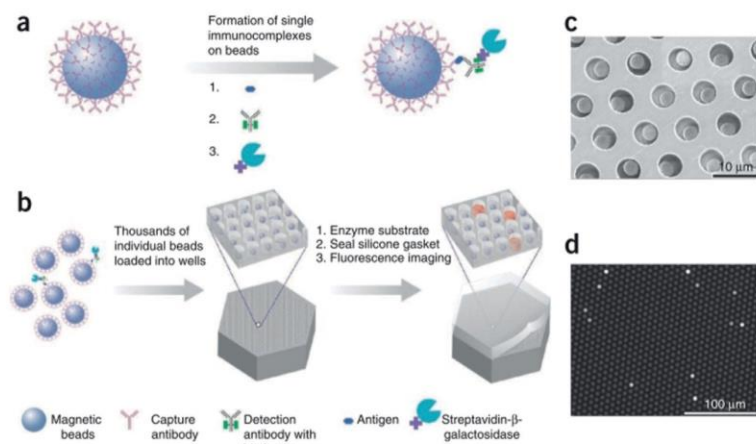
Figure 2. Single-molecule ELISA assay in femtoliter arrays. a) Many magnetic beads coated with capture antibody are dispersed in the analyte sample. After an analyte molecule has been caught, a biotinylated antibody forms the sandwich complex and serves as an anchor for a streptavidin-modified β-galactosidase. b) The beads are loaded—together with a fluorogenic substrate—onto a femtoliter array and sealed by a PDMS gasket. c) Scanning electron microscopy shows that only one bead is loaded per femtoliter well. d) Fluorescence microscopy records the fluorescence increase in wells that contain a bead with a captured analyte molecule. Reprinted with permission from ref. [38]. Copyright 2010 Nature America.

143
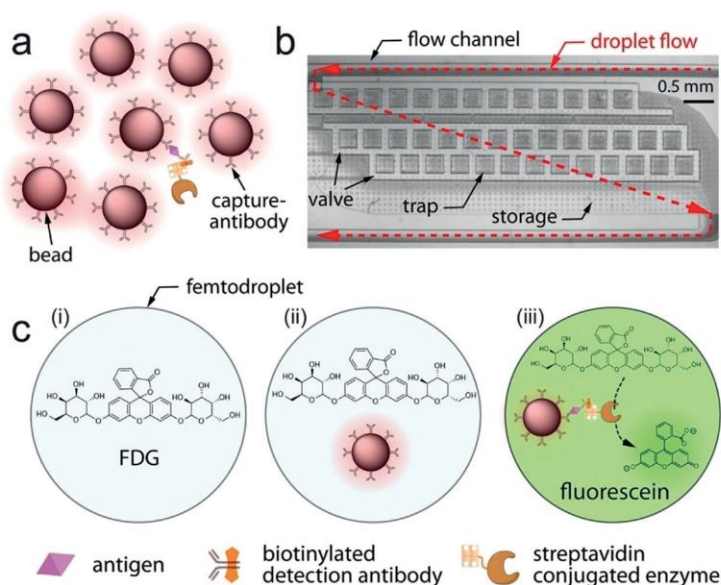
Figure 3. Scheme of single-molecule immunoassay in femtoliter-sized droplets. a) Antibody–antigen complex formation on beads. b) Beads with or without immunocomplex are encapsulated in droplets with the substrate and incubated on chip in traps to collect the fluorescent products of single-enzyme labels. c) Three droplet populations can be distinguished: i) droplets without a bead, ii) those containing a bead without immunocomplex, and iii) those containing both a bead and immunocomplex, which exhibit a positive fluorescence signal due to the enzymatic activity of a single β-galactosidase label. Reprinted with permission from ref. [51]. Copyright 2013 American Chemical Society.

escence. The microdroplet assay achieved an LOD of 46 fM and a linear range of 0.046–4.62 pM.

Liu et al.[52] developed another type of enzyme-linked immunoassay on magnetic beads for single-exosome counting in microdroplets (droplet digital ExoELISA). Magnetic beads were equipped with an anti-CD63 antibody to capture exosomes. After sample incubation, a biotinylated detection antibody and a streptavidin–β-galactosidase conjugate were added to the beads. The beads were enclosed in 40 μm droplets (≈ 33 fL) containing FDG. The fluorescence increase of fluorescein was detected in each droplet containing a magnetic bead with captured exosome. A bead-to-droplet ratio of 0.3 was employed to ensure that only one magnetic bead was enclosed in a given droplet. The assay achieved an LOD down to 10 enzyme-labeled exosome complexes per microliter (≈ 10 aM).

An competitive bead-based immunoassay utilizing microdroplets was reported for the detection of α-fetal protein (AFP).[53] AFP was captured by antibody-coated magnetic beads followed by the addition of a biotinylated detection antibody and a streptavidin–β-galactosidase conjugate. After magnetic separation, the unbound streptavidin–β-galactosidase was injected into a microfluidic chip to generate microdroplets with FDG. The microdroplets were collected into a microtiter plate and fluorescent droplets containing free streptavidin–β-galactosidase were counted under a fluorescence microscope. This indirect digital concentration readout reached an LOD in the fM concentration range.

The Di Carlo group[54] developed a microfluidic digital homogeneous entropy-driven biomolecular assay (dHEBA) for the detection of influenza A. Upon nucleoprotein binding, nucleic acid labeled antibodies formed a catalytically active complex that drove a hybridization/displacement reaction on a multicomponent nucleic acid substrate and generated many fluorescence-labeled oligonucleotides. The dHEBA format enabled the detection of influenza A nucleoprotein in a concentration of 4 aM in approximately 10 min without the need for a purification step.

3. DNA Labels for PCR Amplification

The polymerase chain reaction (PCR) amplifies DNA—in principle starting from a single template strand—exponentially to very high copy numbers of DNA.[55] Droplet microfluidics on a microchip enables the rapid isolation of single DNA strands and subsequent PCR amplification in pico- or femtoliter reaction containers.[56] For example, a digital PCR was performed in rotational chips to detect viral RNA isolated from single HIV viruses.[57] Wells of different volumes were employed in the chip to enable quantification over a wider dynamic range. The assay achieved an LOD of 40 RNA molecules per mL.

Similar to the digital readout of single enzyme molecule labels, a digital immuno-PCR can be implemented if the PCR reaction is enclosed in microdroplets. The droplet-based digital immuno-PCR (ddIPCR) used magnetic beads as a solid support, DNA as a marker and PCR for signal amplification, for example, for the detection of PSA.[58] The ddIPCR was performed in three steps as shown in Figure 4. First, the PCR reaction mixture was emulsified to generate tens of thousands of water-in-oil droplets per microchip. Subsequently, the samples underwent thermal amplification cycles and the number of positive droplets was determined by end-point fluorescence detection. In the last step, the number of DNA copies was calculated based on the Poisson distribution. The ddIPCR can usually improve the LOD by 100- to 10000-fold compared to a standard ELISA. It was noted, however, that the washing steps and the microfluidic droplet system cannot be easily combined. The LOD for PSA was 0.48 ng mL^{-1} with a linear range of 0.5–30 ng mL^{-1}. The concentration analysis of human serum samples correlated well with a commercial reference immunoassay.

The digital PCR was combined with a proximity ligation assay (PLA) to improve the precision of the assay.[59] Target proteins such as the cytokine IL-6 were immobilized on magnetic beads and detected by two types of DNA-modified antibodies that are capable of forming a pair of PLA probes. If both antibodies bound to the protein, the PLA probes were

144
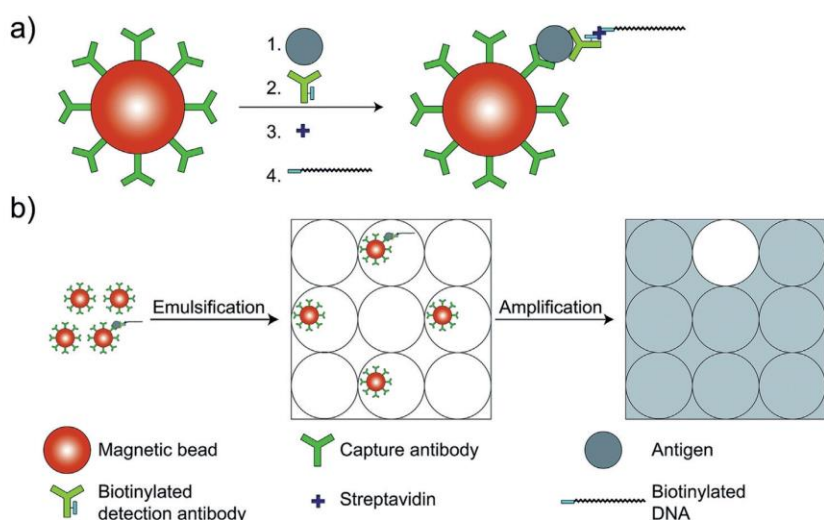
Figure 4. Scheme of ddIPCR. a) Antibody-coated magnetic beads capture the antigen (1). A biotinylated antibody (2), streptavidin (3), and biotinylated DNA sequence from *Aspergillus fumigatus* (4) are sequentially added. b) The magnetic beads are resuspended in a reaction mixture and emulsified. After ddIPCR, the numbers of negative and positive droplets are counted. Reprinted with permission from ref. [58]. Copyright 2018 Royal Society of Chemistry.

joined by DNA ligation. The ligated DNA reporter strand was then amplified by rolling circle amplification, and the amplified DNA was detected via fluorescent DNA probes. Because standard rolling circle amplification is not quantitative, the ligated DNA strands were compartmentalized individually by using a microfluidic device, and the protein concentration was determined digitally by counting fluorescent microdroplets.

4. Fluorescent Molecular Labels

The detection of molecular labels at the single-molecule level relies on fluorescence spectroscopy and microscopy. Confocal microscopy and total internal reflection microscopy (TIRF) efficiently reduce the detection volume and the concomitant background signal, which enables the detection of single fluorescent label molecules. When crossing a focused laser beam in a confocal microscope set-up, individual fluorophores emit bursts of photons that are detected.[60] The residence time depends on the diffusion of the fluorophore through the beam path (with a typical active volume of a few femtoliters) and on photobleaching. Cyanine dyes were proposed for such applications as the excitation within 650–700 nm is well compatible with the spectral window of low light scattering and autofluorescence of biological substances including blood. Even epifluorescence has more recently been reported to enable single-fluorophore detection. However, the type of microscopy is not relevant for the assay design as long as it allows for the detection of a single fluorescent molecule. Thus, we have organized this section according to different assay formats. Fluorescence counting of single protein analyte molecules immobilized on a surface by

capture antibodies seems in general to be more sensitive than correlation techniques in solution.

4.1. Detection of Surface-Bound Analytes

Löscher et al.[61] developed a sandwich assay for the detection of single cardiac actin molecules. The scanning system employed a single-photon-counting avalanche photodiode together with a CCD camera for imaging under 635-nm laser excitation. A glass surface was coated with a cellulose layer to reduce nonspecific binding. Confocal microscopy reduced the optical background by minimizing the detection volume, which enabled the evaluation of photon bursts originating from individual molecules.

A particular kind of bioaffinity assay, the so-called pull-down assay, has been used for the identification of protein–protein interactions. The Ha group[62] developed a single-molecule pull-down assay (Figure 5). A capture antibody was immobilized in a flow chamber coated with polyethylene glycol (PEG) and biotin. Streptavidin was added to the flow chamber, followed by the addition of a biotinylated anti-His antibody, which captured overexpressed His6-tagged yellow fluorescent protein (YFP) from cell extracts. Individual YFP molecules were detected by TIRF microscopy. A stepwise decrease of the fluorescence intensity during single-molecule bleaching experiments enabled the identification of dimeric and trimeric YFP molecules. Individual protein kinase A (PKA) complexes were detected by a two-color single-molecule pull-down assay. In its inactive form, PKA is present as a tetramer that consists of two catalytic and two regulatory subunits. Cyclic adenosine monophosphate (cAMP) activates the enzyme and leads to tetramer dissociation. The investigation of the stoichiometry of individual PKA complexes is essentially not possible using conventional analog detection.

Burgin et al.[64] developed a single-molecule assay for the detection of enhanced green fluorescent protein (EGFP) and tumor suppressor protein p53. A microfluidic chip was mounted onto a TIRF microscope under 473-nm laser excitation. Two methods for absolute protein quantification were used for the digital readout. In the accumulation method (Figure 6a), the analyte was observed over a defined time period, during which the number of fluorescent spots increased until individual EGFP molecules were no longer distinguishable as diffraction-limited spots. In the detect and bleach method (Figure 6b), fluorescent spots were counted, bleached, and after a fixed time interval counted again. Both images were subtracted to identify newly arrived and

145
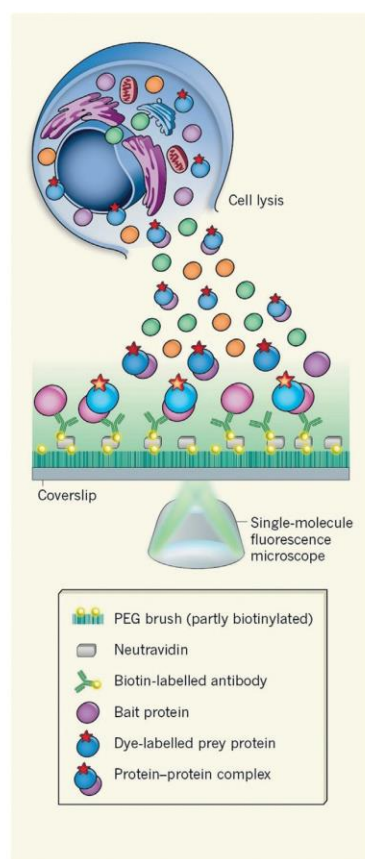
Figure 5. Scheme of single-molecule pull-down assay. A cell lysate is applied directly onto a coverslip for single-molecule TIRF microscopy. Specific antibodies on the coverslip capture protein complexes. Prey proteins associated with the bait protein are detected via a fluorescent dye fused to the prey. Reprinted with permission from ref. [63]. Copyright 2011 Macmillan Publishers Limited.

bleached molecules. Protein p53 was detected in the accumulation method by using a labeled detection antibody.

Zhang et al.[65] developed a digital ATP assay using split aptamers. A coverslip was bound to a glass slide with a 5-mm hole in the center, followed by surface activation with plasma. A mixture of poly(L-lysine)-poly(ethylene glycol)-biotin (PLL-PEG-biotin) and PLL-PEG was added to the activated coverslip. Next, streptavidin was added, and a biotinylated Cy3-3′-labeled split aptamer was bound to streptavidin. The analyte ATP was added together with the other Cy5-3′-labeled aptamer. The coverslip was placed on an epifluorescence microscope, and the emission of the two dyes was collected simultaneously on the same EM-CCD camera. Diffraction-limited spots of a mixed color indicated specific binding, whereas spots with only one color indicated nonspecific binding. The assay achieved an LOD of 100 fM and a working range of 1 pM to 5 nM.

Weng et al.[66] developed an aptasensor for the detection of small molecules. The hairpin-shaped aptamer immobilized
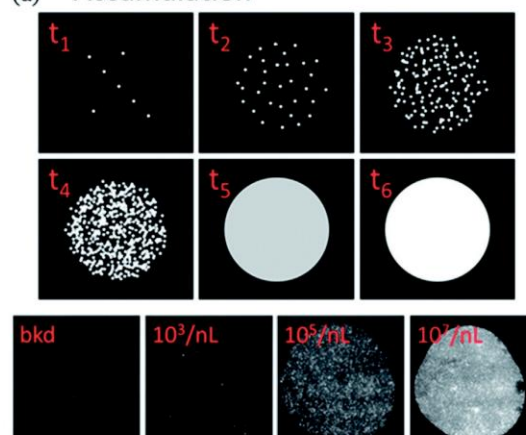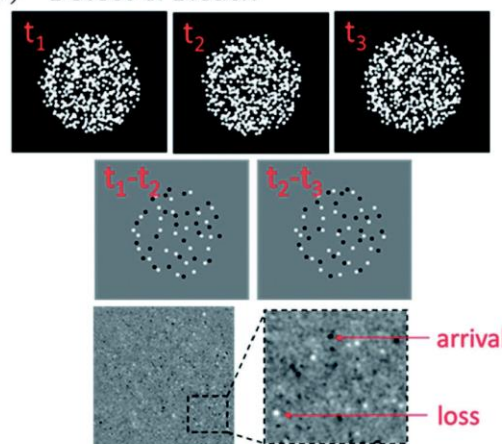
Figure 6. Different approaches for digital protein quantification. a) For low analyte concentrations, the accumulation method counts the increasing number of fluorescent spots. If the distance between two fluorescent molecules is below the diffraction limit, they appear as one spot and cannot be distinguished anymore. b) In the detect and bleach method, fluorescent molecules are counted after a certain time interval and subsequently bleached. The bleaching step keeps the average number of fluorophores bound to the surface at a constant level such that higher concentrations can be determined. Reprinted with permission from ref. [64]. Copyright 2014 Royal Society of Chemistry.

on a glass slide changes its conformation to an open state upon analyte binding (Figure 7). Fluorescently labeled short ssDNA probes bound preferably (but not exclusively) to the open conformation and the fluorescence trajectories of individual aptamers were monitored by TIRF microscopy. As the binding of the fluorescent probe followed different kinetic patterns depending on the conformation of the aptamer, the kinetic fingerprints were used to distinguish between nonspecific binding and analyte binding. Only spots that showed the signature of specific binding were counted to determine the analyte concentration. The assay achieved

146
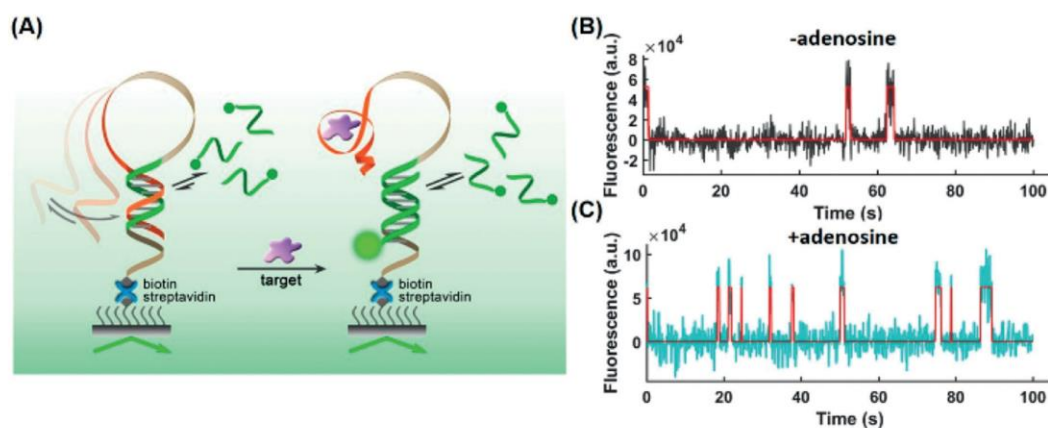
Figure 7. A) Scheme of a hairpin-shaped aptasensor immobilized on a slide surface. Analyte binding results in a conformational change and binding of a complementary fluorescent ssDNA probe. Single-molecule trajectories B) without and C) with 50 pM adenosine are distinguishable. Reprinted with permission from ref. [66]. Copyright 2019 American Chemical Society.

LODs of 0.3 pM for adenosine, 0.35 pM for acetamiprid, and 0.72 pM for PCB-77 in spiked chicken meat extract.

4.2. Laser-Induced Fluorescence Detection inside a Capillary

The Yeung group pioneered the use of capillary electrophoresis for single-molecule detection.[36] In capillary electrophoresis, an electric field drives the sample through the illumination volume, which is small enough to allow for the detection of individual fluorescent molecules. Based on the electrophoretic mobility of individual fluorescently labeled antibodies, fluorescent immunoassays were established.[67] Antibodies bound to an analyte molecule have lower electrophoretic mobility and can thus be distinguished from free antibodies using cross-correlation. Individual fluorescence-labeled antibodies were recorded in the capillary by widefield microscopy using a 20× objective (numerical aperture (NA) 0.75) and an intensified CCD camera.

Stimulated by the need for reliable and sensitive assays for cardiac troponin, a diagnostic marker of acute myocardial infarction, the Erenna platform was developed.[68] First, a sandwich immunoassay was performed in a microtiter plate, and the bound labels were then released and inserted into a capillary electrophoresis device. As only a single fluorescent molecule passed through the detection volume during the observation interval, individual analyte molecules were counted, and an LOD of 1.7 pg mL^{-1} was achieved. In combination with magnetic beads, it was possible to detect troponin I levels of 0.2 pg mL^{-1}, which are typically found in healthy individuals (0.3 to 9 pg mL^{-1}).[69] Esparza et al.[70] used the Erenna assay to study amyloid-beta (Aβ) aggregation and deposition in Alzheimer's disease. Concentrations as low as 1.56 pg mL^{-1} (0.18 pM) of soluble Aβ oligomers were detectable above background, and the limit of quantification (LOQ) was 6.25 pg mL^{-1} (0.72 pM). The method was applied to measure the Aβ oligomers in human cortical tissue homogenate. Wild et al.[71] detected mutant huntingtin protein (mHTT) in cerebrospinal fluid. The mHTT is a promising biomarker for monitoring Huntington disease progression, but due to its predominantly intracellular localization, the concentration in the cerebrospinal fluid is very low (below pM even in patients in an advanced state of the disease) and conventional methods are not sensitive enough to detect it. The Erenna assay provided an LOD of 40 fM and the authors found a significant difference in levels of mHTT in carriers of the genetic mutation in the premanifest stage and in different later stages of the disease.

For the detection of the fertility-related human gonadotropin follicle-stimulating hormone (FSH), the laser beam was shaped into stripes, and 10 "superpixel" zones were evaluated using a CCD camera.[72] Magnetic beads served as a solid support for the immunoassay. The LOD for FSH was 34 fM for a few hundreds of fluorescent events counted above the background in 12 s corresponding to a few zeptomoles of labeled antibodies.

The combination of several excitation lasers (blue 488 nm; green 543 nm; red 635 nm; infrared 730 nm) and four single-photon-counting modules allowed for the implementation of multiplexed assays.[73] Confocal microsecond-scale alternating-laser excitation (ALEX) single-molecule fluorescence spectroscopy was used to probe the fluorescent acceptor (A) without energy transfer (FRET) and provided donor (D) excitation-based data for each single molecule. Distinct emission signatures were recovered for interacting species through determination of the FRET efficiency E, which relates to the D–A distance, and distance-independent stoichiometry-based ratio S. The combination of E and S on two-dimensional histograms allowed for a virtual sorting of single molecules. This technique was evaluated by determining 25 DNA sequences, 6 tumor markers, 8 bacterial gene markers, and 3 drug-resistance determinants.

147

4.3. Fluorescence Correlation Spectroscopy

Fluorescence correlation spectroscopy (FCS) records diffusion at the single-molecule level. Equilibrium concentration fluctuations due to Brownian motion are measured as spikes of fluorescence intensity within a small sampling volume. A concentration in the nanomolar range should be attained for sub-femtoliter detection volumes to allow for following individual fluorescence-labeled molecules. Such a small detection volume can be obtained using confocal microscopy or multiphoton microscopy. The sensitivity of FCS depends mainly on the brightness of the fluorescent probe and on the detection volume.[74] Evaluating fluorescence intensity fluctuations over time by an autocorrelation function yields information on the diffusion rates and the concentration of the fluorescent molecule.[75] The diffusion time depends on the size and shape of the target molecule, on the viscosity of the solution, and on the size of the focused laser beam. FCS can be exploited to follow molecular interactions with other molecules because the diffusion time decreases each time when another molecule has bound.[76] FCS has found applications in in vitro and in vivo studies of protein–protein interactions, nucleic acid interactions, enzymatic activities, and membrane diffusion.[77]

The detection of fluorescence-labeled molecules at the single-molecule level by FCS is applicable for the implementation of homogeneous immunoassays that avoid washing and separation steps as well as nonspecific binding to surfaces, which becomes increasingly important at low analyte concentrations.[75] On the other hand, FCS is prone to background interferences caused by autofluorescence, light scattering, quenching, and potential aggregation of the assay components. The simplest scheme of an FCS immunoassay is based on following the changes in the diffusion rate after the formation of the immunocomplex (Figure 8). Chatterjee et al.[76] employed a sandwich assay for the detection of the neuronal cell adhesion molecule contactin-2 in cerebrospinal fluid. The assay was based on two different anti-contactin antibodies. One antibody was labeled with Alexa Fluor 488 and the other one was unlabeled. The formation of the sandwich immunocomplex of both antibodies with the analyte increased the diffusion time, which was evaluated from the autocorrelation curve. The authors reached a limit of quantification of 0.2 ng mL^{-1}.

Changes in the diffusion rates were also recorded by FCS to implement a competitive assay for the detection of the mycotoxin fumonisin B$_1$ (FB$_1$).[78] The analyte FB$_1$ competed with a tracer consisting of FB$_1$ and Alexa Fluor 488 for the free binding site of the antibody. The assay provided an LOD of 1 ng mL^{-1}.

The sensitivity towards the formation of immunocomplexes closer in size can be enhanced by using fluorescence cross-correlation spectroscopy (FCCS). FCCS uses two spectrally different fluorescent probes, which can be simultaneously excited using two separate excitation wavelengths and detected in two different channels. The amplitudes of the cross-correlation curves are calculated to measure the interactions of the fluorescent probes with the analyte. Compared to conventional FCS, the use of two labels increases the sensitivity and especially the selectivity of FCCS in the quantitative measurement of biomolecules.

The Klenerman group[79] developed a sandwich assay based on the counting of coincidence spikes of two labeled antibodies. Compared to conventional FCCS, the data evaluation was simplified because only the number of spikes was counted, which corresponds to both labels being present in the confocal volume at the same time. Protein G and herpes simplex virus were detected with an LOD of 50 fM.

Miller et al.[80] demonstrated a sandwich FCCS-based assay for the detection of human chorionic gonadotropin and the prion protein (Figure 9). Two lasers were alternated, and the emissions of different fluorescent labels were measured using separate detectors to eliminate spectral cross-talk and reduce the probability of false positive cross-correlation.[81] The fluorophores were chosen in such a way that their emission is separated, reducing the overlap of the emission and the possible energy transfer. To eliminate aggregation effects on the cross-correlation curves, cross-correlations on short time sections were calculated and those displaying the highest level of fluorescence (top 1% of the intensity distribution) were discarded. The method provided

Figure 8. a) FCS setup. A laser is focused to excite fluorescent molecules in a confocal volume. Fluorescence intensity fluctuations due to Brownian motion are measured in solution by a photodiode connected to an optical fiber. b) The emitted photons are collected and plotted as time-dependent intensity changes. c) The autocorrelation curves show an increase in the diffusion time after formation of the immunocomplex (••••) compared to the antibody alone (——). Reprinted with permission from ref. [76]. Copyright 2017 Elsevier.

Figure 9. In FCCS, two fluorescence-labeled antibodies bind to the analyte. Black line: cross-correlation of labeled antibodies without analyte (antigen); red line: cross-correlation of labeled antibodies in the presence of the analyte. Reprinted with permission from ref. [80]. Copyright 2009 American Chemical Society.

LODs of 100 pM (human chorionic gonadotropin) and 2 nM (prion protein) with an analysis time of 40 min.

5. Nanoparticle Labels

In recent years, various kinds of nanomaterials have been introduced as labels for immunoassays in order to enhance the assay performance.[20a] In particular, NPs with luminescent or plasmonic properties, which allow for a convenient optical readout, are suitable for single-molecule analysis.[82] Compared to molecular labels, NPs display generally higher signals, which allows for an easier readout. On the other hand, their larger size can be a drawback in terms of steric hindrance of the immunocomplex formation as well as a potentially higher degree of nonspecific binding.

5.1. Semiconductor Nanoparticles

Quantum dots (QDs) are fluorescent semiconductor nanocrystals with dimensions typically between 1 and 10 nm. The photoluminescence properties of QDs can be tuned by changing the nanocrystal size, making it possible to adjust emission wavelengths in the range of 380 to 2000 nm.[83] Compared to conventional fluorophores, QDs provide higher emission intensities, better photostability, wider excitation spectra, and narrower emission bandwidths.[84] This allows for an easier detection of individual QDs compared to conventional fluorophores.

5.1.1. *Detection of Surface-Bound Analytes*

Liu et al.[85] developed a sandwich immunoassay based on QD labels. Capture antibody-coated QDs and detection antibody-coated QDs were mixed with the sample, and then immobilized onto a positively charged coverslip. Mixed color spots (yellow) were counted under a fluorescence microscope. Carcinoembryonic antigen (CEA) was detected with an LOD of 6.1 pM. The same group[86] implemented a homogeneous sandwich immunoassay that employed only one type of label. Capture and detection antibodies were conjugated separately to 655QD. After formation of a sandwich immunocomplex with the analyte, the QD emission was monitored through a diffraction grating placed in front of a CMOS camera of the microscope. The grating divided the emission into a zeroth-order spot and a first-order streak. Because of the diffraction limit, it was not possible to distinguish between unbound QDs and the immunocomplexes. The QDs were oxidized during excitation, and the first order streak shifted to shorter wavelengths. The oxidation of the QDs started at different times and proceeded at different rates, which split the first order streak into two smaller streaks. The number of split streaks was proportional to the number of analyte molecules. The LODs for CEA and AFP were 6.7 fM and 3.4 fM, respectively.

5.1.2. *Detection in Microchannels*

The Nie group[87] implemented a sandwich immunoassay for virus detection based on the parallel detection of red and green fluorescent NPs in a microfluidic channel under 488-nm laser excitation. The immunocomplex was detected by monitoring the coincidence of photon bursts in the red and green detection channels. In this way, wild-type and mutated respiratory syncytial viruses were quantified in parallel with an LOD of 4×10^6 plaque-forming units (PFU).

Zhang et al.[88] developed an aptamer-based single-QD FRET assay for the detection of cocaine. They first designed a signal-off assay by assembling a sandwich of a 3′-biotinylated oligonucleotide, a cocaine aptamer and a 3′-Cy5-labeled oligonucleotide. The sensitivity of the system was investigated by plotting the Cy5 burst counts against the ratio of Cy5 to 605QD from 0 to 24. It was possible to distinguish between single Cy5 labels. The sandwich complex was dispersed in a diluted cocaine sample to capture the analyte, and then a commercial streptavidin-functionalized 605QD (605 nm emission) was added to capture the aptamer complex. In the presence of a high amount of cocaine, no FRET signal was observed due to the release of the Cy5-oligonucleotide after analyte binding. The signal-off assay achieved an LOD of 0.5 μM for cocaine, which is comparable to other electrochemical and enzyme-based assays. The generally low sensitivity was explained by the poor affinity of the aptamer towards cocaine. Additionally, a signal-on assay was designed by forming a sandwich of a 3′-biotinylated oligonucleotide and 5′-Cy5-oligonucleotide, the cocaine aptamer, and a 3′-Iowa-black-oligonucleotide, which quenched the emission of the 605QD/Cy5 FRET. In the presence of cocaine, the quencher containing the oligonucleotide was released, and

149

the FRET emission between the 605QD and Cy5 was detected. A 488-nm argon laser was focused on the capillary (50 μm inner diameter), and photon bursts of 605QD and Cy5 were detected simultaneously by two avalanche photodiodes (APD).

A high-throughput assay was developed in a very narrow channel (1–2 μm width and height) integrated in a chip system (Figure 10).[89] Semiconducting polymer dots (Pdots) were modified with streptavidin and the binding of biotin-Alexa647 was investigated. Au NPs were added to the solution as an internal standard to compensate for instrumental fluctuations. The platform combined confocal fluorescence detection with narrow channels, which made it possible to count photon bursts corresponding to individual NP-labeled molecules. Additionally, the dual laser excitation scheme enabled the quantification of the number of fluorophores per NP. This is a very promising technique for the characterization of different nanoconjugates.

5.1.3. Fluorescence Correlation Spectroscopy

To distinguish two components by FCS, at least a twofold difference in their diffusion coefficients is required, which corresponds to approximately an eightfold mass difference (in the case of an idealized compact hydrodynamic sphere).[90] This can be a limiting factor for the analysis of associations of particles with similar mass. If small fluorescent label molecules are replaced by larger NPs, however, the difference in the diffusion times between the free immunoreagents and the formed immunocomplex increases, and the sensitivity of FCS is improved. For example, a sandwich aptamer-based FCS assay utilizing QD-based probes was reported for the detection of thrombin in serum with an LOD of 2.6 nM and a working range of 5–500 nM.[91]

The general configuration of the FCCS requires the alignment of the two lasers with different wavelengths to the same focal spot, which makes the optical setup more complicated than the conventional single-laser FCS. The misalignment of the detection volumes can lead to a decrease of apparent cross-correlation. The single-wavelength excitation FCCS (SW-FCCS) developed by Wohland's group[92] overcame this limitation by the use of two probes, which can be excited using the same wavelength, but their emission is separated due to a large difference of the Stokes shifts. This can be conveniently achieved by the use of QDs[93] or long Stokes shift fluorescent proteins.[94] The group of Ren[95] designed sandwich and competitive assays based on SW-FCCS for the detection of alpha-fetoprotein (AFP). In both approaches, 655QDs (655 nm emission) and Alexa Fluor 488 (520 nm emission) were chosen as the labels. The achieved LODs were 20 pM (sandwich assay) and 180 pM (competitive assay).

5.2. Photon-Upconversion Nanoparticles

The optical background of traditional fluorescence read-out can be avoided by using photon-upconversion nanoparticles (UCNPs) that emit shorter-wavelength light under near-infrared (NIR) excitation (anti-Stokes emission).[96] UCNPs are lanthanide-doped nanocrystals and the most efficient UCNPs consist of a hexagonal $NaYF_4$ host crystal doped with Yb^{3+} and Er^{3+} or Tm^{3+}. The anti-Stokes emission strongly reduces autofluorescence and light scattering. Fur-
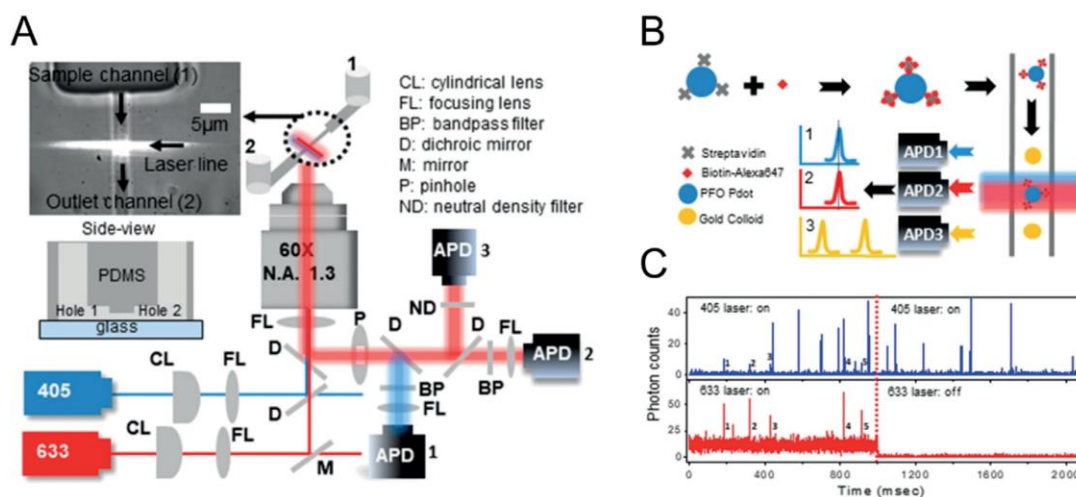
Figure 10. A) Optical setup of the single-particle flow platform. Avalanche photodiodes APD1 and APD2 detect the fluorescence of Pdots and Alexa647, respectively, while APD3 detects the backscattered light of Au NPs. B) Labeling and measurement procedure to quantify the number of streptavidin molecules bound to the surface of Pdots. C) Fluorescence intensity traces of single-particle flow measurements of the Pdot-SA-biotin-Alexa647 complex. Blue (top) and red (bottom) traces are from Pdots and biotin-Alexa647, respectively. The dotted red line indicates the time at which the 633 nm laser was turned off. The five labeled peaks indicate the Pdot-SA-biotin-Alexa647 complex since both blue (Pdot) and red (biotin) fluorescence were detected simultaneously. Reprinted with permission from ref. [89]. Copyright 2018 American Chemical Society.

150

ther advantages of UCNPs include a high photostability and multiple and narrow emission bands that can be tuned individually for the multiplexed detection of several analytes in parallel.[97] For example, the group of Soukka[98] developed a multiplexed array-in-well assay to determine the immune status against virus infections in human serum samples by the spatial arrangement of several virus antigens on a microtiter plate. Additionally, two types of UCNP labels with different emission colors (Er-doped: green; Tm-doped: blue) were used to distinguish between IgG and IgM antibody classes.

The groups of Fan[99] and Jin[100] further enhanced the multiplexing capabilities of UCNPs by combining wavelength- and lifetime-based encoding. The combination of several lifetime populations and emission bands laid the foundation for a very high encoding capacity. This approach was used for the detection and differentiation between the DNA of nine subtypes of human papillomavirus,[99] but can also be readily adapted for multiplexed antibody-based assays.

5.2.1. Detection of Surface-Immobilized Analytes

We have developed a method for visualizing individual UCNPs ($NaYF_4$:Yb^{3+},Er^{3+}) by conventional epiluminescence microscopy and applied it for the sensitive detection of the cancer marker PSA.[22a] Individual sandwich immunocomplexes consisting of 1) an anti-PSA antibody immobilized on the surface of a microtiter well, 2) PSA, and 3) an anti-PSA antibody–UCNP conjugate were counted under an upconversion wide-field microscope equipped with a 980-nm laser excitation source (Figure 11). The single-molecule (digital) ULISA provided an LOD of 1.2 pg mL^{-1} (42 fM) PSA in 25% blood serum and covered a dynamic range of three orders of magnitude. The digital readout provided single-particle resolution without instrumental background, which resulted in ten times lower LOD compared to the classical (analog) readout of luminescence intensity. An important advantage of the digital readout is the resistance against NP aggregation. In

the analog mode, a large aggregate containing hundreds of luminescent NPs can lead to a very high background signal. By contrast, in the digital mode, each aggregate—regardless of its size—only counts as a single binding event and has only a marginal effect on the background signal. Recently, we have prepared a detection label based on a conjugate of PEG-coated UCNPs with streptavidin, which allowed to decrease the label concentration and further improved the LOD by a factor of 50 to ≈20 fg mL^{-1}.[22b]

Li et al.[101] designed a digital homogeneous sandwich immunosorbent assay based on UCNPs ($NaYF_4$:Yb^{3+},Er^{3+}, 42 nm in diameter) for PSA. An antibody-coated UCNP, PSA, and an antibody-coated Au NP formed an immunocomplex. As the green upconversion luminescence overlapped strongly with the absorption spectrum of 50 nm Au NPs, luminescence energy transfer (LRET) strongly quenched the upconversion luminescence. Consequently, the ratio of the visible particles in a flow cell and the amount of UCNPs that was visible in the negative control decreased. The assay achieved an LOD of 1.0 pM in buffer and 2.3 pM in serum.

5.2.2. Fluorescence Correlation Spectroscopy

If a sample such as blood or plasma is strongly autofluorescent, the FCS/FCCS signal of a label present in sub-nanomolar concentrations is not detectable due to spectral overlap. This effect can either be reduced by using brighter labels or by measuring the cross-correlation of UCNP labels to avoid optical background interference. Lahtinen et al.[102] developed an assay based on upconversion cross-correlation spectroscopy for the detection of thyroid-stimulating hormone (TSH). Green ($NaYF_4$:Yb^{3+},Er^{3+})- and blue (NaYF$_4$:Yb^{3+},Tm^{3+})-emitting UCNPs were conjugated with anti-TSH antibodies, and the cross-correlation was measured upon binding of the analyte TSH. Compared to small organic fluorophores, NP labels have a higher tendency to form aggregates, bind non-specifically, and induce bridging of more
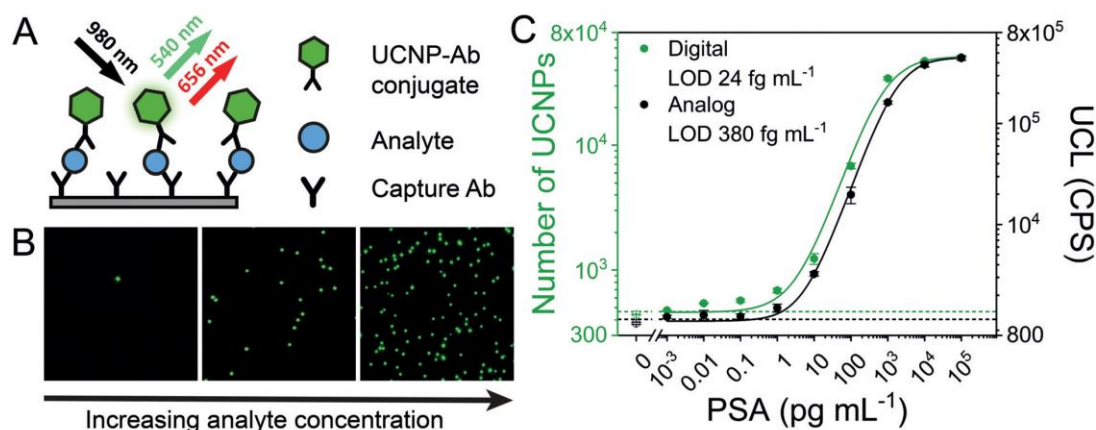
Figure 11. Single-molecule ULISA. A) Scheme of sandwich immunoassay; Ab = antibody. B) Wide-field upconversion microscope images of single immunocomplexes carrying a UCNP label. C) Calibration curves of the digital (green) and analog ULISA (black). The number of UCNPs is given by the diffraction-limited spots in (B) and the upconversion luminescence (UCL) is recorded by a microtiter plate reader.[22]

151

than two NPs. To suppress these effects, large intensity bursts that were attributed to aggregates were removed before calculating the auto- and cross-correlation functions.[103] However, the smaller bursts were still causing strong variations of the amplitude, which affected the assay sensitivity. The achieved LOD was 15 mIU L^{-1}, which is above the range of normal TSH concentrations in serum (0.3–5.0 mIU L^{-1}).

5.3. Plasmonic Nanoparticles

Plasmonic NPs have been used in single-molecule immunoassays because they enable a highly sensitive readout based on their light-scattering properties and spectral changes upon analyte binding. The most common materials include gold (Au NPs) and silver (Ag NPs). Au NPs are labels that are most frequently used in immunoassays in general, finding applications in lateral flow assays, electrochemistry, colorimetric assays, and plasmonic sensing.[104] Ag NPs are less stable because they are oxidized more easily, but they possess higher extinction coefficients and stronger Raman and fluorescence enhancement.[105] In both cases, the plasmonic properties are strongly dependent on the shape and the size of the NP.[106]

5.3.1. Dark-Field Microscopy

Dark-field microscopy is the most common method for the detection of single plasmonic particles. In dark-field microscopy, the illumination light is prevented from entering the objective acceptance cone, whereas the light scattering from immobilized NPs is collected by the objective lens. Background scattering and reflection from interfaces can be further reduced by optimizing the refractive indices.

Poon et al.[107] developed an antibody-based single-particle scattering intensity assay for the detection of various clinical cancer markers such as AFP, CEA, and PSA. A gold nanoprobe coated with a capture antibody was immobilized in a flow cell on microscope coverslips. Then the analyte was added, followed by a second Ag NP carrying the detection antibody. Binding of Au and Ag NPs resulted in a threefold increase of the scattering intensity and a spectral shift. The LODs for all three analytes were in the range of 1 to 6 pm.

Wu et al.[108] developed a magnetic-bead-based sandwich immunoassay for AFP, CEA, and PSA using Au NP detection. First, a sandwich immunocomplex was formed by incubating the sample with a biotinylated antibody and a second unlabeled antibody (Figure 12). The immunocomplexes were captured on streptavidin-coated magnetic beads. Au NPs coated with a secondary antibody were added, and unbound labels were removed by magnetic separation. After washing, the Au NPs were released from the beads by treatment with 8 M urea. The free Au NPs were then immobilized on a cationic coverslip and counted under a dark-field microscope. Zhu et al.[109] developed a similar sandwich immunoassay for PSA using a preconcentration step on magnetic beads.

The Gooding group[110] showed the potential use of commercial cameras as they appear in smartphones for the high-throughput spectral readout of the localized surface plasmon resonance (LSPR) spectra of up to 5000 individual Au NPs (Figure 13). Anti-interleukin-6 (IL-6) antibodies were conjugated to Au NPs and spin-coated on a glass slide. A biotinylated anti-IL-6 antibody was attached to a 10-nm streptavidin-modified satellite Au NP and then added to the Au NPs immobilized on glass. The binding of the satellite Au NP resulted in a redshift of the LSPR signal due to plasmon coupling. The spectral shift of single Au NPs before and after the addition of IL-6 was used to calculate the analyte concentration. While the setup was not sensitive enough to detect single binding events, single-molecule sensitivity may be achieved by using bigger satellite particles (20–80 nm).

A method for extracting affinity constants based on statistical fluctuations in equilibrium was proposed by Luthgens and Janshoff.[111] It is based on a single-molecule readout of an array of isolated sensors, which can accommodate a high amount of simultaneously bound analyte molecules. Aćimović et al.[112] employed this principle to follow antibody–antigen binding kinetics on long timescales on the single-molecule level. First, Au nanorods were modified with

antigen ⟶ biotin-Ab1 ⟶ Ab2 ✳ secondary antibody-AuNP ✳ streptavidin-magnetic bead
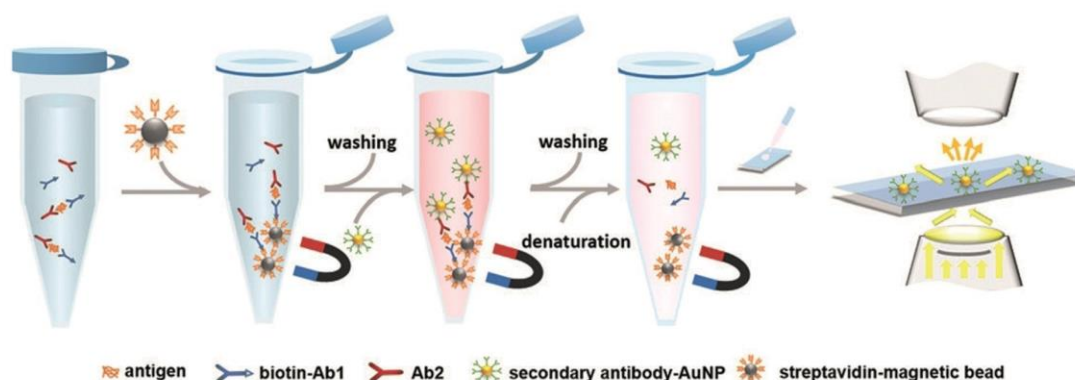
Figure 12. Au NP-based detection of PSA with dark-field microscopy readout. Reprinted with permissions from ref. [108]. Copyright 2017 Royal Society of Chemistry.

152
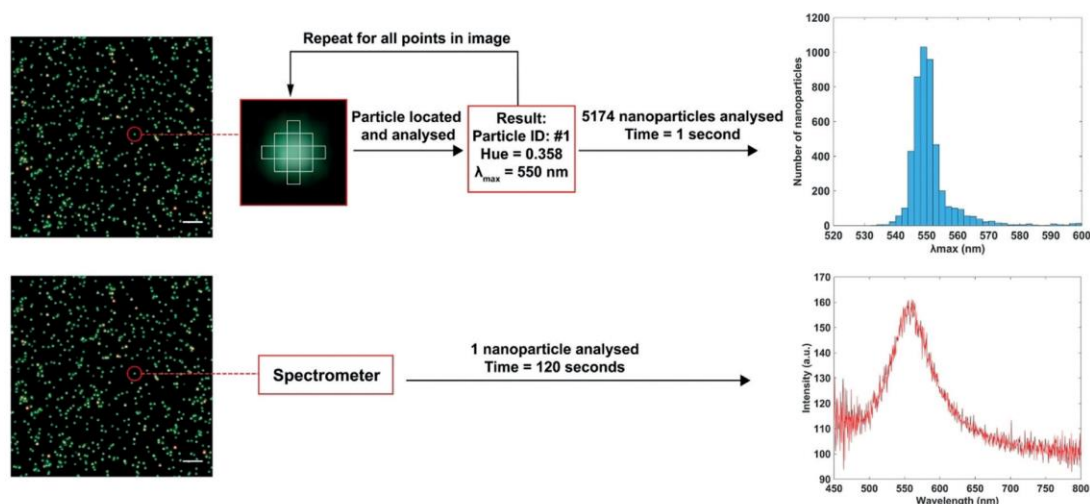
Figure 13. Top: Color analysis using a commercial camera. The color of the Au NPs is transformed into a hue value that corresponds to a specific wavelength and plotted in a histogram. Bottom: Color analyses using a spectrometer; each spot has to be processed individually. Reprinted with permission from ref. [110]. Copyright 2018 Elsevier.

thiolated PEG followed by binding of an anti-PEG antibody. The signal fluctuations at equilibrium enabled the calculation of kinetic parameters and analyte concentrations.

Yang et al.[113] developed a digital aptamer-based assay for the detection of thrombin. A biotinylated anti-thrombin aptamer was immobilized on streptavidin-coated magnetic beads. Au NPs coated with a DNA sequence complementary to the aptamer were introduced and bound to the aptamer. In the presence of thrombin, the Au NPs were released, and the beads were magnetically separated. The free Au NPs in the supernatant were either counted individually under a dark-field microscope by dispersing a drop on a coverslip (digital detection) or—at high concentrations—by measuring the absorption resulting from NP aggregation (analog detection). Another aptamer-based thrombin assay was developed by Li et al.[114] A glass slide was modified by Au NPs to bind a thrombin-specific aptamer. Thrombin was specifically captured, followed by another anti-thrombin aptamer to form a sandwich complex. After the addition of Au NPs, NP oligomers formed through Au–S binding, and the color changed from green to yellow and red. Individual NPs were detected under a dark-field microscope, and the thrombin concentration was estimated from the intensity change of the Au NPs. The assay detected thrombin with an LOD of 10 fM.

Chen et al.[115] increased the LSPR signal of individual Au NPs by enzymatic amplification. When a single streptavidin horseradish peroxidase conjugate bound to a biotinylated Au NP, the resulting LSPR shift enabled the detection of single molecules. The enzymatic precipitation of 3,3′-diaminobenzidine further increased the colorimetric response by a factor of 50. This method can potentially be developed into a sandwich immunoassay by coating the Au NPs with a capture antibody and conjugating horseradish peroxidase with a detection antibody.

5.3.2. Light Scattering Correlation Spectroscopy

Resonance light scattering correlation spectroscopy (RLSCS) measures the fluctuations of resonance light scattering in small volumes due to the Brownian motion of single NPs. Noble metal NPs are excellent labels for RSLCS because of their efficient resonance light scattering, which is several orders of magnitude higher than scattering of small organic molecules.[116] The RSLCS instrumentation is similar to that of FCS, but no emission filter is needed. Like FCS, the RLSCS immunoassays are based on the increase of the characteristic diffusion time in the detection volume due to the formation of an immunocomplex. RLSCS was used in a sandwich immunoassay for AFP (LOD 1 pM)[117] and in competitive assays for AFP (LOD 100 pM) and 17-β-estradiol (LOD 10 pM).[118] Similar to FCS and FCCS, one of the major limitations of RLSCS is the significant effect of NP label aggregation. Although in both studies the particles were coated by PEG to suppress the NP aggregation, in the presence of a real sample matrix, the assay reproducibility in serum was lower compared to the standard ELISA.

Fluorescence and scattering light cross-correlation spectroscopy (FSCCS) was used by Wang et al.[119] in a confocal setup for measuring the scattering of labels based on Au NPs and a fluorescent dye (Alexa Fluor 488) as a probe pair (Figure 14). The advantage of FSCCS is the use of a single 488-nm laser as the excitation source for both the Au NP and the fluorescent label. A sandwich immunoassay based on this setup achieved an LOD of 3.1 pM AFP.

5.3.3. Surface Plasmon Microscopy

The adsorption of individual plasmonic NPs can be followed in real time using surface plasmon microscopy.[120] Changes in surface plasmon resonance (SPR) properties

153
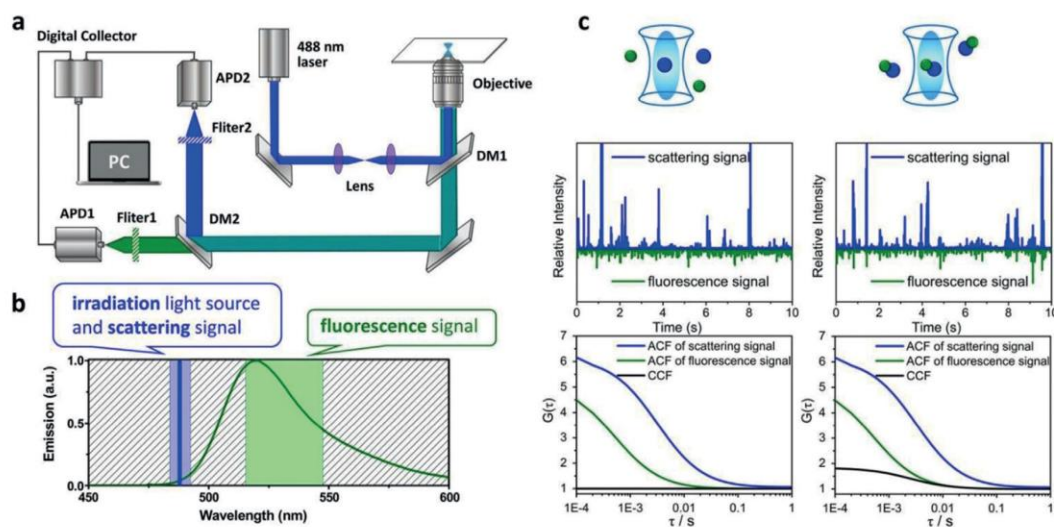
Figure 14. a) Setup for FSCCS. b) Spectral separation of excitation and emission wavelengths. c) Scattering and fluorescence signals and their correlation curves for labeled species diffusing independently (left) or linked (right). ACF = autocorrelation curve, CCF = cross-correlation curve. Reprinted with permission from ref. [119]. Copyright 2017 American Chemical Society.

affect the reflected light intensity, which is detected by an image sensor.[121] The measurement can be based either on the setup with a high-NA microscope objective[122] or on the standard Kretschmann configuration.[123] While a high-NA objective provides high resolution, the field of view is typically limited to an area of 0.01 mm². On the other hand, the Kretschmann configuration provides a wider field of view (over 1 mm²), but imperfections in the arrangement of object, lens, and image planes degrade the performance and resolution of the optical system. SPR imaging is typically used for the characterization of homogenous films, where high resolution is not necessary.[124]

The group of Mirsky developed a wide-field approach for the detection and quantification of single NPs[121] and applied it for the analysis of Au and Ag NPs in complex samples such as wine, apple juice, and sunscreen (Figure 15).[125] The large imaging area of the wide-field setup increased the probability of detecting single NP adsorption events at low concentrations. The signal strength was mainly determined by the size and refractive index of the NPs, the distance from the plasmonic substrate, and the performance of the optical system. The adsorption of a single NP, however, only led to a small signal change. To enhance the sensitivity, differential images of local temporal and spatial intensity changes were evaluated based on the changes between the two subsequently captured frames. The method provided an LOD of 10^6 NPs mL^{-1} (≈ 1.6 fM) and a working range of 10^6–10^{10} NPs mL^{-1} with a measurement time of 1 min. The sensitivity can be further improved by increasing the analysis time or the sensing surface area.

Furthermore, the combination of surface plasmon microscopy with electrochemical analysis made it possible to determine the composition of NPs.[126] This technique was applied to the analysis of Ag and Cu NPs and achieved an

LOD of 10^4 NPs mL^{-1}. Surface plasmon microscopy was also employed for single-molecule detection of DNA hybridization,[127] and the application to single-molecule immunoassays would be straightforward.

5.3.4. Detection in Microarrays

Sevenler et al.[128] used Au nanorods as labels for the detection of hepatitis B virus surface antigen (HBsAg) on a protein microarray. An anti-HBsAg antibody was spotted on an interferometric reflectance imaging sensing (IRIS) substrate and incubated with the antigen, followed by the addition of Au nanorods coated with another anti-HBsAg antibody, and the particles were counted in an automated imaging device under illumination by circularly polarized light. Light reflected by the IRIS substrate was also polarized, but the light scattered by Au nanorods was linearly polarized along the longitudinal axis of the NPs and was separated from the reflected light. The assay achieved an LOD of 3.2 pg mL^{-1}.

Belushkin et al.[129] designed a sandwich immunoassay for C-reactive protein (CRP). A gold nanohole array was coated with an anti-CRP capture antibody. The array was immersed in the analyte medium, washed, and immersed in a dispersion of Au NPs that were coated with an anti-CRP antibody. Au NPs in or close to the nanoholes could be detected because of a decrease in the extraordinary optical transmission (EOT). EOT is an SPR-based phenomenon that occurs when light passes through a subwavelength-sized regularly shaped metallic film. Particles too far away from nanoholes were not detected. Single Au NPs were counted under a microscope.

154
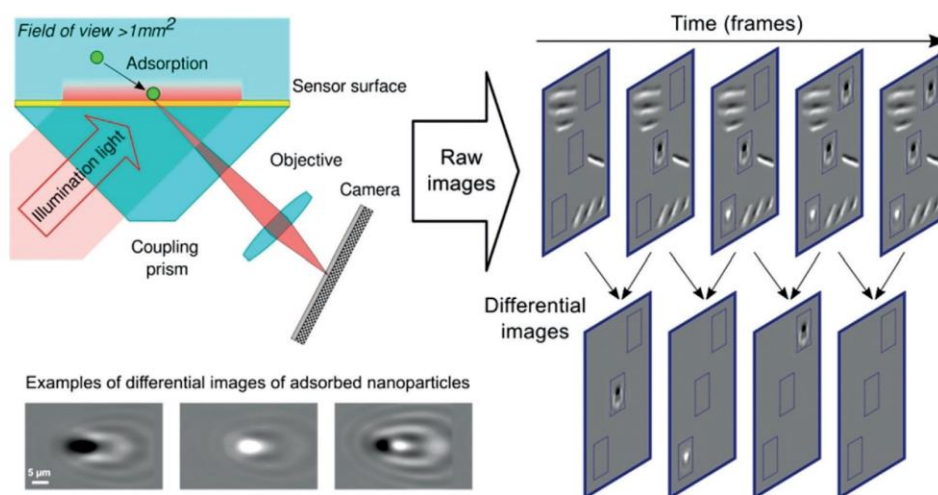
Figure 15. Surface plasmon microscopy for the detection of single NPs adsorbing to the sensor surface. Reprinted with permission from ref. [125]. Copyright 2016 American Chemical Society.

6. Bead Labels

6.1. Fluorescence Microscopy

While it is not possible to make a sharp separation between NPs and beads, here we define beads as labels larger than 100 nm in diameter. The larger size, on the one hand, offers an easier way for detection but, on the other hand, impedes the accessibility of the label to the analyte. The Lövgren group[130] was one of the first to employ a bead label for the detection of single analyte molecules. Individual europium-doped beads—with a diameter of 107 nm, very close to NP size—were detected by time-resolved fluorescence (TRF). A microtiter plate was coated with a monoclonal anti-PSA antibody and biotinylated PSA was added, followed by the streptavidin-coated Eu beads. The analyte binding was measured in the analog mode by time-resolved fluorometry and in the digital mode by counting single bead labels under a time-resolved microscope equipped with a $10\times$ objective and a CCD camera. The assay achieved an LOD of 0.38 pg mL^{-1} of biotinylated PSA.

Wu et al.[131] used color-encoded magnetic beads to simultaneously detect single virus particles of three different types of avian influenza (Figure 16). Polystyrene beads were coated first with γ-Fe$_2$O$_3$, then with QDs displaying different emission colors (green, yellow, red) and with antibodies against avian influenza. The three bead types, each one specific for a certain avian influenza type, were dispersed in the sample and magnetically separated. The beads were then loaded onto a PDMS microarray that was coated with antibodies for the different virus types. After washing, only beads that captured a virus particle remained in the array. The assay resulted in an LOD of 0.02 pg mL^{-1}.

Zhang et al.[132] embedded UCNPs of different colors and in different ratios into polymer microbeads to generate codes for the multiplexed detection of DNA. The combination of

n intensity levels with m colors resulted in (n^m-1) unique codes. The labels were detected at the single-bead level under 980-nm excitation by confocal microscopy. The DNA sequence was identified based on the upconversion encoding signal, while the presence and amount of the target sequence was indicated by conventional fluorescent dyes.

Gite et al.[133] developed a sandwich assay consisting of 1) a magnetic particle, 2) an anti-*Clostridium difficile* capture antibody, 3) *C. difficile,* 4) an anti-*C. difficile* detection antibody, and 5) a fluorescent microparticle. A mixture of a visible-light-absorbing dye-cushion reagent and the density agent iodixanol was dried on the bottom of each microwell (Figure 17). The immunoreagents were added, and the magnetic beads were pulled to the bottom of the microplate with a magnet. The dye absorbed all visible light and stayed at the bottom due to the density agent, resulting in a strong reduction of the background fluorescence of unbound fluorescent particles. Single fluorescent beads appeared as bright pixels on a digital camera chip.

6.2. Bright-Field Microscopy

Tekin et al.[134] developed a microfluidic-based magnetic bead counting assay for the detection of proteins in serum (Figure 18). Magnetic beads (2.8 μm) were modified with a capture antibody to preconcentrate a target protein from fetal bovine serum. The beads were passed over a glass surface patterned with smaller antibody-modified magnetic beads (1 μm). The larger beads were attracted to the surface by a magnetic field, which allowed them to "roll" over multiple smaller beads due to dipolar magnetic forces. An immunocomplex formed when the antigen had a suitable orientation on the bead. The drag force caused by the flow had to be strong enough to release the particles when only dipolar forces were present. The analyte concentration was

155
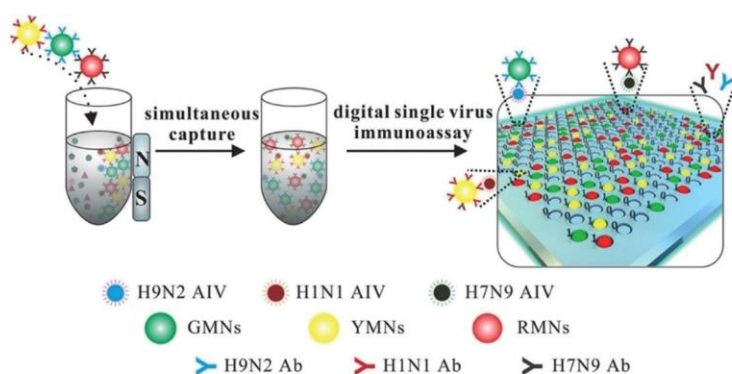
Figure 16. Scheme of the multiplex assay for avian influenza viruses. Color-encoded magnetic spheres—each coated with a specific anti-avian influenza virus antibody—are dispersed in the virus sample. After magnetic purification, the particles are loaded onto a PDMS array and digitally counted. Reprinted with permission from ref. [131]. Copyright 2019 American Chemical Society.
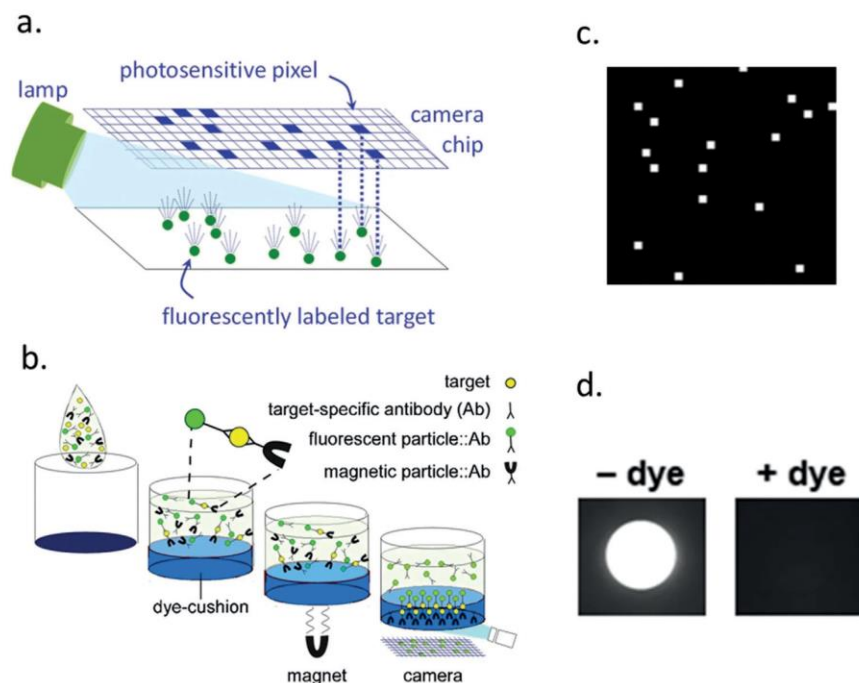
Figure 17. a) Detection of single fluorescent beads on one or a small group of pixels of a camera chip without the need for microscope magnification. b) After immunocomplex formation, a magnet immobilizes the magnetic beads at the bottom of a microwell. Only fluorescent beads near the surface are excited because the dye absorbs the excitation light that penetrates deeper into the well. c) Fluorescent beads appear as bright pixels on the digital camera. d) A comparison of a well with and without dye shows the efficiency of a dye-cushion layer. Reprinted from ref. [133] with the permission of Creative Commons Attribution 4.0 International License.

($\approx 1\ \mathrm{fg\,mL^{-1}}$) TNF-$\alpha$, equivalent to ≈ 200 molecules in 5 µL of the sample.

6.3. Dark-Field Microscopy

Tethered particle monitoring is a biophysical technique used to characterize changes in the length of a polymer tethered to a particle on one end and a surface on the other end. The Brownian motion of the particle limited by the tether is usually monitored optically. Schafer et al.[135] introduced tethered particle monitoring in 1991 to follow the transcription of a DNA template bound to an Au NP by RNA polymerase immobilized on a glass slide. Various modifications of the principle are possible and can be used for monitoring single-molecule binding events in an immunoassay.

Visser et al.[136] utilized the tethered particle monitoring in an aptamer-based sandwich assay for thrombin. Magnetic beads were modified with an anti-thrombin capture aptamer and the glass surface of a flow chip was modified by a detection aptamer. The beads were tethered to the glass surface by a 40-nm-long dsDNA strand. When the analyte was captured between the aptamers, the bead was anchored onto the surface, and its mobility was strongly reduced (Figure 19), which was monitored over time by dark-field microscopy. The binding and unbinding events of hundreds of beads were detected simultaneously. The rate of switching between the two states, and especially the lifetime of the unbound state, was dependent on the concentration of thrombin in a range of 10–300 nM. As the interaction was reversible and all recognition elements were bound in the flow cell, the system is amenable for continuous biomarker monitoring.

Silver et al.[137] developed a sandwich immunoassay for the detection of PSA based on tethered particle monitoring. Magnetic beads (2.8 µm) with immobilized antibody captured

determined by counting the bound large beads on a conventional optical microscope. The combination of a magnetic preconcentration step and digital counting of bound magnetic beads in a microfluidic chip afforded an LOD of 60 aM

156
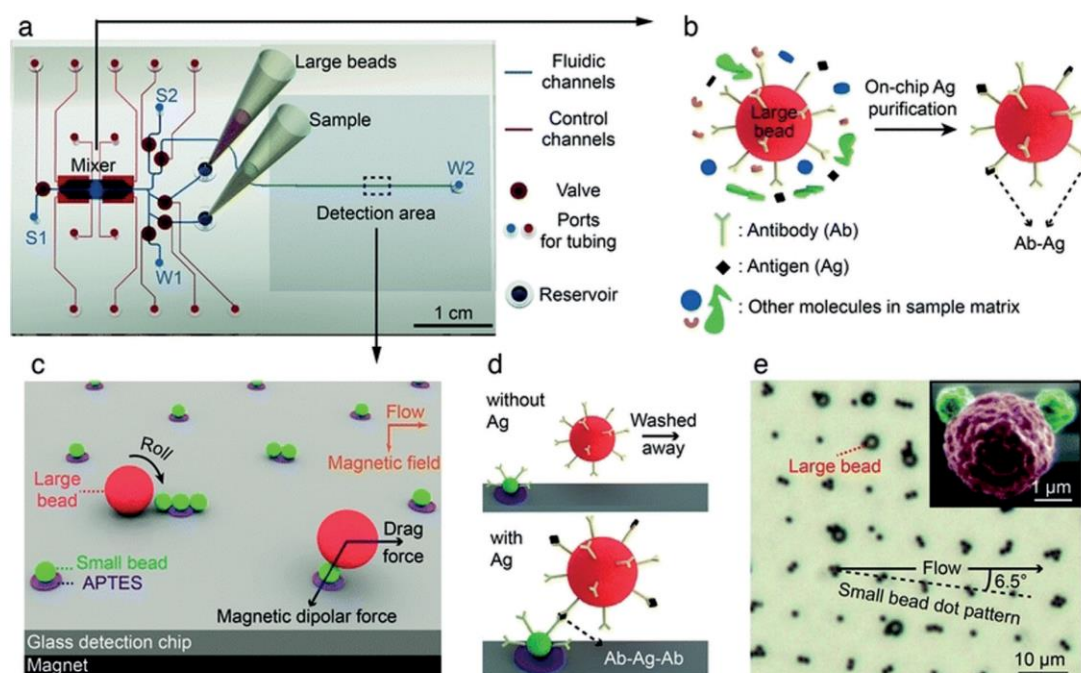
Figure 18. Microfluidic-based magnetic counting assay. a) Scheme of a microfluidic chip. b) Large magnetic beads separate the target protein from the matrix. c) The large beads roll over the patterned array of smaller beads that are magnetically attracted to the surface. d) A sandwich immunocomplex is formed when the antigen and the large bead have a suitable orientation. e) Optical micrograph of the captured large beads on the patterned array of small beads. A colored SEM photograph in the inset shows the large bead captured on the small beads. Reprinted with permission from ref. [134]. Copyright 2013 Royal Society of Chemistry.

PSA from the sample matrix. After magnetic separation, the beads were incubated with the biotinylated detection antibody and introduced into a flow cell. The beads carrying the immunocomplex were captured by a streptavidin-terminated DNA tether. This tether allowed the beads to move 12 μm back and forth when the flow direction was changed by manual syringe operation. Thus, specifically bound beads were distinguished from nonspecifically bound beads and counted using a low-magnification (10×) dark-field microscope. The assay achieved an LOD of 1 pM PSA.

Akama et al.[138] combined tethered particle monitoring with an immunoassay in femtoliter arrays. In the "digital homogeneous non-enzymatic immunosorbent assay" (HoNon-ELISA), antibody-decorated magnetic particles were used to separate the analyte from the sample matrix. Then, they were magnetically pulled into the microreactors of a femtoliter array chip for the confinement of the antibody–antigen reaction. The antigen was recognized by another antibody immobilized through a PEG linker to the well surface. The sandwich complex tethered the particle to the surface and limited its Brownian motion, which was monitored for thousands of wells in parallel using bright-field or dark-field microscopy and particle tracking analysis. According to the movement patterns, selectively captured particles were discerned from nonspecifically bound ones, and individual binding events were counted. The procedure did not require any washing or signal amplification steps and reached an LOD of 0.093 pg mL^{-1} PSA.

7. Label-Free Detection

Most label-free detection schemes are based on plasmonic effects. While Section 5.3 describes the use of plasmonic NPs as labels, here we focus on the arrangement of plasmonic nanostructures to generate local hot spots, which are very sensitive to analyte binding.[139] Localized surface plasmon resonance (LSPR) has been used to follow the changes of local refractive indices near plasmonic NPs. There are various possibilities to link the refractive index changes to the presence of the analyte, as demonstrated by numerous reports of bulk LSPR-based immunoassays.[20a, 140] The high sensitivity of LSPR can be exploited to characterize statistical distributions of molecular properties and to follow single-molecule binding events.[141] Beuwer et al.[142] used correlated atomic force microscopy (AFM) and optical microscopy to study how the binding location affects the changes of LSPR signals. Au NPs were used as a model analyte and bound to single-crystal Au nanorods using cysteine–cysteine coupling.[143] In the correlative approach, AFM was used to study the binding locations, and the plasmon shifts were evaluated by single-particle spectroscopy. A broad distribution of LSPR shifts was
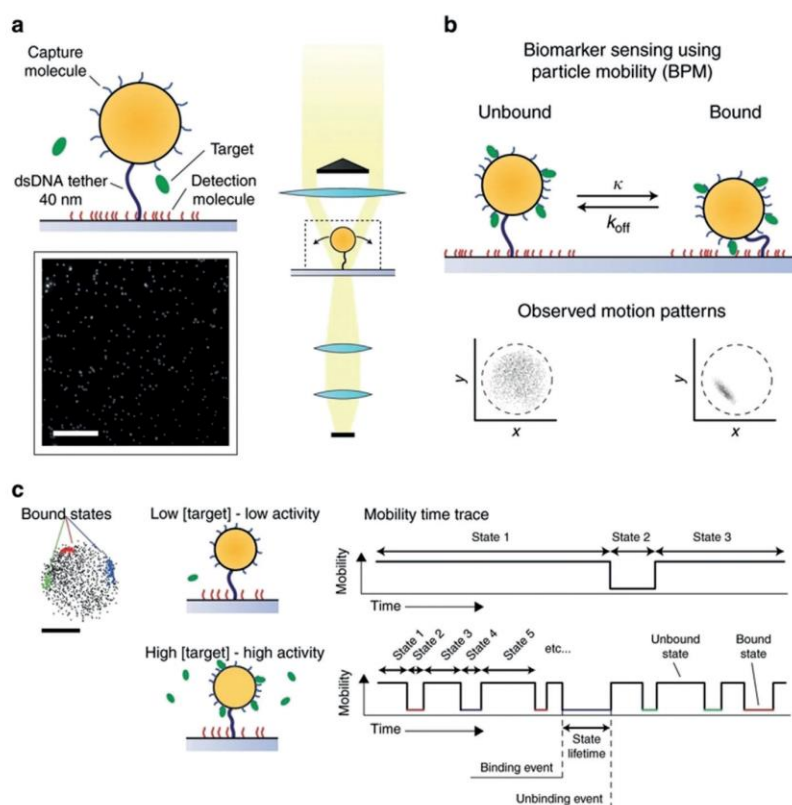
Figure 19. Tethered particle monitoring. a) Particles (orange) are modified by capture aptamers (blue) and tethered to the substrate by a 40-nm dsDNA strand (black). The substrate is decorated with detection aptamers (red). The image was recorded by dark-field microscopy (scale bar: 50 μm). b) After thrombin (green) binding, the particle's movement is restricted, which changes the motion pattern. c) The particle mobility is continuously analyzed for hundreds of particles in parallel. The mobility time traces of low and high analyte concentration reveal individual binding and unbinding events. Reprinted from ref. [136] with the permission of Creative Commons Attribution 4.0 International License.

individual nanorods. When the plasmon wavelength of a particle was shorter than the 795-nm illumination light, the scattered signal increased upon antibody binding. The intensity change was stepwise and irreversible due to the strong biotin–antibody interaction. The binding constants were calculated from the mean waiting times and followed a Poisson distribution. The LOD was influenced by the number of binding events in a certain timeframe. As low analyte concentration resulted in long waiting times, a high number of particles had to be observed, which was limited by the field of view of the objective (ca. 50000 NPs). The high rate of binding events at high analyte concentrations required a fast camera image acquisition. The shorter exposure times were compensated by a higher excitation power, which was limited by photothermal heating of the particles.

Another emerging label-free technique for the detection of single molecules are whispering gallery mode (WGM) microring resonators, which trap light due to multiple total internal reflections at a curved boundary (Figure 21). Analyte binding to the optical ring resonators results in a shift of the resonance wavelength. Arrays of microring resonators were used for the multiplexed detection of five protein biomarkers.[148] Single-molecule sensitivity for protein or DNA

observed for similar binding locations, which was attributed to the size dispersion of the Au NPs. Binding of the Au NPs to the tip of the rod led to stronger plasmon shifts than binding to its sides. Since the probability of binding to various locations of a nanorod differs,[144] the knowledge of the binding location can help not only to determine the level of sensor response but also to evaluate the binding constants. Site-specific functionalization techniques can be used to maximize the sensitivity and reduce the signal distribution.[145] Lee et al.[146] designed plasmon rulers as sensors for the detection of single molecules of matrix metalloproteinase (MMP3). When two noble metal NPs exhibiting LSPR approach each other, their individual surface plasmon resonances couple, which generates a shift in the scattering spectrum and can be detected by dark-field microscopy.

Beuwer et al.[147] used Au nanorods to detect the interaction of biotin and an anti-biotin antibody (Figure 20). They functionalized the tips of Au nanorods with thiolated biotin and detected the change in the scattering intensity of

has been achieved. More recently, even single ions such as Hg^{2+} and Zn^{2+} have been detected using a gold antenna coupled to a WGM microresonator.[149]

Surface-enhanced (SERS) and tip-enhanced Raman spectroscopy (TERS) also enable the label-free detection of single protein molecules.[151] It is, however, difficult to employ these techniques for measuring protein concentrations in routine analytical applications.

8. Summary and Outlook

As new and low-abundance disease markers are investigated, there is a growing need for developing more sensitive detection methods. Tables 1–3 summarize various assay types for the digital readout of analytes that have been discussed in the Review.

Single-molecule immunoassays have gained popularity in clinical research and diagnostics and some platforms have

158
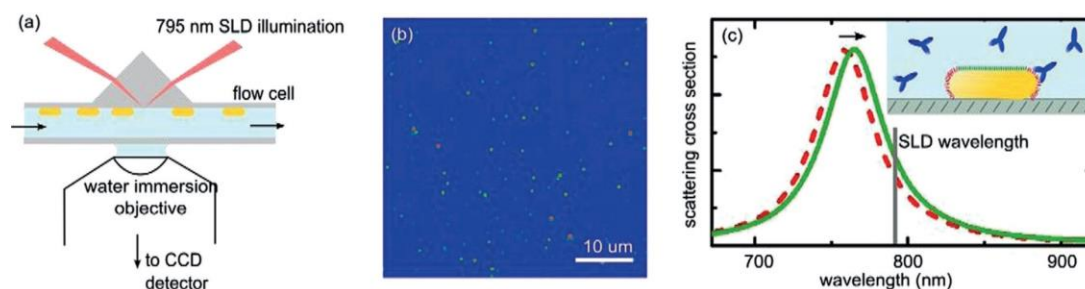
Figure 20. a) Scheme of a dark-field microscope with a superluminescent diode (SLD). b) Image of surface-immobilized gold nanorods shown in pseudocolors. c) The tips of the gold nanorods are functionalized by receptors (red), while the sides are blocked by tetraethylene glycol (green). An individual antibody-binding event results in a redshift of the plasmon resonance. The vertical gray line indicates the SLD center wavelength. Reprinted with permission from ref. [147]. Copyright 2015 American Chemical Society.
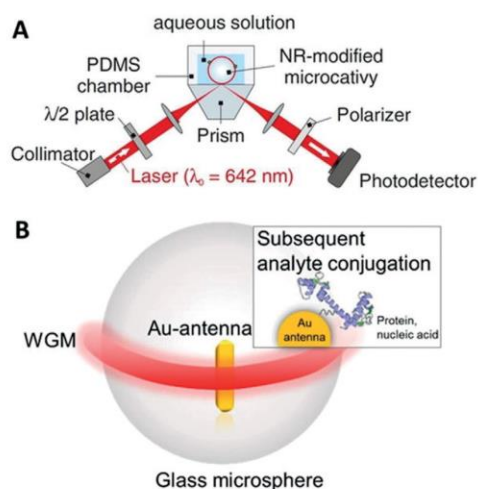
Figure 21. Scheme of optical ring resonators. A) Instrument setup for coupling a laser into an optical ring resonator. B) A glass microsphere serves as an optical microcavity to measure physical, chemical, and biological properties. Near total internal reflection of light results in an optical resonance (WGM, red). The WGM couples to a gold nanorod where it excites plasmon resonance. Single analyte molecules can be detected if they bind inside plasmonic hot spots. Reprinted with permission from ref. [150]. Copyright 2017 IOP Publishing.

been commercialized. Commercial single-molecule immunoassays offer complete solutions for the detection of a wide range of biomarkers in clinical research, including cytokines, hormones, and signaling proteins. As of September 2019, Merck offered 49 ready-to-use immunoassay kits for the Erenna system,[152] and Quanterix offered 130 kits for the Simoa platform.[153] Furthermore, custom development services and kits for in-house development of new assays by the customer are available.

Although the detection of individual optical labels is relatively easy using state-of-the-art detectors, it is still a challenge to achieve the superior sensitivity of single-molecule assays compared to that of analog assays. Recently, the advantages of analog and digital detection modes have

been compared systematically using the same TIRF platform.[154] Furthermore, the same analyte was used to evaluate the performance of different assays.[155] Three immunoassay platforms were assessed regarding their ability to detect sub-picomolar concentrations of the protein biomarker GAD65.[156]

Another important challenge is the simplicity and robustness of the assay procedure. Even though single-molecule assays can reach extremely high sensitivity, the need for highly sophisticated instrumentation, well-trained personnel, and long operation times can impede their commercialization. Despite these challenges, single-molecule assays are finding their way into real-world applications and can replace conventional methods such as the ELISA or electrochemiluminescence assays. The possibility to detect only a few biomarker molecules in a sample opens up many new possibilities for enhanced diagnostics.

Conflict of interest

The authors declare no conflict of interest.

[1] a) S. Weiss, *Science* **1999**, *283*, 1676–1683; b) W. E. Moerner, D. P. Fromm, *Rev. Sci. Instrum.* **2003**, *74*, 3597–3619; c) C. Joo,

159

Table 1: Digital assays for cancer biomarkers. The LODs were converted into molar concentrations wherever applicable.

Assay type	Analyte	Matrix	LOD	Working range	Assay time (min)	Sample volume	Ref.
FCCS with QDs	AFP	buffer	20 pM	20 pM–5 nM	120	10 µL	[95]
Resonance light scattering correlation spectroscopy	AFP	buffer	1 pM	1 pM–1 nM	50	20 µL	[117]
Fluorescence and scattering light cross-correlation spectroscopy	AFP	buffer	3.1 pM	5–580 pM	120	10 µL	[119]
Light scattering correlation spectroscopy	AFP	buffer	100 pM	100 pM–10 nM	120	20 µL	[118]
Counting of spatially overlapping two-color QDs	CEA	plasma in buffer	6.1 pM	10.4–666.7 pM	30	n/a	[85]
Droplet microfluidics	exosomes	n/a	17 aM	10 aM–1 pM	n/a	n/a	[52]
Simoa	PSA	25% newborn calf serum in buffer	98 fM	100 fM–500 pM	n/a	n/a	[39]
Droplet array	PSA	buffer	2 aM	1 aM–100 fM	120	n/a	[45]
Femtoliter microfluidic droplets	PSA	buffer	46 fM	0.046–4.62 pM	270	200 µL	[51]
Droplet-based immunoPCR	PSA	buffer	17 pM	17 pM–1 nM	120	30 µL	[58]
Digital ULISA with UCNPs	PSA	25% bovine serum in buffer	42 fM	350 fM–35 pM	150	100 µL	[22a]
Digital ULISA with streptavidin-coated UCNPs	PSA	25% bovine serum in buffer	800 aM	3.5 fM–3.5 pM	210	100 µL	[22b]
Single-UCNP enumeration	PSA	buffer	1 pM	0–500 pM	120	n/a	[101]
Au NP enumeration with dark-field microscopy	PSA	buffer	35 pM	35–700 pM	170	95 µL	[108]
Counting of gold nanorods by dark-field microscopy	PSA	buffer	280 aM	350 aM–350 fM	195	100 µL	[109]
Digital HoNon-ELISA	PSA	buffer	3.2 fM	3.2 fM–3.2 pM	n/a	n/a	[138]
Tethered-bead immunoassay	PSA	buffer	1 pM	1–10 pM	n/a	50 µL	[137]
Simoa	PSA, TNF-α	25% bovine serum	50 aM, 150 aM	100 aM–1 pM	360	100 µL	[38]
Fluorescence-aided multiplexed molecule sorting	CEA, PSA, AFP	50% human serum in buffer	14 pM, 100 pM, 100 pM	10 pM–1 nM, 100 pM–10 nM, 100 pM–10 nM	120	n/a	[73]
Immunoassay based on spectral blueshifts of QDs	CEA, AFP	25% plasma in buffer	6.7 fM, 3.4 fM	10 fM–100 pM	n/a	n/a	[86]
Scattering-based quantitative single-particle intensity measurement	CEA, PSA, AFP	human serum	1.7 pM, 3.3 pM, 5.9 pM	0–300 pM	n/a	n/a	[107]

n/a = not available; AFP = alpha-fetoprotein; CEA = carcinoembryonic antigen; PSA = prostate specific antigen; TNF-a = tumor necrosis factor alpha.

160

Table 2: Summary of digital assays for other clinical biomarkers. The LODs were converted into molar concentrations wherever applicable.

Assay type	Analyte	Matrix	LOD	Working range	Assay time (min)	Sample volume	Ref.
Fluorescence colocalization	ATP	buffer	100 fM	1 pM–5 nM	45	25 µL	[65]
FCS	contactin-2	17% CSF in buffer	1.5 pM	n/a	60	10 µL	[76]
Microarray-based plasmonic biosensor	CRP	buffer	225 fM	n/a	120	100 µL	[129]
Erenna	cTnI	25% human plasma in buffer	74 fM	n/a	n/a	10 µL	[68]
Bead-based Erenna	cTnI	25% human plasma in buffer	8.7 fM	10 fM–500 pM	180	100 µL	[69]
Light scatting correlation spectroscopy	17-β-estradiol, AFP	buffer	10 pM, 100 pM	10 pM–1 nM, 100 pM–10 nM	120	20 µL	[118]
Single-molecule fluorescence counting	FSH	n/a	34 fM	100 fM–1 nM	n/a	100 µL	[72]
FCCS	hCG PrP	buffer	100 pM 2 nM	100 pM–10 nM (hCG)	40	n/a	[80]
Proximity ligation assay	IL-6	n/a	5 fM	10 fM–1 nM	n/a	n/a	[59]
Counting of Au NPs using dark-field microscopy with digital color analysis	IL-6	buffer	4.76 nM	n/a	n/a	n/a	[110]
Erenna	mutant huntingtin	30% cerebrospinal fluid in buffer	40 fM	40 fM–1 nM	n/a	45 µL	[71]
Simoa	NF-L	25% human serum in buffer	4.3 fM	4.2 fM–26 pM	n/a	152 µL	[42]
Simoa	tau	25% human plasma in buffer	180–250 aM	250 aM–15 pM	n/a	152 µL	[43]
Single-molecule counting fluorescence immunoassay	synthetic Aβ dimers	buffer	0.18 pM	n/a	overnight + 90 min	20 µL	[70]
Aptamer-based assay using QDs	thrombin	buffer	2.6 nM	5–500 nM	60	10 µL	[91]
Core–shell based aptasensor using dark-field microscopy	thrombin	buffer	2.54 fM	6–100 fM	30	n/a	[113]
Aptamer sandwich sensor with Au Np oligomers	thrombin	buffer	10 fM	20 fM–20 nM	n/a	n/a	[114]
Upconversion cross-correlation spectroscopy	thyroid-stimulating hormone	buffer	15 mIU L^{-1}	28.8–2880 mIU L^{-1}	30	30 µL	[102]
Magnetic bead surface coverage assay	TNF-α	serum	60 aM	n/a	20	5 µL	[134]
Single-molecule microarray	tumor suppressor protein p53	buffer	35 fM	100 fM–100 pM	n/a	0.2 nL	[64]

CRP = c-reactive protein; cTnI = cardiac troponin I; AFP = alpha-fetoprotein; FSH = follicle stimulating hormone; hCG = human chorionic gonadotropin; NF-L = neurofilament light chain; TNF-a = tumor necrosis factor alpha.

Table 3: Digital assays for bacteria, viruses, toxins, and other contaminants. The LODs were converted into molar concentrations wherever applicable.

Assay type	Analyte	Matrix	LOD	Working range	Assay time (min)	Sample volume	Ref.
Multiplexed single-virus immunoassay	avian influenza H9N2, H1N1, H7N9	buffer	0.02 pg mL^{-1}	n/a	60	n/a	[131]
Digital MultiPath immunoassay	*C. difficile* toxin B	8% pooled stool sample diluted in buffer	170 fм	100 fм– 1 nм	30	100 µL	[133]
Single-QD-based aptamer nanosensor	cocaine	buffer	500 nм	500 nм– 10 µм	n/a	n/a	[88]
FCS	fumonisin B$_1$	buffer	1.4 nм	1.4 nм– 35 nм	15	9 µL	[78]
Microfluidic digital HEBA	influenza A nucleo-protein	buffer	4 aм	10 aм– 10 pм	10	10 µL	[54]
Bead-based digital ELISA	hepatitis B surface antigens	buffer	139 aм	100 aм– 1 pм	210	n/a	[29]
Digital microarray with interferometric detection of plasmonic nanorods	hepatitis B surface antigens	buffer	126 fм	100 fм– 100 nм	270	n/a	[128]
Fluorescence coincidence detection	herpes simplex virus	buffer	50 fм	100 fм– 100 pм	180	n/a	[79]
Simoa	HIV p24 capsid	human plasma	117 aм	100 aм– 100 fм	210	100 µL	[41]
Counting assay with color-coded NPs	respiratory syncytial virus	buffer	20–30 fм	100 fм– 100 pм	100	n/a	[87]
Simoa	ricin	buffer	166 aм	100 aм– 100 pм	64	n/a	[44]
Single-molecule aptasensor	adenosine, acetamiprid, PCB-77	chicken extract 100× diluted in buffer	300 fм, 350 fм, 720 fм	500 fм– 50 pм	n/a	n/a	[66]

H. Balci, Y. Ishitsuka, C. Buranachai, T. Ha, *Annu. Rev. Biochem.* **2008**, *77*, 51–76.

[2] a) L. Cohen, D. R. Walt, *Chem. Rev.* **2019**, *119*, 293–321; b) P. Holzmeister, G. P. Acuna, D. Grohmann, P. Tinnefeld, *Chem. Soc. Rev.* **2014**, *43*, 1014–1028; c) L. Chang, D. M. Rissin, D. R. Fournier, T. Piech, P. P. Patel, D. H. Wilson, D. C. Duffy, *J. Immunol. Methods* **2012**, *378*, 102–115; d) J. J. Gooding, K. Gaus, *Angew. Chem. Int. Ed.* **2016**, *55*, 11354–11366; *Angew. Chem.* **2016**, *128*, 11526–11539; e) Y. F. Wu, R. D. Tilley, J. J. Gooding, *J. Am. Chem. Soc.* **2019**, *141*, 1162–1170.

[3] a) R. J. Yu, Y. L. Ying, Y. X. Hu, R. Gao, Y. T. Long, *Anal. Chem.* **2017**, *89*, 8203–8206; b) A. Arima, I. H. Harlisa, T. Yoshida, M. Tsutsui, M. Tanaka, K. Yokota, W. Tonomura, J. Yasuda, M. Taniguchi, T. Washio, M. Okochi, T. Kawai, *J. Am. Chem. Soc.* **2018**, *140*, 16834–16841.

[4] a) U. Wienken, H. E. Gaub, *Biophys. J.* **2013**, *105*, 2687–2694; b) S. Mandal, D. Koirala, S. Selvam, C. Ghimire, H. B. Mao, *Angew. Chem. Int. Ed.* **2015**, *54*, 7607–7611; *Angew. Chem.* **2015**, *127*, 7717–7721.

[5] S. Subramanian, H. Y. Wu, T. Constant, J. Xavier, F. Vollmer, *Adv. Mater.* **2018**, *30*, 1801246.

[6] I. Surugiu, B. Danielsson, L. Ye, K. Mosbach, K. Haupt, *Anal. Chem.* **2001**, *73*, 487–491.

[7] J. Foote, H. N. Eisen, *Proc. Natl. Acad. Sci. USA* **1995**, *92*, 1254–1256.

[8] N. M. Green, *Methods Enzymol.* **1990**, *184*, 51–67.

[9] R. S. Yalow, S. A. Berson, *Nature* **1959**, *184*, 1648–1649.

[10] R. Peltomaa, E. Benito-Pena, M. C. Moreno-Bondi, *Anal. Bioanal. Chem.* **2018**, *410*, 747–771.

[11] A. Kunze, L. Pei, D. Elsasser, R. Niessner, M. Seidel, *J. Virol. Methods* **2015**, *222*, 132–137.

[12] N. L. Anderson, N. G. Anderson, *Mol. Cell. Proteomics* **2002**, *1*, 845–867.

[13] a) S. M. Hanash, S. J. Pitteri, V. M. Faca, *Nature* **2008**, *452*, 571–579; b) N. L. Henry, D. F. Hayes, *Mol. Oncol.* **2012**, *6*, 140–146; c) M. J. Aernecke, J. Guo, S. Sonkusale, D. R. Walt, *Anal. Chem.* **2009**, *81*, 5281–5290; d) D. R. Walt, *J. Clin. Invest.* **2019**, *129*, 3472–3473.

[14] J. F. Rusling, C. V. Kumar, J. S. Gutkind, V. Patel, *Analyst* **2010**, *135*, 2496–2511.

[15] A. St John, C. P. Price, *Clin. Biochem. Rev.* **2014**, *35*, 155–167.

[16] D. J. Litman, T. M. Hanlon, E. F. Ullman, *Anal. Biochem.* **1980**, *106*, 223–229.

[17] L. Hood, *Annu. Rev. Anal. Chem.* **2008**, *1*, 1–43.

[18] H. Siitari, I. Hemmila, E. Soini, T. Lovgren, V. Koistinen, *Nature* **1983**, *301*, 258–260.

[19] M. Rui, C. S. Hampe, C. Wang, Z. D. Ling, F. K. Gorus, A. Lernmark, D. G. Pipeleers, P. E. M. De Pauw, *J. Immunol. Methods* **2007**, *319*, 133–143.

[20] a) Z. Farka, T. Juřík, D. Kovář, L. Trnková, P. Skládal, *Chem. Rev.* **2017**, *117*, 9973–10042; b) M. Pastucha, Z. Farka, K. Lacina, Z. Mikušová, P. Skládal, *Microchim. Acta* **2019**, *186*, 26.

[21] H. H. Gorris, O. S. Wolfbeis, *Angew. Chem. Int. Ed.* **2013**, *52*, 3584–3600; *Angew. Chem.* **2013**, *125*, 3668–3686.

[22] a) Z. Farka, M. J. Mickert, A. Hlaváček, P. Skládal, H. H. Gorris, *Anal. Chem.* **2017**, *89*, 11825–11830; b) M. J. Mickert, Z. Farka, U. Kostiv, A. Hlaváček, D. Horák, P. Skládal, H. H. Gorris, *Anal. Chem.* **2019**, *91*, 9435–9441.

[23] C. Hofmann, A. Duerkop, A. J. Baeumner, *Angew. Chem. Int. Ed.* **2019**, *58*, 12840–12860; *Angew. Chem.* **2019**, *131*, 12970–12992.

[24] a) A. Shalev, A. H. Greenberg, P. J. Mcalpine, *J. Immunol. Methods* **1980**, *38*, 125–139; b) C. C. Harris, R. H. Yolken, H. Krokan, I. C. Hsu, *Proc. Natl. Acad. Sci. USA* **1979**, *76*, 5336–5339.

[25] M. Böhmer, J. Enderlein, *ChemPhysChem* **2003**, *4*, 793–808.

[26] P. Haas, P. Then, A. Wild, W. Grange, S. Zorman, M. Hegner, M. Calame, U. Aebi, J. Flammer, B. Hecht, *Anal. Chem.* **2010**, *82*, 6299–6302.

[27] C. F. Woolley, M. A. Hayes, P. Mahanti, S. D. Gilman, T. Taylor, *Anal. Bioanal. Chem.* **2015**, *407*, 8605–8615.

[28] B. Rotman, *Proc. Natl. Acad. Sci. USA* **1961**, *47*, 1981–1991.

[29] K. Akama, K. Shirai, S. Suzuki, *Anal. Chem.* **2016**, *88*, 7123–7129.

[30] H. H. Gorris, D. R. Walt, *Angew. Chem. Int. Ed.* **2010**, *49*, 3880–3895; *Angew. Chem.* **2010**, *122*, 3970–3986.

[31] a) R. Liebherr, A. Hutterer, M. Mickert, F. Vogl, A. Beutner, A. Lechner, H. Hummel, H. Gorris, *Anal. Bioanal. Chem.* **2015**, *407*, 7443–7452; b) D. M. Rissin, H. H. Gorris, D. R. Walt, *J. Am. Chem. Soc.* **2008**, *130*, 5349–5353.

[32] D. B. Craig, E. A. Arriaga, J. C. Y. Wong, H. Lu, N. J. Dovichi, *J. Am. Chem. Soc.* **1996**, *118*, 5245–5253.

[33] M. Comellas-Aragonès, H. Engelkamp, V. I. Claessen, N. A. J. M. Sommerdijk, A. E. Rowan, P. C. M. Christianen, J. C. Maan, B. J. M. Verduin, J. J. L. M. Cornelissen, R. J. M. Nolte, *Nat. Nanotechnol.* **2007**, *2*, 635–639.

[34] H. M. Piwonski, M. Goomanovsky, D. Bensimon, A. Horovitz, G. Haran, *Proc. Natl. Acad. Sci. USA* **2012**, *109*, E1437–E1443.

[35] H. Gorris, T. Blicharz, D. Walt, *FEBS J.* **2007**, *274*, 5462–5470.

[36] Q. Xue, E. S. Yeung, *Nature* **1995**, *373*, 681–683.

[37] Y. Rondelez, G. Tresset, K. V. Tabata, H. Arata, H. Fujita, S. Takeuchi, H. Noji, *Nat. Biotechnol.* **2005**, *23*, 361–365.

[38] D. M. Rissin, C. W. Kan, T. G. Campbell, S. C. Howes, D. R. Fournier, L. Song, T. Piech, P. P. Patel, L. Chang, A. J. Rivnak, E. P. Ferrell, J. D. Randall, G. K. Provuncher, D. R. Walt, D. C. Duffy, *Nat. Biotechnol.* **2010**, *28*, 595–599.

[39] D. H. Wilson, D. W. Hanlon, G. K. Provuncher, L. Chang, L. N. Song, P. P. Patel, E. P. Ferrell, H. Lepor, A. W. Partin, D. W. Chan, L. J. Sokoll, C. D. Cheli, R. P. Thiel, D. R. Fournier, D. C. Duffy, *Clin. Chem.* **2011**, *57*, 1712–1721.

[40] A. D. Warren, S. T. Gaylord, K. C. Ngan, M. D. Milutinovic, G. A. Kwong, S. N. Bhatia, D. R. Walt, *J. Am. Chem. Soc.* **2014**, *136*, 13709–13714.

[41] L. Chang, L. N. Song, D. R. Fournier, C. W. Kan, P. P. Patel, E. P. Ferrell, B. A. Pink, K. A. Minnehan, D. W. Hanlon, D. C. Duffy, D. H. Wilson, *J. Virol. Methods* **2013**, *188*, 153–160.

[42] P. Shahim, M. Gren, V. Liman, U. Andreasson, N. Norgren, Y. Tegner, N. Mattsson, N. Andreasen, M. Ost, H. Zetterberg, B. Nellgard, K. Blennow, *Sci. Rep.* **2016**, *6*, 36791.

[43] A. Olivera, N. Lejbman, A. Jeromin, L. M. French, H. S. Kim, A. Cashion, V. Mysliwiec, R. Diaz-Arrastia, J. Gill, *JAMA Neurol.* **2015**, *72*, 1109–1116.

[44] S. T. Gaylord, T. L. Dinh, E. R. Goldman, G. P. Anderson, K. C. Ngan, D. R. Walt, *Anal. Chem.* **2015**, *87*, 6570–6577.

[45] S. H. Kim, S. Iwai, S. Araki, S. Sakakihara, R. Iino, H. Noji, *Lab Chip* **2012**, *12*, 4986–4991.

[46] Y. Obayashi, R. Iino, H. Noji, *Analyst* **2015**, *140*, 5065–5073.

[47] X. Wang, L. Cohen, J. Wang, D. R. Walt, *J. Am. Chem. Soc.* **2018**, *140*, 18132–18139.

[48] M. T. Guo, A. Rotem, J. A. Heyman, D. A. Weitz, *Lab Chip* **2012**, *12*, 2146–2155.

[49] H. Song, R. F. Ismagilov, *J. Am. Chem. Soc.* **2003**, *125*, 14613–14619.

[50] J. J. Agresti, E. Antipov, A. R. Abate, K. Ahn, A. C. Rowat, J. C. Baret, M. Marquez, A. M. Klibanov, A. D. Griffiths, D. A. Weitz, *Proc. Natl. Acad. Sci. USA* **2010**, *107*, 4004–4009.

[51] J. U. Shim, R. T. Ranasinghe, C. A. Smith, S. M. Ibrahim, F. Hollfelder, W. T. S. Huck, D. Klenerman, C. Abell, *ACS Nano* **2013**, *7*, 5955–5964.

[52] C. C. Liu, X. N. Xu, B. Li, B. Situ, W. L. Pan, Y. Hu, T. X. An, S. H. Yao, L. Zheng, *Nano Lett.* **2018**, *18*, 4226–4232.

[53] S. B. Tian, Z. Zhang, J. Y. Chen, M. Y. Du, Z. Li, H. Yang, X. H. Ji, Z. K. He, *Talanta* **2018**, *186*, 24–28.

[54] D. Kim, O. B. Garner, A. Ozcan, D. Di Carlo, *ACS Nano* **2016**, *10*, 7467–7475.

[55] D. Schenk, G. Song, Y. Ke, Z. H. Wang, *PLOS One* **2017**, *12*, e0181062.

[56] N. R. Beer, B. J. Hindson, E. K. Wheeler, S. B. Hall, K. A. Rose, I. M. Kennedy, B. W. Colston, *Anal. Chem.* **2007**, *79*, 8471–8475.

[57] F. Shen, B. Sun, J. E. Kreutz, E. K. Davydova, W. B. Du, P. L. Reddy, L. J. Joseph, R. F. Ismagilov, *J. Am. Chem. Soc.* **2011**, *133*, 17705–17712.

[58] W. H. Zhou, *Anal. Methods* **2018**, *10*, 3690–3695.

[59] R. Q. Ke, R. Y. Nong, S. Fredriksson, U. Landegren, M. Nilsson, *Plos One* **2013**, *8*, 5.

[60] B. Oswald, M. Gruber, M. Bohmer, F. Lehman, M. Probst, O. S. Wolfbeis, *Photochem. Photobiol.* **2001**, *74*, 237–245.

[61] F. Löscher, S. Böhme, J. Martin, S. Seeger, *Anal. Chem.* **1998**, *70*, 3202–3205.

[62] A. Jain, R. J. Liu, B. Ramani, E. Arauz, Y. Ishitsuka, K. Ragunathan, J. Park, J. Chen, Y. K. Xiang, T. Ha, *Nature* **2011**, *473*, 484–488.

[63] P. Tinnefeld, *Nature* **2011**, *473*, 461–462.

[64] E. Burgin, A. Salehi-Reyhani, M. Barclay, A. Brown, J. Kaplinsky, M. Novakova, M. A. A. Neil, O. Ces, K. R. Willison, D. R. Klug, *Analyst* **2014**, *139*, 3235–3244.

[65] H. D. Zhang, Y. J. Liu, K. Zhang, J. Ji, J. W. Liu, B. H. Liu, *Anal. Chem.* **2018**, *90*, 9315–9321.

[66] R. Weng, S. T. Lou, L. D. Li, Y. Zhang, J. Qiu, X. Su, Y. Z. Qian, N. G. Walter, *Anal. Chem.* **2019**, *91*, 1424–1431.

[67] Y. F. Ma, M. R. Shortreed, H. L. Li, W. H. Huang, E. S. Yeung, *Electrophoresis* **2001**, *22*, 421–426.

[68] A. H. B. Wu, N. Fukushima, R. Puskas, J. Todd, P. Goix, *Clin. Chem.* **2006**, *52*, 2157–2159.

[69] J. Todd, B. Freese, A. Lu, D. Held, J. Morey, R. Livingston, P. Goix, *Clin. Chem.* **2007**, *53*, 1990–1995.

[70] T. J. Esparza, H. Z. Zhao, J. R. Cirrito, N. J. Cairns, R. J. Bateman, D. M. Holtzman, D. L. Brody, *Ann. Neurol.* **2013**, *73*, 104–119.

[71] E. J. Wild, R. Boggio, D. Langbehn, N. Robertson, S. Haider, J. R. C. Miller, H. Zetterberg, B. R. Leavitt, R. Kuhn, S. J. Tabrizi, D. Macdonald, A. Weiss, *J. Clin. Invest.* **2015**, *125*, 1979–1986.

[72] E. A. Nalefski, C. M. D'Antoni, E. P. Ferrell, J. A. Lloyd, H. Q. Qiu, J. L. Harris, D. H. Whitney, *Clin. Chem.* **2006**, *52*, 2172–2175.

163

[73] S. W. Yim, T. Kim, T. A. Laurence, S. Partono, D. S. Kim, Y. Kim, S. M. Weiss, A. M. Reitmair, *Clin. Chem.* **2012**, *58*, 707–716.

[74] Z. Foldes-Papp, U. Demel, G. P. Tilz, *Proc. Natl. Acad. Sci. USA* **2001**, *98*, 11509–11514.

[75] S. Y. Tetin, K. M. Swift, E. D. Matayoshi, *Anal. Biochem.* **2002**, *307*, 84–91.

[76] M. Chatterjee, B. Noding, E. A. J. Willemse, M. J. A. Koel-Simmelink, W. M. van der Fliere, D. Schild, C. E. Teunissen, *Clin. Biochem.* **2017**, *50*, 1061–1066.

[77] S. T. Hess, S. H. Huang, A. A. Heikal, W. W. Webb, *Biochemistry* **2002**, *41*, 697–705.

[78] Y. N. Bian, X. Y. Huang, J. C. Ren, *Anal. Methods* **2016**, *8*, 1333–1338.

[79] H. T. Li, D. J. Zhou, H. Browne, S. Balasubramanian, D. Klenerman, *Anal. Chem.* **2004**, *76*, 4446–4451.

[80] A. E. Miller, C. W. Hollars, S. M. Lane, T. A. Laurence, *Anal. Chem.* **2009**, *81*, 5614–5622.

[81] a) A. N. Kapanidis, N. K. Lee, T. A. Laurence, S. Doose, E. Margeat, S. Weiss, *Proc. Natl. Acad. Sci. USA* **2004**, *101*, 8936–8941; b) E. Thews, M. Gerken, R. Eckert, J. Zapfel, C. Tietz, J. Wrachtrup, *Biophys. J.* **2005**, *89*, 2069–2076.

[82] M. Seydack, *Biosens. Bioelectron.* **2005**, *20*, 2454–2469.

[83] E. Petryayeva, W. R. Algar, I. L. Medintz, *Appl. Spectrosc.* **2013**, *67*, 215–252.

[84] U. Resch-Genger, M. Grabolle, S. Cavaliere-Jaricot, R. Nitschke, T. Nann, *Nat. Methods* **2008**, *5*, 763–775.

[85] X. J. Liu, C. H. Huang, C. H. Zong, A. Y. Liang, Z. J. Wu, Y. S. Zhang, Q. Q. Zhang, W. F. Zhao, H. W. Gai, *ACS Sens.* **2018**, *3*, 2644–2650.

[86] X. J. Liu, C. H. Huang, X. L. Dong, A. Y. Liang, Y. S. Zhang, Q. Q. Zhang, Q. Wang, H. W. Gai, *Chem. Commun.* **2018**, *54*, 13103–13106.

[87] A. Agrawal, C. Y. Zhang, T. Byassee, R. A. Tripp, S. M. Nie, *Anal. Chem.* **2006**, *78*, 1061–1070.

[88] C. Y. Zhang, L. W. Johnson, *Anal. Chem.* **2009**, *81*, 3051–3055.

[89] S. R. Jung, R. Han, W. Sun, Y. F. Jiang, B. S. Fujimoto, J. B. Yu, C. T. Kuo, Y. Rong, X. H. Zhou, D. T. Chiu, *Anal. Chem.* **2018**, *90*, 6089–6095.

[90] U. Meseth, T. Wohland, R. Rigler, H. Vogel, *Biophys. J.* **1999**, *76*, 1619–1631.

[91] J. J. Yin, A. D. Zhang, C. Q. Dong, J. C. Ren, *Talanta* **2015**, *144*, 13–19.

[92] L. C. Hwang, T. Wohland, *ChemPhysChem* **2004**, *5*, 549–551.

[93] F. Fujii, M. Kinjo, *ChemBioChem* **2007**, *8*, 2199–2203.

[94] T. Kogure, S. Karasawa, T. Araki, K. Saito, M. Kinjo, A. Miyawaki, *Nat. Biotechnol.* **2006**, *24*, 577–581.

[95] J. J. Wang, H. Liu, X. Y. Huang, J. C. Ren, *Microchim. Acta* **2016**, *183*, 749–755.

[96] a) M. Haase, H. Schäfer, *Angew. Chem. Int. Ed.* **2011**, *50*, 5808–5829; *Angew. Chem.* **2011**, *123*, 5928–5950; b) U. Resch-Genger, H. H. Gorris, *Anal. Bioanal. Chem.* **2017**, *409*, 5855–5874; c) H. H. Gorris, U. Resch-Genger, *Anal. Bioanal. Chem.* **2017**, *409*, 5875–5890.

[97] Y. Fan, S. F. Wang, F. Zhang, *Angew. Chem. Int. Ed.* **2019**, *58*, 13208–13219; *Angew. Chem.* **2019**, *131*, 13342–13353.

[98] V. Kale, H. Pakkila, J. Vainio, A. Ahomaa, N. Sirkka, A. Lyytikainen, S. M. Talha, A. Kutsaya, M. Waris, I. Julkunen, T. Soukka, *Anal. Chem.* **2016**, *88*, 4470–4477.

[99] L. Zhou, Y. Fan, R. Wang, X. M. Li, L. L. Fan, F. Zhang, *Angew. Chem. Int. Ed.* **2018**, *57*, 12824–12829; *Angew. Chem.* **2018**, *130*, 13006–13011.

[100] Y. Q. Lu, J. B. Zhao, R. Zhang, Y. J. Liu, D. M. Liu, E. M. Goldys, X. S. Yang, P. Xi, A. Sunna, J. Lu, Y. Shi, R. C. Leif, Y. J. Huo, J. Shen, J. A. Piper, J. P. Robinson, D. Y. Jin, *Nat. Photonics* **2014**, *8*, 33–37.

[101] X. Li, L. Wei, L. L. Pan, Z. Y. Yi, X. Wang, Z. J. Ye, L. H. Xiao, H. W. Li, J. F. Wang, *Anal. Chem.* **2018**, *90*, 4807–4814.

[102] S. Lahtinen, S. Krause, R. Arppe, T. Soukka, T. Vosch, *Chem. Eur. J.* **2018**, *24*, 9229–9233.

[103] W. Becker, in *Springer Ser. Chem. Phys. Bd. 81*, Springer-Verlag, Berlin, Heidelberg, **2005**, S. I-387.

[104] C. Fenzl, T. Hirsch, A. J. Baeumner, *TRAC Trends Anal. Chem.* **2016**, *79*, 306–316.

[105] R. Nooney, A. Clifford, X. LeGuevel, O. Stranik, C. McDonagh, B. D. MacCraith, *Anal. Bioanal. Chem.* **2010**, *396*, 1127–1134.

[106] C. J. Murphy, A. M. Gole, J. W. Stone, P. N. Sisco, A. M. Alkilany, E. C. Goldsmith, S. C. Baxter, *Acc. Chem. Res.* **2008**, *41*, 1721–1730.

[107] C. Y. Poon, L. Wei, Y. L. Xu, B. Chen, L. H. Xiao, H. W. Li, *Anal. Chem.* **2016**, *88*, 8849–8856.

[108] X. Wu, T. Li, G. Y. Tao, R. Y. Lin, X. J. Pei, F. Liu, N. Li, *Analyst* **2017**, *142*, 4201–4205.

[109] L. Zhu, G. H. Li, S. Q. Sun, H. Tan, Y. H. He, *RSC Adv.* **2017**, *7*, 27595–27602.

[110] M. Sriram, B. P. Markhali, P. R. Nicovich, D. T. Bennett, P. J. Reece, D. B. Hibbert, R. D. Tilley, K. Gaus, S. R. C. Vivekchand, J. J. Gooding, *Biosens. Bioelectron.* **2018**, *117*, 530–536.

[111] E. Lüthgens, A. Janshoff, *ChemPhysChem* **2005**, *6*, 444–448.

[112] S. S. Aćimović, H. Šípová-Jungová, G. Emilsson, L. Shao, A. B. Dahlin, M. Käll, T. J. Antosiewicz, *ACS Nano* **2018**, *12*, 9958–9965.

[113] R. Yang, S. W. Liu, Z. J. Wu, Y. Tan, S. Q. Sun, *Talanta* **2018**, *182*, 348–353.

[114] J. J. Li, Y. F. Jiao, Q. Y. Liu, Z. B. Chen, *Anal. Chim. Acta* **2018**, *1028*, 66–76.

[115] S. Chen, M. Svedendahl, R. P. Van Duyne, M. Kall, *Nano Lett.* **2011**, *11*, 1826–1830.

[116] X. Liu, Q. Dai, L. Austin, J. Coutts, G. Knowles, J. H. Zou, H. Chen, Q. Huo, *J. Am. Chem. Soc.* **2008**, *130*, 2780–2782.

[117] T. Lan, C. A. Dong, X. Y. Huang, J. C. Ren, *Analyst* **2011**, *136*, 4247–4253.

[118] T. Lan, C. Q. Dong, X. Y. Huang, J. C. Ren, *Talanta* **2013**, *116*, 501–507.

[119] J. J. Wang, X. Y. Huang, H. Liu, C. Q. Dong, J. C. Ren, *Anal. Chem.* **2017**, *89*, 5230–5237.

[120] B. Rothenhäusler, W. Knoll, *Nature* **1988**, *332*, 615–617.

[121] I. Sidorenko, S. Nizamov, R. Hergenroder, A. Zybin, A. Kuzmichev, B. Kiwull, R. Niessner, V. M. Mirsky, *Microchim. Acta* **2016**, *183*, 101–109.

[122] B. Huang, F. Yu, R. N. Zare, *Anal. Chem.* **2007**, *79*, 2979–2983.

[123] A. Zybin, Y. A. Kuritsyn, E. L. Gurevich, V. V. Temchura, K. Uberla, K. Niemax, *Plasmonics* **2010**, *5*, 31–35.

[124] J. Homola, *Chem. Rev.* **2008**, *108*, 462–493.

[125] S. Nizamov, V. Scherbahn, V. M. Mirsky, *Anal. Chem.* **2016**, *88*, 10206–10214.

[126] S. Nizamov, O. Kasian, V. M. Mirsky, *Angew. Chem. Int. Ed.* **2016**, *55*, 7247–7251; *Angew. Chem.* **2016**, *128*, 7363–7367.

[127] A. R. Halpern, J. B. Wood, Y. Wang, R. M. Corn, *ACS Nano* **2014**, *8*, 1022–1030.

[128] D. Sevenler, G. G. Daaboul, F. E. Kanik, N. L. Unlu, M. S. Unlu, *ACS Nano* **2018**, *12*, 5880–5887.

[129] A. Belushkin, F. Yesilkoy, H. Altug, *ACS Nano* **2018**, *12*, 4453–4461.

[130] H. Härmä, T. Soukka, T. Lövgren, *Clin. Chem.* **2001**, *47*, 561–568.

[131] Z. Wu, T. Zeng, W. J. Guo, Y. Y. Bai, D. W. Pang, Z. L. Zhang, *ACS Appl. Mater. Interfaces* **2019**, *11*, 5762–5770.

[132] F. Zhang, Q. H. Shi, Y. C. Zhang, Y. F. Shi, K. L. Ding, D. Y. Zhao, G. D. Stucky, *Adv. Mater.* **2011**, *23*, 3775–3779.

164

[133] S. Gite, D. Archambault, M. P. Cappillino, D. Cunha, V. Dorich, T. Shatova, A. Tempesta, B. Walsh, J. A. Walsh, A. Williams, J. E. Kirby, J. Bowers, D. Straus, *Sci. Rep.* **2018**, *8*, 8.

[134] H. C. Tekin, M. Cornaglia, M. A. M. Gijs, *Lab Chip* **2013**, *13*, 1053–1059.

[135] D. A. Schafer, J. Gelles, M. P. Sheetz, R. Landick, *Nature* **1991**, *352*, 444–448.

[136] E. W. A. Visser, J. H. Yan, L. J. van Ijzendoorn, M. W. J. Prins, *Nat. Commun.* **2018**, *9*, 2541.

[137] J. Silver, Z. Y. Li, K. Neuman, *Biosens. Bioelectron.* **2015**, *63*, 117–123.

[138] K. Akama, N. Iwanaga, K. Yamawaki, M. Okuda, K. Jain, H. Ueno, N. Soga, Y. Minagawa, H. Noji, *ACS Nano* **2019**, *13*, 13116–13126.

[139] A. B. Taylor, P. Zijlstra, *ACS Sens.* **2017**, *2*, 1103–1122.

[140] B. Sepúlveda, P. C. Angelomé, L. M. Lechuga, L. M. Liz-Marzán, *Nano Today* **2009**, *4*, 244–251.

[141] N. J. Halas, S. Lal, W. S. Chang, S. Link, P. Nordlander, *Chem. Rev.* **2011**, *111*, 3913–3961.

[142] M. A. Beuwer, B. van Hoof, P. Zijlstra, *J. Phys. Chem. C* **2018**, *122*, 4615–4621.

[143] M. Garai, T. S. Zhang, N. Y. Gao, H. Zhu, Q. H. Xu, *J. Phys. Chem. C* **2016**, *120*, 11621–11630.

[144] A. Kinkhabwala, Z. F. Yu, S. H. Fan, Y. Avlasevich, K. Mullen, W. E. Moerner, *Nat. Photonics* **2009**, *3*, 654–657.

[145] P. Zijlstra, P. M. R. Paulo, K. Yu, Q. H. Xu, M. Orrit, *Angew. Chem. Int. Ed.* **2012**, *51*, 8352–8355; *Angew. Chem.* **2012**, *124*, 8477–8480.

[146] S. E. Lee, Q. Chen, R. Bhat, S. Petkiewicz, J. M. Smith, V. E. Ferry, A. L. Correia, A. P. Alivisatos, M. J. Bissell, *Nano Lett.* **2015**, *15*, 4564–4570.

[147] M. A. Beuwer, M. W. J. Prins, P. Zijlstra, *Nano Lett.* **2015**, *15*, 3507–3511.

[148] A. L. Washburn, M. S. Luchansky, A. L. Bowman, R. C. Bailey, *Anal. Chem.* **2010**, *82*, 69–72.

[149] M. D. Baaske, F. Vollmer, *Nat. Photonics* **2016**, *10*, 733–739.

[150] M. F. S. Ferreira, E. Castro-Camus, D. J. Ottaway, J. M. Lopez-Higuera, X. Feng, W. Jin, Y. Jeong, N. Picque, L. M. Tong, B. M. Reinhard, P. M. Pellegrino, A. Mendez, M. Diem, F. Vollmer, Q. M. Quan, *J. Optics* **2017**, *19*, 083001.

[151] A. B. Zrimsek, N. H. Chiang, M. Mattei, S. Zaleski, M. O. McAnally, C. T. Chapman, A. I. Henry, G. C. Schatz, R. P. Van Duyne, *Chem. Rev.* **2017**, *117*, 7583–7613.

[152] Single Molecule Counting (SMC) Erenna Instrument, Software and Kits http://www.merckmillipore.com/CZ/cs/life-science-research/protein-detection-quantification/Immunoassay-Platform-Solutions/single-molecule-counting-immunoassay-technology/SMC-Erenna-Instrument-Software-and-Kits/VS.b.qB.N.UAAAFfn7lc20.J,nav.

[153] Simoa assay kits https://www.quanterix.com/products-technology/simoa-assay-kits.

[154] L. Smith, M. Kohli, A. M. Smith, *J. Am. Chem. Soc.* **2018**, *140*, 13904–13912.

[155] D. Yeung, S. Ciotti, S. Purushothama, E. Gharakhani, G. Kuesters, B. Schlain, C. Shen, D. Donaldson, A. Mikulskis, *J. Immunol. Methods* **2016**, *437*, 53–63.

[156] O. R. Costa, K. Verhaeghen, S. Roels, G. Starige, Z. D. Ling, D. Pipeleers, F. K. Gorus, G. A. Martens, *PLOS One* **2018**, *13*, e0193670.

Paper III

Rapid immunosensing of *Salmonella* Typhimurium using electrochemical impedance spectroscopy: the effect of sample treatment

Farka, Z.; Juřík, T.; Pastucha, M.; Kovář, D.; Lacina, K.; Skládal, P.

(Z.F. and T.J. contributed equally)

Contribution:

Design of experiments, development and optimization of EIS immunosensor, characterization of sensing surface by AFM, data evaluation, manuscript writing

Full Paper

Rapid Immunosensing of *Salmonella* Typhimurium Using Electrochemical Impedance Spectroscopy: the Effect of Sample Treatment

Zdeněk Farka,[a] Tomáš Juřík,[a] Matěj Pastucha,[a] David Kovář,[a] Karel Lacina,[a] and Petr Skládal*[a, b]

Abstract: A label-free immunosensor for rapid detection of *Salmonella* Typhimurium based on electrochemical impedance spectroscopy was developed. Specific antibody was immobilized to a screen-printed electrode via cysteamine monolayer activated with glutaraldehyde and the impedance was measured between two gold electrodes. Different procedures for sample treatment (combinations of heat and sonication) were tested and their impact on the assay performance was compared. Atomic force microscopy was used to study the effect of the treatment on the cell shape and to confirm the specific binding of *Salmonella* to the sensing surface. The immunosensor allowed detection of 1×10^3 CFU·mL^{-1} in 20 min with negligible interference from other bacteria. Wide linear response was obtained in the range between 10^3 CFU·mL^{-1} and 10^8 CFU·mL^{-1}. The successful detection of *Salmonella* in spiked milk demonstrates the suitability of sensor for the analysis of real samples.

Keywords: Atomic force microscopy · Biosensor · Immunosensor · Label-free detection · Salmonella Typhimurium

1 Introduction

Rapid detection of low levels of bacterial cells integrated into a portable device remains challenging for point-of-care clinical diagnosis, food testing and environmental screening. Screen-printed electrodes (SPE) represent a powerful tool for the development of miniaturized chips for the in-field detection [1]. This approach allows mass production of disposable and low-cost immunosensors suitable for a fast analysis of various pathogenic bacteria in very low sample volumes. Our research was focused on *Salmonella enterica* serovar Typhimurium, a non-typhoidal strain, which is one of the leading agents of gastrointestinal diseases. *Salmonella* is a gram-negative bacterium causing diarrhea, fever and abdominal spasm within 12 to 72 hours after infection. In the worst case, *Salmonella* may intervene into the blood stream, bones, brain and nervous system and occasionally result in lethal infections [2]. Humans become infected particularly by consumption of the contaminated food [3]. The bacteria are present mostly in raw food products from animals, such as meat, eggs and unpasteurized dairy products. It was estimated that 94 million cases of gastroenteritis with 155,000 deaths attributed to *Salmonella* occur globally each year [4]. The Centers for Disease Control and Prevention (CDC) published the approximation of 1.2 million illnesses and 450 deaths per year in the United States initiated by non-typhoidal *Salmonella* [4]. These statistics make *Salmonella* a considerable threat for human health. Furthermore, the United States Department of Agriculture (USDA) calculated the crude annual costs associated with food-borne diseases caused by *Salmonella* to be $3.3 million [5]. The analytical device capable of fast and sensitive detection of *Salmonella* is hence of a great importance.

Conventional methods for the detection of *Salmonella* comprise the cell culturing and colony counting, immunoassay techniques and polymerase chain reaction (PCR). The culture based methods became the gold standard for *Salmonella* detection due to the high sensitivity and selectivity. The long-term analysis of 5–7 days including labor-intensive procedures makes it rather disadvantageous [6]. Enzyme-linked immunosorbent assay (ELISA) represents another sensitive method providing results in approximately 24 h [7]. Generally, the time-consuming pre-enrichment step to increase the population of target organism is compulsory [8]. The speed of analysis and sensitivity has been improved by the PCR incorporating amplification of a specific short DNA sequence. However, the complex processes including cell extraction, nucleic acid purification and amplification with subsequent detection makes PCR complicated approach requiring expensive instrumentation and trained personnel [9]. Moreover, the application of all above mentioned techniques is typically limited only to the laboratory environment. The detailed

[a] Z. Farka,[†] T. Juřík,[†] M. Pastucha, D. Kovář, K. Lacina, P. Skládal
CEITEC MU, Masaryk University, Kamenice 5, 625 00 Brno, Czech Republic
*e-mail: skladal@chemi.muni.cz

[b] P. Skládal
Department of Biochemistry, Faculty of Science, Masaryk University
Kotlářská 2, 611 37 Brno, Czech Republic

[†] These authors contributed equally

Supporting information for this article is available on the WWW under http://dx.doi.org/10.1002/elan.201600093.

overview of commonly used methods and commercially available systems for the detection of *Salmonella* was summarized by Odumeru and León-Velarde [10].

Besides the traditional methods, biosensor technologies have been extensively developed as an alternative for rapid and sensitive detection, robustness, ease of operation and potential in-field application. Quartz crystal microbalance (QCM) [11] and surface plasmon resonance (SPR) [12],[13] biosensors appeared to be promising tools regarding the sensitive determination of *Salmonella* reaching the limit of detection down to 102 CFU·mL^{-1}. Nevertheless, these systems usually require sandwich arrangements accompanied by additional enhancers [14]. Recently, electrochemical biosensors have emerged as a powerful instrument overcoming the discussed limitations [15–17].

Electrochemical impedance spectroscopy (EIS) represents an efficient method capable of detecting small changes occurring on the electrode-solution interface. EIS combines a rapid response with very high sensitivity and enables real-time detection [18]. Moreover, signal generation can be readily interfaced with a portable instrumentation. The EIS based biosensors for the bacterial detection are generally based on the immobilization of antibodies on the electrode leading to a specific binding of the target cells. Thus, the label-free operation may be attained, which brings important benefits as simplicity and robustness.

Current research is also focused on EIS biosensors using labels and signal enhancers to increase the sensitivity. Gold nanoparticles (AuNPs) belong probably to the most convenient labels enabling the signal amplification either through the enlargement of electroactive surface area [19] or due to their electrocatalytic activity [20]. AuNPs also possess biocompatibility and allow for additional modification by other biomolecules (enzymes [21], antibodies [22], DNA [23]) or nanoparticles (magnetic beads [24],[25], quantum dots [26]). A simple screen-printed immunosensor for the detection of *Salmonella* was developed by Fei et al. The AuNPs improved the immobilization of antibodies, while conjugate of the secondary antibody and horseradish peroxidase generated the signal [27]. Magnetic nanoparticles (MNPs) conjugated with antibodies represent another approach allowing the immunomagnetic preconcentration, separation and clean-up of the target bacteria [28]. Application of MNPs also helped to overcome the time-consuming immobilization process; Xu et al. [29] developed a system based on the immunomagnetic separation of *Salmonella* cells with simultaneous labeling by antibody-glucose oxidase.

Despite all the advantages of labels and nanoparticles, the laborious and time-consuming preparation of conjugates and high cost of antibodies and enzymes must be taken into consideration regarding the potential applications in point-of-care diagnostics.

In this work, we focused on the development of a simple, easy to fabricate and low-cost immunosensor for *Salmonella* Typhimurium. The self-assembled monolayer (SAM) created on the SPE provided a thin, well-ordered and reproducible layer for immobilization of antibody. The EIS was used for the monitoring of impedance changes after the specific binding of bacteria. Various methods of the cell treatment were applied and the efficiency of binding on the sensor was investigated. Atomic force microscopy (AFM) provided further perspective on the bacteria shape and verified the binding.

2 Experimental

2.1 Chemicals and Reagents

Cysteamine, glutaraldehyde and bovine serum albumin (BSA) were obtained from Sigma-Aldrich (USA). Phosphate buffered saline pH 7.4 (PBS) consisted of 50 mM sodium hydrogen phosphate/sodium dihydrogen phosphate and 150 mM sodium chloride (PENTA, Czech Rep.). The sensor surface was blocked by BSA in PBS containing 0.01 % Tween 20 (Fluka, Germany). All solutions were filtered through 0.22 μm PTFE membrane (Merck Millipore, USA).

The solution for electrochemical measurements consisted of 2.5 mM potassium ferrocyanide and 2.5 mM potassium ferricyanide (Lachema, Czech Rep.) in 0.1 M KCl. The solution was stored at 4 °C and purged by argon gas before measurement.

2.2 Microorganisms and Antibodies

Salmonella enterica subsp. *enterica* serovar Typhimurium (strain ATCC 14028) and *E. coli* K-12 (for cross-reactivity testing) were obtained from Czech Collection of Microorganisms (CCM). All work with *Salmonella* was carried out in Biosafety Level 2 laboratory. For the cultivation, 100 μL of the stock solution was inoculated into 25 mL of low salt LB broth (Duchefa Biochemie, Netherlands) in Erlenmeyer flask and incubated overnight at 37 °C. The obtained bacterial suspension was centrifuged two times for 10 min at 6800 g and resuspended in PBS.

The microbe concentrations were determined by measurement of optical density at 600 nm with calibration using the McFarland scale. The bacteria samples were optionally heat-treated at 80 °C for 40 min with mild shaking on Thermomixer Comfort (Eppendorf, Germany). Selected samples were also homogenized using sonicator Q700 (Qsonica, USA) with 1.6 mm Microtip probe. The microtube containing 1 mL of sample was cooled in ice bath. Amplitude of 70 % was maintained for approximately 10 min to reach the total energy of 1000 J consumed by the sample. The concentrations of thus treated bacteria (most probably killed) are expressed as CFU·mL^{-1} corresponding to the native cells before treatment [30].

Monoclonal anti-*Salmonella* antibody ab8274 specific against the lipopolysaccharides (LPS) of *S.* Typhimurium was obtained from Abcam (UK).

168

2.2 Preparation of Biosensing Layer

The electrochemical measurements were performed using a gold 2-channel screen-printed electrode (SPE) AC2.W1.RS (BVT Technologies, Czech Rep.). The silver reference electrode included in the layout of SPE was not used. Prior to the immobilization, the electrodes were cleaned in acetone for 20 min. In each step, the 1 µL drop of reagents for immobilization was placed on both electrodes. After each incubation step, the electrodes were thoroughly washed with deionized water.

In the first step, a self-assembled monolayer of cysteamine (20 mg·mL^{-1} in water) was allowed to form during 2 h followed by binding of glutaraldehyde (3 % in PBS) for 1 hour at room temperature. Then, the sensor was incubated with antibody (100 µg·mL^{-1} in PBS) overnight at 4 °C [31,32]. Blocking was done by BSA (20 mg·mL^{-1} in PBS with 0.01 % Tween 20) for 30 min. The further blocking by milk (30 min) was employed for analysis of real samples. The prepared electrodes (Au-cys-GA-Ab/BSA) were stored in dry conditions at 4 °C. The blank electrodes (Au-cys-GA-BSA) were prepared by the same procedure excluding the antibody step. The immobilization procedure is shown in Fig. 1.

2.3 Electrochemical Immunoassay

The electrochemical impedance spectroscopy experiments were carried out with PGSTAT302N (Autolab, Netherlands) in the two-electrode setup. The analyzed frequency range was from 0.1 Hz to 100 kHz with amplitude of 5 mV.

For the binding of bacteria, the electrode was placed inside a microtube containing 1 mL of *Salmonella* sample in PBS or the spiked milk. The incubation was done

under mild shaking for 15 min at room temperature. The sensor was then thoroughly washed with PBS followed by water, placed inside the measuring solution and EIS spectra were acquired.

The results were evaluated in Nova software (Autolab, Netherlands) using the Randles equivalent circuit [33]. It consists of the solution resistance (R_S), double layer capacitance at the electrode surface (C_{DL}), charge transfer resistance (R_{CT}) and Warburg impedance (Z_W). The data were plotted in Nyquist diagrams representing the real (Z') and imaginary (Z'') parts of impedance. Warburg impedance is generally observed in the diffusion-controlled low frequency region, whereas the charge transfer resistance occurs in the kinetically controlled high frequency region [34]. The attachment of bacteria to the electrode surface results in the increase of R_{CT} which appears as a larger semicircle in the plot. The relative change of charge transfer resistance ΔR_{CT} (%) was calculated as:

$$\Delta R_{CT} = (R_{CT(\text{with microbe})} - R_{CT(\text{blank})})/R_{CT(\text{blank})} \cdot 100\%$$

The limit of detection (LOD) was evaluated from the calibration curve as a concentration for which the signal was higher than three times the standard deviation of blank measurements.

The glass slides (Menzel Gläser, Germany) and sensors with captured bacteria were visualized by atomic force microscopy (AFM). Dimension FastScan Bio (Bruker, USA) with FastScan-A probe in the tapping mode was used. The data was processed by NanoScope Analysis (Bruker, USA) and Gwyddion (Czech Metrology Institute, Czech Rep.) software.

3 Results and Discussion

3.1 AFM Study of *Salmonella* Treated under Different Conditions

The sample treatment procedures were initially evaluated in order to obtain optimal binding of bacteria to the specific antibody. Due to rather complex topography of SPE sensors and the expected changes of *Salmonella* during heat-treatment and sonication, the microbes were first visualized on glass after non-specific adsorption. The collected cells were centrifuged at 6800 g, resuspended in water, treated under different conditions and diluted to the concentration of 10^8 CFU·mL^{-1}. A droplet of 2 µL was placed on a cover slip, left to dry and the surface was imaged with AFM. Both *height* and *error* signals were evaluated. The resulting scans are shown in Fig. S1 in the Supporting Information. The cover slip has proven to be sufficiently flat for the visualization of bacteria (Fig. S1A). Compared to the native *Salmonella* (Fig. S1B), the heat-treated sample (Fig. S1C) consisted of entire cells surrounded by small particles, probably cell debris and material released from the disrupted cells. Additionally, the combination of heat-treatment and sonication resulted in more fragmented cells represented by
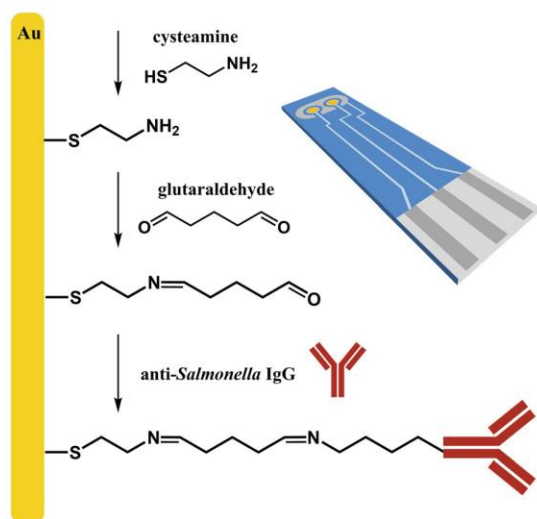
Fig. 1. Scheme of antibody immobilization (blocking by BSA not shown); design of the SPE electrode (right).

169

small particles of various size (Fig. S1D). In parallel, the treated samples were tested for binding on the immunosensors.

3.2 Preparation of Biosensing Layer

The process of immobilization was monitored by EIS. The electrode was washed with water after each immobilization step and impedance spectra were measured in ferro/ferricyanide (Fig. S2). Formation of electrically inactive layer on gold surface generally leads to the isolation of surface and thus increased values of R_{CT}. However, after binding of cysteamine, a decrease of R_{CT} was observed due to the interaction between positively charged amine groups of cysteamine and the negatively charged redox probe [35]. The following immobilization steps led to gradual increases of R_{CT}, as expected. The covalent binding of proteins (either antibody or BSA) caused higher signal changes than smaller glutaraldehyde molecule. The absolute impedance values varied among individual SPE sensors, therefore the further data evaluation

was based on the calculated ΔR_{CT}, with significantly more reliable results.

3.3 Detection of Whole *Salmonella* Cells

To determine the optimal way of sample preparation, the specificity of antibody was tested with bacteria treated under different conditions (viable, heat-treated, sonicated, heat-treated and sonicated, part 3.1).

The results from EIS indicated that the utilized antibody did not provide sufficient affinity to native *Salmonella* cells. Only small signal changes were observed in case of untreated *Salmonella*. According to the manufacturer's information, the antibody is specific against LPS of *S.* Typhimurium. In the previous reports, the antibody was used for labeling of *Salmonella* in specimens of fixed and permeabilized eukaryotic cells (where the damage of *Salmonella* can be expected) [36, 37].

After the treatment of *Salmonella* by heat (80 °C, 40 min) the affinity of microbe to the antibody significantly increased. The EIS spectra for the detection of heat-treated cells are depicted in Fig. 2A. The LOD of
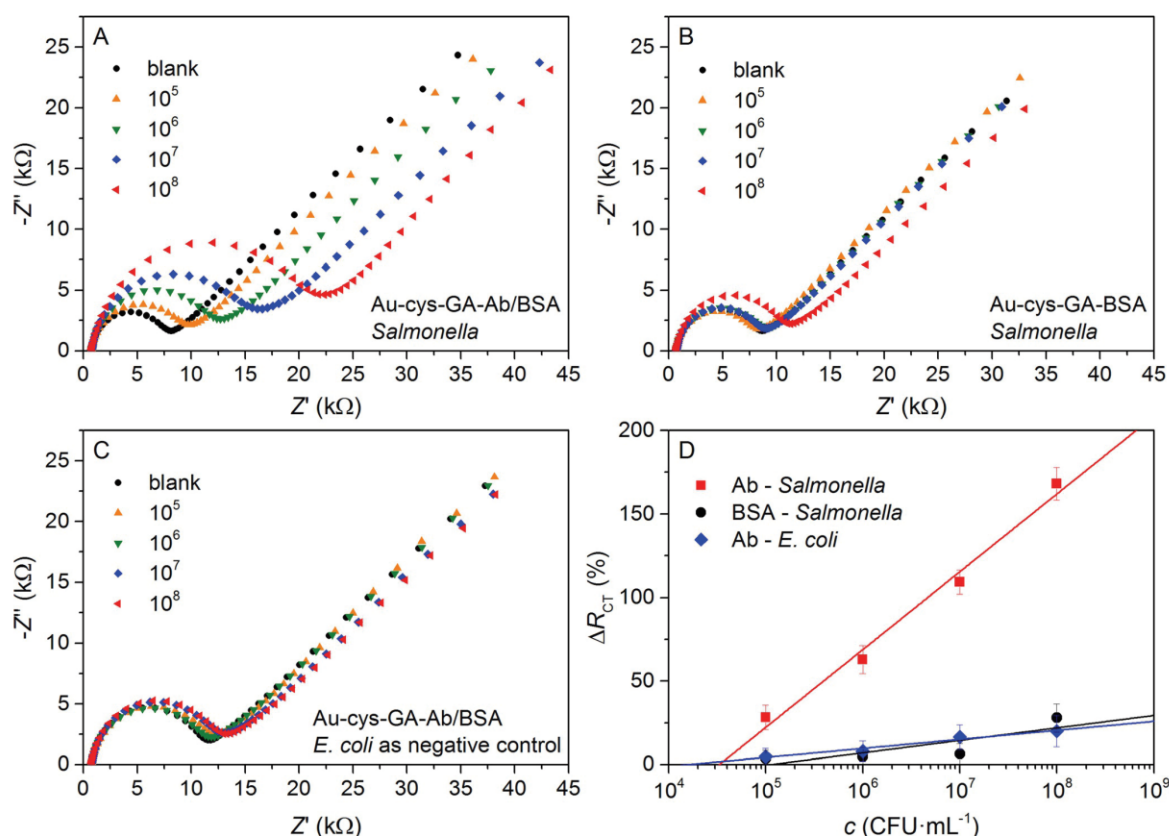
Fig. 2. EIS response of immunosensor to heat-treated bacterial cells (concentrations in CFU·mL^{-1}). A) Specific binding of *Salmonella* to sensor with Ab; B) negative control – interaction of *Salmonella* with sensor not modified by Ab; C) cross reactivity – interaction of *E. coli* with anti-*Salmonella* Ab; D) calibration curves.

7×10^4 CFU·mL^{-1} and wide linear range up to 10^8 CFU·mL^{-1} was achieved. The heat-treatment does not pose a major technical complication for the potential analysis of real samples. Furthermore, the manipulation with killed or weakened bacteria can be even advantageous because of the reduced pathogenicity.

To assess the extent of non-specific binding, the blank sensor with no immobilized antibody was prepared and the same samples were tested (Fig. 2B). Only negligible levels of binding were registered except for the high concentration of 10^8 CFU·mL^{-1}.

Different blocking procedures were also examined. The sensor surface blocked with BSA in PBS without Tween 20 exhibited slightly higher non-specific binding. The blocking with 1 M ethanolamine was tested as well. However, the sensor prepared in such way was more prone to non-specific binding than sensor blocked with BSA. Significant increase of impedance was observed after the blocking of surface by milk. However, the binding ability was not deteriorated by this approach.

For the cross reactivity tests, the anti-*Salmonella* antibody-modified sensor was incubated with corresponding concentrations of heat-treated *E. coli* K-12 (Fig. 2C). The impedance signals increased negligibly, confirming low interactions with *E. coli* and high selectivity of the antibody. Both *Salmonella* and *E. coli* are gram-negative, therefore very low cross-reactivity can be expected also for other more phylogenetically distant bacteria [38]. The calibration curve for the detection of heat-treated cells and negative controls are shown in Fig. 2D. The error bars represent standard deviations.

An alternative method of sensor incubation with sample was based on the deposition of a small droplet (10 µL) on the gold electrodes. The mixing of solution was limited and the absolute amount of bacteria present in the sample was lower compared to the incubation in microtube. Consequently, smaller signal changes were observed and this approach was not further employed. However, such procedure can be advantageous for the analysis of *Salmonella* in very small sample volumes.

The sensors incubated with *Salmonella* were visualized using AFM to confirm the presence of bacterial cells. The SPE electrodes exhibited very high roughness with height differences in some areas over 3 µm. The *error* signal has shown to be advantageous for finding of bacteria on the complex surface compared to the *height* signal, where small cells were easily overlooked (Fig. S3). Specifically bound *Salmonella* was present on the sensor with antibody (Fig. 3) while no captured cells were detected in the case of blank electrodes without antibody. Small particles that might correspond to the material released from disrupted cells (as shown on glass substrate in Fig. S1) were also found (Fig. S3).

3.4 Detection of Sonicated *Salmonella* Cells

To further improve sensitivity, sonication of the heat-treated and native *Salmonella* was tested. According to
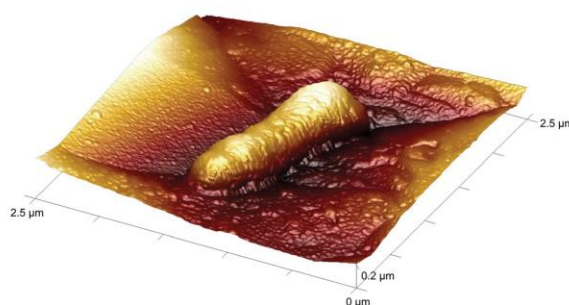
Fig. 3. AFM image of the SPE sensor with immobilized antibody and specifically bound heat-treated *Salmonella*.

the previous study, the treatment of cells can influence the interaction between antibody and microbe [39]. In case of the heat-treated and sonicated sample, the antibody has shown considerably higher affinity compared to the whole cells (Fig. 4A). The evaluated LOD was 1×10^3 CFU·mL^{-1} with linear range up to 10^8 CFU·mL^{-1}. The calibration curve is shown in Fig. 5, the comparison of assay parameters with other sensors published in the literature is shown in Table 1. The signals obtained with blank sensor (without immobilized antibody) were also slightly higher than in the case of whole cells (Fig. 4C).

Nevertheless, the specific binding of *Salmonella* in concentration of 10^4 CFU·mL^{-1} provided higher signal than non-specific interaction of microbe in concentration of 10^8 CFU·mL^{-1}. This proves that the possible interferences were not significant. The fact that smaller cell fragments can bind better than whole cells is in a good agreement with the declared specificity of antibody against
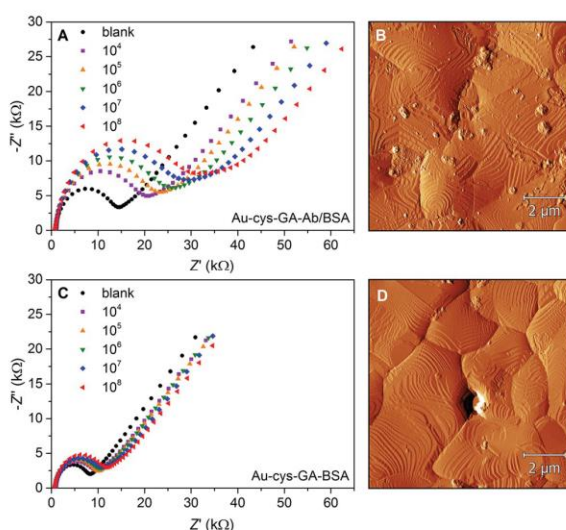
Fig. 4. A) EIS response of SPE sensor to different concentrations of heat-treated and sonicated *Salmonella*; B) AFM scan of electrode after binding (*error* signal); C) negative control (no antibody on the surface); D) AFM scan of the blank electrode.

171

Table 1. Comparison of EIS biosensors for the detection of *Salmonella*

Electrode	LOD (CFU·mL^{-1})	Lin. range (CFU·mL^{-1})	Time (min)	Ref.
Interdigitated SPE*,†	3.4×10^2	10^2–10^6	105	[29]
NP modified GCE	5×10^2	10^3–10^7	60	[41]
Interdigitated MEA*	1×10^3	10^3–10^7	30	[42]
Macroporous silicon	1×10^3	10^3–10^6	30	[43]
SPE	1×10^3	10^3–10^8	20	This work

* pre-enrichment by magnetic nanoparticles; † label required
NP – nanoparticle; GCE – glassy carbon electrode; MEA – microelectrode array
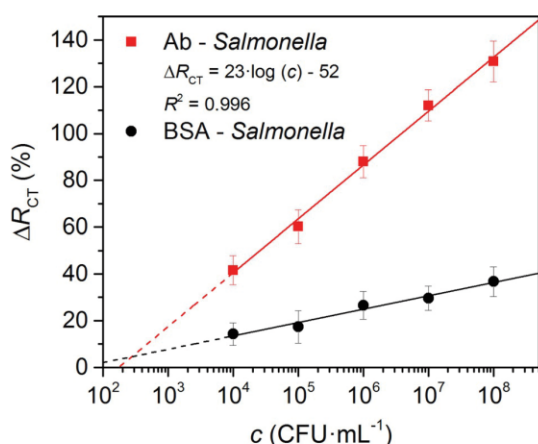
Fig. 5. Calibration curve for the EIS detection of heat-treated and sonicated *Salmonella*.

LPS of *Salmonella*. In case of homogenized cells, better availability of antigenic determinants can be expected.

The AFM was used to confirm the presence of bacteria on the sensor surface. After the EIS measurement of heat-treated and sonicated *Salmonella* (10^8 CFU·mL^{-1}), the sensor was washed with deionized water and scanned in dry state (Fig. 4B,D). The antibody-modified sensor captured high amount of cell fragments with the size and structure clearly corresponding to the heat-treated and sonicated *Salmonella* as imaged on glass (Fig. S1D).

The blank electrode contained insignificant amount of captured cells. This result is in correlation with the data obtained from EIS. The non-specific binding was more significant than in the case of whole cells, but still much lower than specific interaction with antibody.

The real samples of milk were spiked by heat-treated and sonicated bacteria and analyzed on electrodes blocked by milk (Fig. S4). Thorough washing of sensors after incubation in real-samples was crucial, insufficient washing resulted in gradual non-specific increases of impedance. The binding ability of thus prepared electrodes slightly decreased due to higher surface coverage, resulting in the LOD of 9×10^3 CFU·mL^{-1} and linear range up to 10^7 CFU·mL^{-1}.

The analysis of sonicated (without heat-treatment) *Salmonella* provided similar results as in case of heat-treated

and sonicated sample (Fig. S5). A lower LOD of 6×10^2 CFU·mL^{-1} was achieved, but slight increase of non-specific interactions was also observed. A comparison of assay parameters for all tested cell treatment methods is shown in Table S1.

For the analysis of real samples, the pretreatment by sonication (and heat) is not a major technical complication. Despite the additional requirements on the instrumentation, the sonication can be advantageous, because it is less time-consuming than the treatment by heat. Sample preparation by heat-treatment only is still sufficient with the LOD comparable to infection dose of *Salmonella* [40] and smaller requirements for the equipment.

4 Conclusions

Label-free immunosensor based on electrochemical impedance spectroscopy was developed for rapid and sensitive detection of *S.* Typhimurium. The specific antibody was immobilized via cysteamine and glutaraldehyde to the SPE and impedance spectra were measured between two gold electrodes. Microbial cells were treated by heat and sonication and the effect of treatment was studied using AFM and EIS. The optimal results were achieved with the heat-treated and sonicated *Salmonella*, which provided LOD of 1×10^3 CFU·mL^{-1} and wide linear range up to 10^8 CFU·mL^{-1}. The specificity and cross-reactivity tests confirmed high selectivity of the assay. The total time of analysis (including incubation of sensor with sample) was 20 min. The binding of *Salmonella* to the sensor was also confirmed by AFM. Samples of milk spiked by *Salmonella* were successfully analyzed; this demonstrates the suitability of the developed methods for the detection of bacteria in real samples.

References

[1] M. Badihi-Mossberg, V. Buchner, J. Rishpon, *Electroanalysis* **2007**, *19*, 2015–2028.
[2] R. L. Scharff, *J. Food Prot.* **2012**, *75*, 123–131.

172

[3] T. S. Desin, W. Koster, A. A. Potter, *Expert Rev. Vaccines* **2013**, *12*, 87–96.

[4] S. E. Majowicz, J. Musto, E. Scallan, F. J. Angulo, M. Kirk, S. J. O'Brien, T. F. Jones, A. Fazil, R. M. Hoekstra, *B. Int Collaboration Enteric Dis, Clin. Infect. Dis.* **2010**, *50*, 882–889.

[5] S. Hoffmann, M. B. Batz, J. G. Morris, *J. Food Prot.* **2012**, *75*, 1292–1302.

[6] E. C. Alocilja, S. M. Radke, *Biosens. Bioelectron.* **2003**, *18*, 841–846.

[7] A. Roda, M. Mirasoli, B. Roda, F. Bonvicini, C. Colliva, P. Reschiglian, *Microchim. Acta* **2012**, *178*, 7–28.

[8] E. de Boer, R. R. Beumer, *Int. J. Food Microbiol.* **1999**, *50*, 119–130.

[9] V. Velusamy, K. Arshak, O. Korostynska, K. Oliwa, C. Adley, *Biotechnol. Adv.* **2010**, *28*, 232–254.

[10] J. A. Odumeru, C. G. León-Velarde, in *Salmonella – A Dangerous Foodborne Pathogen* (Ed.: B. S. M. Mahmoud), InTech, Croatia, **2012**, pp. 373–392.

[11] X. L. Su, Y. B. Li, *Biosens. Bioelectron.* **2005**, *21*, 840–848.

[12] S. D. Mazumdar, M. Hartmann, P. Kampfer, M. Keusgen, *Biosens. Bioelectron.* **2007**, *22*, 2040–2046.

[13] H. Vaisocherová-Lísalová, I. Víšová, M. L. Ermini, T. Špringer, X. C. Song, J. Mrázek, J. Lamačová, N. Scott-Lynn Jr, P. Šedivák, J. Homola, *Biosens. Bioelectron.* **2016**, *80*, 84–90.

[14] F. Salam, Y. Uludag, I. E. Tothill, *Talanta* **2013**, *115*, 761–767.

[15] M. D. Morales, B. Serra, A. G. V. de Prada, A. J. Reviejo, J. M. Pingarron, *Analyst* **2007**, *132*, 572–578.

[16] S. Liebana, D. Brandao, S. Alegret, M. I. Pividori, *Anal. Methods* **2014**, *6*, 8858–8873.

[17] N. Pal, S. Sharma, S. Gupta, *Biosens. Bioelectron.* **2016**, *77*, 270–276.

[18] M. B. Mejri, H. Baccar, E. Baldrich, F. J. Del Campo, S. Helali, T. Ktari, A. Simonian, M. Aouni, A. Abdelghani, *Biosens. Bioelectron.* **2010**, *26*, 1261–1267.

[19] D. Wang, W. C. Dou, G. Y. Zhao, Y. Chen, *J. Microbiol. Methods* **2014**, *106*, 110–118.

[20] J. F. Fei, W. C. Dou, G. Y. Zhao, *RSC Adv.* **2015**, *5*, 74548–74556.

[21] C. L. Xiang, R. Li, B. Adhikari, Z. She, Y. X. Li, H. B. Kraatz, *Talanta* **2015**, *140*, 122–127.

[22] X. N. Zhang, W. J. Lu, E. Han, S. Wang, J. Z. Shen, *Electrochim. Acta* **2014**, *141*, 384–390.

[23] D. Zhu, Y. R. Yan, P. H. Lei, B. Shen, W. Cheng, H. X. Ju, S. J. Ding, *Anal. Chim. Acta* **2014**, *846*, 44–50.

[24] Y. J. Sung, H. J. Suk, H. Y. Sung, T. Li, H. Poo, M. G. Kim, *Biosens. Bioelectron.* **2013**, *43*, 432–439.

[25] D. Brandao, S. Liebana, S. Campoy, S. Alegret, M. I. Pividori, *Talanta* **2015**, *143*, 198–204.

[26] G. Kim, J. H. Moon, C. Y. Moh, J. G. Lim, *Biosens. Bioelectron.* **2015**, *67*, 243–247.

[27] J. F. Fei, W. C. Dou, G. Y. Zhao, *Microchim. Acta* **2015**, *182*, 2267–2275.

[28] Q. Chen, J. H. Lin, C. Q. Gan, Y. H. Wang, D. Wang, Y. H. Xiong, W. H. Lai, Y. T. Li, M. H. Wang, *Biosens. Bioelectron.* **2015**, *74*, 504–511.

[29] M. Xu, R. H. Wang, Y. B. Li, *Talanta* **2016**, *148*, 200–208.

[30] A. D. Taylor, J. Ladd, Q. M. Yu, S. F. Chen, J. Homola, S. Y. Jiang, *Biosens. Bioelectron.* **2006**, *22*, 752–758.

[31] Z. Farka, D. Kovar, J. Pribyl, P. Skladal, *Int. J. Electrochem. Sci.* **2013**, *8*, 100–112.

[32] M. C. Canbaz, C. S. Simsek, M. K. Sezginturk, *Anal. Chim. Acta* **2014**, *814*, 31–38.

[33] J. E. B. Randles, *Discuss. Faraday Soc.* **1947**, *1*, 11–19.

[34] E. P. Randviir, C. E. Banks, *Anal. Methods* **2013**, *5*, 1098–1115.

[35] R. K. Shervedani, M. Farahbakhsh, M. Bagherzadeh, *Anal. Chim. Acta* **2007**, *587*, 254–262.

[36] A. Rydstrom, M. J. Wick, *J. Immunol.* **2007**, *178*, 5789–5801.

[37] A. Eulalio, K. S. Frohlich, M. Mano, M. Giacca, J. Vogel, *Plos One* **2011**, *6*, 10.

[38] M. K. Aydintug, T. J. Inzana, T. Letonja, W. C. Davis, L. B. Corbeil, *J. Infect. Dis.* **1989**, *160*, 846–857.

[39] Z. Farka, D. Kovar, P. Skladal, *Sensors* **2015**, *15*, 79–92.

[40] M. H. Kothary, U. S. Babu, *J. Food Saf.* **2001**, *21*, 49–73.

[41] J. Dong, H. Zhao, M. R. Xu, Q. Ma, S. Y. Ai, *Food Chem.* **2013**, *141*, 1980–1986.

[42] P. D. Nguyen, T. B. Tran, D. T. X. Nguyen, J. Min, *Sens. Actuators B Chem.* **2014**, *197*, 314–320.

[43] R. D. Das, R. RoyChaudhuri, S. Maji, S. Das, H. Saha, *Biosens. Bioelectron.* **2009**, *24*, 3215–3222.

173

Paper IV

Detection of aerosolized biological agents using the piezoelectric immunosensor

Kovář, D.; Farka, Z.; Skládal, P.

(D.K. and Z.F. contributed equally)

Contribution:

Development and optimization of QCM immunosensor, data evaluation, manuscript writing

Detection of Aerosolized Biological Agents Using the Piezoelectric Immunosensor

David Kovář,[‡] Zdeněk Farka,[‡] and Petr Skládal*

National Centre for Biomolecular Research and CEITEC MU, Masaryk University, Kotlářská 2, 611 37 Brno, Czech Republic

Ⓢ Supporting Information

ABSTRACT: Airborne microorganisms are a major cause of respiratory diseases. Detection of pathogenic bacteria in the form of bioaerosols is required not only in peacetime but also in the threat of biological attacks. The label-free and direct detection of aerosolized biological agents is presented here. A desktop bioaerosol chamber for safe work with aerosolized microbial cells was constructed, and its functionality was tested. The model organisms (*Escherichia coli*) were disseminated using an aerosol generator in the chamber filled with either common laboratory indoor air or sterile air. The particles from the generated aerosol were collected using the cyclone SASS 2300, suspended in buffer and then analyzed using the piezoelectric immunosensor modified with specific capture antibodies. The frequency shifts indicated presence of the model biological agent with limit of detection of 1.45×10^4 CFU·L^{-1} of air. The total time from sample collection to detection was 16 min. The system was fully automated and controlled remotely through a local network.
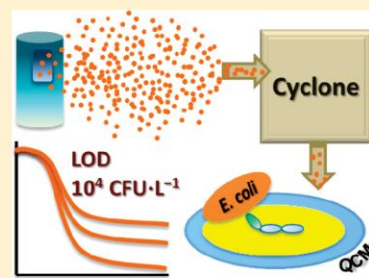
INTRODUCTION

Airborne microorganisms (bacteria, viruses, fungi, etc.) are integral part of the natural and urban environments. Airborne bacteria originate from natural and anthropogenic sources, sometimes with the intent of targeted biological attacks or serious incidents.[1,2] Bioterrorism is emerging as a real threat of the 21st century. The potential for abuse of biological warfare agents (BWAs) is too high as it was shown several times in modern history.[3]

The outdoor and indoor contamination of air with bacteria can relatively quickly lead to a large number of infected people. BWAs can be spread as contaminants of water supply and food or as bioaerosol contaminating indoor ventilation systems or disseminated outdoor by aircraft attacks.[4] The detection of BWAs in the form of bioaerosol or pathogenic airborne bacteria is challenging due to the low concentration of target microbes and potential complexity of the sample matrix. The samples usually contain pollen grains, mold, fungi, dust, and ubiquitous microbial organisms.[5] Also, a large number of industrial products emitted to the atmosphere by man may in principle interfere with the detection methods and make the detection of the target microorganisms highly complicated or even impossible. The composition of microorganisms in the atmosphere is still not well-defined. Together with these interferences, the low visibility, odorless, tasteless, and problematic sampling makes the analysis complicated. The delayed effect of biological agents in contrary to chemical agents, infectious character, and potentially larger number of casualties make it well suited for military or bioterrorist purposes.[3] Also, the occurrence of pathogenic microorganisms in the air in places with a high population density contributes to the spread of epidemics and pandemics. In such cases, early treatment must be initiated based on rapid detection and identification of the pathogen.

The two key parts should be resolved during analysis of bioaerosols: collection of aerosol and detection of the bioagent. Extensive attention was focused on bioaerosol collecting systems: samplers.[6] The function of the samplers is based on different physical principles and structural designs.[7−10] The prime features characterizing samplers include operational flow rate of air, sampling time, volume of the collected samples, and cutoff size of the captured particles. Xu and Yao compared several portable widely used samplers on indoor and outdoor aerosols.[11] The study summarized that different samplers resulted in different culturable bacterial bioaerosol diversity in various environments.

Two different approaches toward detection of bioaerosols are used: either detection of general biological compounds present in air or direct specific detection of the target BWAs. The former choice utilizes optical methods, mainly fluorescence of the molecules present in biological systems[12−14] (ATP, NADH, tryptophan, etc.). However, there are two disadvantages: (1) fluorescence-based instruments cannot distinguish between harmful or ubiquitous microorganisms, and (2) atmospheric pollutants may also fluoresce and consequently trigger false positive indications.[15] Also, this concept is feasible only for living bacteria. The spores as a dormant form of certain bacterial species (e.g., *Bacillus*, *Clostridium*) exhibit very low levels of ATP and cannot be detected directly.[16]

175

The second approach exploits the direct detection using culture-based methods, Raman spectroscopy, mass spectrometry,[17,18] PCR techniques,[19−21] particle ionization with potentiometric detection,[22] alternatively FISH,[7] surface-enhanced Raman spectroscopy (SERS),[23] and differential mobility spectrometry (DMS).[24] Personal bioaerosol sampler coupled with PCR was used for detection of vaccinia virus.[25] However, complexities of analyzed samples containing interfering (bio)-substances put PCR methods, which are by no means universally applicable to real-time monitoring of environmental samples, at a disadvantage,[26] and additional methods are needed to avoid false conclusions.[27] In the case of mass spectrometry (MS), extensive instrumentation limits widespread use for field detection.

There is a need for reliable, quick-response, real-time, and on-site detection systems for use on a massive scale. Conventional microbiological methods are time-consuming and usually require collection of samples for subsequent laboratory analysis. This strongly depends on aerosol samplers used for collection of the microorganisms and on the desiccation stress characterized on the sampler.[11] In contrary, biosensors have gained potential. Biosensors have many advantages in contrast with other developed methods for detection of microbes. The most important is the specificity given by the biological recognition factor which is followed by portability, miniaturization, and rapid response. The biosensors merge a convenient transducer with the efficient biological factor. As the transducer, optical,[28−30] electrochemical,[31,32] and piezoelectric[33,34] sensors were successfully adopted. Either antibodies or nucleic acids (DNA probes, aptamers) can serve for the recognition. The viability or desiccation of microbes is not as relevant as in the case of the culture methods. The main question is the sensitivity of such biosensors. The United States Department of Homeland Security[35] (DHS, USA) requires the sensitivity of field devices in the range from 10^2 to 10^5 organisms·L^{-1}.

Numerous protocols for detection of microorganisms employ the label-free assays. The main convenience is simplified protocol, quick response and no need of secondary labeled bioreagents. The most popular are impedance spectroscopy,[36] surface plasmon resonance[21,29,37,38] (SPR), and quartz crystal microbalance[39,40] (QCM) sensors. In our previous study, we compared sensitivity of the SPR system Biacore with the QCM sensor on a *Bacillus anthracis* surrogate, concluding that both methods provided similar sensitivity.[41] The use of QCM for label-free direct detection of bioaerosols should be feasible due to the preconcentration effect of the sampler. The QCM as a cheaper alternative to SPR is advantaged to widespread use for field detection and this possibility is evaluated in this work. The QCM is a relatively simple and sensitive device formed by thin quartz plate with gold electrodes on the opposite sides. The antibodies immobilized on its surface make QCM highly sensitive to the target antigen. The antigens interact with antibodies on the surface and increase the mass loaded on the surface which directly corresponds to the decreased frequency of the resonator.

Nevertheless, the label free biosensors were not yet seriously considered for detection of bacteria from air. Several papers have been published about the detection of particles from air using QCM,[42,43] but only two papers describe detection of bacteria.[34,44] Here we present the detection of aerosolized bacteria using QCM, also comparing with culture based method and particle counter.

■ EXPERIMENTAL SECTION

Chemicals and Reagents. Cysteamine and sulfosuccinimidyl-4-(N-maleimidomethyl)cyclohexane-1-carboxylate (Sulfo-SMCC) were purchased from Sigma (Germany). The chemicals for preparation of buffers (PBS, PBS-EDTA, and citrate), sulfuric acid, and potassium chromate for preparation of chromic acid were supplied from Penta (Czech Republic). Phosphate buffered saline (PBS, 50 mM sodium hydrogen phosphate/sodium dihydrogen phosphate; 150 mM sodium chloride; pH 7.4) was used for dissemination and QCM experiments. Citrate buffer (100 mM sodium citrate/citric acid; pH 4.0) was used for regeneration of the immunosensing surface. The buffers were filtered through a 0.22 μm PTFE membrane (Millipore, Germany) and autoclaved before use. Household bleach for disinfection of the aerosol chamber and contaminated parts of the apparatus was purchased from a local shop. The polyclonal antibody against *Escherichia coli* (4329-4906) was purchased from AbD Serotec (UK).

BWA Model. As a model microorganism, *E. coli* strain K 12 was used. The strain (CCM 7929) was obtained as a lyophilized sample from Czech Collection of Microorganisms. The sample was revived in the Luria−Bertani low salt broth (Duchefa Biochemie, Netherlands) for 12 h, and the aliquots were stored frozen. *E. coli* was cultivated by the standard procedure. A volume of 100 μL of stock aliquot was inoculated in 100 mL of the low salt LB broth and aerobically cultivated overnight at 37 °C under gentle mixing. The bacteria were centrifuged at 4500 rcf for 10 min, and the pellet was washed thrice with PBS. The final PBS suspension was used for dilution of samples for aerosol experiments. Concentration of cells was determined by measuring absorbance at 600 nm using the McFarland calibration scale. The microbial suspensions for dissemination as the bioaerosol were diluted in PBS before use.

Preparation of QCM Immunosensors. The antibody (Ab) was reduced by cysteamine.[45] Briefly, the stock Ab was diluted in PBS-EDTA (100 mM PBS, 10 mM EDTA, pH 7.2) to a concentration of 2 mg·mL^{-1}, and 1 μL of cysteamine (60 mg·mL^{-1}, water solution) was added per each 10 μL of the Ab solution. The mixture was incubated for 90 min at 37 °C. The reduced antibodies (rIgG) were purified using the Microcon centrifugal unit YM 10,000 in accordance with the manufacturer's instructions. The final concentration of rIgG was 3.5 mg·mL^{-1}.

Quartz crystals (10 MHz, AT-cut, gold electrodes) were purchased from International Crystal Manufacturing (USA). Prior to use, the gold electrodes were cleaned in chromic acid for 60 min and thoroughly washed with deionized water. The self-assembled monolayer was formed from aqueous cysteamine solution (20 mg·mL^{-1}, 10 μL per electrode). The crystals were incubated in the dark for 2 h at 4 °C, washed with deionized water, and allowed to dry. Amine-containing surfaces were incubated with Sulfo-SMCC (3 mg·mL^{-1}) for 1 h at room temperature, washed, and incubated directly with the reduced antibodies (rIgG, 100 μg·mL^{-1}) for 18 h at 4 °C. After the last washing step, the crystals were either used or stored in dry state in refrigerator. The resonance frequency was measured after each modification step for verification of the immobilization steps (data not shown).

Construction of the Air Chamber. The aerosol chamber was made of poly(methyl methacrylate). The dimensions of the box were 93 × 63 × 59 cm^3 (total volume 0.346 m^3). The removable front panel with attached handling gloves was locked

176
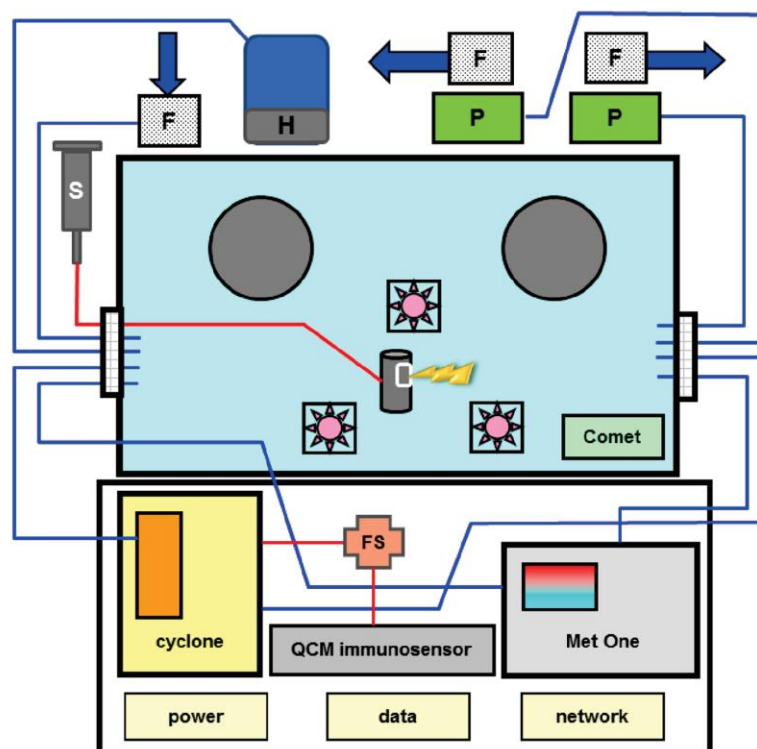
Figure 1. Scheme of desktop air chamber (not in scale): F, HEPA filters; P, air pumps; H, humidifier; S, syringe for filing the aerosol generator; FS, fluids switching unit. The sensor Comet was placed inside the chamber. Below the chamber, sensor systems, cyclone sampler linked to the immunosensor, network modules, and power supply adapters were placed. The blue lanes represent the airflow tracks, and the red lanes the liquid tracks. See the Supporting Information for the overall photo (Figure S3) and the diagram of flow-through system (Figure S4).

by screws. On the side panels, there were grommets for cables and valve hose brushings for safe manipulation and unplugging of the chamber with contaminated content from the rest of the measuring apparatus. Three fans with diameter of 12 cm and PWM speed control were placed inside the chamber to provide the turbulence and rapid mixing of the air inside. The axis of one fan was placed vertically to the bottom; the axes of the next two fans were placed angle-wise of $45°$ to the bottom. Aerosol generator was centered among the fans, it consisted of the ultrasonic piezoelectric element for terrariums (Reptile One, Australia) placed in beaker and covered with routing plastic plate streamlining the aerosol (Figure S1 in the Supporting Information). The samples were applied to this beaker from outside of the chamber using syringe and Teflon tube. The relative humidity, temperature and air pressure inside the chamber were monitored using the Comet 7511 sensor (Comet, Czech Republic). The particles size distribution, the outer temperature and outer relative humidity were measured using Met One 3400 (Hach). The counter measures particles in the range from 0.3 to 10 μm. The Met One was placed outside the chamber and the air from the interior was circulated through using the connected hose. The air humidifier SuperFog (LuckyReptile, Germany) was used for increasing the internal humidity where appropriate. Two air pumps (Hurricane, Italy) supplemented by HEPA filters (AirFilters, Czech Republic) were used for rapid exchange of sterile air inside the chamber. A Smart Air Sampler System, model SASS 2300 (Research

International) was used for collection of air samples. The SASS is a portable, wetted-wall cyclone sampler system developed for the collection of airborne materials. According to the user manual, it is particularly effective to capture aerosolized pathogenic bacteria and spores in the range of 0.5–10 μm. The cyclone collects the samples in liquid volume maintained constant during the sampling process. All apparatus used were controlled by software developed in-house (Delphi, Windows) for this purpose. The apparatus (Cyclone, Met One and all electronic accessories) were connected to the Serial Ethernet Server ESP904 (B&B Electronics) and controlled remotely via Ethernet link (see diagram of connections in Figure S2).

Measuring Setup. Before the experiment and sampling the blank, normal air, the chamber was cleaned and the inner surfaces were sterilized using bleach. Prior to each experimental cycle, the chamber was ventilated out using two air pumps and then flushed by filtered air (HEPA filter) for 60 min. Then 10 mL samples (*E. coli* suspensions or PBS as blank) were loaded to the aerosol generator, and the humidity was increased to 80%. Three source concentrations of *E. coli* were used for dissemination: 10^7, 10^8, and 10^9 CFU·mL^{-1}. To limit heating of the piezoelectric generator, five shorter cycles (60 s dissemination and 30 s break) were performed, hereafter referred to as full-cycle. Approximately 0.5 mL of BWA model suspension was disseminated as a bioaerosol fog per each full-cycle. Considering the total volume of the chamber (0.346 m^3) and initial concentration of suspension, the initial concen-

177
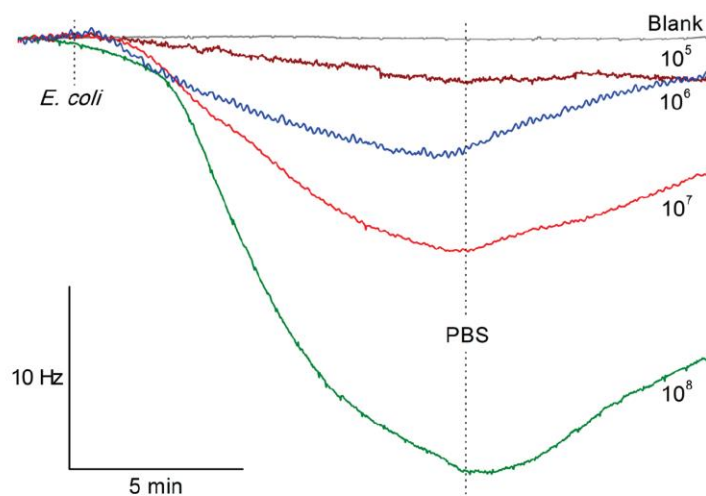
Figure 2. Immunosensor responses for *E. coli* K 12 suspensions in PBS buffer. The association phase (10 min) and spontaneous dissociation of the formed immunocomplex due to flowing PBS are shown. Concentrations of bacteria are given in CFU·mL^{-1}.

trations of the spread BWA model were calculated as 1.45×10^4, 1.45×10^5, and 1.45×10^6 CFU·L^{-1} of air. The aerosol generation efficiency and the turbulence effect of fans were verified by culturing disseminated *E. coli* on agar plates placed in several parts inside the chamber (Figure S6).

During the collection, the cyclone sampled the air from the chamber with a flow rate 360 L air/min. This means that the volume of the air chamber was passed approximately 4.8-times through the cyclone during the 5 min collection. The resulting preconcentration effect was theoretically 100-times, assuming that all fogged microorganisms were collected. Final volume of collected samples was 4.5 mL/5 min cycle. The sample holding loop (internal volume 400 μL) was implemented for dosing of collected samples to the immunosensor. The loop was always filled with the middle stream of liquid sample pumped from SASS 2300 using programmable electric valves. The forward and backward volumes were captured in vials. The scheme is shown in Figure S4; the system consists of two switching valves, sample loop, milliGAT pump (Global FIA, USA), in-house made flow-through cell with the QCM immunosensor, and vials for collection of the remaining sample volume.

The QCM detection followed immediately after sampling. During the collection, the baseline of the immunosensor was stabilized in flowing PBS buffer. After filling the sample loop, the valves were switched and the sample was flown through the cell for 10 min followed by dissociation in PBS (10 min) and regeneration by citrate buffer (2 min). The pH change was sufficient for regeneration of the surface, and it allowed its reusability for 12−15 cycles. Then the activity of the sensor decreased rapidly. The sensor response to *E. coli* suspension throughout the whole experiment including regeneration phase is shown in Figure S9. The frequency changes were measured in real-time using the QCM analyzer (KEVA, Czech Republic). The flow rate for all solutions was 40 μL·min^{-1} except for the sample loop filling when the internal peristaltic pump of SASS 2300, which operates with constant flow rate of 4 mL·min^{-1}.

RESULTS AND DISCUSSION

Preparation of Immunosensors. Initially, eight individual immunosensors were modified with anti-*E. coli* antibody as described above. From this set, three immunosensors with similar final frequency shifts (sensors A−C) were chosen for performing measurements because of good reproducibility of individual immunosensors.[46] The standard suspensions of bacteria were prepared by diluting the stock solution. The calibration curve for microbes in solution was measured using sensor A; the incubation period in flowing standard was 10 min. Typical frequency shifts for standard solutions (*E. coli* spiked in PBS) are shown in Figure 2; the regeneration phases are not shown. The frequency response was linear over a range from 10^5 to 10^7 CFU·mL^{-1}, while the linear regression equation was $\Delta f = -5.079\log(\text{CFU·mL}^{-1}) + 24.40$ ($R^2 = 0.997$). The limit of detection (LOD) was obtained as the concentration of *E. coli* in a sample for which the response reached 3 times the standard deviation (3σ) of the signal shifts of blank (3 repetitions). From the calibration graph presented in Figure S11, the LOD 7.5×10^4 CFU·mL^{-1} was determined for *E. coli* samples spiked in PBS. The matrix effect of environmental air samples was also studied. The outdoor air samples were collected using the cyclone sampler as described above. The air flow was constant and the same as in the case of collection from the chamber; only the time was increased for obtaining a sufficiently large volume of the working buffer. Afterward, *E. coli* was spiked into the working buffer (airPBS) in the same concentrations as before. The standard solutions were measured using sensor B (Figure S10), and the LOD was obtained similarly. The LOD 1.3×10^5 CFU·mL^{-1} was determined for spiked airPBS samples. The linear regression equation for graph shown in Figure S11 was $\Delta f = -5.860\log(\text{CFU·mL}^{-1}) + 28.43$ ($R^2 = 0.937$). Based on these values, it can be assumed there is no significant matrix effect. The values suggest that the sensor provides similar results as published in the literature; *Salmonella typhimurium* was detected[47] with LOD of 10^5 CFU·mL^{-1}. The better LOD was achieved only through enhancing of the signal by nanoparticles.[48] Jiang et al.[49] compared different particles for amplifying and improving detection of *E. coli* O157:H7. Jiang's

178
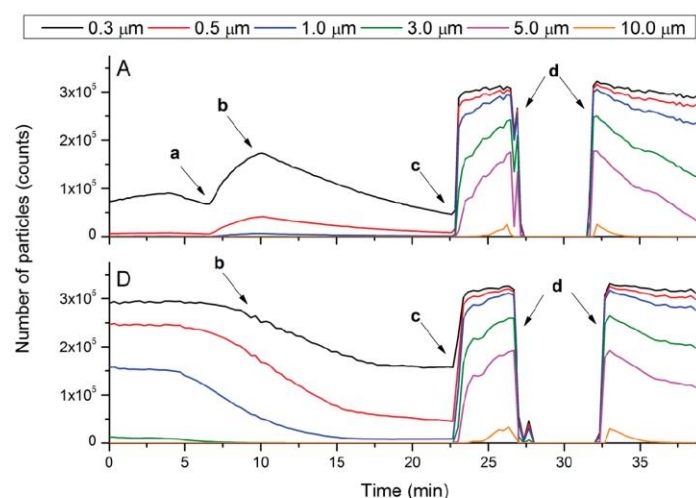
Figure 3. Comparison of data sets for particle size measurements: for blank (A) and disseminated concentration of *E. coli* 10^9 CFU·mL^{-1} (D). There are no significant differences between the blank and sample of dispersed *E. coli* in the measured aerosol. The data set (A) was started in a sterile and more or less particle-free air chamber. At point a, the humidity was increased to 80% and the internal environment was left to stabilize, point b. At point c, either the blank (A) or the sample (D) was dispersed. The increase in the concentration of particles is observed due to dispersing. The gaps in signal defined at points d indicate cyclone sampling.

group achieved the LOD of 10^6 CFU·mL^{-1} for label-free settings and lowered the LOD by 3 orders of magnitude using immunobeads. The preincubation of the samples or direct preconcentration using magnetic beads could further reduce the LOD value, but to the detriment of measuring time. In our case, the preconcentration step is provided via the cyclone air sampler, and the further preincubation or preconcentration seems not necessary for online real-time monitoring.

The ability of antibodies to bind *E. coli* K 12 was imaged by atomic force microscope NanoWizard 3 BioScience (JPK Instruments, Germany) in the semicontact mode (Figure S7). The gold surface of QCM sensor was modified as described above. The surface was incubated with bacterial suspension in PBS (10^7 CFU·mL^{-1}) for 1 h and consequently washed with sterile filtered PBS and shortly with sterile water. The nonincubated surface was used as a blank. The obtained images confirmed the expected function of the capture antibody.

Testing Performance of the Aerosol Chamber. Initially, the dissemination efficiency was tested with the help of culturing of agar plates. The opened plates were placed inside the chamber in different positions and the suspension (10^7 CFU·mL^{-1}) was disseminated in full-cycle to generate the bioaerosol. The plates were contacting the aerosol inside the chamber during the dissemination and cyclone collection. Afterward, the air containing bioaerosol was filtered out; the plates were removed, cultivated for 24 h at 37 °C and evaluated. The sterile PBS was used as blank and the plates were processed identically.

The agar plate placed near the aerosol generator contained big microbial spots resulting from direct dropping of microbial suspension during the dissemination. The plates on the walls of the air chamber contained very small and well isolated point colonies, demonstrating sufficient quality of dissemination of the bacteria inside the air chamber (Figure S6).

The amount of particles inside the air chamber was also monitored in real-time using the portable particle counter Met

One; this system provides distribution of particles in eight channels of increasing size intervals. The dissemination data sets of blank and concentration of *E. coli* of 10^9 CFU·mL^{-1} are shown in Figure 3. Comparison of other concentrations is shown in Figure S8. Each data set is characterized by increasing concentration of particles during the dissemination full-cycle and typical "gap" resulting from the cyclone collection; in the closed system, the much higher flow rate of air through the cyclone practically stopped the flow of air to the particle counter. Unfortunately, there was no apparent difference among the three disseminated concentration levels of bacteria or the blank and the counts of particles measured using Met One (with cyclone being switched off). When considering the size interval over 3 orders of magnitude, it was surprising that there were no differences for neither 1 nor 3 μm measuring channels. It seems that the response of the particle counter was mostly indicating different sizes of microdrops of the disseminated solutions.

Detection of Bioaerosols. The bioaerosol samples were prepared by dissemination of several bacterial suspensions in the air chamber. For each concentration, two independent full-cycle disseminations were done and the "contaminated" air was collected by the cyclone sampler. The disseminated PBS without any microbes was used as a blank. The detection of samples was done in the flow-through immunosensor system connected online to the SASS cyclone. The responses (frequency shifts of sensor C) are shown in Figure 4. The data indicated that the minimal disseminated concentration was detectable and the concentration in the analyzed samples is below 1.5×10^4 CFU·L^{-1} of air.

Assuming that 0.5 mL of the source suspensions dispersed throughout the volume of the air chamber, the theoretical concentrations of *E. coli* in the air and transferred in the buffer samples were calculated and are summarized in Table 1. Of course, this is the highest expected value, not considering partial condensation of the drops of the aerosol and sorption of microbial cells on the internal surfaces. However, the real

179

Table 1. Levels of *E. coli* in Air and in the Cyclone Samples during Dissemination of Bioaerosols

disseminated concentration CFU·mL^{-1}	level expected in air CFU·L^{-1}	expected in PBS after capture CFU·mL^{-1}	cultivation of samples CFU·mL^{-1}	calculated from QCM response CFU·mL^{-1}
10^7	1.45×10^4	1.11×10^6	90	6.69×10^4
10^8	1.45×10^5	1.11×10^7	2.5×10^3	1.63×10^5
10^9	1.45×10^6	1.11×10^8	8.1×10^3	2.89×10^6
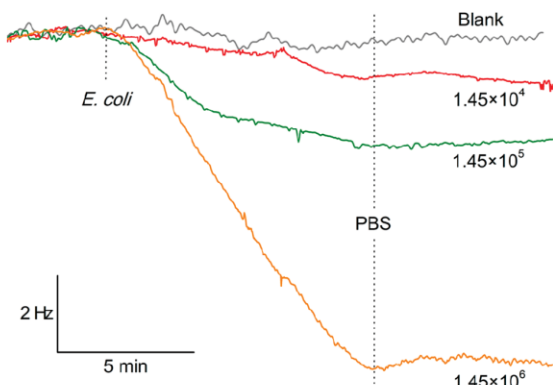
Figure 4. Frequency responses to samples collected by the SASS 2300 sampler. PBS buffer was disseminated as blank. The theoretically expected concentrations of *E. coli* in the generated bioaerosols are expressed in CFU·L^{-1} of air.

observed response of the immunosensor was approximately 2 orders of magnitude lower than one should expect from the theoretical calculation. The collected samples were also cultivated (Figure S12), and the real concentrations were extrapolated. The 100 μL of samples from the cyclone were smeared on the LB agar plates and cultivated for 24 h at 37 °C. The counted colonies were extrapolated using analytical software Icy (Institut Pasteur, France). This nondirect culture based detection method provided much lower real concentrations of *E. coli* in individual samples. The concentrations in the cultivated cyclone samples were calculated and are summarized also in Table 1. It should be mentioned that this is the lower limit of the microbes in the captured samples; the immunosensor should be responding also to the dead or partially damaged cells which are not appearing in the agar plates. In our experience with this kind of immunosensor, there are no significant differences between living, damaged, or dead bacteria. The total amount of lipopolysaccharides as main antigen does not vary in living suspension or suspension damaged by ultrasonication; hence, the signal is comparable for both suspensions with the same concentration of bacteria at the beginning. Accordingly, we use the CFU·mL^{-1} for expression of bacteria concentration; this is expected to be quite near values expressed as bacteria·mL^{-1}.

Previous information about coupling direct label-free immunosensors for detection of microbes in air is rather limited. Alava et al. used *E. coli* MRE 162 with a detection limit of 2.4×10^7 CFU·mL^{-1} in the collected air samples.[44] However, details about preparation of air samples were missing in this paper. Usachev et al. used surface plasmon resonance for label-free real-time detection of the viral surrogate MS2 bacteriophage in bioaerosol; however, the LOD was not mentioned clearly.[38] The aerosolized virus of influenza type A was detected using QCM coated with specific antibodies.[34] Unfortunately, there are no other papers or studies concerning

detection of bacteria in aerosol using QCM. For this reason, the data measured here support the usefulness of combining the cyclone sampler with a piezoelectric immunosensor for reasonably fast detection of the target microbial cells in bioaerosols.

CONCLUSION

The aerosol chamber was constructed for safe and controlled dissemination of biological agents and applied for experiments with model bacterial aerosols of *E. coli*. The quartz crystal microbalance based piezoelectric immunosensor was used for label-free detection of bioaerosols after coupling with the air sampling cyclone SASS 2300. The whole setup was fully automated; the included liquid flow system was used for online delivery of the cyclone samples to the immunosensor detector, resulting in one detection cycle being completed in 16 min. The demonstrated limit of detection of *E. coli* in the collected aerosol samples was around 10^4 CFU·L^{-1} of air, based on the levels expected from the disseminated amounts of microbes. Total time needed for sample collection, detection, sensor regeneration, and ventilation of the chamber was 40 min. The reference culture based method proved that the disseminated concentration of *E. coli* in the air chamber was significantly reduced due to the surface adsorption, desiccation, or mechanical stress evoked by the cyclone. The important advantage of the developed system is the completely remote operation: the users are not in contact with the potentially dangerous bioagents during the experiments. Furthermore, the small dimensions, a desktop system, provide full portability of the experimental system; only power and Ethernet sources are required.

The obtained data confirmed feasibility of the proposed combination of piezoelectric immunodetector with cyclone for promising detection of bioaerosols. The parallel detection of the most relevant pathogens using monoclonal antibodies immobilized on several sensors may in the future allow revealing a biological threat in reasonably short time intervals. The simple direct indication of the captured microbes is a single-step assay, and thus, the minimal complexity is favorable for high robustness and reliability of the whole system.

ASSOCIATED CONTENT

Ⓢ Supporting Information

Additional information as noted in the text. This material is available free of charge via the Internet at http://pubs.acs.org.

AUTHOR INFORMATION

Corresponding Author

*E-mail: skladal@chemi.muni.cz. Phone: +420 549 497 010.

Author Contributions

‡These authors contributed equally. The manuscript was written through contributions of all authors. All authors have given approval to the final version of the manuscript.

Notes

The authors declare no competing financial interest.

180

■ REFERENCES

(1) Sternbach, G. J. Emerg. Med. 2003, 24, 463−467.
(2) Török, T. J.; Tauxe, R. V.; Wise, R. P.; Livengood, J. R.; Sokolow, R.; Mauvais, S.; Birkness, K. A.; Skeels, M. R.; Horan, J. M.; Foster, L. R. J. Am. Med. Assoc. 1997, 278, 389−395.
(3) Danzig, R.; Berkowsky, P. B. J. Am. Med. Assoc. 1997, 278, 431−432.
(4) Khardori, N.; Kanchanapoom, T. Clin. Microbiol. Newsl. 2005, 27, 1−8.
(5) Polymenakou, P. N. Atmosphere 2012, 3, 87−102.
(6) Mandal, J.; Brandl, H. Open Environ. Biol. Monit. J. 2011, 4, 83−96.
(7) Deloge-Abarkan, M.; Ha, T. L.; Robine, E.; Zmirou-Navier, D.; Mathieu, L. J. Environ. Monit. 2007, 9, 91−97.
(8) King, M. D.; McFarland, A. R. Aerosol Sci. Technol. 2012, 46, 82−93.
(9) Su, W.-C.; Tolchinsky, A. D.; Chen, B. T.; Sigaev, V. I.; Cheng, Y. S. J. Environ. Monit. 2012, 14, 2430−2437.
(10) Pan, Y.-L.; Boutou, V.; Bottiger, J. R.; Zhang, S. S.; Wolf, J.-P.; Chang, R. K. Aerosol Sci. Technol. 2004, 38, 598−602.
(11) Xu, Z.; Yao, M. Aerosol Sci. Technol. 2011, 45, 1143−1153.
(12) Joshi, D.; Kumar, D.; Maini, A. K.; Sharma, R. C. Spectrochim. Acta, Part A 2013, 112, 446−456.
(13) Park, C. W.; Park, J.-W.; Lee, S. H.; Hwang, J. Biosens. Bioelectron. 2014, 52, 379−383.
(14) Lee, S. J.; Park, J. S.; Im, H. T.; Jung, H.-I. Sens. Actuators, B 2008, 132, 443−448.
(15) Pöhlker, C.; Huffman, J. A.; Pöschl, U. Atmos. Meas. Technol. 2012, 5, 37−71.
(16) Venkateswaran, K.; Hattori, N.; La Duc, M. T.; Kern, R. J. Microbiol. Methods 2003, 52, 367−377.
(17) Alam, S. I.; Kumar, B.; Kamboj, D. V. Anal. Chem. 2012, 84, 10500−10507.
(18) van Wuijckhuijse, A. L.; Stowers, M. A.; Kleefsman, W. A.; van Baar, B. L. M.; Kientz, C. E.; Marijnissen, J. C. M. J. Aerosol Sci. 2005, 36, 677−687.
(19) Fykse, E. M.; Langseth, B.; Olsen, J. S.; Skogan, G.; Blatny, J. M. J. Appl. Microbiol. 2008, 105, 351−358.
(20) Hospodsky, D.; Yamamoto, N.; Peccia, J. Appl. Environ. Microbiol. 2010, 76, 7004−7012.
(21) Usachev, E. V.; Agranovski, I. E. J. Environ. Monit. 2012, 14, 1631−1637.
(22) Sarantaridis, D.; Caruana, D. J. Anal. Chem. 2010, 82, 7660−7667.
(23) Sengupta, A.; Laucks, M. L.; Dildine, N.; Drapala, E.; Davis, E. J. J. Aerosol Sci. 2005, 36, 651−664.
(24) Krebs, M. D.; Zapata, A. M.; Nazarov, E. G.; Miller, R. A.; Costa, I. S.; Sonenshein, A. L.; Davis, C. E. IEEE Sens. J. 2005, 5, 696−703.
(25) Agranovski, I. E.; Safatov, A. S.; Sergeev, A. A.; Pyankov, O. V.; Petrishchenko, V. A.; Mikheev, M. V.; Sergeev, A. N. Atmos. Environ. 2006, 40, 3924−3929.
(26) Green, H. C.; Field, K. G. Water Res. 2012, 46, 3251−3260.
(27) Maher, N.; Dillon, H. K.; Vermund, S. H.; Unnasch, T. R. Appl. Environ. Microbiol. 2001, 67, 449−452.
(28) Ligler, F. S.; Anderson, G. P.; Davidson, P. T.; Foch, R. J.; Ives, J. T.; King, K. D.; Page, G.; Stenger, D. A.; Whelan, J. P. Environ. Sci. Technol. 1998, 32, 2461−2466.
(29) Naimushin, A. N.; Spinelli, C. B.; Soelberg, S. D.; Mann, T.; Stevens, R. C.; Chinowsky, T.; Kauffman, P.; Yee, S.; Furlong, C. E. Sens. Actuators, B 2005, 104, 237−248.

(30) Rowe-Taitt, C. A.; Golden, J. P.; Feldstein, M. J.; Cras, J. J.; Hoffman, K. E.; Ligler, F. S. Biosens. Bioelectron. 2000, 14, 785−794.
(31) Skládal, P.; Švábenská, E.; Žeravík, J.; Přibyl, J.; Šišková, P.; Tjärnhage, T.; Gustafson, I. Electroanalysis 2012, 24, 539−546.
(32) Švábenská, E.; Kovář, D.; Krajíček, V.; Přibyl, J.; Skládal, P. Int. J. Electrochem. Sci. 2011, 6, 5968−5979.
(33) Liang, D.; Shih, W. P.; Chen, C. S.; Dai, C. A. Sensors 2010, 10, 3641−3654.
(34) Owen, T. W.; Al-Kaysi, R. O.; Bardeen, C. J.; Cheng, Q. Sens. Actuators, B 2007, 126, 691−699.
(35) Sabelnikov, A.; Zhukov, V.; Kempf, R. Biosens. Bioelectron. 2006, 21, 2070−2077.
(36) Yang, L. Talanta 2008, 74, 1621−1629.
(37) Usachev, E. V.; Tam, A. M.; Usacheva, O. V.; Agranovski, I. E. J. Aerosol Sci. 2014, 76, 39−47.
(38) Usachev, E. V.; Usacheva, O. V.; Agranovski, I. E. J. Appl. Microbiol. 2013, 115, 766−773.
(39) Taylor, A. D.; Yu, Q.; Chen, S.; Homola, J.; Jiang, S. Sens. Actuators, B 2005, 107, 202−208.
(40) Reddy, B. S. K.; Kumar, K. R.; Balakrishnaiah, G.; Gopal, K. R.; Reddy, R. R.; Reddy, L. S. S.; Narasimhulu, K.; Rao, S. V. B.; Kiran Kumar, T.; Balanarayana, C.; Moorthy, K. K.; Babu, S. S. J. Atmos. Sol.-Terr. Phys. 2011, 73, 1727−1738.
(41) Farka, Z.; Kovář, D.; Přibyl, J.; Skládal, P. Int. J. Electrochem. Sci. 2013, 8, 100−112.
(42) Raghavendra Kumar, K.; Narasimhulu, K.; Balakrishnaiah, G.; Suresh Kumar Reddy, B.; Rama Gopal, K.; Reddy, R. R.; Moorthy, K. K.; Suresh Babu, S. Sci. Total Environ. 2009, 407, 5589−5604.
(43) Pillai, P. S.; Moorthy, K. K. Atmos. Environ. 2001, 35, 4099−4112.
(44) Alava, T.; Berthet-Duroure, N.; Ayela, C.; Trévisiol, E.; Pugnière, M.; Morel, Y.; Rameil, P.; Nicu, L. Sens. Actuators, B 2009, 138, 532−538.
(45) Hermanson, G. T. Bioconjugate techniques; Academic Press: London, 1996.
(46) Pohanka, M.; Skladal, P.; Pavlis, O. J. Immunoassay Immunochem. 2008, 29, 70−79.
(47) Su, X. L.; Li, Y. Biosens. Bioelectron. 2005, 21, 840−848.
(48) Salam, F.; Uludag, Y.; Tothill, I. E. Talanta 2013, 115, 761−767.
(49) Jiang, X.; Wang, R.; Wang, Y.; Su, X.; Ying, Y.; Wang, J.; Li, Y. Biosens. Bioelectron. 2011, 29, 23−28.

181

Paper V

Cyclopropylamine plasma polymer surfaces for label-free SPR and QCM immunosensing of *Salmonella*

Makhneva, E.; Farka, Z.; Skládal, P.; Zajíčková, L.

Contribution:

Development and optimization of SPR and QCM immunosensors, characterization of sensing surface by AFM, data evaluation, participation in manuscript writing

Cyclopropylamine plasma polymer surfaces for label-free SPR and QCM immunosensing of *Salmonella*

Ekaterina Makhneva[a,b], Zdeněk Farka[c], Petr Skládal[c,d], Lenka Zajíčková[a,b,*]

[a] *RG Plasma Technologies, Central European Institute of Technology (CEITEC), Masaryk University, Purkyňova 123, Brno 612 00, Czech Republic*
[b] *Department of Physical Electronics, Faculty of Science, Masaryk University, Kotlářská 2, Brno 611 37, Czech Republic*
[c] *RG Nanobiotechnology, CEITEC, Masaryk University, Kamenice 5, Brno 625 00, Czech Republic*
[d] *Department of Biochemistry, Faculty of Science, Masaryk University, Kamenice 5, Brno 625 00, Czech Republic*

A B S T R A C T

We report on the first successful application of nitrogen-containing functional surfaces prepared by plasma polymerization in surface plasmon resonance (SPR) immunosensing. The plasma polymers (PPs) were deposited from cyclopropylamine (CPA) vapors onto gold surfaces of SPR and quartz crystal microbalance (QCM) sensors. It provided an excellent platform for a stable immobilization of antibodies using glutaraldehyde (GA) activation. The performance of the SPR immunosensor was proven by a model pair of monoclonal antibody (Ab) AL-01 and human serum albumin as well as by the selective detection of bacterial pathogen *Salmonella* Typhimurium using the immobilized anti-*Salmonella* Ab. A baseline drift of the measured SPR signal, caused by the long-term reactivity of CPA plasma polymers, was well stabilized by 18 h immersion in phosphate buffered saline prior to the GA activation. The immunosensors can be successfully regenerated several times using 10 mM NaOH. The limit of detection of 10^5 CFU/mL and a wide linear response were achieved for *Salmonella*. The assay parameters are comparable to the conventional label-free methods. However, the replacement of conventional immobilization matrix with the CPA PPs offers an advantage of excellent adhesion to gold QCM and SPR surfaces achieved by fast and eco-friendly procedure compatible with the vacuum deposition of gold.

1. Introduction

Salmonella is a pathogenic gram-negative bacterium causing diarrhea, fever and abdominal spasm. *Salmonella* can also intervene into the blood stream, bones, brain and nervous system and can occasionally result in lethal infections [1]. Therefore, there is a need for analytical devices capable of sensitive and fast detection of this pathogen. Conventional methods for the detection of bacteria include the cell culturing, polymerase chain reaction (PCR) and enzyme-linked immunosorbent assay (ELISA). These methods provide very high sensitivity, though the required long analysis times make them not suitable for point-of-care testing [2]. The comprehensive overview of currently used methods for the detection of *Salmonella* was done by Odumeru and Leon-Velarde [3].

Many biosensors for microorganism detection have been recently developed as an alternative to conventional methods trying to combine a high sensitivity and short analysis time. Quartz crystal microbalance (QCM) [4] and surface plasmon resonance (SPR) [5,6], biosensors appeared to be promising tools regarding the sensitive determination of

bacteria. The advantage of direct label-free operations is a short analysis time (~10 min). The limits of detection (LODs) are typically around 10^4–10^5 CFU/mL [2,7]. Lower LODs down to 10^2 CFU/mL can be achieved using sandwich arrangements accompanied by additional signal enhancing approaches [8–10], but such assays prolong to an hour or longer.

Plasma enhanced chemical vapor deposition (PECVD) is an ecological friendly, fast and efficient method for preparation of thin films with unique fine-tuned physical and chemical properties [11,12]. The combination of low-temperature processing with high reactivity makes PECVD very powerful because it enables the implementation of processes otherwise requiring very high temperatures or noxious and aggressive chemicals [13,14]. Plasma polymer (PP) films prepared by PECVD exhibit excellent adhesion to many different surfaces including gold [15,16], and PECVD is compatible with the gas-phase deposition of gold layer used in SPR and QCM sensors. In particular, the amine group providing PP films can be deposited in plasma discharges fed by various monomer vapors and they appear successful in preparation of biomaterials [17,18]. The most studied amine PP processes employ the

allylamine monomer. The films exhibit high hemocompatibility [19] and improved cell adhesion and proliferation as tested with fibroblasts [20,21]. Further step in eco-friendly plasma processing of reactive amine surfaces is the replacement of toxic allylamine with the relatively non-toxic cyclopropylamine (CPA). Besides, it can ensure a slightly higher retention of the functional groups in the obtained PP films [22].

Previously, we investigated how the plasma deposition conditions influenced the chemical composition and water stability of CPA PPs prepared in two different capacitively coupled plasma (CCP) reactors characterized by different ion energy flux towards growing film [23,24]. The films were also tested as matrix layers for the immobilization of biomolecules [25]. Although the films deposited in different reactors had similar chemical composition the differences in their structure were demonstrated for example by different water stability. It resulted in a different QCM immunosensing performance. The optimized CPA PP film was obtained in the low ion energy tubular reactor. It provided a stable baseline signal, good selectivity and high immunochemical response using either GA or sulfosuccinimidyl 4-(N-maleimidomethyl)cyclohexane-1-carboxylate (sulfo-SMCC) based immobilization procedures.

The sensitivity of immunoassays and immunosensors is governed by affinity of the chosen Ab towards the target antigen (Ag). However, the experimental set-up and the method for immobilization of the immunoreagents play significant role in the final performance. For this reason, novel approaches for immunolayer construction and efficient Ab (or Ag) immobilization need to be developed. The technique based on the CPA PP films seems very perspective but it needs a better understanding of the CPA PP behavior in liquids and convincing up-to-date examples of its applications. In this work, the stability and chemical reactions of the CPA PP films in solutions are studied in-depth followed by the demonstration of the practical potential of the films for the SPR and QCM immunosensing of *Salmonella*.

2. Experimental section

2.1. Chemicals and materials

Cyclopropylamine (98% purity, used without any further purification), glutaraldehyde (GA, 25% aqueous solution), human serum albumin, Staphylococcal protein A (SpA) and dimethyl pimelimidate (DMP) were purchased from Sigma Aldrich (USA). Sodium hydrogen phosphate, sodium dihydrogen phosphate and sodium chloride for the preparation of phosphate buffered saline (PBS, pH 7.4) were supplied from Penta (Czech Republic). Anti-HSA monoclonal Ab (clone AL01) was obtained from Exbio (Czech Republic). The detection of *Salmonella* was done using rabbit polyclonal Ab Serotec 8209-4006 (AbD Serotec, UK). Argon with purity of 99.998% was supplied by Messer (Czech Republic). Double-side polished single crystal silicon (c-Si) wafers (< 111 > , N-type phosphorus doped, resistance 0.5 Ωcm) from ON-SEMI (Czech Republic) were cut into 10×15 mm substrates. Round shaped QCM sensors (AT-cut, 14 mm in diameter, resonance frequency of 10 MHz) coated by Au with a Cr interlayer were purchased from Krystaly Hradec Králové (Czech Republic). MP-SPR (multi-parametric SPR) Navi gold sensors, SPR102 Au were purchased from BioNavis (Finland). All the substrates and sensors were cleaned by sonication in isopropanol (Penta, 99.8%) for 10 min All solutions were filtered through a 0.22 μm polyethersulfone membrane (Merck Millipore, Germany).

2.2. Plasma polymerization in tubular reactor

The plasma polymerization from CPA/Ar gas mixture was performed in pulsed radio frequency (13.56 MHz) CCP discharge described in details elsewhere [23]. The substrates (polished c-Si, QCM sensors and SPR chips) were cleaned in pulsed Ar discharge for 10 min prior to the deposition. Both, the Ar plasma cleaning and the polymerization,

were carried out at the pressure of 120 Pa with the on-time power of 20 W. The flow rate of Ar and CPA vapors were set to 28 and 0.3 sccm, respectively. All plasma processes (surface cleaning and CPA/Ar plasma polymerization) were carried out in square-pulsed mode with the pulse repetition frequency of 500 Hz and 33% duty cycle.

The utilized deposition conditions were selected as a compromise between sufficient nitrogen and especially NH_2 content in the resulting film and reasonably low thickness losses in liquid. The film provided a stable baseline, good selectivity and high response in previous study of the QCM immunosensor [25]. The biosensing experiments were carried out using 40 nm thick CPA PP films deposited on the gold electrodes of QCM and SPR. The atomic C:N:O composition ratio of this film was 77:20:3 as determined by X-ray photoelectron spectroscopy (XPS). The samples were stored 1–5 days at 4 °C prior to the immobilization of biomolecules. The films on Si substrates used for FT-IR analyses were thicker, 120 nm, but their composition varied only within the error of XPS (1–2 at. %). The amount of primary amine groups in the CPA PP was 1.3 at. %. Although the films exhibited 16% thickness loss after 24 h in water, further prolongation of the water contact did not change the film thickness.

2.3. Preparation of microorganism samples

Salmonella enterica subsp. *enterica* serovar Typhimurium (ATCC 14028) was obtained from Czech Collection of Microorganisms. For the cultivation, 100 μL of the stock solution was inoculated into 25 mL of low salt LB broth (Duchefa Biochemie, Netherlands) in Erlenmeyer flask, the incubation was done aerobically overnight at 37 °C. The obtained bacterial suspension was centrifuged twice for 10 min at 6800 g and resuspended in PBS. The samples of bacteria were heat-treated for 40 min at 80 °C with mild shaking (400 rpm) using Thermomixer Comfort (Eppendorf, Germany). The microbe concentrations were determined by measurement of optical density at 600 nm (OD_{600}) with calibration using the McFarland scale. The concentrations of heat-treated bacteria are expressed as CFU/mL corresponding to the native cell concentration before the treatment [26].

2.4. SPR immunosensing

The SPR studies were carried out using the MP-SPR Navi gold sensors SPR102 Au and SPR Navi 210 A system from BioNavis (Finland). The instrument is equipped with a built-in degasser, automated valves and syringe pumps. MP-SPR enables a wide angular scan mode (40-78°) that records a complete SPR curve with absolute angle information or the fixed-angle mode which provides faster response times. PBS was used as a running buffer with a flow rate of 20 μL/min. The injections of different solutions were programmed using SPR-Navi software. The flow cell consists of two channels: binding (with immobilized Ab) and reference (modified in the same way as binding but without the Ab). The changes of resonant angle due to the interactions on the sensor surface were measured at two wavelengths: 670 and 785 nm. For the evaluation, the 670 nm data were used due to the higher sensitivity. The position (angle) of surface plasmon resonance peak was determined using the build-in centroid fitting function.

2.4.1. Glutaraldehyde-based immobilization method

The surface of SPR chip coated with 40 nm thick CPA PP was activated with GA (droplet of 3% solution in PBS, 1 h at room temperature) providing free aldehyde groups. It is known that GA can react with several functional groups of proteins, such as amine, thiol, phenol, and imidazole [27]. The activation was carried out off-line (outside of the SPR system) in order to prevent binding of GA to the tubing. The chip was then washed in PBS and sterile water, dried and inserted into BioNavis system. At first, each chip was maintained in PBS (flow rate 20 μL/min) for 40 min to reach stable baseline. Afterwards, the solution of Ab (either anti-HSA AL-01 or anti-*Salmonella* Ab Serotec) in concentration of 50 μg/mL or 100 μg/mL was

184

injected to the binding channel at the flow rate of 4 μL/min for 54 min. In the reference channel, only PBS was flowing at the same rate (parallel injection mode). Free reactive groups were deactivated by applying 2 mg/mL solution of BSA in PBS at 10 μL/min for 20 min to both channels (serial injection mode).

2.4.2. Protein A based immobilization method

The GA-modified chip was inserted into the system and, after the baseline establishment, the 100 μg/mL solution of Protein A was injected into both the channels at 4 μL/min for 54 min. Afterwards, 2 mg/mL BSA was applied for 20 min to both the channels at the flow rate of 10 μL/min to deactivate free aldehyde groups. Next, the Ab solution at the concentration of 100 μg/mL (AL-01 or Ab Serotec) was injected into the binding channel at 4 μL/min for 54 min (PBS was flowing through the reference channel). Finally, the fresh 20 mM DMP solution was injected at 10 μL/min for 20 min to stabilize the complex between the Protein A and Ab.

After the immobilization of Ab and blocking of non-specific sites with BSA the immunosensing was carried out using the solutions of either HSA or *Salmonella* at the flow rate of 20 μL/min for 10 min each followed by 10 min dissociation. The solution of 10 mM NaOH was used as a regeneration agent at 20 μL/min for 2 min.

2.5. QCM immunosensing

QCM sensors with the CPA plasma polymer, 40 nm in thickness, were immersed overnight in PBS, washed with water, dried and GA activation (3% in PBS, 1 h, r.t.) was applied. Then the Ab Serotec was covalently bound (100 μg/mL in PBS, 18 h at 4 °C). The sensor surface blocking was done using BSA (200 μg/mL, 20 min, r.t.). After each step, the sensors were thoroughly washed with deionized water, allowed to dry and the resonant frequency was measured. Standard deviations of the frequency measurements were calculated from the series of three QCM sensors characterized for each procedure.

The bacteria detection experiments involved a binding interaction between the Ab Serotec immobilized on the QCM electrode and the suspension of *Salmonella* as Ag. The QCM crystals were placed in a flow-through cell (design and construction by Dr. Karel Lacina). The measurements were performed using the QCM Analyzer (KEVA, Czech Republic) that served as both the oscillator and the frequency counter. The flow of solutions was driven by the milliGAT pump (Global FIA, USA) and a selection valve (Valco Instruments, USA). The whole system was controlled via the in-house developed software LabTools that allowed fully automated operation. PBS was used as a running buffer with a flow rate of 40 μL/min. After baseline stabilization, the samples of *Salmonella* were injected for 10 min followed by 10 min of dissociation phase.

2.6. Characterization of plasma polymer thin films

Chemistry of films on the IR transparent c-Si substrates was assessed by Fourier transformed infrared (FT-IR) spectroscopy using the Bruker Vertex 80v spectrophotometer. The transmittance measurements were performed with a parallel beam transmittance accessory in the spectral range 370–7500 cm^{-1} (resolution 4 cm^{-1}, 500 scans) at 2.5 mbar. The FT-IR spectra are shown as the ratio of transmittance of the film on Si substrate and the transmittance of bare Si in the range 1400–3700 cm^{-1} only because no significant absorption peaks belonging to the films were identified outside this range and the identification of weak absorption peaks below 1400 cm^{-1} was difficult due to the strong absorption peaks in c-Si that could not be reliably subtracted by this procedure.

The ellipsometric data were measured in the spectral region of 0.6–6.5 eV using a phase modulated Jobin Yvon UVISEL ellipsometer at the incidence angle of 65°. The optical data obtained for as-deposited films on Si, dried films on Si after immersion in PBS and after reaction

with GA were fitted by the model of one homogeneous non-uniform film on Si substrate using a PJDOS dispersion model for SiO$_2$-like materials [26], assuming a wedge-shaped non-uniformity [28]. The following parameters were fitted: thickness, thickness non-uniformity, and dispersion model parameters describing the electronic structure. The agreement between the data and the fit achieved for all the as-deposited films revealed that the assumption of the homogeneous film in the direction perpendicular to the substrate was valid. After immersion in PBS, the films exhibited defects such as surface roughness or inhomogeneity but the determination of the film thickness using the above mentioned structural model was still possible with a sufficient precision.

The properties of SPR chips with CPA PP films after individual sensor preparation steps and after binding of bacteria were studied using atomic force microscopy (AFM). Dimension FastScan Bio (Bruker, USA) with FastScan-A probe was used to scan the surface in dry state after washing with deionized water, the data was evaluated in the software Gwyddion.

3. Results and discussion

3.1. Understanding the stability of CPA PP for effective use in SPR sensing

The SPR sensors with the optimized CPA PP film activated by GA were studied at first with the model pair, Ab AL-01 and HSA, because this pair provides a reliable immunocomplex under different conditions and assay formats [29]. Unlike for the QCM immunosensing [25], a high drift of the baseline limited the sensitivity of SPR assays (Fig. S1A in the Supporting information). The reason for such significantly different results of QCM and SPR experiments is seen in the vastly different time of film immersion in liquids. In the case of QCM, the films were in contact with the solution of Ab in PBS for 18 h before the next step was carried out. When the same procedure was applied to the SPR chips the baseline was stable but the sensitivity was twice lower (Fig. S1B in the Supporting information and [30]). These results opened a question about the behavior of the CPA plasma polymers (and other amine-PPs) in the PBS solution and the answer was crucial for the improvement of the SPR immunosensing procedure.

The amine-PPs are polyfunctional compounds with a high level of unsaturation degree [31–33]. In the FT-IR spectra of the as-deposited CPA PP (Fig. 1A) the N−H stretching (3350 cm^{-1}) and N−H bending (1650 cm^{-1}) signals were observed, which can originate from amine (−NH$_2$, > NH), imine (−CH=NH) and enamine (−CH=CH−NH$_2$) groups. In the region of triple bonds, the signals at 2240 and 2190 cm^{-1} corresponded to nitrile, isonitrile and different unsaturated structures (−C≡N, −$^+$N≡C−, −N=C=N−, −C=C=N− or −C≡C−). All these groups can undergo the hydrolysis in PBS.

Since the films may not be always used for the biosensing experiments immediately after the deposition, two types of the films were examined for the stability in PBS: as-deposited and two weeks old surface stored in air (room temperature). The long term stability of the films in air was investigated for 2 months old CPA PP film. This film exhibited +1% thickness change and increase of C=O and N−H stretching signals (Fig. 1A). It leads to a conclusion that, in the process of aging of the CPA PP films at air, the hydrolysis of nitriles and isonitriles plays the major role and it does not cause any thickness losses. Different thickness losses were observed for as-deposited and two weeks old films after an immersion in PBS for short time (Fig. 1B). However, the thickness loss was about 14% for both the films after 18 h of immersion and no further significant changes in thickness were recorded for a longer immersion time. The film thickness losses for the long-term immersion in PBS were comparable to the losses observed after long-term immersion in water [23].

The changes in thickness were accompanied by an increase of C=O and decrease of C−H, C=C, −C≡N, −$^+$N≡C−, −NH$_2$, > NH, −CH=NH, −CH=CH−NH$_2$ absorption in FT-IR spectra (Fig. 1A). No hydroxyl
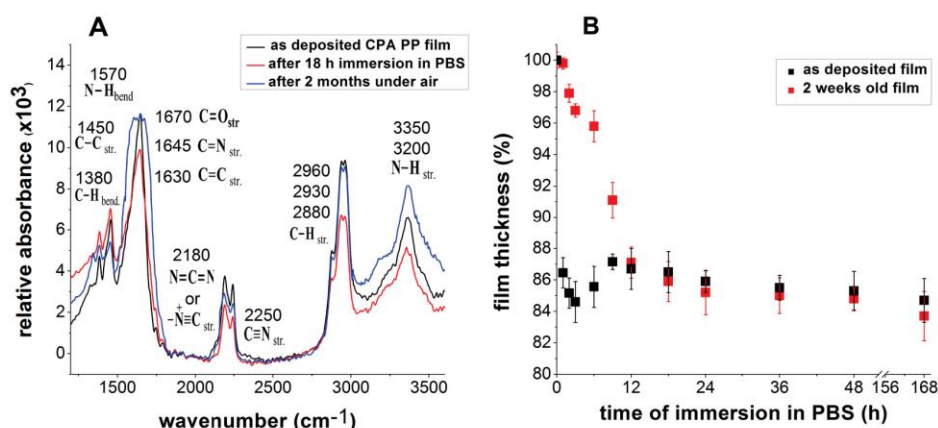
Fig. 1. Stability and aging of the CPA PP films: (A) FT-IR spectra of as-deposited film (black), after 18 h immersion in PBS (red) and after 2 months under air (blue); (B) Thickness losses of the CPA PP films after different times of immersion in PBS measured by ellipsometry, for as deposited film (black) and 2 weeks old film (red) (For interpretation of the references to colour in this figure legend, the reader is referred to the web version of this article).

absorption was observed in the FT-IR spectra even after 1 week of immersion. The changes taking place during the immersions in water and aqueous buffer solutions can be attributed to several mechanisms, protonation of amines and hydrolysis of enamines, imines and nitriles, as discussed in Fig. S2 of the Supporting information. The hydrolysis of nitriles (Fig. S2D) evidenced by the FT-IR in the region 2180–2250 cm^{-1} cannot cause the observed thickness loss (up to 17%). In order to explain it the hydrolysis of enamines or imines (Figs. S2B and S2C) has to be taken into account. The increased IR absorption in the region of C=O can be explain by all three mechanisms of hydrolysis whereas the hydrolysis of amines has the opposite effect on the N−H absorption than the hydrolysis of enamines and imines. The activation of CPA PP by GA did not prevent the reactions of the film with water and buffer ions and, therefore, the large drift of the baseline was observed during the SPR immunosensing after the GA activation of the fresh as-deposited film (Fig. S1A).

3.2. Optimized SPR immunosensor tested with a model pair, AL-01 and HSA

Based on the understanding of the CPA PP stabilization in PBS, the SPR chips with CPA PPs were immersed into PBS overnight (18 h, r.t.), prior to the GA activation. Indeed, this procedure significantly improved the baseline stability (Fig. S1B).

The thickness increase of 5–7 nm was recorded by ellipsometry after 1 h reaction of the CPA PP film with the GA solution. The CPA PP binds the GA and GA-oligomers through primary and secondary amines forming a Schiff base or enamine. Imines (enamines) of the CPA PP participate on the nucleophile exchange with the aldehydes forming aldehydes or ketones at the surface. Nitriles (isonitriles) undergo hydrolysis forming amides, which are active in nucleophile addition of carbonyls [33]. Then, further aldol condensation of the newly formed free reactive aldehydes occurs (Fig. 2).

The structure 1 in Fig. 2 represents the average structure of the unsaturated polymerized GA in the aqueous solution [34]. GA-oligomers participate in the same reactions as GA (presented in Fig. 2) and also on the Michael-type reactions (nucleophile addition to the double bond of α,β-unsaturated compound) [35], which would also contribute to the desired result – free reactive aldehydes on the surface.

Aldol reactions generally require catalysis by H$^+$ or OH$^-$. It was shown that nitrogen plasma-treated surfaces are strongly basic environment due to the presence of amines and imines and therefore the catalysts are not necessary for aldol reactions [33]. Similarly, it was observed that the CPA PP surface was active to the GA binding and the

aldol condensation happened during 1 h to form 5–7 nm thick layer of poly-GA. It was shown by Babacan et al. that longer times of reaction of the surface with the GA lead to less active poly-GA with higher cross-linkage level (less free reactive aldehyde groups) [36].

The CPA PP film on the surface of a gold SPR chip was further studied by AFM. The AFM enabled to observe individual particles of the evaporated gold (Fig. 3A). The as-deposited film closely followed the topography of the substrate (Fig. 3B), in agreement with our previous scanning electron microscopy (SEM) results [23]. After the 18 h of washing in PBS, inhomogeneities increasing the surface roughness were formed due to a partial hydrolysis of the PP (Fig. 3C). The observed smoothing of the surface after the activation by GA (Fig. 3D) is explained by a growth of poly-GA film with the thickness of 5–7 nm, as determined by ellipsometry.

The CPA PP film activated by GA was successfully used for the immobilization of the Ab observed as ΔR of 200 mdeg in the binding channel (Fig. S3). Then, the blocking agent – BSA was applied to both the channels (ΔR of 100 mdeg in the binding channel and 150 mdeg in the reference channel) and the reactions with the Ag (HSA) solutions were followed with the SPR angular scan mode. The aim of the work was to develop procedure for multiple-usage of immunosensors based on the CPA PP. The optimal regeneration agent, 10 mM NaOH solution, was found to dissociate the Ab-Ag complex without losing the immobilized Ab from the chip surface. In all the measurements, the drift of the baseline disappeared after the first or second regeneration. In average, each sensor allowed 7–9 regenerations (Fig. S4) without activity losses. Each test including antigen binding, dissociation (could be shortened to about 2 min) and regeneration phase took 35 min, the analysis time itself was only 10 min. The sensorgrams obtained for different concentrations of HSA with one SPR chip regenerated after each measurements are shown in Fig. 4. Starting from the HSA concentration of 20 µg/mL the saturation character of the response became evident.

As an alternative method of the SPR detection discussed above, the fixed angle mode was tested. This mode allowed obtaining faster response (more data points per second) than the angular scan mode, during which the whole resonance spectrum was measured. However, the experimental data contained more noise (Fig. S5) than the data from the angular scan mode that employed the fitting of plasmon resonance peak.

3.3. SPR immunosensing of Salmonella

The sensor with Ab Serotec immobilized directly via GA was used

186
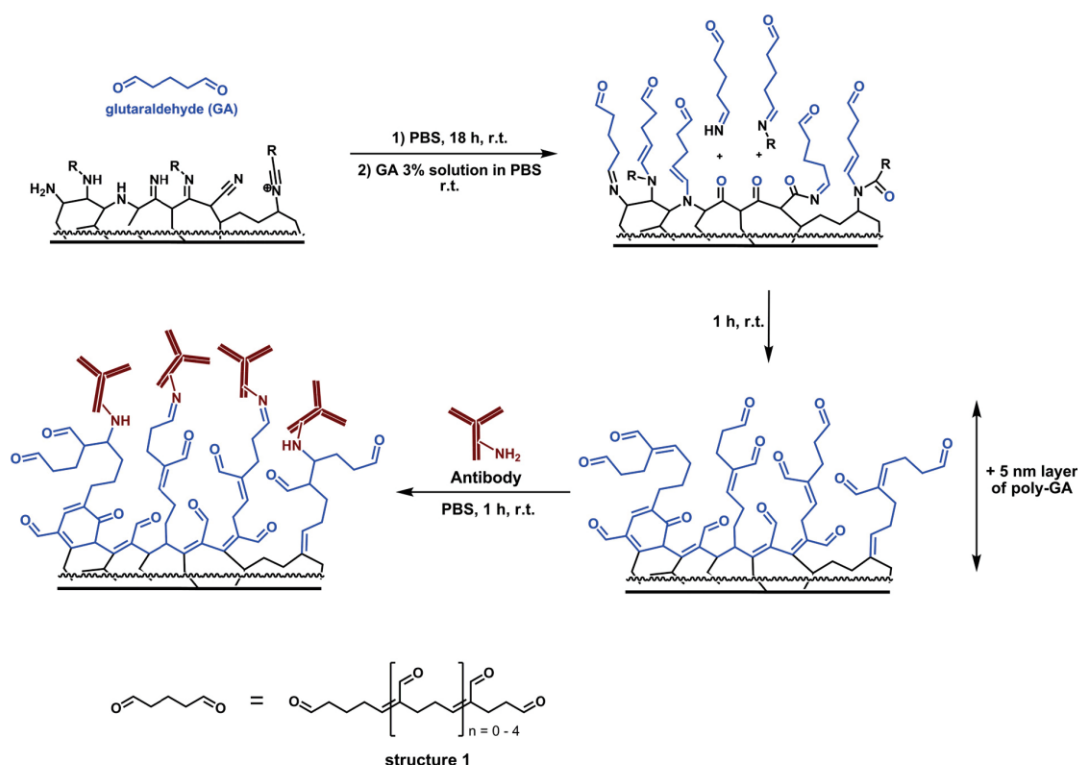
Fig. 2. The scheme of Ab immobilization approach utilizing the GA activation of the CPA PP film. The structure 1 represents the average structure of the unsaturated polymerized GA in the commercial aqueous solution.

for the detection of the heat-treated *Salmonella* cells. The regeneration with NaOH (discussed in Section 3.2) allowed reproducible detection of more than 7 samples with a single sensor. No signal changes were observed for blank (PBS) injections. The sensorgrams of *Salmonella* binding are shown in Fig. 5.

The dependence of immunosensor response on the bacteria concentration exhibited a saturation character and, therefore, the linearization was achieved by plotting the concentration in logarithmic scale [2]. The LOD of 10^5 CFU/mL was achieved with the analysis time of 10 min. A wide linear response allowed analysis of *Salmonella* concentrations between 10^5 and 10^8 CFU/mL. The AFM scans of the measurement and reference channels after binding *Salmonella* (10^7 CFU/mL) are shown in Fig. 6. The AFM confirmed the specific binding of microbial cells in the measurement channel. The blank channel contained only small fragments non-specifically bound to the sample matrix.

The immobilization of Ab via Protein A was also tested for the detection of both HSA and *Salmonella*. Protein A provides oriented immobilization of antibodies because it binds their Fc fragment [37]. Nevertheless, the amount of immobilized Ab Serotec was significantly lower than in the case of GA-based immobilization method (approximately 25%) and the complex between Protein A and Ab was not stable enough for the detection, despite the crosslinking with DMP. The measurements had a higher level of noise and the regeneration was practically impossible due to the loss of Ab. Therefore, the immobilization of Ab directly via GA is preferred compared to the immobilization method based on Protein A.

3.4. QCM immunosensing of Salmonella

The binding interactions between *Salmonela* and the anti-*Salmonella*

Ab Serotec were studied also with QCM because it allowed to follow the mass changes during all the individual steps. The QCM resonance frequency, i.e. the mass changes, was measured in a dry state after washing with deionized water (Table 1). The measurements were performed with 10 min binding phase, the same as in the case of SPR. Separately, the reference crystal with immobilized GA and blocking agent (BSA) but without anti-*Salmonella* Ab was measured. The regeneration was carried out with 10 mM NaOH, thus allowing several (7–9) experiments with a single sensor. The results of the QCM detection are shown in Fig. 7.

The LOD of 10^5 CFU/mL was achieved, which is comparable to widely used ELISA methods [3] and other methods of label-free immunosensing using self-assembled monolayers (SAMs) [38–41]. Only very small signal changes were observed in the case of QCM sensor not modified by the Ab, which confirms the high specificity of the interaction. The comparable LOD in case of label-free detection of bacteria using SPR and QCM methods is in agreement with previously published results [42].

4. Conclusions

Pulsed plasma polymerization of CPA is a fast and eco-friendly method for the preparation of reactive polyfunctional nitrogen-containing films. The investigation of the CPA PP films in aqueous media showed that the long-term reactivity of the CPA PP is stabilized by 18 h immersion in buffer (PBS) prior to the GA activation. Therefore, this work leads to a novel approach replacing the preparation of self-assembled monolayers on the gold surfaces of SPR and QCM sensors by the procedure combining the plasma polymerization of CPA with the immersion in PBS. The FT-IR and ellipsometry revealed the decrease of amine content and the thickness loss up to 17% after the CPA PP

187
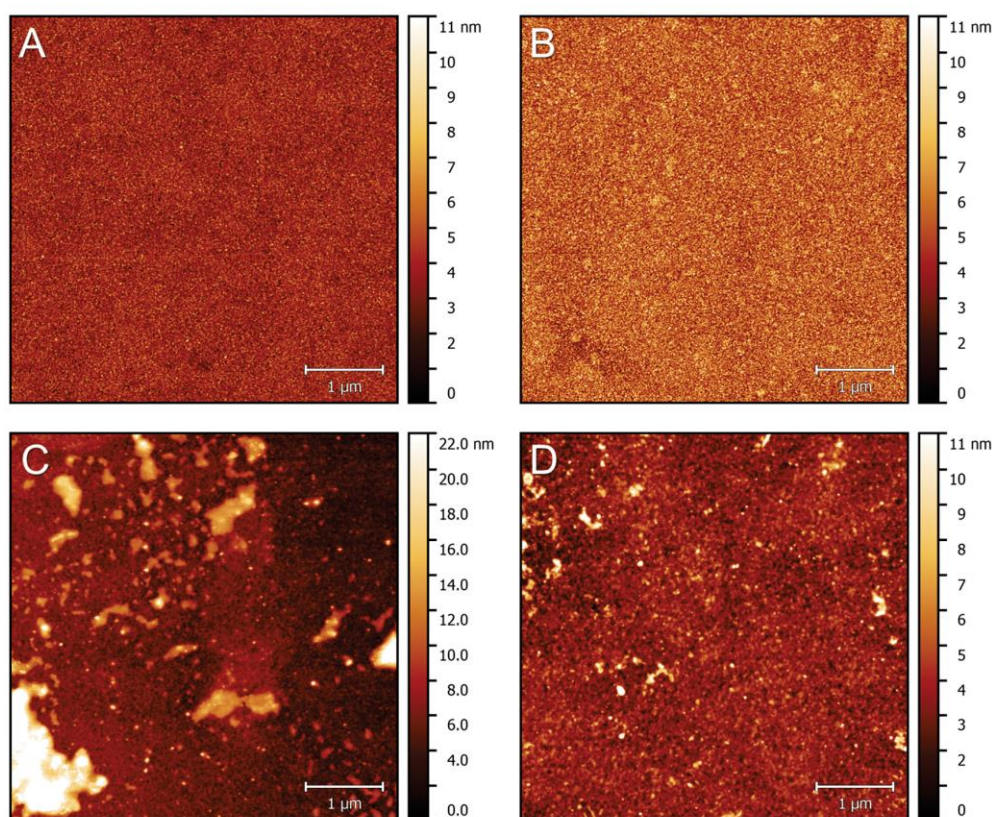
Fig. 3. AFM scans (height signal) of the CPA PP films on the surface of gold SPR chip after individual sensor modification steps: (A) bare gold; (B) as-deposited CPA PP film; (C) CPA PP film after 18 h immersion in PBS; (D) CPA PP activated by GA.
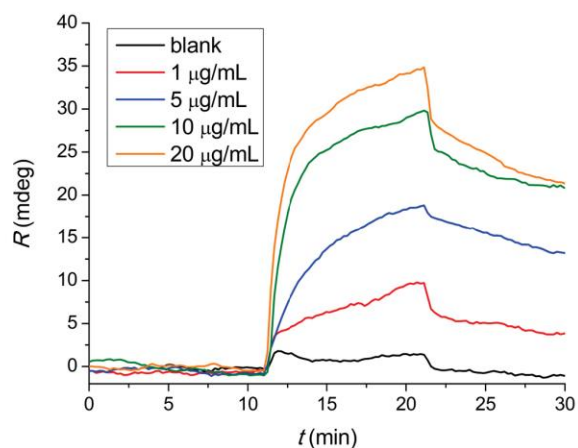
Fig. 4. Binding interactions between immobilized anti-HSA Ab AL-01 and solutions of HSA antigen measured by SPR in angular scan mode. 10 min zone of HSA Ag was followed by 10 min of dissociation in PBS. Each HSA concentration was applied after regeneration with 10 mM NaOH.

Fig. 5. Binding interaction (10 min) between immobilized anti-*Salmonella* Ab Serotec and different concentration of *Salmonella* (concentrations in CFU/mL), followed by 10 min of dissociation in PBS. Changes of differential response ΔR are shown together with the calibration curve in the inset graph.

immersion in PBS. These results can be explained by the hydrolysis of enamines or imines in the CPA PP whereas the chemical changes without a thickness loss are caused by the hydrolysis of nitriles. The GA activation of the CPA PP surface carried out for 1 h led to the growth of 5–7 nm thick film of GA and GA-oligomers on which the antibodies,

anti-HSA Ab AL01 or anti-*Salmonella* Ab Serotec, were immobilized for the detection of HSA or *Salmonella* bacteria, respectively. The sensor regeneration with 10 mM NaOH was successful allowing several measurements (7–9) with a single sensor. A linear response was obtained in
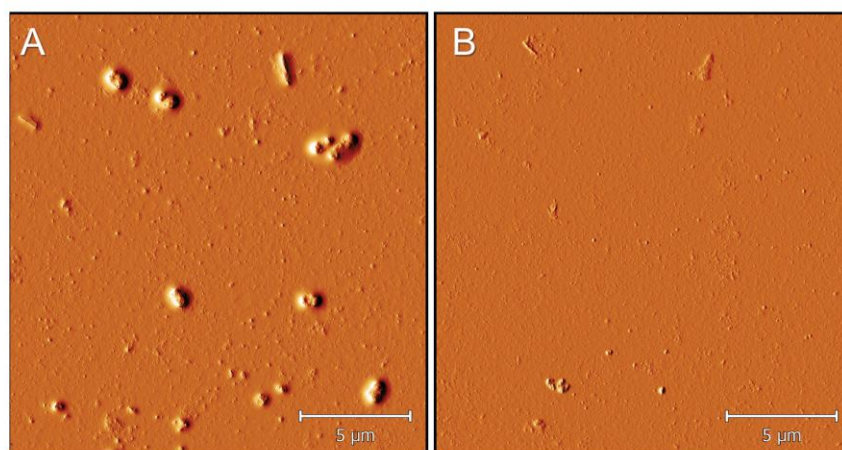
Fig. 6. AFM scans (error signal) of the CPA PP film on surface of SPR chip after the interaction with *Salmonella* (10^7 CFU/mL): (A) Ab modified surface; (B) reference channel without immobilized Ab.

Table 1
Changes of the QCM resonance frequency after individual steps of the immobilization procedure, i.e. after the deposition of plasma polymer, overnight immersion in PBS, activation of plasma polymer with GA, immobilization of antibody and blocking by BSA. The measurements were carried out in a dry state after washing.

Procedure step:	plasma polymerization	immersion in PBS	GA	Ab Serotec	BSA
Frequency changes $\Delta f = f_2 - f_1$ (Hz) Binding crystal	-1645 ± 21	$+350 \pm 14$	-417 ± 10	-180 ± 7	-68 ± 8
Reference crystal	-1627 ± 23	$+361 \pm 12$	-422 ± 13	–	-160 ± 6
Mass changes Δm (ng) Binding crystal	$+1428 \pm 18$	-304 ± 12	$+362 \pm 9$	$+156 \pm 6$	$+59 \pm 7$
Reference crystal	$+1412 \pm 20$	-313 ± 11	$+366 \pm 11$	–	$+139 \pm 5$
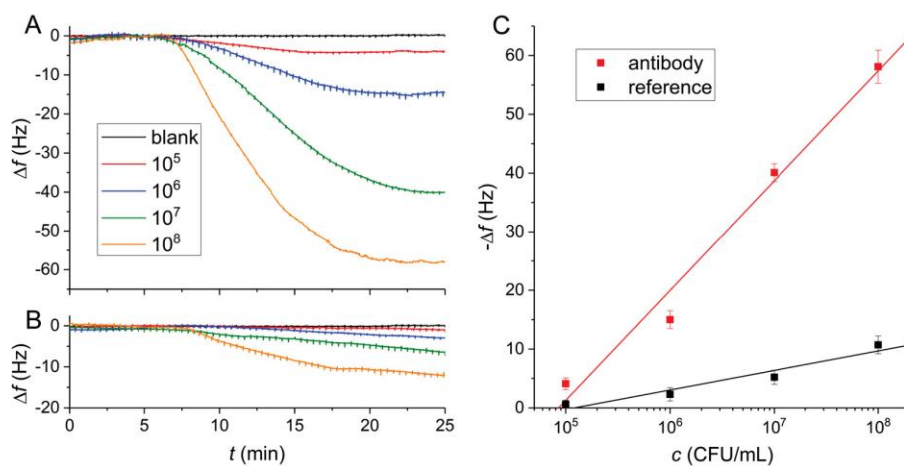
Fig. 7. (A) QCM detection of *Salmonella* using CPA PP modified chip and Ab Serotec immobilized via GA. The concentrations are in CFU/mL. (B) Reference sensor (without immobilized Ab), (C) Calibration curve.

the wide range 1–20 µg/mL for HSA and 10^5–10^8 CFU/mL for *Salmonella*. The LOD was comparable to the widely used ELISA methods and other methods of label-free immunosensing using SAMs. The achieved results confirmed that the developed methodology for the grafting of biomolecules on the gold surfaces have great potential for biosensing applications focused on protein markers as well as microbial cells.

Acknowledgements

Appendix A. Supplementary data

Supplementary material related to this article can be found, in the online version, at doi:https://doi.org/10.1016/j.snb.2018.08.055.

References

[1] R.L. Scharff, Economic burden from health losses due to foodborne illness in the United States, J. Food Prot. 75 (2012) 123–131, https://doi.org/10.4315/0362-028X.JFP-11-058.

[2] Z. Farka, D. Kovář, P. Skládal, Rapid detection of microorganisms based on active and passive modes of QCM, Sensors (Switzerland) 15 (2015) 79–92, https://doi.org/10.3390/s150100079.

[3] B.S.M. Mahmoud (Ed.), Salmonella – A Dangerous Foodborne Pathogen, IntechOpen, 2012, , https://doi.org/10.5772/1308.

[4] J.W.-F. Law, N.-S.Ab Mutalib, K.-G. Chan, L.-H. Lee, Rapid methods for the detection of foodborne bacterial pathogens: principles, applications, advantages and limitations, Front. Microbiol. 5 (2015) 1–20, https://doi.org/10.3389/fmicb.2014.00770.

[5] Y. Wang, Z. Ye, C. Si, Y. Ying, Subtractive inhibition assay for the detection of E. coli O157:H7 using surface plasmon resonance, Sensors 11 (2011) 2728–2739, https://doi.org/10.3390/s110302728.

[6] H. Vaisocherová-Lísalová, I. Víšová, M. Ermini, T. Špringer, X. Song, J. Mrázek, J. Lamačová, N. Scott Lynn, P. Šedivák, J. Homola, Low-fouling surface plasmon resonance biosensor for multi-step detection of foodborne bacterial pathogens in complex food samples, Biosens. Bioelectron. 80 (2016) 84–90, https://doi.org/10.1016/j.bios.2016.01.040.

[7] X.L. Su, Y. Li, A QCM immunosensor for Salmonella detection with simultaneous measurements of resonant frequency and motional resistance, Biosens. Bioelectron. 21 (2005) 840–848, https://doi.org/10.1016/j.bios.2005.01.021.

[8] F. Salam, Y. Uludag, I.E. Tothill, Real-time and sensitive detection of Salmonella Typhimurium using an automated quartz crystal microbalance (QCM) instrument with nanoparticles amplification, Talanta 115 (2013) 761–767, https://doi.org/10.1016/j.talanta.2013.06.034.

[9] Z. Farka, T. Juřík, M. Pastucha, P. Skládal, Enzymatic precipitation enhanced surface plasmon resonance immunosensor for the detection of Salmonella in powdered milk, Anal. Chem. 88 (2016) 11830–11836, https://doi.org/10.1021/acs.analchem.6b03511.

[10] N.A. Masdor, Z. Altintas, I.E. Tothill, Sensitive detection of Campylobacter jejuni using nanoparticles enhanced QCM sensor, Biosens. Bioelectron. 78 (2016) 328–336, https://doi.org/10.1016/j.bios.2015.11.033.

[11] A. Kuzminova, A. Shelemin, O. Kylián, M. Petr, J. Kratochvíl, P. Solař, H. Biederman, From super-hydrophilic to super-hydrophobic surfaces using plasma polymerization combined with gas aggregation source of nanoparticles, Vacuum 110 (2014) 58–61, https://doi.org/10.1016/j.vacuum.2014.08.014.

[12] S. Subhash Latthe, A. Basavraj Gurav, C. Shridhar Maruti, R. Shrikant Vhatkar, Recent progress in preparation of superhydrophobic surfaces: a review, J. Surf. Eng. Mater. Adv. Technol. 2 (2012) 76–94, https://doi.org/10.4236/jsemat.2012.22014.

[13] L. O'Neill, A. O'Hare, A. Goodwin, Method for coating a substrate using plasma, US 8,178,168 B2, 2006.

[14] A.J.C. Eun, L. Huang, F.T. Chew, S.F.Y. Li, S.M. Wong, Detection of two orchid viruses using quartz crystal microbalance (QCM) immunosensors, J. Virol. Methods 99 (2002) 71–79, https://doi.org/10.1016/S0166-0934(01)00382-2.

[15] C.E. Nwankire, A. Venkatanarayanan, R.J. Forster, J. Ducrée, Enhanced gold-to-polymer adhesion for integrated electrochemical biosensing on cost-efficient lab-on-a-chip cartridges, 19th Int. Conf. Miniaturized Syst. Chem. Life Sci. (2015) 1707–1709.

[16] R. Förch, Tutorial review: surface modification and adhesion, in: R. Förch, H. Schönherr, A.T.A. Jenkins (Eds.), Design: Applications in Bioscienceand Nanotechnology, Wiley, 2009.

[17] G. Aziz, N. De Geyter, R. Morent, 2 − Incorporation of primary amines via plasma technology on biomaterials, in: P. Andrea Serra (Ed.), Advances in Bioengineering, IntechOpen, 2015, pp. 21–48, , https://doi.org/10.5772/59691.

[18] P. Cools, R. Morent, N. De Geyter, Plasma modified textiles for biomedical applications, Adv. Bioeng. (2015) 1–32, https://doi.org/10.5772/59770.

[19] Z. Yang, J. Wang, R. Luo, M. Maitz, F. Jing, H. Sun, N. Huang, The covalent immobilization of heparin to pulsed-plasma polymeric allylamine films on 316L stainless steel and the resulting effects on hemocompatibility, Biomaterials 31 (2010) 2072–2083, https://doi.org/10.1016/j.biomaterials.2009.11.091.

[20] H. Wen-Juan, X. Fen-Yan, C. Qiang, W. Jing, Amine-containing film deposited in pulsed dielectric barrier discharge at a high pressure and its cell adsorption behaviours, Chin. Phys. B 18 (2009) 1276, https://doi.org/10.1088/1674-1056/18/3/073.

[21] T.B. Ren, T. Weigel, T. Groth, A. Lendlein, Microwave plasma surface modification of silicone elastomer with Allylamine for improvement of biocompatibility, J. Biomed. Mater. Res. – Part A 86 (2008) 209–219, https://doi.org/10.1002/jbm.a.31508.

[22] L. Denis, P. Marsal, Y. Olivier, T. Godfroid, R. Lazzaroni, M. Hecq, J. Cornil, R. Snyders, Deposition of functional organic thin films by pulsed plasma polymerization: a joint theoretical and experimental study, Plasma Process. Polym. 7 (2009) 172–181, https://doi.org/10.1002/ppap.200900131.

[23] A. Manakhov, L. Zajíčková, M. Eliáš, J. Čechal, J. Polčák, J. Hnilica, Š. Bittnerová, D. Nečas, Optimization of cyclopropylamine plasma polymerization toward enhanced layer stability in contact with water, Plasma Process. Polym. 11 (2014) 532–544, https://doi.org/10.1002/ppap.201300177.

[24] A. Manakhov, M. Landová, J. Medalová, M. Michlíček, J. Polčák, D. Nečas, L. Zajíčková, Cyclopropylamine plasma polymers for increased cell adhesion and growth, Plasma Process. Polym. 14 (2017) 1–12, https://doi.org/10.1002/ppap.201600123.

[25] E. Makhneva, A. Manakhov, P. Skládal, L. Zajíčková, Development of effective QCM biosensors by cyclopropylamine plasma polymerization and antibody immobilization using cross-linking reactions, Surf. Coat. Technol. 290 (2016) 116–123, https://doi.org/10.1016/j.surfcoat.2015.09.035.

[26] Z. Farka, T. Juřík, M. Pastucha, D. Kovář, K. Lacina, P. Skládal, Rapid immunosensing of Salmonella Typhimurium using electrochemical impedance spectroscopy: the effect of sample treatment, Electroanalysis 28 (2016) 1–8, https://doi.org/10.1002/elan.201600093.

[27] A.J. Habeeb, R. Hiramoto, Reaction of proteins with glutaraldehyde, Arch. Biochem. Biophys. 126 (1968) 16–26, https://doi.org/10.1016/0003-9861(68)90554-7.

[28] D. Nečas, I. Ohlídal, D. Franta, Variable-angle spectroscopic ellipsometry of considerably non-uniform thin films, J. Opt. 13 (2011) 85705, https://doi.org/10.1088/2040-8978/13/8/085705.

[29] I. Navrátilová, P. Skládal, V. Viklický, Development of piezoelectric immunosensors for measurement of albuminuria, Talanta 55 (2001) 831–839, https://doi.org/10.1016/S0039-9140(01)00512-4.

[30] E. Makhneva, Z. Farka, P. Skládal, L. Zajíčková, Brno, Czech Repub.Conference Proceedings, Proc. 8th Int. Conf. Nanomater. - Res. Appl. (Nanocon)2016, Conference Proceedings, Proc. 8th Int. Conf. Nanomater. - Res. Appl. (Nanocon) (2016) 395–401.

[31] A. Shard, J. Whittle, A. Beck, P. Brookes, N. Bullett, R. Talib, A. Mistry, D. Barton, S. McArthur, A NEXAFS examination of unsaturation in plasma polymers of allylamine and propylamine, J. Phys. Chem. B 108 (2004) 12472–12480, https://doi.org/10.1021/jp048250f.

[32] K.S. Siow, L. Britcher, S. Kumar, H.J. Griesser, Plasma methods for the generation of chemically reactive surfaces for biomolecule immobilization and cell colonization – a review, Plasma Process. Polym. 3 (2006) 392–418, https://doi.org/10.1002/ppap.200600021.

[33] C.P. Klages, Z. Khosravi, A. Hinze, Some remarks on chemical derivatization of polymer surfaces after exposure to nitrogen-containing plasmas, Plasma Process. Polym. 10 (2013) 307–312, https://doi.org/10.1002/ppap.201200142.

[34] I. Migneault, C. Dartiguenave, M.J. Bertrand, K.C. Waldron, Glutaraldehyde: behavior in aqueous solution, reaction with proteins, and application to enzyme crosslinking, Biotechniques 37 (2004) 790–802, https://doi.org/10.2144/3705A0790.

[35] F.M. Richards, J.R. Knowles, Glutaraldehyde as a protein cross-linkage reagent, J. Mol. Biol. 37 (1968) 231–233, https://doi.org/10.1016/0022-2836(68)90086-7.

190

[36] S. Babacan, P. Pivarnik, S. Letcher, A.G. Rand, Evaluation of antibody im-
mobilization methods for piezoelectric biosensor application, Biosens. Bioelectron.
15 (2000) 615–621, https://doi.org/10.1016/S0956-5663(00)00115-9.

[37] C.P. Johnson, I.E. Jensen, A. Prakasam, R. Vijayendran, D. Leckband, Engineered
protein A for the orientational control of immobilized proteins, Bioconjug. Chem.
14 (2003) 974–978, https://doi.org/10.1021/bc034063t.

[38] R. Robelek, Surface plasmon resonance sensors in cell biology: basics and appli-
cation, Bioanal. Rev. 1 (2009) 57–72, https://doi.org/10.1007/s12566-009-0005-y.

[39] J.R. Son, G. Kim, A. Kothapalli, M.T. Morgan, D. Ess, Detection of *Salmonella* en-
teritidis using a miniature optical surface plasmon resonance biosensor, J. Phys.
Conf. Ser. 61 (2007) 1086–1090, https://doi.org/10.1088/1742-6596/61/1/215.

[40] M. Farré, L. Kantiani, D. Barceló, Microfluidic Devices: Biosensors, (2012), https://
doi.org/10.1016/B978-0-12-384862-8.00007-8.

[41] G.C.A.M. Bokken, R.J. Corbee, F. Van Knapen, A.A. Bergwerff, Immunochemical
detection of Salmonella group B, D and E using an optical surface plasmon re-
sonance biosensor, FEMS Microbiol. Lett. 222 (2003) 75–82, https://doi.org/10.
1016/S0378-1097(03)00250-7.

[42] Z. Farka, D. Kovář, J. Přibyl, P. Skládal, Piezoelectric and surface plasmon re-
sonance biosensors for Bacillus atrophaeus spores, Int. J. Electrochem. Sci. 8 (2013)
100–112.

Ekaterina Makhneva graduated from Novosibirsk State University with M.Sc. in Organic Chemistry in 2012. She worked as a researcher in the Laboratory of Medicinal Chemistry at NIOCH SB RAS (Russia) and started her Ph.D. study in 2014 at the Masaryk University (Brno, Czechia) under the supervision of Lenka Zajíčková. In 2018, she received Ph.D. in Advanced Materials and Nanosciences. In her thesis, she developed plasma polymeriza-tion processes applicable in immunosensing and investigated the interactions of proteins with plasma-chemically prepared surfaces. Currently, she is a post-doctoral research as-sociate in the Junior Research Group of Bio-sensing Surfaces at the INP Greifswald and her research interests continue in the direction of development of effective biosensors using plasma polymers.

Zdeněk Farka received his Ph.D. in Structural Biology in 2017 under the supervision of Petr Skládal at CEITEC, Masaryk University, Czech Republic. His research interests in-clude the detection of bacteria and proteins via immunoanalytical techniques. He is de-veloping label-free point-of-care sensors and examines the amplification of the im-munosensor response by means of nanoparticles and enzymes. He spent three internships at the University of Regensburg (Germany), working on applications of photon-upcon-version nanoparticles under the supervision of Hans-Heiner Gorris.

Petr Skládal is an Associated Professor at the Department of Biochemistry, Faculty of Science, Masaryk University. He received his Ph.D. in the field of amperometric biosensors in 1992. After completing research stays (1991, 1993) at the University of Florence, Italy, with Marco Mascini, he continued to investigate biosensors at Masaryk University. He currently heads the Nanobiotechnology Laboratory at the Central European Institute of Technology in Brno. His research is focused on enzyme and immunochemical biosensors using electrochemical and pie-zoelectric transducers; affinity kinetics with surface plasmon resonance systems; and applications of atomic force microscopy in life sciences.

Lenka Zajíčková received her Ph.D. in Plasma Physics from the Masaryk University in Brno (Czech Republic) in 1999. She stayed as post-doc at the Ruhr University Bochum (Germany), the Commenius University in Bratislava (Slovak Republic) and the University of Minnesota, Minneapolis, (U.S.). Currently, she is leading the research group of Plasma Technologies at Central European Institute of Technology (CEITEC), Masaryk University. Her work encompasses plasma enhanced chemical vapor deposition (PECVD) of func-tional plasma polymers, organosilicon and hydrogenated carbon films, plasma synthesis of iron oxide nanoparticles and carbon nanotubes. She works on the applications of these materials as protective and optical coatings, in sensing and bioapplications. She is the Chair of Technology Advisory Committee for Plasma Processing at the Society of Vacuum Coaters, one of the organizers of the symposium on Carbon- and/or nitrogen-containing thin films and nanomaterials at European Material Research Society (EMRS) Spring Meeting 2018 and the member of the International Union of Pure and Applied Physics (IUPAP) Commission C16 for Plasma Physics.

191

Paper VI

Maleic anhydride and acetylene plasma copolymer surfaces for SPR immunosensing

Makhneva, E.; Farka, Z.*; Pastucha, M.; Obrusník, A.; Horáčková, V.; Skládal, P.; Zajíčková, L.

Contribution:

Design of experiments, development and optimization of SPR immunosensor, characterization of sensing surface by AFM, data evaluation, manuscript writing

RESEARCH PAPER

Maleic anhydride and acetylene plasma copolymer surfaces for SPR immunosensing

Ekaterina Makhneva [1,2] · Zdeněk Farka [3] · Matěj Pastucha [3,4] · Adam Obrusník [1,2] · Veronika Horáčková [3] ·
Petr Skládal [3,4] · Lenka Zajíčková [1,2]

Abstract

We report on the successful application of carboxyl-rich plasma polymerized (PP) films as a matrix layer for bioreceptor immobilization in surface plasmon resonance (SPR) immunosensing. Composition and chemical properties of the carboxyl-rich PP films deposited from a mixture of maleic anhydride and acetylene were investigated. Changes in the films stored in air, water, and buffer were studied and the involved chemical changes were described. Performance in SPR immunosensing was evaluated on interactions of human serum albumin (HSA) with a specific monoclonal antibody. The comparison with the mixed self-assembled monolayer of mercaptoundecanoic acid and mercaptohexanol (MUA/MCH) and one of the most widely used surfaces for SPR, the 2D and 3D carboxymethylated dextran (CMD), was presented to show the efficacy of plasma polymerized matrix layers for biosensing. The PP film-based SPR immunosensor provided a similar detection limit of HSA (100 ng/mL) as MUA/MCH- (100 ng/mL) and 3D CMD (50 ng/mL)-based sensors. However, the response levels were about twice higher in case of the PP film-based immunosensor than in case of MUA/MCH-based alternative. The PP film surfaces had similar binding capacity towards antibody as the 3D CMD layers. The response of PP film-based sensor towards HSA was comparable to 3D CMD-based sensor up to 2.5 μg/mL. For the higher concentrations (> 10 μg/mL), the response of PP film-based immunosensor was lower due to inaccessibility of active sites of the immobilized antibody inside the flat PP film surface. We have demonstrated that due to its high stability and cost-effective straightforward preparation, the carboxyl-rich PP films represent an efficient alternative to self-assembled monolayers (SAM) and dextran-based layers in label-free immunosensing.

Keywords Plasma polymerization · Carboxyl-rich films · Immobilization · Surface plasmon resonance biosensor · Label-free detection

✉ Zdeněk Farka
farka@mail.muni.cz

1 RG Plasma Technologies, CEITEC MU, Masaryk University, Kamenice 5, 625 00 Brno, Czech Republic

2 Department of Physical Electronics, Faculty of Science, Masaryk University, Kotlářská 2, 611 37 Brno, Czech Republic

3 RG Nanobiotechnology, CEITEC MU, Masaryk University, Kamenice 5, 625 00 Brno, Czech Republic

4 Department of Biochemistry, Faculty of Science, Masaryk University, Kamenice 5, 625 00 Brno, Czech Republic

Introduction

Biosensors are being extensively developed and applied for biomedical and environmental studies. Quartz crystal microbalance (QCM) [1] and surface plasmon resonance (SPR) [2] biosensors proved to be very promising tools for sensitive label-free determination of various analytes including proteins and bacteria [3]. Efficient immobilization of the biorecognition molecules onto the sensor surface is always required for the biosensor development. Coatings containing chemical groups capable of the formation of covalent linkages between biomolecules and the surface are of high interest for biological applications [4–6]. A sufficiently high surface concentration of functional groups as well as the layer stability under various pH is required.

Plasma polymerized (PP) films are extensively used in the field of biomedical applications. The amine-rich PP films are

� Springer

the most widely used and known to be convenient for immobilization of biomolecules and binding of cells [7–11]. There were plenty of reports describing the use of amine-rich PP films in biosensing, cell proliferation, and other biological applications [12–15]. Compared to the conventionally used layers, such as carboxymethylated dextran (CMD), the plasma polymerization can provide faster and cost-effective layer preparation. Furthermore, PP surfaces provide good adhesion to common substrates, which results in stable signal and good regeneration capabilities. Carboxyl-rich PP films are typically generated by plasma polymerization of various acrylates [16, 17]. Examples of using gas mixtures of CO_2 and ethylene were also presented [18, 19]. Another approach relied on the use of PP films deposited from maleic anhydride (MA), which provided highly reactive coatings, but the process required fine tuning, because the level of stability was initially not sufficient [20]. There were several impressive results for biological applications using the grafting of MA onto hydrocarbon surfaces [21, 22]; however, these PP layers were not yet employed as a matrix layer for biomolecule immobilization.

Because the carboxyl-based layers are otherwise the gold standard within matrices for label-free biosensing [23, 24], our work was dedicated to the development of effective carboxyl-rich PP films. The preliminary tests were carried out to show the potential of PP films in SPR immunosensing [25]. Two different types of carboxyl-rich PP films were prepared at different plasma conditions by polymerization from MA/C_2H_2/Ar gas mixture and from CO_2/C_2H_4/Ar gas mixture. Their binding capacity towards monoclonal anti-human serum albumin (HSA) antibody was evaluated and the potential to bind antigen was demonstrated by applying HSA solution (single concentration of 5 μg/mL). However, the CO_2/C_2H_4 PP film-based immunosensor provided lower stability and smaller binding capacity towards the antibody, which resulted in constant drift of the baseline and a low level of response towards HSA. On the other hand, the MA/C_2H_2 PP film was able to efficiently bind the antibody, provided a stable baseline during the measurements, and the response towards HSA was selective and much larger compared to the CO_2/C_2H_4 PP film-based immunosensor.

Based on the obtained results, we continued the studies of the MA/C_2H_2 PP film and its properties with the aim of developing a robust immunosensing layer. Here, we present a detailed study on the characterization of chemical properties of the MA/C_2H_2 PP film, its stability and use as a matrix suitable for bioreceptor immobilization in SPR immunosensing. Chemical composition of the obtained PP films was analyzed by Fourier transform infrared spectroscopy (FTIR) and the chemical changes were followed right after the deposition, after storage in air, water, and buffer. The changes of surface topography and stiffness were evaluated by atomic force microscopy (AFM). The performance of the developed PP film-based immunosensor was characterized and compared with sensors based on mixed self-assembled monolayer (SAM) of mercaptoundecanoic acid and mercaptohexanol (MUA/MCH) and on the widely used CMD.

Materials and methods

Chemicals and materials

Maleic anhydride (MA) (98%), 1-ethyl-3-(3-dimethylaminopropyl)carbodiimide hydrochloride (EDC), N-hydroxysuccinimide (NHS), bovine serum albumin (BSA), and human serum albumin (HSA) were purchased from Sigma-Aldrich (Germany). Sodium hydrogen phosphate, sodium dihydrogen phosphate, and sodium chloride for preparation of the phosphate-buffered saline (PBS; 50 mM phosphate, 150 mM NaCl, pH 7.4) were supplied from Penta (Czech Republic). Anti-HSA monoclonal antibody (clone AL-01, purified immunoglobulin G) was obtained from Exbio (Czech Republic). Argon (99.998%) was supplied by Messer (Czech Republic). Double-side polished single crystalline silicon (c-Si) wafers (⟨111⟩, N-type phosphorus doped, resistance 0.5 Ω cm) from ON-SEMI (USA) were cut into 10×15 mm^2 substrates. MP-SPR (multi-parametric surface plasmon resonance) Navi gold sensors, SPR102 Au were purchased from BioNavis (Finland). All substrates were cleaned by sonication in isopropanol (Penta, 99.8%) for 10 min. All buffers were filtered using vacuum filtration system Stericup with 0.22-μm polyethersulfone (PES) membrane (Merck Millipore, USA).

Plasma polymerization in atmospheric pressure dielectric barrier discharge

The mixture of MA/C_2H_2/Ar was plasma polymerized in an atmospheric pressure dielectric barrier discharge (AP-DBD) reactor. The reactor was powered by 4 kHz AC voltage with peak-to-peak voltage of 4 kV. The reactor geometry and a detailed study of the correlation of plasma parameters with the PP film properties was reported before [26]. The polymerization time was adjusted to obtain the PP films with a thickness of 20 nm (0.5 min) for the SPR tests and AFM measurements, and 120 nm (3 min) for the FTIR studies [25].

FTIR analysis

Vertex 80v spectrometer (Bruker Optik, Germany) was used to obtain the FTIR spectra of the PP films. The measurements were carried out in the transmission mode on the IR-transparent Si substrates using parallel beam transmittance accessory in the spectral range from 400 to 4500 cm^{-1}. The reference spectra were recorded from a bare double-side

194

polished Si wafer. Absorbance was calculated based on the measured transmittance and data were normalized by thickness. The FTIR spectra are plotted in the range of 1000–4000 cm^{-1}, and there were no significant absorption peaks of the PP films identified outside the given range [25]. The spectrum assignments were done according to [27].

Ellipsometric measurements

The Jobin Yvon UVISEL ellipsometer (Horiba, Japan) was used to determine the thickness of PP films. The data were collected in the spectral range from 0.6 to 6.5 eV at the incidence angle of 65°. The model of one homogeneous non-uniform film using a PJDOS dispersion model assuming a wedge-shaped non-uniformity was used to fit the optical data obtained for the as-deposited PP films and dried PP films after immersion in PBS [11]. In all cases, the thickness determination was possible with a sufficient level of precision.

Atomic force microscopy

The surface topography and stiffness were studied using AFM. Dimension FastScan Bio (Bruker, USA) with FastScan-A probe was used to scan the surface of bare gold SPR chips, chips with freshly deposited MA/C$_2$H$_2$ PP film and chips with PP film after overnight immersion in PBS. The data were evaluated in software Gwyddion (Czech Metrology Institute, Czech Republic).

SPR immunosensing

For the SPR studies, system MP-SPR Navi 210A (BioNavis, Finland) was used; the injection of samples was controlled using the SPR-Navi software. The sensor response was evaluated as the surface plasmon resonance angle determined in angular scan mode by a *centroid* fitting function. Prior to insertion into BioNavis system, the PP-modified SPR chips were washed using PBS, followed by washing with water and drying by nitrogen. First, the baseline signal was established with the degassed PBS as a running buffer with a flow rate of 20 μL/min. Afterwards, the freshly prepared mixture of EDC (200 mM) and NHS (50 mM) in water was injected for 7 min to activate the sensor surface. The anti-HSA antibody was diluted in acetate buffer (pH 4.5) to the concentration of 50 μg/mL and injected to the binding channel for 20 min using the flow rate of 10 μL/min. The reference channel was modified by a solution of BSA under the same experimental conditions using a parallel injection mode. The blocking of reactive surface was performed in both channels using 2 mg/mL solution of BSA in PBS (10 min, 10 μL/min). For the immunosensing experiments, the samples of HSA were injected for 10 min (20 μL/min) with another 10 min as a dissociation time [25].

The performance of PP film-based layer was compared with the surface based on SAM and with commercial CMD chips. For the SAM formation, the gold SPR chip was first washed in acetone (10 min) and isopropanol (10 min) under ultrasonication. The chip was then immersed overnight in a mixture of 3 mM 11-mercaptoundecanoic acid (MUA) and 7 mM 6-mercapto-1-hexanol (MCH). The commercial 2D (CMDP) and 3D (CMD50) CMD-based chips (XanTec bioanalytics, Germany) were used without prior pre-treatment. The conditions of activation using EDC/NHS, antibody binding and surface blocking remained the same as in case of the PP-based sensor.

The binding kinetics was fitted in software TraceDrawer (Ridgeview Instruments AB, Sweden). The one-to-one binding model was employed, and the k_a and k_d values were fitted globally from binding curves shown in graphs.

Results and discussion

Chemical composition and properties of MA/C$_2$H$_2$ plasma copolymers

The primary challenge for the development of effective biosensors using plasma polymerization is the creation of thin polymer layers stable in an aqueous environment, which would at the same time be suitable for the immobilization of biomolecules. In this paper, copolymerization of maleic anhydride with acetylene was employed to create stable carboxyl-rich PP films suitable for antibody immobilization. Acetylene is known as one of the most reactive hydrocarbons in terms of plasma polymerization [28]. The use of maleic anhydride and acetylene mixture allowed obtaining plasma copolymers consisting of anhydride groups incorporated along unsaturated hydrocarbon chains. Such copolymerization approach allowed obtaining coatings with desired properties.

To study the chemical changes in the MA/C$_2$H$_2$ PP films, FTIR analysis was employed (Fig. 1), which showed that anhydrides, α,β-unsaturated esters, and carboxylic acids were present in the as-deposited films. When the films were immersed in water or PBS right after the deposition, the stability was very poor and the films disappeared from the substrate due to the rapid hydrolysis of the anhydride groups. Due to this fact, the as-deposited films were stored in air and the slow hydrolysis of the anhydride groups was observed by an increase of carboxylic acid signals (at 1725 and 1690 cm^{-1}) and a decrease of anhydride group signals (at 1865 and 1780 cm^{-1}), which completely disappeared after approximately 5 days (120 h) of storage in air. No changes in FTIR spectra were observed during further storage in air. The FTIR spectra of MA/C$_2$H$_2$ PP films after various times of storage in air are shown in Fig. S1 in the Electronic Supplementary Material (ESM). After stabilization in air (196 h), the films were

195
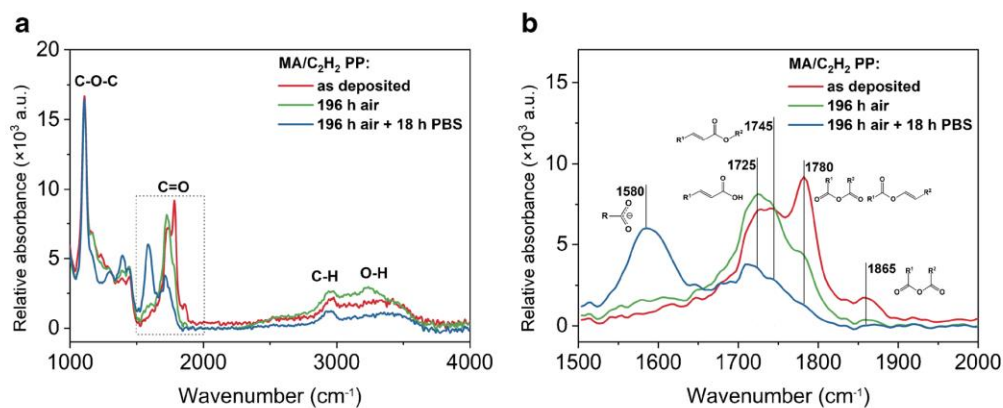
Fig. 1 FTIR spectra of MA/C$_2$H$_2$ PP films: **a** full range spectra, **b** double bonds region

immersed in PBS, and after 18 h of immersion, they exhibited approximately 28% thickness loss. During the immersion in PBS, the formation of carboxylate ions was observed, which was indicated by the appearance of a signal at 1580 cm^{-1}.

The 20-nm-thick (as determined by ellipsometry) MA/C$_2$H$_2$ PP layers deposited on gold SPR chips were studied using AFM (Fig. 2). Compared to the bare gold, surface

roughness increased after the PP film deposition, followed by flattening after the overnight immersion in PBS. Particles observed at the surface of MA/C$_2$H$_2$ PP layers were formed due to the production of dust particles in the plasma gas phase that, after reaching a critical size, fell down and stuck to the surface. Acetylene-containing plasmas are well-known for their high production of dust particles and the formation of
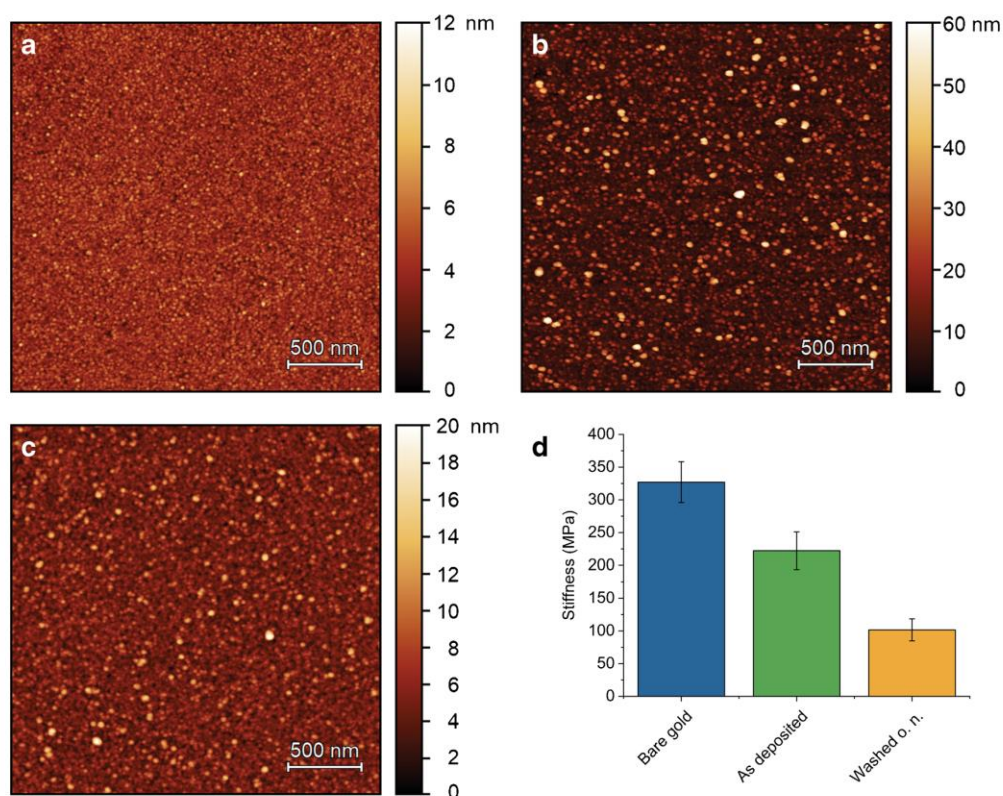
Fig. 2 AFM images of **a** bare gold surface of SPR chip, **b** as-deposited MA/C$_2$H$_2$ PP film, and **c** MA/C$_2$H$_2$ PP film after overnight immersion in PBS. **d** Surface stiffness evaluated using the AFM

Springer

196

rough films during MA/C_2H_2 plasma polymerization was studied in detail previously [29]. The PP surface flattening after overnight immersion in PBS was caused by the thickness losses of the PP layers, which resulted in partial removal of the loosely bound particles from the surface. After the PP film deposition, the stiffness of the surface decreased, which is connected with covering of the rather rigid gold surface with soft polymer layer. Further decrease of stiffness was observed after the overnight immersion in PBS, which indicates loosening of the PP film structure. Such change was generally beneficial as it provided higher flexibility during the interactions with soft biomolecules.

Performance of MA/C_2H_2 PP films in SPR immunosensing

Performance of the PP layers in SPR immunosensing was evaluated by probing the interactions of immobilized AL-01 antibody and HSA antigen as a model pair. It is known that this pair provides a reliable immunocomplex formation under different conditions and assay formats [30, 31]. SPR chips with the deposited 20-nm-thick MA/C_2H_2 PP films were stabilized in air and by overnight immersion in PBS and inserted into the system. Before antibody immobilization, the PBS was flown to establish a stable baseline signal. After this step, the sensor surface was activated by the reaction with EDC/NHS, which transformed the carboxyl groups into esters reactive towards amino groups of the antibody (Fig. 3).

After the antibody immobilization (Fig. 4a), reactions with HSA solutions of different concentrations were carried out (Fig. 4b). After the individual HSA injections, 10 mM HCl solution was applied for 2 min to regenerate the chip surface. The immunocomplex was dissociated during the regeneration,

the antigen molecules were washed away revealing the active sites of antibodies, and the sensor surface was fully active again. Regeneration allowed to carry out multiple measurements with a single SPR chip, the sensorgram of sensor surface regeneration is shown in Fig. S2 in the ESM.

Limit of detection (LOD; evaluated as $S/N > 3$) of 100 ng/mL of HSA was achieved with the MA/C_2H_2 PP film-based chips, which is comparable to the conventionally used SAM-based sensors [32, 33]. For HSA concentrations above 10 μg/mL, saturation of the sensor surface was observed. The raw signals from the measuring and reference channels are shown in Fig. S3 A-B in the ESM. The negligible signal changes in the reference channel confirm the high efficiency of the used blocking conditions and the low level of non-specific interactions. Overall, the developed sensor provided excellent level of stability and selective response towards analyte.

To critically evaluate the suitability of the developed sensor for immunosensing, a comparison with the standard MUA/MCH self-assembled monolayer (Fig. 4c) and with the most widely used CMD-based sensors (Fig. 4d) was carried out using exactly the same procedure for the sensor preparation and the same antibody-antigen pair. The raw signals from the measuring and reference channel are shown in Fig. S3 C-F in the ESM. The signals obtained during the antibody immobilization are summarized in Table 1.

The MUA/MCH mixed self-assembled monolayer was formed based on carboxyl bearing mercaptoundecanoic acid (MUA) and inert mercaptohexanol (MCH). Compared to the MA/C_2H_2 PP film, the MUA/MCH-based sensor provided lower capacity towards antibody binding, which resulted in subsequent lower capacity towards binding of HSA antigen (lower signals and working range limited to 5 μg/mL). Compared to PP film- and CMD-based sensor surface
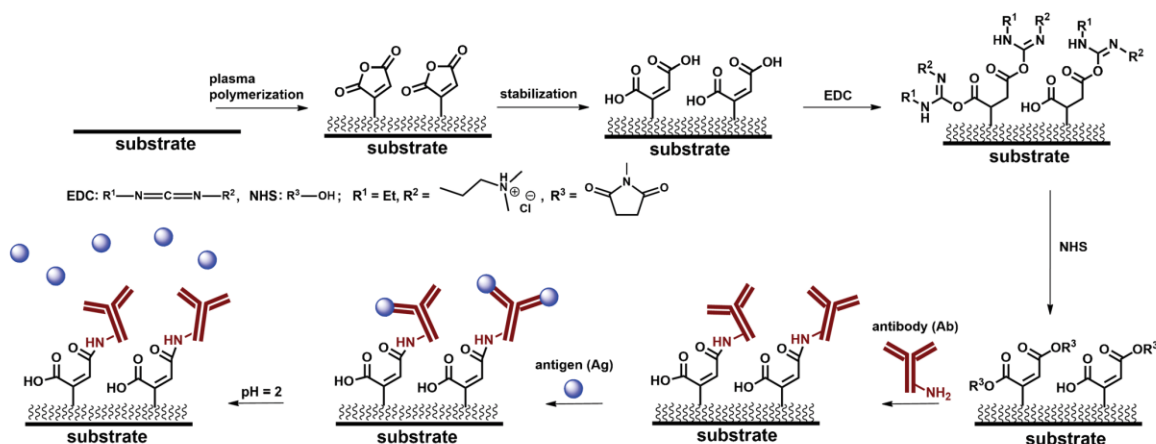
Fig. 3 Individual steps of the immunosensor surface preparation and measurement. Anhydride groups deposited during the plasma polymerization of MA were transformed to carboxyl groups during the stabilization in air. The carboxyl groups were then activated by the EDC/ NHS, which allowed to covalently bind the amino groups of the antibody. After the capture of the antigen, the immunocomplex can be regenerated by the introduction of acidic pH, which dissociates the antigen and allows further experiments
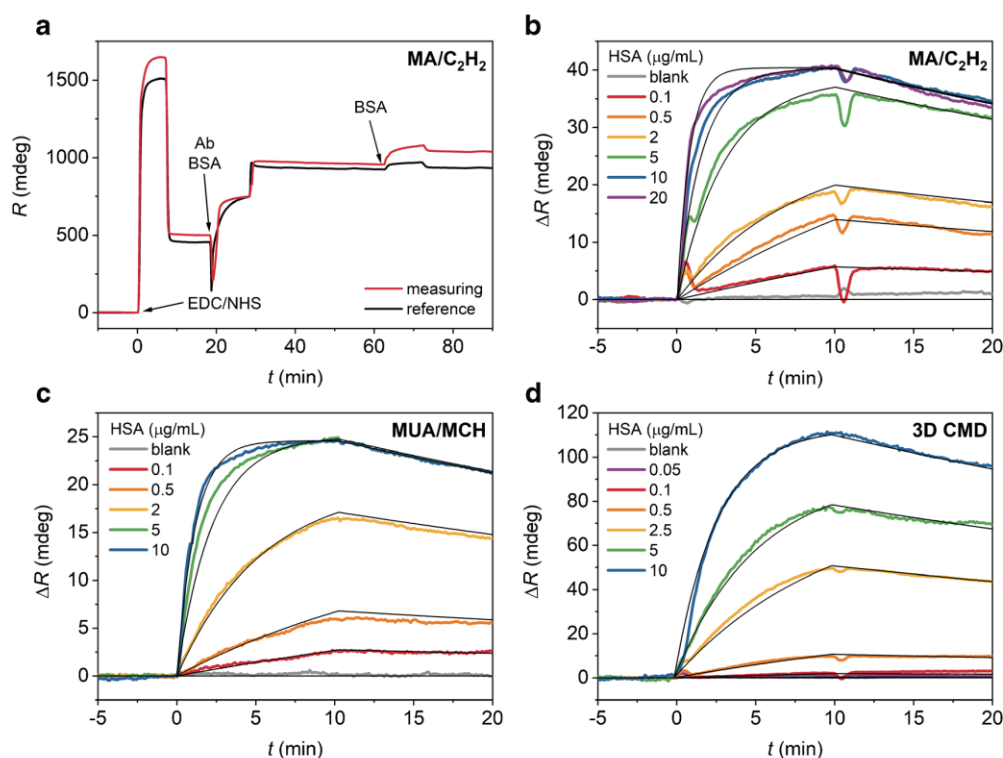
Fig. 4 **a** SPR sensorgram of the antibody immobilization on MA/C$_2$H$_2$ PP film surface. SPR binding curves of HSA on antibody-modified gold SPR chip based on **b** MA/C$_2$H$_2$ PP film, **c** MUA/MCH, and **d** 3D CMD. Differential signals (ΔR; calculated as the difference between channel with immobilized antibody and reference) are shown. The black lines correspond to the fitted kinetics model

matrices, the highest amount of BSA was adsorbed during the blocking step to the binding channel of the MUA/MCH sensor, suggesting there was still space for further protein immobilization. Different pH values of the immobilization solution were tested to enhance the electrostatic interaction and the efficiency of the antibody immobilization; however, no significant changes in immobilization were observed. To optimize the sensor surface blocking, the approaches based on binding of BSA (2 mg/mL) and ethanolamine (1 M, pH 8.5) were compared (Fig. S4 in the ESM). Both methods provided low

level of non-specific protein adsorption, blocking by BSA was used for further experiments due the possibility to be performed at neutral pH.

In case of the CMD, the comparison with 2D CMD layer was done first (since the MA/C$_2$H$_2$ PP films are also 2D surfaces), followed by the same tests with the 50-nm-thick 3D CMD layer. PP films and CMD layers performed differently during the sensor preparation procedure. PP films exhibited a much larger response to the reaction with EDC/NHS mixture compared to the CMD layers, whereas the response during the

Table 1 Relative SPR responses (mdeg) after individual steps of antibody immobilization procedure

Type of matrix layer (channel)	Activation by EDC/NHS	Immobilization of antibody (binding channel) and BSA (reference)	Blocking by BSA	Binding of HSA (0.5 µg/mL)
MA/C$_2$H$_2$ (binding)	501	455	83	13
MA/C$_2$H$_2$ (reference)	456	460	11	−1
MUA/MCH (binding)	139	158	162	5
MUA/MCH (reference)	117	252	23	0
2D CMD (binding)	27	30	9	2
2D CMD (reference)	21	260	2	1
3D CMD (binding)	17	405	2	9
3D CMD (reference)	17	690	−2	0

antibody immobilization was comparable for the PP films and 3D CMD. The worst performance during the antibody immobilization was observed with the 2D CMD layer; the very low signal change suggests that only very limited number of antibody molecules was immobilized. Due to this fact, no response was observed during further tests with HSA solutions for the 2D CMD-based sensor and no sensorgram was obtained.

After the successful antibody immobilization onto the 3D CMD layer, tests with HSA solutions were carried out (Fig. 4d). The 3D CMD-based sensor provided LOD of 50 ng/mL, which is similar to MA/C_2H_2 PP film-based sensor. The level of response to relatively small concentrations (up to 0.5 or 2.5 μg/mL of HSA) was also comparable. However, the response to the concentration of 10 μg/mL of HSA was about twice lower in case of the MA/C_2H_2 PP film-based sensor. Interesting to note that the amount of immobilized antibody on the surfaces of MA/C_2H_2 PP film-based sensor and 3D CMD-based sensor was almost the same, which means that about a half of antibody molecules immobilized on the MA/C_2H_2 PP film-based sensor were not binding the analyte. This could be due to the 2D structure of the MA/C_2H_2 PP film with relatively large—but not selective—binding capacity. A sufficient amount of antibody molecules was capable of binding to the MA/C_2H_2 PP film surface, but the active sites of the antibody were not accessible for the analyte. The 3D CMD layers have "tree-like" structured brushes, where many of antibody molecules can be effectively immobilized—active sites of antibody molecules are more accessible for the antigen [34]. The comparison of the measured signals for all tested sensor types is shown in Fig. 5. The kinetic parameters of the interaction between AL-01 antibody and HSA antigen for the different layers are summarized in Table 2. The MUA/MCH-based chip provided the fastest association reaction, probably due to the perfectly plain surface and no re-binding. Also the MA/C_2H_2

Table 2 Comparison of the evaluated kinetic parameters for the interaction between anti-HSA antibody AL-01 and HSA antigen on different surfaces

Type of matrix layer	k_a (M^{-1} s^{-1})	k_d (s^{-1})	K_D (M)
MA/C_2H_2	7.0×10^4	3.0×10^{-4}	4.3×10^{-9}
MUA/MCH	9.5×10^4	2.5×10^{-4}	2.6×10^{-9}
3D CMD	3.9×10^4	2.5×10^{-4}	6.3×10^{-9}

PP film-based immobilization resulted in quite fast association, providing significantly higher k_a value compared to the CMD surface. The evaluated K_D values did not significantly differ among the layers, confirming the potential of the MA/C_2H_2 PP film-based surface for kinetic studies.

Conclusions

Plasma copolymerization of MA and acetylene in DBD reactor is an efficient method for the preparation of carboxyl-containing films that are proposed as an alternative to widely used SAMs and CMD layers on the gold surfaces of SPR sensors. The obtained MA/C_2H_2 PP films were highly reactive surfaces; their chemical properties in air and aqueous environment were studied by FTIR. After stabilization in air (5 days of storage), approximately 30% thickness loss was observed during the immersion in PBS due to the partial hydrolysis of the MA/C_2H_2 polymer film. Nevertheless, a stable signal was obtained during the subsequent SPR immunosensing and a selective response towards analyte was recorded.

The comparison of the performance of MA/C_2H_2 PP films, MUA/MCH, 2D and 3D CMD layers in SPR immunosensing of human serum albumin was carried out. The MA/C_2H_2 PP films showed enhanced performance compared to MUA/
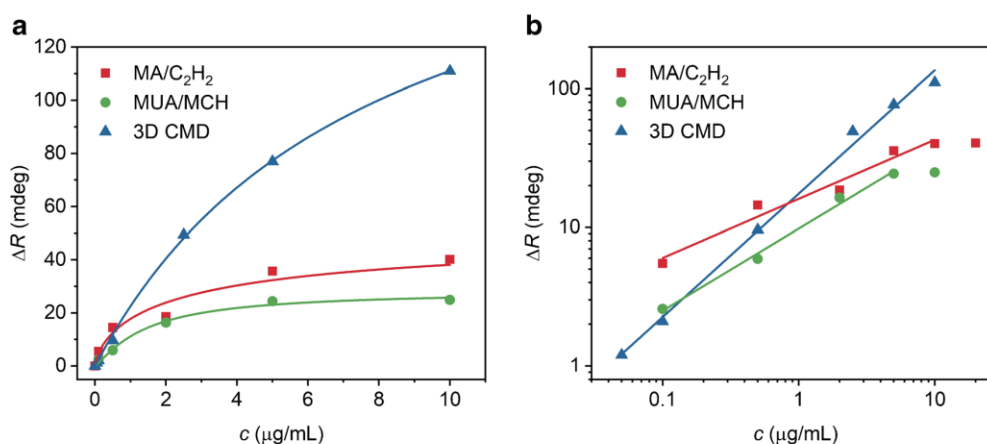
Fig. 5 Comparison of the obtained signals for HSA detection using surfaces based on MA/C_2H_2 PP film, MUA/MCH, and 3D CMD. **a** Linear scale fitted by the Langmuir model and **b** double-logarithmic plot fitted by line (the points in saturation were not included in the fit)

199

MCH and 2D CMD layers. The LOD achieved on the MA/C_2H_2 PP-based sensor (100 ng/mL) was similar to the MUA/MCH- and 3D CMD-based sensors. The level of response of the MA/C_2H_2 PP film-based sensors was about twice larger than in the case of MUA/MCH-based sensors. However, the level of response of the MA/C_2H_2 PP film-based sensor was lower compared to the 3D CMD-based sensor, especially in case of high antigen concentrations. This is due to the random distribution of functional groups in PP film, smaller surface area compared to the 3D CMD surface, and random orientation of the antibody molecules immobilized via amino groups. The achieved results demonstrate that plasma polymerization is a one-step eco-friendly procedure (not requiring the use of aggressive chemicals) for creation of highly reactive surfaces and prove a great potential of carboxyl-containing PP films as a matrix for immobilization of bioreagents in the field of biosensing.

Compliance with ethical standards

Conflict of interest The authors declare that they have no conflict of interest.

References

1. Skládal P. Piezoelectric biosensors. Trends Anal Chem. 2016;79:127–33.
2. Caucheteur C, Guo T, Albert J. Review of plasmonic fiber optic biochemical sensors: improving the limit of detection. Anal Bioanal Chem. 2015;407(14):3883–97.
3. Farka Z, Juřík T, Kovář D, Trnková L, Skládal P. Nanoparticle-based immunochemical biosensors and assays: recent advances and challenges. Chem Rev. 2017;117(15):9973–10042.
4. Wadu-Mesthrige K, Amro NA, Liu GY. Immobilization of proteins on self-assembled monolayers. Scanning. 2000;22(6):380–8.
5. Howell S, Kenmore M, Kirkland M, Badley RA. High-density immobilization of an antibody fragment to a carboxymethylated dextran-linked biosensor surface. J Mol Recognit. 1998;11(1–6):200–3.
6. Jadhav SA. Self-assembled monolayers (SAMs) of carboxylic acids: an overview. Cent Eur J Chem. 2011;9(3):369–78.
7. Jung D, Yeo S, Kim J, Kim B, Jin B, Ryu DY. Formation of amine groups by plasma enhanced chemical vapor deposition and its application to DNA array technology. Surf Coat Technol. 2006;200(9):2886–91.
8. Crespin M, Moreau N, Masereel B, Feron O, Gallez B, Vander Borght T, et al. Surface properties and cell adhesion onto allylamine-plasma and amine-plasma coated glass coverslips. J Mater Sci Mater Med. 2011;22(3):671–82.
9. Chen Q, Forch R, Knoll W. Characterization of pulsed plasma polymerization allylamine as an adhesion layer for DNA adsorption/hybridization. Chem Mater. 2004;16(4):614–20.
10. Wu ZY, Yan YH, Shen GL, Yu RQ. A novel approach of antibody immobilization based on n-butyl amine plasma-polymerized films for immunosensors. Anal Chim Acta. 2000;412(1–2):29–35.
11. Makhneva E, Farka Z, Skládal P, Zajíčková L. Cyclopropylamine plasma polymer surfaces for label-free SPR and QCM immunosensing of *Salmonella*. Sensors Actuators B Chem. 2018;276:447–55.
12. Yang ZL, Wang J, Luo RF, Maitz MF, Jing FJ, Sun H, et al. The covalent immobilization of heparin to pulsed-plasma polymeric allylamine films on 316L stainless steel and the resulting effects on hemocompatibility. Biomaterials. 2010;31(8):2072–83.
13. Hu WJ, Xie FY, Chen Q, Weng J. Amine-containing film deposited in pulsed dielectric barrier discharge at a high pressure and its cell adsorption behaviours. Chin Phys B. 2009;18(3):1276–82.
14. Ren TB, Weigel T, Groth T, Lendlein A. Microwave plasma surface modification of silicone elastomer with allylamine for improvement of biocompatibility. J Biomed Mater Res A. 2008;86A(1):209–19.
15. Makhneva E, Manakhov A, Skládal P, Zajíčková L. Development of effective QCM biosensors by cyclopropylamine plasma polymerization and antibody immobilization using cross-linking reactions. Surf Coat Technol. 2016;290:116–23.
16. Batan A, Nisol B, Kakaroglou A, De Graeve I, Van Assche G, Van Mele B, et al. The impact of double bonds in the APPECVD of acrylate-like precursors. Plasma Process Polym. 2013;10(10):857–63.
17. Nisol B, Watson S, Lerouge S, Wertheimer MR. Energetics of reactions in a dielectric barrier discharge with argon carrier gas: III esters. Plasma Process Polym. 2016;13(9):900–7.
18. Korner E, Fortunato G, Hegemann D. Influence of RF plasma reactor setup on carboxylated hydrocarbon coatings. Plasma Process Polym. 2009;6(2):119–25.
19. Rupper P, Vandenbossche M, Bernard L, Hegemann D, Heuberger M. Composition and stability of plasma polymer films exhibiting vertical chemical gradients. Langmuir. 2017;33(9):2340–52.
20. Mishra G, McArthur SL. Plasma polymerization of maleic anhydride: just what are the right deposition conditions? Langmuir. 2010;26(12):9645–58.
21. Chu LQ, Zhang Q, Forch R. Surface plasmon-based techniques for the analysis of plasma deposited functional films and surfaces. Plasma Process Polym. 2015;12(9):941–52.
22. Pearson HA, Urban MW. Simple click reactions on polymer surfaces leading to antimicrobial behavior. J Mater Chem B. 2014;2(15):2084–7.
23. Rich RL, Myszka DG. Advances in surface plasmon resonance biosensor analysis. Curr Opin Biotechnol. 2000;11(1):54–61.
24. Johnsson B, Lofas S, Lindquist G. Immobilization of proteins to a carboxymethyldextran-modified gold surface for biospecific interaction analysis in surface-plasmon resonance sensors. Anal Biochem. 1991;198(2):268–77.
25. Makhneva E, Obrusník A, Farka Z, Skládal P, Vandenbossche M, Hegemann D, et al. Carboxyl-rich plasma polymer surfaces in surface plasmon resonance immunosensing. Jpn J Appl Phys. 2018;57(1):5.
26. Obrusník A, Jelínek P, Zajíčková L. Modelling of the gas flow and plasma co-polymerization of two monomers in an atmospheric-pressure dielectric barrier discharge. Surf Coat Technol. 2017;314:139–47.
27. Coates J. Interpretation of infrared spectra, a practical approach. Encyclopedia of analytical chemistry. 2006.
28. Nisol B, Watson S, Lerouge S, Wertheimer MR. Energetics of reactions in a dielectric barrier discharge with argon carrier gas: V hydrocarbons. Plasma Process Polym. 2017;14(8):9.

29. Zajíčková L, Jelínek P, Obrusník A, Vodák J, Nečas D. Plasma-enhanced CVD of functional coatings in Ar/maleic anhydride/C$_2$H$_2$ homogeneous dielectric barrier discharges at atmospheric pressure. Plasma Phys Control Fusion. 2017;59(3):13.

30. Navrátilová I, Skládal P, Viklický V. Development of piezoelectric immunosensors for measurement of albuminuria. Talanta. 2001;55(4):831–9.

31. Farka Z, Čunderlová V, Horáčková V, Pastucha M, Mikušová Z, Hlaváček A, et al. Prussian blue nanoparticles as a catalytic label in a sandwich nanozyme-linked immunosorbent assay. Anal Chem. 2018;90(3):2348–54.

32. Farré M, Kantiani L, Barceló D. Microfluidic devices: biosensors. Chemical analysis of food: techniques and applications; 2012. p. 177–217.

33. Farka Z, Kovář D, Přibyl J, Skládal P. Piezoelectric and surface plasmon resonance biosensors for *Bacillus atrophaeus* spores. Int J Electrochem Sci. 2013;8(1):100–12.

34. Lofas S, Johnsson B. A novel hydrogel matrix on gold surfaces in surface-plasmon resonance sensors for fast and efficient covalent immobilization of ligands. J Chem Soc Chem Commun. 1990;(21):1526–8.

Paper VII

Functional Plasma Polymerized Surfaces for Biosensing

Makhneva, E.; Barillas, L.; Farka, Z.; Pastucha, M.; Skládal, P.; Weltmann, K. D.; Fricke, K.

Contribution:

Development and optimization of SPR immunosensor, data evaluation, participation in manuscript writing

Functional Plasma Polymerized Surfaces for Biosensing

Ekaterina Makhneva,* Laura Barillas, Zdeněk Farka, Matěj Pastucha, Petr Skládal,
Klaus-Dieter Weltmann, and Katja Fricke

ACCESS | Metrics & More | Article Recommendations | Supporting Information

ABSTRACT: The capabilities of biosensors for fast, economic, and user-friendly analysis of complex samples has led to the exploitation of analytical devices for detection, quantification, and monitoring of specific chemical species for various applications. For a sufficiently high surface reactivity toward the adopted bioreceptors, a thin functional layer is required to enable coupling of the target biomolecules and to provide good stability in the presence of a sample matrix. In this work, the generation of water-stable oxygen-rich plasma polymerized (pp) films deposited by atmospheric-pressure jet plasma for reliable immobilization of biomolecules is presented. Three types of pp films were developed and characterized. All of the obtained pp films were successfully used as a matrix layer in the SPR immunosensors, which provided excellent level of sensitivity, stability, and regenerability. The achieved results show that atmospheric pressure plasma-induced polymerization is a powerful alternative method for the preparation of matrix layers for a wide range of applications in the biological field.

KEYWORDS: *atmospheric-pressure plasma-induced polymerization, functional polymers, chemical composition, thin films, biosensing*
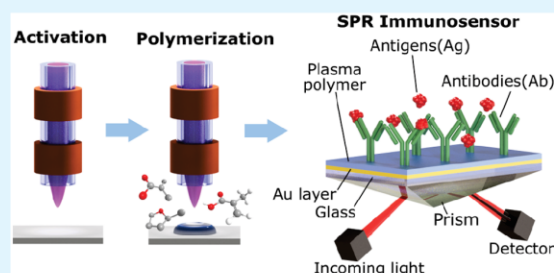
1. INTRODUCTION

Detecting and quantifying specific molecular compounds in solutions is indispensable when analyzing biological samples in general and in particular for rapid detection of low concentrations of specific analytes in small sample volumes. A molecular compound can be identified according to its chemical or physical properties or by the interactions with a specific molecular partner. A biosensor detects the presence of a target molecule directly or indirectly through interactions with biomolecules. The biological recognition element is a pivotal part of a biosensing system providing specific quantitative or semiquantitative analytical information. For biomolecule immobilization, polymers are becoming indispensable for the preparation of biosensor platforms, whereas its equipment with functional groups must interface with the analyte. In particular, reactive organic polymer thin films which are capable of covalent attachment of various biomolecules are of great interest in the field of biotechnology. Usually, the binding of the biomolecule is performed via a primary amine or carboxyl group, thus the surface should contain either carboxyl or primary amine groups to utilize the common carbodiimide/*N*-hydroxysuccinimide zero-length coupling reactions providing amide-based links. A wide range of functionalization methodologies have been investigated to equip surfaces with the desired reactive chemical groups. The most common way is via wet-chemical procedures, which are time-consuming and rely on aggressive chemicals, e.g., the case of thiols attacking noble metal surfaces.[1−3]

An alternative and efficient method is plasma polymerization, which is a fast and eco-friendly procedure for the formation of thin polymer films on various surfaces that does not require washing steps and additions of reagents. Physical plasma is an (partially) ionized gas, which is also referred to as the fourth state of matter. It is composed of photons, electrons, positive and negative ions, atoms, free radicals, and excited or nonexcited molecules. Plasma is generated at low-, atmospheric-, and high-pressure conditions by applying energy. Nonthermal plasmas have reached considerable importance in various plasma processing applications due to its ability to provide enhanced gas phase chemistry with high concentrations of chemically active species without the need for elevated gas temperatures. Resulting plasma polymer coatings are generally highly branched and cross-linked, with an excellent level of adhesion to any kind of surface and high level of stability. The majority of the work related to plasma polymerization is reported on the low-pressure glow discharge plasmas. A variety of low-pressure discharges differing in the principles of coupling the power from the external electrical source have been developed.[4−8]
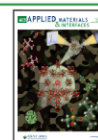
Atmospheric-pressure plasmas have become of increasing interest in recent years due to their better cost-efficiency as they require less sophisticated or even no vacuum equipment.[9] Successful atmospheric-pressure plasma polymerization from a range of monomers has been reported by several teams in the past few years.[10−12] The most frequently used type of plasma sources for atmospheric pressure plasma polymerization is the dielectric-barrier discharge,[13−15] in which one or both of the electrodes are separated by a dielectric layer to limit the plasma current and prevent arcing.

Plasma polymerized (pp) surfaces containing O-rich reactive functional groups are typically created from various acrylates and methacrylates,[16−19] as their vinyl or vinylidene groups are active toward free radical polymerization. There are plenty of successful examples of the plasma polymerization of acrylates for the creation of biocompatible surfaces available in the literature.[20−23] The most widely used monomer for deposition of such types of coatings is acrylic acid. Nevertheless, the plasma conditions have to be carefully optimized due to reactive carboxylic groups that are lost through the CO_2 release during the deposition process.[24] Methyl methacrylate is another widely used monomer, which also exhibits significant chemical degradation under plasma conditions.[25,26] To overcome this issue, the monomer structure has to be carefully examined prior to use. It was recently shown that the plasma polymerization of glycidyl methacrylate strongly favors a conventional pathway of the free radical polymerization process.[27] The presented epoxide groups acted as a chemical buffer, effectively protecting the molecule from a statistical breakdown. Other popular approaches for the creation of O-rich pp films for bioapplications rely on the use of CO_2 and ethylene mixtures.[28] Such types of pp films deposited under low pressure were successfully employed for the development of immunosensors with a limit of detection comparable to conventionally used biosensing techniques.[29] Another promising approach utilizing the copolymerization of maleic anhydride (MA) and acetylene in a dielectric barrier discharge reactor resulted in the O-rich pp surfaces with a sufficient level of stability in aqueous environment. The MA-co-acetylene pp films were efficiently used as an antibody immobilization matrix layer, and SPR immunosensors were successfully developed.[30]

Within the past few years, numerous studies on the application of high frequency driven atmospheric-pressure plasma jets (APPJ) for surface modifications or for deposition of thin polymer films appeared.[31−35] Recently, the deposition of poly(methyl methacrylate) (PMMA) coatings using APPJ was reported using a novel setup containing an inner capillary through which the monomer vapors were introduced.[36] It was shown that the obtained PMMA films had a radial gradient in surface chemistry, morphology, and thickness, and the coatings properties strongly depended on the monomer flow rate. All of the aforementioned publications are using single polymerizable monomers, monomer mixtures, or gas mixtures containing hydrocarbon-based precursors for the deposition of functional coatings. The monomers are typically introduced into the plasma directly in the form of vapors (in the case of liquid monomers) or gaseous compounds are used. This leads to a high level of fragmentation of the monomer molecules, and the resulting pp films have a highly branched structure. In our work, the liquid monomers were spread onto the substrate surface and treated by APPJ plasma, which resulted in a more conventional-like mechanism of the plasma-induced polymerization process and reduced the irregularity of the pp chains.

Two key criteria were identified as critical for the assessment of a functional polymer coating for biosensing: (1) stability in aqueous media regarding elemental composition, thickness, and morphology, and (2) the type and amount of functional groups providing active binding sites for the biomolecule immobilization. In this contribution, pp coatings derived from chemically different monomers and mixtures thereof were submitted to an extensive surface characterization as-deposited and after storage in distilled water for 24 h. The monomers choice was based on their intrinsic oxygen content and on their capability to be polymerized. Hence, 1,2,4-trivinylcyclohexane (TVC) that contains no oxygen, tetrahydrofurfuryl methacrylate (THFMA) that has a high content of oxygen, and a 1:2 volume ratio mixture thereof were chosen as monomers. THFMA was chosen as a monomer due to the well-known activity of vinylidene group toward polymer chain growth, whereas tetrahydrofuran (THF) presented in its structure acted as a protecting group against statistical breakdown of the THFMA molecule. TVC contains three vinyl groups active toward free radical polymerization, and it was effective as a monomer itself, or used as a source of carbon functionalities to adjust the carbon content and stability of the resulting pp films. The ring opening of the THF or cyclohexane, which is probable under plasma-induced polymerization conditions, resulted in additional cross-linking of the polymer chains. As far as the TVC is a very volatile compound, a mixture with a double excess of TVC was chosen to obtain a copolymer of TVC and THFMA, with a sufficient level of TVC incorporation into the polymer chains. Both of the monomers used in this study are also nontoxic chemicals, which perfectly fits with the eco-friendly APPJ polymerization procedure.

The chemical composition of the pp films was analyzed by FT−IR and XPS. Film morphology was studied by AFM before and after immersion in water. Thickness losses after storage in water were determined by ellipsometric measurements. After the characterization of the obtained pp films, the SPR immunosensors for the detection of human serum albumin (HSA) were developed based on the immobilization of monoclonal anti-HSA antibody AL-01.

2. EXPERIMENTAL SECTION

2.1. Chemicals and Materials. Tetrahydrofurfuryl methacrylate (THFMA, $C_9H_{14}O_3$) (97% purity, containing 75 ppm hydroquinone (HQ), 900 ppm methylhydroquinone (MEHQ) as stabilizers), and 1,2,4-trivinylcyclohexane (TVC, $C_6H_9(CH = CH_2)_3$) (98%, mixture of isomers) were purchased from Sigma-Aldrich and used for polymerization without any further purification. Argon (Ar) with purity of 99.998% was supplied by Messer and used for APPJ plasma as a process gas. Single-side polished silicon (Si) wafers and double-side polished single crystal silicon (c-Si) wafers (⟨111⟩, N-type phosphorus doped, resistance 1−5 Ωcm) were purchased from MicroChemicals and were cut into substrates of 10×10 mm². Double-side polished Si wafers were used for FT−IR studies, while single-side polished Si wafers were used for XPS and AFM analysis as well as for ellipsometric measurements. 1-Ethyl-3-(3-(dimethylamino)propyl)carbodiimide hydrochloride (EDC), N-hydroxysuccinimide (NHS), bovine serum albumin (BSA), and human serum albumin (HSA), were purchased from Sigma-Aldrich. Sodium hydrogen phosphate, sodium dihydrogen phosphate, and sodium chloride for the preparation of phosphate buffered saline (PBS; 50 mM phosphate, 150 mM NaCl) with pH 7.4, were supplied from Penta. Anti-HSA monoclonal antibody (clone AL-01, purified immunoglobulin G) was obtained from Exbio. MP-SPR (multiparametric surface plasmon resonance) Navi gold sensors, SPR102 Au were purchased from BioNavis. All the substrates were cleaned by sonication in isopropanol (Sigma, 99.8%) for 10 min. All

solutions were filtered through a 0.22-μm poly(tetrafluoroethylene) (PTFE) membrane (Merck Millipore).

2.2. Plasma-Induced Polymerization. Plasma-induced polymerization was carried out using APPJ described elsewhere.[37] APPJ is composed of two copper ring electrodes (width = 5 mm, distance between electrodes = 4.7 mm) attached to the quartz capillary (outer diameter = 6, inner diameter = 4 mm). The upper electrode is capacitively coupled to a RF generator working at the frequency of 27.12 MHz over a matching network, whereas the lower electrode is connected to the ground potential (Figure 1).
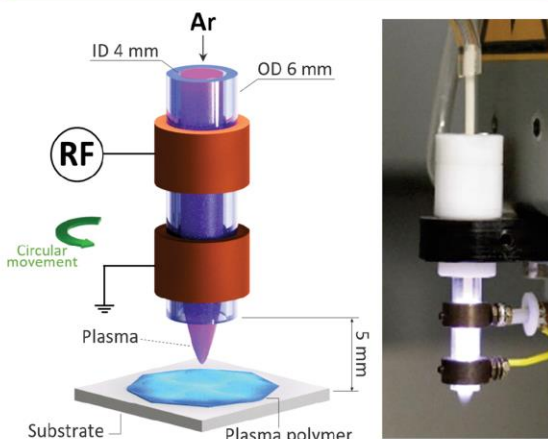
Figure 1. Schematic of the APPJ (left) and photograph of the APPJ operating with 1 slm Argon.

First, the surface of substrate was activated by applying APPJ Ar plasma for 30 s. Then, a thin film of a liquid monomer was nebulized on the surface of plasma-activated substrate and the APPJ Ar plasma was applied again until the formation of thin solid film was observed (polymerization process was complete). Both processes were carried out with an input power of 5 W, Ar flow rate $Q(Ar)$ = 1 slm, and a nozzle outlet to substrate distance of 5 mm. Circular movement of the jet (d = 5 mm) was used to increase the uniformity of the obtained pp films. The thickness of films was controlled by the time of monomer nebulization onto the substrate surface and by the plasma treatment time. For the deposition of 120−140 nm thick pp films from TVC monomer, the nebulization time was 3 s and the plasma-induced polymerization time was 20 s, from THFMA monomer: nebulization—1 s, plasma-induced polymerization—30 s; from THFMA/TVC (1:2 v.r.) monomer mixture: nebulization—2 s, and plasma-induced polymerization—25 s. For the deposition of thin 20−40 nm pp layers the nebulization time was kept at 0.5 s for all of the used monomers. Plasma-induced polymerization time for TVC monomer was 5 s, THFMA—10 s, and THFMA:TVC (1:2 v.r.)—7 s.

2.3. Fourier Transformed Infrared (FT−IR) Spectroscopy. FT−IR spectra were obtained for the films deposited on the IR-transparent c-Si substrates in the transmission mode using the Bruker Vertex 80v spectrometer. The measurements were performed with a parallel beam transmittance accessory in the spectral range from 400 to 4000 cm^{-1}. The data were collected at a pressure of 2.5 mbar with the resolution of 4 cm^{-1} and 500 scans. The transmittance of the films on Si substrate was divided by the transmittance of bare Si substrate for the thin film analysis.

2.4. X-ray Photoelectron Spectroscopy (XPS). The chemical surface composition was determined by high-resolution scanning XPS. The spectra were acquired using an Axis Supra DLD electron spectrometer (Kratos Analytical) with a monochromatic Al Kα source (1486.6 eV). The instrument was set to the medium magnification lens mode (field of view 2) and by selecting the slot mode, providing an analysis area of approximately 250 μm in diameter. Core level spectra of

O 1s, C 1s, and Si 2p were collected at a pass energy of 80 eV. Data acquisition and processing were carried out using CasaXPS software, version 2.14dev29 (Casa Software, Ltd.). Due to sample charging, the binding energy scale was corrected for all samples by setting the C 1s binding energy to 285.0 eV. Concentrations are provided in atomic percent (at.%). Depth profiles were generated by alternating cycles of spectral acquisition of the sample surface followed by 10 keV Ar$_{1000}^{+}$ bombardment of the sample surface. The beam was rastered over an area of 1.5 × 1.5 mm^2.

2.5. Water Contact Angle (WCA). WCA measurements were performed on the pp surfaces at room temperature under ambient air by the sessile drop method using an OCA 30 contact angle analyzer (DataPhysics Instruments GmbH) and a drop of distilled water with a volume of 0.5 μL. The contact angle of the resting drop was determined utilizing the SCA20 software.

2.6. Atomic Force Microscopy (AFM). AFM analysis was carried out using CoreAFM (nanoSurf) to obtain the film surface morphology right after the deposition process and after 24 h of storage in water. The AFM imaging was conducted in noncontact mode, using a PPP-XYNCHR tip with a spring constant of 42 N/m. The obtained data were evaluated in the Gwyddion software.

2.7. Ellipsometry. The ellipsometric data were measured using a J.A. Woollam Co. M-2000 V ellipsometer at incidence angles of 55°, 65°, and 75°. The optical data obtained for as-deposited films and after storage in water were fitted by the Cauchy model including film nonuniformity and roughness using Complete EASE (J.A. Woolam) software. The agreement between the data and the fit was achieved for all the as-deposited films. After the storage in water, the films exhibited increased surface roughness and inhomogeneity, but the determination of the film thickness using the above-mentioned model was still possible with sufficient precision.

2.8. Surface Plasmon Resonance (SPR) Immunosensing. SPR Navi 210A system from BioNavis was used for SPR studies. The flow cell of the device consisted of two channels: binding (with antibody) and reference (no antibody). SPR-Navi software enabled programming of injections of different solutions. The position of SPR peak was determined via build-in centroid fitting function. SPR chips with the deposited approximately 20 nm thick pp films were first immersed overnight in PBS, washed with sterile water, dried, and inserted into the device. First, the baseline of every sample was recorded under the 20 μL/min flow of PBS for about 40 min. Then EDC/NHS (200 mM/50 mM) activation was applied for 7 min under the same flow rate. The EDC/NHS step resulted in formation of reactive NHS esters to which the Ab (anti-HSA, clone AL-01; 100 μg/mL, pH = 4.5; flow rate of 10 μL/min for 20 min) was successfully bonded in the binding channel. In parallel to Ab injection a BSA solution was applied to a reference channel at the same concentration, pH, flow rate, and time. Next, the free reactive groups left at the sensor surface were blocked by BSA solution applied to both of the channels (2 mg/mL in PBS, flow rate of 20 μL/min for 10 min). Then the immunosensing of different concentrations of HSA (50 ng/mL to 10 μg/mL) was carried out at the flow rate of 20 μL/min for 10 min with 10 min dissociation time.

3. RESULTS

3.1. Chemical Composition and Stability in Water of pp Films. During plasma-induced polymerization, reactive processes such as ion bombardment and cross-linking reactions are creating polymer networks with complex structures, whereas, depending on the process parameters, functional groups of the precursor can be retained or new functionalities are introduced. THFMA, TVC, and a mixture of THFMA and TVC (1:2 volume ratio) were used as monomers for the deposition of pp films. FT−IR analysis revealed the functional chemical groups present in the pp films and helped to follow chemical changes after storage in water (Figure 2). FT−IR spectra of the monomers were recorded to compare the chemical composition of the resulting pp films with the corresponding initial
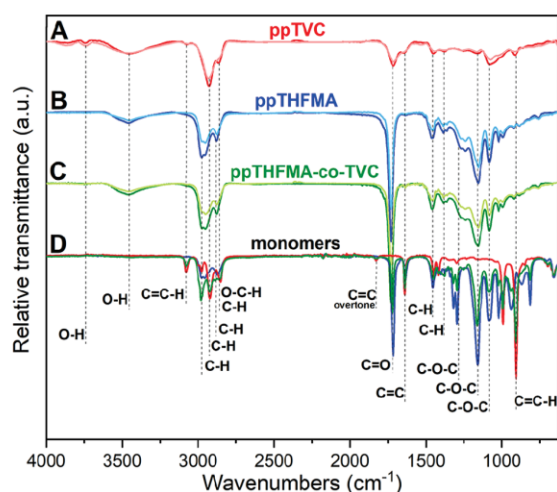
Figure 2. FT−IR spectra: A: ppTVC—red, ppTVC after 24 h of immersion in water—light-red; B: ppTHFMA—blue, ppTHFMA after 24 h of immersion in water—light-blue; C: ppTHFMA-*co*-TVC—green, ppTHFMA-*co*-TVC after 24 h of immersion in water—light-green; D: spectra of monomers: TVC—red, THFMA—blue, and THFMA-TVC (1:2 volume ratio)—green, the spectra of the monomers were divided by 10.

(nonpolymerized) monomers. Assignment of the observed signals is presented in Table S1.[38]

In the FT−IR spectra of all of the freshly deposited pp films, the OH stretching signal was observed at 3455 cm^{-1}. The C═O stretching signal at 1730 cm^{-1} corresponding to esters was found in the THFMA-derived pp films. The C═O signal in the ppTVC spectrum was slightly shifted to lower wavenumbers and appeared at 1720 cm^{-1}, whereas the signal intensity was remarkably lower compared to the THFMA-containing polymers. Only traces of vinyl groups (1640 cm^{-1}) were found in the structure of the resulting pp films from THFMA and THFMA-*co*-TVC. The vinyl group signal in ppTVC was seen more clearly, but the intensity was remarkably lower than in case of the nonpolymerized TVC monomer. For all deposited films, C−H stretching signals were observed at 2980 and 2945 cm^{-1}, which correspond to alkane fragments in the pp films structure. The C−H stretching at 2870 cm^{-1} might be assigned to either alkane chains or to the O−C−H groups, corresponding to different ethers.

The chemical stability of the obtained pp films was examined upon immersion in water for 24 h. No dramatic changes in the presence of chemical groups can be seen, however, the overall intensity of signals was slightly lower compared to the freshly deposited pp films. Thus, the decreased signal intensities in FT−IR spectra were assigned to the thickness losses of the coatings.

Ellipsometric measurements were conducted to determine the film thickness before and after the immersion in water. After 24 h of storage in water, ppTVC, ppTHFMA, and ppTHFMA-*co*-TVC exhibited thickness losses of 6 ± 1%, 18 ± 2%, and 16 ± 2%, respectively, whereas within the further 168 h of storage in water, no more significant changes in thickness were recorded. More detailed data including results for the short-term and long-term immersions in water are presented in Figure S1 of the Supporting Information (SI).

All deposited pp films were analyzed by XPS right after the deposition and after 24 h of immersion in water (Figure 3). The elemental composition of the as-deposited films and after storage in water for 24 h is listed in Table S2.
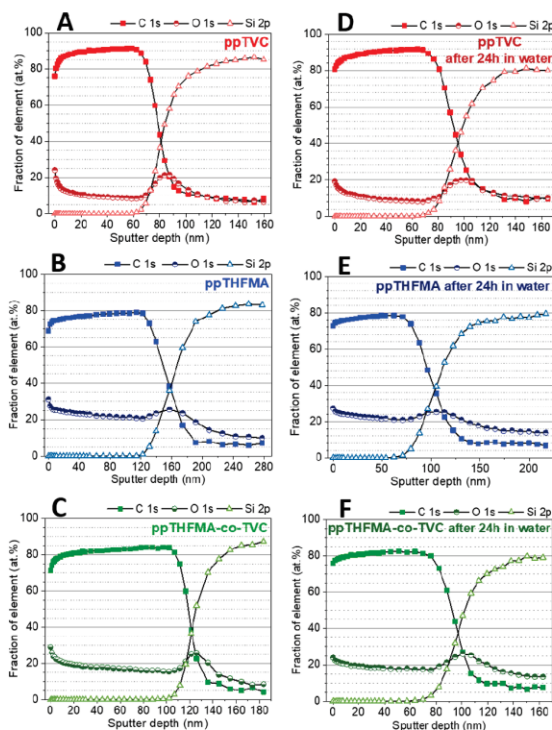
Figure 3. XPS depth profiles of ppTVC, ppTHFMA, and ppTHFMA-*co*-TVC films: A, B, C: right after the deposition process; D, E, F: after 24 h of storage in water.

The pp films were composed of carbon and oxygen, which were the constituents of the monomer used for the plasma-induced polymerization (except of hydrogen, which cannot be analyzed by the XPS technique).[39] Surprisingly, no traces of nitrogen were detected although the experiments were conducted at ambient conditions. However, more important for the pp film analysis is the oxygen to carbon ratio (O/C). Although the monomer of TVC contains only carbon and hydrogen, an O/C ratio of 0.32 was determined for the ppTVC film. Compared with the monomer structure of THFMA (O/C ratio of 0.33) a remarkable increase in the oxygen content was observed for ppTHFMA films (O/C ratio of 0.45). Furthermore, the pp films were characterized after 24 h of storage in distilled water to assess their stability in terms of elemental composition. For all analyzed pp films, a decrease in the oxygen fraction was observed after the immersion.

While the surface composition determines interfacial properties, the bulk of the film provide information about the stability of the underlying polymer layer. XPS depth profiling allows the probing of the vertical compositional profiles to study compositional variations across the film up to the bottom interface, the silicon wafer. For the in-depth analysis of the deposited films, an argon gas cluster ion source with a cluster size of 1000 (Ar_{1000}^{+}) and a raster size of 1.5 × 1.5 mm^2 was used.

Unlike monatomic ions, the level of chemical damage induced through cluster ion beam exposure is far lower (the depth of penetration of cluster ions is within the top 2−5 nm of a sample surface), which enables the depth profiling of organic materials.[40]

The time required to reach the half-maximum of the silicon substrate concentration was used together with the thickness of the film determined by ellipsometry to convert the sputtering time to sputtered depth. Depending on the coating, different etch rates were calculated: 0.18, 0.43, and 0.24 nm/s for ppTVC, ppTHFMA, and ppTHFMA-co-TVC, respectively. The XPS-derived elemental composition determined after each argon cluster ion etching cycle is presented as a function of depth in Figure 3 for all the studied pp films. Carbon and oxygen were the only elements detected in the survey scans of the films, whereas silicon originated from the substrate. Near surface, a high amount of oxygen was detected, even for the ppTVC film. With the increasing sputter depth, the oxygen content decreased whereas the portion of carbon rose. The relatively gradual rise in silicon portion with depth indicates that there is a broad interface between the organic pp film and the inorganic SiO_2/Si phases.

To investigate the functional composition of the sputtered films, component peaks for the C 1s spectrum were chosen based upon the shape of the core level envelope. The high-resolution XP C 1s spectra were fitted with four subpeak components (C1−C4) (Figure S2). The C1 component was assigned to C−C/C−H (binding energy (BE) = 285.0 eV) bonds, while C2 (BE = 286.6 eV) included hydroxyl and ether groups (C−O). The C3 was assigned to C═O (BE = 287.8 eV) and C4 included O−C═O (BE = 289.0 eV).[41] The additional component at BE = 285.7 eV originated from a 0.7 eV secondary (β) chemical shift produced by the ester carbon (primary shift of 4 eV). It should be noted that no attempt has been made to distinguish between the carboxylic acid group (COOH) and the ester group (COOC). Both chemical groups have identical chemical shifts in the XPS spectrum.

Figure S2 represents C 1s high-resolution spectra of the freshly deposited films (labeled as near-surface) and after sputtering (labeled as bulk; sputter depth >50 nm). Upon sputtering, it was observed that the portion of oxygen-bearing functional groups decreased, which was in agreement with the decreasing oxygen content with rising sputter depth as shown in Figure 3.

The functional composition of the coatings was determined from curve fitting of the C 1s region and was plotted versus the sputtered depth in Figure 4. Sputtering caused a significant increase in the CH/CC component whereas for all oxygen-containing bindings, a decrease was observed.

Water contact angle (WCA) measurements were carried out on the as deposited pp films and on the pp films stored in water for 24 h. The results are presented in Table S3. All the freshly deposited pp films were quite hydrophilic, whereas after 24 h of storage in water an increase of WCA was seen in all of the cases.

AFM analysis was used to study the morphology of the freshly deposited films and changes after 24 h of storage in water (Figure 5). The freshly deposited pp films were characterized by a uniform smooth surface topography. Among the coatings, the ppTHFMA-co-TVC film exhibited a slightly rougher surface (Table S4).

Changes in the topography of coatings can be seen after 24 h of storage in water. In particular, formation of pinhole-like dips with various depths was observed at the surface of ppTHFMA
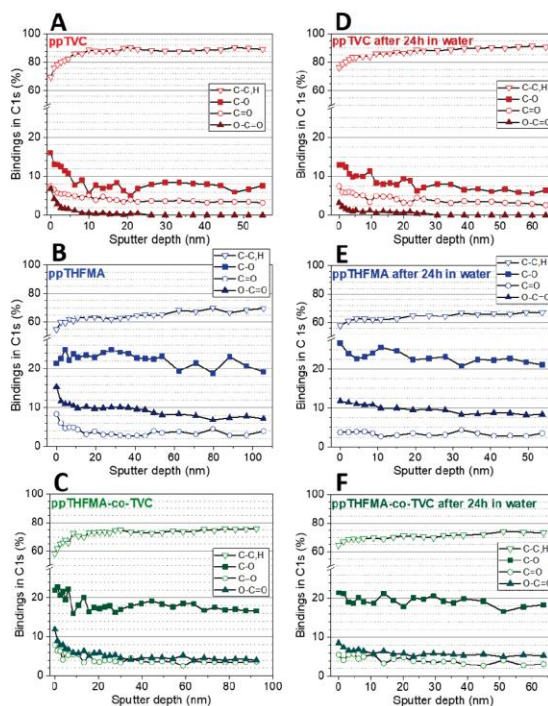
Figure 4. Evolution of the relative C 1s components of the ppTVC, ppTHFMA, and ppTHFMA-co-TVC films during sputtering by a 10 keV Ar GCIS with a cluster size of 1000 (Ar_{1000}^+). A, B, C: right after the deposition process; D, E, F: after 24 h of storage in water.

film. Although the ppTVC layer remained smooth, AFM images revealed a nanostructure comprising round-shaped particles densely packed over the whole area after the immersion in water. Remarkable changes in the topography can be seen for the ppTHFMA-co-TVC films, the surface was covered by irregular shaped donut-like rings of different height (0.3−1 μm).

3.2. SPR Immunosensing Using pp Films as Matrix Layers for Ab Immobilization. For the pp films thicker than 40 nm the SPR min angle peak was out of the range of the measurements. Owing to the thickness limitations only thin pp films could be used for the SPR measurements. Prior to the immunosensors development, chemical composition, morphology, and stability in water of the thin (20−40 nm) pp layers were compared to the thicker layers used for characterization. The thin pp films deposition process was adjusted to achieve the same level of conversion by decreasing the amount of liquid monomer spread at the substrate surface and the plasma-induced polymerization time. By XPS analysis and ellipsometric measurements it was shown that thin pp coatings had similar chemical composition and stability level in water (Table S5). The ppTVC thin films had approximately 5 at. % higher content of oxygen in its bulk, whereas ppTHFMA and ppTHFMA-co-TVC thin films were almost the same as the thicker pp films (differences were within 2 at. %). The level of stability of all of the thin films remained the same as for the thicker films. AFM analysis of the thin pp films before and after immersion in water showed that the 20−40 nm pp films have morphological features similar to the 120−140 nm pp films, but of a smaller scale (Figure S3). Ring-like structures were observed at the surface of

207
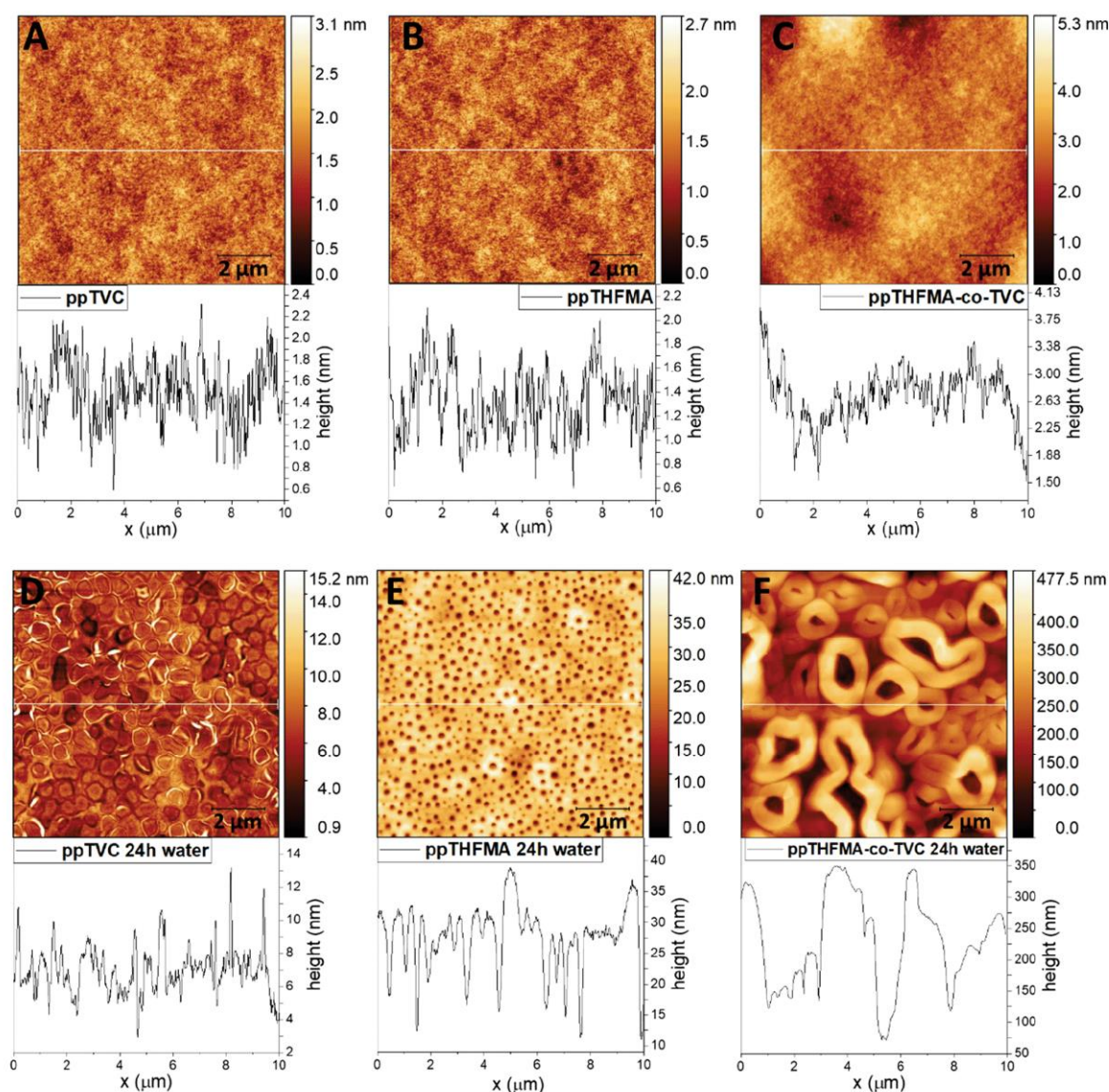
Figure 5. AFM images $(10 \times 10 \ \mu m^2)$ of ppTVC, ppTHFMA, and ppTHFMA-*co*-TVC films: A, B, C: as-deposited; D, E, F: after 24 h of storage in water. Corresponding height profiles are shown for each picture, which were extracted from the solid lines in the micrographs.

thin ppTVC layer, tiny pin-holes were seen at the surface of ppTHFMA layers, and donut-like structures were observed at the surface of ppTHFMA-*co*-TVC layers. Overall, the thin pp films were much smoother compared to the thicker coatings characterized before. The roughest coating still remained the copolymer ppTHFMA-*co*-TVC. Taking into account the similar chemical composition and levels of stability in water of both sets of the pp films (20−40 nm and 120−140 nm) we can conclude that roughness of pp films is increasing with the increasing thickness of the layers.

After it was shown that the thin pp films have a similar chemical composition and the same level of stability as the thicker pp films, SPR immunosensors using the pp films as matrix layers for immobilization of biorecognition element were

developed. First thin pp films were deposited on the surface of SPR chips, then the SPR chips were immersed overnight (18 h) in PBS for stabilization, then washed with water, dried, and inserted into the SPR device.

After inserting the SPR chips with the deposited pp film into the device the baseline of the sensor was recorded for about 40 min. The SPR chips used in our study have two channels: binding and reference. After the baseline establishment, EDC/NHS activation was applied to both channels (Figure S4). This zero-length cross-linker is typically applied to activate carboxyl groups forming NHS esters, reactive toward the primary amines.[42] The primary amines present in the antibody (Ab) molecule bind to the NHS esters yielding stable amide bonds (Scheme 1). Even though the shapes of the signals obtained in

Scheme 1. Immunosensor Preparation Procedure: 1: Plasma-Induced Polymerization, 2: EDC/NHS Activation, 3: Ab Immobilization, 4: Binding of Ag to Ab, 5: Regeneration of the Sensor Surface by Applying 10 mM HCl
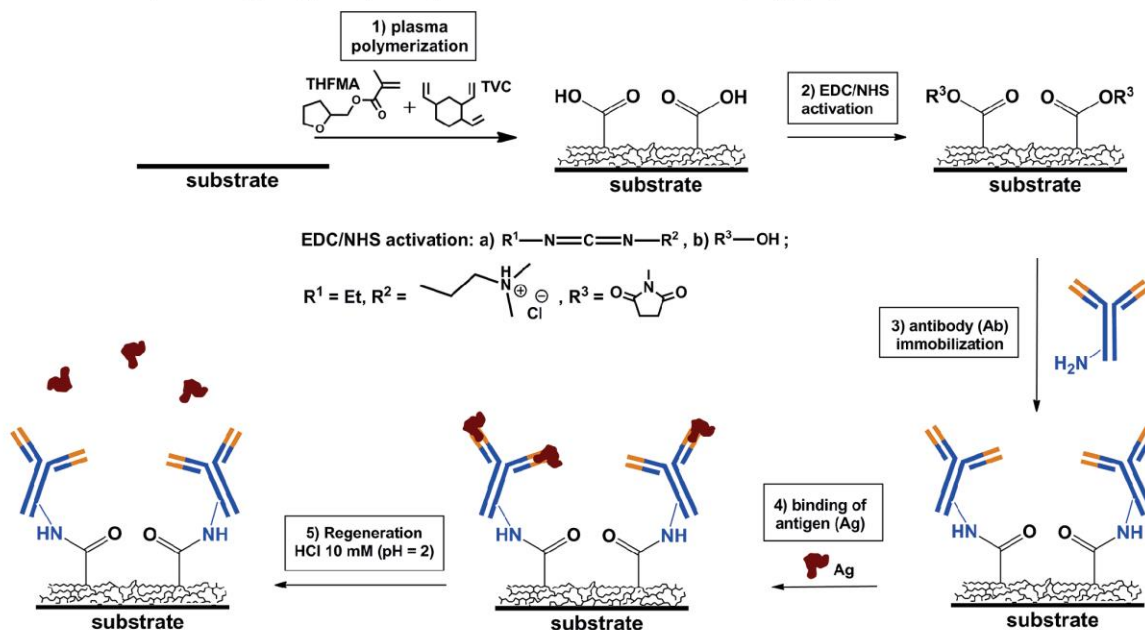
Table 1. Relative SPR Responses (mdeg) after Individual Steps of Antibody Immobilization Procedure

type of matrix layer (channel)	activation by EDC/NHS	immobilization of antibody (binding channel) and BSA (reference)	blocking by BSA	response to 1 μg/mL of HSA
ppTVC (binding)	45	250	245	30
ppTVC (reference)	42	495	2	1
ppTHFMA (binding)	54	160	185	23
ppTHFMA (reference)	52	390	5	1
ppTHFMA-co-TVC (binding)	57	300	150	22
ppTHFMA-co-TVC (reference)	55	635	−5	1
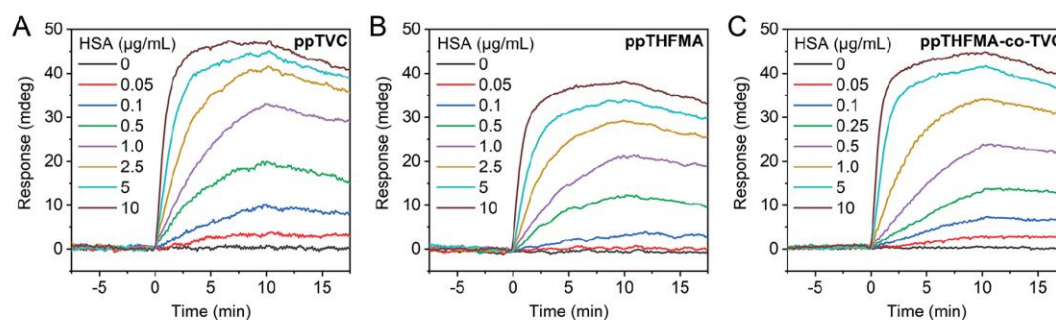
Figure 6. Sensorgrams: A: ppTVC based immunosensor, B: ppTHFMA based immunosensor, and C: ppTHFMA-co-TVC based immunosensor (reference channel is subtracted, real data are in the SI Figure S5).

the sensorgram during the interaction of the pp coatings with the EDC/NHS were quite different for each type of the pp layer, the level of the sensors response after EDC/NHS activation was almost the same in all of the cases (Table 1).

After the activation step, the solution of Al-01 Ab was applied to the binding channel and the BSA solution to the reference

channel at the same time. The shapes of the response curves were similar in all of the cases. The largest amount of Ab molecules was bound to the surfaces of ppTHFMA-co-TVC layer. Even though the amount of OH groups presented in the pp films was the largest in ppTVC (determined by FT−IR) and the amount of O−C═O groups was the largest in ppTHFMA

(determined by XPS), the copolymer pp film had better capacity in terms of immobilizing proteins. After Ab immobilization step free reactive sites left were blocked by BSA applied to both channels, and the immunotests with HSA antigen solutions were carried out (Figure 6).

The 10 mM solution of HCl was used as a regeneration agent and allowed to test from 7 to 9 concentrations with a single chip. The regeneration of SPR immunosensors worked perfectly for the ppTHFMA-co-TVC and ppTHFMA layers, whereas the ppTVC based immunosensor had a slight drift (Figure S6). The ppTVC based immunosensor also had the noisiest signal during the measurements. The ppTVC and ppTHFMA-co-TVC based sensors had an LOD of 50 ng/mL. ppTHFMA surface had the lowest capacity of binding proteins which resulted in LOD of 100 ng/mL and lower level of response to high concentration of HSA.

The sensors provided a linear response up to 10 μg/mL concentration of HSA. For each type of the developed immunosensor calibration curves were constructed (Figure 7). A good agreement with a log linear fit was achieved for the all of the pp films.
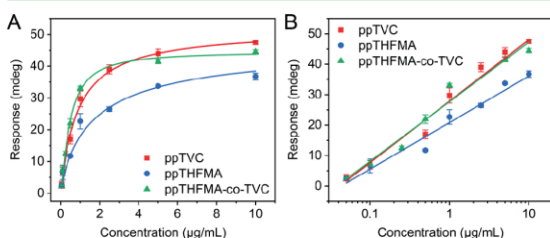
Figure 7. Calibration curves obtained for the developed SPR immunosensors. A: linear scale and B: log linear scale.

4. DISCUSSION

The main challenge for the development of effective biosensors using pp films is the creation of thin polymer layers that are stable in aqueous environment (in terms of thickness and elemental composition) and at the same time are reactive toward biomolecules. Polymer surfaces rich of oxygen functionalities such as −COOH, −OH, or −CH═O are of high interest in the field of bioapplications due to their ability of covalent binding of proteins and other bioligands.[43−46]

Here, three different types of O-rich pp films were prepared and investigated for chemical and morphological characteristics before and after storage in water prior to the SPR immunosensors development. First, the chemical functional groups presented in the pp films were analyzed by FT−IR spectroscopy and compared to the spectra of the used monomers. Both monomers contained no hydroxyl groups in their structure, however, all of the obtained pp films contained OH groups. These OH groups can originate from acids or alcohols formed during the plasma-induced polymerization process by interactions of monomers with the reactive oxygen species produced by the reactions of plasma with the surrounding air. Furthermore, for all studied coatings a decrease of vinyl group signals was clearly seen, which indicates that the vinyl bond played a major role in the polymerization process. A decrease of signal intensities and broadening of the peaks were seen for the pp films, which are typical features of a polymer FT−IR spectra. Almost all of the carbon signals presented in the

obtained spectra correspond to alkane parts of the polymeric chains. For the THFMA-based pp films, C═O and C−O−C corresponding to different esters were observed. Interestingly, in the structure of ppTVC, free OH groups were seen, as well as the position of the C═O stretching corresponded to carboxylic acids. Ether signals were found in all of the pp films. Overall, except the appearance of hydroxyl group and decrease of vinyl group intensity, there was no considerable chemical change in the structure of the monomer during the plasma-induced polymerization process. These differences in the monomer and polymer structures suggests that the polymerization followed a conventional free radical mechanisms via initiation by reactive oxygen species (mainly by alkoxy-radicals formed by dissociation of various peroxides) formed in the plasma.[47] No chemical changes were seen in the FT−IR spectra of the pp films immersed in water for 24 h; drop of intensity of all of the film signals resulted from the thickness losses. The ppTVC appeared to be the most stable, due to the lowest content of oxygen functionalities in its structure. Initial thickness losses during storage in water might originate from the less stable oligomer species formed during the process in the near-surface region. These oligomers were loosely bound and washed away when the films were immersed in water. It was shown that no more significant thickness losses happen after 24 h of storage in water, which is a typical trend of majority of pp surfaces.[30] Typically, a water contact angle measurements or oxygen content determination by XPS are carried out for investigation of stability of pp surfaces in water, however, such measurements do not provide sufficient information about the stability of the films in terms of their mass or thickness losses.[28,48,49] In our study, thickness losses after immersion in water were determined by ellipsometric measurements. The obtained results proved an excellent level of stability in water for all stabilized films after removal of loosely bound oligomer particles.

XPS analysis of the as-deposited pp films have shown that all of the obtained films had an increased content of oxygen in the near surface region. Larger amount of oxygen at the surface of pp films can be caused by postoxidation processes (reactions with activated air molecules) due to the radical nature of the plasma-induced polymerization.[50] The long-lived radicals trapped inside the polymer chains have a tendency to absorb oxygen. Another explanation of larger content of O−C═O groups in the near surface region of the films is a higher oxidation degree due to the direct interaction of plasma with the surface. A clear transition between the film and the substrate was recorded in all cases. All of the analyzed films had a peak in oxygen content in the film−substrate transition region. This peak appeared due to the plasma pretreatment procedure during which oxygen functionalities were formed at the substrate surface. The plasma-activated substrate surface was reactive toward the monomer and efficiently bound the growing film by formation of the Si−O−C thin interlayer. All of the deposited pp films contained alkane chains, which is another sign of a conventional-like free radical polymerization mechanism via vinyl or vinylidene bonds. In the bulk of the layers, the chemistry of the organic film remained almost unchanged as shown by rather stable atomic concentrations of carbon and oxygen. This can be used as an indicator of regularity of the obtained polymer chains. The period of regularity though can be relatively large as far as the process was rather rapid and involved many interactions with reactive radicals formed by the plasma (Figure 8) (e.g., R−CH$_2$−O$^\bullet$, R−C(O)−O$^\bullet$, R−CH$_2$−O−O$^\bullet$, HO$^\bullet$, HOO$^\bullet$). Densities of ions in atmospheric pressure plasmas are

210
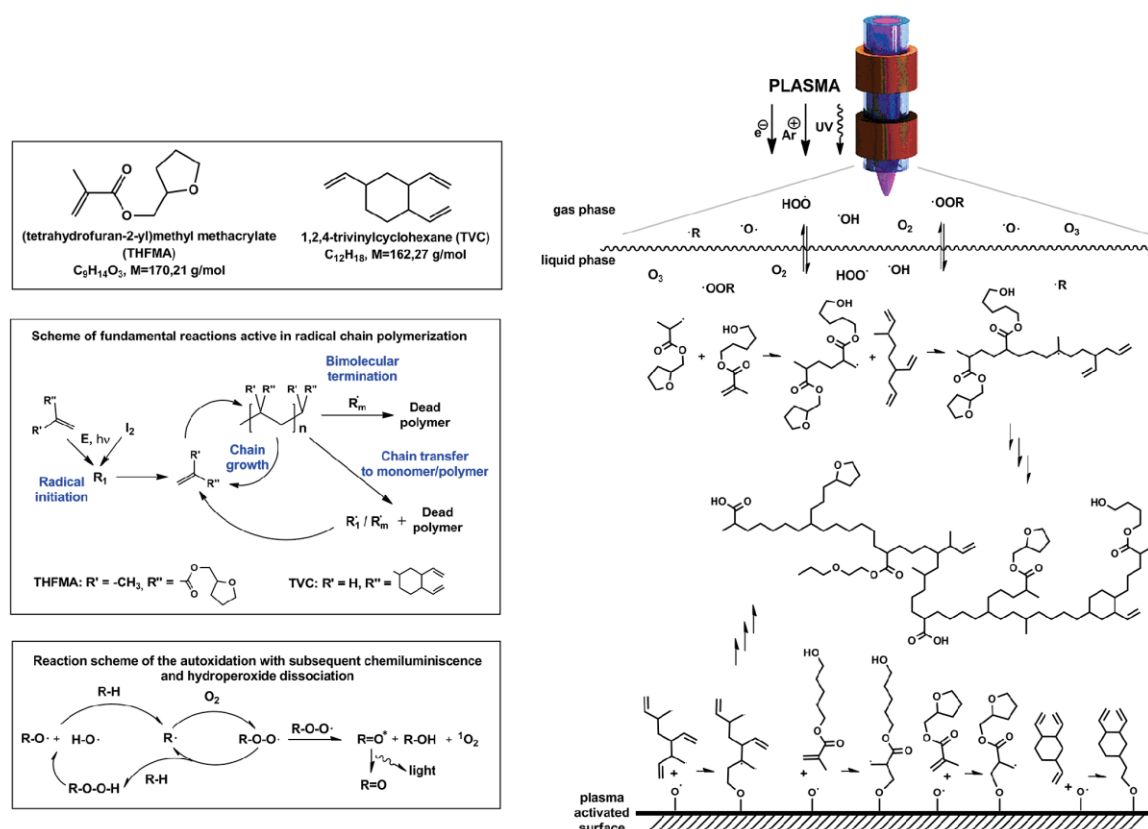
Figure 8. Schematic illustration of pp film formation during the APPJ polymerization.

insignificant, and their role in the polymer film formation can be neglected.[51−54]

The ppTVC had about 10 at. % of oxygen in its bulk, whereas the TVC itself did not contain any oxygen at all. This makes oxygen incorporation into carbon chains of the polymer evident. Oxygen found in the bulk of ppTVC film was mostly in the form of ethers and aldehydes (ketones), which can be caused by the action of R—O• that are known to be reactive toward carbon double bonds and are typically used as initiators of free radical polymerization (Figure 8).[55,56] In the near surface region of the ppTVC film, the O—C=O groups were present, which by taking into account the FT−IR spectrum corresponded to carboxylic acids. ppTHFMA (as well as THFMA) had the largest oxygen content compared to all other obtained films. The amount of ethers in the ppTHFMA was about three times larger than in ppTVC. THFMA monomer contained ethers in its structure and about one-third of the ethers content was a result of oxygen incorporation during the plasma-induced polymerization process. The ppTHFMA-co-TVC film had composition in between the ppTHFMA and ppTVC. It was shown that it is possible to adjust the carbon content by using a mixture of the monomers. The amount of aldehyde (ketone) functionalities remained constant (about 5 at. %) in all films. As far as none of the monomers had this functional group in their structure, all of the aldehydes (ketones) appeared in the course of the plasma-induced polymerization as a result of reactions with oxygen. It is interesting to note that none of the films contained any nitrogen,

even though there are plenty of reports about the formation of various nitrogen-containing reactive species during interactions of plasma with surrounding air.[57−59]

After 24 h of immersion of the films in water, XPS depth profiling results showed no chemical changes except of a slight loss of oxygen content from the film surfaces (app. 4 at.%). No signal from the substrate was detected in any of the cases. Even though the films exhibited different levels of thickness losses after 24 h of storage in water, all of them were stable in terms of their chemical composition.

WCA results have shown that all of the freshly deposited pp films were hydrophilic surfaces with similar values of WCA (Table S3). Such results were caused by a thin oxygen-rich layer that was found at their surfaces by XPS depth profiling. After 24 h of storage in water the WCA results showed a decrease of hydrophilicity for all of the pp layers. The increase of WCA of the pp films after immersion was related to the loss of thin oxygen-rich layer from their surfaces. The ppTVC had the largest increase in WCA after 24 h of storage in water caused by the lowest concentration of oxygen functionalities in its structure.

The morphology of the deposited films was studied by AFM. All of the freshly deposited pp films appeared as smooth surfaces. The ppTHFMA-co-TVC film had slightly higher roughness compared to single monomer films (Table S4). After 24 h of storage in water, different characteristic morphological changes appeared on the surfaces of the deposited films. Generally, a high

211

increase of surface roughness after the immersion in water was found in all cases. Furthermore, different morphological features were found at the surfaces of pp films after the immersion in water; these can originate from the different polymer chain growth mechanisms during the plasma-induced polymerization. The rings observed on the surface of ppTVC films can be a result of island-like formation of the polymer film. The pinhole-like dips on the surface of ppTHFMA can originate from the removal of oxygen-rich particles left from the bulk polymerization. The ppTHFMA-co-TVC layers exhibited morphological changes that represented a sum of the rings and pin holes formations; large donut-like structures were found over the whole surface. The copolymer exhibited the most dramatic changes on its surface after immersion in water, which resulted in an increase of the surface area by 10−12%. Generally, the increased total surface area can be beneficial for more efficient immobilization of biomolecules.

After thorough characterization of the obtained pp films, thin (20−40 nm) pp layers were deposited on SPR chips and SPR immunosensors were successfully elaborated. During the immunosensors preparation procedure the level of response of pp films toward EDC/NHS mixture was similar in all of the cases, but the amount of Ab bonded to the surface was different. The largest volume of Ab loaded at the sensor surface was in case of ppTHFMA-co-TVC layer, which can be due to a larger surface area resulted from the formation of donut-like structures at its surface. During the immunotests the performance of ppTVC and ppTHFMA-co-TVC based sensors was very similar, the ppTHFMA based sensor had the smallest amount of Ab bonded to its surface and was worse in terms of sensitivity and level of response. Even though the ppTVC based sensor had a slight drift and a relatively noisy signal because of the nonuniformity of its thickness resulting from high volatility of TVC the level of response toward analyte was slightly larger than that in the case of the ppTHFMA-co-TVC based sensor. The constructed calibration curves showed a good linearity in all of the cases, but the best agreement with the linear fit was achieved for the ppTHFMA-co-TVC based sensor.

The developed SPR immunosensors had the same sensitivity as the conventionally used SAMs and CMD based immuno-sensors, but offered a better stability and regenerability. The level of response was larger than that in the case of SAMs based sensors, but smaller than in case of CMD based sensors.[60] Such results can be explained by the fact that the surface area of SAMs is smaller than of the pp films, but CMD layers are a loose 3D network and have a much larger surface area.[61] We have previously reported on the use of pp films for immunosensors development, but the level of response, sensitivity, and stability of such sensors was worse compared to our APPJ pp films.[30,62] Our results have shown an importance of presence of morphological features at the film surface leading to an increase of surface area and the load proteins.

5. CONCLUSIONS

Plasma-induced polymerization using APPJ is an efficient alternative to conventional methods for the creation of thin layers suitable for bioreceptor immobilization. The fast (overall time of the plasma-induced polymerization procedure takes just one minute) and easy procedure for the preparation of the pp surfaces makes it compatible with industrial applications. The plasma-induced polymerization method brings advantages of interactions of the substrate surface with highly reactive species

without any damage, which results in a much better level of adhesion of pp films to the substrate surface.

A detailed study of the obtained pp films showed that the plasma-induced polymerization under the described conditions followed a conventional-like free radical pathway, via vinyl or vinylidene bond. The main difference between the conventional free radical mechanism and the plasma-induced polymerization mechanism was much higher concentration of reactive oxygen species (e.g., $R-CH_2-O^\bullet$, $R-C(O)-O^\bullet$, $R-CH_2-O-O^\bullet$, $HO^\bullet$, $HOO^\bullet$) presented in plasma. This resulted in oxygen incorporation into the film structure mostly in the form of ethers. The chemical structure of the obtained pp films contained branched alkane chains and hydroxyl groups, which appeared in the film structure from the reactions with plasma-activated molecules of the surrounding air. The largest amount of oxygen functional groups was found at the surface and in the near surface region of all obtained films. The stability of pp films in aqueous environment was studied as it is critical for bioanalytical applications. A general trend of no substantial thickness losses after 24 h of storage in liquid was observed. The most stable pp film was the ppTVC coating, which had the lowest amount of oxygen in its structure. The ppTHFMA and ppTHFMA-co-TVC had more significant thickness losses during the initial storage in water, however, the chemical composition of all of the studied films remained unchanged. The initial thickness losses were caused by the removal of loosely bound oligomer species present at the surface of the films. The AFM analysis revealed different characteristic morphological changes for each type of the pp film.

High level of stability and presence of various oxygen functional groups (such as carboxyl and hydroxyl groups) in the structure of the obtained pp films make them perfect candidates for the use in biosensing applications as bioreceptor immobilization matrices. The morphological features formed at the surfaces of the pp films increased the surface area, enabling higher yield and structural variability for bioreceptor immobilization. The developed SPR immunosensors based on pp films showed an excellent level of stability and regenerability allowing from 7 to 9 measurements with a single sensor. Achieved LODs of 50 ng/mL were comparable to the conventionally used SAMs and CMD layers. The level of response was larger than that in the case of SAM layers, but smaller than CMD layers, which are a 3D loose networks. All of the developed immunosensors provided selective and linear response to the analyte in the range of the used concentrations (from 50 ng/mL to 10 μg/ mL). Our results have shown that not just the amount of functional groups presented in the pp layers is crucial for the performance of SPR immunosensors, but also the morphology of the layers plays an important role. The ppTHFMA-co-TVC layer was the roughest among the obtained pp films and had the largest capacity for binding proteins. ppTVC layer based SPR immunosensor was just slightly worse in terms of performance: there was quite a noisy signal during the measurements and a slight drift during regenerations, but the level of the response to analyte was the largest among the tested pp films.

■ ASSOCIATED CONTENT

ⓈI Supporting Information

The Supporting Information is available free of charge at https://pubs.acs.org/doi/10.1021/acsami.0c01443.

> Details on pp films surface characterization by XPS, FT−IR, WCA, AFM, and SPR sensorgrams (PDF)

■ AUTHOR INFORMATION

Corresponding Author

Ekaterina Makhneva − *RG Bio Sensing Surfaces, Leibniz Institute for Plasma Science and Technology (INP), 17489 Greifswald, Germany;* ⊙ orcid.org/0000-0001-7059-0200; Email: ekaterina.makhneva@inp-greifswald.de

Authors

Laura Barillas − *RG Bio Sensing Surfaces, Leibniz Institute for Plasma Science and Technology (INP), 17489 Greifswald, Germany*

Zdeněk Farka − *RG Nanobiotechnology, Central European Institute of Technology (CEITEC), Masaryk University, 625 00 Brno, Czech Republic;* ⊙ orcid.org/0000-0002-6842-7081

Matěj Pastucha − *RG Nanobiotechnology, Central European Institute of Technology (CEITEC), Masaryk University, 625 00 Brno, Czech Republic*

Petr Skládal − *RG Nanobiotechnology, Central European Institute of Technology (CEITEC), Masaryk University, 625 00 Brno, Czech Republic;* ⊙ orcid.org/0000-0002-3868-5725

Klaus-Dieter Weltmann − *RG Bio Sensing Surfaces, Leibniz Institute for Plasma Science and Technology (INP), 17489 Greifswald, Germany*

Katja Fricke − *RG Bio Sensing Surfaces, Leibniz Institute for Plasma Science and Technology (INP), 17489 Greifswald, Germany*

Complete contact information is available at:
https://pubs.acs.org/10.1021/acsami.0c01443

Author Contributions

The manuscript was written through contributions of all authors. All authors have given approval to the final version of the manuscript.

Notes

The authors declare no competing financial interest.

■ ACKNOWLEDGMENTS

■ ABBREVIATIONS

TVC, 1,2,4-trivinylcyclohexane
THFMA, tetrahydrofurfurylmethacrylate
APPJ, atmospheric pressure plasma jet
pp, plasma polymerized
MA, maleic anhydride
PMMA, polymethylmethacrylate
PBS, phosphate buffered saline
EDC, 1-ethyl-3-(3-dimethylaminopropyl)carbodiimide hydrochloride
NHS, N-hydroxysuccinimide
BSA, bovine serum albumin
HSA, human serum albumin
Ab, antibody
LOD, limit of detection
CMD, carboxymethylated dextran
SAM, self-assembled monolayer.

■ REFERENCES

(1) Vericat, C.; Vela, M. E.; Benitez, G.; Carro, P.; Salvarezza, R. C. Self-Assembled Monolayers of Thiols and Dithiols on Gold: New Challenges for a Well-Known System. *Chem. Soc. Rev.* **2010**, *39*, 1805−1834.

(2) Nurmalasari, R.; Gaffar, Y. S.; Hartati, Y. W. Label-Free Electrochemical DNA Biosensor for the Detection of Mycobacterium Tuberculosis Using Gold Electrode Modified by Self-Assembled Monolayer of Thiol. *Procedia Chem.* **2015**, *17*, 111−117.

(3) Bergström, A. SPR Sensor Surfaces Based on Self-Assembled Monolayers, **2009**.

(4) Denis, L.; Cossement, D.; Godfroid, T.; Renaux, F.; Bittencourt, C.; Snyders, R.; Hecq, M. Synthesis of Allylamine Plasma Polymer Films: Correlation between Plasma Diagnostic and Film Characteristics Plasma. *Plasma Processes Polym.* **2009**, *6*, 199−208.

(5) Chen, Q.; Förch, R.; Knoll, W. Characterization of Pulsed Plasma Polymerization Allylamine as an Adhesion Layer for DNA Adsorption/Hybridization. *Chem. Mater.* **2004**, *16*, 614−620.

(6) Ryan, M. E.; Hynes, A. M.; Badyal, J. P. S. Pulsed Plasma Polymerization of Maleic Anhydride. *Chem. Mater.* **1996**, *8*, 37−42.

(7) Choukourov, A.; Biederman, H.; Slavinska, D.; Hanley, L.; Grinevich, A.; Boldyryeva, H.; Mackova, A. Mechanistic Studies of Plasma Polymerization of Allylamine. *J. Phys. Chem. B* **2005**, *109*, 23086−23095.

(8) Li, Y. P.; Zhang, Z. C.; Shi, W.; Lei, M. K. Adhesion Enhancement of Polyethylene Modified by Capacitively Coupled Radio Frequency Plasma Polymerization of Ethanol. *Surf. Coat. Technol.* **2014**, *259*, 77−82.

(9) Mori, Y.; Yoshii, K.; Kakiuchi, H.; Yasutake, K. Atmospheric Pressure Plasma Chemical Vapor Deposition System for High-Rate Deposition of Functional Materials. *Rev. Sci. Instrum.* **2000**, *71*, 3173−3177.

(10) Girard-Lauriault, P. L.; Mwale, F.; Iordanova, M.; Demers, C.; Desjardins, P.; Wertheimer, M. R. Atmospheric Pressure Deposition of Micropatterned Nitrogen-Rich Plasma-Polymer Films for Tissue Engineering Plasma. *Plasma Processes Polym.* **2005**, *2*, 263−270.

(11) Kurniawan, D.; Kim, B. S.; Lee, H. Y.; Lim, J. Y. Atmospheric Pressure Glow Discharge Plasma Polymerization for Surface Treatment on Sized Basalt Fiber/Polylactic Acid Composites. *Composites, Part B* **2012**, *43*, 1010−1014.

(12) Trunec, D; Zajickova, L; Bursikova, V; Studnicka, F; Stahel, P; Prysiazhnyi, V; Perina, V; Houdkova, J; Navratil, Z; Franta, D Deposition of Hard Thin Films from HMDSO in Atmospheric Pressure Dielectric Barrier Discharge. *J. Phys. D: Appl. Phys.* **2010**, *43*, 225403.

(13) Barekzi, N.; Laroussi, M. Effects of Low Temperature Plasmas on Cancer Cells Plasma. *Plasma Processes Polym.* **2013**, *10*, 1039−1050.

(14) Cools, P.; Declercq, H.; Ghobeira, R.; Morent, R.; De Geyter, N. Acrylic Acid Plasma Coatings for Enhanced Cell Migration in PCL 3D Additive Manufactured Scaffolds. *Surf. Coat. Technol.* **2018**, *350*, 925−935.

(15) Beck, A. J.; Short, R. D.; Matthews, A. Deposition of Functional Coatings from Acrylic Acid and Octamethylcyclotetrasiloxane onto Steel Using an Atmospheric Pressure Dielectric Barrier Discharge. *Surf. Coat. Technol.* **2008**, *203*, 822−825.

(16) Nisol, B.; Batan, A.; Dabeux, F.; Kakaroglou, A.; De Graeve, I.; Van Assche, G.; Van Mele, B.; Terryn, H.; Reniers, F. Surface Characterization of Atmospheric Pressure Plasma-Deposited Allyl Methacrylate and Acrylic Acid Based Coatings Plasma. *Plasma Processes Polym.* **2013**, *10*, 564−571.

(17) Bardon, J.; Dieden, R.; Grysan, P.; Mertz, G.; Martin, A.; Delmée, M.; Ruch, D. Mechanical Properties of Thin Plasma Polymer Coatings from Hexanediol Dimethacrylate and Relations with Their Chemical Properties. *Surf. Coat. Technol.* **2019**, *358*, 320−330.

(18) Loyer, F.; Frache, G.; Choquet, P.; Boscher, N. D. Atmospheric Pressure Plasma-Initiated Chemical Vapor Deposition (AP-PiCVD) of Poly(Alkyl Acrylates): An Experimental Study. *Macromolecules* **2017**, *50*, 4351−4362.

(19) Mertz, G.; Delmée, M.; Bardon, J.; Martin, A.; Ruch, D.; Fouquet, T.; Garreau, S.; Airoudj, A.; Marguier, A.; Ploux, L.; Roucoules, V. Atmospheric Pressure Plasma Co-Polymerization of Two Acrylate Precursors: Toward the Control of Wetting Properties Plasma. *Plasma Processes Polym.* **2018**, *15*, 1800073.

(20) Donegan, M.; Dowling, D. P. Protein Adhesion on Water Stable Atmospheric Plasma Deposited Acrylic Acid Coatings. *Surf. Coat. Technol.* **2013**, *234*, 53−59.

(21) Francesch, L.; Garreta, E.; Balcells, M.; Edelman, E. R.; Borrós, S. Fabrication of Bioactive Surfaces by Plasma Polymerization Techniques Using a Novel Acrylate-Derived Monomer Plasma. *Plasma Processes Polym.* **2005**, *2*, 605−611.

(22) Bitar, R.; Cools, P.; De Geyter, N.; Morent, R. Acrylic Acid Plasma Polymerization for Biomedical Use. *Appl. Surf. Sci.* **2018**, *448*, 168−185.

(23) Notara, M.; Bullett, N. A.; Deshpande, P.; Haddow, D. B.; MacNeil, S.; Daniels, J. T. Plasma Polymer Coated Surfaces for Serum-Free Culture of Limbal Epithelium for Ocular Surface Disease. *J. Mater. Sci.: Mater. Med.* **2007**, *18*, 329−338.

(24) Nisol, B.; Watson, S.; Lerouge, S.; Wertheimer, M. R. Energetics of Reactions in a Dielectric Barrier Discharge with Argon Carrier Gas: III Esters Plasma. *Plasma Processes Polym.* **2016**, *13*, 900−907.

(25) Pan, Y. V.; Denton, D. D. Plasma Dissociation Reaction Kinetics. I. Methyl Methacrylate. *J. Appl. Polym. Sci.* **1999**, *73*, 1−16.

(26) Pan, Y. V.; Denton, D. D. Plasma Dissociation Reaction Kinetics. II. Precursors Related to Methyl Methacrylate: Methyl Crotonate, Methyl Isobutyrate, Ethyl Methacrylate, and Vinyl Acetate. *J. Appl. Polym. Sci.* **1999**, *73*, 17−27.

(27) Loyer, F.; Bengasi, G.; Frache, G.; Choquet, P.; Boscher, N. D. Insights in the Initiation and Termination of Poly(Alkyl Acrylates) Synthesized by Atmospheric Pressure Plasma-Initiated Chemical Vapor Deposition (AP-PiCVD) Plasma. *Plasma Processes Polym.* **2018**, *15*, 1800027.

(28) Rupper, P.; Vandenbossche, M.; Bernard, L.; Hegemann, D.; Heuberger, M. Composition and Stability of Plasma Polymer Films Exhibiting Vertical Chemical Gradients. *Langmuir* **2017**, *33*, 2340−2352.

(29) Hegemann, D.; Indutnyi, I.; Zajíčková, L.; Makhneva, E.; Farka, Z.; Ushenin, Y.; Vandenbossche, M. Stable, Nanometer-Thick Oxygen-Containing Plasma Polymer Films Suited for Enhanced Biosensing Plasma. *Plasma Processes Polym.* **2018**, *15*, No. 1800090.

(30) Makhneva, E.; Obrusník, A.; Farka, Z.; Skládal, P.; Vandenbossche, M.; Hegemann, D.; Zajíčková, L. Carboxyl-Rich Plasma Polymer Surfaces in Surface Plasmon Resonance Immunosensing. *Jpn. J. Appl. Phys.* **2018**, *57*, 01AG06.

(31) Daeschlein, G.; Von Woedtke, T.; Kindel, E.; Brandenburg, R.; Weltmann, K. D.; Jünger, M. Antibacterial Activity of an Atmospheric Pressure Plasma Jet against Relevant Wound Pathogens in Vitro on a Simulated Wound Environment Plasma. *Plasma Processes Polym.* **2010**, *7*, 224−230.

(32) Carton, O.; Ben Salem, D.; Bhatt, S.; Pulpytel, J.; Arefi-Khonsari, F. Plasma Polymerization of Acrylic Acid by Atmospheric Pressure Nitrogen Plasma Jet for Biomedical Applications Plasma. *Plasma Processes Polym.* **2012**, *9*, 984−993.

(33) Lu, Q.; Liu, D.; Song, Y.; Zhou, R.; Niu, J. Inactivation of the Tomato Pathogen Cladosporium Fulvum by an Atmospheric-Pressure Cold Plasma Jet Plasma. *Plasma Processes Polym.* **2014**, *11*, 1028−1036.

(34) Trizio, I.; Intranuovo, F.; Gristina, R.; Dilecce, G.; Favia, P. He/O2Atmospheric Pressure Plasma Jet Treatments of PCL Scaffolds for Tissue Engineering and Regenerative Medicine Plasma. *Plasma Processes Polym.* **2015**, *12*, 1451−1458.

(35) Neretti, G.; Tampieri, F.; Borghi, C. A.; Brun, P.; Cavazzana, R.; Cordaro, L.; Marotta, E.; Paradisi, C.; Seri, P.; Taglioli, M.; Zaniol, B.; Zuin, M.; Martines, E. Characterization of a Plasma Source for Biomedical Applications by Electrical, Optical, and Chemical Measurements Plasma. *Plasma Processes Polym.* **2018**, *15*, 1800105.

(36) Van Vrekhem, S.; Morent, R.; De Geyter, N. Deposition of a PMMA Coating with an Atmospheric Pressure Plasma Jet. *J. Coatings Technol. Res.* **2018**, *15*, 679−690.

(37) Schäfer, J.; Foest, R.; Quade, A.; Ohl, A.; Weltmann, K. D. Local Deposition of SiOx Plasma Polymer Films by a Miniaturized Atmospheric Pressure Plasma Jet (APPJ). *J. Phys. D: Appl. Phys.* **2008**, *41*, 194010.

(38) Coates, J. Interpretation of Infrared Spectra, A Practical Approach. *Encyclopedia of Analytical Chemistry* **2006**, 10815−10837.

(39) Watts, J. F.; Wolstenholme, J. An Introduction to Surface Analysis by XPS and AES, **2003**. DOI: 10.1002/0470867930

(40) Cumpson, P. J.; Portoles, J. F.; Barlow, A. J.; Sano, N.; Birch, M. Depth Profiling Organic/Inorganic Interfaces by Argon Gas Cluster Ion Beams: Sputter Yield Data for Biomaterials, in-Vitro Diagnostic and Implant Applications. *Surf. Interface Anal.* **2013**, *45*, 1859−1868.

(41) Castner, D. G.; Ratner, B. D. Surface Characterization of Butyl Methacrylate. *Surf. Interface Anal.* **1990**, *15*, 479−486.

(42) Fischer, M. J. E. Amine Coupling Through EDC/NHS: A Practical Approach. In Surface Plasmon Resonance. *Methods Mol. Biol.* **2010**, *627*, 55−73.

(43) Howell, S.; Kenmore, M.; Kirkland, M.; Badley, R. A. High-Density Immobilization of an Antibody Fragment to a Carboxymethy-lated Dextran-Linked Biosensor Surface. *J. Mol. Recognit.* **1998**, *11*, 200−203.

(44) Wadu-Mesthrige, K.; Amro, N. A.; Liu, G. Immobilization of Proteins on Self-Assembled Monolayers. *Scanning* **2000**, *22*, 380−388.

(45) Ducker, R. E.; Montague, M. T.; Leggett, G. J. A Comparative Investigation of Methods for Protein Immobilization on Self-Assembled Monolayers Using Glutaraldehyde, Carbodiimide, and Anhydride Reagents. *Biointerphases* **2008**, *3*, 59−65.

(46) Jadhav, S. A. Self-Assembled Monolayers (SAMs) of Carboxylic Acids: An Overview. *Cent. Eur. J. Chem.* **2011**, *9*, 369−378.

(47) Guerrero-Santos, R.; Saldivar-Guerra, E.; Bonilla-Cruz, J. Free Radical Polymerization. *In Handbook of Polymer Synthesis, Characterization, and Processing* **2013**, 65−83.

(48) Loyer, F.; Combrisson, A.; Omer, K.; Moreno-Couranjou, M.; Choquet, P.; Boscher, N. D. Thermoresponsive Water-Soluble Polymer Layers and Water-Stable Copolymer Layers Synthesized by Atmos-pheric Plasma Initiated Chemical Vapor Deposition. *ACS Appl. Mater. Interfaces* **2019**, *11*, 1335−1343.

(49) Detomaso, L.; Gristina, R.; Senesi, G. S.; D'Agostino, R.; Favia, P. Stable Plasma-Deposited Acrylic Acid Surfaces for Cell Culture Applications. *Biomaterials* **2005**, *26*, 3831−3841.

(50) Meyer-Plath, A. Identification of Surface Radicals on Polymers. *Vak. Forsch. Prax.* **2005**, *17*, 40−46.

(51) Waskoenig, J.; Niemi, K.; Knake, N.; Graham, L. M.; Reuter, S.; Schulz-Von Der Gathen, V.; Gans, T. Atomic Oxygen Formation in a Radio-Frequency Driven Micro-Atmospheric Pressure Plasma Jet Plasma Sources. *Plasma Sources Sci. Technol.* **2010**, *19*, 045018.

(52) Willems, G.; Hecimovic, A.; Sgonina, K.; Carbone, E.; Benedikt, J. Mass Spectrometry of Neutrals and Positive Ions in He/CO2 Non-Equilibrium Atmospheric Pressure Plasma Jet Plasma. *Plasma Phys. Controlled Fusion* **2020**, *62*, 034005.

(53) Petersen, J.; Becker, C.; Fouquet, T.; Addiego, F.; Toniazzo, V.; Dinia, A.; Ruch, D. Nano-Ordered Thin Films Achieved by Soft Atmospheric Plasma Polymerization. *RSC Adv.* **2013**, *3*, 4416−4424.

(54) Klages, C. P.; Czerny, A. K.; Philipp, J.; Becker, M. M.; Loffhagen, D. DBD-Based Plasma Polymerization from Monomer-Argon Mixtures: Analytical Model of Monomer Reactions with Excited Argon Species Plasma. *Plasma Processes Polym.* **2017**, *14*, No. 1700081.

(55) Wittenberg, N. F. G.; Buback, M.; Hutchinson, R. A. Kinetics and Modeling of the Radical Polymerization of Acrylic Acid and of Methacrylic Acid in Aqueous Solution, *Macromol. React. Eng.* **2013**, *7*, 267.

(56) Coqueret, X.Radiation-Induced Polymerization of ionizing radiation in materials processing in applications. **2017**, 143−165

(57) Gorbanev, Y.; Soriano, R.; O'Connell, D.; Chechik, V. An Atmospheric Pressure Plasma Setup to Investigate the Reactive Species Formation. *J. Vis. Exp.* **2016**, *117*, 1−6.

(58) Reuter, S.; Von Woedtke, T.; Weltmann, K. D. The KINPen - A Review on Physics and Chemistry of the Atmospheric Pressure Plasma Jet and Its Applications. *J. Phys. D: Appl. Phys.* **2018**, *51*, 233001.

214

(59) Boxhammer, V. Development of a Safe Therapeutic Window for Cold Atmospheric Plasma Treatments, **2014**.

(60) Makhneva, E.; Farka, Z.; Pastucha, M.; Obrusník, A.; Horáčková, V.; Skládal, P.; Zajíčková, L. Maleic Anhydride and Acetylene Plasma Copolymer Surfaces for SPR Immunosensing. *Anal. Bioanal. Chem.* **2019**, *411*, 7689−7697.

(61) Song, S.; Lu, Y.; Li, X.; Cao, S.; Pei, Y.; Aastrup, T.; Pei, Z. Optimization of 3D Surfaces of Dextran with Different Molecule-weights for Real-Time Detection of Biomolecular Interactions by a QCM Biosensor. *Polymers (Basel, Switz.)* **2017**, *9*, 409.

(62) Makhneva, E.; Farka, Z.; Skládal, P.; Zajíčková, L. Cyclopropyl-amine Plasma Polymer Surfaces for Label-Free SPR and QCM Immunosensing of Salmonella Sensors. *Sens. Actuators, B* **2018**, *276*, 447−455.

215

Paper VIII

Amperometric Immunosensor for Rapid Detection of Honeybee Pathogen *Melissococcus plutonius*

Mikušová, Z.; <u>Farka, Z.*</u>; Pastucha, M.; Poláchová, V.; Obořilová, R.; Skládal, P.

Contribution:

Design of experiments, preparation of immunization antigen and antibody, optimization of electrochemical immunosensor, data evaluation, manuscript writing

Amperometric Immunosensor for Rapid Detection of Honeybee Pathogen *Melissococcus Plutonius*

Zuzana Mikušová,[a, b] Zdeněk Farka,*[a] Matěj Pastucha,[a, b] Veronika Poláchová,[a, b] Radka Obořilová,[b] and Petr Skládal*[a, b]

This contribution is dedicated to the memory of Professor Emil Paleček.

Abstract: European foulbrood (EFB) is a honeybee larvae disease caused by a bacterium *Melissococcus plutonius*. An amperometric immunosensor based on a sandwich assay was developed for rapid point-of-care detection of this pathogen. An in-house made anti-*Melissococcus* antibody was immobilized to a gold surface of a screen-printed sensor *via* self-assembled monolayer of cysteamine activated with glutaraldehyde. The direct impedimetric detection of captured microbial cells was tested, however, a better performance was obtained after the formation of sandwich with the peroxidase-labeled antibody in the amperometric mode. The label-free assay was limited by higher non-specific binding. The limit of detection of the immunosensor was 6.6×10^4 CFU mL^{-1} (colony-forming units) with wide linear range between 10^5 CFU mL^{-1} and 10^9 CFU mL^{-1}. The whole analysis was completed within 2 h, which is shorter compared to common laboratory diagnostic tools, such as enzyme-linked immunosorbent assay or polymerase chain reaction. Furthermore, atomic force microscopy was used for confirmation of the bacteria presence on the electrode surface. The developed immunosensor was successfully employed in the analysis of real samples of honeybees and larvae. The achieved results demonstrate the potential of the amperometric immunosensor for practical in-field diagnosis of EFB, which can prevent infection spreading and connected losses of honeybee colonies.

Keywords: biosensor · amperometry · sandwich assay · antibody · European foulbrood · *Apis mellifera*

1 Introduction

Western honeybee (*Apis mellifera*) is considered as the most important pollinator and therefore, an indispensable part of the ecosystem. However, in the last decades, serious losses of honeybee colonies attributed mostly to climate changes and diseases of various origin, including parasites, microorganisms, and viruses, were observed. One of the most relevant microbial honeybee diseases is European foulbrood (EFB). This infectious disease is caused by a bacterial Gram-positive pathogen *Melissococcus plutonius* [1]. EFB affects mainly four to five days old honeybee larvae, which become infected after ingesting food contaminated with the bacteria. EFB can be visually detected by several symptoms; the color of larvae changes from pearl white to yellow or brown and larvae usually die displaced in the brood cells, instead of normal coiled position [2]. The infection affects large percentage of the brood, leading to weakening of the colony and its possible collapse.

Due to the economic and environmental consequences, the prevention of the uncontrolled spreading of the EFB is crucial to prevent losses of honeybee colonies. With this intention, the development of a reliable method to detect the causative agent of the disease, *M. plutonius*, in early stages of the infection, ideally in the point-of-care (POC) format, is highly demanded. The basic method for the detection is based on microscopic evaluation of carbol fuchsin-stained smears. However, this method is not sensitive enough to reveal the infection in its early stages or in honeybee products. Traditionally, very sensitive but time-consuming cultivation-based methods are complicated by low cultivation recoveries of the bacterium and its overgrowing by secondary invaders [2]. A relatively new option for the EFB diagnosis is a test kit based on lateral flow immunoassay; however, it was developed mainly for qualitative confirmation of the disease, suggesting room for more sensitive methods of EFB diagnosis [3]. On the other hand, the detection of EFB based on real-time polymerase chain reaction (PCR) provides improved sensitivity; however, the drawback of this approach lies in its feasibility only in laboratory conditions [4].

In recent years, biosensors are being developed as an alternative to common laboratory equipment for pathogen detection [5,6]. The early identification of pathogens

[a] Z. Mikušová, Z. Farka, M. Pastucha, V. Poláchová, P. Skládal
CEITEC MU, Masaryk University, Kamenice 5, 625 00 Brno, Czech Republic
E-mail: farka@mail.muni.cz
[b] Z. Mikušová, M. Pastucha, V. Poláchová, R. Obořilová, P. Skládal
Department of Biochemistry, Masaryk University, Kamenice 5, 625 00 Brno, Czech Republic
E-mail: skladal@chemi.muni.cz

needs to be realized in-field as POC test to initiate early response [7]. Electrochemical approaches, including amperometry and electrochemical impedance spectroscopy (EIS), provide high sensitivity, operational simplicity, short analysis times, and are compatible with systems for POC testing [8]. In case of the amperometric sensors, the electrochemical reaction is measured as a current flow difference at constant voltage [9]. EIS is a technique for interpreting changes occurring at the electrode-solution interface. Impedance is a complex resistance calculated through model circuit (typically Randles circuit) formed by combination of resistors, inductors, and capacitors [10]. Recently, many papers describing the development of various biosensors for pathogen detection were reported using different electrochemical techniques, including amperometry, voltammetry, potentiometry, and EIS [11,12].

The most frequent bacterial targets for biosensors are foodborne pathogens including *Escherichia coli* [13,14,15], *Salmonella enterica* [16,17,18], *Listeria monocytogenes* [19] and *Vibrio parahaemolyticus* [20]. The EIS biosensors for bacteria provide typical limits of detection (LODs) of 10^2–10^4 $CFU\,mL^{-1}$ (colony-forming units) with no pre-enrichment and analysis time around 1–2 hours [19,21,22]. Further improvement of the sensitivity can be achieved by the use of suitable labels [23]. In case of amperometric detection, LODs are typically around 10^2 $CFU\,mL^{-1}$ with analysis times ranging from 1 to 3 h [17,24]. The sensitivity can be further enhanced e.g. by the use of magnetic microparticles, as reviewed recently [7]. These works proved that POC immunoassays based on electrochemical transducers can achieve high sensitivity with reasonable analysis times.

The antibody with high affinity and low cross-reactivity is a key element of a functional immunosensor. In our case, no antibodies were commercially available for *M. plutonius*. For this reason, we have recently prepared a rabbit polyclonal anti-*Melissococcus* antibody, which was used in microtiter-plate based enzyme-linked immunosorbent assay (ELISA) [25]. The sandwich assay scheme was employed; thus, we have also conjugated the antibody with peroxidase from horseradish (HRP) to provide signal development *via* enzymatically catalyzed reaction.

The aim of this work was to transfer the immunoassay from the ELISA format to a rapid and miniaturized assay based on electrochemical transducer. Gold screen-printed electrodes (SPEs) were used due to their low cost, mass production possibilities, portability, and suitability for in-field detection [18]. The practical capabilities of the developed amperometric immunosensor were verified on the analysis of real samples of spiked bees and larvae.

2 Materials and Methods

2.1 Chemicals and Reagents

Bovine serum albumin (BSA), bovine γ-globulin (BGG), cysteamine hydrochloride, glutaraldehyde solution (25 %), peroxidase from horseradish (EC 1.11.1.7 type VI, specific activity >250 purpurogallin units mg^{-1}), Tween 20, 3,3′,5,5′-tetramethylbenzidine (TMB), L-cysteine hydrochloride, tris(hydroxymethyl)aminomethane (Tris), ethylenediaminetetraacetic acid (EDTA), peptone, starch, tryptone, yeast extract, and Nutrient broth No. 4 were obtained from Sigma-Aldrich (Germany). Potassium hexacyanoferrate(III) was purchased from Fluka (Germany). Poly(vinyl alcohol) (PVA; 6 kDa) was from Polysciences (USA). Dimethylsulfoxide (DMSO), glucose, and potassium hexacyanoferrate(II) trihydrate were purchased from Lach-Ner (Czech Republic). Potassium hydrogenphosphate, potassium dihydrogen phosphate, sodium hydrogen phosphate dodecahydrate, sodium dihydrogen phosphate dihydrate, potassium hydroxide, sodium chloride, and hydrogen peroxide solution (30 %) were obtained from Penta (Czech Republic). All solutions were filtered through a 0.22 μm PES membrane (Merck Millipore, Germany).

Phosphate-buffered saline (PBS, pH 7.4) consisted of 50 mM NaH_2PO_4/Na_2HPO_4 with 150 mM NaCl; assay buffer (pH 7.5) contained of 0.2 % BSA, 0.5 % BGG, 50 mM Tris, 150 mM NaCl, 5 mM EDTA, 0.2 % PVA, 1 % glucose and 0.01 % Tween 20.

Melissococcus plutonius medium (modified ATCC Medium 1430) was prepared using 7.5 g peptone, 2 g tryptone, 10 g glucose, 2.5 g yeast extract, 2 g starch, 50 mL of 1 M KH_2PO_4/K_2HPO_4 (pH 6.7), and 950 mL of water, pH 7.2 adjusted with 5 M KOH; after autoclaving at 121 °C for 15 min and cooling down, 2.5 mL of filter-sterilized 10 % solution of L-cysteine hydrochloride was added.

2.2 Preparation of Microorganisms

Melissococcus plutonius (ATCC 35311) and *Paenibacillus alvei* (ATCC 6344) were obtained from the Czech Collection of Microorganisms (CCM, Czech Republic). The bacteria were cultivated as described in our previous work [25]. Briefly, *M. plutonius* was cultivated anaerobically for 3 days at 34 °C in a closed Duran bottle without shaking. *P. alvei*, serving as a negative control, was cultivated aerobically in Nutrient broth No. 4 (8 g L^{-1}) for 2 days at 30 °C in a Duran bottle with shaking.

The bacteria were harvested to PBS and their concentrations were determined using McFarland standards and optical density measurement at 600 nm. The aliquots of bacteria in PBS were stored for further use at −30 °C in concentration of 1×10^{10} $CFU\,mL^{-1}$.

2.3 Real Sample Collection and Processing

Real beehive material of healthy bees and larvae was collected in June 2018 from an apiary in the South Moravian Region, Czech Republic. Adult bees were collected from the brood nests into plastic bags and immediately placed on dry ice. Larvae before capping (4–5 days old) were extracted from the brood cells by a spatula and frozen in the same manner. The samples were transported to the laboratory and stored for further use at −30 °C.

To prepare the samples for analysis, bees were homogenized by cooling with liquid nitrogen and grinding using mortar and pestle [26], followed by shaking in PBS–T extraction buffer (0.5 mL per bee, 50 mM NaH_2PO_4/Na_2HPO_4, pH 7.4, 150 mM NaCl, 0.01 % Tween 20) for 10 min. After centrifugation at 500 g for 2 min and discarding the pellet to clean the sample of large fragments, the supernatant was diluted 10 times and spiked with the bacteria. Samples of larvae were homogenized using a Potter-Elvehjem homogenizer at room temperature and 0.5 mL of PBS–T per larva was used for the extraction. Centrifugation, dilution of the matrix and spiking procedure remained the same as in case of bees [25].

2.4 Preparation of Antibody

Anti-*Melissococcus* antibody was prepared by immunization of rabbits with bacterial antigen emulsified with Freud's complete adjuvant. After booster injection of antigen in incomplete Freud's adjuvant, blood samples for antisera preparation were collected. As the final step, the immunoglobulin G fraction was purified using Protein G column. The antibody was stored at −30 °C in concentration of 4.6 mg mL^{-1}.

For the preparation of the detection conjugate of anti-*Melissococcus* antibody with HRP (Ab-HRP), the HRP was oxidized by sodium periodate to form a covalent bond with the lysine residues of the antibody. Sodium cyanoborohydride was used to reduce the formed Schiff base to a more stable secondary amine and the remaining reactive groups were blocked by ethanolamine [27,28]. The conjugate was purified to PBS, diluted to 4.6 mg mL^{-1}, and stored at 4 °C. The antibody preparation process, as well as its conjugation with HRP and functional verification using ELISA, are described in detail in our previous work [25].

2.5 Immunosensing Based on Electrochemical Impedance Spectroscopy (EIS)

Dual-channel gold screen-printed sensors (AC2.W1.RS, BVT Technologies, Czech Republic) were cleaned in acetone for 15 min. Between all modification steps, the sensors were rinsed with deionized water and dried with compressed air. A droplet of cysteamine (2 µL, 20 mg mL^{-1} in water) was deposited on the working electrode surface for 2 h at room temperature to form a self-assembled monolayer [29]. After rinsing, the sensors were incubated with 2 µL of glutaraldehyde (5 % in PBS) for 1 h at room temperature, washed and incubated overnight with 2 µL of antibody solution (concentration 0.81 mg mL^{-1} in PBS) at 4 °C. This was followed by blocking using 1 % BSA in assay buffer for 1 h at room temperature. Impedance spectra were acquired after blocking using the potentiostat Autolab PGSTAT302N with FRA module (Metrohm, The Netherlands). The measurements were performed in a frequency range from 10^5 to 2 Hz with amplitude of 10 mV in solution of hexacyanoferrate(II)/(III) (final concentration of 5 mM) in PBS as a supporting electrolyte. Data from these measurements were used as a background signal for further evaluation.

The immunosensing procedure consisted of incubation of the sensor in 500 µL of different concentrations of *M. plutonius* (specific target) and *P. alvei* (negative control representing other bacteria commonly present in the infected honeybees) in PBS in 2 mL Eppendorf tube for 1 h under gentle agitation. After washing, the impedance spectra were measured and the obtained Nyquist diagrams were fitted with Nova software (Metrohm) using the Randles circuit model to evaluate charge transfer resistance (R_{CT}). To determine the amount of bacteria captured on the electrode surface, the ΔR_{CT} was calculated by subtracting the R_{CT} after bacteria binding from R_{CT} after the blocking [18].

2.6 Amperometric Immunosensor

Single-channel gold screen-printed sensors (AC1.W1.RS, BVT Technologies) were modified with antibody as described above (2.5); the immobilization scheme is shown in Figure 1A. The modified electrodes were stored dry at 4 °C. Each sensor was used for a single measurement with the sample. The consumed electrodes, as well as all used solutions, were sterilized to inactivate the microbes before disposal.

The first step of the immunoassay (Figure 1B) was the incubation for 1 h with the samples of *M. plutonius* and *P. alvei* in PBS. The sensors were immersed in 500 µL of the solution in 2 mL Eppendorf tubes under gentle agitation. After brief washing with PBS, this was followed by 1 h incubation with 0.46 mg mL^{-1} Ab-HRP conjugate in assay buffer (2 µL droplet on working electrode). The amperometric measurements were performed using the Autolab PGSTAT302N potentiostat, based on the successive additions of H_2O_2 and TMB (final concentrations of 1 mM and 10 µM, respectively) in PBS working solution. All measurements were carried out with stirring in a beaker (5 mL) at a potential of −50 mV against the Ag/AgCl pseudoreference electrode on the SPE.

The current change (ΔI) after TMB addition to the working solution (mean value from the 20 to 30 s interval after mixing) was used as a sensor response for data evaluation; the shown data are means from 3 individual

219

Full Paper
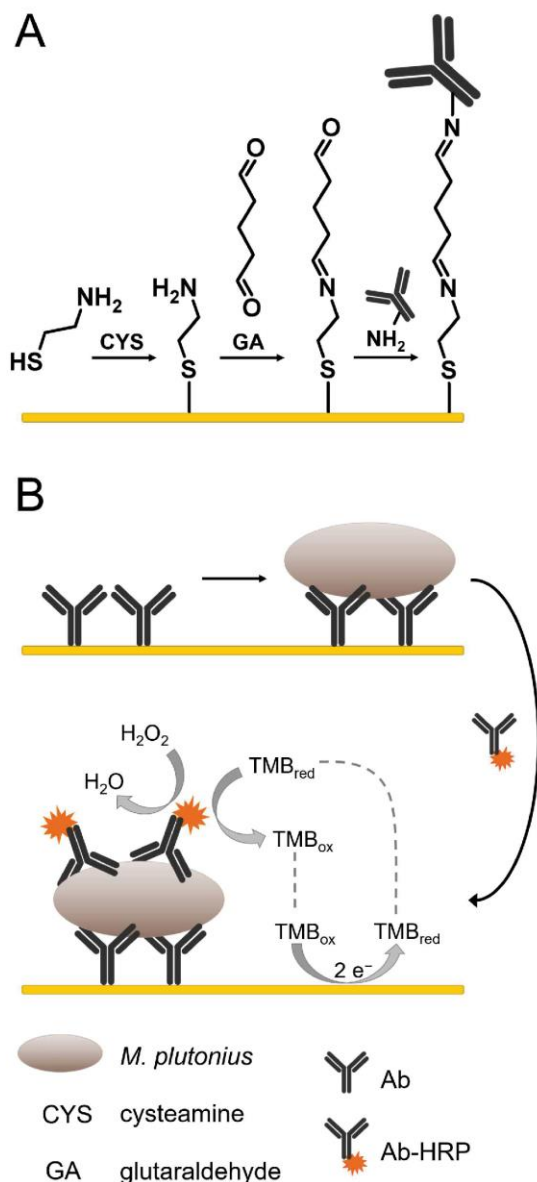
Fig. 1. (A) Scheme of antibody immobilization on gold surface of SPE sensor. (B) Scheme of amperometric immunoassay.

measurements including standard errors as bars. The LOD was calculated from the calibration curve as a concentration corresponding to the signal change in case of blank measurement plus 3 times the standard deviation of the blank signal.

2.7 Atomic Force Microscopy

M. plutonius captured on the antibody-modified SPE surface was imaged using atomic force microscopy (AFM). Bare gold sensor, surface after formation of cysteamine self-assembled monolayer, antibody-modified and blocked surface, and surface after specific binding of *M. plutonius* cells were compared. The washed and gently dried samples were imaged using the Dimension FastScan Bio AFM system (Bruker, USA) with ScanAsyst-Air probe. The AFM scanning was done in PeakForce Tapping mode with a scan rate of 0.2 Hz and resolution of 1024×1024. Due to the high roughness of the gold SPE sensors, tapping amplitude of 150 nm and 1 nN setpoint were chosen. The resulting scans were processed in software NanoScope Analysis (Bruker) and Gwydion (Czech Metrology Institute, Czech Republic).

3 Results and Discussion

3.1 Impedimetric Immunosensor

EIS offers simple one-step detection principle; however, it is very dependent on the level of non-specific binding, therefore the blocking conditions had to be carefully optimized. Two blocking solutions were compared: 1 % BSA in PBS and 1 % BSA in assay buffer. Due to the more complex composition, the latter one showed better suppression of the non-specific binding at the working electrode surface, leading to lower impedance changes in case of negative controls. Besides the incubation of the sensor in 500 µL of the sample, incubation with a 2 µL droplet placed on the working electrode was also tested. Smaller signal changes were observed in the case of the droplet, probably because of the reduced number of bacteria available for binding and limited mixing of the solution. This procedure was not pursued further, however, it can be beneficial when only limited amount of sample is available.

Figure 2A shows the measured EIS spectra for the different concentrations of *M. plutonius*. The specific signal increases correspond to the amount of bacteria captured on the sensing surface and thus to their concentration in the sample [30]. The LOD of the *M. plutonius* detection in PBS using EIS within 1 h analysis was calculated from the calibration curve in Figure 2B to be 9.1×10^4 CFU mL^{-1}. The sensor provided wide linear range up to 10^9 CFU mL^{-1}. The sensitivity of EIS is slightly lower than in other reports; this is probably because the polyclonal antibody was used without affinity purification step [31,32]. As a confirmation that the developed EIS immunosensor provides specific response to *M. plutonius*, samples of negative control of *P. alvei* were analyzed. Relatively small, yet not negligible signal changes were observed, which were growing with the increasing microbe levels. This indicates non-specific binding of the control microbe.

One of the significant advantages of EIS is that it does not require a detection step based on labelled antibody. This makes it a simple one-step procedure; however, the method is then prone to non-specific binding of the material from the sample matrix. This problem does not

220
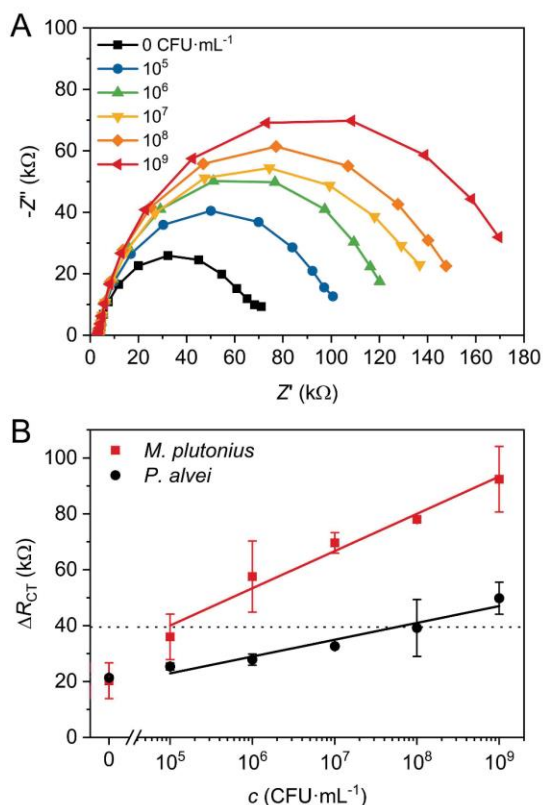
Fig. 2. (A) EIS response of immunosensor to *M. plutonius* (concentrations in $CFU\,mL^{-1}$). (B) Calibration curve of EIS-based detection of *M. plutonius*, with *P. alvei* as a negative control. The dotted line represents the LOD ($9.1 \times 10^4\,CFU\,mL^{-1}$).

Fig. 3. (A) Amperometric detection of *M. plutonius* (concentrations in $CFU\,mL^{-1}$). The arrow represents addition of TMB. (B) Calibration curve of amperometric detection of *M. plutonius*, with *P. alvei* as a negative control. The dotted line represents the LOD ($6.6 \times 10^4\,CFU\,mL^{-1}$).

usually pronounce when the detection is performed in buffer, however, the real samples of bee and larvae extracts can further adsorb on the electrode surface and thus further deteriorate the sensor performance.

Alternatively, we plan for the future to combine the EIS procedure with the sandwich assay format and HRP label with substrate providing precipitating products. This approach helped us to enhance the surface plasmon resonance sensing of *Salmonella* [28].

3.2 Amperometric Immunosensor

The amperometric detection was based on a sandwich immunoassay. It is an indirect method and requires Ab-HRP label, which makes it one step longer compared to the EIS. On the other hand, the use of a label allows to suppress the effect of non-specific binding of other bacterial cells to the electrode surface (based on the slopes of *P. alvei* curves in Figures 2B and 3B). In the case of amperometry, SPE selection, blocking conditions,

dilution of the antibody solution and Ab-HRP conjugate, and H_2O_2/TMB substrate concentration were optimized.

Various types of SPE sensors were compared. The dual-channel carbon sensors (DRP-X1110SWCNT, Metrohm DropSens, Spain) with carbon nanotubes and carboxyl groups, activated by *N*-(3-(dimethylamino) propyl)-*N'*-ethylcarbodiimide (EDC) and *N*-hydroxysuccinimide (NHS), were the least suitable due to the relatively low signal response and high levels of non-specific binding. Single-channel gold sensors DRP-220AT and DRP-C220AT (Metrohm DropSens) were less reproducible and less sensitive to lower bacterial concentrations compared to gold single- and dual-channel sensors AC1. W1.RS and AC2.W1.RS (BVT Technologies). The single-channel AC1.W1.RS provided the lowest signals in case of negative controls and were therefore selected for the immunosensor optimization.

For the blocking, 1 % BSA in assay buffer was used due to the lower non-specific signals, which is in agreement with the observations from the EIS. The concentration of the capture antibody solution was optimized for the final immunoassay to $0.81\,mg\,mL^{-1}$. The completed

221

immunosensors were stored in dry state in refrigerator; during 2 months period, no significant (<5%) decrease of response was noticed. During the assay procedure after incubation with sample, concentration of the Ab-HRP conjugate was set at 0.46 mg mL^{-1} as a compromise between the assay sensitivity, signal-to-background ratio and antibody consumption. After optimization of all steps, the developed amperometric immunosensor was used for sandwich assay of *M. plutonius*.

Typical signal traces for the amperometric measurement are shown in Figure 3A. The measured current changes corresponded linearly to the logarithm of concentration of *M. plutonius* in the sample. The dotted line in calibration graph (Figure 3B) represents the LOD determined to be 6.6×10^4 CFU mL^{-1}, the total analysis time was 2 h. Wide linear range from 10^5 to 10^9 CFU mL^{-1} was achieved. It can be clearly seen from the obtained responses for the negative control (*P. alvei*) that the HRP-conjugated anti-*Melissococcus* antibody tracer does not cross-react with other bacteria. This was also verified in the case of ELISA detection in our previous work [25]. The non-specific signals of *P. alvei* were significantly lower compared to the EIS-based detection. In the case of EIS, the measured signals correspond to all molecules (and bacteria) from sample matrix attached onto the electrode, including those bound non-specifically. However, in the case of amperometry, the Ab-HRP detection conjugates bind specifically only to the *M. plutonius* cells. In case of real samples, the measurement reproducibilities were 7.5% and 7.9% for bee and larvae samples, respectively. Furthermore, the sensitivity of the amperometric detection was higher compared to the EIS detection, which is probably connected with the amplification effect of the HRP. The achieved sensitivity is comparable with the published ELISA assays for *M. plutonius* detection with LODs around 10^5–10^6 CFU mL^{-1} [3,33], however, it is lower than in the case of PCR-based detection with LODs reaching units of CFU mL^{-1} [34,35].

The amperometric immunosensor, unlike ELISA and PCR, provides shorter analysis time and has a miniaturization and mass production potential for POC screening applications. The amperometric detection will probably never be the most sensitive method available on the market, however, it can find its place as a device for in-field pre-screening of EFB. The laboratory-based PCR analysis can follow after the pre-screening for further confirmation of the indicated EFB infections. According to Roetschi et al., when EFB manifests in a beehive, bacterial loads above 5×10^4 CFU per bee can be expected and this value can be used as a threshold in screening of health status of suspected colonies [35]. As 500 μL of buffer was used for sample extraction, the threshold value corresponds to ca 10^5 CFU mL^{-1}; the LOD of the developed amperometric immunosensor complies with this requirement.

The use of Ab-HRP label allows to suppress the effect of complex matrix in real samples, which is the main limitation in case of EIS. Therefore, the amperometric

detection was chosen for the subsequent measurements of real samples of bees and larvae.

3.3 AFM Scanning of SPE Immunosensor Surface

AFM was used to study the surface of the SPE-based immunosensor. The data from the Peak Force Error channel are displayed due to large height differences on the rough surface of the sensors resulting from the screen-printing production method. The differences between individual assay steps were successfully displayed. A bare electrode surface before modification is shown in Figure 4A; the surface after modification with cysteamine is shown in Figure 4B. The new shapes with the depth of about 120 nm and diameter from 0.1 to 1 μm appeared and were probably caused by partial disruption of the SPE surface. The surface after antibody immobilization and blocking by BSA is shown in Figure 4C. After blocking, the electrode surface appears flatter, which is probably a result of surface coverage by the protein layer.

Finally, the surface of the gold electrode with bacteria captured *via* affinity interaction with the antibody was visualized (Figure 4D). To keep the surface comparable with the electrochemical experiments, the electrode preparation procedure and the bacteria binding conditions remained unchanged. However, higher bacterial concentration of 10^{10} CFU mL^{-1} (in PBS) was used in order to achieve denser surface coverage. The optimal area for scanning of the rough electrode surface was 10×10 μm^2; only a few bacteria were captured per this area when using the highest concentration used in the electrochemical immunoassay (10^9 CFU mL^{-1}). *M. plutonius* is shown as an oval, pointed cocci with length of approximately 1 μm, typically in a pair or forming short chains. The shape of *M. plutonius* bacterial cell corresponds to a scanning electron micrograph published by Forsgren [36]. The AFM successfully illustrated that the developed sensor is capable of binding whole *M. plutonius* cells.

3.4 Analysis of Real Samples

Finally, to prove that the developed immunosensor is suitable for the real sample analysis, samples of healthy bees and larvae were prepared and spiked with known concentrations of bacteria. During the last year, EFB infections were not detected in the Czech Republic, thus real infected samples were not available. A calibration curve was established for each of the matrices to assess their effect on the sensitivity of the sensor (Figure 5).

LODs obtained for the bacteria spiked in the matrices of bees and larvae were 2.4×10^5 and 7.0×10^5 CFU mL^{-1}, respectively. These values are comparable with the LOD of 1.4×10^5 CFU mL^{-1} achieved with the ELISA published in our previous work using the same antibody [25]. The LODs from the real samples are approximately one order of magnitude higher than in the case of pure bacteria in buffer, however, such behavior of real samples has been also previously reported by other authors [24,37]. The
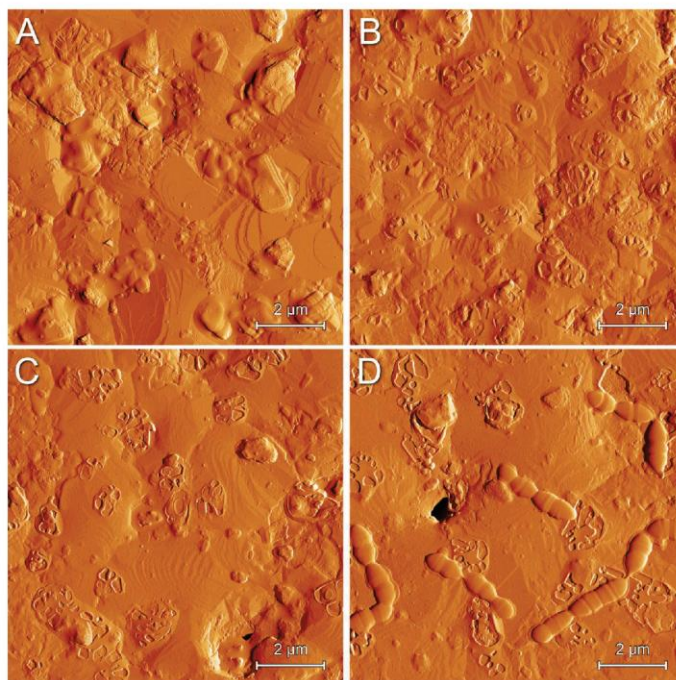
Fig. 4. AFM scans of gold SPE sensor (A) before modification, (B) after formation of self-assembled monolayer of cysteamine, (C) after modification with antibody and blocking by BSA, and (D) after specific binding of bacteria (10^{10} CFU mL^{-1} in PBS). PeakForce Error signals are shown due to the high roughness of the SPE surface.
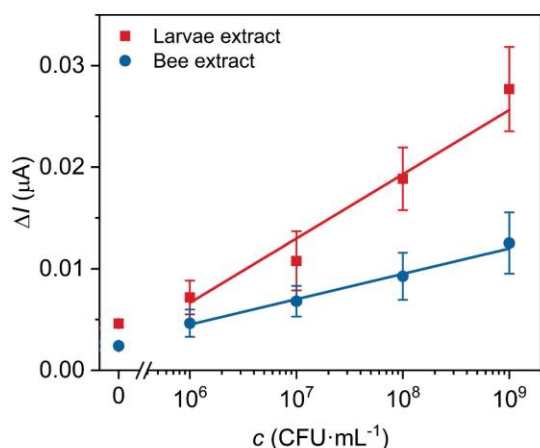
Fig. 5. Calibration curves for amperometric detection of *M. plutonius* in real samples of spiked larvae (LOD 7.0×10^5 CFU mL^{-1}) and bees (LOD 2.4×10^5 CFU mL^{-1}).

reason probably is that the complex matrix of bees and larvae contains various molecules (fats, proteins, etc.), which can block the electrode surface and lower the sensitivity of the immunodetection. The change in calibration dependency is not ideal for the practical application; however, it can be compensated by making calibration dependencies separately for bees and larvae and using the appropriate calibration when analyzing the corresponding real samples. The successful analysis of real samples with spiked bacteria confirmed the suitability of the amperometric immunosensor for in-field EFB diagnosis.

4 Conclusions

A portable amperometric immunosensor based on sandwich assay was developed for rapid detection of *M. plutonius* without the need for expensive, complicated, and time-consuming laboratory instrumentation. The specific anti-*Melissococcus* antibody was immobilized to the gold working electrode of SPE sensor *via* self-assembled monolayer of cysteamine and glutaraldehyde to serve as a biorecognition element. The conjugate of antibody with HRP was used as a detection label to allow simple electrochemical detection based on reduction of the enzymatically oxidized TMB. The use of sandwich assay format allowed to suppress the effect of real sample matrix compared to the label-free procedure of EIS. Consequently, the amperometric approach was chosen for the detection of *M. plutonius* in real samples of bees and larvae. The specific binding of *M. plutonius* to the antibody-modified gold electrode was confirmed by AFM; despite the high roughness of the screen-printed surface, the typical chains of microbes were visible.

223

The amperometric immunosensor provided LOD of 6.6×10^4 CFU mL^{-1} for pure bacterial sample in buffer. The calibration dependency was linear in logarithmic concentration scale up to 10^9 CFU mL^{-1}, the whole analysis was completed within 2 h. The immunosensor was also used to the analysis of real samples. The LODs achieved in the complex matrices of homogenized bees and larvae were 2.4×10^5 and 7.0×10^5 CFU mL^{-1}, respectively. The measurements with negative control of *P. alvei* confirmed the high selectivity of the assay. The achieved results demonstrate the suitability of the amperometric immunosensor for the rapid in-field diagnosis of EFB.

5 Live Subject Statement

The animals were maintained and handled in accordance with the Act. No. 246/1992 Coll. on the Protection of Animals against Cruelty, as amended and with internal guidelines. The experimental procedures were approved by the Branch Commission for Animal Welfare of the Ministry of Agriculture of the Czech Republic.

References

[1] L. Bailey, M. D. Collins, *J. Appl. Bacteriol.* **1982**, *53*, 215–217.
[2] E. Forsgren, G. E. Budge, J. D. Charriere, M. A. Z. Hornitzky, *J. Apic. Res.* **2013**, *52*, 14.
[3] V. Tomkies, J. Flint, G. Johnson, R. Waite, S. Wilkins, C. Danks, M. Watkins, A. G. S. Cuthbertson, E. Carpana, G. Marris, G. Budge, M. A. Brown, *Apidologie* **2009**, *40*, 63–72.
[4] M. J. Ansari, A. Al-Ghamdi, A. Nuru, A. M. Ahmed, T. H. Ayaad, A. Al-Qarni, Y. Alattal, N. Al-Waili, *Saudi J. Biol. Sci.* **2017**, *24*, 1327–1335.
[5] Z. Farka, T. Juřík, D. Kovář, L. Trnková, P. Skládal, *Chem. Rev.* **2017**, *117*, 9973–10042.
[6] G. Vasquez, A. Rey, C. Rivera, C. Iregui, J. Orozco, *Biosens. Bioelectron.* **2017**, *87*, 453–458.
[7] M. Pastucha, Z. Farka, K. Lacina, Z. Mikušová, P. Skládal, *Microchim. Acta* **2019**, *186*, 312.
[8] K. K. Mistry, K. Layek, T. N. Chell, C. R. Chaudhuri, H. Saha, *Anal. Methods* **2016**, *8*, 3096–3101.
[9] K. K. Mistry, K. Layek, A. Mahapatra, C. RoyChaudhuri, H. Saha, *Analyst* **2014**, *139*, 2289–2311.
[10] J. E. B. Randles, *Discuss. Faraday Soc.* **1947**, *1*, 11–19.
[11] P. Skládal, *Electroanalysis* **1997**, *9*, 737–745.
[12] C. Kokkinos, A. Economou, M. I. Prodromidis, *TrAC Trends Anal. Chem.* **2016**, *79*, 88–105.
[13] A. Hassan, A. de la Escosura-Muniz, A. Merkoci, *Biosens. Bioelectron.* **2015**, *67*, 511–515.
[14] F. C. Huang, H. L. Zhang, L. Wang, W. H. Lai, J. H. Lin, *Biosens. Bioelectron.* **2018**, *100*, 583–590.
[15] F. J. Zhu, G. Y. Zhao, W. C. Dou, *Microchim. Acta* **2018**, *185*, 11.
[16] M. Freitas, S. Viswanathan, H. P. A. Nouws, M. Oliveira, C. Delerue-Matos, *Biosens. Bioelectron.* **2014**, *51*, 195–200.
[17] D. Brandao, S. Liebana, S. Campoy, S. Alegret, M. I. Pividori, *Talanta* **2015**, *143*, 198–204.
[18] Z. Farka, T. Juřík, M. Pastucha, D. Kovář, K. Lacina, P. Skládal, *Electroanalysis* **2016**, *28*, 1803–1809.
[19] Q. Chen, J. H. Lin, C. Q. Gan, Y. H. Wang, D. Wang, Y. H. Xiong, W. H. Lai, Y. T. Li, M. H. Wang, *Biosens. Bioelectron.* **2015**, *74*, 504–511.
[20] Y. H. Sha, X. Zhang, W. R. Li, W. Wu, S. Wang, Z. Y. Guo, J. Zhou, X. R. Su, *Talanta* **2016**, *147*, 220–225.
[21] M. Xu, R. H. Wang, Y. B. Li, *Talanta* **2016**, *148*, 200–208.
[22] R. H. Wang, J. Lum, Z. Callaway, J. H. Lin, W. Bottje, Y. B. Li, *Biosensors* **2015**, *5*, 791–803.
[23] J. F. Fei, W. C. Dou, G. Y. Zhao, *RSC Adv.* **2015**, *5*, 74548–74556.
[24] M. Xu, R. H. Wang, Y. B. Li, *Analyst* **2016**, *141*, 5441–5449.
[25] V. Poláchová, M. Pastucha, Z. Mikušová, M. J. Mickert, A. Hlaváček, H. H. Gorris, P. Skládal, Z. Farka, *Nanoscale* **2019**, *11*, 8343–8351.
[26] J. D. Evans, R. S. Schwarz, Y. P. Chen, G. Budge, R. S. Cornman, P. De la Rua, J. R. de Miranda, S. Foret, L. Foster, L. Gauthier, E. Genersch, S. Gisder, A. Jarosch, R. Kucharski, D. Lopez, C. M. Lun, R. F. A. Moritz, R. Maleszka, I. Munoz, M. A. Pinto, *J. Apic. Res.* **2013**, *52*, 53.
[27] G. T. Hermanson, *Bioconjugate Techniques (Second Edition)*, Academic Press, New York, **2008**.
[28] Z. Farka, T. Juřík, M. Pastucha, P. Skládal, *Anal. Chem.* **2016**, *88*, 11830–11836.
[29] Z. M. Li, Y. C. Fu, W. H. Fang, Y. B. Li, *Sensors* **2015**, *15*, 19212–19224.
[30] C. K. Joung, H. N. Kim, M. C. Lim, T. J. Jeon, H. Y. Kim, Y. R. Kim, *Biosens. Bioelectron.* **2013**, *44*, 210–215.
[31] G. Lillie, P. Payne, P. Vadgama, *Sens. Actuators B Chem.* **2001**, *78*, 249–256.
[32] D. Wang, Q. Chen, H. L. Huo, S. S. Bai, G. Z. Cai, W. H. Lai, J. H. Lin, *Food Control* **2017**, *73*, 555–561.
[33] D. E. Pinnock, N. E. Featherstone, *J. Apic. Res.* **1984**, *23*, 168–170.
[34] S. P. Djordjevic, K. Noone, L. Smith, M. A. Z. Hornitzky, *J. Apic. Res.* **1998**, *37*, 165–173.
[35] A. Roetschi, H. Berthoud, R. Kuhn, A. Imdorf, *Apidologie* **2008**, *39*, 362–371.
[36] E. Forsgren, *J. Invertebr. Pathol.* **2010**, *103*, S5–S9.
[37] Y. H. Lin, S. H. Chen, Y. C. Chuang, Y. C. Lu, T. Y. Shen, C. A. Chang, C. S. Lin, *Biosens. Bioelectron.* **2008**, *23*, 1832–1837.

Paper IX

Enzymatic Precipitation Enhanced Surface Plasmon Resonance Immunosensor for the Detection of *Salmonella* in Powdered Milk

Farka, Z.; Juřík, T.; Pastucha, M.; Skládal, P.

Contribution:

Design of experiments, development and optimization of precipitation-enhanced SPR assay, characterization of precipitation reaction by AFM, data evaluation, manuscript writing

Enzymatic Precipitation Enhanced Surface Plasmon Resonance Immunosensor for the Detection of *Salmonella* in Powdered Milk

Zdeněk Farka,[†] Tomáš Juřík,[†,‡] Matěj Pastucha,[†,‡] and Petr Skládal*,[†,‡]

[†]CEITEC MU and [‡]Department of Biochemistry, Faculty of Science, Masaryk University, Kamenice 5, 625 00 Brno, Czech Republic

S *Supporting Information*

ABSTRACT: Contamination of food by pathogenic bacteria has always been a serious threat for human health. The amount of food exports and imports has been increasing in recent years which requires precise food quality control with short analysis time and simplified sample treatment. Surface plasmon resonance (SPR) immunosensor enhanced by biocatalyzed precipitation was developed for the analysis of *Salmonella* in dairy products. The specific capture antibody was immobilized on the SPR chip which allowed a direct label-free detection of *Salmonella* Typhimurium with the limit of detection (LOD) of 10^4 CFU·mL^{-1} and the analysis time of 10 min. Alternatively, the secondary detection antibody was conjugated with horseradish peroxidase to provide a signal enhancement by the biocatalyzed conversion of 4-chloro-1-naphthol to insoluble benzo-4-chlorocyclohexadienone. The formation of precipitate was studied in detail by atomic force microscopy (AFM). The sensitivity was increased 40 times in case of the precipitation-enhanced detection compared to the label-free approach. The optimized method provided LOD of 100 CFU·mL^{-1} with linear range up to 10^6 CFU·mL^{-1}. The total time of analysis including bacteria binding and enhancement step was below 60 min. The capability to analyze real samples with complex matrices was demonstrated on the detection of *Salmonella* in powdered milk. The developed sensor represents simple and robust approach for routine monitoring of food contamination.
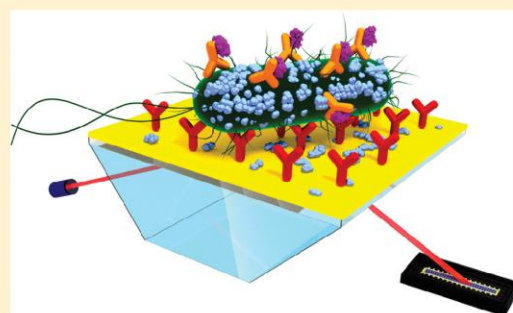
*S*almonella belongs to the most widespread foodborne bacterial pathogens causing an extensive number of food poisoning, illnesses and deaths worldwide.[1] According to the Centers for Disease Control and Prevention (CDC), *Salmonella* was evaluated as a leading cause of foodborne infections in the United States with approximately 1.2 million illnesses and 450 deaths per year.[2] Even more critical situation occurs in developing countries. It was estimated that approximately 3.4 million illnesses and 680 thousand deaths originated from nontyphoidal *Salmonella* in Africa in 2010.[3] It has a big impact not only on human health, but also on the expenses associated with *Salmonella* control program.[4] *Salmonella* is a Gram-negative facultative anaerobic bacteria occurring mostly in the intestinal tract of animals. It is transmitted to humans predominantly by meat, eggs and milk products.[5] Currently, over 2,500 serotypes of *Salmonella* have been reported; the most common serotypes associated with human illnesses in the United States and European countries are *Salmonella enterica* serovar Typhimurium (*S.* Typhimurium) and *S. enterica* serovar Enteritidis (*S.* Enteritidis).[6] European Union (EU) established high food safety standards, however, according to the Rapid Alert System for Food and Feed (RASFF), the reported incidence of *Salmonella* has been gradually growing (Figure S1 in the Supporting Information). In 2015, 517 notifications of *Salmonella* presence in food were registered in the EU and 397 of them were classified as a serious risk for public health.[7] Thus, a rapid detection of

Salmonella represents a considerable challenge for the food industry and safety analytics.

Conventional techniques for *Salmonella* detection include culturing method, enzyme-linked immunosorbent assay (ELISA) and polymerase chain reaction (PCR). In spite of being reliable, these methods are generally time-consuming, labor-intensive and require complex sample pretreatment and trained personnel.[8] In the last decades, biosensors have emerged as a powerful instrument for rapid and sensitive detection of bacteria.[9] Several electrochemical sensors exhibiting good sensitivity, specificity and fast response were developed for the determination of *Salmonella*.[10,11] Electrochemical impedance spectroscopy (EIS) allows a label-free detection and potential construction of a portable device.[12,13] Quartz crystal microbalance (QCM)[14] and surface plasmon resonance (SPR)[15−17] have gained substantial attention owing to the possibility of a real-time monitoring of bacteria binding to the sensor surface.

Recent trends in immunosensing have been frequently connected with various approaches leading to signal enhancement. For instance, gold nanoparticles (AuNPs) were incorporated into a sandwich format resulting in a significant

increase of refractive index during the SPR detection of *Salmonella*.[18] AuNPs conjugated with a detection antibody were also applied in order to extend the mass load on the QCM sensor and improve the sensitivity of *Campylobacter jejuni*[19] and *Francisella tularensis* detection.[20] Magnetic nanoparticles (MNPs) appeared to be a useful tool providing a favorable dual benefit regarding the signal amplification: immunomagnetic separation/preconcentration of the sample[21] and simultaneous mass enhancement on the sensor surface. Very low limits of detection (LOD) around 10−100 CFU·mL^{-1} were achieved for *Salmonella* detection by SPR[22] and QCM[23] using MNPs. Another abundantly utilized approach for the improvement of immunosensor sensitivity involves various nanocrystal-based tracers, such as CuS, PbS and CdS, conjugated with the detection antibody. After binding to bacteria, these crystals are dissolved in nitric acid, releasing Cu^{2+}, Pb^{2+}, or Cd^{2+} ions, which can be further detected by anodic stripping voltammetry. By employing this method, the LODs were reduced to 4100 CFU·mL^{-1}[24] and even 13 CFU·mL^{-1}[25] in case of *Salmonella*, and 10 CFU·mL^{-1} for *E. coli*,[26] respectively. Finally, the enzyme-catalyzed precipitation of solid product on the sensing surface has been adopted for increasing the signal intensity.[27,28] Highly sensitive electrochemical immunosensors for the detection of prostate specific antigen (PSA)[29,30] and carcinoembryonic antigen (CEA)[31] were developed, horseradish peroxidase (HRP) produced insoluble precipitate resulting in hindrance of the electron transfer. Although the above-mentioned enzyme-enhanced immunoassays of low molecular weight antigens became progressive, sensing of whole cells is not common. An impedance biosensor for the detection of *E. coli* based on biocatalyzed precipitation of 5-bromo-4-chloro-3-indolyl phosphate by alkaline phosphatase (ALP) was constructed[32] and the LOD of 10^3 CFU·mL^{-1} was achieved. SPR detection of *E. coli* amplified by HRP-catalyzed conversion of 3,3′,5,5′-tetramethylbenzidine (TMB) to an insoluble product enabled to obtain the LOD of 10^4 CFU·mL^{-1} in spinach leaves.[33]

According to the literature, we introduce the analysis of *Salmonella* using SPR enhanced by biocatalyzed precipitation for the first time. Our strategy is aimed on simplicity and robustness of the assay while maintaining reasonably short analysis time and high sensitivity. A sandwich immunocomplex consisting of the monoclonal capture antibody, *Salmonella* and the detection antibody conjugated with HRP (HRP-Ab$_2$) was formed on the SPR chip. The biocatalyzed conversion of 4-chloro-1-naphthol to insoluble benzo-4-chlorocyclohexadienone (Figure S2) was carried out resulting in a significant change of the SPR signal. Based on epidemiological data, *Salmonella* is considered to be a serious hazard that has to be controlled during manufacturing of dried dairy products, because several outbreaks of salmonellosis have been caused by contaminated milk powder.[34] Therefore, our study was focused on the analysis of milk powder samples spiked with *Salmonella*.

■ EXPERIMENTAL SECTION

Chemicals and Reagents. Sodium periodate, sodium cyanoborohydride, *N*-(3-(dimethylamino)propyl)-*N*′-ethylcarbodiimide (EDC), *N*-hydroxysuccinimide (NHS), ethanolamine (EA), bovine serum albumin (BSA), 4-chloro-1-naphthol (4-CN), and 4-(2-hydroxyethyl)piperazine-1-ethanesulfonic acid (HEPES) were obtained from Sigma-Aldrich (USA). Horseradish peroxidase (HRP), glycerol and Tween 20 were purchased from Fluka (Germany). Hydrogen peroxide, sodium hydrogen phosphate, sodium dihydrogen phosphate and sodium chloride were from PENTA (Czech Republic).

HBS-P buffer (pH 7.4) consisted of 10 mM HEPES, 150 mM sodium chloride, and 0.005% Tween 20. Phosphate buffered saline (PBS, pH 7.4) was made from 50 mM sodium hydrogen phosphate/sodium dihydrogen phosphate and 150 mM sodium chloride. The precipitation substrate was prepared by freshly mixing 2 mM 4-CN (in 12% ethanol) and 2 mM hydrogen peroxide (in PBS) in ratio 1:1 (v/v). All solutions were filtered through 0.22 μm PTFE membrane (Merck Millipore, USA).

Mouse monoclonal anti-*Salmonella* antibody ab8274 (Abcam, UK) was used as a capture antibody. Rabbit polyclonal anti-*Salmonella* antibody 8209−4006 (detection antibody, Ab$_2$; AbDSerotec, UK) was conjugated with HRP and served as a signal enhancer.

Preparation of HRP-Ab$_2$ Conjugate. Oxidation of HRP and its conjugation to antibody was done according to Hermanson[35] and Catty,[36] with minor modifications. HRP (1 mg·mL^{-1} in water) was oxidized using 8 mM sodium periodate (10 min, 22 °C, dark, mild shaking). The reaction was quenched by adding 50 μL of glycerol per 1 mL of solution and the oxidized enzyme was purified using the Microcon centrifugal unit YM-10 (10 kDa MWCO; Merck Millipore, USA) by 3 repeated additions of 1 mM sodium acetate buffer pH 4.4 and subsequent centrifugations. The final concentration of HRP (1.33 mg·mL^{-1}) was adjusted to 1 mg·mL^{-1} using 200 mM carbonate/bicarbonate buffer pH 9.5.

For the conjugation, the oxidized HRP was added to the antibody solution (1 mg·mL^{-1} in 50 mM carbonate/bicarbonate buffer pH 9.5) in a ratio of 1:1 (v/v) resulting in 3.4 molar excess of the enzyme. After 2 h of gentle mixing (22 °C, dark), 10 μL of sodium cyanoborohydride (5 M solution in 1 M NaOH) per 1 mL of the mixture was added to specifically reduce the formed Schiff base (4 °C, overnight). The unreacted aldehyde groups on the oxidized HRP were blocked by the addition of 50 μL of 1 M EA (pH 9.5) per 1 mL of solution (30 min, 22 °C, mild shaking). The conjugate was purified using the Microcon YM-100 (100 kDa MWCO), transferred to PBS and stored at 4 °C for further use. The final concentration of HRP-Ab$_2$ conjugate was equivalent to 2 μg·mL^{-1} of the antibody.

Preparation of Microorganism Samples. *Salmonella enterica* subsp. *enterica* serovar Typhimurium (ATCC 14028) and *Escherichia coli* K-12 (for testing of cross-reactivity) were obtained from the Czech Collection of Microorganisms (CCM, Czech Republic). The work with *Salmonella* was carried out in the BSL-2 laboratory. For cultivation, 100 μL of the stock solution was inoculated into 25 mL of low salt LB broth (Duchefa Biochemie, Netherlands) in Erlenmeyer flask. The incubation was done aerobically overnight at 37 °C with mild shaking. The obtained bacterial suspension was centrifuged twice for 10 min at 6800 g and resuspended in HBS-P. The microbe concentrations were determined from optical density at 600 nm (OD$_{600}$) using the McFarland calibration scale. The bacteria samples were heat-treated at 80 °C for 30 min with mild shaking (500 rpm) on Thermomixer Comfort (Eppendorf, Germany). Concentrations of thus treated bacteria are expressed as CFU·mL^{-1} corresponding to viable cells before the treatment.[13] The powdered milk (Laktino, Czech Republic) was dissolved in the HBS-P buffer to the concentration of 1% and spiked with varying concentrations of *Salmonella* cells.

227

Preparation of Biosensing Layers. The SPR measurements were carried out using two systems: Biacore 3000 (GE Healthcare, Sweden) and BioNavis 210A (BioNavis, Finland). Carboxymethylated dextran chips CM3 (GE Healthcare) and CMD500l (XanTec bioanalytics, Germany) were used in case of Biacore and BioNavis, respectively. The immobilization protocol was the same for both systems, but the flow rates varied because of the different size of the fluidic systems: 5 μL·min^{-1} for Biacore and 20 μL·min^{-1} for BioNavis.

First, the sensor surface was cleaned with a solution of 2 M NaCl and 10 mM NaOH for 5 min, followed by the activation of carboxylic groups using a freshly prepared mixture of EDC (200 mM) and NHS (50 mM) for 7 min. The capture antibody (and BSA for reference channel) was diluted to 10 μg·mL^{-1} in acetate buffer (50 mM, pH 4.5) and allowed to bind for 10 min in case of Biacore and 40 min (flow rate reduced to 5 μL·min^{-1}) in case of BioNavis. The remaining reactive groups were blocked by EA (1 M, pH 8.5, 5 min) followed by BSA (2 mg·mL^{-1} in HBS-P, 10 min).[37] The sensors for analysis of real samples were additionally blocked by 10 min injection of 1% powdered milk in HBS-P. The individual steps of the immobilization procedure (for BioNavis) are displayed in Figure S3.

SPR Detection of Bacteria. The testing of antibodies and label-free detection was carried out using Biacore 3000 with the flow rate of 5 μL·min^{-1}. The samples were injected using the *KINJECT* function with 10 min for both association and dissociation phases. After each concentration of bacteria, the sensor was regenerated (1 min, 50 mM HCl).

The HRP substrate 4-CN was diluted in ethanolic solution, which is not recommended for the integrated fluidic chip of Biacore 3000. Therefore, the biocatalyzed precipitation-enhanced assay was carried out on the BioNavis 210A which provides more robust fluidic system. The bacteria were injected for 10 min (with another 10 min for dissociation and signal stabilization), followed by 10 min injection of the HRP-Ab$_2$ conjugate (10 min dissociation) and 10 min of precipitation substrate solution (10 min dissociation) resulting in the total analysis time of 60 min. After the experiment, the tubing was cleaned by 98% ethanol. The schematic representation of individual reaction steps is shown in Figure 1.

The measurements on BioNavis were done in the angular scan mode, where full SPR curves in the range of 57−78 deg were recorded in real time. The resonance angles were evaluated using the *Centroid* algorithm in the SPR Navi software (BioNavis). Differential signals ΔR corresponding to the difference between measuring and reference channel are plotted in graphs. The calibration graphs were evaluated from the ΔR values at the end of the precipitation phase; the baseline levels before the precipitation step were subtracted. The error bars correspond to standard deviations. Limits of detection were evaluated based on the signal-to-noise ratio as the lowest concentration for which the signal was higher than 3 times the noise level ($S/N > 3$).

After the analysis, the chips were removed, washed with sterile water and scanned by AFM in dry state using Dimension FastScan Bio (Bruker, USA) with FastScan-A probe. The data were evaluated in NanoScope Analysis (Bruker) and Gwyddion (Czech Metrology Institute, Czech Republic). Optical microscopy images were acquired by Olympus BX41 microscope equipped with U-PCD2 phase contrast condenser and Olympus E-510 camera (Olympus, Japan). Evaluation of
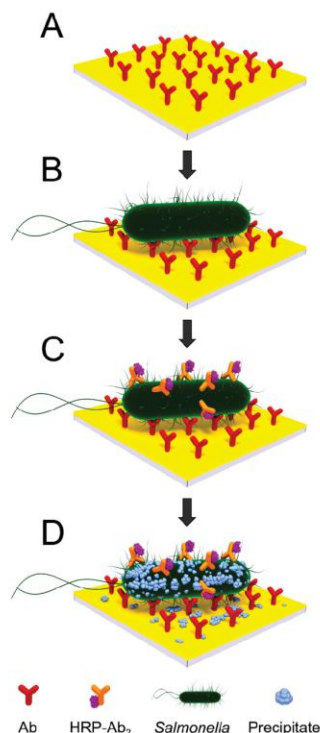
Figure 1. Scheme of biocatalyzed precipitation-enhanced SPR detection of *Salmonella*. (A) SPR chip with immobilized capture antibody; (B) binding of *Salmonella*; (C) binding of HRP-Ab$_2$ conjugate; and (D) HRP-catalyzed conversion of 4-chloro-1-naphthol to insoluble benzo-4-chlorocyclohexadienone.

images was done in ImageJ software (National Institutes of Health, USA).

■ RESULTS AND DISCUSSION

Label-Free SPR Detection of Salmonella. Label-free detection was performed to confirm the efficiency of the selected immobilization procedure and to evaluate the affinity of the antibody to the microbial cells. Biacore 3000, generally considered a highly sensitive SPR instrument, was adopted for this experiment. Antibody Abcam ab8274 was previously tested with heat-treated and sonicated *Salmonella* cells using an electrochemical immunosensor;[13] therefore, the specific binding was expected. The sensorgrams of heat-treated *Salmonella* detection are shown in Figure 2. The LOD of 10^4 CFU·mL^{-1} was achieved with a wide linear range up to 10^8 CFU·mL^{-1}. The main advantage of the label-free approach was the possibility of a real-time detection with a short assay time of 10 min. However, the obtained LOD may not be sufficient for a reliable analysis of real food samples.

After each measurement, the sensor was regenerated using 50 mM HCl; the signal did not return to the baseline level completely, however, up to 20 measurements were possible without significant loss of sensitivity. Subsequent injection of 50 mM NaOH provided more thorough regeneration. Due to the harsh conditions, maximum of 7 regenerations by NaOH could have been carried out before the sensing performance deteriorated.
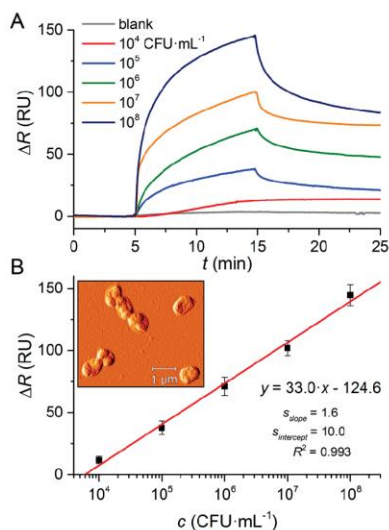
Figure 2. Label-free SPR detection of *Salmonella* using Biacore 3000. (A) SPR sensorgrams, 10 min association with sample followed by 10 min dissociation; (B) calibration curve; the inset shows AFM scan of the SPR chip in the zone corresponding to the binding channel.

Figure 3. SPR sensorgrams of the biocatalyzed precipitation-enhanced *Salmonella* detection. (A) Concentration of 10^2 CFU·mL^{-1} and (B) 10^7 CFU·mL^{-1}. The insets show details of binding of microbe and HRP-Ab$_2$ conjugate.

The sensor surface with specifically bound microbes was scanned using AFM. The results are shown as inset of Figure 2 and more details are provided in Figure S4. A high amount of cells was captured in the measuring channel (Figure S4A) compared to the reference one (Figure S4B) where practically no cells were bound.

SPR Detection of Salmonella Enhanced by Biocatalyzed Precipitation. The signal enhancement was carried out by binding of the HRP-Ab$_2$ conjugate followed by injection of the precipitation reaction mixture (4-CN and H$_2$O$_2$). In this case, the measurements were performed on BioNavis 210A providing good resistance to ethanolic solutions. The sensorgrams of interactions during all binding steps for the precipitation-enhanced detection are shown in Figure 3. In case of a high concentration (10^7 CFU·mL^{-1}), a significant signal increase was observed during each step. The signal change after precipitation reaction was 40× higher than after *Salmonella* binding. Our approach represents a substantial improvement compared to the previously reported TMB-based enzymatic enhancement of *E. coli* detection[33] which provided only 2.5× increased sensitivity.

The comparison of binding interactions in the measuring and reference channels is shown in Figure S5, the full SPR curves are given in Figure S6. A slight response was observed for the nonspecific bacteria binding in the reference channel, followed by a negligible signal increase after injection of the HRP-Ab$_2$ conjugate. The ratio between the signal in measuring and reference channels raised from 3.5 (direct binding) to 8.6 (precipitation reaction). In case of a very low concentration of 100 CFU·mL^{-1}, the signal of *Salmonella* and the HRP-Ab$_2$ conjugate binding might be arguable compared to the noise level, but the following enzymatic reaction strongly enhanced the signal so the presence of bacteria in the sample became clearly confirmed. The nonspecific adsorption of interferents to the sensor surface might lead to a signal increase in the first binding step. However, the HRP-Ab$_2$ conjugate is specific to *Salmonella*, therefore this nonspecific binding in the primary
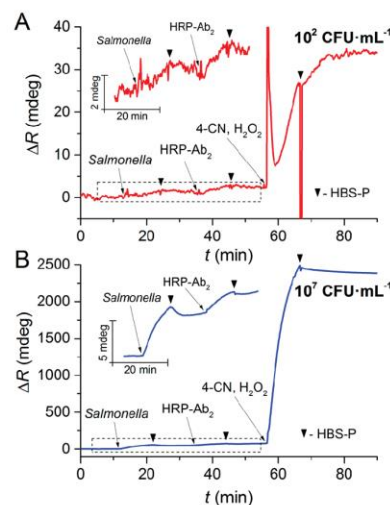
step is not further amplified. This contributes to the improved selectivity.

The cross-reactivity was tested with *E. coli* K-12 as a Gram-negative bacteria relatively similar to *Salmonella*.[38] Negligible nonspecific adsorption to both channels (resulting in no change of the differential signal) was followed by no binding of the HRP-Ab$_2$ conjugate and very low amount of the precipitate formation in both channels (no change of differential signal). This confirms the high specificity of both the capture antibody and the enhancement step.

The presence of surfactant in the running buffer was essential for a smooth analysis. When the experiment was performed in buffers without Tween 20 (either HEPES or PBS), the precipitation started already inside the inlet tubing before reaching the measuring chip. The cell debris and the HRP-Ab$_2$ conjugate was probably nonspecifically adsorbed to the tubing surface resulting in undesired early precipitation.

The sensorgrams of final enhancement step (precipitation of 4-CN) corresponding to various bacteria concentrations are shown in Figure 4. The signal changes were increased exponentially with the increasing concentration of microbes, suggesting that a single *Salmonella* cell could capture several HRP-Ab$_2$ conjugates that subsequently catalyzed the precipitation of a large amount of 4-CN molecules. This brings a major advantage compared to the amplification by nanoparticles, where only linear signal enhancement can be achieved.[39] The obtained dependence of $\log(\Delta R)$ on $\log(c)$ was linear from 10^2 to 10^6 CFU·mL^{-1} and the LOD was evaluated to be 100 CFU·mL^{-1}.

The total analysis time of 60 min is significantly shorter than the conventional methods for bacteria detection, such as cultivation (~days),[40] ELISA (~10 h)[41] and PCR (~hours).[42,43] It is also faster than other reported SPR immunosensors based on signal amplification by nanoparticles[18,39] while providing comparable or better LOD. The overview of immunosensing methods for *Salmonella* detection is presented in Table 1. If required, the dissociation segments of individual measuring steps (binding of microbe, binding of the

229
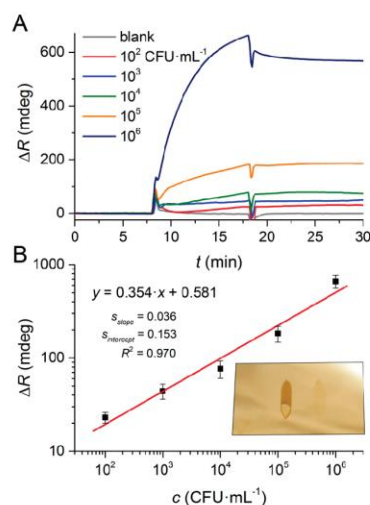
Figure 4. (A) SPR sensorgram showing the final step of biocatalyzed precipitation enhancement for different concentrations of *Salmonella*. (B) calibration curve. The inset image shows the measuring chip (specific channel−left, reference−right) after the precipitation reaction.

labeled antibody, stabilization of signal after the precipitation) could be shortened; in our case, the detailed monitoring of stability of immunocomplexes was preferred. Furthermore, the results are recorded in real-time during each binding step, therefore a rapid reaction (∼10 min) can be realized in the presence of a higher amount of bacteria in the sample before the amplification process. On the other hand, the signal can be further increased by prolonging the precipitation reaction, thus even lower concentrations of bacteria (below 100 CFU·mL^{-1}) might be detectable. However, the linear range and time of analysis would be influenced.

After the chip was removed from the SPR system, overview photo and optical microscopy images were captured and the chip was scanned using AFM. Significantly higher amount of the precipitate (visible by naked eye) was formed in the specific measuring channel (left channel in the inset of Figure 4) compared to the reference channel (right). The AFM (Figure 5) confirmed the presence of bacteria in the measuring channel, as well as large amount of precipitate particles (∼22 000 particles on the area of 20 × 20 μm^2). Also the reference channel contained some precipitate particles, but the amount was considerably lower (∼3000 particles on 20 × 20 μm^2). The binding channel contained 6.9 times more particles which
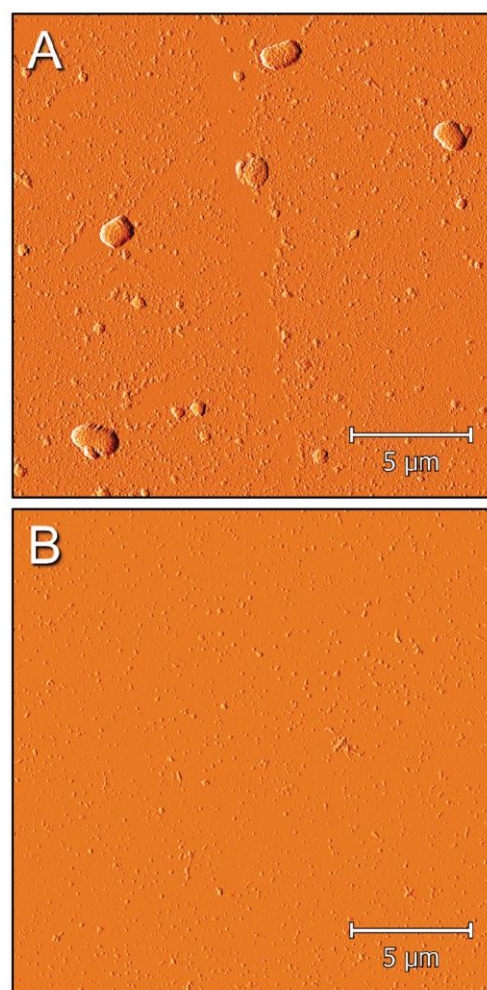
Figure 5. AFM scan of the measuring (A) and reference (B) channel of the SPR chip after *Salmonella* binding (10^7 CFU·mL^{-1}) and signal enhancement by the biocatalyzed precipitation. *Error* signal is shown.

correlates with the difference in the SPR signals (8.6 times higher response). Similarly, the surface area covered by precipitate (evaluated from AFM) was 6.3 times higher in the measuring channel. The antibody does not capture only whole cells, but also small cell debris.[13] When the HRP-Ab$_2$ conjugate

Table 1. Overview of Immunosensors for *Salmonella* Detection[a]

method	signal enhancement	LOD (CFU·mL^{-1})	linear range (CFU·mL^{-1})	analysis time (min)	ref
EIS	MNPs	340	10^2–10^6	105	44
EIS	AuNPs and MWCNTs	500	10^3–10^7	60	12
DPV	MNPs and AuNPs	143	10^3–10^6	90	45
Colorimetry	Silica NPs	88	not quantitative	60	46
Fluorimetry	MNPs and QDs	3400	10^4–10^6	50	47
SPR	AuNPs	7400	10^3–10^6	80	18
SPR	Label-free	10 000	10^4–10^8	10	this work
SPR	Enzymatic precipitation	100	10^2–10^6	60	this work

[a]DPV, differential pulse voltammetry; MWCNT, multiwalled carbon nanotube; QD, quantum dot.

230
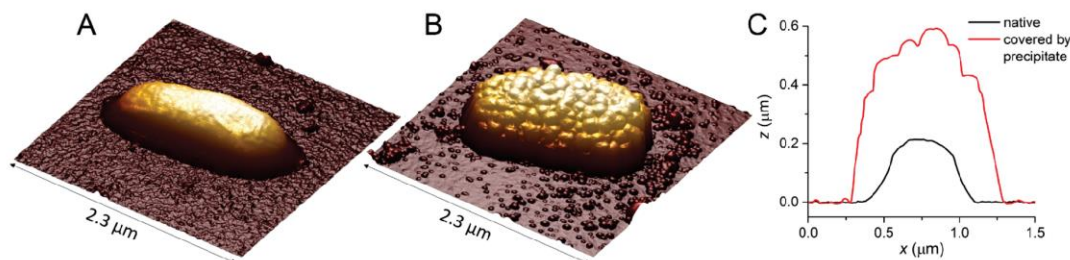
Figure 6. 3D representation of the AFM scan of (A) native and (B) precipitate-covered individual *Salmonella* cells. (C) Cross section of the bacteria made as a perpendicular line in the center.

is bound to such debris, the precipitate is formed in its vicinity. Therefore, there are more precipitate particles on the gold surface of the measuring channel (actually bound on cell debris) than in the reference channel, as can be seen in AFM images. The comparison of optical microscopy images of the measuring and reference channel is shown in Figure S7.

The shape of individual bacterial cells before and after precipitation reaction is compared in Figure 6 (detailed image of the precipitate-covered bacteria in 2D *height* and *error* signals is shown in Figure S8). The sample was scanned in dry state; the height of unfixed dry cells is typically smaller than the size of native cells.[48] The height of bacteria was increased three times after the precipitation reaction. Individual precipitate particles were visible on both bacteria and the gold surface.

Analysis of Real Samples. Detection of *Salmonella* in powdered milk was performed to demonstrate the ability of the developed sensor to analyze real samples with complex matrices. Even though the immunosensors rely on specific antibodies, there is still a risk of nonspecific adsorption of various molecules and particles from food samples. The enhancement by the biocatalyzed precipitation becomes an advantage due to the ability to improve the selectivity. The nonspecific adsorption with concomitant signal increase might occur in the first step of the analysis, but the binding of the HRP-Ab$_2$ conjugate and the precipitation reaction appear only in the presence of bacteria. The LOD of 10^3 CFU·mL^{-1} was achieved in the sample of powdered milk (Figure 7). This represents 1 order of magnitude deterioration compared to the samples diluted in buffer. The amount of the antibody immobilized to the sensor surface was the same in both cases, but the nonspecific adsorption of components of milk might has blocked some of the antigen binding sites on immobilized antibodies or concealed some epitopes on bacteria in the sample. The optical microscopy images of the SPR chip after precipitation-enhanced analysis of powdered milk are shown in Figure S9.

The ID$_{50}$ (the amount of microorganisms that needs to be ingested to cause 50% probability of infection) for *Salmonella* is considered to be >10^4 CFU.[49] It was reported that low levels of bacteria (<10^2 CFU·g^{-1}) do not represent a risk to human health.[34] Thus, the developed immunosensor is suitable for the practical analysis of real food samples.

■ CONCLUSIONS

Advanced surface plasmon resonance immunosensor was developed for a rapid and sensitive analysis of *Salmonella* in food samples. The detection antibody was conjugated with horseradish peroxidase to allow the signal enhancement by the biocatalyzed conversion of 4-chloro-1-naphthol to insoluble
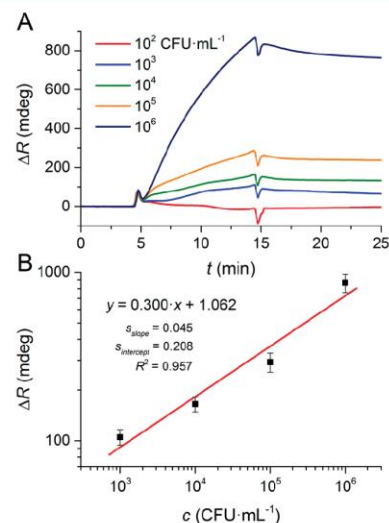
Figure 7. (A) SPR sensorgram showing the final step of biocatalyzed precipitation enhancement for the analysis of *Salmonella* in powdered milk. (B) Calibration curve.

benzo-4-chlorocyclohexadienone. This approach provided 40 times improvement of sensitivity of the *Salmonella* detection compared to label-free approach resulting in low limit of detection of 10^2 CFU·mL^{-1} and linear range up to 10^6 CFU·mL^{-1}. Additionally, the whole analysis including the injection of bacteria and the HRP-Ab$_2$ conjugate followed by the precipitation reaction did not exceed 60 min. The interaction of *Salmonella* with antibody and the precipitate formation were studied in detail by atomic force microscopy. The cross-reactivity was tested with *E. coli* K-12 and confirmed high specificity of both antibodies and the enhancement step. The powdered milk was selected as a representative example of a dairy product, typically contaminated by foodborne pathogens. *Salmonella* was successfully detected in real samples with LOD of 10^3 CFU·mL^{-1}, confirming the suitability of the developed immunosensor for practical food screening.

■ ASSOCIATED CONTENT

Ⓢ Supporting Information

The Supporting Information is available free of charge on the ACS Publications website at DOI: 10.1021/acs.analchem.6b03511.

Salmonella incidence in the EU, SPR sensorgram of antibody immobilization, SPR sensorgram of precipita-

231

tion-enhanced *Salmonella* detection, and AFM and optical microscopy images of SPR chips (PDF)

■ AUTHOR INFORMATION

Corresponding Author

*E-mail: skladal@chemi.muni.cz. Telephone: +420 54949 7010.

ORCID ⊙

Petr Skládal: 0000-0002-3868-5725

Notes

The authors declare no competing financial interest.

■ REFERENCES

(1) Bell, R. L.; Jarvis, K. G.; Ottesen, A. R.; McFarland, M. A.; Brown, E. W. *Microb. Biotechnol.* **2016**, *9* (3), 279−292.

(2) Scallan, E.; Hoekstra, R. M.; Angulo, F. J.; Tauxe, R. V.; Widdowson, M. A.; Roy, S. L.; Jones, J. L.; Griffin, P. M. *Emerging Infect. Dis.* **2011**, *17* (1), 7−15.

(3) Crump, J. A.; Heyderman, R. S. *Clin. Infect. Dis.* **2015**, *61*, S235−S240.

(4) Li, S. Q.; Li, Y. G.; Chen, H. Q.; Horikawa, S.; Shen, W.; Simonian, A.; Chin, B. A. *Biosens. Bioelectron.* **2010**, *26* (4), 1313−1319.

(5) Lopez, F. E.; de las Mercedes Pescaretti, M.; Morero, R.; Delgado, M. A. *Food Res. Int.* **2012**, *45* (2), 842−851.

(6) Lee, K. M.; Runyon, M.; Herrman, T. J.; Phillips, R.; Hsieh, J. *Food Control* **2015**, *47*, 264−276.

(7) RASFF: The Rapid Alert System for Food and Feed. https://webgate.ec.europa.eu/rasff-window/portal/.

(8) Salam, F.; Uludag, Y.; Tothill, I. E. *Talanta* **2013**, *115*, 761−767.

(9) Kirsch, J.; Siltanen, C.; Zhou, Q.; Revzin, A.; Simonian, A. *Chem. Soc. Rev.* **2013**, *42* (22), 8733−8768.

(10) Morales, M. D.; Serra, B.; Guzmán-Vázquez de Prada, A.; Reviejo, A. J.; Pingarron, J. M. *Analyst* **2007**, *132* (6), 572−578.

(11) Liebana, S.; Brandao, D.; Alegret, S.; Pividori, M. I. *Anal. Methods* **2014**, *6* (22), 8858−8873.

(12) Dong, J.; Zhao, H.; Xu, M. R.; Ma, Q.; Ai, S. Y. *Food Chem.* **2013**, *141* (3), 1980−1986.

(13) Farka, Z.; Juřík, T.; Pastucha, M.; Kovář, D.; Lacina, K.; Skládal, P. *Electroanalysis* **2016**, *28* (8), 1803−1809.

(14) Wong, Y. Y.; Ng, S. P.; Ng, M. H.; Si, S. H.; Yao, S. Z.; Fung, Y. S. *Biosens. Bioelectron.* **2002**, *17* (8), 676−684.

(15) Koubova, V.; Brynda, E.; Karasova, L.; Skvor, J.; Homola, J.; Dostalek, J.; Tobiska, P.; Rosicky, J. *Sens. Actuators, B* **2001**, *74* (1−3), 100−105.

(16) Oh, B. K.; Kim, Y. K.; Park, K. W.; Lee, W. H.; Choi, J. W. *Biosens. Bioelectron.* **2004**, *19* (11), 1497−1504.

(17) Taylor, A. D.; Ladd, J.; Yu, Q. M.; Chen, S. F.; Homola, J.; Jiang, S. Y. *Biosens. Bioelectron.* **2006**, *22* (5), 752−758.

(18) Vaisocherová-Lísalová, H.; Víšová, I.; Ermini, M. L.; Špringer, T.; Song, X. C.; Mrázek, J.; Lamačová, J.; Scott Lynn, N., Jr; Šedivák, P.; Homola, J. *Biosens. Bioelectron.* **2016**, *80*, 84−90.

(19) Masdor, N. A.; Altintas, Z.; Tothill, I. E. *Biosens. Bioelectron.* **2016**, *78*, 328−336.

(20) Kleo, K.; Schafer, D.; Klar, S.; Jacob, D.; Grunow, R.; Lisdat, F. *Anal. Bioanal. Chem.* **2012**, *404* (3), 843−851.

(21) Brandao, D.; Liebana, S.; Campoy, S.; Alegret, S.; Pividori, M. I. *Talanta* **2015**, *143*, 198−204.

(22) Liu, X.; Hu, Y.; Zheng, S.; Liu, Y.; He, Z.; Luo, F. *Sens. Actuators, B* **2016**, *230*, 191−198.

(23) Su, X. L.; Li, Y. B. *Biosens. Bioelectron.* **2005**, *21* (6), 840−848.

(24) Viswanathan, S.; Rani, C.; Ho, J. A. A. *Talanta* **2012**, *94*, 315−319.

(25) Freitas, M.; Viswanathan, S.; Nouws, H. P. A.; Oliveira, M.; Delerue-Matos, C. *Biosens. Bioelectron.* **2014**, *51*, 195−200.

(26) Wang, Y.; Fewins, P. A.; Alocilja, E. C. *IEEE Sens. J.* **2015**, *15* (8), 4692−4699.

(27) Juřík, T.; Skládal, P. *Chem. Pap.* **2015**, *69* (1), 167−175.

(28) Li, J.; Wang, J. J.; Guo, X.; Zheng, Q.; Peng, J.; Tang, H.; Yao, S. Z. *Anal. Chem.* **2015**, *87* (15), 7610−7617.

(29) Akter, R.; Rahman, M. A.; Rhee, C. K. *Anal. Chem.* **2012**, *84* (15), 6407−6415.

(30) Hou, L.; Tang, Y.; Xu, M. D.; Gao, Z. Q.; Tang, D. P. *Anal. Chem.* **2014**, *86* (16), 8352−8358.

(31) Hou, L.; Cui, Y. L.; Xu, M. D.; Gao, Z. Q.; Huang, J. X.; Tang, D. P. *Biosens. Bioelectron.* **2013**, *47*, 149−156.

(32) Ruan, C. M.; Yang, L. J.; Li, Y. B. *Anal. Chem.* **2002**, *74* (18), 4814−4820.

(33) Linman, M. J.; Sugerman, K.; Cheng, Q. *Sens. Actuators, B* **2010**, *145* (2), 613−619.

(34) Scott, V. N.; Powell, M.; Cabrera, J.; Carullo, M. E.; Martinez, I.; Lohachoompol, V. *Food Control* **2015**, *58*, 12−16.

(35) Hermanson, G. T. *Bioconjugate Techniques*, 2nd ed.; Academic Press: New York, 2008.

(36) Catty, D. *Antibodies Volume II: A Practical Approach*; IRL Press: Oxford, 1989.

(37) Farka, Z.; Kovar, D.; Skladal, P. *Sensors* **2015**, *15* (1), 79−92.

(38) Aydintug, M. K.; Inzana, T. J.; Letonja, T.; Davis, W. C.; Corbeil, L. B. *J. Infect. Dis.* **1989**, *160* (5), 846−857.

(39) Torun, O.; Hakki Boyaci, I.; Temur, E.; Tamer, U. *Biosens. Bioelectron.* **2012**, *37* (1), 53−60.

(40) Fratamico, P. M. *Mol. Cell. Probes* **2003**, *17* (5), 215−221.

(41) Cudjoe, K. S.; Hagtvedt, T.; Dainty, R. *Int. J. Food Microbiol.* **1995**, *27* (1), 11−25.

(42) Li, Y.; Mustapha, A. *J. Food Prot.* **2004**, *67* (1), 27−33.

(43) Rodriguez-Lazaro, D.; D'Agostino, M.; Herrewegh, A.; Pla, M.; Cook, N.; Ikonomopoulos, J. *Int. J. Food Microbiol.* **2005**, *101* (1), 93−104.

(44) Xu, M.; Wang, R. H.; Li, Y. B. *Talanta* **2016**, *148*, 200−208.

(45) Afonso, A. S.; Perez-Lopez, B.; Faria, R. C.; Mattoso, L. H. C.; Hernandez-Herrero, M.; Roig-Sagues, A. X.; Maltez-da Costa, M.; Merkoci, A. *Biosens. Bioelectron.* **2013**, *40* (1), 121−126.

(46) Sun, Q.; Zhao, G. Y.; Dou, W. C. *Sens. Actuators, B* **2016**, *226*, 69−75.

(47) Guo, P. L.; Tang, M.; Hong, S. L.; Yu, X.; Pang, D. W.; Zhang, Z. L. *Biosens. Bioelectron.* **2015**, *74*, 628−636.

(48) Liu, B. Y.; Zhang, G. M.; Li, X. L.; Chen, H. *Scanning* **2012**, *34* (1), 6−11.

(49) Teunis, P. F. M.; Kasuga, F.; Fazil, A.; Ogden, I. D.; Rotariu, O.; Strachan, N. J. C. *Int. J. Food Microbiol.* **2010**, *144* (2), 243−249.

Paper X

Prussian Blue Nanoparticles as a Catalytic Label in a Sandwich Nanozyme-Linked Immunosorbent Assay

Farka, Z.*; Čunderlová, V.; Horáčková, V.; Pastucha, M.; Mikušová, Z.; Hlaváček, A.; Skládal, P.

(Z.F. and V.Č. contributed equally)

Contribution:

Design of experiments, bioconjugation and characterization of PBNPs, development and optimization of sandwich assay, data evaluation, manuscript writing

Prussian Blue Nanoparticles as a Catalytic Label in a Sandwich Nanozyme-Linked Immunosorbent Assay

Zdeněk Farka,*,[†,‖] Veronika Čunderlová,[†,‡,‖] Veronika Horáčková,[†] Matěj Pastucha,[†,‡] Zuzana Mikušová,[‡] Antonín Hlaváček,[†,§] and Petr Skládal*,[†,‡]

[†]Central European Institute of Technology and [‡]Department of Biochemistry, Faculty of Science, Masaryk University, Kamenice 5, 625 00 Brno, Czech Republic

[§]Institute of Analytical Chemistry, Czech Academy of Sciences, 602 00 Brno, Czech Republic

Ⓢ *Supporting Information*

ABSTRACT: Enzyme immunoassays are widely used for detection of analytes within various samples. However, enzymes as labels suffer several disadvantages such as high production cost and limited stability. Catalytic nanoparticles (nanozymes) can be used as an alternative label in immunoassays overcoming the inherent disadvantages of enzymes. Prussian blue nanoparticles (PBNPs) are nanozymes composed of the $Fe_4[Fe(CN)_6]_3$-based coordination polymer. They reveal peroxidase-like activity and are capable of catalyzing the oxidation of colorless 3,3′,5,5′-tetramethylbenzidine in the presence of H_2O_2 to form intensely blue product. Here, we introduce the method for conjugation of PBNPs with antibodies and their application in nanozyme-linked immunosorbent assay (NLISA). Sandwich NLISA for detection of human serum albumin in urine was developed with limit of detection (LOD) of 1.2 ng·mL^{-1} and working range up to 1 μg·mL^{-1}. Furthermore, the microbial contamination of *Salmonella* Typhimurium in powdered milk was detected with LOD of 6×10^3 colony-forming units (cfu)·mL^{-1} and working range up to 10^6 cfu·mL^{-1}. In both cases, a critical comparison with the same immunoassay but using native peroxidase as label was realized. The achieved results confirmed the suitability of PBNPs for universal and robust replacement of enzyme labels.
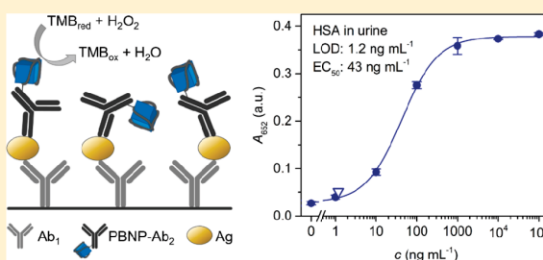
Enzyme-linked immunosorbent assay (ELISA) is considered the gold standard for highly sensitive qualitative and quantitative detection of analytes within various samples. In ELISA, an enzyme is conjugated with either antibody or antigen to be used as a signal amplification label, which catalyzes the conversion of substrate molecules to easily detectable product. For example, the conversion of a colorless substrate to a colored or fluorescent product may be applied.[1] The most commonly used enzymatic labels for immunochemical detection and imaging are peroxidases, such as horseradish peroxidase (HRP). However, high production cost, short shelf life, and decrease of activity during conjugation reactions of natural enzymes create an increasing demand for cheap and more stable nanozymes.[2,3] Nanozymes are nanomaterials mimicking catalytic activity of enzymes, such as peroxidases.[4−6]

Catalytically active nanozymes with high signal amplification and good stability generally improve the performance of immunoassays[7] and have excellent potential for the detection of single molecules in digital (immuno)assays.[8]

Nanozymes can be commonly synthesized from benign precursors in aqueous dispersants.[9] The applicability of nanozymes for practical use is also promoted by thermal and chemical stability of inorganic nanomaterials.[10] Nanozymes with high peroxidase-like activity were studied for their potential use in immunochemical assays.[3−6] Initially, magnetite

nanoparticles (Fe_3O_4) of different sizes were characterized for their activity, high turnover number, and good stability.[10] Later on, peroxidase-like activity was described for CeO_2,[11] CuO,[12] Co_3O_4,[13] bimetallic,[14] and MnO_2 nanoparticles,[15] graphene oxide nanoplates,[16] mesoporous silica nanoparticles coated by catalytic metal complexes,[7] and hemin block copolymer micelles.[17]

Coordination polymers[18] are solids, which have been studied recently for their exceptional catalytic properties. Prussian blue nanoparticles (PBNPs)[19] are nanozymes composed of coordination polymer with chemical formula $Fe_4[Fe(CN)_6]_3$ that reveal peroxidase-like activity.[20,21] Previously, we reported the biotinylation scheme of PBNPs allowing for competitive nanozyme-linked immunosorbent assay (NLISA) of protein markers.[22] However, competitive immunoassays typically possess lower sensitivity than sandwich variants.[23] Here, we introduce a method for direct conjugation of PBNPs with antibodies. The nanomaterial is characterized by transmission electron microscopy (TEM), atomic force microscopy (AFM), and dynamic light scattering (DLS). Two sandwich NLISAs were developed, for the detection of human serum albumin

234

(HSA) in urine and the detection of bacterial pathogen *Salmonella* Typhimurium in milk, and their performance was critically compared with the corresponding classic ELISA format using similar conjugates based on the natural HRP. In comparison with our previous reported competitive NLISA for HSA, the limit of detection was improved by 3 orders of magnitude.[22] This demonstrates that antibody-conjugated PBNPs can be used as an enzyme replacement and provide a universal detection system for sandwich immunoassays.

■ MATERIALS AND METHODS

Chemicals and Reagents. Bovine γ-globulin (BGG), bovine serum albumin (BSA), HSA, HRP, iron(III) chloride hexahydrate, poly-L-lysine hydrobromide (30−70 kDa), sodium azide, sodium borohydride, sodium cyanoborohydride, sodium periodate, 3,3′,5,5′- tetramethylbenzidine (TMB), Tris, and Tween 20 were obtained from Sigma−Aldrich. Ethylenediaminetetraacetic acid (EDTA), glucose, and potassium ferrocyanide trihydrate were purchased from Lachema. Poly(vinyl alcohol) (6 kDa) was purchased from Polysciences. All other common chemicals were obtained in the highest quality available from Penta.

Phosphate buffer (PB; 50 mM NaH_2PO_4/Na_2HPO_4, pH 7.4), phosphate-buffered saline (PBS; 50 mM NaH_2PO_4/Na_2HPO_4, pH 7.4, containing 150 mM NaCl), washing buffer (50 mM NaH_2PO_4/Na_2HPO_4, pH 7.4, 0.01% Tween 20, and 0.05% NaN_3), and assay buffer (0.2% BSA, 0.5% BGG, 50 mM Tris, 150 mM NaCl, 5 mM EDTA, 0.2% PVA (w/w), 1% glucose, 0.05% NaN_3, and 0.01% Tween 20, pH 7.5) were used throughout this work.

For the detection of HSA, mouse monoclonal antibody (mAb) clone AL-01 (Exbio) and fluorescein isothiocyanate (FITC)-labeled swine polyclonal antibody (pAb-F; Sevapharma) were used. The detection of *Salmonella* was based on mouse mAb ab8274 (Abcam) and rabbit pAb 8209-4006 (AbD Serotec).

Preparation of Antibody-Modified Prussian Blue Nanoparticles. PBNPs and denatured bovine serum albumin (dBSA) were prepared according to our previous work.[22] Briefly, PBNPs were synthesized by mixing 20 mL of aqueous solution of 1 mM $K_4[Fe(CN)_6]$ and 25 mM citric acid with 20 mL of 1 mM $FeCl_3$ and 25 mM citric acid, which was preheated to 55 °C. The resulting blue PBNP dispersion was stirred for 10 min and cooled to room temperature. The molar concentration of the synthesized PBNPs was 33 nM; this was based on the amounts of Fe^{2+} and Fe^{3+} ions used in the synthesis and the average nanoparticle size determined by TEM.

For preparation of dBSA, 10 mg of BSA was reduced by addition of 0.7 mg of $NaBH_4$ in 3.1 mL of water and the mixture was shaken for 60 min at room temperature. In order to decompose excess $NaBH_4$, the mixture was heated to 80 °C for 30 min until bubbles of H_2 were no longer formed. Then, prepared dBSA was mixed in a ratio of 10:1 with phosphate buffer (0.5 M, pH 8.0) and stored at −20 °C. The dBSA-modified PBNPs (PBNP-dBSA) were prepared by mixing PBNPs (33 nM) and dBSA (0.36 mg·mL^{-1}) at a volume ratio of 1:1 with subsequent heating to 70 °C for 5 min.

To prepare antibody-modified PBNPs, pAb-F (or alternatively pAb Serotec in the case of *Salmonella* assay) was diluted in 10 mM PBS to a concentration of 3 mg·mL^{-1}. The antibody was oxidized by addition of 100 μL of 0.1 M $NaIO_4$ per 1 mL of antibody solution, and the mixture was incubated at room temperature for 30 min under shaking (Thermomixer

Comfort, Eppendorf). Subsequently, the oxidized pAb-F was purified with a Microcon centrifugal unit YM-10 [10K molecular weight cutoff (MWCO); Merck Millipore]. The oxidized antibody was diluted in 10 mM PBS to a concentration of 0.2 mg·mL^{-1}, mixed with 16.5 nM PBNP-dBSA conjugate solution at a volume ratio of 1:1, and incubated at room temperature for 2 h, followed by incubation at 4 °C overnight. The formed Schiff base was reduced by addition of 50 μL of 1 M $NaBH_3CN$ per 1 mL of solution and the mixture was incubated for 4 h at room temperature. The free reactive groups were blocked by addition of 50 μL of 1 M Tris-HCl per 1 mL of solution, and this was mixed at room temperature for 30 min. The final PBNP-Ab conjugates were stored at 4 °C. The synthesis of PBNP−Ab conjugates is summarized in Figure 1.
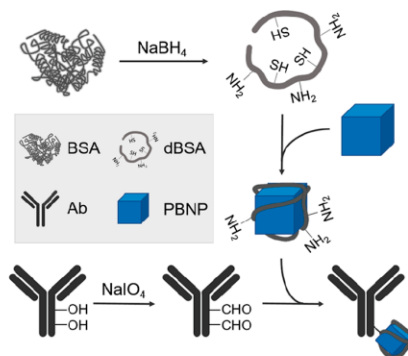
Figure 1. Scheme of PBNP−Ab conjugate synthesis. The PBNPs are modified by denatured BSA to introduce amino groups on their surface, and the oxidized antibody is conjugated via the aldehyde groups.

Characterization of Nanoparticles. Samples of PBNPs and their conjugates were diluted 10-fold with PBS, and hydrodynamic diameters were estimated from dynamic light scattering utilizing a Zetasizer Nano ZS instrument (Malvern).

For characterization of PBNPs by AFM, mica (grade V-1 muscovite, SPI Supplies) was cleaned with adhesive tape and impurities on the surface were removed by compressed air. A droplet of poly-L-lysine (20 μL of 10 μg·mL^{-1} solution in 0.1 M PB, pH 6.9) was deposited on mica for 20 min at room temperature, and then the mica was washed with distilled water and dried. The sample of PBNPs (15 μL) was incubated on the mica surface for 20 min, and the mica was washed and scanned in dry state on a Dimension Fast Scan AFM with Fast Scan-A probe (Bruker); the images were evaluated by use of Gwyddion software.

For TEM characterization, the dispersion of nanomaterial (~4 μL) was deposited onto 400-mesh copper EM grids coated with a continuous carbon layer. Dried grids were imaged by TEM (Tecnai F20, FEI). The dimensions of individual particles were analyzed by use of ImageJ software (National Institutes of Health).

Detection of Human Serum Albumin. A sandwich assay based on antibody-modified PBNPs as a label was developed for detection of human serum albumin (HSA) in urine (Figure 2). Due to the presence of HSA in urine from healthy patients,[24,25] the urine was first deproteinized by use of the Microcon centrifugal unit YM-10 and then spiked with known

235
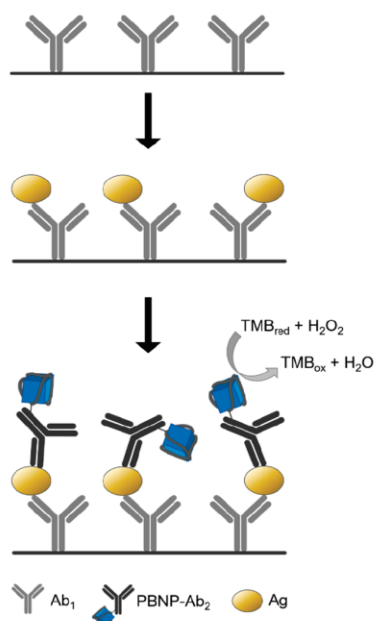
Figure 2. Scheme of PBNP-based sandwich NLISA. The microtiter plate is coated by capture antibody (Ab₁), followed by specific binding of antigen (Ag) and formation of sandwich with the detection PBNP–Ab₂ label. The colorimetric readout is based on PBNP-catalyzed oxidation of TMB in the presence of H_2O_2.

HSA concentrations. Nunc MaxiSorp 96-well microtiter plates (Thermo Fisher Scientific) were coated with monoclonal anti-HSA antibody AL-01 (4 μg·mL^{-1} in PBS, 100 μL/well) and

incubated overnight at 4 °C. All following steps were carried out at room temperature; after each step, the plate was washed four times with 200 μL of washing buffer. The plate was blocked with 200 μL of 5% powdered milk (Laktino) in PBS for 60 min. Then, either standard dilutions of HSA in assay buffer or spiked and 10× diluted urine samples (1 ng·mL^{-1} to 100 μg·mL^{-1} HSA) were added (100 μL/well), and the plates were incubated for 60 min. Subsequently, PBNP–pAb-F conjugates in the assay buffer were added (750 pM, 100 μL/well) and the plates were incubated for 60 min. Finally, the color was developed by addition of freshly prepared substrate solution (0.5 mM TMB and 125 mM H_2O_2 in 200 mM sodium acetate, pH 3.5, 100 μL/well), and absorbance at 652 nm (A_{652}) was measured after 120 min on a Synergy 2 reader (BioTek). Alternatively, the reaction was stopped by addition of 100 μL of 1 M H_2SO_4 and the absorbance was read at 450 nm (A_{450}).

Furthermore, the classic sandwich ELISA was developed and optimized to provide a comparison of NLISA with the standard approach. The conjugation of detection pAb-F with HRP was done according to our previous work.[26] The assay protocol remained the same as in the case of NLISA except for the detection conjugate binding and biocatalytic step. HRP–pAb-F conjugate (100 μL; concentration equivalent to 2.5 μg·mL^{-1} antibody) was allowed to bind for 60 min, followed by addition of commercial TMB substrate solution (Enzymo Plus). The color change was read after 30 min as A_{652}; end-point measurement at 450 nm was carried out as well after addition of 100 μL of 1 M H_2SO_4.

Detection of *Salmonella* Typhimurium. *Salmonella enterica* subsp. *enterica* serovar Typhimurium (ATCC 14028) was obtained from the Czech Collection of Microorganisms (CCM). The previously optimized sample preparation protocol that yields *Salmonella* with high affinity to the used antibodies was employed.[27] The stock solution of *Salmonella* (100 μL) was
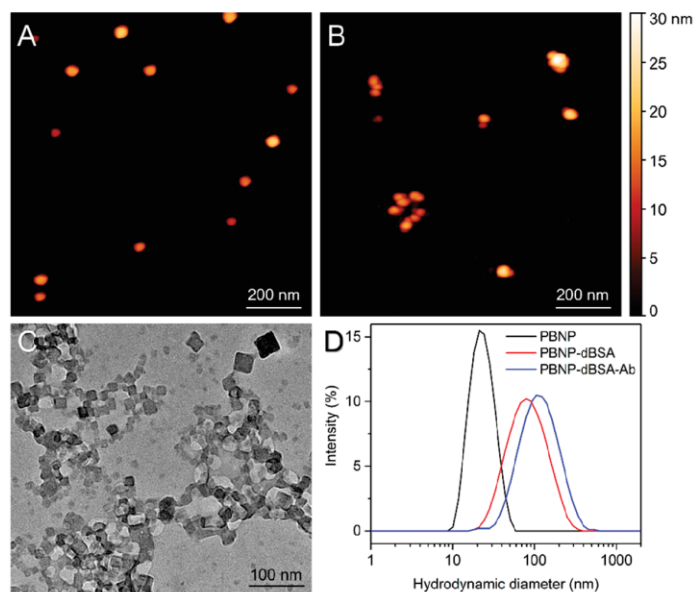
Figure 3. (A, B) AFM images of (A) PBNPs (average diameter 22.1 ± 2.9 nm) and (B) PBNP-dBSA–Ab (116 ± 29 nm) conjugates. (C) TEM image of PBNPs (15.3 ± 3.4 nm). (D) DLS of PBNPs (hydrodynamic diameter $\varnothing_{HD}$ 24 nm); PBNP-dBSA ($\varnothing_{HD}$ 92 nm), and PBNP-dBSA–Ab ($\varnothing_{HD}$ 128 nm).
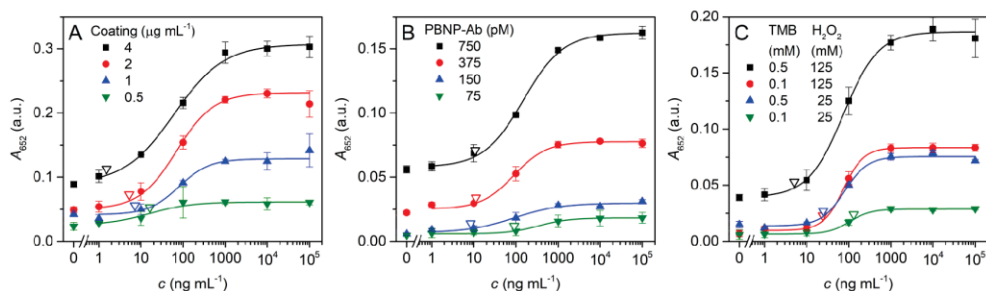
Figure 4. Optimization of NLISA for HSA detection. (A) Optimization of coating concentration of primary anti-HSA mAb. (B) Different concentrations of PBNP−Ab conjugate are used to generate the signal for a plate coated by 1 μg·mL^{-1} capture mAb. (C) Optimization of substrate concentration. Open triangles represent LOD values.

inoculated into 25 mL of low-salt Lysogeny broth (LB) broth (Duchefa Biochemie) in an Erlenmeyer flask, which was incubated aerobically overnight (37 °C, mild shaking). The bacterial suspension was centrifuged twice for 10 min at 6800g and resuspended in PBS.

The microorganism samples were treated by heat at 80 °C for 30 min with mild shaking (900 rpm) in a Thermomixer Comfort instrument. Selected samples were also homogenized by use of a Q700 sonicator (Qsonica). The 1.6 mm Microtip probe was placed into a microtube with 1 mL of *Salmonella* sample, and amplitude of 70% was maintained for approximately 10 min until the total energy consumed by the sample reached 1 kJ. The concentrations of thus-treated bacteria are expressed as colony-forming units per milliliter (cfu·mL^{-1}) corresponding to the initial amount of viable cells. The real samples were prepared by dissolving powdered milk in assay buffer to a concentration of 1% and spiking it with varying *Salmonella* concentrations.

For *Salmonella* detection, the surface of the microtiter plate was coated by monoclonal anti-*Salmonella* antibody Abcam ab8274 (2 μg·mL^{-1}), and the detection label consisted of PBNPs modified by polyclonal antibody Serotec 8209-4006. Other assay steps remained the same as in the case of HSA detection. The reference ELISA experiments were performed utilizing the same experimental conditions; the only difference was use of the conjugate of HRP with polyclonal antibody Serotec at a concentration of 2.5 μg·mL^{-1}.

Data Analysis. For each concentration, the mean and standard deviation were calculated from three replicate wells. A four-parameter logistic function was used for regression analysis of the calibration curves:

$$y = \frac{y_{max} - y_{bg}}{1 + \left(\frac{c}{EC_{50}}\right)^s} + y_{bg}$$

where c is the concentration of either HSA or *Salmonella* and y is the measured absorbance at 652 nm (A_{652}). The equation yields as parameters the maximum (y_{max}) and background (y_{bg}) signals, the concentration that reduced ($y_{max} - y_{bg}$) by 50% (EC_{50}), and the slope at the inflection point (s). The limit of detection (LOD) was calculated from the regression curve as the concentration corresponding to the y_{LOD} value:

$$y_{LOD} = y_{bg} + 3s_0$$

where s_0 is the standard deviation of blank measurement (no analyte present in the sample).

RESULTS AND DISCUSSION

Characterization of Prussian Blue Nanoparticles and Their Conjugates. For the first time, we describe the direct covalent conjugation of PBNPs with antibodies. The employed synthetic method provided PBNPs with cubic shape; the nanoparticles were characterized by TEM, AFM, and DLS. The average size estimated by AFM was 22.1 ± 2.9 nm (Figure 3A), the size determined by TEM was 15.3 ± 3.4 nm (Figure 3C), and DLS revealed hydrodynamic diameter of 24 nm with polydispersity index 0.213 (Figure 3D). The surface of PBNPs was modified with reductively denatured bovine serum albumin and as we reported previously; the attachment of dBSA was accompanied by slight aggregation of PBNPs.[22] The size of these aggregates estimated by AFM was 107 ± 20 nm; DLS provided a hydrodynamic diameter of 92 nm with polydispersity index of 0.222. Then prepared PBNP−dBSA was conjugated with antibodies by a reductive amination method,[28] resulting in the PBNP-Ab tracer. The size of the final PBNP−Ab conjugate provided by AFM was 116 ± 29 nm (Figure 3B); the hydrodynamic diameter was 128 nm with polydispersity index 0.232.

Design of Nanozyme-Linked Immunosorbent Assay. Synthesized conjugates of PBNPs with anti-HSA antibody were employed in the sandwich immunoassay for HSA. Due to the simple conjugation and shorter analysis time (fewer incubation steps), PBNPs conjugated with detection antibody were used as tracer directly instead of the universal biotin-labeling protocol, which is also possible but prolongs the assay.[22]

The assay procedure was based on two anti-HSA antibodies: monoclonal AL-01 and polyclonal pAb-F. As expected, the most efficient binding was observed when the mAb was used for analyte capture and pAb as the label conjugated on the PBNPs (Figure S1). This arrangement allows oriented binding of the analyte on the surface and reduces probability that the label could not bind to the analyte due to inaccessible binding sites. Furthermore, binding of HSA via the capture antibody enhanced its accessibility for the PBNP−Ab tracer, which resulted in higher signals in sandwich compared to the direct assay with HSA coated on the microtiter plate surface.

The coating concentration and blocking conditions were optimized in order to achieve high sensitivity and wide working range. Unlike the competitive assays where the coating concentration needs to be fine-tuned to achieve a compromise between efficient competition and measured signal intensity,[29] the sandwich format generally provides higher responses for higher coating concentrations. In agreement with theory, the measured signals increased with increasing coating concen-

237
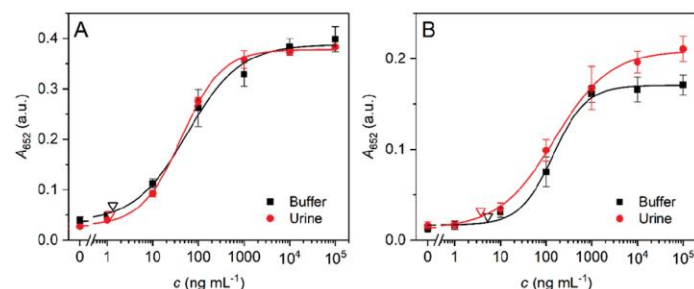
Figure 5. (A) Calibration curve of sandwich NLISA for detection of HSA in buffer (black; LOD 1.3 ng·mL^{-1}, EC$_{50}$ 57 ng·mL^{-1}) and spiked urine (red; LOD 1.2 ng·mL^{-1}, EC$_{50}$ 43 ng·mL^{-1}) under optimized conditions (4 μg·mL^{-1} coating, 750 pM PBNP–Ab). (B) Calibration curve of standard ELISA for HSA detection in buffer (black; LOD 5.3 ng·mL^{-1}, EC$_{50}$ 142 ng·mL^{-1}) and spiked urine (red; LOD 3.7 ng·mL^{-1}, EC$_{50}$ 152 ng·mL^{-1}). Open triangles represent LOD values.

tration (Figure 4A). However, the background also increased proportionally, which led to a constant signal-to-background ratio of 3–4:1 that did not depend significantly on the coating level. The coating from the higher part of the tested scale (4 μg·mL^{-1}) was selected since the higher signals in general allow readout less prone to instrumental and pipetting errors. This leads to smaller standard deviations and hence better LOD values. The effects of different blocking conditions on assay performance are shown in Figure S2A. Compared to blocking with pure BSA (10 mg·mL^{-1} in PBS), the more complex solutions of milk (50% in PBS) and powdered milk (5% in PBS) provided lower degrees of nonspecific binding. Powdered milk was selected due to slightly lower background and expected higher reproducibility.

During preparation, centrifugation was used to conveniently separate PBNP–Ab conjugates from the unbound antibody that might potentially compete with the conjugate for binding on HSA. The comparison of centrifuged and uncentrifuged conjugates of two PBNP–Ab samples (based on two different antibody oxidation times) is shown in Figure S2B. For both conjugates, significant signal decrease was observed after centrifugation. Even though high centrifugation speed (14000g) and long centrifugation time (30 min) were used, a substantial amount of PBNPs remained in the supernatant, while the sedimented particles were rather difficult to resuspend. On the other hand, no significant interference from the unseparated free antibody was observed in the case of uncentrifuged particles; therefore, this sample was used for further immunoassays. The concentration of detection PBNP–Ab conjugate substantially influenced the overall measured signals (Figure 4B); however, it did not affect the signal-to-background ratio, as there were more particles that could bind nonspecifically to the surface. Unlike enzymes, the nanoparticle labels catalyze conversions of high concentrations of substrate for longer times; such conditions usually cause denaturation of natural biocatalysts. The optimization of substrate concentration is shown in Figure 4C, and the time dependence of product formation is shown in Figure S3. The readout after 120 min was selected as a compromise between the overall measured signal and assay time requirements. Stopping the reaction by H$_2$SO$_4$ provided higher absorbance values; however, it did not affect the LOD values as the errors were increased proportionally (Figure S4). To evaluate reproducibility, the assay was performed multiple times with different batches of PBNP–Ab conjugate. Only small variations in the LOD (1.3–4.0 ng·mL^{-1}) and EC$_{50}$ (28.3–77.3 ng·mL^{-1})

values were observed (Figure S5), which confirms the high reliability of both conjugate preparation and the assay itself; the accuracy of results is further ensured by measuring the calibration curve as a part of each microtiter plate with unknown samples.

The ability to analyze real samples was demonstrated by detection of HSA in human urine. Because of the high sensitivity of the developed NLISA and trace amounts of HSA in urine from healthy patients, HSA was first removed from the urine sample by filtration through a 10 kDa centrifugal microfilter, followed by spiking of known HSA concentrations. The calibration curve comparing HSA detection in buffer and urine is shown in Figure 5A. Possible interference from various ions present in urine, which might potentially catalyze substrate conversion, is suppressed by the washing step; therefore, no large difference in the response was observed when HSA was analyzed in buffer and in the urine samples.

To compare the capabilities of PBNP- and enzyme-based labels, ELISA based on the same combination of antibodies was developed, optimized (Figure S6), and employed for analysis of HSA in spiked urine (Figure 5B). The LOD of NLISA (1.2 ng·mL^{-1}) was slightly better than in the case of ELISA (3.7 ng·mL^{-1}). The similar results suggest that the assay is limited mainly by the affinity of the selected antibodies for the target analyte and not by the detection step. However, the catalytic nanoparticles provide several practical advantages compared to the enzymatic label, such as simple and cheap preparation, higher stability, and possibility to function at much higher substrate concentrations. The PBNPs alone provide practically unlimited shelf life (several years at 4 °C); the stability-limiting element is the antibody as the biorecognition molecule. Further enhancements in label stability could be achieved by functionalizing the PBNPs with artificial aptamers or molecularly imprinted polymers. A detailed comparison of NLISA and ELISA with respect to properties and preparation of catalytic label and assay performance is shown in Table S1.

The overall analysis time was 4 h starting from the coated and blocked plate. The concentration range typical for microalbuminuria, which is a diagnostic hallmark for diabetic nephropathy, is from 20 to 200 μg·mL^{-1} in the 24 h specimens. The optimized assay provided LOD of 1.2 ng·mL^{-1} for HSA in urine, with a working range up to 1 μg·mL^{-1}. Therefore, the parameters of developed NLISA are sufficient to discriminate positive microalbuminuria samples.[30] The achieved detection limit is better than values reported for competitive ELISA (LOD 89 ng·mL^{-1}),[31] competitive fluoroimmunoassays (LOD
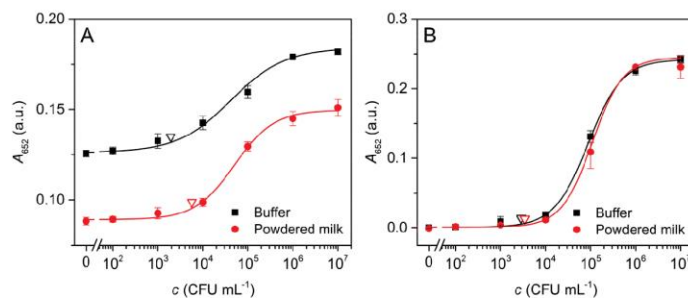
Figure 6. (A) Calibration curve for NLISA-based detection of *Salmonella* Typhimurium in buffer (black; LOD 2×10^3 cfu·mL^{-1}, EC$_{50}$ 4×10^4 cfu·mL^{-1}) and spiked powdered milk (red; LOD 6×10^3 cfu·mL^{-1}, EC$_{50}$ 5×10^4 cfu·mL^{-1}). (B) Calibration curve for ELISA-based detection of *Salmonella* Typhimurium in buffer (black; LOD 3×10^3 cfu·mL^{-1}, EC$_{50}$ 9×10^4 cfu·mL^{-1}) and spiked powdered milk (red; LOD 3×10^3 cfu·mL^{-1}, EC$_{50}$ 1×10^5 cfu·mL^{-1}). Open triangles represent LOD values.

1 μg·mL^{-1}),[32] competitive NLISA (LOD 0.27 μg·mL^{-1}),[22] method based on specific fluorescence probe (LOD 0.4 μg·mL^{-1}),[33] immunonephelometry (LOD 2 μg·mL^{-1}),[34] immunoturbidimetry (LOD 6 μg·mL^{-1}),[34] and the semiquantitative dipstick method (LOD 10 μg·mL^{-1}).[35] The developed sandwich NLISA provided LOD comparable to radioimmunoassay (LOD 16 ng·mL^{-1})[34] and sandwich ELISA (LOD 6.25 ng·mL^{-1}),[36] as summarized in Table S2.

Detection of *Salmonella* Typhimurium. To demonstrate the universal applicability of PBNPs as labels in immunoassays, *Salmonella* Typhimurium was detected as a representative example of a large microbial antigen. The assay was optimized on the basis of findings obtained during the detection of HSA; the optimization of coating concentration is shown in Figure S7A. Also in this case, the coating concentration influenced the total measured signals but did not have an effect on the signal-to-background ratio. It was previously shown that the selected antibodies exhibit higher affinity toward heat-treated samples compared to native *Salmonella*,[27] therefore, heat treatment and sonication were tested for sample preparation (Figure S7B). The sonicated *Salmonella* provided a wider working range compared to the heat-treated sample; however, similar LOD values were achieved. Heat treatment is preferable for sample preparation due to lower requirements for equipment and time.

Detection in powdered milk (diluted by assay buffer) spiked with the microbe was carried out to demonstrate the ability of NLISA to detect *Salmonella* in real samples (Figure 6A). The presence of milk matrix during the *Salmonella* binding step served to further block the surface and allowed us to decrease the level of nonspecific binding with minimal effect on the LOD. The optimized assay provided LOD of 6×10^3 cfu·mL^{-1} in powdered milk, with a working range up to 10^6 cfu·mL^{-1}. The obtained results are better than values for traditional ELISA that provide typical LODs in the range between 10^4 and 10^6 cfu·mL^{-1}.[37-39] The sandwich ELISA developed here, utilizing the same combination of capture and detection antibodies, provided LOD of 3×10^3 cfu·mL^{-1} in powdered milk (Figure 6B). This is in agreement with the results for the detection of HSA, which suggest that the affinity of antibodies has a more significant impact on the LOD than the label used. Another assay scheme based on direct ELISA was also tested and compared (Figure S8); however, the LOD did not improve compared to the sandwich arrangement.

The LOD can be further improved by a shortened cultivation-based pre-enrichment; however, such assays have higher demands on analysis time (~1 day instead of several

hours).[40] A faster way to concentrate the analyte and separate it from a complex matrix is immunomagnetic separation. This approach is often used in biosensor-based detection.[41] It is not regularly used in immunoassays, though microfluidics-based ELISA utilizing magnetic beads was recently reported for the detection of C-reactive protein.[42]

Various nanoparticle-based approaches were recently reported to improve the properties of traditional ELISA for *Salmonella* detection.[43] One of the most popular ways is to improve the catalytic properties of the label. For example, conjugation of detection antibody and HRP on single-walled carbon nanotubes[44] allowed researchers to reach LOD of 10^3 and 10^4 cfu·mL^{-1} for direct and sandwich assay, respectively. This method provided higher catalytic activities than simple conjugates of HRP with antibody; however, it was still limited by the instability of the enzyme label. PBNPs, on the other hand, not only provide comparable LOD but also can be used to catalyze higher substrate concentrations (allowing higher measured signals) and are significantly more stable (which provides longer shelf life of the label). The comparison of immunoassays for *Salmonella* detection without pre-enrichment steps is shown in Table S3.

■ CONCLUSIONS

The straightforward method for conjugation of Prussian blue nanoparticles with antibodies was developed and applied in nanozyme-linked immunosorbent assay (NLISA). The assay protocol is based on the oxidation of TMB forming blue product; therefore a common colorimetric reader can be used without special requirements for instrumentation. The universal applicability of PBNPs as labels is demonstrated by the development of two sandwich immunoassays. Human serum albumin was detected in urine for the diagnosis of albuminuria. The assay provided LOD of 1.2 ng·mL^{-1} and a working range of 3 orders of magnitude, up to 1 μg·mL^{-1}. NLISA was also employed for the detection of bacterial pathogen *Salmonella* Typhimurirum in powdered milk with LOD of 6×10^3 cfu·mL^{-1} and a working range up to 10^6 cfu·mL^{-1}. For comparison, the same antibodies were also used in standard sandwich ELISA formats with natural HRP enzyme. Comparable assay parameters were achieved, which suggests that the assay is limited mainly by the affinity of the antibodies for the target analyte and not by the detection step. However, PBNPs provide several practical advantages compared to the enzymatic label, such as easy synthesis from cheap precursors and higher stability. The results achieved in the NLISA are also highly

comparable with other recent nanoparticle-based immuno-assays, including those based on gold nanoparticles, quantum dots, and carbon nanotubes (Table S3).

■ ASSOCIATED CONTENT

ⓢ Supporting Information

The Supporting Information is available free of charge on the ACS Publications website at DOI: 10.1021/acs.anal-chem.7b04883.

Eight figures and three tables showing optimization of NLISA assay, reference ELISA measurements, and comparison of assay parameters with literature (PDF)

■ AUTHOR INFORMATION

Corresponding Authors
*E-mail farka@mail.muni.cz (Z.F.).
*E-mail skladal@chemi.muni.cz; telephone +420 54949 7010 (P.S.).

ORCID ⓘ
Zdeněk Farka: 0000-0002-6842-7081
Petr Skládal: 0000-0002-3868-5725

Author Contributions
‖Z.F. and V.Č. contributed equally to this work.

Notes
The authors declare no competing financial interest.

■ ACKNOWLEDGMENTS

■ REFERENCES

(1) Wild, D. *The Immunoassay Handbook*, 4th ed.; Elsevier: Oxford, U.K., 2013.

(2) Lavery, C. B.; MacInnis, M. C.; MacDonald, M. J.; Williams, J. B.; Spencer, C. A.; Burke, A. A.; Irwin, D. J. G.; D'Cunha, G. B. *J. Agric. Food Chem.* **2010**, *58* (15), 8471−8476.

(3) Wei, H.; Wang, E. K. *Chem. Soc. Rev.* **2013**, *42* (14), 6060−6093.

(4) Kuah, E.; Toh, S.; Yee, J.; Ma, Q.; Gao, Z. Q. *Chem. - Eur. J.* **2016**, *22* (25), 8404−8430.

(5) Ragg, R.; Tahir, M. N.; Tremel, W. *Eur. J. Inorg. Chem.* **2016**, *2016* (13−14), 1906−1915.

(6) Nasir, M.; Nawaz, M. H.; Latif, U.; Yaqub, M.; Hayat, A.; Rahim, A. *Microchim. Acta* **2017**, *184* (2), 323−342.

(7) Kumari, S.; Dhar, B. B.; Panda, C.; Meena, A.; Sen Gupta, S. *ACS Appl. Mater. Interfaces* **2014**, *6* (16), 13866−13873.

(8) Walt, D. R. *Anal. Chem.* **2013**, *85* (3), 1258−1263.

(9) Shokouhimehr, M.; Soehnlen, E. S.; Khitrin, A.; Basu, S.; Huang, S. P. D. *Inorg. Chem. Commun.* **2010**, *13* (1), 58−61.

(10) Gao, L. Z.; Zhuang, J.; Nie, L.; Zhang, J. B.; Zhang, Y.; Gu, N.; Wang, T. H.; Feng, J.; Yang, D. L.; Perrett, S.; Yan, X. *Nat. Nanotechnol.* **2007**, *2* (9), 577−583.

(11) Xu, C.; Qu, X. G. *NPG Asia Mater.* **2014**, *6*, No. e90, DOI: 10.1038/am.2013.88.

(12) Chen, W.; Chen, J.; Liu, A. L.; Wang, L. M.; Li, G. W.; Lin, X. H. *ChemCatChem* **2011**, *3* (7), 1151−1154.

(13) Dong, J. L.; Song, L. N.; Yin, J. J.; He, W. W.; Wu, Y. H.; Gu, N.; Zhang, Y. *ACS Appl. Mater. Interfaces* **2014**, *6* (3), 1959−1970.

(14) He, W. W.; Liu, Y.; Yuan, J. S.; Yin, J. J.; Wu, X. C.; Hu, X. N.; Zhang, K.; Liu, J. B.; Chen, C. Y.; Ji, Y. L.; Guo, Y. T. *Biomaterials* **2011**, *32* (4), 1139−1147.

(15) Liu, X.; Wang, Q.; Zhao, H. H.; Zhang, L. C.; Su, Y. Y.; Lv, Y. *Analyst* **2012**, *137* (19), 4552−4558.

(16) Song, Y. J.; Qu, K. G.; Zhao, C.; Ren, J. S.; Qu, X. G. *Adv. Mater.* **2010**, *22* (19), 2206−2210.

(17) Qu, R.; Shen, L. L.; Chai, Z. H.; Jing, C.; Zhang, Y. F.; An, Y. L.; Shi, L. Q. *ACS Appl. Mater. Interfaces* **2014**, *6* (21), 19207−19216.

(18) Kitagawa, S.; Kitaura, R.; Noro, S. *Angew. Chem., Int. Ed.* **2004**, *43* (18), 2334−2375.

(19) Herren, F.; Fischer, P.; Ludi, A.; Halg, W. *Inorg. Chem.* **1980**, *19* (4), 956−959.

(20) Zhang, X. Q.; Gong, S. W.; Zhang, Y.; Yang, T.; Wang, C. Y.; Gu, N. *J. Mater. Chem.* **2010**, *20* (24), 5110−5116.

(21) Zhang, W. M.; Ma, D.; Du, J. X. *Talanta* **2014**, *120*, 362−367.

(22) Čunderlová, V.; Hlaváček, A.; Horňáková, V.; Peterek, M.; Němeček, D.; Hampl, A.; Eyer, L.; Skládal, P. *Microchim. Acta* **2016**, *183* (2), 651−658.

(23) Jackson, T. M.; Ekins, R. P. *J. Immunol. Methods* **1986**, *87* (1), 13−20.

(24) Datta, P.; Dasgupta, A. *J. Clin. Lab. Anal.* **2009**, *23* (5), 314−318.

(25) Tsai, J. Z.; Chen, C. J.; Settu, K.; Lin, Y. F.; Chen, C. L.; Liu, J. T. *Biosens. Bioelectron.* **2016**, *77*, 1175−1182.

(26) Farka, Z.; Juřík, T.; Pastucha, M.; Skládal, P. *Anal. Chem.* **2016**, *88* (23), 11830−11836.

(27) Farka, Z.; Juřík, T.; Pastucha, M.; Kovář, D.; Lacina, K.; Skládal, P. *Electroanalysis* **2016**, *28* (8), 1803−1809.

(28) Algar, W. R.; Prasuhn, D. E.; Stewart, M. H.; Jennings, T. L.; Blanco-Canosa, J. B.; Dawson, P. E.; Medintz, I. L. *Bioconjugate Chem.* **2011**, *22* (5), 825−858.

(29) Hlaváček, A.; Farka, Z.; Hübner, M.; Horňáková, V.; Němeček, D.; Niessner, R.; Skládal, P.; Knopp, D.; Gorris, H. H. *Anal. Chem.* **2016**, *88* (11), 6011−6017.

(30) Doumas, B. T.; Peters, T. *Clin. Chim. Acta* **1997**, *258* (1), 3−20.

(31) Zhao, L. X.; Lin, J. M.; Li, Z. J. *Anal. Chim. Acta* **2005**, *541* (1−2), 197−205.

(32) Hlaváček, A.; Bouchal, P.; Skládal, P. *Microchim. Acta* **2012**, *176* (3−4), 287−293.

(33) Kessler, M. A.; Meinitzer, A.; Petek, W.; Wolfbeis, O. S. *Clin. Chem.* **1997**, *43* (6), 996−1002.

(34) Busby, D. E.; Bakris, G. L. *J. Clin. Hypertens.* **2004**, *6*, 8−12.

(35) Marshall, S. M.; Shearing, P. A.; Alberti, K. *Clin. Chem.* **1992**, *38* (4), 588−591.

(36) Watts, G. F.; Bennett, J. E.; Rowe, D. J.; Morris, R. W.; Gatling, W.; Shaw, K. M.; Polak, A. *Clin. Chem.* **1986**, *32* (8), 1544−1548.

(37) Magliulo, M.; Simoni, P.; Guardigli, M.; Michelini, E.; Luciani, M.; Lelli, R.; Roda, A. *J. Agric. Food Chem.* **2007**, *55* (13), 4933−4939.

(38) Roda, A.; Mirasoli, M.; Roda, B.; Bonvicini, F.; Colliva, C.; Reschiglian, P. *Microchim. Acta* **2012**, *178* (1−2), 7−28.

(39) Wang, W. B.; Liu, L. Q.; Song, S. S.; Tang, L. J.; Kuang, H.; Xu, C. L. *Sensors* **2015**, *15* (3), 5281−5292.

(40) Wu, X. L.; Wang, W. B.; Liu, L. Q.; Kuang, H.; Xu, C. L. *Anal. Methods* **2015**, *7* (21), 9047−9053.

(41) Liebana, S.; Brandao, D.; Alegret, S.; Pividori, M. I. *Anal. Methods* **2014**, *6* (22), 8858−8873.

(42) Liu, D.; Li, X. R.; Zhou, J. K.; Liu, S. B.; Tian, T.; Song, Y. L.; Zhu, Z.; Zhou, L. J.; Ji, T. H.; Yang, C. Y. *Biosens. Bioelectron.* **2017**, *96*, 332−338.

(43) Farka, Z.; Juřík, T.; Kovář, D.; Trnková, L.; Skládal, P. *Chem. Rev.* **2017**, *117* (15), 9973−10042.

(44) Chunglok, W.; Wuragil, D. K.; Oaew, S.; Somasundrum, M.; Surareungchai, W. *Biosens. Bioelectron.* **2011**, *26* (8), 3584−3589.

Paper XI

Competitive Upconversion-Linked Immunosorbent Assay for the Sensitive Detection of Diclofenac

Hlaváček, A.; <u>Farka, Z.</u>; Hübner, M.; Horňáková, V.; Němeček, D.; Skládal, P.; Knopp, D.; Gorris, H. H.

Contribution:

Design of experiments, bioconjugation and characterization of UCNPs, development and optimization of competitive immunoassay, data evaluation, participation in manuscript writing

analytical chemistry

Competitive Upconversion-Linked Immunosorbent Assay for the Sensitive Detection of Diclofenac

Antonín Hlaváček,[†,‡,§] Zdeněk Farka,[†,‡] Maria Hübner,[||] Veronika Horňáková,[‡] Daniel Němeček,[‡] Reinhard Niessner,[||] Petr Skládal,[‡] Dietmar Knopp,[||] and Hans H. Gorris*,[†]

[†]Institute of Analytical Chemistry, Chemo- and Biosensors, University of Regensburg, 93040 Regensburg, Germany
[‡]CEITEC—Central European Institute of Technology, Masaryk University, Brno 625 00, Czech Republic
[§]Institute of Analytical Chemistry AS CR, v. v. i., Brno 602 00, Czech Republic
[||]Chair of Analytical Chemistry and Institute of Hydrochemistry, Technical University of Munich, 81377 Munich, Germany

S *Supporting Information*

ABSTRACT: Photon-upconverting nanoparticles (UCNPs) emit light of shorter wavelength under near-infrared excitation and thus avoid optical background interference. We have exploited this unique photophysical feature to establish a sensitive competitive immunoassay for the detection of the pharmaceutical micropollutant diclofenac (DCF) in water. The so-called upconversion-linked immunosorbent assay (ULISA) was critically dependent on the design of the upconversion luminescent detection label. Silica-coated UCNPs (50 nm in diameter) exposing carboxyl groups on the surface were conjugated to a secondary anti-IgG antibody. We investigated the structure and monodispersity of the nanoconjugates in detail. Using a highly affine anti-DCF primary antibody, the optimized ULISA reached a detection limit of 0.05 ng DCF per mL. This performance came close to a conventional enzyme-linked immunosorbent assay (ELISA) without the need for an enzyme-mediated signal amplification step. The ULISA was further employed for analyzing drinking and surface water samples. The results were consistent with a conventional ELISA as well as liquid chromatography—mass spectrometry (LC—MS).
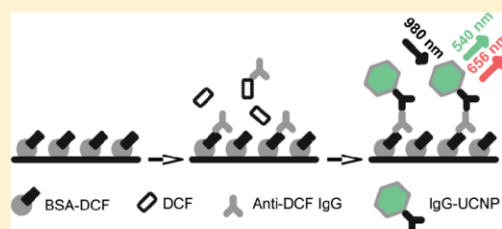
The enzyme-linked immunosorbent assay (ELISA) is a cost efficient tool for the specific and highly sensitive detection of many toxic analytes in food and environmental samples as well as clinical diagnosis. There are, however, some disadvantages of a classic ELISA such as an inherent instability of enzymes and time-consuming signal development. Consequently, many research efforts have been made to replace the enzymes by using nanoparticles (NPs) as signal amplifiers, e.g., fluorescent dye-doped polymer or silica NPs,[1] metal NPs,[2] magnetic NPs,[3] catalytic NPs,[4] or quantum dots.[5] Recently, photon-upconverting nanoparticles (UCNPs) have been used as a new generation of luminescent labels for sensitive immunochemical detection. UCNPs are lanthanide-doped nanocrystals that can be excited by near-infrared light and emit light of shorter wavelengths (anti-Stokes emission),[6,7] which strongly reduces autofluorescence and light scattering. Further advantages of UCNPs include (A) a very high photostability, (B) large anti-Stokes shifts allowing for an excellent separation of excitation and detection channels, and (C) multiple and narrow emission bands that can be tuned individually for the multiplexed detection of analytes.[8–10]

These distinct photophysical features of UCNPs have been used for the design of heterogeneous microtiter plate immunoassays, e.g., for the detection of prostate-specific antigen (limit of detection, LOD, 0.15 ng mL^{-1}/6 pM)[11] or

human chorionic gonadotropin (LOD, 3.8 ng mL^{-1}/200 pM).[12] The advantages of UCNPs in lateral flow assays, e.g., for the detection of worm parasite antigens (LOD, 0.01 ng mL^{-1}/0.1 pM)[13] have also been well documented. There have been a few reports on the use of homogeneous competitive immunoassays for the detection of small molecules such as estradiol (LOD, ~0.1 ng mL^{-1}/400 pM)[14] and folate (LOD, 0.4 ng mL^{-1}/1000 pM)[15] in blood and a bead-based immunoassay for the detection of mycotoxins in food samples (LOD, ~0.01 ng mL^{-1}/50 pM).[16]

The development and widespread availability of more sensitive analytical techniques has resulted in an increasing number of pharmaceuticals that can be detected in the environment after medical or veterinary use.[17,18] Diclofenac (2-[2-(2,6-dichlorophenyl) aminophenyl] ethanoic acid; DCF) is a widely used nonsteroidal anti-inflammatory drug (NSAID). In the Indian subcontinent, the widespread use of DCF for veterinary treatment of cattle since the 1990s has led to a precipitous decline of the indigenous vulture population because DCF leads to renal failure in vultures that feed on contaminated carcasses.[19] In Europe, DCF belongs to the most

frequently detected pharmaceuticals in the water-cycle because it is not easily degraded when passing through sewage treatment plants. DCF has been detected in low μg L^{-1} amounts in wastewater effluents and also in ng L^{-1} amounts in surface waters,[20] groundwater, and drinking water.[21] Very low amounts of DCF can be detected by liquid chromatography–time-of-flight-mass spectrometry (LC–TOF-MS) or high-resolution mass spectrometers.[22,23] These instrumental techniques, however, are expensive, time-consuming, labor intensive and need trained personnel. By contrast, immunoassays are more suitable for on-site testing directly in the field or for the analysis of large numbers of samples in small laboratories.[24]

Here, we have optimized the preparation of monodisperse and stable upconversion reporters for the sensitive detection of DCF in water samples by a competitive upconversion-linked immunosorbent assay (ULISA). Anti-mouse IgG antibodies were conjugated to silica-coated UCNPs exposing carboxyl function on the surface and the conjugates were characterized by gel electrophoresis.[25] The competitive detection of DCF was performed using a monoclonal mouse anti-DCF antibody (Figure 1). This antibody was characterized in detail as
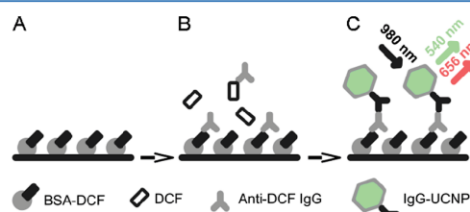
Figure 1. Scheme of the indirect competitive ULISA for the detection of diclofenac (DCF). (A) A microtiter plate is coated with a bovine serum albumin-DCF conjugate (BSA-DCF). (B) Dilution series of DCF are prepared in the microtiter plate followed by the addition of anti-DCF mouse antibody. (C) The attachment of anti-DCF antibody is then detected by an anti-mouse IgG-UCNP secondary antibody conjugate. The upconversion luminescence is recorded under 980 nm laser excitation.

described recently[26] and showed about 10% cross-reactivity with DCF metabolites such as 5-OH-DCF, 4'-OH-DCF, and DCF-acyl glucuronide but only less than 1% with other structurally related nonsteroidal anti-inflammatory drugs. The performance of the optimized ULISA was compared with a conventional ELISA as well as LC−MS.

■ EXPERIMENTAL SECTION

Chemicals. All standard chemicals and diclofenac sodium salt (D6899, purity ≥98%) were obtained from Sigma-Aldrich (Steinheim, Germany). Carboxyethylsilanetriol sodium salt; 25% (w/v) in water was obtained from ABCR GmbH (Karlsruhe, Germany). The horseradish peroxidase-labeled horse anti-mouse IgG was from Axxora (Lörrach, Germany) and horse anti-mouse IgG was from Vector Laboratories (Burlingame). The monoclonal anti-diclofenac antibody 12G5 was generated in mice using a DCF-thyroglobulin conjugate as described previously.[26] An antibody stock solution of 0.45 mg mL^{-1} was prepared in 20 mM NaH$_2$PO$_4$, 0.1 M Tris-HCl, 0.02% NaN$_3$, pH 7.4 and stored at 4 °C. Buffers and solutions were prepared with ultrapure water, which was obtained by

reverse osmosis with UV treatment (Milli-RO 5 Plus, Milli-Q185 Plus, Eschborn, Germany).

Synthesis of Carboxyl-Silica-Coated UCNPs. UCNPs of 42.5 ± 4.9 nm in diameter were synthesized by high-temperature coprecipitation[27] as described in the Supporting Information. The mass concentration was determined by gravimetric analysis and a concentration of 1.0 mg mL^{-1} of UCNPs was estimated to be equivalent to the molar concentration of 9.8×10^{-9} mol L^{-1} (Supporting Information).

Carboxyl-silica-coated UCNPs (COOH-UCNPs) were prepared by a reverse microemulsion method:[25] UCNPs (80 mg) were diluted in cyclohexane to a final volume of 23 mL. This dispersion was mixed with 1800 mg of Igepal CO-520 and 100 μL of tetraethyl orthosilicate (TEOS) and stirred intensively for 10 min. A mixture of 55 μL 25% (w/v) of aqueous ammonium hydroxide and 55 μL of water was added to form a microemulsion that was slowly stirred overnight. Then, 25 μL of TEOS were added and the microemulsion was again stirred for 180 min. After adding 50 μL of 25% (w/v) sodium carboxyethylsilanetriol in water, the microemulsion was first sonicated for 15 min and then stirred for 60 min. The COOH-UCNPs were extracted with 1000 μL of dimethylformamide and washed four times with 20 mL of propan-2-ol, three times with 5000 μL of water and finally dispersed in water to yield a final concentration of 150 mg mL^{-1}. The COOH-UCNPs in water were stable at 4 °C for several months.

Conjugation of COOH-UCNP and Secondary Antibody. COOH-UCNPs were first activated by 1-ethyl-3-(3-(dimethylamino)propyl)carbodiimide (EDC) and N-hydroxy-sulfosuccinimide (sulfo-NHS). In a typical synthesis, 0.5 mg (∼5 pmol) of COOH-UCNPs was dispersed in water to a final volume of 200 μL. The volume of 50 μL of a mixture containing 2.1 μmol of EDC and 5.5 μmol of sulfo-NHS in 100 μL of 100 mM sodium 2-(N-morpholino)ethanesulfonate (MES) buffer, pH 6.1 was added and mixed for 30 min. A dispersion of 100 μL of activated COOH-UCNPs (1 mg mL^{-1} or ∼10 nmol L^{-1}) were mixed with 100 μL of horse anti-mouse IgG in borate buffer (100 mM sodium borate, pH 9.0). Three IgG concentrations were employed and incubated for 90 min at room temperature: (1) 330 nmol L^{-1} IgG resulting in a ratio 33 IgG molecules per UCNP (sample IgG-UCNP-33:1), (2) 67 nmol L^{-1} IgG resulting in a ratio of 7 IgG molecules per UCNP (IgG-UCNP-7:1), and (3) 33 nmol L^{-1} IgG resulting in a ratio of 3 IgG molecules per UCNP (IgG-UCNP-3:1). The bioconjugates were centrifuged for 10 min at 4 000g, dispersed in UCNP assay buffer (50 mM Tris, 150 mM NaCl, 0.05% NaN$_3$, 0.01% Tween 20, 0.05% bovine γ-globulin (BGG), 0.5% bovine serum albumin (BSA), 0.2% poly(vinyl alcohol) 6000 (PVA), pH 7.75) and sonicated for 5 min.

Nanoparticle Characterization. Transmission electron microscopy (TEM) was performed on a Tecnai F20 FEI instrument (Eindhoven, The Netherlands). About 4 μL of UCNPs were deposited on a 400-mesh copper EM grid coated with a continuous carbon layer and negatively stained with 2% (w/v) aqueous solution of uranyl acetate to increase the contrast of the silica shell. The dried grids were then imaged at 50 000× magnification (2.21 Å pixel^{-1}). The size of individual particles in the TEM images was measured by the imaging software ImageJ (http://imagej.nih.gov).[28] The hydrodynamic diameter and zeta potential of UCNP suspensions were determined on a Zetasizer Nano SZ from Malvern Instruments (Malvern, U.K.). FT-IR spectra were recorded on an Alpha FT-IR spectrometer from Bruker (Billerica, MA).

Agarose Gel Electrophoresis. Following our previous work,[25] COOH-UCNPs and their bioconjugates were characterized by agarose gel electrophoresis (0.5% w/v agarose, 45 mM Tris, 45 mM H_3BO_3 with pH 8.6, 15 min at 100 V). Samples were mixed in a ratio of 10:1 with 50% w/w glycerol and 8 μL aliquots were loaded onto the gel. A custom-built upconversion reader (Chameleon multilabel microplate reader, Hidex, Turku, Finland) equipped with a continuous 980 nm laser (4 W) was used to scan agarose gels with a spatial resolution of 0.5 mm as described earlier.[29]

Conjugation of Diclofenac to BSA. BSA-DCF conjugates were prepared using either 1.5 μmol or 7.5 μmol of DCF and 9.7 μmol of sulfo-NHS added to a mixture of 400 μL of MES buffer and 100 μL of dimethylformamide. DCF was activated by the addition of 47 μmol of EDC and incubation at room temperature for 30 min. After adding 500 μL of 0.15 μmol BSA in water and 250 μL of 50 mM aqueous Na_2CO_3, the mixture was incubated at room temperature for 4 h and then dialyzed (cellulose membrane, $MW_{cut-off}$: 14 kDa, D9277, Sigma-Aldrich) three times against 150 mL of 50 mM Na_2CO_3. BSA-DCF was adjusted to a concentration of 1.6 mg mL^{-1} by adding 50 mM of Na_2CO_3 and stored at 4 °C in the presence of 0.05% NaN_3. The conjugate was analyzed by matrix-assisted laser desorption ionization (MALDI)-TOF-MS (Bruker, Ultra-flex TOF/TOF, N_2-laser, 337 nm, positive mode).

Water Samples. Munich tap water and two surface water samples were collected in Southern Bavaria from Lake Wörthsee and the Würm River. The fresh water samples were filtrated over a glass microfiber filter (GF/C, Whatman catalog no. 1822 047) and stored at 4 °C. The concentrations of Ca^{2+}, Mg^{2+}, and total organic content (TOC) as well as the conductivity and pH were determined (Supporting Information, Table S1). ELISA and ULISA were performed with undiluted and spiked samples. For LC−MS, the samples were subjected to generic solid phase extraction (SPE) and analyzed by an Orbitrap-based Exactive benchtop mass spectrometer (Thermo Scientific, Dreieich, Germany) as described earlier.[26]

Upconversion-Linked Immunosorbent Assay. A transparent 96-well microtiter plate with high protein binding capacity (Corning, Wiesbaden, Germany) was coated with BSA-DCF in coating buffer (optimal concentration, 1 μg mL^{-1} BSA-DCF in 50 mM NaHCO$_3$/Na$_2$CO$_3$, 0.05% NaN$_3$, pH 9.6; 200 μL per well) at 4 °C overnight. All subsequent steps were carried out at room temperature. The plate was washed manually four times with 250 μL of washing buffer (50 mM NaH$_2$PO$_4$/Na$_2$HPO$_4$, 0.01% Tween 20, 0.05% NaN$_3$, pH 7.4). The free binding sites in each well were blocked with 250 μL of 1% BSA in 50 mM NaH$_2$PO$_4$/Na$_2$HPO$_4$, 0.05% NaN$_3$, pH 7.4 for 1 h. The plate was washed four times with washing buffer. Either standard dilutions of DCF in double distilled water or environmental samples (100 μL per well) were added, immediately followed by the anti-DCF monoclonal mouse antibody (12G5; optimal concentration, 0.225 μg mL^{-1} in 100 mM NaH$_2$PO$_4$/Na$_2$HPO$_4$, 300 mM NaCl, 100 μL per well) and incubated for 1 h. After four washing steps, the microtiter plate was incubated for 1 h with 100 μL of the IgG-UCNP conjugate (optimal concentration, 10 μg mL^{-1} in 50 mM Tris, 150 mM NaCl, 0.05% NaN$_3$, 0.01% Tween 20, 0.05% BGG, 0.5% BSA, 0.2% PVA, pH 7.75). After four washing steps, the upconversion luminescence was read out from empty wells using a custom-built upconversion microplate reader (Chameleon multilabel microplate reader, Hidex, Turku, Finland) equipped with a continuous 980 nm laser (4 W). A collimated

laser spot of ∼0.8 mm was focused on the bottom of the microtiter wells. Each well was scanned 100 times in a raster with the step size of 0.4 mm and 500 ms signal integration time. The truncated mean was calculated for each well after discarding the 10 highest and 10 lowest measurements of the luminescence intensity to account for local irregularities on the microtiter well surface that result in signal outliers.

Enzyme-Linked Immunosorbent Assay. The ELISA was performed as described earlier.[26] A transparent 96-well microtiter plate with high protein binding capacity (Greiner Bio-one, Frickenhausen, Germany) was coated with 0.5 μg mL^{-1} of ovalbumin-DCF conjugate in coating buffer (50 mM NaHCO$_3$/Na$_2$CO$_3$, 0.05% NaN$_3$, pH 9.6; 200 μL per well) at 4 °C overnight. All subsequent steps were carried out at room temperature. The plate was automatically washed with a plate washer (ELx405 Select, Bio-Tek Instruments, Bad Friedrichshall, Germany) four times with washing buffer (50 mM KH$_2$PO$_4$/K$_2$HPO$_4$, 146 mM NaCl, 0.05% Tween 20, pH 7.6; PBST). The free binding sites in each well were blocked with 300 μL of 1% BSA in PBST for 1 h. The plate was washed four times with washing buffer. First, standard dilutions of DCF in double distilled water or environmental samples (100 μL per well) were added, immediately followed by the anti-DCF monoclonal mouse antibody (12G5, 0.5 μg mL^{-1} in PBS; 100 μL per well) and incubated for 30 min. After four washing steps, the secondary horseradish peroxidase-labeled antibody was added (0.2 mg mL^{-1} in PBS; 200 μL per well) and incubated for 1 h. After final washing, the substrate solution (200 μL per well) was added and the plates were shaken for about 15 min for color development. The substrate solution consisted of 25 mL substrate buffer (prepared with 46.0 mL of potassium dihydrogen citrate and 0.1 g of potassium sorbate in 1 L of water, pH 3.8), 500 μL of 3,3′,5,5′-tetramethylbenzidine stock solution (375 mg in 30 mL of dimethyl sulfoxide), and 100 μL of 1% hydrogen peroxide. The enzyme reaction was stopped by adding 100 μL of 5% sulfuric acid per well. The absorbance was read at 450 nm by a microplate reader (Synergy HT, Bio-Tek Instruments).

Data Analysis. A four-parameter logistic function (eq 1) was used for a regression analysis of the calibration curves:

$$Y = \frac{Y_{max} - Y_{bg}}{1 + \left(\frac{[DCF]}{IC_{50}}\right)^S} + Y_{bg}$$
(1)

where [DCF] is the concentration of diclofenac, and Y is either the upconversion luminescence or the absorbance at 450 nm. Equation 1 yields the maximum (Y_{max}) and background (Y_{bg}) signal, the DCF concentration that reduces ($Y_{max} - Y_{bg}$) by 50% (IC_{50}) and the slope at the inflection point (s). All measurements were made at least in triplicate. The concentration of DCF in real water samples was determined by utilizing an inverse function of eq 1 and the limit of detection (LOD) was defined as before:[26]

$$Y(LOD) = 0.85 \times (Y_{max} - Y_{bg}) + Y_{bg}$$
(2)

■ RESULTS AND DISCUSSION

Surface Modification and Characterization of UCNPs. The development of a competitive upconversion immunoassay (ULISA) for the detection of DCF (Figure 1) critically depends on the design of the luminescent reporter that replaces the conventional enzyme amplification steps.[30] Oleic acid-capped
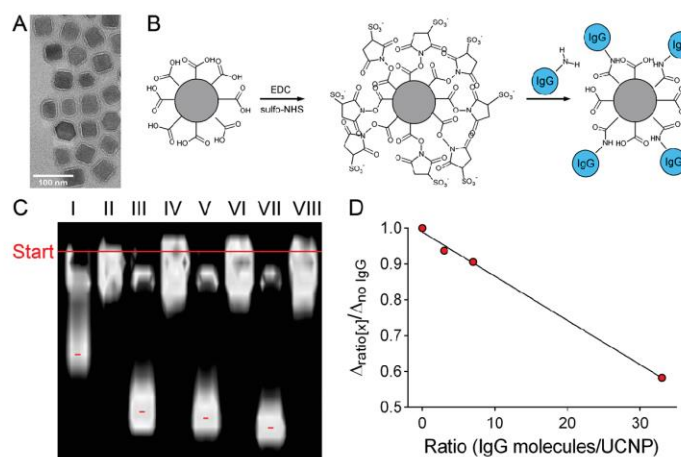
Figure 2. Preparation and characterization of IgG-UCNP conjugates. (A) TEM image of silica-coated UCNPs exposing carboxyl groups on the surface (COOH-UCNPs, Supporting Information Figure S3). (B) The carboxyl groups are activated by EDC/sulfo-NHS and conjugated to anti-mouse IgG. (C) The conjugates are prepared by using different ratios of anti-mouse IgG and COOH-UCNPs (I/II, 33 to 1; III/IV, 7 to 1; V/VI, 3 to 1; VII/VIII, no IgG). Each sample is centrifuged either with 4 000g (I, III, V, VII) or with 10 000g (II, IV, VI, VIII) and characterized by agarose gel electrophoresis. The migration distance (Δ) is indicated with red lines. (D) The relative electrophoretic mobility ($\Delta_{ratio[x]}/\Delta_{no\ IgG}$) of the conjugates is linearly dependent on the ratio of IgG molecules per UCNP.

UCNPs were coated with a silica shell exposing carboxylic acid functional groups on the surface. The carboxyl groups improve the dispersibility in water and serve as attachment sites for subsequent conjugation steps. We previously described a one-step water-in-oil microemulsion protocol for coating the surface of small UCNPs (~12 nm in diameter) with a carboxylated silica shell that showed only a weak upconversion luminescence.[25] For the immunoassay, we have synthesized larger UCNPs of 42.5 ± 4.9 nm in diameter (Supporting Information Figure S1) that are much brighter because they are less affected by surface quenching effects.[31] The one step silica-coating protocol, however, resulted in aggregation when directly applied to bigger nanoparticles. Therefore, we developed a two-step protocol to prepare a thicker, compact, and more stable silica shell on the surface of UCNPs.[32] First, TEOS was added to the microemulsion to generate a thin layer of bare silica (2.4 ± 0.4 nm, Supporting Information Figure S2). This step alone was not sufficient to prevent aggregation. Therefore, TEOS was added for a second time, which changed the thickness of the silica shell only slightly. The second carboxylation step ensured an excellent dispersibility of COOH-UCNP in water.[33] The total diameter of COOH-UCNPs was consistent as determined by transmission electron microscopy (TEM, 46.9 ± 5.0 nm; Supporting Information Figure S3 and Figure 2A) and atomic force microscopy (AFM, 45.4 ± 7.6 nm; Supporting Information Figure S4). Dynamic light scattering measurements confirmed an increase of the hydrodynamic diameter from 55 to 65 nm after silica coating (Supporting Information Figure S5).

The optimized COOH-UCNPs were then conjugated to a secondary anti-IgG antibody via standard EDC/sulfo-NHS chemistry (Figure 2B).[34,35] A low concentration of COOH-UCNP was utilized to prevent that one antibody molecule binds to several UCNPs, which would lead to aggregation. The conjugates were characterized by agarose gel electrophoresis (Figure 2C), dynamic light scattering (DLS), zeta potential measurements, and FT-IR spectroscopy (Supporting Information Figures S6−S8). The lowest degree of aggregation was observed when the concentration of COOH-UCNPs in the reaction mixture was 1 mg mL^{-1}. The conjugation of the secondary antibody reduced the negative surface potential of the COOH-UCNPs as shown by zeta potential measurements and led to a stronger retardation in the agarose gel.[36] The shift of the electrophoretic mobility was linearly dependent on the ratio of IgG molecules per UCNP and indicated the degree of surface modification (Figure 2D). Additionally, larger aggregates of nanoparticles remained in the gel pockets and could not enter the agarose matrix. Sample IgG-UCNP-33:1 shows a main fraction of monodisperse bioconjugates separated as a distinct band and a smaller fraction of slowly moving components, which are probably partially aggregated and cross-linked bioconjugates. This result is consistent with a bimodal particle distribution and a higher polydispersity index observed in the DLS measurement.

The IgG-UCNP conjugates were purified from an excess of unbound secondary anti-mouse IgG and components of the reaction mixture by differential centrifugation. At first, the bioconjugates were centrifuged at 10 000g, which however, led to strong nanoparticle aggregation (Figure 2C). When the centrifugal speed was reduced to 4 000g followed by short sonication, purified, and monodisperse IgG-UCNP were obtained. Further lowering of the centrifugal field was not efficient since the sedimentation of IgG-UCNP was too slow. The small retardation coefficient of UCNPs prepared with the lowest amount of IgG (IgG-UCNP-3:1, Figure 2C, lane V) indicated an insufficient surface modification. Therefore, this bioconjugate was not used for the following ULISA experiments.

Design of Upconversion-Linked Immunosorbent Assay. In a competitive immunoassay, a low concentration of coating antigen ensures that the free analyte can compete efficiently for the binding sites of the detection antibodies. On the other hand, the signal generation has to be strong enough for a reliable readout. Here, we prepared two different coating conjugates consisting of BSA-DCF. The conjugates were analyzed by MALDI-TOF mass spectrometry, which showed
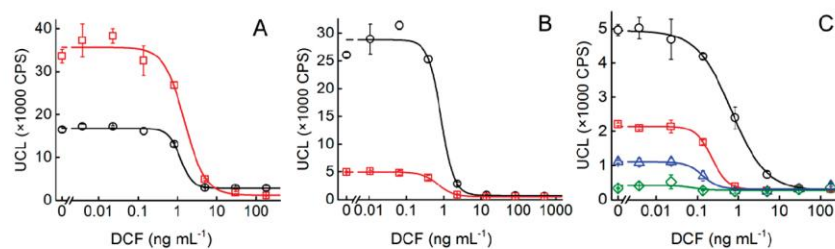
Figure 3. ULISA optimization. (A) Microtiter plates are coated with 1 μg mL^{-1} of BSA carrying either 10 (red $\square$) or 5.7 ($\bigcirc$) DCF residues. (B) The upconversion luminescent (UCL) signal is generated by using 10 μg mL^{-1} of IgG-UCNP-33:1 ($\bigcirc$) or IgG-UCNP-7:1 (red $\square$), respectively. (C) The detection of DCF is optimized by using the monoclonal anti-DCF antibody in concentrations of 0.5 μg mL^{-1} ($\bigcirc$) (IC$_{50}$, 0.68 ng mL^{-1}), 0.25 μg mL^{-1} (red $\square$) (IC$_{50}$, 0.23 ng mL^{-1}), 0.1 μg mL^{-1} (blue $\triangle$) (IC$_{50}$, 0.13 ng mL^{-1}) or 0.02 μg mL^{-1} (green $\diamond$) (IC$_{50}$, 0.08 ng mL^{-1}). Error bars represent standard deviations in upconversion signals from three replicate wells.

a coupling density of either 5.7 or 10 DCF residues per BSA molecule (Supporting Information Figures S9−S11). When the conjugate with the higher degree of derivatization was used for coating in the immunoassay, the signals were, as expected, about twice as high but also showed stronger signal fluctuation and a hook effect (Figure 3A), which may be the consequence of two binding sites of IgG molecules forming cyclic complexes (Supporting Information Figure S12).[37] By contrast, the conjugate exposing 5.7 DCF residues per BSA molecule yielded more stable signals and a slightly lower IC$_{50}$ value (1.2 ng mL^{-1} compared to 1.5 ng mL^{-1}) and a lower detection limit for DCF. Consequently, this coating conjugate was used in all further experiments. An optimal signal generation was observed with a coating concentration of 1 μg mL^{-1} (Supporting Information Figure S13).

The competition step including free DCF and anti-DCF detection antibody was performed in analogy to a sensitive conventional ELISA.[26] Only the enzyme-mediated color generation was replaced by an IgG-UCNP conjugate as a direct luminescent reporter (Figure 3B). The higher degree of UCNP surface coverage (IgG-UCNP ratio of 33:1 compared to 7:1) increased the maximum signal intensity by a factor of 5 although both conjugates were prepared with a molar excess of IgG molecules per nanoparticle. This difference can be explained because not every surface-conjugated antibody may have the right orientation or be fully functional in order to bind efficiently to the primary antibody. Consequently, a higher degree of derivatization resulted in a proportionally higher number of functional antibodies. On the downside, using IgG-UCNP-33:1 resulted in strong signal fluctuations as well as a hook effect, which impedes the reproducible determination of DCF. It should also be noted that the degree of surface substitution did not significantly affect IC$_{50}$ or the LOD, and a concentration of 10 μg mL^{-1} IgG-UCNP-7:1 resulted in the most reproducible upconversion signal generation (Supporting Information Figure S14).

In contrast to the UCNP-bound secondary antibody, the primary anti-DCF antibody is directly involved in the competition step. Figure 3C shows that both the upconversion signal intensity and the IC$_{50}$/LOD for DCF strongly depend on the antibody concentration. A higher primary antibody concentration leads to a higher signal intensity because more antibodies can bind to the DCF-BSA coating conjugate, but they also consume a larger amount of free DCF and thus deteriorate the assay sensitivity. A concentration of 0.25 μg mL^{-1} primary anti-DCF antibody yielded an optimal balance

between signal generation and sensitivity for the determination of DCF and was used in all further experiments.

Calibration and Sensitivity of ULISA and ELISA. For each type of competitive immunoassay, it is necessary to find the optimal balance between detection sensitivity for an analyte and signal development. It should also be noted that a high affinity and a low cross-reactivity of the primary antibody are the most distinctive features that determine the sensitivity and specificity of the analyte detection. Figure 4 shows calibration
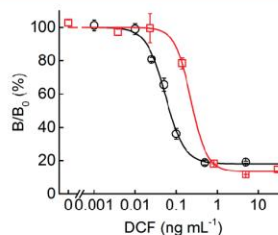
Figure 4. Normalized calibration curves of ULISA (red $\square$, replotted red curve from Figure 3C; IC$_{50}$, 0.23 ng mL^{-1}; LOD, 0.05 ng mL^{-1}) and ELISA ($\bigcirc$, IC$_{50}$, 0.05 ng mL^{-1}; LOD, 0.01 ng mL^{-1}). Error bars represent standard deviations of three replicate wells.

curves of ULISA and ELISA recorded under similar conditions and using the same anti-DCF primary antibody. In both cases a signal to background ratio (Y_{max}/Y_{bg}) of 5:1 was adjusted to achieve the most sensitive detection of DCF but also to obtain a reliable signal generation. The competitive ULISA (LOD, 0.05 ng mL^{-1}/170 pM) has a 5 times higher detection limit than a conventional ELISA (LOD, 0.01 ng mL^{-1}/ 34 pM) but allows for an easier and faster signal generation. As the detection sensitivity is ultimately dependent on the anti-DCF antibody, it can be expected that the ULISA can be further optimized by developing brighter UCNPs reporter conjugates.

Competitive immunoassays for small molecules are typically less sensitive than sandwich immunoassays where the signal generation is directly proportional to the analyte concentration. The highest sensitivity was described for the detection of *Schistosoma* circulating anodic antigen by using micrometer-sized upconversion particles in a lateral flow assay (LOD, 0.01 ng mL^{-1}/0.1 pM).[13] This particular analyte displays repetitive surface epitopes and facilitates binding of several primary antibodies per analyte molecule. The competitive immunoassay for DCF affords a similar sensitivity as a magnetic bead-based competitive immunoassay for the detection of aflatoxin that was

246

Table 1. Detection of DCF in Unspiked and Spiked Real Water Samples

sample	spiked (ng mL^{-1})	ULISA (ng mL^{-1})	ELISA (ng mL^{-1})	LC−MS (ng mL^{-1})
		<LOD	<LOD	<LOD
Lake Wörthsee	1	1.81 ± 0.06	1.11 ± 0.26	1.1 ± 0.09
	10	10.2 ± 3.8	9.9 ± 1.5	8.2 ± 0.7
		<LOD	<LOD	<LOD
Würm River	1	1.05 ± 0.26	1.16 ± 0.04	1.30 ± 0.35
	10	10.9 ± 1.6	11.9 ± 1.5	8.7 ± 0.8
		<LOD	<LOD	<LOD
Munich tap water	1	1.53 ± 0.28	1.06 ± 0.01	1.32 ± 0.10
	10	15.0 ± 5.4	10.3 ± 1.6	8.9 ± 0.2

reported to reach an LOD of 0.01 ng mL^{-1} (50 pM) under optimal conditions.[16] The additional magnetic separation step, however, demands a more sophisticated instrumentation and is more time-consuming.

Detection of Diclofenac in Real Water Samples. Two surface water samples and drinking water were collected in Southern Bavaria and the matrix was analyzed (Supporting Information Table S1) to assess possible interferences with the detection of DCF. These interferences should be as low as possible because matrix effects can suppress the immunoassay signal and lead to an overestimation of analyte concentrations. The monoclonal primary antibody 12G5 is resistant to matrix interferences over a wide pH range, humic acid concentrations up 20 mg L^{-1}, and Ca^{2+} concentrations up to 75 mg L^{-1} as described earlier.[26] The drinking water sample from Munich, however, contained relatively high Ca^{2+} and Mg^{2+} concentrations of 110 mg L^{-1} in total, which is probably the reason for a signal suppression (defined as $100 \times (Y_{sample} - Y_{bg})/(Y_{max} - Y_{bg})$) to 60 ± 7% in the ULISA and 73 ± 10% in the ELISA in the undiluted samples without DCF. By contrast, the surface water samples contained less Ca^{2+} and Mg^{2+} and were less affected by signal suppression.

The concentration of DCF was too low to be detectable in the unspiked water samples. Thus, each sample was additionally spiked with either 1 ng mL^{-1} or 10 ng mL^{-1} of DCF. The spiked samples were typically diluted at least by a factor of 3 prior to the immunoassay to keep matrix effects to a minimum. Table 1 shows the concentrations of DCF as determined by ULISA, ELISA, and LC−MS. The ULISA led to slightly stronger deviations from the spiking concentration compared to the ELISA because the matrix may also have an impact on the binding of the nanoparticulate luminescent reporter unit, which is relatively large compared to the enzyme antibody conjugate used for the ELISA. These differences in the immunoassay performance are subject to further investigation and will be optimized to unfold the full potential of the ULISA for the background-free detection of analytes.

CONCLUSION

The first immunoassays employed radionuclides that are very small, can be directly attached to the tracer or detection antibody, and generate a signal without background interference. Radioimmunoassays, however, have been largely replaced by ELISAs because of shorter signal acquisition times, lower costs, and safety considerations. Compared to the fluorescent immunoassay (FIA), the ELISA is typically preferred because the enzyme-mediated signal amplification results in a lower background signal. As a new assay format, the competitive

ULISA can achieve simultaneously a highly sensitive and background-free detection of analytes without the need for enzyme-mediated signal amplification. The design of the luminescent IgG-UCNP conjugate turned out to be critical in order to yield the most robust readout and the lowest detection limit for the environmental pollutant DCF (0.05 ng mL^{-1}). It is expected that further control over nanoparticle bioconjugation, e.g., by optimizing the orientation of IgG molecules on the nanoparticle surface, and enhancing the brightness of UCNPs will allow to reach (or even surpass) the detection limit of conventional ELISAs.

ASSOCIATED CONTENT

Supporting Information

The Supporting Information is available free of charge on the ACS Publications website at DOI: 10.1021/acs.analchem.6b01083.

Synthesis of UCNPs, calculation of nanoparticle concentrations, TEM and AFM images, DLS and zeta potential measurement, FT-IR spectra, MALDI-TOF analyses, explanation of the hook effect, optimization of the ULISA, and characterization of water samples (PDF)

AUTHOR INFORMATION

Corresponding Author

*Phone: +49-941-943-4015. Fax: +49-941-943-4064. E-mail: hans-heiner.gorris@ur.de.

Notes

The authors declare no competing financial interest.

247

■ REFERENCES

(1) Wang, L.; Wang, K. M.; Santra, S.; Zhao, X. J.; Hilliard, L. R.; Smith, J. E.; Wu, J. R.; Tan, W. H. *Anal. Chem.* **2006**, *78*, 646−654.

(2) Jans, H.; Huo, Q. *Chem. Soc. Rev.* **2012**, *41*, 2849−2866.

(3) Osterfeld, S. J.; Yu, H.; Gaster, R. S.; Caramuta, S.; Xu, L.; Han, S. J.; Hall, D. A.; Wilson, R. J.; Sun, S. H.; White, R. L.; Davis, R. W.; Pourmand, N.; Wang, S. X. *Proc. Natl. Acad. Sci. U. S. A.* **2008**, *105*, 20637−20640.

(4) Čunderlová, V.; Hlaváček, A.; Horňáková, V.; Peterek, M.; Němeček, D.; Hampl, A.; Eyer, L.; Skládal, P. *Microchim. Acta* **2016**, *183*, 651−658.

(5) Hlaváček, A.; Bouchal, P.; Skládal, P. *Microchim. Acta* **2012**, *176*, 287−293.

(6) Auzel, F. *Chem. Rev.* **2004**, *104*, 139−173.

(7) Haase, M.; Schäfer, H. *Angew. Chem., Int. Ed.* **2011**, *50*, 5808−5829.

(8) Ehlert, O.; Thomann, R.; Darbandi, M.; Nann, T. *ACS Nano* **2008**, *2*, 120−124.

(9) Li, X. M.; Zhang, F.; Zhao, D. Y. *Chem. Soc. Rev.* **2015**, *44*, 1346−1378.

(10) Gorris, H. H.; Ali, R.; Saleh, S. M.; Wolfbeis, O. S. *Adv. Mater.* **2011**, *23*, 1652−1655.

(11) Päkkilä, H.; Ylihärsilä, M.; Lahtinen, S.; Hattara, L.; Salminen, N.; Arppe, R.; Lastusaari, M.; Saviranta, P.; Soukka, T. *Anal. Chem.* **2012**, *84*, 8628−8634.

(12) Huang, P.; Zheng, W.; Zhou, S. Y.; Tu, D. T.; Chen, Z.; Zhu, H. M.; Li, R. F.; Ma, E.; Huang, M. D.; Chen, X. Y. *Angew. Chem., Int. Ed.* **2014**, *53*, 1252−1257.

(13) Corstjens, P. L. A. M.; van Lieshout, L.; Zuiderwijk, M.; Kornelis, D.; Tanke, H. J.; Deelder, A. M.; van Dam, G. J. *J. Clin. Microbiol.* **2008**, *46*, 171−176.

(14) Kuningas, K.; Päkkilä, H.; Ukonaho, T.; Rantanen, T.; Lövgren, T.; Soukka, T. *Clin. Chem.* **2007**, *53*, 145−146.

(15) Arppe, R.; Mattsson, L.; Korpi, K.; Blom, S.; Wang, Q.; Riuttamaki, T.; Soukka, T. *Anal. Chem.* **2015**, *87*, 1782−1788.

(16) Wu, S. J.; Duan, N.; Zhu, C. Q.; Ma, X. Y.; Wang, M.; Wang, Z. P. *Biosens. Bioelectron.* **2011**, *30*, 35−42.

(17) Ternes, T. A. *TrAC, Trends Anal. Chem.* **2001**, *20*, 419−434.

(18) Perez, S.; Barcelo, D. *TrAC, Trends Anal. Chem.* **2007**, *26*, 494−514.

(19) Oaks, J. L.; Gilbert, M.; Virani, M. Z.; Watson, R. T.; Meteyer, C. U.; Rideout, B. A.; Shivaprasad, H. L.; Ahmed, S.; Chaudhry, M. J. I.; Arshad, M.; Mahmood, S.; Ali, A.; Khan, A. A. *Nature* **2004**, *427*, 630−633.

(20) Koutsouba, V.; Heberer, T.; Fuhrmann, B.; Schmidt-Baumler, K.; Tsipi, D.; Hiskia, A. *Chemosphere* **2003**, *51*, 69−75.

(21) Heberer, T. *Toxicol. Lett.* **2002**, *131*, 5−17.

(22) Sacher, F.; Lange, F. T.; Brauch, H. J.; Blankenhorn, I. *J. Chromatogr. A* **2001**, *938*, 199−210.

(23) Petrovic, M.; Hernando, M. D.; Diaz-Cruz, M. S.; Barcelo, D. *J. Chromatogr. A* **2005**, *1067*, 1−14.

(24) Deng, A. P.; Himmelsbach, M.; Zhu, Q. Z.; Frey, S.; Sengl, M.; Buchberger, W.; Niessner, R.; Knopp, D. *Environ. Sci. Technol.* **2003**, *37*, 3422−3429.

(25) Hlaváček, A.; Sedlmeier, A.; Skládal, P.; Gorris, H. H. *ACS Appl. Mater. Interfaces* **2014**, *6*, 6930−6935.

(26) Huebner, M.; Weber, E.; Niessner, R.; Boujday, S.; Knopp, D. *Anal. Bioanal. Chem.* **2015**, *407*, 8873−8882.

(27) Wang, F.; Han, Y.; Lim, C. S.; Lu, Y. H.; Wang, J.; Xu, J.; Chen, H. Y.; Zhang, C.; Hong, M. H.; Liu, X. G. *Nature* **2010**, *463*, 1061−1065.

(28) Schneider, C. A.; Rasband, W. S.; Eliceiri, K. W. *Nat. Methods* **2012**, *9*, 671−675.

(29) Sedlmeier, A.; Hlavacek, A.; Birner, L.; Mickert, M. J.; Muhr, V.; Hirsch, T.; Corstjens, P. L.; Tanke, H. J.; Soukka, T.; Gorris, H. H. *Anal. Chem.* **2016**, *88*, 1835−1841.

(30) Liebherr, R. B.; Soukka, T.; Wolfbeis, O. S.; Gorris, H. H. *Nanotechnology* **2012**, *23*, 485103.

(31) Arppe, R.; Hyppänen, I.; Perälä, N.; Peltomaa, R.; Kaiser, M.; Würth, C.; Christ, S.; Resch-Genger, U.; Schäferling, M.; Soukka, T. *Nanoscale* **2015**, *7*, 11746−11757.

(32) Wong, Y. J.; Zhu, L.; Teo, W. S.; Tan, Y. W.; Yang, Y.; Wang, C.; Chen, H. *J. Am. Chem. Soc.* **2011**, *133*, 11422−11425.

(33) Bagwe, R. P.; Hilliard, L. R.; Tan, W. H. *Langmuir* **2006**, *22*, 4357−4362.

(34) Algar, W. R.; Prasuhn, D. E.; Stewart, M. H.; Jennings, T. L.; Blanco-Canosa, J. B.; Dawson, P. E.; Medintz, I. L. *Bioconjugate Chem.* **2011**, *22*, 825−858.

(35) Sedlmeier, A.; Gorris, H. H. *Chem. Soc. Rev.* **2015**, *44*, 1526−1560.

(36) Sapsford, K. E.; Tyner, K. M.; Dair, B. J.; Deschamps, J. R.; Medintz, I. L. *Anal. Chem.* **2011**, *83*, 4453−4488.

(37) Barbarakis, M. S.; Qaisi, W. G.; Daunert, S.; Bachas, L. G. *Anal. Chem.* **1993**, *65*, 457−460.

Paper XII

Rapid single-step upconversion-linked immunosorbent assay for diclofenac

Hlaváček, A.; Peterek, M.; <u>Farka, Z.</u>; Mickert, M. J.; Prechtl, L.; Knopp D.; Gorris, H. H.

Contribution:

Development and optimization of competitive immunoassay, data evaluation, participation in manuscript writing

CrossMark

ORIGINAL PAPER

Rapid single-step upconversion-linked immunosorbent assay for diclofenac

Antonín Hlaváček [1,2,3] · Miroslav Peterek [2] · Zdeněk Farka [1,2] · Matthias J. Mickert [1] ·
Leonhard Prechtl [4] · Dietmar Knopp [4] · Hans H. Gorris [1]

Abstract The non-steroidal anti-inflammatory drug and analgesic diclofenac is a common micropollutant in water. A direct competitive upconversion-linked immunosorbent assay (ULISA) for diclofenac has been developed that is based on a nanoparticulate tracer consisting of a $NaYF_4$:Yb,Er core (diameter of ~90 nm, excitation and emission wavelenghts 980 and 535 nm, respectively) enclosed by a carboxylated silica shell and finally coated with diclofenac-conjugated bovine γ-globulin. The proteinaceous coating prevents non-specific adsorption of the tracer to the microtiter plate and provides a structurally flexible linker for surface-exposed diclofenac to warrant efficient competition with free (analyte) diclofenac in real water samples. The tracer was purified by gel electrophoresis and lyophilized. Both processes have no adverse effects on the immunoassay. All assay components can be stored in a dry state without a cooling chain, and can be reactivated on demand. Hence, this ULISA is well suited for environmental monitoring in low-resource settings. The ULISA has a similar limit of detection (20 pg mL^{-1}; equivalent to 70 pM) as the conventional ELISA, but the time for analysis is reduced to 70 min because no enzymatic amplification steps are involved.

Keywords Bioconjugation · Electrophoretic purification · Immunoassay · Luminescence · Pharmaceutical micropollutant · Photon-upconversion

Introduction

The enzyme-linked immunosorbent assay (ELISA) is the most widely employed immunochemical method for the sensitive detection of analytes in complex matrices such as food, environmental, or clinical samples. Nanoparticles have been recognized as a more stable reporter system for immunoassays compared to enzymes. For example, fluorescent dye-doped polymer or silica nanoparticles [1], metal nanoparticles [2], magnetic nanoparticles [3], catalytic nanoparticles [4] and quantum dots [5] have been used as direct labels in immunoassays. Photon-upconversion nanoparticles (UCNPs) were introduced as luminescent labels for a so-called upconversion-linked immunosorbent assay (ULISA) [6–8]. UCNPs are nanocrystals, which convert near-infrared (NIR) light to light of shorter wavelengths (anti-Stokes emission) [9–11]. Advantages of UCNPs over conventional fluorescent labels include negligible autofluorescence, excellent photostability, large anti-Stokes shifts facilitating sensitive detection, and lower scattering of long-wavelength excitation light [12].

Many pharmaceuticals for medical and veterinary use are not easily degraded in sewage treatment plants [13, 14], and therefore released into the environmental water cycle. The non-steroidal anti-inflammatory drug (NSAID) diclofenac (2-[2-(2,6-dichlorophenyl) aminophenyl] ethanoic acid) appeared as one of the most frequently detected micropollutants

✉ Hans H. Gorris
hans-heiner.gorris@ur.de

[1] Institute of Analytical Chemistry, Chemo- and Biosensors, University of Regensburg, Universitätsstr. 31, 93040 Regensburg, Germany

[2] CEITEC - Central European Institute of Technology, Masaryk University, 625 00 Brno, Czech Republic

[3] Institute of Analytical Chemistry of the Czech Academy of Siences, v. v. i, 602 00 Brno, Czech Republic

[4] Institute of Hydrochemistry, Technical University of Munich, 81377 Munich, Germany

Springer

in wastewater effluents (low ng mL^{-1} concentrations) and also in ground waters, drinking water and surface waters (pg mL^{-1} concentrations) [15–17]. Trace amounts of diclofenac can be measured by LC-TOF-MS or high resolution mass spectrometers [18]. However, these instrumental techniques require well-equipped laboratories, the detection is time consuming and expensive, and well-trained personnel is necessary. Consequently, immunoassays are a less resource-demanding alternative for the detection of environmental micropollutants and are suitable for on-site testing [19]. We have developed an indirect competitive ULISA for the detection of diclofenac based on a UCNP-labeled secondary antibody [6]. The detection of diclofenac by the ULISA (LOD: 0.05 ng mL^{-1}), however, was slightly less sensitive compared to a conventional ELISA (LOD: 0.0078 ng mL^{-1}) using the same detection antibody (mAb 12G5) for diclofenac [20]. This antibody showed only about 10% cross-reactivity with diclofenac metabolites and less than 1% with other structurally related NSAIDs. Furthermore, it was resistant to matrix interferences over a wide pH range, humic acid concentrations up to 20 µg mL^{-1}, and Ca^{2+} concentrations up to 75 µg mL^{-1} [20].

Here, we have established a single-step direct competitive ULISA for the sensitive detection of diclofenac as shown in Fig. 1. The performance and sensitivity of the ULISA was critically dependent on the surface architecture of the luminescent tracer [21], which consisted of bright UCNPs (type NaYF$_4$:Yb,Er, ~90 nm in diameter) embedded in a carboxylated silica shell and coated with diclofenac-modified bovine-γ-globulin (diclofenac-BGG) [22]. The tracer was purified by preparative gel electrophoresis and lyophilized without influence on the assay performance. Essentially, all assay components can be prepared in a dry state for long-time storage and transportation and reactivated on demand. The reduced number of assay steps compared to a conventional ELISA and storage without a cooling chain renders the ULISA an excellent choice for environmental monitoring in

Fig. 1 Scheme of the direct competitive ULISA for the detection of diclofenac. A microtiter plate is coated with a monoclonal anti-diclofenac antibody. Water samples are mixed with a tracer consisting of a diclofenac-BGG-UCNP conjugate and added to the microtiter plate. Free diclofenac in the sample competes with the tracer for the limited amount of antibody binding sites. The upconversion luminescence (535 nm, green emission) is recorded under 980-nm laser excitation. As a consequence of the competition step, the luminescence intensity decreases when the diclofenac concentration is increased

low-resource settings [17, 23, 24]. The performance of the immunoassay was tested on real water samples (surface and tap water).

Experimental

Chemicals and samples

The monoclonal anti-diclofenac antibody 12G5 was produced in mice using a diclofenac-thyroglobulin conjugate and stored as 5 mg mL^{-1} solution in 20 mM NaH$_2$PO$_4$, 0.1 M Tris-HCl, 0.02% NaN$_3$, pH 7.4 at 4 °C [20]. All other standard chemicals and diclofenac sodium salt were obtained from Sigma-Aldrich. Bidistilled water was utilized for all experiments. Three surface water samples from the rivers *Donube*, *Naab* and *Regen* and tap water were collected in Regensburg (Bavaria, Germany), filtrated over a paper filter (Grade 1289 Sartorius Stedim Biotech, www.sartorius.com) and stored at 4 °C.

Preparation of the diclofenac-BGG-UCNP tracer

Conjugation of diclofenac to bovine γ-globulin (diclofenac-BGG) Diclofenac (0.11 mg, 0.33 µmol), N-(3-dimethylaminopropyl)-N′-ethylcarbodiimide hydrochloride (EDC, 5 mg, 26 µmol) and N-hydroxysulfosuccinimide sodium salt (sulfo-NHS, 0.9 mg, 4 µmol) were dissolved in 400 µL of 100 mM sodium 2-(N-morpholino)ethanesulfonate (MES) buffer, pH 6.0 and 100 µL of dimethylformamide. After an activation time of 30 min, the solution was mixed with bovine γ-globulin (BGG) (100 mg, 0.66 µmol) dissolved in 1500 µL of 80 mM Na$_2$CO$_3$ and 100 mM H$_3$BO$_3$ for 4 h at room temperature. The diclofenac-BGG solution was transferred to a dialyzing sleeve (MW$_{cut-off}$ 14 kDa) and dialyzed for 64 h at 4 °C against 3000 mL of a buffer containing 80 mM Na$_2$CO$_3$ and 100 mM H$_3$BO$_3$, pH 9.4. The dialyzed diclofenac-BGG was diluted with this buffer to a concentration of 20 mg mL^{-1} and stored at 4 °C.

Preparation of the upconversion tracer by binding the diclofenac-BGG conjugate to the surface of UCNPs UCNPs were prepared by high-temperature co-precipitation, coated with carboxylated silica and characterized as described in the Electronic Supporting Material (ESM) [25]. Carboxylated UCNPs (4 mg, ~2.6 pmol) were centrifuged (1000×g, 15 min), redispersed in 5000 µL of 100 mM sodium MES, pH 6.0, and activated by adding EDC (10 mg, 52 µmol) and sulfo-NHS (5 mg, 23 µmol). The dispersion was incubated at room temperature for 30 min followed by centrifugation (600×g, 1 min). The pellet containing activated UCNPs was subsequently redispersed in 5000 µL of 100 mM sodium MES, pH 6.0 and mixed with 5000 µL of the diclofenac-BGG conjugate in a

buffer containing 80 mM Na_2CO_3 and 100 mM H_3BO_3 (1.5 mg mL^{-1}, 50 nmol). After 4 h at room temperature, the diclofenac-UCNP conjugate was centrifuged (1000×g, 20 min) five times and redispersed in a buffer containing 65 mM Tris and 20 mM H_3BO_3, pH 9.0 to a final UCNP concentration of 8.0 mg mL^{-1}.

Purification and lyophilization of the diclofenac-BGG-UCNP tracer A preparative agarose gel electrophoresis was used for tracer purification (0.4% agarose, 65 mM Tris and 20 mM H_3BO_3, pH 9.0, ESM Fig. S3). The purified tracer dispersed in 65 mM Tris and 20 mM H_3BO_3, pH 9.0, was supplemented with cryoprotective glucose (20% w/w) to facilitate lyophilization [26]. The freeze-dried tracer can be stored for at least several months and reconstituted to the original UCNP concentration by the addition of water.

Upconversion-linked immunosorbent assay (ULISA)

A white polystyrene 96-well microtiter plate with high binding capacity (Greiner Bio-one, Frickenhausen, Germany, www.gbo.com) was coated with 700 ng mL^{-1} mAb 12G5 dissolved in coating buffer (50 mM $NaHCO_3$/Na_2CO_3, pH 9.6; 90 μL per well) at 4 °C overnight. Subsequent steps were performed at room temperature. A volume of 60 μL was removed from microtiter plate wells, replaced by assay buffer (50 mM Tris, 150 mM NaCl, 0.05% NaN_3, 0.01% Tween 20, 0.5% BGG, 0.2% BSA, 0.2% poly(vinyl alcohol) 6000 g mol^{-1}, 1.0% glucose, 5 mM ethylenediaminetetraacetic acid, pH 7.5) and incubated for 60 min. The plate was washed six times with washing buffer (50 mM NaH_2PO_4/Na_2HPO_4, 0.05% Tween 20, pH 7.5; 300 μL per well) using a plate washer (HydroFlex, Tecan, www.tecan.com). Empty plates were allowed to dry under ambient conditions. Standard dilutions in the range of 13 pg mL^{-1} to 20 ng mL^{-1} diclofenac as well as environmental samples were prepared in water. The tracer diclofenac-BGG-UCNP dispersed in double concentrated assay buffer (100 mM Tris, 300 mM NaCl, 0.10% NaN_3, 0.02% Tween 20, 1.0% BGG, 0.4% BSA, 0.4% poly(vinyl alcohol) 6000 g mol^{-1}, 2.0% glucose, 10 mM ethylenediaminetetraacetic acid, pH 7.5) was mixed in a ratio of 1:1 with the diclofenac dilutions. Then, 90 μL of the mixture was applied per well and incubated for 15, 30 or 60 min. After six washing steps, the plate was dried and the upconversion luminescence was recorded using a microplate reader (Chameleon multilabel microplate reader, Hidex, www.hidex.com) equipped with a continuous 980 nm 4 W laser and band pass filter of 535 ± 25 nm [27]. A focused laser beam with ~0.8 mm diameter was projected on the bottom of the microtiter wells. In each well, 16 points were raster scanned using a step size of 0.5 mm and a signal integration time of 500 ms. To account for irregularities in the luminescence readout of the well surface and obtain a more robust signal, the truncated mean was calculated after discarding the highest two and the lowest two luminescence measurements. All measurements were made in triplicate.

A four-parameter logistic function (Eq. (1)) was used for the regression of the calibration curve. The diclofenac concentrations in environmental samples were calculated by an inverse function of Eq. (1):

$$UCL = \frac{UCL_{max} - UCL_{bg}}{1 + \left(\frac{[diclofenac]}{IC_{50}}\right)^s} + UCL_{bg} \qquad (1)$$

where $[diclofenac]$ is the diclofenac concentration, and UCL is the upconversion luminescence signal. The parameters of Eq. (1) yield the maximum signal (UCL_{max}), the background signal (UCL_{bg}), the diclofenac concentration that reduces $UCL_{max} - UCL_{bg}$ by 50% (IC_{50}), and the slope (s) at the inflection point. The limit of detection (LOD) was estimated as follows:

$$UCL(LOD) = 0.85 \times \left(UCL_{max} - UCL_{bg}\right) + UCL_{bg} \qquad (2)$$

Results and discussion

Preparation and characterization of the diclofenac-BGG-UCNP tracer

The competitive upconversion-linked immunosorbent assay (ULISA) shown in Fig. 1 required the careful design of a luminescent tracer. The diclofenac tracer was prepared in four steps: (1) Conjugation of diclofenac to BGG, (2) synthesis of UCNPs, which yielded ~90 nm hexagonal prisms as confirmed by transmission electron microscopy (TEM, Fig. 2a, for a larger image section see Fig. S1, ESM), (3) encapsulation of UCNPs by a carboxylated silica shell of 3.7 ± 0.5 nm thickness (Fig. 2b and Fig. S2, ESM), and (4) surface coating with the diclofenac-BGG conjugate. Dynamic light scattering was recorded after each surface modification step to confirm the monodispersity of UCNPs (Fig. 2c).

The diclofenac-BGG conjugate had a dual function because (1) it served as a structurally flexible linker between diclofenac and the nanoparticle surface and (2) it prevented non-specific adsorption of the tracer to the microtiter plate. We reported previously that a moderate ratio of protein to UCNPs results in partial crosslinking of nanoconjugates (~33:1 for UCNPs with a diameter of 47 nm) [6]. Here, we employed a higher ratio of diclofenac-BGG to UCNPs (~19,000:1) to obtain a high surface modification, but could not completely prevent crosslinking since a substantial fraction of the diclofenac-BGG-UCNP tracer was aggregated. Thus, we developed an agarose gel electrophoresis system (ESM Fig. S3) to purify the monodisperse fraction of diclofenac-BGG-

Fig. 2 TEM images of (**a**) oleic acid-capped UCNPs and (**b**) silica-coated UCNPs exposing carboxyl groups on their surface. UCNPs have the shape of hexagonal prisms (height (*H*): 91.0 ± 3.4 nm, diameter (*D*): 94.1 ± 5.7 nm) as depicted in the inset of panel (**a**). **c** Hydro(solvo)dynamic diameters of oleic acid-capped UCNPs in cyclohexane (△, 113 nm, polydispersity index 0.024), silica-coated UCNPs in 65 mM Tris and 20 mM H_3BO_3 (○, 119 nm, polydispersity index 0.039) and the final tracer diclofenac-BGG-UCNPs (□, 164 nm, polydispersity index 0.111) after electrophoretic purification using the device shown in ESM Fig. S3. **d** Agarose gel of purified diclofenac-BGG-UCNPs (40 µg mL^{-1}, left two lines) and carboxylated UCNPs (4 mg mL^{-1}, right two lanes) imaged by an upconversion scanner [27]
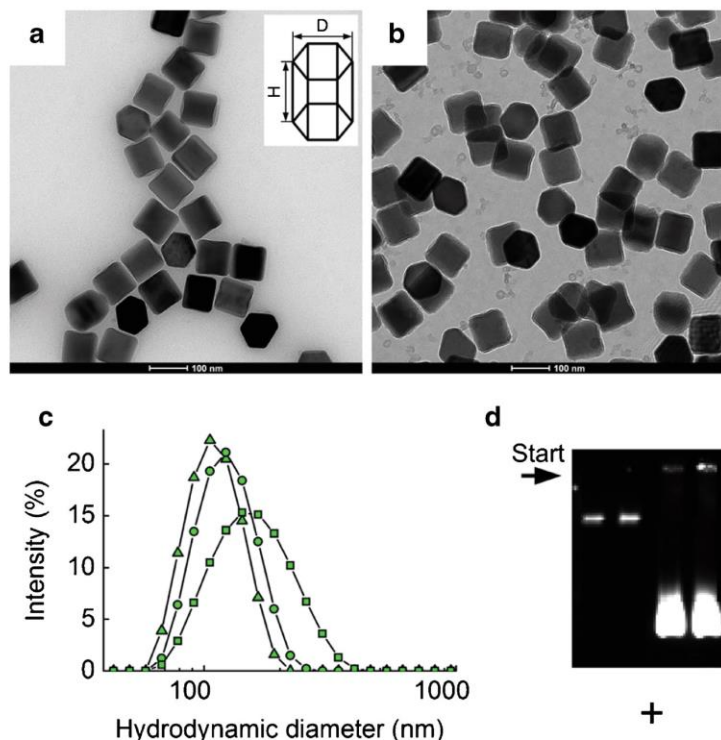
UCNP in a yield of 10% (0.4 mg of UCNPs / 64 µg mL^{-1}) [22]. The surface attachment of diclofenac-BGG led to a change of the zeta potential of carboxylated UCNPs from −36.5 mV to −21.5 mV and the hydrodynamic diameter increased from 119 nm to 164 nm (Fig. 2c). The higher polydispersity of the conjugate may result from some variability in the number and the orientation of diclofenac-BGG conjugates (Fig. 2c). These results were further confirmed by agarose gel electrophoresis, which revealed a lower electrophoretic mobility of the diclofenac-BGG-UCNP tracer compared to carboxylated UCNPs (Fig. 2d).

Direct competitive upconversion-linked immunosorbent assay (ULISA)

Calibration curves were generated by first coating microtiter plates with anti-diclofenac antibody mAb 12G5, blocking and letting them dry. Then, serial dilutions of diclofenac were prepared in water, mixed with the diclofenac-BGG-UCNP tracer and immediately transferred to the coated microtiter plate. The optimization steps are detailed in the ESM and the assay performance under optimized conditions is shown in Fig. 3.

A maximum incubation time of 60 min was used to keep the assay time fast. The total time of analysis starting from the dry coated and blocked microtiter plate was reduced to only

70 min compared to a conventional ELISA (125 min, see ESM for a detailed comparison). Under optimized assay conditions, the signal to background ratio (UCL_{max}/UCL_{bg}) was 82. By contrast, the signal to background ratio of both ULISA and ELISA reported previously was only 5 [6]. One reason for the excellent signal to background ratio is the relatively high brightness of UCNPs (diameter of 90 nm) that can be detected without optical background interference. Additionally, the
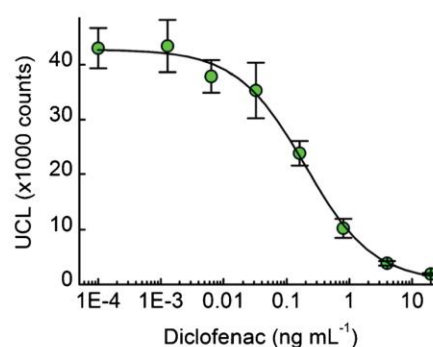
Fig. 3 ULISA calibration curve for the detection of diclofenac under optimal assay conditions. (a) 700 ng mL^{-1} antibody coating concentration, (b) 40 ng mL^{-1} tracer concentration and (c) 60 min incubation time, which yields an LOD of 0.02 ng mL^{-1} (70 pM). Error bars indicate the standard deviations of three replicate wells

introduction of a protein layer on the UCNP surface efficiently blocks non-specific surface interactions of the tracer. Finally, each tracer nanoparticle exposes multiple diclofenac moieties (multivalency) on the surface to ensure an efficient immobilization by the coating antibody even if the tracer is present in much lower molar concentrations than free diclofenac.

Different methods for the sensitive detection of diclofenac are summarized in Table 1. The direct competitive ULISA described in this study is more sensitive (LOD: 0.02 ng mL^{-1}) than our previously reported indirect competitive ULISA (0.05 ng mL^{-1}) and comparable to a conventional indirect competitive ELISA (0.008 ng mL^{-1}) using the same monoclonal antibody 12G5. Earlier work based on a polyclonal anti-diclofenac antibody yielded a slightly better LOD of 0.006 ng mL^{-1} [19]. Instrumental techniques such as isotachophoresis (ITP) – mass spectrometry (MS) [34] or gas chromatography (GC) – mass spectrometry (MS) [32] yielded lower LODs of 0.0006 ng mL^{-1} or 0.001 ng mL^{-1}, respectively, but required a longer time for sample pretreatment. Exceptionally low LODs (<< pg mL^{-1}) and rapid operation were reported for electrochemical aptasensors [30, 31]. Surface waters, however, were not investigated in these studies.

Preparation of an all dry reagent immunoassay for in-field testing

The antibody was dried on the microtiter plate without influencing the assay performance as shown in the last section. In a conventional ELISA, the catalytic activity of the enzyme is one of the most delicate elements in an immunoassay and requires a permanent cooling chain because lyophilization or freezing of enzymes typically can strongly impair their activity. The need for permanent cooling is a particular limitation in low resource settings and in-field testing. Since we have replaced the enzymatic by a nanoparticulate detection label, we also tested the option to lyophilize the tracer suspension in order to further extend the shelf life of the tracer at ambient temperature. The tracer suspension in buffer was supplemented with 20% (w/w) glucose to avoid freezing during lyophilization. After storage at room temperature for any length of time, the lyophilized tracer was readily resuspended by the addition of water to reconstitute the original tracer concentration. Figure 4 shows that the lyophilization and the subsequent storage at room temperature did not affect the immunoassay performance. Consequently, all components of the ULISA can be stored at room temperature.

Analysis of real water samples

Three water samples from rivers and drinking water were collected in Regensburg (Bavaria, Germany). The concentration of diclofenac in these samples was below the detection limit of immunoassays, which is consistent with our previous finding in other Bavarian water samples [6]. Therefore, each water sample was additionally spiked to obtain concentrations of 1 ng mL^{-1}, 3 ng mL^{-1}, and 10 ng mL^{-1} diclofenac. Table 2 shows the concentrations of diclofenac as determined by the direct competitive ULISA. Deviations from the spiked diclofenac concentrations can be explained by two reasons. First, high Ca^{2+} ion concentrations of >70 mg L^{-1} in undiluted water samples can lead to matrix effects as reported earlier [6, 20] because the metal ion can disrupt non-covalent interactions by shielding charges and destabilizing hydrogen bonds.

Table 1 Comparison of methods for the detection of diclofenac in water

Methods and mode of detection	LOD (ng mL^{-1})	Time of analysis	Reference
Indirect competitive ELISA; polyclonal antibody	0.006	200 min	[19]
Indirect competitive ELISA; mAb (12G5)	0.008	125 min	[20]
Indirect competitive ULISA; mAb (12G5)	0.05	140 min	[6]
Direct competitive ULISA; mAb (12G5)	0.02	70 min	This work
Solid-phase extraction/HPLC-MS	0.01	Sample pretreatment ~60 min; elution time ~ 10 min	[28]
Surface plasmon resonance; molecularly imprinted polymer	1.2	~12 min	[29]
Impedimetry; aptamer	0.0009	Several minutes	[30]
Impedimetry; aptamer	1×10^{-6}	Several minutes	[31]
Solid-phase extraction/GC-MS	0.001	Sample pretreatment ~6 h; elution time ~ 25 min	[32]
Solid-phase extraction/CE-MS	33	Sample pretreatment ~60 min; electrophoresis ~30 min	[33]
Solid-phase extraction/ITP-MS	0.0006	Sample pretreatment ~60 min, isotachophoresis ~15 min	[34]
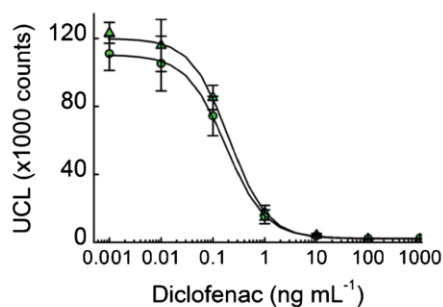
Fig. 4 Comparison of assay performance using the same diclofenac-BGG-UCNP tracer before (○, IC_{50} 0.18 ng mL^{-1}) and after lyophilization and redispersion (Δ, IC_{50} 0.21 ng mL^{-1}). Error bars indicate the standard deviations of three replicate wells

Second, the concentrations of spiked diclofenac are not in the most sensitive range of the calibration curve. For a more quantitative determination of diclofenac, the water samples can be pre-diluted, which, however, would negatively affect the LOD of the assay.

Conclusion

The sensitivity of the direct competitive ULISA for diclofenac (LOD 0.02 ng mL^{-1}) is comparable to the classic indirect competitive ELISA (0.008 ng mL^{-1}) using the same monoclonal anti-diclofenac antibody but higher than the sensitivity of our previously reported indirect competitive ULISA (LOD 0.05 ng mL^{-1}) [6]. Furthermore, the assay performance was simplified by (1) reducing the number of assay steps to only one analyte/tracer incubation step and one washing step and (2) reducing the assay time to only 70 min starting from pre-coated plates (ESM Table S2). The careful design of the diclofenac-BGG-UCNP tracer (diameter of ~90 nm) was the key element for eliminating the background signal due to optical interference as well as non-specific adsorption to the microtiter plate surface. Consequently, the assay achieved an excellent signal to background ratio (UCL_{max}/UCL_{bg} = 82). Finally, lyophilization of the tracer ensured its long-time

Table 2   Detection of diclofenac in unspiked and spiked water samples

Spiked (ng mL^{-1})	Danube (ng mL^{-1})	Naab (ng mL^{-1})	Regen (ng mL^{-1})	Tap water (ng mL^{-1})
-	≤ LOD	≤ LOD	≤ LOD	≤ LOD
1.0	0.86 ± 1.1	1.3 ± 1.0	1.4 ± 0.7	1.2 ± 0.6
3.0	2.9 ± 2.3	3.0 ± 0.7	4.5 ± 1.2	4.1 ± 3.6
10.0	8.9 ± 5.0	9.1 ± 0.3	15.2 ± 5.1	8.4 ± 2.7

stability and avoided the need for a cooling chain during transportation. All assay components can be prepared in a dry state and reactivated on demand, which is beneficial for in-field monitoring of analytes in low resource settings [17, 23, 24].

References

1. Wang L, Wang KM, Santra S, Zhao XJ, Hilliard LR, Smith JE, Wu JR, Tan WH (2006) Watching silica nanoparticles glow in the biological world. Anal Chem 78:646–654. doi:10.1021/ac0693619
2. Jans H, Huo Q (2012) Gold nanoparticle-enabled biological and chemical detection and analysis. Chem Soc Rev 41:2849–2866. doi:10.1039/c1cs15280g
3. Osterfeld SJ, Yu H, Gaster RS, Caramuta S, Xu L, Han SJ, Hall DA, Wilson RJ, Sun SH, White RL, Davis RW, Pourmand N, Wang SX (2008) Multiplex protein assays based on real-time magnetic nanotag sensing. Proc Natl Acad Sci U S A 105:20637–20640. doi:10.1073/pnas.0810822105
4. Čunderlová V, Hlaváček A, Horňáková V, Peterek M, Němeček D, Hampl A, Eyer L, Skládal P (2016) Catalytic nanocrystalline coordination polymers as an efficient peroxidase mimic for labeling and optical immunoassays. Microchim Acta 183:651–658. doi:10.1007/s00604-015-1697-z
5. Hlaváček A, Bouchal P, Skládal P (2012) Biotinylation of quantum dots for application in fluoroimmunoassays with biotin-avidin amplification. Microchim Acta 176:287–293. doi:10.1007/s00604-011-0729-6
6. Hlaváček A, Farka Z, Hübner M, Horňáková V, Němeček D, Niessner R, Skládal P, Knopp D, Gorris HH (2016) Competitive upconversion-linked immunosorbent assay for the sensitive detection of diclofenac. Anal Chem 88:6011–6017. doi:10.1021/acs.analchem.6b01083
7. Päkkilä H, Ylihärsilä M, Lahtinen S, Hattara L, Salminen N, Arppe R, Lastusaari M, Saviranta P, Soukka T (2012) Quantitative multianalyte microarray immunoassay utilizing upconverting phosphor technology. Anal Chem 84:8628–8634. doi:10.1021/ac301719p
8. Achatz DE, Ali R, Wolfbeis OS (2011) Luminescent chemical sensing, biosensing, and screening using upconverting nanoparticles. Top Curr Chem 300:29–50. doi:10.1007/128_2010_98
9. Auzel F (2004) Upconversion and anti-stokes processes with f and d ions in solids. Chem Rev 104:139–173. doi:10.1021/cr020357g
10. Haase M, Schäfer H (2011) Upconverting nanoparticles. Angew Chem Int Ed 50:5808–5829. doi:10.1002/anie.201005159

11. Yang Y (2014) Upconversion nanophosphors for use in bioimaging, therapy, drug delivery and bioassays. Microchim Acta 181:263–294. doi:10.1007/s00604-013-1139-8

12. Gorris HH, Ali R, Saleh SM, Wolfbeis OS (2011) Tuning the dual emission of photon-upconverting nanoparticles for ratiometric multiplexed encoding. Adv Mater 23:1652–1655. doi:10.1002/adma.201004697

13. Ternes TA (2001) Analytical methods for the determination of pharmaceuticals in aqueous environmental samples. Trac-Trend Anal Chem 20:419–434. doi:10.1016/S0165-9936(01)00078-4

14. Perez S, Barcelo D (2007) Application of advanced MS techniques to analysis and identification of human and microbial metabolites of pharmaceuticals in the aquatic environment. Trac-Trend Anal Chem 26:494–514. doi:10.1016/j.trac.2007.05.004

15. Heberer T (2002) Occurrence, fate, and removal of pharmaceutical residues in the aquatic environment: a review of recent research data. Toxicol Lett 131:5–17. doi:10.1016/S0378-4274(02)00041-3

16. Koutsouba V, Heberer T, Fuhrmann B, Schmidt-Baumler K, Tsipi D, Hiskia A (2003) Determination of polar pharmaceuticals in sewage water of Greece by gas chromatography-mass spectrometry. Chemosphere 51:69–75. doi:10.1016/S0045-6535(02)00819-6

17. Oaks JL, Gilbert M, Virani MZ, Watson RT, Meteyer CU, Rideout BA, Shivaprasad HL, Ahmed S, Chaudhry MJI, Arshad M, Mahmood S, Ali A, Khan AA (2004) Diclofenac residues as the cause of vulture population decline in Pakistan. Nature 427:630–633. doi:10.1038/nature02317

18. Petrovic M, Hernando MD, Diaz-Cruz MS, Barcelo D (2005) Liquid chromatography-tandem mass spectrometry for the analysis of pharmaceutical residues in environmental samples: a review. J Chromatogr A 1067:1–14. doi:10.1016/j.chroma.2004.10.110

19. Deng AP, Himmelsbach M, Zhu QZ, Frey S, Sengl M, Buchberger W, Niessner R, Knopp D (2003) Residue analysis of the pharmaceutical diclofenac in different water types using ELISA and GC-MS. Environ Sci Technol 37:3422–3429. doi:10.1021/es0341945

20. Huebner M, Weber E, Niessner R, Boujday S, Knopp D (2015) Rapid analysis of diclofenac in freshwater and wastewater by a monoclonal antibody-based highly sensitive ELISA. Anal Bioanal Chem 407:8873–8882. doi:10.1007/s00216-015-9048-9

21. Sedlmeier A, Gorris HH (2015) Surface modification and characterization of photon-upconverting nanoparticles for bioanalytical applications. Chem Soc Rev 44:1526–1560. doi:10.1039/c4cs00186a

22. Hlaváček A, Sedlmeier A, Skládal P, Gorris HH (2014) Electrophoretic characterization and purification of silica-coated photon-upconverting nanoparticles and their bioconjugates. ACS Appl Mater Interfaces 6:6930–6935. doi:10.1021/am500732y

23. Petrie B, Barden R, Kasprzyk-Hordern B (2015) A review on emerging contaminants in wastewaters and the environment: current knowledge, understudied areas and recommendations for future monitoring. Water Res 72:3–27. doi:10.1010/j.watres.2014.08.053

24. Osório MV, Reis S, Lima JLFC, Segundo MA (2017) Analytical features of diclofenac evaluation in water as a potential marker for anthropogenic pollution. Curr Pharm Anal 13:39–47. doi:10.2174/1573412912666160422123841

25. Wang F, Han Y, Lim CS, Lu YH, Wang J, Xu J, Chen HY, Zhang C, Hong MH, Liu XG (2010) Simultaneous phase and size control of upconversion nanocrystals through lanthanide doping. Nature 463:1061–1065. doi:10.1038/nature08777

26. Fuller BJ (2004) Cryoprotectants: the essential antifreezes to protect life in the frozen state. Cryo-Lett 25:375–388

27. Sedlmeier A, Hlaváček A, Birner L, Mickert MJ, Muhr V, Hirsch T, Corstjens PL, Tanke HJ, Soukka T, Gorris HH (2016) Highly sensitive laser scanning of photon-upconverting nanoparticles on a macroscopic scale. Anal Chem 88:1835–1841. doi:10.1021/acs.analchem.5b04147

28. Al-Odaini NA, Zakaria MP, Yaziz MI, Surif S (2010) Multiresidue analytical method for human pharmaceuticals and synthetic hormones in river water and sewage effluents by solid-phase extraction and liquid chromatography-tandem mass spectrometry. J Chromatogr A 1217:6791–6806. doi:10.1016/j.chroma.2010.08.033

29. Altintas Z, Guerreiro A, Piletsky SA, Tothill IE (2015) NanoMIP based optical sensor for pharmaceuticals monitoring. Sensors Actuators B Chem 213:305–313. doi:10.1016/j.snb.2015.02.043

30. Shiravand T, Azadbakht A (2017) Impedimetric biosensor based on bimetallic AgPt nanoparticle-decorated carbon nanotubes as highly conductive film surface. J Solid State Electrochem 21:1699–1711. doi:10.1007/s10008-017-3532-4

31. Azadbakht A, Beirnvand S (2017) Voltammetric aptamer-based switch probes for sensing diclofenac using a glassy carbon electrode modified with a composite prepared from gold nanoparticles, carbon nanotubes and amino-functionalized Fe_3O_4 nanoparticles. Microchim Acta 184:2825–2835. doi:10.1007/s00604-017-2285-1

32. Guitart C, Readman JW (2010) Critical evaluation of the determination of pharmaceuticals, personal care products, phenolic endocrine disrupters and faecal steroids by GC/MS and PTV-GC/MS in environmental waters. Anal Chim Acta 658:32–40. doi:10.1016/j.aca.2009.10.066

33. Ahrer W, Scherwenk E, Buchberger W (2001) Determination of drug residues in water by the combination of liquid chromatography or capillary electrophoresis with electrospray mass spectrometry. J Chromatogr A 910:69–78. doi:10.1016/S0021-9673(00)01187-0

34. Malá Z, Gebauer P, Boček P (2016) Capillary isotachophoresis with ESI-MS detection: methodology for highly sensitive analysis of ibuprofen and diclofenac in waters. Anal Chim Acta 907:1–6. doi:10.1016/j.aca.2015.11.040

Paper XIII

Competitive upconversion-linked immunoassay using peptide mimetics for the detection of the mycotoxin zearalenone

Peltomaa, R.; <u>Farka, Z.</u>; Mickert, M. J.; Brandmeier, J. C.; Pastucha, M.; Hlaváček, A.; Martínez-Orts, M.; Canales, Á.; Skládal, P.; Benito-Peña, E.; Moreno-Bondi, M. C.; Gorris, H. H.

Contribution:

Design of experiments, bioconjugation and characterization of UCNPs, development and optimization of competitive immunoassay, data evaluation, participation in manuscript writing

Competitive upconversion-linked immunoassay using peptide mimetics for the detection of the mycotoxin zearalenone

Riikka Peltomaa [a,b,1], Zdeněk Farka [a,c], Matthias J. Mickert [a,2], Julian C. Brandmeier [a], Matěj Pastucha [c], Antonín Hlaváček [d], Mónica Martínez-Orts [e], Ángeles Canales [e], Petr Skládal [c], Elena Benito-Peña [b], María C. Moreno-Bondi [b,**], Hans H. Gorris [a,*]

[a] Institute of Analytical Chemistry, Chemo- and Biosensors, University of Regensburg, Universitätsstraße 31, 93040, Regensburg, Germany
[b] Department of Analytical Chemistry, Faculty of Chemistry, Universidad Complutense de Madrid, Plaza de las Ciencias, Ciudad Universitaria, 28040, Madrid, Spain
[c] Department of Biochemistry, Faculty of Science, Masaryk University, Kamenice 5, 625 00, Brno, Czech Republic
[d] Institute of Analytical Chemistry of the Czech Academy of Sciences, Veveří 97, 602 00, Brno, Czech Republic
[e] Department of Organic Chemistry, Faculty of Chemistry, Universidad Complutense de Madrid, Plaza de las Ciencias, Ciudad Universitaria, 28040, Madrid, Spain

ABSTRACT

Due to increasing food safety standards, the analysis of mycotoxins has become essential in the food industry. In this work, we have developed a competitive upconversion-linked immunosorbent assay (ULISA) for the analysis of zearalenone (ZEA), one of the most frequently encountered mycotoxins in food worldwide. Instead of a toxin-conjugate conventionally used in competitive immunoassays, we designed a ZEA mimicking peptide extended by a biotin-linker and confirmed its excellent suitability to mimic ZEA by nuclear magnetic resonance (NMR) and surface plasmon resonance (SPR) analysis. Upconversion nanoparticles (UCNP, type NaYF$_4$:Yb,Tm) served as background-free optical label for the detection of the peptide mimetic in the competitive ULISA. Streptavidin-conjugated UCNPs were prepared by click reaction using an alkyne-PEG-neridronate linker. The UCNP conjugate clearly outperformed conventional labels such as enzymes or fluorescent dyes. With a limit of detection of 20 pg mL^{-1} (63 pM), the competitive ULISA is well applicable to the detection of ZEA at the levels set by the European legislation. Moreover, the ULISA is specific for ZEA and its metabolites (α- and β-zearalenol) without significant cross-reactivity with other related mycotoxins. We detected ZEA in spiked and naturally contaminated maize samples using liquid chromatography–tandem mass spectrometry (UPLC-MS/MS) as a reference method to demonstrate food analysis in real samples.

1. Introduction

Zearalenone (ZEA) is a non-steroidal estrogenic mycotoxin that is produced as a secondary metabolite by several fungi species in the *Fusarium* genus (Bennett and Klich, 2003; Zinedine et al., 2007). Although ZEA is acknowledged to exhibit relatively low acute toxicity, it is chronically toxic and has been frequently implicated in reproductive disorders of farm animals, especially pigs (Kuiper-Goodman et al., 1987; Zinedine et al., 2007). Estrogenic activity accounts for its most critical mode of action, although ZEA has also been implicated in anabolic, haematotoxic, and genotoxic effects (Kuiper-Goodman et al., 1987;

IARC, 1993; Maaroufi et al., 1996; European Commission, 2000). Alongside with other mycotoxins, ZEA is a common contaminant in many agricultural commodities, such as maize, barley, oats, wheat, and rice (EFSA Panel, 2011). Maize and maize-based products are the most frequently contaminated food commodities. As much as 79% of tested samples have been reported to be contaminated with ZEA at detectable levels (Gareis et al., 2003). Due to their widespread and extensive biological effects, current international and national regulations encompass ZEA and other major mycotoxins (van Egmond et al., 2007). Current maximum limits for ZEA in Europe vary from 20 to 3000 μg kg^{-1} depending on the foodstuffs or animal feed in question (European

---

Commission, 2006a, 2006b). The legislation inevitably calls for sensitive and accurate analytical methods to detect the toxins and to ensure safe food for the consumer.

High-performance liquid chromatography (HPLC) coupled with fluorescence (De Saeger et al., 2003; Drzymala et al., 2015) or mass spectrometry (Romera et al., 2018; Hidalgo-Ruiz et al., 2019) detectors are commonly used as reference methods for the detection of ZEA. Besides these sensitive yet complex and costly chromatographic techniques, immunochemical methods such as enzyme-linked immunosorbent assays (ELISAs) are fast and straightforward screening techniques for on-site mycotoxin analysis (EFSA Panel, 2011; Nolan et al., 2019; Caglayan et al., 2020). Small molecules such as ZEA are conventionally detected in a competitive ELISA format, which, however, suffers from certain inherent limitations (Wild, 2013; Nolan et al., 2019). The synthesis of competing mycotoxin-conjugates accounts for one of the main challenges (Xiong et al., 2020). For instance, ZEA has no suitable reactive groups available for coupling such that the conjugation to a carrier protein or a label requires large amounts of the pure toxin, involves several reaction steps that may result in a heterogeneous mixture of conjugates with different stoichiometries and a challenging purification (Liu et al., 1985; Thouvenot and Morfin, 1983). Large batch-to-batch variations and overuse of organic solvents in the conjugation account for additional limitations. There is also a potential toxicity hazard for the manufacturer, user, and the environment (Chauhan et al., 2016).

Epitope mimicking peptides, also known as mimotopes, have been introduced as a valuable alternative to the traditional analyte-conjugates in competitive immunoassays and biosensors. Such peptides mimic the epitope of the analyte sufficiently to compete with the native analyte for antibody binding. Therefore, the cumbersome conjugation step and the aforementioned limitations can be avoided (Xiong et al., 2020; Peltomaa et al., 2018a). It should also be noted that although high-affinity antibodies are of crucial importance for high sensitivity in all immunoassays, a lower affinity of the peptide competitor compared to the analyte shifts the equilibrium in favor of analyte binding (Peltomaa et al., 2019; Xiong et al., 2020). As less analyte is required to achieve the same response, the assay is more sensitive. Peptide mimetics for many mycotoxins have been identified from peptide libraries by phage display (Yuan et al., 1999; He et al., 2011, 2013; Liu et al., 2013; Peltomaa et al., 2017). From such a phage-borne peptide mimetic for ZEA, we have previously constructed a recombinant peptidomimetic fusion protein with *Gaussia* luciferase. This bioluminescent tracer was directly used for the detection of ZEA without the need for secondary antibodies or further labeling steps and achieved a limit of detection (LOD) of 4.2 ng mL^{-1} (Peltomaa et al., 2020).

The progress in nanotechnology-based biosensors (Farka et al., 2017) has also inspired the field of mycotoxin detection. Several nanoparticles (NP) have been used as the detection label, for example, lanthanide-doped inorganic NPs (Niazi et al., 2018), gold (Peltomaa et al., 2018b; Liu et al., 2020) and silver NPs (Jiang et al., 2020), quantum dots (Fang et al., 2014; Li et al., 2019), silica NPs (Taghdisi et al., 2016; Tan et al., 2019) as well as photon-upconversion nanoparticles (UCNP) (Dai et al., 2017; Wu et al., 2018; Yang et al., 2018; He et al., 2020). UCNPs are lanthanide-doped nanomaterials capable of converting near-infrared (NIR) excitation light to emission at shorter wavelengths, typically in the visible range. The upconversion—or anti-Stokes—emission can be detected without optical background interference or light scattering, and the autofluorescence is completely eliminated by spectral separation (Haase and Schäfer, 2011). Owing to these unique optical properties, UCNPs have gained significant attention and become an intriguing alternative for enzymatic or fluorescent labels in immunoassays (Hlaváček et al., 2016; Farka et al., 2020a), lateral flow assays (Sedlmeier et al., 2016; Zhang et al., 2020) as well as biosensors (Farka et al., 2017; Zhang et al., 2019; Kim et al., 2020).

To account for the growing need for the rapid analysis of ZEA, we introduce a highly sensitive competitive upconversion-linked immunosorbent assay (ULISA) for the detection of ZEA based on a synthetic peptide mimetic and UCNPs as the label. As shown schematically in Fig. 1, our approach relies on the use of the previously identified ZEA mimicking peptide (Peltomaa et al., 2020), which was chemically synthesized and modified with a biotin linker, and thoroughly characterized. To the best of our knowledge, we have analyzed for the first time both the interaction of peptide mimetic and antibody by nuclear magnetic resonance (NMR) and its binding kinetics by surface plasmon resonance (SPR). We functionalized UCNPs with a PEG-linker and streptavidin (UCNP-PEG-SA) as a highly sensitive label for ZEA detection. After confirming the specificity of the method in cross-reactivity studies, spiked and naturally contaminated maize samples were analyzed.

2. Experimental section

2.1. Materials

Monoclonal anti-zearalenone (anti-ZEA) antibody was purchased from Soft Flow Ltd (Pécs, Hungary). The biotinylated peptide mimetic (GWWGPYGEIELLGGGSK(Bio)-NH$_2$) was synthesized at Peptide Synthetics (Fareham, UK). Mycotoxins zearalenone (ZEA), α-zearalenol and β-zearalenol were supplied by Sigma-Aldrich (St. Louis, MO, USA), whereas fumonisin B$_1$, deoxynivalenol, T-2 toxin, and ochratoxin A were from Fermentek Ltd. (Jerusalem, Israel). Human serum albumin-conjugated ZEA (HSA-ZEA) was from BioTez (Berlin, Germany). SuperBlock (TBS) Blocking Buffer was purchased from Thermo Fisher Scientific (Waltham, MA, USA), bovine γ-globulin (BGG), bovine serum albumin (BSA), and Tween-20 were purchased from Sigma-Aldrich. The 96-well microtiter plates with a clear bottom (μClear, high binding) were obtained from Greiner Bio-One (Kremsmünster, Austria). The preparation, surface conjugation, and characterization of UCNPs are described in the supporting information (SI).

2.2. Peptide characterization by NMR spectroscopy and SPR analysis

Saturation transfer difference (STD) experiments were performed using a Bruker AVANCE 600 MHz spectrometer equipped with a cryogenic probe, with 4096 scans, at 298 K. The irradiation conditions were set at −1.0 ppm for the on-resonance and 100 ppm for the off-resonance spectra, respectively. Samples were dissolved in deuterated PBS buffer to a final concentration of 0.4 mM for the peptide mimetic and 3 μM for the anti-ZEA antibody. For the competitive binding experiment, ZEA was added to the peptide/antibody sample to a final concentration of 0.2 mM (peptide–toxin ratio 2:1). The binding kinetics of the peptide mimetic was studied on an MP-SPR Navi 210 A (BioNavis, Finland) SPR system. Details of the affinity measurements can be found in the SI.

2.3. Competitive immunoassays

The ELISA and fluorescent immunoassay (FIA) are described in the SI. For the ULISA, a 96-well microtiter plate was coated with 2 μg mL^{-1} of anti-ZEA monoclonal antibody in coating buffer (50 mM NaHCO$_3$/Na$_2$CO$_3$, pH 9.6, supplemented with 0.05% (w/v) NaN$_3$; 100 μL per well) by overnight incubation at 4 °C. After washing the wells four times with washing buffer (50 mM Tris, pH 7.5; 0.05% (w/v) Tween 20, 0.05% (w/v) NaN$_3$) using a plate washer (HydroFlex, Tecan, Switzerland), they were blocked with 175 μL of blocking buffer (50 mM Tris-HCl, pH 7.4; 10% (v/v) SuperBlock, 0.05% (w/v) NaN$_3$; 150 mM NaCl) for 1 h at room temperature. After repeating the washing steps, standard dilutions of ZEA in the range of 0–100 ng mL^{-1} were added to the wells in triplicates together with the peptide mimetic (2 μg mL^{-1}) in a total volume of 100 μL per well in assay buffer (50 mM Tris-HCl, pH 7.5; 150 mM NaCl, 0.05% (w/v) NaN$_3$, 0.01% (w/v) Tween 20, 0.5% (w/v) BGG, 0.2% (w/v) BSA, 0.2% (w/v) poly(vinyl alcohol) 6000, 1% (w/v) glucose, 5 mM ethylenediaminetetraacetic acid). For the cross-reactivity

2
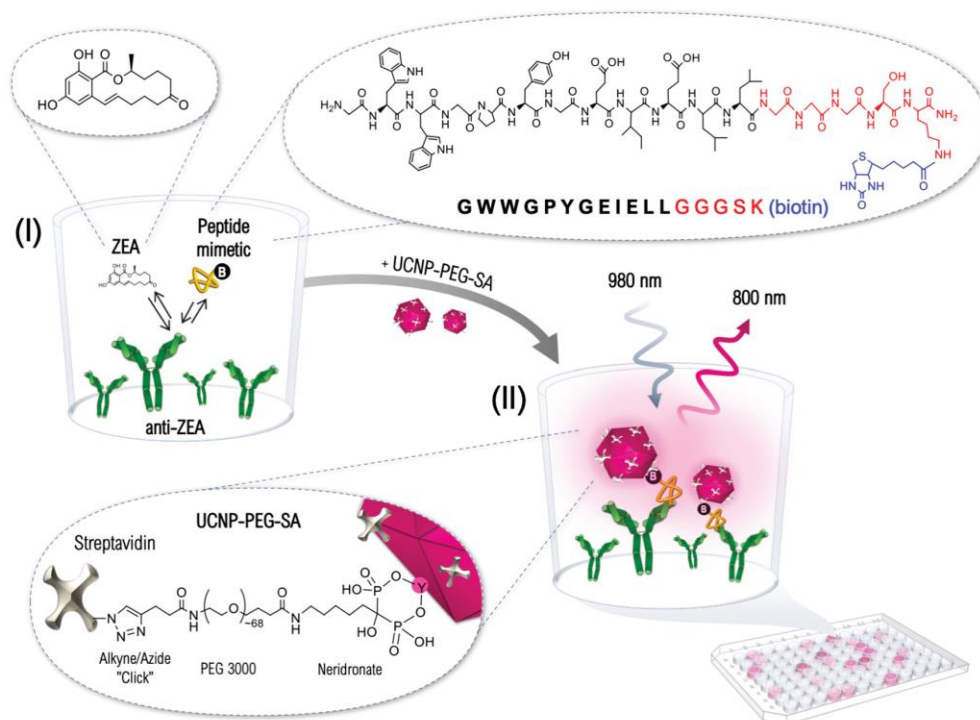
Fig. 1. Scheme of the competitive ULISA for the detection of zearalenone (ZEA). In the first step (I), a microtiter plate is coated with anti-ZEA antibody, and ZEA in the sample competes with the peptide mimetic for a limited amount of antibody binding sites. The peptide of 12 amino acids was extended by a GGGSK-linker (red) on the C-terminus including biotin (blue) for coupling. In the second step (II), the UCNP-PEG-SA-conjugates bind to the biotinylated peptide, and high upconversion luminescence signals are measured in the absence of ZEA. Streptavidin is bound to the surface of UCNPs by using a PEG-neridronate linker (bottom left). (For interpretation of the references to color in this figure legend, the reader is referred to the Web version of this article.)

study, ZEA was replaced by other mycotoxins. The incubation was continued for another 1 h, and after washing the wells four times, the UCNP-PEG-SA-conjugate (12.5 µg mL^{-1} in assay buffer) was added to each well. After 1 h of incubation and four washing steps, the plate was dried, and the upconversion luminescence was measured using a microtiter plate reader (Chameleon, Hidex, Finland) (Sedlmeier et al., 2016). In each well, 64 points were raster-scanned using a step size of 1 mm and a signal integration time of 1 s.

2.4. Analysis of real samples

Maize samples were provided by an external laboratory in Madrid (Spain), and the concentration of ZEA in the samples was determined by ultra-performance liquid chromatography–tandem mass spectrometry (UPLC-MS/MS) (Romera et al., 2018). For validation purposes and following current legislation (Magnusson and Örnemark, 2014), blank maize samples (1 g) that did not contain ZEA at levels detectable by UHPLC-MS/MS were spiked to 20–80 µg kg^{-1} of ZEA by adding a standard ZEA solution in methanol. After allowing the spiked samples to equilibrate overnight at room temperature, 5 mL of methanol:water mixture (80:20, v/v) was added, and the suspensions were shaken for 30 min at room temperature. Similarly, 5 mL of the solvent was added to 1 g of naturally contaminated maize samples that were also analyzed by UPLC-MS/MS according to a previously reported method (Romera et al., 2018). The sample extracts were purified by centrifugation (7000×g, 10 min). Finally, the extracts were diluted 10 or 20 times in the assay buffer for the ULISA analysis.

2.5. Data analysis

The truncated average of the 64 measurement points was calculated for each well after discarding the 16 highest and 16 lowest measurements to account for irregularities in the luminescence readout of the well surface. The average luminescence signals obtained for different toxin concentrations were then analyzed with the data analysis and graphing software Origin (OriginLab, USA) using a four-parameter logistic regression model:

$$y = A_{min} + \frac{A_{max} - A_{min}}{1 + \left(\frac{x}{IC_{50}}\right)^{b}} \tag{1}$$

where A_{max} is the asymptotic maximum (*i.e.*, the signal in the absence of analyte), A_{min} is the asymptotic minimum, and b and IC_{50} are the slope of the curve and the analyte concentration at the inflection point, respectively.

The limit of detection (LOD) was determined as the toxin concentration at which the antibody binding to the peptide was inhibited by 10%, and the dynamic range was evaluated as the toxin concentration corresponding to 20–80% inhibition (Marco et al., 1995). Cross-reactivity (CR) was calculated from the IC_{50} values using the equation:

$$CR = \frac{IC_{50}(ZEA)}{IC_{50}(other\ mycotoxins)} \times 100\% \tag{2}$$

The apparent recovery from each spiked sample was calculated as the ratio of observed toxin concentration and the reference value.

3. Results and discussion

3.1. Design of the peptide mimetic for the competition with ZEA

The rapid analysis of low-molecular weight analytes such as ZEA using competitive immunoassays poses particular challenges. These intrinsic limitations can be partially avoided by epitope mimicking peptides. A ZEA mimicking peptide (peptide mimetic) was identified by phage display without prior knowledge of the interaction between the antibody and ZEA. The selectivity of the peptide mimetic was ensured during the phage display selections using a competitive elution step with the target analyte in the panning process. Only those phages that displayed peptides capable of competing with ZEA were selected for the next round in the iterative panning process. A thorough selectivity study with the identified peptide mimetic showed that it interacted only with the anti-ZEA antibody and that it could be only displaced by ZEA and not by other mycotoxins (Peltomaa et al., 2020). In this work, we extended the C-terminus of the previously identified peptide mimetic by a short GGGSK(biotin) sequence as shown in Fig. 1 to (1) obtain a similar structure as the recombinant fusion and phage-displayed peptides, and (2) to introduce a biotin handle for the immobilization of the peptide to a solid surface or to a label via streptavidin. Moreover, in order to mimic the structure of the phage-displayed peptide as closely as possible, the C-terminus of the synthetic peptide was amidated to mask the negatively charged carboxylate group that was not present in the phage during the panning selections.

3.2. Analysis of the peptide–antibody interaction by NMR

To identify the key amino acids in the peptide mimetic (Fig. 1; top right inset) that contribute to the antibody binding, we studied the peptide–antibody interaction by NMR. The interaction between the peptide mimetic and anti-ZEA antibody was assessed using saturation transfer difference (STD) experiments, which are based on the magnetization transfer from a protein to the hydrogens of a bound ligand. When the resonances of the protein, here the anti-ZEA antibody, are selectively saturated, the signals of a specifically bound peptide show changes in the resonance intensity, and these signals can be detected in the STD. As the STD is the difference spectrum between the experiment with protein saturation and the reference spectrum without saturation, those signals that are not involved in the interaction are canceled in the STD (Mayer and Meyer, 1999). Clear STD signals were detected from the peptide mimetic in the presence of anti-ZEA, showing that the peptide is recognized by the antibody (Fig. 2A, the 2D experiments acquired for the aromatic signal assignment are given in Figs. S1–S2). In addition, STD intensities provided information about the binding epitope since the peptide regions that are more strongly involved in the interaction display higher STD values. Here, high STD values were detected for the aromatic residues tryptophan 2 and 3, and tyrosine 6. Tryptophan 3 was the residue with the highest STD effect (Fig. 2D). These results indicate
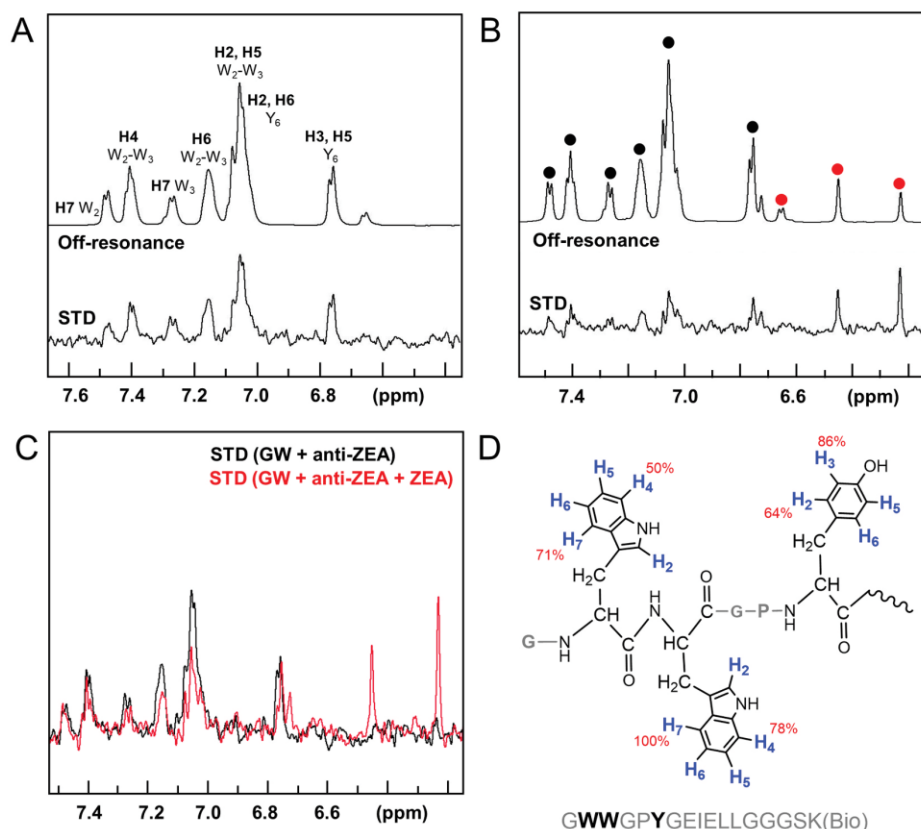
Fig. 2. Analysis of peptide–antibody interaction by STD-NMR experiments. Expansion of the aromatic region of the ^{1}H-NMR reference spectra (off-resonance) and STD spectra of the peptide mimetic in the presence of the anti-ZEA antibody (A) before and (B) after the addition of ZEA. The new peaks appearing in (B) are marked with red circles. (C) Overlay of STD spectra shown in panels (A) and (B). (D) Peptide regions that strongly interact with the antibody expressed as STD percentages of the differential spectrum normalized to H_7 of tryptophan 3 (W_3), which shows the highest STD value (100%). (For interpretation of the references to color in this figure legend, the reader is referred to the Web version of this article.)

that the aromatic amino acids of the peptide mimetic are the key interaction points with the antibody. This information can be of help for redesigning the peptide mimetic, for example, to a shorter format which could be more convenient and cost-effective for future studies. As a control experiment, the STD spectrum of the peptide was acquired in the absence of the antibody to check that no signals were detectable under these conditions (Fig. S3). Additionally, competitive binding experiments were performed by adding ZEA to the peptide/antibody sample and acquiring a new STD spectrum. As expected, we observed the signals of ZEA and a decrease of the peptide STD signals (Fig. 2B and C). This effect has been quantified by the measurement of the STD intensities in presence of 0.5 equivalents of ZEA. Under these conditions, the STD effect of the H7 signal from the tryptophan 3 (which is the most representative nucleus involved in the interaction) shows a decrease of 43% upon toxin addition. Simultaneously, the signals corresponding to ZEA display the highest STD effects (with intensities almost three times greater than the STD of the peptide signals). This confirms that both molecules—the peptide and the toxin—are competing for the same antibody binding site, and the interaction is specific.

3.3. Analysis of the peptide-binding kinetics by SPR

The binding kinetics of both the peptide mimetic and ZEA with the anti-ZEA antibody were evaluated and compared by SPR analysis (Fig. 3). For the investigation of the peptide mimetic (MW: 2031 g mol^{-1}), the antibody was immobilized on the chip, and the peptide mimetic was present in solution (Fig. 3A). Both fitting this kinetic data (one-to-one binding model) and a Langmuir equilibrium fit (Fig. S4) resulted in similar equilibrium constants (K_D) of 5.2×10^{-7} M or 2.2×10^{-7}, respectively. A similar K_D of 1.7×10^{-7} M was also found for a fumonisin mimetic peptide selected from the same phage-displayed peptide library in a previous study (Peltomaa et al., 2019).

However, due to the small size of ZEA (MW: 318 g mol^{-1}), it was not possible to investigate the binding kinetics of ZEA in the same direct assay based on the immobilized antibody (data not shown). Therefore, an HSA-ZEA conjugate was immobilized on the SPR chip to capture the antibody in solution (Fig. 3B). In this case, K_D for the interaction of antibody and ZEA was much higher compared to the antibody–peptide interaction. While the association rates (k_a) are quite similar, the 10,000-fold faster dissociation rate (k_d) of the antibody-peptide complex accounts for the overall low K_D. Since each HSA molecule was conjugated on average to 12 ZEA molecules according to the manufacturer, both binding sites of the antibody may have been involved in binding to the HSA-ZEA conjugate, thus giving information on the stronger avidity rather than affinity. Nevertheless, these results show that the peptide mimetic binds less strongly to the antibody than ZEA, which renders the
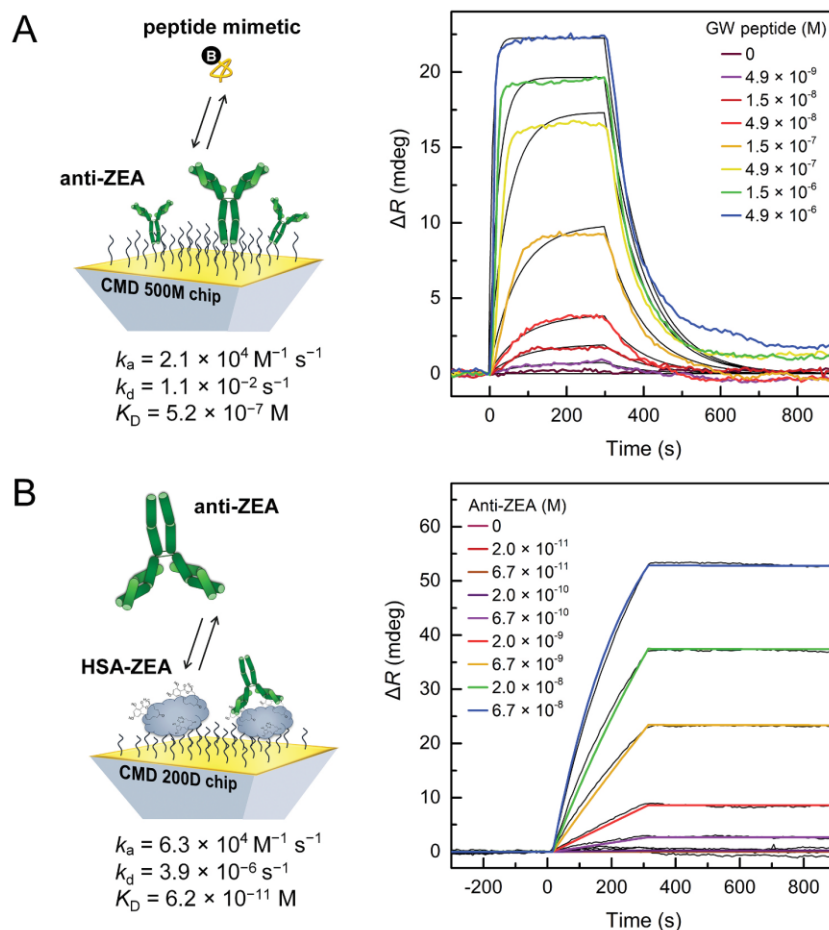
Fig. 3. Kinetic analyses by SPR using (A) the immobilized anti-ZEA antibody and free peptide mimetic, or (B) anti-ZEA antibody with immobilized HSA-ZEA. Binding curves with different peptide or antibody concentrations in colors are shown together with the kinetic fits in black. The differential signals ΔR were calculated from the sample and reference channels. (For interpretation of the references to color in this figure legend, the reader is referred to the Web version of this article.)

peptide a suitable competitor for the development of immunoassays.

3.4. Competitive ELISA and FIA

Conventional ELISA and fluorescence-linked immunoassay (FIA) are commonly used bioanalytical methods for mycotoxin analysis. In order to find the optimal label for the detection of ZEA using the synthetic peptide mimetic, we performed the assay with streptavidin conjugated either to horseradish peroxidase (SA-HRP) or carboxyfluorescein (SA-FAM). The functionality of both streptavidin labels was first confirmed by a binding study in a BSA-biotin assay. Relatively high BSA-biotin coating concentrations (10 µg mL^{-1}) were required for the reliable detection of the labels (Fig. S5) and resulted in signal-to-background ratios (S/B) of 69 for SA-HRP and 39 for SA-FAM.

In the competitive assay, using a capture antibody concentration of 2 µg mL^{-1}, the signal decreased slightly in response to increasing ZEA concentrations (Figs. S6A and S6B). Neither SA-HRP nor SA-FAM, however, were suitable to determine ZEA concentrations reliably. The insufficient label performance can be explained by the lower affinity of the peptide mimetic to the antibody as compared to ZEA (Fig. 3). While the lower affinity has the advantage that ZEA can compete more efficiently with the peptide mimetic, the relatively high dissociation rate of 1.1×10^{-2} s^{-1} may lead to a loss of the signal generating labels during subsequent washing steps. Higher concentrations of the capture antibody and peptide mimetic would possibly lead to higher signals in ELISA and FIA. For practical reasons, however, this is not an option because higher antibody coating concentrations would drastically increase the assay costs, and higher concentrations of the peptide mimetic would decrease the sensitivity of the competitive immunoassay. Therefore, we replaced SA-FAM and SA-HRP by a UCNP-PEG-SA label to develop a robust method for the detection of ZEA in food samples. In addition to the background-free optical detection, each UCNP label exposes several streptavidin molecules on its surface connected via a highly flexible PEG-linker structure. We expected that the UCNP label with its ability to strongly bind to several peptides simultaneously via the biotin-streptavidin interaction (multivalency) would partially compensate for

the relatively weak affinity of the peptide bound to the capture antibody.

3.5. Characterization of UCNP labels

Oleic acid-capped UCNPs (NaYF$_4$:Yb^{3+},Tm^{3+}) were modified with alkyne-PEG-neridronate ligand and streptavidin-azide (Fig. 1; bottom left inset) by a Cu-catalyzed click-reaction (Mickert et al., 2019; Farka et al., 2020b). The as-synthesized UCNPs and the UCNP-PEG-SA-bioconjugates were thoroughly characterized before employing them as a label in the competitive immunoassay. Transmission electron microscopy (TEM) revealed a uniform spherical shape (Fig. 4A) with an average diameter of 37 nm (Fig. 4B). In the emission spectrum (Fig. 4C), the UCNPs displayed the strongest luminescence at 800 nm. Moreover, the hydrodynamic properties of particles before and after the conjugation were compared by dynamic light scattering (DLS). The increase of the hydrodynamic diameter (Fig. 4D and E) indicated the successful surface modification of UCNPs. As the distribution of the hydrodynamic diameter did not broaden considerably, the conjugation procedure did not lead to particle aggregation. Finally, the functional properties of the conjugate were tested in a BSA-biotin assay (Fig. 4F). The UCNP-PEG-SA conjugate resulted in a S/B of 622 for 100 ng mL^{-1} of immobilized BSA-biotin and 35 µg mL^{-1} of UCNP-PEG-SA. At this BSA-biotin concentration, SA-HRP or SA-FAM achieved only a S/B of 4 or 7, respectively, which shows the superior performance of UCNP labels.

3.6. Competitive upconversion-linked immunosorbent assay (ULISA)

The anti-ZEA capture antibody was immobilized onto a well of a microtiter plate, and the competition between ZEA and the biotinylated peptide mimetic was detected using the UCNP-PEG-SA label as shown in Fig. 1. The competitive ULISA was optimized in terms of the antibody and peptide concentrations, assay and blocking buffer, as well as the UCNP label concentration (Fig. S7). High concentrations of the capture antibody and peptide mimetic resulted in higher absolute signals in the absence of free ZEA (Fig. S7A). Lowering these concentrations improved
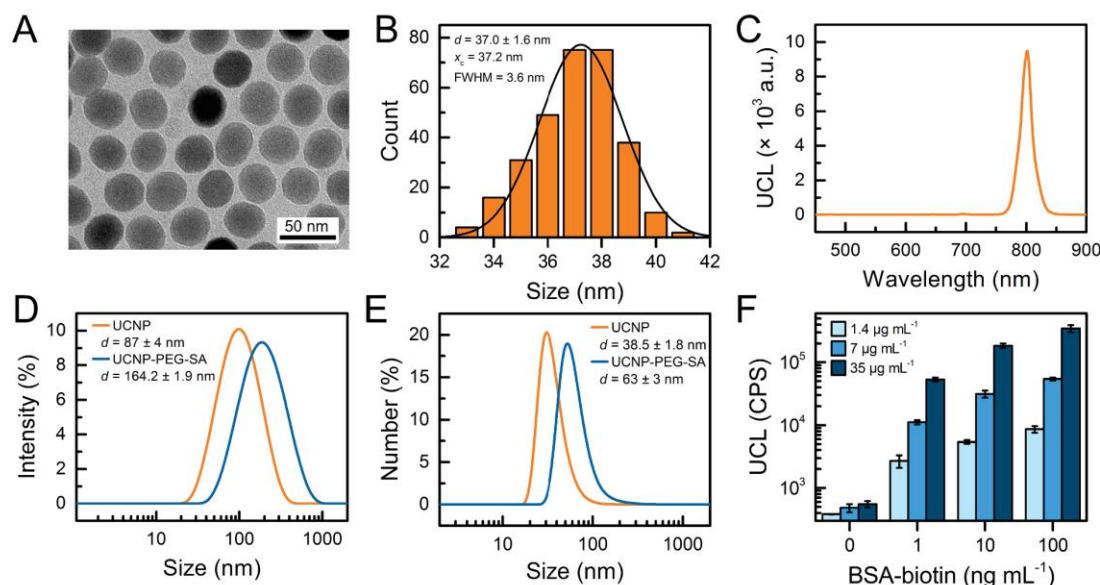
Fig. 4. Characterization of UCNPs. (A) TEM image of oleic-acid capped UCNPs. (B) Size distribution of UCNPs determined from TEM. (C) Emission spectrum of UCNPs measured under 980-nm excitation. DLS measurements (D: intensity; E: number distribution) of oleic acid-capped UCNPs in cyclohexane and UCNP-PEG-SA-conjugates in TBS. (F) Binding of UCNP-PEG-SA-conjugates (concentrations of 1.4–35 µg mL^{-1}) to immobilized BSA-biotin. The error bars show the standard error of the mean in replicate wells ($n = 3$).

the sensitivity towards ZEA detection. The optimal concentrations were high enough to provide reliable signals but also resulted in good sensitivity for the detection of ZEA. The effect of the assay buffer composition was also studied, but the tested buffers exerted only minor effects on the assay sensitivity (Fig. S7B). The assay buffer containing BGG and BSA-based blocking buffer was selected as it provided slightly better sensitivity to ZEA, albeit lower absolute signals compared to the SuperBlock-based buffer (Fig. S7B). The more complex BGG-containing assay buffer led to lower background signals, thus strongly improving the S/B to 45 compared to the SuperBlock-based buffer (S/B: 17). The same assay buffer composition was used previously in a highly sensitive ULISA for the detection of prostate-specific antigen (PSA) in serum (Mickert et al., 2019), and it is considered to be particularly suitable for complex samples and difficult matrices. Similarly, the assay performance was only marginally influenced by using either BSA or SuperBlock as the blocking buffer. However, the use of BSA resulted in a better S/B of 45 compared to SuperBlock (S/B 31), and it was selected for subsequent experiments. Higher UCNP concentrations provided higher absolute signals but did not affect the sensitivity, and similar IC_{50} values of 0.19 (± 0.03) ng mL^{-1} and 0.18 (± 0.09) ng mL^{-1} were observed with 12.5 and 30 μg mL^{-1} UCNPs, respectively (Fig. S7C).

Fig. 5A shows the excellent performance of the optimized ULISA with an IC_{50} value of 0.16 ± 0.08 ng mL^{-1} and a dynamic range (IC_{20}–IC_{80}) from 50 pg mL^{-1} to 0.5 ng mL^{-1}. The LOD of 20 pg mL^{-1} was more than 200 times lower than our earlier bioluminescent immunoassay based on the same antibody and the same peptide mimetic sequence in the form of a fusion protein (Peltomaa et al., 2020). Also, the dynamic range was improved by a factor of 3 compared to the bioluminescent method. Overall, the LOD of the ULISA is comparable or lower than most of the previously reported methods (Table S1) and commercially available assays (Table S2). Although few lower LODs have been reported in the literature, the ULISA benefits from a simple and straightforward assay protocol and measurement scheme.

3.7. Cross-reactivity

The specificity of the ULISA was evaluated by determining the cross-reactivity with related mycotoxins. Metabolites of ZEA, such as the stereoisomers α-zearalenol and β-zearalenol, showed strong cross-reactivities of 320% and 133%, respectively (Fig. 5B) because they share a high structural similarity with ZEA (Fig. S8). Furthermore, the

monoclonal anti-ZEA antibody was raised against an ovalbumin-ZEA conjugate, which consisted of ZEA attached to ovalbumin in the very position that is varied among these metabolites (Fig. S8). Thus, the antibody cannot differentiate between these metabolites in line with previous reports on antibodies raised against ZEA-oxime-coupled conjugates (Thouvenot and Morfin, 1983; Liu et al., 1985). In any case, cross-reactivity with these metabolites can be considered useful as both of them are *in vivo* metabolites of ZEA and have been shown to occur naturally (De Ruyck et al., 2020). Notably, no cross-reactivity was observed with other mycotoxins produced by the same *Fusarium* species (deoxynivalenol, ochratoxin A, fumonisin B_1, T-2 toxin).

3.8. Real sample analysis

We confirmed the functionality of the ULISA in a real sample matrix by spiking blank maize samples that were confirmed to be free of ZEA by UPLC-MS/MS analysis with 20–80 μg kg^{-1} of ZEA. Sample extracts in methanol were diluted in assay buffer and analyzed by the ULISA. Recoveries between 77% and 105% (Table 1) indicated an acceptable accuracy of the method for the quantitative detection of ZEA in real samples. The relative standard deviation (RSD) of three replicate measurements varied between 3 and 9%, thus also fulfilling the performance criteria for ZEA detection set in the European Commission regulations No 1881/2006 and 401/2006, which established a maximum residue limit of 350 μg kg^{-1} for unprocessed maize products and the acceptable recoveries and RSDs, respectively (European Commission, 2006a, 2014). The analysis of naturally contaminated maize samples by both the competitive ULISA and UPLC-MS/MS yielded in general consistent results (Table 2). Depending on the type of sample, however, significant variations were observable between these methods that can be

Table 1
Analysis of ZEA in spiked samples.

Spiked ZEA (μg kg^{-1})	Measured ZEA (μg kg^{-1})	RSD[a]	Recovery
0	< LOD	6%	n.d.
20	18.3	4%	91%
40	41.8	3%	105%
60	61.2	4%	102%
80	61.3	9%	77%

[a] RSD, relative standard deviation ($n = 3$).
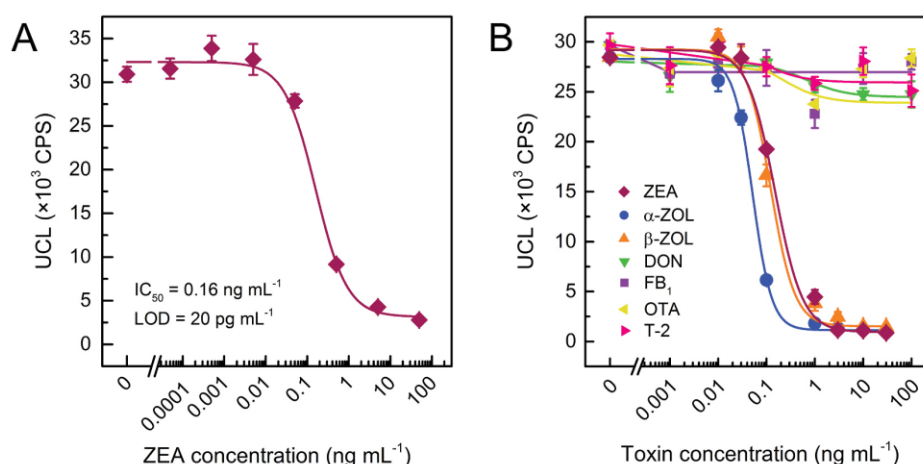
Fig. 5. (A) Calibration curve of the optimized ULISA for the detection of ZEA in buffer. (B) Cross-reactivities (CR) of zearalenone (ZEA, IC_{50}: 0.16 ± 0.08 ng ml^{-1}, CR: 100%); α-zearalenol (α-ZOL, IC_{50}: 0.05 ± 0.01 ng ml^{-1}, CR: 320%) and β-zearalenol (β- ZOL, IC_{50}: 0.12 ± 0.05 ng ml^{-1}, CR: 133%). No cross-reactivities (IC_{50} not determinable) are found for the toxins deoxynivalenol (DON), fumonisin B_1 (FB_1), ochratoxin A (OTA), and T-2 toxin (T-2). The molecular structures of the toxins are shown in Fig. S6. The error bars the standard error of the mean in replicate wells ($n = 3$).

Table 2
Analysis of ZEA in naturally contaminated maize samples.

Measured ZEA ($\mu g\ kg^{-1}$) by UPLC-MS/MS	Measured ZEA ($\mu g\ kg^{-1}$) by ULISA	RSD[a] of ULISA
70	88	6%
114	108	12%
124	151	6%
250	184	4%
350	334	17%

[a] RSD, relative standard deviation ($n = 3$).

explained by matrix effects affecting the UPLC-MS/MS and ULISA measurement to a different degree. The stronger matrix effect in naturally contaminated samples is also evident from larger RSD values of the ULISA compared to the spiked samples. Despite these variations, the ULISA readily enables detection of ZEA concentration above maximum residue limits in naturally contaminated cereal samples.

4. Conclusions

We have demonstrated the advantages of using peptide mimetics in a competitive ULISA for the sensitive detection of the mycotoxin ZEA. The design of the competitive ULISA rests on two interdependent pillars: (1) A biotinylated peptide mimetic serves as a substitute for the conventional ZEA-protein conjugate that competes efficiently with the analyte ZEA as shown by NMR and SPR analyses of the peptide–antibody interaction. (2) A UCNP-PEG-SA conjugate serves as a substitute for the conventional enzyme label that attaches the label more strongly and can be detected without optical background interference. With an LOD of 20 pg mL^{-1} (63 pM), the competitive ULISA is about $1000 \times$ more sensitive than commercial assays for ZEA detection. Furthermore, no complex sample pre-treatment is required as for common reference methods such as HPLC-MS. The method showed good analytical performance not only in buffer but also in spiked and naturally contaminated maize samples. Therefore, our competitive ULISA is a valuable tool for the simple analysis of mycotoxin-contaminated food samples with a sensitivity that meets the requirements set by the European legislation.

CRediT authorship contribution statement

Riikka Peltomaa: Conceptualization, Methodology, Investigation, Formal analysis, Writing - original draft, Writing - review & editing, Visualization. **Zdeněk Farka:** Conceptualization, Methodology, Investigation, Formal analysis, Writing - original draft, Writing - review & editing, Visualization. **Matthias J. Mickert:** Methodology, Investigation. **Julian C. Brandmeier:** Methodology, Investigation. **Matěj Pastucha:** Investigation, Writing - review & editing. **Antonín Hlaváček:** Investigation, Writing - review & editing. **Mónica Martínez-Orts:** Investigation, Writing - review & editing. **Ángeles Canales:** Writing - review & editing, Supervision, Funding acquisition. **Petr Skládal:** Writing - review & editing, Supervision. **Elena Benito-Peña:** Conceptualization, Writing - review & editing, Supervision. **María C. Moreno-Bondi:** Conceptualization, Resources, Writing - review & editing, Supervision, Funding acquisition. **Hans H. Gorris:** Conceptualization, Resources, Writing - review & editing, Supervision, Project administration, Funding acquisition.

Declaration of competing interest

The authors declare that they have no known competing financial interests or personal relationships that could have appeared to influence the work reported in this paper.

Appendix A. Supplementary data

Supplementary data to this article can be found online at https://doi.org/10.1016/j.bios.2020.112683.

References

Bennett, J.W., Klich, M., 2003. Mycotoxins. Clin. Microbiol. Rev. 16, 497–516.

Caglayan, M.O., Şahin, S., Üstündağ, Z., 2020. Detection strategies of zearalenone for food safety: a review. Crit. Rev. Anal. Chem. 26, 1–20.

Chauhan, R., Singh, J., Sachdev, T., Basu, T., Malhotra, B.D., 2016. Recent advances in mycotoxins detection. Biosens. Bioelectron. 81, 532–545.

Dai, S., Wu, S., Duan, N., Chen, J., Zheng, Z., Wang, Z., 2017. An ultrasensitive aptasensor for Ochratoxin A using hexagonal core/shell upconversion nanoparticles as luminophores. Biosens. Bioelectron. 91, 538–544.

De Ruyck, K., Huybrechts, I., Yang, S., Arcella, D., Claeys, L., Abbeddou, S., De Keyzer, W., De Vries, J., Ocke, M., Ruprich, J., De Boevre, M., De Saeger, S., 2020. Mycotoxin exposure assessments in a multi-center European validation study by 24-hour dietary recall and biological fluid sampling. Environ. Int. 137, 105539.

De Saeger, S., Sibanda, L., Van Peteghem, C., 2003. Analysis of zearalenone and α-zearalenol in animal feed using high-performance liquid chromatography. Anal. Chim. Acta 487, 137–143.

Drzymala, S.S., Weiz, S., Heinze, J., Marten, S., Prinz, C., Zimathies, A., Garbe, L.-A., Koch, M., 2015. Automated solid-phase extraction coupled online with HPLC-FLD for the quantification of zearalenone in edible oil. Anal. Bioanal. Chem. 407, 3489–3497.

EFSA Panel on Contaminants in the Food Chain (CONTAM), 2011. Scientific Opinion on the risks for public and animal health related to the presence of zearalenone in food. EFSA Journal 2011, 2197.

European Commission, 2006a. Commission regulation (EC) No 1881/2006. Off. J. Eur. Union L364, 5–24.

European Commission, 2006b. Commission recommendation (EC) No 576/2006. Off. J. Eur. Union L229, 7–9.

European Commission, 2014. Commission regulation (EC) No 519/2014. Off. J. Eur. Union L147, 29–43.

European Commission, 2000. Opinion of the scientific committee on food on *Fusarium* toxins. Part 2: zearalenone (ZEA). Available at: https://ec.europa.eu/food/sites/food/files/safety/docs/cs_contaminants_catalogue_fusarium_out65_en.pdf.

Fang, G., Fan, C., Liu, H., Pan, M., Zhu, H., Wang, S., 2014. A novel molecularly imprinted polymer on CdSe/ZnS quantum dots for highly selective optosensing of mycotoxin zearalenone in cereal samples. RSC Adv. 4, 2764–2771.

Farka, Z., Juřík, T., Kovář, D., Trnková, L., Skládal, P., 2017. Nanoparticle-based immunochemical biosensors and assays: recent advances and challenges. Chem. Rev. 117, 9973–10042.

Farka, Z., Mickert, M.J., Mikušová, Z., Hlaváček, A., Bouchalová, P., Xu, W., Bouchal, P., Skládal, P., Gorris, H.H., 2020b. Surface design of photon-upconversion nanoparticles for high-contrast immunocytochemistry. Nanoscale 12, 8303–8313.

Farka, Z., Mickert, M.J., Pastucha, M., Mikušová, Z., Skládal, P., Gorris, H.H., 2020a. Advances in optical single-molecule detection: en route to supersensitive bioaffinity assays. Angew. Chem. Int. Ed. 59, 10746–10773.

Gareis, M., Schothorst, R.C., Vidnes, A., Bergsten, C., Paulsen, B., Brera, C., Miraglia, M., 2003. Collection of occurrence data of Fusarium toxins in food and assessment of dietary intake by the population of EU Member States. Report of Experts Participating in SCOOP Task 3.2.10. available at: https://ec.europa.eu/food/sites/food/files/safety/docs/cs_contaminants_catalogue_fusarium_task3210.pdf.

Haase, M., Schäfer, H., 2011. Upconverting nanoparticles. Angew. Chem. Int. Ed. 50, 5808–5829.

Hlaváček, A., Farka, F., Hübner, M., Horňáková, V., Němeček, D., Niessner, R., Skládal, P., Knopp, D., Gorris, H.H., 2016. Competitive upconversion-linked immunosorbent assay for the sensitive detection of diclofenac. Anal. Chem. 88, 6011–6017.

He, D., Wu, Z., Cui, B., Jin, Z., Xu, E., 2020. A fluorometric method for aptamer-based simultaneous determination of two kinds of the *Fusarium* mycotoxins zearalenone and fumonisin B_1 making use of gold nanorods and upconversion nanoparticles. Microchim. Acta 187, 254.

He, Q.-H., Xu, Y., Huang, Y.-H., Liu, R.-R., Huang, Z.-B., Li, Y.-P., 2011. Phage-displayed peptides that mimic zearalenone and its application in immunoassay. Food Chem. 126, 1312–1315.

He, Z., He, Q., Xu, Y., Li, Y., Liu, X., Chen, B., Lei, D., Sun, C., 2013. Ochratoxin A mimotope from second-generation peptide library and its application in immunoassay. Anal. Chem. 85, 10304–10311.

Hidalgo-Ruiz, J.L., Romero-González, R., Martínez Vidal, J.L., Garrido Frenich, A., 2019. A rapid method for the determination of mycotoxins in edible vegetable oils by ultra-high performance liquid chromatography-tandem mass spectrometry. Food Chem. 288, 22–28.

IARC, International Agency for Research on Cancer, 1993. Monographs on the Evaluation of Carcinogenic Risks to Humans, Some Naturally Occurring Substances: Food Items and Constituents, Heterocyclic Aromatic Amines and Mycotoxins. International Agency for Research on Cancer, Lyon, France.

Jiang, F., Li, P., Zong, C., Yang, H., 2020. Surface-plasmon-coupled chemiluminescence amplification of silver nanoparticles modified immunosensor for high-throughput ultrasensitive detection of multiple mycotoxins. Anal. Chim. Acta 1114, 58–65.

Kim, K., Jo, E.-J., Lee, K.J., Park, J., Jung, G.Y., Shin, Y.-B., Lee, L.P., Kim, M.-G., 2020. Gold nanocap-supported upconversion nanoparticles for fabrication of a solid-phase aptasensor to detect ochratoxin A. Biosens. Bioelectron. 150, 111885.

Kuiper-Goodman, T., Scott, P.M., Watanabe, H., 1987. Risk assessment of the mycotoxin zearalenone. Regul. Toxicol. Pharmacol. 7, 253–306.

Li, R., Meng, C., Wen, Y., Fu, W., He, P., 2019. Fluorometric lateral flow immunoassay for simultaneous determination of three mycotoxins (aflatoxin B_1, zearalenone and deoxynivalenol) using quantum dot microbeads. Microchim. Acta 186, 748.

Liu, M.-T., Ram, B.P., Hart, L.P., Pestka, J.J., 1985. Indirect enzyme-linked immunosorbent assay for the mycotoxin zearalenone. Appl. Environ. Microbiol. 50, 5.

Liu, X., Xu, Y., He, Q., He, Z., Xiong, Z., 2013. Application of mimotope peptides of fumonisin B_1 in peptide ELISA. J. Agric. Food Chem. 61, 4765–4770.

Liu, Z., Hua, Q., Wang, J., Liang, Z., Li, J., Wu, J., Shen, X., Lei, H., Li, X., 2020. A smartphone-based dual detection mode device integrated with two lateral flow immunoassays for multiplex mycotoxins in cereals. Biosens. Bioelectron. 158, 112178.

Maaroufi, K., Chekir, L., Creppy, E.E., Ellouz, F., Bacha, H., 1996. Zearalenone induces modifications of haematological and biochemical parameters in rats. Toxicon 34, 535–540.

Magnusson, B., Örnemark, U. (Eds.), 2014. Eurachem Guide: the Fitness for Purpose of Analytical Methods – A Laboratory Guide to Method Validation and Related Topics, second ed. Available at: http://www.eurachem.org

Marco, M.-P., Gee, S., Hammock, B.D., 1995. Immunochemical techniques for environmental analysis I. Immunosensors. Trends Anal. Chem. 14, 341–350.

Mayer, M., Meyer, B., 1999. Characterization of ligand binding by saturation transfer difference NMR spectroscopy. Angew. Chem. Int. Ed. 38, 1784–1788.

Mickert, M.J., Farka, Z., Kostiv, U., Hlaváček, A., Horák, D., Skládal, P., Gorris, H.H., 2019. Measurement of sub-femtomolar concentrations of prostate-specific antigen through single-molecule counting with an upconversion-linked immunosorbent assay. Anal. Chem. 91, 9435–9441.

Niazi, S., Wang, X., Pasha, I., Khan, I.M., Zhao, S., Shoaib, M., Wu, S., Wang, Z., 2018. A novel bioassay based on aptamer-functionalized magnetic nanoparticle for the detection of zearalenone using time resolved-fluorescence NaYF$_4$: Ce/Tb nanoparticles as signal probe. Talanta 186, 97–103.

Nolan, P., Auer, S., Spehar, A., Elliott, C.T., Campbell, K., 2019. Current trends in rapid tests for mycotoxins. Food Addit. Contam. A 36, 800–814.

Peltomaa, R., Agudo-Maestro, I., Más, V., Barderas, R., Benito-Peña, E., Moreno-Bondi, M.C., 2019. Development and comparison of mimotope-based immunoassays for the analysis of fumonisin B_1. Anal. Bioanal. Chem. 411, 6801–6811.

Peltomaa, R., Amaro-Torres, F., Carrasco, S., Orellana, G., Benito-Peña, E., Moreno-Bondi, M.C., 2018b. Homogeneous quenching immunoassay for fumonisin B_1 based on gold nanoparticles and an epitope-mimicking yellow fluorescent Protein. ACS Nano 12, 11333–11342.

Peltomaa, R., Benito-Peña, E., Barderas, R., Sauer, U., González Andrade, M., Moreno-Bondi, M.C., 2017. Microarray-based immunoassay with synthetic mimotopes for the detection of fumonisin B_1. Anal. Chem. 89, 6216–6223.

Peltomaa, R., Benito-Peña, E., Moreno-Bondi, M.C., 2018a. Bioinspired recognition elements for mycotoxin sensors. Anal. Bioanal. Chem. 410, 747–771.

Peltomaa, R., Fikacek, S., Benito-Peña, E., Barderas, R., Head, T., Deo, S., Daunert, S., Moreno-Bondi, M.C., 2020. Bioluminescent detection of zearalenone using recombinant peptidomimetic *Gaussia* luciferase fusion protein. Microchim Acta 187, 547.

Romera, D., Mateo, E.M., Mateo-Castro, R., Gómez, J.V., Gimeno-Adelantado, J.V., Jiménez, M., 2018. Determination of multiple mycotoxins in feedstuffs by combined use of UPLC–MS/MS and UPLC–QTOF–MS. Food Chem. 267, 140–148.

Sedlmeier, A., Hlaváček, A., Birner, L., Mickert, M.J., Muhr, V., Hirsch, T., Corstjens, P.L.A.M., Tanke, H.J., Soukka, T., Gorris, H.H., 2016. Highly sensitive laser scanning of photon-upconverting nanoparticles on a macroscopic scale. Anal. Chem. 88, 1835–1841.

Taghdisi, S.M., Danesh, N.M., Beheshti, H.R., Ramezani, M., Abnous, K., 2016. A novel fluorescent aptasensor based on gold and silica nanoparticles for the ultrasensitive detection of ochratoxin A. Nanoscale 8, 3439–3446.

Tan, H., Ma, L., Guo, T., Zhou, H., Chen, L., Zhang, Y., Dai, H., Yu, Y., 2019. A novel fluorescence aptasensor based on mesoporous silica nanoparticles for selective and sensitive detection of aflatoxin B_1. Anal. Chim. Acta 1068, 87–95.

Thouvenot, D., Morfin, R.F., 1983. Radioimmunoassay for zearalenone and zearalanol in human serum: production, properties, and use of porcine antibodies. Appl. Environ. Microbiol. 45, 16–23.

van Egmond, H.P., Schothorst, R.C., Jonker, M.A., 2007. Regulations relating to mycotoxins in food: perspectives in a global and European context. Anal. Bioanal. Chem. 389, 147–157.

Wild, D. (Ed.), 2013. The Immunoassay Handbook: Theory and Applications of Ligand Binding, ELISA, and Related Techniques, fourth ed. Elsevier, Oxford ; Waltham, MA.

Wu, S., Liu, L., Duan, N., Wang, W., Yu, Q., Wang, Z., 2018. A test strip for ochratoxin A based on the use of aptamer-modified fluorescence upconversion nanoparticles. Microchim. Acta 185, 497.

Xiong, Ying, Leng, Y., Li, X., Huang, X., Xiong, Yonghua, 2020. Emerging strategies to enhance the sensitivity of competitive ELISA for detection of chemical contaminants in food samples. Trends Anal. Chem. 126, 115861.

Yang, M., Zhang, Y., Cui, M., Tian, Y., Zhang, S., Peng, K., Xu, H., Liao, Z., Wang, H., Chang, J., 2018. A smartphone quantitative detection platform of mycotoxins based on multiple-color upconversion nanoparticles. Nanoscale 10, 15865–15874.

Yuan, Q., Pestka, J.J., Hespenheide, B.M., Kuhn, L.A., Linz, J.E., Hart, L.P., 1999. Identification of mimotope peptides which bind to the mycotoxin deoxynivalenol-specific monoclonal antibody. Appl. Environ. Microbiol. 65, 8.

Zhang, S., Sun, Y., Sun, Y., Wang, H., Shen, Y., 2020. Semiquantitative immunochromatographic colorimetric biosensor for the detection of dexamethasone based on up-conversion fluorescent nanoparticles. Microchim. Acta, 187, 447.

Zhang, Z., Shikha, S., Liu, J., Zhang, J., Mei, Q., Zhang, Y., 2019. Upconversion nanoprobes: recent advances in sensing applications. Anal. Chem. 91, 548–568.

Zinedine, A., Soriano, J.M., Moltó, J.C., Mañes, J., 2007. Review on the toxicity, occurrence, metabolism, detoxification, regulations and intake of zearalenone: an oestrogenic mycotoxin. Food Chem. Toxicol. 45, 1–18.

9

Paper XIV

Click-conjugated photon-upconversion nanoparticles in an immunoassay for honeybee pathogen _Melissococcus plutonius_

Poláchová, V.; Pastucha, M.; Mikušová, Z.; Mickert, M. J.; Hlaváček, A.; Gorris, H. H.; Skládal, P.; Farka, Z.*

Contribution:

Design of experiments, preparation of immunization antigen and antibody, bioconjugation and characterization of UCNPs, development and optimization of sandwich immunoassay, data evaluation, manuscript writing

Click-conjugated photon-upconversion nanoparticles in an immunoassay for honeybee pathogen *Melissococcus plutonius*†

Veronika Poláchová,[a,b] Matěj Pastucha,[a,b] Zuzana Mikušová,[a,b] Matthias J. Mickert, [iD][c] Antonín Hlaváček,[d] Hans H. Gorris, [iD][c] Petr Skládal [iD][a,b] and Zdeněk Farka [iD]*[a]

European foulbrood (EFB) is an infectious disease affecting honeybee larvae caused by the bacterium *Melissococcus plutonius*. The enzyme-linked immunosorbent assay (ELISA) is the gold standard for antibody-based bacteria detection, however, its sensitivity is not high enough to reveal early-stage EFB infection. Photon-upconversion nanoparticles (UCNPs) are lanthanide-doped nanomaterials that emit light of shorter wavelength under near-infrared (NIR) excitation and thus avoid optical background interference. After conjugation with specific biorecognition molecules, UCNPs can be used as ultrasensitive labels in immunoassays. Here, we introduce a method for conjugation of UCNPs with streptavidin based on copper-free click chemistry, which involves surface modification of UCNPs with alkyne-modified bovine serum albumin (BSA) that prevents the non-specific binding and provides reactive groups for conjugation with streptavidin-azide. To develop a sandwich upconversion-linked immunosorbent assay (ULISA) for *M. plutonius* detection, we have prepared a rabbit polyclonal anti-*Melissococcus* antibody. The specific capture of the bacteria was followed by binding of biotinylated antibody and UCNP–BSA–streptavidin conjugate for a highly sensitive upconversion readout. The assay yielded an LOD of 340 CFU mL^{-1} with a wide working range up to 10^9 CFU mL^{-1}, which is 400 times better than the LOD of the conventional ELISA. The practical applicability of the ULISA was successfully demonstrated by detecting *M. plutonius* in spiked real samples of bees, larvae and bottom hive debris. These results show a great potential of the assay for early diagnosis of EFB, which can prevent uncontrolled spreading of the infection and losses of honeybee colonies.

Introduction

The western honeybee (*Apis mellifera*) is the most remarkable insect pollinator invaluable to agriculture and biodiversity. The value of crop production attributed to honeybee pollina-

[a]CEITEC MU, Masaryk University, Kamenice 5, 625 00 Brno, Czech Republic. E-mail: farka@mail.muni.cz
[b]Department of Biochemistry, Masaryk University, Kamenice 5, 625 00 Brno, Czech Republic
[c]Institute of Analytical Chemistry, Chemo- and Biosensors, University of Regensburg, 93053 Regensburg, Germany
[d]Institute of Analytical Chemistry of the Czech Academy of Sciences, Veveří 97, 602 00 Brno, Czech Republic

†Electronic supplementary information (ESI) available: Protocols of microorganism cultivation, antigen preparation, antibody conjugation, ELISA assay, UCNP synthesis, UCNP characterization, and data analysis; results from antibody testing using ELISA, LC-MS/MS analysis, single-particle microscopy, non-specific binding tests, and optimization of ULISA; tables comparing approaches for EFB diagnosis and UCNP-based assays for bacteria detection. See DOI: 10.1039/c9nr01246j

tion in the USA was estimated to be 17 billion USD in 2009,[1] which represents above 10% of the total crop production value in the USA. European foulbrood (EFB) is a honeybee disease caused by a Gram-positive bacterium *Melissococcus plutonius*. It infects honeybee larvae and causes their death before they are capped, which can be detected by visual inspection of the brood. To minimize the risk of disease spreading, early and reliable detection of diseased colonies is critical, ideally before clinical symptoms develop.[2]

Microscopic evaluation of carbol fuchsin stained smears of diseased larvae is the basic method for laboratory confirmation of EFB. However, it can be hampered by secondary bacteria invading the infected brood and it is not sensitive enough to confirm the absence of bacterium in honeybee products. Cultivation on selective media is a traditional method of choice for the isolation and identification of bacteria. However, *M. plutonius* is a fastidious organism with low cultivation recoveries, which limits the sensitivity of this otherwise very sensitive, straightforward, but lengthy method.[3]

268

Molecular detection methods based on either DNA or antibodies offer an improvement in sensitivity, time-requirements and throughput of the analysis. Real-time PCR represents a standard approach in research and laboratory confirmation of this pathogen nowadays.[3] While antibody-based immunoassays and immunosensors have been reported for the detection of diverse pathogens,[4] these methods have not been widely applied to the detection of *M. plutonius* yet. One of the reasons might be the lack of commercially available antibodies and the need to develop them in-house. Recently, a field test based on lateral flow immunoassay has been developed.[5] This ready-to-use kit is commercially available (Vita Europe Ltd) and can be used to confirm infections by *M. plutonius* in diseased larvae directly in the apiary. Furthermore, an ELISA assay for laboratory confirmation of the bacteria was reported.[6]

Although the ELISA is considered a gold standard of immunoassays due to its high sensitivity, robustness of detection and widespread use, it is still challenging to improve the detection limits for an early-stage diagnosis.[7] Furthermore, the use of enzyme labels for signal amplification is limited by low stability, high production costs and time-consuming preparation.[8] Therefore, detection labels that afford a higher sensitivity and sustainable preparation are highly desirable. Nanoparticles provide a great potential to substitute traditional labels in a variety of detection schemes. Immuno-based detection using nanomaterials such as gold nanoparticles,[9] catalytic nanoparticles,[10] quantum dots,[11] or carbon-based materials[12] have been reported to provide enhanced assay properties.

Photon-upconversion nanoparticles (UCNPs) are lanthanide-doped nanomaterials, typically consisting of a crystalline NaYF$_4$ host matrix doped with Yb^{3+} and Er^{3+} ions, which emit high energy photons of shorter wavelength under excitation by near-infrared (NIR) radiation (anti-Stokes emission).[13,14] Due to the very low autofluorescence and light scattering of the NIR radiation in biomaterials, the background luminescence is minimized, thus making UCNPs popular in bioanalytical applications,[15] including upconversion-linked immunosorbent assays (ULISAs),[16–18] lateral-flow assays,[19] chemical sensing,[20,21] and *in vitro* and *in vivo* imaging.[22–24] In addition, unlike classic fluorescent labels, UCNPs do not photobleach and are chemically more stable.[25]

UCNPs are typically prepared in hydrophobic solvents, such as oleic acid and octadecene. Hence, for biological applications their surface needs to be modified.[26] One of the most common methods of surface modification is silanization. This process involves the hydrolysis and condensation of siloxane precursors, typically tetraethyl orthosilicate[27] and other silane-derivatives providing functional groups for further conjugation.[28,29] Another approach involves the exchange of the hydrophobic surface ligands by hydrophilic ligands. Ligands with carboxylate or phosphonate groups can coordinate to the lanthanide ions on the surface of UCNPs. Other parts of such ligands are then employed for conjugation reactions.[30] Typically, the hydrophobic ligand is first exchanged by nitrosonium tetrafluoroborate, followed by subsequent

exchange with the functionalized ligand.[31] One of the most frequently used ligands are citric acid,[32] polyacrylic acid[33] and polyethylene glycol (PEG).[34] PEG is popular in biological applications due to its low toxicity, no immunogenicity and no metabolic degradation during clearance from the body.[35] Due to steric hindrance and repulsion effects it also contributes to the reduction of non-specific binding towards proteins or protein-modified solid support.[36] However, as the non-specific binding is recently becoming one of the major challenges in ultrasensitive assays, especially for the analysis of real samples with complex matrices,[30] alternative approaches that can further improve the binding specificity are highly demanded.

In this work, we introduce a highly sensitive method for the detection of *M. plutonius* in samples of bees, larvae and bottom hive debris using conjugates of UCNPs with streptavidin, tailored to minimize their non-specific binding. We have developed a polyclonal anti-*Melissococcus* antibody and introduced a method for conjugation of UCNPs with biomolecules based on copper-free click reaction between alkyne-modified BSA on the UCNP surface and azide-modified streptavidin. This conjugation method results in uniform conjugates allowing universal use in bioanalytical applications based on biotinylated detection probes. Moreover, the method is well suited for the attachment of any azide-modified proteins such as antibodies to thus prepared alkyne-derivatized UCNPs.

Experimental section

Chemicals and reagents

5-Azidopentanoic acid (APA), (1R,8S,9s)-bicyclo[6.1.0]non-4-yn-9-ylmethyl *N*-succinimidyl carbonate (BCN-NHS), bovine serum albumin (BSA), bovine γ-globulin (BGG), 5(6)-carboxyfluorescein (CF), 5-carboxyrhodamine *N*-succinimidyl ester (Rh-NHS), *N*-(3-dimethylaminopropyl)-*N*′-ethylcarbodiimide (EDC), *N*-hydroxysulfosuccinimide sodium salt (sulfo-NHS), 2-(*N*-morpholino)ethanesulfonic acid (MES), streptavidin (SA), tris(hydroxymethyl)aminomethane (Tris), and Tween 20 were purchased from Sigma-Aldrich (Germany). Poly(vinyl alcohol) (PVA; 6 kDa) was purchased from Polysciences (USA). Blotting grade powdered milk was obtained from Carl Roth (Germany). Substrate solution TMB-Complete 2 was purchased from TestLine (Czech Republic). All other common chemicals were obtained in the highest quality available from Penta (Czech Republic).

Dialysis buffer (100 mM H$_3$BO$_3$, 80 mM Na$_2$CO$_3$, pH 9.4), phosphate buffer (PB; 50 mM NaH$_2$PO$_4$/Na$_2$HPO$_4$, pH 7.4), phosphate-buffered saline (PBS; PB with 150 mM NaCl), washing buffer (PB with 0.01% Tween 20, and 0.05% NaN$_3$), and assay buffer (0.2% BSA, 0.5% BGG, 50 mM Tris, 150 mM NaCl, 5 mM EDTA, 0.2% PVA, 1% glucose, 0.01% Tween 20, and 0.05% NaN$_3$, pH 7.5) were used throughout this work.

Melissococcus plutonius (ATCC 35311), *Paenibacillus alvei* (ATCC 6344), *Paenibacillus larvae* (CCM 4484), and *Brevibacillus laterosporus* (ATCC 64) were obtained from the Czech Collection of Microorganisms (CCM, Czech Republic). The

269

details of microorganism cultivation, preparation of antigen for immunization, and processing of real samples are provided in the ESI.†

Preparation of antibody

New Zealand white rabbits were immunized with 0.75 mL of 100× diluted antigen in PBS emulsified in 0.75 mL of Freund's complete adjuvant. The booster antigen injection using Freund's incomplete adjuvant followed after 35 days. After 10 days, blood samples for the preparation of antisera were collected, and the sera were stored at −20 °C.[37] The rabbit sera were screened by an indirect ELISA to evaluate their specificity towards whole cells of *M. plutonius* as target analyte and *P. alvei* as a negative control. Serum of the rabbit exhibiting better specific reactivity and lower cross-reactivity was selected for further use. The immunoglobulin G fraction from the serum was purified on a protein G column (Thermo Scientific, USA) using FPLC and stored in concentration of 4.6 mg mL^{-1} at −30 °C. The protocols of antibody conjugation with horseradish peroxidase (HRP) and biotin and of the ELISA assay for the antibody testing are provided in the ESI.†

Synthesis of UCNPs

UCNPs with composition of $NaY_{0.895}Yb_{0.10}Er_{0.005}F_4$ were prepared by thermal decomposition of oleate precursors.[38] The resulting oleate-capped UCNPs were coated with carboxylated silica using a water in oil microemulsion.[39] The carboxylated UCNPs (see ESI† for details) were stored as a water dispersion in concentration of 37 mg mL^{-1}.

Preparation of UCNP-streptavidin conjugates

For the preparation of fluorescent click-reactive BSA–alkyne conjugate, BCN-NHS (2.92 mg) was dissolved in 20 μL of dimethylformamide (DMF) and mixed with 1.72 mg of Rh-NHS dissolved in 100 μL of DMF. The solution was subsequently mixed with 1880 μL of dialysis buffer containing 132 mg of BSA and after 4 h of mixing, the carboxyrhodamine-labelled BSA–alkyne conjugate was dialyzed four times overnight against 500 mL of dialysis buffer.

To prepare click-reactive UCNPs, carboxylated UCNPs (1 mg) were centrifuged (1700g, 10 min), redispersed in 200 μL of 100 mM sodium MES, 30 mM Na_2CO_3, pH 6.0, containing 0.4 mg of EDC and 0.2 mg of sulfo-NHS. The dispersion was sonicated at room temperature for 10 min followed by a short centrifugation (3300g, 1 min). The pellet containing activated UCNPs was immediately redispersed in 200 μL of 100 mM sodium MES, 30 mM Na_2CO_3, pH 6.0 containing 0.5 mg of BSA–alkyne. After 90 min of mild mixing at room temperature, the UCNP–BSA–alkyne conjugate was centrifuged/redispersed five times in 50 mM Tris with 50 mM H_3BO_3 pH 8.6 (1700g, 15 min, 200 μL of buffer).[39]

To prepare fluorescent click-reactive streptavidin-azide, free carboxyl groups of APA and CF were activated using EDC/sulfo-NHS chemistry to make them reactive towards free amino groups of streptavidin.[40] APA (1.4 mg) was dissolved in 100 μL of DMF and mixed with 100 μL of 100 mM sodium MES, pH 6.1 containing EDC (3.8 mg) and sulfo-NHS (4.3 mg). The solution was shaken gently for 1 h at room temperature. CF (1.5 mg) was dissolved in 100 μL of DMF and mixed with 400 μL of 100 mM sodium MES, pH 6.1 containing EDC (15 mg) and sulfo-NHS (3.5 mg). After 1 h of activation, 50 μL of activated CF and 20 μL of activated APA solutions were mixed together with 5.2 mg of streptavidin dissolved in 60 μL of dialysis buffer. After 4 h of mild mixing at room temperature, the CF-labelled click-reactive streptavidin-azide was dialyzed five times overnight against 500 mL of dialysis buffer.

For the final copper-free click-conjugation[41] of UCNPs with streptavidin, 1 mg of click-reactive UCNP–BSA–alkyne was centrifuged for 15 min at 1700g and the pellet was redispersed with 2.5 mg of click-reactive streptavidin-azide in 500 μL of dialysis buffer. The solution of UCNP–BSA–alkyne and streptavidin-azide was subsequently dialyzed four times overnight against 250 mL of 100 mM sodium MES, pH 4.5, which allowed their electrostatic attraction and enabled an efficient click-conjugation. The UCNP–BSA–SA conjugates were centrifuged (1700g, 15 min), redispersed in 50 mM Tris, 50 mM H_3BO_3, pH 8.6 to a final concentration of 5 mg mL^{-1} and stored at 4 °C. The conjugation scheme is shown in Fig. 1.
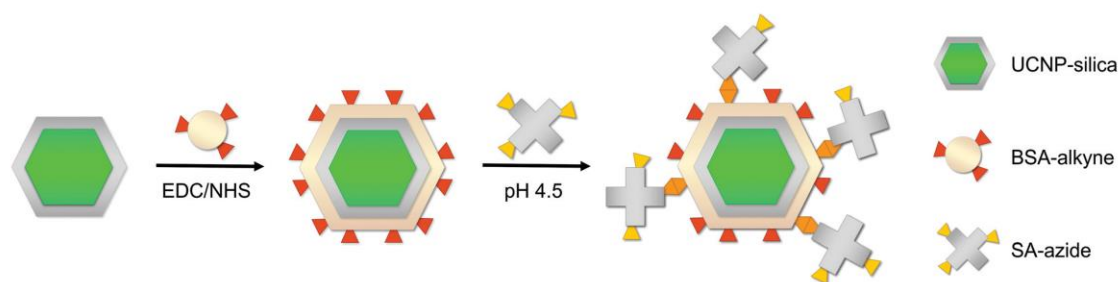
Fig. 1 Scheme of conjugation of UCNPs with streptavidin based on copper-free click chemistry. Carboxylated silica-coated UCNPs (UCNP-silica) were activated by EDC/NHS and coupled with BCN-modified bovine serum albumin (BSA–alkyne). Afterwards, APA-modified streptavidin (SA-azide) was introduced and the click-reaction started after dialysis to pH 4.5.

270

The UCNPs and their conjugates were characterized using transmission electron microscopy (TEM), agarose gel electrophoresis, liquid chromatography coupled with tandem mass spectrometry (LC-MS/MS), dynamic light scattering (DLS), and single-particle upconversion microscopy; the level of non-specific binding of the UCNPs was studied in a microtiter plate-based assay. Detailed protocols are provided in ESI.†

Development of upconversion-linked immunosorbent assay (ULISA) for EFB diagnosis

A transparent 96-well microtiter plate with high binding capacity (Microlon, Greiner Bio-One, Austria) was coated with 200× diluted anti-*Melissococcus* antibody in PBS (100 µL per well) at 4 °C overnight. All subsequent steps were carried out at room temperature. After each step, the plate was washed four times with 250 µL of washing buffer. The plate was blocked with 200 µL of 5% powdered milk in PBS for 1 h. Afterwards, either standard dilutions of bacteria in assay buffer or spiked in bee, larvae or bottom hive debris extracts diluted with assay buffer were added (100 µL per well) and incubated for 2 h. Then, the microtiter plate was incubated for 1 h with 100 µL of 500× diluted biotin-conjugated anti-*Melissococcus* antibody. Afterwards, the plate was incubated with the UCNP–BSA–SA conjugate (10 µg mL^{-1} in assay buffer, 100 µL per well) for 1 h. Finally, the plate was washed four times, allowed to dry, and the upconversion luminescence was measured using an upconversion microplate reader equipped with a continuous 980 nm laser (5 W; Laserland, China) and CCD spectroscope QE65 Pro (Ocean Optics, USA) as a detector. In each well of the microtiter plate, photon-upconversion luminescence intensities in the range of 646–672 nm were recorded as a Cartesian grid of 64 points with a spacing of 600 µm. The truncated average was calculated for each well after discarding 16 highest and 16 lowest recorded values. The assay scheme is shown in Fig. 2. The ULISA and ELISA calibration curves were fitted using a four-parameter logistic function. The ESI† contains details of the statistical evaluation and LOD calculation.

Results and discussion

Testing of antibodies and enzyme-linked immunosorbent assay

Since there were no commercially available antibodies against *M. plutonius*, a rabbit polyclonal antibody was prepared to afford a sensitive and selective recognition of the target bacteria. Cell wall fractions of *M. plutonius* were used as an antigen for immunization. The discussion of the antigen preparation and the optical microscopy images illustrating the antigen preparation (Fig. S1†) are available in ESI.†

The specificity of the prepared rabbit anti-*Melissococcus* antibody was tested using an indirect ELISA as the most simple and reliable method. First, the blocking conditions were optimized (Fig. S2A†) and blocking by 5% powdered milk in PBS was selected for further use. The specificity of the anti-*Melissococcus* antibody was evaluated by binding studies to the target *M. plutonius* and compared to negative controls of *P. alvei*, *P. larvae*, and *B. laterosporus* representing other relevant honeybee pathogens (Fig. 3A). The results show a negligible level of non-specific binding to negative controls, while providing strong specific response to *M. plutonius*. The indirect ELISA provided an LOD of 7.1×10^4 CFU mL^{-1} with a working range up to 10^9 CFU mL^{-1}. This is comparable with other ELISA assays for bacteria detection, which typically provide LODs in the range between 10^4 and 10^6 CFU mL^{-1}.[42,43] It was previously found that clinical symptoms of EFB can be expected above a cut-off bacterial load of 5×10^4 CFU of *M. plutonius* per bee, corresponding to *ca.* 10^5 CFU mL^{-1} when 500 µL of buffer are used for sample extraction.[44] Therefore, a higher assay sensitivity would be preferred for an efficient early-stage diagnosis, when lower bacterial loads are present. Furthermore, the indirect ELISA is not well suited for the detection of analytes in real samples due to the high complexity of the matrix, which can negatively affect the bacteria coating efficiency and thus decrease the assay sensitivity. Therefore, we aimed to design a sandwich ELISA for *M. plutonius* detection, which would be suitable for real sample analysis and in the next step would allow to replace the
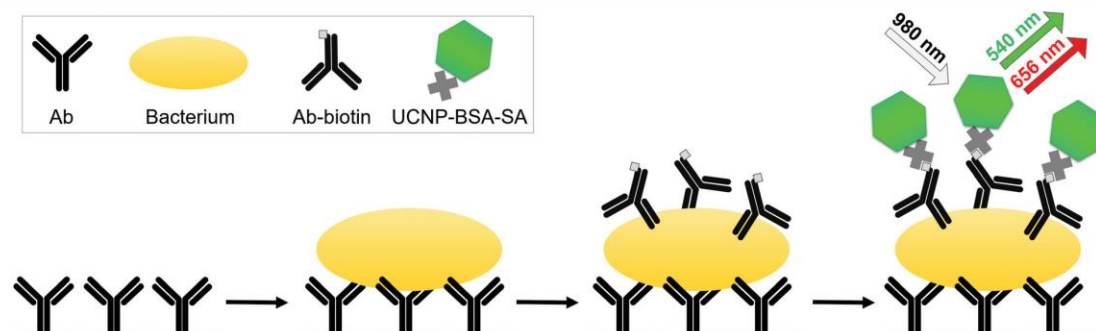
Fig. 2 Scheme of sandwich upconversion-linked immunosorbent assay (ULISA) for diagnosis of European foulbrood. The microtiter plate was coated by a capture antibody, followed by the specific binding of *M. plutonius*, biotinylated antibody, and the conjugate of UCNP with BSA and streptavidin. Finally, upconversion luminescence corresponding to bacteria concentration was measured under 980 nm excitation.

271
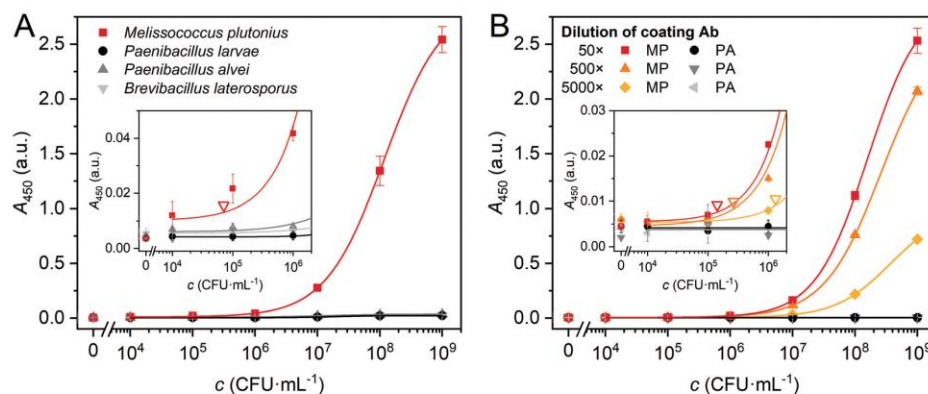
Fig. 3 (A) Specificity of the developed anti-*Melissococcus* antibody tested using indirect ELISA (LOD 7.1 × 10⁴ CFU mL⁻¹). (B) Effect of varying concentration of coated anti-*Melissococcus* antibody on the performance of sandwich ELISA for detection of *M. plutonius* (MP) with *P. alvei* (PA) as a negative control. The 50× diluted Ab provides an LOD of 1.4 × 10⁵ CFU mL⁻¹; 500× diluted Ab provides an LOD of 2.7 × 10⁵ CFU mL⁻¹ and 5000× diluted Ab results in an LOD of 1.3 × 10⁶ CFU mL⁻¹. Open triangles represent the LOD values.

HRP-based label by UCNP–BSA–SA conjugate to enhance the assay sensitivity. For the sandwich detection, conjugate of anti-*Melissococcus* antibody with HRP (Ab-HRP) was prepared and its function was confirmed in a direct ELISA (Fig. S2B†).

To develop a sandwich immunoassay with high sensitivity and wide working range, the concentrations of coating antibody and Ab-HRP conjugate were optimized. In both cases, the increasing concentration led to higher signals with small effect on the background level. Therefore, the optimized dilutions, found as a compromise between antibody consumption and signal-to-background ratio, were 200× for anti-*Melissococcus* coating antibody (Fig. 3B) and 500× for the detection Ab-HRP conjugate (Fig. S3A†). The optimized sandwich assay provided an LOD of 1.4 × 10⁵ CFU mL⁻¹ with a working range up to 10⁹ CFU mL⁻¹, which is comparable with the performance of the indirect ELISA. Furthermore, the sandwich ELISA was utilized to assess the performance of the conjugate of the anti-*Melissococcus* antibody with biotin (Ab-biotin) (Fig. S3B†). This conjugate was necessary for the development of sandwich immunoassay based on the UCNP–BSA–SA label. The optimized sandwich ELISA was employed for the real sample analysis (Fig. S4†). The samples of spiked bees (LOD 3.4 × 10⁵ CFU mL⁻¹), larvae (LOD 2.3 × 10⁴ CFU mL⁻¹) and bottom hive debris (LOD 3.4 × 10⁴ CFU mL⁻¹) were successfully analyzed, which confirms the low level of cross-reactivity of the prepared antibody to other components present in the samples.

Characterization of UCNPs and their conjugates

UCNPs coated with a carboxylated silica shell were characterized by TEM (Fig. 4A). The particles had a hexagonal prism shape with height of 80.5 ± 4.7 nm and diameter of 105.6 ± 4.3 nm. The thickness of the silica shell was 3.3 ± 0.5 nm. The emission spectrum of silica-coated UCNPs is shown in Fig. 4B.

To develop a high-performance detection label, we have introduced a method for the conjugation of UCNPs with strep-
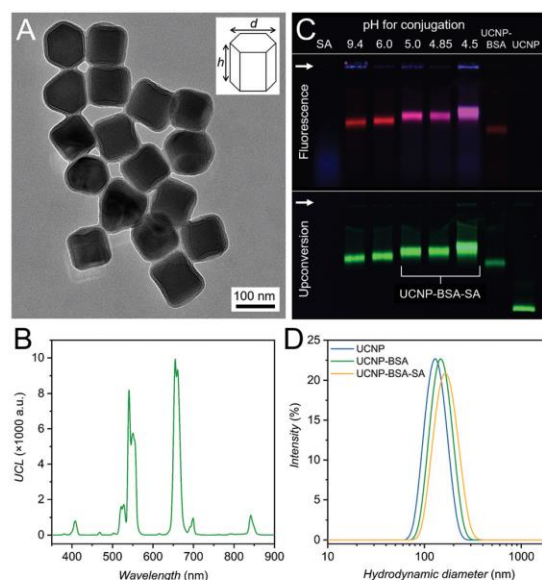
Fig. 4 (A) TEM image of silica-coated UCNPs with shape of hexagonal prism (height (*h*): 80.5 ± 4.7 nm, diameter (*d*): 105.6 ± 4.3 nm) as depicted in scheme in the inset. The thickness of the silica layer was 3.3 ± 0.5 nm. (B) Upconversion luminescence spectrum of silica-coated UCNPs measured under 980 nm excitation. (C) Agarose gel electrophoresis of carboxyrhodamine-stained UCNP–BSA–alkyne (red channel) conjugated with carboxyfluorescein-stained streptavidin-azide (blue channel) at different pH visualized by fluorescence and upconversion (green). The arrows indicate the starting point of electrophoresis. (D) DLS of UCNPs (hydrodynamic diameter Φ_{HD}: 133.2 nm); UCNP–BSA–alkyne (Φ_{HD}: 152.1 nm), and UCNP–BSA–SA (Φ_{HD}: 170.8 nm). The experimental data points were plotted using a B-spline function.

tavidin and other biomolecules *via* copper-free click chemistry. This approach is based on bioorthogonal reaction between BCN-modified BSA (BSA–alkyne) attached to the UCNP surface

272

and APA-modified streptavidin (streptavidin-azide).[41] The BSA has two functions: it serves as a linker between the click-reactive BCN-group and the UCNP and helps to prevent the non-specific binding of UCNPs towards protein-modified solid support.

BSA–alkyne and streptavidin-azide were fluorescently labeled to monitor the surface modification of UCNPs by BSA–alkyne and subsequent conjugation with streptavidin-azide. Samples of silanized UCNPs (visible in the upconversion scan only), carboxyrhodamine-stained UCNP–BSA–alkyne (red channel), carboxyfluorescein-stained streptavidin-azide (blue channel) and UCNP–BSA–SA conjugates prepared at different pH were characterized using agarose gel electrophoresis (Fig. 4C). Narrow bounded bands and no visible UCNP aggregates in the gel pockets suggest that the silanized UCNPs and their conjugates were uniform.[45] The successful conjugation was confirmed by overlapping bands in blue and red channels and mobility shifts of conjugates. The optimal conjugation pH was 4.5. This pH probably reduces electrostatic repulsion between UCNP–BSA–alkyne and streptavidin-azide and suggests two-step conjugation mechanism. Firstly, streptavidin molecules approach UCNPs and, secondly, nearby alkyne and azide groups react.

The presence of BSA and streptavidin conjugated on UCNPs was further confirmed by mass spectrometry. The UCNP conjugates were mixed with trypsin to digest the proteins, followed by removal of UCNPs by centrifugation and analysis of peptide mixtures using LC-MS/MS. Both the samples of UCNP–BSA (Table S1†) and UCNP–BSA–SA (Table S2†) contained BSA as the most abundant protein, with integrated intensities of 1.38×10^{10} and 1.58×10^{10} a.u., respectively. While there was no streptavidin found in the UCNP–BSA samples, the UCNP–BSA–SA extract contained streptavidin fragments with integrated intensity of 1.63×10^9 a.u. These results suggest there is approximately 10 times excess of BSA compared to streptavidin bound on the UCNP surface.

The uniformity of the silanized UCNPs and their conjugates was confirmed by DLS measurement. The DLS shows a hydrodynamic diameter of 133.2 nm with a polydispersity index (PDI) of 0.019 for silica-coated UCNPs. After conjugation with BSA–alkyne, the size increased to 152.1 nm (PDI of 0.024), followed by another increase to 170.8 nm (PDI of 0.045) after the conjugation with streptavidin-azide (Fig. 4D). The zeta-potential (Fig. S5†) of UCNPs (−44.2 mV) successively increased after conjugation with BSA–alkyne (−23.5 mV) and streptavidin-azide (−14.4 mV). These results are in agreement with the gel electrophoresis, because both increasing hydrodynamic diameter and zeta-potential contribute to the drop of electrophoretic mobility.

The distribution of the luminescence intensities of the UCNP–BSA–SA conjugate was studied using single-particle upconversion microscopy (Fig. S6†). The presence of a single Gaussian peak in the histogram and coefficient of variation (CV) of 29.8% further confirm the high uniformity of the conjugate. For comparison, the previously studied silica-coated UCNPs without any protein coating provided CVs in the range between 26 and 61%.[18]

The effect of the UCNP surface modification on the non-specific binding was studied in microtiter plate-based assay. Compared to bare silica-coated UCNPs, the non-specific binding of BSA-modified UCNPs was lower on a coated and blocked microtiter plate (Fig. S7†). After the modification with streptavidin (UCNP–BSA–SA), the non-specific binding increased, however, it was lower than in case of silanized UCNPs conjugated with streptavidin directly *via* carboxyl groups (UCNP–SA). In case of the microtiter plate without blocking (Fig. S8†), a sequential decrease of non-specific binding was observed after conjugation with BSA and streptavidin. The additional benefit of the BSA-based conjugation is the effect on prevention of conjugate aggregation. This can be seen from lower error bars in the non-specific binding tests, as well as from the comparison of gel electrophoresis of UCNP–BSA–SA (Fig. 4C) containing highly uniform particles and UCNP–SA (Fig. S9†) containing large amount of aggregates. These results confirm the advantages of the UCNP–BSA design compared to the coating with silica layer only.

Upconversion-linked immunosorbent assay (ULISA)

One of the most important limiting factors in nanoparticle-based immunoassays is the level of non-specific binding of nanoparticles to the surface, which generally increases with increasing label concentration.[46] Therefore, we have focused on the optimization of the detection steps (Ab-biotin and UCNP–BSA–SA concentration). In both cases, the observed signals, as well as the level of non-specific binding, were increasing with increasing label concentration. With respect to minimizing the LOD, 500× diluted Ab-biotin conjugate (Fig. S10A†) and 10 µg mL^{-1} of UCNP–BSA–SA conjugate (Fig. S10B†) were selected for further experiments. The coating concentration and blocking conditions were based on the parameters optimized in the sandwich ELISA.

The optimized ULISA was first employed for the detection of *M. plutonius* in assay buffer and the specificity of the detection was verified using *P. larvae* and *B. laterosporus* as negative controls (Fig. 5). The use of UCNP–BSA–SA label allowed to reach the LOD of 340 CFU mL^{-1} with a wide working range up to 10^9 CFU mL^{-1}. The achieved LOD is 400 times better compared to the conventional sandwich ELISA (Fig. S11†) and fits into the range suitable for practical analysis of infected bees and larvae. Because the same immunoreagents were used in both the ELISA and ULISA assay, the biggest effect on the improved sensitivity is provided by the background-free detection of the anti-Stokes emission and by the low level of non-specific binding of the BSA-modified UCNPs.

The presented ULISA for *M. plutonius* detection achieved significantly better sensitivity compared to older *M. plutonius* immunoassays: ELISAs with LODs 10^5 and 10^6 CFU mL^{-1}.[5,6] It is often not possible to easily compare detection limits with PCR-based methods, as they usually state only the minimum detectable amount of template DNA after extraction. Some authors tried to assess the minimum concentration of bacteria needed in the sample before extraction. A hemi-nested PCR was reported to successfully detect *M. plutonius* concentrations

273
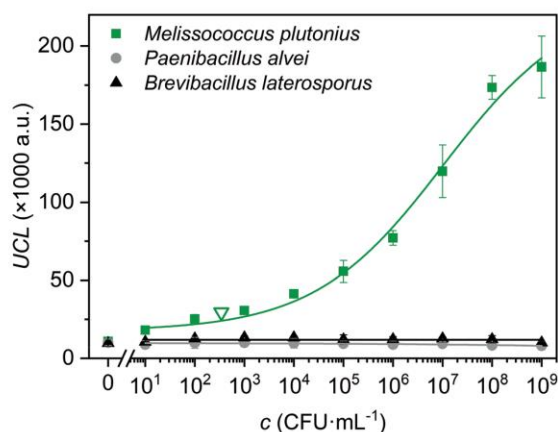
Fig. 5 Calibration curve of sandwich ULISA for the detection of *M. plutonius* in buffer (LOD 340 CFU mL^{-1}, EC$_{50}$ 1.0 × 10^7 CFU mL^{-1}), with negative controls of *P. alvei* and *B. laterosporus*. Open triangle represents the LOD.

down to 6 CFU mL^{-1}, however, the DNA was isolated from bacterial cultures of *M. plutonius* and not from the real samples of honeybee material.[47] A modified hemi-nested PCR was used to analyze larvae and honey samples with an LOD of 10^3 CFU mL^{-1},[48] which is comparable to our results. Finally, a real-time PCR was used for the detection of *M. plutonius* in honeybee samples with an LOD of 3.5 CFU mL^{-1}.[44] An overview of different approaches for the detection of *M. plutonius* is provided in Table S3.†

As far as we know, this is the first report of a UCNP-based immunoassay for detecting bacteria in a microtiter plate. Other detection approaches include an assay based on binding of antibody-conjugated UCNPs to *E. coli*, followed by separation of unbound UCNPs and luminescence intensity measurement (LOD 10 CFU mL^{-1});[49] a lateral flow assay for *Yersinia*

pestis and *Burkholderia pseudomallei* based on a sandwich scheme with antibody-conjugated UCNPs (LOD 10^5 CFU mL^{-1});[50] and a FRET assay based on UCNP–cDNA and AuNP–aptamer conjugates for the detection of *E. coli* (LOD of 3 CFU mL^{-1}).[51] The comparison of assay parameters of various methods for bacteria detection based on UCNPs is shown in Table S4.† One of the reasons for slightly lower sensitivity of our ULISA assay compared to some other literature reports is the use of in-house prepared polyclonal antibody, whereas commercial monoclonal antibodies are typically reported in the literature. Generally, different procedures can be reliably compared only in case of using the same antibody–antigen pair. Nevertheless, the achieved sensitivity of this ULISA is fully sufficient for the diagnosis of EFB in infected apiaries.

Analysis of real samples

The practical applicability of the ULISA was demonstrated by analyzing spiked real samples of bees, larvae, and bottom hive debris, which are the typical matrices where *M. plutonius* is present in case of an EFB infection. The real samples were diluted with assay buffer to 10% and 25% in order to suppress the matrix effects. Therefore, the sensitivity was only slightly deteriorated compared to the detection in buffer. In case of bee extracts, LODs of 540 CFU mL^{-1} and 1.6 × 10^3 CFU mL^{-1} were achieved for 10% and 25% sample, respectively (Fig. 6A). The more diluted sample provided a slightly higher sensitivity, however considering the dilution of target bacteria, the dilution to 25% is preferable. A similar phenomenon was observed also in case of larvae (Fig. 6B), with LODs of 8.5 × 10^3 CFU mL^{-1} and 1.3 × 10^4 CFU mL^{-1} for 10% and 25% extracts, respectively. In case of the bottom hive debris (Fig. 6B), an LOD of 570 CFU mL^{-1} was reached. The generally lower sensitivity of *M. plutonius* detection in larvae compared to bees and bottom hive debris is probably given by the different character of the sample in connection with its processing. Bees and the bottom hive debris contain more insoluble components,
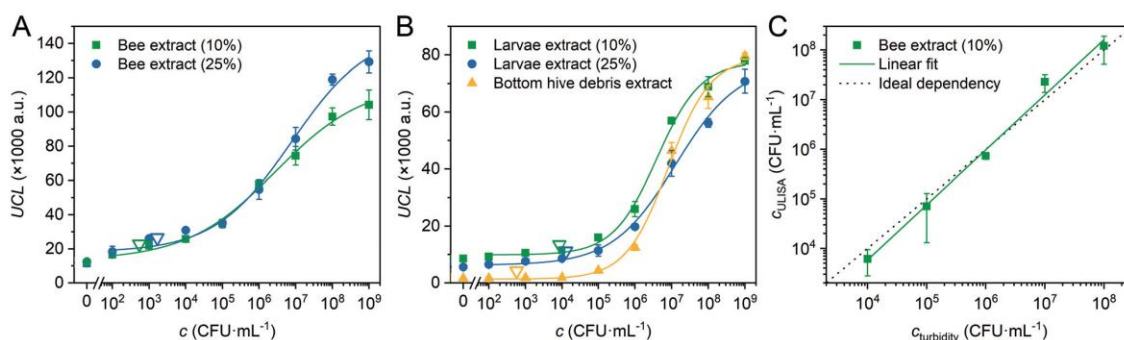
Fig. 6 Calibration curves of sandwich ULISA-based detection of *M. plutonius* spiked in real samples. (A) Bee extract diluted by assay buffer to 10% (LOD 540 CFU mL^{-1}) and 25% (LOD 1.6 × 10^3 CFU mL^{-1}). (B) Larvae extract diluted to 10% (LOD 8.5 × 10^3 CFU mL^{-1}) and 25% (LOD 1.3 × 10^4 CFU mL^{-1}) and bottom hive debris extract (LOD 570 CFU mL^{-1}). Open triangles represent the LOD values. (C) Correlation between the *M. plutonius* concentration in 10% bee extract determined by ULISA and turbidimetry.

274

which are removed during the sample processing, whereas the soft tissues from larvae are retained during the sample processing and can affect the assay. The precision of the assay was validated by the analysis of real samples spiked with known amounts of *M. plutonius*. Good agreement of the ULISA and turbidimetry was achieved, which can be demonstrated by the slope of 1.1 and R^2 of 0.992 of the correlation dependency (Fig. 6C).

In general, the LODs for all types of real samples are below the amount of *M. plutonius* found in infected apiaries with clinical symptoms (typically 10^5 CFU mL^{-1}).[44] This, in combination with easy sample preparation based on standardized approaches, makes the ULISA based on UCNP–BSA–SA conjugate a method suitable for practical early-stage diagnosis of EFB infections.

Conclusions

We report a method for the simple and fast conjugation of UCNPs with streptavidin based on copper-free click chemistry. The prepared conjugates can be used as universal labels in immunoassays based on biotinylated antibodies. The method involves surface modification of UCNPs with alkyne-modified BSA, which prevents non-specific binding and provides reactive groups for conjugation with streptavidin-azide. The proposed conjugation protocol is universally applicable for the conjugation of click-reactive UCNPs with any click-activated biomolecules.

The UCNP–BSA–SA conjugates were applied as a luminescent label for implementing a highly sensitive immunoassay for *M. plutonius*, the causative agent of EFB. Rabbit polyclonal antibody was prepared to provide sensitive and selective recognition of *M. plutonius*. The antibody coated on the microtiter plate captured bacteria from the complex samples, followed by binding of the biotinylated anti-*Melissococcus* antibody and the UCNP–BSA–SA conjugate. The sensitive upconversion readout provided an LOD of 340 CFU mL^{-1} and a wide working range up to 10^9 CFU mL^{-1}, which is 400 times better than the LOD of conventional ELISA performed under the same conditions. Finally, the optimized assay was employed for the detection of *M. plutonius* in spiked real samples of bees, larvae, and bottom hive debris, with LODs of 540, 8.5×10^3 and 570 CFU mL^{-1}, respectively. The assay sensitivity fits into the range suitable for practical analysis of infected apiaries, thus this approach shows a great potential for early-stage diagnosis of EFB and prevention of uncontrolled spreading of infection and losses of honeybee colonies.

Live subject statement

The animal experiments complied with the Act. No. 246/1992 Coll. on the Protection of Animals against Cruelty, as amended and were approved by the Branch Commission for Animal Welfare of the Ministry of Agriculture of the Czech Republic.

Conflicts of interest

There are no conflicts to declare.

Acknowledgements

References

1 N. W. Calderone, *PLoS One*, 2012, **7**, 27.
2 T. Erban, O. Ledvinka, M. Kamler, B. Hortova, M. Nesvorna, J. Tyl, D. Titera, M. Markovic and J. Hubert, *PeerJ*, 2017, **5**, 28.
3 E. Forsgren, G. E. Budge, J. D. Charriere and M. A. Z. Hornitzky, *J. Apic. Res.*, 2013, **52**, 14.
4 A. Ahmed, J. V. Rushworth, N. A. Hirst and P. A. Millner, *Clin. Microbiol. Rev.*, 2014, **27**, 631–646.
5 V. Tomkies, J. Flint, G. Johnson, R. Waite, S. Wilkins, C. Danks, M. Watkins, A. G. S. Cuthbertson, E. Carpana, G. Marris, G. Budge and M. A. Brown, *Apidologie*, 2009, **40**, 63–72.
6 D. E. Pinnock and N. E. Featherstone, *J. Apic. Res.*, 1984, **23**, 168–170.
7 Z. Farka, T. Juřík, D. Kovář, L. Trnková and P. Skládal, *Chem. Rev.*, 2017, **117**, 9973–10042.
8 H. Wei and E. K. Wang, *Chem. Soc. Rev.*, 2013, **42**, 6060–6093.
9 J. H. Kwon, H. T. Kim, J. H. Lee, R. Kim, M. Heo, J. Shin, H. Y. Lee, Y. J. Cha and J. Lee, *Nanoscale*, 2017, **9**, 16476–16484.
10 Z. Farka, V. Čunderlová, V. Horáčková, M. Pastucha, Z. Mikušová, A. Hlaváček and P. Skládal, *Anal. Chem.*, 2018, **90**, 2348–2354.
11 G. Annio, T. L. Jennings, O. Tagit and N. Hildebrandt, *Bioconjugate Chem.*, 2018, **29**, 2082–2089.
12 Y. X. Lin, Q. Zhou, D. P. Tang, R. Niessner and D. Knopp, *Anal. Chem.*, 2017, **89**, 5637–5645.
13 M. Haase and H. Schafer, *Angew. Chem., Int. Ed.*, 2011, **50**, 5808–5829.

275

14 B. Zhou, B. Y. Shi, D. Y. Jin and X. G. Liu, *Nat. Nanotechnol.*, 2015, **10**, 924–936.

15 Z. Zhang, S. Shikha, J. Liu, J. Zhang, Q. Mei and Y. Zhang, *Anal. Chem.*, 2019, **91**, 548–568.

16 A. Hlaváček, Z. Farka, M. Hübner, V. Horňáková, D. Němeček, R. Niessner, P. Skládal, D. Knopp and H. H. Gorris, *Anal. Chem.*, 2016, **88**, 6011–6017.

17 N. Sirkka, A. Lyytikainen, T. Savukoski and T. Soukka, *Anal. Chim. Acta*, 2016, **925**, 82–87.

18 Z. Farka, M. J. Mickert, A. Hlaváček, P. Skládal and H. H. Gorris, *Anal. Chem.*, 2017, **89**, 11825–11830.

19 P. L. A. M. Corstjens, C. J. De Dood, D. Kornelis, E. Fat, R. A. Wilson, T. M. Kariuki, R. K. Nyakundi, P. T. Loverde, W. R. Abrams, H. J. Tanke, L. Van Lieshout, A. M. Deelder and G. J. Van Dam, *Parasitology*, 2014, **141**, 1841–1855.

20 R. Arppe, T. Nareoja, S. Nylund, L. Mattsson, S. Koho, J. M. Rosenholm, T. Soukka and M. Schaferling, *Nanoscale*, 2014, **6**, 6837–6843.

21 X. X. Hu, T. Wei, J. Wang, Z. E. Liu, X. Y. Li, B. H. Zhang, Z. H. Li, L. L. Li and Q. Yuan, *Anal. Chem.*, 2014, **86**, 10484–10491.

22 J. Wang, T. Wei, X. Y. Li, B. H. Zhang, J. X. Wang, C. Huang and Q. Yuan, *Angew. Chem., Int. Ed.*, 2014, **53**, 1616–1620.

23 L. Frances-Soriano, M. A. Zakharko, M. Gonzalez-Bejar, P. A. Panchenko, V. Herranz-Perez, D. A. Pritmov, M. A. Grin, A. F. Mironov, J. M. Garcia-Verdugo, O. A. Fedorova and J. Perez-Prieto, *Chem. Mater.*, 2018, **30**, 3677–3682.

24 D. Y. Jin, P. Xi, B. M. Wang, L. Zhang, J. Enderlein and A. M. van Oijen, *Nat. Methods*, 2018, **15**, 415–423.

25 S. W. Wu, G. Han, D. J. Milliron, S. Aloni, V. Altoe, D. V. Talapin, B. E. Cohen and P. J. Schuck, *Proc. Natl. Acad. Sci. U. S. A.*, 2009, **106**, 10917–10921.

26 M. Wang, G. Abbineni, A. Clevenger, C. B. Mao and S. K. Xu, *Nanomedicine*, 2011, **7**, 710–729.

27 Z. Q. Li and Y. Zhang, *Angew. Chem., Int. Ed.*, 2006, **45**, 7732–7735.

28 A. Hlaváček, A. Sedlmeier, P. Skládal and H. H. Gorris, *ACS Appl. Mater. Interfaces*, 2014, **6**, 6930–6935.

29 Z. E. Liu, J. Wang, Y. Li, X. X. Hu, J. W. Yin, Y. Q. Peng, Z. H. Li, Y. W. Li, B. M. Li and Q. Yuan, *ACS Appl. Mater. Interfaces*, 2015, **7**, 19416–19423.

30 A. Sedlmeier and H. H. Gorris, *Chem. Soc. Rev.*, 2015, **44**, 1526–1560.

31 A. G. Dong, X. C. Ye, J. Chen, Y. J. Kang, T. Gordon, J. M. Kikkawa and C. B. Murray, *J. Am. Chem. Soc.*, 2011, **133**, 998–1006.

32 Z. G. Chen, H. L. Chen, H. Hu, M. X. Yu, F. Y. Li, Q. Zhang, Z. G. Zhou, T. Yi and C. H. Huang, *J. Am. Chem. Soc.*, 2008, **130**, 3023–3029.

33 S. Wilhelm, M. Kaiser, C. Wurth, J. Heiland, C. Carrillo-Carrion, V. Muhr, O. S. Wolfbeis, W. J. Parak, U. Resch-Genger and T. Hirsch, *Nanoscale*, 2015, **7**, 1403–1410.

34 U. Kostiv, V. Lobaz, J. Kucka, P. Svec, O. Sedlacek, M. Hruby, O. Janouskova, P. Francova, V. Kolarova, L. Sefc and D. Horak, *Nanoscale*, 2017, **9**, 16680–16688.

35 J. M. Harris and R. B. Chess, *Nat. Rev. Drug Discovery*, 2003, **2**, 214–221.

36 E. L. Bentzen, I. D. Tomlinson, J. Mason, P. Gresch, M. R. Warnement, D. Wright, E. Sanders-Bush, R. Blakely and S. J. Rosenthal, *Bioconjugate Chem.*, 2005, **16**, 1488–1494.

37 M. Franek, I. Diblikova, I. Cernoch, M. Vass and K. Hruska, *Anal. Chem.*, 2006, **78**, 1559–1567.

38 F. Wang, Y. Han, C. S. Lim, Y. H. Lu, J. Wang, J. Xu, H. Y. Chen, C. Zhang, M. H. Hong and X. G. Liu, *Nature*, 2010, **463**, 1061–1065.

39 A. Hlaváček, M. Peterek, Z. Farka, M. J. Mickert, L. Prechtl, D. Knopp and H. H. Gorris, *Microchim. Acta*, 2017, **184**, 4159–4165.

40 G. T. Hermanson, *Bioconjugate Techniques (Second Edition)*, Academic Press, New York, 2008.

41 C. R. Becer, R. Hoogenboom and U. S. Schubert, *Angew. Chem., Int. Ed.*, 2009, **48**, 4900–4908.

42 A. Roda, M. Mirasoli, B. Roda, F. Bonvicini, C. Colliva and P. Reschiglian, *Microchim. Acta*, 2012, **178**, 7–28.

43 B. Pang, C. Zhao, L. Li, X. L. Song, K. Xu, J. Wang, Y. S. Liu, K. Y. Fu, H. Bao, D. D. Song, X. J. Meng, X. F. Qu, Z. P. Zhang and J. Li, *Anal. Biochem.*, 2018, **542**, 58–62.

44 A. Roetschi, H. Berthoud, R. Kuhn and A. Imdorf, *Apidologie*, 2008, **39**, 362–371.

45 A. Hlaváček, M. J. Mickert, T. Soukka, S. Lahtinen, T. Tallgren, N. Pizúrová, A. Król and H. H. Gorris, *Anal. Chem.*, 2019, **91**, 1241–1246.

46 S. Lahtinen, A. Lyytikainen, N. Sirkka, H. Pakkila and T. Soukka, *Microchim. Acta*, 2018, **185**, 8.

47 S. P. Djordjevic, K. Noone, L. Smith and M. A. Z. Hornitzky, *J. Apic. Res.*, 1998, **37**, 165–173.

48 E. Forsgren, A. C. Lundhagen, A. Imdorf and I. Fries, *Microb. Ecol.*, 2005, **50**, 369–374.

49 W. X. Pan, J. W. Zhao and Q. S. Chen, *J. Agric. Food Chem.*, 2015, **63**, 8068–8074.

50 Z. Q. Liang, X. C. Wang, W. Zhu, P. P. Zhang, Y. X. Yang, C. Y. Sun, J. J. Zhang, X. R. Wang, Z. Xu, Y. Zhao, R. F. Yang, S. L. Zhao and L. Zhou, *ACS Appl. Mater. Interfaces*, 2017, **9**, 3497–3504.

51 B. R. Jin, S. R. Wang, M. Lin, Y. Jin, S. J. Zhang, X. Y. Cui, Y. Gong, A. Li, F. Xu and T. J. Lu, *Biosens. Bioelectron.*, 2017, **90**, 525–533.

276

Paper XV

Versatile bioconjugation strategies of PEG-modified upconversion nanoparticles for bioanalytical applications

Kostiv, U.; Farka, Z.; Mickert, M. J.; Gorris, H. H.; Velychkivska, N.; Pop-Georgievski, O.; Pastucha, M.; Odstrčilíková, E.; Skládal, P.; Horák, D.

(U.K. and Z.F. contributed equally)

Contribution:

Design of experiments, bioconjugation of UCNPs, development and optimization of sandwich immunoassay, data evaluation, participation in manuscript writing

Versatile Bioconjugation Strategies of PEG-Modified Upconversion Nanoparticles for Bioanalytical Applications

Uliana Kostiv,[⊥] Zdeněk Farka,[⊥] Matthias J. Mickert, Hans H. Gorris, Nadiia Velychkivska, Ognen Pop-Georgievski, Matěj Pastucha, Eliška Odstrčilíková, Petr Skládal, and Daniel Horák*

ACCESS | Metrics & More | Article Recommendations | Supporting Information

ABSTRACT: Lanthanide-doped upconversion nanoparticles (UCNPs) display highly beneficial photophysical features for background-free bioimaging and bioanalysis; however, they are instable in high ionic strength buffers, have no functional groups, and are nonspecifically interacting. Here, we have prepared NIR-excitable UCNPs that are long-term colloidally stable in buffered media and possess functional groups. Heterobifunctional poly(ethylene glycol) (PEG) linkers bearing neridronate and alkyne or maleimide were attached to UCNPs via a ligand exchange. Streptavidin (SA)-conjugates were prepared by click reaction of UCNP@PEG-alkyne and SA-azide. Antihuman serum albumin pAbF antibody was modified with azide groups and conjugated to UCNP@PEG-alkyne via click reaction; alternatively, the antibody, after mild reduction of its disulfide bonds, was conjugated to UCNP@PEG-maleimide. We employed these nanoconjugates as labels for an upconversion-linked immunosorbent assay. SA-based labels achieved the lowest LOD of 0.17 ng/mL for the target albumin, which was superior compared to a fluorescence immunoassay (LOD 0.59 ng/mL) or an enzyme-linked immunoassay (LOD 0.56 ng/mL).
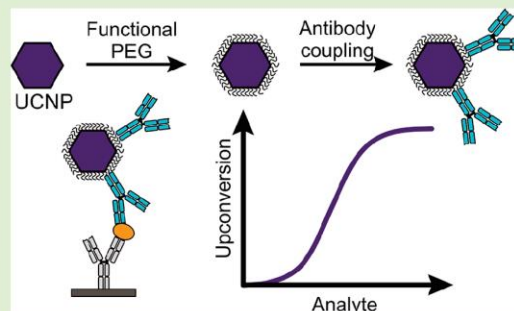
INTRODUCTION

Lanthanide-doped UCNPs have gained strong interest in various biomedical applications such as *in vitro*[1] and *in vivo* imaging,[2] drug and gene delivery,[3] optogenetics,[4] photodynamic and photothermal therapy,[5] bioassays, and biosensors.[6,7] The main advantage of UCNPs is the ability to convert two or more absorbed low-energy near-infrared (NIR) photons to one emitted photon of higher energy.[8] Compared to conventional luminescent materials, such as organic dyes, semiconductor nanocrystals, or metal complexes, UCNPs have many favorable optical properties, including a narrow line-like emission, high photostability, long emission lifetime, no blinking, and tunable emission wavelengths.[9] As the UCNPs absorb NIR irradiation, light scattering and photoinduced damage of living tissues is minimized.[10] Moreover, NIR radiation delivers light deep into the tissue, which is beneficial for many biological applications.[11] UCNPs can be detected in the organism in real-time with low optical background interference and a high signal-to-noise ratio, which is vital for sensing applications, including food assays, hazard detection, and medical diagnosis.[12,13]

UCNPs are typically composed of an optically inert crystal host lattice codoped with optically active lanthanide ions.[14] The most efficient host matrix is the hexagonal (β) phase structure of alkaline rare-earth fluoride nanocrystals doped

with an optically active sensitizer (Yb^{3+}) and activator (Er^{3+}, Ho^{3+}, or Tm^{3+}).[15] Variations in selection of activators lead to a corresponding shift of the anti-Stokes emission, allowing one to tune the emission wavelength according to the requirements. An optically inert NaYF$_4$-shell prevents surface quenching by water increasing the brightness of the particle.[16]

UCNPs are commonly synthesized in high-boiling nonpolar solvents at elevated temperatures in the presence of stabilizers, yielding high-quality monodisperse nanocrystals that are, however, hydrophobic in nature.[17] Subsequent surface modification of the hydrophobic particles is therefore essential to render them dispersible in aqueous media, minimize nonspecific interactions with proteins and cells, and introduce reactive functional groups for conjugations with biomolecules.[18] Various surface modification strategies were developed, such as coating with polyelectrolytes via a layer-by-layer approach, encapsulation into a silica shell, and ligand exchange with amphiphilic and hydrophilic polymers, for example, PEG,

poly(acrylic acid), polyethylenimine, poly(vinylpyrrolidone), poly(maleic anhydride-alt-1-octadecene), dextran, chitosan, and so forth.[19−21] Polymers containing anchoring end-groups, such as hydroxyl, amine, carboxylic or sulfonic acid, and phosphate or phosphonate groups, have also been exploited to modify the surface of UCNPs.[22] While all these coating strategies yield water dispersible UCNPs, an optimal modification that produces colloidally stable, even in high ionic strength buffers, and functional particles is still missing. Up-to-date, researchers described coating with PEG terminated by bisphosphonate or tetraphosphonate anchoring end-groups that proved to be stable in phosphate buffered saline (PBS).[23,24] These coatings are effective because phosphates and phosphonates strongly bind to lanthanide ions.[25]

The aim of this work was to develop a simple surface modification strategy for UCNPs, which would ensure their long-term colloidal stability in buffered media and introduce functional groups for subsequent conjugation with biomolecules. Monodisperse $NaYF_4:Yb^{3+}/Tm^{3+}@NaYF_4$ core−shell nanoparticles were prepared and modified by neridronate-PEG-alkyne or neridronate-PEG-maleimide via one-step ligand exchange and subsequently conjugated to streptavidin or an anti-HSA antibody. These biomacromolecular labels were employed in a sandwich immunoassay for the detection of human serum albumin (HSA), a marker of the albuminuria, pathological condition of the kidney.

■ EXPERIMENTAL SECTION

Materials and Chemicals. Anhydrous lanthanide chlorides, that is, yttrium(III), ytterbium(III), and thulium(III) chloride (99%), ammonium hydrogen difluoride, biotin N-hydroxysuccinimide ester, octadec-1-ene (90%), sodium L-ascorbate, tris(2-carboxyethyl)-phosphine hydrochloride (TCEP), sodium azide, human serum albumin (HSA), bovine serum albumin (BSA), bovine γ-globulin (BGG), horseradish peroxidase (HRP), ethanolamine, Tween 20, potassium fluoride, and glucose were purchased from Sigma-Aldrich (St. Luis, MO, U.S.A.). NHS-PEG-N$_3$ (M_w = 388 Da) was purchased from Thermo Fisher Scientific (Waltham, MA, U.S.A.) and α-NHS-ω-alkyne poly(ethylene glycol) (NHS-PEG-Alk; $M_{w,PEG}$ = 5,475 Da) and α-maleimidohexanoic-ω-NHS (NHS-PEG-Mal; $M_{w,PEG}$ = 5,475 Da) were obtained from Rapp Polymere (Tübingen, Germany). Streptavidin-azide (SA-azide) was obtained from Protein Mods (Madison, WI, U.S.A.). Sodium neridronate [(6-amino-1-hydroxy-1-phosphono-hexyl)phosphonic acid monosodium salt] was synthesized according to previous reports.[26,27] The monoclonal mouse-anti HSA antibody (clone AL-01) was purchased from Exbio (Prague, Czech Republic). UCNPs conjugated with a fluorescein isothiocyanate (FITC)-labeled swine polyclonal antibody (pAbF; Sevapharma; Prague, Czech Republic) were used as a detection label. Cellulose dialysis membranes (MWCO = 3.5, 14, 100, and 300 kDa) were purchased from Spectrum Europe (Breda, Netherlands). Ultracel YM-10 and YM-100 Microcon centrifugal filters (MWCO = 10 and 100 kDa, respectively) were obtained from Sigma-Aldrich. All other chemicals were purchased from commercial sources and used without further purification. Buffers were prepared with ultrapure water obtained by reverse osmosis with UV treatment (Milli-Q Gradient A10 system; Millipore, Darmstadt, Germany).

Conjugation of Detection Antibody with Biotin. The detection antibody was biotinylated according to our previous work.[28,29] In short, the pAbF was diluted in PBS (50 mM phosphate, 150 mM NaCl; pH 7.4) to a concentration of 5 mg/mL and NHS-biotin was dissolved in anhydrous dimethylformamide (20 mg/mL). Subsequently, the antibody was mixed with a 20-fold molar excess of NHS-biotin (100 μL of pAbF + 1.5 μL NHS-biotin) and incubated at room temperature (RT) for 2 h. The pAbF-biotin conjugate was then purified using a Microcon centrifugal unit YM-100 transferred to PBS and stored at 4 °C in the concentration of 2 mg/mL.

Conjugation of Detection Antibody and HRP. The pAbF was conjugated to HRP according to our previous work.[29−31] HRP (3.5 mg/mL in water) was oxidized with 8 mM sodium periodate (added as 88 mM solution in water) at 22 °C for 10 min in the dark under mild shaking for the generation of aldehyde groups. The reaction was quenched by adding 6.5 μL of 10% glycerol per 1 mL of solution (final concentration 50 mM), followed by the purification of the oxidized HRP using a Microcon centrifugal unit YM-10 with three repeated additions of 5 mM sodium acetate buffer (pH 4.4) and subsequent centrifugations. The HRP had a final concentration of 2.94 mg/mL.

For the conjugation reaction, the oxidized HRP was added to the antibody solution (2 mg/mL in 100 mM carbonate/bicarbonate buffer; pH 9.5) in a 1:1 (v/v) ratio, resulting in a 5-fold molar excess of the enzyme. The solution was mixed gently at 22 °C for 2 h in the dark. Then, 10 μL of a solution containing 5 M sodium cyanoborohydride in 1 M NaOH was added per 1 mL of the mixture to specifically reduce the Schiff base at 4 °C overnight. Blocking of the unreacted aldehyde groups on the oxidized HRP was done by the addition of 1 M ethanolamine (50 μL; pH 9) per 1 mL of solution (30 min, 22 °C, mild shaking). Finally, the pAbF-HRP conjugate was purified using a Microcon YM-100 unit, transferred to PBS, and stored at 4 °C in the concentration equivalent to 2 mg of the antibody/mL.

Synthesis of $NaYF_4:Yb^{3+}/Tm^{3+}$ Core Nanoparticles. $NaYF_4:Yb^{3+}/Tm^{3+}$ nanoparticles were synthesized according to an earlier procedure with minor modifications.[32] Typically, YCl_3 (0.795 mmol), $YbCl_3$ (0.2 mmol), $TmCl_3$ (0.005 mmol), oleic acid (6 mL), and octade-1-ene (15 mL) were mixed in a 100 mL three-neck flask. The mixture was heated to 160 °C for 30 min under a gentle flow of argon to get a homogeneous yellowish solution that was cooled down to RT. NaOH (4 mmol) and $NH_4F\cdot HF$ (2.5 mmol) were dissolved in methanol (10 mL); the solution was added dropwise to the mixture and was slowly heated to 70 °C under an argon flow. After evaporation of methanol, the temperature was increased to 300 °C and held for 1.5 h. The resulting $NaYF_4:Yb^{3+}/Tm^{3+}$ nanoparticles were collected by centrifugation (3,460 g, 30 min), washed with hexane, and precipitated in ethanol. This procedure was repeated twice. To prepare oleic acid-free $NaYF_4:Yb^{3+}/Tm^{3+}$ nanoparticles, the particles were thoroughly washed with ethanol (14 mL, 5 times), ethanol/water mixture (1:1 v/v, 14 mL, 5 times), and water (14 mL, 5 times) using sedimentation/redispersion.

Synthesis of $NaYF_4:Yb^{3+}/Tm^{3+}@NaYF_4$ Core−Shell Nanoparticles. $NaYF_4:Yb^{3+}/Tm^{3+}@NaYF_4$ core−shell particles were synthesized according to a previously described protocol.[33] A mixture of YCl_3 (1 mmol) and oleic acid (6 mL) in octade-1-ene (30 mL) was heated at 160 °C for 30 min with stirring under an argon atmosphere and cooled down to RT. A dispersion of 150 mg $NaYF_4:Yb^{3+}/Tm^{3+}$ core nanoparticles in hexane, 4 mmol NaOH, and 2.5 mmol $NH_4F\cdot HF$ in methanol was added dropwise. The mixture was gently heated to 120 °C under an argon atmosphere until hexane and methanol evaporated. The temperature was increased to 300 °C, kept constant for 1.5 h, and cooled to RT. The resulting $NaYF_4:Yb^{3+}/Tm^{3+}@NaYF_4$ nanoparticles were separated by centrifugation (3,460 g, 30 min), washed with hexane, and precipitated in ethanol. The procedure was repeated two times. To prepare oleic acid-free $NaYF_4:Yb^{3+}/Tm^{3+}@NaYF_4$ core−shell nanoparticles, the particles were thoroughly washed with ethanol (14 mL, 5 times), ethanol/water mixture (1:1 v/v, 14 mL, 5 times), and water (14 mL, 5 times) using sedimentation/redispersion.

Synthesis of Neridronate-PEG-Alkyne (Ner-PEG-Alk) and Neridronate-PEG-Maleimide (Ner-PEG-Mal). Ner-PEG-Alk and Ner-PEG-Mal (Figure 1) were prepared according to previously published reports.[27,34] Sodium neridronate (0.32 g) was dissolved in 0.1 M PBS (10 mL, pH 7.4), the solution was cooled to 5 °C, NHS-PEG-Alk or NHS-PEG-Mal (0.5 g) was added, and the mixture was stirred at 5 °C for 12 h and dialyzed (MWCO = 3.5 kDa) against water for 7 days (water was exchanged twice per day) and freeze-dried.
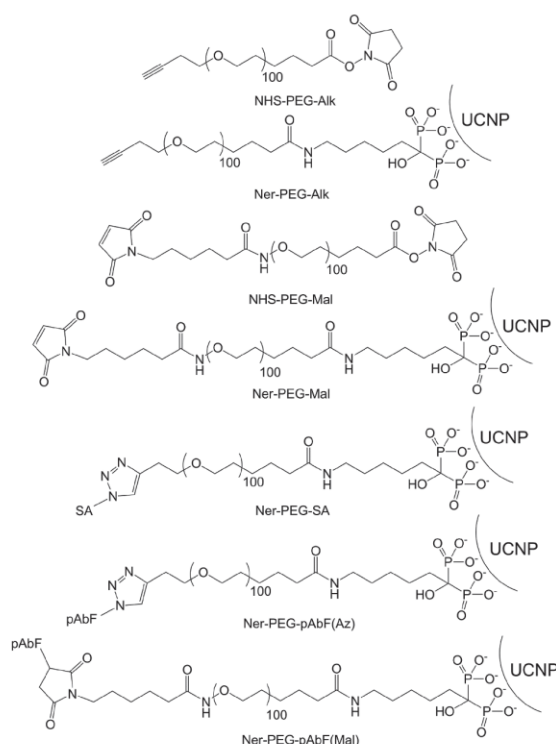
Figure 1. Compounds used for the modification of UCNPs. α-NHS-ω-alkyne poly(ethylene glycol) (NHS-PEG-Alk), neridronate-PEG-alkyne (Ner-PEG-Alk), α-maleinimidohexanoic-ω-NHS (NHS-PEG-Mal), neridronate-PEG-maleimide (Ner-PEG-Mal), Ner-PEG-pAbF-(Az), Ner-PEG-pAbF(Mal), and Ner-PEG-SA. NHS, N-hydroxysuccinimide; SA, streptavidin; pAbF, FITC-labeled swine polyclonal antibody; Az, azide.

Substitution of NHS end-groups (k) of NHS-PEG-Alk or NHS-PEG-Mal with neridronate was calculated from ^{1}H NMR spectra as $k = (2 \times I_6/2 \times I_{a'}) \times 100$, where I_6 and $I_{a'}$ are the integrals of peaks 6 and a', multiplied with the number of protons in the corresponding group (Figure 2).

Modification of UCNPs with Ner-PEG-Alk. Ner-PEG-Alk (6 or 16 mg) was added to 4 mL of an aqueous dispersion of NaYF$_4$:Yb^{3+}/Tm^{3+} (6 mg/mL) or NaYF$_4$:Yb^{3+}/Tm^{3+}@NaYF$_4$ nanoparticles (16 mg/mL), and the mixture was stirred at RT for 12 h. The resulting NaYF$_4$:Yb^{3+}/Tm^{3+}-PEG-Alk and NaYF$_4$:Yb^{3+}/Tm^{3+}@NaYF$_4$-PEG-Alk nanoparticles were dialyzed (MWCO = 14 kDa) against water to remove unreacted Ner-PEG-Alk. NaYF$_4$:Yb^{3+}/Tm^{3+}-PEG-Alk and NaYF$_4$:Tm^{3+}@NaYF$_4$-PEG-Alk nanoparticles had a final concentration of 6 or 16 mg/mL, respectively, as determined by thermogravimetric analysis (>350 °C).

Conjugation of NaYF$_4$:Yb^{3+}/Tm^{3+}@NaYF$_4$-PEG-Alk Nanoparticles with pAbF Antibody. To prepare the azide (Az)-modified pAbF antibody, the antibody (6 mg/mL; 14.7 μL) and NHS-PEG-N$_3$ (24.7 or 247 μL; 4 mM) were mixed at RT for 2 h and washed three times with PBS (0.5 mL; pH 7.5) using YM-10 Ultracel filters (centrifugation for 30 min at 14,000 g) to remove the residual NHS-PEG-N$_3$. The final volume of pAbF-azide was 125 μL.

To prepare NaYF$_4$:Yb^{3+}/Tm^{3+}@NaYF$_4$-PEG-pAbF(Az) particles, pAbF-azide (75 μL), sodium L-ascorbate (20 μL; 20 mg/mL), and NaYF$_4$:Yb^{3+}/Tm^{3+}@NaYF$_4$-PEG-Alk nanoparticles (4.25 mg) in 25 mM Tris buffer (1 mL; pH 7.5) were purged with Ar for 30 min. The click reaction was started by the addition of 0.05 M CuSO$_4$ (10 μL). The NaYF$_4$:Yb^{3+}/Tm^{3+}@NaYF$_4$-PEG-pAbF(Az) nanoparticles were

dialyzed twice (MWCO = 300 kDa) against 50 mM Tris buffer (2 l; pH 7.5) containing 0.05% NaN$_3$ and 1 mM KF at 4 °C for 12 h and stored in the same buffer at 4 °C.

Conjugation of NaYF$_4$:Yb^{3+}/Tm^{3+}@NaYF$_4$-PEG-Mal Nanoparticles with pAbF Antibody. To prepare NaYF$_4$:Yb^{3+}/Tm^{3+}@NaYF$_4$-PEG-pAbF(Mal) particles, disulfide bonds of pAbF were mildly reduced, and the resulting free thiols reacted with NaYF$_4$:Yb^{3+}/Tm^{3+}@NaYF$_4$-PEG-Mal nanoparticles. pAbF (6 μL; 11 mg/mL) and 8 mM TCEP (5 μL) in 0.1 M PBS were mixed at RT for 1 h, NaYF$_4$:Yb^{3+}/Tm^{3+}@NaYF$_4$-PEG-Mal nanoparticles (5.5 mg) in 25 mM Tris buffer (0.5 mL; pH 7.5) were added and the mixture was stirred at RT for 1 h. The resulting NaYF$_4$:Yb^{3+}/Tm^{3+}@NaYF$_4$-PEG-pAbF(Mal) particles were dialyzed twice (MWCO = 300 kDa) against 50 mM Tris buffer (2 l; pH 7.5) containing 0.05% NaN$_3$ (0.5 g) and 1 mM KF at 4 °C for 12 h and stored in the same buffer at 4 °C.

Conjugation of UCNPs with Streptavidin (SA). SA-conjugated nanoparticles were prepared via Cu(I)-catalyzed click reaction with SA-azide according to previous publications.[1,34] SA-azide (9, 50, or 25 μL; 1 mg/mL), sodium L-ascorbate (20 μL; 20 mg/mL), and NaYF$_4$:Yb^{3+}/Tm^{3+}-PEG-Alk core (24 nm; 3 mg), NaYF$_4$:Yb^{3+}/Tm^{3+}-PEG-Alk core (44 nm; 7 mg) or NaYF$_4$:Yb^{3+}/Tm^{3+}@NaYF$_4$-PEG-Alk core−shell nanoparticles (38 × 28 nm; 8 mg) in 25 mM Tris buffer (1 mL; pH 7.5) were purged with Ar for 30 min to remove oxygen. The click reaction was catalyzed by Cu(I) generated *in situ* from sodium L-ascorbate and 0.05 M CuSO$_4$ (10 μL). Resulting SA-conjugated nanoparticle dispersions were sonicated for 10 min, dialyzed twice (MWCO = 100 kDa) against 50 mM Tris buffer (pH 7.5) containing 0.05% NaN$_3$ (0.5 g) and 1 mM KF at 4 °C for 12 h, and stored in the same buffer at 4 °C.

Characterization of Nanoparticles. The particle morphology was investigated by a Tecnai G2 Spirit Twin 12 transmission electron microscope (TEM; FEI, Czech Republic). The size of the particles was determined by measuring at least 300 nanoparticles from TEM micrographs using the software ImageJ.

Hydrodynamic particle diameter (D_h), size distribution (polydispersity PD), and ζ-potential were determined by dynamic light scattering (DLS) in water or Tris buffer on a ZEN 3600 Zetasizer Nano (Malvern Instruments, U.K.) at 25 °C. D_h and PD were taken from the intensity-weighted distribution function obtained by CONTIN analysis of the correlation function obtained in the Malvern software.

Thermogravimetric analysis (TGA) was performed using a PerkinElmer TGA 7 analyzer (Norwalk, CT, U.S.A.) from 30 to 850 °C in air at a heating rate of 10 °C/min. Grafting density of PEG (σ; molecules per nm^2) on the particle surface was calculated from TGA using eq 1[18]

$$\sigma = \frac{w_{PEG} \cdot \rho \cdot V \cdot N_A}{(1 - w_{PEG}) \cdot M_{PEG} \cdot S} \tag{1}$$

where w_{PEG} is the weight fraction of PEG, ρ is the bulk density of NaYF$_4$ (4.21 g/cm^3), V and S are the volume and surface area of a particle, respectively, N_A is Avogadro's number, and M_{PEG} is the molecular weight of Ner-PEG-Alk or Ner-PEG-Mal (5,637 g/mol).

ATR FTIR spectra were recorded on a Thermo Nicolet Nexus 870 FTIR spectrometer (Madison, WI, U.S.A.) purged with dry air and equipped with a liquid nitrogen-cooled mercury cadmium telluride detector. Spectra were measured using a Golden Gate single reflection ATR cell (Specac; Orpington, U.K.) equipped with a diamond internal reflection ATR crystal. A typical spectrum contained 256 scans acquired with a resolution of 4 cm^{-1}. From the acquired spectra, a spectrum of water vapor (an atmosphere spectrum) was subtracted and the linear baseline correction and ATR correction were applied. Note, the spectral region 2,500−1,850 cm^{-1} was not shown due to presence of the bands of the ATR crystal.

^{1}H NMR and ^{1}H−^{1}H correlation spectroscopy (COSY) spectra were acquired with a Bruker Avance III 600 spectrometer (Bruker; Billerica, MA, U.S.A.). Measurement conditions were as follows: 90° pulse width 10 μs, relaxation delay 10 s, spectral width 10,822 Hz,

280
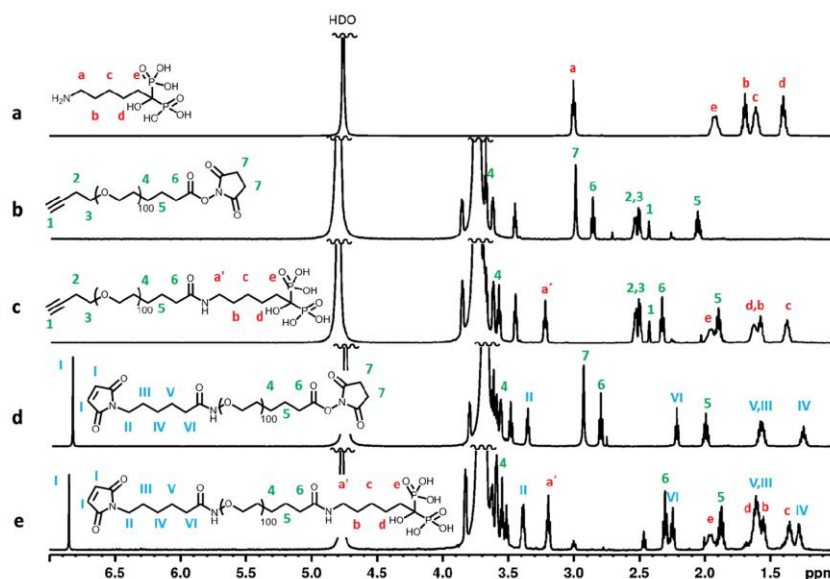
Figure 2. High-resolution ^{1}H NMR spectra (600 MHz) of (a) neridronate, (b) NHS-PEG-Alk, (c) Ner-PEG-Alk, (d) NHS-PEG-Mal, and (e) Ner-PEG-Mal in D_2O at 25 °C.

acquisition time 3.02 s, and 16 scans. Two-dimensional COSY spectra were collected with 1,024 points in F2 and 128 points in F1 dimensions over a sweep width of 18 ppm with 64 scans. The spectra were processed in Topspin 4.0.5 using standard methods with zero-degree shifted sine-squared apodization in both dimensions and zero filling in F1 to yield a transformed 2D data set of 1,024 by 1,024 points. The integrated intensities were determined using the spectrometer integration software with an accuracy of ±1%. During the measurement, the temperature was kept constant within ±0.2 K using a BVT 3000 temperature unit.

X-ray photoelectron spectroscopy was performed using a K-Alpha$^+$ XPS spectrometer (Thermo Fisher Scientific, U.K.) operating at a base pressure of 1.0×10^{-7} Pa. Data acquisition and processing were performed using the Thermo Avantage software. All particles analyzed by XPS were dialyzed (MWCO = 300 kDa) against water before measurements. The nanoparticles were spread on silicon substrates and analyzed using a microfocused (spot size 400 μm), mono-chromated Al Kα X-ray radiation with a pass energy of 200 eV for survey and 50 eV for high-energy resolution core level spectra. The X-ray angle of incidence was 30° and the emission angle was along the surface normal. Dual-charge compensation system employing electrons and low energy Ar$^+$ ions was employed during the measurements. The analyzer transmission function, Scofield sensitivity factors, and effective attenuation lengths (EALs) for photo-electrons were applied for quantification. EALs were calculated using the standard TPP-2 M formalism. The binding energy scale of the XPS spectrometer was calibrated by the well-known positions of the C 1s C—C and C—H, C—O, and C(=O)—O peaks of poly(ethylene terephthalate) and Cu 2p, Ag 3d, and Au 4f peaks of Cu, Ag, and Au metals, respectively. All measured spectra were charge referenced to the C 1s contribution at a binding energy of 285.0 eV attributed to C—C and C—H moieties.

Upconversion emission spectra were recorded on a FS5 spectrofluorometer (Edinburgh Instruments; Livingston, U.K.) coupled with a 980 nm CW infrared diode laser with nominal power 2 W (MDL-III-980; CNI Optoelectronics; Changchun, China).

BSA-Biotin Assay. A 96-well microtiter plate (μClear, high binding; Greiner) was coated with serial dilutions of BSA-biotin (0.1, 1, and 10 μg/mL, Sigma-Aldrich) in coating buffer (50 mM

NaHCO$_3$/Na$_2$CO$_3$, 0.05% NaN$_3$, pH 9.6; 100 μL) at 4 °C overnight. The plate was washed with washing buffer (50 mM NaH$_2$PO$_4$/Na$_2$HPO$_4$, 0.01% Tween 20, 0.05% NaN$_3$; pH 7.4, 250 μL) four times in a HydroFlex microplate washer (Tecan; Männedorf, Switzerland) and blocked with blocking buffer (50 mM NaH$_2$PO$_4$/Na$_2$HPO$_4$, 0.05% NaN$_3$; pH 7.4, 1% BSA, 200 μL) for 1 h. After four washings steps, uncoated wells (negative control) and BSA-biotin-coated wells were incubated with 100 μL of serial dilutions of the 24 nm NaYF$_4$:Yb^{3+}/Tm^{3+}-PEG-SA core and 37 × 27 nm core−shell NaYF$_4$:Yb^{3+}/Tm^{3+}@NaYF$_4$-PEG-SA particles in assay buffer (0.2% BSA, 0.5% BGG, 50 mM Tris, 150 mM NaCl, 5 mM EDTA, 0.2 wt % poly(vinyl alcohol) (M_w = 6,000 Da), 1% glucose, 0.05% NaN$_3$, 1 mM KF, and 0.01% Tween 20; pH 7.5) for 1 h. After the last incubation step, the plate was washed four times, dried on air, and scanned using a custom-build upconversion microtiter plate reader Hidex Chameleon (Finland).

Upconversion-Linked Immunosorbent Assay. For the ULISA with UCNP-antibody conjugates, a μClear plate was coated with monoclonal anti-HSA antibody (AL-01, 42 μg/mL in coating buffer, 100 μL/well) and incubated at 4 °C overnight. All the following steps were carried out at RT; after each step, the plate was washed four times with 250 μL of washing buffer. The plate was blocked for 1 h with 200 μL of washing buffer containing 25% SuperBlock. Standard dilutions of HSA in assay buffer were added (100 μL/well) and the mixture was incubated for 1 h. Subsequently, the UCNP-Ab conjugates (100 μL in assay buffer) were added and incubation continued for 1 h, as described earlier.[35] After the last washing step, the plate was dried at RT.

The ULISA with UCNP-SA conjugates was performed using the above-described procedure with different detection steps. After the incubation with HSA, 100 μL of the biotinylated detection antibody (pAbF-biotin) in assay buffer was added and incubated for 1 h, followed by washing and incubation with UCNP-SA (100 μL in assay buffer) for 1 h.

Because off the presence of HSA in urine from healthy patients,[36,37] the urine for real sample analysis was first deproteinized by use of the Micron centrifugal unit YM-10 and then spiked with known HSA concentrations.[35]

The scanning was performed using a Hidex plate reader. Each well was scanned in a rectangular grid of 8 × 8 pixels with 1 s exposure

281
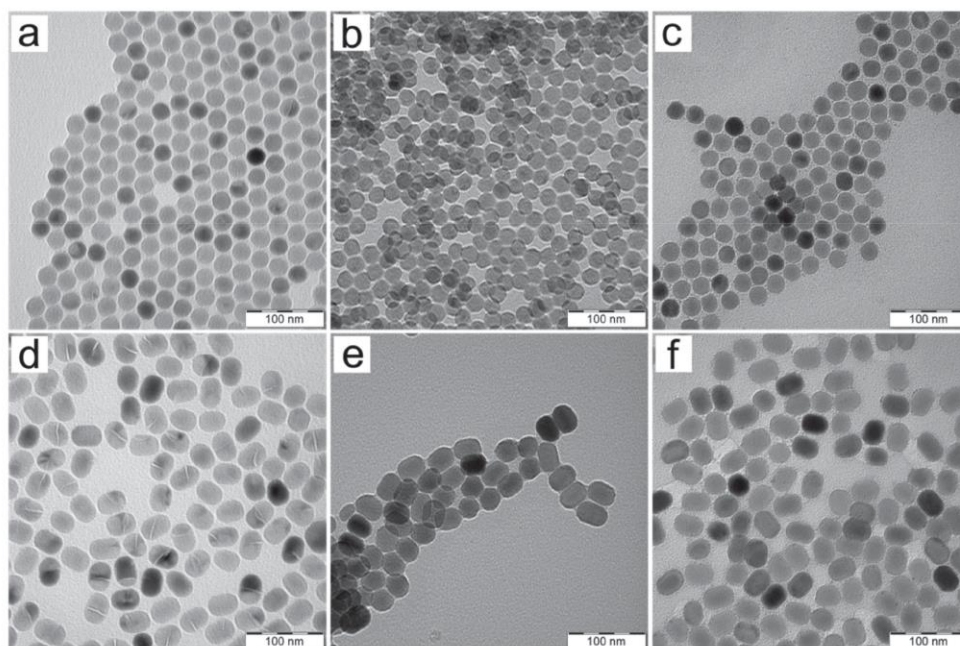
Figure 3. TEM micrographs of (a) OA-stabilized $NaYF_4$:Yb^{3+}/Tm^{3+}, (b) washed $NaYF_4$:Yb^{3+}/Tm^{3+}, (c) $NaYF_4$:Yb^{3+}/Tm^{3+}-PEG-SA, (d) OA-stabilized $NaYF_4$:Yb^{3+}/Tm^{3+}@$NaYF_4$, (e) washed $NaYF_4$:Yb^{3+}/Tm^{3+}@$NaYF_4$, and (f) $NaYF_4$:Yb^{3+}/Tm^{3+}@$NaYF_4$-PEG-SA nanoparticles.

time per pixel and a scanning step size of 0.1 mm. The truncated average of the luminescence intensities was calculated, excluding the 16 highest and 16 lowest values. A four-parameter logistic function was used for regression analysis of the calibration curves. The LOD was calculated from the regression curve as the concentration corresponding to the fitted background level plus three times the standard deviation of the blank measurement.[34] The signal-to-background (S/B) ratios were calculated as the ratio between the signal for the highest HSA concentration (10 μg/mL) and blank (no HSA in the sample).

Fluorescence- and Enzyme-Based Immunoassays. The performance of the sandwich upconversion-linked immunosorbent assay (ULISA) was compared to a fluorescence immunoassay (FIA) and an enzyme-linked immunoassay (ELISA) for HSA. The FIA was performed in a 96-well black high-binding microtiter plate. Immobilization of the capture antibody, blocking, and washing procedures were the same as described for the ULISA. After capturing the HSA, pAbF-biotin in assay buffer (100 μL, 1 h) was used as a detection conjugate. The readout was done using a Synergy 2 reader (BioTek; Winooski, VT, U.S.A.) with Xe flash lamp excitation, excitation filter 485/20 nm, emission filter 528/20 nm, and dichroic mirror Top 510 nm.

For the ELISA, the same assay protocol was used except for the detection conjugate binding and the enzymatic amplification step. HRP-pAbF conjugate (20 μg/mL; 100 μL) was allowed to bind for 1 h, followed by the addition of 100 μL of 3,3′,5,5′-tetramethylbenzidine/hydrogen peroxide substrate solution (TestLine Clinical Diagnostics; Brno, Czech Republic). The enzymatic reaction was monitored using a Synergy 2 reader as the change of absorbance at 652 nm (A_{652}), followed by stopping using 1 M H_2SO_4 (100 μL) and readout at 450 nm (A_{450}).

■ RESULTS AND DISCUSSION

Upconversion Nanoparticles. To prepare uniformly sized UCNPs, high-temperature coprecipitation of lanthanide chlorides was used in the presence of oleic acid (OA) as a stabilizer. The morphology, size, and distribution of the nanoparticles were analyzed by TEM, which revealed uniformity and spherical shape of the OA-stabilized $NaYF_4$:Yb^{3+}/Tm^{3+} core nanoparticles with a diameter of D_n = 24 ± 1 nm (Figures 3a and S1a). To enhance the upconversion luminescence and prevent surface quenching, an inert epitaxial $NaYF_4$ shell was grown around the OA-stabilized $NaYF_4$:Yb^{3+}/Tm^{3+} core nanoparticles. The shape of the OA-stabilized $NaYF_4$:Yb^{3+}/Tm^{3+}@$NaYF_4$ core−shell nanoparticles was ellipsoidal due to the prevalent anisotropic shell formation. Anisotropic epitaxial shell growth could be caused by several factors, such as selective adsorption of OA ligands, ligand etching, and/or crystal lattice mismatch between core and shell.[38] The average size of the OA-stabilized $NaYF_4$:Yb^{3+}/Tm^{3+}@$NaYF_4$ core−shell nanoparticles was 38 ± 2 × 28 ± 2 nm, which includes a 14 × 4 nm-thick $NaYF_4$ shell (Figures 3d and S1d).

After the synthesis, the nanoparticles were hydrophobic due to the adsorbed OA stabilizer on their surface. To remove OA, both core and core−shell nanoparticles were thoroughly washed and transferred in water without any treatment with acid, which could damage the particles and reduce their luminescence efficacy.[19] Shape and size of the $NaYF_4$:Yb^{3+}/Tm^{3+} core and $NaYF_4$:Yb^{3+}/Tm^{3+}@$NaYF_4$ core−shell nanoparticles did not change after washing (D_n = 24 ± 1 and 38 ± 2 × 29 ± 1 nm, respectively; Figure 3b,e and S1b,e). After washing, the chemical compositions of the $NaYF_4$:Yb^{3+}/Tm^{3+} core and $NaYF_4$:Yb^{3+}/Tm^{3+}@$NaYF_4$ core−shell particles were confirmed by XPS analysis (Figure 4a). Let us note that the formation of shell decreased the XPS signals from the core, as the photoemission arises from the most outer layer of the particles (7−12 nm). The high-resolution XPS spectra of $NaYF_4$:Yb^{3+}/Tm^{3+} core showed the presence of the dominant

282
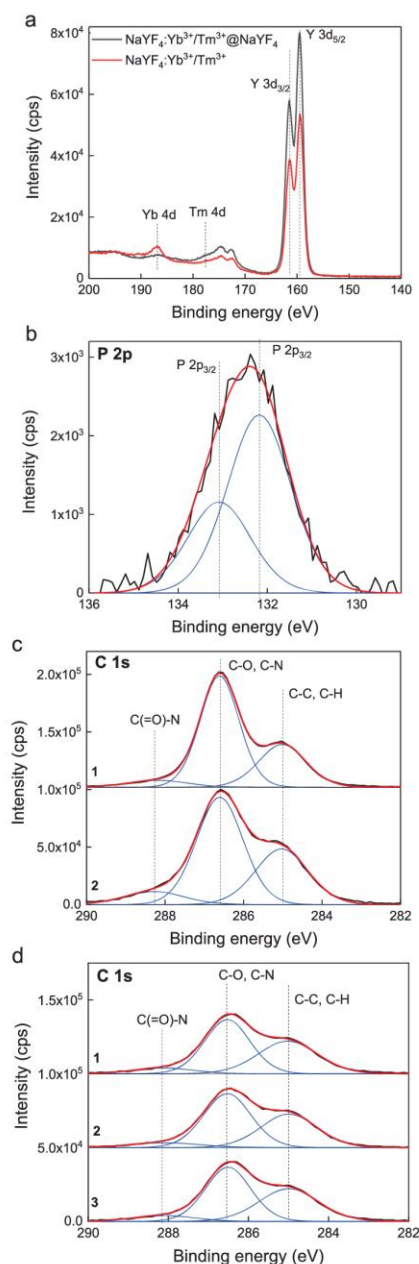
Figure 4. (a) Comparison of high-resolution XPS spectra of neat $NaYF_4$:Yb^{3+}/Tm^{3+} (red) and $NaYF_4$:Yb^{3+}/Tm^{3+}@$NaYF_4$ nanoparticles (black). (b) Representative P 2p high-resolution XPS spectra proving the immobilization of PEG-Ner on $NaYF_4$:Yb^{3+}/Tm^{3+} core and $NaYF_4$:Yb^{3+}/Tm^{3+}@$NaYF_4$ core−shell nanoparticles. (c) Representative C 1s high-resolution XPS spectra of $NaYF_4$:Yb^{3+}/Tm^{3+}@$NaYF_4$-PEG-Mal core−shell nanoparticles before (1) and after (2) immobilization of pAbF antibody. (d) Representative C 1s high-resolution XPS spectra of $NaYF_4$:Yb^{3+}/Tm^{3+}@$NaYF_4$-PEG-Alk nanoparticles before (1) and after immobilization of SA-azide (2) and pAbF-azide antibody (3). Black, measured data; red, fitted data; blue, individual contributions of functional groups on the nanoparticle surface.

Y 3d double peak at 159.5 eV and a minor Yb 4d peak at 186.9 eV. The Tm 4d peak at 177.6 eV could not be uniquely distinguished due to a low Tm amount and strong overlap with broad peak of the Y 3d plasmon loss. The successful formation of the $NaYF_4$ shell around the $NaYF_4$:Yb^{3+}/Tm^{3+} core was proven by increasing Y 3d contributions in the high-resolution XPS spectrum and the concomitant drop of the Yb 4d signals.

PEGylation of UCNPs. Even though the bare nanoparticles were dispersible in aqueous media, they irreversibly aggregated in higher ionic strength buffers, for example, PBS, due to the strong affinity of phosphate anions to lanthanides, leading to rapid loss of colloidal stability and aggregation of UCNPs.[19] This tendency to aggregation was observed also with other lanthanide-based[39] magnetic[40] and gold nanoparticles.[41] Therefore, $NaYF_4$:Yb^{3+}/Tm^{3+} core and $NaYF_4$:Yb^{3+}/Tm^{3+}@$NaYF_4$ core−shell nanoparticles were modified by heterotelechelic PEG containing both neridronate and alkyne or maleimide functional end-groups according to the following considerations: (i) PEG is widely used to prevent undesirable nonspecific adsorption of biomolecules and cells, as well as to sterically stabilize nanoparticles;[42] (ii) neridronate, a bisphosphonate, strongly binds to upconversion nanoparticles via chelation with lanthanide ions;[25] and (iii) the presence of a functional end-group on PEG chain enables subsequent immobilization of biomolecules, such as, antibodies and oligonucleotides, yielding bioconjugated nanoparticles with specificity for target structures.[43]

Ner-PEG-Alk and Ner-PEG-Mal were prepared by coupling of NHS-PEG-Alk or NHS-PEG-Mal with neridronate (Figure 1). To investigate the reaction, high-resolution ^{1}H NMR spectra of neridronate, NHS-PEG-Alk, Ner-PEG-Alk, NHS-PEG-Mal, and Ner-PEG-Mal were recorded (Figure 2). The spectrum of neridronate showed four characteristic peaks at 1.4−2.0 ppm and one triplet peak at 3.0 ppm assigned to CH_2 in α-position to the amine group (Figure 2a; signal "a"). The spectrum of NHS-PEG-Alk displayed two CH_2 peaks, one CH≡ peak at 2.4−2.6 ppm, and three CH_2 peaks next to PEG at 3.68, 2.86, and 2.06 ppm (Figure 2b; signals 4, 6, and 5, respectively), and one singlet peak from two CH_2 groups of NHS at 2.99 ppm (Figure 2b; signal 7). When neridronate was coupled to NHS-PEG-Alk, an amide bond was formed, resulting in a downfield shift of neridronate peak from 3.00 to 3.22 ppm (Figure 2c; signal "a" was shifted to "a′ "). Moreover, the upfield shift of the CH_2 peaks next to PEG was detected (Figure 2c; signals 4, 5, and 6). The most pronounced change was detected for CH_2 peak assigned to O=C−NH group of Ner-PEG-Alk (Figure 2c; signal 6 shifted from 2.86 to 2.33 ppm). Furthermore, the absence of neridronate and NHS peaks (Figure 2c; signal 7 and signal "a", respectively) confirmed high purity of Ner-PEG-Alk product without any residual NHS-PEG-Alk or neridronate.

Neridronate reacted with NHS-PEG-Mal in a similar way (Figure 2d,e). The substitution of NHS end-groups of NHS-PEG-Alk or NHS-PEG-Mal with neridronate, calculated from ^{1}H NMR spectra, reached 99.5 and 97.6% for Ner-PEG-Alk and Ner-PEG-Mal, respectively. Analysis of 2D COSY ^{1}H NMR spectra of Ner-PEG-Alk and Ner-PEG-Mal enabled assignment of proton chemical shifts to chemical structures of aforementioned substances (Figures S2 and S3, respectively).

Physicochemical Characterization of UCNPs. In the high-resolution XPS spectra, the presence of the neridronate on the $NaYF_4$:Yb^{3+}/Tm^{3+} core and $NaYF_4$:Yb^{3+}/Tm^{3+}@ $NaYF_4$ core−shell nanoparticles after the surface modification

by Ner-PEG-Alk and Ner-PEG-Mal led to the appearance of phosphorus P 2p doublet signals at about 132 eV (Figure 4b). The binding of Ner-PEG-Alk and Ner-PEG-Mal on the surface of the nanoparticles was further evidenced by the appearance of the characteristic dominating ethylene glycol C—O contribution in the high-resolution XPS C 1s spectrum at 286.7 eV (Figure 4c,d).[44]

To investigate the behavior of PEG-modified core and core–shell nanoparticles in aqueous media, hydrodynamic diameter (D_h) and polydispersity (PD) were measured by dynamic light scattering (DLS). D_h of NaYF$_4$:Yb^{3+}/Tm^{3+}-PEG-Alk and NaYF$_4$:Yb^{3+}/Tm^{3+}@NaYF$_4$-PEG-Alk nanoparticles in water was 113 nm (PD = 0.17; Figure S4a,b) and 116 nm (PD = 0.18; Figure S5a,b), respectively. D_h of NaYF$_4$:Yb^{3+}/Tm^{3+}-PEG-Mal core and NaYF$_4$:Yb^{3+}/Tm^{3+}@NaYF$_4$-PEG-Mal core–shell nanoparticles was 128 nm (PD = 0.23; Figure S4c,d) and 160 nm (PD = 0.13; Figure S5a,c), respectively. ζ-potential of the NaYF$_4$:Yb^{3+}/Tm^{3+} core and NaYF$_4$:Yb^{3+}/Tm^{3+}@NaYF$_4$ core–shell nanoparticles in water reached 40 and 33 mV, respectively. Such a high surface charge can be explained by the presence of Ln^{3+} ions on the particle surface. After surface modification by Ner-PEG-Alk, surface charge changed to 10 and 11 mV for NaYF$_4$:Yb^{3+}/Tm^{3+}-PEG-Alk and NaYF$_4$:Yb^{3+}/Tm^{3+}@NaYF$_4$-PEG-Alk nanoparticles, respectively. The ζ-potential of NaYF$_4$:Yb^{3+}/Tm^{3+}-PEG-Mal and NaYF$_4$:Yb^{3+}/Tm^{3+}@NaYF$_4$-PEG-Mal nanoparticles was almost neutral (−1 and 2 mV, respectively). Change in the particle surface charge proved successful modification of the particles by Ner-PEG-Alk and Ner-PEG-Mal. Moreover, the presence of PEG, serving as a steric barrier against aggregation, ensured colloidal stability of the UCNPs in water and Tris buffer.

The XPS results were further corroborated by ATR FTIR spectroscopy of washed NaYF$_4$:Yb^{3+}/Tm^{3+}@NaYF$_4$, NaYF$_4$:Yb^{3+}/Tm^{3+}@NaYF$_4$-PEG-Alk, and NaYF$_4$:Yb^{3+}/Tm^{3+}@NaYF$_4$-PEG-Mal nanoparticles (Figure S6). The spectrum of washed nanoparticles exhibited the characteristic bands of oleyl groups at 2,854 and 2,927 cm^{-1} attributed to symmetric and asymmetric CH$_2$ stretching vibrations.[45] The intensity of these bands was rather low, confirming efficient removal of OA from the particles during washing. Spectra of nanoparticles modified by Ner-PEG-Alk or Ner-PEG-Mal showed characteristic bands of CH$_2$ groups of PEG at 842, 962, 1,105, 1,241, 1,342, 1,465, and 2,881 cm^{-1}, confirming its presence on the NaYF$_4$:Yb^{3+}/Tm^{3+}@NaYF$_4$-PEG-Alk and NaYF$_4$:Yb^{3+}/Tm^{3+}@NaYF$_4$-PEG-Mal nanoparticles. Characteristic bands of alkyne and maleimide were not detected due to overlap with much stronger peaks of PEG. Despite thorough drying of the samples, some residual water remained adsorbed on the particles, as the ATR FTIR spectra presented broad peaks of water O—H stretching vibrations in 3,700–3,100 cm^{-1} region, which also overlapped with stretching vibrations of N—H groups of Ner and Mal.

The TGA of the NaYF$_4$:Yb^{3+}/Tm^{3+}@NaYF$_4$, NaYF$_4$:Yb^{3+}/Tm^{3+}@NaYF$_4$-PEG-Alk, and NaYF$_4$:Yb^{3+}/Tm^{3+}@NaYF$_4$-PEG-Mal nanoparticles is shown in Figure S7. The mass loss was considered between 150 and 600 °C, because adsorbed water was evaporated (<1 wt % loss) up to 150 °C. Weight loss of washed NaYF$_4$:Yb^{3+}/Tm^{3+}@NaYF$_4$ nanoparticles amounted to 1.3 wt %, which corresponded to residual OA bound to the particle surface. After surface modification with Ner-PEG-Alk and Ner-PEG-Mal, the weight loss of NaYF$_4$:Yb^{3+}@NaYF$_4$-PEG-Alk and NaYF$_4$:Yb^{3+}/Tm^{3+}@NaYF$_4$-PEG-Mal

nanoparticles corresponded to 20.4 and 21.4 wt %, that is, grafting density of PEG chains bound to the particle surface was 0.93 and 0.99 PEG/nm^2, respectively. These results correlated with the ATR FTIR and XPS analysis, indicating the presence of PEG on the particle surface.

Conjugation of UCNPs with Biomolecules. In the following experiments, biomolecules, SA or pAbF antibody, were conjugated to PEGylated nanoparticles, using three different routes (Figure 1): (i) attachment of SA-azide to the NaYF$_4$:Yb^{3+}/Tm^{3+}@NaYF$_4$-PEG-Alk nanoparticles via click reaction, (ii) modification of pAbF antibody by NHS-PEG-N$_3$ and its subsequent click reaction with NaYF$_4$:Yb^{3+}/Tm^{3+}@NaYF$_4$-PEG-Alk nanoparticles, and (iii) reduction of disulfide bonds of pAbF antibody and conjugation to the NaYF$_4$:Yb^{3+}/Tm^{3+}@NaYF$_4$-PEG-Mal nanoparticles.

After conjugation of SA-azide, the morphology, size, and particles size distribution of the NaYF$_4$:Yb^{3+}/Tm^{3+}-PEG-SA core and NaYF$_4$:Yb^{3+}/Tm^{3+}@NaYF$_4$-PEG-SA core–shell nanoparticles remained similar (D_n = 24 ± 1 and 37 ± 2 × 27 ± 1.4 nm, respectively; Figure 3c,f and Figure S1c,f) as those of starting OA-stabilized particles. Hydrodynamic diameter of NaYF$_4$:Yb^{3+}/Tm^{3+}-PEG-SA and NaYF$_4$:Yb^{3+}/Tm^{3+}@NaYF$_4$-PEG-SA particles in 50 mM Tris buffer slightly increased, reaching D_h = 118 nm, PD = 0.22 and D_h = 125 nm, PD = 0.18, respectively (Figure S4e,f and Figure S5e,f, respectively), compared to NaYF$_4$:Yb^{3+}/Tm^{3+}@NaYF$_4$-PEG-Alk. Azide-modified pAbF antibody-conjugated NaYF$_4$:Yb^{3+}/Tm^{3+}@NaYF$_4$-PEG-Alk particles exhibited D_h = 124 nm and PD = 0.19 (Figure S5g,h). After conjugation of pAbF antibody to NaYF$_4$:Yb^{3+}/Tm^{3+}@NaYF$_4$-PEG-Mal nanoparticles, hydrodynamic diameter in 50 mM Tris buffer slightly increased (D_h = 170 nm, PD = 0.13; Figure S5i,j), compared to NaYF$_4$:Yb^{3+}/Tm^{3+}@NaYF$_4$-PEG-Mal nanoparticles.

The successful conjugation of the SA and pAbF antibody to the NaYF$_4$:Yb^{3+}/Tm^{3+}@NaYF$_4$-PEG-Alk and/or NaYF$_4$:Yb^{3+}/Tm^{3+}@NaYF$_4$-PEG-Mal nanoparticles was evidenced by XPS (Figure 4c,d). The presence of SA and pAbF antibody on the nanoparticle surface could not be verified from the increase of the N 1s signals (note that the N 1s signals strongly overlapped with the Y 3s signals) but led to direct changes in the C 1s spectra of the NaYF$_4$:Yb^{3+}/Tm^{3+}@NaYF$_4$-PEG-SA, NaYF$_4$:Yb^{3+}/Tm^{3+}@NaYF$_4$-PEG-pAbF(Az), and NaYF$_4$:Yb^{3+}/Tm^{3+}@NaYF$_4$-PEG-pAbF(Mal) nanoparticles. The conjugation led to an increase of the amide C=O—NH signals at 288.2 eV and a decrease of the C—O signals coming from the PEG chains. At the same time, an increase of the C—C and C—H signals was observed at 285.0 eV (Figure 4c,d). It is worth noting that the NaYF$_4$:Yb^{3+}/Tm^{3+}@NaYF$_4$-PEG-Mal core–shell nanoparticles showed more significant changes in the C 1s high-resolution spectra upon the immobilization of pAbF antibody than the NaYF$_4$:Yb^{3+}/Tm^{3+}@NaYF$_4$-PEG-Alk nanoparticles upon immobilization of SA-azide and pAbF-azide antibody. This is probably connected with the higher loading capacity of NaYF$_4$:Yb^{3+}/Tm^{3+}@NaYF$_4$-PEG-Mal core–shell nanoparticles stemming from the higher density of PEG chains, that is, maleimide groups over the nanoparticle surface.

To investigate the optical properties of the 24-nm NaYF$_4$:Yb^{3+}/Tm^{3+}-PEG-Alk core and 37 × 27-nm NaYF$_4$:Yb^{3+}/Tm^{3+}@NaYF$_4$-PEG-Alk core–shell nanoparticles, their upconversion photoluminescence spectra were recorded at 980 nm excitation (Figure 5). The spectrum of the NaYF$_4$:Yb^{3+}/Tm^{3+}-PEG-Alk core showed typical emission
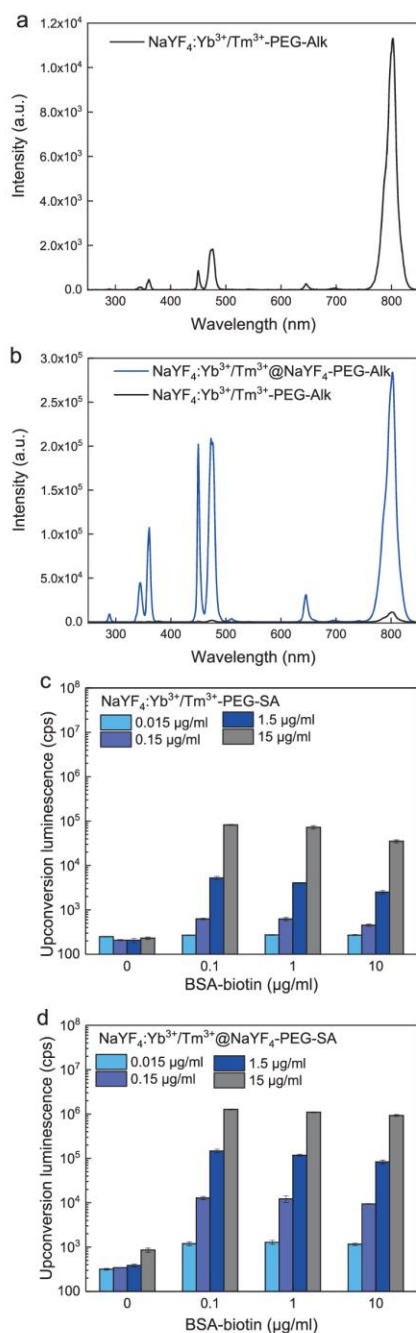
284

Figure 5. Upconversion luminescence emission spectra of (a) NaYF$_4$:Yb^{3+}/Tm^{3+}-PEG-Alk core and (b) NaYF$_4$:Yb^{3+}/Tm^{3+}@NaYF$_4$-PEG-Alk core−shell nanoparticles in water (1 mg/mL), excitation at 980 nm, power density 1 W/cm^2. Plate-based binding test of (c) NaYF$_4$:Yb^{3+}/Tm^{3+}-PEG-SA and (d) NaYF$_4$:Yb^{3+}/Tm^{3+}@NaYF$_4$-PEG-SA nanoparticles to different concentrations of BSA-biotin (0−10 μg/mL). BSA-biotin was immobilized on a microtiter plate and incubated with different concentrations of the particles (0.015−15 μg/mL). The error bars correspond to standard deviation of upconversion luminescence of three different wells.

lines of Tm^{3+} at 343, 360, 450, 475, 645, and 802 nm, corresponding to $^1I_6 \rightarrow {}^3F_4$, $^1D_2 \rightarrow {}^3H_6$, $^1D_2 \rightarrow {}^3F_4$, $^1G_4 \rightarrow {}^3H_6$, $^1G_4 \rightarrow {}^3F_4$, and $^3H_4 \rightarrow {}^3H_6$ electronic transitions (Figure 5a). After introduction of the NaYF$_4$ shell, the intensity of emission peaks increased significantly (Figure 5b). The brightness of the 24-nm NaYF$_4$:Yb^{3+}/Tm^{3+}-PEG-SA core and 37 × 27-nm NaYF$_4$:Yb^{3+}/Tm^{3+}@NaYF$_4$-PEG-SA core−shell particles and activity of SA bound to the nanoparticles was tested using a BSA-biotin assay (Figure 5c,d). Both conjugates showed high level of specific binding; however, the brightness of NaYF$_4$:Yb^{3+}/Tm^{3+}@NaYF$_4$-PEG-SA was 1 order of magnitude higher compared to that of core NaYF$_4$:Yb^{3+}/Tm^{3+}-PEG-SA particles. Consequently, the core−shell nanoparticles were selected as a label for the detection of HSA in the sandwich immunoassay.

Performance of Upconversion-Linked Immunoassay. The prepared conjugates (Figure 6) were employed as a label
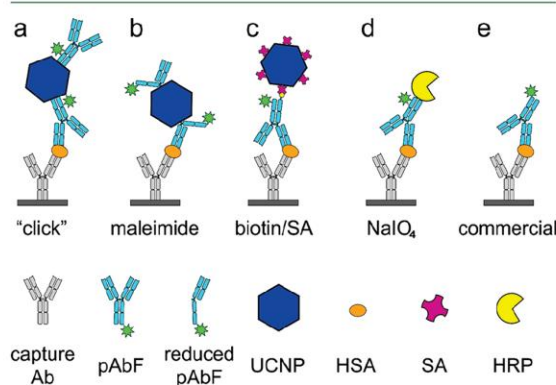
Figure 6. Scheme of sandwich immunoassays. Five different labels were prepared and employed for the detection of HSA. (a−c) Representation of different implements of a ULISA where antibodies or streptavidin are attached to UCNPs via bifunctional cross-linkers. (d) ELISA and (e) FIA are included for comparison to conventional immunoassays.

in sandwich assay for the detection of HSA. The performance of sandwich immunoassays strongly depends on the affinity of immunoreagents, closely followed by the performance of the detection label.[35] In the case of the nanoparticle-based labels, a good conjugation efficiency is required to allow for a specific binding. Furthermore, the good particle uniformity and absence of aggregates is important to ensure consistent results with low errors within wells. The results of the sandwich immunoassays with NaYF$_4$:Yb^{3+}/Tm^{3+}@NaYF$_4$-PEG-pAbF-(Az) particles are shown in Figure 7a. The two different samples were based on different amount of NHS-PEG-N$_3$ in the antibody-modification step (1:2.3 or 1:0.2 w/w). The particles containing antibody with a higher number of N$_3$ reactive groups provided higher signals, however, without positive effect on the LOD. This can be attributed to a higher number of aggregates, which is connected to higher signal fluctuations between wells. The higher label concentrations provided significantly higher signals, however, also the background increased, which resulted in nearly identical LOD values for different dilutions of the same label type. The NaYF$_4$:Yb^{3+}/Tm^{3+}@NaYF$_4$-PEG-pAbF(Az) nanoparticles

285
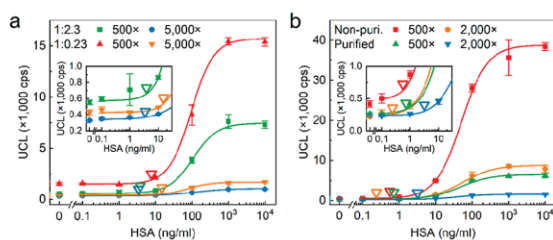
Figure 7. (a) ULISA for the detection of HSA with $NaYF_4$:Yb^{3+}/Tm^{3+}@$NaYF_4$-PEG-pAbF(Az) labels. Different ratios of NHS-PEG-N_3 and pAbF (1:2.3 or 1:0.23 w/w) were used for antibody activation before the click reaction. (b) ULISA for HSA based on $NaYF_4$:Yb^{3+}/Tm^{3+}@$NaYF_4$-PEG-pAbF(Mal) labels. The particle concentrations are expressed as the dilutions of the stock solution. The insets show a magnified part of the plots for low HSA concentrations. The error bars correspond to standard deviations of three wells; the empty triangles correspond to the LOD values.

provided an LOD of 3.5 ng/mL for HSA, with a working range up to 1 μg/mL.

The other particle design was based on maleimide coupling. The performance of $NaYF_4$:Yb^{3+}/Tm^{3+}@$NaYF_4$-PEG-pAb-F(Mal) particles is shown in Figure 7b. Compared to $NaYF_4$:Yb^{3+}/Tm^{3+}@$NaYF_4$-PEG-pAbF(Az) particles, a similar concentration provided higher signals and a slightly lower background, which resulted in an improved LOD down to 0.24 ng/mL and a working range up to 1 μg/mL. The $NaYF_4$:Yb^{3+}/Tm^{3+}@$NaYF_4$-PEG-pAbF(Mal) particles provided a high signal-to-background (S/B) value of 92 (ratio of signal for highest HSA concentration in the assay and signal for blank). Suspecting that the LOD can be affected by the presence of particle aggregates, we have purified the particles by sucrose gradient centrifugation.[34] The specific signals decreased due to the particle dilution during the purification, however, no improvement of the LOD was achieved, suggesting that the LOD was affected more by the level of specific and nonspecific binding rather than the amount of aggregates.

Apart from the labels directly conjugated with the antibodies, labels based on SA were also tested. The assay based on $NaYF_4$:Yb^{3+}/Tm^{3+}-PEG-SA provided higher sensitivity, represented by an LOD of 0.17 ng/mL (Figure 8a). The results agreed with our previous observation, where the combination of biotinylated antibody and streptavidin-based label also improved the LOD compared to the direct
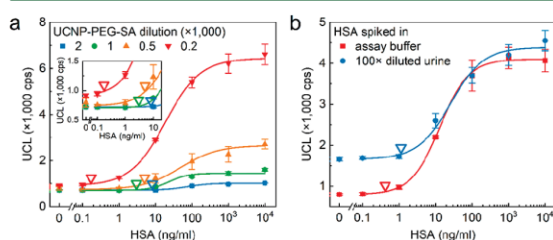
Figure 8. ULISA for the detection of HSA with $NaYF_4$:Yb^{3+}/Tm^{3+}-PEG-SA label. (a) Detection in assay buffer with varying label concentration; (b) detection in spiked 100 times diluted urine with 200 times diluted label. The inset shows the magnified part of the plot for low HSA concentrations. The error bars correspond to standard deviations of three wells. The empty triangles correspond to the LOD values.

application of the antibody-based label.[34] Because of the low level of nonspecific binding, the higher label concentrations provided higher signal with negligible effect on the background level. Therefore, 200 times dilution of the label was selected for further experiments as a compromise between the signal level and conjugate consumption. Finally, the optimized assay was employed for the analysis of real samples of spiked urine (Figure 8b). The baseline level in the case of urine was slightly higher than in the case of assay buffer, which can be explained by the presence of some proteins even in the purified urine sample. Nevertheless, the specific detection of HSA was demonstrated, proving the practical applicability of the ULISA for real sample analysis.

To compare the ULISA with standard methods, we performed the equivalent fluorescence- and enzyme-based immunoassays for HSA detection. The fluorescence immunoassay provided LOD of 0.59 ng/mL with S/B ratio of 4.8 (Figure 9a). The ELISA provided similar LOD value (0.56 ng/
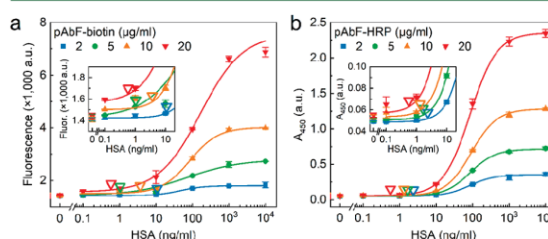
Figure 9. Detection of HSA using (a) FIA (with pAbF-biotin) and (b) ELISA (with pAbF-HRP). The insets show magnified part of the plots for low HSA concentrations. The error bars correspond to standard deviations of three wells; the empty triangles correspond to the LOD values.

mL) and S/B ratio of 43 (Figure 9b). The results demonstrated that the ULISA offered improvement compared to the standard methods in terms of both LOD and S/B ratio. The achieved results were also superior to those from other methods for the HSA detection, as shown in Table 1.

■ CONCLUSIONS

We have introduced a straightforward strategy for the surface modification and bioconjugation of UCNPs with focus on

Table 1. Comparison of Immunoanalytical Methods for the Detection of HSA

method	LOD (ng/mL)	reference
ULISA	0.17	this work
FIA	0.59	this work
ELISA	0.56	this work
nanozyme-linked immunosorbent assay	1.2	35
chemiluminescence lateral flow immunoassay	2,500	46
isotachophoresis with laser-induced fluorescence readout	0.5	47
fluorometric immunoassay	30	48
microtiter plate immunoassay with laser-induced breakdown spectroscopy readout	10	28
magnetoelastic immunosensor	10	49
electrochemical immunosensor	1,550	50
surface plasmon resonance immunosensor	50	51

286

bioanalytical applications, such as immunoassays. Uniformly sized $NaYF_4$:Yb^{3+}/Tm^{3+} core and $NaYF_4$:Yb^{3+}/Tm^{3+}@$NaYF_4$ core—shell nanoparticles were successfully prepared by thermal coprecipitation of lanthanide precursors. To make the particles compatible with aqueous buffers, ensure their colloidal stability, and enable a successful bioconjugation, Ner-PEG-Alk and Ner-PEG-Mal were prepared by coupling NHS-PEG-Alk or NHS-PEG-Mal with neridronate. The substitution of NHS end-groups with neridronate reached 99.5 and 97.6%, respectively. Bioconjugation involved the click reaction of pAbF-azide or SA-azide with $NaYF_4$:Yb^{3+}/Tm^{3+}@$NaYF_4$-PEG-Alk nanoparticles and the reaction of reduced disulfide bonds of pAbF antibody with $NaYF_4$:Yb^{3+}/Tm^{3+}@$NaYF_4$-PEG-Mal particles. The emission spectra confirmed a much higher emission intensity of core—shell nanoparticles compared to that of the bare cores. This observation was supported by the results of the BSA-biotin test, where $NaYF_4$:Yb^{3+}/Tm^{3+}@$NaYF_4$-PEG-SA nanoparticles provided 1 order of magnitude higher signals than the $NaYF_4$:Yb^{3+}/Tm^{3+}-PEG-SA particles. The particles were then employed in an immunoassay for the detection of HSA. All compared types were useful as the labels in the assay; the best performance was achieved with the streptavidin-based conjugate, which provided LOD of 0.17 ng/mL. This value represents more than a three-fold improvement to conventional labels based on fluorescein and horseradish peroxidase.

■ ASSOCIATED CONTENT

Ⓢ Supporting Information

The Supporting Information is available free of charge at https://pubs.acs.org/doi/10.1021/acs.biomac.0c00459.

> Figure S1. Histograms of OA-stabilized $NaYF_4$:Yb^{3+}/Tm^{3+}, washed $NaYF_4$:Yb^{3+}/Tm^{3+}, $NaYF_4$:Yb^{3+}/Tm^{3+}-PEG-SA, OA-stabilized $NaYF_4$:Yb^{3+}/Tm^{3+}@$NaYF_4$, washed $NaYF_4$:Yb^{3+}/Tm^{3+}@$NaYF_4$, and $NaYF_4$:Yb^{3+}/Tm^{3+}@$NaYF_4$-PEG-SA nanoparticles. Figure S2. Interpretation of 2D-COSY ^{1}H NMR spectrum of Ner-PEG-Alk measured at 25 °C. Figure S3. Interpretation of 2D-COSY ^{1}H NMR spectrum of Ner-PEG-Mal measured at 25 °C. Figure S4. Size distribution calculated from intensity-weighted distribution function and autocorrelation decay plot of $NaYF_4$:Yb^{3+}/Tm^{3+}-PEG-Alk, $NaYF_4$:Yb^{3+}/Tm^{3+}-PEG-Mal, and $NaYF_4$:Yb^{3+}/Tm^{3+}-PEG-SA nanoparticles. Figure S5. Size distribution calculated from intensity-weighted distribution function and autocorrelation decay plot of $NaYF_4$:Yb^{3+}/Tm^{3+}@$NaYF_4$-PEG-Alk, $NaYF_4$:Yb^{3+}/Tm^{3+}@$NaYF_4$-PEG-Mal, $NaYF_4$:Yb^{3+}/Tm^{3+}@$NaYF_4$-PEG-SA, $NaYF_4$:Yb^{3+}/Tm^{3+}@$NaYF_4$-PEG-pAbF(Az), and $NaYF_4$:Yb^{3+}/Tm^{3+}@$NaYF_4$-PEG-pAbF(Mal) nanoparticles. Figure S6. ATR FTIR spectra of $NaYF_4$:Yb^{3+}/Tm^{3+}@$NaYF_4$, $NaYF_4$:Yb^{3+}/Tm^{3+}@$NaYF_4$-PEG-Alk, and $NaYF_4$:Yb^{3+}/Tm^{3+}@$NaYF_4$-PEG-Mal nanoparticles. Figure S7. TGA of $NaYF_4$:Yb^{3+}/Tm^{3+}@$NaYF_4$, $NaYF_4$:Yb^{3+}/Tm^{3+}@$NaYF_4$-PEG-Alk, and $NaYF_4$:Yb^{3+}/Tm^{3+}@$NaYF_4$-PEG-Mal nanoparticles (PDF)

■ AUTHOR INFORMATION

Corresponding Author

Daniel Horák − *Institute of Macromolecular Chemistry of the Czech Academy of Sciences, 162 06 Prague 6, Czech Republic;* ⓘ orcid.org/0000-0002-6907-9701; Email: horak@imc.cas.cz

Authors

Uliana Kostiv − *Institute of Macromolecular Chemistry of the Czech Academy of Sciences, 162 06 Prague 6, Czech Republic*

Zdeněk Farka − *Department of Biochemistry, Faculty of Science and CEITEC − Central European Institute of Technology, Masaryk University, 625 00 Brno, Czech Republic;* ⓘ orcid.org/0000-0002-6842-7081

Matthias J. Mickert − *Institute of Analytical Chemistry, Chemo- and Biosensors, University of Regensburg, 93053 Regensburg, Germany*

Hans H. Gorris − *Institute of Analytical Chemistry, Chemo- and Biosensors, University of Regensburg, 93053 Regensburg, Germany*

Nadiia Velychkivska − *Institute of Macromolecular Chemistry of the Czech Academy of Sciences, 162 06 Prague 6, Czech Republic*

Ognen Pop-Georgievski − *Institute of Macromolecular Chemistry of the Czech Academy of Sciences, 162 06 Prague 6, Czech Republic;* ⓘ orcid.org/0000-0001-7938-9271

Matěj Pastucha − *Department of Biochemistry, Faculty of Science and CEITEC − Central European Institute of Technology, Masaryk University, 625 00 Brno, Czech Republic*

Eliška Odstrčilíková − *Department of Biochemistry, Faculty of Science, Masaryk University, 625 00 Brno, Czech Republic*

Petr Skládal − *Department of Biochemistry, Faculty of Science and CEITEC − Central European Institute of Technology, Masaryk University, 625 00 Brno, Czech Republic;* ⓘ orcid.org/0000-0002-3868-5725

Complete contact information is available at:
https://pubs.acs.org/10.1021/acs.biomac.0c00459

Author Contributions

[1]U.K. and Z.F. contributed equally to the work.

Notes

The authors declare no competing financial interest.

■ ACKNOWLEDGMENTS

■ REFERENCES

(1) Farka, Z.; Mickert, M. J.; Mikušová, Z.; Hlaváček, A.; Bouchalová, P.; Xu, W.; Bouchal, P.; Skládal, P.; Gorris, H. H. Surface design of photon-upconversion nanoparticles for high-contrast immunocytochemistry. *Nanoscale* **2020**, *12*, 8303−8313.

(2) Xu, J.; Gulzar, A.; Yang, P.; Bi, H.; Yang, D.; Gai, S.; He, F.; Lin, J.; Xing, B.; Jin, D. Recent advances in near-infrared emitting lanthanide-doped nanoconstructs: Mechanism, design and application for bioimaging. *Coord. Chem. Rev.* **2019**, *381*, 104−134.

(3) Lee, G.; Il Park, Y. I. Lanthanide-doped upconversion nanocarriers for drug and gene delivery. *Nanomaterials* **2018**, *8*, 511.

287

(4) All, A. H.; Zeng, X.; Teh, D. B. L.; Yi, Z.; Prasad, A.; Ishizuka, T.; Thakor, N.; Hiromu, Y.; Liu, X. Expanding the toolbox of upconversion nanoparticles for *in vivo* optogenetics and neuro-modulation. *Adv. Mater.* **2019**, *31*, 1803474.

(5) Rostami, I.; Rezvani Alanagh, H.; Hu, Z.; Shahmoradian, S. H. Breakthroughs in medicine and bioimaging with up-conversion nanoparticles. *Int. J. Nanomed.* **2019**, *14*, 7759−7780.

(6) Farka, Z.; Juřík, T.; Kovář, D.; Trnková, L.; Skládal, P. Nanoparticle-based immunochemical biosensors and assays: Recent advances and challenges. *Chem. Rev.* **2017**, *117*, 9973−10042.

(7) Farka, Z.; Mickert, M. J.; Pastucha, M.; Mikušová, Z.; Skládal, P.; Gorris, H. H. Advances in optical single-molecule detection: En route to super-sensitive bioaffinity assays. *Angew. Chem., Int. Ed.* **2020**, *52*, 2−30.

(8) Haase, M.; Schäfer, H. Upconverting nanoparticles. *Angew. Chem., Int. Ed.* **2011**, *50*, 5808−5829.

(9) Wolfbeis, O. S. An overview of nanoparticles commonly used in fluorescent bioimaging. *Chem. Soc. Rev.* **2015**, *44*, 4743−4768.

(10) Gorris, H. H.; Wolfbeis, O. S. Photon-upconverting nano-particles for optical encoding and multiplexing of cells, biomolecules, and microspheres. *Angew. Chem., Int. Ed.* **2013**, *52*, 3584−3600.

(11) Chamanzar, M.; Garfield, D. J.; Iafrati, J.; Chan, E. M.; Sohal, V.; Cohen, B. E.; Schuck, P. J.; Maharbiz, M. M. Upconverting nanoparticle micro-lightbulbs designed for deep tissue optical stimulation and imaging. *Biomed. Opt. Express* **2018**, *9*, 4359−4371.

(12) Zhang, Z.; Shikha, S.; Liu, J.; Zhang, J.; Mei, Q.; Zhang, Y. Upconversion nanoprobes: Recent advances in sensing applications. *Anal. Chem.* **2019**, *91*, 548−568.

(13) Lee, S. Y.; Lin, M.; Lee, A.; Park, Y. I. Lanthanide-doped nanoparticles for diagnostic sensing. *Nanomaterials* **2017**, *7*, 411.

(14) Heer, S.; Kömpe, K.; Güdel, H. U.; Haase, M. Highly efficient multicolour upconversion emission in transparent colloids of lanthanide-doped $NaYF_4$ nanocrystals. *Adv. Mater.* **2004**, *16*, 2102−2105.

(15) Wen, S.; Zhou, J.; Zheng, K.; Bednarkiewicz, A.; Liu, X.; Jin, D. Advances in highly doped upconversion nanoparticles. *Nat. Commun.* **2018**, *9*, 2415.

(16) Würth, C.; Fischer, S.; Grauel, B.; Alivisatos, A. P.; Resch-Genger, U. Quantum yields, surface quenching, and passivation efficiency for ultrasmall core/shell upconverting nanoparticles. *J. Am. Chem. Soc.* **2018**, *140*, 4922−4928.

(17) Sedlmeier, A.; Gorris, H. H. Surface modification and characterization of photon-upconverting nanoparticles for bioanalyt-ical applications. *Chem. Soc. Rev.* **2015**, *44*, 1526−1560.

(18) Tong, L.; Lu, E.; Pichaandi, J.; Cao, P.; Nitz, M.; Winnik, M. A. Quantification of surface ligands on $NaYF_4$ nanoparticles by three independent analytical techniques. *Chem. Mater.* **2015**, *27*, 4899−4910.

(19) Mandl, G. A.; Cooper, D. R.; Hirsch, T.; Seuntjens, J.; Capobianco, J. A. Perspective: Lanthanide-doped upconverting nanoparticles. *Methods Appl. Fluoresc.* **2019**, *7*, 012004.

(20) Wilhelm, S.; Kaiser, M.; Würth, C.; Heiland, J.; Carrillo-Carrion, C.; Muhr, V.; Wolfbeis, O. S.; Parak, W. J.; Resch-Genger, U.; Hirsch, T. Water dispersible upconverting nanoparticles: Effects of surface modification on their luminescence and colloidal stability. *Nanoscale* **2015**, *7*, 1403.

(21) Gee, A.; Xu, X. Surface functionalisation of upconversion nanoparticles with different moieties for biomedical applications surfaces. *Surfaces* **2018**, *1*, 96−121.

(22) Duong, H. T. T.; Chen, Y.; Tawfik, S. A.; Wen, S.; Parviz, M.; Shimoni, O.; Jin, D. Systematic investigation of functional ligands for colloidal stable upconversion nanoparticles. *RSC Adv.* **2018**, *8*, 4842−4849.

(23) Zhao, G.; Tong, L.; Cao, P.; Nitz, M.; Winnik, M. A. Functional PEG-PAMAM-tetraphosphonate capped $NaLnF_4$ nanoparticles and their colloidal stability in phosphate buffer. *Langmuir* **2014**, *30*, 6980−6989.

(24) Bekah, D.; Cooper, D.; Kudinov, K.; Hill, C.; Seuntjens, J.; Bradforth, S.; Nadeau, J. Synthesis and characterization of biologically stable, doped LaF_3 nanoparticles co-conjugated to PEG and photosensitizers. *J. Photochem. Photobiol., A* **2016**, *329*, 26−34.

(25) Nsubuga, A.; Sgarzi, M.; Zarschler, K.; Kubeil, M.; Hübner, R.; Steudtner, R.; Graham, B.; Joshi, T.; Stephan, H. Facile preparation of multifunctionalisable 'stealth' upconverting nanoparticles for bio-medical applications. *Dalton Trans.* **2018**, *47*, 8595−8604.

(26) Kieczykowski, G. R.; Jobson, R. B.; Melillo, D. G.; Reinhold, D. F.; Grenda, V. J.; Shinkai, I. Preparation of (4-amino-1-hydroxybutylidene)bisphosphonic acid sodium salt, MK-217 (alendr-onate sodium). An improved procedure for the preparation of 1-hydroxy-1,1-bisphosphonic acids. *J. Org. Chem.* **1995**, *60*, 8310−8312.

(27) Kostiv, U.; Lobaz, V.; Kučka, J.; Švec, P.; Sedláček, O.; Hrubý, M.; Janoušková, O.; Francová, P.; Kolářová, V.; Šefc, L.; Horák, D. A simple neridronate-based surface coating strategy for upconversion nanoparticles: Highly colloidally stable ^{125}I-radiolabeled $NaYF_4$:Yb^{3+}/Er^{3+}@PEG nanoparticles for multimodal *in vivo* tissue imaging. *Nanoscale* **2017**, *9*, 16680−16688.

(28) Modlitbová, P.; Farka, Z.; Pastucha, M.; Pořízka, P.; Novotný, K.; Skládal, P.; Kaiser, J. Laser-induced breakdown spectroscopy as a novel readout method for nanoparticle-based immunoassays. *Micro-chim. Acta* **2019**, *186*, 629.

(29) Hermanson, G. *Bioconjugate Techniques*, 3rd ed.; Academic Press, 2013.

(30) Farka, Z.; Juřík, T.; Pastucha, M.; Skládal, P. Enzymatic precipitation enhanced surface plasmon resonance immunosensor for the detection of *Salmonella* in powdered milk. *Anal. Chem.* **2016**, *88*, 11830−11836.

(31) Catty, D. *Antibodies Vol. II: A Practical Approach*; IRL Press: Oxford, 1989.

(32) Kostiv, U.; Patsula, V.; Noculak, A.; Podhorodecki, A.; Větvička, D.; Poučková, P.; Sedláková, Z.; Horák, D. Phthalocyanine-conjugated upconversion $NaYF_4$:Yb^{3+}/Er^{3+}@SiO$_2$ nanospheres for NIR-triggered photodynamic therapy in a tumor mouse model. *ChemMedChem* **2017**, *12*, 2066−2073.

(33) Podhorodecki, A.; Krajnik, B.; Golacki, L. W.; Kostiv, U.; Pawlik, G.; Kaczmarek, M.; Horák, D. Percolation limited emission intensity from upconverting $NaYF_4$:Yb^{3+},Er^{3+} nanocrystals − a single nanocrystal optical study. *Nanoscale* **2018**, *10*, 21186−21196.

(34) Mickert, M. J.; Farka, Z.; Kostiv, U.; Hlaváček, A.; Horák, D.; Skládal, P.; Gorris, H. H. Measurement of sub-femtomolar concentrations of prostate-specific antigen through single-molecule counting with an upconversion-linked immunosorbent assay. *Anal. Chem.* **2019**, *91*, 9435−9441.

(35) Farka, Z.; Čunderlová, V.; Horáčková, V.; Pastucha, M.; Mikušová, Z.; Hlaváček, A.; Skládal, P. Prussian blue nanoparticles as a catalytic label in a sandwich nanozyme-linked immunosorbent. *Anal. Chem.* **2018**, *90*, 2348−2354.

(36) Datta, P.; Dasgupta, A. An improved microalbumin method (μALB_2) with extended analytical measurement range evaluated on the ADVIA® chemistry systems. *J. Clin. Lab. Anal.* **2009**, *23*, 314−318.

(37) Tsai, J.-Z.; Chen, C.-J.; Settu, K.; Lin, Y.-F.; Chen, C.-L.; Liu, J.-T. Screen-printed carbon electrode-based electrochemical immuno-sensor for rapid detection of microalbuminuria. *Biosens. Bioelectron.* **2016**, *77*, 1175−1182.

(38) Zhang, C.; Lee, J. Y. Prevalence of anisotropic shell growth in rare earth core−shell upconversion nanocrystals. *ACS Nano* **2013**, *7*, 4393−4402.

(39) Kostiv, U.; Kučka, J.; Lobaz, V.; Kotov, N.; Janoušková, O.; Šlouf, M.; Krajnik, B.; Podhorodecki, A.; Francová, P.; Šefc, L.; Jirák, D.; Horák, D. Highly colloidally stable trimodal ^{125}I-radiolabeled PEG-neridronate-coated upconversion/magnetic bioimaging nanop-robes, submitted.

(40) Patsula, V.; Horák, D.; Kučka, J.; Macková, H.; Lobaz, V.; Francová, P.; Herynek, V.; Heizer, T.; Páral, P.; Šefc, L. Synthesis and modification of uniform PEG-neridronate-modified magnetic nano-particles determines prolonged blood circulation and biodistribution in a mouse preclinical model. *Sci. Rep.* **2019**, *9*, 10765.

288

(41) Du, S.; Kendall, K.; Toloueinia, P.; Mehrabadi, Y.; Gupta, G.; Newton, J. Aggregation and adhesion of gold nanoparticles in phosphate buffered saline. *J. Nanopart. Res.* **2012**, *14*, 758.

(42) Schöttler, S.; Becker, G.; Winzen, S.; Steinbach, T.; Mohr, K.; Landfester, K.; Mailänder, V.; Wurm, F. R. Protein adsorption is required for stealth effect of poly(ethylene glycol)- and poly-(phosphoester)-coated nanocarriers. *Nat. Nanotechnol.* **2016**, *11*, 372−377.

(43) Gorris, H. H.; Resch-Genger, U. Perspectives and challenges of photon-upconversion nanoparticles - Part II: bioanalytical applications. *Anal. Bioanal. Chem.* **2017**, *409*, 5875−5890.

(44) Pop-Georgievski, O.; Zimmermann, R.; Kotelnikov, I.; Proks, V.; Romeis, D.; Kučka, J.; Caspari, A.; Rypáček, F.; Werner, C. Impact of bioactive peptide motifs on molecular structure, charging, and nonfouling properties of poly(ethylene oxide) brushes. *Langmuir* **2018**, *34*, 6010−6020.

(45) Shukla, N.; Liu, C.; Jones, P. M.; Weller, D. FTIR study of surfactant bonding to FePt nanoparticles. *J. Magn. Magn. Mater.* **2003**, *266*, 178−184.

(46) Zangheri, M.; Di Nardo, F.; Mirasoli, M.; Anfossi, L.; Nascetti, A.; Caputo, D.; De Cesare, G.; Guardigli, M.; Baggiani, C.; Roda, A. Chemiluminescence lateral flow immunoassay cartridgewith integrated amorphous silicon photosensors array for humanserum albumin detection in urine samples. *Anal. Bioanal. Chem.* **2016**, *408*, 8869−8879.

(47) Reza Mohamadi, M.; Kaji, N.; Tokeshi, M.; Baba, Y. Online preconcentration by transient isotachophoresis in linear polymer on a poly(methyl methacrylate) microchip for separation of human serum albumin immunoassay mixtures. *Anal. Chem.* **2007**, *79*, 3667−3672.

(48) Marukhyan, S. S.; Gasparyan, V. K. Fluorometric immunoassay for human serum albumin based on its inhibitory effect on the immunoaggregation of quantum dots with silver nanoparticles. *Spectrochim. Acta, Part A* **2017**, *173*, 34−38.

(49) Liu, R.; Guo, X.; Wang, J.; Guo, J.; Zhang, Y.; Zhang, W.; Sang, S. High sensitivity detection of human serum albumin using a novel magnetoelastic immunosensor. *J. Mater. Sci.* **2019**, *54*, 9679−9688.

(50) Stanković, V.; Đurđić, S.; Ognjanović, M.; Antić, B.; Kalcher, K.; Mutić, J.; Stanković, D. M. Anti-human albumin monoclonal antibody immobilized on EDC-NHS functionalized carboxylic graphene/AuNPs composite as promising electrochemical HSA immunosensor. *J. Electroanal. Chem.* **2020**, *860*, 113928.

(51) Makhneva, E.; Farka, Z.; Pastucha, M.; Obrusník, A.; Horáčková, V.; Skládal, P.; Zajíčková, L. Maleic anhydride and acetylene plasma copolymer surfacesfor SPR immunosensing. *Anal. Bioanal. Chem.* **2019**, *411*, 7689−7697.

289

Paper XVI

Upconversion-linked Immunoassay for the Diagnosis of Honeybee Disease American Foulbrood

Pastucha, M.; Odstrčilíková, E.; Hlaváček, A.; Brandmeier, J. C.; Vykoukal, V.; Weisová, J.; Gorris, H. H.; Skládal, P.; Farka Z.*

Contribution:

Design of experiments, preparation of immunization antigen and antibody, bioconjugation and characterization of UCNPs, development and optimization of sandwich immunoassay, data evaluation, manuscript writing

Upconversion-Linked Immunoassay for the Diagnosis of Honeybee Disease American Foulbrood

Matěj Pastucha, Eliška Odstrčilíková, Antonín Hlaváček, Julian C. Brandmeier, Vít Vykoukal, Julie Weisová, Hans H. Gorris, Petr Skládal, and Zdeněk Farka

(Invited Paper)

Abstract—American foulbrood (AFB) caused by the bacterium *Paenibacillus larvae* is the most destructive disease of the honeybee brood. Therefore, rapid and sensitive detection methods are required to limit spreading of this pathogen, which has a major impact on agriculture and biodiversity. While *P. larvae* is typically detected by microbial cultivation or polymerase chain reaction, antibody-based detection represents a viable alternative. Here, we prepared an antibody specific for *P. larvae* and used it for the development of an upconversion-linked immunosorbent assay (ULISA). Photon-upconversion nanoparticles (UCNP) were conjugated to streptavidin *via* a PEG-linker using copper-catalyzed click chemistry to replace the enzyme label in conventional enzyme-linked immunosorbent assay (ELISA). The ULISA showed low cross-reactivity and provided a limit of detection of 2.9×10^3 CFU/mL, representing a 22-fold improvement compared to the ELISA. This level is within the bacterial loads present in honeybee larvae during an AFB infection. The assay was successfully applied to the analysis of spiked samples of bees, larvae, and hive debris.

Index Terms—American foulbrood, bacterial pathogens, *Paenibacillus larvae*, photon-upconversion nanoparticle, upconversion-linked immunosorbent assay.

I. INTRODUCTION

THE western honeybee (*Apis mellifera*) is the most frequent single species pollinator of flowering plants, making it invaluable to agriculture and biodiversity [1]. American foulbrood (AFB) is the most destructive disease of the honeybee brood, causing significant economic losses worldwide [2]. The disease is caused by a spore-forming Gram-positive bacterium *Paenibacillus larvae*. The spores infect young honeybee larvae through contaminated feed, they germinate and colonize the midgut of the larvae. Later, the proliferating bacteria cross the midgut epithelium and invade the larval body cavity (hemocoel) [3]. The dead larvae are converted to a glue-like "ropy" mass sticking to the side of the honeycomb cell (the typical diagnostic sign of the AFB), eventually drying to a hard scale. During this process, the bacteria begin to sporulate, and in the end, over 10^9 spores can be present in a single larva (however, only 0.2% of the total spore count is germinating *in vitro*) [4]. Afterward, adult bees spread the spores around the hive and more larvae get infected through the contaminated food reserves. The range of infectious materials is rather large – diseased larvae and the resulting dry scales, adult worker bees, honey, pollen, hive debris, beehive surfaces, and beekeeping equipment [5].

The high resilience of the spores [6] typically requires that infected colonies and contaminated equipment are burned down. Other colonies in the restriction area are examined and – depending on the national regulations – further monitored to eradicate the disease [7]. In any case, a sensitive and reliable detection of the pathogen is a prerequisite to efficiently prevent further spreading of the disease. The classical diagnosis is based on the clinical signs in the hive. The bacterium and its spores can also be identified by microscopy of stained smears prepared from the diseased larvae [8]; however, this method is not sensitive enough for samples containing lower levels of bacteria. Microbial cultivation is the gold standard for the isolation and identification of bacteria [9], e.g., by their morphology, their biochemical profile, or the bacteriophage sensitivity assay [10]. The cultivation-based methods are very sensitive and do not

291

require sophisticated instrumentation, but they are lengthy (days to weeks) and not suited for automation. This is a disadvantage when it is necessary to run many tests in a short time for screening purposes.

The first polymerase chain reaction (PCR) test for the identification of *P. larvae* was developed in 1999 [11], followed by numerous other reports [9], [12], [13]. PCR-based methods allow precise genotyping of the bacteria, are very sensitive [14] and fast, can analyze a large number of samples in parallel, and can address problems with limited spore germination of some bacterial strains [15]. However, the use of PCR is limited by contaminations, and the presence of PCR-inhibitors in the bee material, making the DNA isolation and purification a critical step and a possible source of problems [16].

Antibody-based methods offer an adequate alternative to the classical diagnostic methods [9]. First antibody-based techniques for the detection of *P. larvae* were developed in the 1970s, including the immunofluorescence with microcopy detection [17] and an immunodiffusion test [18]. An enzyme-linked immunosorbent assay (ELISA) for the confirmation of AFB was first reported in 1990 [19]. ELISAs are sensitive and specific, even in complex matrices, can analyze multiple samples in parallel, and can detect a wide range of analytes (based on the used antibody). Recently, Vita Europe Ltd. developed a commercial lateral flow immunoassay test [20] for rapid confirmation of the AFB diagnosis in diseased larvae by beekeepers or bee inspectors directly in the apiary and within a few minutes. However, the development of new antibody-based methods is generally hampered by the lack of commercially available antibodies against *P. larvae*, which need to be prepared in-house. The conventional ELISA is also not sensitive enough for the detection of sub-clinical levels of the bacterium.

The recent progress in nanotechnology allowed the development of various nanomaterials, which can be used as sensitive labels in immunoassays to enhance the sensitivity [21], [22]. Photon-upconversion nanoparticles (UCNP, e.g., $NaYF_4$:Yb,Er) are lanthanide-doped nanocrystals that possess the unique photophysical ability to absorb near-infrared light and emit at shorter wavelengths [23], [24]. This anti-Stokes emission avoids autofluorescence and light scattering of the surrounding material and thus ensures a sensitive detection without optical background interference. Due to the strong reduction of the background signal, it is even possible to detect individual UCNPs, which allows single-molecule (digital) immunoassays [25].

Common synthesis routes result in oleic acid-capped UCNPs. Therefore, a surface modification step is typically required to prepare labels that are dispersible in water and display antibodies (Ab) or streptavidin (SA) on their surface. In addition to the background-free detection, it is equally important to reduce the non-specific binding to achieve the highest sensitivity in immunoassays. We previously investigated several surface modification techniques [26]–[28] and the lowest non-specific binding was achieved by a heterobifunctional PEG linker carrying a surface-coordinating bisphosphonate group on the one end and an alkyne group on the other end [28]. A click reaction was subsequently employed to conjugate the alkyne group to an azide-modified antibody or streptavidin.

The modified UCNPs can be used as a label in various formats of immunoassays [29], [30], including the microtiter plate-based upconversion-linked immunosorbent assay (ULISA). Sensitive ULISAs were developed for the detection of various analytes, including prostate-specific antigen [28], human serum albumin [31], cardiac troponin I [32], and zearalenone [33]. We have recently employed UCNPs with bovine serum albumin coating to detect *M. plutonius*, the causative agent of the European foulbrood. The assay was 400 times more sensitive compared to a conventional ELISA and enabled the detection of 340 colony forming units (CFU) per mL [34].

Here, we introduce (ULISA) for the diagnosis of AFB. A specific rabbit polyclonal anti-*P. larvae* antibody was prepared and characterized using ELISA. Luminescent labels were prepared by conjugating UCNPs with the antibody or streptavidin and employed in a sandwich ULISA (Fig. 1). Finally, the practical potential of the assay was demonstrated by the analysis of real samples of bees, larvae, and hive debris.

II. MATERIALS AND METHODS

A. Chemicals and Reagents

Tween 20, $NHS-dPEG_8$-azide, horseradish peroxidase (HRP), and succinimidyl-6-(biotinamido)hexanoate (NHS-LC-biotin) were purchased from Sigma-Aldrich (USA). Dry dimethylformamide (DMF), streptavidin, and SuperBlock TBS (SB) were obtained from Thermo Fisher Scientific (USA). Polyethylene glycol (PEG; M_W 6000) was purchased from Carl Roth (Germany). α-N-hydroxysuccinimide-ω-alkyne polyethylene glycol (PEG M_W 3000, Alkyne-PEG-NHS) was purchased from Iris Biotech (Germany). HRP-conjugated anti-rabbit antibody (111-035-008) was obtained from Jackson ImmunoResearch (U.K.). Streptavidin-HRP conjugate (SA-HRP; ab7403) was purchased from Abcam (U.K.). 3,3',5,5'-tetramethylbenzidine substrate solution (TMB-Complete 2) was obtained from TestLine Clinical Diagnostics (Czech Republic). All other common chemicals were obtained in the highest quality available from Sigma-Aldrich (USA), Carl Roth (Germany), and Penta (Czech Republic).

The buffers used include phosphate buffer (PB; 50 mM NaH_2PO_4/Na_2HPO_4, pH 7.4), phosphate buffered saline (PBS; PB with 150 mM NaCl), Tris buffer (TB; 50 mM Tris, pH 7.5), Tris buffered saline (TBS; TB with 150 mM NaCl), washing buffer (TB with 0.05% Tween 20, 0.05% NaN_3, and 1 mM KF), coating buffer (50 mM $NaHCO_3/Na_2CO_3$, 0.05% NaN_3, pH 9.6), and assay buffer (TBS with 10% SB, 1 mM KF, 0.5% PEG 6000, 0.05% Tween 20, 0.05% NaN_3, pH 7.5).

B. Cultivation of Bacteria

The bacterial strains were obtained from the Czech Collection of Microorganisms (CCM). *Paenibacillus larvae* (CCM 4484) was used for the preparation of the antibody and for the assay optimizations. *Melissococcus plutonius* (ATCC 35311) was selected as a negative control, as it is a causative agent of the European foulbrood, a honeybee brood disease, which can be
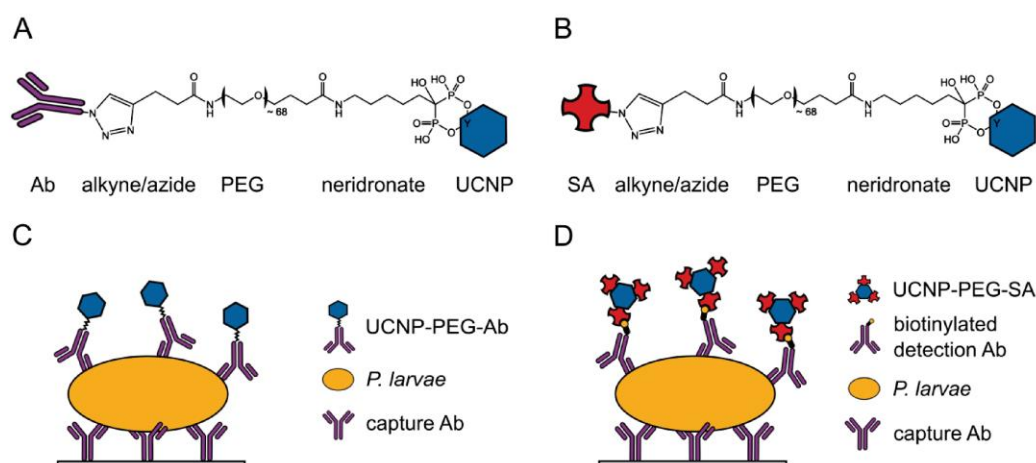
Fig. 1. Structure of **(A)** UCNP-PEG-Ab, and **(B)** UCNP-PEG-SA conjugates. Scheme of sandwich ULISA based on **(C)** UCNP-PEG-Ab, and **(D)** UCNP-PEG-SA label for the detection of *P. larvae*.

mistaken for AFB because of similarities in clinical signs. Furthermore, *Paenibacillus alvei* (ATCC 6344), and *Brevibacillus laterosporus* (ATCC 64) were used to further verify the assay specificity, as these bacteria are also found in the beehives and are often associated with bee brood diseases as secondary invaders [35].

P. larvae was cultivated in the MYPGP broth (1% Müller-Hinton broth, 1.5% yeast extract, 0.3% K_2PO_4, 0.2% glucose, 0.1% sodium pyruvate, pH 7.1; autoclaved for 15 min at 121 °C; all components were obtained from Sigma-Aldrich, USA) at 37 °C for 2 days with moderate aeration [36]. *P. alvei*, *M. plutonius*, and *B. laterosporus* were cultivated according to our previous work [34].

All bacteria were harvested by centrifugation into PBS (7,000 g, 10 min, twice with discarding the supernatant and resuspending the bacteria in fresh PBS). The aliquots of bacterial suspension (concentration of 1–2×10^{10} CFU/mL) were stored at −30 °C.

C. Preparation of Antibody

The immunization antigen was prepared according to our previous work [34]. The *P. larvae* suspension in PBS (1×10^{10} CFU/mL) was thoroughly sonicated with a tip sonicator to disintegrate the cells (Q700, Qsonica, USA, 1.6 mm Microtip probe, 60% amplitude, 5 s on time, 3 s off time, 45 min total on time). The cell wall fraction was subsequently purified by centrifugation. The homogenate was first centrifuged at 300 g for 15 min twice, with pellet discarded in each run to purge the samples of the remaining large cell fragments. The supernatant was then centrifuged at 20,000 g for 2 h, and the resulting supernatant containing small cellular components and soluble content of the cell was discarded. The pellet containing disintegrated cell walls was resuspended in PBS to $OD_{600} = 3.6$ and stored at −30 °C.

New Zealand white rabbits were used for polyclonal antibody production [37]. Two rabbits were immunized with 90 μL of the *P. larvae* antigen (cell wall fraction) emulsified in Incomplete

Freund's Adjuvant (IFA). The booster injection consisting of 90 μL of the *P. larvae* antigen emulsified in IFA followed on day 21. On day 35, small aliquots of blood were collected (∼100 μL), and the serum reactions were checked by indirect ELISA against *P. larvae*; cross-reactivity was checked against *M. plutonius*. However, only one rabbit exhibited the desired reactivity with negligible cross-reactivity to *M. plutonius*. This rabbit was injected on day 42 with the third booster injection (90 μL antigen emulsified in IFA) with the aim to increase the antibody titer in the serum. After another testing of the sera by indirect ELISA on day 49, the blood was collected on day 50, and serum was stored at −30 °C. The IgG fraction of the antisera was isolated by FPLC using HiTrap Protein G HP column (GE Healthcare, USA). The elution of the antibodies was done using 100 mM glycine-HCl (pH 2.7), followed by neutralization and transfer to PBS using a Sephadex G-25 column. The purified IgGs were diluted to a concentration of 2.5 mg/mL, and stored at −30 °C.

The anti-*P. larvae* antibody was conjugated to horseradish peroxidase (Ab-HRP) and to biotin (Ab-bt) as described in our previous work [31].

D. Enzyme-Linked Immunosorbent Assay (ELISA)

1) Testing the Antibody Specificity: For the indirect ELISA, a 96-well high-binding microtiter plate (Microlon, Greiner, Austria) was coated with varying concentrations of bacterial cells in coating buffer (100 μL per well) and incubated overnight at 4 °C. All following steps were carried out at RT; after each step, the plate was washed four times with 250 μL of the washing buffer. The microtiter plate was blocked with 200 μL of 20% SB in the washing buffer for 1 h. Then, the anti-*P. larvae* antibody (purified IgG fraction) in the assay buffer was added (50 μg/mL; 100 μL per well) and incubated for 1 h under mild shaking. Subsequently, the HRP-conjugated anti-rabbit antibody (0.8 μg/mL) was added to each well (100 μL) and incubated for 1 h.

The testing of Ab-biotin conjugate was performed using the above-described procedure with a difference in antibody-binding steps. After the blocking step, Ab-bt conjugate in assay buffer was added (125 μg/mL; 100 μL per well) and incubated for 1 h, followed by the addition of 100 μL of SA-HRP (1 μg/mL in assay buffer) with another 1 h of incubation.

After the last washing step, 100 μL of TMB-Complete 2 substrate solution was added, and the enzymatic reaction was monitored in kinetic mode using a Synergy 2 reader (BioTek Instruments, USA) as the change of absorbance at 652 nm (A_{652}). When the highest absorbance value in the plate was near 0.8, the reaction was stopped using 1 M H_2SO_4 (100 μL per well), connected with a color change from blue to yellow, and the absorbance at 450 nm (A_{450}) was read out.

2) Sandwich ELISA: For the sandwich ELISA, the microtiter plate was first coated with anti-*P. larvae* antibody (125 μg/mL in coating buffer) overnight at 4 °C. After each step, the plate was washed four times with 250 μL of the washing buffer per well. After 1 h of blocking (20% SB in the washing buffer, 200 μL per well), the bacteria in the assay buffer were added (100 μL per well) and incubated for 1 h under mild shaking. The detection was based either on an Ab-HRP or Ab-bt plus SA-HRP. In both cases, the antibody conjugate (50 μg/mL for Ab-HRP and 125 μg/mL for Ab-bt) in the assay buffer was added for 1 h; in the case of Ab-bt, 1 h incubation with SA-HRP in assay buffer (1 μg/mL; 100 μL per well) followed. The substrate conversion was detected in the same way as in the case of the indirect ELISA.

E. Preparation of UCNP Labels

1) Synthesis of UCNPs: UCNP labels were prepared according to the previously described methods utilizing the growth of seed nanoparticles [38]. The seed nanoparticles ($NaYF_4$ doped with 18% Yb^{3+} and 2% Tm^{3+}, 205 mg; hydrodynamic diameter 30.1 nm by DLS) were dispersed in 5.5 mL of oleic acid and 17 mL of 1-octadecene and heated to 300 °C under the nitrogen atmosphere. During 100 min at 300 °C, the growth was carried out by injecting trifluoroacetate precursors into the hot nanoparticle dispersion (73 mL 50% oleic acid and 50% 1-octadecene (v/v) containing 167 mM sodium trifluoroacetate, 134 mM yttrium trifluoroacetate, 30 mM ytterbium trifluoroacetate, and 3.3 mM thulium trifluoroacetate).

2) Synthesis of Alkyne-PEG-Ner Linker: For the synthesis of the Alkyne-PEG-Ner linker, 30 mg of neridronate (Ner; Merck, Germany) were dissolved in NaOH (1 M, 128 μL), PB was added (398 μL, pH 7.6), and the solution was sonicated for 5 min. The 15 mM Alkyne-PEG-NHS in PB (500 μL, pH 7.6) was added, incubated under shaking initially for 2 h at room temperature, and then overnight at 4 °C. The reaction mixture was dialyzed against double-distilled water in a Spectra/Por Float-A-Lyzer G2 dialysis device (MWCO: 500–1000 Da; Carl Roth, Germany). The solution was transferred to a glass vial, lyophilized (Alpha 1-2, Christ, Germany) for 24 h, and stored at 4 °C for further use.

3) Preparation of Click-Reactive Proteins: Click-reactive antibody-azide and streptavidin-azide were prepared using the NHS-dPEG$_8$-azide linker. In the case of antibody, 1.96 μL of NHS-dPEG$_8$-azide (200 mM) in DMF was added to 200 μL of the antibody (2.5 mg/mL) in PB together with 150 μL of PB. In the case of streptavidin, 31.25 μL of NHS-dPEG$_8$-azide (200 mM) in DMF were added to 150 μL of the streptavidin (4.0 mg/mL) in PB together with 187.5 μL of PB. The reaction mixture was incubated for 2 h at room temperature and then stopped by the addition of 50 μL of TB. The conjugate was purified *via* centrifuge filtration (14,000 g, 6 × 20 min) using Amicon ultra (MWCO 30 kDa for antibody; MWCO 10 kDa for streptavidin), and stored at 4 °C in a concentration of 1 mg/mL in PB.

4) Preparation of Alkyne-PEG-Ner-UCNP Conjugates: UCNPs (10 mg) dispersed in cyclohexane were mixed with an equal volume of 200 mM HCl, incubated under shaking for 30 min at 38 °C, and sonicated for 15 min to remove oleic acid from the UCNP surface and mediate a phase transfer from cyclohexane to water. The upper phase was transferred to another vial, an excess of acetone was added, and the solution was centrifuged (1,000 g, 20 min). The UCNP pellet was dispersed in 500 μL of double-distilled water and sonicated for 5 min. Alkyne-PEG-Ner (2 mg) was dissolved in 500 μL of double-distilled water, added to the UCNP dispersion, and incubated overnight at 38 °C under shaking. The alkyne-PEG-Ner-UCNP conjugates were purified by dialysis in a Spectra/Por Float-A-Lyzer G2 dialysis device (MWCO 100 kDa; Carl Roth, Germany) at 4 °C against double-distilled water containing 1 mM KF.

5) Functionalization of UCNPs with Antibody and Streptavidin: For the functionalization of UCNPs with click-reactive antibody (Fig. 1A) and streptavidin (Fig. 1B), 100 μL of TB (375 mM, pH 7.5) and 20 μL of an aqueous solution of sodium ascorbate (20 mg/mL) were added to alkyne-PEG-Ner-UCNPs (10 mg in 1.4 mL of double-distilled water). The mixture was purged with argon for 40 min, 100 μL of either antibody-azide or streptavidin-azide (1 mg/mL in PB) were added, and the mixture was purged for another 10 min. The click-reaction was started by the addition of 10 μL of $CuSO_4$ solution in double-distilled water (6.25 mM for antibody conjugate, 12.5 mM for streptavidin conjugates), the suspension was purged for 30 min with argon, and another 10 μL of $CuSO_4$ solution was added. The dispersion was purged with argon for 30 min and then dialyzed in a Float-A-Lyzer G2 dialysis device (MWCO 300 kDa) against dialysis buffer (50 mM Tris, 0.05% NaN$_3$, 1 mM KF, pH 7.5) at 4 °C.

F. Characterization of UCNP Labels

For the transmission electron microscopy (TEM) analysis, a dispersion of UCNPs in cyclohexane (5 μL) was dispensed on a copper grid coated with in-house made 12-nm continual carbon foil. The excess dispersion was removed by a paper tissue, and the grid was dried on air. The grids were imaged on Titan Themis (FEI, Czech Republic) with a FEI Ceta 16-megapixel CMOS camera. The dimensions of individual particles were analyzed using ImageJ software.

The emission spectrum of UCNP-cyclohexane dispersion (30 mg/mL) was recorded by a laboratory-made epiluminescence

detector equipped with a 400-mW laser with a wavelength of 980 nm [39].

Hydrodynamic diameters were determined by dynamic light scattering (DLS) experiments on a Zetasizer Nano ZS (Malvern, U.K.). The particles were diluted to a concentration of 20 μg/mL using cyclohexane (oleic acid-capped UCNPs) or TBS (bioconjugates), respectively.

A BSA-biotin assay was used to confirm the binding properties of the UCNP-PEG-SA conjugate. The BSA-biotin (BSA-bt) conjugate was prepared by mixing BSA in PBS buffer (5 mg/mL) with a 15-fold molar excess of NHS-biotin in anhydrous DMF (40 mg/mL). The conjugate was purified using Amicon Ultra centrifugal filters (MWCO 10 kDa). The 96-well microtiter plate was coated with serial dilutions of BSA-bt in coating buffer overnight at 4 °C. After four washing steps (250 μL of washing buffer per well), the plate was blocked using 20% SB in washing buffer (200 μL per well) for 1 h. After four washing steps, the plate was incubated with UCNP-PEG-SA conjugate in assay buffer (100 μL per well) for 1 h. After the last incubation and washing, the plate was dried on air and scanned using a laboratory-made laser microscanner.

G. Upconversion-Linked Immunosorbent Assay (ULISA)

1) Sandwich ULISA: The sandwich ULISA based on either UCNP-PEG-Ab (Fig. 1C) or UCNP-PEG-SA (Fig. 1D) was performed in a 96-well microtiter plate. The immobilization of the capture antibody (125 μg/mL in coating buffer) and blocking (20% SB in washing buffer) were the same as in the case of the sandwich ELISA; after each step, the plate was washed four times with 250 μL of the washing buffer per well. The UCNP-Ab was added after the bacteria-binding step (1 mg/mL; 100 μL per well in assay buffer, 1 h incubation). In the case of the biotin-streptavidin approach, the Ab-bt conjugate in assay buffer was added after the bacteria-binding step (125 μg/mL; 100 μL per well in assay buffer, 1 h incubation), followed by the addition of UCNP-PEG-SA conjugate (500 μg/mL; 100 μL per well in assay buffer) and incubation for 1 h. After the last incubation and washing step, the plate was dried on air and scanned using a laboratory-made laser microscanner.

2) Analysis of Real Samples: To demonstrate the practical applicability of the ULISA, the analysis was carried out using spiked honeybee material – adult bees, larvae, and bottom hive debris. The samples were collected from a healthy apiary in the South Moravian Region of the Czech Republic in September 2020. The larvae were homogenized using a Potter-Elvehjem homogenizer, with 0.5 mL of washing buffer added per larva. Adult bees, due to their rigid nature, were cooled with liquid nitrogen and ground using a mortar and pestle [40], followed by the addition of 0.5 mL of washing buffer per bee. The hive debris was directly mixed with the washing buffer (1 mL per 0.5 g of debris). All samples were shaken vigorously for 10 min. To remove the insoluble components that would interfere with the analysis, the suspensions were centrifuged at 500 g for 2 min and only the liquid part was collected. The resulting extracts were stored at −30 °C. Prior to the analysis, the extracts were diluted 4 times using the assay buffer to reduce the matrix effects

and spiked with known amounts of *P. larvae*. For the ULISA analysis, Ab-bt (125 μg/mL) and UCNP-PEG-SA (500 μg/mL) served as the detection label.

3) Upconversion Scanning: A laboratory-made laser microscanner was used for recording photon-upconversion from microtiter plates. The device is equipped with a 980-nm excitation laser (5 W), and utilizes a CCD array spectrometer as a detector (QE65000, Ocean Optics). An integrated emission intensity from 764 nm to 822 nm was recorded as a Cartesian grid of 8 × 8 points with a spacing of 600 μm. The truncated average was calculated for each well after discarding 16 highest and 16 lowest recorded values [34].

H. Data Analysis

The average and the standard deviation were calculated from three replicate wells for each concentration, and a four-parameter logistic function was used for the regression analysis of the calibration curves. The limit of detection (LOD) was calculated from the regression curve as the concentration corresponding to the signal value of y_{BG} (lowest point corresponding to the four-parameter logistic function) plus three times the standard deviation of the blank [34].

III. RESULTS AND DISCUSSION

A. ELISA Characterization of Polyclonal Antibodies

We generated polyclonal antibodies in rabbits as no antibody specific for *P. larvae* was commercially available for the immunoassay. Two rabbits were immunized with cell wall fractions of *P. larvae* to raise an immune response against surface antigens of the bacteria. Only one serum, however, was selected for further experiments because of its low level of non-specific interaction with other bacteria. The second rabbit did show sensitivity towards *P. larvae*, but a high level of non-specific reactivity was present, too (data not shown). The cross-reactivity can be suppressed by affinity purification of the antibody using the immunization antigen, but this was not possible due to the complex nature of the antigen used [41]. Therefore, only the standard protein G affinity chromatography was used, isolating the whole panel of IgGs from the antiserum.

The specificity of the prepared rabbit anti-*P. larvae* antibody (purified IgG fraction) was first tested in an indirect ELISA assay based on bacteria coated on the surface of the microtiter plate and HRP-conjugated anti-rabbit secondary antibody (Fig. 2A). The results demonstrate the high specificity of the prepared antibody, *P. larvae* provides a high signal (LOD 2.4 × 10^4 CFU/mL) whereas *P. alvei*, *M. plutonius*, and *B. laterosporus* – other common bacteria infecting honeybees – provide only a negligible signal change. In the case of *P. larvae*, the signal-to-background ratio (*S*/*B*; evaluated as the ratio of the signal for the concentration of 10^9 CFU/mL and the background) of 55 was achieved.

However, due to the necessity of coating the microtiter plate directly with the sample, the indirect assay scheme is not suitable for the analysis of complex samples. Therefore, we proceeded to a sandwich ELISA, initially based on the direct conjugate
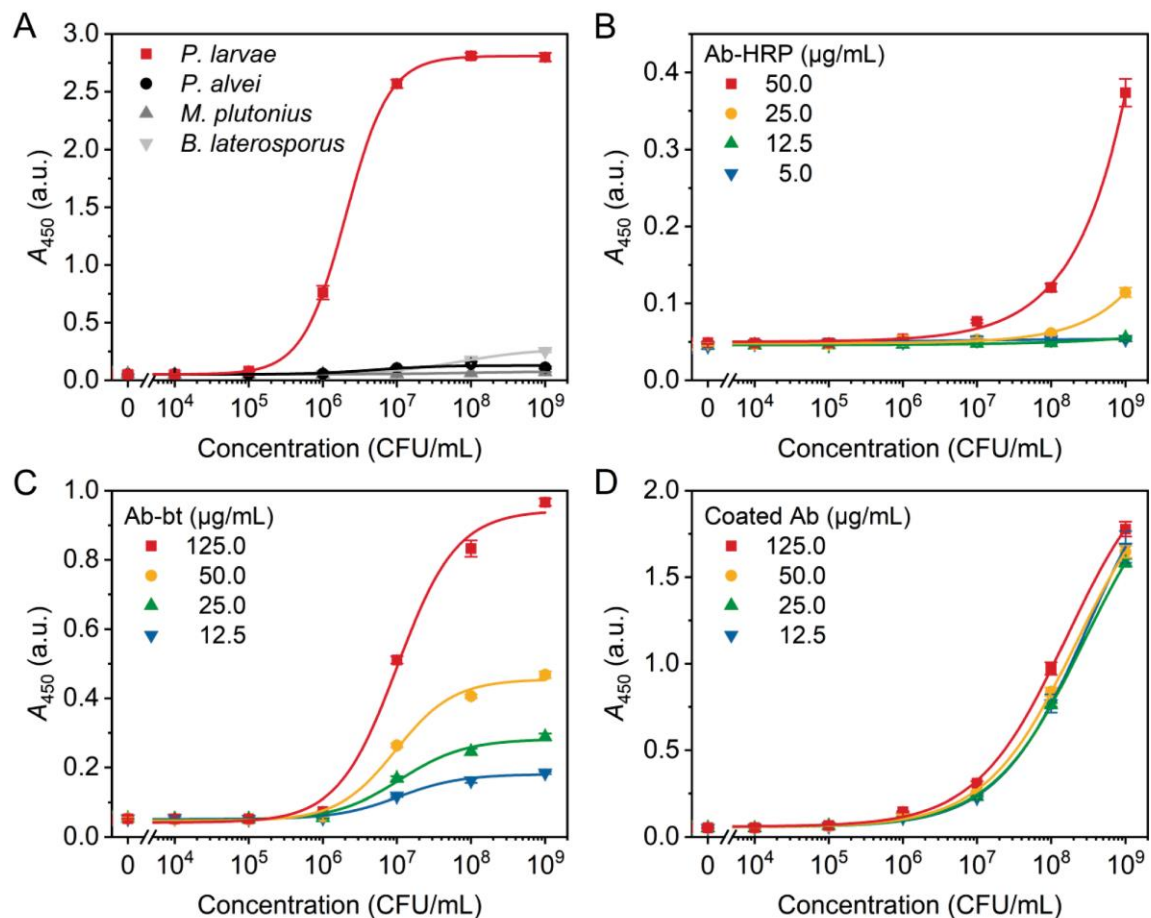
295

Fig. 2.   Detection of *P. larvae* using ELISA. (**A**) Testing of antibody specificity with *P. larvae* and negative controls of *P. alvei*, *M. plutonius*, and *B. laterosporus* in an indirect assay with anti-*P. larvae* Ab and HRP-conjugated anti-rabbit Ab. (**B**) Sandwich assay with HRP-conjugated anti-*P. larvae* Ab. (**C**) Testing of biotin-conjugated anti-*P. larvae* Ab in an indirect assay with SA-HRP label. (**D**) Sandwich assay with biotin-conjugated anti-*P. larvae* Ab and SA-HRP label.

of anti-*P. larvae* Ab with HRP (Fig. 2B). Even though the specific binding was observed, the conversion of TMB substrate was very slow (A_{652} was below 0.2 a.u. after 40 min of reaction), resulting in an unsatisfactory value of LOD of 1.0 $\times$ 10^6 CFU/mL (S/B of 8) for 50 μg/mL of Ab-HRP; even higher LOD value was obtained for lower detection conjugate concentrations. The deterioration of the LOD compared to the assay based on the unconjugated anti-*P. larvae* antibody was probably caused by the fact that the antibody was purified only on the protein G column, but no other affinity purification was performed. Therefore, even though using high antibody concentrations, a significant portion of the direct Ab-HRP conjugates might not be specific against the target bacterium.

In order to overcome this limitation, the anti-*P. larvae* antibody was also labeled with biotin and tested in an indirect assay based on coated bacteria and SA-HRP conjugate as the detection label. The increasing concentration of SA-HRP led to the increased assay sensitivity (data not shown). However, in the case of a 500$\times$ diluted label, the very fast

reaction with substrate led to faster saturation and larger error bars, probably due to the precipitation of TMB product at high concentrations. Therefore, 1000$\times$ diluted SA-HRP was used. The Ab-bt conjugates allowed to achieve higher sensitivity compared to the Ab-HRP conjugates. The increasing Ab-bt concentration led basically only to the increase of the specific signals with a small effect on the background level (Fig. 2C). The saturation occurred at $\sim$100 μg/mL (data not shown); therefore, the label concentration of 125 μg/mL (providing LOD of 2 $\times$ 10^5 CFU/mL) was selected for further experiments.

Ab-bt and SA-HRP were applied as detection labels in a sandwich assay (Fig. 2D). Compared to the strong effect of antibody concentration when used as a label, increasing the coating concentration did not affect the sensitivity significantly. The sandwich assay provided an LOD of 6.5 $\times$ 10^4 CFU/mL. This value is 15-fold better than in the case of sandwich assay with the Ab-HRP conjugate. Furthermore, the S/B ratio of 34 was 4 times better than in the case of the Ab-HRP conjugate. The achieved LOD is comparable with the ELISA for

296
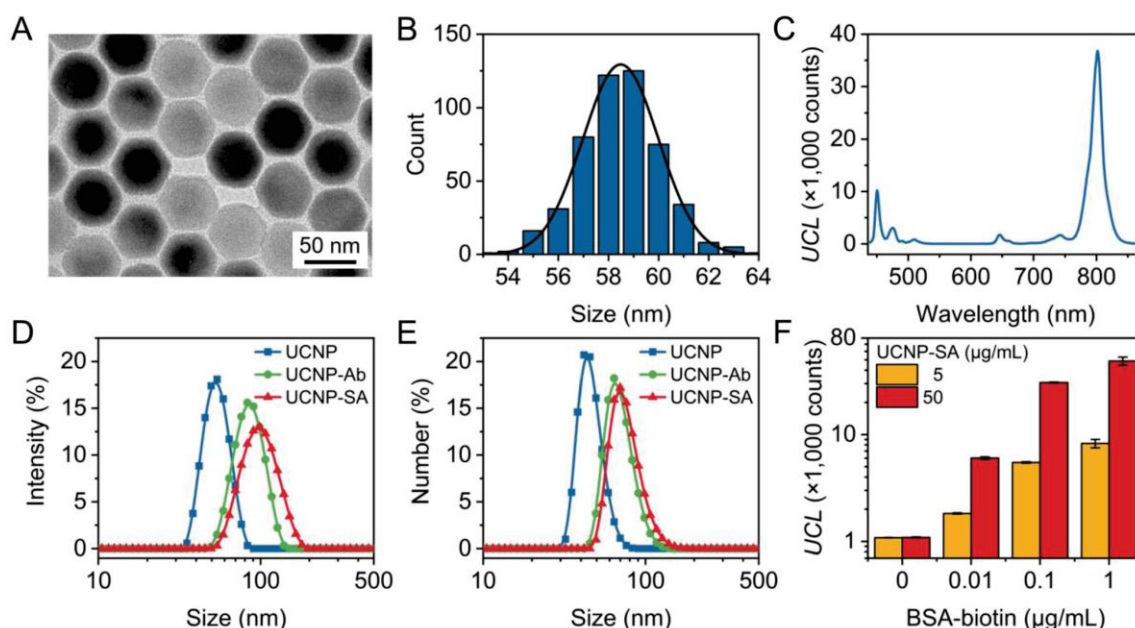
Fig. 3. **(A)** TEM image of oleic acid-capped UCNPs ($d = 58.5 \pm 1.6$ nm) and **(B)** histogram of particle sizes with Gaussian fit ($x_c = 58.5$ nm; FWHM = 3.6 nm). **(C)** Emission spectrum of UCNPs under 980-nm excitation. **(D)** Intensity DLS particle size distribution of oleic acid capped UCNPs in cyclohexane (UCNP; $d = 54.2 \pm 1.1$ nm), and UCNP-PEG-Ab (UCNP-Ab; $d = 88 \pm 2$ nm) and UCNP-PEG-SA (UCNP-SA; $d = 97 \pm 3$ nm) in TBS. **(E)** Number DLS particle size distribution of UCNPs ($d = 46.5 \pm 0.6$ nm), UCNP-PEG-Ab ($d = 69 \pm 3$ nm), and UCNP-PEG-SA ($d = 71 \pm 5$ nm). The DLS data were connected using a B-spline function. **(F)** Testing of UCNP-PEG-SA conjugates in a BSA-biotin assay.

P. larvae as reported by Olsen et al., providing an LOD of 1 $\times$ 10^5 CFU/mL [19]. In comparison with our assay, they used a monoclonal antibody sensitive to vegetative bacteria and spores. With comparable sensitivity to ours, the ELISA was satisfactory for confirmation of the diagnosis in diseased larvae. However, an improved sensitivity would be required for the detection of sub-clinical levels of the pathogen or confirmatory diagnosis in larvae with a lower bacterial load.

B. Characterization of UCNP Labels

The oleic acid-capped UCNPs were characterized using TEM (Fig. 3A). The arithmetic average of particle sizes (vertex to vertex; $n = 500$) was 58.5 ± 1.6 nm; the histogram of sizes (Fig. 3B) also revealed the average size of 58.5 nm, with an FWHM of 3.6 nm. The spectrum of the UCNPs under 980-nm excitation is shown in Fig. 3C; the emission exhibits a dominant peak at 802 nm.

The changes in hydrodynamic diameter after conjugation were followed using DLS. The size distribution based on intensity (Fig. 3D) revealed the average size of oleic acid-capped UCNPs of 54.2 ± 1.7 nm with the polydispersity index (PDI) of 0.105 ± 0.014. After the conjugation with antibody, the hydrodynamic diameter increased to 88 ± 2 nm (PDI 0.128 ± 0.014). In the case of the streptavidin conjugate, the size increased to 97 ± 3 nm (PDI 0.140 ± 0.009). The size increase suggests the successful bioconjugation; the bigger difference between the bare particles and conjugate in the case of streptavidin (which is

approximately 1/3 the size of the antibody) is probably caused by the higher amount of streptavidin molecules on the UCNP surface compared to the amount of the conjugated antibody molecules. The relatively small changes in PDI suggest that only a small fraction of aggregates was formed during the conjugation reaction. The DLS size distribution by number (Fig. 3E) showed the diameter increase from 46.5 ± 0.6 nm in the case of oleic acid-capped UCNPs to 69 ± 3 nm and 97 ± 3 nm in the case of UCNP-PEG-Ab and UCNP-PEG-SA, respectively. As expected, the distribution by number provides a smaller size but otherwise, the results are comparable.

The functional properties of the UCNP-PEG-SA conjugate were tested in a BSA-biotin assay (Fig. 3F). The prepared label provided a high level of specific binding to the surface-coated BSA biotin with a low level of non-specific interaction with the blocked surface. The *S/B* ratio of 8 and 45 was achieved for the UCNP-PEG-SA concentration of 5 μg/mL and 50 μg/mL, respectively.

C. Upconversion-Linked Immunosorbent Assay (ULISA)

The sandwich ULISA was first tested based on the direct UCNP-PEG-Ab conjugates (Fig. 4). Even though specific binding was observed, the obtained signals were rather low. The *S/B* ratio was in the range between 8 and 12, with the highest value observed for the high label concentration of 1 mg/mL. This concentration provided an LOD of 4.7×10^6 CFU/mL. These values are comparable with the sandwich ELISA based on the

297
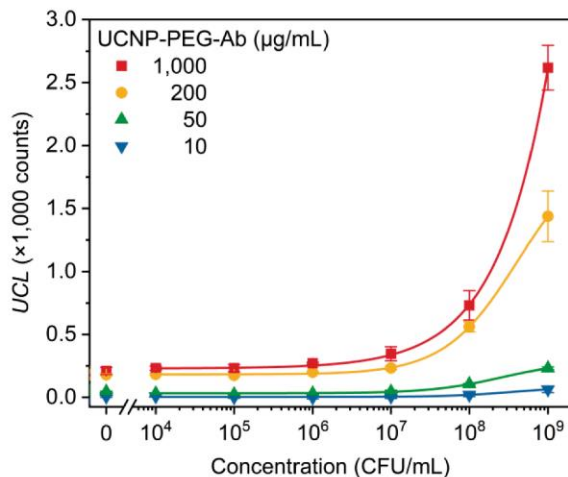
Fig. 4. Detection of *P. larvae* using sandwich ULISA with UCNP-PEG-Ab conjugate as the detection label.

Ab-HRP conjugate, but worse compared to the Ab-bt conjugate with SA-HRP. Again, this is probably caused by the polyclonal nature of the prepared antibody. Even though the nanoparticles have a relatively high surface-to-volume ratio, the number of alkyne groups available for the binding of the azide-modified antibody is limited. Therefore, when the polyclonal antibody contains a high percentage of "bulk" IgG molecules not specific for the analyte, some of the nanoparticles might not show a specific binding at all. This explains the necessity to use high concentrations of UCNP-PEG-Ab. However, as the use of the Ab-bt conjugate provided a significant improvement in the case of ELISA, it was expected that it can lead to enhanced performance also in the case of ULISA.

The ULISA with Ab-bt and UCNP-PEG-SA (Fig. 5A) was based on the same procedure as the ULISA with UCNP-Ab, only changing the antibody-binding steps. Similarly to the improvement in the case of ELISA, also ULISA with Ab-bt provided a significant improvement of the detection capabilities. The achieved signals for 10^9 CFU/mL were two orders of magnitude higher in both cases with the high UCNP label concentration (note that the same UCNP core was used in both labels). Due to the low level of non-specific binding of the PEG-based conjugates, the increasing label concentration led to the increase of specific signals with a low impact on the background. This was connected with the increase of *S/B* from 5 (20 μg/mL) to 110 (200 μg/mL) (Fig. 5A). Further increase of label concentration to 500 μg/mL (Fig. 5B) allowed to achieve the *S/B* of 128. This value is not only 11 times higher compared to the ULISA with UCNP-PEG-Ab conjugate, but also 4 times higher compared to the ELISA assay with Ab-bt conjugate. The negative controls of *P. alvei*, *M. plutonius*, and *B. laterosporus* provided only minor signal changes compared to the specific target *P. larvae*. The LOD of the optimized ULISA was 2.9×10^3 CFU/mL. This represents a 22-fold improvement compared to the ELISA based on the same immunoreagents, which clearly shows the benefit of the UCNP-based labels.

The exact concentration of vegetative bacteria in diseased bee larvae was probably never quantified as only spores are traditionally detected through cultivation-based methods. Therefore, the LOD necessary for reliable diagnosis is not directly accessible. However, the diseased larvae were found to contain as many as 2.8×10^9 spores [4]. During bacterial sporulation, only one endospore is formed by one vegetative cell. Therefore, the number of bacterial cells that appear in each larva during the disease progression is necessarily equal to or higher than the number of endospores. In cultivation-based approaches, only the viable bacteria (or spores) are counted. In antibody-based detection, the viability is not required, and only the presence of the surface antigen in the sample matters. As a result, even the bacteria inaccessible to conventional techniques can be detected by the immunoassay, making it a promising alternative to traditional methods. Direct comparison of the sensitivity of different methods (e.g., analyzing the same set of samples) is difficult but is indeed desirable in future research.

A comparison with the published PCR methods is possible, but the reported LODs vary significantly from 10^5 spores per gram of hive debris [42], to 283 spores/g of honey [43], and down to incredible 2 spores/g [44] and 1 spore/g [14] of honey and hive debris, respectively. This difference can be explained by the problematic estimation of the total spore count, as only a small fraction of all spores in the sample are viable [36] and if cultivation is used, the spore count can be underestimated. Another reason and an important aspect limiting the practical sensitivity of PCR is the presence of PCR inhibitors in bee materials, which makes the DNA isolation and purification a critical step and a possible source of this discrepancy [16].

D. Analysis of Real Samples

To demonstrate the practical potential of the developed assay, real samples of bees, larvae, and hive debris were analyzed. Typically, vegetative cells would be expected only in bee larvae, but bees and hive debris were tested as matrices as well to thoroughly test the inhibitory effects that the different matrices can have on the assay performance. In the case of the 25% extract of bees and larvae (Fig. 6A), the specific detection was achieved; however, the performance was worse compared to the analysis in buffer. Both samples have shown a decrease of specific signals, as well as the increase of the background, leading to the *S/B* of 5 in the case of bee extract and 9 in the case of the larvae extract. The larvae had the lowest background signal of all samples tested, suggesting the lowest concentration of substances causing non-specific binding of the antibodies or UCNP conjugates. The LODs of 1.1×10^6 CFU/mL (bee extract) and 4.8×10^5 CFU/mL (larvae extract) are on the limit to allow reliable distinction of AFB with regards to the bacterial load in honeybee material. Furthermore, a separate calibration based on healthy bees or larvae would be necessary for quantitative results due to the changes in the calibration curve shape compared to the buffer.

On the other hand, the bottom hive debris provided comparable results to the analysis in buffer (Fig. 6B). The LOD was 2.8×10^3 CFU/mL, the decrease of the *S/B* ratio to 14 is connected with
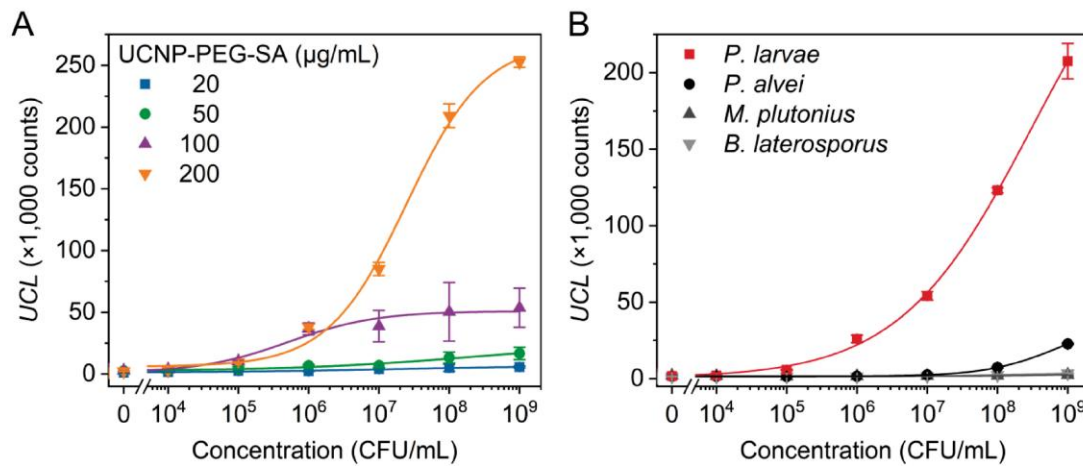
Fig. 5. Detection of *P. larvae* using sandwich ULISA. **(A)** Optimization of UCNP-PEG-SA label concentration. **(B)** Testing of assay specificity with *P. larvae* and negative controls of *P. alvei*, *M. plutonius*, and *B. laterosporus*.
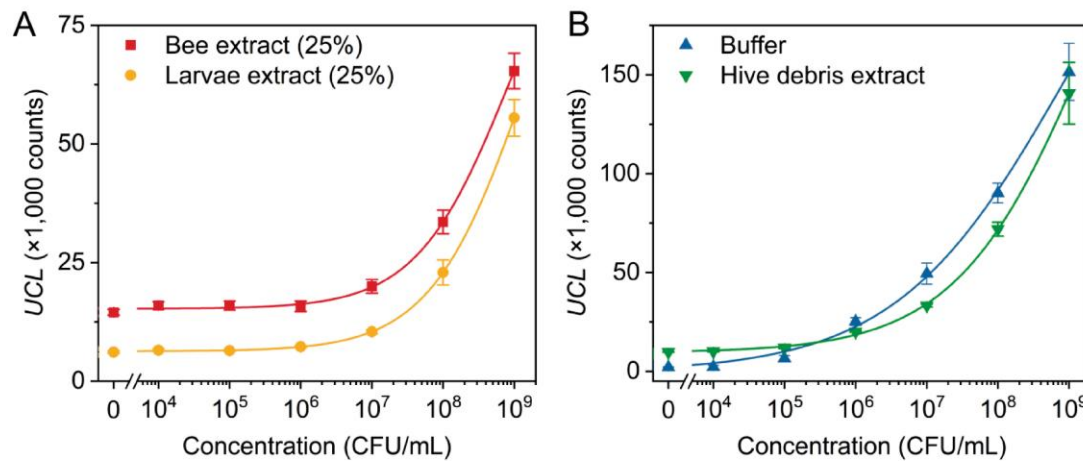

Fig. 6. Sandwich ULISA for the detection of *P. larvae* in real samples of **(A)** bee and larvae extract, and **(B)** bottom hive debris extract.

the slight increase of the level of background signal. Sensitive detection of *P. larvae* in hive debris is desirable for screening purposes [16]. Our results show that hive debris extract does not substantially affect the assay performance.

Overall, the results achieved with the real samples demonstrate the practical applicability of the ULISA assay for the diagnosis of AFB in different matrices. In the future, we also want to focus on the detection of spores with the aim to develop a combined assay to widen the applicability of the presented UCNP-based AFB diagnosis.

IV. CONCLUSION

In this work, we have introduced an ULISA for the diagnosis of American foulbrood, based on the detection of its surface epitopes in the sample. We prepared a rabbit polyclonal antibody specific to *P. larvae* using the disintegrated and purified cell walls as the immunization antigen. The antibody was tested in an ELISA; specific binding and only low levels of cross-reactivity with other bacteria potentially present in bees (*P. alvei*, *M. plutonius*, *B. laterosporus*) were observed. Conjugates of UCNPs based on Alkyne-PEG-Ner linker and either antibody-azide or streptavidin-azide were prepared using copper-catalyzed click chemistry. The sandwich ULISA with UCNP-PEG-SA provided an LOD of 2.9×10^3 CFU/mL, which represents a 22-fold improvement compared to the ELISA and is within the range of typical bacterial loads present during AFB infections. Finally, we have demonstrated the practical applicability of the ULISA in the analysis of real samples of bees, larvae, and bottom hive debris.

REFERENCES

[1] K. L. J. Hung, J. M. Kingston, M. Albrecht, D. A. Holway, and J. R. Kohn, "The worldwide importance of honey bees as pollinators in natural habitats," *Proc. R. Soc. B-Biol. Sci.*, vol. 285, no. 1870, Jan. 2018, Art no. 20172140.

[2] E. Genersch, "American foulbrood in honeybees and its causative agent, *Paenibacillus larvae*," *J. Invertebr. Pathol.*, vol. 103, pp. S10–S19, Jan. 2010.

[3] J. Ebeling, H. Knispel, G. Hertlein, A. Funfhaus, and E. Genersch, "Biology of *Paenibacillus larvae*, a deadly pathogen of honey bee larvae," *Appl. Microbiol. Biotechnol.*, vol. 100, no. 17, pp. 7387–7395, Sep. 2016.

[4] A. Lindstrom, S. Korpela, and I. Fries, "The distribution of *Paenibacillus larvae* spores in adult bees and honey and larval mortality, following the addition of American foulbrood diseased brood or spore-contaminated honey in honey bee (*Apis mellifera*) colonies," *J. Invertebr. Pathol.*, vol. 99, no. 1, pp. 82–86, Sep. 2008.

[5] W. Dobbelaere *et al.*, "Disinfection of wooden structures contaminated with *Paenibacillus larvae* subsp *larvae* spores," *J. Appl. Microbiol.*, vol. 91, no. 2, pp. 212–216, Aug. 2001.

[6] J. G. Stephan, J. R. de Miranda, and E. Forsgren, "American foulbrood in a honeybee colony: Spore-symptom relationship and feedbacks," *BMC Ecol.*, vol. 20, no. 1, pp. 14, Mar. 2020, Art. no. 15.

[7] B. Locke, M. Low, and E. Forsgren, "An integrated management strategy to prevent outbreaks and eliminate infection pressure of American foulbrood disease in a commercial beekeeping operation," *Prev. Vet. Med.*, vol. 167, pp. 48–52, Jun. 2019.

[8] M. A. Z. Hornitzky and S. C. Wilson, "A system for the diagnosis of the major bacterial brood diseases of honeybees," *J. Apic. Res.*, vol. 28, no. 4, pp. 191–195, 1989.

[9] D. C. de Graaf *et al.*, "Diagnosis of American foulbrood in honey bees: A synthesis and proposed analytical protocols," *Lett. Appl. Microbiol.*, vol. 43, no. 6, pp. 583–590, Dec. 2006.

[10] D. P. Stahly *et al.*, "PPL1c, a virulent mutant bacteriophage useful for identification of *Paenibacillus larvae* subspecies *larvae*," *J. Invertebr. Pathol.*, vol. 74, no. 3, pp. 295–296, Nov. 1999.

[11] V. A. Govan, M. H. Allsopp, and S. Davison, "A PCR detection method for rapid identification of *Paenibacillus larvae*," *Appl. Environ. Microbiol.*, vol. 65, no. 5, pp. 2243–2245, May 1999.

[12] B. Sopko *et al.*, "Detection and quantification of *Melissococcus plutonius* in honey bee workers exposed to european foulbrood in czechia through conventional PCR, qPCR, and barcode sequencing," *J. Apic. Res.*, vol. 59, no. 4, pp. 503–514, Aug. 2020.

[13] H. Beims, M. Janke, W. von der Ohe, and M. Steinert, "Rapid identification and genotyping of the honeybee pathogen *Paenibacillus larvae* by combining culturing and multiplex quantitative PCR," *Open Vet. J.*, vol. 10, no. 1, pp. 53–58, Apr. 2020.

[14] F. Rossi, C. Amadoro, A. Ruberto, and L. Ricchiuti, "Evaluation of quantitative PCR (qPCR) *Paenibacillus larvae* targeted assays and definition of optimal conditions for its detection/quantification in honey and hive debris," *Insects*, vol. 9, no. 4, pp. 12, Dec. 2018, Art. no. 165.

[15] S. Crudele, L. Ricchiuti, A. Ruberto, and F. Rossi, "Quantitative PCR (qPCR) vs culture-dependent detection to assess honey contamination by *Paenibacillus larvae*," *J. Apic. Res.*, vol. 59, no. 2, pp. 218–222, Mar. 2020.

[16] E. Forsgren and A. T. Laugen, "Prognostic value of using bee and hive debris samples for the detection of American foulbrood disease in honey bee colonies," *Apidologie*, vol. 45, no. 1, pp. 10–20, Jan. 2014.

[17] E. Otte, "Ein Beitrag zur Labordiagnose der Bösartigen Faulbrut der Honigbiene unter besonderer Berücksichtigung der Immunofluoreszenzmethode," *Apidologie*, vol. 4, no. 4, pp. 331–339, 1973.

[18] Y.-s. Peng and K.-y. Peng, "A study on the possible utilization of immunodiffusion and immunofluorescence techniques as the diagnostic methods for American foulbrood of honeybees (*Apis mellifera*)," *J. Invertebr. Pathol.*, vol. 33, no. 3, pp. 284–289, May 1979.

[19] P. E. Olsen, G. A. Grant, D. L. Nelson, and W. A. Rice, "Detection of American foulbrood disease of the honeybee, using a monoclonal antibody specific to *Bacillus larvae* in an enzyme-linked immunosorbent assay," *Can. J. Microbiol.*, vol. 36, no. 10, pp. 732–735, Oct 1990.

[20] Vita Bee Health, "AFB diagnostic test kit," [Online]. Available: https://www.vita-europe.com/beehealth/products/afb-diagnostic-test-kit/. accessed 2020-10-29

[21] X. M. Pei *et al.*, "Sandwich-type immunosensors and immunoassays exploiting nanostructure labels: A review," *Anal. Chim. Acta*, vol. 758, pp. 1–18, Jan. 2013.

[22] Z. Farka, T. Juřík, D. Kovář, L. Trnková, and P. Skládal, "Nanoparticle-Based immunochemical biosensors and assays: Recent advances and challenges," *Chem. Rev.*, vol. 117, no. 15, pp. 9973–10042, Aug. 2017.

[23] M. Haase and H. Schafer, "Upconverting nanoparticles," *Angew. Chem. Int. Ed.*, vol. 50, no. 26, pp. 5808–5829, Jun. 2011.

[24] G. Y. Chen, H. L. Qju, P. N. Prasad, and X. Y. Chen, "Upconversion nanoparticles: Design, nanochemistry, and applications in theranostics," *Chem. Rev.*, vol. 114, no. 10, pp. 5161–5214, May 2014.

[25] Z. Farka *et al.*, "Advances in optical single-molecule detection: En route to supersensitive bioaffinity assays," *Angew. Chem. Int. Ed.*, vol. 59, no. 27, pp. 10746–10773, Jun. 2020.

[26] R. B. Liebherr, T. Soukka, O. S. Wolfbeis, and H. H. Gorris, "Maleimide activation of photon upconverting nanoparticles for bioconjugation," *Nanotechnology*, vol. 23, no. 48, Dec. 2012, Art. no. 485103.

[27] A. Hlaváček *et al.*, "Rapid single-step upconversion-linked immunosorbent assay for diclofenac," *Microchim. Acta*, vol. 184, no. 10, pp. 4159–4165, Oct. 2017.

[28] M. J. Mickert *et al.*, "Measurement of Sub-femtomolar concentrations of prostate-specific antigen through single-molecule counting with an upconversion-linked immunosorbent assay," *Anal. Chem.*, vol. 91, no. 15, pp. 9435–9441, Aug. 2019.

[29] J. Kim *et al.*, "Rapid and background-free detection of avian influenza virus in opaque sample using NIR-to-NIR upconversion nanoparticle-based lateral flow immunoassay platform," *Biosens. Bioelectron.*, vol. 112, pp. 209–215, Jul. 2018.

[30] Z. B. Luo *et al.*, "Branched polyethylenimine-modified upconversion nanohybrid-mediated photoelectrochemical immunoassay with synergistic effect of dual-purpose copper ions," *Anal. Chem.*, vol. 91, no. 6, pp. 4149–4156, Mar. 2019.

[31] U. Kostiv *et al.*, "Versatile bioconjugation strategies of PEG-Modified upconversion nanoparticles for bioanalytical applications," *Biomacromolecules*, vol. 21., no. 11, pp. 4502–4513, Nov. 2020.

[32] N. Sirkka, A. Lyytikainen, T. Savukoski, and T. Soukka, "Upconverting nanophosphors as reporters in a highly sensitive heterogeneous immunoassay for cardiac troponin I," *Anal. Chim. Acta*, vol. 925, pp. 82–87, Jun. 2016.

[33] R. Peltomaa *et al.*, "Competitive upconversion-linked immunoassay using peptide mimetics for the detection of the mycotoxin zearalenone," *Biosens. Bioelectron.*, vol. 170, Dec. 2020, Art. no. 112683.

[34] V. Poláchová *et al.*, "Click-conjugated photon-upconversion nanoparticles in an immunoassay for honeybee pathogen *Melissococcus plutonius*," *Nanoscale*, vol. 11, no. 17, pp. 8343–8351, May 2019.

[35] A. M. Alippi, A. C. Lopez, and O. M. Aguilar, "Differentiation of *Paenibacillus larvae* subsp. *larvae*, the cause of American foulbrood of honeybees, by using PCR and restriction fragment analysis of genes encoding 16S rRNA," *Appl. Environ. Microbiol.*, vol. 68, no. 7, pp. 3655–3660, Jul. 2002.

[36] D. W. Dingman and D. P. Stahly, "Medium promoting sporulation of *Bacillus larvae* and metabolism of medium components," *Appl. Environ. Microbiol.*, vol. 46, no. 4, pp. 860–869, Oct. 1983.

[37] M. Fránek, I. Diblíková, I. Černoch, M. Vass, and K. Hruška, "Broad-specificity immunoassays for sulfonamide detection: Immunochemical strategy for generic antibodies and competitors," *Anal. Chem.*, vol. 78, no. 5, pp. 1559–1567, Mar. 2006.

[38] S. Fischer, J. K. Swabeck, and A. P. Alivisatos, "Controlled isotropic and anisotropic shell growth in beta-NaLnF$_4$ nanocrystals induced by precursor injection rate," *J. Am. Chem. Soc.*, vol. 139, no. 35, pp. 12325–12332, Sep. 2017.

[39] A. Hlaváček, J. Křivánková, J. Přikryl, and F. Foret, "Photon-Upconversion barcoding with multiple barcode channels: Application for droplet microfluidics," *Anal. Chem.*, vol. 91, no. 20, pp. 12630–12635, Oct. 2019.

[40] J. D. Evans *et al.*, "Standard methods for molecular research in *Apis mellifera*," *J. Apic. Res.*, vol. 52, no. 4, Apr 2013, Art. no. 52.4.11.

[41] K. Huse, H.-J. Böhme, and G. H. Scholz, "Purification of antibodies by affinity chromatography," *J. Biochem. Biophys. Methods*, vol. 51, no. 3, pp. 217–231, May 2002.

[42] S. Ryba, D. Titera, M. Haklova, and P. Stopka, "A PCR method of detecting American foulbrood (*Paenibacillus larvae*) in winter beehive wax debris," *Vet. Microbiol.*, vol. 139, no. 1-2, pp. 193–196, Oct. 2009.

[43] A. M. Alippi, A. C. Lopez, and O. M. Aguilar, "A PCR-based method that permits specific detection of *Paenibacillus larvae* subsp. *larvae*, the cause of American foulbrood of honey bees, at the subspecies level," *Lett. Appl. Microbiol.*, vol. 39, no. 1, pp. 25–33, May 2004.

[44] J. Martinez, V. Simon, B. Gonzalez, and P. Conget, "A real-time PCR-based strategy for the detection of *Paenibacillus larvae* vegetative cells and spores to improve the diagnosis and the screening of American foulbrood," *Lett. Appl. Microbiol.*, vol. 50, no. 6, pp. 603–610, Jun. 2010.

Matěj Pastucha received the master's degree in analytical biochemistry in 2015 and is currently working toward the Ph.D. under the supervision of Petr Skládal. He is the Ph.D. student of Biochemistry with Masaryk University, Brno, Czech Republic. His research focuses on the development of immunochemical assays and sensors for the detection of proteins and bacteria. This includes antibody immobilization to diverse substrates, their conjugation with nanoparticles or other labels, and detection utilizing optical or electrochemical readout.

Eliška Odstrčilíková received the bachelor's degree in biochemistry from Masaryk University in 2020. She is currently working toward the master's degree in analytical biochemistry under the supervision of Zdeněk Farka. She specializes in bioanalytical applications of photon-upconversion nanoparticles, especially for microtiter plate-based and lateral flow immunoassay.

Antonín Hlaváček received the Ph.D. degree in biochemistry in 2012 under the supervision of Petr Skládal with the Department of Biochemistry, Masaryk University, Czech Republic. From 2013 to 2017, he experienced several research internships with the University of Regensburg, Germany (laboratory of Hans-Heiner Gorris). He is currently working as a Researcher with the Department of Bioanalytical Instrumentation of the Institute of Analytical Chemistry of the Czech Academy of Sciences. His research interests include the synthesis of nanoparticles, bioconjugation, immunoassays, microfluidics, and bioanalytical instrumentation.

Julian C. Brandmeier is a master's student with the Institute of Analytical Chemistry, Chemo- and Biosensors at the University of Regensburg in the group of Hans-Heiner Gorris. He is currently focusing on the sensitive detection of cardiac troponin using photon-upconversion nanoparticles as background-free luminescent labels in microtiter plate-based and lateral flow immunoassays. He is specialized in the surface modification, characterization, and imaging of photon-upconversion nanoparticles.

Vít Vykoukal received the Ph.D. degree in advanced materials and nanosciences in 2018 under the supervision of Jiří Pinkas with CEITEC, Masaryk University, Czech Republic. Since 2019, he is a member of Cryo-Electron Microscopy and Tomography Core Facility with CEITEC MU where he works as a Research Specialist. He supervises the project for the application a new contrast agent in cryo-electron microscopy, and evolves synthesis of bio-compatible metal nanoparticles and their uptake into cells. He is responsible for the characterization of inorganic materials of core-facility customers.

Julie Weisová is studying for a bachelor's degree in biochemical technology with the University of Technology, Brno, Czech Republic. She is currently on an internship with the Department of Bioanalytical Instrumentation of the Institute of Analytical Chemistry of the Czech Academy of Sciences. She focuses on the synthesis and electrophoretic characterization of photon-upconversion nanoparticles under the supervision of Antonín Hlaváček.

Hans H. Gorris studied biology with the University of Münster, Germany and received the Ph.D. degree from the University of Lübeck, Germany. After working on single-molecule enzyme assays with David Walt with Tufts University, USA, he joined the Institute of Analytical Chemistry, Chemo- and Biosensors with the University of Regensburg, Germany, in 2009. He has been a Heisenberg-Fellow of the DFG since 2016. His research interests include background-free luminescent bioaffinity assays based on UCNPs with single-molecule sensitivity as well as new methods for investigating enzyme kinetics at the single-molecule level.

Petr Skládal received the Ph.D. degree in the field of amperometric biosensors in 1992. After completing research stays (1991, 1993) with the University of Florence, Italy, with Marco Mascini, he continued to investigate biosensors. He is an Associated Professor and Head of the Department of Biochemistry, Faculty of Science, Masaryk University. He currently also heads the Nanobiotechnology Research Group with the Central European Institute of Technology in Brno. His research is focused on enzyme and immunochemical biosensors using electrochemical and piezoelectric transducers, affinity kinetics with surface plasmon resonance systems, nanomechanical transducers, and applications of atomic force microscopy in life sciences.

Zdeněk Farka received the Ph.D. degree in structural biology in 2017 under the supervision of Petr Skládal with CEITEC, Masaryk University, Czech Republic. He completed research internships with the University of Regensburg, Germany, with Hans-Heiner Gorris and with the University of Rouen, France, with Niko Hildebrandt. He is currently working as an Assistant Professor with the Department of Biochemistry, Faculty of Science, Masaryk University. His research interests include the detection of proteins and bacteria *via* immunoanalytical techniques. He develops label-free point-of-care sensors based on optical and electrochemical transducers and examines the amplification of immunoassay response by various kinds of nanoparticles.

301

Paper XVII

Single Molecule Upconversion-Linked Immunosorbent Assay with Extended Dynamic Range for the Sensitive Detection of Diagnostic Biomarkers

Farka, Z.; Mickert, M. J.; Hlaváček, A.; Skládal P.; Gorris, H. H.

(Z.F. and M.J.M. contributed equally)

Contribution:

Design of experiments, optimization of single-particle microscope setup, bioconjugation and characterization of UCNPs, development and optimization of sandwich immunoassay, data evaluation, manuscript writing

Single Molecule Upconversion-Linked Immunosorbent Assay with Extended Dynamic Range for the Sensitive Detection of Diagnostic Biomarkers

Zdeněk Farka,[†,‡] Matthias J. Mickert,[†] Antonín Hlaváček,[†,‡,§] Petr Skládal,[‡] and Hans H. Gorris*,[†]

[†]Institute of Analytical Chemistry, Chemo- and Biosensors, University of Regensburg, 93040 Regensburg, Germany
[‡]CEITEC—Central European Institute of Technology, Masaryk University, 625 00 Brno, Czech Republic
[§]Institute of Analytical Chemistry of the Czech Academy of Sciences, v. v. i., 602 00 Brno, Czech Republic

S *Supporting Information*

ABSTRACT: The ability to detect disease markers at the single molecule level promises the ultimate sensitivity in clinical diagnosis. Fluorescence-based single-molecule analysis, however, is limited by matrix interference and can only probe a very small detection volume, which is typically not suitable for real world analytical applications. We have developed a microtiter plate immunoassay for counting single molecules of the cancer marker prostate specific antigen (PSA) using photon-upconversion nanoparticles (UCNPs) as labels that can be detected without background fluorescence. Individual sandwich immunocomplexes consisting of (1) an anti-PSA antibody immobilized to the surface of a microtiter well, (2) PSA, and (3) an anti-PSA antibody-UCNP conjugate were counted under a wide-field epifluorescence microscope equipped with a 980 nm laser excitation source. The single-molecule (digital) upconversion-linked immunosorbent assay (ULISA) reaches a limit of detection of 1.2 pg mL^{-1} (42 fM) PSA in 25% blood serum, which is about ten times more sensitive than commercial ELISAs, and covers a dynamic range of three orders of magnitude. This upconversion detection mode has the potential to pave the way for a new generation of digital immunoassays.
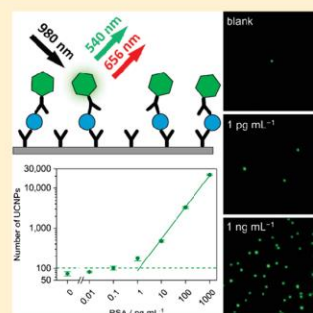
Information on the onset and the progression of diseases is essential to start a therapy as early as possible. Consequently, sensitive diagnostic tests (assays) are required to measure the presence of diagnostic markers with the lowest possible limit of detection (LOD).[1] The development of single molecule immunoassays has recently attracted wide attention[2−4] because the detection and quantification of individual analyte molecules—also termed a digital readout—obviates the need for a (sometimes disputed) classical definition of an LOD and in principle can reach a much higher sensitivity.

A single fluorescent molecule conjugated to an analyte-specific antibody can only be detected in a (sub)femtoliter volume by using confocal microscopy[5] or total internal reflection fluorescence microscopy (TIRF)[6,7] to minimize the background fluorescence and light scattering of billions of surrounding molecules. The high microscopic demands and extremely small detection volumes are not practicable for analyzing real samples because it takes too long for an analyte molecule present in subpicomolar concentrations to diffuse into such a small detection volume.[8] Mainly two strategies have been developed to make single molecule immunoassays applicable in real analytical assays: First, the analyte can be preconcentrated on the surface of magnetic microbeads rather than using a planar surface to access a larger probe volume and improve the binding kinetics of surface-bound capture antibody and analyte free in solution. Second, if the detection antibody is labeled with an enzyme, thousands of fluorescent product molecules can be generated per analyte molecule, which yields a much stronger and more robust signal detectable by conventional wide-field microscopy. The enzymatic signal amplification step is in line with an enzyme-linked immunosorbent assay (ELISA)—the gold standard in immunodiagnostics—but diffusion of the fluorescent product has to be prevented to obtain a high local fluorophore concentration. A local confinement of the fluorescent product has been achieved either by using large arrays of femtoliter-sized wells[9] to enclose microbeads containing the preassembled single enzyme-analyte sandwich complex with a fluorogenic substrate[10] or by using a substrate that is converted to an insoluble fluorescent product and directly deposits on the surface of the microbeads.[11]

Photon-upconversion nanoparticles (UCNPs) are lanthanide-doped nanocrystals that can be excited by near-infrared (NIR, 980 nm) light and, depending on the lanthanide dopant composition, emit various colors of short wavelength light. The anti-Stokes emission strongly reduces autofluorescence and light scattering of the surrounding matrix.[12] UCNPs have been used as optical background-free luminescent labels for so-called upconversion-linked immunosorbent assays (ULISAs)[13] to

detect environmental analytes such as diclofenac[14,15] and clinical analytes such as cardiac troponin I[16] or prostate-specific antigen (PSA, M_w = 28.7 kDa).[17]

PSA is the most important diagnostic marker for prostate cancer, one of the most common cancers in men.[18] PSA levels in serum are in particular important for monitoring the response to therapy and recurrence in patients after radical prostatectomy.[19,20] The biochemical recurrence is defined as PSA concentrations rising from <0.1 ng mL^{-1} to persistently >0.2 ng mL^{-1}, and occurs in up to 40% after surgery.[21] Therefore, sensitive assays and high-affinity anti-PSA antibodies are required that allow for the reliable detection of PSA concentrations below 0.1 ng mL^{-1}.

Here, we present a single molecule (digital) ULISA for PSA (Figure 1), which is more easily amenable to standard
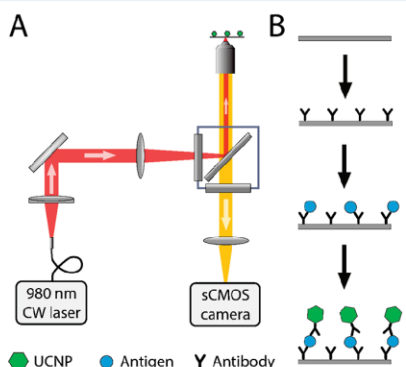
Figure 1. (A) Scheme of upconversion microscopy. An inverted wide-field epiluminescence microscope is equipped with a fiber-coupled 980 nm continuous-wave laser diode and a sensitive sCMOS camera. (B) Scheme of sandwich upconversion-linked immunosorbent assay (ULISA) involving (1) immobilization of the anti-PSA capture antibody, (2) binding of the antigen PSA, and (3) analyte detection by a UCNP-antibody conjugate.

immunoassay protocols compared to single enzyme molecule amplification systems because (1) there is no need to confine the diffusion of the fluorescent product, (2) no preconcentration step is required, and (3) single analyte molecules can be detected in a conventional 96-well microtiter plate format using wide-field epiluminescence microscopy.[22]

■ EXPERIMENTAL SECTION

Preparation of the UCNP-Antibody Conjugate. UCNPs (β-NaYF$_4$:18 mol % Yb^{3+}, 2 mol % Er^{3+}) of different sizes (SI Table 1) were synthesized by high-temperature coprecipitation[23] and coated with a carboxylated silica layer using a reverse microemulsion method (SI Table 2).[24] The affinity of anti-PSA antibodies was analyzed by surface plasmon resonance (SPR, SI Figure 1). A polyclonal anti-PSA antibody (AF1344, R&D Systems, USA) was conjugated to the surface of UCNPs via EDC/sulfo-NHS activation. The Supporting Information contains experimental details.

Characterization of Nanoparticles. For transmission electron microscopy (TEM, Tecnai F20, FEI, USA), ~4 μL of UCNPs were placed onto a 400-mesh copper EM grid coated with a continuous layer of carbon. Size and shape of individual UCNPs were analyzed with the software ImageJ. Dynamic light scattering (DLS) and zeta potential measure-

ments were performed on a Zetasizer Nano ZS (Malvern, UK). For agarose gel electrophoresis,[25,26] UCNP samples were mixed in a ratio of 10:1 with glycerol (80% w/w), and 6 μL were applied into the pockets of the agarose gel (0.5% w/v agarose, 45 mM Tris, 45 mM borate, pH 8.6). After electrophoresis (40 min at 100 V), the gel was scanned with a step size of 0.5 mm using a custom-built upconversion scanner (Chameleon, Hidex, Finland) equipped with a continuous 980 nm laser (4 W). The integrated upconversion luminescence intensity of the gel pockets divided by the integrated luminescence over the whole gel lane yielded information on the fraction of aggregated UCNPs. Additionally, the calculation of UCNP mass concentrations is described in the Supporting Information.

Upconversion Epiluminescence Microscopy. A 980 nm continuous wave laser diode (4 W, WSLS-980−004-H-T, Wavespectrum, China) was connected to a motorized TIRF/Epifluorescence illuminator unit (Ti-TIRF-E, Nikon, Japan) of an inverted microscope (Eclipse Ti-E, Nikon) via a multimode optical fiber (105 μm fiber core, 0.22 NA, Wavespectrum). A computer was equipped with an analog output module (PCI-6723, National Instruments, USA) to control the laser power (SI Figure 2). The optical filter set included a long-pass excitation filter ($\lambda_{\text{cut-on}}$ = 830 nm, Schott, Germany), a multiphoton dichroic mirror ($\lambda_{\text{cut-on}}$ = 875 nm, AHF Analysentechnik, Germany), and a band-pass filter for the green emission of Er-doped UCNPs (λ = 535 ± 70 nm, OD$_{980nm}$ ≈ 6, Chroma, USA). Images were taken with a 100× objective (NA = 1.49, CFI HP Apochromat TIRF, Nikon) and a cooled 5.5 megapixel sCMOS camera (Neo, Andor Technology, UK). The maximum laser power of 4 W resulted in a power density of 640 W cm^{-2} in the focal plane. The optimization of the single UCNP detection on glass slides is described in the Supporting Information.

Upconversion-Linked Immunosorbent Assay (ULISA). A 96-well polystyrene microtiter plate with 190 μm thick bottom foil (high protein binding capacity, μCLEAR, Greiner, Germany) was coated with 0.3 μg mL^{-1} of monoclonal anti-PSA antibody (ab403, Abcam, UK) in coating buffer (50 mM NaHCO$_3$/Na$_2$CO$_3$, 0.05% NaN$_3$, pH 9.6; 200 μL per well) at 4 °C overnight. All subsequent steps were carried out at room temperature. After four washing steps with 250 μL of washing buffer (50 mM NaH$_2$PO$_4$/Na$_2$HPO$_4$, 0.01% Tween 20, 0.05% NaN$_3$, pH 7.4), the microtiter plate was blocked with 250 μL of 1% bovine serum albumin (BSA, Sigma-Aldrich) in 50 mM NaH$_2$PO$_4$/Na$_2$HPO$_4$, 0.05% NaN$_3$, pH 7.4, for 1 h. After four washing steps, serial PSA (ab78528, Abcam) dilutions were prepared either in assay buffer (50 mM Tris, 150 mM NaCl, 0.05% NaN$_3$, 0.5% bovine gamma globulin (Sigma-Aldrich), 0.2% BSA, 0.01% Tween 20, 0.2% poly(vinyl alcohol) (M_w: 6000 g mol^{-1}), 1% glucose and 5 mM EDTA, pH 7.5) or in 4-fold diluted bovine serum (Sigma-Aldrich). On each well, 100 μL of the PSA dilution was incubated for 1 h. After four washing steps, the microtiter plate was incubated with 100 μL of the UCNP-antibody conjugate (10 μg mL^{-1} in assay buffer) for 1 h. After four washing steps, the wells were left empty to determine the PSA concentration in each well in two different modes:

Analog Mode. The integrated upconversion luminescence of the UCNP label was detected in the microtiter plate wells by using a custom-built upconversion microtiter plate reader (Chameleon, Hidex). The continuous 980 nm laser (4 W) was focused on the bottom of the microtiter plate wells resulting in a collimated laser spot size of ~0.8 mm.[14] Each well was

scanned 64 times with a raster step size of 0.4 mm and 500 ms signal integration time. The truncated average was calculated for each well after discarding the eight highest and eight lowest luminescence intensities to exclude outliers.

Digital Mode. The number of single UCNP labels in the microtiter plate wells was counted by upconversion epiluminescence microscopy. Adding 100 μL of glycerol to the wells facilitated heat dissipation of the high-power laser beam. Nine images of $166 \times 140\ \mu m^2$ were recorded per well with a step size of 300 μm in a rectangular grid. Single UCNPs were counted automatically using a built-in function of the software NIS Elements (Nikon).

Data Analysis. For each detection mode, the mean and standard deviation were calculated from three replicate wells and two types of regression analyses were applied for the calibration curves. (1) In the four-parameter logistic function

$$Y = \frac{Y_{max} - Y_{bg}}{1 + \left(\frac{[PSA]}{EC_{50}}\right)^s} + Y_{bg}$$

[PSA] is the concentration of prostate specific antigen and Y is either the upconversion luminescence (analog ULISA) or the number of UCNPs (digital ULISA). The equation yields the maximum (Y_{max}) and background (Y_{bg}) signal, the PSA concentration that reduces ($Y_{max} - Y_{bg}$) by 50% (EC_{50}), and the slope at the inflection point (s).

(2) In the logit−log analysis, a linear regression was applied to the steepest part of the calibration curve and the background level was conventionally defined as the luminescence signal or number of UCNPs, respectively, detected in the absence of PSA plus three times the standard deviation. The intersection of the regression line and the background level defined the LOD.

■ RESULTS AND DISCUSSION

The development of the single molecule ULISA critically depended on the design of a homogeneous and monodisperse UCNP label. The TEM images show a homogeneous size and shape of UCNPs covered by a closed silica shell (Figure 2). The shift of the electrophoretic mobility (Figure 2C) indicates the successful UCNP-Ab conjugation. Only a small fraction of aggregates (<10%) was present in the gel pockets that did not enter the gel matrix. The main fraction of single UCNPs as well as clusters of two and three UCNPs are visible as distinct bands in the gel. The success of the surface modification steps was further confirmed by an increasing hydrodynamic diameter as well as zeta potential measurements (SI Figure 4).

Wide-field upconversion microscopy (Figure 1A) of single UCNPs was optimized by immobilizing different types of carboxylated UCNPs in a size range of 37−90 nm on a glass slide modified with cationized bovine serum albumin (cBSA) (Figure 3). The carboxylated UCNPs exposing a negative surface potential (SI Figure 4) strongly bind to the cBSA-coated glass slides such that the number of immobilized UCNPs increased linearly with the UCNP concentration (SI Figure 5). Excitation in the upconversion mode ensured a very low background signal that, in absence of UCNPs, only depended on the camera noise (Figure 3A). The four types of UCNPs were visible individually (Figure 3B−E) as diffraction limited spots of ∼400 nm in diameter (Figure 3F). The brightness of the spots increased so strongly with the size of UCNPs (Figure 3G) that the exposure time for the largest
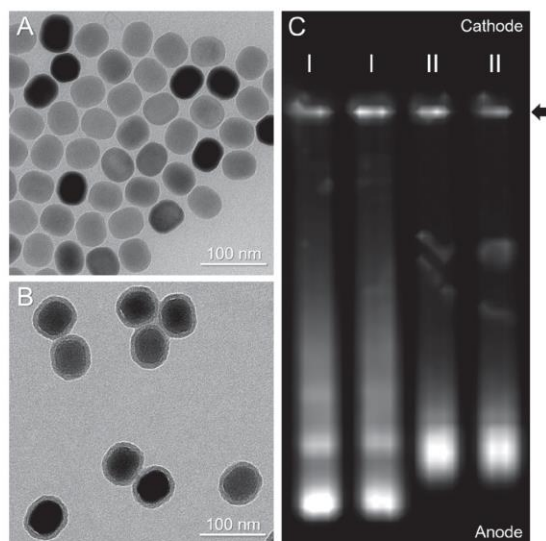
Figure 2. TEM images of (A) oleic acid-capped UCNPs (diameter 48.2 ± 3.4 nm) and (B) UCNPs with carboxylated silica shell (thickness 7.1 ± 1.2 nm). (C) Agarose gel electrophoresis of (I) carboxylated UCNPs and (II) UCNP-antibody conjugates in duplicates (6% of nanoparticle aggregates in I and 8% in II). The arrow indicates the starting point of electrophoresis.

UCNPs had to be reduced in order to avoid detector saturation. The histograms in Figure 3H follow a single Gaussian distribution, which indicates some heterogeneity in the emission intensity of individual UCNPs—rather than clusters of one, two or more nanoparticles that would result in distinct peaks. Thus, both gel electrophoresis (Figure 2C, lines I) and the intensity distribution confirm that the majority of UCNPs are monodisperse. UCNPs with a size of 48 nm showed highly homogeneous and strong luminescence intensities suitable for all further experiments.

The sandwich immunoassay (Figure 1B) was performed on high-binding microtiter plates with a thin foil (190 μm) at the bottom of each well to account for the short working distance of the high NA microscope objective. The microtiter plate format allowed for an easier immobilization of the capture antibody and for an improved assay handling and automation compared to glass slides. Serial dilutions of PSA spiked into 25% serum (diluted in assay buffer) were prepared on the microtiter plate. After binding of the UCNP−antibody conjugate, the microtiter plates were read both by measuring the upconversion luminescence in a microtiter plate reader (analog ULISA) and by counting individual sandwich immunocomplexes as diffraction limited spots under the microscope (digital ULISA, Figure 4).

The small number of spots in the absence of PSA (Figure 4A) can be attributed to some nonspecific binding of the UCNP−antibody conjugate to the microtiter plate surface and defines the LOD of the immunoassay, similar to that in a conventional assay. Several advantages of the digital readout over an analog readout, however, should be noted: (1) Nonspecific binding of the luminescent reporter and the instrumental background can be assessed separately in each measurement. (2) Counting single immunocomplexes is not affected by variations in the signal intensity of the reporter, for
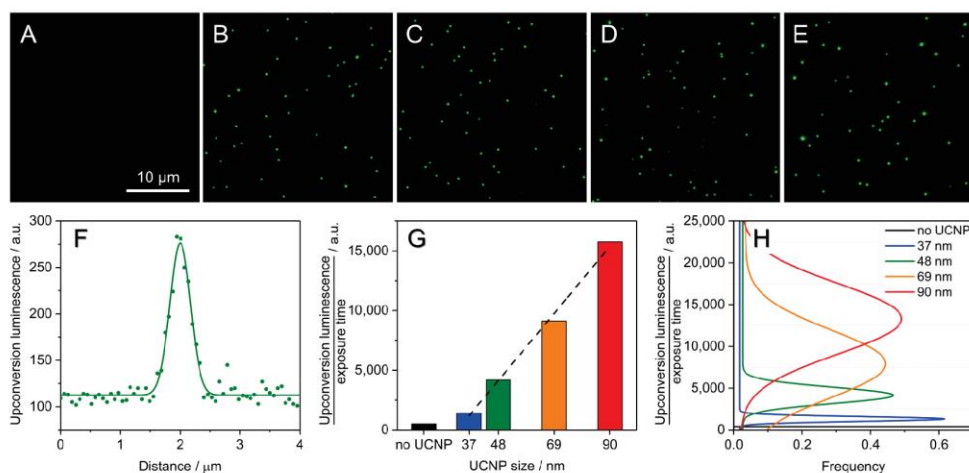
Figure 3. Image sections of individual UCNPs (green spots) bound to cBSA-modified glass slide taken by wide-field microscopy. (A) No UCNP, 7 s exposure time; (B) 37 nm, 7 s exposure time; (C) 48 nm, 5 s exposure time; (D) 69 nm 4 s exposure time; (E) 90 nm, 2 s exposure time. (F) Upconversion luminesce intensity cross-section of a single UCNP (diameter of 48 nm) evaluated from microscope image. (G) The upconversion luminescence intensities normalized to 1 s exposure time increase with the size of UCNPs. (H) Gaussian distributions of luminescence intensities with coefficients of variation (CV) of 26% (37 nm), 28% (48 nm), 61% (69 nm), and 37% (90 nm).
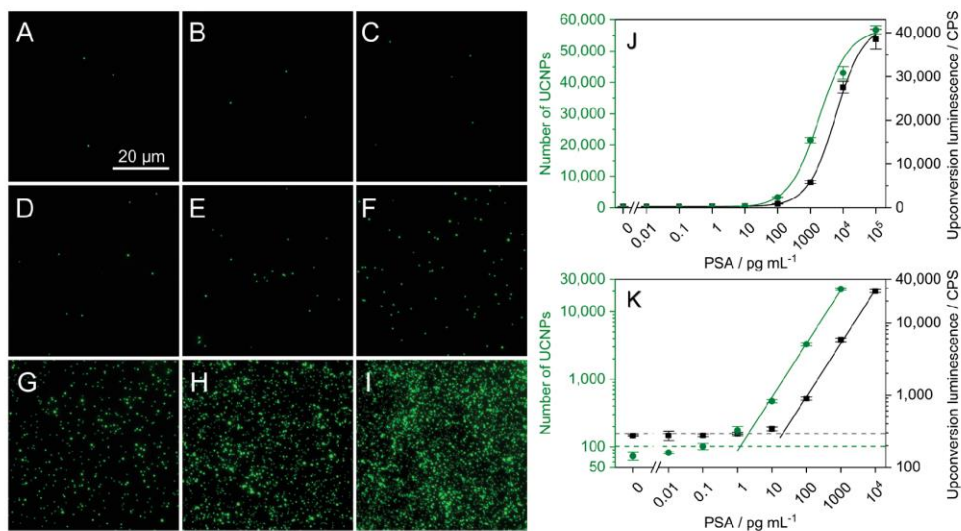
Figure 4. Upconversion microscopy images of serial PSA dilutions in 25% serum: (A) no PSA; (B) 10 fg mL^{-1}; (C) 100 fg mL^{-1}; (D) 1 pg mL^{-1}; (E) 10 pg mL^{-1}; (F) 100 pg mL^{-1}; (G) 1 ng mL^{-1}; (H) 10 ng mL^{-1}; (I) 100 ng mL^{-1}. PSA is captured on microtiter plate wells and detected by a UCNP−antibody conjugate. A small section (3600 μm^2) of the analyzed area (166 × 140 μm^2) is shown. (J) Calibration based on a 4-parameter logistic regression model shows a test midpoint (EC$_{50}$) of 1.8 ng mL^{-1} for the digital readout (green line) and 5.9 ng mL^{-1} for the analog readout (black line). (K) Linear regression after logit transformation yields an LOD of 1.2 pg mL^{-1} in the digital readout and 20.3 pg mL^{-1} in the analog readout. The hatched lines are the background levels defined either as mean number of spots (green) or upconversion luminescence (black) without PSA + 3× standard deviation. Error bars indicate the standard deviation from three replicate wells.

example, as a result of luminescence heterogeneity or aggregation of UCNPs.[27] By contrast, the size of an aggregate strongly affects the integrated signal in the analog mode even if only very few aggregates are present. To reduce the effect of large aggregates in the analog readout, we raster scanned 64 points on each well with the microtiter plate reader and determined a truncated average for further data evaluation. (3) The number of spots counted on a fraction of the microtiter well area covered by the PSA sample is a direct measure of the

detection efficiency of PSA (Supporting Information), which depends on several factors such as diffusion rates, binding kinetics and steric hindrance due to the nanoparticle size. Here, we have calculated an average detection efficiency of approximately 1% in the linear detection range of the assay.

For a good precision of the assay, the imaging area must be large enough to minimize the sampling error,[28] or in physical terms, the Poisson noise. While either a 100× or a 60× microscope objective were suitable for counting single UCNPs,

306

the 100× objective was more sensitive (SI Figure 6). To account for the small field of view of the 100× objective, we acquired consecutive images of nine areas per microtiter plate well. The total imaging area of 0.2 mm² per well was large enough to reduce the Poisson noise below 10%, and counting of individual immunocomplexes in repeated measurements was highly reproducible (CV < 15%) (SI Table 4).

Data obtained by single molecule counting (digital ULISA) and by a microtiter plate reader (analog ULISA) were analyzed by a four-parameter regression model commonly used for microtiter plate immunoassays (Figure 4J) as well as a logit–log model (Figure 4K) to zoom in on low counts of UCNPs and signals close to the background. The digital ULISA achieved an LOD of 1.2 pg mL^{-1} and a linear working range between 10 pg mL^{-1} and 1 ng mL^{-1} of PSA in 25% serum; this corresponds to the LOD of 4.8 pg mL^{-1} in the original serum. Higher PSA concentrations were outside the linear range because too many spots with overlapping point-spread functions (Figures 4H and 4I) cannot be resolved individually. Higher PSA concentrations were analyzed by switching from the digital to the analog mode.[29] The sensitivity (LOD: 20.3 pg mL^{-1}) and the linear working range (100 pg mL^{-1}–10 ng mL^{-1}) of the analog ULISA were comparable to commercial ELISAs for the diagnosis of PSA (SI Table 5). The combination of both detection modes, however, improves the sensitivity by 1 order of magnitude and extends the linear working range to 3 orders of magnitude from 10 pg mL^{-1} to 10 ng mL^{-1}. The analysis of PSA spiked into buffer yielded essentially the same results (SI Figure 7 and SI Table 3) and indicates that matrix effects of 25% serum are negligible.

In the future, the single molecule immunoassay can be improved by (1) optimizing the blocking procedure to reduce nonspecific binding, (2) tuning the antibody sandwich combination specifically for single molecule immunoassays,[30] and (3) by reducing the size of the UCNP-antibody reporter. In an earlier report,[31] fluorescence lifetime imaging of relatively large Eu(III)-doped nanoparticles (107 nm in diameter) did not improve the detection of PSA by counting single immunocomplexes compared to the analog mode. By contrast, we have achieved a 10× higher sensitivity in the digital mode by reducing the label size to 48 nm. It is likely that smaller nanoparticle can further increase the detection efficiency above 1% by providing better access to the surface-bound PSA. The single molecule ULISA is also amenable to the multiplexed detection of several analytes in parallel by using UCNP–antibody combinations that can be excited by 980 nm light but display different emission colors.[32–34]

CONCLUSION

We have developed a digital sandwich immunoassay using UCNPs as a luminescent label for counting single PSA molecules without background fluorescence. With an LOD of 1.2 pg mL^{-1} and a wide dynamic range of 3 orders of magnitude, the ULISA is superior to commercial ELISAs for the clinical diagnosis of PSA. While some more sensitive immunoassays have been described in the literature (SI Table 5), none of these are compatible with conventional microtiter plate assay protocols that can be readily adapted for the detection of any other diagnostic markers. Thus, we expect that the ability to detect single analyte molecules reliably and with a relatively simple detection scheme will have a strong impact on the development of future immunoassays.

ASSOCIATED CONTENT

Supporting Information

The Supporting Information is available free of charge on the ACS Publications website at DOI: 10.1021/acs.anal-chem.7b03542.

> Characterization of anti-PSA antibodies, the preparation and characterization of UCNP-antibody conjugates, the optimization of the upconversion microscope, additional ULISA experiments, and a comparison to other (commercial) immunoassays for the detection of PSA (PDF)

AUTHOR INFORMATION

Corresponding Author

*Phone: +49-941-943-4015. Fax: +49-941-943-4064. E-mail: hans-heiner.gorris@ur.de.

ORCID

Antonín Hlaváček: 0000-0003-3358-3858
Petr Skládal: 0000-0002-3868-5725
Hans H. Gorris: 0000-0003-1148-4293

Author Contributions

Z.F. and M.J.M. contributed equally to the work.

Notes

The authors declare no competing financial interest.

REFERENCES

(1) Farka, Z.; Juřík, T.; Kovář, D.; Trnková, L.; Skládal, P. *Chem. Rev.* **2017**, *117*, 9973−10042.

(2) Holzmeister, P.; Acuna, G. P.; Grohmann, D.; Tinnefeld, P. *Chem. Soc. Rev.* **2014**, *43* (4), 1014−1028.

(3) Gooding, J. J.; Gaus, K. *Angew. Chem., Int. Ed.* **2016**, *55* (38), 11354−11366.

(4) Zhang, Y.; Noji, H. *Anal. Chem.* **2017**, *89* (1), 92−101.

(5) Löscher, F.; Böhme, S.; Martin, J.; Seeger, S. *Anal. Chem.* **1998**, *70* (15), 3202−3205.

(6) Tessler, L. A.; Reifenberger, J. G.; Mitra, R. D. *Anal. Chem.* **2009**, *81* (17), 7141−7148.

(7) Jain, A.; Liu, R. J.; Ramani, B.; Arauz, E.; Ishitsuka, Y.; Ragunathan, K.; Park, J.; Chen, J.; Xiang, Y. K.; Ha, T. *Nature* **2011**, *473* (7348), 484−489.

(8) Schreiber, G.; Haran, G.; Zhou, H. X. *Chem. Rev.* **2009**, *109* (3), 839−860.

(9) Gorris, H. H.; Walt, D. R. *Angew. Chem., Int. Ed.* **2010**, *49* (23), 3880−3895.

(10) Rissin, D. M.; Kan, C. W.; Campbell, T. G.; Howes, S. C.; Fournier, D. R.; Song, L.; Piech, T.; Patel, P. P.; Chang, L.; Rivnak, A. J.; Ferrell, E. P.; Randall, J. D.; Provuncher, G. K.; Walt, D. R.; Duffy, D. C. *Nat. Biotechnol.* **2010**, *28* (6), 595−599.

(11) Akama, K.; Shirai, K.; Suzuki, S. *Anal. Chem.* **2016**, *88* (14), 7123−7129.

(12) Haase, M.; Schäfer, H. *Angew. Chem., Int. Ed.* **2011**, *50* (26), 5808−5829.

(13) Gorris, H. H.; Resch-Genger, U. *Anal. Bioanal. Chem.* **2017**, *409*, 5875−5890.

(14) Hlaváček, A.; Farka, Z.; Hübner, M.; Horňáková, V.; Němeček, D.; Niessner, R.; Skládal, P.; Knopp, D.; Gorris, H. H. *Anal. Chem.* **2016**, *88* (11), 6011−6017.

(15) Hlaváček, A.; Peterek, M.; Farka, Z.; Mickert, M. J.; Prechtl, L.; Knopp, D.; Gorris, H. H. *Microchim. Acta* **2017**, *184* (10), 4159−4165.

(16) Sirkka, N.; Lyytikäinen, A.; Savukoski, T.; Soukka, T. *Anal. Chim. Acta* **2016**, *925*, 82−87.

(17) Ukonaho, T.; Rantanen, T.; Jämsen, L.; Kuningas, K.; Päkkilä, H.; Lövgren, T.; Soukka, T. *Anal. Chim. Acta* **2007**, *596* (1), 106−115.

(18) Siegel, R. L.; Miller, K. D.; Jemal, A. *Ca-Cancer J. Clin.* **2016**, *66* (1), 7−30.

(19) Hayes, J. H.; Barry, M. J. *JAMA-J. Am. Med. Assoc.* **2014**, *311* (11), 1143−1149.

(20) Stephan, C.; Ralla, B.; Jung, K. *Biochim. Biophys. Acta, Rev. Cancer* **2014**, *1846* (1), 99−112.

(21) Thaxton, C. S.; Elghanian, R.; Thomas, A. D.; Stoeva, S. I.; Lee, J. S.; Smith, N. D.; Schaeffer, A. J.; Klocker, H.; Horninger, W.; Bartsch, G.; Mirkin, C. A. *Proc. Natl. Acad. Sci. U. S. A.* **2009**, *106* (44), 18437−18442.

(22) Park, Y. I.; Kim, J. H.; Lee, K. T.; Jeon, K. S.; Na, H. B.; Yu, J. H.; Kim, H. M.; Lee, N.; Choi, S. H.; Baik, S. I.; Kim, H.; Park, S. P.; Park, B. J.; Kim, Y. W.; Lee, S. H.; Yoon, S. Y.; Song, I. C.; Moon, W. K.; Suh, Y. D.; Hyeon, T. *Adv. Mater.* **2009**, *21* (44), 4467−4471.

(23) Wang, F.; Han, Y.; Lim, C. S.; Lu, Y. H.; Wang, J.; Xu, J.; Chen, H. Y.; Zhang, C.; Hong, M. H.; Liu, X. G. *Nature* **2010**, *463* (7284), 1061−1065.

(24) Sedlmeier, A.; Gorris, H. H. *Chem. Soc. Rev.* **2015**, *44* (6), 1526−1560.

(25) Sedlmeier, A.; Hlaváček, A.; Birner, L.; Mickert, M. J.; Muhr, V.; Hirsch, T.; Corstjens, P.; Tanke, H. J.; Soukka, T.; Gorris, H. H. *Anal. Chem.* **2016**, *88* (3), 1835−1841.

(26) Hlaváček, A.; Sedlmeier, A.; Skládal, P.; Gorris, H. H. *ACS Appl. Mater. Interfaces* **2014**, *6* (9), 6930−6935.

(27) Liebherr, R. B.; Hutterer, A.; Mickert, M. J.; Vogl, F. C.; Beutner, A.; Lechner, A.; Hummel, H.; Gorris, H. H. *Anal. Bioanal. Chem.* **2015**, *407* (24), 7443−7452.

(28) Crawford, A. C.; Skuratovsky, A.; Porter, M. D. *Anal. Chem.* **2016**, *88* (12), 6515−6522.

(29) Rissin, D. M.; Fournier, D. R.; Piech, T.; Kan, C. W.; Campbell, T. G.; Song, L. A.; Chang, L.; Rivnak, A. J.; Patel, P. P.; Provuncher, G. K.; Ferrell, E. P.; Howes, S. C.; Pink, B. A.; Minnehan, K. A.; Wilson, D. H.; Duffy, D. C. *Anal. Chem.* **2011**, *83* (6), 2279−2285.

(30) Dinh, T. L.; Ngan, K. C.; Shoemaker, C. B.; Walt, D. R. *Anal. Chem.* **2016**, *88* (23), 11335−11339.

(31) Härmä, H.; Soukka, T.; Lövgren, T. *Clin. Chem.* **2001**, *47* (3), 561−568.

(32) Gorris, H. H.; Ali, R.; Saleh, S. M.; Wolfbeis, O. S. *Adv. Mater.* **2011**, *23* (14), 1652−1655.

(33) Gorris, H. H.; Wolfbeis, O. S. *Angew. Chem., Int. Ed.* **2013**, *52* (13), 3584−3600.

(34) Kale, V.; Päkkilä, H.; Vainio, J.; Ahomaa, A.; Sirkka, N.; Lyytikäinen, A.; Talha, S. M.; Kutsaya, A.; Waris, M.; Julkunen, I.; Soukka, T. *Anal. Chem.* **2016**, *88* (8), 4470−4477.

308

Paper XVIII

Measurement of Sub-femtomolar Concentrations of Prostate-Specific Antigen through Single-Molecule Counting with an Upconversion-Linked Immunosorbent Assay

Mickert, M. J.; Farka, Z.; Kostiv, U.; Hlaváček, A.; Horák, D.; Skládal, P.; Gorris, H. H.

(M.J.M and Z.F. contributed equally)

Contribution:

Design of experiments, bioconjugation and characterization of UCNPs, development and optimization of sandwich immunoassay, data evaluation, manuscript writing

analytical chemistry

Measurement of Sub-femtomolar Concentrations of Prostate-Specific Antigen through Single-Molecule Counting with an Upconversion-Linked Immunosorbent Assay

Matthias J. Mickert,[†,¶] Zdeněk Farka,[†,‡,¶] Uliana Kostiv,[†,§] Antonín Hlaváček,[⊥] Daniel Horák,[§] Petr Skládal,[‡] and Hans H. Gorris*,[†]

[†]Institute of Analytical Chemistry, Chemo- and Biosensors, University of Regensburg, 93053 Regensburg, Germany
[‡]CEITEC—Central European Institute of Technology, Masaryk University, 625 00 Brno, Czech Republic
[§]Institute of Macromolecular Chemistry, Czech Academy of Sciences, 162 06 Prague, Czech Republic
[⊥]Institute of Analytical Chemistry, Czech Academy of Sciences, 602 00 Brno, Czech Republic

S *Supporting Information*

ABSTRACT: Single-molecule (digital) immunoassays provide the ability to detect much lower protein concentrations than conventional immunoassays. As photon-upconversion nanoparticles (UCNPs) can be detected without optical background interference, they are excellent labels for so-called single-molecule upconversion-linked immunosorbent assays (ULISAs). We have introduced a UCNP label design based on streptavidin-PEG-neridronate and a two-step detection scheme involving a biotinylated antibody that efficiently reduces nonspecific binding on microtiter plates. In a microtiter plate immunoassay, individual sandwich immune complexes of the cancer marker prostate-specific antigen (PSA) are detected and counted by wide-field epiluminescence microscopy (digital readout). The digital detection is 16× more sensitive than the respective analogue readout and thus expands the limit of detection to the sub-femtomolar concentration range (LOD: 23 fg mL^{-1}, 800 aM). The single molecule ULISA shows excellent correlation with an electrochemiluminescence reference method. Although the analogue readout can routinely measure PSA concentrations in human serum samples, very low concentrations have to be monitored after radical prostatectomy. Combining the digital and analogue readout covers a dynamic range of more than 3 orders of magnitude in a single experiment.
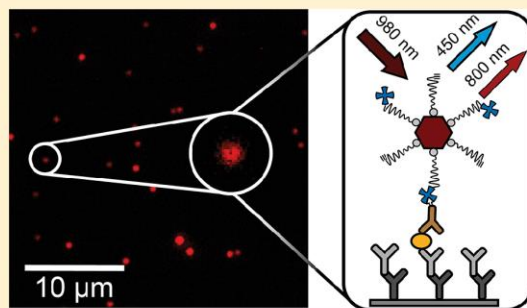
In recent years, the development of immunoassays has been strongly driven by new nanomaterial-based detection labels,[1] such as quantum dots,[2] europium-based nanoparticles,[3] carbon nanotubes,[4] gold nanoparticles,[5] silicon nanowires,[6] nanozymes,[7] and upconversion nanoparticles (UCNPs).[8] Unlike enzymes, nanomaterials are chemically and physically stable,[9] and their properties can be tuned by size or composition.[10,11] In particular, the anti-Stokes emission of UCNPs under NIR excitation (980 nm) prevents autofluorescence and minimizes light scattering, thus enabling the detection of analytes without optical background interference. UCNPs sequentially absorb two or more photons and emit light of shorter wavelengths (NaYF$_4$:Yb,Er: green/red emission or NaYF$_4$:Yb,Tm: blue/800 nm emission).[12,13] In contrast to organic fluorophores, UCNPs are highly photostable over long periods of time and under high excitation intensities,[14] which is especially important for the design of labels in single-molecule immunoassays.[15] The ability to detect and count single molecules of an analyte of interest (digital readout) opens up the door to reaching the ultimate sensitivity in analytical chemistry,[16−18] because the signal-to-background ratio is not affected when analytes have to be measured at ever lower concentrations.[19−22]

Prostate cancer is the most frequently diagnosed type of cancer among men and the fifth leading cause of death from cancer worldwide.[23] Epithelial cells of the prostate secrete prostate-specific antigen (PSA) with typical serum concentrations of less than 4 ng mL^{-1} in healthy men. Higher PSA concentrations are an important indicator of prostate cancer.[24−26] The removal of the carcinoma by radical prostatectomy leads to a drastic drop of PSA levels,[27] which, however, must be monitored repeatedly and with high sensitivity in order to detect cancer recurrence as early as possible.[22] Conventional enzyme-linked immunosorbent assays (ELISAs) reach limits of detection (LOD) in the range of 100 pg mL^{-1} as shown in Supplemental Table S1. We previously developed a single-molecule upconversion-linked immuno-

sorbent assay (ULISA) by using silica-coated UCNPs conjugated to an anti-PSA antibody as a detection label.[28] With an LOD of 1.2 pg mL^{-1}, the ULISA was about 10−100× more sensitive than conventional ELISAs. Nonspecific surface binding and the sterically constrained PSA-capture efficiency of the UCNP-conjugate, however, limited the sensitivity at very low PSA concentrations.

In this work, we have designed a new single-molecule ULISA scheme as shown in Figure 1. We replaced the antibody-silica-
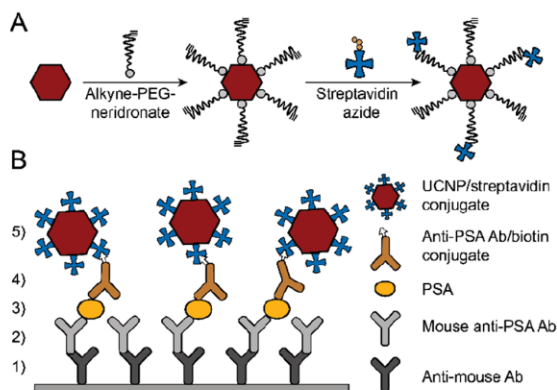
Figure 1. Schematic representation of UCNP conjugation and sandwich ULISA. (A) Alkyne-PEG-neridronate coordinates via two phosphonate groups of neridronate to lanthanide ions exposed on the surface of UCNPs. A click reaction then binds streptavidin azide covalently to the alkyne group of PEG. (B) Steps of the sandwich ULISA: (1) A microtiter well is coated with an antimouse antibody. (2) A mouse monoclonal anti-PSA capture antibody binds to the antimouse antibody. (3) PSA is captured by the monoclonal anti-PSA antibody. (4) A biotinylated polyclonal anti-PSA antibody forms a sandwich immune complex. (5) SA-coated UCNPs bind to the biotinylated detection antibody. The individual assay steps are shown in Figure S1.

UCNPs by streptavidin-coated UCNPs linked via poly-(ethylene glycol) (SA-PEG-UCNPs) on the basis of the following considerations: First, the hydrophilic PEG renders UCNPs highly water dispersible and resistant against aggregation. Second, steric hindrance and repulsion effects of surface-bound PEG reduce nonspecific binding (e.g., of serum proteins).[29−33] Third, the two-step addition of a biotinylated detection antibody followed by SA-UCNPs allows for the use of a relatively high concentration of the detection antibody to efficiently label all PSA molecules immobilized on the surface of the microtiter plate. The concentration of the UCNP label (and associated nonspecific binding effects), however, can be kept much lower because the extremely high affinity of SA and biotin (10^{-15} mol L^{-1}) ensures efficient binding to the detection antibody.[34]

■ MATERIALS AND METHODS

Antibodies were characterized by surface plasmon resonance measurements as described in the SI (Figure S2). Random serum samples and data on PSA levels determined by the Elecsys electrochemiluminescent immunoassay (Roche Diagnostics) were provided by a hospital in Svitavy, Czech Republic. Streptavidin-coated RD Upcon nanoparticles

(Erbium-540-SA, 58 nm in diameter) were provided by Kaivogen (TEM images shown in Figure S3).

Preparation and Characterization of SA-PEG-UCNP Labels. The syntheses of NaYF$_4$:Yb^{3+},Er^{3+}- and NaY-F$_4$:Yb^{3+},Tm^{3+}-doped UCNPs and of the surface ligand alkyne-PEG-neridronate are described in the SI. The surfaces of the UCNPs were modified by mixing an aqueous dispersion of UCNPs (10 mL, 14 mg mL^{-1}) with 28 mg of alkyne-PEG-neridronate ($M_W \sim 5600$ g mol^{-1}) and stirring for 24 h at room temperature (RT). The alkyne-PEG-neridronate-functionalized UCNPs were dialyzed (M_W cutoff of 14 kDa) against water for 48 h at 4 °C. Streptavidin was attached to the surface ligands via a click reaction: A 1 mL dispersion of 7 mg of alkyne-PEG-UCNPs in 25 mM Tris/HCl (pH 7.5) was mixed with 25 μL of streptavidin azide (1 mg mL^{-1}, 7 Bioscience) and 20 μL of sodium L-ascorbate (20 mg mL^{-1}) and purged with argon for 30 min to remove oxygen. The 1,3-cycloaddition was started by the addition of 10 μL of 50 mM CuSO$_4$, which generated the Cu(I) catalyst in situ. The streptavidin-PEG-neridronate-modified nanoparticles (SA-PEG-UCNP, chemical structure shown in Figure S4) were sonicated for 10 min and dialyzed (M_W cutoff of 100 kDa) against 2 L of 50 mM Tris/HCl (pH 7.5) for 12 h at 4 °C (twice exchanged) and stored in the same buffer at 4 °C.

The morphology of the UCNPs was investigated by transmission electron microscopy (TEM; Tecnai G2 Spirit Twin 12, FEI). TEM images were analyzed by ImageJ (NIH) to determine the size of the UCNPs (Figures S5 and S6). Dynamic light scattering (DLS) was recorded on a Zetasizer Nano ZS instrument (Malvern, Figure S7). The activity of the surface-bound streptavidin was tested using a BSA-biotin assay as described in the SI (Figure S8).

Upconversion-Linked Immunosorbent Assay (ULISA). A 96-well microtiter plate (μClear, high binding, Greiner Bio-One) was coated with a polyclonal horse antimouse antibody (3 μg mL^{-1}, 200 μL, Vector Laboratories) in coating buffer (42 mM NaHCO$_3$, 8 mM Na$_2$CO$_3$, 0.05% NaN$_3$, pH 9.6) at 4 °C overnight. The following steps were all performed at RT. The plate was washed four times with 250 μL of washing buffer (10.4 mM NaH$_2$PO$_4$, 39.6 mM Na$_2$HPO$_4$, 150 mM NaCl, 0.05% NaN$_3$, pH 7.4) and blocked for 1 h with 200 μL of washing buffer containing 1% BSA (Carl Roth). After four washing steps, the microtiter plate was incubated with 0.3 μg mL^{-1} of monoclonal mouse anti-PSA antibody (ab403, Abcam) for 1 h in assay buffer (50 mM Tris, 150 mM NaCl, 0.05% NaN$_3$, 0.5% bovine gamma globulin (Sigma-Aldrich), 0.2% BSA, 0.01% Tween 20, 0.2% poly(vinyl alcohol) (M_W 6000 g mol^{-1}), 1% glucose, 5 mM EDTA, and 1 mM KF). The microtiter plate was washed four times. For the calibration curve, serial dilutions of a PSA standard (Abcam, ab78528) were prepared from a stock solution (0.2 mg mL^{-1} PSA in phosphate-buffered saline, stored at −80 °C) in assay buffer containing 25% bovine serum (Sigma-Aldrich). For the analysis of real samples, 2.5 μL of serum was diluted 400× in 1 mL of assay buffer/25% bovine serum. Each sample was added in a volume of 100 μL to the microtiter wells and incubated for 1 h. The microtiter plate was washed four times and incubated with 100 μL of 0.25 μg mL^{-1} biotinylated anti-PSA antibody (BAF1344, R&D Systems) for 1 h. After four washing steps, either 100 μL of 0.7 μg mL^{-1} commercial SA-coated UCNPs (Kaivogen) or 100 μL of 3.5 μg mL^{-1} SA-PEG-UCNPs was applied to each well and incubated for 1 h. The plate was

311

Table 1. Influence of the Type of UCNP Label and the Readout Mode on ULISA Performance

	type of UCNP(Er)					
	SA-PEG-UCNP		commercial SA-UCNP		Ab-silica-UCNP[28]	
size (nm)	30/35[a]		58		48[a]	
label concentration (pM)[b]	~100		~3		~70	
	Analogue	Digital	Analogue	Digital	Analogue	Digital
nonspecific binding[c]	129 ± 7	49 ± 2	45 ± 19	138 ± 13	274 ± 6	73 ± 10
individual spot brightness	n.a.	70 ± 89	n.a.	39 ± 28	n.a.	69 ± 67
test midpoint (pg mL^{-1})	2100	600	930	430	5900	1800
working range (pg mL^{-1})	1–1 000	0.1–100	10–1 000	1–100	100–10 000	10–1 000
combined working range	0.1–1 000		1–1 000		10–10 000	
detection efficiency (%)[d]	n.a.	17	n.a.	3	n.a.	0.5
LOD (pg mL^{-1})	0.41	0.023	1.71	0.24	20.3	1.2
LOD (fM)	14	0.8	60	8.4	700	42
number of PSA molecules[e]	~800 000	~50 000	~3.6 × 10^6	~500 000	~42 × 10^6	~2.5 × 10^6
sensitivity enhancement[f]	18		7		17	

[a]Average diameter/length of 300 UCNPs determined by TEM. [b]Calculation in the SI. [c]Analogue readout: UCL (CPS), digital readout: number of luminescent spots in the background images (0.2 mm^2). [d]Ratio of background corrected PSA molecules and total number of PSA molecules per well (SI). [e]In a microtiter plate well volume of 100 μL. [f]LOD$_{analogue}$/LOD$_{digital}$.
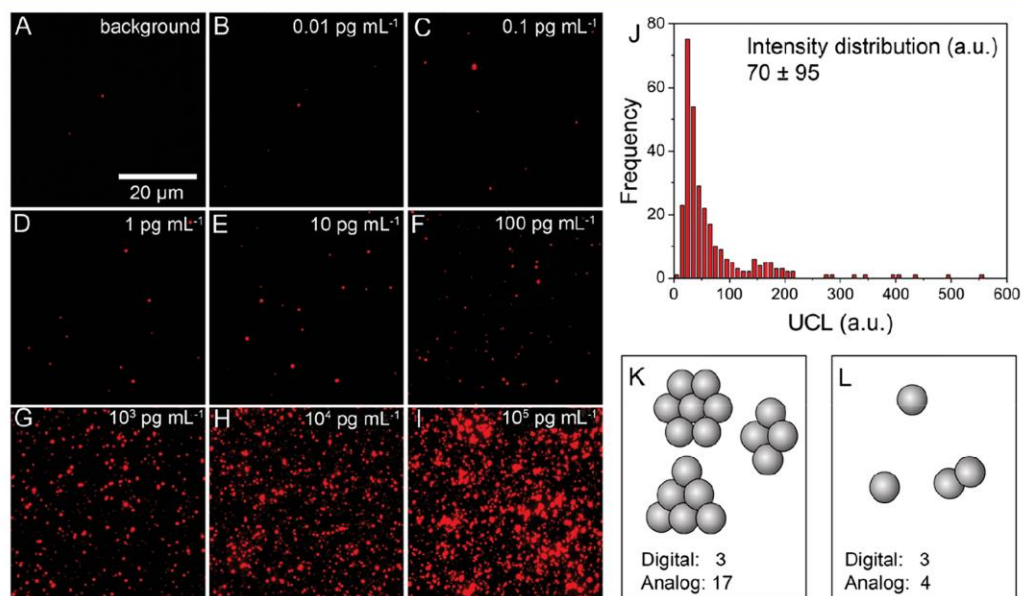
Figure 2. Digital PSA calibration in assay buffer using SA-PEG-UCNP(Tm) labels. (A–I) Wide-field upconversion microscopy (λ_{ex}: 980 nm, λ_{em}: 800 nm) showing small image sections (50 × 50 μm^2) of serial PSA dilutions. The PSA concentrations are indicated in the panels. (J) Brightness distribution of 300 luminescent spots recorded at a PSA concentration of 100 pg mL^{-1}. (K) Small aggregates and (L) homogeneous nanoparticles affecting the background signals of the digital and analogue readouts in different ways.

washed four times and left to air-dry before the analogue and digital readout.

For the analogue readout, a custom-built upconversion microtiter plate reader (Chameleon, Hidex) scanned each well in a rectangular grid of 8 × 8 pixels with 1 s exposure time per pixel and a scanning step size of 0.1 mm.[35] The truncated average of the luminescence intensities was calculated excluding the 16 highest and the 16 lowest values. For the digital readout, 100 μL of glycerol was added to the dry wells to minimize local heating effects during NIR excitation (4 W laser, 640 W cm^{-2}). The thin bottom foil (190 μm) of the microtiter wells compensated for the short working distance of the high numerical aperture objective (NA 1.49). A modified

epifluorescence microscope (SI) recorded nine wide-field images of 166 × 140 μm^2 per well (total imaging area of 0.2 mm^2) in a rectangular grid with a step size of 300 μm and an exposure time of 20 s.[28] The software NIS elements (Nikon) automatically identified and counted single UCNPs in each image. The total number of UCNPs in all nine images was used for the digital data analysis. For both the analogue and digital analysis, the average and standard deviation were calculated from three wells and analyzed using a four-parameter logistic function (SI).[28]
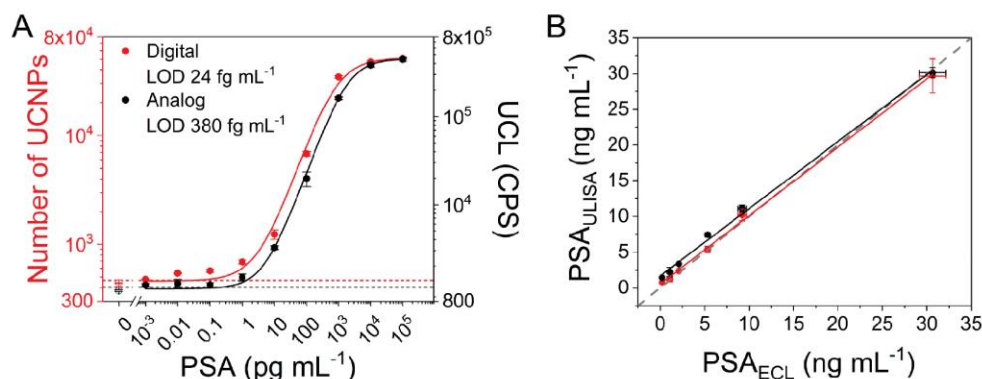
Figure 3. (A) Calibration curves of the ULISA in digital (red, LOD: 24 fg mL^{-1}) and analogue (black, LOD: 380 fg mL^{-1}) modes. The number of UCNPs(Tm) was determined by microscopy (Figure 2), and the upconversion luminescence was determined by a microtiter plate reader. The log scale of the y-axis highlights signals in the lower PSA concentration range. LODs (hatched lines) represent 3 times the standard deviation of the background (no PSA) above the baseline of the regression curve. (B) Correlation between the PSA concentrations in human serum samples determined by using the digital (red line) or analogue (black line) ULISA and an electrochemiluminescent immunoassay (ECL, digital R^2: 0.998, analogue R^2: 0.997, Table S4). Error bars indicate the standard deviations of three replicate experiments.

■ RESULTS AND DISCUSSION

Optimization of the UCNP-Label Design. The sensitivity of the ULISA critically depends on antibodies with a high affinity for the cancer marker as well as on the design of well-defined detection labels (SA-UCNP). The high affinities of the capture and detection antibodies to PSA were confirmed by surface plasmon resonance (SPR) measurements (Figure S2). We optimized the ULISA using PSA from a commercial supplier and Er-doped SA-UCNPs. According to the scheme in Figure 1, a microtiter plate was coated with an anti-IgG antibody followed by an anti-PSA capture antibody to reduce steric hindrance between the microtiter plate surface and the UCNP label. PSA was serially diluted in assay buffer and then transferred to the microtiter plate. A biotinylated anti-PSA antibody was added followed by an SA-UCNP label. The label concentrations were adjusted individually to achieve the optimal balance between high labeling efficiency and low nonspecific binding. The upconversion luminescence was detected both by using an upconversion microtiter plate reader (analogue mode) and by counting individual immune complexes with a wide-field microscope (digital mode). Table 1 shows the effects of different labels and readout modes on the immunoassay performance.

The ULISA involving (1) a biotinylated antibody and (2) SA-PEG-UCNPs was 50 times more sensitive compared with that in our earlier study based on antibody-silica-UCNP conjugates.[28] The lower test midpoint further confirms the improved binding kinetics afforded by the two-step label systems. A comparison including SA-PEG-UCNPs (Figure S9) and commercial SA-UCNPs (Figures S10 and S11) shows that the digital readout yields a 7−18× lower LOD than the respective analogue readout of the same microtiter plate experiment. Although the label design is very important for improving the immunoassay performance in general, the digital readout gives a final boost to the assay sensitivity. Additional experiments confirming the long-time stability (>3 months) of the SA-PEG-UCNPs in suspension and evaluating the effects of label purification by sucrose gradient centrifugation are described and discussed in the SI (Figures S12−S14).

We furthermore determined an analogue microscope readout by integrating the total spot intensity of each microscope image and compared it with the digital readout of the same image. Because the analogue microscope readout was 100-fold less sensitive than the digital readout (Figure S15), the high signal acquisition of the microscope objective (NA 1.49) cannot explain the benefits of the digital readout. The digital readout was rather more sensitive because detecting and counting individual UCNPs in the confined area of a diffraction-limited spot is independent of the total intensity in the entire imaging area. Especially at low PSA concentrations, the total emission of only few UCNPs distributed over a relatively large area of 0.2 mm^2 is not sufficient to increase the signal above the background.

Determination of PSA in Human Serum Samples. For the analysis of PSA in human serum samples, we prepared SA-PEG-UCNPs doped with Tm because the NIR emission (800 nm) of Tm-doped UCNPs is brighter than the emission of Er-doped UCNPs, and single UCNPs can be counted more easily. Figure 2 shows microscope images of the PSA dilution series in microtiter plates used for single-molecule counting (digital readout). In the background image (no PSA, Figure 2A), only 476 luminescent spots were detected on a total area of 0.2 mm^2 because of nonspecific binding of UCNP labels to the microtiter plate surface. As in any conventional immunoassay, low nonspecific binding is essential for ensuring a low background signal. Figure 2J shows the brightness variation of individual luminescent spots that can be attributed to some label aggregation. The following example illustrates the advantage of the digital readout compared with the analogue readout: If two types of UCNP labels containing more or less aggregates show the same degree of nonspecific binding (e.g., three binding events on a given area), the aggregated labels lead to a much higher background signal in the conventional readout scheme (Figure 2K, analogue signal: 17 UCL) than the homogeneous labels (Figure 2L, analogue signal: 4 UCL). Consequently, the digital readout confers robustness against the effects of label aggregation because each aggregate, independent of its size, only counts as a single binding event.
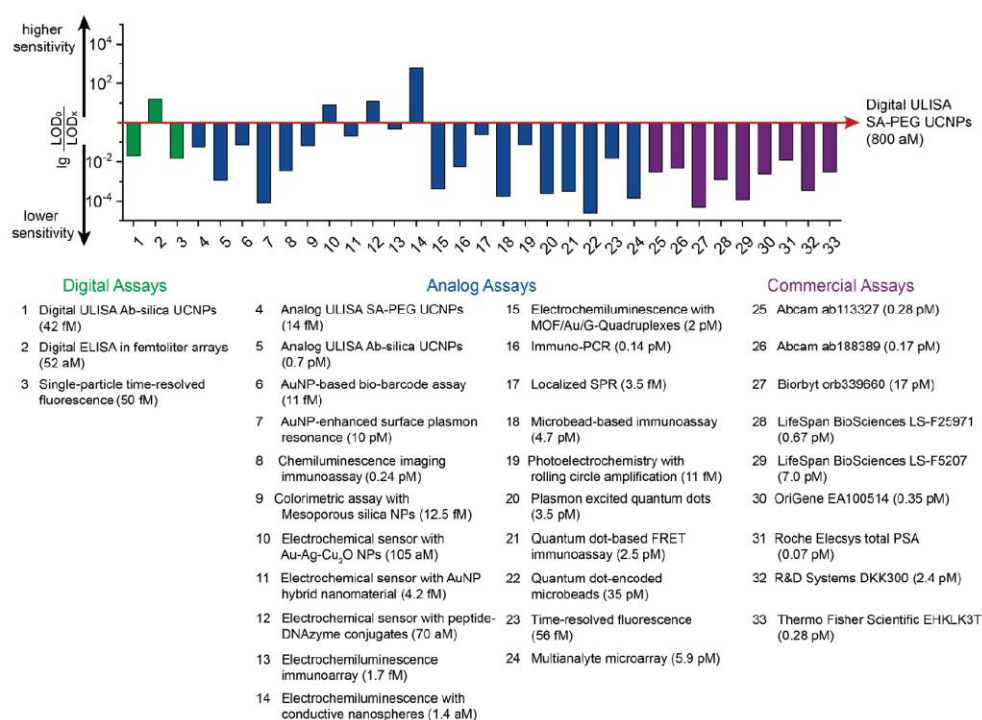
313

Figure 4. Comparison of the digital ULISA to PSA assays described in the literature. The relative assay performance is indicated as the decadic logarithm of the ratio of LOD_0 (digital ULISA) to LOD_x (other PSA assays). Values above 1 refer to lower LODs, and values below 1 refer to higher LODs compared with that of the digital ULISA (red arrow). Green: single-molecule assays (including commercial platforms), blue: noncommercial analogue assays, purple: commercial analogue assays. References are listed in Table S1.

In addition to variations among repeated measurements, the precision of the digital immunoassay depends on the sampling error because a limited number of observed binding events is not necessarily representative of all binding events.[36] The stochastic nature of discrete binding events is also known as the Poisson noise ($\sqrt{n}/n$), which depends on the number of counted spots (n). The Poisson noise is highest at low PSA concentration levels and can be reduced by increasing the imaging area. Table S2 shows a Poisson noise of <5% for all PSA concentrations, which is comparable to the variation among repeated measurements. In the upper concentration range, the digital readout is limited if diffraction-limited spots cannot be distinguished individually any more but rather form a continuous layer.

The ULISA calibration curves in Figure 3A show that the digital readout reaches a 16× lower LOD of 24 fg mL^{-1} (840 aM) than the respective analogue readout of the same microtiter plate experiment. This improvement is similar to the 18× lower LOD achieved by using the digital mode for the readout of the Er-doped SA-PEG-UCNP labels (Table 1). These experiments also confirm that the advantages of the digital detection are independent of the type of UCNP label. In this context, it should be noted that the dynamic range of the ULISA can be extended by 1 order of magnitude (0.1 pg mL^{-1} to 1 ng mL^{-1}) if the digital readout is used for low PSA concentrations and the analogue readout is used for high PSA concentrations.[37,38]

Random human serum samples with PSA concentrations determined by an electrochemiluminescent immunoassay were provided by a hospital. Linearity-of-dilution experiments on a serum sample containing 215 pg mL^{-1} of PSA showed recovery rate fluctuations of less than 25% when comparing the analogue and digital ULISA with the electrochemiluminescent reference method (Table S3). For routine analysis of serum samples, we prediluted the human serum samples by a factor of 400 because the sera of healthy individuals contain PSA concentrations of around 4 ng mL^{-1}.[24] The results of the analogue and digital readouts of the ULISA are in excellent agreement with the values determined by the reference method (Figure 3B).

In conclusion, the digital ULISA achieves a sub-femtomolar LOD. We used Er^{3+}-doped (LOD: 800 aM, 2.3 fg of PSA per well) and Tm^{3+}-doped UCNPs (LOD: 840 aM, 2.4 fg of PSA per well) and demonstrated that the advantages of the digital readout are independent of the type of label. The indirect labeling system consisting of a biotinylated anti-PSA antibody and SA-UCNPs ensures that the biotinylated antibody without nanoparticle has better access to PSA bound to the surface of the microtiter plate. The extremely strong SA–biotin affinity can then compensate for the sterically constrained access of the SA-UCNP conjugates to the biotinylated antibody on the microtiter plate surface. The digital readout further improves the LOD for two reasons: (1) Individual immune complexes (UCNPs) can be distinguished from the local background signal on a very small area, whereas the whole imaging area

314

contributes to the background signal of the analogue readout. (2) The digital readout is largely resistant to label aggregation because each aggregate is detected only as a single binding event. Consequently, the digital detection of PSA always achieved a lower LOD than the respective analogue detection, and the advantages of the digital mode became more distinctive when the level of nonspecific binding was low. Reducing nonspecific binding and using smaller UCNPs to improve the label binding can even further enhance the ULISA performance. A comparison of various PSA assays described in the literature (Figure 4) shows that the digital ULISA can readily outperform commercial analogue immunoassays for the detection of PSA. Although the digital ELISA based on femtoliter arrays achieves an even lower LOD, the digital ULISA can be operated more easily using standard immunoassay protocols. Analyte binding and detection can be performed at the same site on a standard microtiter plate, whereas other digital immunoassays require a separation step between analyte capture on beads and the detection of the labeled immune complex either in femtoliter arrays[22] or in glass capillaries.[19]

■ ASSOCIATED CONTENT

ⓢ Supporting Information

The Supporting Information is available free of charge on the ACS Publications website at DOI: 10.1021/acs.analchem.9b02872.

> Surface plasmon resonance measurements, synthesis of UCNP labels, characterization of UCNPs by TEM and DLS, BSA-biotin assays, description of widefield upconversion microscopy, data analysis, calculation of capture efficiency, purification of UCNPs by gradient centrifugation, influence of particle heterogeneity on the ULISA performance, digital and analogue PSA calibration curves, precision of digital ULISA, linearity-of-dilution experiments, and PSA concentrations in human serum samples (PDF)

■ AUTHOR INFORMATION

Corresponding Author
*Tel.: +49-941-943-4015. Fax.: +49-941-943-4064. E-mail: hans-heiner.gorris@ur.de.

ORCID ⓘ
Matthias J. Mickert: 0000-0002-1542-5998
Zdeněk Farka: 0000-0002-6842-7081
Antonín Hlaváček: 0000-0003-3358-3858
Daniel Horák: 0000-0002-6907-9701
Petr Skládal: 0000-0002-3868-5725
Hans H. Gorris: 0000-0003-1148-4293

Author Contributions
¶M.J.M. and Z.F. contributed equally to the work.

Notes
The authors declare no competing financial interest.

■ ACKNOWLEDGMENTS

■ REFERENCES

(1) Farka, Z.; Juřík, T.; Kovář, D.; Trnková, L.; Skládal, P. *Chem. Rev.* **2017**, *117* (15), 9973−10042.
(2) Bhuckory, S.; Mattera, L.; Wegner, K.; Qiu, X.; Wu, Y.-T.; Charbonnière, L.; Reiss, P.; Hildebrandt, N. *Chem. Commun.* **2016**, *52* (100), 14423−14425.
(3) Härmä, H.; Soukka, T.; Lövgren, T. *Clin. Chem.* **2001**, *47* (3), 561−568.
(4) Yu, X.; Munge, B.; Patel, V.; Jensen, G.; Bhirde, A.; Gong, J. D.; Kim, S. N.; Gillespie, J.; Gutkind, J. S.; Papadimitrakopoulos, F.; Rusling, J. F. *J. Am. Chem. Soc.* **2006**, *128* (34), 11199−11205.
(5) Grubisha, D. S.; Lipert, R. J.; Park, H.-Y.; Driskell, J.; Porter, M. D. *Anal. Chem.* **2003**, *75* (21), 5936−5943.
(6) Cui, Y.; Wei, Q.; Park, H.; Lieber, C. M. *Science* **2001**, *293* (5533), 1289−1292.
(7) Farka, Z.; Čunderlová, V.; Horáčková, V.; Pastucha, M.; Mikušová, Z.; Hlaváček, A.; Skládal, P. *Anal. Chem.* **2018**, *90* (3), 2348−2354.
(8) Hlaváček, A.; Peterek, M.; Farka, Z.; Mickert, M. J.; Prechtl, L.; Knopp, D.; Gorris, H. H. *Microchim. Acta* **2017**, *184* (10), 4159−4165.
(9) Alivisatos, P. *Nat. Biotechnol.* **2004**, *22* (1), 47.
(10) Wang, F.; Deng, R.; Wang, J.; Wang, Q.; Han, Y.; Zhu, H.; Chen, X.; Liu, X. *Nat. Mater.* **2011**, *10*, 968.
(11) Medintz, I. L.; Uyeda, H. T.; Goldman, E. R.; Mattoussi, H. *Nat. Mater.* **2005**, *4*, 435.
(12) Haase, M.; Schafer, H. *Angew. Chem., Int. Ed.* **2011**, *50* (26), 5808−5829.
(13) Nam, S. H.; Bae, Y. M.; Park, Y. I.; Kim, J. H.; Kim, H. M.; Choi, J. S.; Lee, K. T.; Hyeon, T.; Suh, Y. D. *Angew. Chem.* **2011**, *123* (27), 6217−6221.
(14) Gorris, H. H.; Wolfbeis, O. S. *Angew. Chem., Int. Ed.* **2013**, *52* (13), 3584−3600.
(15) Hlaváček, A.; Mickert, M. J.; Soukka, T.; Lahtinen, S.; Tallgren, T.; Pizurova, N.; Król, A.; Gorris, H. H. *Anal. Chem.* **2019**, *91* (2), 1241−1246.
(16) Zhang, Y.; Noji, H. *Anal. Chem.* **2017**, *89* (1), 92−101.
(17) Holzmeister, P.; Acuna, G. P.; Grohmann, D.; Tinnefeld, P. *Chem. Soc. Rev.* **2014**, *43* (4), 1014−1028.
(18) Gooding, J. J.; Gaus, K. *Angew. Chem., Int. Ed.* **2016**, *55* (38), 11354−11366.
(19) Todd, J.; Freese, B.; Lu, A.; Held, D.; Morey, J.; Livingston, R.; Goix, P. *Clin. Chem.* **2007**, *53* (11), 1990−1995.
(20) Wilson, D. H.; Hanlon, D. W.; Provuncher, G. K.; Chang, L.; Song, L.; Patel, P. P.; Ferrell, E. P.; Lepor, H.; Partin, A. W.; Chan, D. W.; et al. *Clin. Chem.* **2011**, *57*, 1712−1721.
(21) Liebherr, R. B.; Gorris, H. H. *Molecules* **2014**, *19* (9), 14417−14445.
(22) Rissin, D. M.; Kan, C. W.; Campbell, T. G.; Howes, S. C.; Fournier, D. R.; Song, L.; Piech, T.; Patel, P. P.; Chang, L.; Rivnak, A.

J.; Ferrell, E. P.; Randall, J. D.; Provuncher, G. K.; Walt, D. R.; Duffy, D. C. *Nat. Biotechnol.* **2010**, *28* (6), 595−599.

(23) Torre, L. A.; Bray, F.; Siegel, R. L.; Ferlay, J.; Lortet-Tieulent, J.; Jemal, A. *Ca-Cancer J. Clin.* **2015**, *65* (2), 87−108.

(24) Stenman, U.-H.; Leinonen, J.; Zhang, W.-M.; Finne, P. *Semin. Cancer Biol.* **1999**, *9* (2), 83−93.

(25) Center, M. M.; Jemal, A.; Lortet-Tieulent, J.; Ward, E.; Ferlay, J.; Brawley, O.; Bray, F. *Eur. Urol.* **2012**, *61* (6), 1079−1092.

(26) Zhang, K.; Lv, S.; Lin, Z.; Li, M.; Tang, D. *Biosens. Bioelectron.* **2018**, *101*, 159−166.

(27) Giljohann, D. A.; Mirkin, C. A. *Nature* **2009**, *462* (7272), 461−464.

(28) Farka, Z.; Mickert, M. J.; Hlaváček, A.; Skládal, P.; Gorris, H. H. *Anal. Chem.* **2017**, *89* (21), 11825−11830.

(29) He, Q.; Zhang, J.; Shi, J.; Zhu, Z.; Zhang, L.; Bu, W.; Guo, L.; Chen, Y. *Biomaterials* **2010**, *31* (6), 1085−1092.

(30) Otsuka, H.; Nagasaki, Y.; Kataoka, K. *Adv. Drug Delivery Rev.* **2012**, *64*, 246−255.

(31) Salvati, A.; Pitek, A. S.; Monopoli, M. P.; Prapainop, K.; Bombelli, F. B.; Hristov, D. R.; Kelly, P. M.; Åberg, C.; Mahon, E.; Dawson, K. A. *Nat. Nanotechnol.* **2013**, *8* (2), 137.

(32) Liebherr, R. B.; Soukka, T.; Wolfbeis, O. S.; Gorris, H. H. *Nanotechnology* **2012**, *23* (48), 485103.

(33) Shi, Y.; Shi, B.; Dass, A. V. E.; Lu, Y.; Sayyadi, N.; Kautto, L.; Willows, R. D.; Chung, R.; Piper, J.; Nevalainen, H.; Walsh, B.; Jin, D.; Packer, H. *Sci. Rep.* **2016**, *6*, 37533.

(34) Weber, P.; Ohlendorf, D.; Wendoloski, J.; Salemme, F. *Science* **1989**, *243* (4887), 85−88.

(35) Sedlmeier, A.; Hlaváček, A.; Birner, L.; Mickert, M. J.; Muhr, V.; Hirsch, T.; Corstjens, P. L. A. M.; Tanke, H. J.; Soukka, T.; Gorris, H. H. *Anal. Chem.* **2016**, *88* (3), 1835−1841.

(36) Crawford, A. C.; Skuratovsky, A.; Porter, M. D. *Anal. Chem.* **2016**, *88* (12), 6515−6522.

(37) Rissin, D. M.; Fournier, D. R.; Piech, T.; Kan, C. W.; Campbell, T. G.; Song, L.; Chang, L.; Rivnak, A. J.; Patel, P. P.; Provuncher, G. K.; et al. *Anal. Chem.* **2011**, *83* (6), 2279−2285.

(38) Smith, L.; Kohli, M.; Smith, A. M. *J. Am. Chem. Soc.* **2018**, *140* (42), 13904−13912.

Paper XIX

Effect of Particle Size and Surface Chemistry of Photon-Upconversion Nanoparticles on Analog and Digital Immunoassays for Cardiac Troponin

Brandmeier, J. C.; Raiko, K.; Farka, Z.*; Peltomaa, R.; Mickert, M. J.; Hlaváček, A.; Skládal, P.; Soukka, T.; Gorris, H. H.

Contribution:

Design of experiments, bioconjugation and characterization of UCNPs, development and optimization of sandwich immunoassay, data evaluation, manuscript writing

RESEARCH ARTICLE

ADVANCED
HEALTHCARE
MATERIALS
www.advhealthmat.de

Check for updates

Effect of Particle Size and Surface Chemistry of Photon-Upconversion Nanoparticles on Analog and Digital Immunoassays for Cardiac Troponin

Julian C. Brandmeier, Kirsti Raiko, Zdeněk Farka,* Riikka Peltomaa, Matthias J. Mickert, Antonín Hlaváček, Petr Skládal, Tero Soukka,* and Hans H. Gorris*

Sensitive immunoassays are required for troponin, a low-abundance cardiac biomarker in blood. In contrast to conventional (analog) assays that measure the integrated signal of thousands of molecules, digital assays are based on counting individual biomarker molecules. Photon-upconversion nanoparticles (UCNP) are an excellent nanomaterial for labeling and detecting single biomarker molecules because their unique anti-Stokes emission avoids optical interference, and single nanoparticles can be reliably distinguished from the background signal. Here, the effect of the surface architecture and size of UCNP labels on the performance of upconversion-linked immunosorbent assays (ULISA) is critically assessed. The size, brightness, and surface architecture of UCNP labels are more important for measuring low troponin concentrations in human plasma than changing from an analog to a digital detection mode. Both detection modes result approximately in the same assay sensitivity, reaching a limit of detection (LOD) of 10 pg mL^{-1} in plasma, which is in the range of troponin concentrations found in the blood of healthy individuals.

J. C. Brandmeier, Z. Farka, R. Peltomaa, M. J. Mickert, H. H. Gorris
Institute of Analytical Chemistry, Chemo- and Biosensors
University of Regensburg
Regensburg 93053, Germany
E-mail: farka@mail.muni.cz; hans-heiner.gorris@ur.de

K. Raiko, R. Peltomaa, T. Soukka
Department of Life Technologies/Biotechnology
University of Turku
Kiinamyllynkatu 10, Turku 20520, Finland
E-mail: tejoso@utu.fi

Z. Farka, P. Skládal
Department of Biochemistry, Faculty of Science
Masaryk University
Kamenice 5, Brno 625 00, Czech Republic

A. Hlaváček
Institute of Analytical Chemistry of the Czech Academy of Sciences
v. v. i., Brno 602 00, Czech Republic

1. Introduction

Heart diseases such as acute myocardial infarction (AMI) are the leading cause of death worldwide.[1] Since there is only a limited time available from the onset of the symptoms to lifesaving treatment, fast and reliable diagnostic tests are essential. In healthy individuals, cardiac troponin (cTn) is located exclusively in myocardial tissue. Therefore, several clinical tests have been employed to measure elevated levels of cTn—the recommended biomarker for AMI—in blood for the early diagnosis of AMI.[2] cTn is a heterotrimeric complex consisting of cTnI, cTnT, and TnC.[3,4] The subunits cTnI and cTnT exist as unique, recognizable isoforms only in the heart muscle (myocardium) and are released into the blood during AMI.[5,6] Highly sensitive, precise, and specific troponin tests are required to discriminate between low cTnI levels in blood and background noise.[7] Commercial chemiluminescence, electrochemical, or fluorescence assays in clinical use[8] reach limits of detection (LOD) in the range of 0.08–2.7 pg mL^{-1}.[9] According to the European Society of Cardiology and the American College of Cardiology, increased cTnI or cTnT levels in blood are defined as the value above the 99th percentile concentration of a healthy reference population, which varies typically between 8.67 and 60.4 pg mL^{-1}.[10,11]

Nevertheless, cTnI is a challenging analyte for immunochemical detection, and quantitative measurements can be influenced by several factors, such as the availability of epitopes for antibody binding. Due to the proteolytic susceptibility of the N- and C-terminal parts of cTnI,[12] antibodies for cTnI assays are often selected to recognize epitopes in the stable central part.[13,14] Furthermore, since cTnI in the blood is mainly present as a binary cTnI–TnC complex,[8] the antibodies should recognize both the free and complexed forms of cTnI. Moreover, phosphorylation or blocking of the epitopes by autoantibodies or heterophile antibodies may hinder the antibody recognition.[15] As it is unlikely that a single antibody pair is not affected by some kind of cTnI modifications or interferences,[16] many cTnI assays use a combination of two capture or two detection antibodies.[9] Furthermore, troponin assays often suffer not only from a low working range but also from rather poor precision at concentrations

318

**ADVANCED
SCIENCE NEWS**

www.advancedsciencenews.com

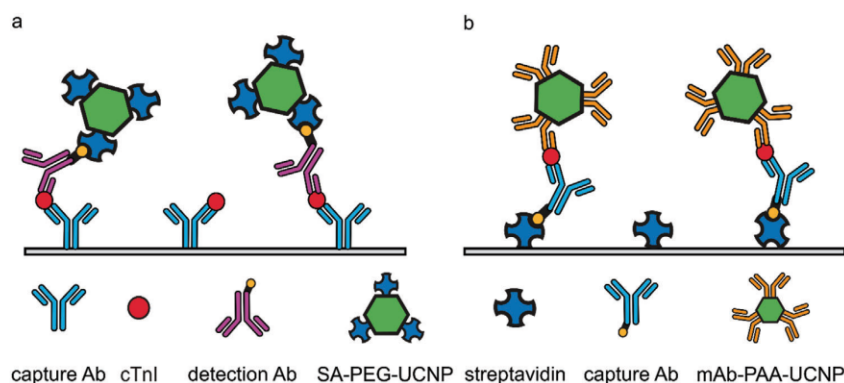**ADVANCED
HEALTHCARE
MATERIALS**

www.advhealthmat.de

Figure 1. ULISA configurations for the detection of cardiac troponin (cTnI). a) SA-PEG-UCNP label: A microtiter well is coated with monoclonal mouse anti-cTnI antibodies to capture cTnI. The biotinylated anti-cTnI antibody binds to cTnI and forms a sandwich immunocomplex, which is detected using SA-PEG-UCNP labels. b) mAb-PAA-UCNP label: A microtiter well is coated with streptavidin to immobilize biotinylated anti-cTnI antibodies, which capture cTnI. Finally, mAb-UCNP conjugates bind to cTnI and form a sandwich immunocomplex.

below the 99th percentile.[17] The choice of signal-generating labels is is of a paramount importance to improve the assay reliability and performance.

Photon-upconversion nanoparticles (UCNP) represent lanthanide-doped luminescent labels emitting shorter-wavelength light under near-infrared excitation (anti-Stokes emission), which strongly reduces background interference because of autofluorescence and light scattering.[18,19] Due to these remarkable optical properties, UCNPs are excellent labels for upconversion-linked immunosorbent assays (ULISA).[20–22] The hydrophobic layer of oleic acid on pristine UCNPs needs to be replaced by a hydrophilic coating to render the UCNPs dispersible in aqueous media and allow further bioconjugation. Alkyne-poly(ethylene glycol) (PEG) conjugated to neridronate, a bisphosphonate, has been shown to strongly coordinate to surface lanthanide ions of UCNPs. The alkyne group reacts with azide-modified streptavidin via click-chemistry.[23,24] Alternatively, surface coating with hydrophilic poly(acrylic acid) (PAA) yields water-dispersible nanoparticles with excellent colloidal stability and high density of surface carboxyl groups for bioconjugation via EDC/NHS activation.[25]

Furthermore, the absence of optical background interferences enables the detection and counting of individual UCNP labels using wide-field optical microscopy.[19,26] This has led to the development of single-molecule (digital) immunoassays[27] as opposed to analog immunoassays where the integrated signal generated by thousands of labels is measured. It is essential that the UCNP labels have the right size and are bright enough to be reliably detectable (and countable) at the single-nanoparticle level. If this condition is met, the digital assay is essentially independent of varying particle brightness, particle aggregation, and the instrumental background. With high-affinity detection antibodies, the LOD is limited by (1) the standard deviation of the nonspecifically bound labels in the control sample without analyte, and (2) counting statistics, as the precision of the measurement depends on the number of counted events (Poisson noise).

We previously developed a digital ULISA with PEG-neridronate-based UCNP labels for the detection of prostate-specific antigen (PSA).[19,26] The digital readout yielded an LOD

of 0.023 pg mL^{-1}, which was 20-fold more sensitive than the analog readout. In another study, we applied PAA-coated UCNPs to the detection of cTnI in the analog mode, which resulted in an LOD of 0.48 pg mL^{-1}.[28,29] Here, we employ both surface modification strategies for UCNPs and critically assess the effect of the UCNP label size on the performance of the analog and digital immunoassay for cTnI. The schemes of the sandwich ULISAs using either type of label are shown in **Figure 1**.

2. Experimental Section

2.1. Chemicals and Reagents

A complete list of chemicals and the preparation of alkyne-PEG-neridronate (Alkyne-PEG-Ner) and the streptavidin-azide are provided in the Supporting Information. The cTn I-T-C complex, and monoclonal anti-cTnI-antibody (mAb) clones 19C7cc, MF4cc, 560cc, and 625cc were purchased from Hytest (Turku, Finland). The mAbs 560cc and 625cc were biotinylated as described in the Supporting Information and mAb 19C7 as previously published.[30] The recombinant anti-cTnI F$_{ab}$ fragment 9707 was cloned from a hybridoma cell line of Medix Biochemica (Espoo, Finland) and produced and site-specifically biotinylated as described previously.[31] Blood for the plasma pool from five anonymized healthy volunteers was collected in lithium-heparin vacuum tubes (BD Vacutainer 10 mL, Plymouth, UK). Volunteers provided written informed consent regarding the use of collected plasma samples according to the principles expressed in the Declaration of Helsinki. Plasma was stored at −20 °C, and the aliquots were freshly thawed and centrifuged for 5 min at 1000 g before each experiment. The STAT troponin I test (Abbot, Chicago, IL, USA) was used to determine the intrinsic cTnI concentration in plasma.

The buffers were prepared using double-distilled water and filtered through a 0.22-µm membrane (Magna Nylon, GVS, USA). The buffers for the dilution of reagents included phosphate buffer (PB; 50×10^{-3} M NaH$_2$PO$_4$/Na$_2$HPO$_4$, pH 7.4), phosphate-buffered saline (PBS; PB with 150×10^{-3} M NaCl), Tris-buffered saline (TBS; 50×10^{-3} M Tris, 150×10^{-3} M

319

**ADVANCED
SCIENCE NEWS**

www.advancedsciencenews.com

**ADVANCED
HEALTHCARE
MATERIALS**

www.advhealthmat.de

NaCl, pH 7.5). Coating buffer consisted of 50×10^{-3} M NaHCO$_3$/Na$_2$CO$_3$, 0.05% NaN$_3$, pH 9.6. Two types of washing buffers were employed: Kaivogen-washing buffer and Tris-washing buffer (50×10^{-3} M Tris, 5×10^{-3} M CaCl$_2$, 0.05% Tween 20, pH 7.5). Several assay buffer combinations were investigated: (1) SuperBlock buffer (10% SuperBlock in TBS, 1×10^{-3} M KF, 0.05% Tween 20, 0.05% PEG, and 0.05% NaN$_3$, pH 7.5), (2) SuperBlock buffer with 5×10^{-3} M CaCl$_2$ (SuperBlock-Ca), (3) Kaivogen assay buffer, (4) modified Kaivogen assay buffer (assay buffer including 0.05% PAA (M_W 1200 Da), 1×10^{-3} M KF, 0.2% milk powder, 0.08% native mouse IgG, 0.005% denatured mouse IgG, pH 8.0), (5) BSA/BGG buffer (37.5×10^{-3} M Tris, 513×10^{-3} M NaCl, 5% D-trehalose, 2.5% BSA, 0.06% BGG, 0.04% NaN$_3$, pH 8.6), and (6) BSA/BGG/IgG buffer (37.5×10^{-3} M Tris, 500×10^{-3} M NaCl, 5% D-trehalose, 2.5% BSA, 0.06% BGG, 0.08% native mouse IgG, 0.005% denatured mouse IgG, 0.2% casein, 37.5 U mL^{-1} heparin, 0.0375% NaN$_3$, pH 7.75). Calibrator dilutions were prepared in 7.5% BSA/TSA (50×10^{-3} M Tris, pH 7.75, 150×10^{-3} M NaCl and 0.05% NaN$_3$, with 7.5% BSA).

2.2. Preparation of and Characterization of UCNP Labels

2.2.1. SA-PEG-UCNP Conjugates

For the preparation of SA-PEG-UCNP labels, UCNPs (NaYF$_4$:Yb,Er, 63 nm in diameter) were synthesized as described in the Supporting Information. The UCNPs (10 mg, 311 µL) dispersed in cyclohexane were mixed with an equal volume of 200×10^{-3} M HCl and incubated for 30 min at 38 °C under shaking and an additional 15 min of sonication to remove the oleic acid from the UCNP surface and mediate a phase transfer from cyclohexane to water. The lower HCl phase was added to an excess of acetone and centrifuged (1000 g, 20 min) to precipitate the UCNPs. The UCNP pellet was redispersed in 500 µL of water, sonicated for 5 min, and 2 mg of the Alkyne-PEG-Ner linker dissolved in 500 µL of water were added and incubated overnight at 38 °C under shaking. The Alkyne-PEG-Ner-UCNP conjugates were dialyzed for 72 h in a Float-A-Lyzer G2 dialysis device (100 kDa M_W cut-off; Fisher Scientific) at 4 °C against 4 L of 1×10^{-3} M KF in water, which was exchanged nine times.

For the functionalization with streptavidin, 100 µL of Tris-HCl (375×10^{-3} M, pH 7.5) and an aqueous solution of sodium ascorbate (20 µL, 100×10^{-3} M) were added to 10 mg of Alkyne-PEG-Ner-UCNPs in 1.4 mL of water. After purging the mixture for 45 min with argon, 100 µL of streptavidin-azide (1 mg mL^{-1} in water) were added, and the mixture was purged for another 10 min. Adding 10 µL of an aqueous solution of 25×10^{-3} M CuSO$_4$ initiated the click reaction. The suspension was purged for 40 min with argon and then dialyzed in a Float-A-Lyzer G2 dialysis device (100 kDa M_W cut-off) against 4 L of dialysis buffer (50×10^{-3} M Tris, 0.05% NaN$_3$, 1×10^{-3} M KF, pH 7.5 at 4 °C for 72 h), which was exchanged nine times.[32]

2.2.2. mAb-PAA-UCNP Conjugates

For the preparation of mAb-PAA-UCNP labels, oleic acid-capped UCNPs (NaYF$_4$:Yb,Er; 40, 48, 56, 64, and 80 nm in diameter)

were obtained from Kaivogen. The oleic acid was removed and replaced with PAA in a two-step ligand exchange with NOBF$_4$, as described previously.[33] The UCNPs (25 mg) dispersed in cyclohexane were mixed with an equal volume of dimethylformamide (DMF). The suspension was sonicated for 1 min, added to 25 mg of NOBF$_4$ and vortexed vigorously. During the following 60 min under shaking (1200 rpm), oleic acid on the nanoparticle surface was replaced by BF$_4^-$, which mediated a phase transfer from cyclohexane to DMF. The UCNP dispersion was split into two aliquots and the particles were precipitated by adding a fourfold volume excess of chloroform to the dispersion in DMF. The UCNPs were washed four times by alternating precipitation with chloroform and centrifugation (11 000 g, 5 min) followed by redispersion in 200 µL of DMF. The UCNP pellet was resuspended in 150 µL DMF, centrifuged (2500 g, 3 min) to remove possible larger aggregates, and the supernatant was transferred to a fresh tube. The yield of UCNPs coated with BF$_4^-$ was determined by comparing the luminescence of the solution to that of 10 mg mL^{-1} UCNP standard, both diluted 200 times in 10×10^{-3} M B$_4$Na$_2$O$_7$, pH 8 with 0.1% Tween-20).

The DMF dispersion of BF$_4^-$-coated UCNPs was mixed with a 10% solution of poly(acrylic acid) (PAA, M_W 2000) in water (adjusted to pH 9 by NaOH) such that a twofold mass excess of PAA compared to UCNPs was obtained. The mixture was further diluted with DMF to yield a PAA concentration of 3.3% and incubated for 24 h at 60 °C under shaking (1400 rpm). The PAA-coated UCNPs were washed three times by centrifugation (20 000 g, 15 min) and resuspended twice in 1 mL of water and finally in 1 mL of sodium borate buffer (50×10^{-3} M H$_3$BO$_3$ with NaOH, pH 8.0). This suspension was centrifuged once more at lower speed (2500 g, 3 min) to sediment possible larger aggregates. The supernatant was carefully collected and stored at room temperature (RT) until further use.

The conjugation of mAb 625cc and mAb 560cc was adapted from a previously published protocol[28] and all steps were performed at RT. A dispersion of 250 µL of PAA-coated UCNPs (2 mg) in 20×10^{-3} M aqueous MES buffer (pH 6.1) was activated using 20×10^{-3} M EDC and 30×10^{-3} M sulfo-NHS for 45 min under shaking. The UCNPs were washed by two centrifugation steps (20 000 g, 7 min), the initial one followed by resuspension in 335 µL and the second in 210 µL of 20×10^{-3} M MES buffer. 40 µL of mAbs solution in 0.9% NaCl was added to yield a final antibody concentration of 0.33 mg mL^{-1} in a total volume of 250 µL. After 2.5 h under rotation, an aqueous solution of 2 M 2-amino-N,N-dimethylacetamide (ADMA) in water (pH 11) was added to yield a final ADMA concentration of 50×10^{-3} M. The mixture was rotated for 30 min to terminate the conjugation reaction and block the nanoparticle surface. After washing twice by centrifugation (20 000 g, 10 min) and resuspension in 500 µL of Tris-buffer (10×10^{-3} M Tris, 0.1% Tween 20, pH 8), the antibody-conjugated UCNPs (mAb-PAA-UCNPs) were resuspended in 5×10^{-3} M Tris, pH 8.5, 0.05% Tween 85, 0.5% BSA, 0.05% NaN$_3$, pH 8.5, and stored at 4 °C.

2.2.3. Characterization of UCNP Labels

The UCNPs and their conjugates were characterized using transmission electron microscopy (TEM), dynamic light scattering

**ADVANCED
SCIENCE NEWS**

www.advancedsciencenews.com

**ADVANCED
HEALTHCARE
MATERIALS**

www.advhealthmat.de

(DLS), and upconversion emission spectroscopy as described in Figures S1–S3 in the Supporting Information.

2.3. ULISA

2.3.1. SA-PEG-UCNP Labels

A high-binding 96-well microtiter plate (μClear with 190-μm-thick bottom foil for microscope detection, Greiner, Austria) was coated with 60 μL of two monoclonal anti-cTnI antibodies (19C7cc and MF4cc, each 50 ng/well) in coating buffer overnight at 4 °C. The following steps were carried out at RT. The plate was washed twice with 250 μL of Tris-washing buffer and blocked for 1 h with 175 μL of SuperBlock buffer. After two washing steps, the cTn I-T-C complex was serially diluted in 60 μL of either BSA/BGG buffer alone, or 20% human plasma in BSA/BGG buffer and incubated for 1 h. The microtiter plate was washed twice and incubated for 1 h with 60 μL of a mixture containing biotinylated anti-cTnI antibodies (560cc and 625cc; each 0.5 μg mL^{-1}) in SuperBlock-Ca buffer. After two washing steps, the plate was incubated with 60 μL of SA-PEG-UCNPs (6.5 μg mL^{-1}) for 1 h in SuperBlock-Ca buffer. After two washing steps, the plate was left to dry on air.

2.3.2. mAb-PAA-UCNP Labels

All steps were carried out at RT. The mAb-PAA-UCNP labels were diluted 30 min before starting the assay in modified Kaivogen assay buffer to a final concentration of either 4 μg mL^{-1} of mAb625-PAA-UCNP alone, or 2 μg mL^{-1} of each label in a mixture of mAb625-PAA-UCNP and mAb560cc-PAA-UCNP.

A high-binding 96-well microtiter plate (μClear with 190-μm-thick bottom foil for microscope detection, Greiner) was coated with streptavidin as described earlier.[34] The plates were first washed with Kaivogen washing buffer. Then, 50 μL of biotinylated mAb 19C7cc (150 ng/well) and F$_{ab}$ 9707 (50 ng/well) in Kaivogen assay buffer were added and incubated for 30 min under shaking. After one washing step, the cTn I-T-C complex was serially diluted in 50 μL/well in 7.5% BSA/TSA or human plasma, respectively, followed by further dilution to 20% in BSA/BGG/IgG buffer, and incubated for 30 min. After one washing step, the mAb-PAA-UCNP labels prepared prior to the assay were sonicated 3× for 0.5 s with 100% amplitude using a VialTweeter (Hielscher Ultrasonics, Teltow, Germany) and added to the microtiter plate (50 μL/well). After 15 min, the microtiter plate was washed four times and left to dry on air.

2.4. Signal Acquisition and Statistical Analysis

2.4.1. Analog Readout

A modified upconversion microtiter plate reader (Chameleon, Hidex, Turku, Finland) equipped with a 980-nm laser excitation source[35] was used for measuring the integrated emission of Er-doped UCNPs at 540 nm. (1) In the case of SA-PEG-UCNP labels, 64 points were scanned in each well with a distance of 100 μm and a signal integration time 1 s. Afterwards, the 16 highest and

16 lowest values were discarded, and the mean value was calculated, providing the truncated average of the intensity in a single well. (2) In the case of mAb-PAA-UCNP labels, the bottom surface of the microtiter plate wells was scanned using a 3 × 3 raster with 1.5 mm step size and an exposure time of 2 s and the average intensity per well was calculated. The plotted averages and standard deviations (mean ± SD) were determined from three independent wells. The data was fitted by a four-parameter logistic function using the software Origin 2020 (OriginLab, USA). The LODs were obtained by adding three times the standard deviation of the background to the baseline values of the regression curve.[26]

2.4.2. Digital Readout

An inverted wide-field epifluorescence microscope (Eclipse Ti, Nikon, Japan) was connected to a continuous-wave 980-nm laser diode (4 W, Wavespectrum, China) via a multimode optical fiber (105 μm fiber core, 0.22 NA, Wavespectrum) and a motorized TIRF/Epifluorescence illuminator unit (Eclipse Ti-E, Nikon, Japan). The filter cube for the detection of Er^{3+}-doped UCNPs consisted of a long-pass excitation filter (λ_{cut-on} = 830 nm, Schott, Germany), a dichroic mirror (λ_{cut-on} = 875 nm, AHF Analysentechnik, Germany), and a band-pass filter (λ = 535 ± 70 nm, OD$_{980}$ ≈ 6, Chroma, USA). The images were acquired on an sCMOS camera (5.5 megapixel, Neo, Andor Technology, UK) and a 100× objective (1.49 NA, CFI HP Apochromat TIRF, Nikon), which resulted in a power density of 640 W cm^{-2}.

The dry microtiter plate wells were filled with 80 μL of glycerol for heat dissipation of the NIR laser beam. The software NIS Elements 4.5 (Nikon) was used for the acquisition of 9 wide-field images per well with an imaging area of 166 × 144 μm^2 and exposure times between 10 and 30 s (depending on the size—and thus brightness—of the UCNPs)[19] and for the counting of individual UCNPs. The total number of UCNPs per well (n = 3) was analyzed using a four-parameter logistic function in Origin 2020. The LODs were obtained by adding three times the standard deviation of the background to the baseline values of the regression curve.[26]

3. Results and Discussion

3.1. Optimization of Antibody Combination and ULISA Configuration

cTnI is a very fragile analyte prone to proteolytic degradation, phosphorylation, or complexing with other proteins and autoantibodies.[16,36–38] As these factors are not relevant when cTnI is present in well-defined buffers, it is necessary to assess the detectability of cTnI in its physiological environment, where many different enzymes, troponins, and other proteins are present in varying concentrations. Therefore, we prepared a plasma pool from five healthy volunteers and determined the intrinsic cTnI concentration using a commercial test (28.8 pg mL^{-1}) to distinguish it from spiked troponin concentrations.

The immunoassay performance further depends on the careful selection of antibodies and the assay configuration. We first
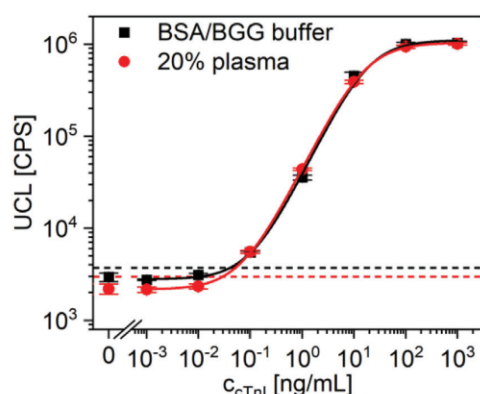
321

ADVANCED
SCIENCE NEWS
www.advancedsciencenews.com

**ADVANCED
HEALTHCARE
MATERIALS**
www.advhealthmat.de

Figure 2. Calibration curves of the analog ULISA using biotinylated mAb 560cc and SA-PEG-UCNP labels. cTnI was serially diluted in either BSA/BGG buffer (LOD: 41 pg mL^{-1}; bg: 3000 CPS), or first in 20% plasma and then in BSA/BGG buffer (LOD: 30 pg mL^{-1}; bg: 2200 CPS). The error bars show the standard deviation of three replicate measurements (mean ± SD, $n = 3$). The hatched lines indicate the LODs.

coated the capture antibodies mAb 19C7cc and MF4cc directly on the microtiter plate surface (Figure 1a). cTnI was then detected using biotinylated detection antibodies and SA-PEG-UCNP labels. When comparing the biotinylated detection antibodies mAb 560cc, mAb 625cc, and a combination of both, mAb 625cc alone was sufficient to achieve the highest sensitivity (Figure S4a, Supporting Information). **Figure 2** shows the calibration curves of cTnI either prepared in BSA/BGG buffer or in 20% plasma and then diluted in BSA/BGG buffer. The LODs of the assay were 41 pg mL^{-1} in BSA/BGG buffer (corresponding to 120 pg mL^{-1} in undiluted sample) and 30 pg mL^{-1} in 20% human plasma (corresponding to 80 pg mL^{-1} in undiluted sample). The only difference between the calibration curves is the slightly lower background (bg) signal as a result of blocking effects of serum proteins, which has a positive effect on the LOD measured in plasma samples. The assay, however, shows no cross-reactivity towards other proteins in plasma, which would have increased the background signal.

In the second assay configuration (Figure 1b), we used streptavidin for coating the microtiter plate surface. Independent of a partial denaturation during the adsorption-based surface attachment, at least one of the four high-affinity binding sites of streptavidin is usually available for binding of biotin. At the same time, the streptavidin layer affords the right orientation of the biotinylated antibody. This is especially important for binding of small biotinylated F$_{ab}$ fragments, which may lose their activity through denaturation after direct adsorption-based surface attachment. In this configuration, we employed a combination of biotinylated F$_{ab}$ 9707 and biotinylated mAb 19C7cc. The smaller size of the F$_{ab}$ fragment enhanced the epitope availability for the detection antibody.[12] On the detection side, two types of mAb-PAA-UCNP labels were compared, one carrying mAb 560cc on the nanoparticle surface and the other mAb 625cc. A combination of both antibody conjugates was also investigated. The LOD was rather independent of the label type in the buffer (Figure S4, Supporting Information), but mAb 625cc-PAA-UCNP resulted in a higher

sensitivity in plasma (data not shown) and thus was used for further experiments.

3.2. Effect of UCNP Label Size

The size of the UCNP-based detection label is another important parameter influencing the immunoassay performance. On the one hand, the size should be small to (1) obtain stable nanoparticle dispersions, (2) reduce nonspecific binding, and (3) minimize their influence on the antibody–antigen interaction. On the other hand, a larger size of UCNPs strongly increases their brightness such that they can be more easily detected. The brightness is particularly important for the detection of the labels at the single-nanoparticle level. Therefore, we conjugated UCNPs of 40, 48, 56, 64, and 80 nm in diameter to mAb 625cc and used them as labels for the detection of cTnI in buffer (**Figure 3**a) and in human plasma (Figure 3b).

While the background signal of mAb-PAA-UCNP labels in BSA/BGG/IgG buffer was in general lower (<2000 CPS) than for the SA-PEG-UCNP labels in buffer and only increased slightly with the label size (see **Table 1** for a detailed comparison), the use of plasma resulted in a ten times higher background signal when the label size increased from 40 to 80 nm. Also, a comparison among the same label sizes showed that the background was 2–20 times higher in plasma than in the buffer. Therefore, the higher background signal of larger UCNP labels cannot be simply explained by a higher brightness of larger UCNPs, but is rather a consequence of plasma components leading to a higher level of nonspecific binding of the larger particles to the microtiter plate. The higher LOD of the ULISA with larger UCNP labels in plasma can be attributed to the higher background signal. The origin of the increased tendency to nonspecific binding of the larger UCNPs may be related to the larger contact area (affected also by the shape of the nanoparticles) with the surface, which may lead a larger number of simultaneous weak interactions.

3.3. Performance of Digital Assays

In our previous work on PSA,[26] we observed that counting single immunocomplexes (digital mode, LOD: 0.02 pg mL^{-1}) resulted in a 20-fold higher sensitivity than the analog mode (LOD: 0.4 pg mL^{-1}) using SA-PEG-UCNP detection labels in the same configuration as shown in Figure 1a. We explained the higher sensitivity of the digital mode by the reduced influence of label aggregation in the digital mode, where each aggregate—independent of its size—is counted only as a single binding event. In the analog mode, by contrast, an aggregate bound non-specifically to the microtiter plate surface can strongly increase the background signal depending on the number of UCNPs in the aggregate.

In our current work, the same microtiter plates prepared for the analog detection of troponin were used for counting individual cTnI immunocomplexes under the upconversion microscope to determine the concentration in the digital mode. **Figure 4** shows microscope images of single immune complexes labeled with mAb-PAA-UCNPs (56 nm; images of other mAb-PAA-UCNP sizes and SA-PEG-UCNPs are shown in Figures S5 and
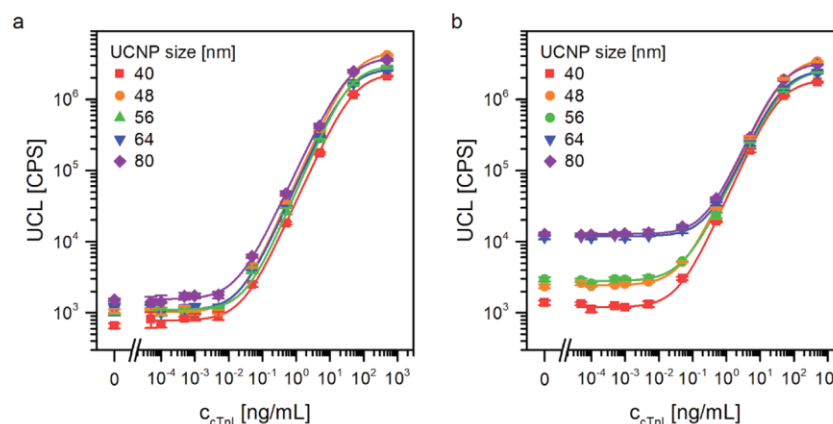
Figure 3. Analog ULISA for the detection of cTnI using different sizes of UCNP-PAA conjugated to mAb 625cc in a) buffer and b) 20% plasma. The error bars show standard deviations of replicate measurements in three wells (mean $\pm$ SD, $n = 3$).

Table 1. Summary of the analog and digital detection of cTnI in buffer and in human plasma using mAb-PAA-UCNP labels.

Detection of cTnI	in buffer				in plasma			
	analog		digital		analog		digital	
UCNP size[a] [nm]	background signal (CPS)	LOD [pg mL^{-1}]	number of UCNPs[b]	LOD [pg mL^{-1}]	background signal (CPS)	LOD [pg mL^{-1}]	number of UCNPs[b]	LOD [pg mL^{-1}]
40	658	6.0	n.d.[c]	n.d.[c]	1387	11.9	n.d.[c]	n.d.[c]
48	1055	3.8	33	3.3	2622	8.6	105	9.8
56	1038	8.3	21	7.0	2958	11.8	74	65.2
64	1129	13.3	15	17.4	11211	57.2	209	17.2
80	1517	2.9	15	4.7	12716	44.9	153	160.0

[a] Average UCNP diameter determined by TEM (Figure S1, Supporting Information); [b] Number of luminescent spots in the background images (0.2 mm^2). Average of 3 wells calculated from the sum of 9 images per well; [c] Not determinable because smaller UCNPs are not bright enough for single-nanoparticle detection.

S6 in the Supporting Information). A minimal size of 48 nm was required for a reliable detection at the single-nanoparticle level. In both buffer and plasma, the distribution of the label brightness was relatively uniform among different types and sizes of labels (Table S1, Supporting Information), indicating that the number of aggregates present in the label samples was relatively small.

The calibration curves of the digital assays are summarized in **Figure 5**. In contrast to the analog readout (Figure 3), the number of nonspecifically bound labels was relatively independent of the label size in BSA/BGG/IgG buffer and in plasma (Figure 5, Table 1). While most of the increased background is a result of more nonspecific binding events in plasma, it should be noted that in the case of small nanoparticles, also the average brightness per diffraction-limited spot increased, which indicates that the plasma has an indirect effect on the label aggregation (Table S1, Supporting Information). As the background mainly determines the assay sensitivity, the sensitivity of the digital detection in buffer was relatively similar among the different label sizes. By contrast, the assay sensitivity decreased in plasma when using larger labels, with exception of the 64-nm conjugates.

We also compared the assay performance in the digital mode using SA-PEG-UCNP labels (Figure S7, Supporting Information), but these labels did not improve the LOD compared to the analog readout (Figure 2), either. Therefore, independent of the assay configuration and the type and size of the label, the analog and digital readout resulted in similar LODs. The number of nonspecifically bound mAb-PAA-UCNP labels in the background image of the blank sample (Figure 5a) was about ten times lower than the number of nonspecifically bound SA-PEG-UCNP labels (Figure S7, Supporting Information), which was consistent with our earlier PSA experiments using SA-PEG-UCNP labels.[26] The lower number of counting events (n) increased the Poisson noise ($\sqrt{n}/n$) and affected the accuracy of the digital readout. For example, in the case of 64-nm UCNPs and 80-nm UCNP, the nonspecific binding was so low that only 15 diffraction-limited spots were detectable in the imaging area. A count of 15, however, results in a relatively high Poisson noise of 26%. In Figure 5a, the lowest baselines show the highest fluctuations, due to the Poisson noise.

An explanation why the digital readout improved the LOD of the PSA assay but not the LOD of the troponin assay may be that
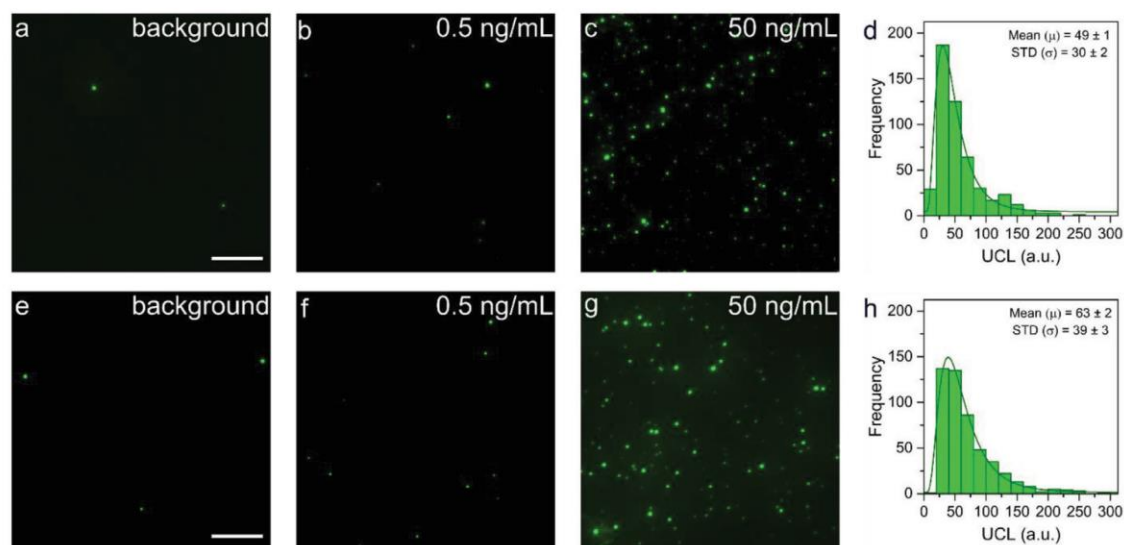
323

**ADVANCED
SCIENCE NEWS**
www.advancedsciencenews.com

**ADVANCED
HEALTHCARE
MATERIALS**
www.advhealthmat.de

Figure 4. Digital ULISA for the detection of troponin using mAb-PAA-UCNP labels (56 nm in diameter). a–c) Wide-field upconversion microscopy images corresponding to serial dilutions of cTnI in BSA/BGG/IgG buffer. d) Brightness distribution histogram of 500 diffraction-limited spots recorded at 50 ng mL^{-1} of cTnI. e–g) Wide-field upconversion microscopy images corresponding to serial cTnI dilutions in plasma. d) Brightness distribution histogram of 500 diffraction-limited spots recorded at 50 ng mL^{-1} of cTnI in plasma. Scale bar: 10 µm.
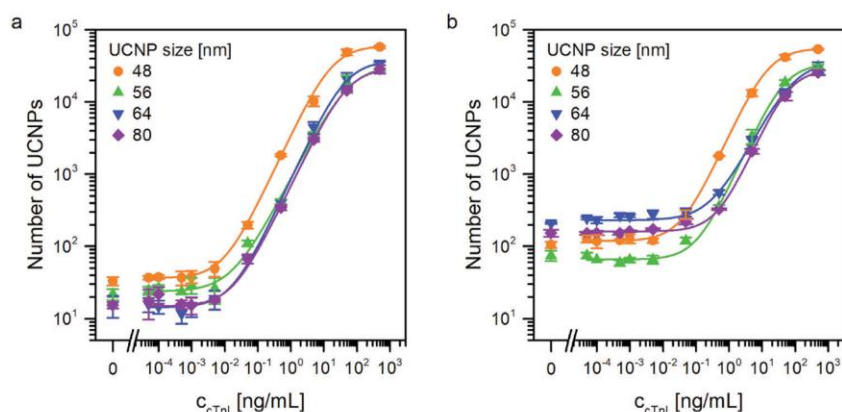
Figure 5. Digital ULISA for the detection of troponin using different sizes of mAb 625cc-PAA-UCNP labels in a) BSA/BGG/IgG buffer and b) 20% plasma. The error bars show the standard deviation of replicate measurements in three wells (mean $\pm$ SD, $n = 3$).

the label preparation was more uniform than in our previous PSA assay. Also, the differences in the particular antibody–antigen interactions may explain why the digital assay confers a higher sensitivity only for some analytes. In the analog mode, the PSA assay was ten times more sensitive than the troponin assay. In the digital mode, the PSA assay was even 200 times more sensitive although the number of nonspecifically bound SA-PEG-UCNP labels was ten times higher than the number of mAb-PAA-UCNP labels. Therefore, it seems to be the first requirement that the affinity of the antibody for the analyte is already very high before the sensitivity can be further improved by the digital readout. Compared to commercial cTnI assays and literature reports,

however, the ULISA results in a similar or even better assay performance (**Table 2**).

4. Conclusions

For the detection of troponin (cTnI), the advantages conferred by optimizing the assay configuration and the size, brightness, and surface chemistry of UCNP labels were more important than changing from an analog to a digital detection mode. In both cases, an LOD of 10 pg mL^{-1} in human plasma was obtained using mAb-PAA-UCNPs (48 nm in diameter). In contrast to conventional analog measurements, the digital readout allowed

324

**ADVANCED
SCIENCE NEWS**

www.advancedsciencenews.com

**ADVANCED
HEALTHCARE
MATERIALS**

www.advhealthmat.de

Table 2. Assay platforms for the detection of cTnI.

	Detection label	LOD [pg mL^{-1}]	linear range [ng mL^{-1}]	Company/reference
Commercial assays	Alkaline phosphatase	20	0.00–50.0	Abbott i-STAT[39]
	Alkaline phosphatase	10	0.01–100	Beckman Access 2[40]
	Alkaline phosphatase	10		Beckman Coulter DxI[41]
	Alkaline phosphatase	2.5	0.0023–27000	Beckman Coulter Access hs-cTnI[42]
	Horseradish peroxidase	12		Ortho-Clinical Diagnostics Vitros[43]
	Horseradish peroxidase	100	0.125–8.0	Invitrogen: Human Troponin I (TNNI3) ELISA[44]
Literature reports	5′-6-FAM-modified aptamer	70	0.1–6.0	[45]
	SERS using graphene oxide/gold NP	5	0.01–1000	[46]
	Cyclovoltammetry using whiskered nanofibers	40	0.5–100	[47]
	48-nm UCNP (analog/digital readout)	10	0.04–38 (analog readout)	This work

for distinguishing between the number of nonspecific binding events (observable as the number of diffraction-limited spots) and the degree of label aggregation (observable as an increase in the brightness of individual diffraction-limited spots). In particular, measurements in human plasma were strongly affected by the size of the UCNP labels. While the number of nonspecific binding events strongly increased with the label size, smaller labels led to slightly more aggregated UCNPs. The digital readout also showed that a low background signal is important to achieve a high sensitivity, but ultimately, the digital assay is limited by the counting noise. When comparing different analytes (troponin and PSA) measured under similar experimental conditions, the particular antibody–analyte interaction had a stronger effect on the assay sensitivity than the degree of nonspecific binding.

Supporting Information

Supporting Information is available from the Wiley Online Library or from the author.

Acknowledgements

Conflict of Interest

The authors declare no conflict of interest.

Data Availability Statement

The data that support the findings of this study are available from the corresponding author upon reasonable request.

Keywords

[1] WHO, www.who.int/data/gho/data/themes/mortality-and-global-health-estimates (accessed: July 2021).

[2] K. Thygesen, J. S. Alpert, A. S. Jaffe, M. L. Simoons, B. R. Chaitman, H. D. White, E. S. C. A. A. H. A. W. H. F. T. F. f. t. U. D. o. M. I. Joint, H. A. Katus, B. Lindahl, D. A. Morrow, P. M. Clemmensen, P. Johanson, H. Hod, R. Underwood, J. J. Bax, R. O. Bonow, F. Pinto, R. J. Gibbons, K. A. Fox, D. Atar, L. K. Newby, M. Galvani, C. W. Hamm, B. F. Uretsky, P. G. Steg, W. Wijns, J. P. Bassand, P. Menasche, J. Ravkilde, E. M. Ohman, E. M. Antman, L. C. Wallentin, P. W. Armstrong, M. L. Simoons, J. L. Januzzi, M. S. Nieminen, M. Gheorghiade, G. Filippatos, R. V. Luepker, S. P. Fortmann, W. D. Rosamond, D. Levy, D. Wood, S. C. Smith, D. Hu, J. L. Lopez-Sendon, R. M. Robertson, D. Weaver, M. Tendera, A. A. Bove, A. N. Parkhomenko, E. J. Vasilieva, S. Mendis, *Circulation* **2012**, *126*, 2020.

[3] S. Takeda, A. Yamashita, K. Maeda, Y. Maeda, *Nature* **2003**, *424*, 35.

[4] I. A. Katrukha, *Biochemistry (Moscow)* **2013**, *78*, 1447.

[5] A. S. Jaffe, J. Ravkilde, R. Roberts, U. Naslund, F. S. Apple, M. Galvani, H. Katus, *Circulation* **2000**, *102*, 1216.

[6] K. Thygesen, J. Mair, H. Katus, M. Plebani, P. Venge, P. Collinson, B. Lindahl, E. Giannitsis, Y. Hasin, M. Galvani, M. Tubaro, J. S. Alpert, L. M. Biasucci, W. Koenig, C. Mueller, K. Huber, C. Hamm, A. S. Jaffe, *Eur. Heart J.* **2010**, *31*, 2197.

[7] D. Westermann, J. T. Neumann, N. A. Sorensen, S. Blankenberg, *Nat. Rev. Cardiol.* **2017**, *14*, 472.

[8] F. S. Apple, Y. Sandoval, A. S. Jaffe, J. Ordonez-Llanos, *Clin. Chem.* **2017**, *63*, 73.

[9] IFCC, https://www.ifcc.org/media/478592/high-sensitivity-cardiac-troponin-i-and-t-assay-analytical-characteristics-designated-by-manufacturer-v072020.pdf (accessed: July 2021).

325

**ADVANCED
SCIENCE NEWS**

www.advancedsciencenews.com

**ADVANCED
HEALTHCARE
MATERIALS**

www.advhealthmat.de

[10] E. Antman, J. P. Bassand, W. Klein, M. Ohman, J. L. Sendon, L. Rydén, M. L. Simoons, M. Tendera, *J. Am. Coll. Cardiol.* **2000**, *36*, 959.

[11] F. S. Apple, C. A. Parvin, K. F. Buechler, R. H. Christenson, A. H. Wu, A. S. Jaffe, *Clin. Chem.* **2005**, *51*, 2198.

[12] A. G. Katrukha, A. V. Bereznikova, V. L. Filatov, T. V. Esakova, O. V. Kolosova, K. Pettersson, T. Lovgren, T. V. Bulargina, I. R. Trifonov, N. A. Gratsiansky, K. Pulkki, L. M. Voipio-Pulkki, N. B. Gusev, *Clin. Chem.* **1998**, *44*, 2433.

[13] M. Panteghini, W. Gerhardt, F. S. Apple, F. Dati, J. Ravkilde, A. H. Wu, *Clin. Chem. Lab. Med.* **2001**, *39*, 175.

[14] M. Panteghini, *Clin. Chim. Acta* **2009**, *402*, 88.

[15] D. S. Herman, P. A. Kavsak, D. N. Greene, *Am. J. Clin. Pathol.* **2017**, *148*, 281.

[16] F. S. Apple, P. O. Collinson, I. T. F. o. C. A. o. C. Biomarkers, *Clin. Chem.* **2012**, *58*, 54.

[17] C. Chenevier-Gobeaux, E. Bonnefoy-Cudraz, S. Charpentier, M. Dehoux, G. Lefevre, C. Meune, P. Ray, S. F. C. S. T. w. Sfbc, *Arch. Cardiovasc. Dis.* **2015**, *108*, 132.

[18] Z. Farka, T. Jurik, D. Kovar, L. Trnkova, P. Skladal, *Chem. Rev.* **2017**, *117*, 9973.

[19] Z. Farka, M. J. Mickert, A. Hlavacek, P. Skladal, H. H. Gorris, *Anal. Chem.* **2017**, *89*, 11825.

[20] A. Hlavacek, Z. Farka, M. Hubner, V. Hornakova, D. Nemecek, R. Niessner, P. Skladal, D. Knopp, H. H. Gorris, *Anal. Chem.* **2016**, *88*, 6011.

[21] V. Polachova, M. Pastucha, Z. Mikusova, M. J. Mickert, A. Hlavacek, H. H. Gorris, P. Skladal, Z. Farka, *Nanoscale* **2019**, *11*, 8343.

[22] R. Peltomaa, Z. Farka, M. J. Mickert, J. C. Brandmeier, M. Pastucha, A. Hlavacek, M. Martinez-Orts, A. Canales, P. Skladal, E. Benito-Pena, M. C. Moreno-Bondi, H. H. Gorris, *Biosens. Bioelectron.* **2020**, *170*, 112683.

[23] U. Kostiv, V. Lobaz, J. Kucka, P. Svec, O. Sedlacek, M. Hruby, O. Janouskova, P. Francova, V. Kolarova, L. Sefc, D. Horak, *Nanoscale* **2017**, *9*, 16680.

[24] Z. Farka, M. J. Mickert, Z. Mikusova, A. Hlavacek, P. Bouchalova, W. Xu, P. Bouchal, P. Skladal, H. H. Gorris, *Nanoscale* **2020**, *12*, 8303.

[25] L. Xiong, T. Yang, Y. Yang, C. Xu, F. Li, *Biomaterials* **2010**, *31*, 7078.

[26] M. J. Mickert, Z. Farka, U. Kostiv, A. Hlavacek, D. Horak, P. Skladal, H. H. Gorris, *Anal. Chem.* **2019**, *91*, 9435.

[27] Z. Farka, M. J. Mickert, M. Pastucha, Z. Mikusova, P. Skladal, H. H. Gorris, *Angew. Chem., Int. Ed. Engl.* **2020**, *59*, 10746.

[28] S. Lahtinen, A. Lyytikainen, N. Sirkka, H. Pakkila, T. Soukka, *Mikrochim. Acta* **2018**, *185*, 220.

[29] N. Sirkka, A. Lyytikainen, T. Savukoski, T. Soukka, *Anal. Chim. Acta* **2016**, *925*, 82.

[30] S. Eriksson, M. Junikka, P. Laitinen, K. Majamaa-Voltti, H. Alfthan, K. Pettersson, *Clin. Chem.* **2003**, *49*, 1095.

[31] J. Ylikotila, J. L. Hellstrom, S. Eriksson, M. Vehniainen, L. Valimaa, H. Takalo, A. Bereznikova, K. Pettersson, *Clin. Biochem.* **2006**, *39*, 843.

[32] M. Pastucha, E. Odstrcilikova, A. Hlavacek, J. C. Brandmeier, V. Vykoukal, J. Weisova, H. H. Gorris, P. Skladal, Z. Farka, *IEEE J. Sel. Top. Quantum Electron.* **2021**, *27*, 1.

[33] S. Lahtinen, M. Baldtzer Liisberg, K. Raikko, S. Krause, T. Soukka, T. Vosch, *ACS Appl. Nano Mater.* **2021**, *4*, 432.

[34] L. Välimaa, K. Pettersson, M. Vehniäinen, M. Karp, T. Lövgren, *Bioconjug. Chem.* **2003**, *14*, 103.

[35] A. Sedlmeier, A. Hlavacek, L. Birner, M. J. Mickert, V. Muhr, T. Hirsch, P. L. Corstjens, H. J. Tanke, T. Soukka, H. H. Gorris, *Anal. Chem.* **2016**, *88*, 1835.

[36] T. Savukoski, J. Jacobino, P. Laitinen, B. Lindahl, P. Venge, N. Ristiniemi, S. Wittfooth, K. Pettersson, *Clin. Chem. Lab. Med.* **2014**, *52*, 1041.

[37] T. Savukoski, A. Twarda, S. Hellberg, N. Ristiniemi, S. Wittfooth, J. Sinisalo, K. Pettersson, *Clin. Chem.* **2013**, *59*, 512.

[38] A. G. Katrukha, in *Cardiac Markers* (Ed.: A. H. B. Wu), 2nd Ed., Humana Press, Totowa, NJ **2002**, pp. 173.

[39] G. Bozkaya, A. R. Sisman, *Ann. Transl. Med.* **2020**, *8*, 1237.

[40] F. S. Apple, Y. Sandoval, A. S. Jaffe, J. Ordonez-Llanos, *Clin. Chem.* **2017**, *63*, 73,.

[41] F. S. Apple, M. M. Murakami, *Clin. Chem.* **2007**, *53*, 1558.

[42] S. Kim, S. J. Yoo, J. Kim, *Clin. Biochem.* **2020**, *79*, 48.

[43] F. S. Apple, R. Ler, A. Y. Chung, M. J. Berger, M. M. Murakami, *Clin. Chem.* **2006**, *52*, 322.

[44] https://www.thermofisher.com/elisa/product/Cardiac-Troponin-I-TNNI3-Human-ELISA-Kit/EHTNNI3 (accessed: July 2021).

[45] D. Liu, X. Lu, Y. Yang, Y. Zhai, J. Zhang, L. Li, *Anal. Bioanal. Chem.* **2018**, *410*, 4285.

[46] X. L. Fu, Y. Q. Wang, Y. M. Liu, H. T. Liu, L. W. Fu, J. H. Wen, J. W. Li, P. H. Wei, L. X. Chen, *Analyst* **2019**, *144*, 1582.

[47] B. Rezaei, A. M. Shoushtari, M. Rabiee, L. Uzun, W. C. Mak, A. P. F. Turner, *Talanta* **2018**, *182*, 178.

326

Paper XX

Surface design of photon-upconversion nanoparticles for high-contrast immunocytochemistry

Farka, Z.*; Mickert, M. J.; Mikušová, Z.; Hlaváček, A.; Bouchalová, P.; Xu, W.; Bouchal, P.; Skládal, P.; Gorris, H. H.

(Z.F. and M.J.M. contributed equally)

Contribution:

Design of experiments, optimization of microscope setup, bioconjugation and characterization of UCNPs, development and optimization of ICC assay, data evaluation, manuscript writing

PAPER

Check for updates

Surface design of photon-upconversion nanoparticles for high-contrast immunocytochemistry†

Zdeněk Farka, ID *‡a,b Matthias J. Mickert, ID ‡a Zuzana Mikušová,a,b,c
Antonín Hlaváček, ID d Pavla Bouchalová,c Wenshu Xu,e Pavel Bouchal, ID c
Petr Skládal ID b,c and Hans H. Gorris ID *a

Immunohistochemistry (IHC) and immunocytochemistry (ICC) are routinely employed for the micro-
scopic identification and diagnosis of cancerous cells in histological tissues and cell cultures. The maxi-
mally attainable contrast of conventional histological staining techniques, however, is low. While the anti-
Stokes emission of photon-upconversion nanoparticles (UCNP) can efficiently eliminate optical back-
ground interference, excluding non-specific interactions of the label with the histological sample is
equally important for specific immunolabeling. To address both requirements, we have designed and
characterized several UCNP-based nanoconjugates as labels for the highly specific detection of the
cancer biomarker HER2 on various breast cancer cell lines. An optimized streptavidin-PEG-neridronate-
UCNP conjugate provided an unsurpassed signal-to-background ratio of 319, which was 50-fold better
than conventional fluorescent labeling under the same experimental conditions. In combination, the
absence of optical interference and non-specific binding lays the foundation for computer-based data
evaluation in digital pathology.

1 Introduction

Breast cancer is the second most frequent type of cancer world-
wide, with approximately 2.1 million new cases reported every
year.[1] The incidence continues to increase despite the
implementation of mammography screening, and improve-
ment of adjuvant systemic therapy.[2] Human epidermal growth
factor receptors (HER or ErbB) are membrane receptors that
play important roles in biological processes like apoptosis, cell
migration, differentiation, and proliferation. In 10–30% of all
breast cancer patients, the HER2 receptor is overexpressed on
cancer cells, which increases the rate of cell proliferation. The

association with rapid cancer growth and poor prognosis
renders HER2 an important cancer biomarker.[3–5]

Immunohistochemistry (IHC) enables the detection and
localization of antigens in histological tissues, which is routi-
nely employed for the identification and diagnosis of cancer-
ous cells.[6] Protocols, antibody labeling, and new staining
techniques can be optimized by immunocytochemistry (ICC),
where target cells are cultivated and prepared similarly as real
tissue samples. While the combination of hematoxylin and
eosin (H&E) represents the principle chemical counterstain-
ing approach,[7] antibodies labeled with enzymes,[8]
fluorophores,[9,10] or nanoparticles[11–13] are required for the
specific detection of cancer biomarkers in IHC and ICC. For
example, antibody-conjugated horseradish peroxidase oxi-
dizes 3,3′-diaminobenzidine (DAB) with hydrogen peroxide,
and the brown product precipitating at the target site is
visible by light microscopy.[14,15]

Typically, pathologists screen images of tissue sections indi-
vidually by visual inspection, which is a time-demanding pro-
cedure. Digital pathology aims at an accurate, automated, and
faster screening and diagnosis of tissue slides aided by artifi-
cial intelligence[16] to account for a growing population, longer
life expectation, as well as the need for personalized medicine.
To improve the accuracy and analysis time in clinical diagno-
sis, it is desirable to have high-quality images based on labels

*aInstitute of Analytical Chemistry, Chemo- and Biosensors, University of Regensburg,
93053 Regensburg, Germany. E-mail: farka@mail.muni.cz, hans-heiner.gorris@ur.de;
Fax: +49-941-943-4064; Tel: +49-941-943-5714*
*bCEITEC – Central European Institute of Technology, Masaryk University, 625 00
Brno, Czech Republic*
*cDepartment of Biochemistry, Faculty of Science, Masaryk University, 625 00 Brno,
Czech Republic*
*dInstitute of Analytical Chemistry of the Czech Academy of Sciences, v. v. i., 602 00
Brno, Czech Republic*
eTTP plc, Melbourn Science Park, SG8 6EE Melbourn, UK
†Electronic supplementary information (ESI) available. See DOI: 10.1039/
c9nr10568a
‡These authors contributed equally to the work.

that generate a high signal-to-background ratio and are compatible with other staining techniques like the H&E staining.[17]

Photon-upconversion nanoparticles (UCNP), such as $NaYF_4$:Yb,Er or $NaYF_4$:Yb,Tm, were used as an alternative labeling strategy in IHC and ICC experiments.[18–20] Unlike conventional fluorophores, UCNPs sequentially absorb two or more photons and emit light of shorter wavelengths (anti-Stokes emission), which prevents autofluorescence, minimizes light scattering, and opens the possibility for multiplexing with standard fluorescence but also with counterstaining methods like the H&E staining.[21] Additionally, UCNPs are not affected by self-quenching and are resistant against photobleaching.[22,23] Non-specific adsorption of labels to cells and other surfaces, however, strongly influences the practical detection capabilities. Thus, UCNPs with low levels of non-specific binding are urgently needed. We previously used UCNPs coated either with bovine serum albumin (BSA)[24] or polyethylene glycol (PEG)[25] to reduce non-specific binding in microtiter plate-based immunoassays.

In pioneering work, the Tanke group[18] introduced the first upconversion labeling technique for IHC and ICC based on sub-micron-sized ground phosphor powders covered with a silica shell. Other groups[26] have since employed silanization,[19,20] encapsulation by 5-mercaptosuccinic acid and polyallylamine hydrochloride,[27] or PEG[28] to prepare upconversion labels for IHC or ICC. Here, we have designed several well-defined UCNP-streptavidin (SA) nanoconjugates for labeling the HER2 receptor on the surface of breast cancer cells (Fig. 1). We have evaluated the labeling performance of the upconversion labels in terms of non-specific binding and background reduction. A quantitative comparison to fluorescent labels demonstrated that UCNP labels are a highly valuable addition to the existent staining repertoire.

2 Materials and methods

2.1 Chemicals and buffers

The list of chemicals is provided in the ESI.† Phosphate buffer (PB; 50 mM NaH_2PO_4/Na_2HPO_4, pH 7.4), phosphate-buffered saline (PBS; PB with 150 mM NaCl), Tris buffered saline (TBS; 50 mM Tris, 150 mM NaCl, pH 7.5), TBS-T buffer (TBS with 0.05% Tween 20), antibody dilution buffer (10% SuperBlock in PBS, 0.05% Tween 20, and 0.05% NaN_3, pH 7.5), SB assay buffer (10% SuperBlock in TBS, 1 mM KF, 0.05% Tween 20, and 0.05% NaN_3, pH 7.5), BSA/BGG assay buffer (0.2% bovine serum albumin, 0.5% bovine γ-globulin, 50 mM Tris, 150 mM NaCl, 5 mM EDTA, 0.2% PVA, 1% glucose, 0.01% Tween 20, 1 mM KF, and 0.05% NaN_3, pH 7.5), and epitope retrieval buffer (10 mM Tris, 1 mM EDTA, 0.05% Tween 20, pH 9) were produced in double-distilled water and filtered through a 0.22 μm membrane (Magna Nylon 47 mm; GVS, USA).

2.2 Preparation of UCNP-streptavidin labels

For the preparation of the Alkyne-PEG-Neridronate linker, 30 mg of neridronate (Ner; Merck, Germany) was dissolved in 128 μL of 1 M NaOH under sonication, followed by the addition of 398 μL of PB (pH 7.6). Then, 500 μL of 15 mM Alkyne-PEG-NHS (α-N-hydroxysuccinimide-ω-alkyne polyethylene glycol, M_W 3000; Iris Biotech, Germany) in PB (pH 7.6) was added and incubated overnight at 4 °C. The reaction mixture was dialyzed against double-distilled water (1.8 L) in a Float-A-Lyzer G2 dialysis device (MWCO = 500–1000 Da, Fisher Scientific, Germany) at 4 °C for 72 h; double-distilled water was 12× changed. The purified, colorless Alkyne-PEG-Ner was lyophilized (Alpha 1–2, Christ, Germany) and stored at 4 °C.[29]

Oleic acid-capped UCNPs were synthesized by high-temperature co-precipitation, as described in the ESI.†[30] UCNPs (10 mg) dispersed in cyclohexane were mixed with an equivalent volume of dimethylformamide (DMF) and approx. 1 mg of $NOBF_4$ (Merck, Germany) was added per mg of UCNPs. UCNPs were incubated for 20 min at 30 °C under shaking to remove oleic acid from the nanoparticle surface and mediate a phase transfer from cyclohexane to DMF. After discarding the upper cyclohexane phase, chloroform was added in excess to the dispersion in DMF to precipitate the UCNPs. UCNPs were then purified for 5 min by centrifugation ($1000g$), redispersed in DMF, precipitated with chloroform and separated for 5 min by centrifugation ($1000g$). The UCNP pellet was redispersed in 1 mL of double-distilled water containing 2 mg of the Alkyne-PEG-Ner linker and incubated overnight at 4 °C. The Alkyne-PEG-Ner-UCNP conjugates were dialyzed for 72 h in a Float-A-Lyzer G2 dialysis device (MWCO = 100 kDa, Fisher Scientific)
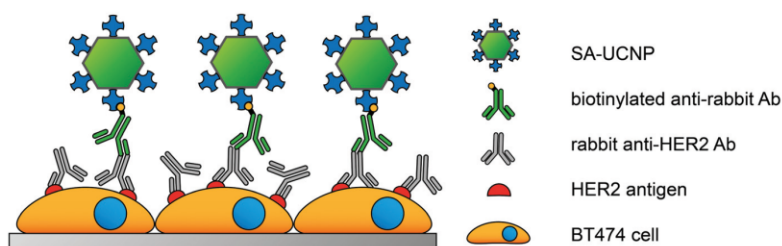

Fig. 1 Scheme of ICC assay. After blocking of the surface (not shown), the primary antibody binds to the HER2 receptor on the surface of cancer cells, followed by a biotinylated secondary antibody and a SA–UCNP-conjugate.

329

against double-distilled water (1.8 L) containing 1 mM KF at 4 °C. The dialysis medium was 9× exchanged.

For the functionalization with streptavidin, Alkyne-PEG-Ner-UCNPs (7 mg in 700 µL water) were diluted with 300 µL of Tris-HCl (75 mM, pH 7.5) and an aqueous solution of L-ascorbic acid sodium salt (20 µL, 20 mg mL^{-1}). The mixture was purged with argon for 40 min, then 50 µL streptavidin azide (7 Bioscience, Germany; 1 mg mL^{-1}) in 25 mM Tris-HCl (pH 7.5) was added, and the mixture was purged for another 10 min. The click-reaction was started by adding 10 µL of CuSO$_4$·5H$_2$O (25 mM in double-distilled water). After 45 min purging with argon, the suspension was dialyzed in a Float-A-Lyzer G2 dialysis device (MWCO = 100 kDa) against 500 mL of TBS containing 1 mM KF and 0.05% NaN$_3$ at 4 °C for 72 h (dialysis medium 9× exchanged).[25] The structure of SA-PEG-Ner-UCNPs is shown in Fig. 2A. The preparation of SA-PEG-Alendronate-UCNPs (Fig. 2B) and SA-BSA-UCNPs (Fig. 2C) is described in the ESI.†

UCNP-conjugates were purified by sucrose gradient centrifugation. Solutions of 10%, 20%, and 35% w/v sucrose were prepared in TBS (containing 1 mM KF, 0.05% NaN$_3$). A sucrose gradient was formed in a microtube by underlaying successively 50 µL of the UCNP sample, 10% sucrose (200 µL), 20% sucrose (200 µL), and 35% sucrose (200 µL). After centrifugation (750g) for 15 min, the top layer (250 µL) was taken for subsequent experiments. Purified SA-PEG-Ner-UCNPs were stored at 4 °C. KF was included in the storage buffer in order to avoid the dissolution of UCNPs.[31]

2.3 Characterization of UCNP conjugates

The UCNPs and their conjugates were characterized using transmission electron microscopy (TEM), optical spectroscopy, dynamic light scattering (DLS), nanoparticle tracking analysis (NTA), single-particle upconversion microscopy, liquid chromatography coupled with tandem mass spectrometry (LC-MS/MS), and in a microtiter plate assay as described in the ESI.†

2.4 Immunolabeling of cells

Breast cancer cell lines BT-474 (ATCC HTB-20), MCF-7 (ATCC HTB-22), and MDA-MB-231 (ATCC HTB-26) were cultivated in high-glucose Dulbecco's Modified Eagle's Medium (complete DMEM; Sigma-Aldrich, Germany) supplemented with 10% fetal bovine serum in a humidified atmosphere of 5% CO$_2$. The cells were trypsinized 24 h before the fixation, centrifuged at 1000g for 5 min and resuspended in complete DMEM. An aliquot of 50 µL of cell suspension was pipetted onto a sterile glass slide (Knittel Glass, Germany) in a cultivation dish and cultivated in drops for 4 h to confine the cells in a small area appropriate for the staining procedure. After 4 h, the cell slides were overlaid with complete DMEM and cultivated for another 20 h. Then the cell slides were washed 3 times with 100 mM phosphate-buffered saline containing 150 mM NaCl (pH 7.2). After removing buffer residues, the slides were submerged into an ice-cold (−20 °C) methanol : acetone (1 : 1) fixative solution for 6 min. The slides were dried at room temperature and stored at −20 °C.
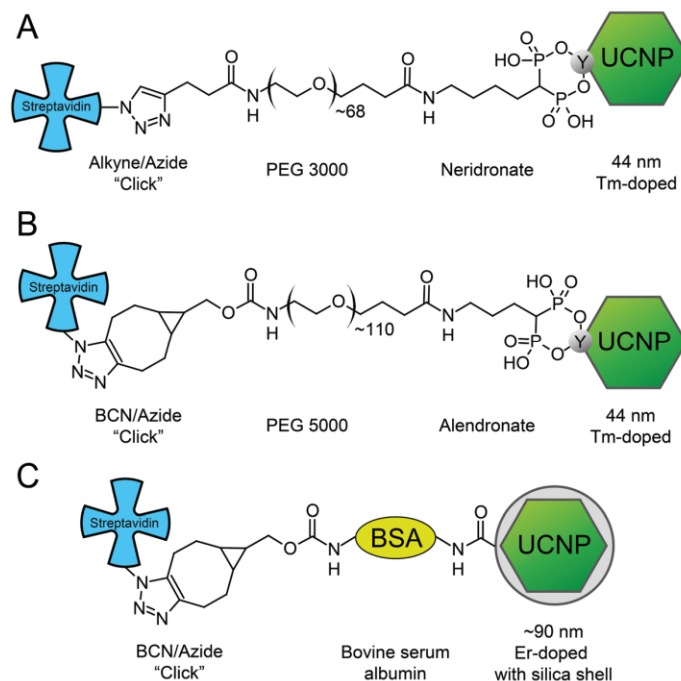

Fig. 2 Linker structures of SA-UCNP labels. (A) SA-PEG-Ner-UCNP, (B) SA-PEG-Alen-UCNP, and (C) SA-BSA-UCNP.

330

Formalin-fixed paraffin-embedded (FFPE) cells and cancer tissue were obtained from AMS Biotechnology (UK). BT-474 and MDA-MB-231 cell pellet slides expressing different levels of the HER2 antigen were used for ICC experiments, and slides with human breast tumor tissue samples from surgical resection (Infiltrative Ductual Carcinoma, HER2 positive; AMS-8009) for IHC experiments. Human tissue samples were collected in the US under informed consent and in accordance with the ethical standards of the responsible committee (institutional and national) and with the 1964 Helsinki declaration and its later amendments. The slides were first dewaxed using xylene (mixture of isomers; 3×5 min) and rehydrated in 99% ethanol (2×5 min), 90% ethanol (2×5 min), and water (5 min). Afterwards, the heat-induced epitope retrieval was performed by placing the slides in epitope retrieval buffer preheated to 60 °C and heating to 80 °C for 20 min in a water bath. The slides were allowed to cool to room temperature for 20 min and then transferred to TBS. After 2 min, the slides were removed from the buffer.

H&E staining was performed according to the manufacturer's instructions (H&E Fast Staining Kit; Carl Roth, Germany). After antigen retrieval, the FFPE slides were incubated in H&E solution 1 for 6 min, rinsed with deionized water for 10 s, followed by differentiation in 0.1% HCl for 10 s. The slides were rinsed under flowing deionized water for 6 min, incubated in H&E solution 2 for 30 s, and washed under flowing deionized water for 30 s.

For HER2-labeling, cell sections (~0.5 cm in diameter) and tissue sections (~1.5 cm in diameter) were encircled with a PAP pen liquid blocker (Science Services, Germany). After drying of the PAP pen marking, the slides were washed for 1 min in TBS. Either 50 μL droplets (for ICC experiments) or 150 μL droplets (for IHC experiments) of the following solutions were applied to the slides at room temperature. After blocking with concentrated SuperBlock containing 0.05% Tween 20 for 60 min and washing 3 times for 5 min with TBS, the slides were incubated with a rabbit anti-HER2 antibody (ab134182, Abcam, UK; 1 μg mL^{-1} in antibody dilution buffer) for 1 h. In a negative control experiment, the slides were incubated in the same dilution buffer without the anti-HER2 antibody. After washing with TBS (3×5 min), biotinylated anti-rabbit antibody was applied (111-065-144, Jackson ImmunoResearch, UK; 2 μg mL^{-1} in antibody dilution buffer, 1 h). Next, the slides were incubated with the purified UCNP conjugate (35 μg mL^{-1}) in SB assay buffer for 1 h. The slides were washed with TBS-T buffer (2×5 min), TBS (5 min), and incubated with DAPI (1 μg mL^{-1} in TBS) for 20 min. Finally, the slides were washed with TBS, a glass cover slip was mounted using 6 μL of TBS, and the slide was imaged under the upconversion microscope.

A streptavidin-5(6)-carboxyfluorescein conjugate (SA-FAM) was synthesized as described in the ESI†[32] and used as a label for conventional fluorescence microscopy. A solution of 10 μg mL^{-1} SA-FAM in SB assay buffer was employed, with the same staining protocol as described for the UCNP labels.

2.5 Microscope imaging

The H&E staining was recorded under a bright-field transmission microscope (OBE 114; Kern Optics, Germany) equipped with a 40× objective (NA 0.65) and an 8.1-megapixel CMOS camera (ODC825; Kern Optics). The ImageJ plugin *Landmark Correspondences* was used to align bright-field images to upconversion luminescence images.

Cells were imaged on a modified inverted wide-field epifluorescence microscope (Eclipse Ti, Nikon, Japan).[33] For UCNP excitation, a 976 nm continuous-wave laser diode (4 W, Wavespectrum, China) was coupled *via* a multi-mode optical fiber (105 μm fiber core, NA = 0.22, Wavespectrum) into a motorized TIRF illuminator unit (Nikon). The optical filters for UCNP excitation consisted of a long-pass excitation filter with a cut-on at 830 nm (Schott, Germany), a dichroic mirror with a cut-on at 875 nm (AHF Analysentechnik, Germany), and either a green band-pass filter (535 ± 70 nm) for the emission of Er^{3+}-doped UCNPs, or a NIR-filter (809 ± 40 nm) for the emission of Tm^{3+}-doped UCNPs. A fiber-optical mercury lamp (Intensilight, Nikon) served as an excitation source for fluorescent dyes and optical filter sets (Chroma, USA) were selected for DAPI ($\lambda_{ex} = 365 \pm 20$ nm, $\lambda_{dichroic} = 357 \pm 35$ nm, $\lambda_{em} = 445 \pm 30$ nm) and carboxyfluorescein ($\lambda_{ex} = 480 \pm 20$ nm, $\lambda_{dichroic} = 470 \pm 20$ nm, $\lambda_{em} = 530 \pm 30$ nm). The emission light was collected with a 40× water immersion objective (CFI Apo LWD 40× WI Lambda-S, NA = 1.15, Nikon) and recorded on a 5.5-megapixel vacuum-cooled sCMOS camera (Neo 5.5; Andor, UK), which resulted in a field of view of 416×351 μm.^{2} The microscope was controlled using NIS Elements 4.5 Advanced Research (Nikon).

For label bleaching experiments, BT-474 cell slides were excited coninuously over a period of 20 min. Time lapse images were acquired every 30 s using an acquistion time of 2s (SA-PEG-Ner-UCNPs) or 200 ms (SA-FAM), respectively. A region of interest of 200×200 μm^2 was selected and the average intensity was measured for each image. After subtraction of the background signal, the intensities were plotted against time.

2.6 Luminescence scanning

For upconversion scanning, a modified microplate reader (Chameleon, Hidex, Finland) was used.[34] Images of the cell pellet slides were acquired by defining several squares that were raster-scanned (18×18 points, 500 μm steps) with an exposure time of 500 ms. A microplate reader (Upcon, Labrox, Finland) was used for fluorescence scanning. Carboxyfluorescein was excited at 485 nm, and the emission light was collected at 535 nm. Squares of 18×18 points with a step size of 500 μm were scanned with an exposure time of 1 s. The imaging data were analyzed with ImageJ (National Institutes of Health, USA).[35] Circular regions of interest (ROI) of identical size were placed over the area containing the cells followed by averaging the gray values of all pixels included in the ROI. After data evaluation, the images were processed in

331

Origin 2019b (OriginLab, USA). Bilinear interpolation increased the image resolution five-fold.

3 Results and discussion

3.1 Characterization of UCNP labels

For efficient immunocytochemistry, it is essential that labels are bright enough for an easy detection without optical background interference and bind to the cancer biomarker with high specificity but not to the support material or non-target cell materials (non-specific binding). We designed UCNP labels coated with PEG or BSA (Fig. 2) that are promising candidates for avoiding non-specific binding.[24,25]

Tm^{3+}-doped UCNPs display strong NIR emission at 801 nm (Fig. S1†) and have a homogeneous size distribution with an average diameter of 44 nm as determined by TEM (Fig. 3A and B). DLS measurements showed that the hydrodynamic diameter increased from 88.7 nm (PDI 0.264) with oleic acid coating to 141.7 nm (PDI 0.234) after the preparation of the SA-PEG-Ner-UCNP conjugate (Fig. S2A†). The presence of streptavidin on the nanoparticle surface was further confirmed by LC-MS/MS (Table S1†). Sucrose gradient centrifugation

removed bigger aggregates, which decreased the average conjugate size to 78.7 nm and improved the particle homogeneity (PDI: 0.187). Nanoparticle tracking analysis (NTA) (Fig. S2B†) showed a main peak at 70.5 nm in both the non-purified and the purified sample, which can be attributed to the non-aggregated conjugate while the decrease in the number of bigger particles (100–250 nm) indicates the successful purification. The dilution of UCNPs during purification was also measured by NTA. A dilution factor of 10.5 ± 3.6 was calculated from three independent purification experiments. The label homogeneity was further investigated on a microtiter plate coated with biotinylated BSA (BSA-biotin). The immobilized SA-PEG-Ner-UCNP labels were detected individually under the upconversion microscope. The non-purified conjugate exhibited a peak of the brightness distribution at 179 a.u. per diffraction-limited spot and a coefficient of variation (CV) of 87% (Fig. 3C). After purification, the peak brightness slightly decreased to 163 a.u. and the labels were more homogeneous (CV: 66%, Fig. 3D). The removal of larger aggregates is evident from the absence of peaks above 600 a.u. Detailed microscopy images are shown in Fig. S3.†

The BSA-biotin microtiter plate assay was further used for the functional characterization of the different nanoconju-
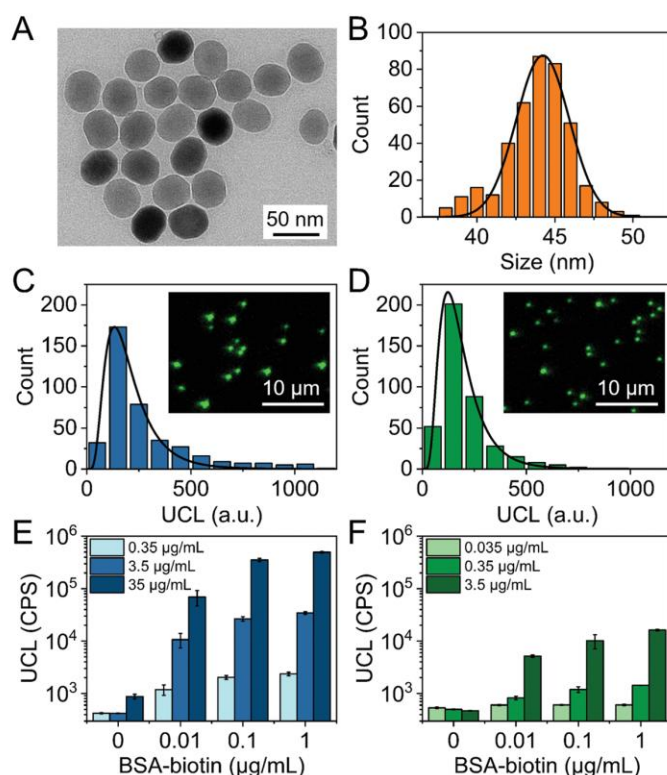
Fig. 3 (A) TEM image of oleic acid-capped UCNPs; (B) UCNP size distribution evaluated by TEM (44.2 ± 4.0 nm). Brightness distribution of (C) non-purified and (D) purified SA-PEG-Ner-UCNPs. The insets show upconversion microscopy images. Functional characterization of (E) non-purified and (F) purified conjugate in a BSA-biotin ULISA assay. The error bars correspond to standard deviations of three independent microtiter plate wells.

gates. Blocking with 10% SuperBlock yielded higher specific signals than BSA blocking, especially at low BSA-biotin coating concentrations. This effect was independent of the UCNP label concentration (Fig. S4†). As the background signal of non-specific binding was in both cases negligible, 10% SuperBlock was chosen for further experiments. Both non-purified (Fig. 3E) and purified (Fig. 3F) SA-PEG-Ner-UCNPs (Fig. 2A) enabled specific binding to BSA-biotin with low levels of non-specific binding. The purification had no significant effect on the signal-to-background ratio (S/B), which increased with label concentration from ~6 at 0.35 µg mL^{-1} SA-PEG-Ner-UCNP to 566 at 35 µg mL^{-1} SA-PEG-Ner-UCNP. Alendronate and a longer PEG (Fig. 2B) were used to conjugate streptavidin to the surface of UCNPs *via* copper-free click chemistry (strain-promoted BCN). Compared to the SA-PEG-Ner-UCNP, the alendronate-based conjugate resulted in a 5–10-fold lower S/B in the BSA-biotin assay (increasing from 1.1 for 0.07 µg mL^{-1} to 12.4 for 7 µg mL^{-1}). This can be explained by a lower amount of reactive PEG linker and, therefore, less streptavidin, which leads to a smaller change of the hydrodynamic diameter after conjugation (Fig. S5 and S6†). SA-BSA-UCNP conjugates (Fig. 2C) were prepared based on larger Er^{3+}-doped UCNPs with a hexagonal prism shape covered by a carboxylated silica layer.[24] Gradient centrifugation had almost no effect on the hydrodynamic diameter, indicating a highly uniform conjugate preparation. Further experiments were performed with the non-purified SA-BSA-UCNP sample. Single-particle microscopy confirmed the highly uniform sample preparation (CV: 43%). In the BSA-biotin assay, the conjugate provided a high S/B of ~100 for all label concentrations (Fig. S7†). The results of all three UCNP nanoconjugates are summarized in Table 1. The SA-FAM conjugate was also characterized by the BSA-biotin microtiter plate assay (Fig. S8†). Due to the generally higher background of fluorescence, lower S/B were observed, however, the general trend of improvement with the increasing label concentration remained (from 5 for 0.4 µg mL^{-1} to 10 for 400 µg mL^{-1}).

3.2 ICC based on UCNP labels

The HER2 antigen expressed on the surface of BT-474 cells was labeled with different UCNP conjugates. DAPI (blue emission) served as a counterstain for visualizing the nucleus. Fig. S9†

shows microscope images after labeling with the SA-BSA-UCNP conjugate. Due to the relatively large UCNP size (~90 nm), individual labels are visible (z-scan experiment is shown in Fig. S10†), but the overall S/B was only 2. This may be explained by two effects: (i) the carboxylated silica shell is not completely shielded by the BSA and leads to non-specific binding, and (ii) the BSA can also contribute to the non-specific binding. This finding is in agreement with the testing of the nanoparticle dilution buffer. In both cases, the presence of BSA (either in the buffer or on the nanoparticle surface) led to the increase of the non-specific binding.

In order to avoid the use of serum proteins for ICC staining and reduce the label size, we developed conjugates based on smaller UCNPs (44 nm). The oleic acid on the as-synthesized UCNPs was replaced by PEG-alendronate *via* a ligand exchange reaction, and streptavidin was subsequently bound by a copper-free click reaction (SA-PEG-Alen-UCNP). The microscope images (Fig. S11†), however, show that this label did not only bind to HER2 on the cell surface but also stained the nucleus as evident from the overlapping DAPI and upconversion channels. In general, the S/B was low (5 at a label concentration of 7 µg mL^{-1} and 2 at a label concentration of 35 µg mL^{-1}).

The third label was also based on 44 nm UCNPs but conjugated to PEG-neridronate and attached to streptavidin *via* copper-mediated click chemistry (SA-PEG-Ner-UCNP). A label concentration of 35 µg mL^{-1} improved the S/B to 29 compared to a concentration of 7 µg mL^{-1} (S/B 6) (Fig. S12†). Individual bright spots in the images of the negative control, however, indicated that aggregated labels deposited on the sample and had a negative impact on the S/B. Therefore, we removed such aggregates by sucrose gradient centrifugation (Table 1). Furthermore, the SA-PEG-Ner-UCNP labeling efficiency strongly depended on the blocking conditions. Both 10% SuperBlock (SB assay buffer) and BSA/BGG assay buffer allowed for a clear distinction between specific labeling of HER2-positive BT-474 cells and respective control experiments without primary antibody (Fig. S13†). The SB assay buffer, however, reduced the non-specific binding much more efficiently, and slightly improved the specific signal, which increased the S/B from 23 to 319 (Fig. S13C and F†; with enhanced contrast of the upconversion background image in

Table 1 Characterization of UCNP labels

Label	SA-PEG-Ner-UCNP		SA-PEG-Alen-UCNP (Fig. S5 and S6†)		SA-BSA-UCNP (Fig. S7†)	
UCNP Diameter (TEM/DLS)	NaY$_{0.80}$Yb$_{0.18}$Tm$_{0.02}$F$_4$ 44.2 ± 4.0 nm/88.7 nm (PDI 0.264)				NaY$_{0.895}$Yb$_{0.100}$Er$_{0.005}$F$_4$ Height 80.5 ± 4.7 nm; diameter 105.6 ± 4.3 nm /126.6 nm (PDI 0.008)	
SA-UCNP-conjugate	Before purification	After purification	Before purification	After purification	Before purification	After purification
Ø$_{HD}$ (DLS)	141.7 nm PDI 0.234	78.7 nm PDI 0.187	106.2 nm PDI 0.143	91.7 nm PDI 0.201	142.4 nm PDI 0.074	135.0 nm PDI 0.128
Single-particle microscopy[a]	179 a.u. CV 87%	163 a.u. CV 66%	186 a.u. CV 99%	193 a.u. CV 70%	126 a.u. CV 43%	not determined

[a] Peak of intensity distribution; the exposure times were adjusted to account for the different brightness of Tm^{3+} and Er^{3+}-doped UCNPs.

333

Fig. S14†). We assume that serum proteins in the BSA/BGG buffer led to a higher degree of non-specific binding in ICC, which is different from the optimal blocking conditions for immunoassays in a microtiter plate format.[25]

Fig. 4 shows microscope image sections (full images are shown in Fig. S15†) and upconversion scans of BT-474 cell pellets labeled with purified SA-PEG-Ner-UCNP in an optimal concentration of 35 μg mL^{-1} and under optimal blocking conditions. The circle around the cell pellet in Fig. 4G shows the hydrophobic marking of the PAP pen, which leads to some non-specific label adsorption. The area where the cells were inspected, however, was not affected. Furthermore, there was no overlap between the green (upconversion) and the blue (DAPI) channel, confirming that SA-PEG-Ner-UCNPs did not bind to DNA. The thickness of the cell pellets did not allow for focusing all cells in a single image. Focusing on different z positions (± 1.6 μm) in the same cell section (Fig. S16†) confirmed that image blurring was a result of the shallow depth of field but independent of the labels. We then compared the HER2-positive FFPE cells to HER2-negative FFPE cells under the same experimental conditions using the SA-PEG-Ner-UCNP label. Upconversion scanning resulted in 40× lower signals on HER2-negative MDA-MB-231 cells than on HER2-positive BT-474 cells. Essentially no signal was visible, neither in the microscopy images nor in the upconversion scans (Fig. S17†).

We have also demonstrated that upconversion-based HER2-labeling is compatible with H&E staining (Fig. S18†). In ICC experiments, H&E staining of the BT-474 FFPE cells did not interfere with the upconversion signal acquisition, which indicates that both procedures are well compatible and are applicable to IHC experiments where H&E staining is a standard procedure. HER2-positive tumor tissue sections were then labeled with SA-PEG-Ner-UCNPs to show their performance in IHC experiments. There was a 12× difference between images taken with and without primary antibody (Fig. S19†). The lower S/B compared to the cultured cell lines can be explained by the more heterogeneous composition of tumor tissues, which contain healthy cells as well as various types of tumor cells and thus display different HER2 expression levels.

To confirm that the efficiency of SA-PEG-Ner-UCNP labeling is independent of the cell preparation, we cultivated the BT-474 cell line as well as two HER2-negative cell lines, MDA-MB-231 and MCF-7, in-house (Fig. 5; individual detection channels shown in Fig. S20†). While HER2-positive BT-474 cells again showed a very high degree of specific labeling, low upconversion signals were detected on the two HER2-negative cell lines. A slightly higher HER2 expression on MCF-7 cells compared to MDA-MB-231 cells was also reported in the literature.[36] The average signal intensities of the cultivated cells were three times lower compared to the FFPE cells because of
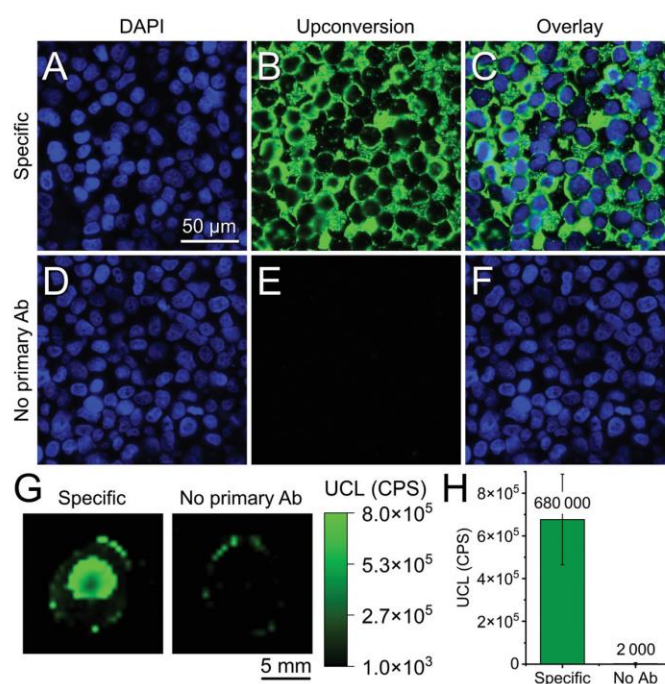
Fig. 4 SA-PEG-Ner–UCNP labeling of HER2-positive FFPE BT-474 cells: (A) DAPI channel, (B) upconversion channel, (C) overlay. Negative controls (without primary antibody): (D) DAPI channel, (E) upconversion channel, (F) overlay. (G) Upconversion scan of the cell pellets; (H) average upconversion intensities. The error bars indicate the standard deviations of intensities in the cell pellet.
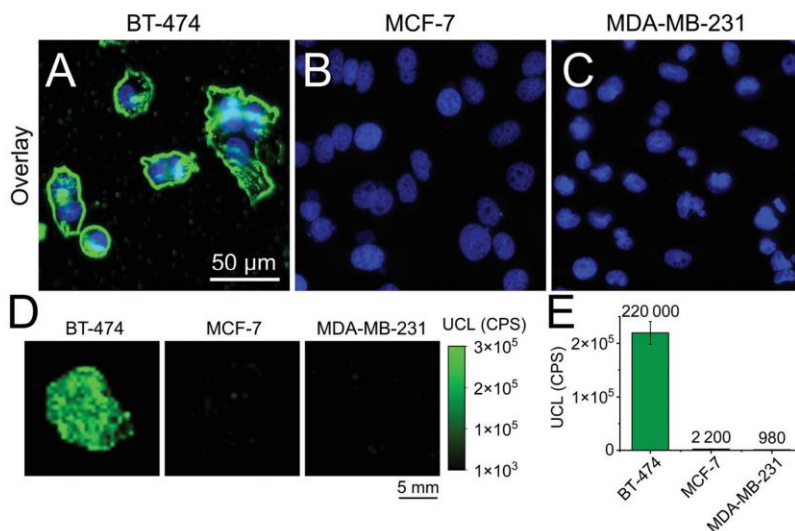
Fig. 5 SA-PEG-Ner-UCNP labeling of cultivated breast cancer cell lines. Overlay images (DAPI and upconversion channels) of (A) BT-474 cells, (B) MCF-7 cells, and (C) MDA-MB-231 cells. (D) Upconversion scans of the cell pellets and (E) average upconversion intensities. The error bars indicate the standard deviation of three independent cell slides.

the lower cell density in the detection area. The results of all labeling experiments are summarized in Table 2.

3.3 ICC based on fluorescent labels

To compare the UCNP label performance with standard fluorescence labeling, FFPE cells (Fig. 6) and cell cultures (Fig. S21 and S22†) were labeled with a fluorescent SA-FAM conjugate. Both the specific and the non-specific signal increased at higher concentrations of SA-FAM, and the S/B improved from 4 at a label concentration of 1 µg mL^{-1} to 6 at 10 µg mL^{-1} (Fig. S23†). Fluorescent labeling, however, always resulted in a relatively high background signal (FFPE cells: Fig. 6K and Fig. S24† shows the fluorescence background of the image with enhanced contrast; cell cultures: Fig. S21E†), which can be explained by cellular autofluorescence, crosstalk between the detection channels and non-specific binding of the SA-FAM conjugate. The bright circles in the fluorescence scan (Fig. 6G–J) indicate the autofluorescence of

the PAP pen marking, but did not affect the analysis of the cell pellet. SA-FAM labeling resulted in a maximum S/B of only 6.1. The results of the fluorescence labeling experiments are summarized in Table 2. The superior performance of the SA-PEG-Ner-UCNP label (S/B 319) is clearly evident from a 50-fold wider dynamic range of upconversion measurements, which enables a much finer distinction between HER2-expression levels on different cancer cell lines. We have also compared the photostability of the SA-PEG-Ner-UCNPs with the SA-FAM (Fig. S25†). The signal of SA-FAM decreased by 59% over a 20 min observation interval. By contrast, the signal of the UCNP labels was stable over the same time period and even increased slightly because the drying sample resulted in a lower quenching effect of the upconversion luminescence by water. Finally, the use of UCNP-based labels avoids the risk of photoconversion of DAPI, which can result in significant interferences with the readout in the fluorescein channel.[38]

Table 2 Summary of cell labeling results

Cell line	HER2 expression[37]	Cell preparation	SA-PEG-Ner-UCNP		SA-FAM	
			UCL ($\times 10^3$ a.u.)	Ratio	Fluorescence ($\times 10^3$ a.u.)	Ratio
BT-474	3+	FFPE	680 ± 210	319[a]	91 ± 10	6.1[a]
		FFPE, no Ab	2 ± 5		14.9 ± 1.3	
		Cell culture	220 ± 21	—	25 ± 7	—
MCF-7	0–1+	Cell culture	2.2 ± 0.4	100[b]	7.8 ± 1.7	3.2[b]
MDA-MB-231	0–1+	Cell culture	0.98 ± 0.11	223[c]	6.36 ± 0.12	3.9[c]

[a] S/B (no primary antibody). [b] Ratio of HER2-positive BT-474 cell culture to HER2-negative MCF-7 cell culture. [c] Ratio of HER2-positive BT-474 cell culture to HER2 negative MDA-MB-231 cell culture.

335
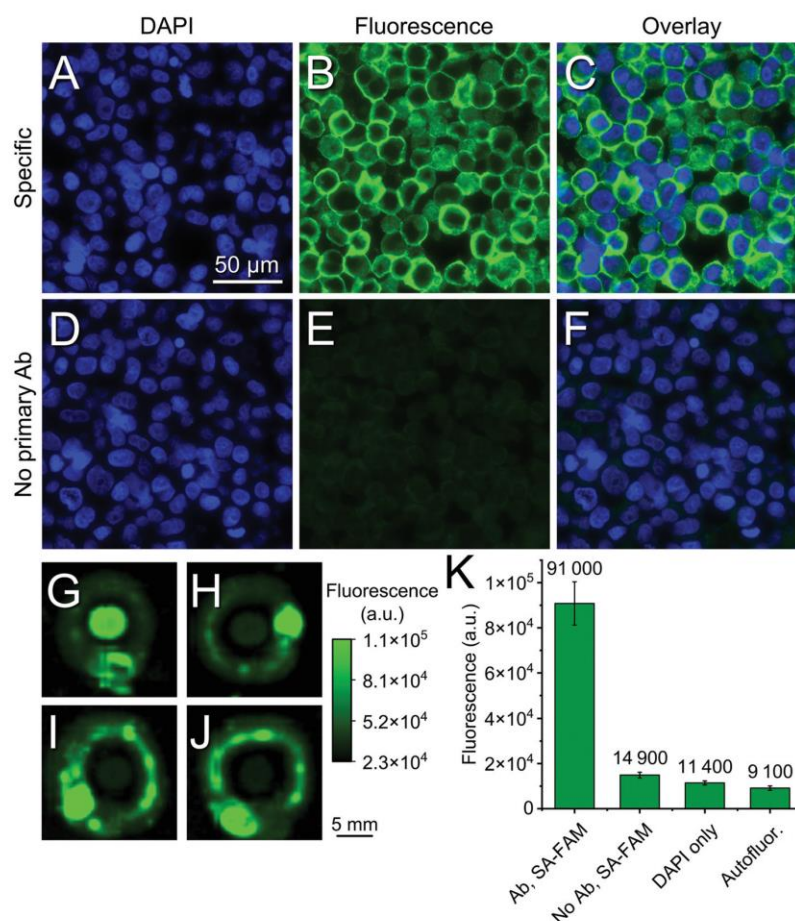
Fig. 6 Fluorescence SA-FAM labeling of HER2-positive FFPE BT-474 cells: (A) DAPI channel, (B) fluorescein channel, (C) overlay. Negative control (without primary Ab): (D) DAPI channel, (E) fluorescein channel, (F) overlay. Fluorescence intensity scans of (G) specific labeling, (H) negative control (no primary antibody), (I) incubation with DAPI only, and (J) autofluorescence. (K) Average fluorescence intensities measured in the cell pellets. The error bars indicate standard deviations of intensities in the cell pellets.

4 Conclusions

We have prepared and characterized three types of streptavidin-UCNP conjugates to evaluate their labeling performance in ICC as compared to conventional fluorescence labeling. The design of the nanoparticle surface architecture and blocking conditions were essential for an efficient ICC procedure. PEG-coated UCNPs showed lower levels of non-specific binding than BSA-coated labels (SA-BSA-UCNP). Similarly, a blocking buffer composition without serum proteins further reduced the level of non-specific binding. HER2-positive BT-474 cells showed the highest specific signals after labeling with SA-PEG-Ner-UCNPs and extremely low background interference as observed by wide-field upconversion microscopy as well as upconversion scanning (S/B 319). By contrast, conventional fluorescence labeling only achieved a S/B of 6. Consequently, the optimized SA-PEG-Ner-UCNP labeling protocol resulted in

a 50-fold wider dynamic range than fluorescence labeling, which allows for a much finer distinction between HER2 expression levels. The absence of optical background interference under 976 nm excitation in combination with extremely low levels of non-specific binding clearly demonstrates the potential of UCNPs as alternative labels in ICC and IHC. The high S/B is a great advantage especially for computer-based data evaluation in digital pathology. Without cross-talk between fluorescence channels, UCNP labeling can readily be combined with H&E staining for multiplexed applications.

Conflicts of interest

336

Acknowledgements

References

1 F. Bray, J. Ferlay, I. Soerjomataram, R. L. Siegel, L. A. Torre and A. Jemal, *CA-Cancer J. Clin.*, 2018, **68**, 394–424.

2 O. Gluz, C. Liedtke, N. Gottschalk, L. Pusztai, U. Nitz and N. Harbeck, *Ann. Oncol.*, 2009, **20**, 1913–1927.

3 S. Dawood, K. Broglio, A. U. Buzdar, G. N. Hortobagyi and S. H. Giordano, *J. Clin. Oncol.*, 2010, **28**, 92–98.

4 H. A. Burris, H. S. Rugo, S. J. Vukelja, C. L. Vogel, R. A. Borson, S. Limentani, E. Tan-Chiu, I. E. Krop, R. A. Michaelson, S. Girish, L. Amler, M. X. Zheng, Y. W. Chu, B. Klencke and J. A. O'Shaughnessy, *J. Clin. Oncol.*, 2011, **29**, 398–405.

5 S. M. Swain, S. B. Kim, J. Cortes, J. Ro, V. Semiglazov, M. Campone, E. Ciruelos, J. M. Ferrero, A. Schneeweiss, A. Knott, E. Clark, G. Ross, M. C. Benyunes and J. Baselga, *Lancet Oncol.*, 2013, **14**, 461–471.

6 J. S. Ross, E. A. Slodkowska, W. F. Symmans, L. Pusztai, P. M. Ravdin and G. N. Hortobagyi, *Oncologist*, 2009, **14**, 320–368.

7 M. Titford, *Biotech. Histochem.*, 2005, **80**, 73–78.

8 P. K. Nakane and G. B. Pierce, *J. Histochem. Cytochem.*, 1966, **14**, 929–931.

9 A. H. Coons, H. J. Creech, R. N. Jones and E. Berliner, *J. Immunol.*, 1942, **45**, 159–170.

10 E. A. Susaki and H. R. Ueda, *Cell Chem. Biol.*, 2016, **23**, 137–157.

11 M. V. Yezhelyev, X. Gao, Y. Xing, A. Al-Hajj, S. M. Nie and R. M. O'Regan, *Lancet Oncol.*, 2006, **7**, 657–667.

12 J. L. Dong, L. N. Song, J. J. Yin, W. W. He, Y. H. Wu, N. Gu and Y. Zhang, *ACS Appl. Mater. Interfaces*, 2014, **6**, 1959–1970.

13 T. R. Nayak, C. Andreou, A. Oseledchyk, W. D. Marcus, H. C. Wong, J. Massague and M. F. Kircher, *Nanoscale*, 2017, **9**, 1110–1119.

14 E. M. Brey, Z. Lalani, C. Johnston, M. Wong, L. V. McIntire, P. J. Duke and C. W. Patrick, *J. Histochem. Cytochem.*, 2003, **51**, 575–584.

15 L. Fan, Y. Y. Tian, R. Yin, D. D. Lou, X. Z. Zhang, M. Wang, M. Ma, S. H. Luo, S. Y. Li, N. Gu and Y. Zhang, *Nanoscale*, 2016, **8**, 8553–8558.

16 K. Bera, K. A. Schalper, D. L. Rimm, V. Velcheti and A. Madabhushi, *Nat. Rev. Clin. Oncol.*, 2019, **16**, 703–715.

17 J. Griffin and D. Treanor, *Histopathology*, 2017, **70**, 134–145.

18 H. Zijlmans, J. Bonnet, J. Burton, K. Kardos, T. Vail, R. S. Niedbala and H. J. Tanke, *Anal. Biochem.*, 1999, **267**, 30–36.

19 M. Wang, C. C. Mi, W. X. Wang, C. H. Liu, Y. F. Wu, Z. R. Xu, C. B. Mao and S. K. Xu, *ACS Nano*, 2009, **3**, 1580–1586.

20 L. Zhou, R. Wang, C. Yao, X. M. Li, C. L. Wang, X. Y. Zhang, C. J. Xu, A. J. Zeng, D. Y. Zhao and F. Zhang, *Nat. Commun.*, 2015, **6**, 6938.

21 C. Y. Liu, Y. F. Qi, R. R. Qiao, Y. Hou, K. Y. Chan, Z. Q. Li, J. Y. Huang, L. H. Jing, J. Du and M. Y. Gao, *Nanoscale*, 2016, **8**, 12579–12587.

22 S. W. Wu, G. Han, D. J. Milliron, S. Aloni, V. Altoe, D. V. Talapin, B. E. Cohen and P. J. Schuck, *Proc. Natl. Acad. Sci. U. S. A.*, 2009, **106**, 10917–10921.

23 M. Haase and H. Schäfer, *Angew. Chem., Int. Ed.*, 2011, **50**, 5808–5829.

24 V. Poláchová, M. Pastucha, Z. Mikušová, M. J. Mickert, A. Hlaváček, H. H. Gorris, P. Skládal and Z. Farka, *Nanoscale*, 2019, **11**, 8343–8351.

25 M. J. Mickert, Z. Farka, U. Kostiv, A. Hlaváček, D. Horák, P. Skládal and H. H. Gorris, *Anal. Chem.*, 2019, **91**, 9435–9441.

26 A. Sedlmeier and H. H. Gorris, *Chem. Soc. Rev.*, 2015, **44**, 1526–1560.

27 Q. Q. Zhan, J. Qian, H. J. Liang, G. Somesfalean, D. Wang, S. L. He, Z. G. Zhang and S. Andersson-Engels, *ACS Nano*, 2011, **5**, 3744–3757.

28 H. He, C. B. Howard, Y. H. Chen, S. H. Wen, G. G. Lin, J. J. Zhou, K. J. Thurecht and D. Y. Jin, *Anal. Chem.*, 2018, **90**, 3024–3029.

29 U. Kostiv, V. Lobaz, J. Kučka, P. Švec, O. Sedláček, M. Hrubý, O. Janoušková, P. Francová, V. Kolářová, L. Šefc and D. Horák, *Nanoscale*, 2017, **9**, 16680–16688.

30 F. Wang, Y. Han, C. S. Lim, Y. H. Lu, J. Wang, J. Xu, H. Y. Chen, C. Zhang, M. H. Hong and X. G. Liu, *Nature*, 2010, **463**, 1061–1065.

31 O. Dukhno, F. Przybilla, V. Muhr, M. Buchner, T. Hirsch and Y. Mely, *Nanoscale*, 2018, **10**, 15904–15910.

32 G. T. Hermanson, *Bioconjugate Techniques*, Academic Press, New York, 2nd edn, 2008.

33 Z. Farka, M. J. Mickert, A. Hlaváček, P. Skládal and H. H. Gorris, *Anal. Chem.*, 2017, **89**, 11825–11830.

337

34 A. Sedlmeier, A. Hlaváček, L. Birner, M. J. Mickert, V. Muhr, T. Hirsch, P. Corstjens, H. J. Tanke, T. Soukka and H. H. Gorris, *Anal. Chem.*, 2016, **88**, 1835–1841.

35 C. A. Schneider, W. S. Rasband and K. W. Eliceiri, *Nat. Methods*, 2012, **9**, 671–675.

36 H. J. Hathaway, K. S. Butler, N. L. Adolphi, D. M. Lovato, R. Belfon, D. Fegan, T. C. Monson, J. E. Trujillo, T. E. Tessier, H. C. Bryant, D. L. Huber, R. S. Larson and E. R. Flynn, *Breast Cancer Res.*, 2011, **13**, R108.

37 K. Subik, J.-F. Lee, L. Baxter, T. Strzepek, D. Costello, P. Crowley, L. Xing, M.-C. Hung, T. Bonfiglio, D. G. Hicks and P. Tang, *Breast Cancer: Basic Clin. Res.*, 2010, **4**, 35–41.

38 M. Jež, T. Bas, M. Veber, A. Košir, T. Dominko, R. Page and P. Rožman, *Histochem. Cell Biol.*, 2013, **139**, 195–204.

338

Paper XXI

Laser-induced breakdown spectroscopy as a novel readout method for nanoparticle-based immunoassays

Modlitbová, P.; Farka, Z.; Pastucha, M.; Pořízka, P.; Novotný, K.; Skládal, P.; Kaiser, J.

Contribution:

Design of experiments, development and optimization of sandwich immunoassay, data evaluation, participation in manuscript writing

ORIGINAL PAPER

Laser-induced breakdown spectroscopy as a novel readout method for nanoparticle-based immunoassays

Pavlína Modlitbová[1] · Zdeněk Farka[2] · Matěj Pastucha[2] · Pavel Pořízka[1] · Karel Novotný[3] · Petr Skládal[2] · Jozef Kaiser[1]

Abstract

Laser-induced breakdown spectroscopy (LIBS) was examined as a novel method for readout of microtiter plate immunoassays involving nanoparticles (NP). The so-called Tag-LIBS technique is a sensitive method for the detection of specific biomarkers. It was applied to the determination of NP labels using nanosecond ablation sampling. The NP labels were examined from the bottom of a standard 96-well microtiter plate. Thanks to the flexibility of LIBS instrumentation, both the plasma emission collection and the focusing optics arrangements can be collinearly arranged. The experiments showed that silver NPs and gold NPs can be readily quantified on the bottom of the microtiter plate. Utilizing this technique, a sandwich immunoassay for human serum albumin using streptavidin-coated AgNP labels was developed. The assay has a 10 ng·mL^{-1} detection limit which is comparable to the sensitivity of fluorometric readout. The main advantage of this LIBS technique is its wide scope in which it enables a detection of almost any type of NP labels, irrespective to any fluorescence or catalytic properties. Owing to the immediate signal response, the relatively simple instrumentation also enables assay automation. The LIBS capability of multi-elemental analyses makes it a promising and fast alternative to other readout techniques, in particular with respect to multiplexed detection of biomarkers.

Keywords Collinear plasma collection · Gold nanoparticles · Laser ablation · Microtiter plate · Sandwich immunoassay · Silver nanoparticles · Streptavidin · Tag-LIBS

Highlights

- LIBS is a suitable readout method for nanoparticle-based immunoassays.
- Collinear LIBS arrangement for collection of plasma emission from the bottom of the standard 96-well microtiter plate was presented.
- Tag-LIBS was employed in a sandwich immunoassay for the detection of human serum albumin.

✉ Pavlína Modlitbová
  Pavlina.Modlitbova@ceitec.vutbr.cz

1   Central European Institute of Technology (CEITEC), Brno University of Technology, Technická 3058/10, 616 00 Brno, Czech Republic

2   Central European Institute of Technology (CEITEC), Masaryk University, Kamenice 5, 625 00 Brno, Czech Republic

3   Department of Chemistry, Faculty of Science, Masaryk University, Kotlářská 2, 611 37 Brno, Czech Republic

Introduction

Immunochemical assays combine the specificity of immunoreagents and the variation in detection approaches enabled by the use of different labels. The assays are usually based on the attachment of one of the immunoreagents to a solid phase and a subsequent addition of reagents that bind to each other (heterogeneous format). The bound and the free components are separated through washing steps [1]. The most widespread assay type – enzyme-linked immunosorbent assay (ELISA) – involves an antibody (or antigen) labeled with enzymes such as horseradish peroxidase or alkaline phosphatase. This labeling enables a quantification via the conversion of suitable substrate to a colored or fluorescent product [2]. The main advantages of enzymatic labels are the easy conjugation with antibodies and the high catalytic activity providing the amplification (a single enzyme molecule

Ⓐ Springer

converts multiple substrate molecules). However, when the enzymes are used as labels, they suffer several disadvantages including the high production costs, limited stability, and time-consuming signal development [3].

The progress in nanotechnology has led to a development of various nanomaterials that can be used to overcome the limitations of enzymes and to improve the assay properties. The applications of nanoparticle (NP) labels in immunoassays can be divided into two main categories: (a) catalytic nanoparticles (nanozymes), and (b) directly detected labels [4]. The detection based on the catalytic NPs employs a transformation of a substrate similar to traditional ELISA [5]. Comparing to ELISA, this process provides better stability and higher catalytic efficiency of nanomaterials such as AuNPs [6], Au@PdNPs [7], iron oxides NPs, Prussian blue NPs [8] or nanocomposite of PtNPs and graphene oxide [9].

The direct immunoassay readout (without the substrate catalysis) is usually based on luminescent labels. Nanomaterials such as quantum dots (QD) [10], carbon-based NPs [11], and photon-upconversion NPs [12] are used as an alternative to the conventional organic dyes and fluorescent proteins. The luminesce-based readout combines a high sensitivity with a simple and affordable instrumentation. Nevertheless, this readout method limits the range of possible labels to the materials exhibiting luminescent properties. Therefore, there is a demand for readout methods providing the universal detection of any label type that is independent on its catalytic or luminescent properties.

Laser-induced breakdown spectroscopy (LIBS) proved to be a suitable method for the NP detection in different matrices; ranging from the detection of QDs applied onto filter paper [13] to a detection of photon-upconversion NPs in the model organisms [14]. On top of that, the LIBS technique is abundantly used for mapping purposes, providing the lateral distribution of elements on the sample surface. This feature is used in a number of applications, for instance a mapping of NPs in mammal [15] and plant [16] tissues. The detection of NPs in aquatic suspensions [17, 18] or the detection of nano-powders in the polymer gels is well known. Also, the detection and characterization of single NPs by Optical Catapulting-Optical Trapping-LIBS (OC-OT-LIBS) [19] was already published. The pioneer LIBS study to detect the biomolecules labeled with CdTe or CdS QDs, followed by using aforementioned immunoassay readout was published by Konečná et al. [20]. On the other hand, the detection of small/scant volumes of liquid samples was studied only once using lab-on-a-chip devices designed especially for the LIBS interfacing [21].

To the best of our knowledge, the LIBS method as an alternative method of signal readout in immunochemical assays was investigated exclusively by Melikechi's re-

search group [22], which also introduced the Tag-LIBS abbreviation [22]. The advanced Tag-femtosecond LIBS detection in microparticle-based immunochemical assays was demonstrated in a case study focused on the multi-element coded assay. The assay was carried out with Fe_2O_3 and TiO_2 microparticles bound to cancer antigen 125 via monoclonal antibodies [22].

In this work, two main experiments were carried out to prove LIBS to be a useful readout method for the common metal NPs-based immunoassays. The initial experiment focused on the most appropriate collection of Ag- and AuNPs plasma emission from the bottom of the standard 96-well microtiter plate and on the optimization of corresponding experimental conditions. The following experiment compared the LIBS method to the fluorescence readout in sandwich immunoassay where these methods are applied to detect the human serum albumin utilizing the label based on streptavidin-coated AgNPs.

Materials and methods

Chemicals and materials

The 20 nm colloid Ag NPs (the mean diameter of 19.9 nm) were obtained from BBI Solutions (www.bbisolutions.com; United Kingdom), 20 nm Au nanospheres citrate NanoXact™ (diameter of 18.9 ± 1.5 nm) were obtained from nanoComposix (www.nanocomposix.com; USA). Streptavidin-conjugated 40 nm AgNPs were purchased from Cytodiagnostics (www.cytodiagnostics.com; Canada). Biotin N-hydroxysuccinimide ester (NHS-biotin), bovine γ-globulin (BGG), bovine serum albumin (BSA), human serum albumin (HSA), N,N'-dimethylformamide (DMF), sodium azide, Tris, and Tween 20 were acquired from Sigma-Aldrich (www.sigmaaldrich.com; Germany). Ethylenediaminetetraacetic acid (EDTA) and glucose were purchased from Lachema (www.erbalachema.com; Czech Republic). Poly(vinyl alcohol) (PVA, 6 kDa) was purchased from Polysciences (www.polysciences.com; Germany). All other common chemicals were obtained in the highest quality available from Penta (www.pentachemicals.eu; Czech Republic). Anti-HSA mouse monoclonal antibody clone AL-01 was purchased from Exbio (www.exbio.cz; Czech Republic), fluorescein isothiocyanate (FITC)-labeled anti-HSA swine polyclonal antibody (AbF) was obtained from Sevapharma (sevapharma.czechtrade.us; Czech Republic).

Buffers used throughout this work were: phosphate buffer (PB; 50 mM NaH_2PO_4/Na_2HPO_4, pH 7.4), phosphate-buffered saline (PBS; PB + 150 mM NaCl), washing buffer (PB + 0.01% Tween 20, and 0.05% NaN_3), and assay buffer

(0.2% BSA, 0.5% BGG, 50 mM Tris, 150 mM NaCl, 5 mM EDTA, 0.2% PVA, 1% glucose, 0.05% NaN_3, and 0.01% Tween 20, pH 7.5).

Deposition of silver and gold nanoparticles in the microtiter plate

First, bare AgNPs and AuNPs were directly deposited on the bottom of the microtiter plate well and consequently ablated in order to optimize the LIBS experimental parameters. The deposition of NP suspensions to the microtiter plate well was performed using two approaches – manually and with an ink-jet deposition system.

For the manual formation of drops, selected volumes in a predetermined concentration were applied using a micropipette onto the bottom of each well. The drops dried at the air atmosphere and the laboratory temperature. The drop volumes were 10.0, 5.0, 2.5, 1.0, and 0.5 μL in the concentration provided by the supplier (AgNPs 3.08 μg·mL^{-1}; AuNPs 53.0 μg·mL^{-1}). Furthermore, the calibration plot was also measured for AgNPs, in a concentration range 3.08; 1.54; 0.77; 0.308; 0.205; 0.154 and 0.062 μg·mL^{-1} in a volume of 10 μL per one drop.

The ink-jet deposition was done using a piezo-driven non-contact dispensing system sciFLEXARRAYER S3 (www.scienion.com; Scienion, Germany). A 60 μm dispense capillary and the pulse parameters of 84 V, 50 μs and 500 Hz were used, resulting in a droplet volume of 250 pL. Four 1 μL drops were formed in each well of the microtiter plate by dispensing 4000 droplets onto each drop in 2 by 2 pattern with 2 mm spacing. The dilution series of AgNPs 3.08; 1.54; 0.77; 0.308; 0.154 and 0.077 μg·mL^{-1} were deposited and dried spontaneously.

Detection of nanoparticle labels in microtiter wells using laser-induced breakdown spectroscopy

Instrumentation and experimental settings

The LIBS measurements were done using the Sci-Trace (www.atomtrace.com; AtomTrace, Czech Republic) including the CageSystem as shown in Fig. 1a, b. The laser pulse (Nd:YAG laser LQ529A, www.solarlaser.com; Solar, Belarus; 532 nm, 10 ns) was used for material ablation (sampling). The laser pulse was focused to a tight spot (a crater diameter of 100 μm) and consequently a laser-induced plasma was created. A characteristic plasma emission was collected using a telescope and delivered via a 50 μm optical fiber to the entrance slit of an echelle spectrometer with a 200–975 nm wavelength range (Mechelle 5000 with the camera iStar 734i Andor, www.andor.oxinst.

com; Oxford Instruments, UK). The software-controlled movement in x,y,z direction enabled scanning the bottoms of individual microtiter plate wells. The samples were measured in the air at the atmospheric pressure and laboratory temperature.

We first evaluated the possibility of a qualitative and a quantitative analysis of both types of selected nanoparticles – AgNPs and AuNPs – in a colinear LIBS arrangement. As mentioned before, the deposition to the microtiter plate was performed by two approaches – (i) manually and (ii) with an ink-jet printer. After drying, the analyses were done using experimental conditions which were optimized a priori. The settings used during the LIBS analysis were: 1.5 μs of the gate delay and 15 μs of the detection integration time, the laser pulse energy was set to 20 mJ. In case of manually (i) applied NPs, each bottom well area was analyzed in a raster of 15 × 15 spots with a 300 μm step as shown in Fig. 1c. After the ink-jet (ii) application of NPs, each bottom well area was analyzed in a raster of 30 × 30 spots with a 150 μm step. To ensure that no plasma emission was lost during the plasma collection from the 12 mm well depth was challenging. In order to handle this, a comparison experiment was carried out utilizing a dried AgNPs drop positioned the flat polystyrene surface (i.e. inverted microtiter plate).

Data processing

The most appropriate emission lines (represented in Fig. 2) of Ag I 338.31 nm (338.17–338.42 nm) and Au I 312.29 nm (312.20–312.34 nm) were selected and defined as the maximum line intensity with a proper background subtraction. The background was defined as the mean of the detected signal (338.54–338.79 nm for Ag and 312.40–312.54 nm for Au) near the selected analytical emission lines. The intensities were depicted as 2D maps representing the spatial distribution of the selected elements separately for each well. All signals for the selected emission line from 225 spectra were accumulated separately for each well after the manual applying of NPs. For the detection of NPs by applying the ink-jet system, 30 × 30 spots per one well with four dried drops were used. However, we only managed to accumulate the selected emission line from 225 spectra covering each drop separately (15 × 15 spots, a quarter of the well bottom). Thus, four accumulated signals of Ag I 338.31 nm emission line per one well were obtained. The accumulated signals were used in all following data evaluation. All LIBS data were processed using the AtomAnalyzer software (AtomTrace, Czech Republic) and visualized with OriginPro 2015 (www.originlab.com; OriginLab Corp., USA).
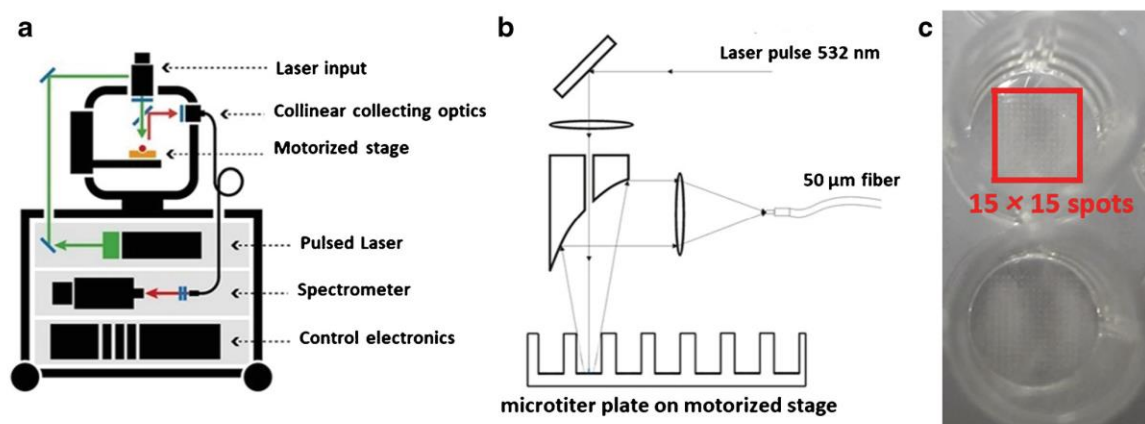
Fig. 1 **a** Scheme of Sci-Trace LIBS system; **b** Scheme of the plasma collection from the bottom of the standard 96-well microtiter plate in 12 mm depth; **c** Photograph of two wells of microtiter plate after LIBS measurements with highlighted area with raster of 15 × 15 ablation craters

Sandwich immunoassay for the detection of human serum albumin

Conjugation of detection antibody with biotin

A biotinylation of the detection antibody was done according to the protocol by Hermanson [23]. AbF was diluted in PBS to the concentration of 5 mg·mL^{-1} and NHS-biotin was dissolved in anhydrous DMF in the concentration of 20 mg·mL^{-1}. Subsequently, 20-times molar excess of NHS-biotin was added to the antibody and the mixture was incubated for 2 h at the room temperature. The AbF-biotin conjugate was purified using the Microcon centrifugal unit YM-100 (100 kDa MWCO; www.merckmillipore.com; Merck

Millipore, USA) to PBS and stored at 4 °C in the concentration of 2 mg·mL^{-1}.

Sandwich immunoassay

A 96-well microtiter plate Nunc MaxiSorp (www.thermofisher.com; Thermo Fisher Scientific, USA) was coated with anti-HSA monoclonal antibody AL-01 (4 μg·mL^{-1} in PBS, 100 μL per well) and incubated overnight at 4 °C. All following incubations were carried out at the room temperature on a microplate shaker; after each step, the plate
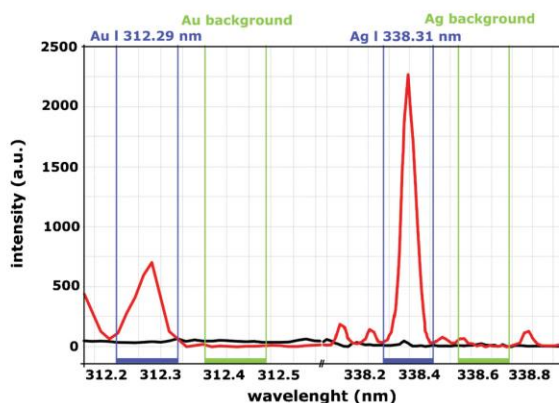
Fig. 2 Sample of spectra of AuNPs and AgNPs (red lines) and matrix (black lines) with highlighted parts of selected ranges of Au I 312.29 nm emission line (312.2–312.34 nm) together with background (312.4–312.54 nm) and Ag I 338.31 nm emission line (338.17–338.42 nm) together with background (338.54–338.79 nm)
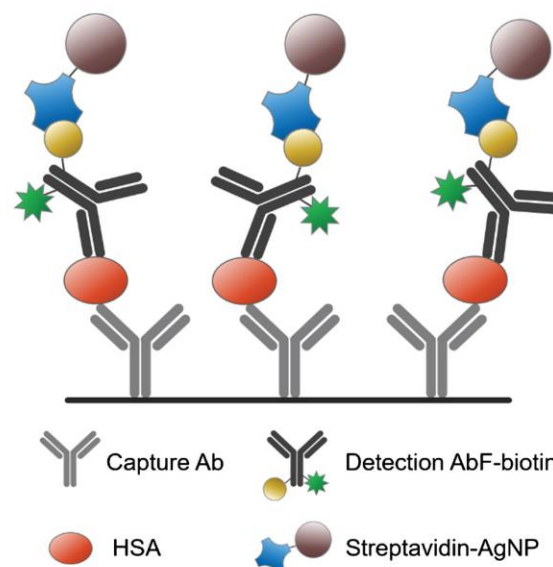
Fig. 3 A scheme of the sandwich immunocomplex in the detection of human serum albumin based on streptavidin-AgNP conjugate

was washed four times with 200 μL of washing buffer. The plate was blocked with 200 μL of 5% powdered milk (www.carlroth.com; Carl Roth, Germany) in PBS for 60 min. Subsequently, standard dilutions of HSA (10 ng·mL^{-1} to 100 μg·mL^{-1}) in the assay buffer were added (100 μL per well), and the plate was incubated for 60 min. Then, AbF-biotin conjugate in the assay buffer was added (the concentration equivalent to 100 μg·mL^{-1} of antibody, 100 μL per well) and incubated for 60 min. Finally, a conjugate of AgNPs with streptavidin (6 μg·mL^{-1}, 100 μL per well) was added for 60 min. After the last washing step, the wells were left empty and the scanning was performed in dry state, the protocol is based on our previously published methodology [8]. The scheme of the sandwich immunocomplex is shown in Fig. 3.

LIBS readout

The LIBS readout of the microtiter plate was based on the evaluation of the Ag I signal from the streptavidin-coated AgNP label. The experimental conditions remained the same as in case of the LIBS experiments with manually deposited nanoparticle drops. The gate delay was 1.5 μs, the detection integration time was 15 μs, the laser pulse energy was 20 mJ, and the raster of single pulses was 15×15 spots with a 300 μm step.

Fluorescence-based readout

To confirm the functionality of the sandwich immunoassay using a reference approach, the fluorescence of the AbF-biotin conjugate was measured using a Synergy 2 reader (www.biotek.com; BioTek, USA). A Tungsten lamp was used as an excitation source, with optics position *Top 510 nm*, the excitation and emission filters were set to 485 nm and 528 nm, respectively. The instrumental background corresponding to the average fluorescence of 12 unmodified wells was subtracted from the signals.

Results and discussion

LIBS detection of nanoparticles in the microtiter plate

Manual deposition of NPs to the microtiter plate

Firstly, the accumulated signal of Au I 312.29 nm emission line from 225 spectra covered a 10 μL drop (concentration 53.0 μg·mL^{-1}). The drop dried on the flat polystyrene surface (inverted microtiter plate). This accumulated signal was compared to accumulated signal values for identical AuNPs drops, which dried on the bottom of microtiter plate well. Differences

between accumulated signals (5 replicates per one condition) showed to be lower than 5%. The accumulated signals from drops that dried on the flat surface were $332,000 \pm 18,000$ (a.u.) and accumulated signals from the spots inside the well were $319,000 \pm 24,000$ (a.u.). Moreover, a collection of plasma emissions from cavities, especially cylindrical, was shown to positively affect the signal repeatability and signal intensity. This influence was attributed to (i) the reflection and compression of the shock wave or to (ii) a more effective collection of plasma radiation caused by the reflection from the chamber walls as previously discussed [24]. The size of the cavities and the distance between the wall and plasma can affect the signal intensities. However, based on our data, we concluded that the plasma emission collection was not affected significantly during the plasma collection from the 12 mm depth and we continued with the LIBS detection from the bottom of a microtiter plate.

Secondly, the LIBS-based readout was used for a qualitative and quantitative determination of AgNP and AuNP suspensions applied with a micropipette onto the bottom of microtiter plate wells. The LIBS results are shown together in Fig. 4, the part (A) presents the accumulated signals of Ag I 338.31 nm for different concentrations of AgNPs (from 3.08 to 0.062 μg·mL^{-1}). The part (B) presents the accumulated signals of Ag I 338.31 nm for dried drops of five different volumes (10.0; 5.0; 2.5; 1.0 and 0.5 μL) of AgNPs in the concentration of 3.08 μg·mL^{-1}. The accumulated signals of Ag I 338.31 nm emission line recalculated to number of NPs on the bottom of the well for each drop are shown together in Fig. 4c. Figure 4d presents the accumulated signals of Au I 312.29 nm for drops of four different volumes (10.0; 5.0; 2.5 and 1.0 μL) of AuNPs in the concentration 53.0 μg·mL^{-1}. Maps representing 2D spatial distribution of AgNPs at the bottom of the well are depicted in Fig. 4 for selected concentrations (E) and volumes (F). It is clearly visible that NPs after manual deposition were non-homogeneously distributed due to the non-uniform drying of drops, which is well known [25].

The LOD for AgNPs (Ag I 338.31 nm) is $6.6 \cdot 10^{6}$ NPs (291 pg Ag) and the LOD for AuNPs (Au I 312.29 nm) is $2.4 \cdot 10^{8}$ NPs (16.1 ng Au). These values were calculated from the accumulated signals from well (raster consisted of 225 laser spots). Different LODs of Ag and Au, as well as the dependence of LODs of the element (Ag or Au) on a selected emission line, the sample matrix, and the concentration range of calibration plot was investigated in detail previously [26]. Furthermore, the well-known influence of the difference in the laser ablation process (single- or double-pulse ablation) was examined as described for the Au element [27]. The LODs for both elements were in the range from 0.4 to 94 ppm based on the experimental conditions [26, 27], which corresponds to

Fig. 4 Dependences of the LIBS accumulated Ag intensity on the concentration (**a**) and volume (**b**) of AgNPs; **c** both dependencies recalculated on the number of AgNPs shown together. **d** Dependency of the LIBS accumulated Au I intensity on the volume of AuNPs. Number of replicates $n = 4$. The symbols on the scatter plot represent mean values and SD as error bars. (**e**) LIBS maps constructed for Ag I 338.31 nm emission line of AgNPs dried drops of various concentration; **f** LIBS maps constructed for Ag I 338.31 nm emission line of AgNPs dried drops of various volumes. The scale bar shows 1 mm. Red letters (a-h) of selected LIBS maps are assigned to their accumulated signal values in graphs (**a**) and (**b**)
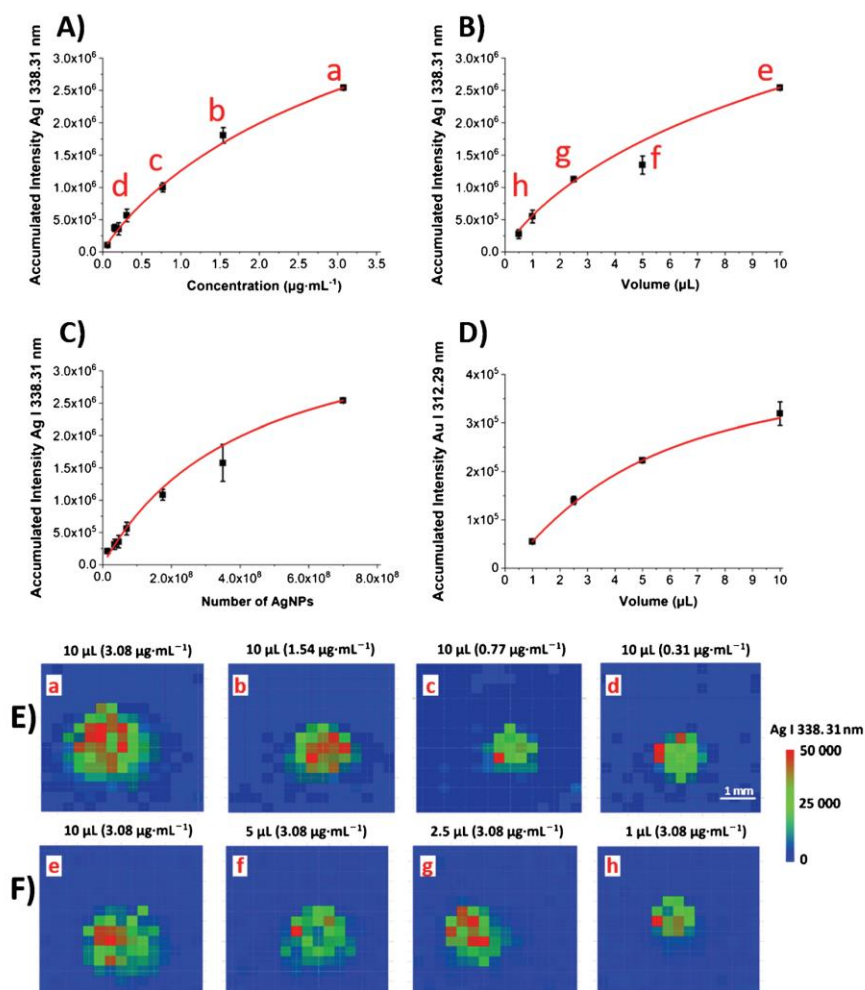
our results (Ag LOD 0.3 ppm for Ag I 338.31 nm and Au LOD 1.6 ppm for Au I 312.29 nm).

Overall, these LIBS results showed that the qualitative and quantitative analysis of both types of NPs is easy to implement and that the number of NPs (a different volume or different concentration applied to a microtiter plate well) is decisive for signal intensities. Due to the lower LODs, the AgNPs were used in all following experiments.

Ink-jet deposition of NPs to the microtiter plate

In this experiment, four 1 μL drops of AgNPs (the concentration range from 3.08 to 0.077 $\mu g \cdot mL^{-1}$) were applied in each well of the microtiter plate using a 2 by 2 pattern with 2 mm spacing. The resulting dried drops were analyzed using LIBS. In comparison to the first LIBS experiment, one difference

appeared. Due to the fact that the drops were of smaller size, the laser ablation step was reduced to 150 μm and the total number of laser spots from one well was 900 (30 × 30). The results are shown in Fig. 5, where the part A presents accumulated signals of Ag I 338.31 nm for six different concentrations (3.08; 1.54; 0.77; 0.308; 0.154 and 0.077 $\mu g \cdot mL^{-1}$) of AgNPs in a volume of 1 μL per one drop. Also, this dependence of the accumulated signal on the concentration was fitted with Langmuir saturation curve. Furthermore, Fig. 5b depicts 2D maps of the spatial distribution of Ag I 338.31 nm emission line for four different concentrations (3.08; 1.54; 0.77; and 0.308 $mg \cdot L^{-1}$) from one well.

The LOD for ink-jet deposited AgNPs was calculated again from the accumulated signals. In this case, the signals were not accumulated from the whole well bottom, but only from one quarter, which corresponded exactly to one drop
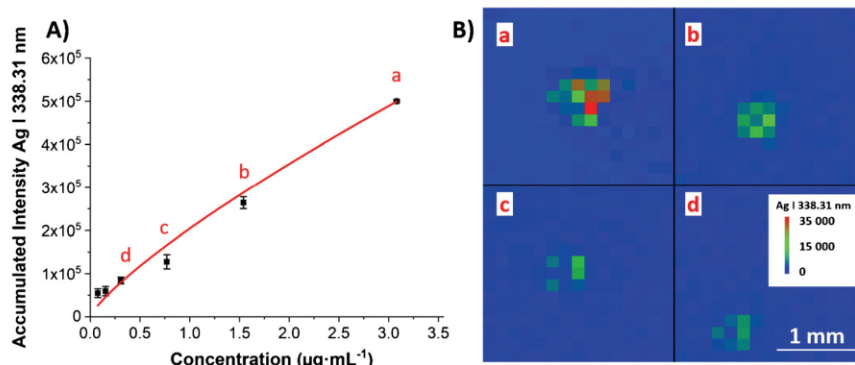
345

Fig. 5 a Dependency of accumulated Ag I 338.31 nm intensity on concentration of AgNPs. Number of replicates $n = 4$. The symbols on the scatter plot represent mean values and SD as error bars. **b** LIBS map constructed for Ag I 338.31 nm emission line of four drops (a: 3.08 $\mu g \cdot mL^{-1}$, b: 1.54 $\mu g \cdot mL^{-1}$, c: 0.77 $\mu g \cdot mL^{-1}$, d: 0.308 $\mu g \cdot mL^{-1}$) of AgNPs applied in a volume of 1 μL on the bottom of one well. The scale bar shows 1 mm

of NPs (15×15 spots from whole 30×30 spots from each well), as indicated in Fig. 5b by black cross lines. The LOD for AgNPs (Ag I 338.31 nm) is $6.7 \cdot 10^6$ NPs (293 pg Ag). The LODs for AgNPs from both experiments were very similar, 291 pg Ag (manual deposition) and 293 pg Ag (ink-jet system). This situation points to the robustness of LIBS method, in case that none of the previously mentioned parameters such as the matrix of samples, and the selected emission line of element or ablation process is changed. The method of NP deposition had no influence on the signal detection and consequently had no influence on LODs. In comparison to the manual application of NPs dispersion with micropipette, the speed, accuracy, and repeatability of the ink-jet system application need to be highlighted together with the space saving and possibility of multiplexing (multiple drops per one well). Considering the following application as a label for immunoassay, the ink-jet deposition resulted in the signal being nearly linearly dependent on the AgNP concentration (Fig. 5a), which was not the case for the manual deposition (Fig. 4a). The linear dependence of the signal on the bound label amount is advantageous as it

does not complicate the interpretation of non-linear immunoanalytical calibration plots.

Sandwich immunoassay for detection of human serum albumin

The optimized LIBS-based readout was used for a determination of streptavidin-coated AgNPs as a label in the sandwich HSA detection. The sandwich assay for HSA was optimized in our previous work [8], therefore we focused here on the optimization of the labeling steps. We analyzed the concentrations of HSA in the range from 10 ng·mL^{-1} to 100 $\mu g \cdot mL^{-1}$. The results are shown in Fig. 6, together with their comparison to the reference readout based on the fluorescence of a conjugate of detection antibody with FITC and biotin. All curves were fitted by a four-parameter logistic function. For the lower concentration of streptavidin-coated AgNPs of 3 $\mu g \cdot mL^{-1}$, LIBS provided lower sensitivity than the fluorescence-based readout. However, when the concentration of streptavidin-AgNP label was increased to 6 $\mu g \cdot mL^{-1}$, the LIBS reached a sensitivity comparable to the fluorescence-based readout. Both

Fig. 6 a Dependences of LIBS accumulated Ag I 338.31 nm intensity on HSA concentration; **b** Dependences of fluorescence signal on HSA concentration. Number of replicates $n = 4$. The symbols on the scatter plot represent mean values and SD as error bars

346
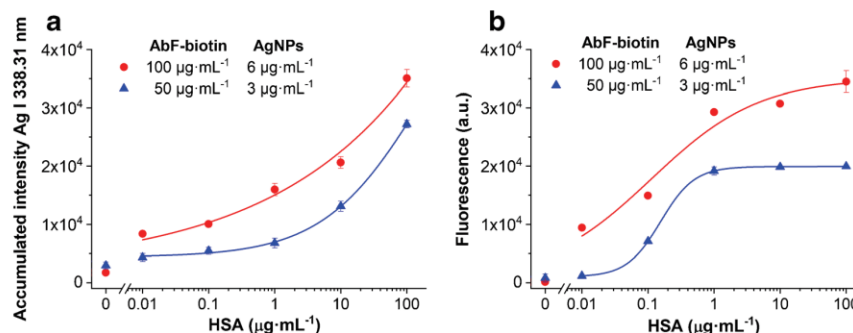
methods provided a detection limit of 10 ng·mL^{-1} of HSA (S/N > 3). Compared to the fluorescence readout where plateau was reached at 1 µg·mL^{-1} of HSA, LIBS offered wider working range up to 100 µg·mL^{-1}. This is a significant advantage considering e.g. the levels typical for albuminuria.

The previous reports about LIBS being used to provide a readout of antibody-based assays are very sparse. Markushin et al. (2015) previously employed femtosecond LIBS for a detection of cancer antigen 125 with LOD of 0.01 U·mL^{-1} [22]. However, the assay was limited because it was necessary to use magnetic particles for an antigen capture, followed by a deposition of resulting sandwich immunocomplexes on the filter paper. Whereas, the system here allows scanning the standard polystyrene microtiter plates without the necessity to significantly change the routine assay procedure. Unfortunately, due to the different experimental settings, different ablation process, various analyte (and units expressed as U·mL^{-1}), the sensitivity of the two approaches cannot be directly compared.

Considering some other approaches, Raman spectroscopy, especially Surface-Enhanced Raman Scattering (SERS) [28, 29], and Inductively Coupled Plasma Mass Spectrometry (ICP-MS) [30] showed to be useable to detect various NPs labels in immunoassays. Quantum dots or metal-doped NPs served as labels for a detection of carcinoembryonic antigen [31], allergens in food [32], or a multiplexed detection of C-reactive protein, alpha-fetoprotein, and neuron-specific enolase [33] by ICP-MS readout method. In comparison of ICP-MS to LIBS, several disadvantages of ICP-MS have to be mentioned, including high cost of instrumentation, high operation costs, high demands on vacuum environment, and a long duration of analysis. On the other hand, SERS showed to be useable for a detection of various labels, so-called SERS-nanotags, in various biosensing of proteins, nucleic acids, and many others, as summarized in a previously published review [34]. Many advantages as the high sensitivity, specificity, multiplexing capability, photostability of SERS-nanotags, and low detection limits (down to the femtomolar level) are compensated by the need of special SERS-nanotags. In contrast, LIBS can detect various commonly used NPs.

Conclusion

We presented Tag-LIBS with nanosecond laser ablation process of sampling as a universal readout method for the immunoassays based on nanoparticle labels. An innovative arrangement of the collinear plasma collection and the focusing optics for LIBS was developed in order to enable a detection of NPs directly in a standard microtiter plate. Using this LIBS setup, we demonstrated the capability to detect AuNPs and AgNPs

with a detection limit of 6.6·10^{6} and 2.4·10^{8} particles for AgNPs and AuNPs, respectively. The LIBS detection of the dried drops on the bottom of a microtiter plate was more appropriate for the drops deposited with the ink-jet system.

The optimized LIBS setup was used for the readout of sandwich immunoassay with streptavidin-coated AgNPs as a label. Human serum albumin, a diagnostic marker of albuminuria, was detected with a LOD of 10 ng·mL^{-1}, which is nearly comparable with the sensitivity of the fluorescence-based readout. Both techniques are complementary readout methods. The fluorescence detection showed a slightly better sensitivity but a substantial tendency to saturation, on the other hand, LIBS presents wider dynamic range, as it is obvious from the immunoassay results. The great LIBS advantage is the fast analysis time, the possibility of a multi-elemental (multi-biomarker) analysis, and the possibility to detect NPs without any photoluminescence or without any effect of potential NPs photoluminescence quenching. Furthermore, LIBS method does not show the broadband interfering spectral emissions.

We expect that Tag-LIBS described here can be applied to detect many types of biomarkers in nanoparticle-based immunochemical assays. It can also be used for a parallel detection of a multiple set of biomarkers in the near future. Moreover, we would like to emphasize the possibility to combine four readout methods (LIBS, SERS, Raman spectroscopy, and fluorescence detection) for their similar detection principles in one optical reader. This multiplexed readout represents a novel strategy for a robust simultaneous determination of various elements, chemical bonds, special nanotags, and fluorescent substances. Thus, this is going to be a subject of our future work.

Compliance with ethical standards The author(s) declare that they have no competing interests.

References

1. Tighe PJ, Ryder RR, Todd I, Fairclough LC (2015) ELISA in the multiplex era: potentials and pitfalls. Proteomics Clin Appl 9:406–422. https://doi.org/10.1002/prca.201400130

2. Lequin RM (2005) Enzyme immunoassay (EIA)/enzyme-linked immunosorbent assay (ELISA). Clin Chem 51:2415–2418. https://doi.org/10.1373/clinchem.2005.051532

347

3. Wei H, Wang E (2013) Nanomaterials with enzyme-like characteristics (nanozymes): next-generation artificial enzymes. Chem Soc Rev 42:6060–6093. https://doi.org/10.1039/c3cs35486e

4. Farka Z, Juřík T, Kovář D, Trnková L, Skládal P (2017) Nanoparticle-based immunochemical biosensors and assays: recent advances and challenges. Chem Rev 117:9973–10042. https://doi.org/10.1021/acs.chemrev.7b00037

5. Wu J, Li S, Wei H (2018) Multifunctional nanozymes: enzyme-like catalytic activity combined with magnetism and surface plasmon resonance. Nanoscale Horizons 3:367–382. https://doi.org/10.1039/c8nh00070k

6. Sang F, Liu J, Zhang X, Pan J (2018) An aptamer-based colorimetric Pt(II) assay based on the use of gold nanoparticles and a cationic polymer. Microchim Acta 185:1–7. https://doi.org/10.1007/s00604-018-2794-6

7. Dehghani Z, Hosseini M, Mohammadnejad J, Bakhshi B, Rezayan AH (2018) Colorimetric aptasensor for campylobacter jejuni cells by exploiting the peroxidase like activity of Au@Pd nanoparticles. Microchim Acta 185:448. https://doi.org/10.1007/s00604-018-2976-2

8. Farka Z, Čunderlová V, Horáčková V, Pastucha M, Mikušová Z, Hlaváček A, Skládal P (2018) Prussian blue nanoparticles as a catalytic label in a Sandwich Nanozyme-linked immunosorbent assay. Anal Chem 90:2348–2354. https://doi.org/10.1021/acs.analchem.7b04883

9. Xu HH, Deng HH, Lin XQ, Wu YY, Lin XL, Peng HP, Liu AL, Xia XH, Chen W (2017) Colorimetric glutathione assay based on the peroxidase-like activity of a nanocomposite consisting of platinum nanoparticles and graphene oxide. Microchim Acta 184:3945–3951. https://doi.org/10.1007/s00604-017-2429-3

10. Wu Y-T, Qiu X, Lindbo S, Susumu K, Medintz IL, Hober S, Hildebrandt N (2018) Quantum dot-based FRET immunoassay for HER2 using Ultrasmall affinity proteins. Small 14:1802266. https://doi.org/10.1002/smll.201802266

11. Yang L, Deng W, Cheng C, Tan Y, Xie Q, Yao S (2018) Fluorescent immunoassay for the detection of pathogenic Bacteria at the single-cell level using carbon dots-encapsulated breakable Organosilica Nanocapsule as labels. ACS Appl Mater Interfaces 10:3441–3448. https://doi.org/10.1021/acsami.7b18714

12. Farka Z, Mickert MJ, Hlaváček A, Skládal P, Gorris HH (2017) Single molecule upconversion-linked immunosorbent assay with extended dynamic range for the sensitive detection of diagnostic biomarkers. Anal Chem 89:11825–11830. https://doi.org/10.1021/acs.analchem.7b03542

13. Škarková P, Novotný K, Lubal P, Jebavá A, Pořízka P, Klus J, Farka Z, Hrdlička A, Kaiser J (2017) 2d distribution mapping of quantum dots injected onto filtration paper by laser-induced breakdown spectroscopy. Spectrochim Acta - Part B At Spectrosc 131:107–114. https://doi.org/10.1016/j.sab.2017.03.016

14. Modlitbová P, Hlaváček A, Švestková T, et al (2019) The effects of photon-upconversion nanoparticles on the growth of radish and duckweed: bioaccumulation, imaging, and spectroscopic studies. Chemosphere 225:723–734. https://doi.org/10.1016/j.chemosphere.2019.03.074

15. Gimenez Y, Busser B, Trichard F, Kulesza A, Laurent JM, Zaun V, Lux F, Benoit JM, Panczer G, Dugourd P, Tillement O, Pelascini F, Sancey L, Motto-Ros V (2016) 3D imaging of nanoparticle distribution in biological tissue by laser-induced breakdown spectroscopy. Sci Rep 6:1–9. https://doi.org/10.1038/srep29936

16. Modlitbová P, Novotný K, Pořízka P, Klus J, Lubal P, Zlámalová-Gargošová H, Kaiser J (2018) Comparative investigation of toxicity and bioaccumulation of Cd-based quantum dots and Cd salt in freshwater plant *Lemna minor* L. Ecotoxicol Environ Saf 147:334–341. https://doi.org/10.1016/j.ecoenv.2017.08.053

17. Sovago M, Buis EJ, Sandtke M (2013) Nanoparticle detection in aqueous solutions using Raman and laser induced breakdown spectroscopy. Spectrochim Acta - Part B At Spectrosc 87:182–187. https://doi.org/10.1016/j.sab.2013.05.033

18. Borowik T, Przybyło M, Pala K, Otlewski J, Langner M (2011) Quantitative measurement of Au and Fe in ferromagnetic nanoparticles with laser induced breakdown spectroscopy using a polymer-based gel matrix. Spectrochim Acta - Part B At Spectrosc 66:726–732. https://doi.org/10.1016/j.sab.2011.09.008

19. Fortes FJ, Fernández-Bravo A, Javier Laserna J (2014) Chemical characterization of single micro- and nano-particles by optical catapulting-optical trapping-laser-induced breakdown spectroscopy. Spectrochim Acta - Part B At Spectrosc 100:78–85. https://doi.org/10.1016/j.sab.2014.08.023

20. Konecna M, Novotny K, Krizkova S, Blazkova I, Kopel P, Kaiser J, Hodek P, Kizek R, Adam V (2014) Identification of quantum dots labeled metallothionein by fast scanning laser-induced breakdown spectroscopy. Spectrochim Acta - Part B At Spectrosc 101:220–225. https://doi.org/10.1016/j.sab.2014.08.037

21. Metzinger A, Nagy A, Gáspár A, Márton Z, Kovács-Széles É, Galbács G (2016) The feasibility of liquid sample microanalysis using polydimethylsiloxane microfluidic chips with in-channel and in-port laser-induced breakdown spectroscopy detection. Spectrochim Acta Part B At Spectrosc 126:23–30. https://doi.org/10.1016/j.sab.2016.10.014

22. Markushin Y, Sivakumar P, Connolly D, Melikechi N (2015) Tag-femtosecond laser-induced breakdown spectroscopy for the sensitive detection of cancer antigen 125 in blood plasma. Anal Bioanal Chem 407:1849–1855. https://doi.org/10.1007/s00216-014-8433-0

23. Hermanson G (2013) Bioconjugate Techniques, 3rd edn. Academic Press

24. Li Y, Tian D, Ding Y, Yang G, Liu K, Wang C, Han X (2018) A review of laser-induced breakdown spectroscopy signal enhancement. Appl Spectrosc Rev 53:1–35. https://doi.org/10.1080/05704928.2017.1352509

25. Park BS, Jung KI, Lee SJ, Lee KY, Jung HW (2018) Effect of particle shape on drying dynamics in suspension drops using multi-speckle diffusing wave spectroscopy. Colloid Polym Sci 296:971–979. https://doi.org/10.1007/s00396-018-4315-x

26. Díaz D, Hahn DW, Molina A (2017) Spectrochimica Acta Part B Quanti fi cation of gold and silver in minerals by laser-induced breakdown spectroscopy. Spectrochim Acta Part B At Spectrosc 136:106–115. https://doi.org/10.1016/j.sab.2017.08.008

27. Rifai K, Laville S, Vidal F, Sabsabi M, Chaker M (2012) Quantitative analysis of metallic traces in water-based liquids by UV-IR double-pulse laser-induced breakdown spectroscopy. J Anal At Spectrom 27:276–283. https://doi.org/10.1039/c1ja10178a

28. Liu R, Liu B, Guan G, Jiang C, Zhang Z (2012) Multilayered shell SERS nanotags with a highly uniform single-particle Raman read-out for ultrasensitive immunoassays. Chem Commun 48:9421–9423. https://doi.org/10.1039/c2cc34115h

29. Wang Y, Vaidyanathan R, Shiddiky MJA, Trau M (2015) Enabling rapid and specific surface-enhanced Raman scattering immunoassay using Nanoscaled surface shear forces. ACS Nano 9:6354–6362. https://doi.org/10.1021/acsnano.5b01929

30. Quinn ZA, Baranov VI, Tanner SD, Wrana JL (2002) Simultaneous determination of proteins using an element-tagged immunoassay coupled with ICP-MS detection. J Anal At Spectrom 17:892–896. https://doi.org/10.1039/b202306g

31. Cao Y, Mo G, Feng J, He X, Tang L, Yu C, Deng B (2018) Based on ZnSe quantum dots labeling and single particle mode ICP-MS coupled with sandwich magnetic immunoassay for the detection of carcinoembryonic antigen in human serum. Anal Chim Acta 1028:22–31. https://doi.org/10.1016/j.aca.2018.04.039

✪ Springer

32. Careri M, Elviri L, Mangia A, Mucchino C (2007) ICP-MS as a novel detection system for quantitative element-tagged immunoassay of hidden peanut allergens in foods. Anal Bioanal Chem 387: 1851–1854. https://doi.org/10.1007/s00216-006-1091-0

33. Ko JA, Lim HB (2016) Metal-doped inorganic nanoparticles for multiplex detection of biomarkers by a sandwich-type ICP-MS immunoassay. Anal Chim Acta 938:1–6. https://doi.org/10.1016/j.aca.2016.07.035

34. Zhang W, Jiang L, Piper JA, Wang Y (2018) SERS Nanotags and their applications in biosensing and bioimaging. J Anal Test 2:26–44. https://doi.org/10.1007/s41664-018-0053-9

Publisher's note Springer Nature remains neutral with regard to jurisdictional claims in published maps and institutional affiliations.

Paper XXII

Laser-Induced Breakdown Spectroscopy as a Readout Method for Immunocytochemistry with Upconversion Nanoparticles

Pořízka, P.; Vytisková, K.; Obořilová, R.; Pastucha, M.; Gábriš, I.; Brandmeier, J. C.; Modlitbová, P.; Gorris, H. H.; Novotný, K.; Skládal, P.; Kaiser, J.; Farka, Z.

Contribution:

Design of experiments, bioconjugation and characterization of UCNPs, development and optimization of ICC assay, data evaluation, manuscript writing

ORIGINAL PAPER

Laser-induced breakdown spectroscopy as a readout method for immunocytochemistry with upconversion nanoparticles

Pavel Pořízka[1] · Karolína Vytisková[2] · Radka Obořilová[3] · Matěj Pastucha[3,4] · Ivo Gábriš[2] · Julian C. Brandmeier[5] · Pavlína Modlitbová[1] · Hans H. Gorris[5] · Karel Novotný[2] ⬤ · Petr Skládal[3,4] · Jozef Kaiser[1] · Zdeněk Farka[3,4]

Abstract

Immunohistochemistry (IHC) and immunocytochemistry (ICC) are widely used to identify cancerous cells within tissues and cell cultures. Even though the optical microscopy evaluation is considered the gold standard, the limited range of useful labels and narrow multiplexing capabilities create an imminent need for alternative readout techniques. Laser-induced breakdown spectroscopy (LIBS) enables large-scale multi-elemental analysis of the surface of biological samples, e.g., thin section or cell pellet. It is, therefore, a potential alternative for IHC and ICC readout of various labels or tags (Tag-LIBS approach). Here, we introduce Tag-LIBS as a method for the specific determination of HER2 biomarker. The cell pellets were labeled with streptavidin-conjugated upconversion nanoparticles (UCNP) through a primary anti-HER2 antibody and a biotinylated secondary antibody. The LIBS scanning enabled detecting the characteristic elemental signature of yttrium as a principal constituent of UCNP, thus indirectly providing a reliable way to differentiate between HER2-positive BT-474 cells and HER2-negative MDA-MB-231 cells. The comparison of results with upconversion optical microscopy and luminescence intensity scanning confirmed that LIBS is a promising alternative for the IHC and ICC readout.

Keywords Immunocytochemistry · Immunohistochemistry · Laser-induced breakdown spectroscopy · Tag-LIBS · Photon-upconversion nanoparticles

Introduction

The specific detection and imaging of biomarkers within cancerous tissues are crucial for early diagnosis and treatment. Traditionally, immunochemical methods combine the specificity of antibodies with various detection schemes [1]. In the most common approaches, antibodies immobilized in microtiter plates are used to capture the molecule of interest, followed by the detection step utilizing labels based on antibodies conjugated with either enzymes (enzyme-linked immunosorbent assay, ELISA) or fluorophores (fluorescence immunoassay, FIA) [2]. The same labels can also be employed for specific detection of target markers within tissue samples (immunohistochemistry, IHC) and cultured cells (immunocytochemistry, ICC) [3]. However, traditional labels suffer from several disadvantages; enzymes have high production costs, limited stability, and a time-consuming signal development [4], while fluorophores are prone to photobleaching and interference from autofluorescence [2].

In recent years, various kinds of nanomaterials have been used to overcome the properties of conventional labels in immunoassays and cell labeling, leading to enhanced detection capabilities [5, 6]. Typically, two basic schemes are implemented: either (i) catalytic nanoparticles (nanozymes), which allow a detection based on substrate conversion [4, 7], or (ii) luminescent nanoparticles, which allow a direct detection [8]. The most commonly

✉ Karel Novotný
    codl@sci.muni.cz

[1] Central European Institute of Technology, Brno University of Technology, Purkyňova 656/123, 612 00 Brno, Czech Republic

[2] Department of Chemistry, Faculty of Science, Masaryk University, Kamenice 5, 625 00 Brno, Czech Republic

[3] Department of Biochemistry, Faculty of Science, Masaryk University, Kamenice 5, 625 00 Brno, Czech Republic

[4] Central European Institute of Technology, Masaryk University, Kamenice 5, 625 00 Brno, Czech Republic

[5] Institute of Analytical Chemistry, Chemo- and Biosensors, University of Regensburg, Universitätsstraße 31, 93040 Regensburg, Germany

🍁 Springer

used luminescent nanoparticle labels include quantum dots (QD) [9, 10]. However, other alternatives are being investigated, including carbon-based nanoparticles (CD) [11], or lanthanide-based photon-upconversion nanoparticles (UCNP) [12, 13]. We have recently investigated the feasibility of UCNP for the background-free visualization of the HER2 biomarker on the surface of breast cancer cells [14]. The luminescence readout provided a high sensitivity with an unsurpassed signal-to-background ratio (SBR). However, this technique allows detecting only the labels with luminescent properties, limiting the capabilities for multiplexing. Therefore, there is a need for novel readout techniques which would allow a universal detection of non-luminescent labels.

Laser-induced breakdown spectroscopy (LIBS) is an optical emission method complementary to conventionally utilized techniques in bioimaging applications [15]. It offers a fast analysis (reduction of turnaround time from minutes to microseconds per single spectrum acquisition), multi-elemental capability and selectivity, a possibility to detect halogens and light elements, and a reduction of operating and maintenance costs by order of magnitude [16, 17]. All these benefits are provided while satisfactorily conserving the sensitivity. The main advantage of LIBS is the ability of multi-elemental imaging with a fine resolution (units of micrometers) on a large scale (few centimeters) [18].

The analytical performance of LIBS has been beneficially used in many different biological applications. Recently, several reviews described the general scope of bioimaging [15, 19] or direct clinical usage [20]. NPs were used for LIBS signal enhancement of other analytes [21, 22]. For the characterization of NPs, optical catapulting-trapping LIBS was used [23]. Repeatedly, LIBS proved to be a useful readout method for various micro- and nanoparticle-based labels in the so-called tag-LIBS arrangement. Barcoding based on LIBS-encoded polystyrene microsphere was used as a coding method for suspension arrays [24]. Ovarian cancer biomarker CA-125 was detected via titanium dioxide and iron oxide microparticles-conjugated antibodies [25], metallothionein via Cd-based QDs [26], and human serum albumin via streptavidin-coated Ag NP labels [18]. The most recent work focused on the readout of lateral-flow immunoassays with Au NPs labeled *Escherichia coli* [27].

The LIBS technique proved to be a relevant alternative for the readout of immunoassays, appropriately applying all its advantages (multi-element capability and high-throughput). Recently, the emphasis has been given to the implementation of LIBS to immunoassays based on various supports (e.g., glass, plastics). Such experimental arrangement may be extended to the analysis of soft tissues or model cell pellets where proteins of interest are marked with various NPs. Selected NPs can be combined to create so-called barcode labels with a specific target conjugation as well as a characteristic emission response. With this approach, a great variety of micro- and nanoparticle labels is available to open new possibilities in barcoding via multi-elemental readout using LIBS. Recently, the need for new readout methods in bioanalytical chemistry (especially in immunoassay application) is increasing, and LIBS represents a suitable alternative. Several milestones were reached, from the identification of NP-labeled proteins [26] to applications in nanoparticle-based immunoassays [18], including lateral-flow assay [27].

The novelty of this work lies in the specific immunochemical labeling of biomarkers on breast cancer tissues, followed by the LIBS readout. This approach pushes forward the LIBS technology in terms of the specific detection of cancer biomarkers up to the final goal—the development of routine cancer diagnostics for biochemical laboratories. Here, we pioneer the application of LIBS for the readout of nanoparticle-labeled immunocytochemistry sections. UCNP were conjugated with streptavidin (SA) and employed for the specific immunolabeling of the HER2 biomarker on the surface of breast cancer cell lines (Fig. 1a). The LIBS setup was optimized for imaging of the cells, and a data evaluation approach that enabled a reliable readout was introduced (Fig. 1b).

Experimental

Chemicals and reagents

Neridronate (Ner), nitrosyl tetrafluoroborate (NOBF$_4$), copper (II) sulfate pentahydrate, L-ascorbic acid sodium salt, and Tween 20 were purchased from Merck (Germany). Dry
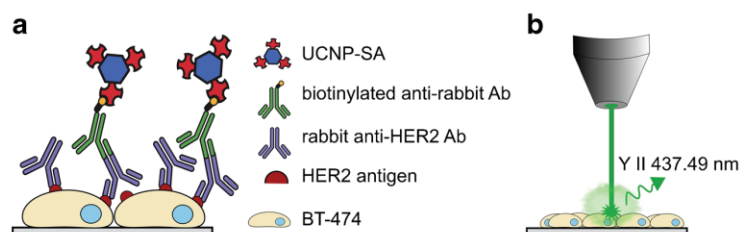

Fig. 1 **a** Scheme of the ICC assay. The primary antibody is used to label the HER2 biomarker on the cell surface, followed by binding of the biotinylated secondary antibody and the UCNP-SA conjugate. **b** Schematic representation of LIBS readout, based on the ablation of material and the detection of Y II 437.49 nm signal

dimethylformamide (DMF) and SuperBlock TBS (SB) were obtained from Thermo Fisher Scientific (USA). Streptavidin-azide was obtained from 7 Bioscience (Germany). α-N-hydroxysuccinimide-ω-alkyne polyethylene glycol (M_W 3 kDa, Alkyne-PEG-NHS) was purchased from Iris Biotech (Germany). All other common chemicals were obtained in the highest quality available from Merck (Germany), Carl Roth (Germany), and Penta (Czech Republic).

Buffers included phosphate buffer (PB; 50 mM NaH_2PO_4/Na_2HPO_4, pH 7.4), phosphate-buffered saline (PBS; PB with 150 mM NaCl), Tris buffered saline (TBS; 50 mM Tris, 150 mM NaCl, pH 7.5), TBS-T buffer (TBS with 0.05% Tween 20), assay buffer (10% SuperBlock in TBS, 1 mM KF, 0.05% Tween 20, and 0.05% NaN_3, pH 7.5), antibody dilution buffer (10% SuperBlock in PBS, 0.05% Tween 20, pH 7.5), 10 mM Tris-HCl (pH 7.5), and epitope retrieval buffer (10 mM Tris, 1 mM EDTA, 0.05% Tween 20, pH 9). The UCNP-SA labels were prepared according to our previous work [14].

Preparation of UCNP-based labels

UCNP-based labels were prepared according to our previous work [28]. The $NaYF_4$:Yb^{3+}, Tm^{3+}-doped UCNP were synthesized by high-temperature co-precipitation [29].

To prepare the Alkyne-PEG-Ner linker, 30 mg of Ner was dissolved under sonication in 128 μL of 1 M NaOH, and 898 μL of PB (pH 7.6) was added. This was followed by the addition of 75 mg Alkyne-PEG-NHS in PB (pH 7.6) and incubation for 3.5 h at room temperature and at 4 °C overnight. The synthesized Alkyne-PEG-Ner linker was dialyzed in a Float-A-Lyzer G2 dialysis device (500–1000 Da MWCO, Fisher Scientific, Germany) against double-distilled water at 4 °C. The linker was then lyophilized using Alpha 1–2 freeze dryer (Christ, Germany) and stored at 4 °C [30].

Oleic acid-capped UCNP (10 mg) dispersed in cyclohexane were mixed with an equivalent volume of dimethylformamide (DMF), followed by the addition of 10 mg of $NOBF_4$. The mixture was shaken at 30 °C for 20 min, during which the oleic acid was removed from the nanoparticle surface, and UCNP transferred from cyclohexane to DMF. The upper cyclohexane phase was discarded, followed by the addition of an excess of chloroform in order to precipitate the UCNP. The purification of UCNP was performed using centrifugation at 1000g for 15 min, followed by a redispersion in DMF, precipitation with chloroform, and another centrifugation step at 1000 g for 15 min. Then, 1 mL of double-distilled water with 2 mg of the Alkyne-PEG-Ner linker was used to redisperse the UCNP pellet, and the mixture was incubated at 4 °C overnight. The alkyne-PEG-Ner-UCNP conjugates were purified by dialysis in a Float-A-Lyzer G2 (100 kDa MWCO, Fisher Scientific) against double-distilled water with 1 mM KF at 4 °C.

For the click reaction, 10 mg of Alkyne-PEG-Ner-UCNPs in 700 μL water was first diluted with 100 μL of 325 mM Tris-HCl (pH 7.5), and 20 μL of 28.6 mg/mL of sodium L-ascorbate in double-distilled water was added. After purging the mixture for 40 min with argon, streptavidin-azide (100 μL of 1 mg/mL solution) was added, followed by purging for another 10 min. The start of the click reaction was catalyzed by the addition of 10 μL of 35.7 mM $CuSO_4$ in double-distilled water, followed by purging with argon for 45 min and sonication for 10 min. The conjugates were purified by dialysis in Float-A-Lyzer G2 (100 kDa MWCO) against Tris-HCl (pH 7.5) with 1 mM KF and 0.05% NaN_3 at 4 °C [12, 14].

Transmission electron microscopy (TEM) revealed a uniform spherical shape with an average diameter of 37 nm. The DLS number distribution of oleic acid-capped UCNP showed the size of 38.5 ± 1.8 nm, which increased to 63 ± 3 nm after the conjugation with streptavidin [28].

Immunochemical labeling of cells

The formalin-fixed paraffin-embedded (FFPE) slides with BT-474 (HER2 3+) and MDA-MB-231 (HER2 0–1+) cells [31] were obtained from AMS Biotechnology (UK). First, xylene (a mixture of isomers) was used to dewax the slides (3× 5 min), followed by the rehydration using 99% ethanol (2× 5 min), 90% ethanol (2× 5 min), and water (5 min). In the next step, the slides were placed in the epitope retrieval buffer (pre-heated to 60 °C) and heated for 20 min to 80 °C using a water bath to perform the heat-induced epitope retrieval. After 20 min of cooling down to room temperature, the slides were transferred to TBS for 2 min, taken out, and dried.

A PAP pen liquid blocker (Science Services, Germany) was used to encircle (~0.5 cm in diameter) the cell section, followed by a washing step in TBS for 1 min. The slide was gently dried; the pellet remained moist. The following steps were performed at room temperature. The solutions were added as 50-μL droplets, and before the incubation with a new reagent, the sample was pre-washed with the reagent applied. First, a blocking using concentrated SuperBlock with 0.05% Tween 20 was done for 60 min, followed by washing with TBS (3× 5 min). Second, the cells were incubated with a rabbit anti-HER2 antibody (ab134182, Abcam, UK) in a concentration of 1 μg/mL in antibody dilution buffer for 60 min. Third, the slides were washed with TBS (3× 5 min), followed by the incubation with 2 μg/mL of a biotinylated anti-rabbit antibody (111-065-144, Jackson ImmunoResearch, UK) in antibody dilution buffer for 60 min. Fourth, the cells were incubated for 60 min with the prepared nanoparticle conjugates (UCNP-SA in varying concentrations) in assay buffer. Finally, the slides were washed with TBS-T buffer (4× 5 min), TBS (5 min), 10 mM Tris (5 min), and dried by compressed

353

air. The prepared samples were then analyzed with LIBS and the luminescence readout [14].

Laser-induced breakdown spectroscopy

The LIBS measurements were performed on a custom-made LIBS Discovery system (CEITEC, Czech Republic) consisting of an ablation chamber, a nanosecond laser (CFR Ultra 400, Quantel by Lumibird, France; Nd:YAG 532 nm, 20 Hz, 10 ns), and a Czerny-Turner spectrometer Shamrock (SR-500i-B2-R, Andor, UK) equipped with a detector iStar sCMOS (iSTAR-sCMOS-18F-E3, Andor, UK). The whole cell pellet was analyzed in a raster of 60×60 spots with a 100 μm step in both directions, one pulse per spot. The setting of the apparatus was as follows: gate width of 50 μs, gate delay of 500 ns, laser pulse energy of 10 mJ, with a purge of argon above the sample surface. The LIBS system was optimized a priori to achieve the best signal-to-noise ratio for the selected emission lines.

The emission line Y II 437.49 nm was chosen based on our previous experiments [32]. The LIBS data was processed using a custom-made C++ software and depicted in the ImageLab (National Institutes of Health, USA) and Origin 2019b (OriginLab, USA). First, each spectrum was internally standardized to the total emissivity to reduce pulse-to-pulse fluctuations. The emission line intensity was estimated as a sum of intensities over the selected wavelength range as done in our former work [18]. No background correction was utilized in the data processing. Consequently, the 2D maps of emission line intensities were created, representing the spatial distribution of Y in the cell pellet.

The data processing strategy was proposed to analytically compare the individual approaches in the sample preparation and intensity response of various label concentrations. LIBS analysis of one single pellet resulted in the map showing Y II 437.49 nm intensity distribution. Then, only spectra from the pellet region were considered; the intensity of Y was estimated for each spectrum (area under the peak) and summed up. Thus, the sample (cell pellet with varied UCNP concentration) was represented by the value of the average Y intensity from the pellet region and was considered as one point in the experiment design. In turn, the averaged Y II intensity value served as a figure of merit for comparing individual measurements. The signal-to-noise ratio (SNR) was estimated for each spectrum in the pilot sample and served for the optimization.

Upconversion microscopy imaging

The UCNP also provided the possibility to monitor their upconversion luminescence (emission of shorter wavelengths under near-IR excitation) as a reference readout technique. A modified wide-field epifluorescence inverted microscope (Eclipse Ti, Nikon, Japan) [33] was used for the visualization of the labeled cells. For the excitation of UCNP, a continuous-wave 980-nm laser diode (4 W; Wavespectrum, China) was coupled to the motorized TIRF illuminator unit (TI-TIRF-E, Nikon) via a multi-mode optical fiber (105 μm fiber core, NA = 0.22, Wavespectrum, China). The used filter set contained a long-pass excitation filter (cut-on 830 nm; Schott, Germany), a short-pass dichroic mirror (cut-on 875 nm; AHF Analysentechnik, Germany), and a NIR band-pass emission filter (809 ± 40 nm). The emission light was collected with a ×20 objective (NA 0.75) and recorded using a Neo 5.5 vacuum-cooled 5.5-megapixel sCMOS camera (Andor, UK), which provided a field of view of 832×702 μm. The software NIS Elements 4.5 Advanced Research (Nikon) was used to control the microscope. The images were evaluated by ImageJ [14].

Luminescence scanning

The upconversion luminescence was scanned using a Chameleon microplate reader (Hidex, Finland) modified for the measurement of upconversion. To obtain the images of the cell pellets, squares of 18×18 points with a step size of 500 μm were raster-scanned with an exposure time of 500 ms. The images were analyzed by ImageJ. The luminescence intensities of individual cell pellets were evaluated by placing circular regions of interest with an identical size over the pellet area, and the gray values of all pixels in the region of interest were averaged. After the quantitative evaluation, a bilinear interpolation was used to increase the resolution of images fivefold, and the resulting images were processed using Origin 2019b [34].

Results and discussion

Characteristic spectra

In conventional immunochemical methods, nanoparticles are used as specific labels to improve the detection performance. The application of nanoparticles also opens new perspectives in the readout strategy and implementation of novel techniques, such as LIBS. The presence of metallic nanoparticles within the sample is more favorable for the laser ablation and the consecutive laser-induced plasma formation resulting in a satisfactory analytical sensitivity. Thus, it is not necessary to target the investigated protein but indirectly evaluate its presence in terms of the characteristic NPs signal.

First, the LIBS experiment was optimized to achieve the highest SNR value for the selected analytical line. It was done in a pulse-to-pulse mode, where each spectrum was considered individually; gate delay and laser pulse energy were the only varied parameters. The optimal conditions were found to be 10 mJ per laser pulse and 500 ns gate delay; all settings are listed

354

in Paragraph 2.5. Interestingly, the use of a 532 nm laser pulse led to a significant, undesirable damage to the glass substrate. Thus, lower pulse energy was chosen as a compromise between the glass damage and good analytical sensitivity. Further optimization is beyond the scope of this work when considering other options in the sample treatment (e.g., using other substrates - polystyrene microplate) and/or laser ablation conditions (266 nm laser pulse) and different experimental settings (e.g., ambient atmosphere and its pressure) [26].

The short-band spectra with characteristic spectral lines were detected for each laser pulse (Fig. 2). The spectral line of yttrium, Y II 437.49 nm, was selected based on our experience [32], and used throughout the experiment. The intensity profiles show distinct differences between positive and control samples (BT-474 or MDA-MB-231 cell pellet with 700 μg/mL of UCNP-SA). The intensity profile of a control spectrum reveals also the Y II 437.49 nm spectral line, which is at the detection limit. Its presence suggests a non-specific binding of UCNP for higher concentrations, which is also the case of the depicted spectra, and a further discussion follows in paragraph 3.2. In addition, the spectrum reveals the possibility of simultaneous detection of multiple elements along with yttrium, and the possibility of simultaneous detection of increased concentrations of other elements associated with cancer growth or with the development of other serious diseases [20]. However, this advantageous feature mainly suggests that LIBS has excellent potential in barcodes and multi-element label readout.

Elemental imaging

After a LIBS system optimization, the LIBS mapping raster was set to cover a square 60×60 points (step size 100 μm) with respect to the size of the cell pellets (ca 0.5 cm in
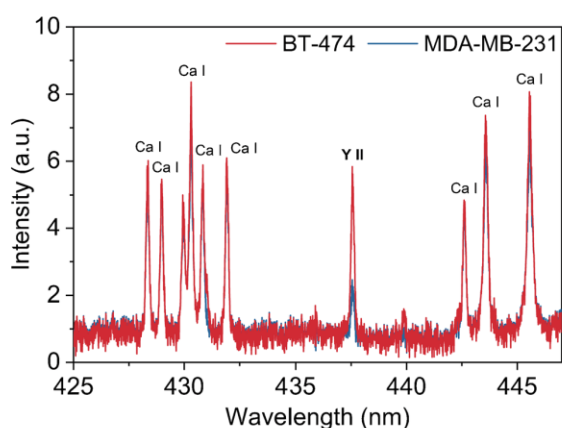

Fig. 2 Characteristic spectra of positive and control samples (BT-474 and MDA-MB-231 cell pellets, respectively) labeled with UCNPs in the concentration of 700 μg/mL, showing distinct intensity values of the Y II 437.49 nm spectral line

diameter), and also to display the immediate surroundings. The center of the scanned area was always set to coincide with the center of a pellet. For the same conditions, the BT-474 pellet was mapped as a HER2-positive representative of breast cancer cell lines, and MDA-MB-231 was selected as a HER2-negative control.

Figure 3a shows the spatial distribution of yttrium-based UCNP in the cell pellets represented by the Y II 437.49 nm emission line intensity with varying UCNP-SA label concentrations. LIBS enabled to specifically map the presence of UCNP, showing an evident difference between the positive and negative samples. However, several undesirable effects were observed, as well. The isolated spikes on the maps, especially for higher label concentrations, probably indicate larger clusters of non-specifically bound nanoparticles [35]. Moreover, the signal tailing on the maps represented by high intensities appears at the top of the pellet map. It should be noted that the mapping was realized by consecutive laser pulses with a bottom-up direction. Lower intensity on the bottom of the pellet and its upward increase are most probably attributed to the redeposition of the ablated material. The redeposition phenomenon has already been observed [32] and is particularly limiting in terms of using the method for mapping the structures of cancerous tissues with an appropriate spatial resolution. As a zigzag-programmed sample motion was used, the signal shifting on every other line was also apparent.

The quantitative evaluation of the obtained intensity maps was based on the integration of yttrium intensities over the cell pellet region (Fig. 3b). This approach allows obtaining one representative value, which can be used for further processing. First of all, the area of the map should be carefully selected (in this case manually) because the pellet area and its position slightly change for each sample. For this purpose, not only maps themselves but also images of the sample before ablation were obtained.

The background signals in the case of the control sample can be considered as the sum of two contributions. The first one might be attributed to the continuum background of LIBS emission spectra which is always present. The background in each LIBS spectrum was not corrected during the evaluation; thus, Y II intensities were considered with a certain background. The second contribution might be attributed to the non-specific adsorption of UCNP on the sample controlled by an adsorption isotherm that could be derived from the slope of the control sample line. Furthermore, the dissolution of UCNP [36] can lead to a release of free Y^{3+} ions, which can non-specifically adsorb to the cells.

Thus, the diminishing of background signals is possible in two ways. Appropriate background subtraction and internal standardization to total emissivity can be used to minimize the LIBS optical background. The non-specific adsorption of the label can be reduced by optimizing the UCNP surface modification and modifying the labeling procedure to

Fig. 3 a 2D LIBS maps of BT-474 and MDA-MB-231 cell pellets with HER2 marker labeled using the UCNP-SA conjugate with concentrations from 7 to 700 μg/mL; the raster size is 100 μm. **b** Dependence of Y II 437.49 nm signal on the UCNP concentration. The error bars correspond to the standard deviations of intensities within the cell pellet region. **c** Signal-to-background ratio evaluated by dividing the BT-474 and MDA-MB-231 cell pellet signals
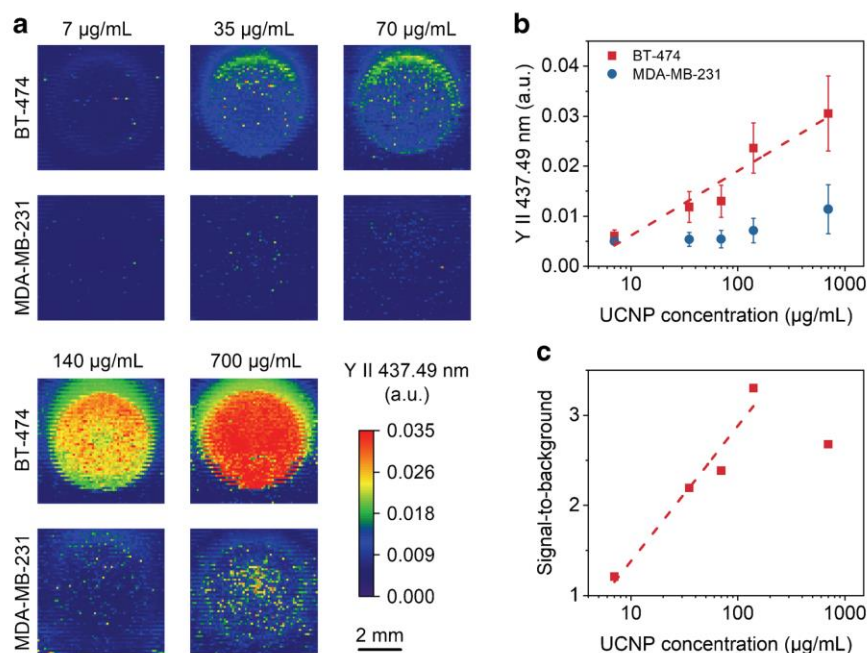
facilitate the removal of non-specifically bound UCNP. Both approaches deserve further investigation and will be the subject of our following experiments.

Overall, an increasing UCNP-SA concentration leads to the increasing signals for the HER2-positive cell line (BT-474) and only a small increase for the negative control (MDA-MB-231). The typical opening scissors shape graph for positive and control samples indicates a more sensitive detection for higher concentrations. The UCNP-SA concentration of 7 μg/mL is near the detection limit of the LIBS system, providing a barely visible signal change and a SBR (Fig. 3c) of 1.2. Increasing the label concentration up to 140 μg/mL led to the increase of the specific signal while keeping the low level of control, reaching a SBR of 3.3. However, further increasing the UCNP-SA concentration to 700 μg/mL was associated

with an increase of the negative control signal, which led to a decrease of SBR to 2.7. This can be explained by the progressive saturation of the specific binding sites on the BT-474 cell line. On the other hand, the number of potential sites for non-specific binding is in excess, making the label concentration the most important factor affecting the SBR.

Finally, the four independent HER2-positive cell pellets were labeled using UCNP-SA conjugates in a concentration of 70 μg/mL to study the repeatability of the measurement (Fig. 4). All the samples provided similar results, showing the higher intensities on the edge of the pellet, which might be connected with the drying of the sample ("coffee ring" effect). Moreover, the rise in the intensity on the top of the map and beyond the pellet region may be attributed to the redeposition of the ablated matter. The variability of

Fig. 4 a 2D LIBS maps of BT-474 cell pellets labeled with UCNP-SA conjugate in a concentration of 70 μg/mL. **b** Average intensities within each of spots 1–4 (error bars correspond to the standard deviations of intensities within spots; marked in red) and the total average of the four mean values obtained from spots 1–4 (error bar corresponds to the standard deviation among the individual averages; marked in blue)
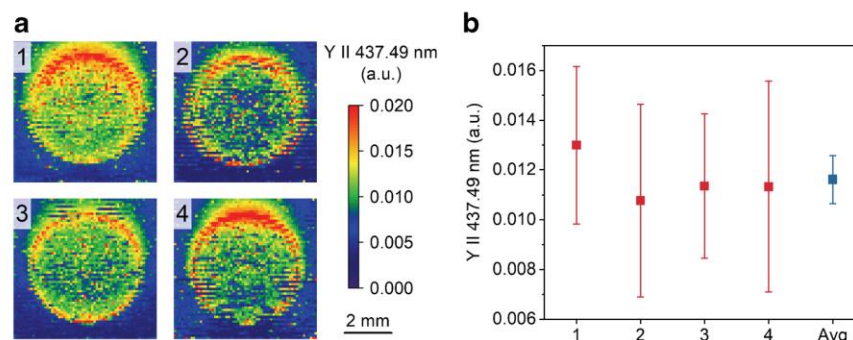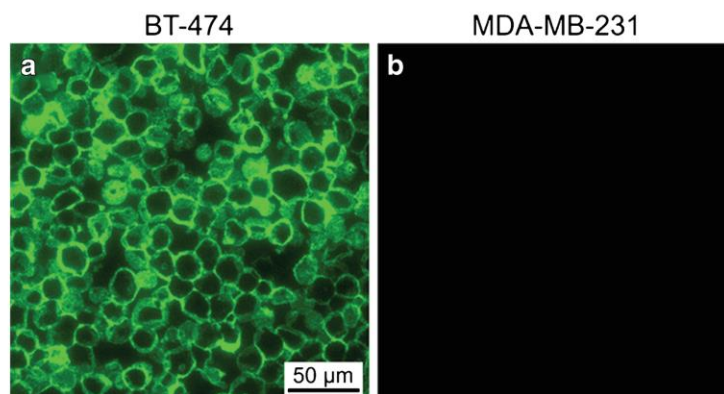
Fig. 5 Wide-field upconversion microscopy images of (**a**) BT-474 and (**b**) MDA-MB-231 FFPE cell pellets after labeling of HER2 biomarker using specific antibodies and UCNP-SA conjugate

intensities within one spot was comparable among the samples; the overall relative standard deviation among the spots was 8% (Fig. 4b).

Comparison with reference techniques

To incorporate the LIBS method in the context of conventional techniques, the same ICC slides were analyzed by upconversion microscopy and luminescence scanning prior to the LIBS measurement. Optical microscopy is traditionally used as a gold standard for the evaluation of the ICC and IHC. We have recently introduced the application of UCNP-based labels in this field. The microscopy images after labeling the BT-474 and MDA-MB-231 cells using UCNP-SA conjugate in the concentration of 700 µg/mL are shown in Fig. 5. Specific labeling of HER2 on the cell membranes was visible on the positive sample of BT-474, whereas practically no signal was observed on the negative control of MDA-MB-231.

The main advantage of microscopy compared to scanning-based approaches is the high resolution, allowing to follow the distribution of the target within the cellular structures. On the other hand, conventional optical microscopy is not optimal for the quantitative determination of the label amount within the whole spot of cells.

Next, LIBS was compared to upconversion luminescence scanning (Fig. 6). Both methods were successful in showing the difference between the HER2-positive and HER2-negative samples. LIBS provides a higher resolution (step size of 100 µm) compared to upconversion scanning (step size of 500 µm); however, it should be noted that both methods might be able to reach a rather high resolution after further optimizations. The LIBS provided a SBR of 5, whereas upconversion scanning reached a SBR of 159. Since the actual amount of UCNP label is the same in both scans, the lower SBR of LIBS is probably caused by a lower readout sensitivity. In comparison with luminescence-based methods, LIBS is
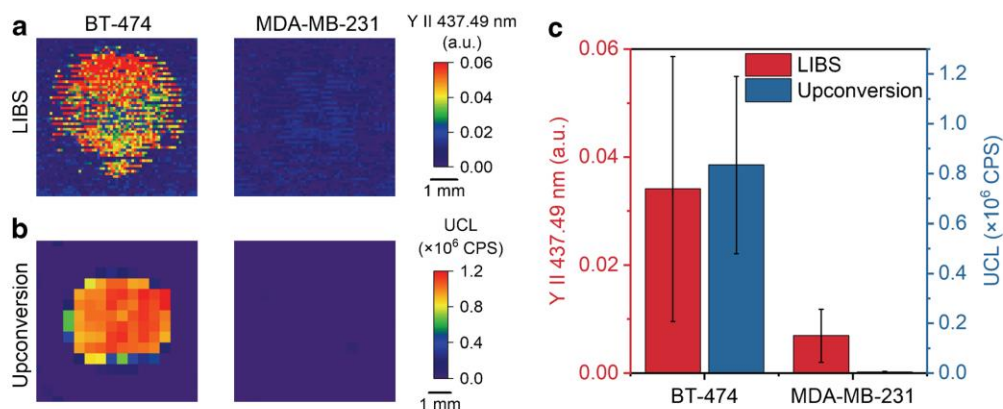

Fig. 6 Comparison of (**a**) LIBS and (**b**) upconversion scanning of BT-474 and MDA-MB-231 cells with HER2 biomarker labeled with UCNP-SA conjugate, using the same scanning area sizes. **c** The average intensities evaluated by the two methods. Error bars correspond to the standard deviation of intensities within the cell pellet

⚙ Springer

357

not limited to labels with luminescent properties, which is an advantage that needs to be highlighted because it opens up possibilities for multiplexing.

Laser ablation inductively coupled plasma mass spectrometry (LA-ICP-MS) method is another widely used laser ablation-based method for the imaging of biomolecules in tissues by using diverse labels. During the last decade, it became a recognizable tool in the identification and localization of various biomarkers by NP-labelling directly in tissue samples, in cultured cells, or even in single-cells [37]. LA-ICP-MS enables the elemental and isotopic determination of metals/metalloids in solid samples with a micrometer spatial resolution (down to 1 μm) at trace levels (achievable sensitivity down to picomoles) [38]. The widespread use of NP-based labels for specific-recognition reactions for the determination of biomolecules by LA-ICP-MS is summarized in the recent review [39]. Compared to LIBS, LA-ICP-MS is very instrumentation-demanding method with high operation and acquisition costs, without the possibility of construction of cheap, simple, and compact tabletop instruments. The technique also has other limitations, and its employing for straightforward, fast, or remote sensing is impossible.

Conclusions

LIBS was introduced as an alternative readout technique for ICC and IHC with upconversion nanoparticle labels. Cell pellets of BT-474 (HER2-positive) and MDA-MB-231 (HER2-negative) were labeled with streptavidin-conjugated UCNPs through primary anti-HER2 antibody and biotinylated secondary antibody.

LIBS enabled a 2D scanning of the sample surface (labeled cell pellets) through the detection of the characteristic signal of the Y II 437.49 nm emission line. This approach allowed indirect imaging of the cell pellets with a resolution of 100 μm. Other elements were detected along with the yttrium signal, which shows the multi-elemental feature of LIBS and outlines its further multiplexing and barcoding capabilities. We have shown that after an appropriate optimization, the LIBS analysis is stable and reproducible. Additionally, we have introduced a novel algorithm for LIBS data processing that provides a platform for the evaluation of 2D scans of biological samples. The results showed a desired LIBS sensitivity to the yttrium signal and specificity of UCNP-SA, clearly demonstrating the difference between the HER2-positive and negative cells in ICC readout. The increasing UCNP-SA concentration led to an increase in the specific binding with a small effect on the negative control, resulting in an optimal SBR at a concentration of 140 μg/mL. Finally, the LIBS results were supported by the upconversion optical microscopy and upconversion luminescence scanning.

Despite the success of our feasibility study, further improvements in terms of lateral resolution and analytical sensitivity are necessary in order to meet the needs of IHC and ICC readouts. In our future work, we want to focus on enhancing the scanning resolution while altering the LIBS experimental apparatus and applying different nanoparticle labels (including multi-metal alloys) to test the feasibility of multiplexing through multi-elemental detection.

Compliance with ethical standards

Conflict of interest The authors declare that they have no conflict of interest.

References

1. Luppa PB, Sokoll LJ, Chan DW (2001) Immunosensors - principles and applications to clinical chemistry. Clin Chim Acta 314(1–2):1–26. https://doi.org/10.1016/s0009-8981(01)00629-5

2. Farka Z, Mickert MJ, Pastucha M, Mikusova Z, Skladal P, Gorris HH (2020) Advances in optical single-molecule detection: en route to supersensitive bioaffinity assays. Angew Chem Int Edit 59(27): 10746–10773. https://doi.org/10.1002/anie.201913924

3. Susaki EA, Ueda HR (2016) Whole-body and whole-organ clearing and imaging techniques with single-cell resolution: toward organism-level systems biology in mammals. Cell Chem Biol 23(1):137–157. https://doi.org/10.1016/j.chembiol.2015.11.009

4. Wang QQ, Wei H, Zhang ZQ, Wang EK, Dong SJ (2018) Nanozyme: an emerging alternative to natural enzyme for biosensing and immunoassay. Trac Trends Anal Chem 105:218–224. https://doi.org/10.1016/j.trac.2018.05.012

5. Yezhelyev MV, Gao X, Xing Y, Al-Hajj A, Nie SM, O'Regan RM (2006) Emerging use of nanoparticles in diagnosis and treatment of breast cancer. Lancet Oncol 7(8):657–667. https://doi.org/10.1016/s1470-2045(06)70793-8

6. Farka Z, Juriik T, Kovaar D, Trnkova L, Sklaadal P (2017) Nanoparticle-based immunochemical biosensors and assays: recent advances and challenges. Chem Rev 117(15):9973–10042. https://doi.org/10.1021/acs.chemrev.7b00037

7. Dong JL, Song LN, Yin JJ, He WW, Wu YH, Gu N, Zhang Y (2014) Co3O4 nanoparticles with multi-enzyme activities and their

application in immunohistochemical assay. ACS Appl Mater Interfaces 6(3):1959–1970. https://doi.org/10.1021/am405009f

8. Seydack M (2005) Nanoparticle labels in immunosensing using optical detection methods. Biosens Bioelectron 20(12):2454–2469. https://doi.org/10.1016/j.bios.2004.11.003

9. Zhou L, Yan J, Tong L, Han X, Wu X, Guo P (2016) Quantum dot-based immunohistochemistry for pathological applications. Cancer Transl Med 2(1):21–28. https://doi.org/10.4103/2395-3977.177562

10. Wu Y-T, Qiu X, Lindbo S, Susumu K, Medintz IL, Hober S, Hildebrandt N (2018) Quantum dot-based FRET immunoassay for HER2 using Ultrasmall affinity proteins. Small 14:1802266. https://doi.org/10.1002/smll.201802266

11. Tang DP, Lin YX, Zhou Q (2018) Carbon dots prepared from Litchi chinensis and modified with manganese dioxide nanosheets for use in a competitive fluorometric immunoassay for aflatoxin B-1. Microchim Acta 185(10):476. https://doi.org/10.1007/s00604-018-3012-2

12. Mickert MJ, Farka Z, Kostiv U, Hlavacek A, Horak D, Skladal P, Gorris HH (2019) Measurement of sub-femtomolar concentrations of prostate-specific antigen through single-molecule counting with an upconversion-linked immunosorbent assay. Anal Chem 91(15): 9435–9441. https://doi.org/10.1021/acs.analchem.9b02872

13. He H, Howard CB, Chen YH, Wen SH, Lin GG, Zhou JJ, Thurecht KJ, Jin DY (2018) Bispecific antibody-functionalized upconversion nanoprobe. Anal Chem 90(5):3024–3029. https://doi.org/10.1021/acs.analchem.7b05341

14. Farka Z, Mickert MJ, Mikusova Z, Hlavacek A, Bouchalova P, Xu WS, Bouchal P, Skladal P, Gorris HH (2020) Surface design of photon-upconversion nanoparticles for high-contrast immunocytochemistry. Nanoscale 12(15):8303–8313. https://doi.org/10.1039/c9nr10568a

15. Modlitbova P, Porizka P, Kaiser J (2020) Laser-induced breakdown spectroscopy as a promising tool in the elemental bioimaging of plant tissues. Trac Trends Anal Chem 122:10. https://doi.org/10.1016/j.trac.2019.115729

16. Hahn DW, Omenetto N (2012) Laser-induced breakdown spectroscopy (LIBS), part II: review of instrumental and methodological approaches to material analysis and applications to different fields. Appl Spectrosc 66(4):347–419. https://doi.org/10.1366/11-06574

17. El Haddad J, Canioni L, Bousquet B (2014) Good practices in LIBS analysis: review and advices. Spectrochim Acta B At Spectrosc 101:171–182. https://doi.org/10.1016/j.sab.2014.08.039

18. Modlitbova P, Farka Z, Pastucha M, Porizka P, Novotny K, Skladal P, Kaiser J (2019) Laser-induced breakdown spectroscopy as a novel readout method for nanoparticle-based immunoassays. Microchim Acta 186(9):10. https://doi.org/10.1007/s00604-019-3742-9

19. Busser B, Moncayo S, Coll JL, Sancey L, Motto-Ros V (2018) Elemental imaging using laser-induced breakdown spectroscopy: a new and promising approach for biological and medical applications. Coord Chem Rev 358:70–79. https://doi.org/10.1016/j.ccr.2017.12.006

20. Gaudiuso R, Melikechi N, Abdel-Salam ZA, Harith MA, Palleschi V, Motto-Ros V, Busser B (2019) Laser-induced breakdown spectroscopy for human and animal health: a review. Spectrochim Acta B At Spectrosc 152:123–148. https://doi.org/10.1016/j.sab.2018.11.006

21. Dell'Aglio M, Alrifai R, Giacomo A (2018) Nanoparticle enhanced laser induced breakdown spectroscopy (NELIBS), a first review. Spectrochim Acta B At Spectrosc 148:105–112. https://doi.org/10.1016/j.sab.2018.06.008

22. Zhao X, Zhao C, Du X (2019) Detecting and mapping harmful chemicals in fruit and vegetables using nanoparticle-enhanced laser-induced breakdown spectroscopy. Sci Rep 9:906. https://doi.org/10.1038/s41598-018-37556-w

23. Fortes FJ, Fernandez-Bravo A, Laserna JJ (2014) Chemical characterization of single micro- and nano-particles by optical catapulting-optical trapping-laser-induced breakdown spectroscopy. Spectrochim Acta B At Spectrosc 100:78–85. https://doi.org/10.1016/j.sab.2014.08.023

24. He Q, Liu Y, He Y (2016) Digital barcodes of suspension array using laser induced breakdown spectroscopy. Sci Rep 6:36511. https://doi.org/10.1038/srep36511

25. Markushin Y, Sivakumar P, Connolly D, Melikechi N (2015) Tag-femtosecond laser-induced breakdown spectroscopy for the sensitive detection of cancer antigen 125 in blood plasma. Anal Bioanal Chem 407(7):1849–1855. https://doi.org/10.1007/s00216-014-8433-0

26. Konecna M, Novotny K, Krizkova S, Blazkova I, Kopel P, Kaiser J, Hodek P, Kizek R, Adam V (2014) Identification of quantum dots labeled metallothionein by fast scanning laser-induced breakdown spectroscopy. Spectrochim Acta B At Spectrosc 101:220–225. https://doi.org/10.1016/j.sab.2014.08.037

27. Gondhalekar C, Biela E, Rajwa B, Bae E, Patsekin V, Sturgis J, Reynolds C, Doh IJ, Diwakar P, Stanker L, Zorba V, Mao XL, Russo R, Robinson JP (2020) Detection of E. coli labeled with metal-conjugated antibodies using lateral-flow assay and laser-induced breakdown spectroscopy. Anal Bioanal Chem 412(6): 1291–1301. https://doi.org/10.1007/s00216-019-02347-3

28. Peltomaa R, Farka Z, Mickert MJ, Brandmeier JC, Pastucha M, Hlaváček A, Martínez-Orts M, Canales Á, Skládal P, Benito-Peña E, Moreno-Bondi MC, Gorris HH (2020) Competitive upconversion-linked immunoassay using peptide mimetics for the detection of the mycotoxin zearalenone. Biosens Bioelectron 170: 112683. https://doi.org/10.1016/j.bios.2020.112683

29. Wang F, Han Y, Lim CS, Lu YH, Wang J, Xu J, Chen HY, Zhang C, Hong MH, Liu XG (2010) Simultaneous phase and size control of upconversion nanocrystals through lanthanide doping. Nature 463(7284):1061–1065. https://doi.org/10.1038/nature08777

30. Kostiv U, Lobaz V, Kucka J, Svec P, Sedlacek O, Hruby M, Janouskova O, Francova P, Kolarova V, Sefc L, Horak D (2017) A simple neridronate-based surface coating strategy for upconversion nanoparticles: highly colloidally stable I-125-radiolabeled NaYF4:Yb3+/Er3+@PEG nanoparticles for multi-modal in vivo tissue imaging. Nanoscale 9(43):16680–16688. https://doi.org/10.1039/c7nr05456d

31. Subik K, Lee J-F, Baxter L, Strzepek T, Costello D, Crowley P, Xing L, Hung M-C, Bonfiglio T, Hicks D, Ping T (2010) The expression patterns of ER, PR, HER2, CK5/6, EGFR, Ki-67 and AR by immunohistochemical analysis in breast cancer cell lines. Breast Cancer 4:35–41. https://doi.org/10.1177/117822341000400004

32. Modlitbova P, Hlavacek A, Svestkova T, Porizka P, Simonikova L, Novotny K, Kaiser J (2019) The effects of photon-upconversion nanoparticles on the growth of radish and duckweed: bioaccumulation, imaging, and spectroscopic studies. Chemosphere 225:723–734. https://doi.org/10.1016/j.chemosphere.2019.03.074

33. Farka Z, Mickert MJ, Hlavacek A, Skladal P, Gorris HH (2017) Single molecule upconversion-linked immunosorbent assay with extended dynamic range for the sensitive detection of diagnostic biomarkers. Anal Chem 89(21):11825–11830. https://doi.org/10.1021/acs.analchem.7b03542

34. Hlavacek A, Farka Z, Hubner M, Hornakova V, Nemecek D, Niessner R, Skladal P, Knopp D, Gorris HH (2016) Competitive upconversion-linked immunosorbent assay for the sensitive detection of diclofenac. Anal Chem 88(11):6011–6017. https://doi.org/10.1021/acs.analchem.6b01083

35. Skarkova P, Novotny K, Lubal P, Jebava A, Porizka P, Klus J, Farka Z, Hrdlicka A, Kaiser J (2017) 2d distribution mapping of quantum dots injected onto filtration paper by laser-induced

breakdown spectroscopy. Spectrochim Acta B At Spectrosc 131: 107–114. https://doi.org/10.1016/j.sab.2017.03.016

36. Dukhno O, Przybilla F, Muhr V, Buchner M, Hirsch T, Mely Y (2018) Time-dependent luminescence loss for individual upconversion nanoparticles upon dilution in aqueous solution. Nanoscale 10(34):15904–15910. https://doi.org/10.1039/c8nr03892a

37. Cid-Barrio L, Calderon-Celis F, Abasolo-Linares P, Fernandez-Sanchez ML, Costa-Fernandez JM, Encinar JR, Sanz-Meder A (2018) Advances in absolute protein quantification and quantitative protein mapping using ICP-MS. Trac Trends Anal Chem 104:148–159. https://doi.org/10.1016/j.trac.2017.09.024

38. Malile B, Brkic J, Bouzekri A, Wilson DJ, Ornatsky O, Peng C, Chen JIL (2019) DNA-conjugated gold nanoparticles as high-mass probes in imaging mass cytometry. ACS Appl Bio Mater 2(10): 4316–4323. https://doi.org/10.1021/acsabm.9b00574

39. Lores-Padin A, Menero-Valdes P, Fernandez B, Pereiro R (2020) Nanoparticles as labels of specific-recognition reactions for the determination of biomolecules by inductively coupled plasma-mass spectrometry. Anal Chim Acta 1128:251–268. https://doi.org/10.1016/j.aca.2020.07.008